

THE UNIVERSITY OF CHICAGO

HARNESSING THE POWER OF PALLADIUM/NORBORNENE COOPERATIVE
CATALYSIS FOR THE MODULAR SYNTHESIS OF ORGANIC MATERIALS

A DISSERTATION SUBMITTED TO
THE FACULTY OF THE DIVISION OF THE PHYSICAL SCIENCES
IN CANDIDACY FOR THE DEGREE OF
DOCTOR OF PHILOSOPHY

DEPARTMENT OF CHEMISTRY

BY

SHINYOUNG CHOI

CHICAGO, ILLINOIS

AUGUST 2024

Copyrights © 2024 by Shinyoung Choi

All rights reserved

To mom, dad, and my fiancé, Jin Sung.

Thank you for your love and unconditional support.

This would not have been possible without you.

TABLE OF CONTENTS

LIST OF SCHEMES.....	vii
LIST OF FIGURES	viii
LIST OF TABLES.....	x
LIST OF ABBREVIATIONS.....	xi
ACKNOWLEDGEMENT	xx
PREFACE.....	xxii
Chapter 1: Rapid and Modular Access to Multifunctionalized 1,2-Azaborines via Palladium/Norbornene Cooperative Catalysis	
1.1 Introduction.....	1
1.2 Results and Discussion.....	4
1.3 Conclusion.....	12
1.4 General Information	12
1.5 Experimental Procedure and Data.....	13
1.6 NMR Spectra.....	86
1.7 References	189
Chapter 2: Modular Synthetic Platform for Interior-Functionalized Dendritic Macromolecules Enabled by the Palladium/Norbornene Catalysis	
2.1 Introduction.....	197

2.2 Results and Discussion.....	199
2.3 Conclusion.....	212
2.4 General Information	213
2.5 Experimental Procedure and Data.....	214
2.6 Absolute Fluorescence Quantum Yield Measurements of AIE Compounds.....	298
2.7 NMR Spectra.....	299
2.8 MALDI-TOF Data	376
2.9 References	384
 Chapter 3: Studies Towards the Bottom-Up Solution-Phase Synthesis of Water/Alcohol Soluble N=5 Armchair Graphene Nanoribbons by the Palladium/Norbornene Catalysis	
3.1 Introduction	388
3.2 Challenges in the Solution-Phase Synthesis of N=5 AGNRs	390
3.3 Results and Discussion.....	393
3.4 Conclusion.....	404
3.5 Characterization Data	405
3.6 NMR Spectra.....	410
3.7 References	417
 Chapter 4: A Review on the Graphene-Based Nanomaterials for Biomedical Applications	
4.1 Introduction	422
4.2 Antimicrobial Activity	425

4.2.1 Physical Damage	425
4.2.2 Chemical Damage.....	429
4.2.3 Applications.....	432
4.3 Cancer Therapeutics	433
4.3.1 Drug Delivery	433
4.3.1.1 pH-Responsive Drug Delivery	435
4.3.1.2 ROS-Responsive Drug Delivery	445
4.3.1.3 Redox-Responsive Drug Delivery.....	445
4.3.1.4 Biomolecule-Responsive Drug Delivery.....	448
4.3.1.5 Magnetic Field-Responsive Drug Delivery.....	450
4.3.1.6 Thermal-Responsive Drug Delivery.....	454
4.3.2 Photothermal Therapy	458
4.3.2.1 Selective/Targeted Photothermal Therapy	460
4.3.2.2 Combined Photothermal Therapy.....	463
4.4 Bone Regeneration	466
4.4.1 Calcium Based Scaffolds.....	468
4.4.2 Natural Polymer Based Scaffolds.....	473
4.4.3 Synthetic Polymer Based Scaffolds.....	475
4.5 Summary and Outlook	478
4.6 References	494

LIST OF SCHEMES

Scheme 1.1 Synthesis and functionalization of 1,2-azaborines	3
Scheme 1.2 Synthetic elaborations.....	10
Scheme 2.1 Pd/NBE-catalyzed generation growth of interior-functionalized dendrons	200
Scheme 2.2 Synthetic pathways to access three prototypes of multifunctional dendrons	207
Scheme 3.1 Structure of the proposed N=5 AGNR bearing piperazine side chains	389
Scheme 3.2 Acid-catalyzed rearrangement of naphthalene derivatives.....	391
Scheme 3.3 Reported solution-phase syntheses of N=5 AGNRs.....	392
Scheme 3.4 Synthetic routes toward G1 and G2	394
Scheme 3.5 Control experiment excluding 1,2-rearrangement under our reaction condition	389
Scheme 3.6 Selected examples of model substrates for the cyclodehydrogenation reaction.....	401
Scheme 3.7 Synthetic route towards G3	402

LIST OF FIGURES

Figure 1.1 Isosteres of benzene.....	1
Figure 2.1 Synthetic strategies for the interior-layer functionalization of dendrons	199
Figure 2.2 Structure-property relationship study of the AIE effect of 2 nd -generation dendrons	210
Figure 2.3 UV-Vis spectra of AIE compounds.....	211
Figure 3.1 Raman spectroscopy data of G1 and G2	395
Figure 3.2 MALDI-TOF spectra of P1 and P2	397
Figure 3.3 MALDI-TOF spectra of G2 and G2	398
Figure 3.4 IR spectra of P1 and G1	399
Figure 3.5 IR spectra of P2 , G2 , and salt form of G2	400
Figure 3.6 MALDI-TOF spectra of G3	403
Figure 3.7 Raman spectra of G3	403
Figure 3.8 UV-vis-NIR spectra of G3	404
Figure 4.1 Schematic illustration of a) Top-down and bottom-up synthesis of graphene derivatives. b) Biomedical applications of graphene-based materials and their physicochemical properties	424
Figure 4.2 Antibacterial activity and cytotoxicity of rGO nanosheets	426
Figure 4.3 Schematic circuitry to illustrate the proposed mechanism	431
Figure 4.4 Chemical structures of GO and DOX.....	435
Figure 4.5 Neutrophil degradation of GO and GO/LMP monitored by Raman spectroscopy ...	439
Figure 4.6 Three different toxicity models for testing MSC-GO-Drug.....	443

Figure 4.7 SEM images of nanofibers	444
Figure 4.8 Schematic diagram of redox-sensitive NGO-SS-mPEG-DXR showing antitumor activity.....	446
Figure 4.9 GSH-responsive drug release profile at pH 7.4 and 5.3	447
Figure 4.10 A schematic illustration of ATP-responsive delivery system	449
Figure 4.11 Schematic representation of GO loaded with Fe ₃ O ₄ nanoparticles and DOX.....	451
Figure 4.12 A thermal-responsive release of GO-PVP-NIPAM-lysine hybrid system	455
Figure 4.13 UV-vis absorption of nano-GO and nano-rGO	461
Figure 4.14 Relative cell viability of EMT6 cells 24 h after treatment	464
Figure 4.15 Structure and synthesis of berberine derivative.....	466
Figure 4.16 Schematic illustration depicting chemo-PTT using rGO/carbon/mesoporous silica nanocookie under NIR irradiation	468
Figure 4.17 The observation of tumor-bearing BALB/c mice on days 0 to 14	470
Figure 4.18 <i>In vivo</i> treatment against mice bearing HeLa tumor.....	472
Figure 4.19 Illustration of a simplified bone structure.....	479

LIST OF TABLES

Table 1.1 Selected control experiments	5
Table 1.2 Substrate scope.....	8
Table 1.3 Less successful examples.....	11
Table 2.1 Selected optimization of the model study	202
Table 2.2 Reaction scope of various electrophiles and nucleophiles.....	203
Table 2.3 Gelation behavior in toluene	207
Table 4.1 A summary of graphene based nanocarriers for drug delivery applications.....	455
Table 4.2 A summary of graphene based nanocarriers for photothermal therapy applications..	475
Table 4.3 A summary of graphene based bone regeneration systems	489

LIST OF ABBREVIATIONS

Ac- β -CD	Acrylated β -cyclodextrin
ADSC	Adipose-derived stem cell
ADH	Adipic acid dihydrazide
AFM	Atomic force microscopy
AGNR	Armchair graphene nanoribbon
AgNP	Silver nanoparticles
AIE	Aggregation induced emission
Apt	Aptamer
Arg	Arginine
ATP	Adenosine-5'-triphosphate
AuNP	Gold nanoparticle
BARF	Tetrakis(3,5-bis(trifluoromethyl)phenyl)borate
BCP	Biphasic calcium phosphate
BMSC	Bone mesenchymal stem cell
Boc	<i>Tert</i> -butyloxycarbonyl
BPEI	Branched polyethyleneimine
B ₂ pin ₂	Bis(pinacolato)diboron
BSA	Bovine serum albumin
CA	Chlorogenic acid
κ -Car	κ -Carrageenan

CDT	Chemodynamic therapy
Ce6	Chlorine C6
CET	Cetuximab
CGC	Critical gelation concentration
CisPt	Cisplatin
CLB	Chlorambucil
CMD	Concerted-metalation-deprotonation
CO	Chito oligosaccharide
Col	Collagen
CPC	Calcium phosphate cement
CPT	Camptothecin
CS	Chitosan
CUR	Curcumin
CVD	Chemical vapor deposition
dba	Dibenzylidene acetone
DBU	1,8-Diazabicyclo(5.4.0)undec-7-ene
DCE	1,2-Dichloroethane
DCTB	<i>Trans</i> -2-[3-(4- <i>tert</i> -butylphenyl)-2-methyl-2-propenylidene]
DDQ	2,3-Dichloro-5,6-dicyano-1,4-benzoquinone
DHB	2,5-Dihydroxybenzoic acid
DIBAL-H	Diisobutylaluminum hydride
DIH	1,3-Diiodo-5,5-dimethylhydantoin
DOX	Doxorubicin

DME	1,2-Dimethoxyethane
DMF	Dimethylformamide
DMP	Dess-Martin Periodinane
DTIC	Dacarbazine
DTX	Docetaxel
EDC	1-ethyl-3-(3-dimethylaminopropyl)carbodiimide
EPR	Enhanced permeability and retention
ESI-TOF	Electrospray ionization time-of-flight
EtOAc	Ethyl acetate
eV	Electron-volt
EXO	Exosomes
FA	Folic acid
FAK	Focal adhesion kinase
FDA	Food and Drug Administration
FET	Field-effect transistor
FG	Functional group
FGO	Fluorinated graphene oxide
fGO	Furin cleavable peptide mediated graphene oxide
fMLP	<i>N</i> -formyl-methionyl-leucyl-phenylalanine
FRT	Ferritin
FT	Fourier-transform
5-FU	5-fluorouracil
Fx	Fucoxanthin

GBM	Graphene-based material
GEF	Gefitinib
Gn	Gelatin
GNR	Graphene nanoribbon
GO	Graphene oxide
GP	Glycerophosphate
GRPR	Gastrin-releasing peptide receptor
GSH	Glutathione
GQD	Graphene quantum dot
HA	Hydroxyapatite
hBMSC	Human bone marrow mesenchymal stem cell
HCCA	α -Cyano-4-hydroxycinnamic acid
HRMS	High-resolution mass spectrometry
HRP	Horseradish peroxidase
HPG	Hyperbranched polyglycerol
IIT	Ion interference therapy
IONP	Iron oxide nanoparticle
IR	Infrared
KGO	Potassium graphene oxide
KLA	Cell apoptosis peptide (KLAKLAK) ₂
LA	Lactic acid
LB	Langmuir-Blodgett
LSCT	Lower critical solution temperature

MA	Methyl acrylate
MALDI-TOF	Matrix-assisted laser desorption ionization time-of-flight
MeOH	Methanol
Mes	Mesityl
Met	Metformin
MF	Magnetic field
MGMSPi	Targeting peptide-modified magnetic graphene-based mesoporous silica
MGO	Magnetic graphene oxide
MHz	Megahertz
MIP	Molecularly imprinted polymer
miRNA	Micro-ribonucleic acid
MitP	Mitochondrion targeting peptide
m.p.	Melting point
mPEG	Methoxy polyethylene glycol
MPO	Myeloperoxidase
MrGO	Magnetic reduced graphene oxide
MRI	Magnetic resonance imaging
MS	Magnetic saturation
MSC	Mesenchymal stem cell
MSN	Mesoporous silica-coated nanostructure
MTX	Mitoxantrone
MWCNT	Multi-walled carbon nanotube
NBE	Norbornene

NBS	<i>N</i> -Bromosuccinimide
NBT	Nitro blue tetrazolium
NCS	<i>N</i> -Chlorosuccinimide
nHA	Nanohydroxyapatite
NIPAM	<i>N</i> -isopropylacrylamide
NIR	Near-infrared
NG	Nanographene
NGO	Nanographene oxide
NGS	Nanographene sheet
NMR	Nuclear magnetic resonance
OAc	Acetoxy
OBz	Benzoyl
OGNR	Oxidized graphene nanoribbon
OSA	Oxidized sodium alginate
OVA	Ovalbumin
P34HB	Poly(3-hydroxybutyrate-co-4-hydroxybutyrate)
PAT	Photoacoustic tomography
PB	Polymer brush
PBS	Phosphate buffer saline
PCA	Protocatechuic acid
PCH- <i>g</i> -HPG	Poly(epichlorohydrin)-graft-hyperbranched polyglycerol
PCL	Poly(caprolactone)
PDEA	Poly(2-diethylamino ethyl methacrylate)

PDI	Polydispersity index
PDT	Photodynamic therapy
PEG	Poly(ethylene glycol)
PEGDA-	Poly(ethylene glycol) diacrylate (PEGDA)-1,2-ethanediol (EDT)
EDT	Copolymer
PEI	Polyethyleneimine
γ -PGA	γ -Polyglutamic acid
P-gp	P-glycoprotein
PhCl	Chlorobenzene
PHEMA	Polyhydroxyethyl methacrylate
PL	Photoluminescence
PLA	Poly(lactic acid)
PMMA	Polymethyl methacrylate
PMN	Polymorphonuclear neutrophil
PNIPAM	poly(<i>N</i> -isopropylacrylamide)
ppm	Parts per million
PSS	Porous silica sheet
PTT	Photothermal therapy
PTX	Paclitaxel
PUU	Polyurethane-urea
PVA	Poly(vinyl alcohol)
PVK	Poly(<i>N</i> -vinylcarbazole)
PVP	Polyvinylpyrrolidone

RBC	Red blood cell
RBLM	Radial-breathing-like-mode
R_f	Retention factor
rGO	Reduced graphene oxide
RES	Reticuloendothelial system
ROMBP	Ring-opening multi-branching polymerization
ROS	Reactive oxygen species
RSV	Resveratrol
RXF	Raloxifene
SA	Sodium alginate
SBF	Simulated body fluid
SEC	Size exclusion chromatography
SF	Silk fibroin
SS	Disulfide bond
SWCNT	Single-walled carbon nanotube
TC	Tamoxifen citrate
TCA	Triformyl cholic acid
TCP	Tricalcium phosphate
TEM	Transmission electron microscopy
TFA	Trifluoroacetic acid
TfOH	Triflic acid
TGF- β	Transforming growth factor beta inhibitor
THF	Tetrahydrofuran

TLC	Thin-layer chromatography
TMS	Trimethylsilyl
TMZ	Temozolomide
TPE	Tetraphenylethylene
TRAIL	Tumor-ecrosis-factor-related apoptosis-inducing ligand
UV	Ultraviolet
vis	Visible
QSR	Quercetin
QY	Quantum yield

ACKNOWLEDGEMENT

First and foremost, I would like to express my gratitude to my advisor, Prof. Guangbin Dong, for allowing me to join his lab and guiding me through my adventure in palladium/norbornene chemistry. I still recall our initial conversation in his office; I had reservations about joining his lab primarily because I was not familiar with organometallics. However, Guangbin was incredibly supportive and optimistic, which gave me the courage and confidence to explore a field that was new to me. Throughout my doctoral journey, his expertise, patience, and kindness had a profound impact on me, both as a researcher and as a person. If I could go back to my first year, I would choose his group all over again.

Next, I would like to thank Prof. Rawal and Prof. Rowan, for agreeing to serve on my dissertation committee. I sincerely appreciate their time and effort in reading my dissertation and providing valuable feedback and insights. I also thank Prof. Snyder, Prof. Yu, and Prof. Levin for their advice and suggestions during my candidacy exam.

Now, I come to my colleagues in Dong lab as well as other members in the chemistry department. I first thank Ki-Young, Jiaxin, and Alex, all of them have been incredible mentors and sources of laughter during my earlier graduate years. I thank my Dong group best friend, Jiangliang, for providing me with daily doses of happy vitamins and engaging in constructive chemistry discussions. I also thank Yifei Wu, a very talented undergraduate mentee, who helped with my project during her last year at UChicago. Special thanks to Michael Reedy for our special fist bump and Laura Luburich for her warm greetings every morning. While I could write a whole book about everyone who has helped me through this long academic journey, it is impossible to acknowledge everyone individually in this short section. However, I would like to extend my gratitude to Sohee Kim, Miao Chen, Cole Wagner, Daniel Pyle, Jule Scholz, Rui Zhang, Dr. Yibin Xue, Dr. Renhe

Li, Dr. Jianchun Wang, Dr. Xin Liu, Dr. Hairong Lyu, Dr. Sihua Hou, and Dr. Tessa Lynch-Colameta.

Finally, I must thank my greatest supporters, my parents and grandparents, whose support and encouragement have accompanied every decision I've made throughout my life. Without their unconditional love and belief in me, I would not be where I am right now. I thank my fiancé, Jin Sung, for bringing joy and stability into my life each and every day. In addition, I thank my lovely guinea pigs; their companionship has truly brightened my days, and I couldn't imagine going through my tough graduate studies without them. I also thank Dawn for her incredible emotional and mental support in the past years. I dedicate my thesis to everyone that supported me throughout, and I look forward to my future life.

PREFACE

The groundbreaking Palladium/norbornene cooperative catalysis, also known as the Catellani reaction, was pioneered by Prof. Marta Catellani in 1997. This transformative reaction integrates the merits of traditional cross-coupling reactions and *ortho*-functionalization into a single process, offering a remarkably step-economical way to access complex polysubstituted aromatic compounds. Its versatility has proven invaluable to both organic chemists and material scientists alike. Within this dissertation, I explore my profound fascination with leveraging the Catellani reaction for methodology development in azaborine functionalization, and the synthesis of various materials such as dendrons and graphene nanoribbons.

While engaging in the synthesis of graphene nanoribbons aimed for potential biomedical applications, my interest in graphene-based nanomaterials for such purposes grew stronger. Consequently, the final chapter of this dissertation offers a comprehensive review of graphene-based nanomaterials within the context of biomedical applications.

Shinyoung Choi

The University of Chicago

May 2024

CHAPTER 1

Rapid and Modular Access to Multifunctionalized 1,2-Azaborines via Palladium/Norbornene Cooperative Catalysis

(Contents of this chapter were published in *J. Am. Chem. Soc.* **2024**, *146*, 9512-9518)

1.1. Introduction

1,2-Azaborine has been an intriguing aromatic isostere of benzene, which replaces a CC unit in benzene ring with a BN unit (Figure 1.1).¹ Owing to their unique polarization induced by the BN fragment, 1,2-azaborine-containing molecules often exhibit better aqueous solubility and bioavailability than the corresponding carbonaceous compounds in medicinal chemistry.² Compared to the saturated bicyclic bioisosteres of benzene, such as bicyclo[1.1.1]pentane (BCP),³ 1,2-azaborines with substantial aromaticity could maintain π - π stacking or CH- π interactions between the drug candidate and protein target when these interactions are critical. In addition, 1,2-azaborines have found interesting applications as conjugated organic materials.⁴ In comparison to their all-carbon analogues, they show different electronic properties, e.g., higher intrinsic hole mobility, owing to the local dipole moment.⁵

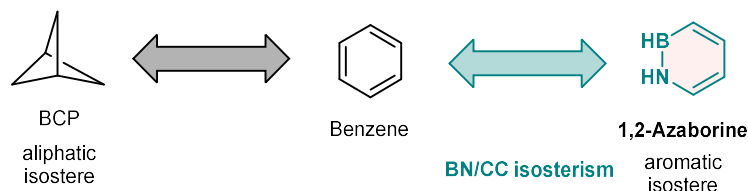


Figure 1.1. Isosteres of benzene

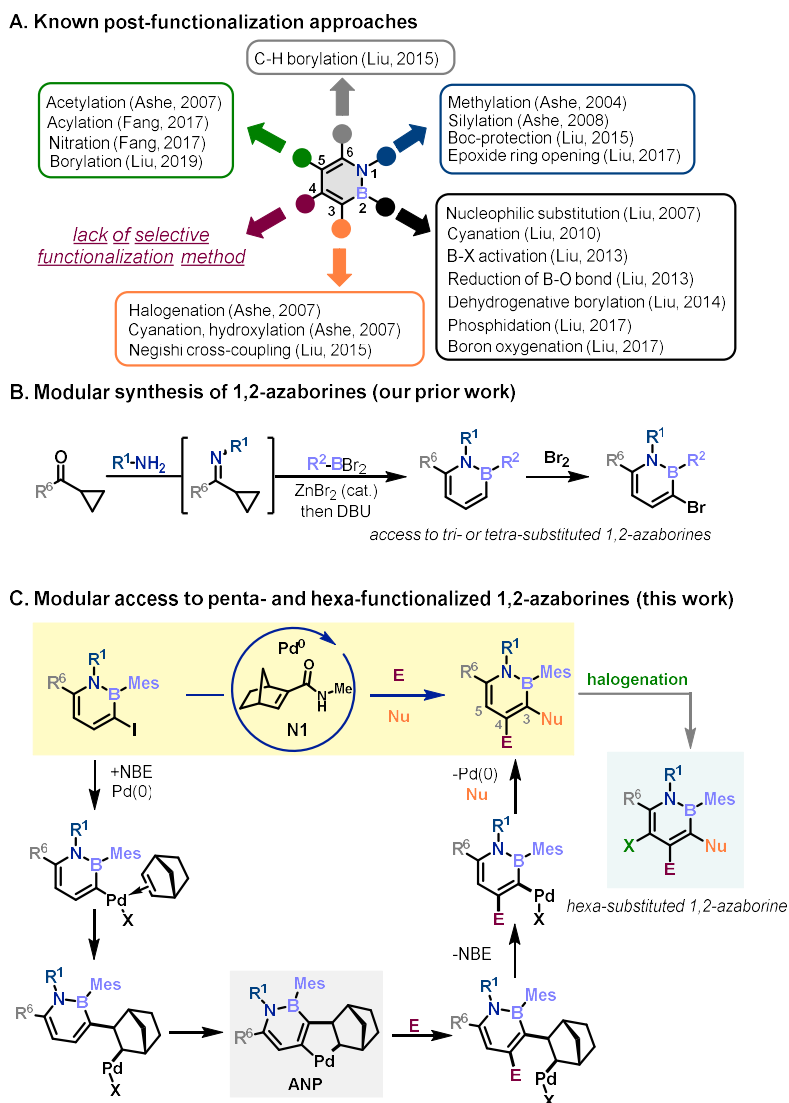
Despite their great potential in drug discovery and material development, synthesis of polysubstituted monocyclic 1,2-azaborines, especially those with five or six different substituents, remains a substantial challenge. Braunschweig et al., reported novel approaches to access hexa-substituted 1,2-azaborines via either the ring expansion of boroles or cyclization between alkynes and iminoboranes, though the substituent scope is limited.⁶⁻⁸ Alternatively, post-functionalization of 1,2-azaborine cores offers a flexible approach to access structural diversity of these heterocycles (Scheme 1.1A).⁹ Impressive works by Ashe¹⁰⁻¹¹ and Liu¹²⁻¹⁸ demonstrated flexible functionalization of the nitrogen and boron positions. Owing to the unique electron distribution in 1,2-azaborine rings, site-selective functionalization of the most electron-rich C3 position via halogenation¹⁹⁻²¹ and the most acidic C6 position via C–H borylation²² have also been realized. Functionalization of the second most electron-rich C5 position via electrophilic substitution can also be achieved when the C3 position is less accessible.^{19, 23-24} However, to the best of our knowledge, site-selective functionalization of the C4 position of 1,2-azaborines remain elusive.²⁵

Recently, our group developed a simple and modular approach to access diverse 1,2,6-trisubstituted 1,2-azaborines from readily available cyclopropyl imines or ketones (Scheme 1.1B).²⁶ The substituents on the boron, nitrogen and the C6 position can be individually controlled and changeable. Given our long-standing interest in the palladium/norbornene (Pd/NBE) cooperative catalysis for arene vicinal difunctionalization,²⁷⁻²⁸ we conceived the idea of merging the modular 1,2-azaborine synthesis with the Pd/NBE catalysis to achieve C4 functionalization and to access penta-substituted 1,2-azaborines (Scheme 1.1C).

It is envisioned that, after the C3 halogenation, the resulting halogenated 1,2-azaborine could undergo oxidative addition with Pd(0), followed by NBE insertion and C4 C–H palladation, to give the key azaborinyl-norbornyl-palladacycle (ANP) intermediate.²⁹ The ANP species can then

react with an external electrophile to introduce a functional group at the C4 position. After the extrusion of NBE by β -carbon elimination, the azaborinyl-Pd(II) species can react with a nucleophile (or an alkene) to render the C3 functionalization and regenerate the Pd(0) catalyst. It can also be imagined that further halogenation at the electron-rich C5 position could lead to hexa-substituted 1,2-azaborines with six independent substituents. Herein, we report our initial discovery of the Pd/NBE-catalyzed C3/C4-difunctionalization of 1,2-azaborines, offering a rapid and modular access to penta-substituted 1,2-azaborines that are otherwise difficult to prepare.

Scheme 1.1. Synthesis and functionalization of 1,2-azaborines.

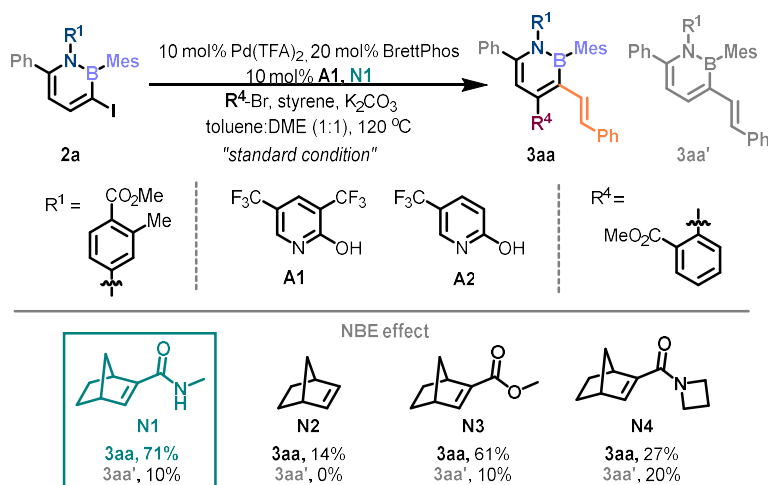


1.2. Results and Discussion

To date, the known substrates for the Pd/NBE catalysis have been limited to arenes, some heteroarenes,³⁰ partially aromatic heterocycles, and electron-neutral alkenes.²⁷ Influenced by the push/pull effect of the nitrogen and boron, the electron distribution in 1,2-azaborines is much less even, compared to normal arenes,^{13, 31} resulting in higher sensitivity to electrophiles and nucleophiles. Thus, there are substantial concerns on how 1,2-azaborines would behave in the C–H palladation process, whether they would be stable in the Pd/NBE catalysis conditions, and how the BN moiety would influence the Pd reactivity.

To address these concerns, we started our exploration of the Pd/NBE-catalyzed *ortho* arylation/*ipso* Heck reaction with 3-iodo-1,2-azaborines (Table 1.1). The *B*-mesityl (Mes)-substituted 1,2-azaborines were used as the substrates owing to their higher stability, which can be efficiently prepared via a slightly modified procedure from our previous report.³² The C3 iodination proceeded smoothly after treatment with 1,3-diiido-5,5-dimethylhydantoin (DIH) in the presence of dimethyl disulfide. The study commenced with 1,2-azaborine **2a** as the substrate, methyl 2-bromobenzoate as the electrophile, and styrene as the nucleophile. The ester moiety in methyl 2-bromobenzoate is known to promote its oxidative addition with the ANP intermediate,³³ which can be removed via post modification (*vide infra*, Scheme 1.2).

Table 1.1 Selected control experiments.^{a,b}



Entry	Changes from the "standard condition"	Yield of 3aa (%)	Yield of 3aa' (%)
1	none	71	10
2	no Pd ^c	0	0
3	no NBE	0	72
4	no ligand	67	18
5	no A1	25	15
6	A2 instead of A1	23	<5
7	100 mol% N1	53	20
8	other NBEs instead of N1	listed above	listed above
9	Pd(OAc) ₂ instead of Pd(TFA) ₂	54	5
10	5 mol% Pd, 10 mol% BrettPhos	65	15
11	5 mol% Pd, no ligand	68	14
12	2.5 mol% Pd, no ligand	51	12
13	CS ₂ CO ₃ instead of K ₂ CO ₃	19	30
14	only toluene	34	<5
15	only DME	59	16

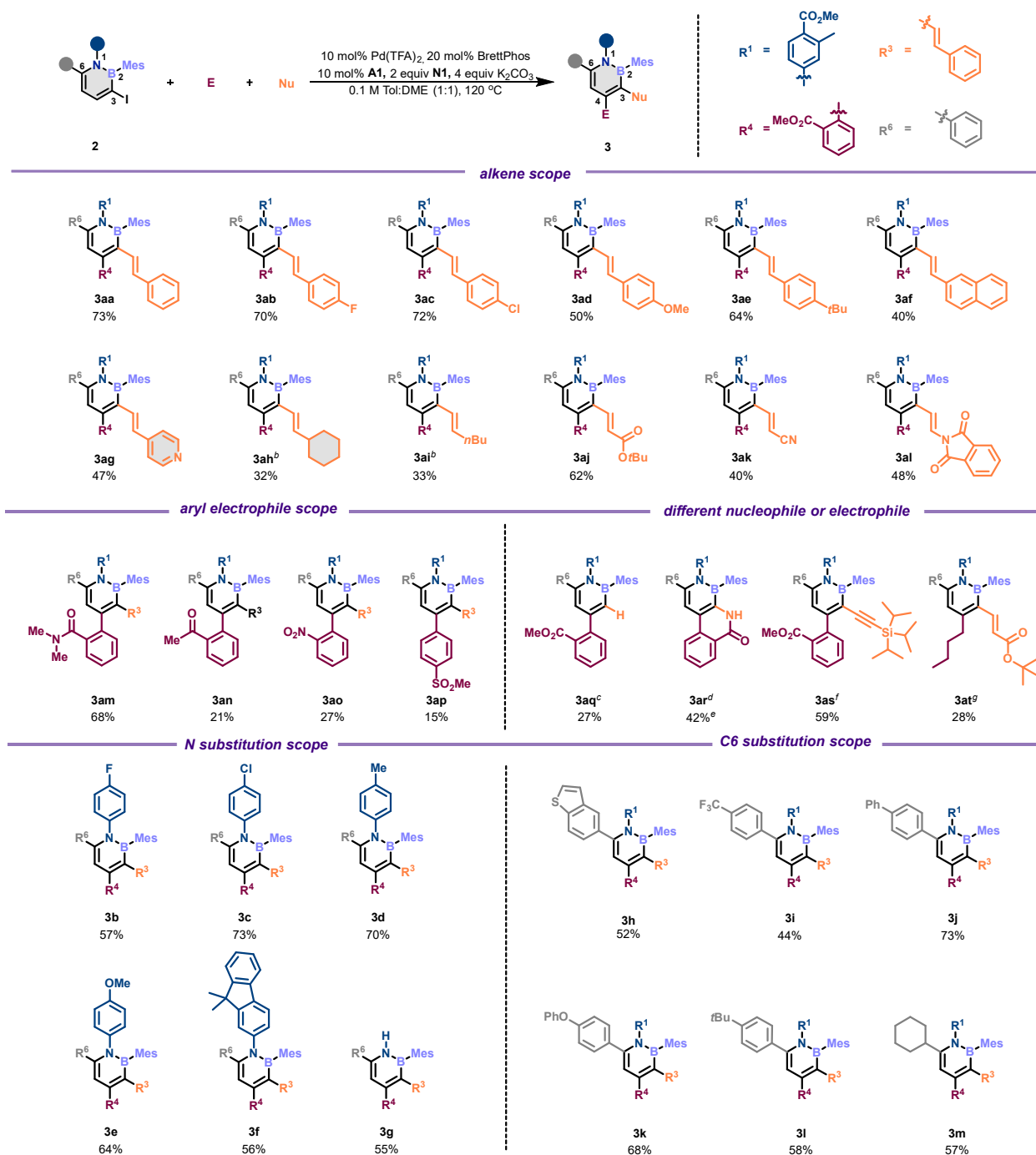
^aReaction conditions: **2a** (0.10 mmol), 2-bromobenzoate (0.10 mmol), styrene (0.105 mmol), Pd(TFA)₂ (0.01 mmol), BrettPhos (0.02 mmol), **N** (0.20 mmol), **A** (0.01 mmol), base (0.40 mmol), toluene:DME (0.1 M, 0.5 mL : 0.5 mL), 120 °C, 18 h. ^bYields (%) were determined by ¹H NMR using CH₂Br₂ as the internal standard. ^c99% of **2a** was recovered.

After careful investigation of various reaction parameters, gratifyingly, the desired C4-arylated C3-vinylated product (**3aa**) was obtained in 71% yield using Pd(TFA)₂ and BrettPhos as the Pd/ligand combination and C2-amide-substituted NBE **N1** as the mediator (entry 1, Table 1.1).³⁴ The major side reaction is the direct C3 Heck coupling, resulting in product **3aa'**. A series of control experiments were next carried out to better understand the role of each reaction component. First, it is not surprising that without Pd or NBE, no desired product was formed (entries 2 and 3). Notably, 99% of **2a** was recovered in the absence of Pd, whereas no 1,2-azaborine substrate was detected for all other entries, suggesting that Pd is most responsible for the decomposition of the substrate. Interestingly, the yield was comparable in the absence of the phosphine ligand, though more direct Heck product was formed (entry 4). It is possible that the 1,2-dimethoxyethane (DME) co-solvent may serve as a ligand to stabilize the Pd during the reaction. Pyridone **A1** serves as a concerted-metalation-deprotonation (CMD) reagent,³⁵ and its absence or employing less acidic **A2** instead led to low yield (entries 5 and 6). The NBE effect was also surveyed. Reducing the loading of **N1** could afford the desired product with a slightly diminished yield (entry 7). Among different NBEs (entry 8),^{27h} the C2-methyl ester-substituted NBE (**N3**)³⁶ could also furnish the desired product in 61% yield; however, simple NBE (**N2**) or more sterically hindered tertiary amide NBE (**N4**) resulted in significantly lower yields of **3aa**. Pd(TFA)₂ was found more reactive than Pd(OAc)₂ (entry 9), and, importantly, good yield can still be obtained when the Pd loading was reduced to 5 mol% or even 2.5 mol% (with or without BrettPhos) (entries 10-12). When Cs₂CO₃ was used as the base, more direct Heck side product and more substrate decomposition were observed compared to when K₂CO₃ was used (entry 13). Finally, the reaction benefited from a combined solvent system in contrast to the use of either toluene or DME alone (entries 14 and 15).

With the optimized condition in hand, the substrate scope was examined (Table 1.2). First, different alkene coupling partners have been tested. Various styrene derivatives bearing either electron-rich, -neutral, or -poor functional groups (**3aa-3ae**) afforded the desired products in moderate to good yields. 2-Vinylnaphthalene and 4-vinylpyridine were also found to be competent (**3af** and **3ag**). Alkenes bearing cyclic or linear alkyl groups were tolerated, albeit with lower yields (**3ah** and **3ai**). Michael acceptors, such as acrylate (**3aj**) and acrylonitrile (**3ak**), can be effectively coupled. Interestingly, vinyl phthalimide (**3al**) also worked reasonably well, which, to the best of our knowledge, has not been used for the *ipso* quench in the Pd/NBE catalysis.

Next, other aryl bromide electrophiles bearing different *ortho*-directing groups was explored. Amide (**3am**) exhibited a comparable directing effect to that of the methyl ester. Methyl ketone (**3an**) and nitro (**3ao**) groups could also furnish the desired products, albeit in lower yields. It is worth noting that the reaction could be accomplished without any *ortho*-directing group (**3ap**). To show the modularity of this strategy, other types of *ortho/ipso* couplings were demonstrated. The *ipso* hydride quench was achieved using borneol as the hydride source (**3aq**). The intramolecular *ipso* amination with 2-bromobenzamide as the coupling partner afford the BN derivative of phenanthridinone (**3ar**). *Ips*o alkylation was successfully accomplished, using (triisopropylsilyl)acetylene as the nucleophile (**3as**). Besides aryl-based electrophiles, preliminary success with *n*-butyl bromide as the electrophile was achieved, giving the desired *ortho*-alkylation *ipso*-Heck product (**3at**).³⁷ Note that the yield of **3at** has not been optimized.

Table 1.2. Substrate scope.^a

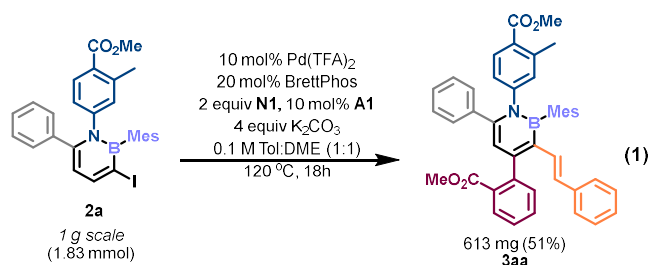


^aReaction conditions: **2** (0.10 mmol), electrophile (0.10 mmol), nucleophile (0.105 mmol), Pd(TFA)₂ (0.01 mmol), BrettPhos (0.02 mmol), **N1** (0.20 mmol), **A1** (0.01 mmol), K₂CO₃ (0.40 mmol), toluene:DME (0.1 M, 0.5 mL : 0.5 mL), 120 °C, 18 h. All yields shown are isolated yields. ^bIsomerization products from olefin chain-walking were observed. ^cBorneol (0.105 mmol) was used as the nucleophile. ^d2-Bromobenzamide (0.1 mmol) was used as both the

electrophile and the nucleophile. ^eReaction performed with Pd(TFA)₂ (0.02 mmol) and BrettPhos (0.04 mmol). ^f(Triisopropylsilyl)acetylene (0.105 mmol) was used as the nucleophile. ^g1-Bromobutane (0.667 mmol) was used as the electrophile, and K₂CO₃ (1.06 mmol) was used.

Additional functional group compatibility and substrate scope were examined by varying the substituents on the nitrogen and C6 positions of 1,2-azaborines. Substrates bearing aryl fluoride (**3b**), aryl chloride (**3c**), toluene (**3d**), anisole (**3e**), or dimethylfluorene (**3f**) on the nitrogen were tolerated. It is noteworthy that *N*-unsubstituted 1,2-azaborine can be synthesized via a modified procedure from NH-cyclopropyl imine and can undergo further functionalization by the Pd/NBE catalysis in good yield. Such NH-1,2-azaborines have *not* been demonstrated by our prior synthetic method.²⁶ On the other hand, various substituents on C6, including sulfur-containing heterocycle (**3h**), benzotrifluoride (**3i**), biphenyl (**3j**), phenyl ether (**3k**), *tert*-butyl benzene (**3l**), and cyclohexyl (**3m**), were found to be compatible.

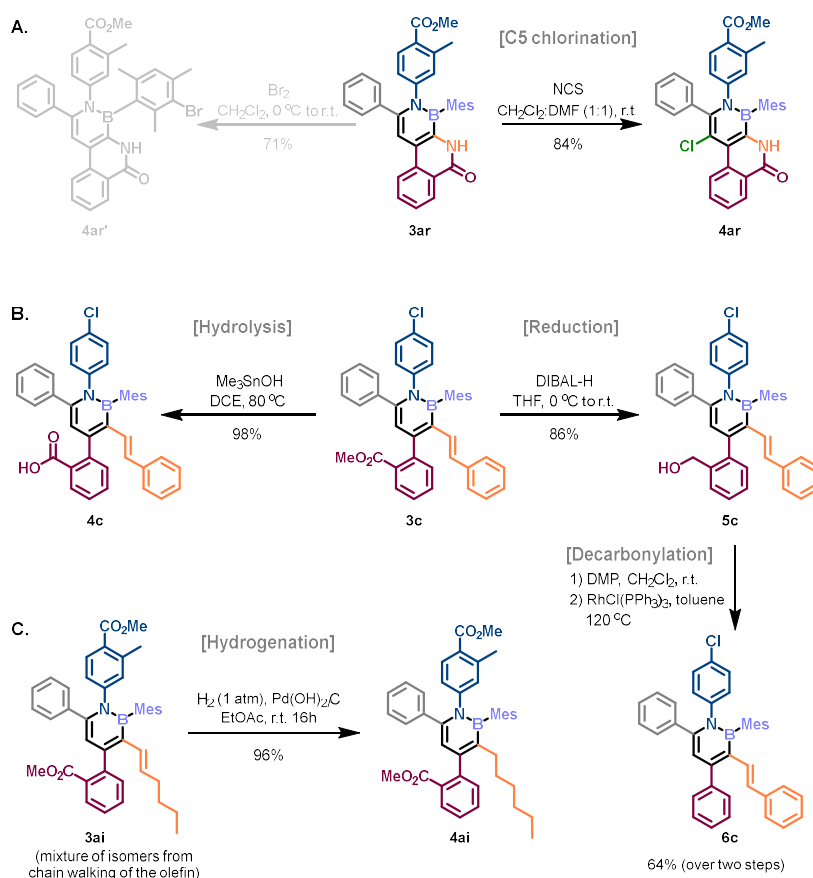
To show the synthetic utility of this method, the scalability of this reaction was first tested (Eq. 1). On a gram scale, the desired product (**3aa**) can be still obtained in good yield under the standard reaction condition.



Next, we explored whether the final C5 position could be further functionalized (Scheme 1.2A). We initially attempted bromination on substrate **3ar**, which selectively brominated the mesityl group over the azaborine ring (**4ar'**). To our delight, chlorination successfully furnished the desired hexa-substituted 1,2-azaborine (**4ar**) in 84% yield. The reason for such selectivity remains unclear at this stage. The chloro group can then potentially undergo standard cross-coupling reactions. To

expand the scope of the C4 aryl substituent, the ester moiety in product **3c** can be hydrolyzed to afford carboxylic acid **4c** almost quantitatively under a mild condition (Scheme 1.2B).³⁸ In addition, the ester group can be reduced by DIBAL-H, to afford alcohol **5c** in a high yield (86%). Notably, the 1,2-azaborine core was found stable under an oxidative condition with treatment of Dess–Martin periodinane (DMP). The corresponding aldehyde can be removed to give the simple phenyl substituent (**6c**) via decarbonylation mediated by Wilkinson’s catalyst.³⁹ Finally, hydrogenation of the alkenyl moiety in compound **3ai** catalyzed by Pearlman’s catalyst [Pd(OH)₂/C], successfully afforded the C3 alkylated 1,2-azaborine (**4ai**) (Scheme 1.2C).

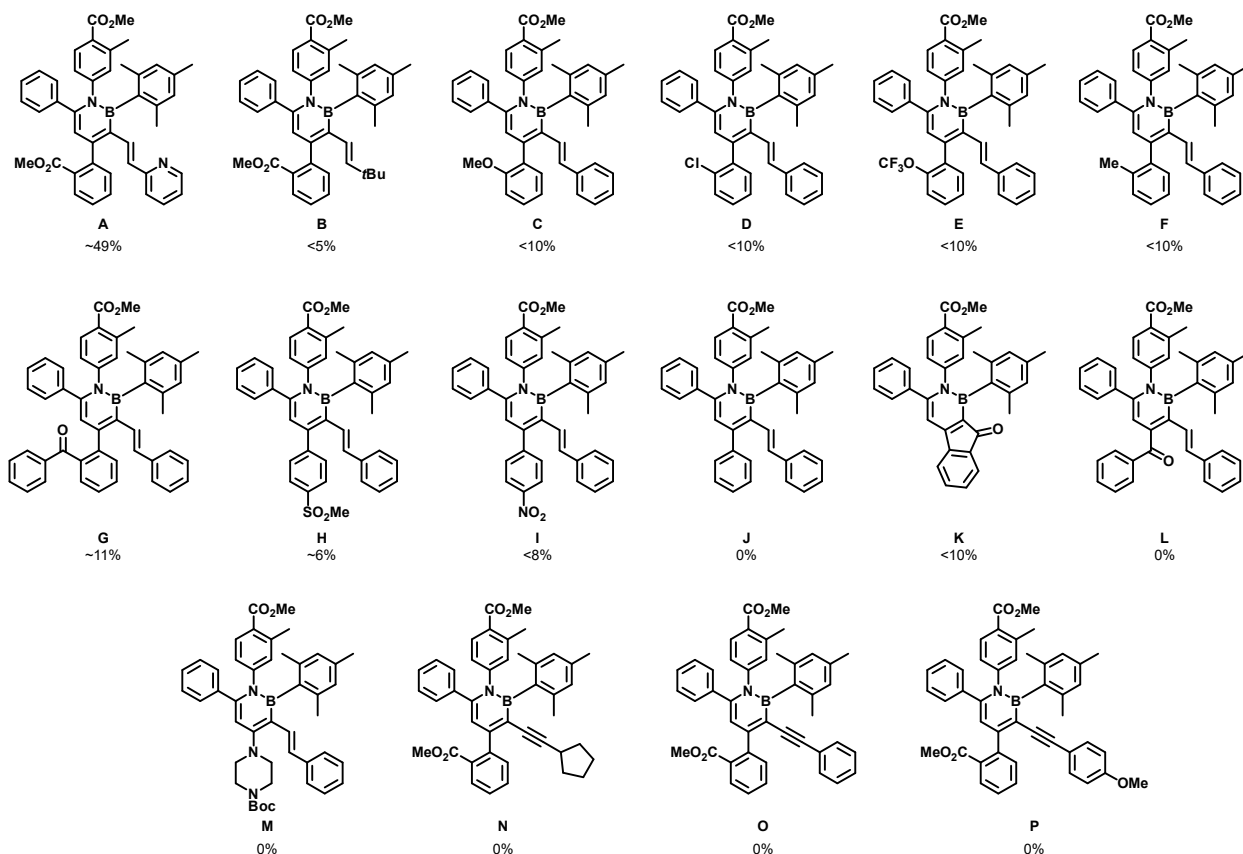
Scheme 1.2. Synthetic elaborations.



In Table 1.3, we present a summary of less successful examples. Compound **A** was successfully synthesized; however, it decomposed rapidly, presumably due to the unstable nature of 2-

vinylpyridine. For compound **B**, the failure could be attributed to either the steric bulk of the *tert*-butyl group or the nucleophile escaping from the reaction solution due to its high volatility at high temperatures. Attempts with other weak *ortho*-directing groups (**C–G**) or without any *ortho*-substituents (**H–J**) on the aryl bromide electrophile resulted in very low yields or no desired product. While 2-bromobenzaldehyde produced the annulation product (**K**), the yield was low. Besides arylation and alkylation, amination and acylation have been explored for the *ortho* coupling, however, they proved challenging under our optimized reaction conditions (**L–M**). Interestingly, other alkynes tethered with cyclopentane or aryl groups failed to yield the desired product (**N–P**) while (triisopropylsilyl)acetylene worked well.

Table 1.3. Less successful examples.



1.3. Conclusion

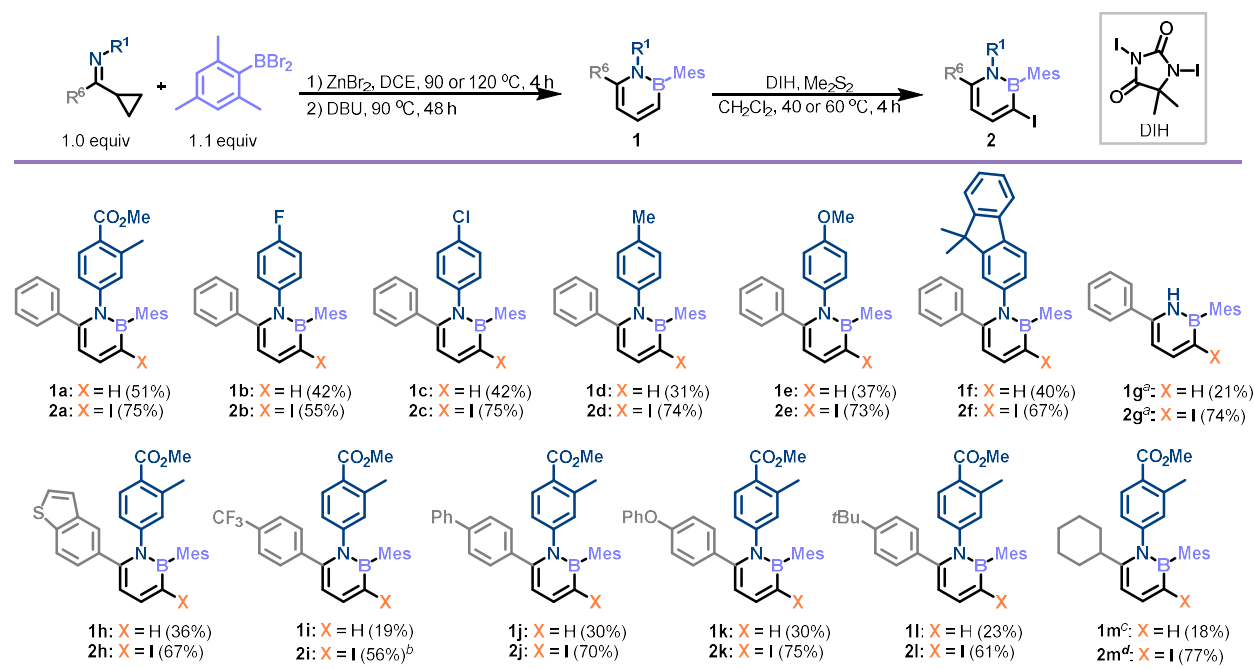
In summary, we have developed the first Pd/NBE-catalyzed C3,C4-difunctionalization of 1,2-azaborines. This method not only fills the gap for site-selective functionalization of the C4 position of 1,2-azaborines, but also enables modular synthesis of hexa-substituted 1,2-azaborines that are otherwise difficult to access. The structurally modified NBE plays a critical role in facilitating this transformation. The broad scope and high functional group tolerance could make this approach attractive for preparing novel BN-analogues of diverse functional aromatic compounds. Efforts on further improving the efficiency and generality of this method are ongoing.

1.4. General Information

All commercially available reagents were purchased from Combi-blocks, Sigma-Aldrich, Fisher Scientific, TCI chemicals, Oakwood, or Ambeed, and used as received. Toluene and 1,2-dimethoxyethane were distilled over sodium, and chlorobenzene (PhCl) and 1,2-dichloroethane (DCE) were distilled over CaH₂. CH₂Cl₂ used in the iodination reactions was processed through a Pure-Solve MD-5 solvent purification system (Inert Corporation). Reaction vials with PTFE lined caps were purchased from Qorpak and flame-dried with a propane torch prior to use. Temperature of the reactions using pie-blocks (Chemglass) were determined using a thermometer placed in a separate vial filled with silicon oil and placed inside the pie-block. Analytical thin-layer chromatography (TLC) was carried out using 0.2 mm silica plates (silica gel 60, F254, EMD chemical), and visualized by irradiation with 254 nm UV light. Column chromatography was performed using silica gel purchased from Macherey-Nagel (Silica 60M, particle size: 0.04-0.063 mm). FT-IR spectra were recorded on a Nicolet iS5 FT-IR spectrometer as a thin film on KBr salt plates. High resolution mass spectra (HRMS) were obtained from Agilent 6223 TOF mass

spectrometer (fragmentation voltage set to 70 V or 130 V) by electrospray ionization (ESI) or atmospheric pressure chemical ionization (APCI) and processed with an Agilent MassHunter Operating System. Nuclear magnetic resonance (NMR) spectra were recorded with a Bruker Avance 400 (^1H at 400 MHz, ^{13}C at 101 MHz, ^{11}B at 128 MHz, ^{19}F at 376 MHz), Bruker Avance 500 (^1H at 400 MHz, ^{13}C at 101 MHz, ^{11}B at 160 MHz, ^{19}F at 470 MHz, ^1H - ^1H COSY, 1D NOE), and Bruker Avance 600 (^1H at 600 MHz, ^{13}C at 151 MHz). Chemical shifts are reported in parts per million (ppm, δ) in reference to the NMR solvent (CDCl_3 $\delta=7.26$ ppm (^1H) and 77.16 ppm (^{13}C)). Coupling constants were reported in Hertz (Hz). Data for ^1H NMR spectra were reported as follows: chemical shift (ppm, referenced to protium, s = singlet, d = doublet, t = triplet, q = quartet, quin = quintet, dd = doublet of doublets, td = triplet of doublets, ddd = doublet of doublet of doublets, m = multiplet, coupling constant (Hz), and integration).

1.5. Experimental Procedure and Data



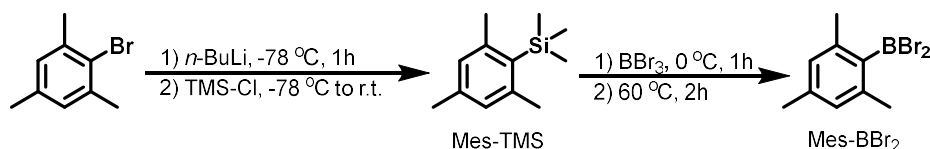
^aReaction condition varies from the general conditions. See below for details. ^bReaction performed at 60 °C with 1.5 equiv DIH. ^cReaction performed at 120 °C.

^dReaction performed at r.t.

1.5.1. Preparation of various imines:

Various imines for the synthesis of 1a-1f and 1h-1m were synthesized following the previously reported literature procedures.²⁶ Imine for the synthesis of 1g was accomplished using a modified literature procedure.⁴⁰ Instead of a bulb to bulb distillation, vacuum distillation was performed to purify the desired imine compound.

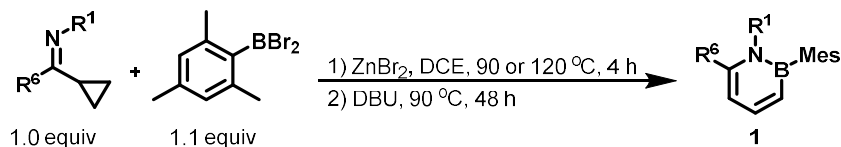
1.5.2. Preparation of Mes-BBr₂:



To a flame-dried 1000 mL round-bottom flask, 2-bromomesitylene (19.9 g, 100 mmol, 1 equiv) and THF (286.0 mL, 0.35 M) were added. The flask was cooled down to -78 °C in a dry-ice/acetone bath. At -78 °C, *n*-BuLi (2.5 M in hexanes, 48.0 mL, 120 mmol, 1.2 equiv) was added dropwise using a dropping funnel, then stirred for 1 h. At the same temperature, trimethylsilyl chloride (25.4 mL, 200 mmol, 2 equiv) was added dropwise. The solution was warmed to r.t. and stirred overnight. Upon completion, the reaction mixture was quenched with water (200 mL), extracted with EtOAc (3 × 200 mL), and dried over MgSO₄. After filtration, the organic solvents were removed under vacuum. The resulting crude mixture was purified by flash column chromatography on silica gel using hexanes to afford Mes-TMS in a quantitative yield.

To a flame-dried Schlenk flask charged with BBr₃ (10.82 mL, 113.97 mmol, 1.05 equiv), Mes-TMS (16.31 g, 108.54 mmol, 1 equiv) was added dropwise at 0 °C and stirred for 1 h. Then, the reaction mixture was heated to 60 °C and stirred for additional 2 h. After cooling down to r.t., the compound was purified by vacuum distillation under heating (vapor temperature was ~96 °C). The NMR data of Mes-BBr₂ matched that of the data reported in literature.⁴¹

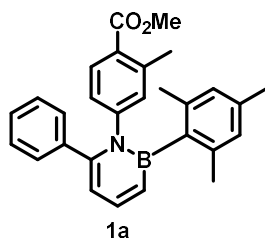
1.5.3. General procedure for the synthesis of 1,2-azaborines **1a-1f** and **1h-1m**:



A flame-dried 4 mL reaction vial was charged with imine (0.2 mmol, 1 equiv) and ZnBr₂ (4.5 mg, 0.1 equiv, 0.02 mmol) in a nitrogen-filled glovebox. Dry 1,2-dichloroethane (DCE, 1.0 mL) was added, followed by the addition of Mes-BBr₂ (63.8 mg, 0.22 mmol, 1.1 equiv). Then the vial was tightly sealed and stirred on a preheated pie-block set to 90 °C or 120 °C. After 4 h, 1,8-diazabicyclo(5.4.0)undec-7-ene (DBU, 90 μL, 0.6 mmol, 3 equiv) was added to the vial under nitrogen atmosphere, and the reaction solution was stirred at the same temperature for 48 h. After cooling down to r.t., the crude mixture was filtered through a short pad of celite, washed with ethyl acetate, and concentrated under reduced pressure. The desired product was purified by flash column chromatography on silica gel (EtOAc:hexanes = 1:20 to 1:9).

1.5.4. Synthetic procedure for the synthesis of **1g**:

A flame-dried 4 mL reaction vial was charged with cyclopropyl(phenyl)methanimine (29.0 mg, 0.2 mmol, 1 equiv) and ZnBr₂ (4.5 mg, 0.02 mmol, 0.1 equiv) in a nitrogen-filled glovebox. Dry chlorobenzene (PhCl, 1.0 mL) was added, followed by the addition of Mes-BBr₂ (63.8 mg, 0.22 mmol, 1.1 equiv). Then the vial was tightly sealed and stirred on a preheated pie-block set to 90 °C. After 4 h, triethylamine (84 μL, 0.6 mmol, 3 equiv) was added to the vial under nitrogen atmosphere, and the reaction solution was stirred at the same temperature for 24 h. After cooling down to r.t., the crude mixture was filtered through a short pad of celite, washed with ethyl acetate, and concentrated under reduced pressure. The desired product was purified by flash column chromatography on silica gel (EtOAc:hexanes = 1:20).



Yield: 51% (a 1:1 mixture of 2 rotamers)

Physical appearance: colorless oil

R_f: 0.4 (EtOAc:hexanes = 1:9)

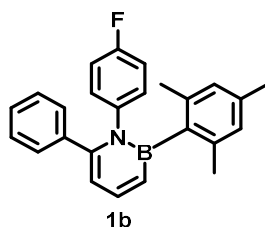
¹H NMR (400 MHz, CDCl₃): δ 7.77 – 7.73 (m, 1H), 7.49 (d, *J* = 8.0 Hz, 1H), 7.13 (m, 5H), 6.86 (d, *J* = 10.3 Hz, 1H), 6.68 (s, 1H), 6.67 (d, *J* = 8.3 Hz, 1H), 6.63 (s, 2H), 6.52 (d, *J* = 6.6 Hz, 1H), 3.76 (s, 3H), 2.26 (s, 3H), 2.18 (s, 3H), 2.07 (s, 3H), 2.05 (s, 3H).

¹³C NMR (101 MHz, CDCl₃): δ 167.49, 148.26, 148.20, 143.36, 140.11, 138.72, 136.58, 131.71, 130.25, 129.52, 127.82, 127.45, 126.88, 126.84, 126.46, 125.54, 114.47, 51.76, 23.21, 23.17, 21.52, 21.21.

¹¹B NMR (128 MHz, CDCl₃): δ 39.3.

IR (KBr, neat): 2951, 2921, 2857, 1723, 1605, 1594, 1573, 1522, 1490, 1411, 1376, 1357, 1256, 1191, 1171, 1143, 1083, 1030, 982, 915, 875, 849, 808, 780, 756, 730, 700, 664 cm⁻¹.

HRMS (ESI-TOF): *m/z* calcd for C₂₈H₂₉BNO₂⁺ [M+H⁺]: 422.2286. Found: 422.2290.



Yield: 42%

Physical appearance: white solid, **m.p.:** 142-144 °C

R_f: 0.6 (EtOAc:hexanes = 1:9)

¹H NMR (500 MHz, CDCl₃): δ 7.75 (dd, *J* = 11.0, 6.7 Hz, 1H), 7.16 – 7.14 (m, 3H), 7.12 – 7.10 (m, 2H), 6.87 (dd, *J* = 11.0, 1.5 Hz, 1H), 6.77 – 6.75 (m, 2H), 6.66 (s, 2H), 6.59 (t, *J* = 8.6 Hz, 2H), 6.52 (dd, *J* = 6.7, 1.5 Hz, 1H), 2.20 (s, 3H), 2.07 (s, 6H).

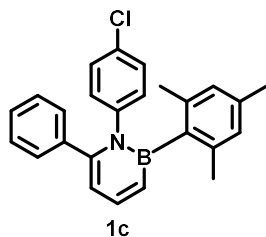
¹³C NMR (126 MHz, CDCl₃): δ 160.42 (d, ¹*J*_{C-F} = 245.2 Hz), 148.73, 143.32, 141.15 (d, ⁴*J*_{C-F} = 3.4 Hz), 138.86, 138.73, 136.57, 129.70, 129.51 (d, ³*J*_{C-F} = 8.5 Hz), 127.81, 127.34, 126.87, 114.34 (d, ²*J*_{C-F} = 22.7 Hz), 114.28, , 23.23, 21.24.

¹¹B NMR (128 MHz, CDCl₃): δ 39.1.

¹⁹F NMR (376 MHz, CDCl₃): δ -116.57.

IR (KBr, neat): 3024, 2915, 2855, 1609, 1593, 1573, 1522, 1506, 1490, 1445, 1420, 1405, 1374, 1359, 1286, 1266, 1218, 1177, 1153, 1094, 1075, 1029, 1014, 989, 966, 838, 822, 782, 772, 757, 731, 717, 699 cm⁻¹.

HRMS (ESI-TOF): *m/z* calcd for C₂₅H₂₄BFN⁺ [M+H⁺]: 368.1980. Found: 368.1987.



Yield: 42%

Physical appearance: yellow oil

R_f: 0.65 (EtOAc:hexanes = 1:9)

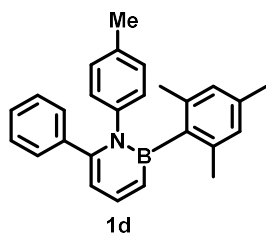
¹H NMR (400 MHz, CDCl₃): δ 7.75 (dd, *J* = 11.0, 6.6 Hz, 1H), 7.17 – 7.15 (m, 3H), 7.11 – 7.09 (m, 2H), 6.88 (d, *J* = 3.2 Hz, 1H), 6.85 (d, *J* = 6.2 Hz, 2H), 6.73 (d, *J* = 8.8 Hz, 2H), 6.66 (s, 2H), 6.52 (d, *J* = 7.1 Hz, 1H), 2.20 (s, 3H), 2.06 (s, 6H).

¹³C NMR (101 MHz, CDCl₃): δ 148.44, 143.73, 143.36, 138.69, 136.63, 131.41, 129.64, 129.40, 127.87, 127.66, 127.42, 126.93, 114.46, 23.22, 21.25.

¹¹B NMR (128 MHz, CDCl₃): δ 38.4.

IR (KBr, neat): 2913, 2855, 1609, 1592, 1574, 1521, 1489, 1445, 1412, 1401, 1358, 1283, 1265, 1238, 1176, 1151, 1086, 1028, 1016, 988, 966, 849, 832, 763, 755, 714, 700 cm⁻¹.

HRMS (ESI-TOF): *m/z* calcd for C₂₅H₂₄BClN⁺ [M+H⁺]: 384.1685. Found: 384.1683.



Yield: 31%

Physical appearance: off-white oil

R_f: 0.65 (EtOAc:hexanes = 1:9)

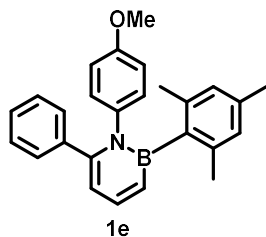
¹H NMR (400 MHz, CDCl₃): δ 7.78 – 7.73 (m, 1H), 7.14 (m, 5H), 6.85 (dd, *J* = 11.0, 1.6 Hz, 1H), 6.70 (s, 4H), 6.66 (s, 2H), 6.51 (dd, *J* = 6.7, 1.4 Hz, 1H), 2.20 (s, 3H), 2.10 (s, 9H).

¹³C NMR (101 MHz, CDCl₃): δ 149.00, 143.07, 142.48, 138.79, 136.19, 135.16, 129.65, 128.09, 127.84, 127.58, 127.04, 126.73, 114.16, 23.27, 21.24, 20.95.

¹¹B NMR (128 MHz, CDCl₃): δ 39.1.

IR (KBr, neat): 3060, 3028, 2919, 2855, 1573, 1609, 1593, 1521, 1510, 1489, 1445, 1408, 1359, 1284, 1264, 1237, 1177, 1150, 1109, 1088, 1022, 989, 848, 822, 769, 756, 730, 716, 700, 699 cm^{-1} .

HRMS (ESI-TOF): m/z calcd for $\text{C}_{26}\text{H}_{27}\text{BN}^+$ $[\text{M}+\text{H}^+]$: 364.2231. Found: 364.2232.



Yield: 37%

Physical appearance: off-white oil

R_f: 0.6 (EtOAc:hexanes = 1:9)

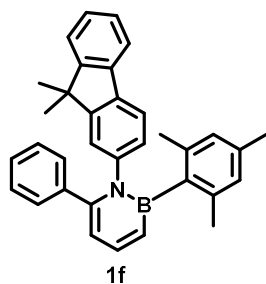
¹H NMR (400 MHz, CDCl₃): δ 7.76 – 7.73 (m, 1H), 7.13 (m, 5H), 6.84 (d, J = 11.0 Hz, 1H), 6.71 (d, J = 7.4 Hz, 2H), 6.65 (s, 2H), 6.50 (d, J = 6.7 Hz, 1H), 6.41 (d, J = 6.8 Hz, 2H), 3.61 (s, 3H), 2.19 (s, 3H), 2.08 (s, 6H).

¹³C NMR (101 MHz, CDCl₃): δ 157.14, 149.16, 143.09, 139.23, 138.80, 138.22, 136.25, 129.68, 128.95, 127.67, 127.08, 126.78, 114.12, 112.61, 55.22, 23.27, 21.25.

¹¹B NMR (128 MHz, CDCl₃): δ 39.8.

IR (KBr, neat): 2909, 1572, 1609, 1522, 1508, 1490, 1460, 1443, 1408, 1359, 1298, 1245, 1179, 1150, 1107, 1088, 1034, 989, 848, 832, 805, 782, 770, 757, 699 cm^{-1} .

HRMS (ESI-TOF): m/z calcd for $\text{C}_{26}\text{H}_{27}\text{BNO}^+$ $[\text{M}+\text{H}^+]$: 380.2180. Found: 380.2187.



Yield: 40% (a 1:1 mixture of 2 rotamers)

Physical appearance: off-white solid, **m.p.:** 73-75 °C

R_f: 0.7 (EtOAc:hexanes = 1:9)

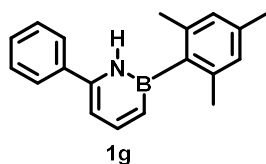
¹H NMR (500 MHz, CDCl₃): δ 7.80 (dd, *J* = 11.0, 6.7 Hz, 1H), 7.53 (dd, *J* = 6.4, 2.0 Hz, 1H), 7.33 (dd, *J* = 6.5, 2.0 Hz, 1H), 7.28 – 7.23 (m, 3H), 7.19 – 7.17 (m, 2H), 7.12 – 7.06 (m, 3H), 6.93 (dd, *J* = 11.0, 1.5 Hz, 1H), 6.81 (d, *J* = 2.0 Hz, 1H), 6.77 (dd, *J* = 8.0, 2.0 Hz, 1H), 6.63 (s, 2H), 6.59 (dd, *J* = 6.7, 1.5 Hz, 1H), 2.14 (s, 3H), 2.12 (s, 6H), 1.14 (s, 3H), 1.13 (s, 3H).

¹³C NMR (126 MHz, CDCl₃): δ 153.78, 152.89, 148.94, 144.27, 143.17, 139.22, 138.90, 138.74, 136.39, 136.26, 129.70, 127.65, 127.11, 127.05, 127.01, 126.97, 126.81, 123.21, 122.67, 119.93, 118.83, 114.09, 46.50, 26.79, 26.40, 23.30, 23.17, 21.13.

¹¹B NMR (128 MHz, CDCl₃): δ 40.6.

IR (KBr, neat): 3204, 3061, 3017, 2959, 2919, 2858, 1609, 1574, 1521, 1490, 1472, 1460, 1448, 1358, 1298, 1281, 1265, 1241, 1174, 1155, 1076, 1029, 1009, 979, 941, 912, 885, 849, 830, 780, 757, 738, 702, 655 cm⁻¹.

HRMS (ESI-TOF): *m/z* calcd for C₃₄H₃₃BN⁺ [M+H⁺]: 466.2701. Found: 466.2704.



Yield: 21%

Physical appearance: colorless oil

R_f: 0.7 (EtOAc:hexanes = 1:9)

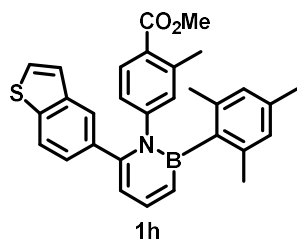
¹H NMR (500 MHz, CDCl₃): δ 8.17 (N-H, br, 1H), 7.84 (dd, *J* = 11.0, 6.9 Hz, 1H), 7.61 (d, *J* = 7.1 Hz, 2H), 7.48 (t, *J* = 7.5 Hz, 2H), 7.42 (t, *J* = 7.3 Hz, 1H), 6.93 (s, 2H), 6.91 (d, *J* = 11.2 Hz, 1H), 6.72 (d, *J* = 6.4 Hz, 1H), 2.35 (s, 3H), 2.26 (s, 6H).

¹³C NMR (126 MHz, CDCl₃): δ 144.83, 144.50, 140.48, 138.29, 137.54, 129.28, 128.85, 127.36, 126.05, 109.08, 23.37, 21.28.

¹¹B NMR (160 MHz, CDCl₃): δ 36.4

IR (KBr, neat): 3375 (br), 3021, 2915, 1608, 1573, 1542, 1490, 1446, 1372, 1287, 1153, 1076, 1035, 990, 922, 849, 784, 753, 727, 696 cm⁻¹.

HRMS (ESI-TOF): *m/z* calcd for C₁₉H₂₁BN⁺ [M+H⁺]: 274.1762. Found: 274.1775.



Yield: 36% (a 1:1 mixture of 2 rotamers)

Physical appearance: colorless oil

R_f: 0.4 (EtOAc:hexanes = 1:9)

¹H NMR (400 MHz, CDCl₃): δ 7.77 (dd, *J* = 11.0, 6.7 Hz, 1H), 7.71 (s, 1H), 7.58 (d, *J* = 8.4 Hz, 1H), 7.47 (d, *J* = 8.3 Hz, 1H), 7.41 (d, *J* = 5.4 Hz, 1H), 7.24 (d, *J* = 5.7 Hz, 1H), 7.01 (d, *J* = 8.4

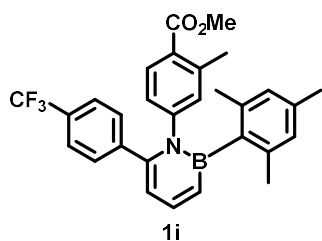
Hz, 1H), 6.89 (d, $J = 10.9$ Hz, 1H), 6.75 (s, 1H), 6.71 (d, $J = 8.4$ Hz, 1H), 6.66 (s, 1H), 6.63 (s, 1H), 6.58 (d, $J = 6.6$ Hz, 1H), 3.74 (s, 3H), 2.24 (s, 3H), 2.19 (s, 3H), 2.12 (s, 3H), 2.04 (s, 3H).

^{13}C NMR (101 MHz, CDCl_3): δ 167.43, 148.27, 148.20, 143.41, 140.17, 139.30, 138.89, 138.72, 136.60, 135.10, 131.65, 130.34, 127.16, 126.89, 126.85, 126.47, 125.76, 125.58, 124.53, 124.01, 121.69, 114.95, 51.74, 23.25, 23.19, 21.58, 21.22.

^{11}B NMR (128 MHz, CDCl_3): δ 39.4.

IR (KBr, neat): 2947, 1719, 1593, 1522, 1499, 1436, 1356, 1254, 1187, 1142, 1081, 1046, 988, 879, 848, 811, 759, 772, 737, 708, 669 cm^{-1} .

HRMS (ESI-TOF): m/z calcd for $\text{C}_{30}\text{H}_{29}\text{BNO}_2\text{S}^+$ [$\text{M}+\text{H}^+$]: 478.2007. Found: 478.2012.



Yield: 19% (a 1:1 mixture of 2 rotamers)

Physical appearance: colorless oil

R_f : 0.45 (EtOAc:hexanes = 1:9)

^1H NMR (400 MHz, CDCl_3): δ 7.75 (dd, $J = 11.0, 6.6$ Hz, 1H), 7.52 (d, $J = 8.2$ Hz, 1H), 7.41 (d, $J = 8.0$ Hz, 2H), 7.25 (d, $J = 5.9$ Hz, 2H), 6.92 (d, $J = 11.0$ Hz, 1H), 6.68 – 6.63 (m, 4H), 6.52 (d, $J = 6.6$ Hz, 1H), 3.77 (s, 3H), 2.27 (s, 3H), 2.18 (s, 3H), 2.07 (s, 3H), 2.03 (s, 3H).

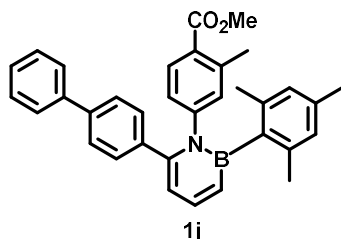
^{13}C NMR (126 MHz, CDCl_3): 167.33, 147.76, 146.53, 143.23, 142.33, 140.44, 138.67, 136.80, 131.54, 130.54, 129.76, 129.51 (q, $^2J_{\text{C-CF}_3} = 32.6$ Hz), 126.97, 126.92, 125.44, 124.86 (q, $^3J_{\text{C-CF}_3} = 3.4$ Hz), 124.05 (q, $^1J_{\text{C-CF}_3} = 272.1$ Hz), 115.06, 51.86, 23.18, 21.56, 21.22.

^{11}B NMR (128 MHz, CDCl_3): δ 40.0.

^{19}F NMR (470 MHz, CDCl_3): δ -62.62.

IR (KBr, neat): 2951, 1721, 1598, 1571, 1527, 1508, 1436, 1408, 1357, 1325, 1255, 1168, 1128, 1110, 1084, 1068, 1016, 983, 844, 775, 754, 728, 706, 671 cm^{-1} .

HRMS (ESI-TOF): m/z calcd for $\text{C}_{29}\text{H}_{28}\text{BF}_3\text{NO}_2^+$ [$\text{M}+\text{H}^+$]: 490.2160. Found: 490.2164.



Yield: 30% (a 1:1 mixture of 2 rotamers)

Physical appearance: off-white oil

R_f : 0.5 (EtOAc:hexanes = 1:9)

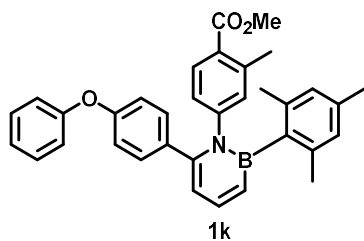
^1H NMR (400 MHz, CDCl_3): δ 7.78 (dd, $J = 11.3, 6.7$ Hz, 1H), 7.53 (dd, $J = 7.8, 5.1$ Hz, 3H), 7.43 – 7.39 (m, 4H), 7.35 – 7.31 (m, 1H), 7.20 (d, $J = 6.9$ Hz, 2H), 6.89 (d, $J = 11.0$ Hz, 1H), 6.75 – 6.71 (m, 2H), 6.66 (d, $J = 7.5$ Hz, 2H), 6.59 (d, $J = 6.7$ Hz, 1H), 3.76 (s, 3H), 2.28 (s, 3H), 2.20 (s, 3H), 2.11 (s, 3H), 2.07 (s, 3H).

^{13}C NMR (101 MHz, CDCl_3): δ 167.46, 148.27, 147.86, 143.39, 140.36, 140.19, 140.03, 138.72, 137.71, 136.61, 131.69, 130.36, 129.92, 128.89, 127.60, 127.08, 126.90, 126.86, 126.54, 126.44, 125.57, 114.62, 51.76, 23.21, 21.58, 21.22.

^{11}B NMR (128 MHz, CDCl_3): δ 39.3.

IR (KBr, neat): 3029, 2994, 2948, 1721, 1607, 1595, 1559, 1510, 1485, 1413, 1398, 1355, 1285, 1270, 1254, 1191, 1171, 1142, 1083, 1007, 982, 875, 841, 777, 763, 712, 697 cm^{-1} .

HRMS (ESI-TOF): m/z calcd for $C_{34}H_{33}BNO_2^+$ $[M+H]^+$: 498.2599. Found: 498.2604.



Yield: 30% (a 1:1 mixture of 2 rotamers)

Physical appearance: off-white oil

R_f: 0.5 (EtOAc:hexanes = 1:9)

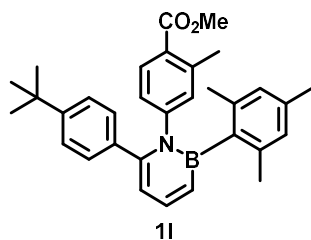
¹H NMR (400 MHz, CDCl₃): δ 7.75 (dd, $J = 11.0, 6.7$ Hz, 1H), 7.54 (d, $J = 8.9$ Hz, 1H), 7.31 (t, $J = 7.8$ Hz, 2H), 7.11 – 7.06 (m, 3H), 6.91 – 6.85 (m, 3H), 6.78 (d, $J = 8.5$ Hz, 2H), 6.69 (d, $J = 6.8$ Hz, 2H), 6.64 (s, 2H), 6.54 (d, $J = 6.7$ Hz, 1H), 3.80 (s, 3H), 2.30 (s, 3H), 2.19 (s, 3H), 2.07 (s, 3H), 2.06 (s, 3H).

¹³C NMR (101 MHz, CDCl₃): δ 167.46, 157.12, 156.49, 148.31, 147.63, 143.38, 140.12, 138.72, 136.62, 133.82, 131.77, 131.03, 130.33, 129.88, 126.90, 126.87, 126.55, 125.60, 123.51, 118.91, 118.28, 114.26, 51.82, 23.26, 23.16, 21.58, 21.22.

¹¹B NMR (128 MHz, CDCl₃): δ 39.5.

IR (KBr, neat): 2948, 2907, 1722, 1596, 1524 1500, 1488, 1435, 1410, 1353, 1286, 1240, 1194, 1169, 1142, 1082, 1014, 982, 870, 848, 807, 775, 692 cm^{-1} .

HRMS (ESI-TOF): m/z calcd for $C_{34}H_{33}BNO_3^+$ $[M+H]^+$: 514.2548. Found: 514.2552.



Yield: 23% (a 1:1 mixture of 2 rotamers)

Physical appearance: colorless oil

R_f: 0.6 (EtOAc:hexanes = 1:9)

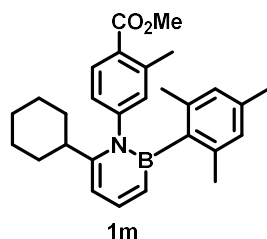
¹H NMR (400 MHz, CDCl₃): δ 7.74 (dd, *J* = 11.0, 6.7 Hz, 1H), 7.50 (d, *J* = 8.3 Hz, 1H), 7.15 (d, *J* = 8.3 Hz, 2H), 7.03 (d, *J* = 8.3 Hz, 2H), 6.85 (d, *J* = 11.0 Hz, 1H), 6.69 – 6.64 (m, 4H), 6.53 (d, *J* = 5.3 Hz, 1H), 3.78 (s, 3H), 2.25 (s, 3H), 2.19 (s, 3H), 2.08 (s, 3H), 2.06 (s, 3H), 1.24 (s, 9H).

¹³C NMR (101 MHz, CDCl₃): δ 167.59, 150.47, 148.36, 148.29, 143.40, 139.97, 138.76, 138.72, 136.53, 135.74, 131.75, 130.19, 129.23, 126.86, 126.84, 126.33, 125.55, 124.66, 114.37, 51.76, 34.61, 31.32, 23.26, 23.13, 21.47, 21.22.

¹¹B NMR (128 MHz, CDCl₃): δ 39.5.

IR (KBr, neat): 2947, 1720, 1585, 1560, 1474, 1437, 1375, 1350, 1290, 1254, 1189, 1131, 1089, 1050, 967, 880, 851, 818, 772, 754, 739, 709, 670 cm⁻¹.

HRMS (ESI-TOF): *m/z* calcd for C₃₂H₃₇BNO₂⁺ [M+H⁺]: 478.2912. Found: 478.2915.



Yield: 18% (a 1:1 mixture of 2 rotamers, reaction performed at 120 °C)

Physical appearance: white solid, **m.p.:** 124-126 °C

R_f: 0.65 (EtOAc:hexanes = 1:9)

¹H NMR (400 MHz, CDCl₃): δ 7.76 (d, *J* = 8.9 Hz, 1H), 7.69 (dd, *J* = 10.9, 6.9 Hz, 1H), 6.92 – 6.90 (m, 2H), 6.62 (dd, *J* = 10.9, 1.3 Hz, 1H), 6.58 (s, 2H), 6.40 (dd, *J* = 7.0, 1.4 Hz, 1H), 3.85 (s, 3H), 2.49 (s, 3H), 2.23 – 2.17 (m, 1H), 2.15 (s, 3H), 2.05 (s, 3H), 2.03 (s, 3H), 1.80 (d, *J* = 12.9 Hz, 2H), 1.69– 1.66 (m, 2H), 1.59 (d, *J* = 13.4 Hz, 1H), 1.41 – 1.28 (m, 2H), 1.23 – 1.11 (m, 1H), 1.01 – 0.90 (m, 2H).

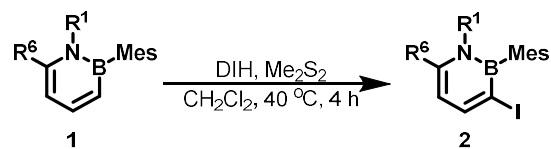
¹³C NMR (101 MHz, CDCl₃): δ 167.57, 153.91, 147.88, 143.78, 140.74, 138.45, 138.39, 136.24, 130.90, 130.47, 127.65, 126.72, 126.69, 124.45, 108.56, 51.93, 40.99, 34.40, 34.19, 26.70, 26.03, 23.36, 23.30, 21.79, 21.19.

¹¹B NMR (128 MHz, CDCl₃): δ 38.8.

IR (KBr, neat): 2928, 2853, 1724, 1599, 1522, 1493, 1434, 1412, 1397, 1345, 1255, 1207, 1191, 1140, 1087, 1017, 847, 764, 710 cm⁻¹.

HRMS (ESI-TOF): *m/z* calcd for C₂₈H₃₅BNO₂⁺ [M+H⁺]: 428.2755. Found: 428.2761.

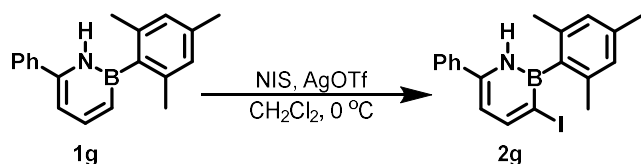
1.5.5. General procedure for the iodination of 1,2-azaborines **2a-2f** and **2h-2m**:



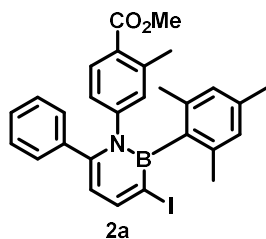
In a 4 mL reaction vial, **1** (0.5 mmol) was dissolved in dichloromethane (10.0 ml). 1,3-Diiodo-5,5-dimethylhydantoin (DIH, 142.5 mg, 0.375 mmol, 0.75 equiv) and Me₂S₂ (2.4 mg, 0.025 mmol, 0.05 equiv) were added sequentially, then the vial was tightly sealed and stirred on a pie-block preheated to 40 °C (for **2i**, 0.75 mmol DIH was used at a reaction temperature of 60 °C, and for **2m**, the reaction was run at r.t.). After 4 h, the reaction mixture was cooled down to r.t., quenched

with triethylamine (1.0 mmol, 2 equiv, 0.14 mL), and concentrated under reduced pressure. The crude mixture was subjected to flash column chromatography on silica gel (EtOAc:hexanes = 1:20 to 1:9) to give the desired azaborine iodide **2**.

1.5.6. Synthetic procedure for the iodination of 1,2-azaborine **2g**:



In a 4 mL reaction vial, **1g** (136.6 mg, 0.5 mmol, 1 equiv) was dissolved in dichloromethane (5.0 ml) and cooled down to 0 °C. Silver triflate (25.7 mg, 0.1 mmol, 0.2 equiv) and *N*-iodosuccinimide (NIS, 123.7 mg, 0.55 mmol, 0.75 equiv) were added sequentially. Upon completion of the reaction, all volatiles were removed under reduced pressure. The crude mixture was subjected to flash column chromatography on silica gel (EtOAc:hexanes = 1:20) to give the desired azaborine iodide **2g**.



Yield: 75% (a 1:1 mixture of 2 rotamers)

Physical appearance: off-white solid, **m.p.:** 64-66 °C

R_f: 0.3 (EtOAc:hexanes = 1:9)

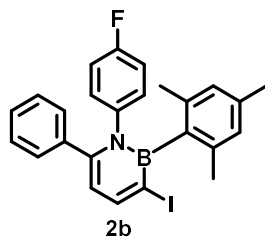
¹H NMR (400 MHz, CDCl₃): δ 8.35 (d, *J* = 7.4 Hz, 1H), 7.49 (d, *J* = 8.1 Hz, 1H), 7.15 – 7.13 (m, 3H), 7.10 – 7.08 (m, 2H), 6.67 (s, 1H), 6.65 (d, *J* = 2.4 Hz, 1H), 6.63 (d, *J* = 6.4 Hz, 2H), 6.30 (d, *J* = 7.4 Hz, 1H), 3.76 (s, 3H), 2.26 (s, 3H), 2.18 (s, 3H), 2.07 (s, 3H), 2.05 (s, 3H).

¹³C NMR (101 MHz, CDCl₃): δ 167.27, 151.35, 148.86, 147.81, 140.25, 138.14, 138.13, 137.79, 137.06, 131.20, 130.35, 129.25, 127.94, 127.84, 126.93, 126.88, 125.08, 115.29, 51.79, 22.54, 21.48, 21.36.

¹¹B NMR (128 MHz, CDCl₃): δ 39.3.

IR (KBr, neat): 3025, 2948, 2913, 2855, 1722, 1866, 1608, 1589, 1572, 1506, 1488, 1445, 1435, 1361, 1339, 1257, 1191, 1169, 1142, 1105, 1084, 1023, 987, 966, 916, 884, 849, 819, 786, 763, 737, 700 cm⁻¹.

HRMS (ESI-TOF): *m/z* calcd for C₂₈H₂₈BINO₂⁺ [M+H⁺]: 548.1252. Found: 548.1256.



Yield: 55%

Physical appearance: white solid, **m.p.:** 67-69 °C

R_f: 0.55 (EtOAc:hexanes = 1:9)

¹H NMR (400 MHz, CDCl₃): δ 8.35 (d, *J* = 7.4 Hz, 1H), 7.16 – 7.14 (m, 3H), 7.10 – 7.07 (m, 2H), 6.75 (dd, *J* = 8.8, 4.8 Hz, 2H), 6.65 (s, 2H), 6.59 (t, *J* = 8.6 Hz, 2H), 6.29 (d, *J* = 7.3 Hz, 1H), 2.20 (s, 3H), 2.07 (s, 6H).

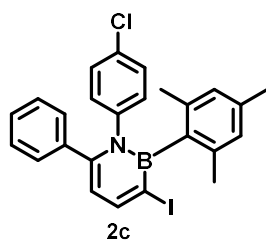
¹³C NMR (126 MHz, CDCl₃): δ 160.61 (d, ¹J_{C-F} = 246.1 Hz), 151.35, 149.41, 140.88 (d, ⁴J_{C-F} = 3.2 Hz), 138.16, 137.97, 137.08, 129.46, 129.11 (d, ³J_{C-F} = 8.5 Hz), 127.96, 127.75, 126.94, 115.15, 114.54 (d, ²J_{C-F} = 22.6 Hz), 22.57, 21.41.

¹¹B NMR (128 MHz, CDCl₃): δ 39.2.

¹⁹F NMR (376 MHz, CDCl₃): δ -115.65.

IR (KBr, neat): 2914, 2853, 1609, 1588, 1572, 1506, 1487, 1444, 1363, 1340, 1234, 1218, 1172, 1153, 1095, 1029, 1014, 980, 839, 824, 763, 740, 699, 599 cm⁻¹.

HRMS (ESI-TOF): m/z calcd for [M+H⁺]: 494.0947. Found: 494.0943.



Yield: 75%

Physical appearance: off-white solid, **m.p.:** 73-75 °C

R_f: 0.55 (EtOAc:hexanes = 1:9)

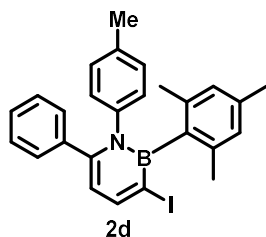
¹H NMR (400 MHz, CDCl₃): δ 8.34 (d, *J* = 7.4 Hz, 1H), 7.17 – 7.15 (m, 3H), 7.09 – 7.06 (m, 2H), 6.87 (d, *J* = 8.6 Hz, 2H), 6.72 (d, *J* = 8.7 Hz, 2H), 6.65 (s, 2H), 6.29 (d, *J* = 7.3 Hz, 1H), 2.21 (s, 3H), 2.06 (s, 6H).

¹³C NMR (101 MHz, CDCl₃): δ 151.40, 149.14, 143.44, 138.15, 137.84, 137.16, 131.93, 129.41, 128.96, 128.03, 127.84, 127.01, 115.30, 22.58, 21.43.

¹¹B NMR (128 MHz, CDCl₃): δ 40.2.

IR (KBr, neat): 3027, 2911, 2855, 1609, 1587, 1560, 1507, 1489, 1459, 1444, 1401, 1363, 1339, 1279, 1264, 1240, 1171, 1091, 1029, 1015, 980, 849, 833, 778, 762, 738, 715, 699 cm^{-1} .

HRMS (ESI-TOF): m/z calcd for $\text{C}_{25}\text{H}_{23}\text{BClIN}^+$ $[\text{M}+\text{H}^+]$: 510.0651. Found: 510.0651.



Yield: 74%

Physical appearance: off-white solid, **m.p.:** 169-171 $^{\circ}\text{C}$

R_f: 0.55 (EtOAc:hexanes = 1:9)

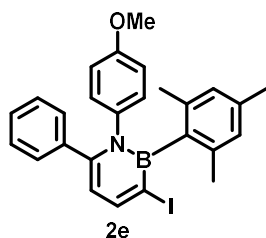
¹H NMR (500 MHz, CDCl₃): δ 8.33 (d, $J = 7.4$ Hz, 1H), 7.14 – 7.08 (m, 5H), 6.67 (s, 4H), 6.64 (s, 2H), 6.27 (d, $J = 7.4$ Hz, 1H), 2.19 (s, 3H), 2.08 (s, 3H), 2.07 (s, 6H).

¹³C NMR (126 MHz, CDCl₃): δ 151.15, 149.73, 142.27, 138.36, 138.27, 136.73, 135.75, 129.44, 128.25, 127.74, 127.47, 127.38, 126.78, 115.04, 22.62, 21.44, 21.01.

¹¹B NMR (128 MHz, CDCl₃): δ 40.1.

IR (KBr, neat): 3029, 2916, 2854, 1610, 1588, 1572, 1509, 1487, 1444, 1362, 1339, 1308, 1280, 1237, 1172, 1109, 1083, 1021, 980, 909, 848, 822, 763, 736, 699, 658, 647, 601, 544 cm^{-1} .

HRMS (ESI-TOF): m/z calcd for $\text{C}_{26}\text{H}_{26}\text{BIN}^+$ $[\text{M}+\text{H}^+]$: 490.1197. Found: 490.1200.



Yield: 73%

Physical appearance: light yellow solid, **m.p.:** 168-170 °C

R_f: 0.5 (EtOAc:hexanes = 1:9)

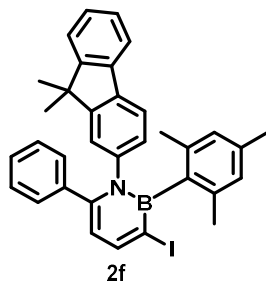
¹H NMR (400 MHz, CDCl₃): δ 8.33 (d, *J* = 7.4 Hz, 1H), 7.15 – 7.13 (m, 3H), 7.11 – 7.08 (m, 2H), 6.70 (d, *J* = 8.8 Hz, 2H), 6.65 (s, 2H), 6.41 (d, *J* = 8.8 Hz, 2H), 6.27 (d, *J* = 7.4 Hz, 1H), 3.60 (s, 3H), 2.20 (s, 3H), 2.08 (s, 6H).

¹³C NMR (101 MHz, CDCl₃): δ 157.41, 151.14, 149.85, 138.30, 138.19, 137.92, 136.72, 129.41, 128.48, 127.81, 127.48, 126.83, 114.99, 112.73, 55.20, 22.60, 21.40.

¹¹B NMR (128 MHz, CDCl₃): δ 39.9.

IR (KBr, neat): 2916, 2852, 1609, 1586, 1571, 1508, 1487, 1442, 1364, 1339, 1298, 1256, 1171, 1107, 1033, 979, 832, 763, 738, 699, 602 cm⁻¹.

HRMS (ESI-TOF): *m/z* calcd for C₂₆H₂₆BINO⁺ [*M*+H⁺]: 506.1147. Found: 506.1153.



Yield: 67% (a 1:1 mixture of 2 rotamers)

Physical appearance: white solid, **m.p.:** 136-138 °C

R_f: 0.6 (EtOAc:hexanes = 1:9)

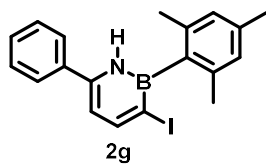
¹H NMR (500 MHz, CDCl₃): δ 8.37 (d, *J* = 7.4 Hz, 1H), 7.50 (d, *J* = 6.4 Hz, 1H), 7.32 – 7.30 (m, 1H), 7.26 – 7.22 (m, 3H), 7.15 – 7.13 (m, 2H), 7.09 – 7.06 (m, 3H), 6.78 (s, 1H), 6.72 (dd, *J* = 8.0, 2.0 Hz, 1H), 6.61 (s, 1H), 6.59 (s, 1H), 6.34 (d, *J* = 7.4 Hz, 1H), 2.12 (s, 6H), 2.09 (s, 3H), 1.14 (s, 3H), 1.12 (s, 3H).

¹³C NMR (126 MHz, CDCl₃): δ 153.76, 153.04, 151.19, 149.64, 143.95, 138.69, 138.32, 138.15, 136.87, 136.74, 129.46, 127.80, 127.52, 127.23, 127.06, 126.88, 126.53, 122.70, 120.01, 118.96, 114.97, 46.55, 26.76, 26.38, 22.60, 22.58, 21.30.

¹¹B NMR (128 MHz, CDCl₃): δ 39.8.

IR (KBr, neat): 2958, 2919, 2856, 1610, 1586, 1571, 1506, 1488, 1472, 1459, 1448, 1421, 1361, 1339, 1297, 1279, 1171, 1155, 1101, 1075, 1028, 995, 847, 828, 761, 738, 698 cm⁻¹.

HRMS (ESI-TOF): *m/z* calcd for C₃₄H₃₂BIN⁺ [M+H⁺]: 592.1667. Found: 592.1664.



Yield: 74% (87% purity)

Physical appearance: off-white oil

R_f: 0.6 (EtOAc:hexanes = 1:9)

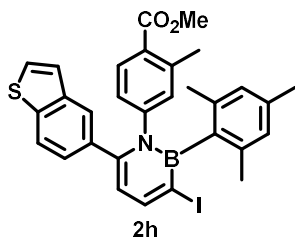
¹H NMR (500 MHz, CDCl₃): δ 8.39 (d, *J* = 7.5 Hz, 1H), 8.09 (N-H, br, 1H), 7.57 (d, *J* = 7.1 Hz, 2H), 7.48 – 7.42 (m, 3H), 6.92 (s, 2H), 6.49 (dd, *J* = 7.5, 2.5 Hz, 1H), 2.35 (s, 3H), 2.20 (s, 6H).

¹³C NMR (126 MHz, CDCl₃): δ 152.51, 145.47, 139.99, 138.00, 137.23, 129.45, 129.36, 127.28, 125.87, 110.47, 22.72, 21.45.

^{11}B NMR (160 MHz, CDCl_3): δ 38.0.

IR (KBr, neat): 3363 (br), 2915, 2853, 1608, 1573, 1528, 1490, 1446, 1374, 1304, 1287, 1182, 1156, 1104, 1077, 1029, 990, 959, 849, 818, 755, 728, 695 cm^{-1} .

HRMS (ESI-TOF): m/z calcd for $\text{C}_{19}\text{H}_{20}\text{BIN}^+$ [$\text{M}+\text{H}^+$]: 400.0728. Found: 400.0727.



Yield: 67% (a 1:1 mixture of 2 rotamers)

Physical appearance: white solid, **m.p.:** 88-90 $^{\circ}\text{C}$

R_f : 0.3 (EtOAc:hexanes = 1:9)

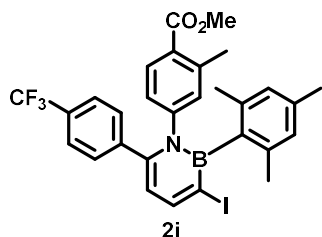
^1H NMR (500 MHz, CDCl_3): δ 8.36 (d, $J = 7.3$ Hz, 1H), 7.67 (s, 1H), 7.58 (d, $J = 8.4$ Hz, 1H), 7.46 (d, $J = 8.4$ Hz, 1H), 7.42 (d, $J = 5.4$ Hz, 1H), 7.24 (d, $J = 5.5$ Hz, 1H), 6.98 (dd, $J = 8.4, 1.8$ Hz, 1H), 6.74 (s, 1H), 6.69 (dd, $J = 8.4, 2.2$ Hz, 1H), 6.65 (s, 1H), 6.61 (s, 1H), 6.35 (d, $J = 7.4$ Hz, 1H), 3.73 (s, 3H), 2.24 (s, 3H), 2.19 (s, 3H), 2.12 (s, 3H), 2.04 (s, 3H).

^{13}C NMR (126 MHz, CDCl_3): δ 167.22, 151.39, 148.89, 147.85, 140.33, 139.29, 139.24, 138.18, 138.12, 137.09, 134.15, 131.17, 130.45, 127.44, 126.96, 126.94, 126.90, 125.33, 125.13, 124.33, 123.93, 121.87, 115.77, 51.77, 22.61, 22.54, 21.54, 21.38.

^{11}B NMR (160 MHz, CDCl_3): δ 39.5.

IR (KBr, neat): 2947, 1718, 1684, 1608, 1585, 1541, 1495, 1473, 1457, 1436, 1362, 1340, 1254, 1187, 1142, 1105, 1086, 1050, 1023, 997, 880, 848, 808, 782, 763, 737, 707, 682, 669 cm^{-1} .

HRMS (ESI-TOF): m/z calcd for $\text{C}_{30}\text{H}_{28}\text{BINO}_2\text{S}^+$ [$\text{M}+\text{H}^+$]: 604.0973. Found: 604.0974.



Yield: 56% (a 1:1 mixture of 2 rotamers)

Physical appearance: white solid, **m.p.:** 168-170 °C

R_f: 0.3 (EtOAc:hexanes = 1:9)

¹H NMR (400 MHz, CDCl₃): δ 8.37 (d, *J* = 7.4 Hz, 1H), 7.52 (d, *J* = 8.2 Hz, 1H), 7.41 (d, *J* = 8.2 Hz, 2H), 7.24 (d, *J* = 8.1 Hz, 2H), 6.69 – 6.62 (m, 4H), 6.29 (d, *J* = 7.4 Hz, 1H), 3.78 (s, 3H), 2.27 (s, 3H), 2.19 (s, 3H), 2.08 (s, 3H), 2.03 (s, 3H).

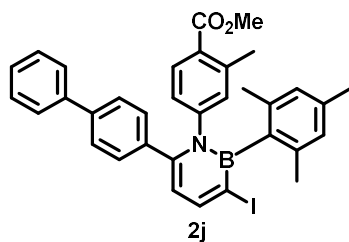
¹³C NMR (151 MHz, CDCl₃): δ 167.15, 151.26, 147.35, 147.12, 141.42, 140.63, 138.14, 138.11, 137.31, 131.05, 130.67, 129.90 (q, ²*J*_{C-CF₃} = 32.7 Hz), 129.55, 127.39, 127.04, 126.98, 125.05, 125.03, 125.00, 124.99, 124.98, 123.92 (q, ¹*J*_{C-CF₃} = 272.4 Hz), 115.76, 51.92, 22.57, 22.55, 21.55, 21.39.

¹¹B NMR (128 MHz, CDCl₃): δ 40.3.

¹⁹F NMR (376 MHz, CDCl₃): δ -62.71.

IR (KBr, neat): 2919, 1723, 1609, 1592, 1570, 1496, 1435, 1409, 1364, 1324, 1257, 1168, 1128, 1110, 1084, 1065, 1017, 885, 848, 816, 780, 757, 706, 678 cm⁻¹.

HRMS (ESI-TOF): *m/z* calcd for C₂₉H₂₇BF₃INO₂⁺ [*M*+H⁺]: 616.1126. Found: 616.1128.



Yield: 70% (a 1:1 mixture of 2 rotamers)

Physical appearance: off-white solid, **m.p.:** 88-90 °C

R_f: 0.4 (EtOAc:hexanes = 1:9)

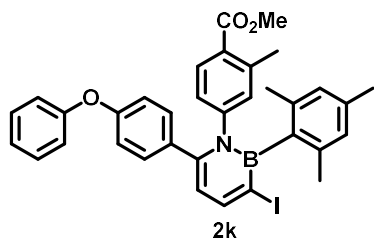
¹H NMR (400 MHz, CDCl₃): δ 8.37 (d, *J* = 7.4 Hz, 1H), 7.52 (d, *J* = 8.2 Hz, 3H), 7.42 – 7.38 (m, 4H), 7.33 (t, *J* = 7.3 Hz, 1H), 7.17 (d, *J* = 8.4 Hz, 2H), 6.74 – 6.70 (m, 2H), 6.65 (d, *J* = 10.6 Hz, 2H), 6.36 (d, *J* = 7.4 Hz, 1H), 3.76 (s, 3H), 2.28 (s, 3H), 2.20 (s, 3H), 2.11 (s, 3H), 2.06 (s, 3H).

¹³C NMR (101 MHz, CDCl₃): δ 167.27, 151.40, 148.54, 147.85, 140.44, 140.36, 140.14, 138.18, 138.15, 137.11, 136.77, 131.20, 130.48, 129.69, 128.91, 127.72, 127.06, 127.03, 126.97, 126.91, 126.56, 125.13, 115.44, 51.80, 22.59, 22.56, 21.55, 21.39.

¹¹B NMR (128 MHz, CDCl₃): δ 41.1.

IR (KBr, neat): 2947, 1722, 1608, 1588, 1495, 1484, 1434, 1403, 1336, 1256, 1191, 1142, 1085, 1022, 1007, 881, 845, 813, 778, 767, 740, 698 cm⁻¹.

HRMS (ESI-TOF): *m/z* calcd for C₃₄H₃₂BINO₂⁺ [M+H⁺]: 624.1565. Found: 624.1567.



Yield: 75% (a 1:1 mixture of 2 rotamers, 94% purity)

Physical appearance: off-white solid, **m.p.:** 75-77 °C

R_f: 0.4 (EtOAc:hexanes = 1:9)

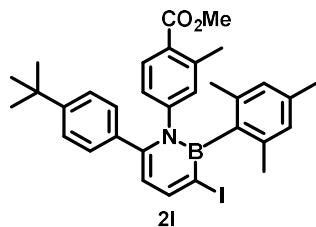
¹H NMR (400 MHz, CDCl₃): δ 8.35 (d, *J* = 7.4 Hz, 1H), 7.54 (d, *J* = 9.0 Hz, 1H), 7.33 – 7.29 (m, 2H), 7.10 (t, *J* = 7.6 Hz, 1H), 7.05 (dd, *J* = 8.7, 1.8 Hz, 2H), 6.89 (d, *J* = 7.6 Hz, 2H), 6.77 (d, *J* = 8.7 Hz, 2H), 6.70 – 6.64 (m, 4H), 6.31 (d, *J* = 7.4 Hz, 1H), 3.80 (s, 3H), 2.31 (s, 3H), 2.19 (s, 3H), 2.07 (s, 6H).

¹³C NMR (101 MHz, CDCl₃): δ 167.28, 156.88, 156.85, 151.38, 148.32, 147.89, 140.31, 138.15, 137.12, 132.78, 131.27, 130.83, 130.46, 129.92, 127.03, 126.97, 126.93, 125.16, 123.69, 119.05, 118.24, 115.13, 51.87, 22.60, 22.55, 21.55, 21.39.

¹¹B NMR (128 MHz, CDCl₃): δ 42.0.

IR (KBr, neat): 2948, 1722, 1608, 1589, 1512, 1488, 1434, 1360, 1336, 1241, 1192, 1168, 1142, 1104, 1085, 1022, 870, 846, 811, 783, 749, 706, 693 cm⁻¹.

HRMS (ESI-TOF): *m/z* calcd for C₃₄H₃₂BINO₃⁺ [M+H⁺]: 640.1514. Found: 640.1512.



Yield: 61% (a 1:1 mixture of 2 rotamers)

Physical appearance: off-white solid, **m.p.:** 81-83 °C

R_f: 0.5 (EtOAc:hexanes = 1:9)

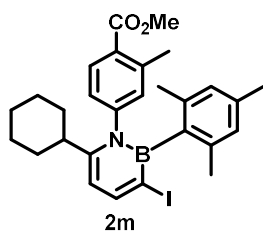
¹H NMR (400 MHz, CDCl₃): δ 8.33 (d, *J* = 7.4 Hz, 1H), 7.50 (d, *J* = 8.2 Hz, 1H), 7.14 (d, *J* = 8.0 Hz, 2H), 7.00 (d, *J* = 8.0 Hz, 2H), 6.67 (d, *J* = 10.8 Hz, 2H), 6.63 (s, 2H), 6.30 (d, *J* = 7.3 Hz, 1H), 3.77 (s, 3H), 2.25 (s, 3H), 2.19 (s, 3H), 2.06 (s, 6H), 1.23 (s, 9H).

¹³C NMR (101 MHz, CDCl₃): δ 167.41, 151.43, 150.95, 149.01, 147.95, 140.16, 138.20, 138.18, 137.04, 134.86, 131.26, 130.31, 129.01, 126.94, 126.89, 126.83, 125.12, 124.83, 115.27, 51.82, 34.65, 31.27, 22.60, 22.54, 21.45, 21.39.

¹¹B NMR (128 MHz, CDCl₃): δ 40.6.

IR (KBr, neat): 2963, 2868, 1723, 1609, 1589, 1494, 1435, 1402, 1362, 1336, 1257, 1192, 1169, 1142, 1114, 1086, 1018, 988, 884, 841, 814, 776, 737, 705, 581 cm⁻¹.

HRMS (ESI-TOF): *m/z* calcd for C₃₂H₃₆BINO₂⁺ [*M*+H⁺]: 604.1878. Found: 604.1881.



Yield: 74% (a 1:1 mixture of 2 rotamers, reaction performed at r.t.)

Physical appearance: white solid, **m.p.:** 145-147 °C

R_f: 0.55 (EtOAc:hexanes = 1:9)

¹H NMR (400 MHz, CDCl₃): δ 8.24 (d, *J* = 7.6 Hz, 1H), 7.76 (d, *J* = 8.9 Hz, 1H), 6.90 – 6.88 (m, 2H), 6.57 (s, 2H), 6.19 (d, *J* = 7.7 Hz, 1H), 3.85 (s, 3H), 2.48 (s, 3H), 2.15 (s, 3H), 2.12 – 2.06 (m, 1H), 2.03 (s, 3H), 2.01 (s, 3H), 1.78 (d, *J* = 12.9 Hz, 2H), 1.68 – 1.65 (m, 2H), 1.58 (d, *J* = 13.3 Hz, 1H), 1.38 – 1.24 (m, 2H), 1.20 – 1.10 (m, 1H), 0.98 – 0.88 (m, 2H).

^{13}C NMR (126 MHz, CDCl_3): δ 167.40, 154.81, 151.56, 147.31, 141.00, 137.90, 137.88, 136.77, 131.08, 129.87, 128.11, 126.82, 126.78, 123.87, 110.12, 51.99, 41.09, 34.19, 33.98, 26.54, 25.89, 22.62, 22.60, 21.76, 21.37.

^{11}B NMR (160 MHz, CDCl_3): δ 38.6.

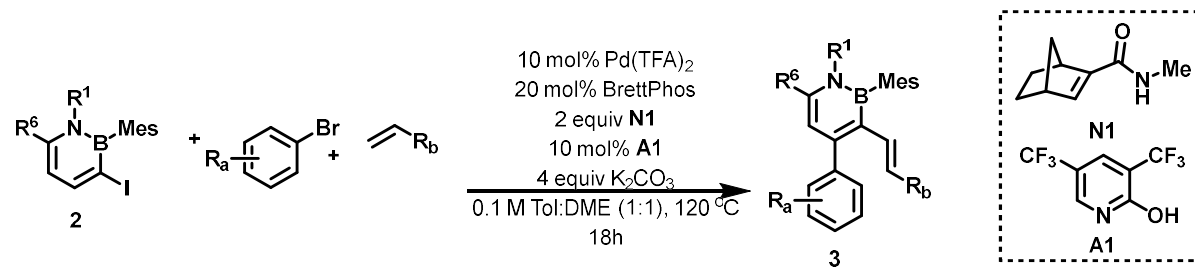
IR (KBr, neat): 2929, 2853, 1724, 1609, 1592, 1502, 1448, 1397, 1348, 1283, 1255, 1191, 1163, 1132, 1107, 1086, 1023, 996, 910, 885, 847, 808, 784, 734, 639 cm^{-1} .

HRMS (ESI-TOF): m/z calcd for $\text{C}_{28}\text{H}_{34}\text{BINO}_2^+$ [$\text{M}+\text{H}^+$]: 554.1722. Found: 554.1721.

1.5.7. Preparation of modified norbornenes and CMD reagents:

N1,⁴² **N3**,⁴³ **N4**,⁴⁴ and **A1**³⁵ are known compounds and were synthesized according to previous reports. **N2** and **A2** are commercially available.

1.5.8. Synthetic procedure of **3aa-3ap** and **3b-3m**:

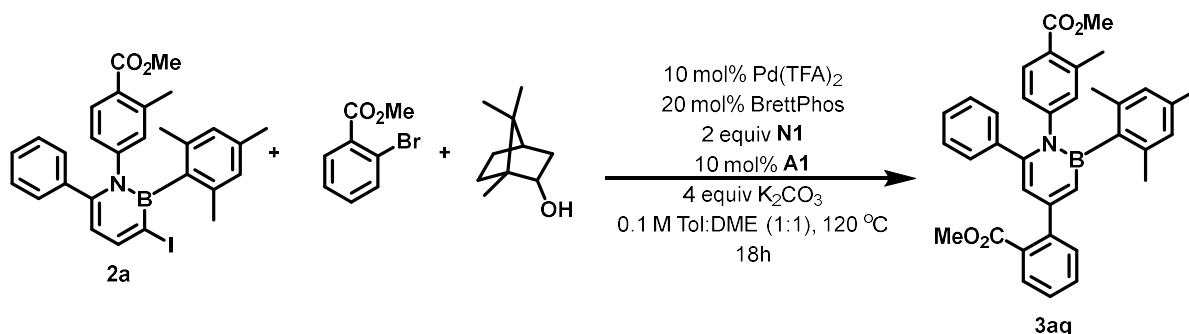


To a flame-dried 4 mL vial A, **2** (0.1 mmol, 1 equiv), Ar-Br (0.1 mmol, 1 equiv), alkene (0.105 mmol, 1.05 equiv), **N1** (30.2 mg, 0.2 mmol, 2 equiv), **A1** (2.3 mg, 0.01 mmol, 10 mol%), and K_2CO_3 (55.3 mg, 0.4 mmol, 4 equiv) were added. In a separate flame-dried 4 mL vial B, $\text{Pd}(\text{TFA})_2$ (3.3 mg, 0.01 mmol, 10 mol%) and BrettPhos (10.7 mg, 0.02 mmol, 20 mol%) were added. Both vials were brought into the glovebox, and 0.5 mL of DME and 0.5 mL of toluene were added to vial A and vial B, respectively. After stirring for 10 minutes, the solution in vial B was transferred

to vial A. The tightly sealed vial was then placed on a pie-block preheated to 120 °C. After 18 h, the reaction mixture was filtered through a pad of celite and washed with ethyl acetate. The crude solution was concentrated to dryness in vacuo and was subjected to flash column chromatography on silica gel (EtOAc:hexanes = 1:20 to 1:2) to give the pentasubstituted 1,2-azaborine **3**.

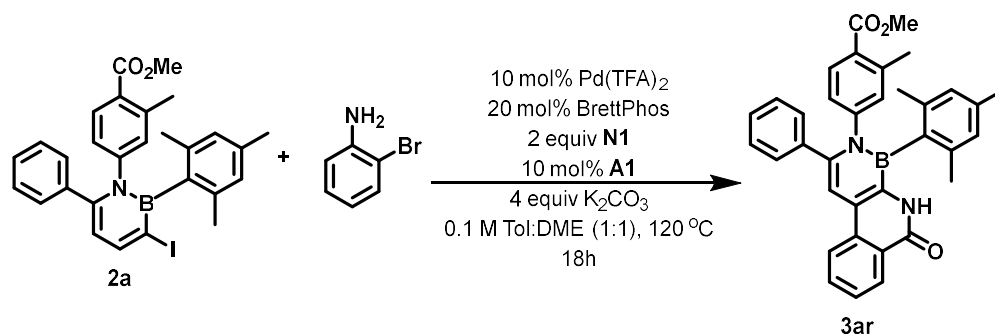
Note: the purity of all the materials, especially **N1** and **A1**, are important for the reaction.

1.5.9. Synthetic procedure of **3aq**:



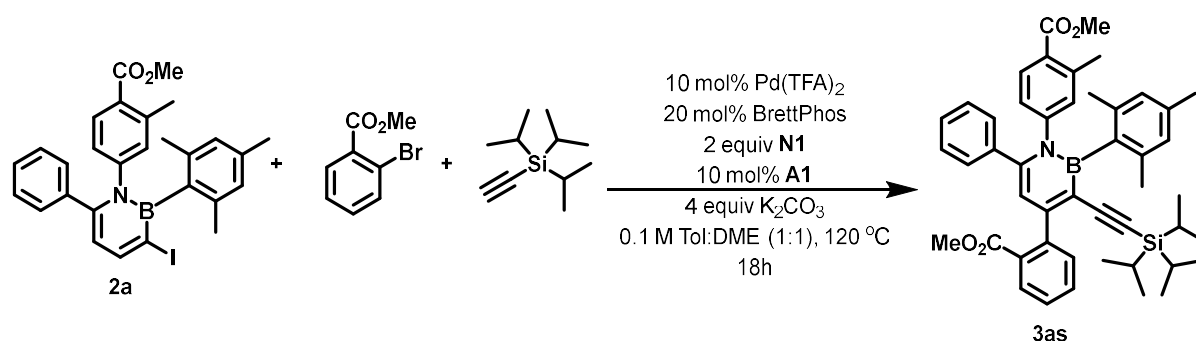
To a flame-dried 4 mL vial A, **2a** (54.7 mg, 0.1 mmol, 1 equiv), Ar-Br (21.5 mg, 0.1 mmol, 1 equiv), borneol (16.2 mg, 0.105 mmol, 1.05 equiv), **N1** (30.2 mg, 0.2 mmol, 2 equiv), **A1** (2.3 mg, 0.01 mmol 10 mol%), and K_2CO_3 (55.3 mg, 0.4 mmol, 4 equiv) were added. In a separate flame-dried 4 mL vial B, $\text{Pd}(\text{TFA})_2$ (10 mol%, 3.3 mg) and BrettPhos (20 mol%, 10.7 mg) were added. Both vials were brought into the glovebox, and 0.5 mL of DME and 0.5 mL of toluene were added to vial A and vial B, respectively. After stirring for 10 minutes, the solution in vial B was transferred to vial A. The tightly sealed vial was then placed on a pie-block preheated to 120 °C. After 18 h, the reaction mixture was filtered through a pad of celite and washed with ethyl acetate. The crude solution was concentrated to dryness in vacuo and was subjected to flash column chromatography on silica gel (EtOAc:hexanes = 1:20 to 1:9) to give **3aq**.

1.5.10. Synthetic procedure of **3ar**:



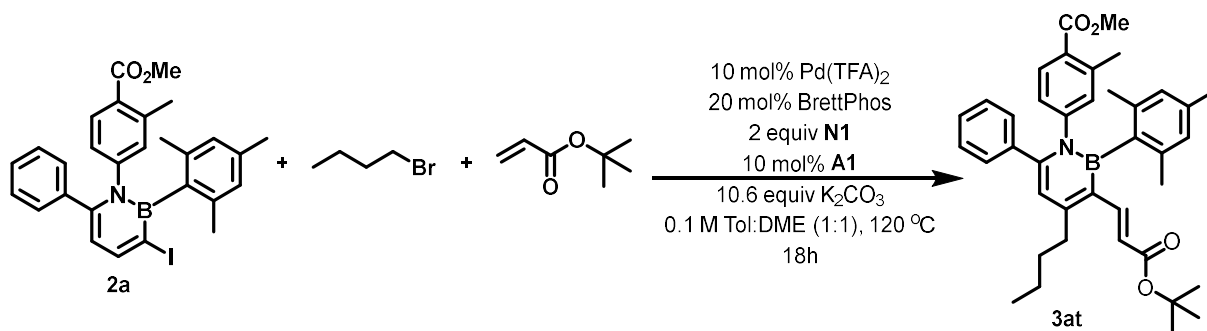
To a flame-dried 4 mL vial A, **2a** (54.7 mg, 0.1 mmol, 1 equiv), 2-bromobenzamide (20.0 mg, 0.1 mmol, 1 equiv), **N1** (30.2 mg, 0.2 mmol, 4 equiv), **A1** (2.3 mg, 0.01 mmol, 10 mol%), and K₂CO₃ (55.3 mg, 0.4 mmol, 4 equiv) were added. In a separate flame-dried 4 mL vial B, Pd(TFA)₂ (3.3 mg, 0.01 mmol, 10 mol%) and BrettPhos (10.7 mg, 0.02 mmol, 20 mol%) were added. Both vials were brought into the glovebox, and 0.5 mL of DME and 0.5 mL of toluene were added to vial A and vial B, respectively. After stirring for 10 minutes, the solution in vial B was transferred to vial A. The tightly sealed vial was then placed on a pie-block preheated to 120 °C. After 18 h, the reaction mixture was filtered through a pad of celite and washed with ethyl acetate. The crude solution was concentrated to dryness in vacuo and was subjected to flash column chromatography on silica gel (EtOAc:hexanes = 1:20 to 1:9) to give **3ar**.

1.5.11. Synthetic procedure of **3as**:



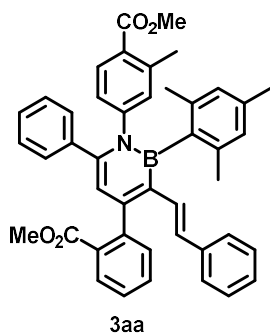
To a flame-dried 4 mL vial A, **2a** (54.7 mg, 0.1 mmol, 1 equiv), Ar-Br (21.5 mg, 0.1 mmol, 1 equiv), (triisopropylsilyl)acetylene (19.1 mg, 0.105 mmol, 1.05 equiv), **N1** (30.2 mg, 0.2 mmol, 2 equiv), **A1** (2.3 mg, 0.01 mmol, 10 mol%), and K₂CO₃ (55.3 mg, 0.4 mmol, 4 equiv) were added. In a separate flame-dried 4 mL vial B, Pd(TFA)₂ (3.3 mg, 0.01 mmol, 10 mol%) and BrettPhos (10.7 mg, 0.02 mmol, 20 mol%) were added. Both vials were brought into the glovebox, and 0.5 mL of DME and 0.5 mL of toluene were added to vial A and vial B, respectively. After stirring for 10 minutes, the solution in vial B was transferred to vial A. The tightly sealed vial was then placed on a pie-block preheated to 120 °C. After 18 h, the reaction mixture was filtered through a pad of celite and washed with ethyl acetate. The crude solution was concentrated to dryness in vacuo and was subjected to flash column chromatography on silica gel (EtOAc:hexanes = 1:20 to 1:9) to give **3as**.

1.5.12. Synthetic procedure of **3at**:



To a flame-dried 4 mL vial A, **2a** (54.7 mg, 0.1 mmol, 1 equiv), 1-bromobutane (91.4 mg, 0.667 mmol, 6.67 equiv), *tert*-butyl acrylate (13.5 mg, 0.105 mmol, 1.05 equiv), **N1** (30.2 mg, 0.2 mmol, 2 equiv), **A1** (2.3 mg, 0.01 mmol, 10 mol%), and K₂CO₃ (146.5 mg, 1.06 mmol, 10.6 equiv) were added. In a separate flame-dried 4 mL vial B, Pd(TFA)₂ (3.3 mg, 0.01 mmol, 10 mol%) and BrettPhos (10.7 mg, 0.02 mmol, 20 mol%) were added. Both vials were brought into the glovebox,

and 0.5 mL of DME and 0.5 mL of toluene were added to vial A and vial B, respectively. After stirring for 10 minutes, the solution in vial B was transferred to vial A. The tightly sealed vial was then placed on a pie-block preheated to 120 °C. After 18 h, the reaction mixture was filtered through a pad of celite and washed with ethyl acetate. The crude solution was concentrated to dryness in vacuo and was subjected to flash column chromatography on silica gel (EtOAc:hexanes = 1:20 to 1:9) to give **3at**.



Yield: 47.9 mg (73%, a 1:1:1:1 mixture of 4 rotamers)

Physical appearance: yellow solid, **m.p.:** 210-212 °C

R_f: 0.25 (EtOAc:hexanes = 1:9)

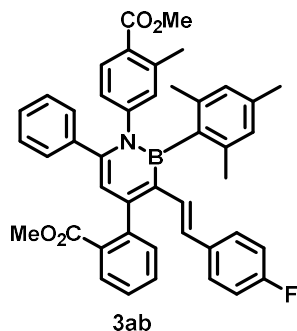
¹H NMR (400 MHz, CDCl₃): δ 7.98 (d, *J* = 7.7 Hz, 1H), 7.58 (t, *J* = 7.5 Hz, 1H), 7.52 (t, *J* = 7.8 Hz, 1H), 7.48 – 7.39 (m, 2H), 7.14 – 7.09 (m, 7H), 7.02 (t, *J* = 7.2 Hz, 1H), 6.81 – 6.77 (m, 4H), 6.73 (d, *J* = 9.4 Hz, 1H), [6.67 (s) + 6.64 (s) + 6.62 (s) = 2H], 6.45 (s, 1H), 5.94 (d, *J* = 16.3 Hz, 1H), 3.78 (s, 3H), 3.65 (s, 3H), [2.30 (s) + 2.28 (s) = 3H], 2.21 (s, 3H), [2.15 (s) + 2.10 (s) = 3H], [2.10 (s) + 2.06 (s) = 3H].

¹³C NMR (101 MHz, CDCl₃): δ 168.21, 167.50, 153.27, 148.16, 146.16, 143.41, 140.06, 139.21, 138.39, 138.35, 138.31, 136.67, 131.82, 131.79, 131.62, 131.09, 130.88, 130.45, 130.20, 130.09, 129.88, 129.54, 128.28, 127.80, 127.48, 127.26, 127.20, 127.12, 127.05, 126.49, 126.13, 125.68, 125.63, 116.98, 52.04, 51.76, 22.89, 22.45, 21.55, 21.53, 21.30.

¹¹B NMR (128 MHz, CDCl₃): δ 39.6.

IR (KBr, neat): 2948, 1723, 1587, 1570, 1473, 1446, 1434, 1375, 1351, 1291, 1255, 1190, 1166, 1132, 1089, 1031, 968, 850, 773, 751, 539, 699 cm⁻¹.

HRMS (ESI-TOF): m/z calcd for C₄₄H₄₁BNO₄⁺ [M+H⁺]: 658.3123. Found: 658.3125.



Yield: 47.5 mg (70%, a 1:1:1:1 mixture of 4 rotamers)

Physical appearance: yellow solid, **m.p.:** 92-94 °C

R_f: 0.2 (EtOAc:hexanes = 1:9)

¹H NMR (400 MHz, CDCl₃): δ 7.98 (d, *J* = 7.8 Hz, 1H), 7.58 (t, *J* = 7.5 Hz, 1H), 7.52 (t, *J* = 7.9 Hz, 1H), 7.49–7.42 (m, 2H), 7.15–7.10 (m, 5H), 6.81–6.71 (m, 7H), [6.67 (s) + 6.65 (s) + 6.62 (s) = 2H], 6.45 (s, 1H), 5.88 (d, *J* = 16.3 Hz, 1H), 3.78 (s, 3H), 3.65 (s, 3H), [2.30 (s) + 2.28 (s) = 3H], 2.21 (s, 3H), [2.14 (s) + 2.10 + 2.06 (s) = 6H].

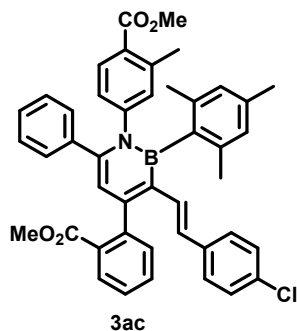
¹³C NMR (126 MHz, CDCl₃): δ 168.22, 167.50, 161.73 (d, ¹*J*_{C-F} = 245.7 Hz), 153.23, 148.12, 146.25, 143.31, 140.09, 138.41, 138.37, 138.34, 138.32, 138.27, 136.71, 135.34 (d, ⁴*J*_{C-F} = 3.1 Hz), 131.80, 131.78, 131.64, 131.18, 130.84, 130.22, 130.19, 130.17, 130.07, 129.54, 128.62, 127.82, 127.55, 127.51, 127.45 (d, ³*J*_{C-F} = 7.8 Hz), 127.26, 127.20, 127.13, 127.06, 126.54, 125.66, 125.62, 116.96, 115.15 (d, ²*J*_{C-F} = 21.6 Hz), 52.07, 51.78, 22.88, 22.87, 22.45, 21.55, 21.53, 21.30.

¹¹B NMR (160 MHz, CDCl₃): δ 39.3.

¹⁹F NMR (376 MHz, CDCl₃): δ -116.08.

IR (KBr, neat): 2949, 1724, 1591, 1570, 1560, 1507, 1484, 1458, 1437, 1375, 1351, 1291, 1255, 1190, 1157, 1132, 1089, 968, 851, 822, 765, 751, 728, 700, 669 cm⁻¹.

HRMS (ESI-TOF): m/z calcd for C₄₄H₄₀BFNO₄⁺ [M+H⁺]: 676.3029. Found: 676.3025.



Yield: 40 mg (72%, a 1:1:1:1 mixture of 4 rotamers)

Physical appearance: yellow solid, **m.p.:** 97-99 °C

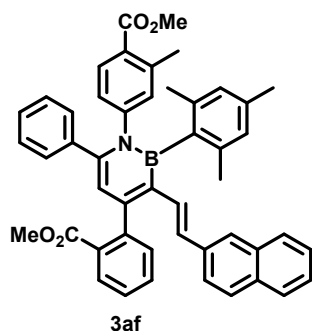
R_f: 0.2 (EtOAc:hexanes = 1:9)

¹H NMR (400 MHz, CDCl₃): δ 7.97 (d, *J* = 7.7 Hz, 1H), 7.58 (t, *J* = 7.4 Hz, 1H), 7.52 (t, *J* = 7.9 Hz, 1H), 7.47 (t, *J* = 7.6 Hz, 1H), 7.42 (d, *J* = 7.6 Hz, 1H), 7.14 – 7.10 (m, 5H), 7.04 (d, *J* = 8.3 Hz, 1H), 6.79 (d, *J* = 15.5 Hz, 1H), 6.74 – 6.62 (m, 6H), 6.46 (s, 1H), 5.86 (d, *J* = 16.3 Hz, 1H), 3.78 (s, 3H), 3.64 (d, *J* = 2.7 Hz, 3H), [2.30 (s) + 2.28 (s) = 3H], 2.21 (s, 3H), [2.13 (s) + 2.09 (s) + 2.05 (s) = 6H].

¹³C NMR (126 MHz, CDCl₃): δ 168.18, 167.49, 153.52, 148.08, 146.49, 143.21, 140.11, 138.41, 138.37, 138.32, 138.23, 137.69, 136.75, 131.91, 131.79, 131.77, 131.65, 131.18, 131.05, 130.82, 130.23, 130.08, 129.53, 128.51, 128.42, 127.83, 127.60, 127.56, 127.28, 127.24, 127.08, 126.58, 125.65, 116.97, 52.08, 51.79, 22.87, 22.45, 21.53, 21.30.

¹¹B NMR (160 MHz, CDCl₃): δ 39.0.

HRMS (ESI-TOF): m/z calcd for $C_{48}H_{49}BNO_4^+$ $[M+H]^+$: 714.3749. Found: 714.3748.



Yield: 28.3 mg (40%, a 1:1:1:1 mixture of 4 rotamers, >95% purity)

Physical appearance: yellow solid, **m.p.:** 90-92 °C

R_f: 0.2 (EtOAc:hexanes = 1:9)

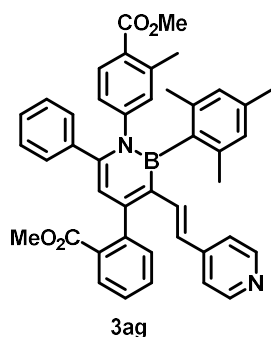
¹H NMR (400 MHz, CDCl₃): δ 8.00 (d, $J = 7.7$ Hz, 1H), 7.66 (d, $J = 7.6$ Hz, 1H), 7.59 (d, $J = 7.5$ Hz, 2H), 7.54 (d, $J = 8.3$ Hz, 2H), 7.49 – 7.46 (m, 2H), 7.32 (td, $J = 7.2, 1.6$ Hz, 2H), 7.17 – 7.11 (m, 5H), 7.07 (d, $J = 8.8$ Hz, 1H), 7.03 (s, 1H), 6.92 (d, $J = 16.3$ Hz, 1H), 6.84 – 6.79 (m, 1H), 6.76 – 6.73 (m, 1H), [6.71 (s) + 6.69 (s) + 6.66 (s) = 2H], 6.47 (s, 1H), 6.08 (d, $J = 16.3$ Hz, 1H), 3.78 (s, 3H), 3.65 (s, 3H), [2.31 (s) + 2.29 (s) = 3H], 2.25 (s, 3H), [2.18 (s) + 2.13 (s) + 2.09 (s) = 6H].

¹³C NMR (101 MHz, CDCl₃): δ 168.25, 167.53, 153.32, 148.18, 146.28, 143.40, 140.10, 138.32, 136.73, 133.68, 132.60, 131.84, 131.67, 131.21, 130.93, 130.24, 130.12, 130.03, 129.56, 127.85, 127.83, 127.80, 127.63, 127.56, 127.51, 127.29, 127.21, 126.55, 125.99, 125.91, 125.71, 125.66, 125.31, 123.48, 117.05, 52.08, 51.79, 22.94, 22.50, 21.55, 21.34.

¹¹B NMR (128 MHz, CDCl₃): δ 38.9.

IR (KBr, neat): 3055, 2948, 2854, 1722, 1596, 1586, 1570, 1474, 1434, 1375, 1350, 1290, 1255, 1190, 1166, 1133, 1089, 1031, 965, 891, 852, 813, 776, 750, 727, 700 cm^{-1} .

HRMS (ESI-TOF): m/z calcd for $C_{48}H_{43}BNO_4^+$ $[M+H]^+$: 708.3280. Found: 708.3277.



Yield: 30.0 mg (47%, a 1:1:1:1 mixture of 4 rotamers)

Physical appearance: yellow solid, **m.p.:** 99-101 °C

R_f: 0.15 (EtOAc:hexanes = 1:2)

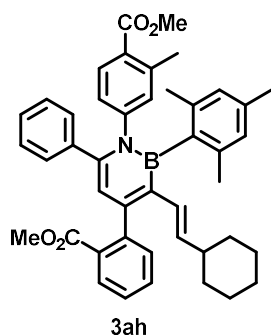
¹H NMR (500 MHz, CDCl₃): δ 8.27 (d, J = 5.4 Hz, 2H), 8.00 (d, J = 7.7 Hz, 1H), 7.60 (t, J = 7.2 Hz, 1H), 7.53 (t, J = 8.7 Hz, 1H), 7.49 (t, J = 7.7 Hz, 1H), 7.42 (d, J = 6.5 Hz, 1H), 7.17–7.09 (m, 5H), 7.01 (d, J = 16.3 Hz, 1H), 6.82–6.78 (m, 1H), 6.75–6.72 (m, 1H), 6.66 (dd, J = 12.1, 9.1 Hz, 2H), [6.63 (s) + 6.62 (s) = 2H], 6.49 (s, 1H), 5.80 (d, J = 16.3 Hz, 1H), 3.77 (s, 3H), [3.66 (s) + 3.65 (s) = 3H], [2.31 (s) + 2.29 (s) = 3H], 2.22 (s, 3H), [2.13 (s) + 2.10 (s) = 3H], [2.10 (s) + 2.06 (s) = 3H].

¹³C NMR (126 MHz, CDCl₃): δ 167.94, 167.41, 155.09, 149.36, 147.84, 147.58, 146.77, 142.83, 140.16, 140.15, 138.35, 138.33, 138.23, 138.01, 136.97, 135.24, 131.73, 131.68, 131.08, 130.70, 130.27, 130.17, 129.50, 127.87, 127.84, 127.74, 127.38, 127.24, 126.75, 125.56, 125.54, 120.57, 116.94, 52.10, 51.79, 22.86, 22.44, 21.54, 21.29.

¹¹B NMR (160 MHz, CDCl₃): δ 38.8.

IR (KBr, neat): 2917, 1723, 1592, 1573, 1485, 1331, 1255, 1189, 1131, 1088, 992, 843, 777, 754, 701 cm^{-1} .

HRMS (ESI-TOF): m/z calcd for $C_{43}H_{40}BN_2O_4^+$ $[M+H]^+$: 659.3076. Found: 659.3083.



Yield: 21.5 mg (32%, 14% chain walking, a 1:1:1:1 mixture of 4 rotamers of each isomer)

Physical appearance: light yellow amorphous solid

R_f: 0.3 (EtOAc:hexanes = 1:9)

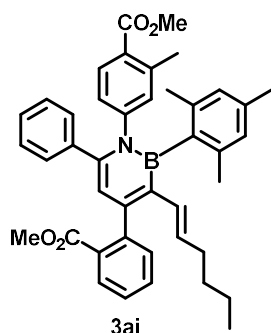
¹H NMR (400 MHz, CDCl₃): δ 7.99 – 7.97 (m, 0.14H), 7.90 (d, J = 7.8 Hz, 0.86H), 7.55 – 7.47 (m, 2H), 7.41 – 7.37 (m, 2H), 7.12 – 7.08 (m, 5H), 6.75 – 6.72 (m, 1H), 6.69 – 6.66 (m, 1H), 6.59 – 6.55 (m, 2H), 6.39 (s, 0.86H), 6.32 (s, 0.14H), 5.84 (d, J = 15.9 Hz, 0.86H), 4.96 – 4.86 (m, 1H), 3.77 (s, 3H), 3.72 – 3.67 (m, 3H), [2.28 (s) + 2.26 (s) = 3H], 2.16 (s, 3H), [2.10 (s) + 2.07 (s) = 3H], 2.08 – 2.06 (m, 1H), [2.06 (s) + 2.00 (s) = 3H], 1.45 – 1.42 (m, 3H), 1.26 – 1.22 (m, 2H), 1.06 – 0.96 (m, 3.36H), 0.62 – 0.56 (m, 1.67H).

¹³C NMR (101 MHz, CDCl₃): δ 168.47, 167.57, 151.28, 148.40, 145.21, 143.78, 139.99, 139.14, 138.56, 138.25, 136.24, 131.85, 131.47, 131.15, 130.77, 130.13, 129.98, 129.56, 127.75, 127.39, 127.27, 127.09, 126.83, 126.29, 125.68, 116.78, 52.06, 51.74, 41.43, 32.57, 26.26, 25.68, 22.84, 22.41, 21.54, 21.25.

¹¹B NMR (128 MHz, CDCl₃): δ 39.7.

IR (KBr, neat): 2923, 2850, 1722, 1590, 1573, 1486, 1446, 1374, 1349, 1291, 1270, 1253, 1190, 1131, 1088, 1031, 967, 850, 700 cm^{-1} .

HRMS (ESI-TOF): m/z calcd for $C_{44}H_{47}BNO_4^+$ $[M+H]^+$: 664.3593. Found: 664.3598.



Yield: 21.1 mg, (33%, 25% chain walking, a 1:1:1:1 mixture of 4 rotamers of each isomer)

Physical appearance: yellow amorphous solid

R_f: 0.3 (EtOAc:hexanes = 1:9)

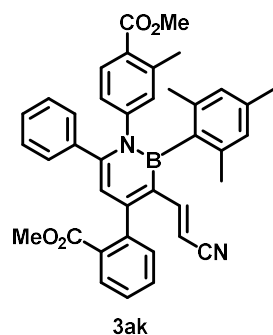
¹H NMR (500 MHz, CDCl₃): δ 7.98 – 7.96 (m, 0.25H), 7.92 (d, J = 7.7 Hz, 0.75H), 7.55 – 7.48 (m, 2H), 7.41 – 7.37 (m, 2H), 7.12 – 7.07 (m, 5H), 6.76 – 6.72 (m, 1H), 6.69 – 6.66 (m, 1H), 6.59 – 6.56 (m, 2H), 6.37 (s, 0.75H), 6.33 – 6.31 (m, 0.25H), 5.91 (d, J = 15.6 Hz, 0.75H), 5.05 – 4.93 (m, 1H), 3.77 (s, 3H), 3.72 – 3.68 (m, 3H), [2.28 (s) + 2.26 (s) = 3H], 2.16 (s, 3H), f [2.11 (s) + 2.06 (s) + 2.02 (s) = 6H], 2.09 – 2.04 (m, 0.8H), 1.69 – 1.65 (m, 1.9H), 0.95 – 0.68 (m, 6.3H).

¹³C NMR (126 MHz, CDCl₃): δ 168.31, 167.43, 151.25, 148.24, 145.07, 143.70, 139.86, 138.39, 138.11, 136.13, 133.27, 131.69, 131.37, 130.87, 130.68, 130.07, 129.99, 129.88, 129.47, 129.43, 127.61, 127.16, 126.99, 126.81, 126.76, 126.67, 126.18, 125.57, 125.52, 116.64, 51.89, 51.61, 33.36, 31.50, 22.75, 22.31, 21.64, 21.40, 21.38, 21.12, 13.87.

¹¹B NMR (160 MHz, CDCl₃): δ 40.9.

IR (KBr, neat): 2951, 2925, 2854, 1723, 1590, 1571, 1486, 1433, 1375, 1350, 1291, 1254, 1190, 1130, 1089, 1031, 967, 849, 774, 752, 725, 700 cm^{-1} .

HRMS (ESI-TOF): m/z calcd for $C_{42}H_{45}BNO_4^+$ $[M+H]^+$: 638.3436. Found: 638.3434.



Yield: 24.3 mg (40%, a 1:1:1:1 mixture of 4 rotamers)

Physical appearance: light yellow solid, **m.p.:** 98-100 °C

R_f: 0.55 (EtOAc:hexanes = 1:2)

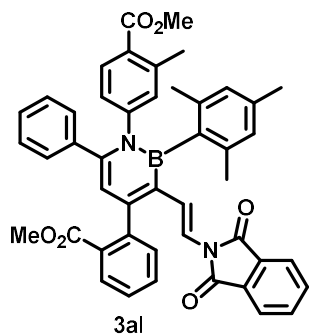
¹H NMR (500 MHz, CDCl₃): δ 8.03 (d, *J* = 7.7 Hz, 1H), 7.60 (t, *J* = 7.6 Hz, 1H), 7.50 (q, *J* = 7.6, 6.8 Hz, 2H), 7.31 (d, *J* = 7.5 Hz, 1H), 7.13 – 7.11 (m, 5H), 7.09 (d, *J* = 7.4 Hz, 1H), 6.75 – 6.68 (m, 2H), [6.65 (s) + 6.62 (s) = 2H], 6.45 (s, 1H), 4.70 (d, *J* = 16.5 Hz, 1H), 3.77 (s, 3H), [3.74 (s) + 3.73 (s) = 3H], [2.29 (s) + 2.27 (s) = 3H], 2.18 (s, 3H), [2.09 (s) + 2.27 (s) = 3H], [2.05 (s) + 2.04 (s) = 3H].

¹³C NMR (126 MHz, CDCl₃): δ 167.34, 167.23, 158.43, 152.70, 149.97, 147.24, 142.06, 140.31, 140.27, 138.03, 138.01, 137.87, 137.64, 137.51, 132.09, 131.47, 130.76, 130.38, 130.36, 130.14, 129.43, 128.34, 128.17, 127.97, 127.83, 127.67, 127.06, 125.37, 120.40, 116.79, 95.65, 52.17, 51.87, 22.73, 22.33, 21.52, 21.29.

¹¹B NMR (128 MHz, CDCl₃): δ 39.1.

IR (KBr, neat): 2949, 2208, 1724, 1606, 1567, 1477, 1435, 1354, 1289, 1256, 1134, 1089, 913, 853, 774, 730, 700 cm⁻¹.

HRMS (ESI-TOF): *m/z* calcd for C₃₉H₃₆BN₂O₄⁺ [M+H⁺]: 607.2763. Found: 607.2764.



Yield: 35.0 mg (48%, a 1:1:1:1 mixture of 4 rotamers)

Physical appearance: yellow solid, **m.p.:** 107-109 °C

R_f: 0.45 (EtOAc:hexanes = 1:2)

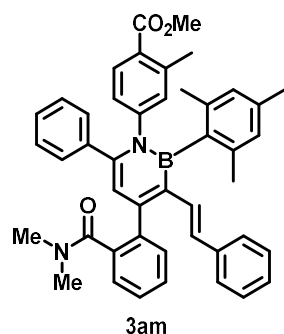
¹H NMR (500 MHz, CDCl₃): δ 8.00 (d, *J* = 7.8 Hz, 1H), 7.66 (dd, *J* = 5.5, 3.0 Hz, 2H), 7.62 – 7.57 (m, 3H), 7.51 (t, *J* = 8.5 Hz, 1H), 7.48 – 7.43 (m, 2H), 7.23 (d, *J* = 15.6 Hz, 1H), 7.15 – 7.09 (m, 5H), 6.80 – 6.72 (m, 2H), [6.69 (s) + 6.66 (s) = 2H], 6.44 (s, 1H), 6.25 (d, *J* = 14.7 Hz, 1H), 3.77 (s, 3H), [3.71 (s) + 3.70 (s) = 3H], [2.30 (s) + 2.28 (s) = 2H], 2.20 (s, 3H), [2.19 (s) + 2.16 (s) = 3H], [2.13 (s) + 2.11 (s) = 3H].

¹³C NMR (126 MHz, CDCl₃): δ 168.15, 167.50, 166.32, 153.72, 148.09, 146.39, 143.33, 143.31, 140.08, 138.25, 138.17, 138.14, 138.09, 136.94, 134.02, 131.96, 131.79, 131.74, 130.65, 130.61, 130.38, 130.19, 129.55, 127.81, 127.64, 127.52, 127.39, 127.29, 126.50, 125.64, 123.25, 122.90, 118.69, 116.81, 52.09, 51.77, 22.87, 22.45, 21.52, 21.32.

¹¹B NMR (128 MHz, CDCl₃): δ 39.7.

IR (KBr, neat): 2928, 2856, 1719, 1605, 1588, 1571, 1474, 1447, 1377, 1290, 1256, 1190, 1132, 1080, 965, 886, 852, 753, 715, 701, 669 cm⁻¹.

HRMS (ESI-TOF): *m/z* calcd for C₄₆H₄₀BN₂O₆⁺ [M+H⁺]: 727.2974. Found: 727.2977.



Yield: 45.5 mg (68%, a mixture of 8 rotamers)

Physical appearance: yellow solid, **m.p.:** 109-111 °C

R_f: 0.55 (EtOAc:hexanes = 1:1)

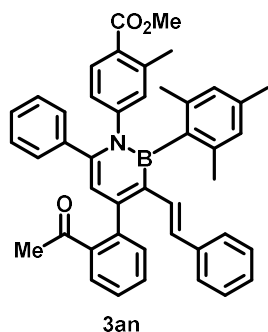
¹H NMR (500 MHz, CDCl₃): δ 7.52 – 7.45 (m, 5H), 7.15 – 7.08 (m, 8H), 7.06 – 7.02 (m, 1H), 6.83 (d, *J* = 7.8 Hz, 3H), 6.71 (d, *J* = 17.2 Hz, 1H), 6.62 – 6.59 (m, 3H), 6.02 (d, *J* = 14.0 Hz, 1H), 3.77 (s, 3H), [2.93 (s) + 2.70 (s) = 6H], 2.30 – 2.19 (6H), 2.22 (s, 3H), [1.99 (s) + 1.93 (s) = 3H]

¹³C NMR (126 MHz, CDCl₃): δ 170.81, 167.46, 151.74, 148.05, 146.25, 140.05, 139.52, 139.13, 138.00, 136.79, 136.59, 131.69, 130.91, 130.39, 130.19, 129.80, 129.53, 128.53, 128.40, 127.89, 127.82, 127.50, 127.47, 127.25, 126.64, 126.54, 126.10, 125.55, 117.70, 51.76, 39.24, 34.89, 22.96, 22.35, 21.53, 21.29.

¹¹B NMR (160 MHz, CDCl₃): δ 39.1.

IR (KBr, neat): 3059, 3921, 2948, 2905, 1722, 1635, 1587, 1569, 1496, 1481, 1446, 1435, 1394, 1351, 1285, 1270, 1255, 1190, 1166, 1142, 1090, 1068, 1031, 971, 849, 775, 696, 637 cm⁻¹.

HRMS (ESI-TOF): *m/z* calcd for C₄₅H₄₄BN₂O₃⁺ [M+H⁺]: 671.3440. Found: 671.3445.



Yield: 13.5 mg (21%, a mixture of 8 rotamers, >95% purity)

Physical appearance: yellow solid, **m.p.:** 94-96 °C

R_f: 0.8 (CH₂Cl₂:hexanes = 6:1)

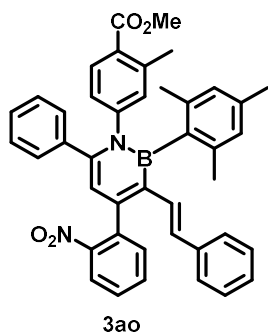
¹H NMR (500 MHz, CDCl₃): δ 7.75 (d, *J* = 7.7 Hz, 1H), 7.57 – 7.51 (m, 2H), 7.47 (t, *J* = 7.5 Hz, 1H), 7.43 (d, *J* = 7.6 Hz, 1H), 7.13 – 7.09 (m, 7H), 7.04 (t, *J* = 7.3 Hz, 1H), 6.86 (d, *J* = 16.4 Hz, 1H), 6.81 – 6.71 (m, 4H), [6.68 (s) + 6.65 (s) + 6.62 (s) = 2H], 6.47 (s, 1H), 5.98 (dd, *J* = 16.3, 2.6 Hz, 1H), 3.78 (s, 3H), [2.34 (s) + 2.33 (s) = 3H], [2.30 (s) + 2.28 (s) = 3H], 2.21 (s, 3H), [2.16 (s) + 2.12 (s) + 2.05 (s) + 2.02 (s) = 6H].

¹³C NMR (101 MHz, CDCl₃): δ 202.31, 167.48, 152.84, 147.94, 146.85, 141.70, 140.15, 139.00, 138.34, 138.32, 137.99, 136.85, 131.77, 131.73, 131.16, 130.80, 130.66, 130.27, 130.04, 129.53, 128.47, 128.39, 127.88, 127.78, 127.69, 127.34, 127.29, 127.21, 127.14, 126.76, 126.20, 125.62, 117.24, 51.81, 29.76, 22.90, 22.49, 21.56, 21.51, 21.31.

¹¹B NMR (128 MHz, CDCl₃): δ 40.9.

IR (KBr, neat): 3023, 2948, 2915, 2848, 1722, 1693, 1586, 1569, 1515, 1480, 1435, 1374, 1353, 1286, 1271, 1252, 1190, 1142, 1090, 1031, 969, 849, 777, 698 cm⁻¹.

HRMS (ESI-TOF): *m/z* calcd for C₄₄H₄₀BNO₃⁺ [*M*⁺]: 641.3096. Found: 641.3091.



Yield: 17.4 mg (27%, a 1:1:1:1 mixture of 4 rotamers)

Physical appearance: yellow solid, **m.p.:** 210-212 °C

R_f: 0.25 (EtOAc:hexanes = 1:9)

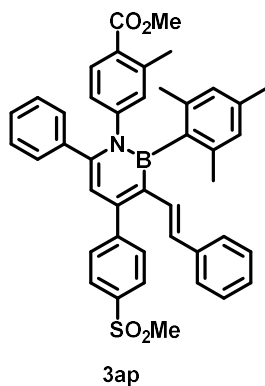
¹H NMR (500 MHz, CDCl₃): δ 8.09 (d, *J* = 8.1 Hz, 1H), 7.68 (t, *J* = 7.5 Hz, 1H), 7.54 (tt, *J* = 8.8, 3.3 Hz, 3H), 7.14 – 7.08 (m, 7H), 7.04 (t, *J* = 7.2 Hz, 1H), 6.78 (q, *J* = 8.5 Hz, 4H), 6.71 (d, *J* = 16.3 Hz, 1H), [6.66 (s) + 6.64 (s) + 6.62 (s) = 2H], 6.41 (s, 1H), 5.97 (d, *J* = 15.7 Hz, 1H), 3.78 (s, 3H), [2.31 (s) + 2.18 (s) = 3H], 2.20 (s, 3H), [2.15 (s) + 2.12 (s) + 2.09 (s) + 2.06 (s) = 6H].

¹³C NMR (126 MHz, CDCl₃): δ 167.52, 167.48, 149.12, 148.91, 147.93, 146.98, 140.25, 140.06, 138.85, 138.74, 138.72, 138.16, 138.00, 137.97, 136.82, 132.93, 132.17, 131.83, 131.65, 131.04, 130.34, 130.19, 129.58, 129.51, 128.53, 128.34, 127.85, 127.68, 127.42, 127.37, 127.02, 126.96, 126.80, 126.71, 126.66, 126.23, 125.69, 125.49, 124.52, 115.60, 51.80, 22.93, 22.50, 21.55, 21.51, 21.31.

¹¹B NMR (128 MHz, CDCl₃): δ 39.5.

IR (KBr, neat): 3057, 3022, 2928, 2856, 1721, 1605, 1586, 1570, 1527, 1496, 1481, 1446, 1437, 1401, 1375, 1351, 1256, 1190, 1166, 1142, 1090, 1030, 967, 915, 883, 857, 809, 786, 770, 749, 738, 700, 675 cm⁻¹.

HRMS (ESI-TOF): *m/z* calcd for C₄₂H₃₈BN₂O₄⁺ [M+H⁺]: 645.2919. Found: 645.2925.



Yield: 10.4 mg (15%, a 1:1 mixture of 2 rotamers. ~90% purity. Product is not stable under silica gel chromatography.)

Physical appearance: yellow solid, **m.p.:** 123-125 °C

R_f: 0.2 (EtOAc:hexanes = 1:4)

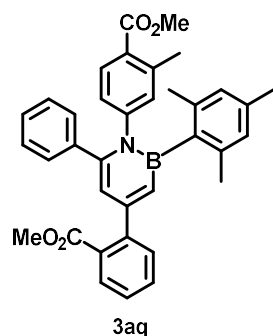
¹H NMR (500 MHz, CDCl₃): δ 8.03 (d, *J* = 7.9 Hz, 2H), 7.72 (d, *J* = 8.0 Hz, 2H), 7.53 (d, *J* = 8.2 Hz, 1H), 7.15 – 7.06 (m, 8H), 6.93 (d, *J* = 16.3 Hz, 1H), 6.83 (d, *J* = 7.6 Hz, 2H), 6.75 (d, *J* = 12.9 Hz, 2H), [6.66 (s) + 6.64 (s) = 2H], 6.51 (s, 1H), 6.03 (d, *J* = 16.4 Hz, 1H), 3.78 (s, 3H), 3.13 (s, 3H), 2.29 (s, 3H), [2.21 (s) + 2.11 (s) = 6H], 2.08 (s, 3H).

¹³C NMR (126 MHz, CDCl₃): δ 167.45, 150.75, 148.51, 147.82, 147.22, 140.18, 139.43, 138.76, 138.34, 138.32, 138.05, 136.93, 131.68, 131.19, 130.71, 130.30, 129.72, 129.46, 128.51, 127.95, 127.80, 127.37, 127.32, 127.25, 126.95, 126.78, 126.22, 125.54, 116.54, 51.83, 44.75, 22.84, 21.54, 21.30.

¹¹B NMR (160 MHz, CDCl₃): δ 41.5.

IR (KBr, neat): 2917, 2849, 1720, 1603, 1589, 1571, 1512, 1492, 1446, 1435, 1376, 1315, 1257, 1147, 1090, 1031, 957, 882, 841, 763, 738, 701, 675, 546, 528 cm⁻¹.

HRMS (ESI-TOF): *m/z* calcd for C₄₃H₄₁BNO₄S⁺ [M+H⁺]: 678.2844. Found: 678.2847.



Yield: 14.8 mg (27%, a 1:1 mixture of 2 rotamers)

Physical appearance: white solid, **m.p.:** 83-85 °C

R_f: 0.25 (EtOAc:hexanes = 1:9)

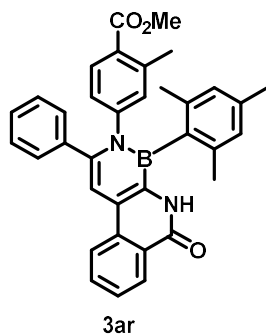
¹H NMR (500 MHz, CDCl₃): δ 7.79 (d, *J* = 7.1 Hz, 1H), 7.53 – 7.51 (m, 3H), 7.40 (ddd, *J* = 7.7, 5.7, 3.1 Hz, 1H), 7.16 – 7.12 (m, 5H), 6.76 (d, *J* = 2.2 Hz, 1H), 6.73 – 6.70 (m, 2H), [6.65 (s) + 6.64 (s) = 2H], 6.53 (d, *J* = 2.2 Hz, 1H), 3.77 (s, 3H), 3.74 (s, 3H), 2.28 (s, 3H), 2.18 (s, 3H), [2.12 (s) + 2.10 (s) = 6H].

¹³C NMR (126 MHz, CDCl₃): δ 169.33, 167.51, 155.52, 148.12, 148.09, 144.16, 140.17, 138.73, 138.57, 136.58, 131.71, 131.33, 130.81, 130.30, 129.91, 129.84, 129.55, 127.87, 127.56, 126.89, 126.86, 126.51, 125.55, 115.69, 52.15, 51.79, 23.20, 23.18, 21.55, 21.23.

¹¹B NMR (160 MHz, CDCl₃): δ 37.9.

IR (KBr, neat): 2949, 1723, 1603, 1573, 1505, 1486, 1445, 1434, 1346, 1289, 1255, 1190, 1130, 1086, 1056, 1031, 987, 878, 849, 768, 754, 733, 701 cm⁻¹.

HRMS (ESI-TOF): *m/z* calcd for C₃₆H₃₅BNO₄⁺ [M+H⁺]: 556.2654. Found: 556.2659.



Yield: 22.6 mg (42%, a 1:1 mixture of 2 rotamers, reaction performed with Pd(TFA)₂ (0.02 mmol) and BrettPhos (0.04 mmol))

Physical appearance: off-white solid, **m.p.:** 114-116 °C

R_f: 0.2 (EtOAc:hexanes = 1:4)

¹H NMR (500 MHz, CDCl₃): δ 8.58 (d, *J* = 8.0 Hz, 1H), 8.33 (N-H, br, 1H), 8.27 (d, *J* = 8.2 Hz, 1H), 7.82 (t, *J* = 7.9 Hz, 1H), 7.68 (t, *J* = 7.6 Hz, 1H), 7.55 (d, *J* = 8.1 Hz, 1H), 7.30 (s, 1H), 7.23 – 7.17 (m, 5H), 6.75 (s, 1H), 6.74 – 6.72 (m, 3H), 3.77 (s, 3H), 2.29 (s, 3H), 2.23 (s, 3H), [2.06 (s) + 2.04 (s) = 6H].

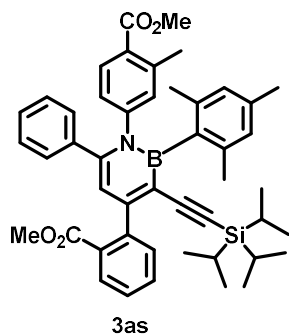
¹³C NMR (126 MHz, CDCl₃): δ 167.34, 161.78, 147.67, 143.10, 140.47, 139.52, 138.46, 138.35, 134.53, 132.72, 131.30, 130.56, 129.70, 128.94, 128.55, 128.47, 128.04, 127.86, 127.81, 127.68, 126.99, 125.18, 124.60, 123.11, 108.17, 51.84, 22.74, 21.57, 21.27.

¹¹B NMR (160 MHz, CDCl₃): δ 35.8.

IR (KBr, neat): 3376, 2926, 1722, 1666, 1605, 1569, 1488, 1446, 1335, 1259, 1146, 1089, 1031, 773, 734, 704 cm⁻¹.

HRMS (ESI-TOF): *m/z* calcd for C₃₅H₃₂BN₂O₃⁺ [M+H⁺]: 539.2500. Found: 539.2507.

¹H-¹H COSY and NOE data of this compound are attached in Section 3.



Yield: 42.3 mg (59%)

Physical appearance: yellow solid, **m.p.:** 70-72 °C

R_f: 0.4 (EtOAc:hexanes = 1:9)

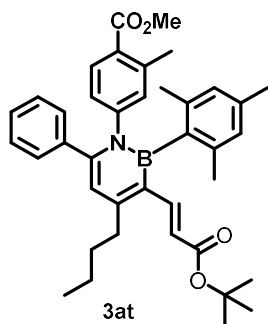
¹H NMR (400 MHz, CDCl₃): δ 7.96 (d, *J* = 8.3 Hz, 1H), 7.55 – 7.52 (m, 2H), 7.47 (d, *J* = 7.0 Hz, 1H), 7.38 (t, *J* = 7.8 Hz, 1H), 7.17 – 7.11 (m, 5H), 6.78 (s, 1H), 6.77 (d, *J* = 6.7 Hz, 1H), 6.55 (s, 2H), 6.52 (s, 1H), 3.77 (s, 3H), 3.74 (s, 3H), 2.29 (s, 3H), 2.12 (s, 3H), 2.11 (s, 6H), 0.69 (s, 18H).

¹³C NMR (126 MHz, CDCl₃): δ 167.77, 167.46, 158.84, 147.96, 147.31, 143.38, 140.29, 138.34, 138.13, 136.24, 131.61, 131.55, 130.40, 130.30, 130.06, 130.04, 129.51, 127.89, 127.72, 127.41, 126.75, 126.72, 126.70, 125.39, 116.19, 108.55, 96.98, 51.95, 51.78, 22.75, 21.56, 21.16, 18.41, 11.26.

¹¹B NMR (160 MHz, CDCl₃): δ 42.6.

IR (KBr, neat): 2943, 2863, 1725, 1602, 1586, 1573, 1463, 1483, 1463, 1446, 1435, 1377, 1345, 1291, 1255, 1210, 1190, 1166, 1133, 1081, 1066, 1031, 1016, 994, 969, 882, 849, 732, 700, 675, 626 cm⁻¹.

HRMS (ESI-TOF): *m/z* calcd for C₄₇H₅₅BNO₄Si⁺ [M+H⁺]: 736.3988. Found: 736.3992.



Yield: 16.6 mg (28%, a 1:1 mixture of 2 rotamers)

Physical appearance: off-white oil

R_f: 0.4 (EtOAc:hexanes = 1:9)

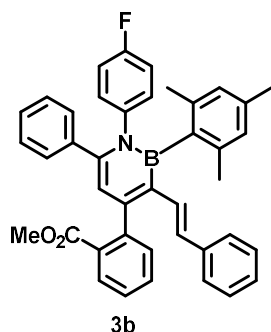
¹H NMR (500 MHz, CDCl₃): δ 7.84 (d, *J* = 16.0 Hz, 1H), 7.47 (d, *J* = 8.2 Hz, 1H), 7.14 – 7.10 (m, 5H), 6.66 – 6.64 (m, 2H), [6.60 (s) + 6.57 (s) = 2H], 6.43 (s, 1H), 5.23 (d, *J* = 16.0 Hz, 1H), 3.76 (s, 3H), 2.80 – 2.77 (m, 2H), 2.25 (s, 3H), 2.15 (s, 3H), [2.00 (s) + 1.97 (s) = 6H], 1.66 (dt, *J* = 15.4, 7.9 Hz, 2H), 1.46 (h, *J* = 7.4 Hz, 2H), 1.40 (s, 9H), 0.98 (t, *J* = 7.3 Hz, 3H).

¹³C NMR (126 MHz, CDCl₃): δ 167.82, 167.47, 158.26, 148.88, 147.86, 144.36, 140.05, 138.32, 138.02, 138.00, 136.70, 131.67, 130.18, 129.42, 127.86, 127.70, 127.23, 127.18, 126.54, 125.52, 120.60, 117.52, 79.31, 51.77, 34.66, 33.28, 28.32, 23.07, 22.72, 21.49, 21.22, 14.16.

¹¹B NMR (160 MHz, CDCl₃): δ 40.5.

IR (KBr, neat): 2956, 2930, 2872, 1723, 1700, 1609, 1585, 1571, 1487, 1446, 1366, 1302, 1255, 1149, 1086, 980, 914, 848, 775, 733, 700, 649 cm⁻¹.

HRMS (ESI-TOF): *m/z* calcd for C₃₉H₄₇BNO₄⁺ [M+H⁺]: 604.3593. Found: 604.3590.



Yield: 34.5 mg (57%, a 1:1 mixture of 2 rotamers)

Physical appearance: yellow solid, **m.p.:** 193-195 °C

R_f: 0.35 (EtOAc:hexanes = 1:9)

¹H NMR (500 MHz, CDCl₃): δ 7.99 (dd, *J* = 7.7, 1.4 Hz, 1H), 7.58 (td, *J* = 7.5, 1.4 Hz, 1H), 7.48 – 7.43 (m, 2H), 7.13 (s, 5H), 7.09 (t, *J* = 7.5 Hz, 2H), 7.04 – 7.01 (m, 1H), 6.89 – 6.86 (m, 1H), 6.84 – 6.78 (m, 4H), 6.67 (d, *J* = 11.7 Hz, 2H), 6.62 (q, *J* = 8.0 Hz, 2H), 6.44 (s, 1H), 5.94 (d, *J* = 16.4 Hz, 1H), 3.65 (s, 3H), 2.23 (s, 3H), [2.14 (s) + 2.09 (s) = 6H].

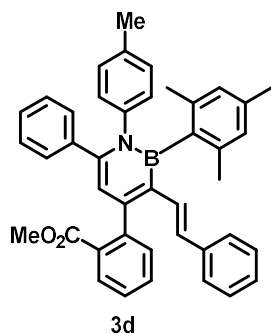
¹³C NMR (126 MHz, CDCl₃): δ 168.27, 160.47 (d, ¹*J*_{C-F} = 245.2 Hz), 153.26, 146.70, 143.45, 141.04 (d, ⁴*J*_{C-F} = 3.3 Hz), 139.26, 138.46, 138.34, 138.31, 136.64, 131.61, 131.13, 130.92, 130.53, 130.10, 129.78, 129.73, 129.59 (dd, ³*J*_{C-F} = 8.3, 2.7 Hz), 128.30, 127.80, 127.48, 127.37, 127.25, 127.10, 126.48, 126.15, 116.77, 114.29 (d, ²*J*_{C-F} = 22.6, 3.3 Hz), 52.04, 22.91, 22.47, 21.33.

¹¹B NMR (128 MHz, CDCl₃): δ 37.7.

¹⁹F NMR (376 MHz, CDCl₃): δ -116.42.

IR (KBr, neat): 3058, 3022, 2948, 2855, 1730, 1608, 1586, 1570, 1507, 1474, 1446, 1376, 1352, 1292, 1255, 1219, 1153, 1127, 1078, 1093, 1029, 1014, 967, 839, 776, 755, 740, 699 cm⁻¹.

HRMS (ESI-TOF): *m/z* calcd for C₄₁H₃₆BFNO₂⁺ [M+H⁺]: 604.2818. Found: 604.2826.



Yield: 42.2 mg (70%, a 1:1 mixture of 2 rotamers)

Physical appearance: yellow solid, **m.p.:** 90-92 °C

R_f: 0.35 (EtOAc:hexanes = 1:9)

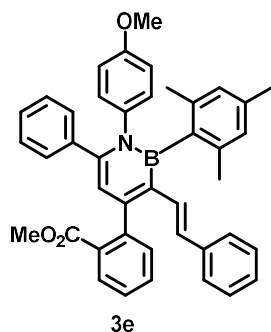
¹H NMR (500 MHz, CDCl₃): δ 7.99 (d, *J* = 7.7 Hz, 1H), 7.57 (t, *J* = 7.4 Hz, 1H), 7.46 (t, *J* = 7.7 Hz, 2H), 7.16 – 7.08 (m, 7H), 7.03 – 6.98 (m, 1H), 6.83 – 6.70 (m, 7H), [6.68 (s) + 6.65 (s) = 2H], 6.43 (s, 1H), 5.89 (d, *J* = 16.4 Hz, 1H), 3.66 (s, 3H), [2.23 (s) + 2.16 (s) = 6H], 2.11 (s, 6H).

¹³C NMR (126 MHz, CDCl₃): δ 168.40, 153.13, 147.06, 143.61, 142.37, 139.40, 138.83, 138.46, 136.30, 135.27, 131.53, 131.19, 130.97, 130.71, 130.05, 129.69, 129.53, 128.26, 128.07, 128.05, 127.94, 127.91, 127.58, 127.38, 127.10, 126.95, 126.35, 126.11, 116.64, 52.02, 22.96, 22.52, 21.35, 21.02.

¹¹B NMR (128 MHz, CDCl₃): δ 39.5.

IR (KBr, neat): 3059, 3026, 2997, 2926, 2856, 1731, 1608, 1587, 1570, 1511, 1474, 1446, 1432, 1376, 1351, 1291, 1254, 1190, 1167, 1127, 1114, 1078, 967, 850, 824, 774, 753, 739, 728, 699 cm⁻¹.

HRMS (ESI-TOF): *m/z* calcd for C₄₂H₃₉BNO₂⁺ [M+H⁺]: 600.3068. Found: 600.3061.



Yield: 39.5 mg (64%, a 1:1 mixture of 2 rotamers)

Physical appearance: yellow solid, **m.p.:** 90-92 °C

R_f: 0.8 (CH₂Cl₂:hexanes = 3:1)

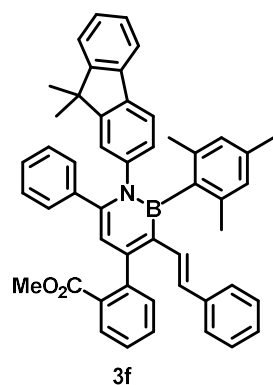
¹H NMR (400 MHz, CDCl₃): δ 7.98 (d, *J* = 7.7 Hz, 1H), 7.57 (t, *J* = 7.1 Hz, 1H), 7.45 (t, *J* = 8.1 Hz, 2H), 7.15 – 7.07 (m, 8H), 7.03 – 6.97 (m, 1H), 6.84 – 6.75 (m, 5H), 6.66 (d, *J* = 10.2 Hz, 2H), 6.44 (t, *J* = 7.2 Hz, 2H), 6.41 (s, 1H), 5.89 (d, *J* = 16.4 Hz, 1H), 3.65 (s, 3H), 3.62 (s, 3H), [2.23 (s) + 2.14 (s) = 6H], 2.10 (s, 3H).

¹³C NMR (101 MHz, CDCl₃): δ 168.38, 157.20, 153.13, 147.19, 143.59, 139.38, 138.81, 138.40, 138.09, 136.32, 131.53, 131.19, 130.96, 130.69, 130.04, 129.70, 129.54, 129.03, 129.00, 128.27, 127.66, 127.38, 127.16, 127.13, 127.01, 126.36, 126.11, 116.60, 112.60, 112.55, 55.23, 52.01, 22.94, 22.51, 21.34.

¹¹B NMR (128 MHz, CDCl₃): δ 39.5.

IR (KBr, neat): 2996, 2931, 2856, 2836, 1723, 1609, 1584, 1570, 1474, 1445, 1376, 1352, 1293, 1246, 1181, 1170, 1126, 1078, 1031, 967, 833, 775, 754, 741, 699 cm⁻¹.

HRMS (ESI-TOF): *m/z* calcd for C₄₂H₃₉BNO₃⁺ [M+H⁺]: 616.3018. Found: 616.3026.



Yield: 39.1 mg (56%, a 1:1:1:1 mixture of 4 rotamers)

Physical appearance: yellow solid, **m.p.:** 108-110 °C

R_f: 0.3 (EtOAc:hexanes = 1:9)

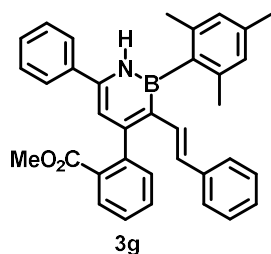
¹H NMR (500 MHz, CDCl₃): δ 8.01 – 7.99 (m, 1H), 7.59 (t, *J* = 7.5 Hz, 1H), 7.53 (d, *J* = 7.3 Hz, 1H), 7.48 (t, *J* = 7.3 Hz, 2H), 7.33 (d, *J* = 6.8 Hz, 1H), 7.28 – 7.23 (m, 3H), 7.18 (d, *J* = 8.0 Hz, 2H), 7.11 – 7.01 (m, 6H), 6.94 – 6.79 (m, 5H), [6.64 (s) + 6.62 (s) + 6.60 (s) + 6.59 (s) = 2H] 6.49 (d, *J* = 4.0 Hz, 1H), 6.03 (dd, *J* = 16.3, 2.9 Hz, 1H), 3.68 (s, 3H), [2.21 (s) + 2.17 (s) = 3H], 2.15 (s, 3H), [2.13 (s) + 2.11 (s) = 3H], [1.19 (s) + 1.17 (s) + 1.15 (s) = 6H].

¹³C NMR (101 MHz, CDCl₃): δ 168.39, 168.29, 153.83, 153.80, 153.18, 153.13, 152.86, 147.00, 146.98, 144.15, 143.64, 143.60, 139.34, 138.94, 138.80, 138.78, 138.41, 138.33, 138.27, 136.40, 136.34, 131.60, 131.56, 131.20, 130.98, 130.74, 130.10, 130.03, 129.72, 129.68, 128.28, 127.65, 127.62, 127.42, 127.17, 127.14, 127.13, 127.10, 127.07, 127.04, 127.02, 126.40, 126.14, 123.27, 123.24, 122.68, 119.97, 119.95, 118.81, 118.79, 116.55, 52.07, 52.05, 46.54, 26.81, 26.79, 26.50, 26.48, 22.94, 22.90, 22.52, 22.50, 21.23.

¹¹B NMR (160 MHz, CDCl₃): δ 38.5.

IR (KBr, neat): 2956, 2920, 2857, 1730, 1585, 1570, 1474, 1460, 1448, 1375, 1352, 1291, 1254, 1127, 1078, 1029, 967, 850, 829, 773, 737, 699 cm⁻¹.

HRMS (ESI-TOF): *m/z* calcd for C₅₀H₄₅BNO₂⁺ [M+H⁺]: 702.3538. Found: 702.3536.



Yield: 28.1 mg (55%, a 1:1 mixture of 2 rotamers)

Physical appearance: yellow solid, **m.p.:** 83-85 °C

R_f: 0.3 (EtOAc:hexanes = 1:9)

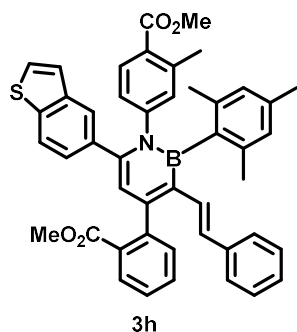
¹H NMR (500 MHz, CDCl₃): δ 8.12 (N-H, br, 1H), 8.01 (d, *J* = 7.7 Hz, 1H), 7.62 – 7.57 (m, 3H), 7.48 (t, *J* = 7.6 Hz, 1H), 7.44 (t, *J* = 7.5 Hz, 2H), 7.38 (dd, *J* = 16.3, 7.7 Hz, 2H), 7.11 (t, *J* = 7.5 Hz, 2H), 7.04 (t, *J* = 7.2 Hz, 1H), 6.94 (d, *J* = 13.0 Hz, 2H), 6.87 (s, 2H), 6.85 (d, *J* = 9.8 Hz, 1H), 6.63 (d, *J* = 2.3 Hz, 1H), 6.26 (d, *J* = 16.2 Hz, 1H), 3.60 (s, 3H), [2.38 (s) + 2.28 (s) = 6H], 2.23 (s, 3H).

¹³C NMR (126 MHz, CDCl₃): δ 168.37, 154.53, 143.74, 142.29, 139.87, 139.72, 139.15, 137.46, 137.25, 131.60, 131.10, 130.96, 130.72, 130.08, 129.61, 129.24, 128.88, 128.34, 127.55, 127.46, 126.54, 126.18, 125.81, 111.83, 52.04, 22.91, 22.56, 21.41.

¹¹B NMR (160 MHz, CDCl₃): δ 38.5.

IR (KBr, neat): 3376 (br), 3023, 2947, 1731, 1595, 1572, 1514, 1490, 1446, 1431, 1397, 1292, 1254, 1189, 1126, 1078, 1029, 967, 910, 850, 767, 733, 693 cm⁻¹.

HRMS (ESI-TOF): *m/z* calcd for C₃₅H₃₃BNO₂⁺ [M+H⁺]: 510.2599. Found: 510.2606.



Yield: 37.0 mg (52%, a 1:1:1:1 mixture of 4 rotamers)

Physical appearance: yellow solid, **m.p.:** 109-111 °C

R_f: 0.2 (EtOAc:hexanes = 1:9)

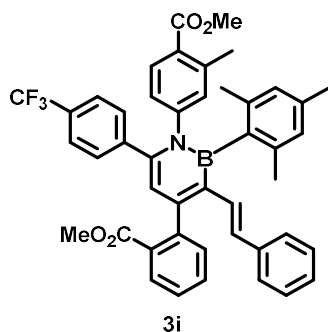
¹H NMR (500 MHz, CDCl₃): δ 7.99 (dd, *J* = 7.7, 1.4 Hz, 1H), 7.73 (s, 1H), 7.60 – 7.55 (m, 2H), 7.52 – 7.44 (m, 3H), 7.39 (d, *J* = 5.4 Hz, 1H), 7.21 (d, *J* = 5.5 Hz, 1H), 7.09 (t, *J* = 7.5 Hz, 2H), 7.05 – 7.01 (m, 2H), 6.89 – 6.75 (m, 5H), [6.69 (s) + 6.66 (s) + 6.65 (s) + (6.62 (s) = 2H], 6.51 (d, *J* = 3.6 Hz, 1H), 5.96 (d, *J* = 16.4 Hz, 1H), 3.75 (s, 3H), [3.67 (s) + 3.66 (s) = 3H], [2.29 (s) + 2.26 (s) = 3H], 2.22 (s), [2.19 (s) + 2.14 (s) = 3H], [2.11 (s) + 2.07 (s) = 3H].

¹³C NMR (126 MHz, CDCl₃): δ 168.22, 168.19, 167.45, 153.33, 153.31, 148.19, 146.16, 143.46, 143.43, 140.13, 139.32, 139.24, 138.91, 138.43, 138.36, 138.32, 136.69, 134.70, 131.78, 131.65, 131.15, 131.09, 130.91, 130.87, 130.49, 130.47, 130.31, 130.29, 130.11, 129.90, 128.30, 127.51, 127.28, 127.22, 127.14, 127.06, 126.51, 126.16, 125.76, 125.73, 125.69, 124.55, 123.98, 121.67, 117.47, 52.09, 51.75, 22.95, 22.89, 22.52, 22.46, 21.61, 21.59, 21.32.

¹¹B NMR (160 MHz, CDCl₃): δ 41.1.

IR (KBr, neat): 2947, 1720, 1585, 1571, 1560, 1541, 1474, 1458, 1437, 1375, 1350, 1290, 1254, 1189, 1131, 1089, 1050, 967, 880, 851, 818, 772, 754, 739, 709 cm⁻¹.

HRMS (ESI-TOF): *m/z* calcd for C₄₆H₄₁BNO₄S⁺ [M+H⁺]: 714.2844. Found: 714.2839.



Yield: 32.1 mg (44%, a 1:1:1:1 mixture of 4 rotamers)

Physical appearance: yellow solid, **m.p.:** 98-100 °C

R_f: 0.2 (EtOAc:hexanes = 1:9)

¹H NMR (500 MHz, CDCl₃): δ 8.00 (d, *J* = 7.8 Hz, 1H), 7.59 (t, *J* = 7.2 Hz, 1H), 7.55 (t, *J* = 7.9 Hz, 1H), 7.48 (t, *J* = 7.6 Hz, 1H), 7.42 (d, *J* = 7.5 Hz, 1H), 7.39 (d, *J* = 8.2 Hz, 2H), 7.28 (d, *J* = 8.1 Hz, 2H), 7.10 (t, *J* = 7.5 Hz, 2H), 7.03 (t, *J* = 7.1 Hz, 1H), 6.82 – 6.73 (m, 5H), [6.68 (s) + 6.66 (s) + 6.65 (s) + 6.63 (s) = 2H], 6.46 (s, 1H), 5.97 (d, *J* = 16.3 Hz, 1H), 3.80 (s, 3H), [3.66 (s) + 3.65 (s) = 3H], [2.32 (s) + 2.30 (s) = 3H], 2.22 (s, 3H), [2.25 (s) + 2.12 (s) + 2.09 (s) + 2.07 (s) = 6H].

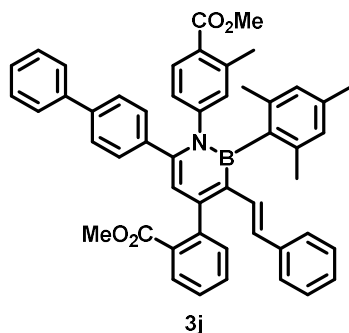
¹³C NMR (126 MHz, CDCl₃): δ 168.01, 167.99, 167.37, 153.03, 147.70, 144.36, 143.17, 143.15, 141.94, 140.40, 140.39, 139.04, 138.41, 138.36, 138.31, 138.28, 136.90, 131.76, 131.65, 131.03, 131.02, 130.53, 130.50, 130.48, 130.18, 130.16, 129.77, 129.46 (q, ²*J*_{C-CF₃} = 32.6 Hz), 128.33, 127.68, 127.36, 127.29, 127.21, 127.14, 126.94, 126.70, 126.22, 125.57, 125.54, 124.84 (q, ³*J*_{C-CF₃} = 3.7 Hz), 124.03 (q, ¹*J*_{C-CF₃} = 272.2 Hz), 117.65, 52.10, 51.87, 22.90, 22.86, 22.48, 22.45, 21.59, 21.57, 21.32.

¹¹B NMR (160 MHz, CDCl₃): δ 41.2.

¹⁹F NMR (376 MHz, CDCl₃): δ -62.61.

IR (KBr, neat): 2950, 2852, 1723, 1597, 1570, 1488, 1435, 1411, 1377, 1351, 1324, 1291, 1255, 1190, 1167, 1128, 1065, 1009, 1018, 968, 842, 777, 693 cm^{-1} .

HRMS (ESI-TOF): m/z calcd for $\text{C}_{45}\text{H}_{40}\text{BF}_3\text{NO}_4^+$ $[\text{M}+\text{H}^+]$: 726.2997. Found: 726.2998.



Yield: 53.4 mg (73%, a 1:1:1:1 mixture of 4 rotamers)

Physical appearance: yellow solid, **m.p.:** 110-112 $^{\circ}\text{C}$

R_f: 0.2 (EtOAc:hexanes = 1:9)

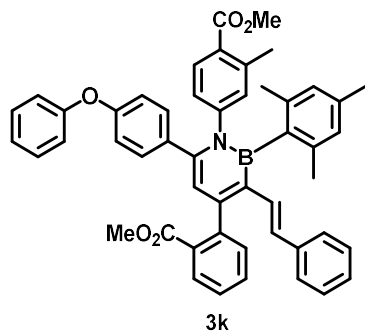
^1H NMR (500 MHz, CDCl_3): δ 8.00 (d, $J = 7.7$ Hz, 1H), 7.61 – 7.58 (m, 1H), 7.55 (d, $J = 8.7$ Hz, 1H), 7.52 (d, $J = 7.4$ Hz, 2H), 7.49 – 7.45 (m, 2H), 7.41 – 7.37 (m, 4H), 7.32 (t, $J = 7.3$ Hz, 1H), 7.22 (d, $J = 8.1$ Hz, 2H), 7.10 (dd, $J = 8.3, 6.8$ Hz, 2H), 7.03 (t, $J = 7.3$ Hz, 1H), 6.88 – 6.77 (m, 5H), [6.70 (s) + 6.67 (s) + 6.66 (s) + 6.64 (s) = 2H], 6.52 (s, 1H), 5.97 (d, $J = 16.3$ Hz, 1H), 3.78 (s, 3H), [3.68 (s) + 3.67 (s) = 3H], [2.33 (s) + 2.31 (s) = 3H], 2.23 (s, 3H), [2.19 (s) + 2.14 (s) = 3H], [2.12 (s) + 2.08 (s) = 3H].

^{13}C NMR (126 MHz, CDCl_3): δ 168.21, 167.49, 153.30, 148.19, 145.80, 143.43, 140.34, 140.15, 140.04, 139.22, 138.43, 138.37, 137.30, 136.70, 131.80, 131.66, 131.11, 131.09, 130.89, 130.46, 130.33, 130.12, 129.94, 128.88, 128.30, 127.59, 127.52, 127.29, 127.22, 127.14, 127.08, 126.60, 126.51, 126.43, 126.16, 125.71, 125.67, 117.15, 52.08, 51.77, 22.93, 22.89, 22.49, 22.46, 21.61, 21.59, 21.32.

^{11}B NMR (128 MHz, CDCl_3): δ 40.0.

IR (KBr, neat): 3028, 2995, 2948, 1723, 1587, 1471, 1483, 1457, 1447, 1435, 1374, 1351, 1290, 1271, 1254, 1190, 1166, 1132, 1089, 1078, 1007, 967, 839, 773, 717, 669, 650 cm^{-1} .

HRMS (ESI-TOF): m/z calcd for $\text{C}_{50}\text{H}_{45}\text{BNO}_4^+$ [$\text{M}+\text{H}^+$]: 734.3436. Found: 734.3439.



Yield: 50.7 mg (68%, a 1:1:1:1 mixture of 4 rotamers)

Physical appearance: yellow solid, **m.p.:** 90-92 °C

R_f: 0.2 (EtOAc:hexanes = 1:9)

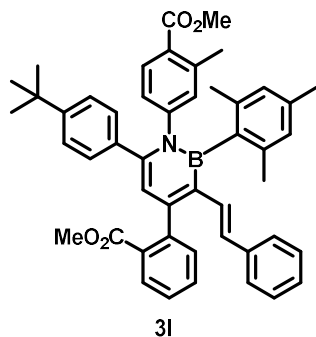
^1H NMR (500 MHz, CDCl_3): δ 7.99 (d, $J = 7.7$ Hz, 1H), 7.58 (q, $J = 7.9$ Hz, 2H), 7.46 (dd, $J = 18.6, 7.5$ Hz, 2H), 7.30 (t, $J = 7.1$ Hz, 2H), 7.11 – 7.08 (m, 5H), 7.03 (d, $J = 7.0$ Hz, 1H), 6.88 (d, $J = 8.3$ Hz, 2H), 6.82 – 6.78 (m, 4H), 6.76 (d, $J = 8.5$ Hz, 3H), [6.67 (s) + 6.65 (s) + 6.64 (s) = 2H] 6.46 (s, 1H), 5.95 (d, $J = 16.3$ Hz, 1H), 3.81 (s, 3H), 3.66 (s, 3H), [2.34 (s) + 2.33 (s) = 3H], 2.22 (s, 3H), [2.14 (s) + 2.12 (s) + 2.11 (s) + 2.09 (s) = 6H].

^{13}C NMR (126 MHz, CDCl_3): δ 168.24, 167.48, 157.11, 156.47, 153.27, 148.20, 145.56, 143.41, 140.10, 139.21, 138.36, 138.32, 136.70, 133.44, 131.87, 131.83, 131.63, 131.06, 130.87, 130.45, 130.28, 130.12, 130.09, 129.88, 129.86, 128.30, 127.51, 127.28, 127.23, 127.14, 127.08, 126.59, 126.50, 126.14, 125.75, 125.70, 123.48, 118.87, 118.86, 118.29, 116.77, 52.07, 51.82, 22.90, 22.88, 22.49, 22.46, 21.59, 21.31.

^{11}B NMR (128 MHz, CDCl_3): δ 39.6.

IR (KBr, neat): 3021, 2997, 2948, 1723, 1589, 1506, 1488, 1457, 1446, 1435, 1374, 1351, 1290, 1271, 1241, 1191, 1167, 1132, 1089, 1078, 1015, 967, 869, 848, 776, 692, 669, 650 cm^{-1} .

HRMS (ESI-TOF): m/z calcd for $\text{C}_{50}\text{H}_{45}\text{BNO}_5^+$ [$\text{M}+\text{H}^+$]: 750.3385. Found: 750.3391.



Yield: 41.1 mg (58%, a 1:1:1:1 mixture of 4 rotamers)

Physical appearance: yellow solid, **m.p.:** 99-101 °C

R_f: 0.35 (EtOAc:hexanes = 1:9)

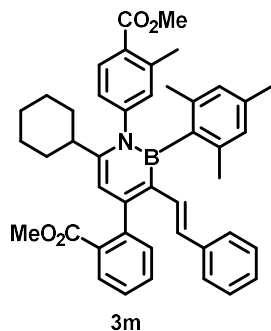
^1H NMR (500 MHz, CDCl_3): δ 7.98 (d, J = 7.7 Hz, 1H), 7.57 (t, J = 6.8 Hz, 1H), 7.54 (t, J = 8.4 Hz, 1H), 7.47 – 7.42 (m, 2H), 7.13 (d, J = 8.4 Hz, 2H), 7.09 (t, J = 7.5 Hz, 2H), 7.05 (d, J = 8.3 Hz, 2H), 7.02 (t, J = 7.4 Hz, 1H), 6.82 – 6.73 (m, 5H), [6.67 (s) + 6.65 (s) + 6.63 (s) = 2H], 6.45 (d, J = 3.3 Hz, 1H), 5.93 (d, J = 16.7 Hz, 1H), 3.79 (s, 3H), 3.65 (s, 3H), [2.30 (s) + 2.28 (s) = 3H], 2.22 (s, 3H), [2.15 (s) + 2.12 (s) + 2.10 (s) + 2.08 (s) = 6H], 1.23 (s, 9H).

^{13}C NMR (126 MHz, CDCl_3): δ 168.26, 167.61, 153.38, 153.36, 150.50, 148.26, 146.28, 146.26, 143.51, 139.96, 139.28, 138.41, 138.37, 136.61, 135.34, 131.86, 131.82, 131.58, 131.13, 131.08, 130.93, 130.87, 130.55, 130.16, 130.09, 130.07, 129.70, 129.24, 128.28, 127.44, 127.24, 127.19, 127.10, 127.04, 126.43, 126.39, 126.12, 125.71, 125.65, 124.67, 116.95, 52.03, 51.77, 34.59, 31.29, 22.90, 22.88, 22.47, 22.45, 21.51, 21.48, 21.31.

^{11}B NMR (128 MHz, CDCl_3): δ 40.8.

IR (KBr, neat): 3023, 2952, 2867, 1722, 1605, 1587, 1572, 1475, 1434, 1352, 1290, 1254, 1191, 1134, 1087, 1020, 968, 883, 836, 776, 733, 707, 694, 669 cm^{-1} .

HRMS (ESI-TOF): m/z calcd for $\text{C}_{48}\text{H}_{49}\text{BNO}_4^+$ [$\text{M}+\text{H}^+$]: 714.3749. Found: 714.3754.



Yield: 37.9 mg (57%, a mixture of 8 rotamers)

Physical appearance: yellow solid, **m.p.:** 88-90 $^{\circ}\text{C}$

R_f : 0.35 (EtOAc:hexanes = 1:9)

^1H NMR (500 MHz, CDCl_3): δ 7.97 (d, $J = 7.7$ Hz, 1H), 7.79 (dd, $J = 20.4, 8.2$ Hz, 1H), 7.56 (t, $J = 7.6$ Hz, 1H), 7.46 (t, $J = 7.7$ Hz, 1H), 7.39 (d, $J = 7.6$ Hz, 1H), 7.06 (t, $J = 7.5$ Hz, 2H), 7.02 – 6.97 (m, 2H), 6.94 – 6.92 (m, 1H), 6.78 – 6.75 (m, 3H), 6.60 – 6.58 (m, 2H), 6.24 (s, 1H), 5.84 (dd, $J = 16.3, 4.2$ Hz, 1H), 3.87 (s, 3H), [3.62 (s) + 3.61 (s) = 3H], [2.54 (s) + 2.49 (s) = 3H], 2.18 (s, 3H), 2.16 – 2.13 (m, 1H), [2.10 (s) + 2.09 (s) + 2.07 (s) + 2.06 (s) = 6H], 1.81 (t, $J = 13.5$ Hz, 2H), 1.65 (br, 2H), 1.56 (d, $J = 12.5$ Hz, 1H), 1.36 – 1.28 (m, 2H), 1.16 – 1.08 (m, 1H), 0.99 – 0.89 (m, 2H).

^{13}C NMR (126 MHz, CDCl_3): δ 168.75, 167.57, 153.70, 153.68, 152.07, 152.05, 147.71, 147.67, 143.92, 143.90, 140.80, 140.72, 139.45, 138.02, 137.98, 136.34, 131.33, 131.27, 131.01, 130.95, 130.85, 130.83, 130.53, 130.41, 129.99, 129.97, 128.78, 128.24, 127.70, 127.31, 127.16, 127.08,

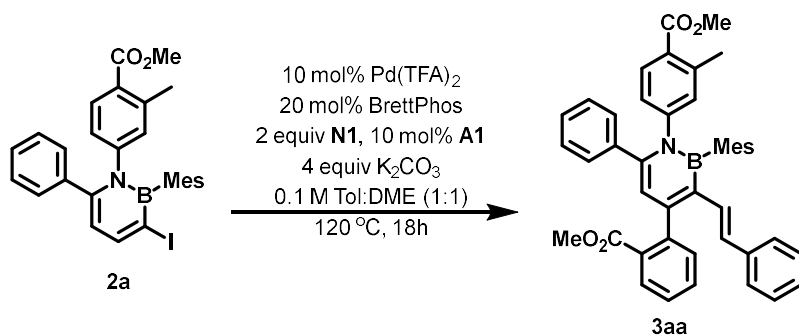
126.98, 126.95, 126.21, 126.01, 124.51, 124.35, 111.38, 51.96, 51.94, 41.04, 34.73, 34.53, 34.06, 33.86, 26.63, 25.90, 22.97, 22.53, 21.79, 21.77, 21.28.

^{11}B NMR (160 MHz, CDCl_3): δ 39.7.

IR (KBr, neat): 2928, 2852, 1723, 1589, 1571, 1475, 1447, 1405, 1342, 1292, 1254, 1190, 1127, 1082, 1053, 967, 910, 846, 757, 775, 734, 712, 693, 647 cm^{-1} .

HRMS (ESI-TOF): m/z calcd for $\text{C}_{44}\text{H}_{47}\text{BNO}_4^+$ [$\text{M}+\text{H}^+$]: 664.3593. Found: 664.3591.

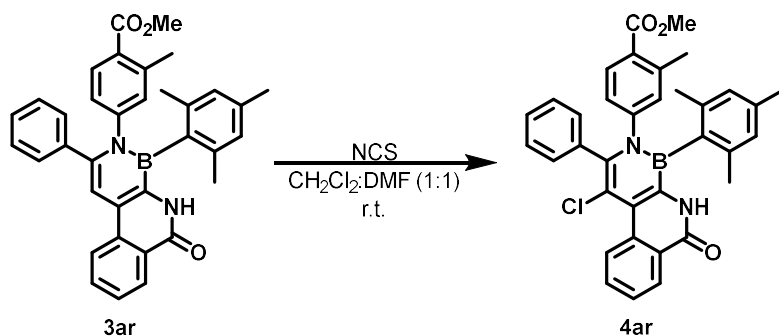
1.5.13. A gram-scale preparation of **3aa**:



To a flame-dried 40 mL vial A, **2a** (1.0 g, 1.827 mmol, 1 equiv), Ar-Br (393.0 mg, 1.827 mmol, 1 equiv), styrene (199.8 mg, 1.919 mmol, 1.05 equiv), **N1** (552.6 mg, 3.655 mmol, 2 equiv), **A1** (42.2 mg, 0.183 mmol, 10 mol%), and K_2CO_3 (1.01 g, 7.309 mmol, 4 equiv) were added. In a separate flame-dried 20 mL vial B, $\text{Pd}(\text{TFA})_2$ (60.7 mg, 0.183 mmol, 10 mol%) and BrettPhos (196.2 mg, 0.366 mmol, 20 mol%) were added. Both vials were brought into the glovebox, and 9.1 mL of DME and 9.1 mL of toluene were added to vial A and vial B, respectively. After stirring for 10 minutes, the solution in vial B was transferred to vial A. The tightly sealed vial was then placed on a pie-block preheated to 120 °C. After 18 h, the reaction mixture was filtered through a pad of celite and washed with ethyl acetate. The crude solution was concentrated to dryness in

vacuo and was subjected to flash column chromatography on silica gel (EtOAc:hexanes = 1:20 to 1:9) to give the pentasubstituted 1,2-azaborine **3aa** in 51% (613.0 mg) yield.

1.5.14. Synthetic procedure of **4ar**:



To a solution of **3ar** (53.8 mg, 0.1 mmol, 1 equiv) in CH₂Cl₂ (1.0 mL) and DMF (1.0 mL), NCS (13.4 mg, 0.1 mmol, 1 equiv) was added in one portion at r.t. The reaction mixture was stirred at r.t. for 16 h. Upon completion of the reaction, the crude solution was concentrated to dryness in vacuo. Then, the crude mixture was subjected to flash column chromatography on silica gel (EtOAc:hexanes = 1:3) to give **4ar**.

Yield: 48.2 mg (84%, a 1:1 mixture of 2 rotamers)

Physical appearance: yellow solid, **m.p.:** 112-114 °C

R_f: 0.25 (EtOAc:hexanes = 1:3)

¹H NMR (500 MHz, CDCl₃): δ 9.37 (d, *J* = 8.4 Hz, 1H), 8.61 (d, *J* = 8.0 Hz, 1H), 8.46 (s, 1H), 7.80 (d, *J* = 8.5 Hz, 1H), 7.69 (t, *J* = 7.2 Hz, 1H), 7.50 (d, *J* = 8.9 Hz, 1H), 7.23 – 7.16 (m, 5H), 6.72 – 6.71 (m, 4H), 3.75 (s, 3H), 2.29 (s, 3H), 2.21 (s, 3H), 2.08 (s, 3H), 2.05 (s, 3H).

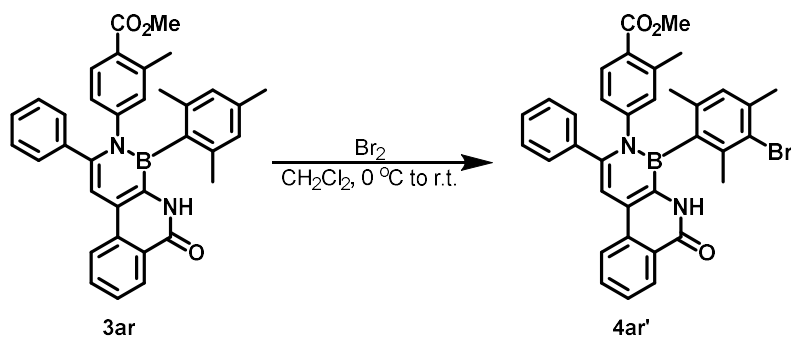
¹³C NMR (126 MHz, CDCl₃): δ 167.17, 161.50, 147.27, 141.55, 140.39, 139.51, 138.89, 136.39, 134.32, 131.74, 131.17, 131.14, 130.93, 130.56, 129.06, 128.97, 128.26, 128.23, 128.06, 128.00, 127.96, 127.90, 127.20, 124.92, 123.46, 115.18, 51.85, 22.84, 22.78, 21.50, 21.25.

^{11}B NMR (160 MHz, CDCl_3): δ 37.7.

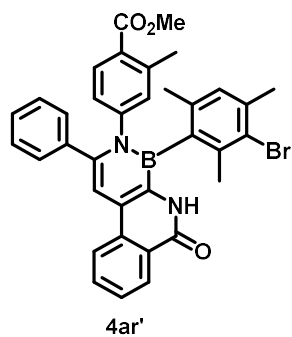
IR (KBr, neat): 3366, 2949, 1718, 1700, 1669, 1605, 1576, 1540, 1521, 1507, 1497, 1481, 1457, 1436, 1325, 1283, 1258, 1172, 1148, 1105, 1083, 1031, 993, 912, 850, 827, 776, 734, 711 cm^{-1} .

HRMS (ESI-TOF): m/z calcd for $\text{C}_{35}\text{H}_{30}\text{BClN}_2\text{NaO}_3^+$ [$\text{M}+\text{Na}^+$]: 595.1930. Found: 595.1923.

1.5.15. Synthetic procedure of **4ar'**:



To a solution of **3ar** (53.8 mg, 0.1 mmol, 1 equiv) in CH_2Cl_2 (2.0 mL), bromine (1.1 mL, 0.11 mmol, 1.1 equiv, 0.1 M in CH_2Cl_2) was added dropwise at $0\text{ }^\circ\text{C}$. The reaction mixture was warmed up to r.t. Upon completion of the reaction, the reaction was quenched with Et_3N (28 μL , 0.2 mmol, 2 equiv) and concentrated to dryness in vacuo. Then, the crude mixture was subjected to flash column chromatography on silica gel (EtOAc:hexanes = 1:20 to 1:9) to give **4ar'**.



Yield: 43.5 mg (71%, a 1:1 mixture of 2 rotamers)

Physical appearance: white solid, **m.p.:** 254-256 °C

R_f: 0.55 (EtOAc:hexanes = 1:2)

¹H NMR (500 MHz, CDCl₃): δ 8.58 (d, *J* = 8.0 Hz, 1H), 8.27 (d, *J* = 8.3 Hz, 1H), 8.25 (N-H, br, 1H) 7.84 (t, *J* = 7.6 Hz, 1H), 7.69 (t, *J* = 7.6 Hz, 1H), 7.57 (dd, *J* = 16.9, 8.3 Hz, 1H), 7.31 (s, 1H), 7.21 (br, 5H), 6.81 (d, *J* = 5.9 Hz, 1H), 6.77 – 6.99 (m, 2H), 3.79 (s, 3H), 2.34 (s, 3H), [2.32 (s) + 2.30 (s) = 3H], [2.24 (s) + 2.23 (s) = 3H], [2.00 (s) + 1.99 (s) = 3H].

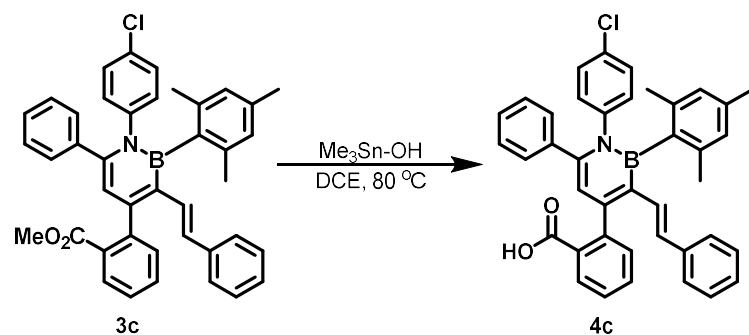
¹³C NMR (126 MHz, CDCl₃): δ 167.29, 167.26, 161.79, 147.43, 143.14, 143.12, 140.70, 140.63, 139.14, 138.88, 138.85, 138.23, 138.09, 134.43, 132.84, 131.16, 131.15, 130.82, 130.72, 130.09, 130.05, 129.75, 129.15, 128.61, 128.49, 128.09, 127.83, 127.30, 125.86, 125.79, 125.06, 124.97, 123.16, 108.28, 51.92, 25.13, 25.02, 24.05, 22.22, 21.62, 21.60.

¹¹B NMR (160 MHz, CDCl₃): δ 37.0.

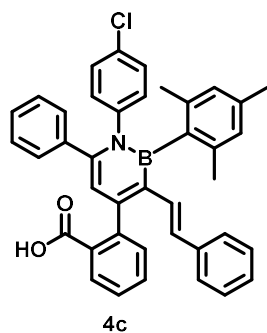
IR (KBr, neat): 3379, 2949, 1722, 1652, 1605, 1569, 1530, 1488, 1446, 1435, 1381, 1340, 1282, 1259, 1203, 1149, 1090, 1068, 1035, 963, 910, 841, 773, 733, 715, 703 cm⁻¹.

HRMS (ESI-TOF): *m/z* calcd for C₃₅H₃₁BBrN₂O₃⁺ [M+H⁺]: 617.1606. Found: 617.1601.

1.5.16. Synthetic procedure of **4c**:



A 4 mL reaction vial was charged with **3c** (62.0 mg, 0.1 mmol, 1 equiv), trimethyltin hydroxide (162.7 mg, 0.9 mmol, 9 equiv), and 1,2-dichloroethane (1.0 mL). The resulting solution was stirred at $80\text{ }^\circ\text{C}$ on a preheated pie-block for 3 days. Upon completion of the reaction, the vial was cooled down to r.t. All volatiles were removed under reduced pressure, and the crude mixture was subjected to flash column chromatography on silica gel (Hexanes: CH_2Cl_2 :MeOH = 6:3:0.5) to give **4c**.



Yield: 59.4 mg (98%, a 1:1 mixture of 2 rotamers)

Physical appearance: light yellow solid, **m.p.:** 191-193 $^\circ\text{C}$

R_f: 0.5 (EtOAc:hexanes = 1:1, R_f obtained from the middle point of the streaking spot)

Poor solubility in CDCl_3 (NMRs were measured at $50\text{ }^\circ\text{C}$)

^1H NMR (600 MHz, CDCl_3): δ 8.09 (d, $J = 7.9$ Hz, 1H), 7.63 (t, $J = 7.6$ Hz, 1H), 7.48 (t, $J = 7.7$ Hz, 1H), 7.44 (d, $J = 7.7$ Hz, 1H), 7.13 – 7.08 (m, 5H), 7.07 (d, $J = 7.8$ Hz, 2H), 7.00 (t, $J = 7.3$

Hz, 1H), 6.90 (d, $J = 8.3$ Hz, 1H), 6.85 – 6.81 (m, 2H), 6.76 (d, $J = 8.1$ Hz, 4H), 6.66 (s, 1H), 6.57 (s, 1H), 6.42 (s, 1H), 5.91 (d, $J = 16.3$ Hz, 1H), 2.21 (s, 3H), 2.12 (s, 3H), 2.01 (s, 3H).

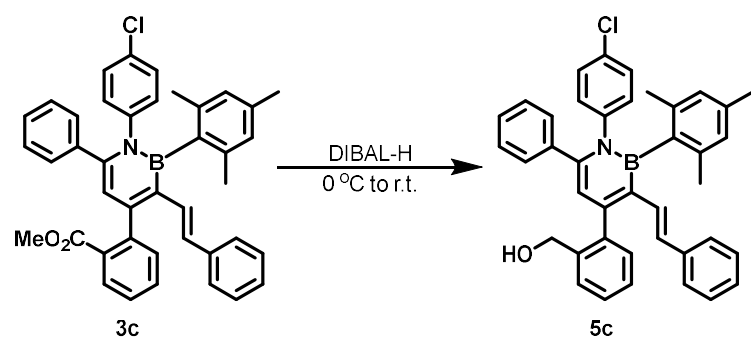
^{13}C NMR (126 MHz, CDCl_3): δ 169.85, 152.94, 146.57, 144.70, 143.76, 139.37, 138.74, 138.46, 138.33, 136.80, 132.51, 131.64, 131.06, 130.40, 130.37, 129.83, 129.66, 129.57, 129.31, 128.32, 127.87, 127.68, 127.58, 127.51, 127.44, 127.12, 126.56, 126.24, 116.79, 22.90, 22.37, 21.29.

^{11}B NMR (160 MHz, CDCl_3): δ 40.8.

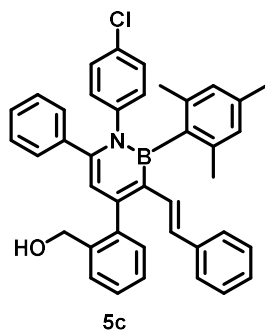
IR (KBr, neat): 3305, 2918, 1680, 1585, 1571, 1489, 1476, 1452, 1402, 1375, 1353, 1302, 1262, 1238, 1165, 1089, 1014, 967, 850, 833, 775, 757, 740, 732, 696, 668 cm^{-1} .

HRMS (ESI-TOF): m/z calcd for $\text{C}_{40}\text{H}_{33}\text{BClNO}_2^+$ [M^+]: 605.2287. Found: 605.2291.

1.5.17. Synthetic procedure of **5c**:



A flame-dried 5 mL round-bottom flask was charged with **3c** (62.0 mg, 0.1 mmol, 1 equiv) and dry THF (1.0 mL). At 0 °C, DIBAL-H (1M solution in hexanes, 0.25 mL, 0.25 mmol, 2.5 equiv) was added dropwise, then the solution was warmed up to r.t. Upon completion of the reaction, the reaction was quenched with 0.1 mL of MeOH. All volatiles were removed under reduced pressure, and the crude mixture was subjected to flash column chromatography on silica gel (EtOAc:hexanes = 1:4) to give **5c**.



Yield: 51.2 mg (86%, a 1:1 mixture of 2 rotamers)

Physical appearance: yellow solid, **m.p.:** 100-102 °C

R_f: 0.3 (EtOAc:hexanes = 1:4)

¹H NMR (500 MHz, CDCl₃): δ 7.61 (d, *J* = 7.4 Hz, 1H), 7.46 – 7.40 (m, 2H), 7.35 (dd, *J* = 7.4, 1.7 Hz, 1H), 7.15 – 7.12 (m, 5H), 7.09 (t, *J* = 7.4 Hz, 2H), 7.03 (t, *J* = 7.3 Hz, 1H), 6.93 – 6.90 (m, 2H), 6.85 (dd, *J* = 8.8, 2.5 Hz, 1H), 6.81 – 6.75 (m, 4H), 6.68 (s, 2H), 6.47 (s, 1H), 5.95 (d, *J* = 16.5 Hz, 1H), [4.62 (s) + 4.61 (s) = 2H], 2.24 (s, 3H), 2.11 (s, 3H), 2.09 (s, 3H), 1.67 (t, *J* = 6.4 Hz, 1H).

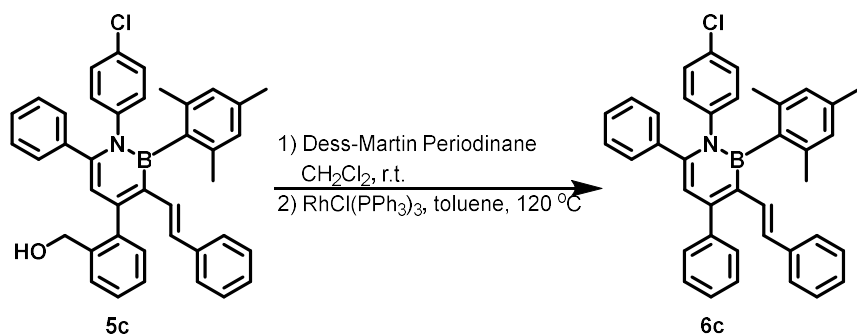
¹³C NMR (126 MHz, CDCl₃): δ 152.33, 147.07, 143.47, 141.27, 138.82, 138.32, 138.26, 138.10, 136.92, 131.64, 130.34, 130.11, 129.65, 129.46, 129.43, 129.08, 128.41, 128.06, 127.97, 127.92, 127.74, 127.70, 127.62, 127.34, 126.81, 126.15, 117.10, 63.67, 22.86, 22.69, 21.35.

¹¹B NMR (160 MHz, CDCl₃): δ 41.1.

IR (KBr, neat): 3421, 3022, 2930, 1608, 1586, 1569, 1490, 1446, 1402, 1375, 1351, 1265, 1167, 1091, 1029, 1015, 971, 908 851, 833, 761, 731, 699 cm⁻¹.

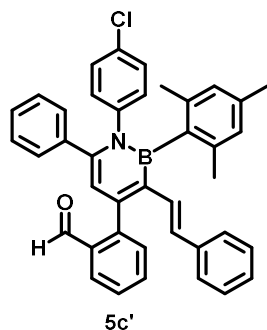
HRMS (ESI-TOF): *m/z* calcd for C₄₀H₃₆BClNO⁺ [M+H⁺]: 592.2573. Found: 592.2575.

1.5.18. Synthetic procedure of **6c**:



A 5 mL round-bottom flask was charged with **5c** (59.2 mg, 0.1 mmol, 1 equiv) was added Dess-Martin Periodinane (DMP, 46.7 mg, 0.11 mmol, 1.1 equiv) and CH₂Cl₂ (1.0 mL). The reaction proceeded very quickly (under 5 min). The solution was filtered through a short pad of celite and washed with EtOAc. All volatiles were removed in vacuo, and the crude mixture was subjected to flash column chromatography on silica gel (EtOAc:hexanes = 1:4) to afford the corresponding aldehyde (**5c'**) in a quantitative yield.

To a flame-dried 4 mL reaction vial charged with the aldehyde and RhCl(PPh₃)₃ (92.5 mg, 0.1 mmol, 1 equiv), toluene (2.0 mL) was added. The solution was heated and stirred at 120 °C on a preheated pie-block overnight. After cooling down to r.t., the crude mixture was passed through a pad of celite and washed with EtOAc. All volatiles were removed in vacuo, and the crude mixture was subjected to flash column chromatography on silica gel (EtOAc:hexanes = 1:4) to afford **6c**.



Yield: 58.8 mg (quantitative yield, a 1:1 mixture of 2 rotamers)

Physical appearance: yellow solid, **m.p.:** 89-91 °C

R_f: 0.6 (EtOAc:hexanes = 1:4)

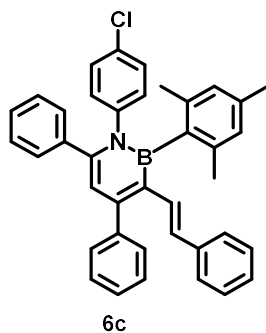
¹H NMR (500 MHz, CDCl₃): δ 10.07 (s, 1H), 8.08 (d, *J* = 6.9 Hz, 1H), 7.70 (t, *J* = 7.3 Hz, 1H), 7.54 (t, *J* = 7.5 Hz, 1H), 7.50 (d, *J* = 7.6 Hz, 1H), 7.16 – 7.12 (m, 6H), 7.08 (t, *J* = 7.3 Hz, 2H), 7.04 – 7.02 (m, 1H), 6.93 – 6.90 (m, 2H), 6.86 – 6.84 (m, 1H), 6.80 (dd, *J* = 8.7, 2.8 Hz, 1H), 6.76 – 6.72 (m, 3H), 6.67 (s, 2H), 6.51 (s, 1H), 5.96 (d, *J* = 16.4 Hz, 1H), 2.24 (s, 3H), 2.12 (s, 3H), 2.07 (s, 3H).

¹³C NMR (126 MHz, CDCl₃): δ 192.36, 148.98, 147.03, 146.72, 143.32, 138.72, 138.34, 138.21, 137.88, 137.04, 134.02, 133.44, 131.79, 131.42, 130.51, 129.71, 129.64, 129.42, 129.38, 128.37, 128.23, 127.99, 127.78, 127.74, 127.42, 127.34, 127.25, 126.93, 126.21, 117.50, 22.88, 22.75, 21.35.

¹¹B NMR (160 MHz, CDCl₃): δ 40.4.

IR (KBr, neat): 3057, 3022, 2917, 2851, 1696, 1608, 1586, 1560, 1491, 1446, 1374, 1351, 1264, 1198, 1167, 1091, 1029, 1015, 969, 897, 851, 833, 775, 764, 732, 699, 669 cm⁻¹.

HRMS (ESI-TOF): *m/z* calcd for C₄₀H₃₄BClNO⁺ [M+H⁺]: 590.2416. Found: 590.2418.



Yield: 36.1 mg (64%)

Physical appearance: yellow solid, **m.p.:** 94-96 °C

R_f: 0.5 (EtOAc:hexanes = 1:9)

¹H NMR (500 MHz, CDCl₃): δ 7.52 (d, *J* = 7.1 Hz, 2H), 7.46 (t, *J* = 7.5 Hz, 2H), 7.39 (t, *J* = 7.3 Hz, 1H), 7.15 – 7.11 (m, 7H), 7.08 (d, *J* = 16.6 Hz, 1H), 7.04 (d, *J* = 7.2 Hz, 1H). 6.90 (d, *J* = 8.7 Hz, 2H), 6.86 (d, *J* = 7.2 Hz, 2H), 6.82 (d, *J* = 8.6 Hz, 2H), 6.67 (s, 2H), 6.60 (s, 1H), 5.96 (d, *J* = 16.4 Hz, 1H), 2.25 (s, 3H), 2.10 (s, 6H).

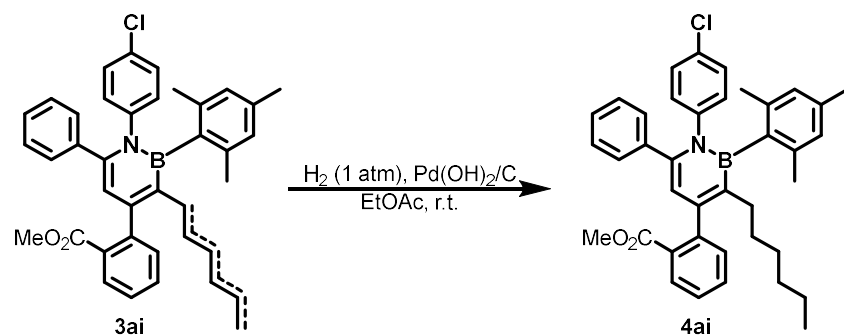
¹³C NMR (126 MHz, CDCl₃): δ 153.30, 146.89, 143.63, 142.46, 139.35, 138.46, 138.40, 136.71, 131.49, 131.05, 129.76, 129.66, 129.60, 129.51, 128.37, 128.20, 127.89, 127.62, 127.55, 127.48, 127.25, 126.45, 126.16, 117.41, 22.86, 21.35.

¹¹B NMR (160 MHz, CDCl₃): δ 40.7.

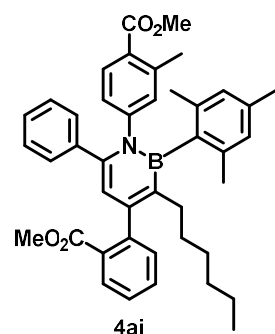
IR (KBr, neat): 3021, 2913, 1608, 1587, 1570, 1491, 1445, 1402, 1375, 1351, 1263, 1167, 1091, 1015, 1030, 968, 897, 850, 833, 775, 765, 732, 699, 653 cm⁻¹.

HRMS (ESI-TOF): *m/z* calcd for C₃₉H₃₄BClN⁺ [M+H⁺]: 562.2467. Found: 562.2472.

1.5.19. Synthetic procedure of **4ai**:



A 5 mL round-bottom flask was charged with **3ai** (63.8 mg, 0.1 mmol, 1 equiv), $\text{Pd}(\text{OH})_2/\text{C}$ (20 wt%, 21.1 mg, 0.03 mmol, 3 mol%) and EtOAc (2.0 mL). The flask was evacuated and backfilled with H_2 three times. Then the reaction was stirred for 16 h in the presence of a H_2 balloon. Upon completion of the reaction, the balloon was removed, and the crude mixture was filtered through a short pad of celite and washed with EtOAc. All volatiles were removed in vacuo, and the resulting product **4ai** was found spectroscopically pure by NMR.



Yield: 20.5 mg (96%, a 1:1 mixture of 2 rotamers)

Physical appearance: off-white amorphous solid

R_f: 0.3 (EtOAc:hexanes = 1:9)

¹H NMR (500 MHz, CDCl₃): δ 7.96 (d, *J* = 7.8 Hz, 1H), 7.54 (t, *J* = 7.4 Hz, 1H), 7.50 (t, *J* = 7.8 Hz, 1H), 7.40 (t, *J* = 7.7 Hz, 1H), 7.37 (d, *J* = 7.6 Hz, 1H), 7.11 – 7.07 (m, 5H), 6.76 – 6.72 (m, 1H), 6.68 – 6.66 (m, 1H), [6.63 (s) + 6.61 (s) + 6.59 (s) = 2H], 6.31 (s, 1H), 3.77 (s, 3H), [3.72 (s) + 3.71 (s) = 3H], [2.28 (s) + 2.26 (s) = 3H], 2.17 (s, 3H), [2.11 (s) + 2.07 (s) = 6H], 2.00 – 1.95 (m, 2H), 1.03 – 0.93 (m, 4H), 0.85 – 0.78 (m, 4H), 0.68 (t, *J* = 7.3 Hz, 3H).

¹³C NMR (126 MHz, CDCl₃): δ 168.31, 168.28, 167.59, 152.96, 148.64, 148.62, 144.35, 143.85, 143.82, 140.01, 138.65, 138.45, 136.20, 131.83, 131.74, 131.42, 130.38, 130.37, 130.20, 130.17, 130.15, 130.13, 129.61, 127.72, 127.18, 127.07, 126.90, 126.88, 126.85, 126.22, 125.67, 125.56, 116.64, 116.63, 51.87, 51.74, 31.91, 31.14, 30.05, 29.48, 23.36, 23.32, 22.79, 22.77, 22.34, 21.54, 21.26, 14.13.

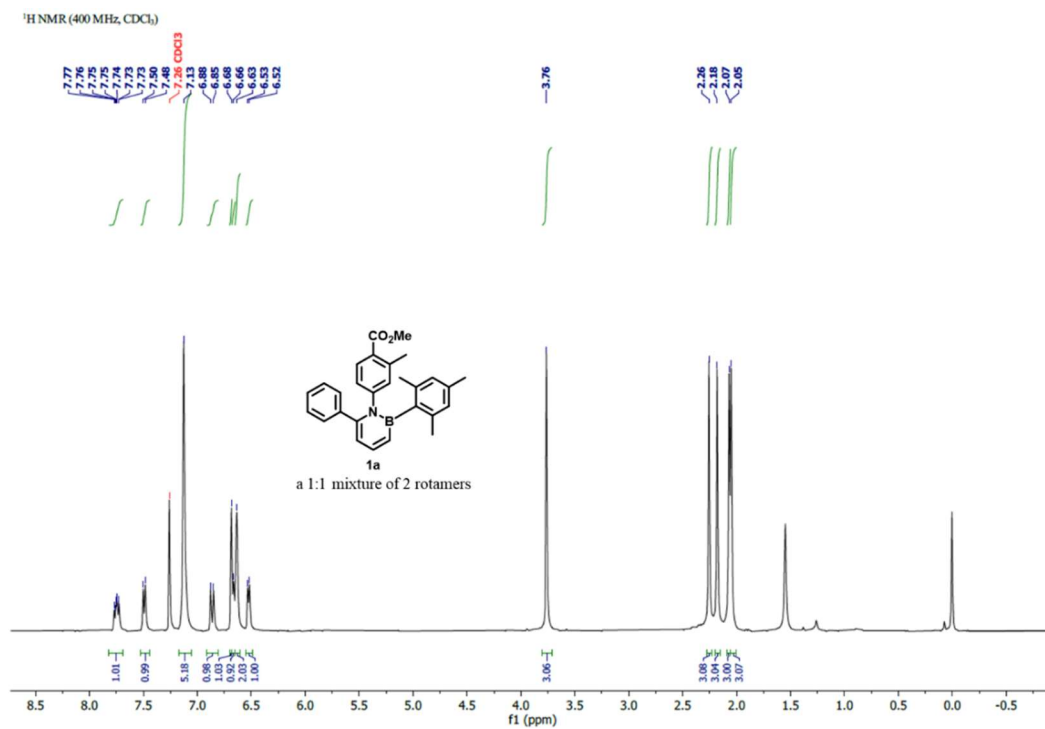
¹¹B NMR (160 MHz, CDCl₃): δ 41.0.

IR (KBr, neat): 2927, 2855, 1722, 1594, 1572, 1488, 1446, 1376, 1254, 1190, 1131, 1089, 849, 753, 700 cm⁻¹.

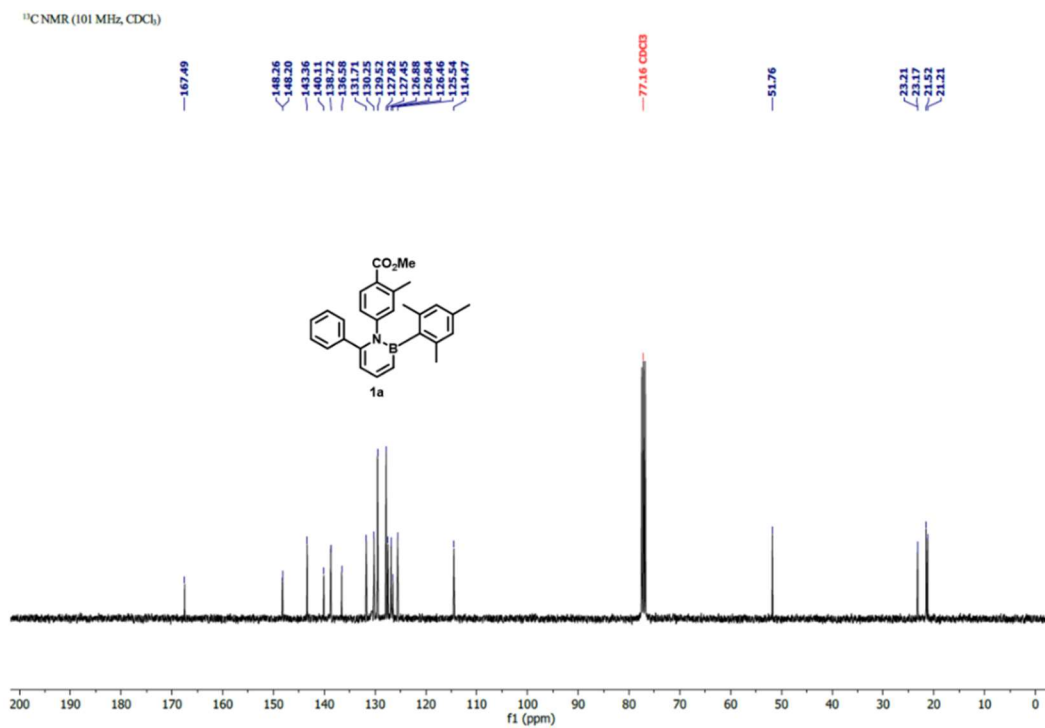
HRMS (ESI-TOF): *m/z* calcd for [M+H⁺]: 640.3593. Found: 640.3595.

1.6. NMR Spectra

^1H NMR of **1a**

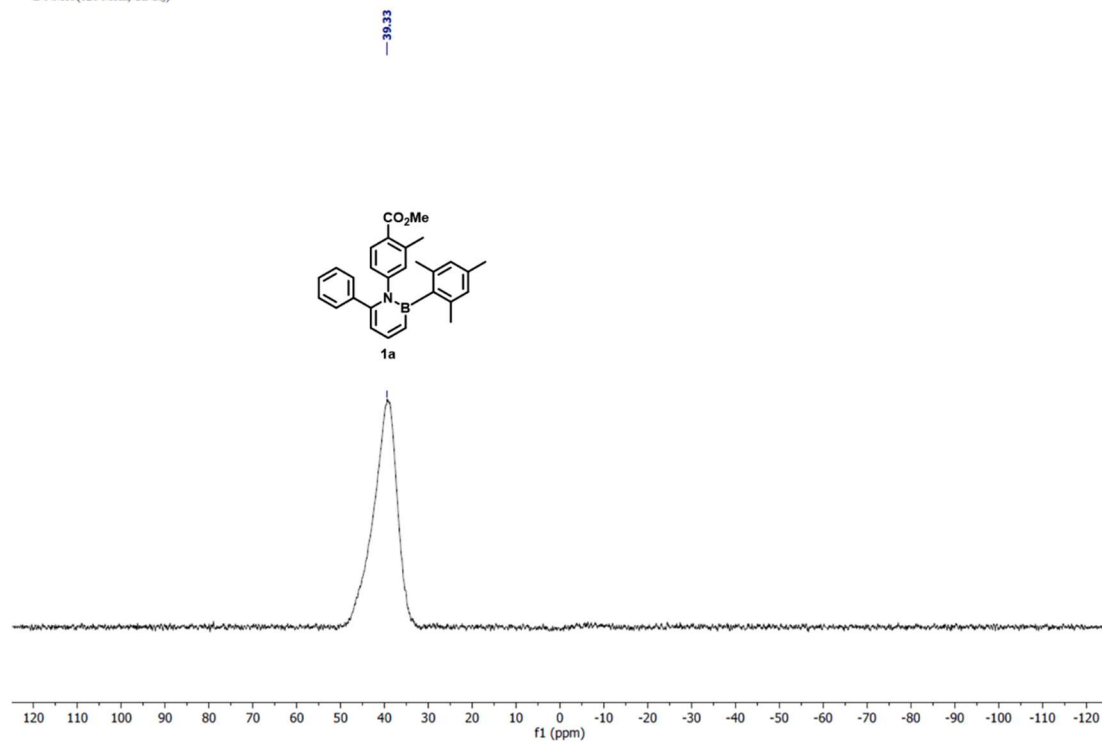


^{13}C NMR of **1a**



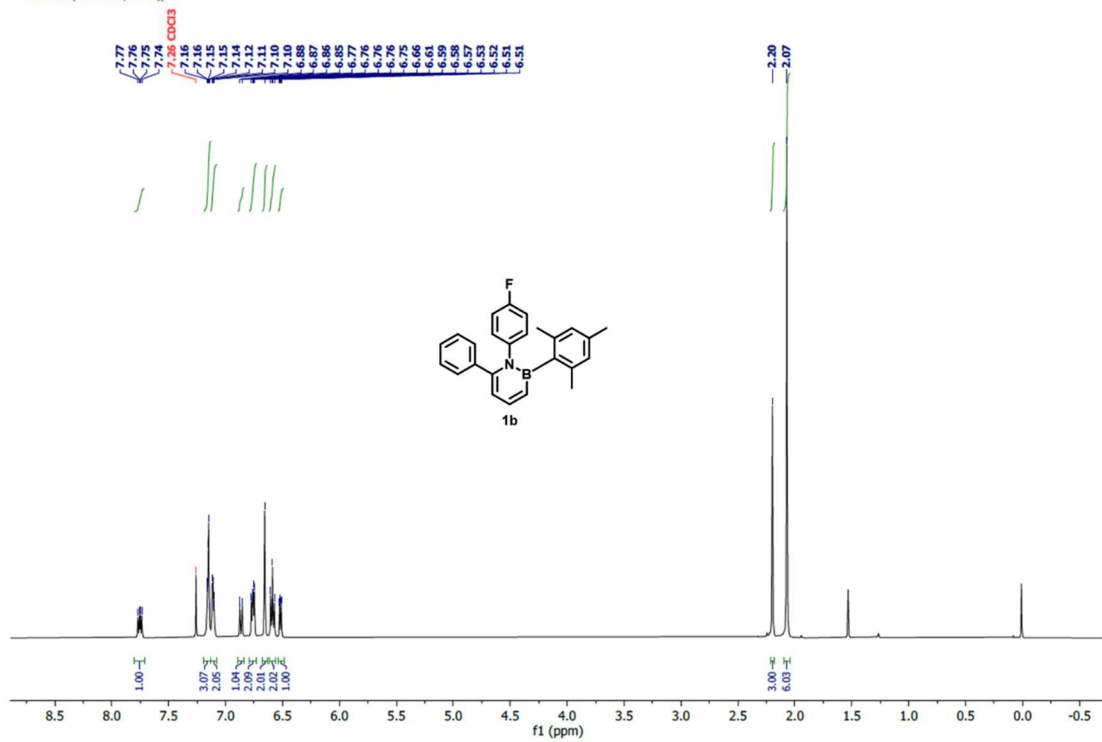
^{11}B NMR of **1a**

^{11}B NMR (128 MHz, CDCl_3)



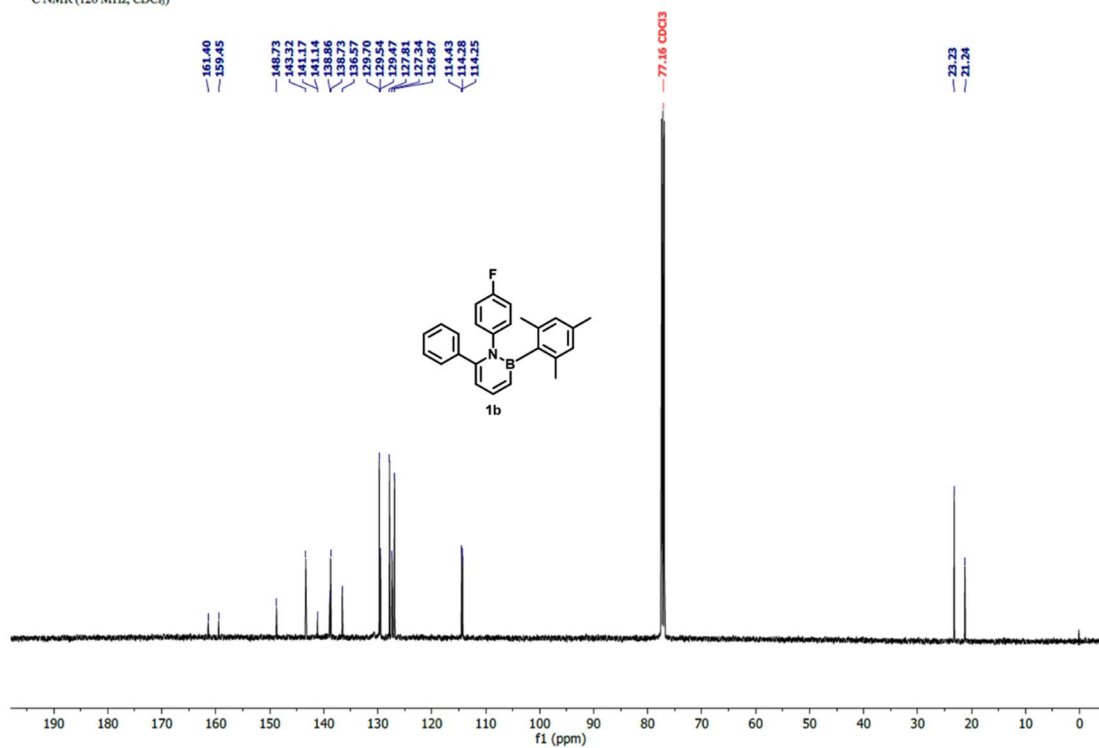
^1H NMR of **1b**

^1H NMR (500 MHz, CDCl_3)



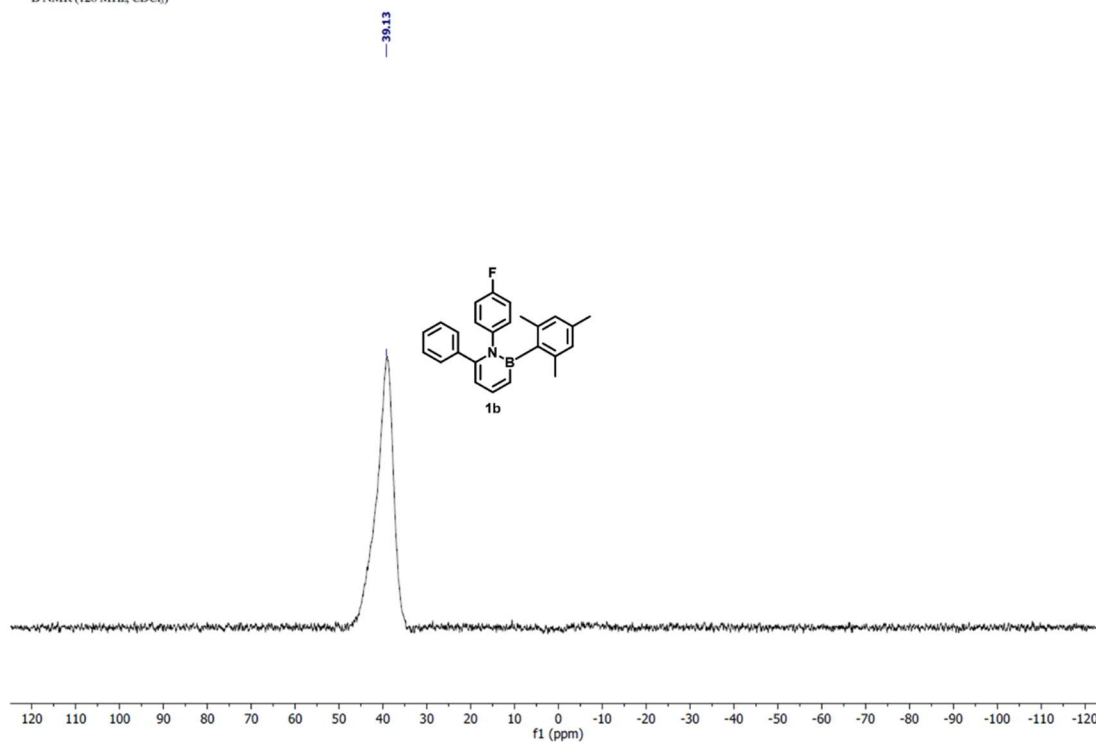
¹³C NMR of **1b**

¹³C NMR (126 MHz, CDCl₃)



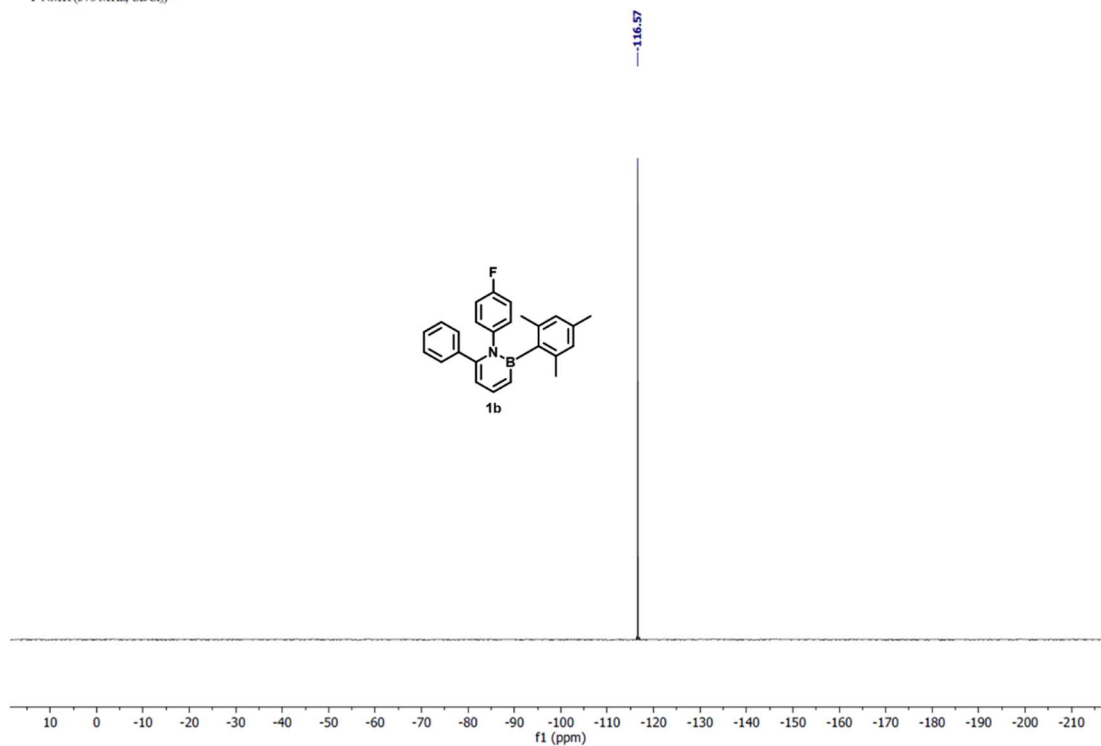
¹¹B NMR of **1b**

¹¹B NMR (128 MHz, CDCl₃)



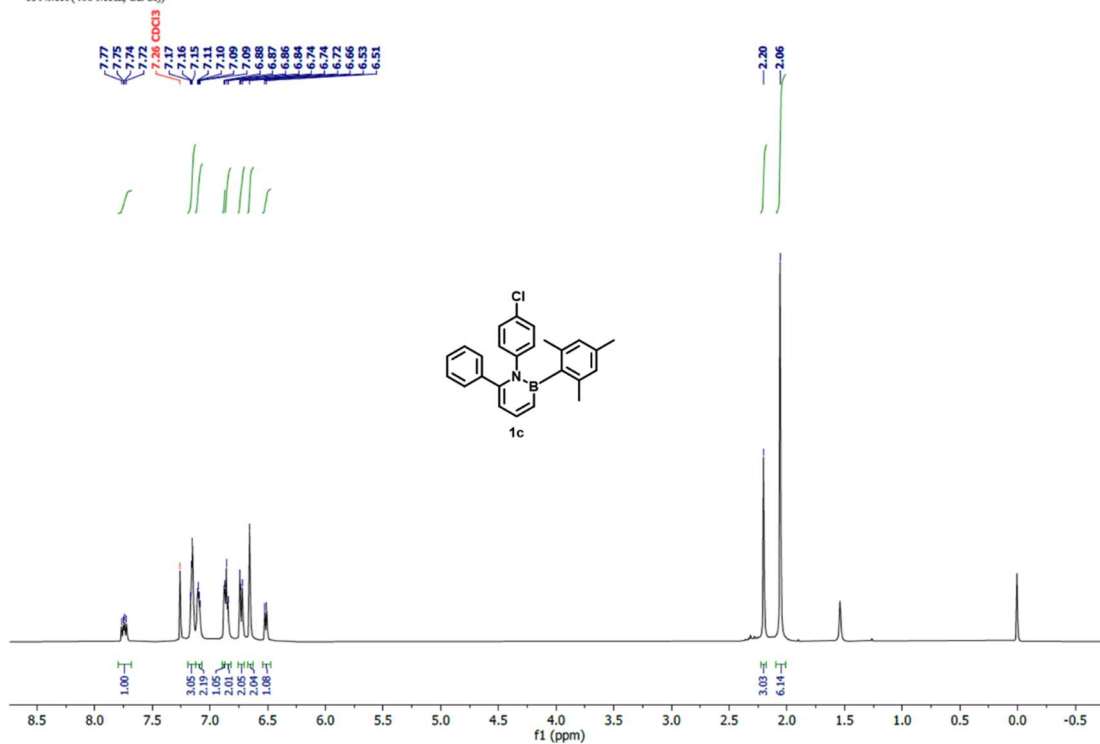
^{19}F NMR of **1b**

^{19}F NMR (376 MHz, CDCl_3)



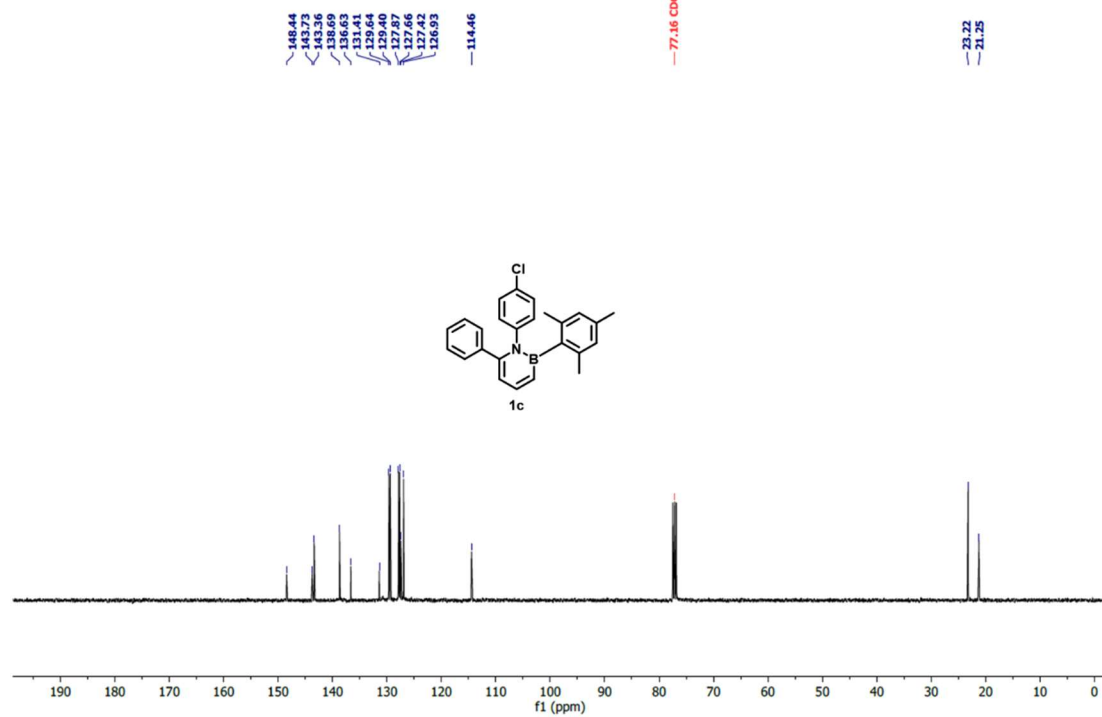
^1H NMR of **1c**

^1H NMR (400 MHz, CDCl_3)



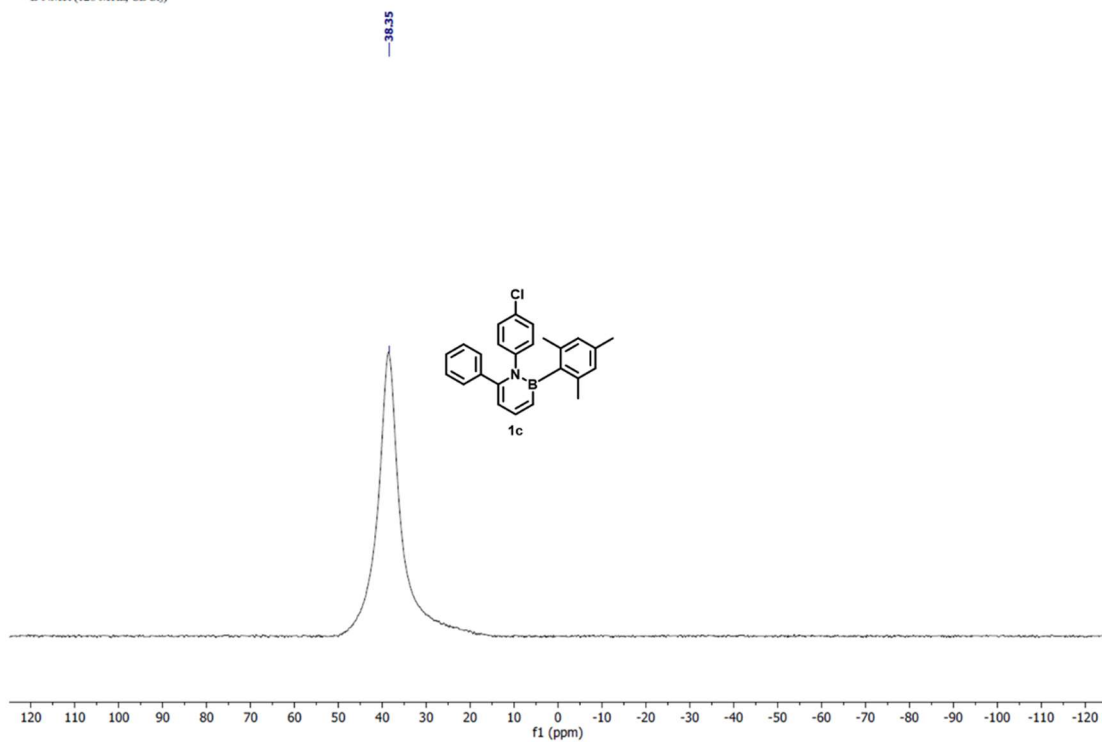
^{13}C NMR of **1c**

^{13}C NMR (101 MHz, CDCl_3)



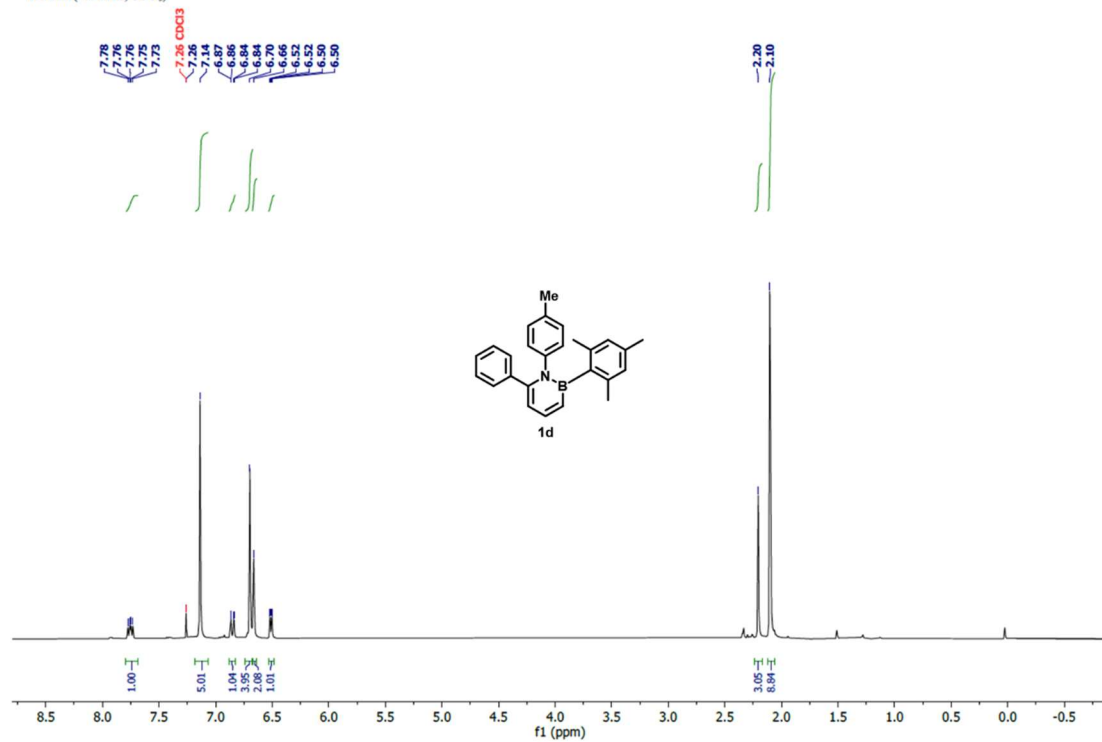
^{11}B NMR of **1c**

^{11}B NMR (128 MHz, CDCl_3)



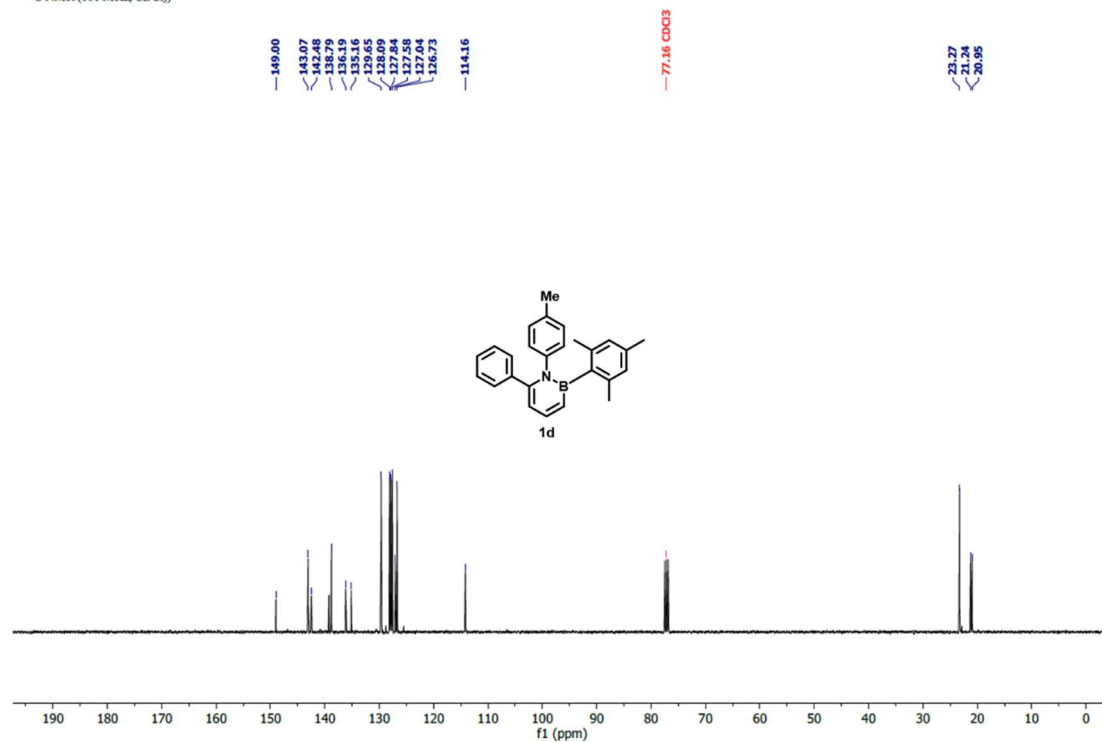
^1H NMR of **1d**

^1H NMR (400 MHz, CDCl_3)



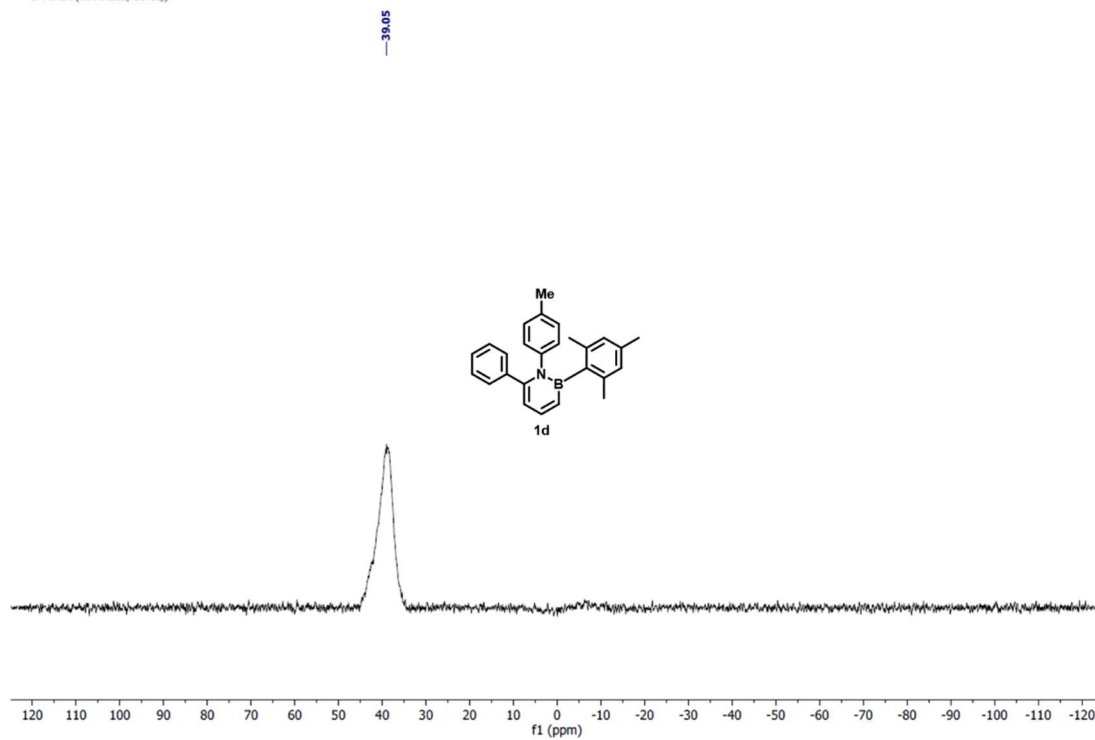
^{13}C NMR of **1d**

^{13}C NMR (101 MHz, CDCl_3)



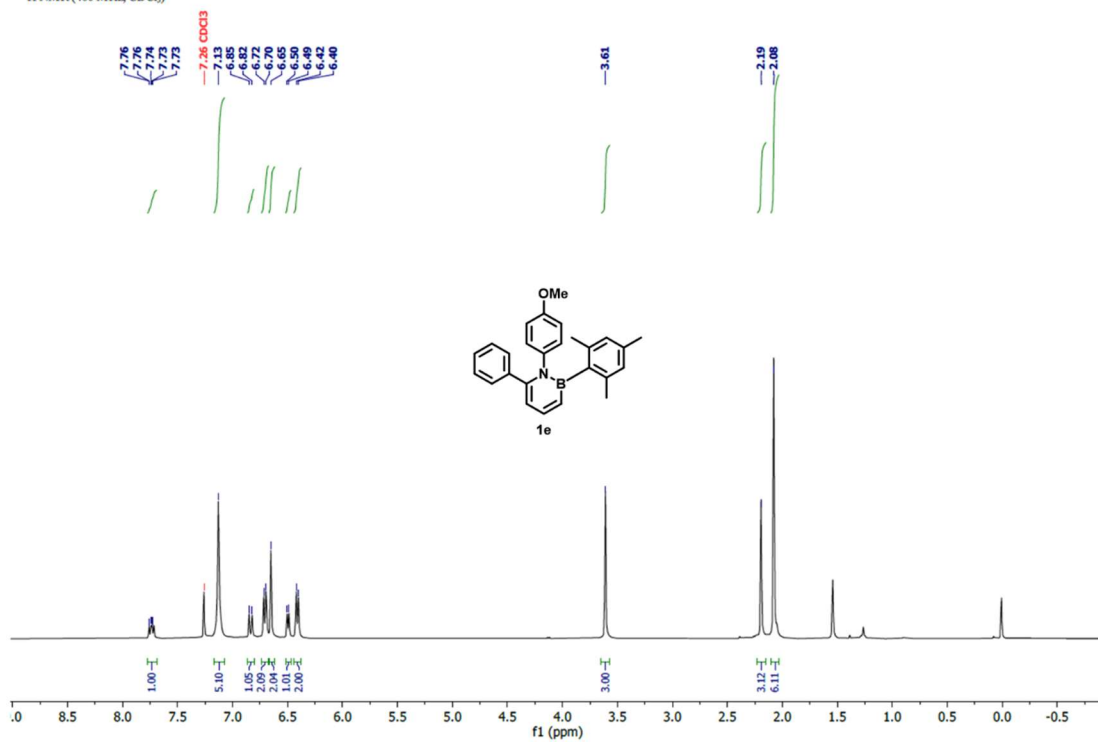
^{11}B NMR of **1d**

^{11}B NMR (128 MHz, CDCl_3)



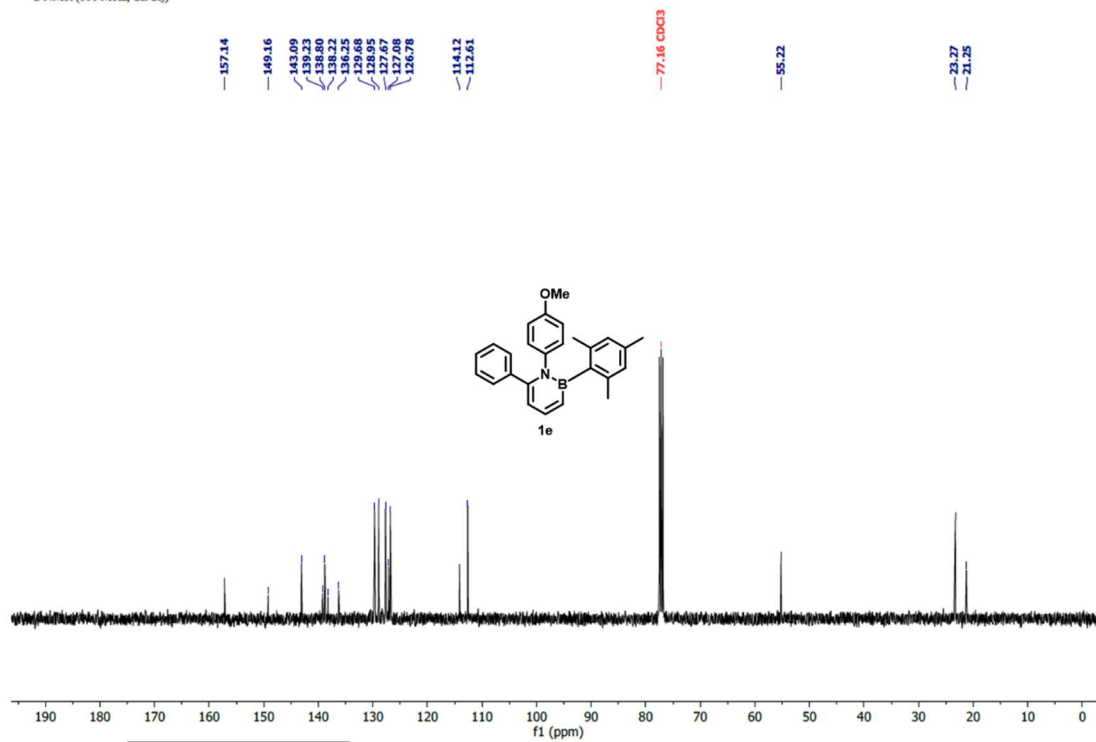
^1H NMR of **1e**

^1H NMR (400 MHz, CDCl_3)



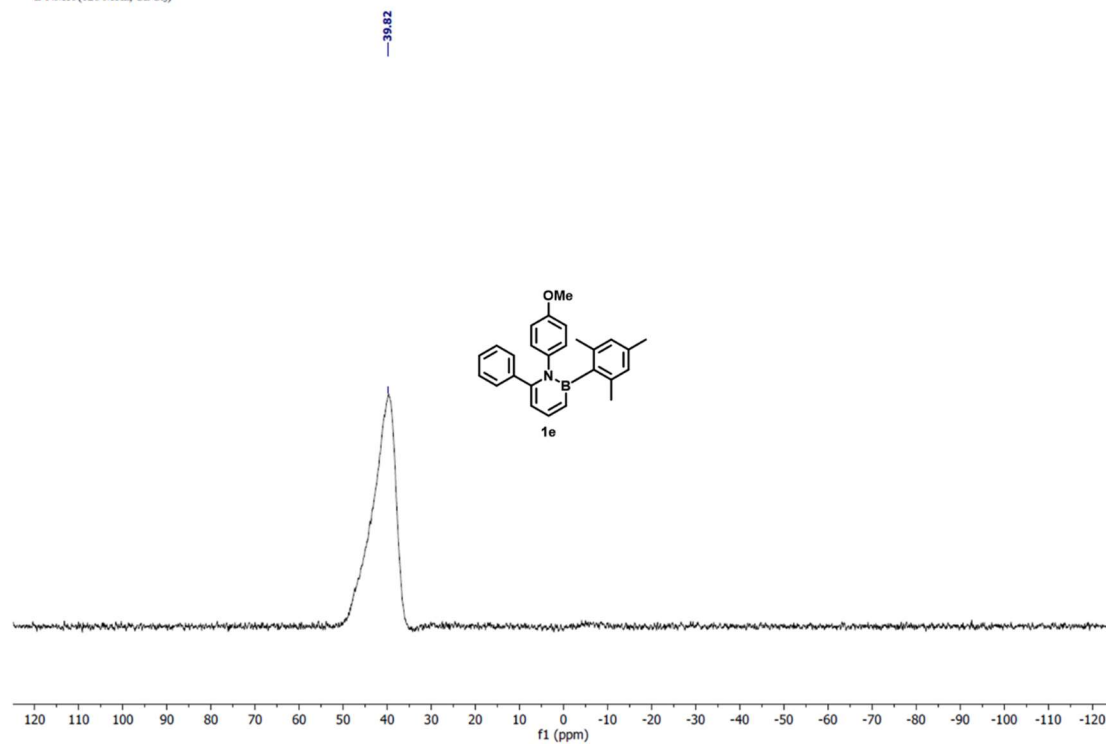
^{13}C NMR of **1e**

^{13}C NMR (101 MHz, CDCl_3)



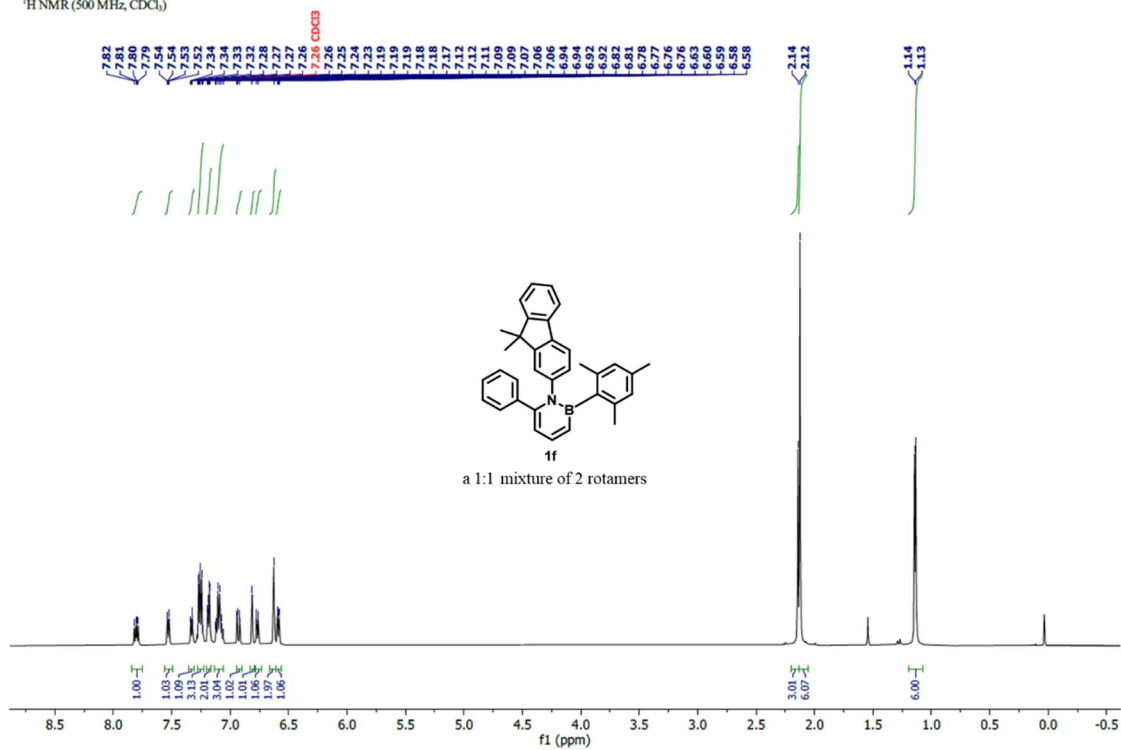
^{11}B NMR of **1e**

^{11}B NMR (128 MHz, CDCl_3)



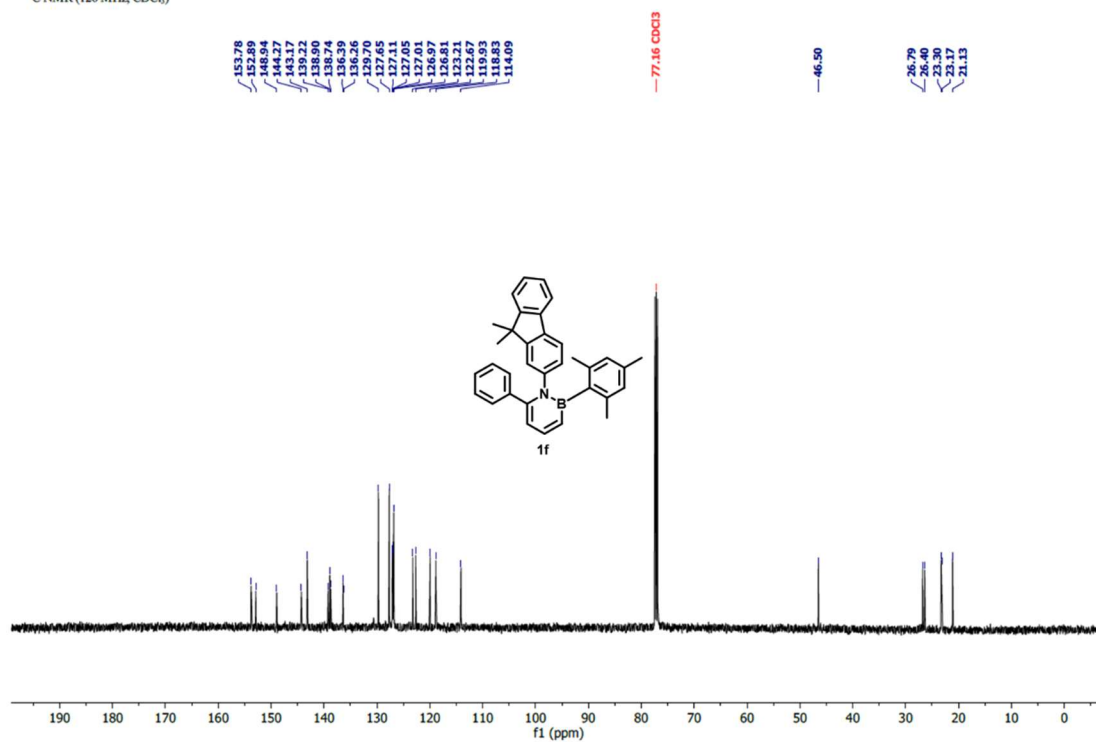
¹H NMR of **1f**

¹H NMR (500 MHz, CDCl₃)



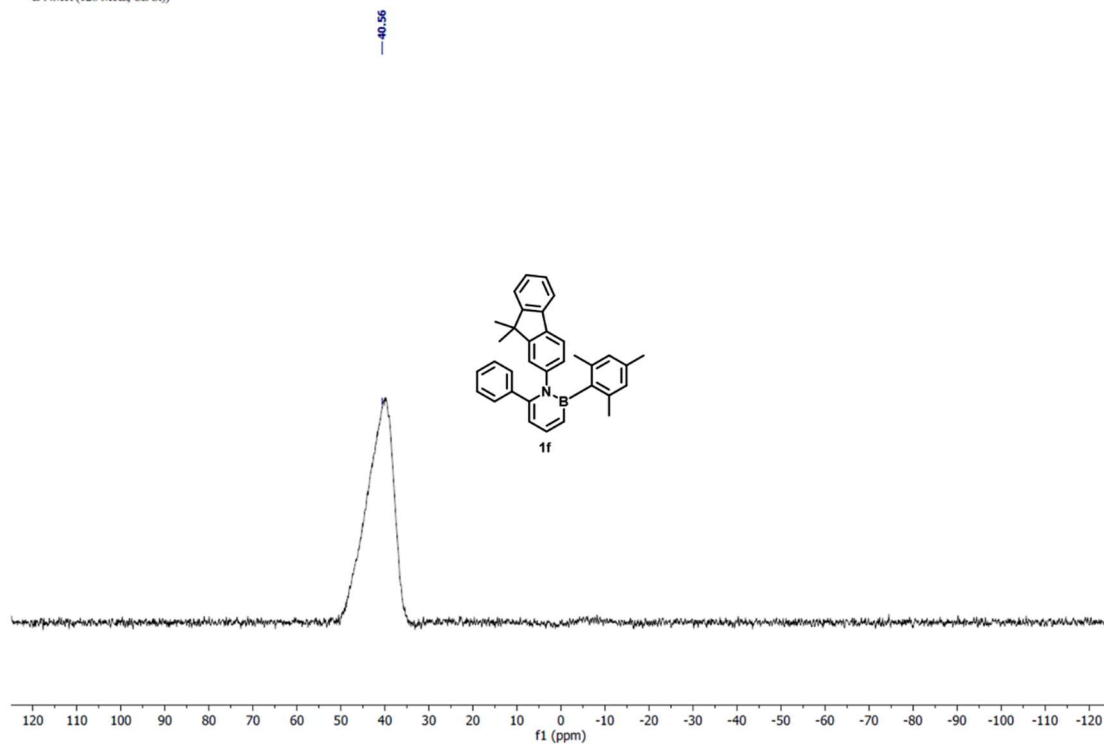
¹³C NMR of **1f**

¹³C NMR (126 MHz, CDCl₃)



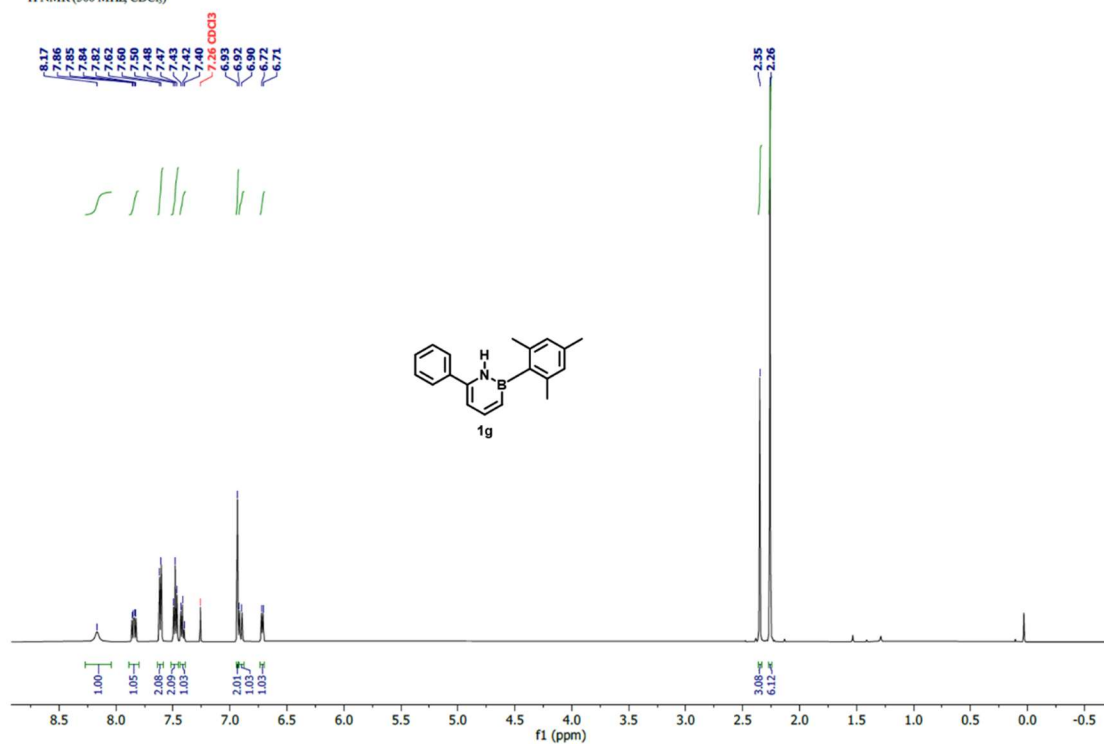
^{11}B NMR of **1f**

^{11}B NMR (128 MHz, CDCl_3)



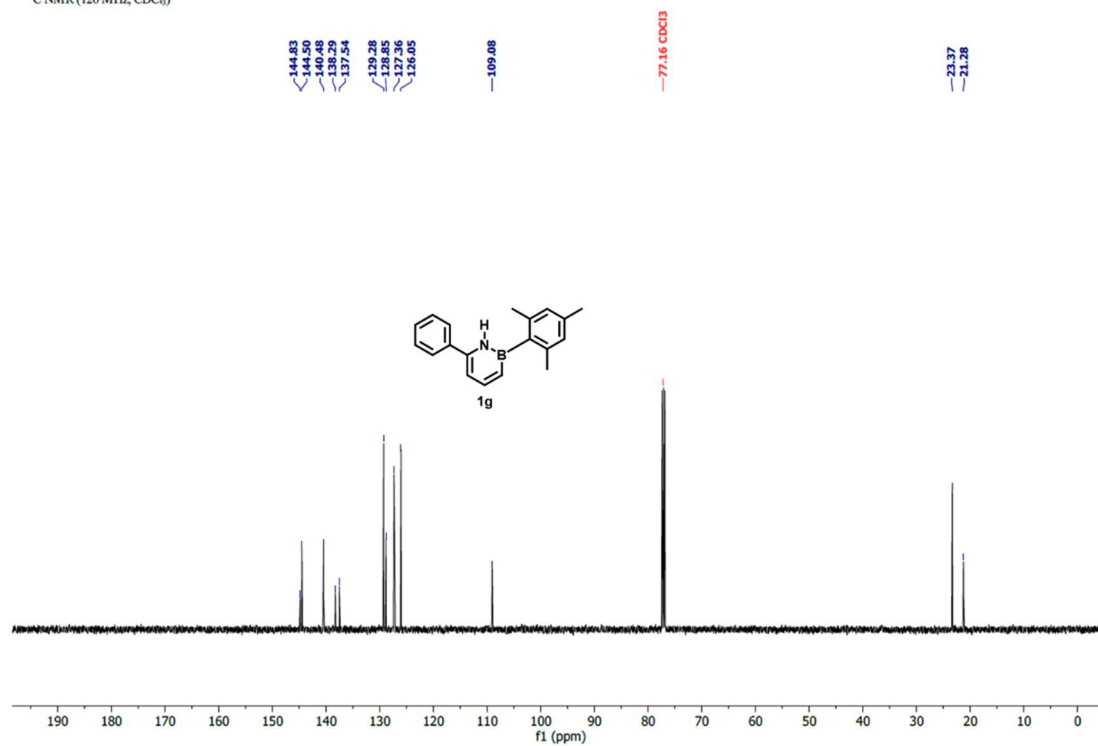
^1H NMR of **1g**

^1H NMR (500 MHz, CDCl_3)



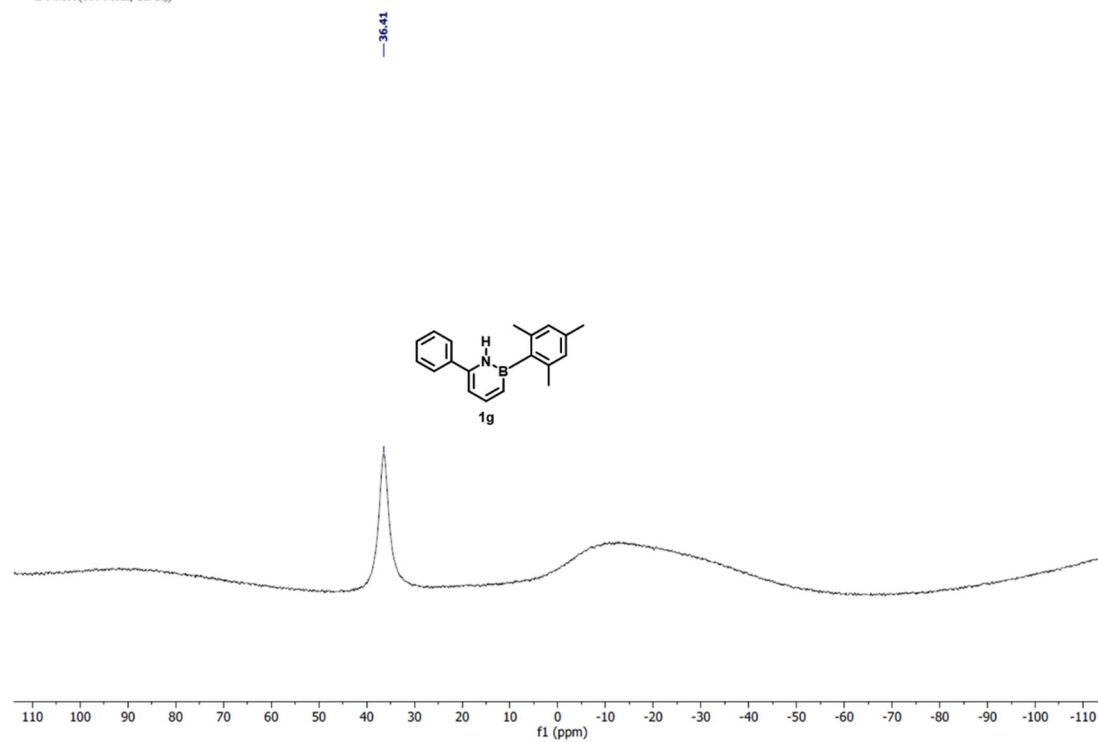
^{13}C NMR of **1g**

^{13}C NMR (126 MHz, CDCl_3)



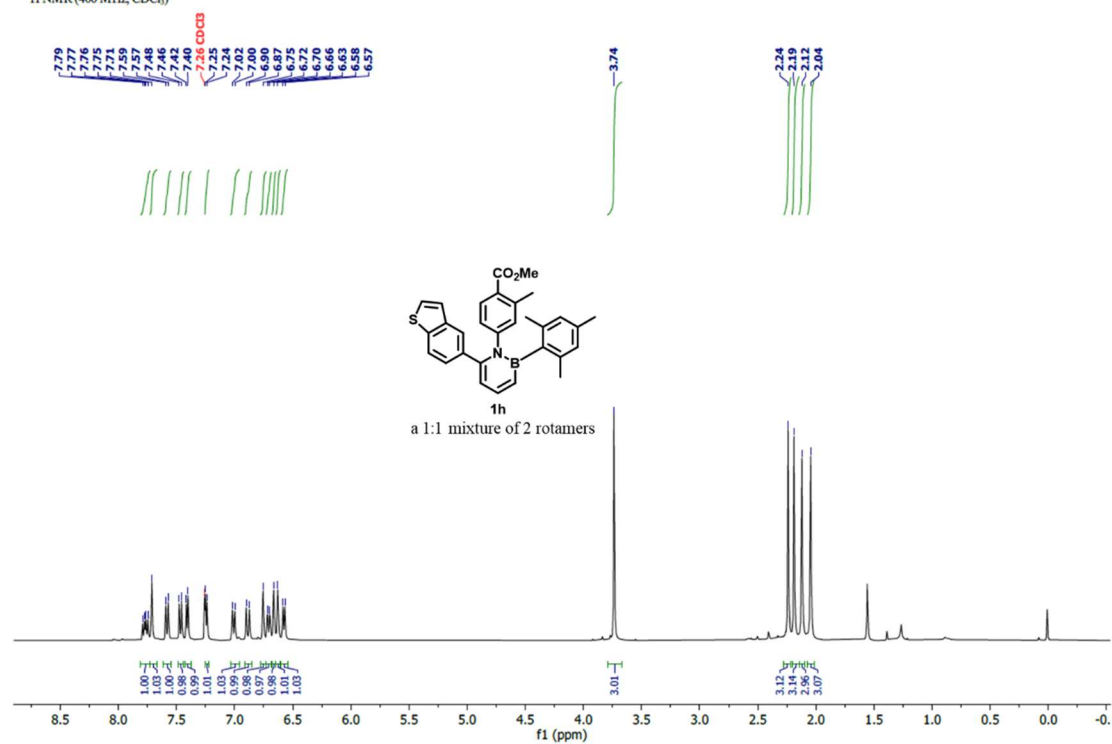
^{11}B NMR of **1g**

^{11}B NMR (160 MHz, CDCl_3)



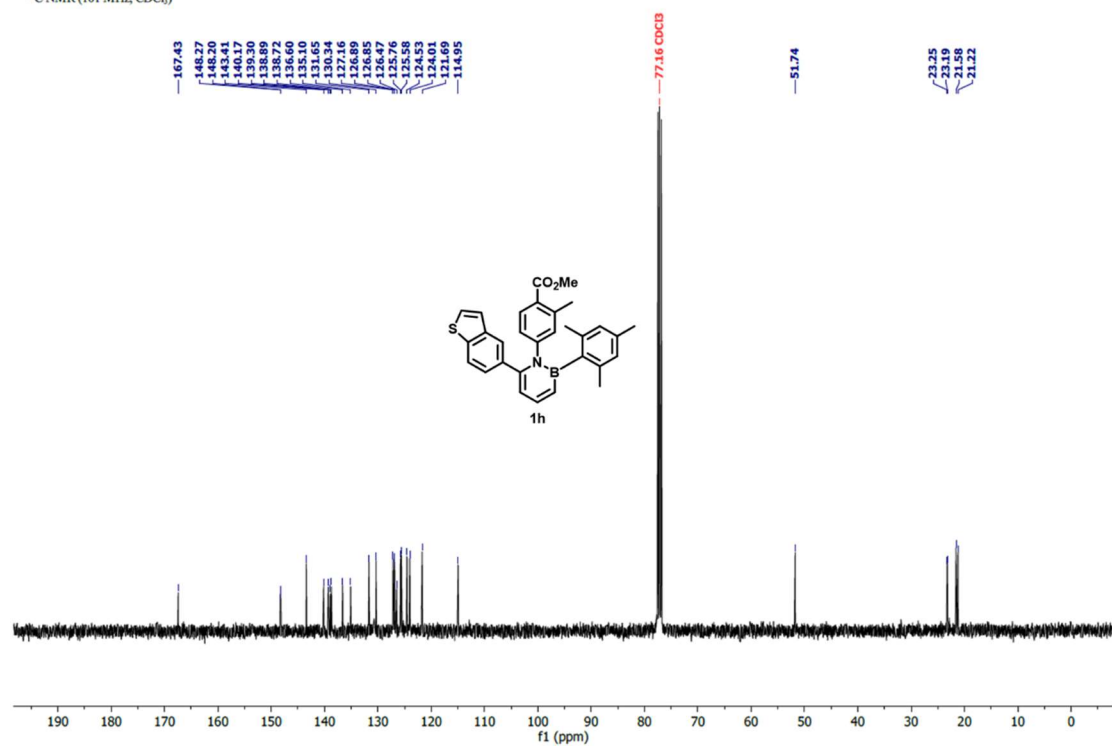
¹H NMR of **1h**

¹H NMR (400 MHz, CDCl₃)



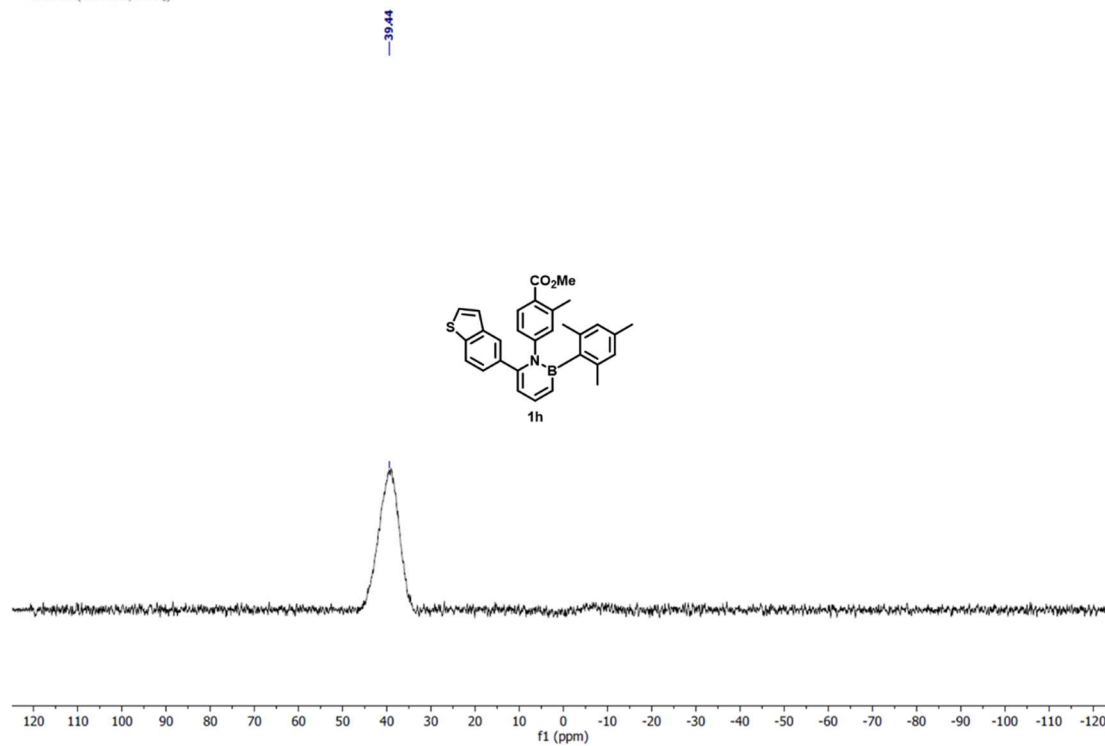
¹³C NMR of **1h**

¹³C NMR (101 MHz, CDCl₃)



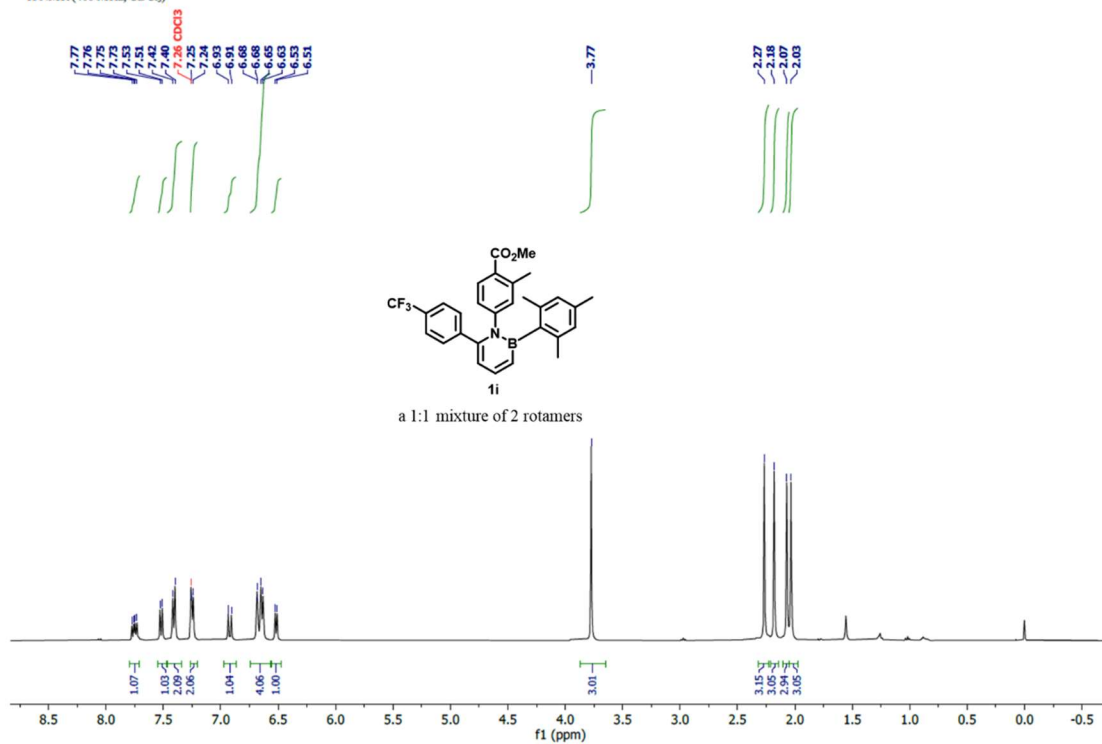
^{11}B NMR of **1h**

^{11}B NMR (128 MHz, CDCl_3)

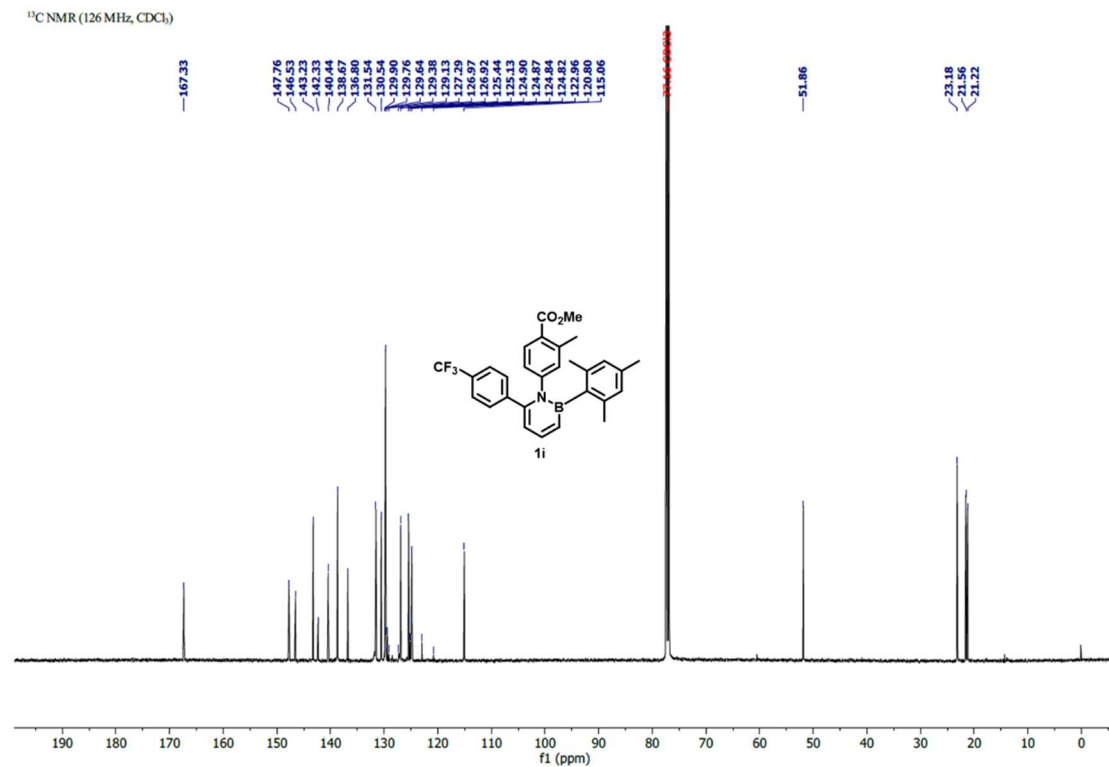


^1H NMR of **1i**

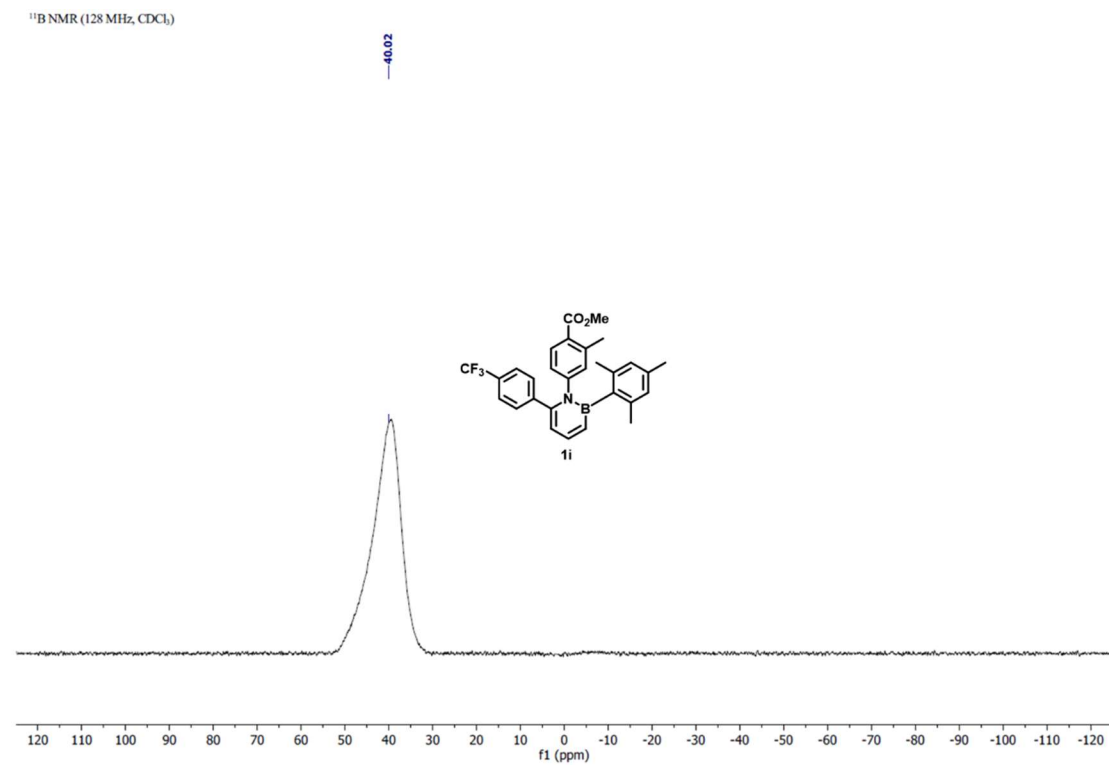
^1H NMR (400 MHz, CDCl_3)



^{13}C NMR of **1i**

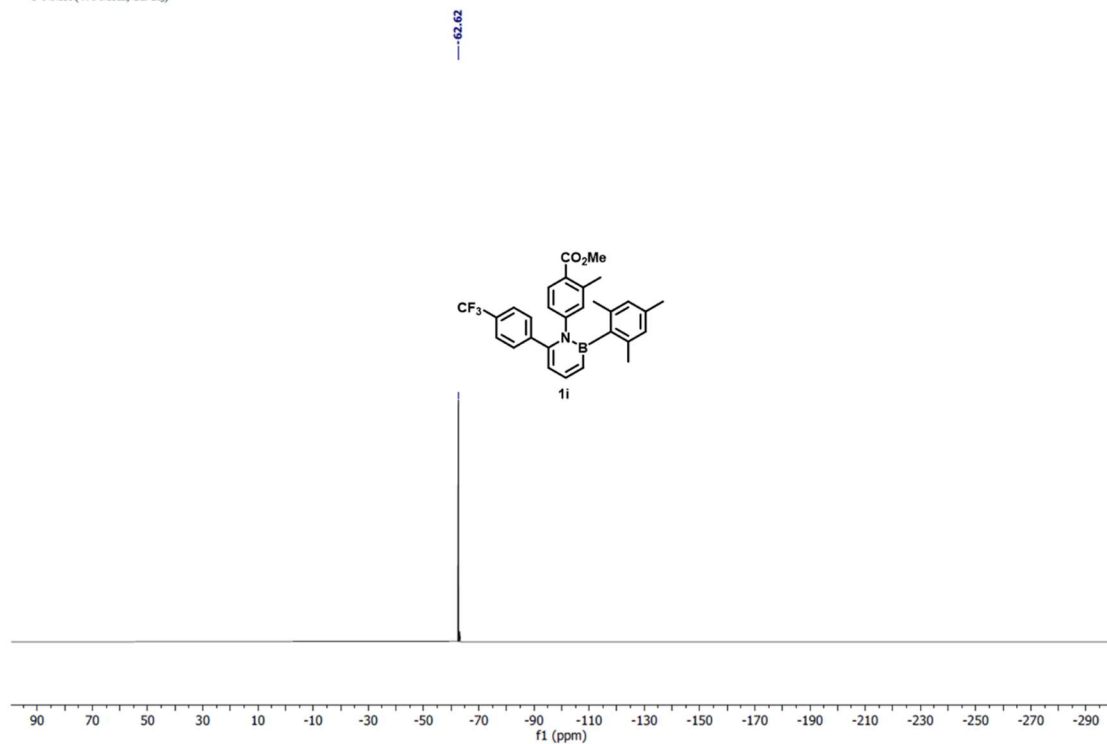


^{11}B NMR of **1i**



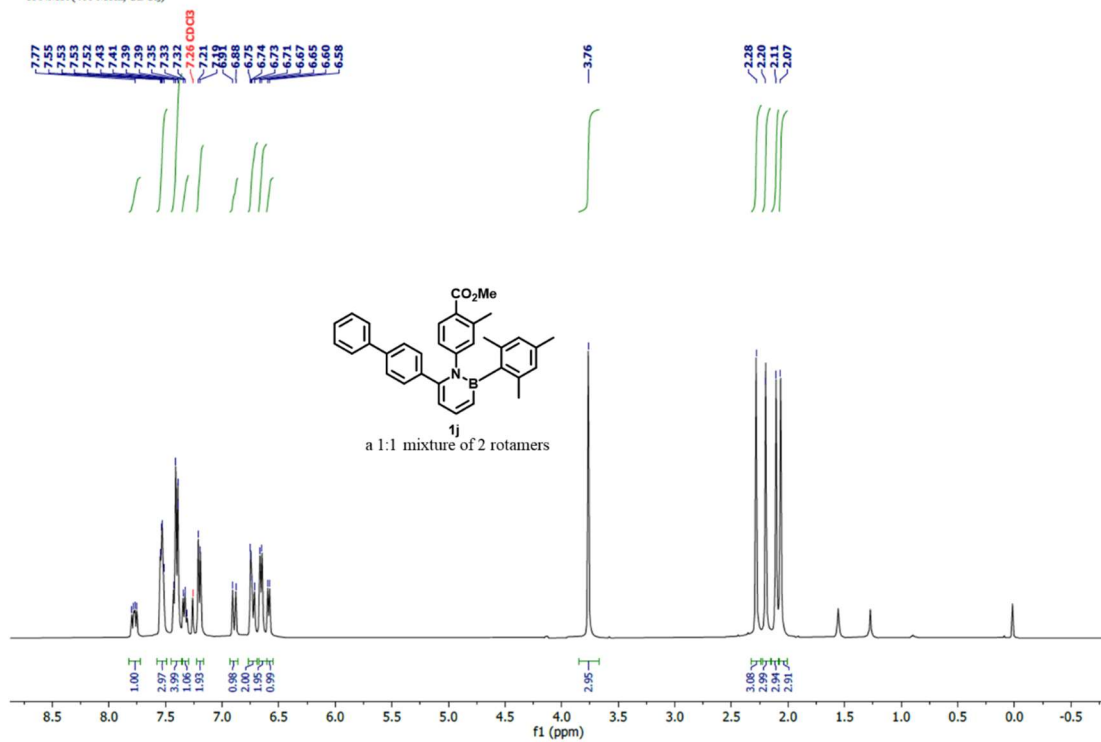
^{19}F NMR of **1i**

^{19}F NMR (470 MHz, CDCl_3)



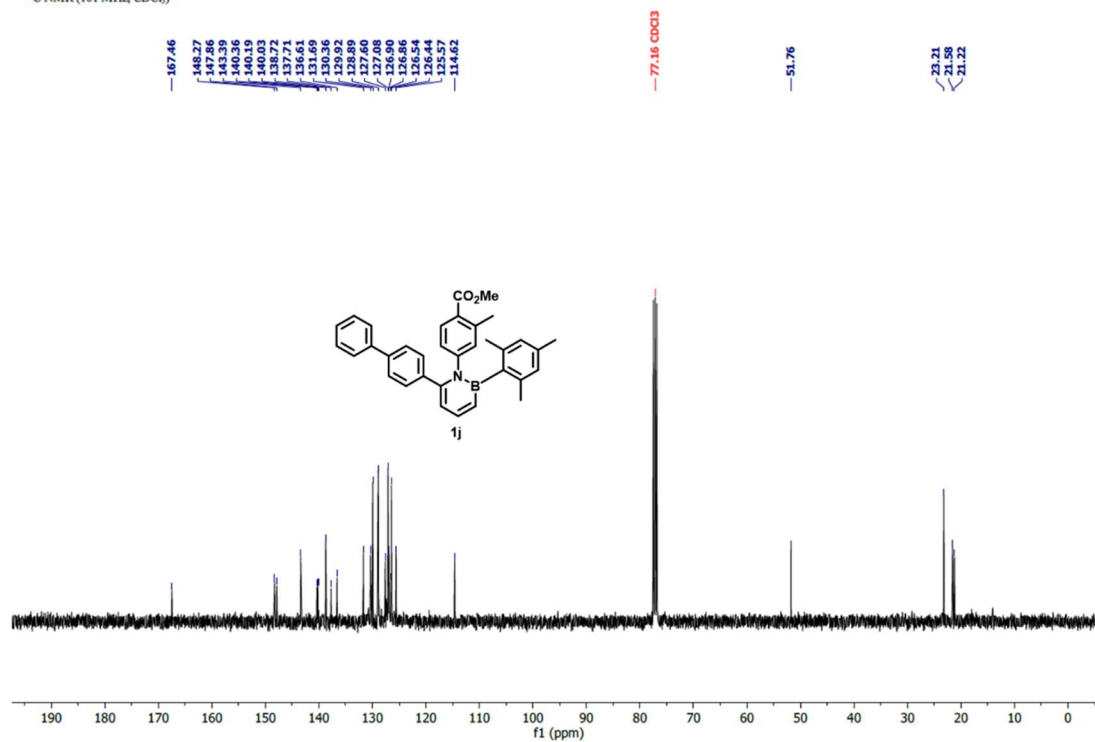
^1H NMR of **1j**

^1H NMR (400 MHz, CDCl_3)



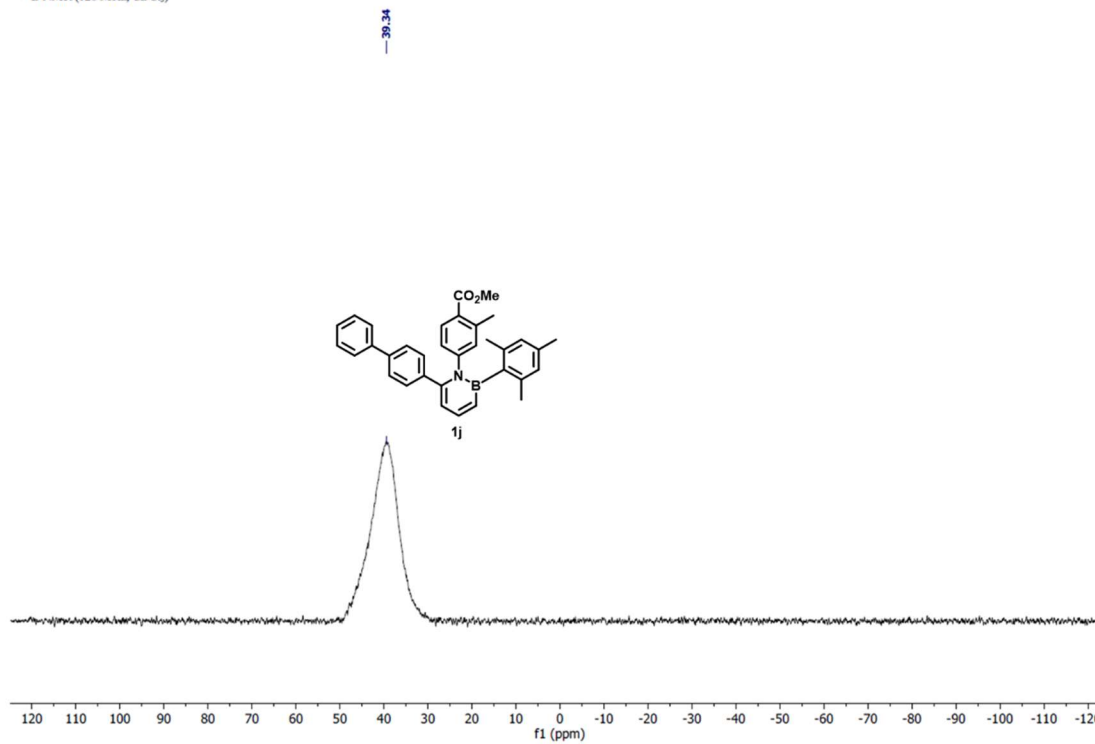
¹³C NMR of **1j**

¹³C NMR (101 MHz, CDCl₃)



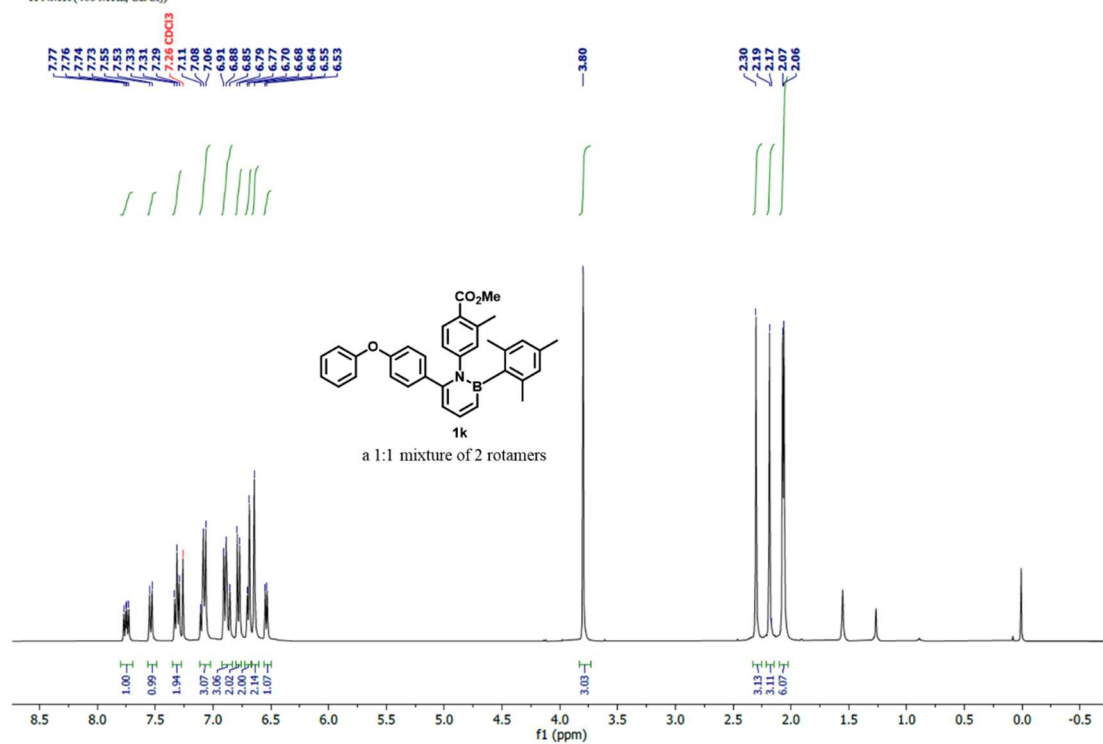
¹¹B NMR of **1j**

¹¹B NMR (128 MHz, CDCl₃)



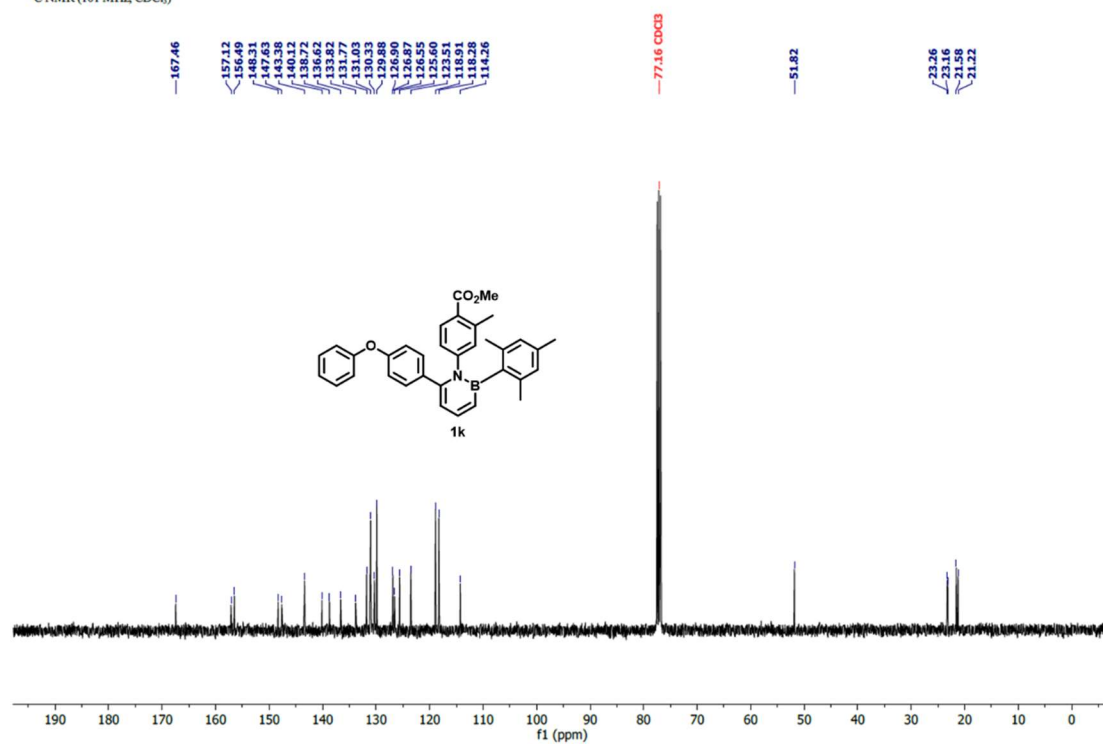
¹H NMR of **1k**

¹H NMR (400 MHz, CDCl₃)



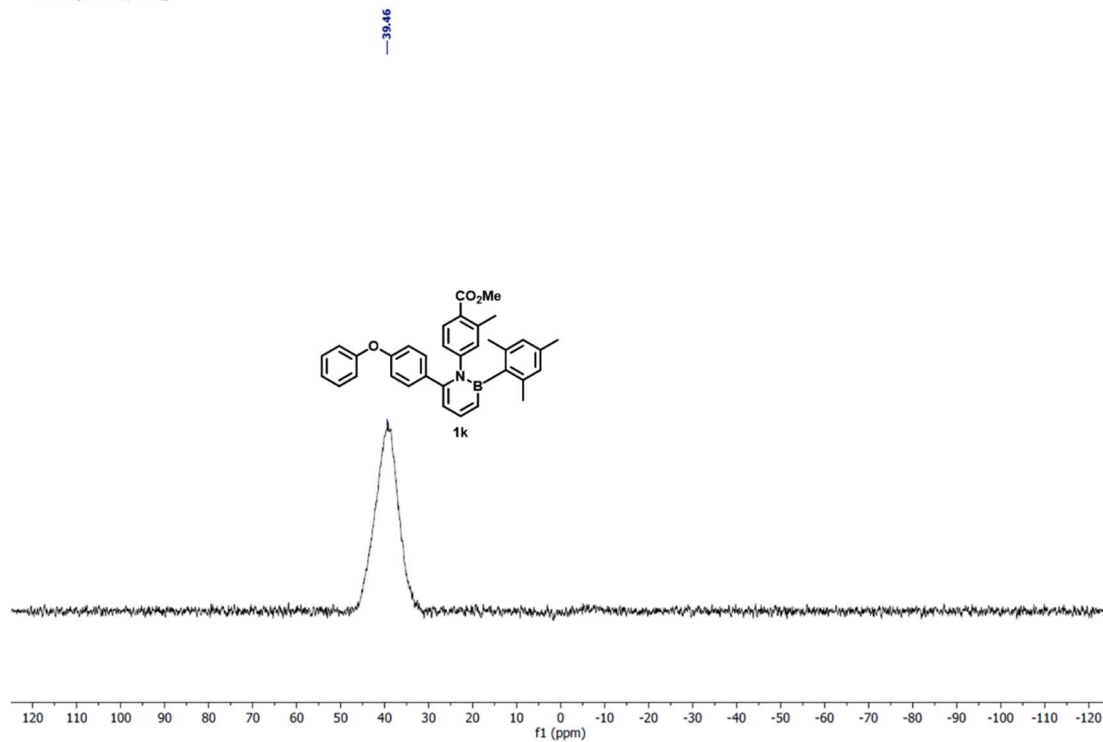
¹³C NMR of **1k**

¹³C NMR (101 MHz, CDCl₃)



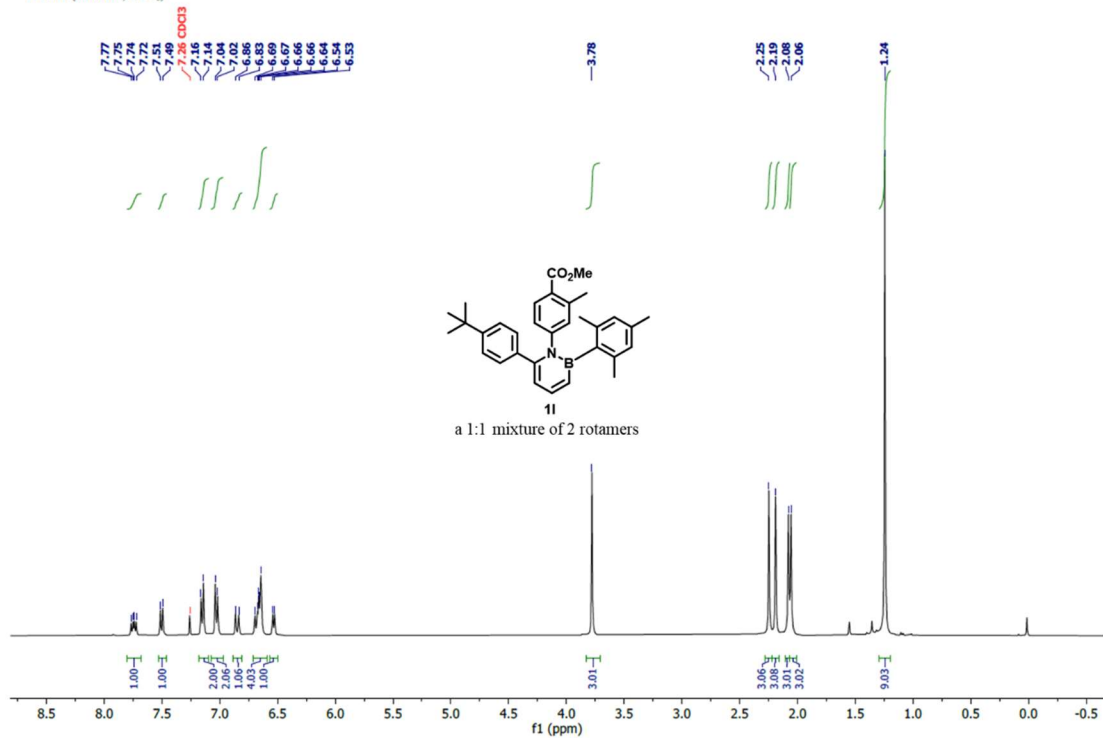
^{11}B NMR of **1k**

^{11}B NMR (128 MHz, CDCl_3)

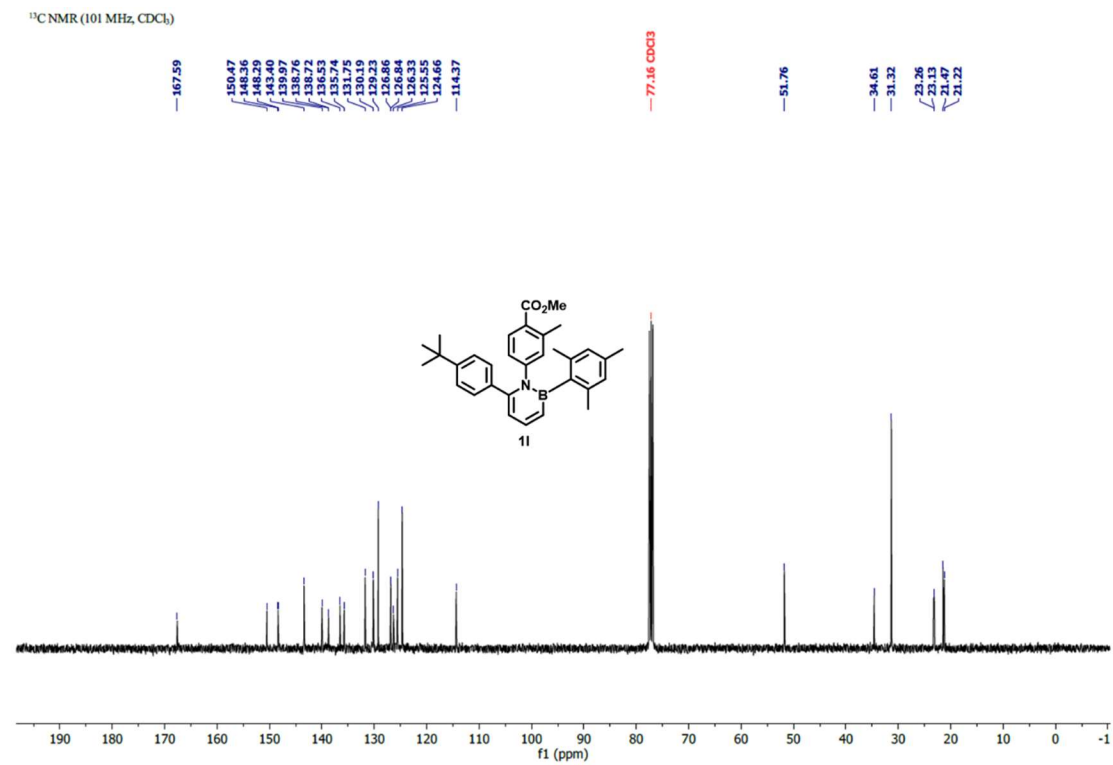


^1H NMR of **1l**

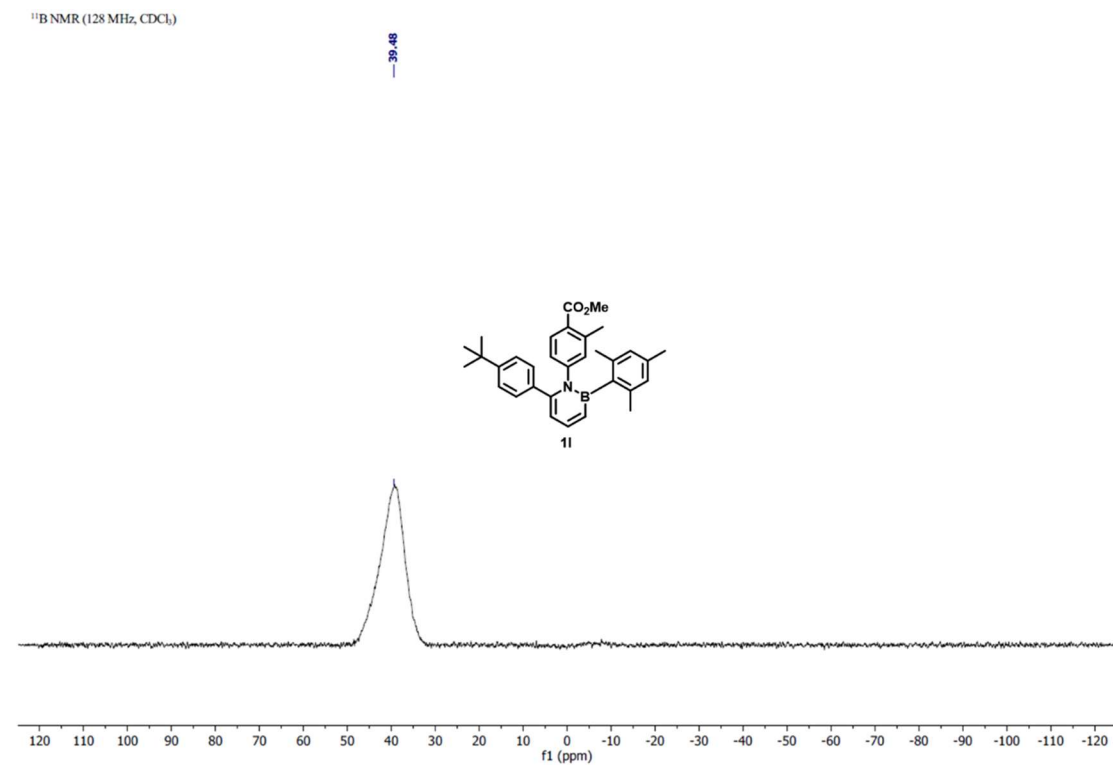
^1H NMR (400 MHz, CDCl_3)



^{13}C NMR of **11**

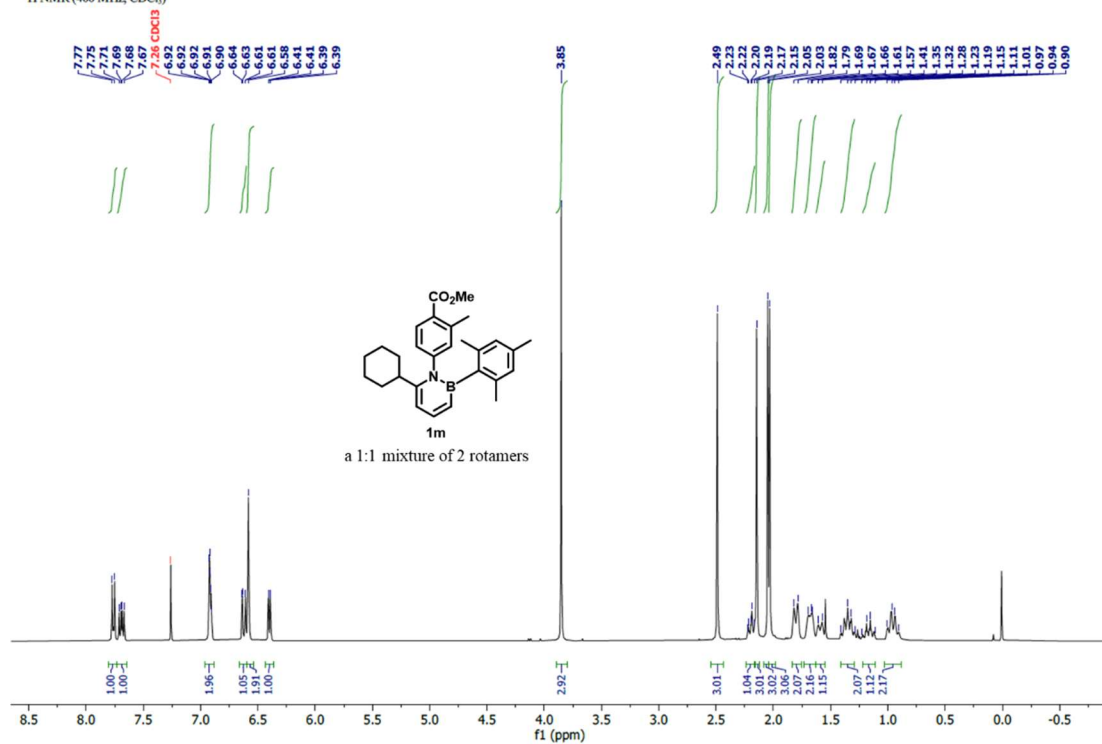


^{11}B NMR of **11**



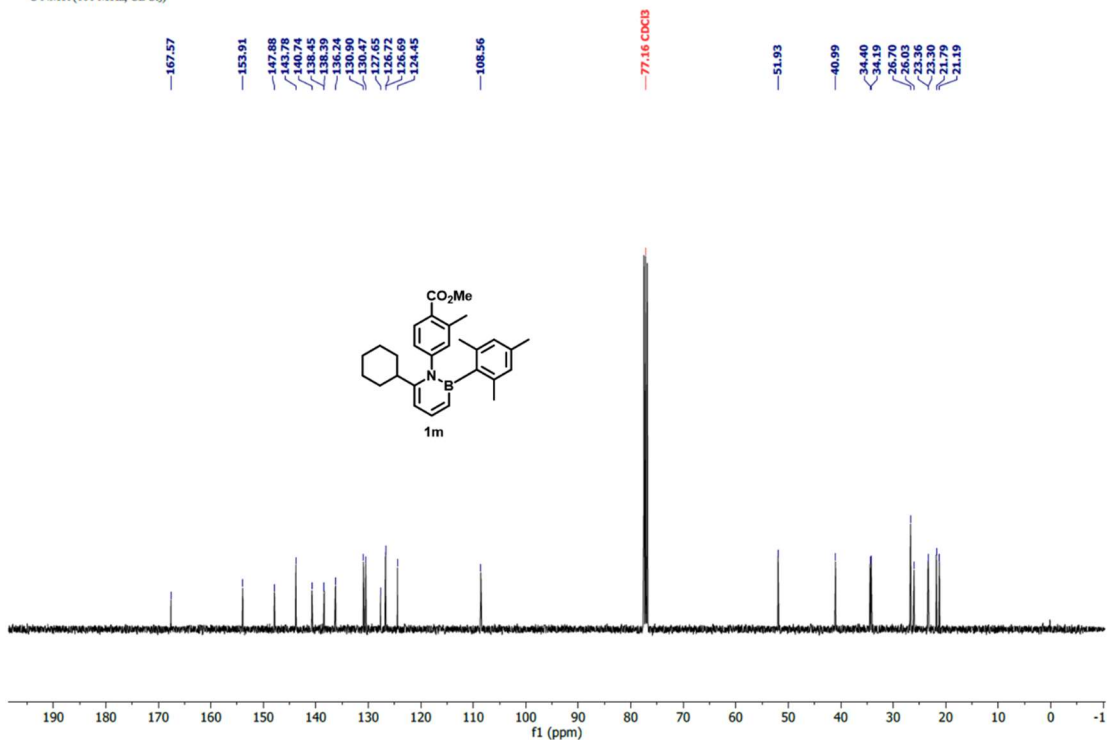
¹H NMR of **1m**

¹H NMR (400 MHz, CDCl₃)



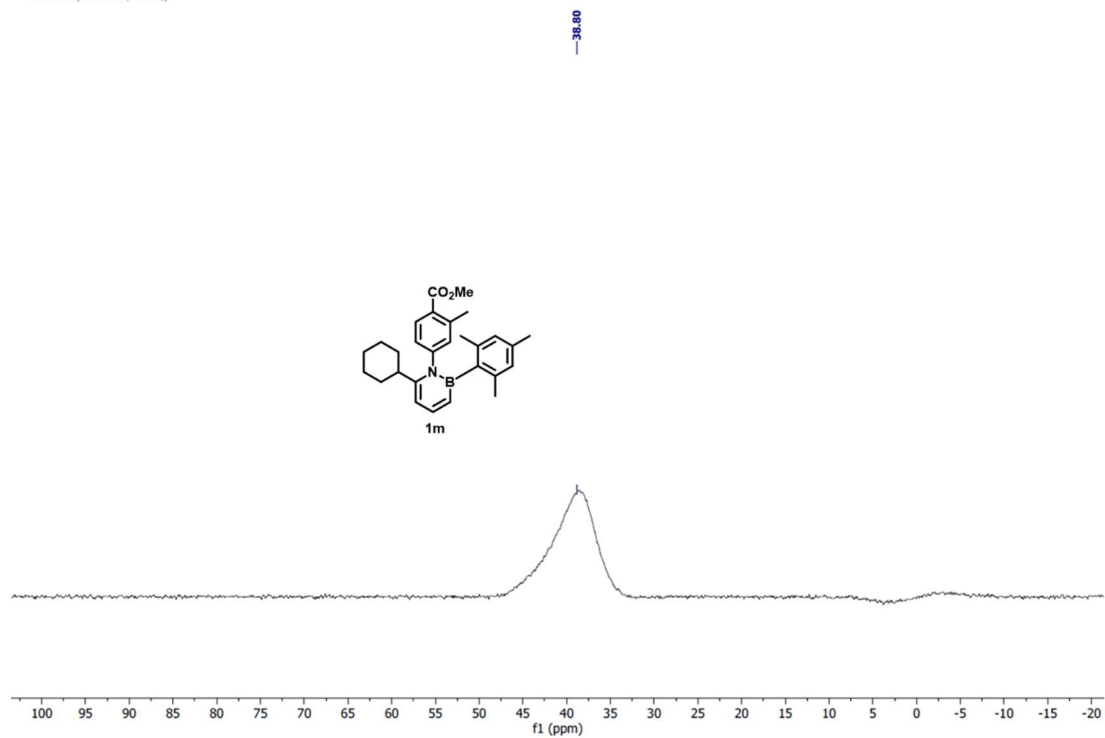
¹³C NMR of **1m**

¹³C NMR (101 MHz, CDCl₃)



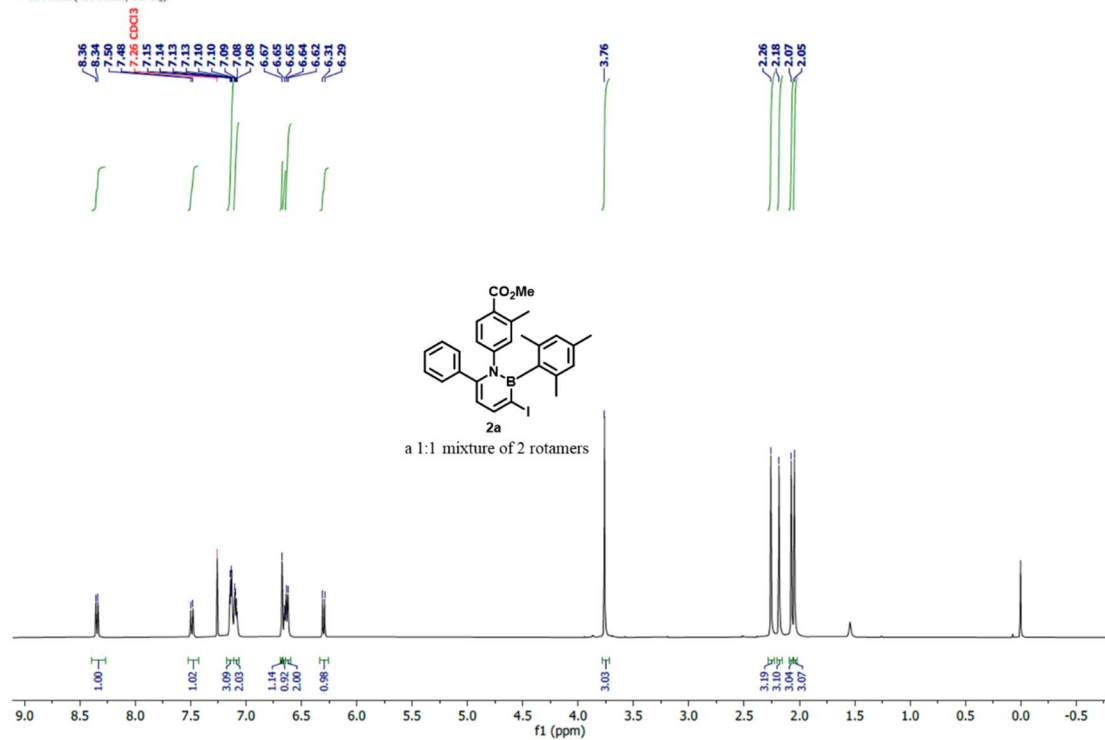
^{11}B NMR of **1m**

^{11}B NMR (128 MHz, CDCl_3)



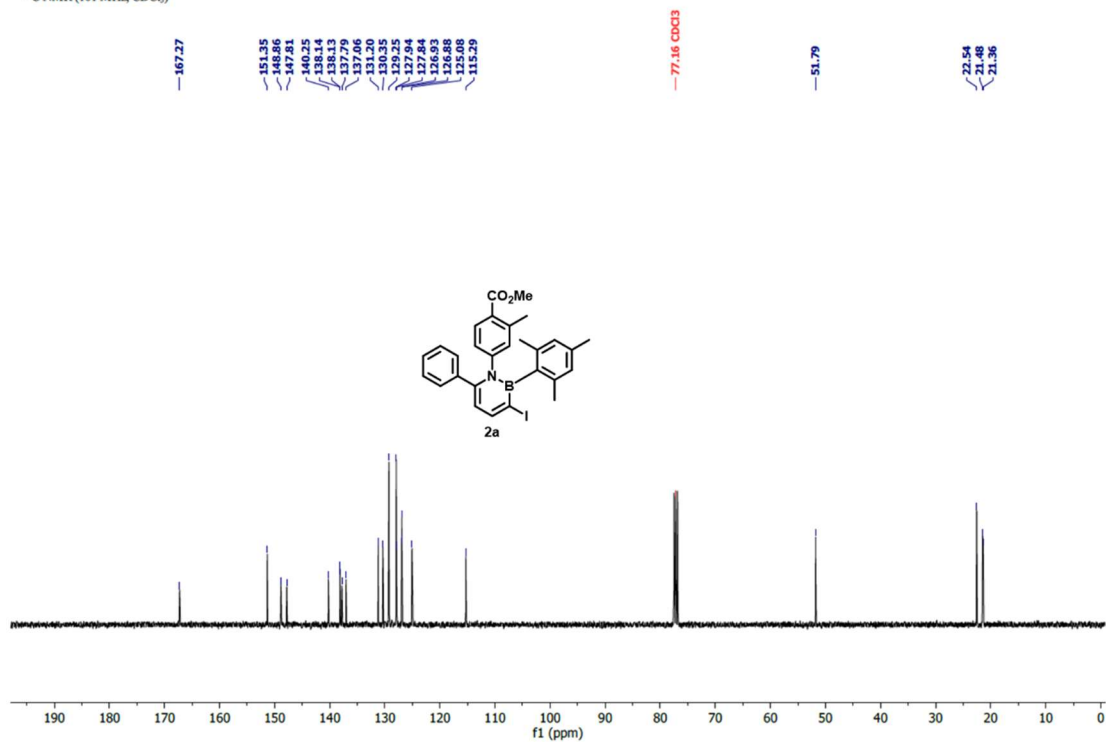
^1H NMR of **2a**

^1H NMR (400 MHz, CDCl_3)



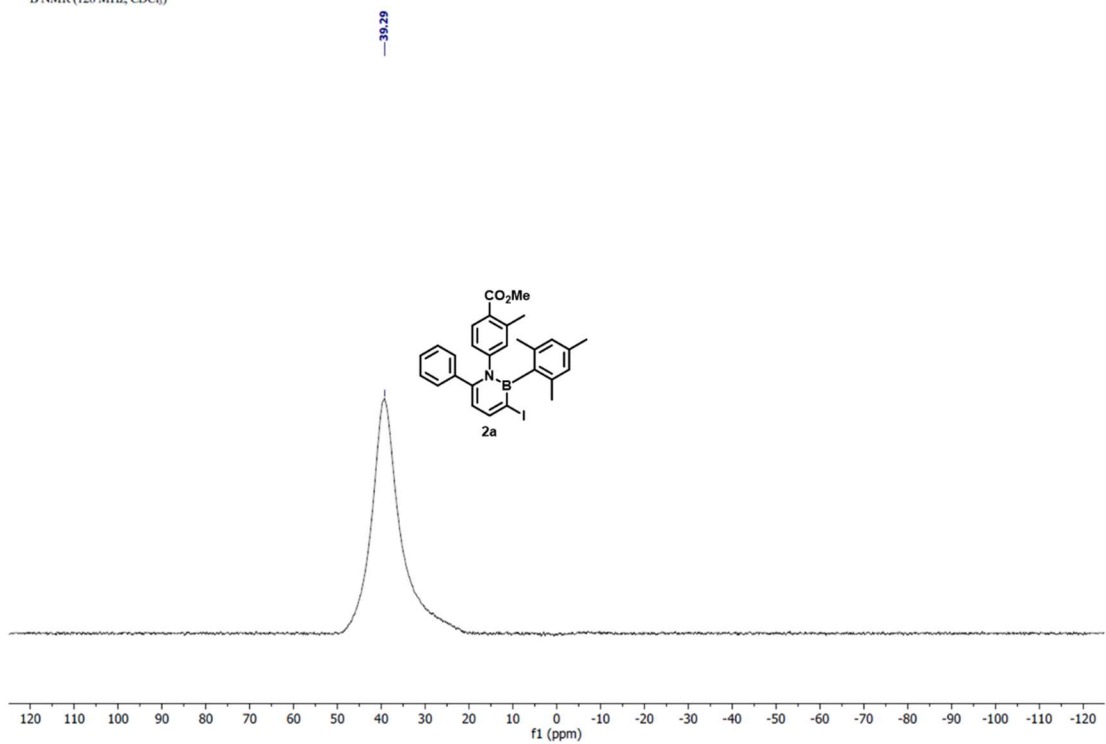
^{13}C NMR of **2a**

^{13}C NMR (101 MHz, CDCl_3)



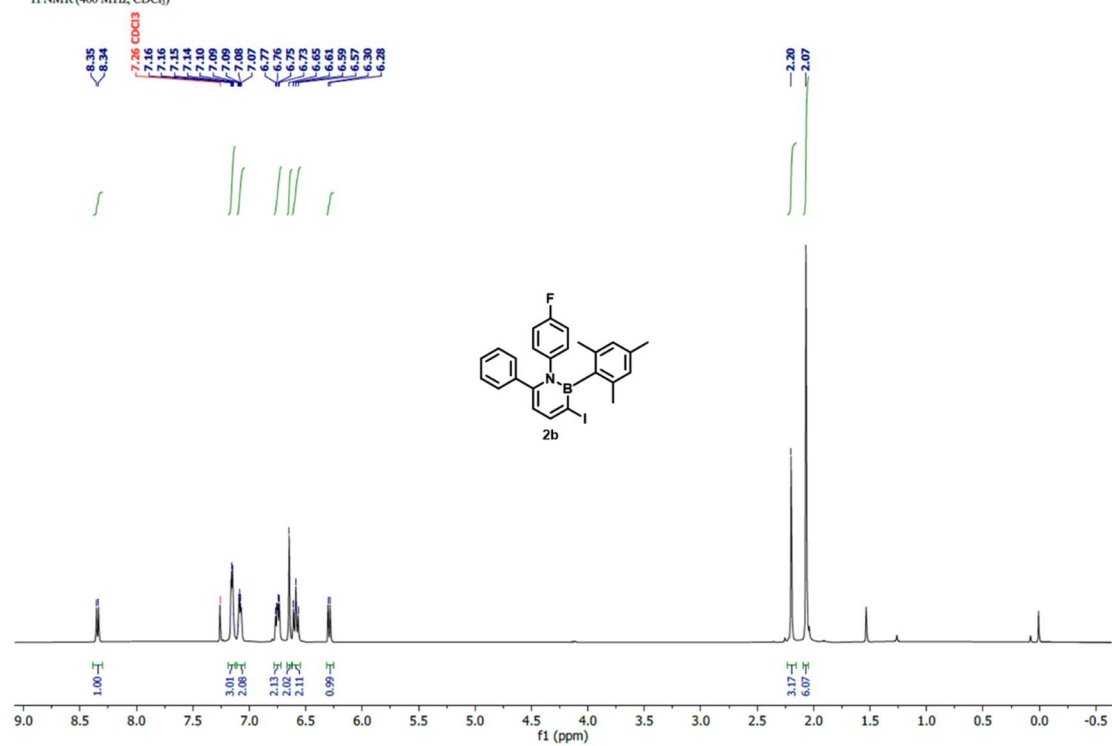
^{11}B NMR of **2a**

^{11}B NMR (128 MHz, CDCl_3)



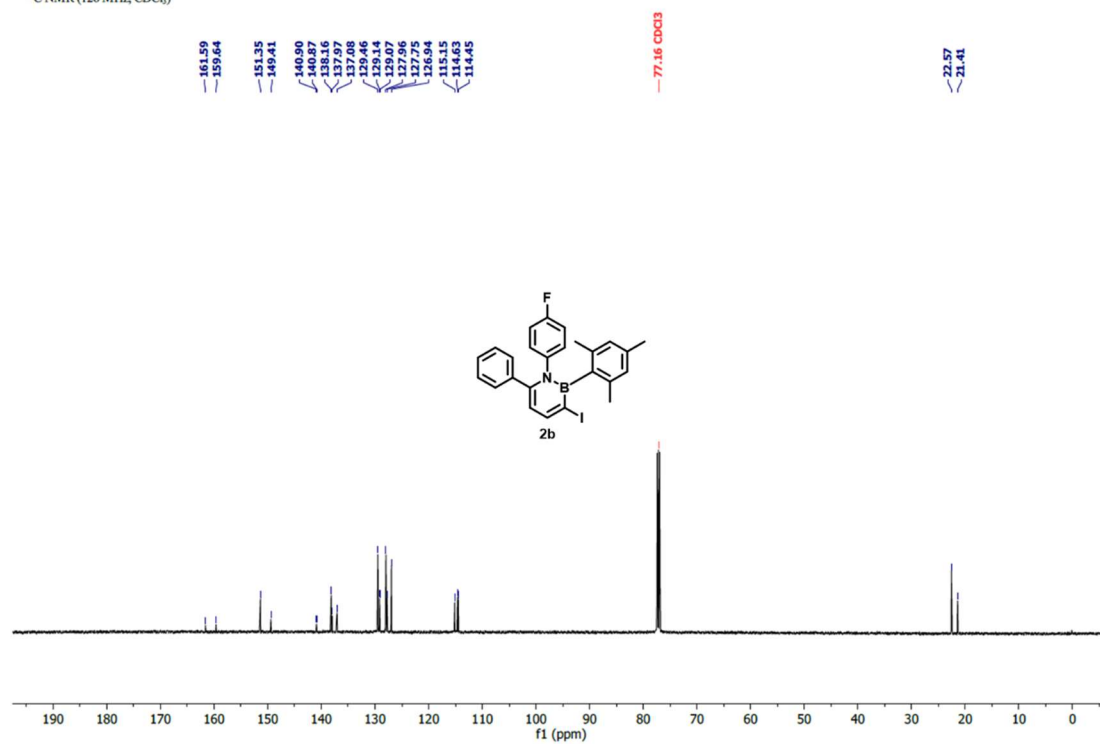
¹H NMR of 2b

¹H NMR (400 MHz, CDCl₃)



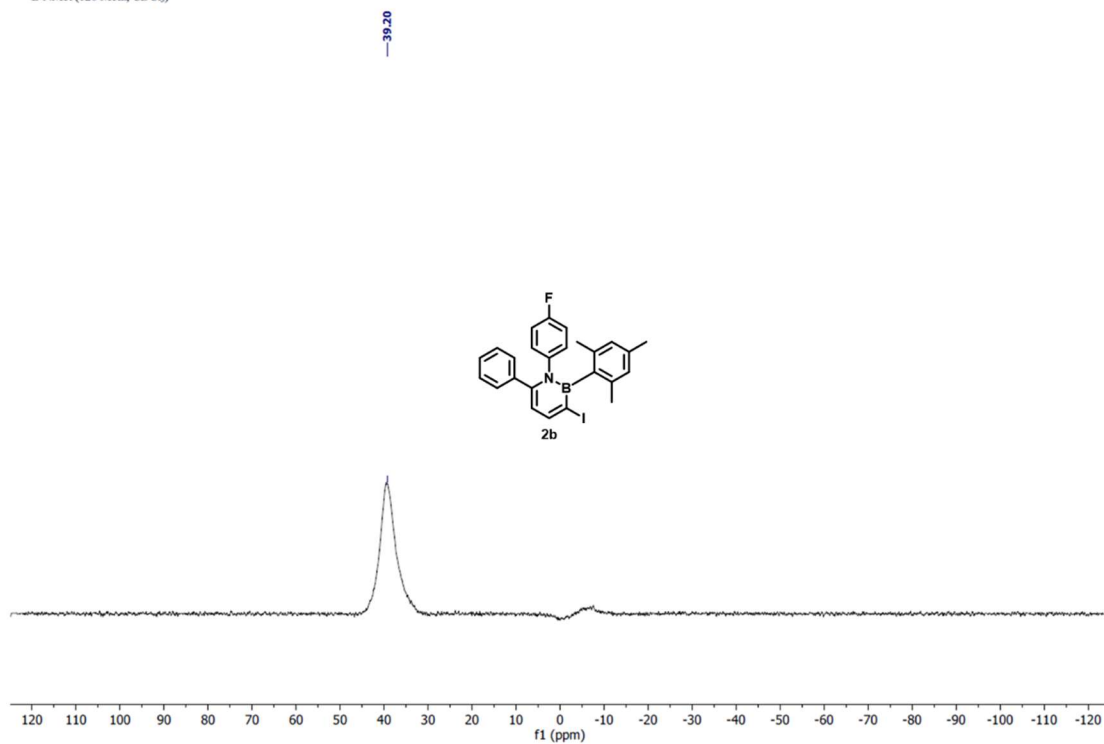
¹³C NMR of 2b

¹³C NMR (126 MHz, CDCl₃)



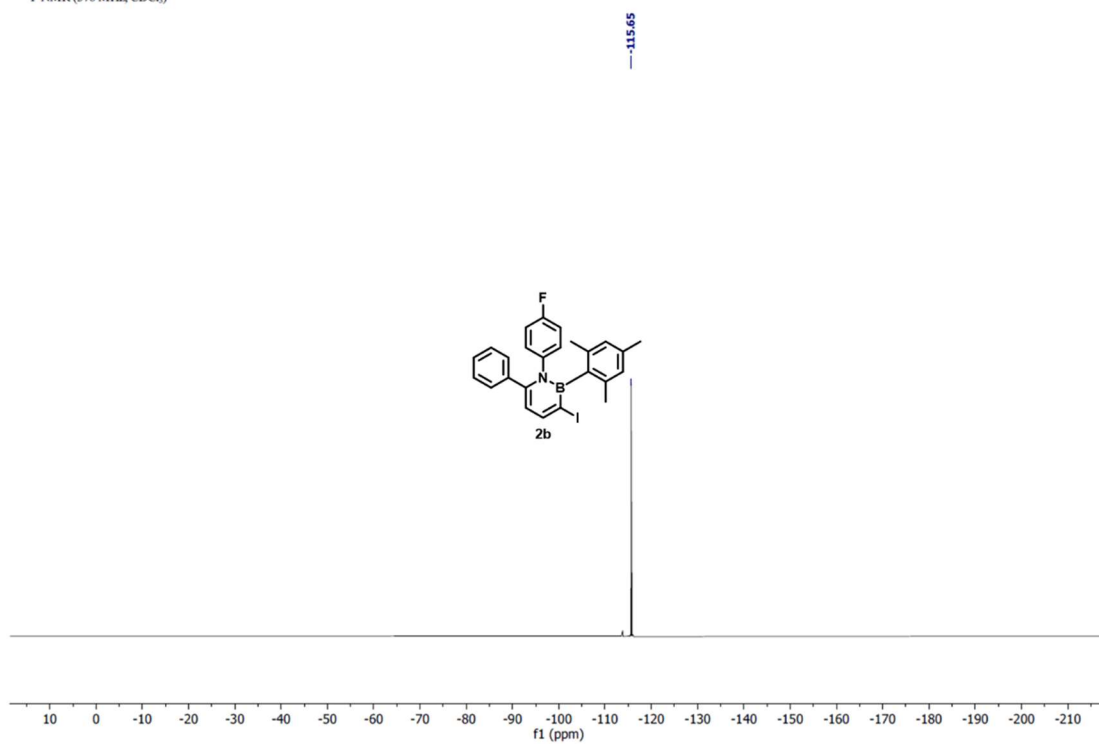
^{11}B NMR of **2b**

^{11}B NMR (128 MHz, CDCl_3)



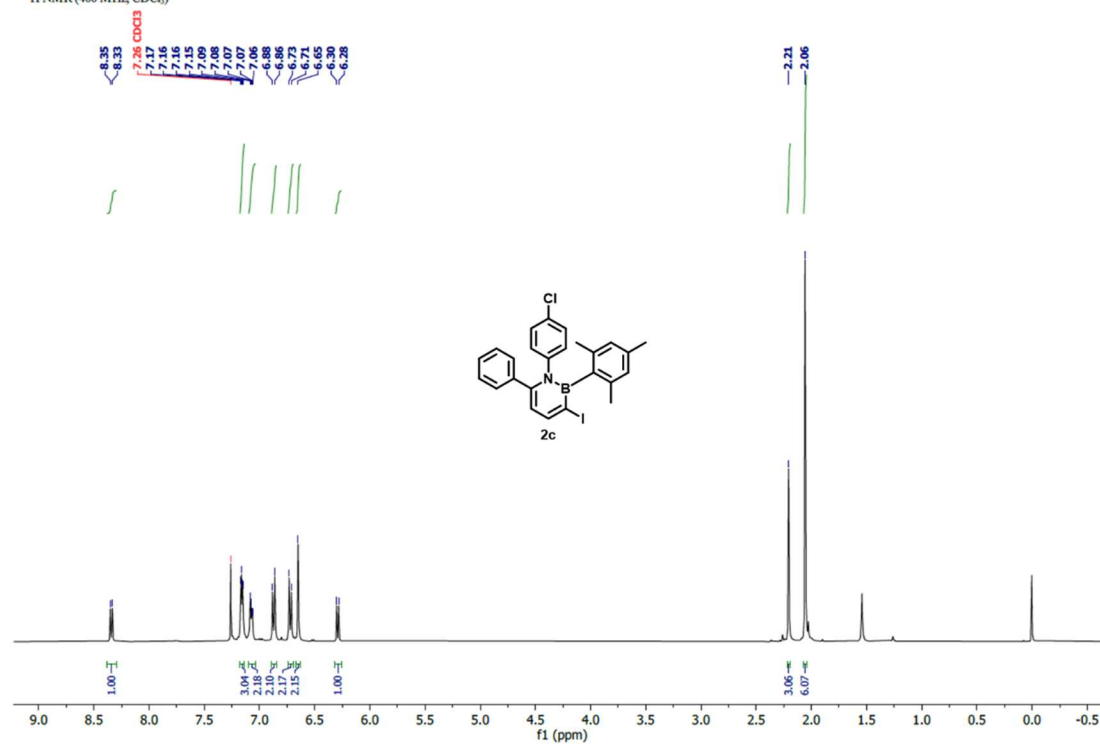
^{19}F NMR of **2b**

^{19}F NMR (376 MHz, CDCl_3)



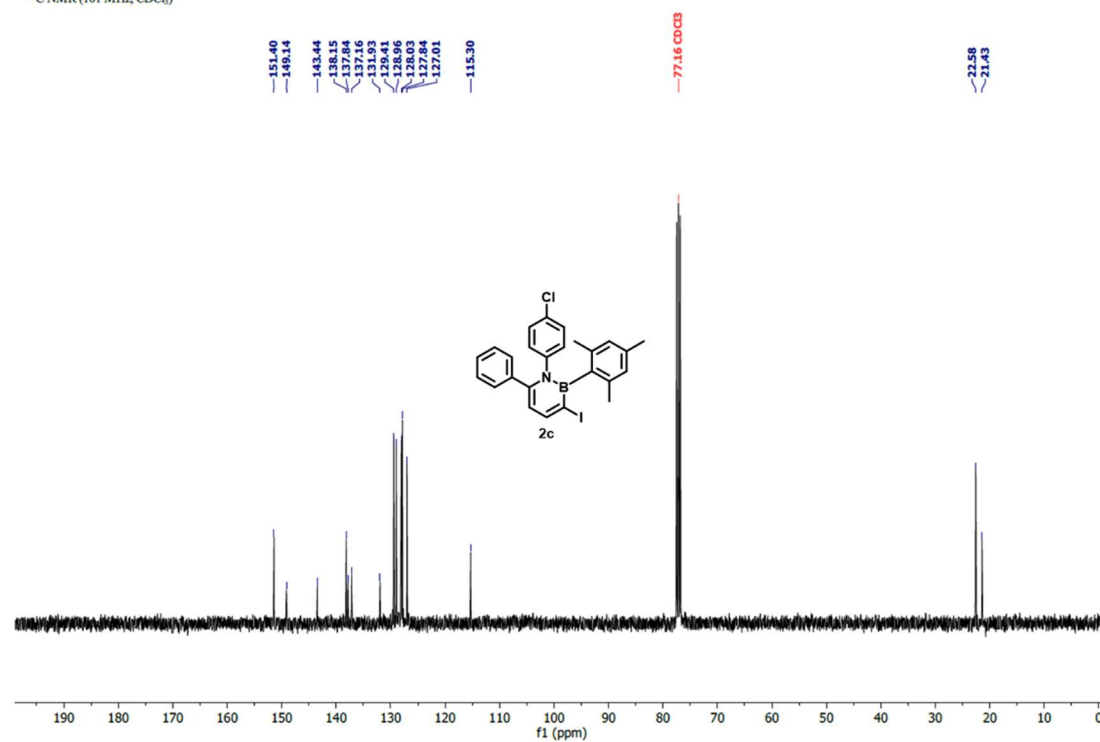
¹H NMR of 2c

¹H NMR (400 MHz, CDCl₃)



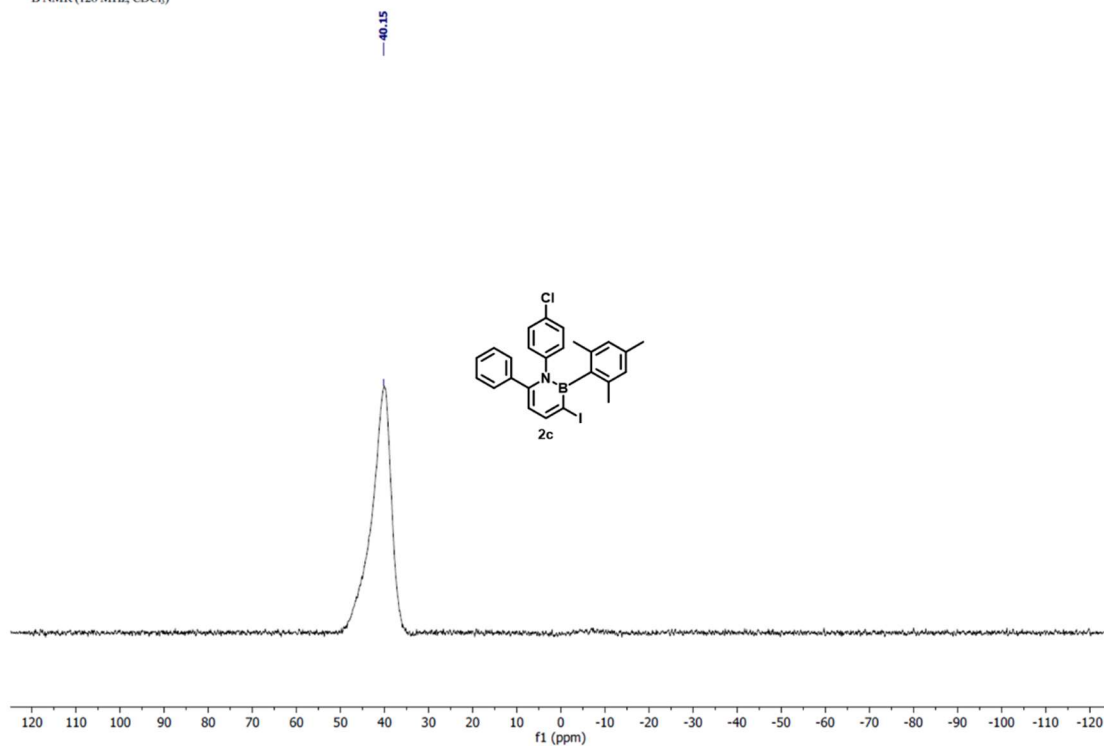
¹³C NMR of 2c

¹³C NMR (101 MHz, CDCl₃)



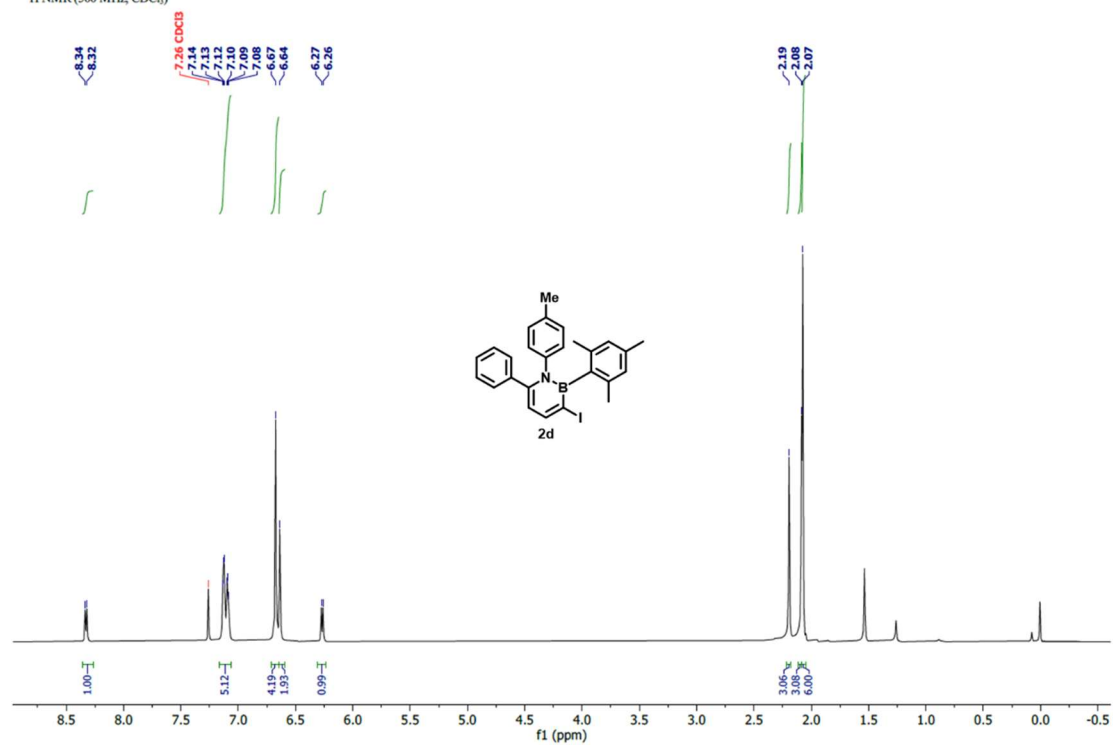
^{11}B NMR of **2c**

^{11}B NMR (128 MHz, CDCl_3)



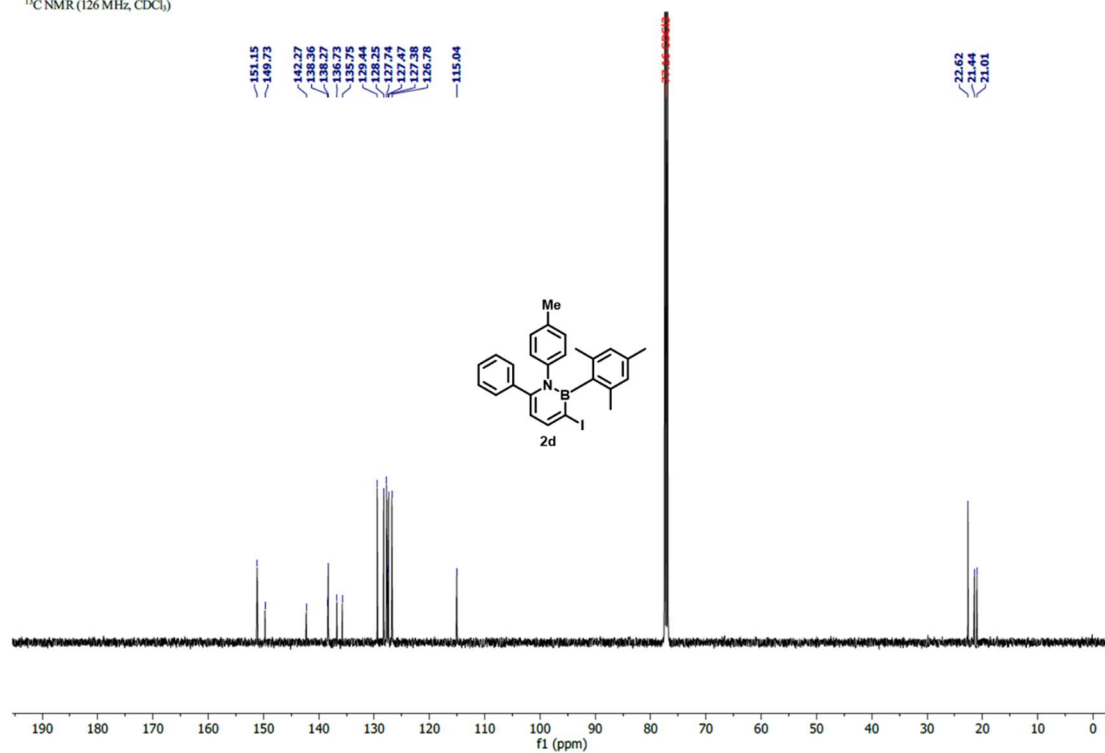
^1H NMR of **2d**

^1H NMR (500 MHz, CDCl_3)



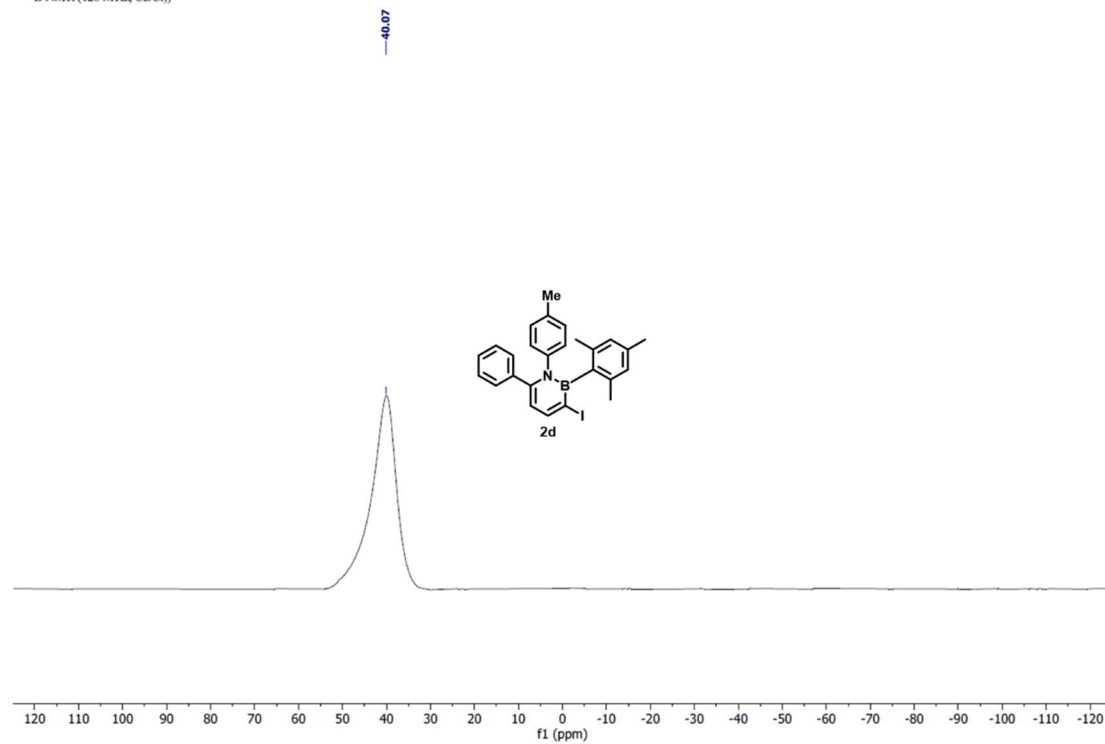
^{13}C NMR of **2d**

^{13}C NMR (126 MHz, CDCl_3)



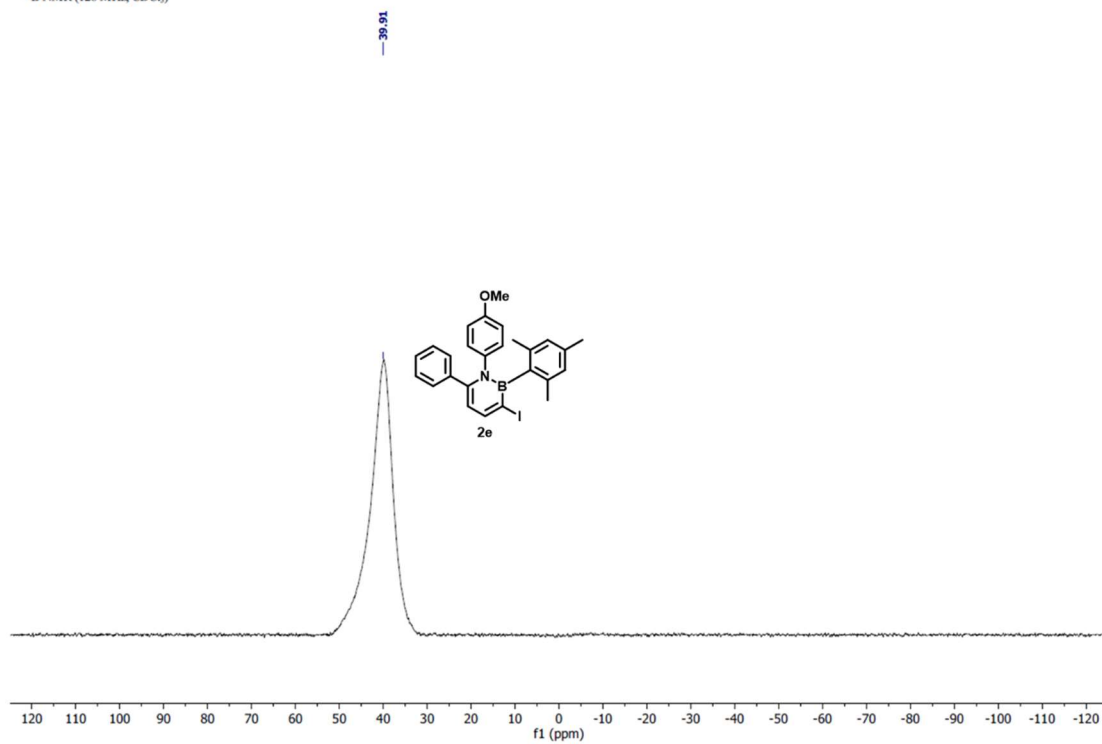
^{11}B NMR of **2d**

^{11}B NMR (128 MHz, CDCl_3)



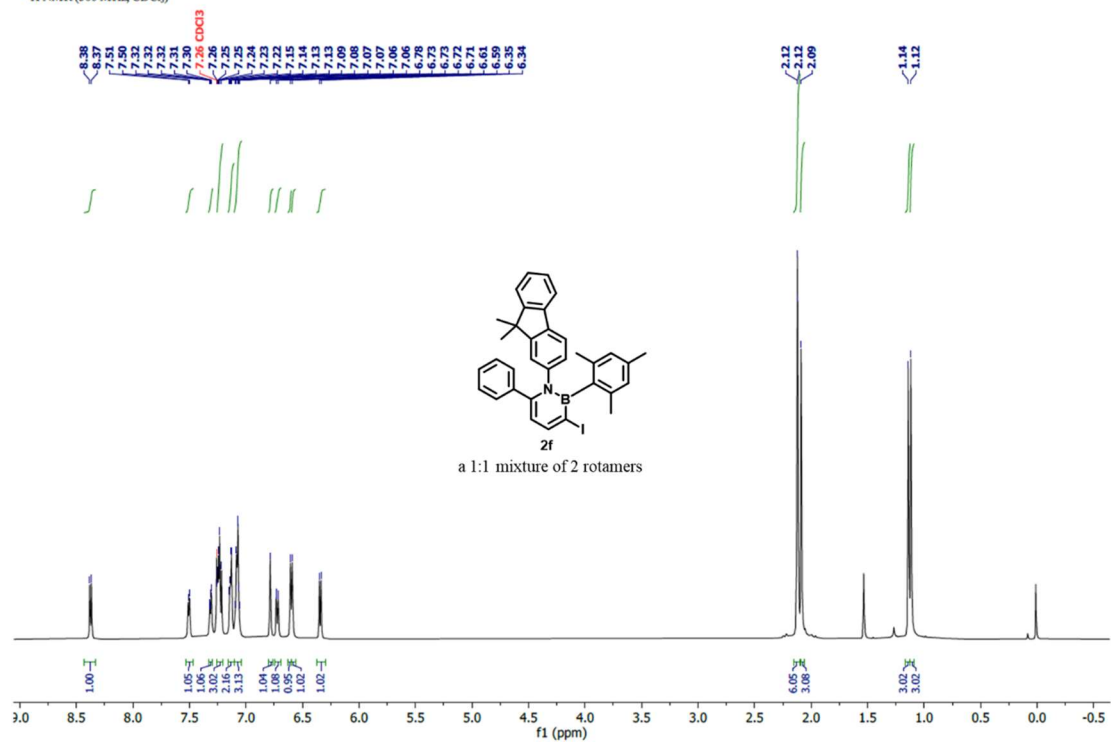
^{11}B NMR of 2e

^{11}B NMR (128 MHz, CDCl_3)



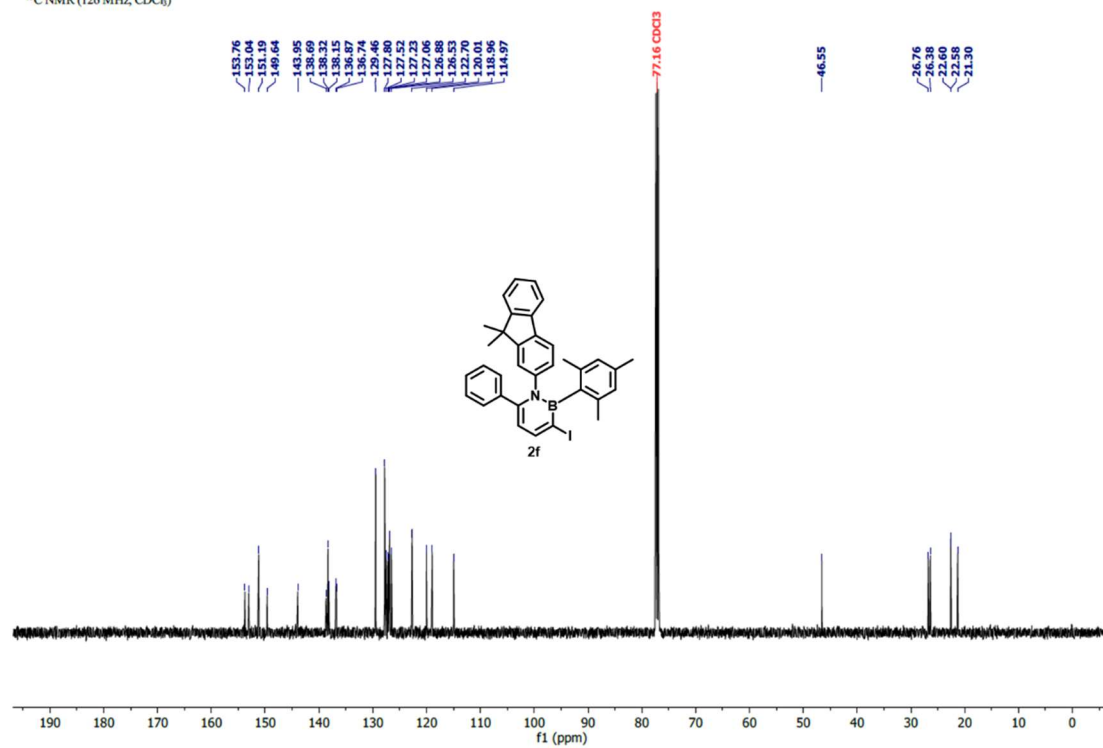
^1H NMR of 2f

^1H NMR (500 MHz, CDCl_3)



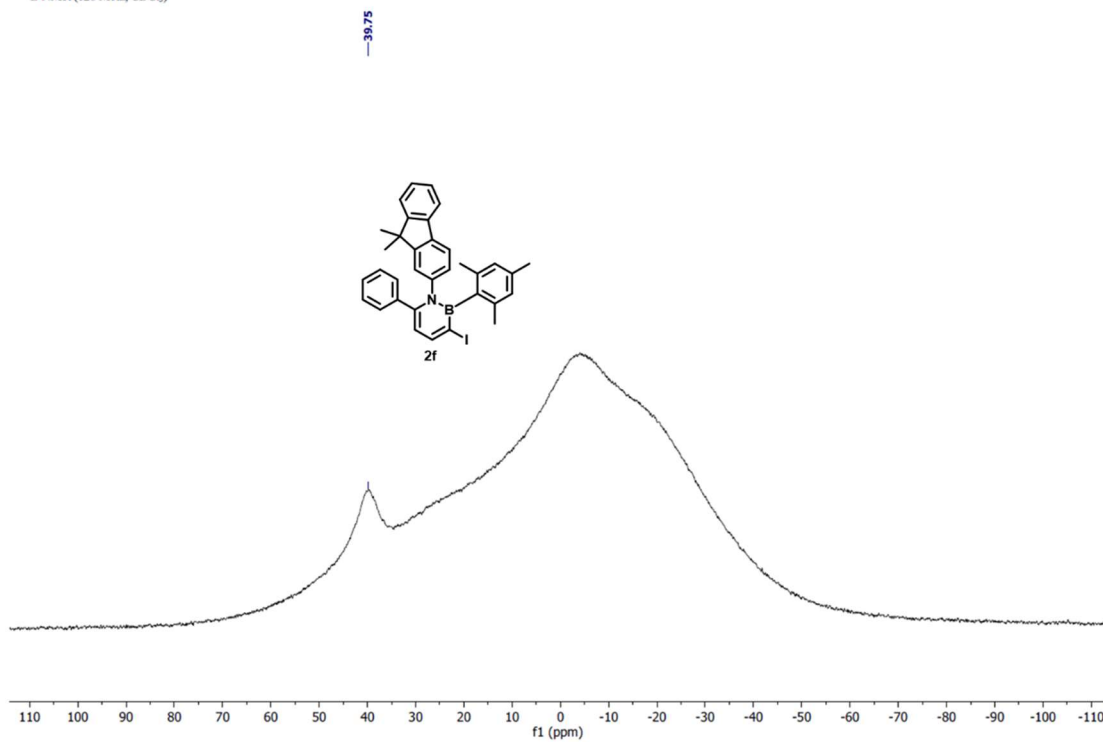
^{13}C NMR of **2f**

^{13}C NMR (126 MHz, CDCl_3)



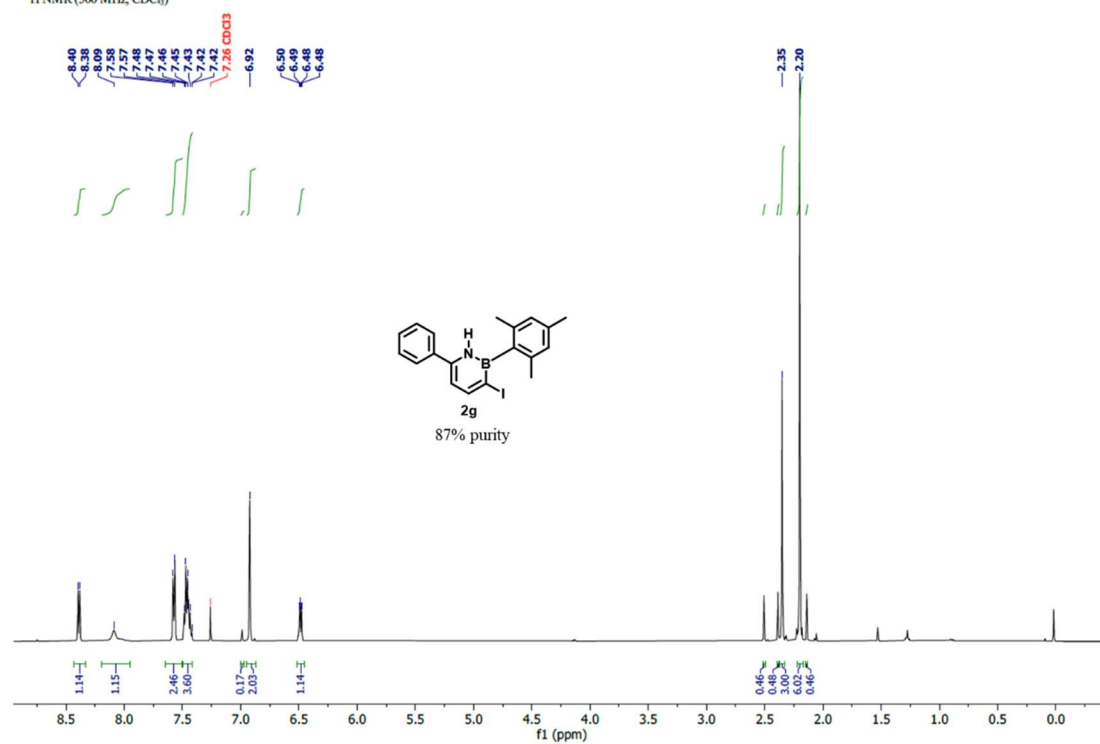
^{11}B NMR of **2f**

^{11}B NMR (128 MHz, CDCl_3)



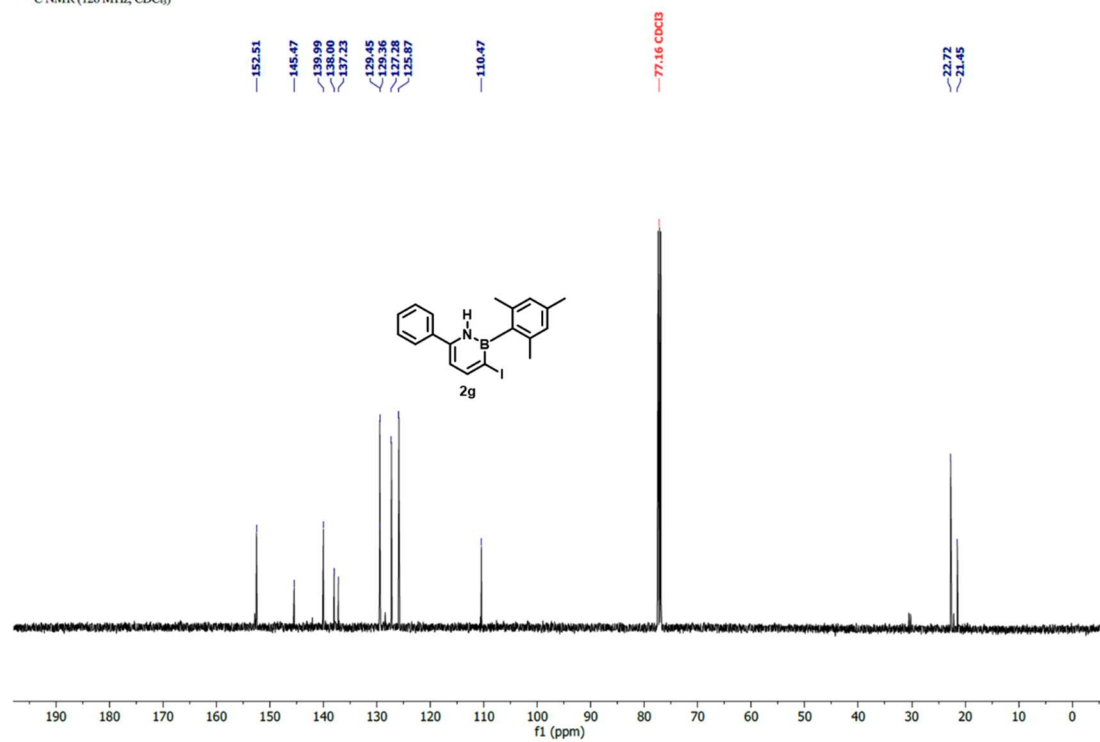
¹H NMR of 2g

¹H NMR (500 MHz, CDCl₃)



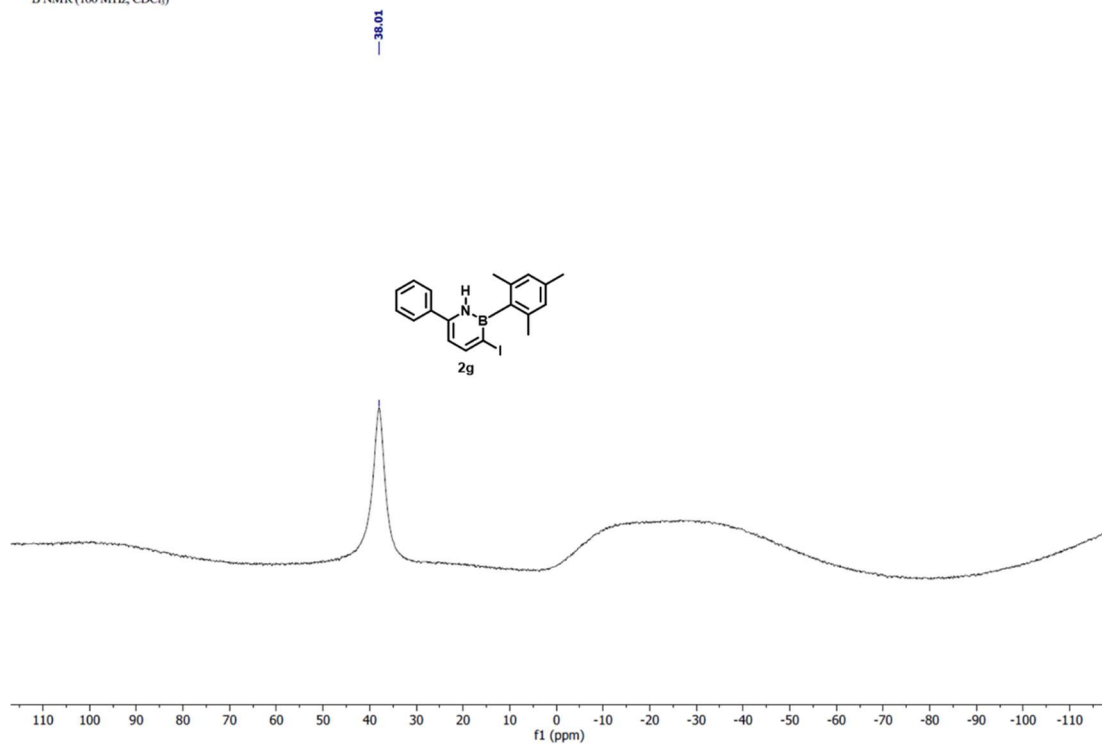
¹³C NMR of 2g

¹³C NMR (126 MHz, CDCl₃)



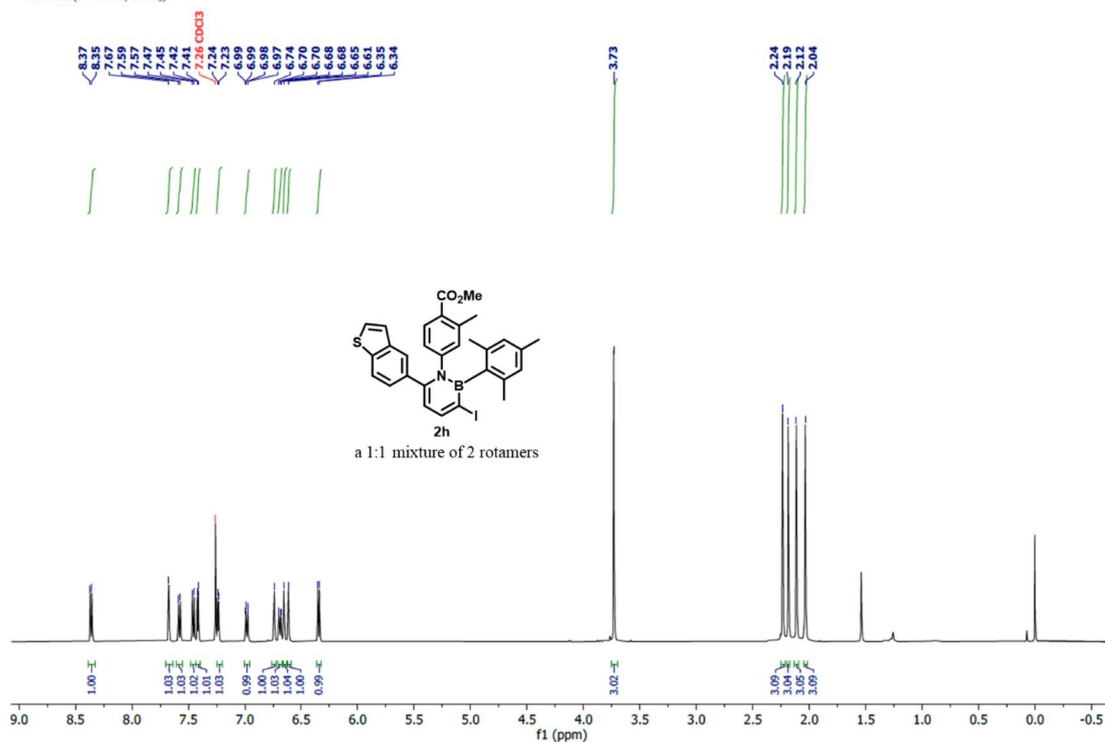
^{11}B NMR of 2g

^{11}B NMR (160 MHz, CDCl_3)



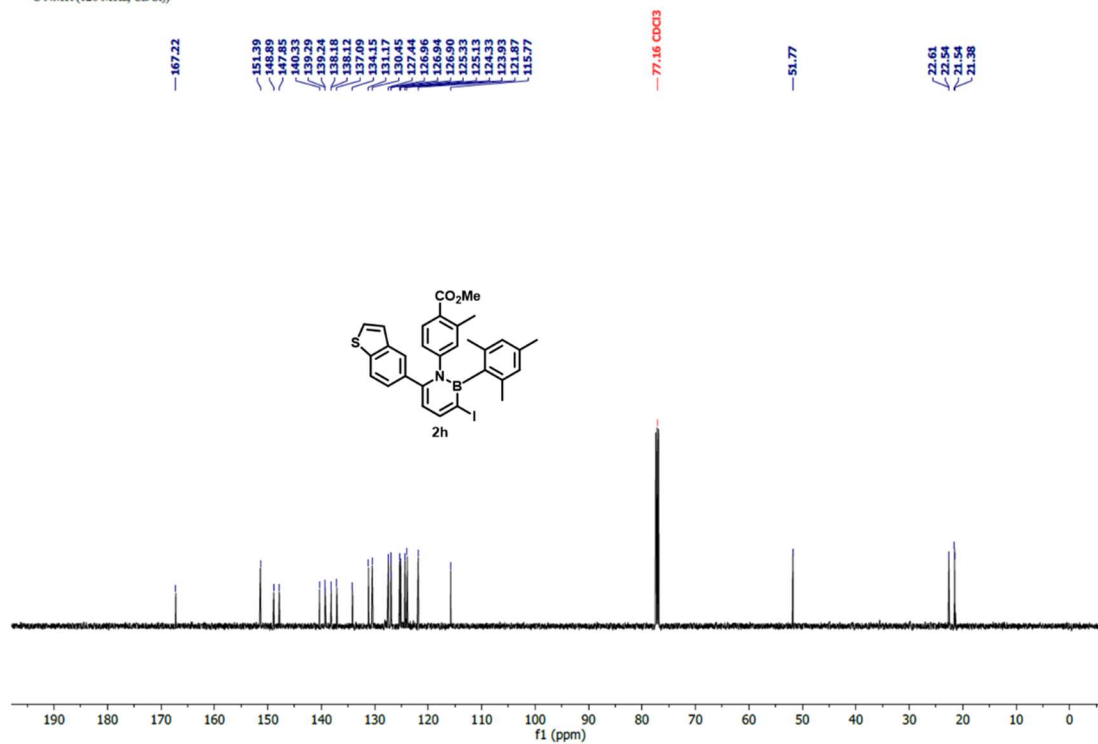
^1H NMR of 2h

^1H NMR (500 MHz, CDCl_3)



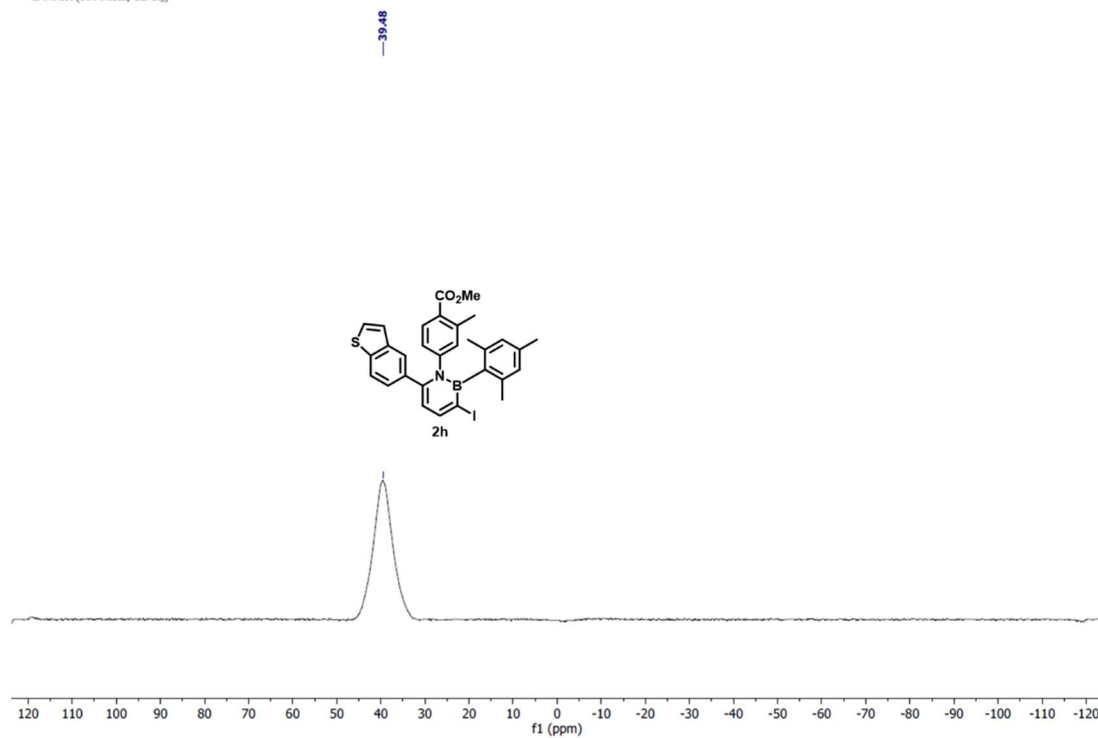
^{13}C NMR of **2h**

^{13}C NMR (126 MHz, CDCl_3)



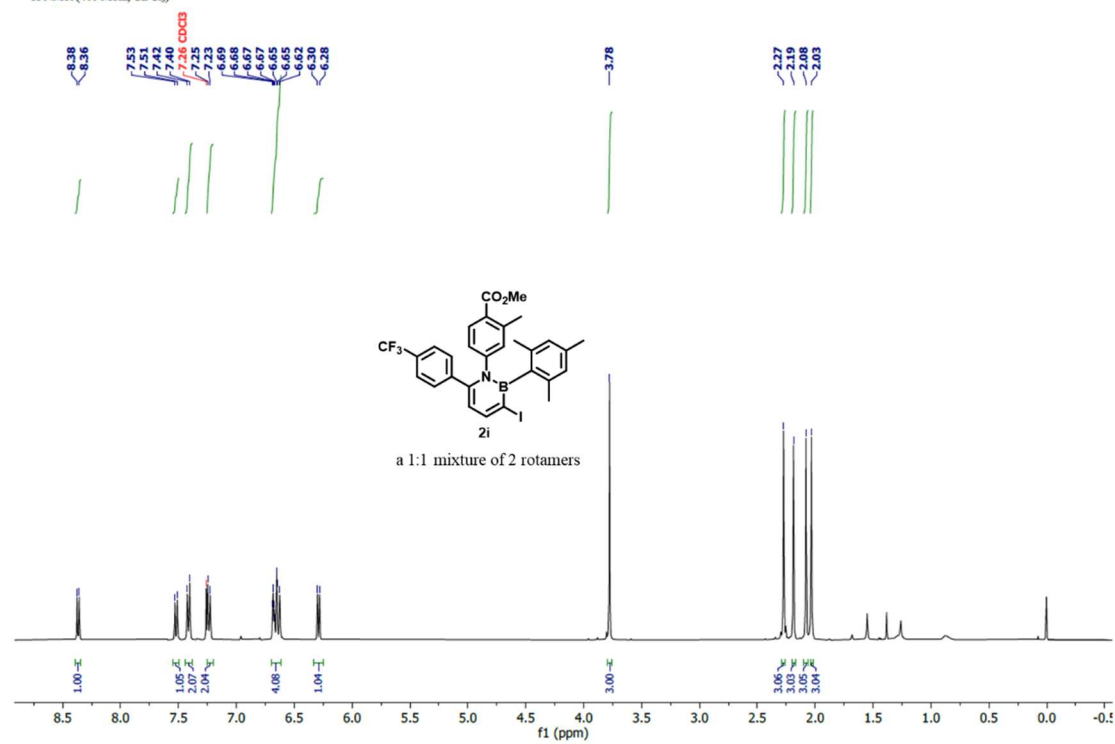
^{11}B NMR of **2h**

^{11}B NMR (160 MHz, CDCl_3)



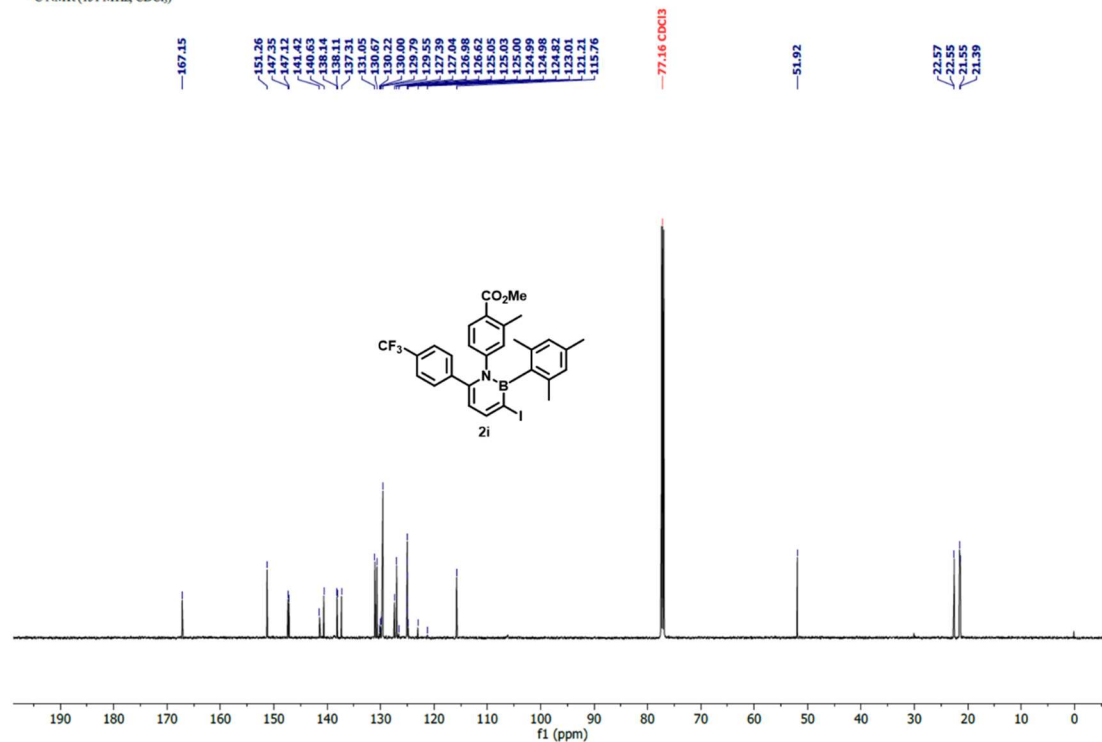
¹H NMR of 2i

¹H NMR (400 MHz, CDCl₃)



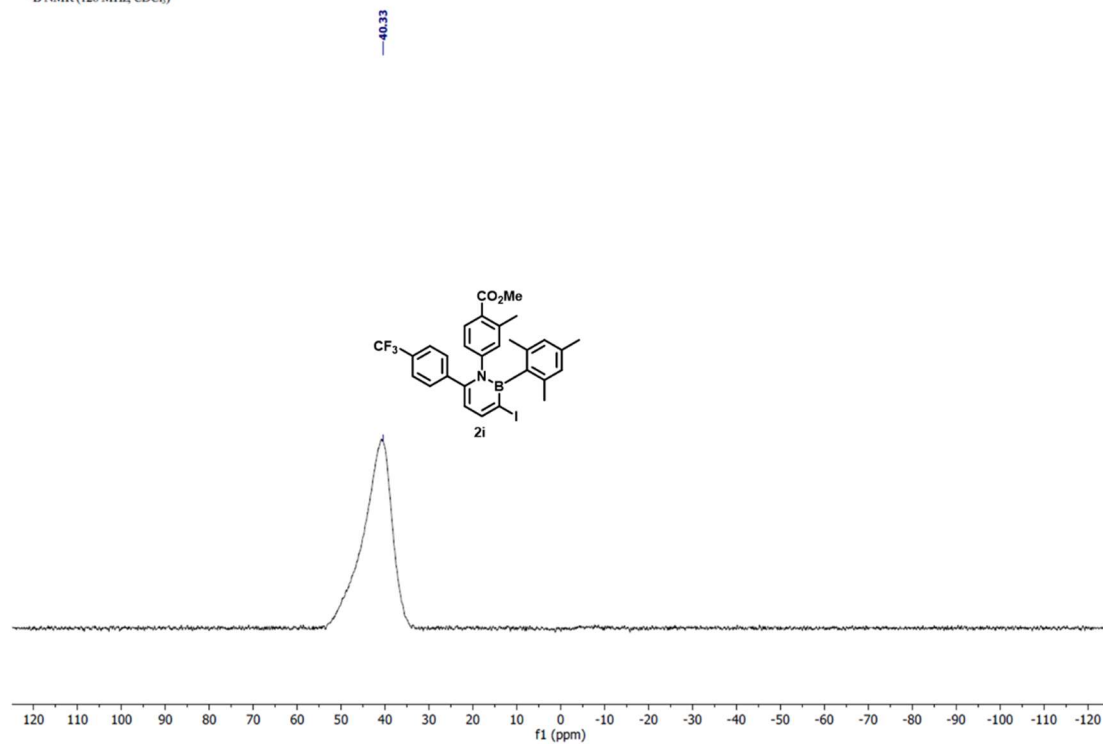
¹³C NMR of 2i

¹³C NMR (151 MHz, CDCl₃)



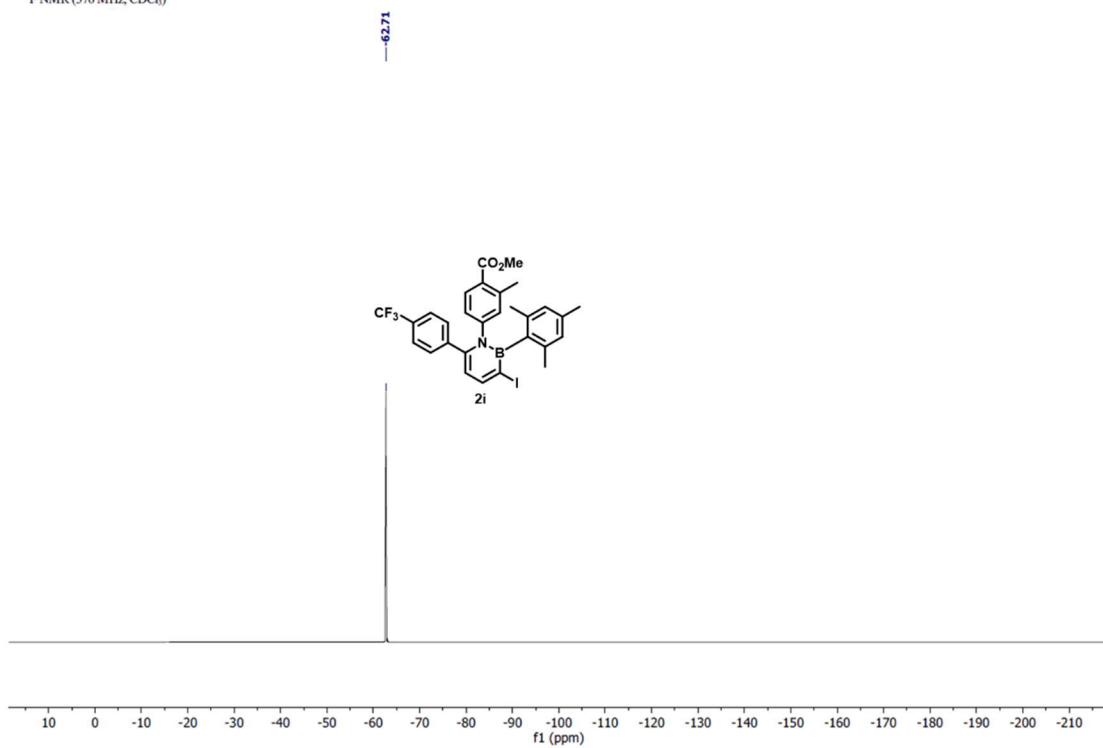
^{11}B NMR of **2i**

^{11}B NMR (128 MHz, CDCl_3)



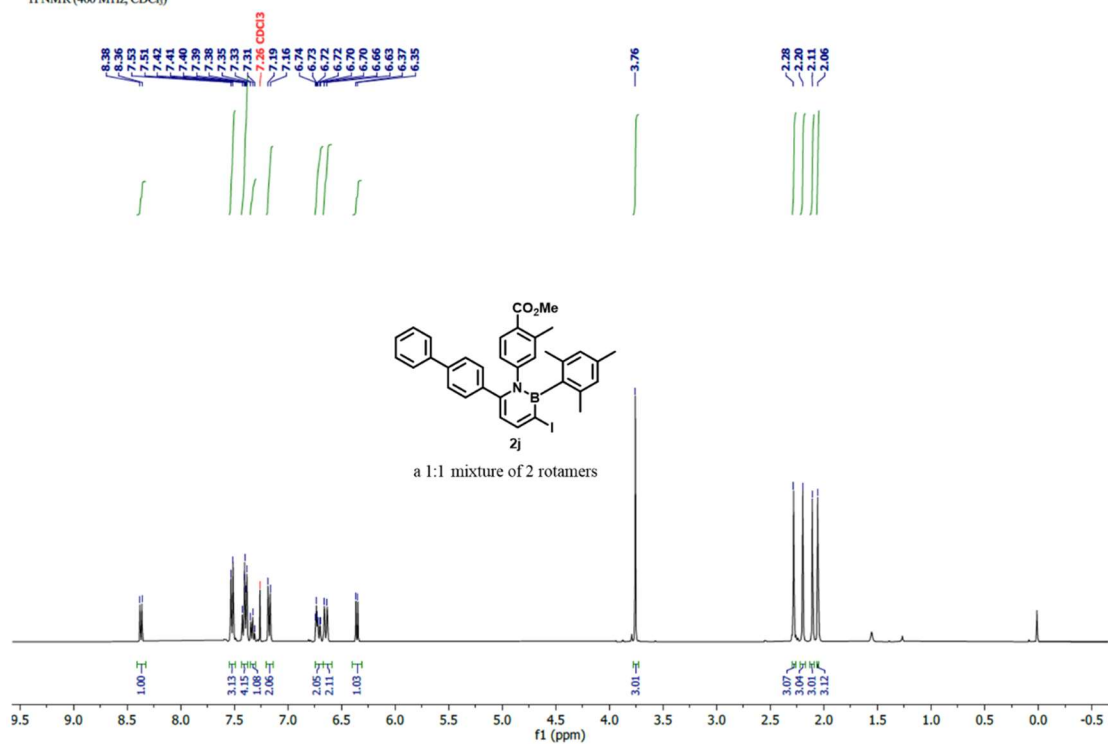
^{19}F NMR of **2i**

^{19}F NMR (376 MHz, CDCl_3)



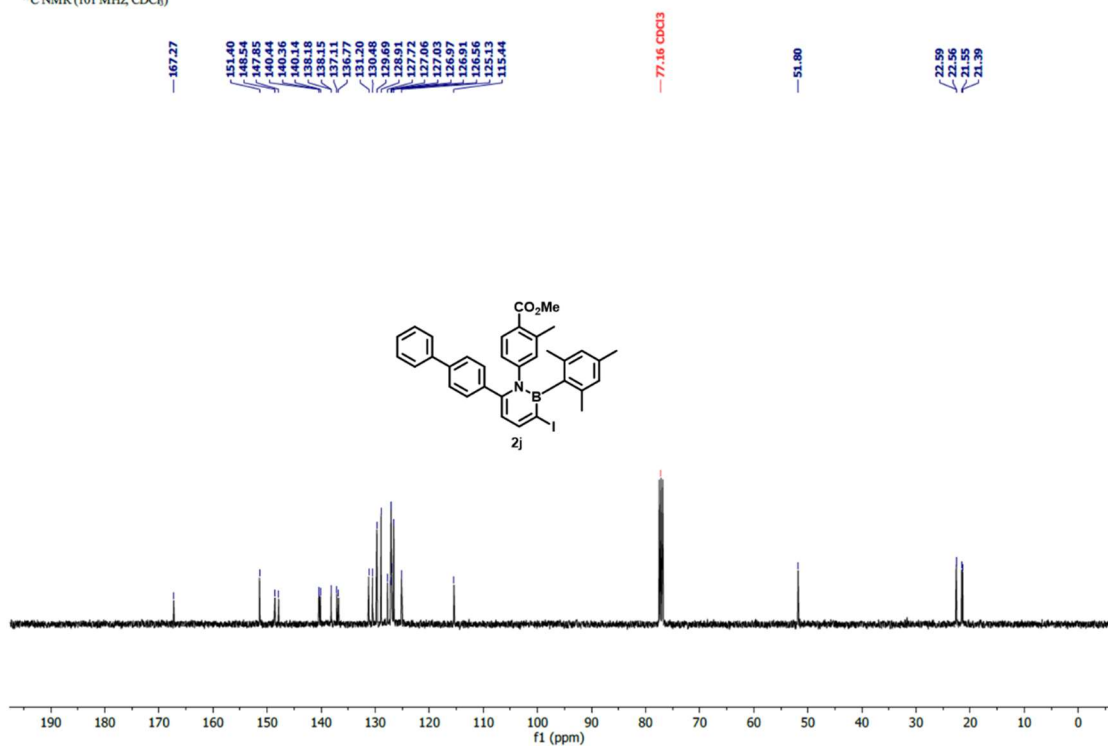
¹H NMR of 2j

¹H NMR (400 MHz, CDCl₃)



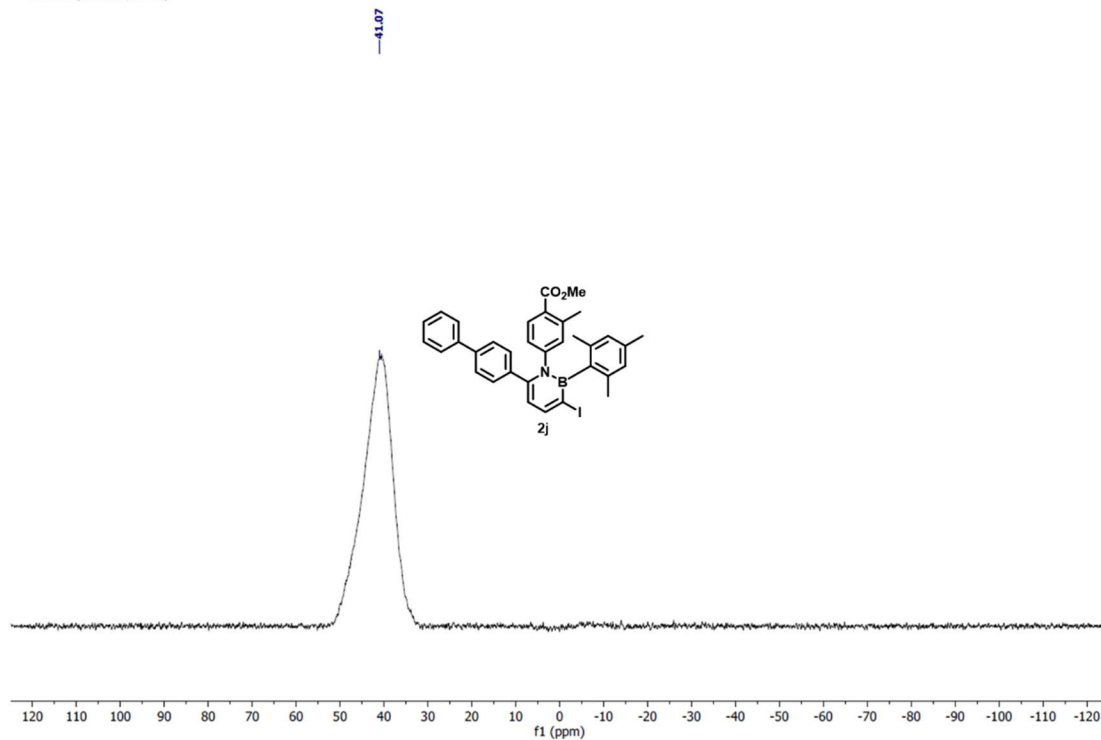
¹³C NMR of 2j

¹³C NMR (101 MHz, CDCl₃)



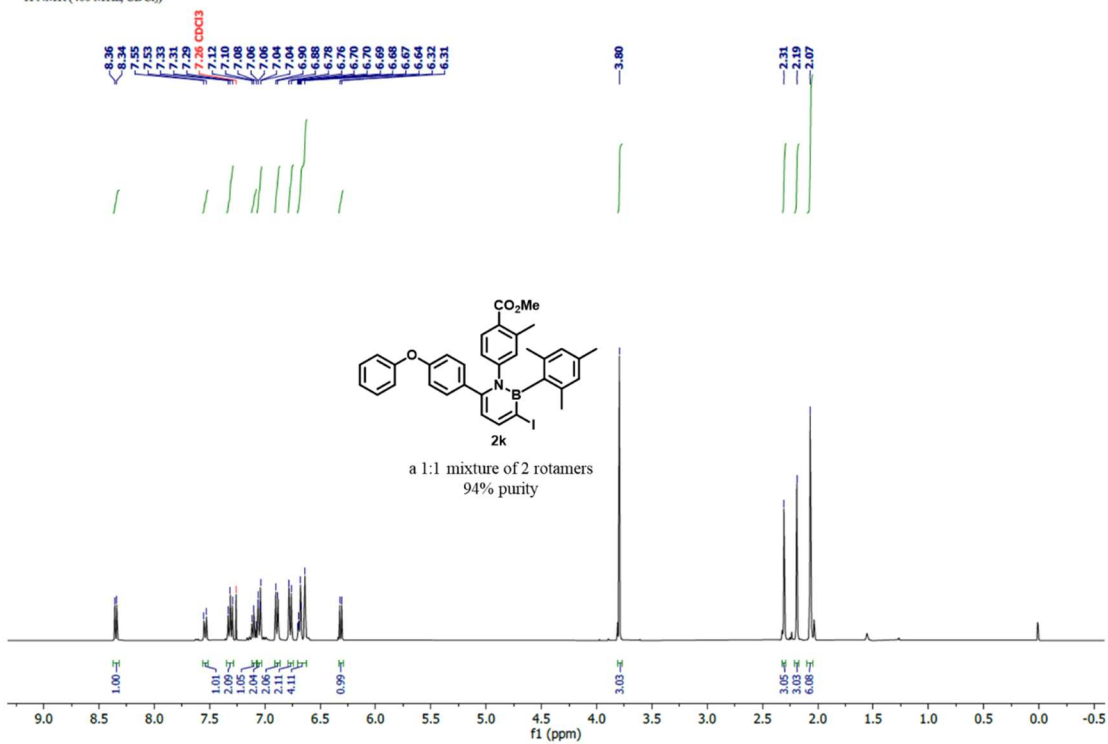
^{11}B NMR of 2j

^{11}B NMR (128 MHz, CDCl_3)



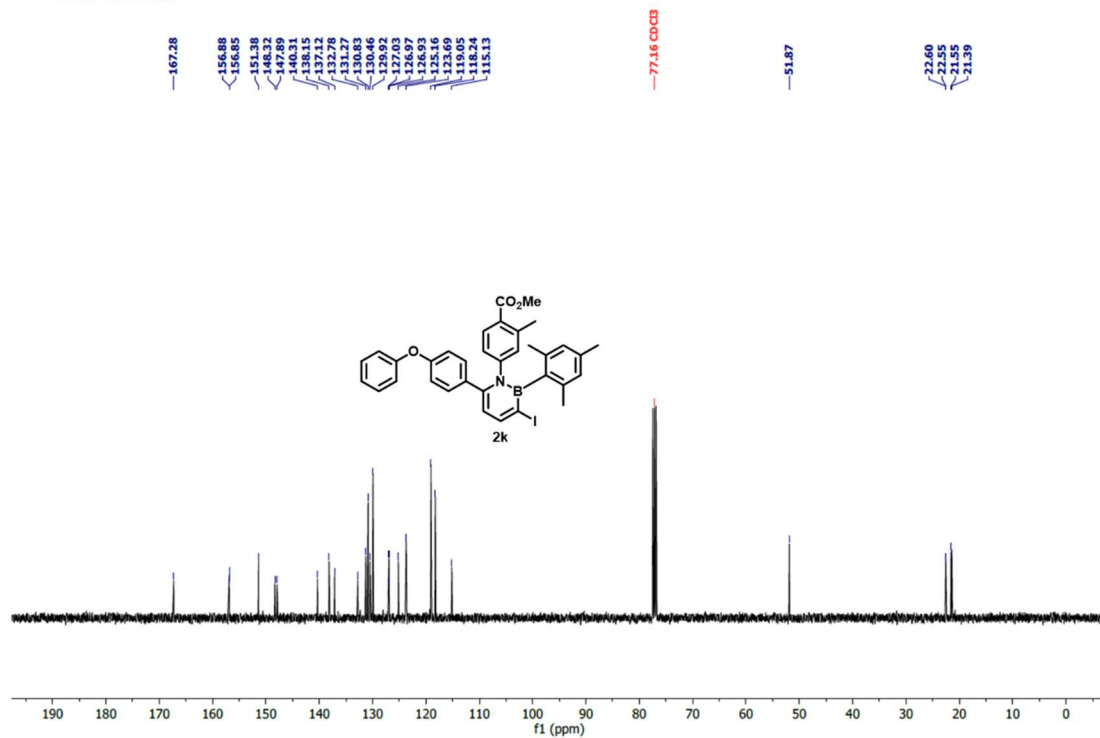
^1H NMR of 2k

^1H NMR (400 MHz, CDCl_3)



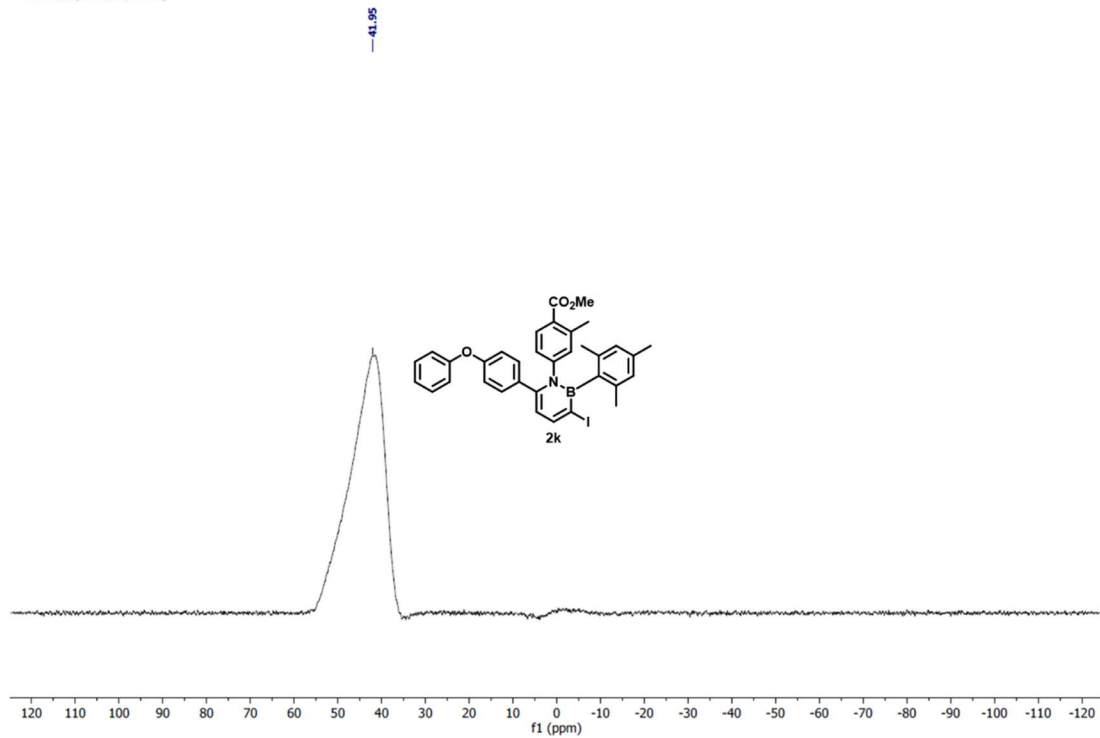
¹³C NMR of 2k

¹³C NMR (101 MHz, CDCl₃)



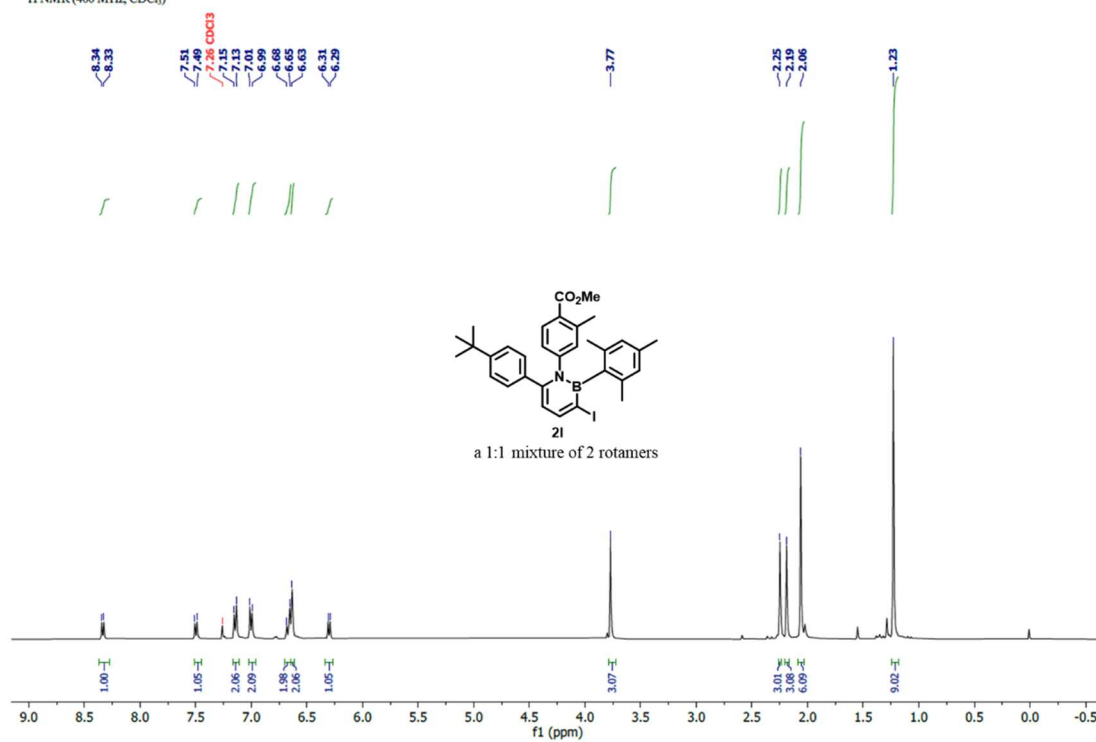
¹¹B NMR of 2k

¹¹B NMR (128 MHz, CDCl₃)



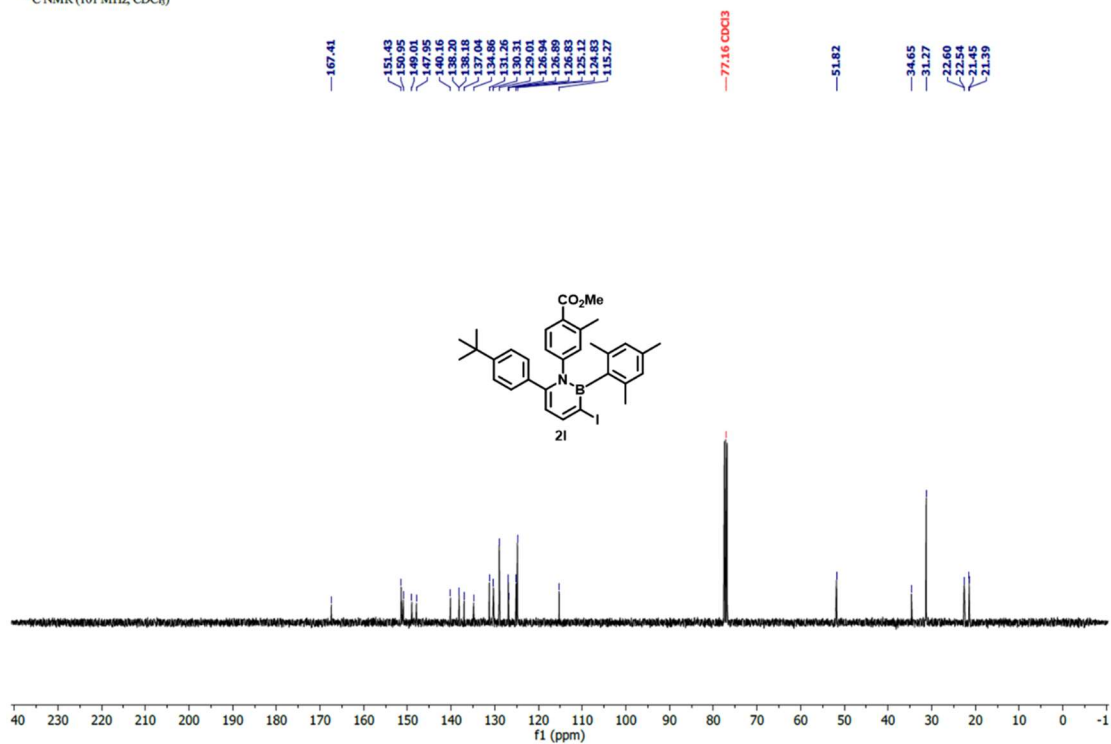
¹H NMR of 21

¹H NMR (400 MHz, CDCl₃)



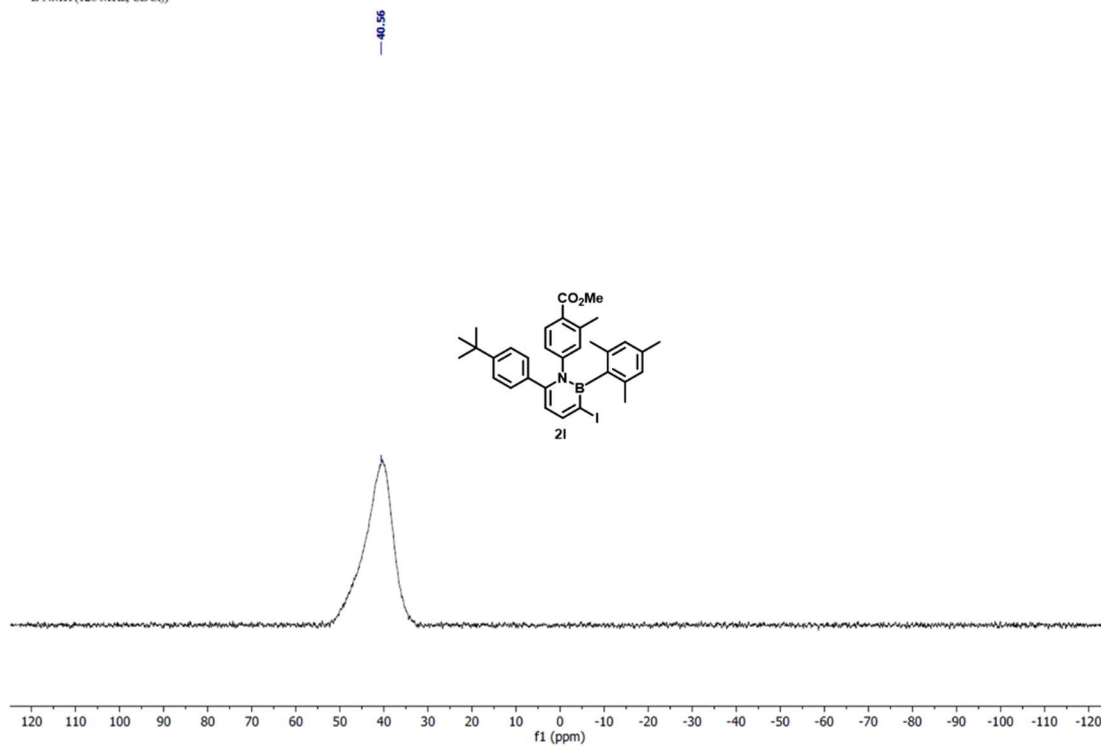
¹³C NMR of 21

¹³C NMR (101 MHz, CDCl₃)



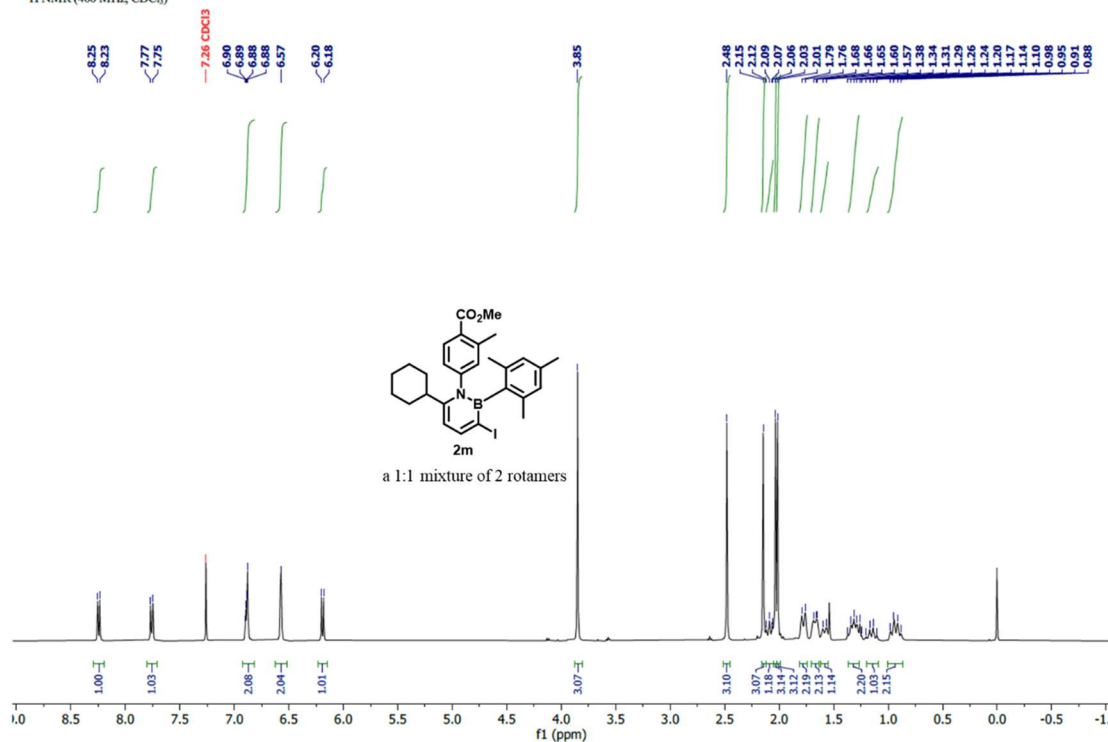
^{11}B NMR of **2l**

^{11}B NMR (128 MHz, CDCl_3)



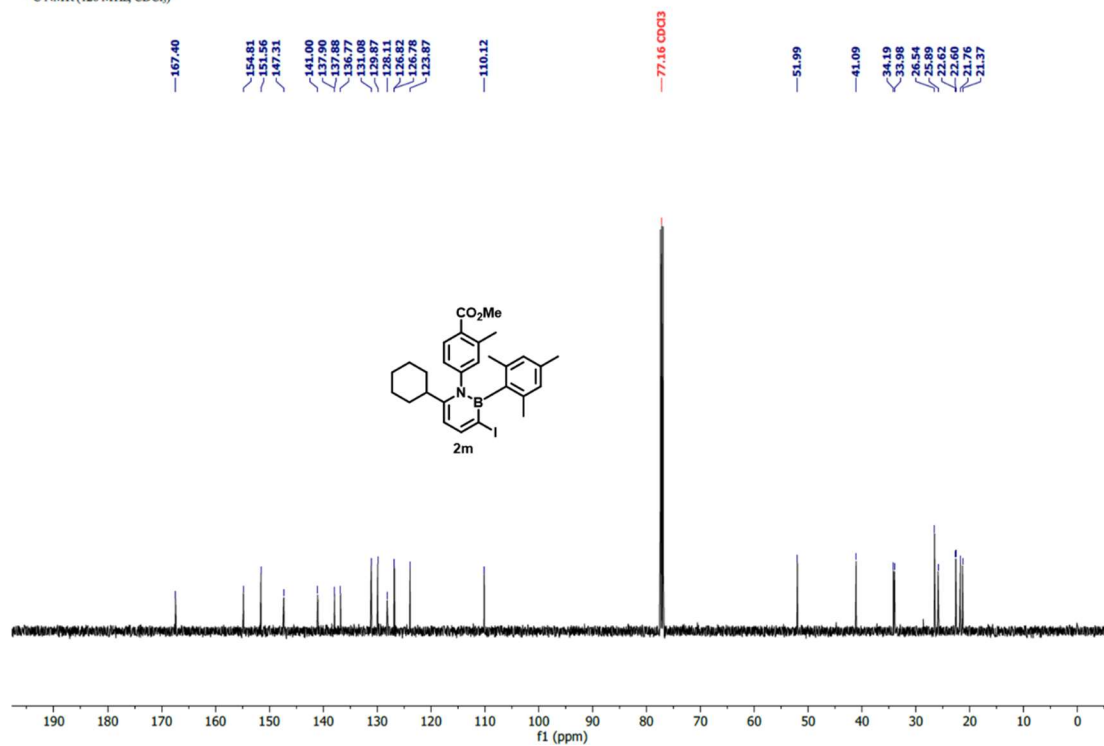
^1H NMR of **2m**

^1H NMR (400 MHz, CDCl_3)



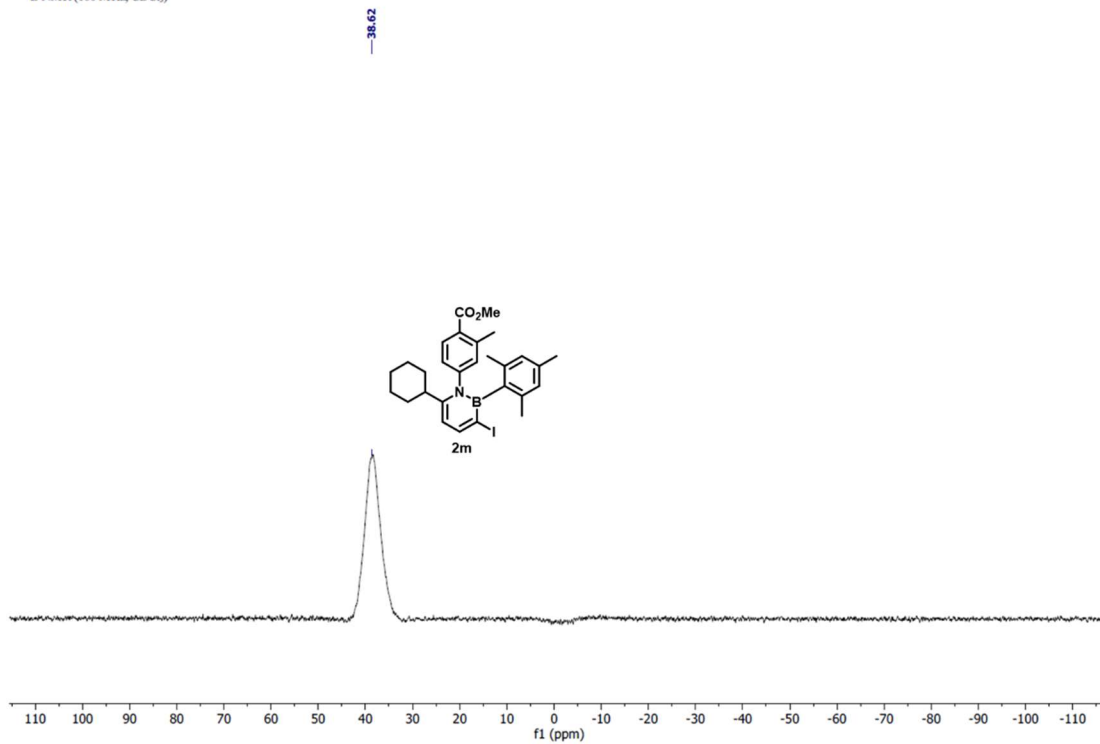
^{13}C NMR of **2m**

^{13}C NMR (126 MHz, CDCl_3)



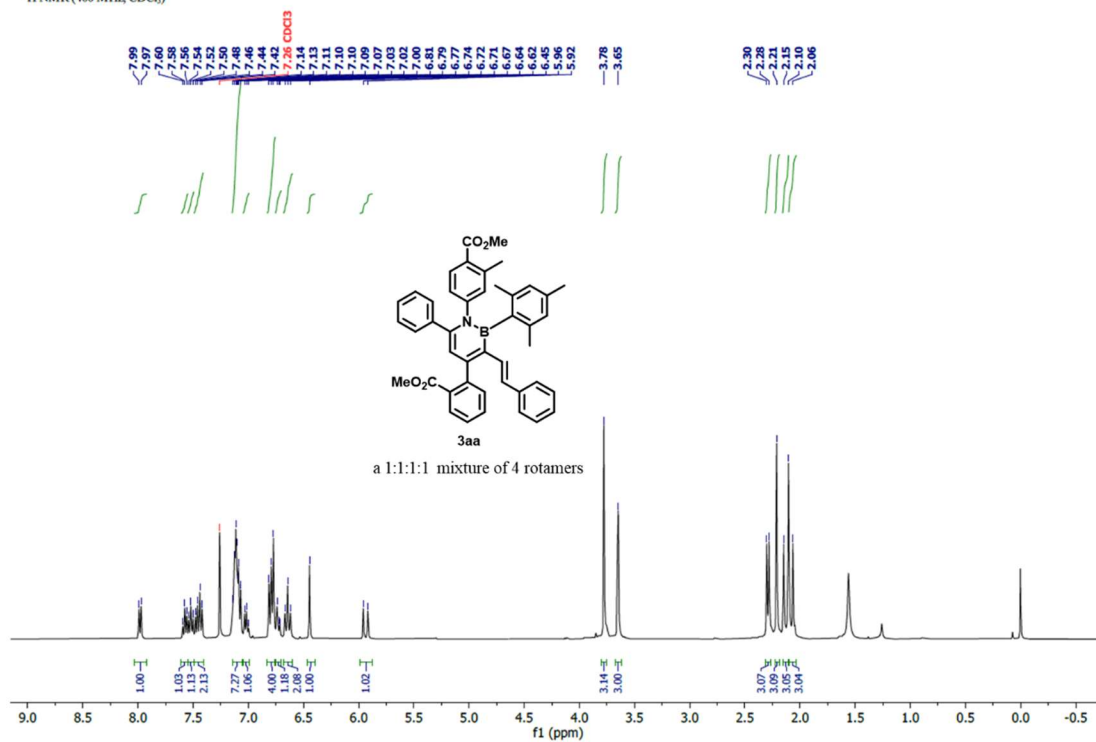
^{11}B NMR of **2m**

^{11}B NMR (160 MHz, CDCl_3)



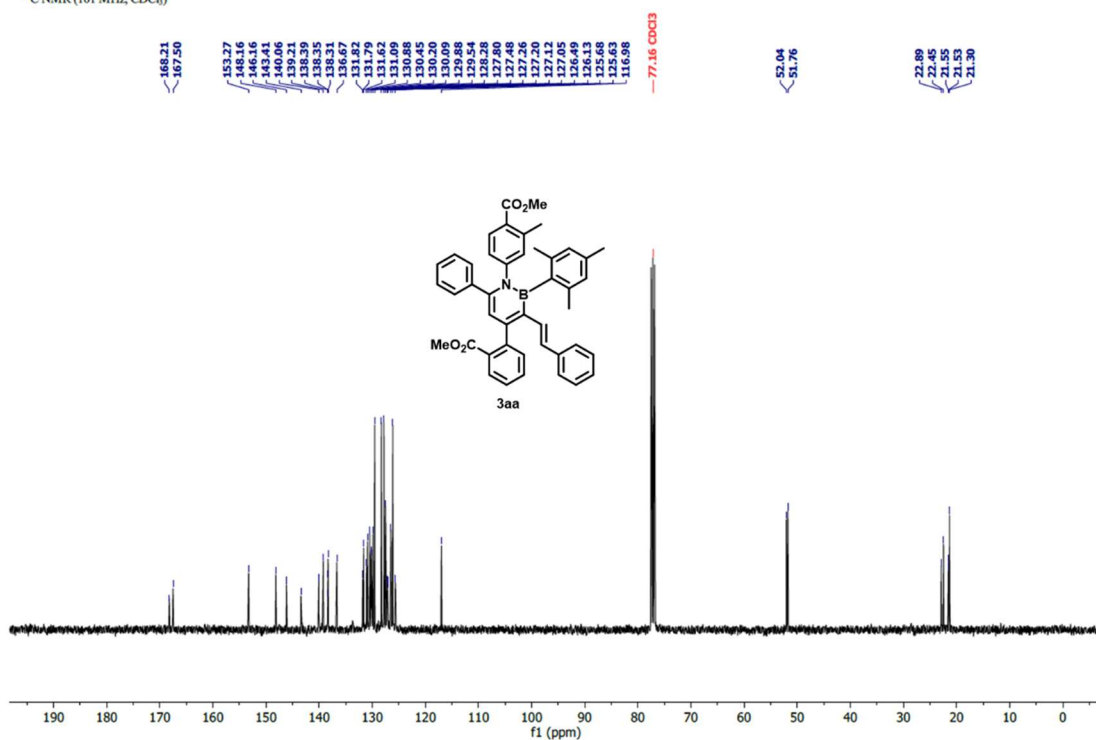
¹H NMR of 3aa

¹H NMR (400 MHz, CDCl₃)



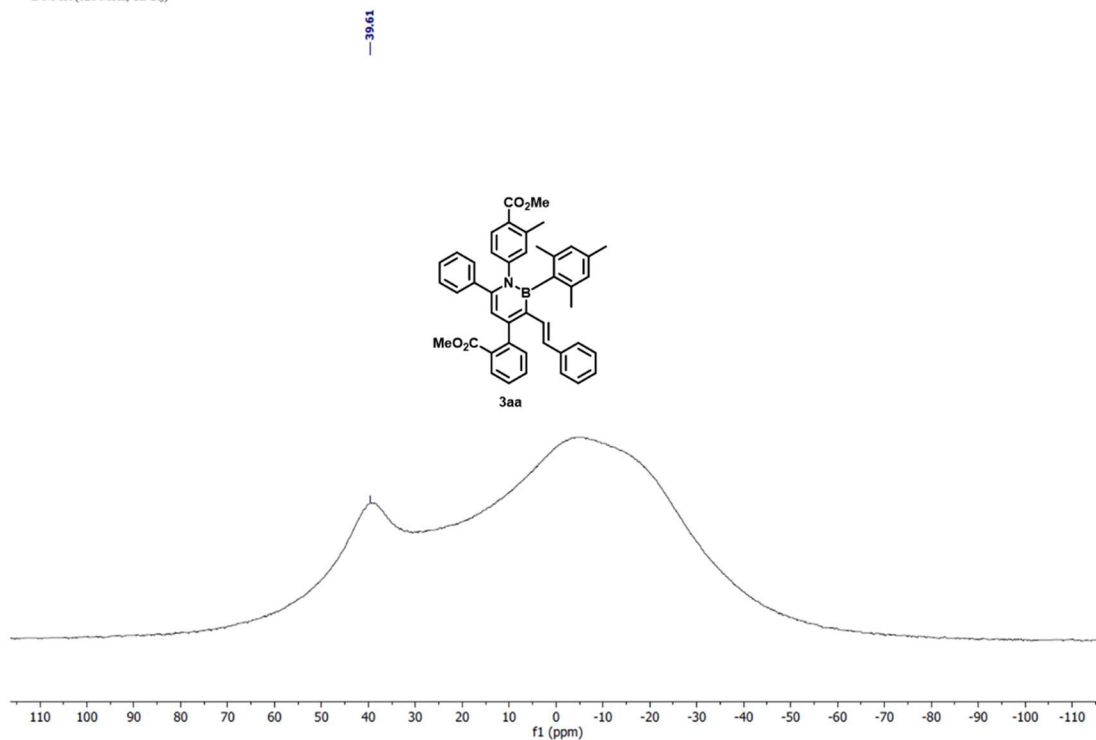
¹³C NMR of 3aa

¹³C NMR (101 MHz, CDCl₃)



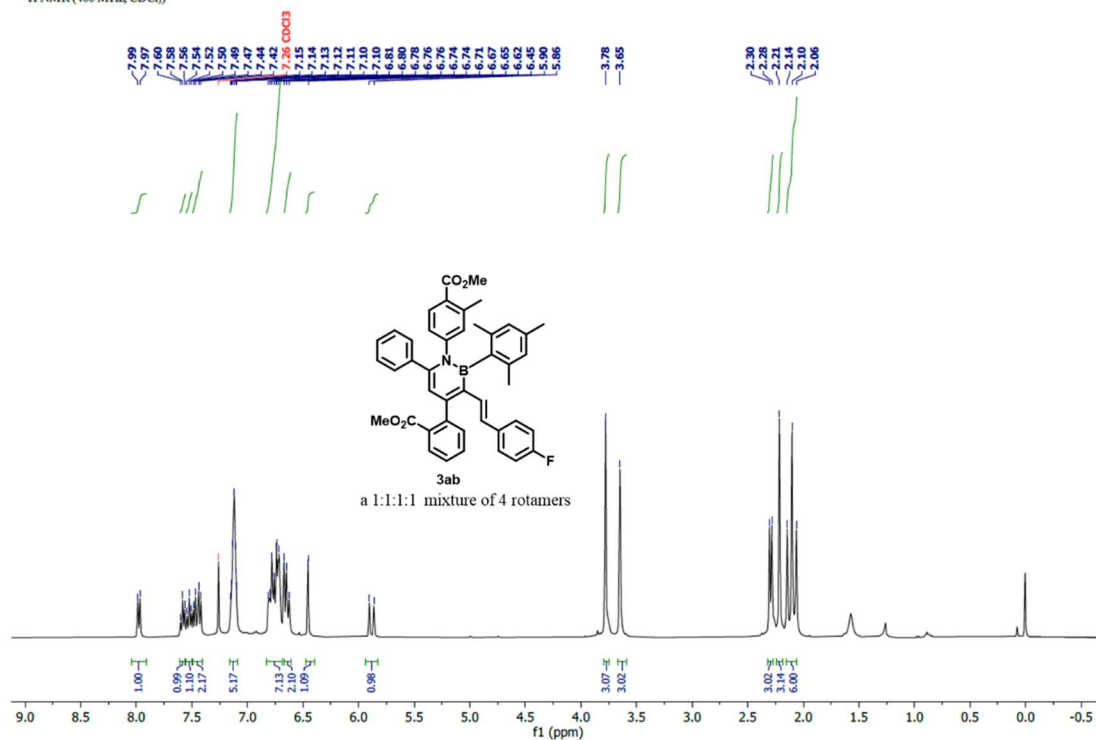
^{11}B NMR of **3aa**

^{11}B NMR (128 MHz, CDCl_3)



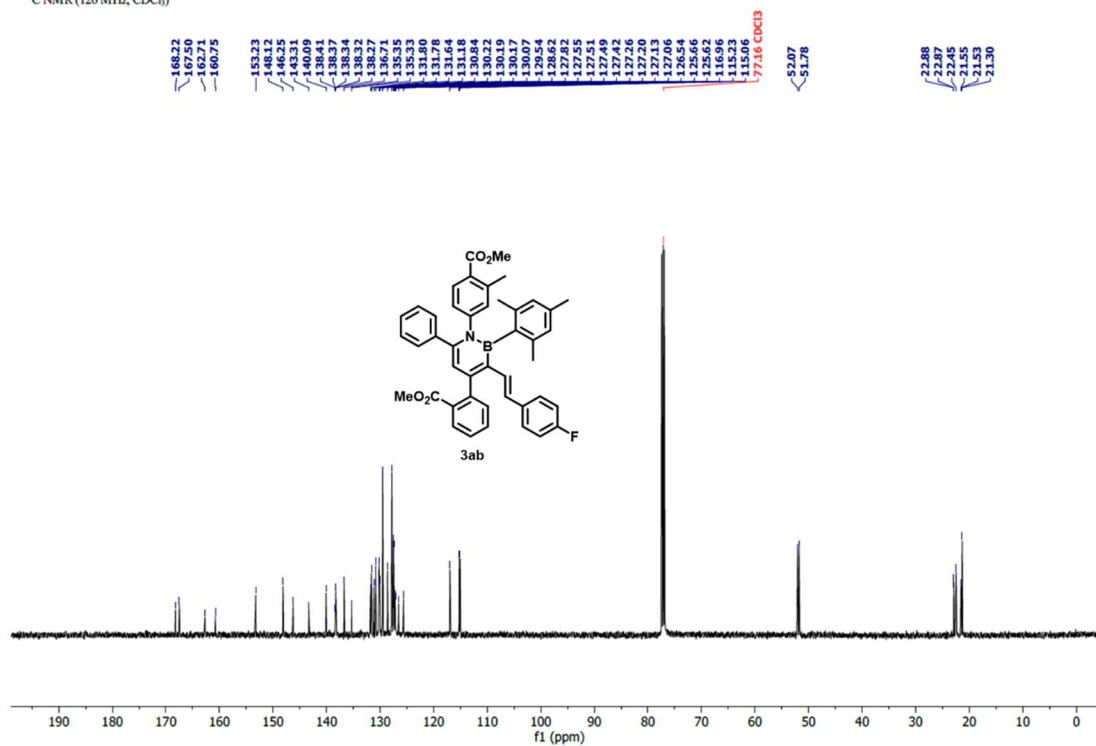
^1H NMR of **3ab**

^1H NMR (400 MHz, CDCl_3)



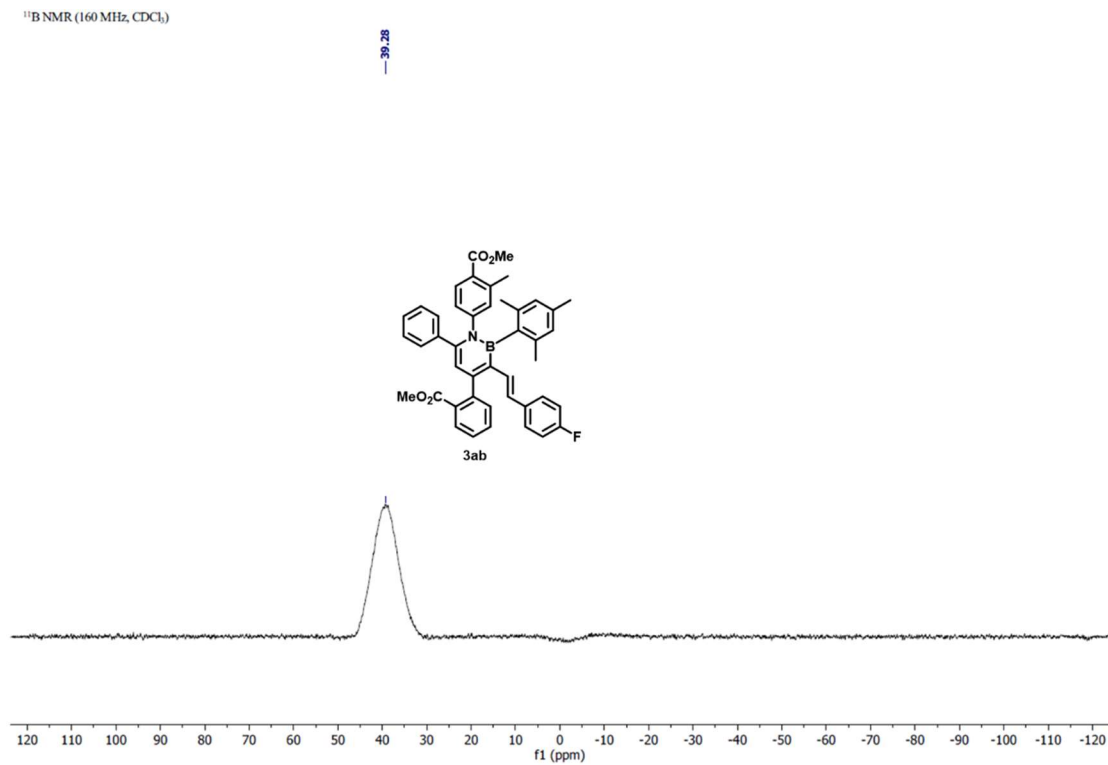
¹³C NMR of 3ab

¹³C NMR (126 MHz, CDCl₃)



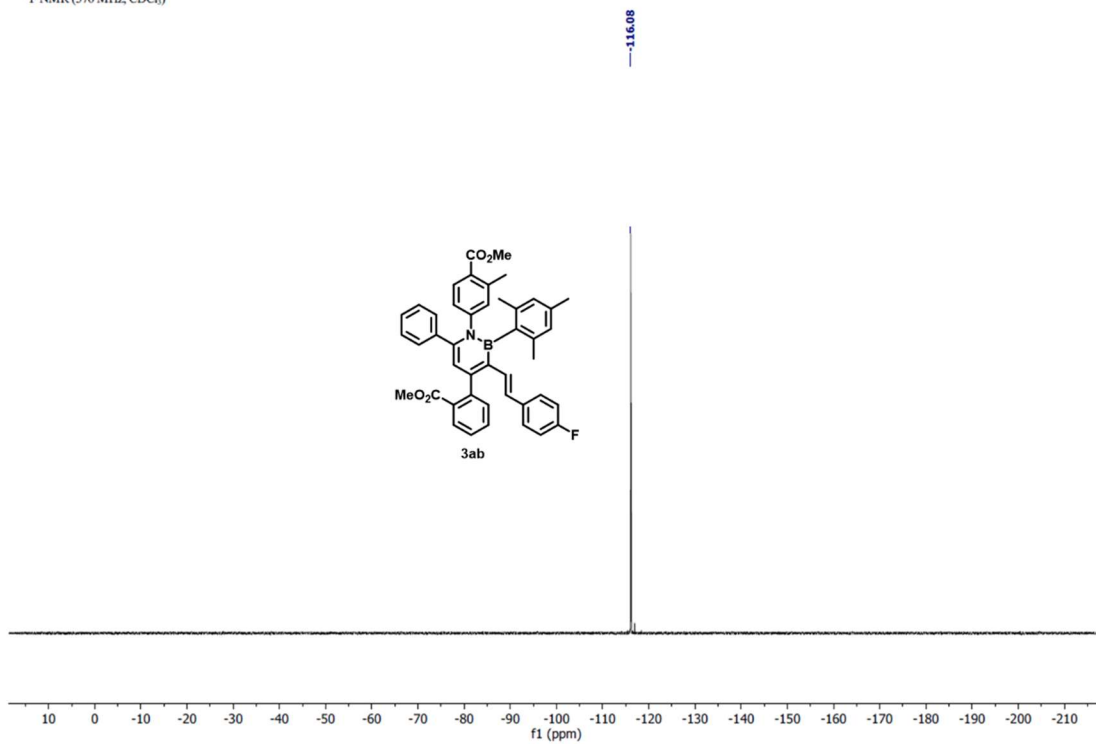
¹¹B NMR of 3ab

¹¹B NMR (160 MHz, CDCl₃)



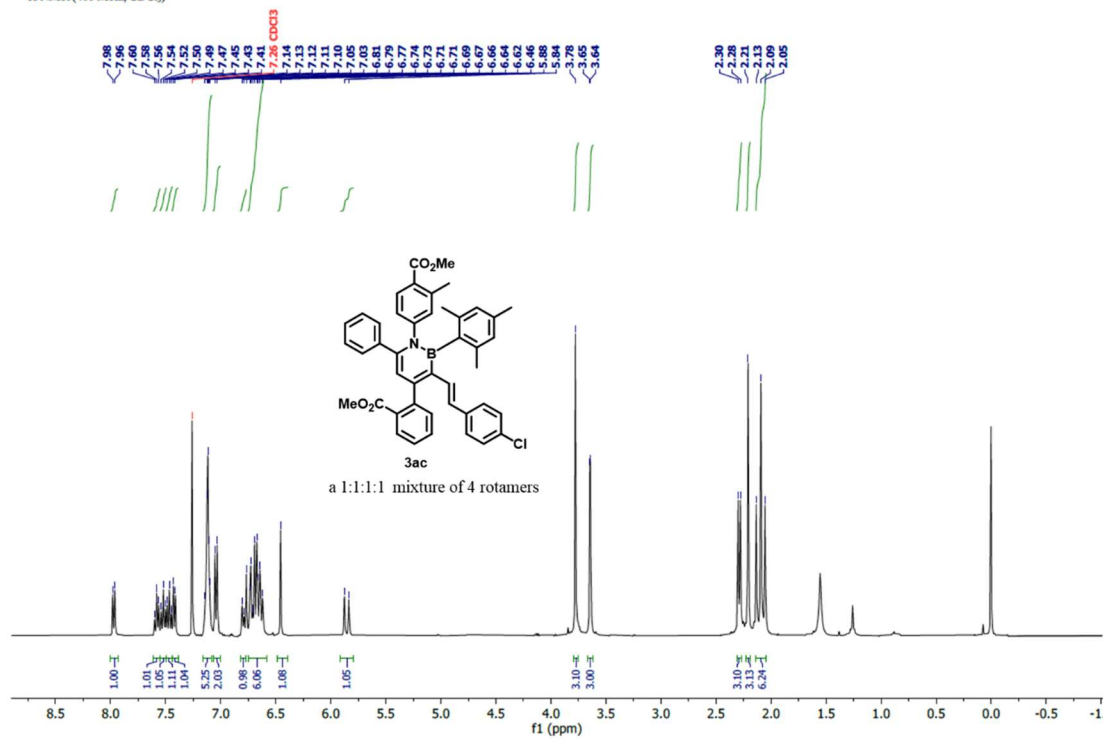
¹⁹F NMR of 3ab

¹⁹F NMR (376 MHz, CDCl₃)



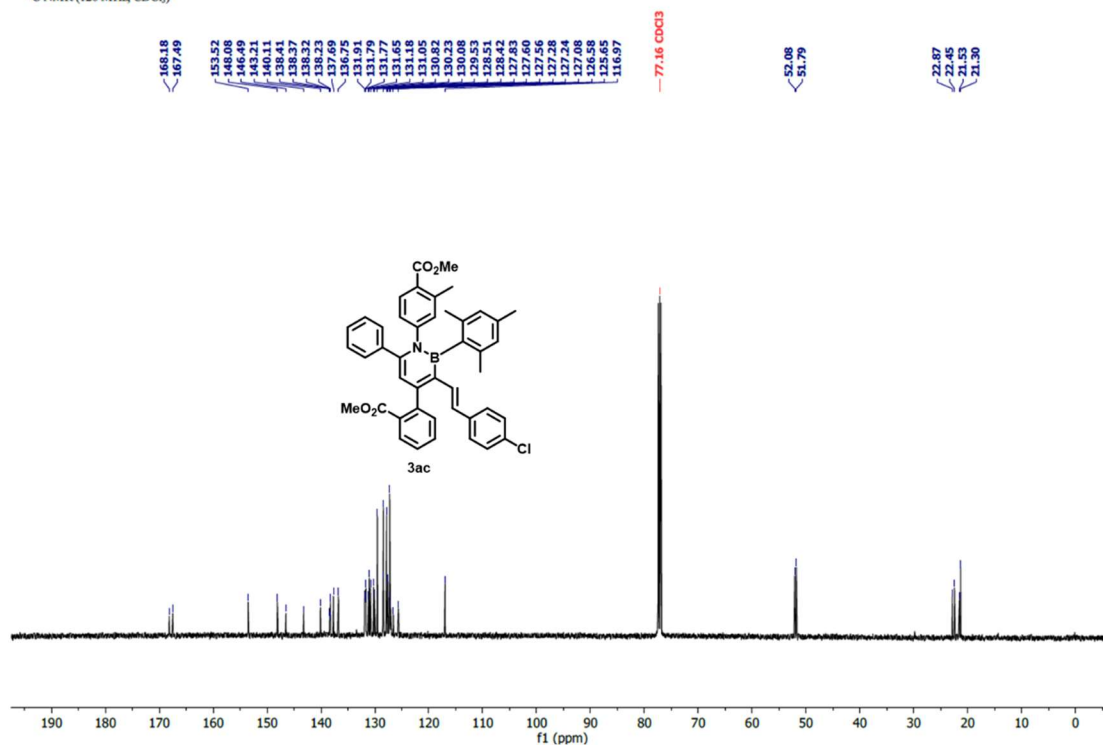
¹H NMR of 3ac

¹H NMR (400 MHz, CDCl₃)



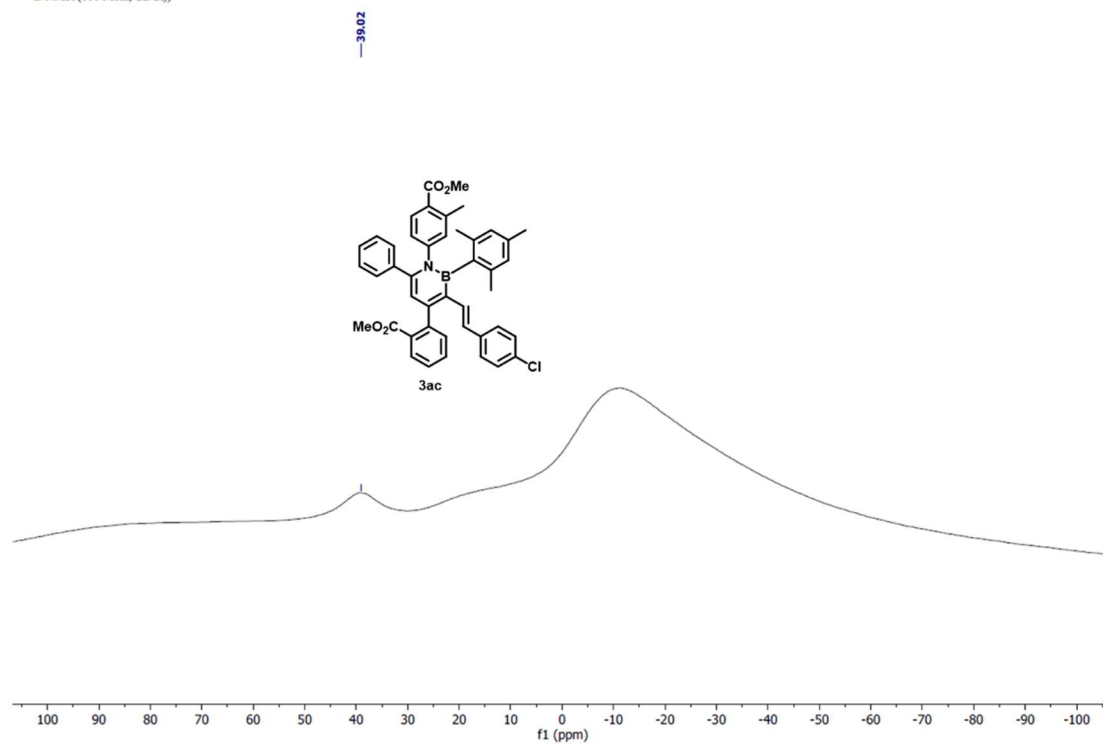
¹³C NMR of 3ac

¹³C NMR (126 MHz, CDCl₃)



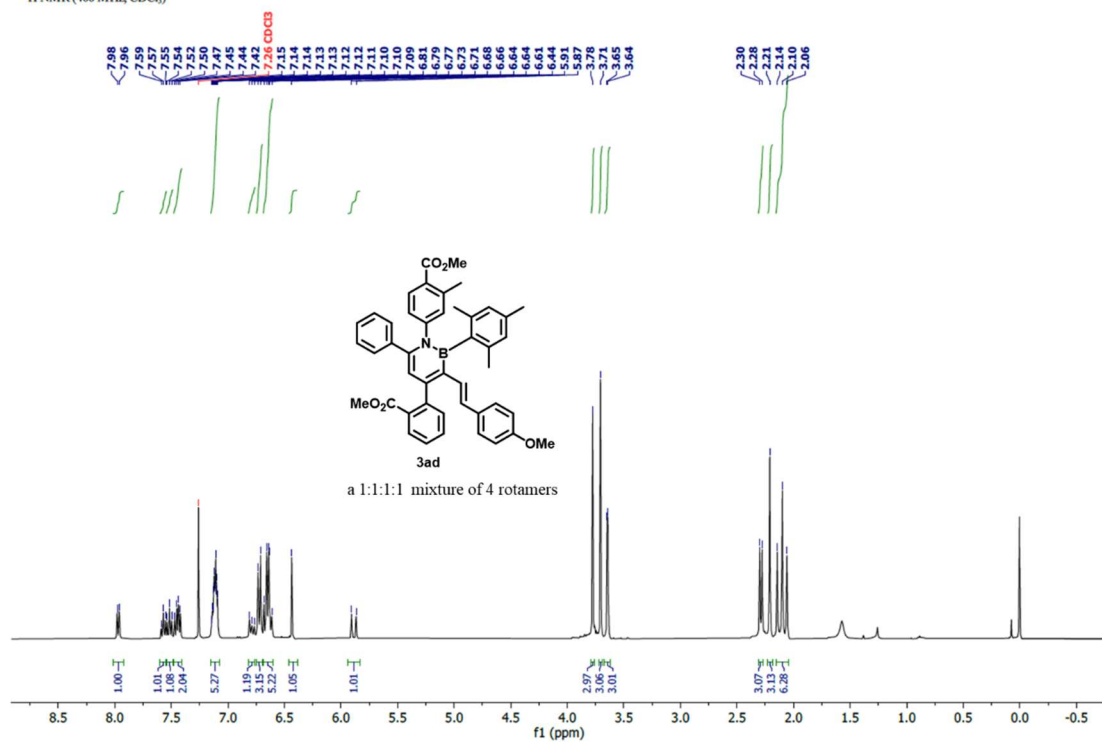
¹¹B NMR of 3ac

¹¹B NMR (160 MHz, CDCl₃)



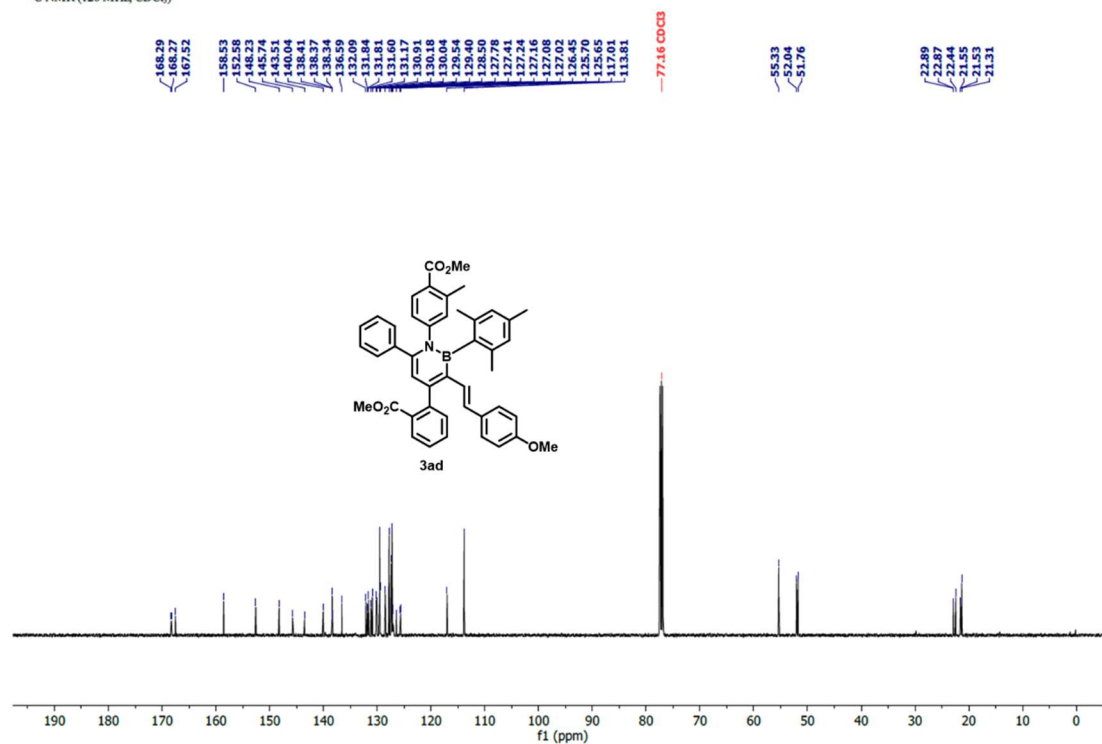
¹H NMR of 3ad

¹H NMR (400 MHz, CDCl₃)



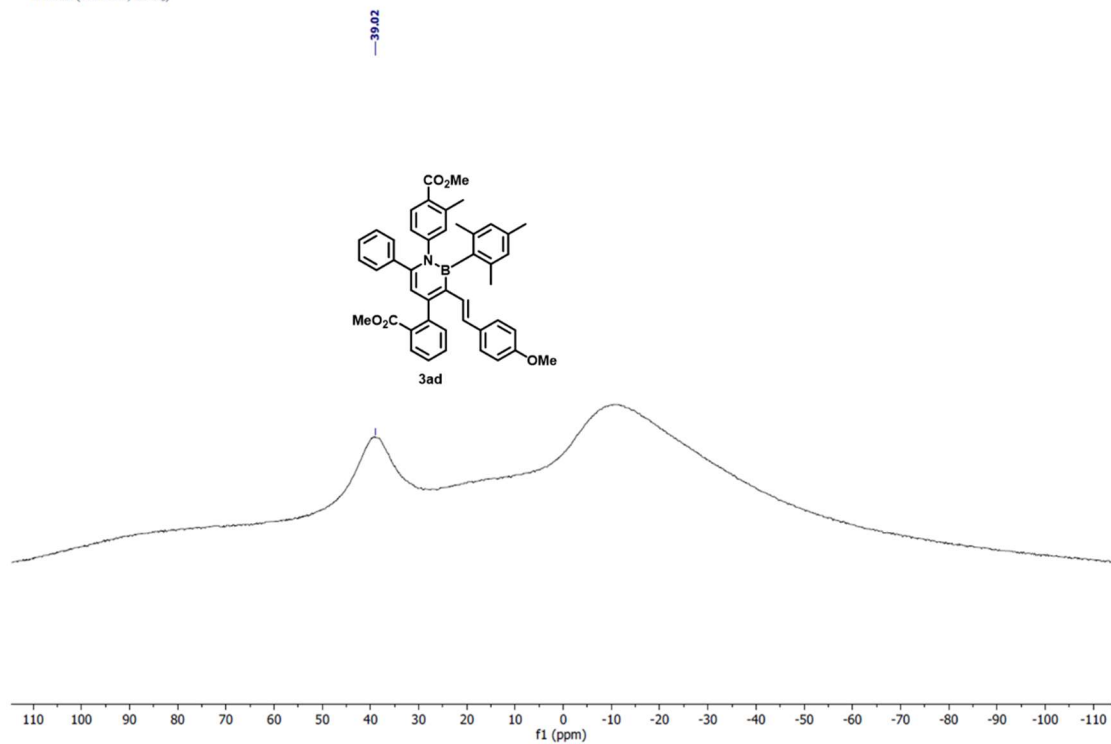
¹³C NMR of 3ad

¹³C NMR (126 MHz, CDCl₃)



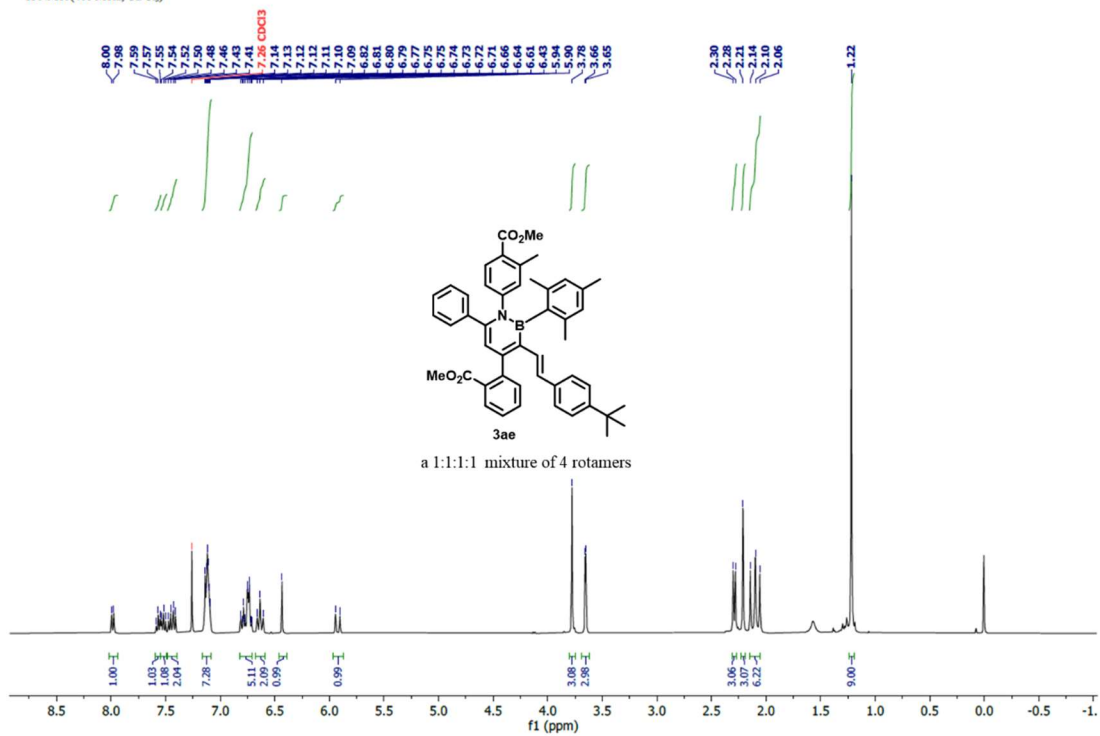
^{11}B NMR of **3ad**

^{11}B NMR (160 MHz, CDCl_3)



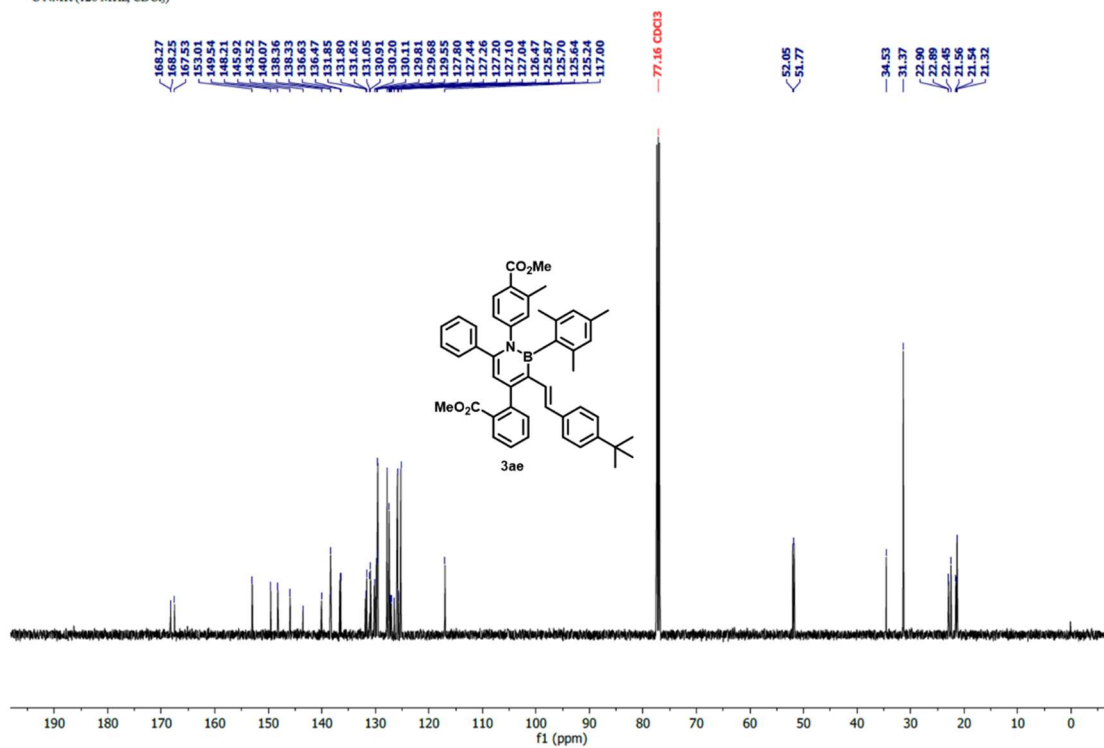
^1H NMR of **3ae**

^1H NMR (400 MHz, CDCl_3)



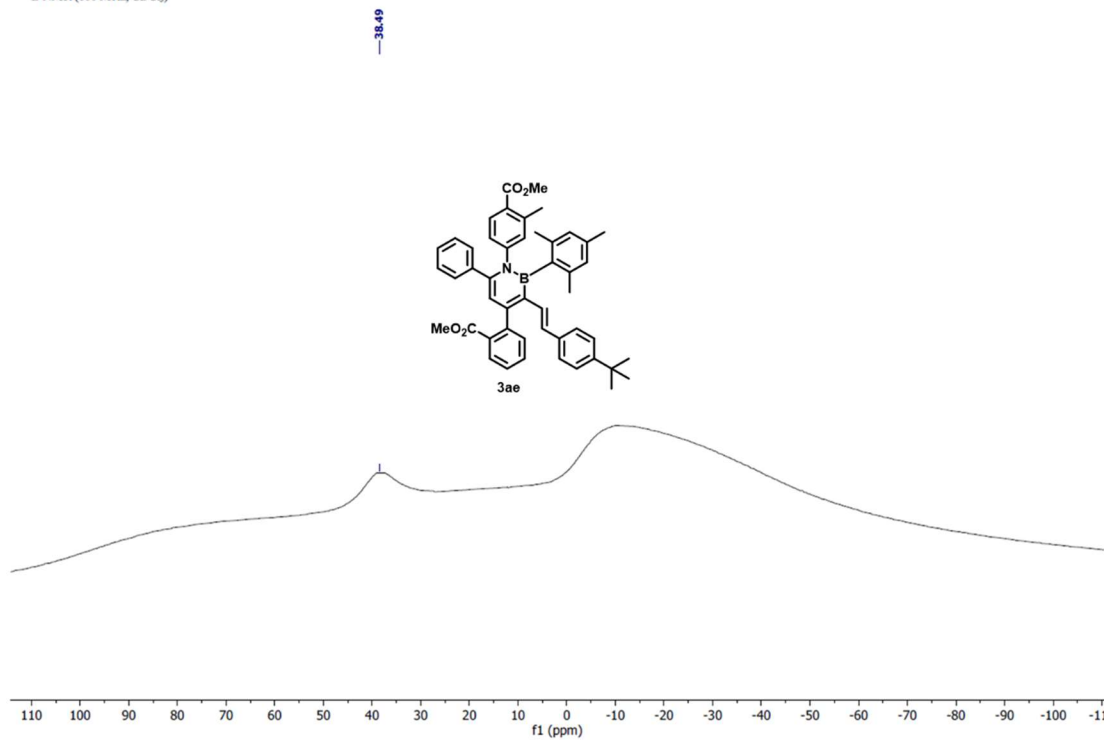
^{13}C NMR of **3ae**

^{13}C NMR (126 MHz, CDCl_3)



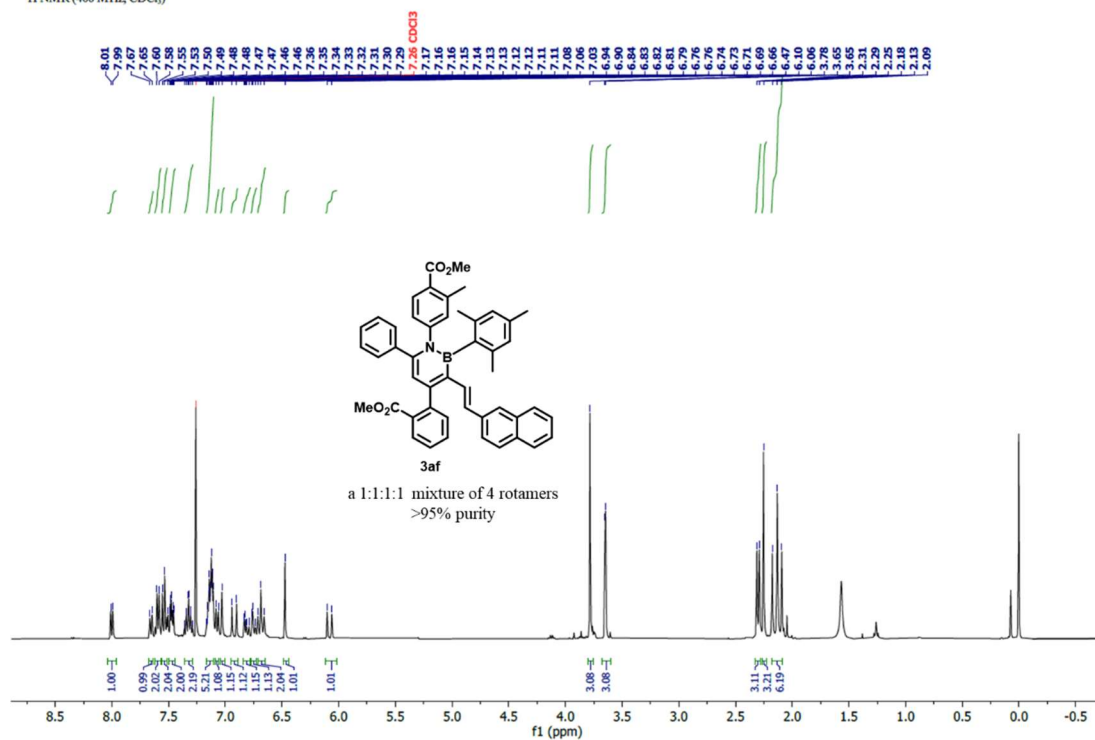
^{11}B NMR of **3ae**

^{11}B NMR (160 MHz, CDCl_3)



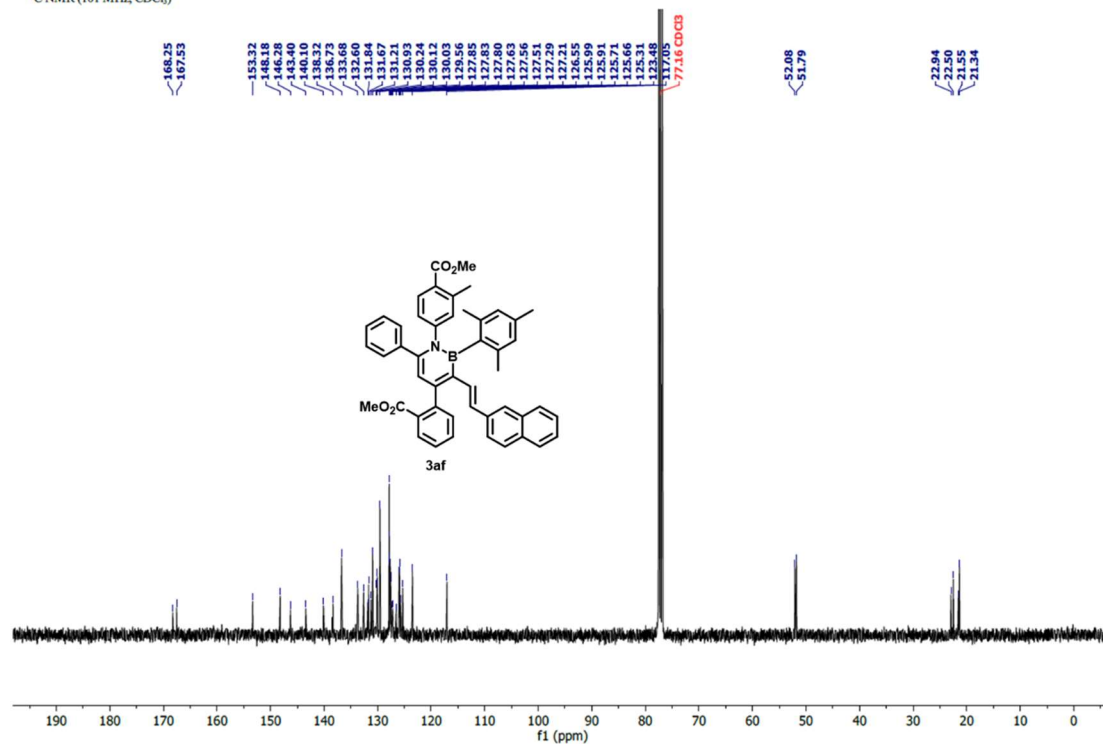
¹H NMR of 3af

¹H NMR (400 MHz, CDCl₃)



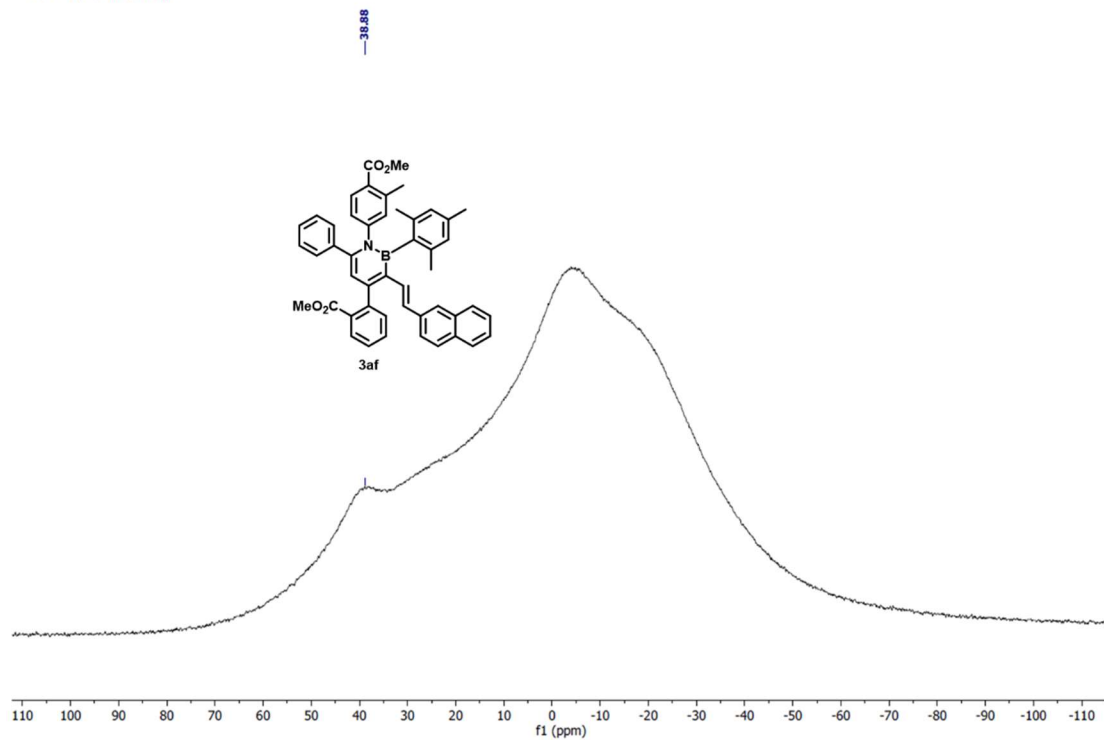
¹³C NMR of 3af

¹³C NMR (101 MHz, CDCl₃)



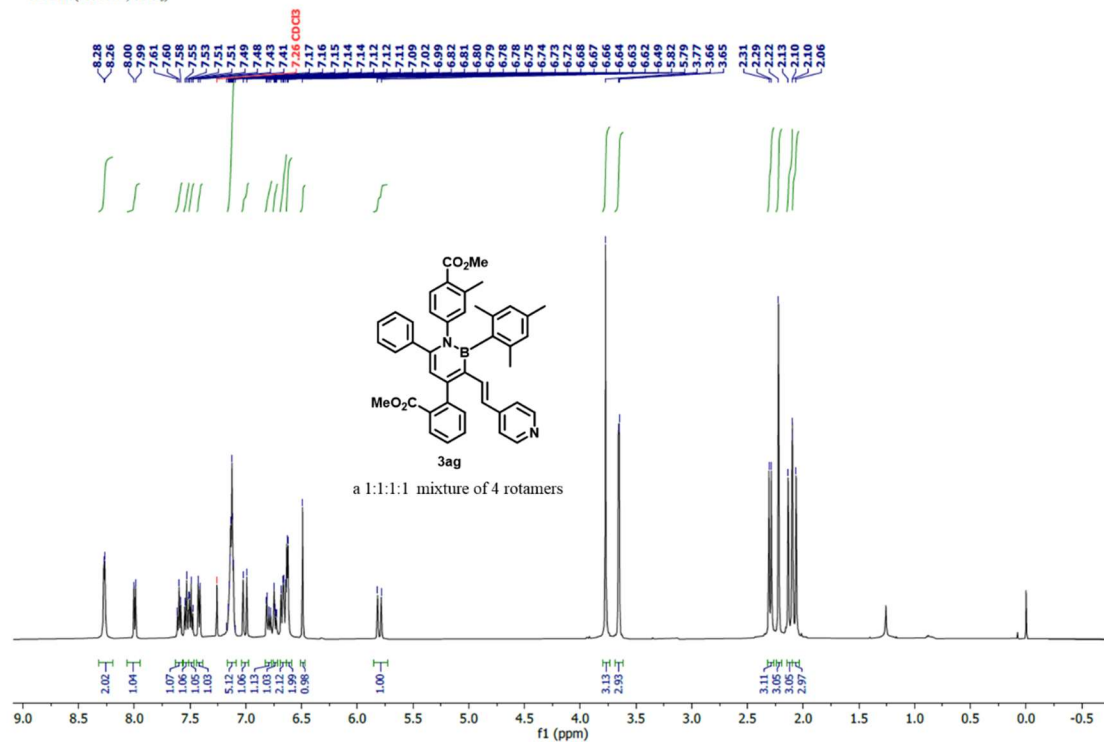
^{11}B NMR of **3af**

^{11}B NMR (128 MHz, CDCl_3)



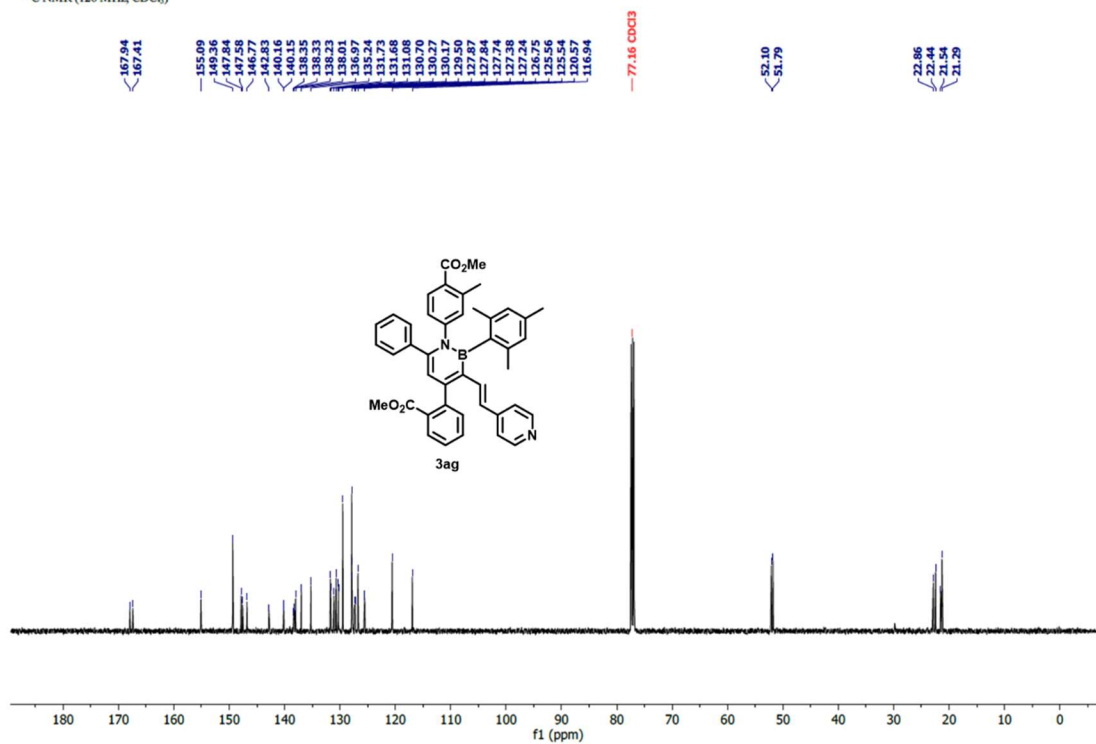
^1H NMR of **3ag**

^1H NMR (500 MHz, CDCl_3)



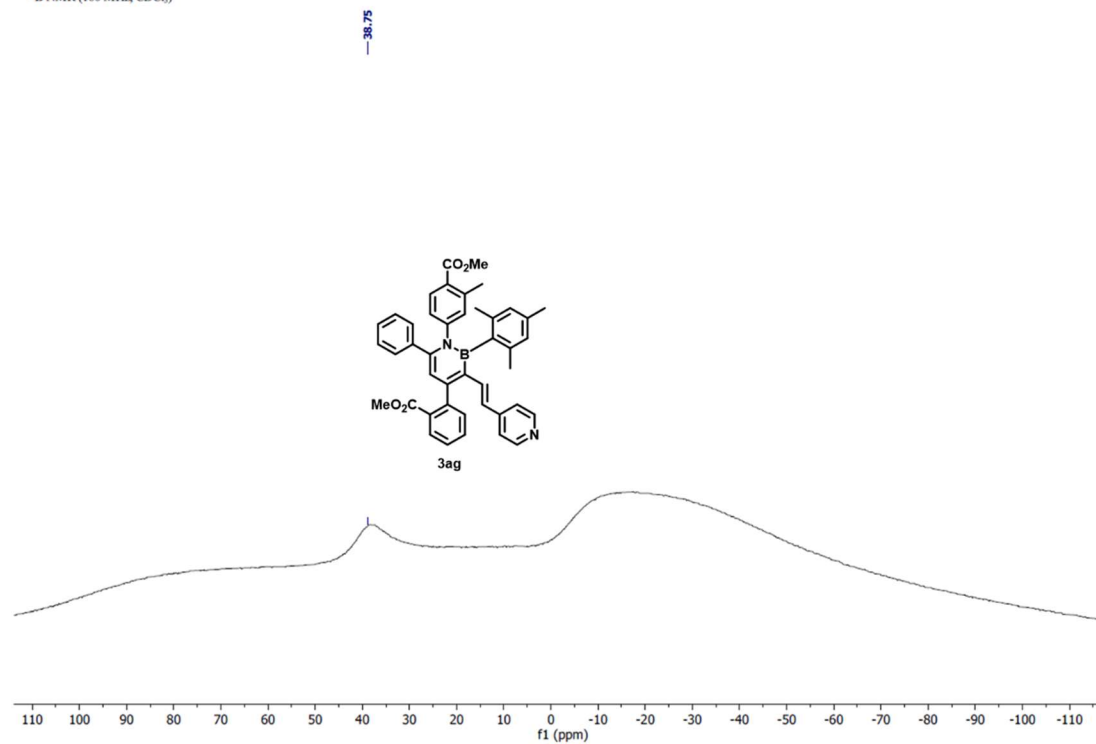
^{13}C NMR of **3ag**

^{13}C NMR (126 MHz, CDCl_3)



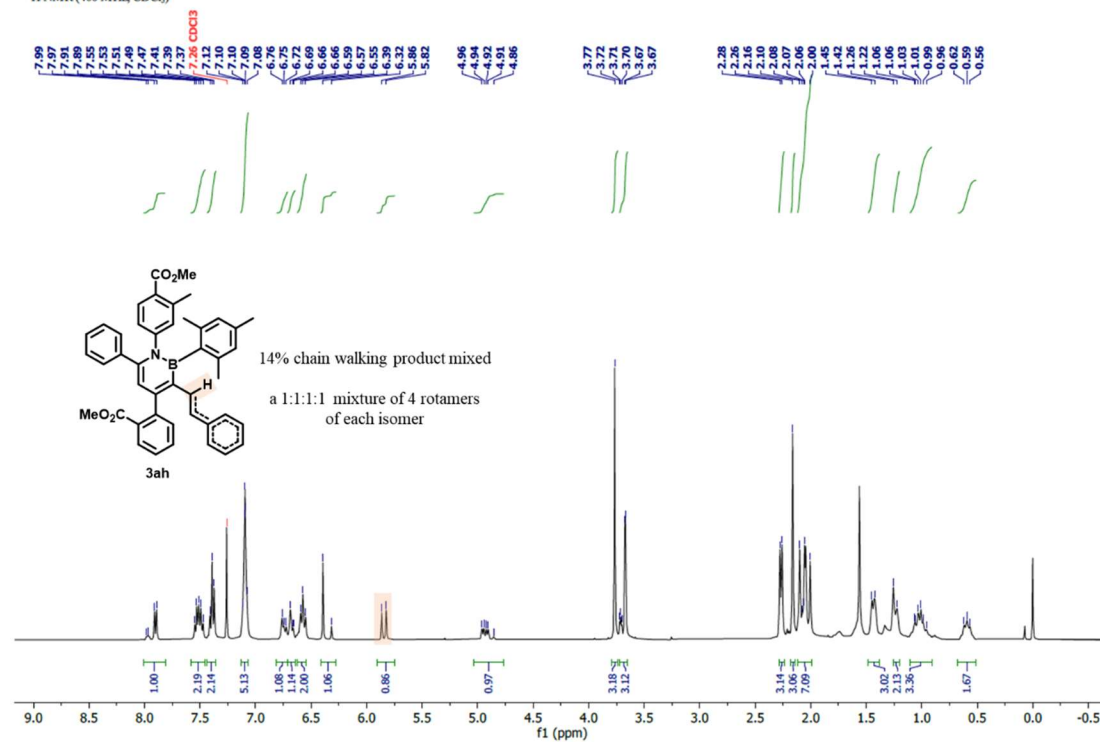
^{11}B NMR of **3ag**

^{11}B NMR (160 MHz, CDCl_3)



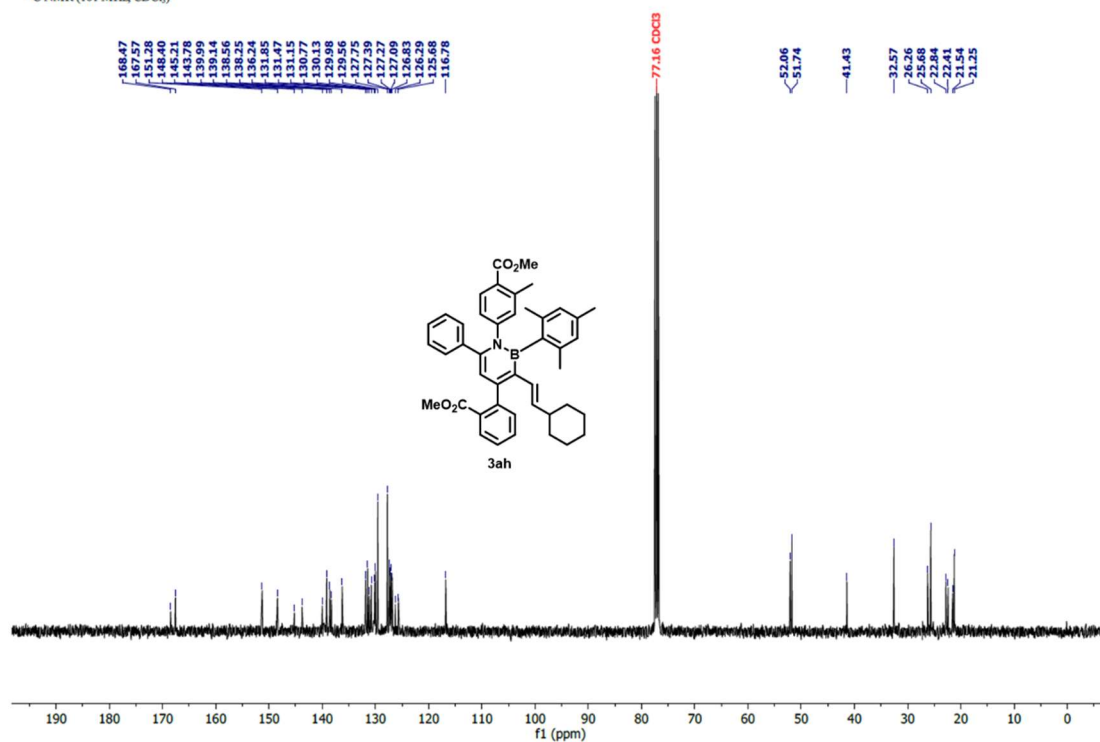
¹H NMR of 3ah

¹H NMR (400 MHz, CDCl₃)



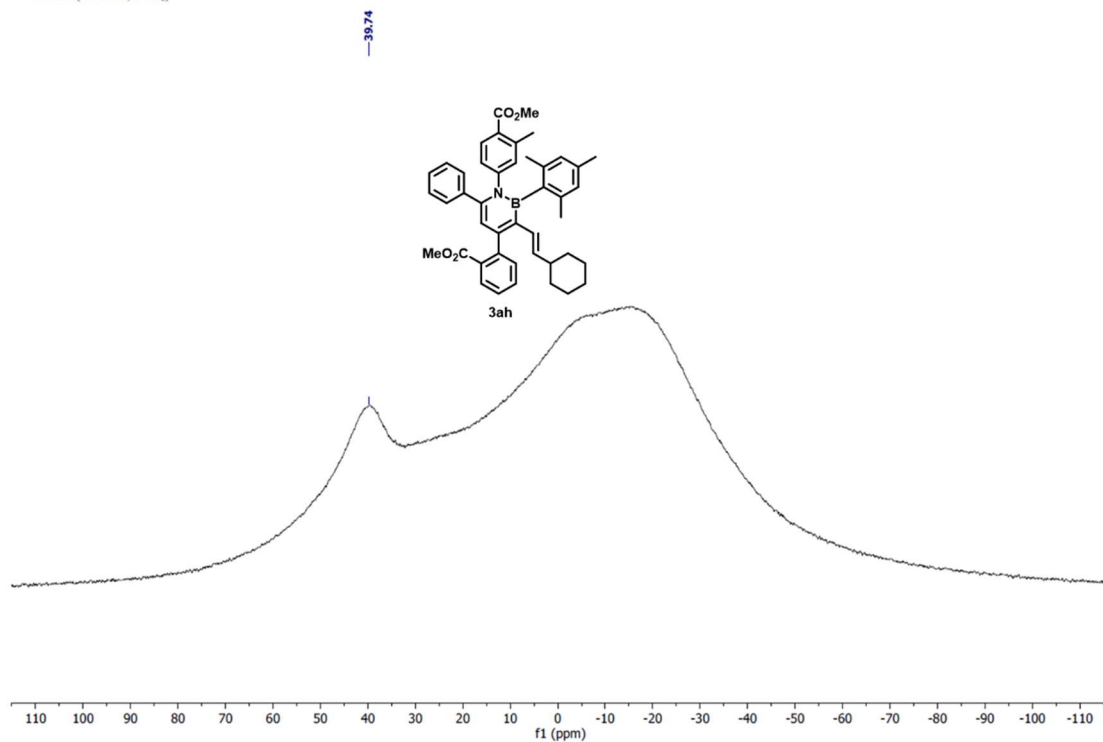
¹³C NMR of 3ah

¹³C NMR (101 MHz, CDCl₃)



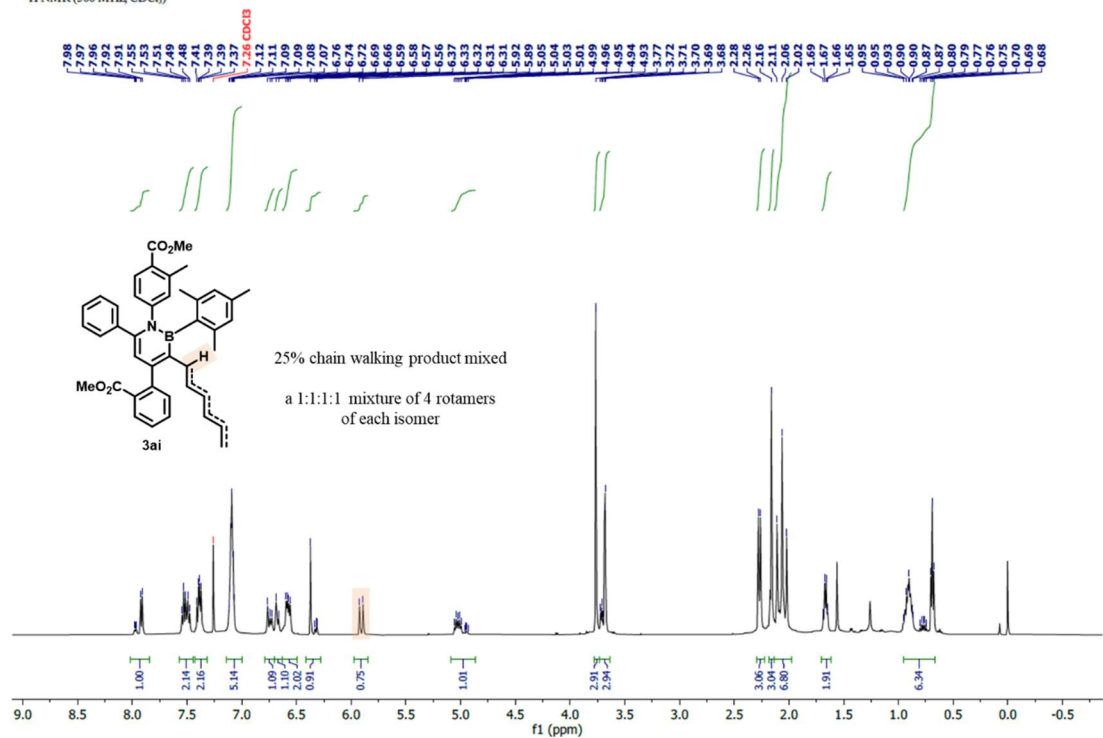
^{11}B NMR of **3ah**

^{11}B NMR (128 MHz, CDCl_3)

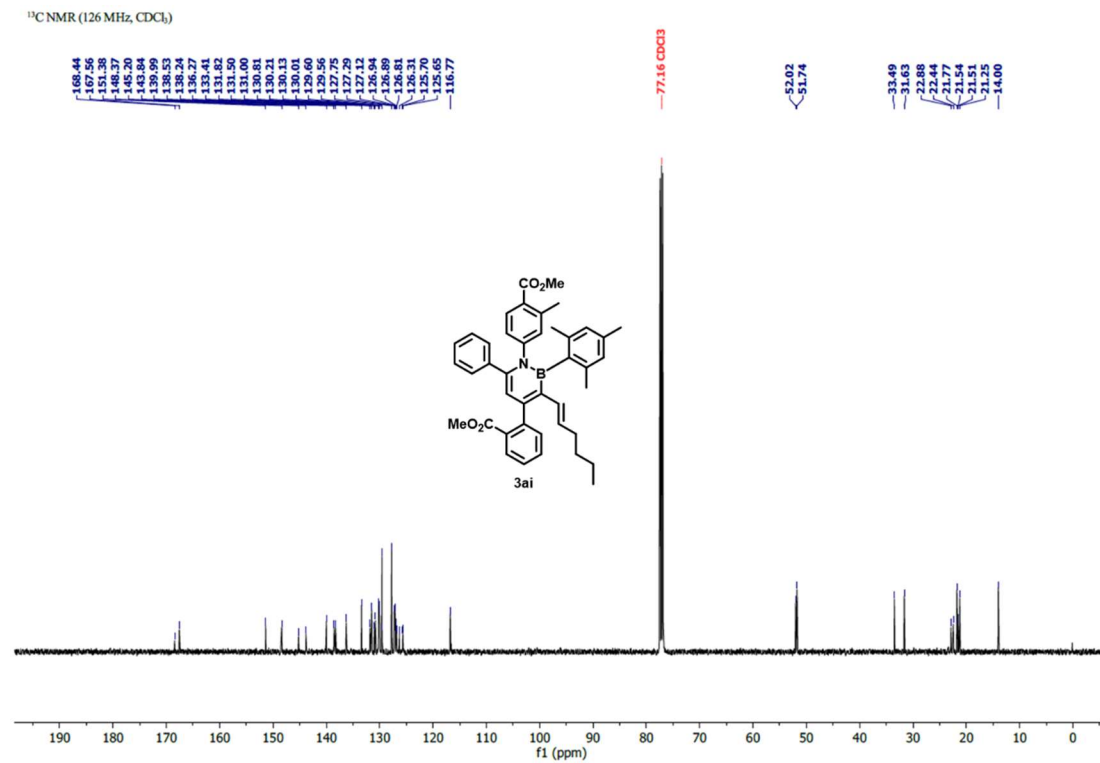


^1H NMR of **3ai**

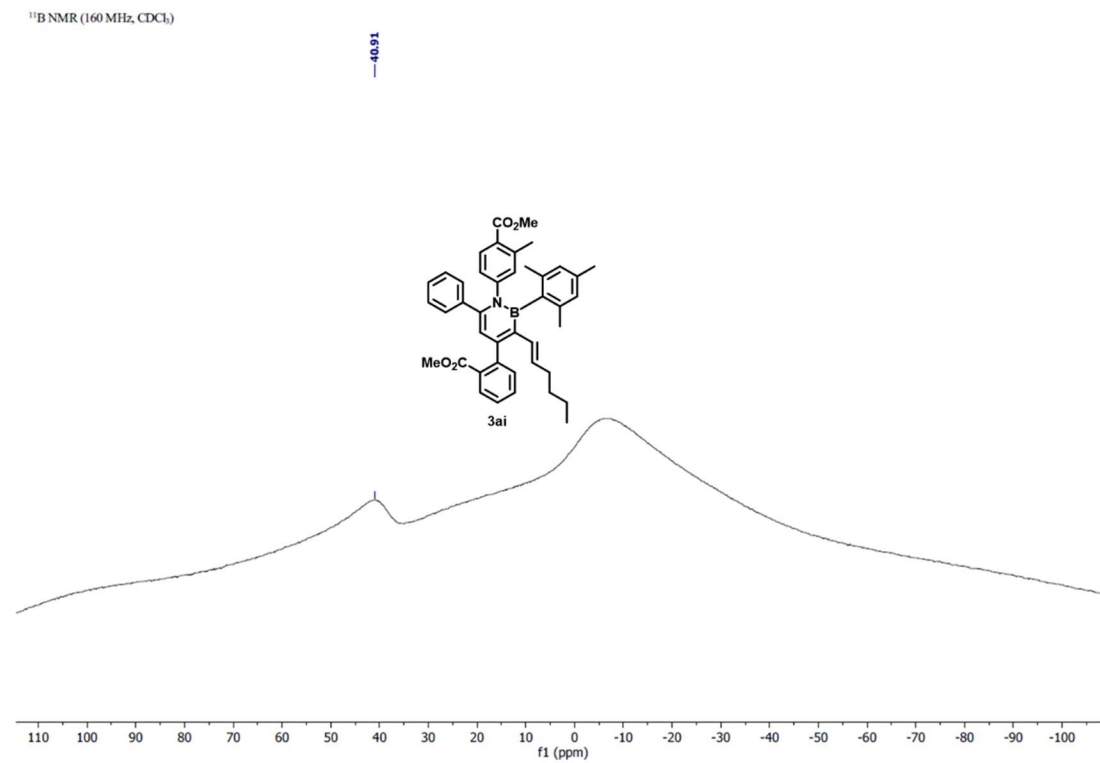
^1H NMR (500 MHz, CDCl_3)



^{13}C NMR of **3ai**

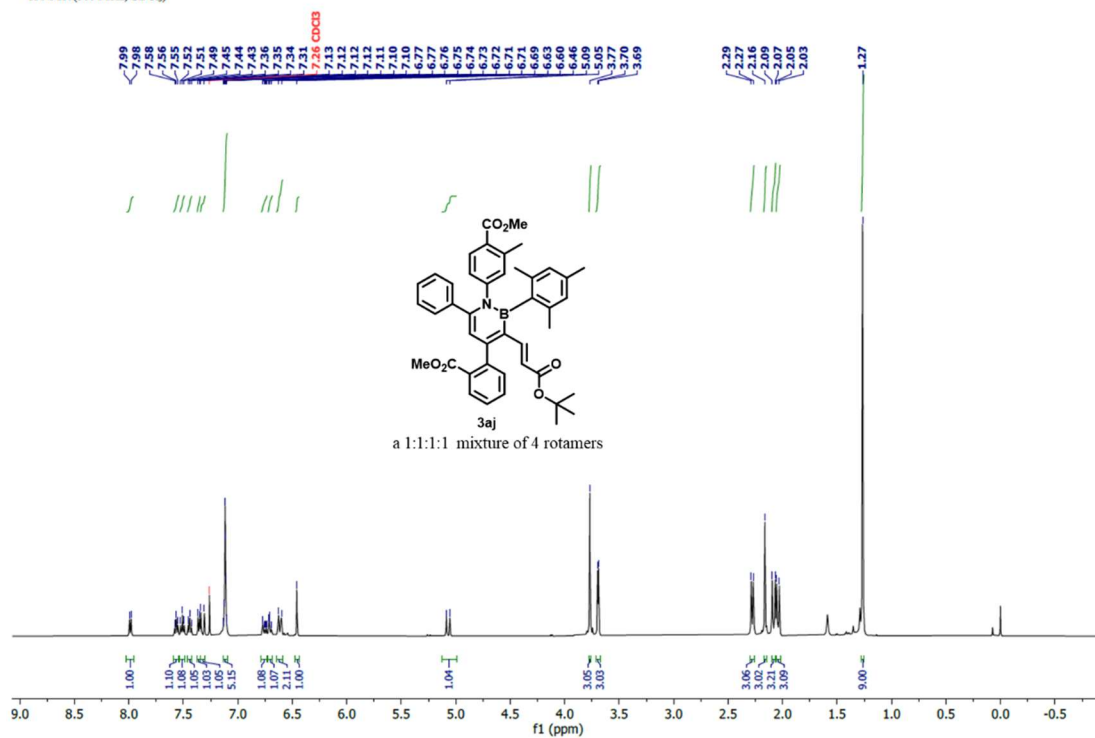


^{11}B NMR of **3ai**



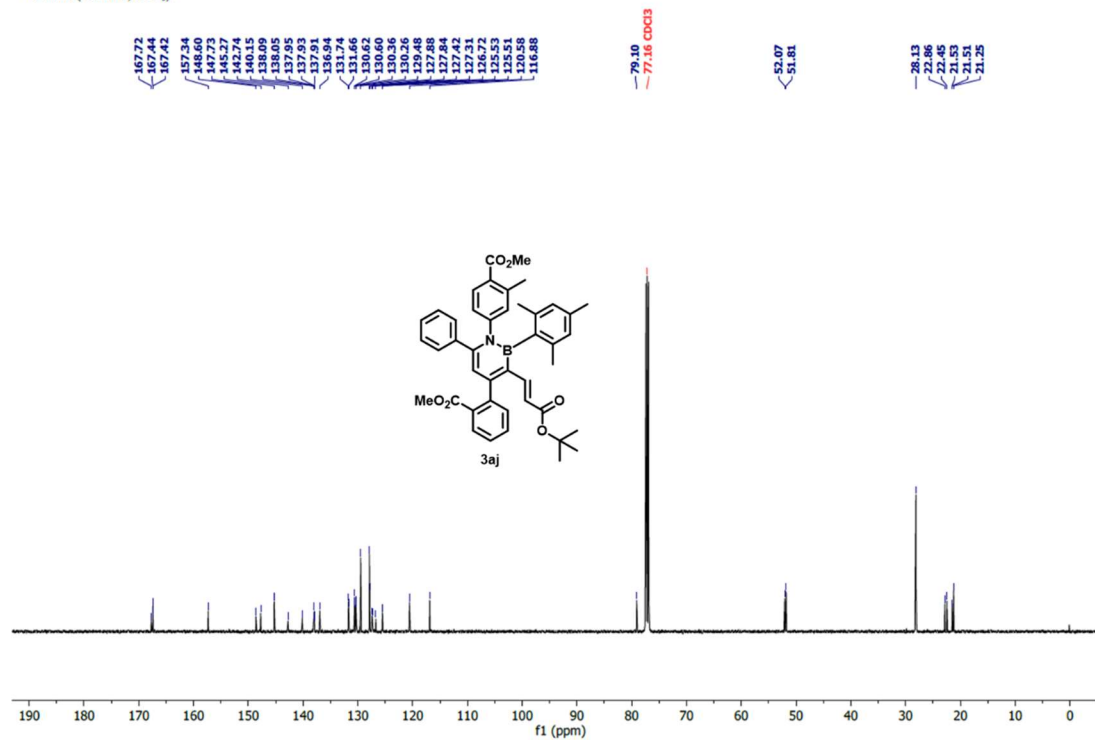
¹H NMR of 3aj

¹H NMR (500 MHz, CDCl₃)



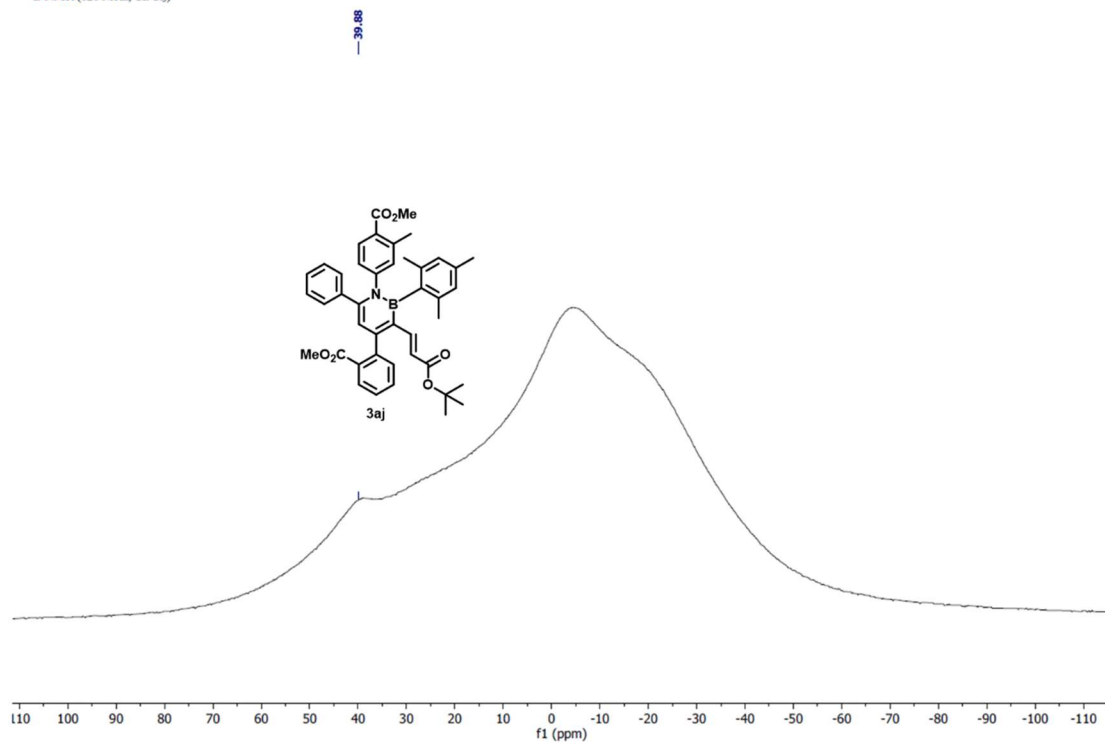
¹³C NMR of 3aj

¹³C NMR (126 MHz, CDCl₃)



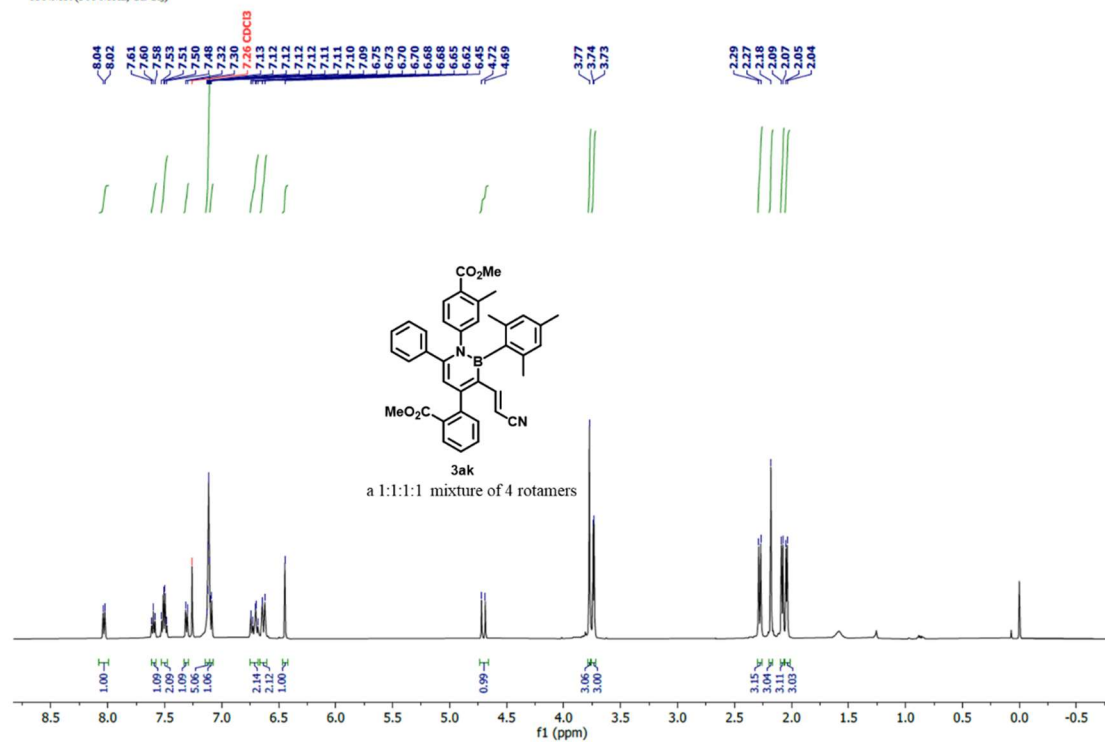
^{11}B NMR of **3aj**

^{11}B NMR (128 MHz, CDCl_3)



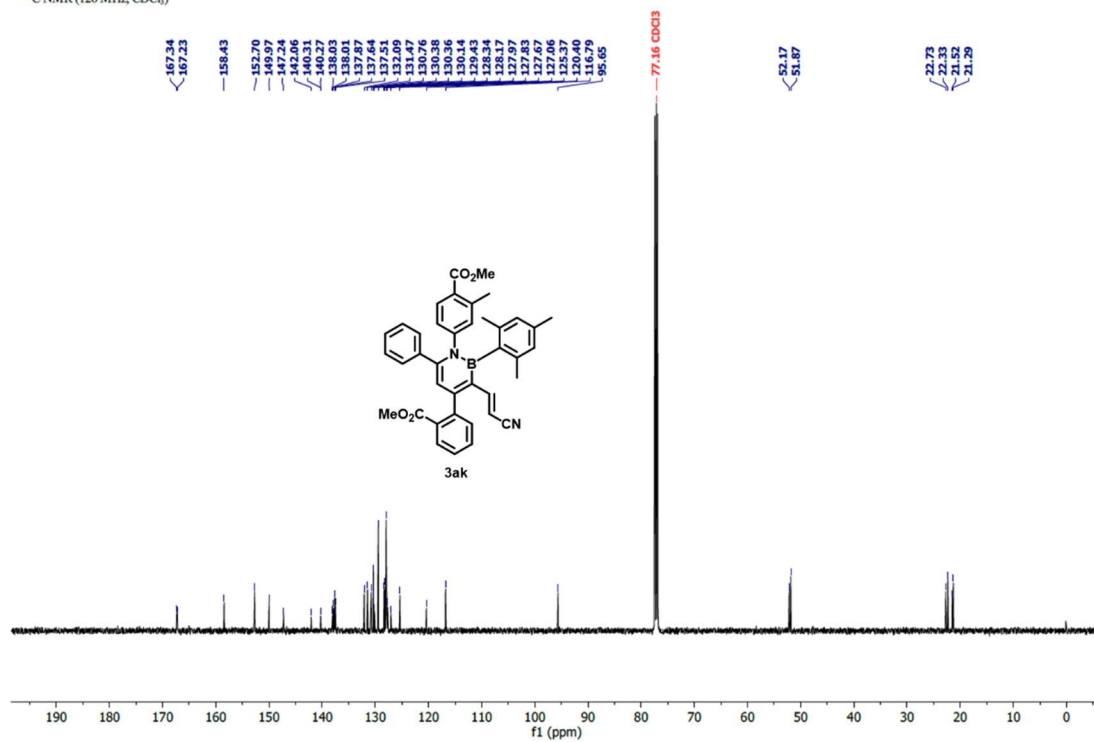
^1H NMR of **3ak**

^1H NMR (500 MHz, CDCl_3)



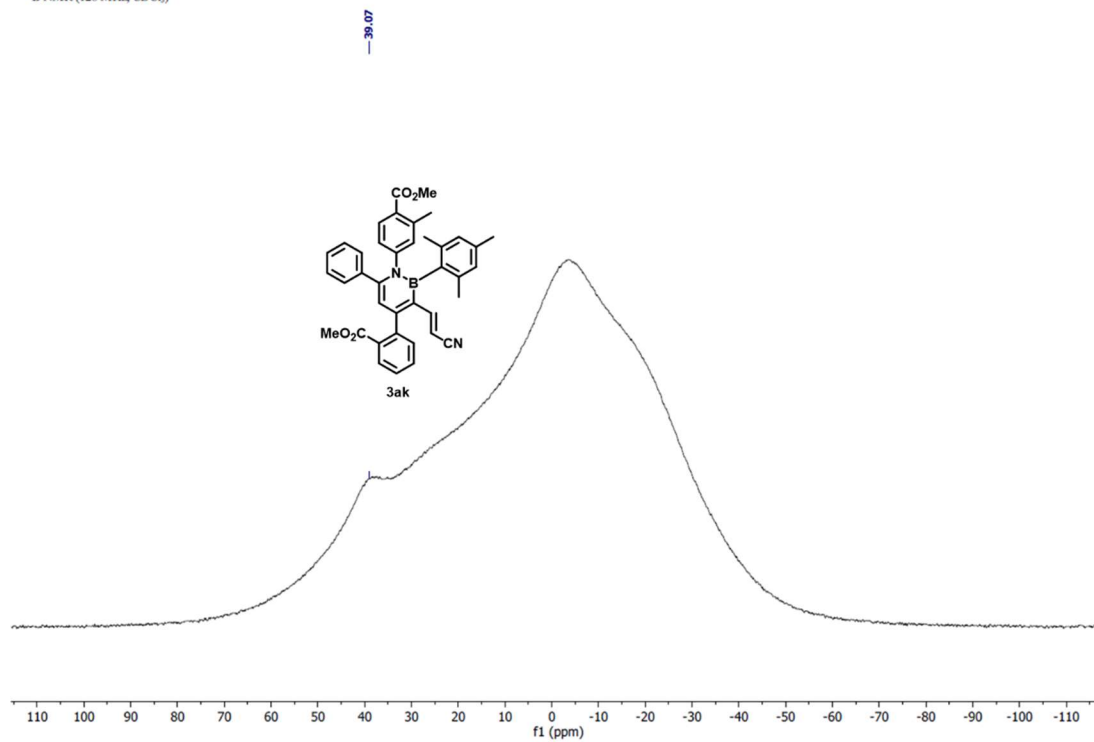
^{13}C NMR of **3ak**

^{13}C NMR (126 MHz, CDCl_3)



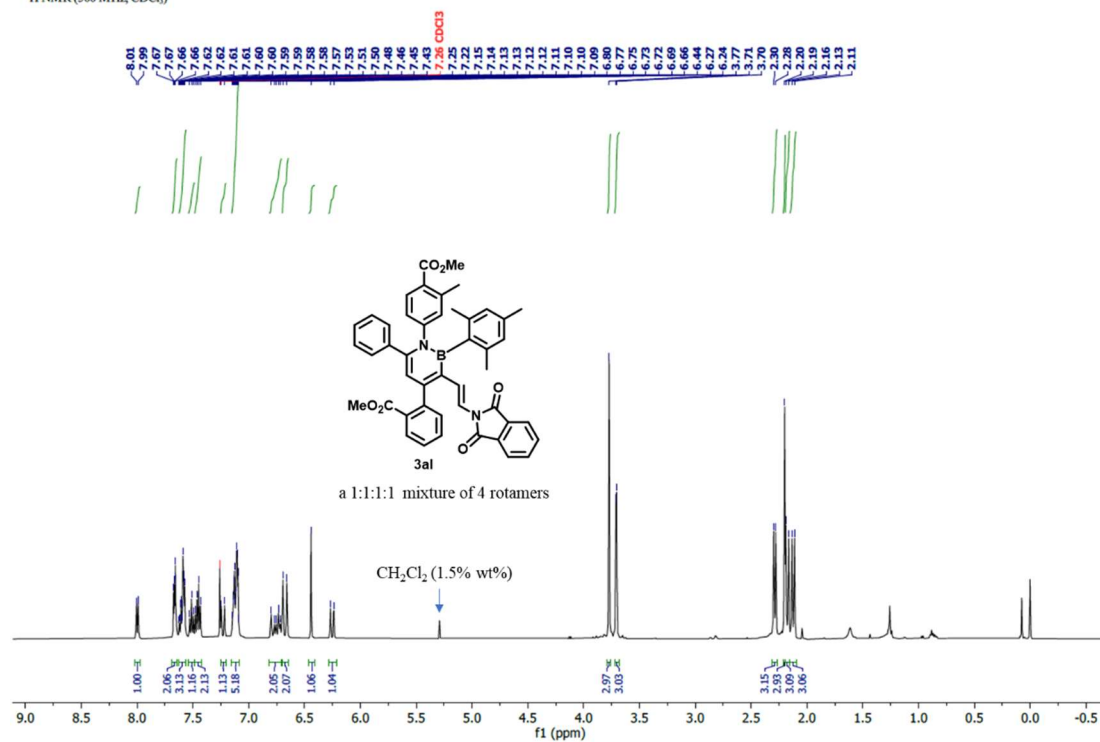
^{11}B NMR of **3ak**

^{11}B NMR (128 MHz, CDCl_3)



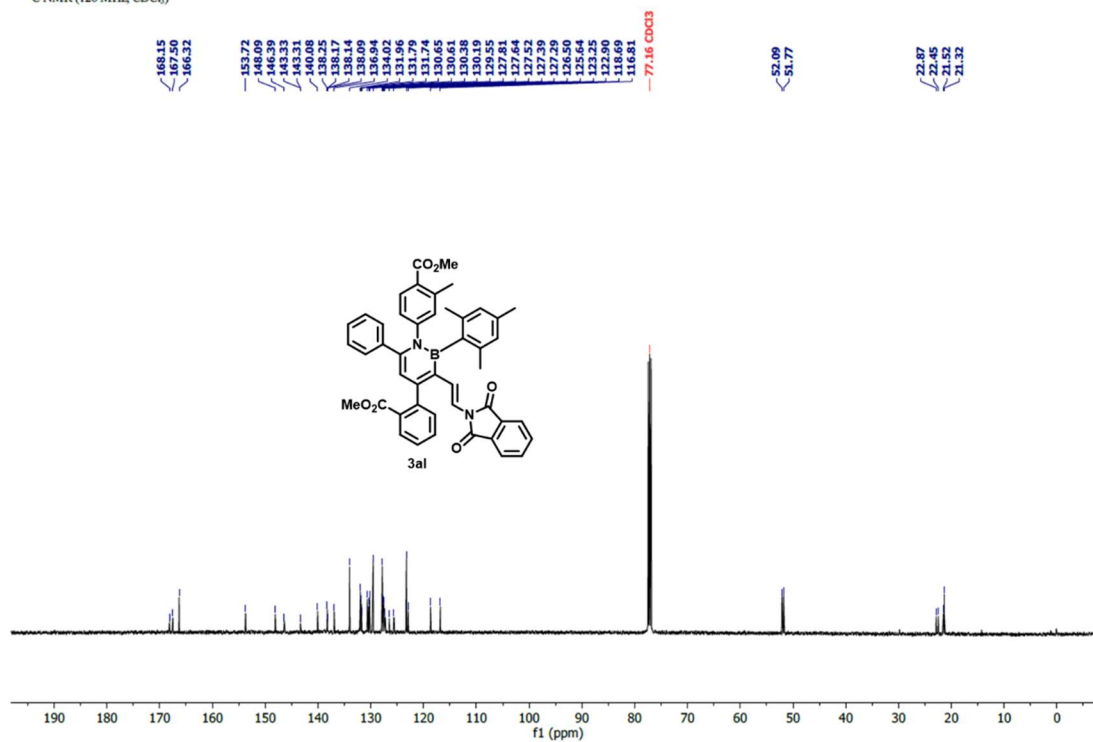
¹H NMR of 3al

¹H NMR (500 MHz, CDCl₃)



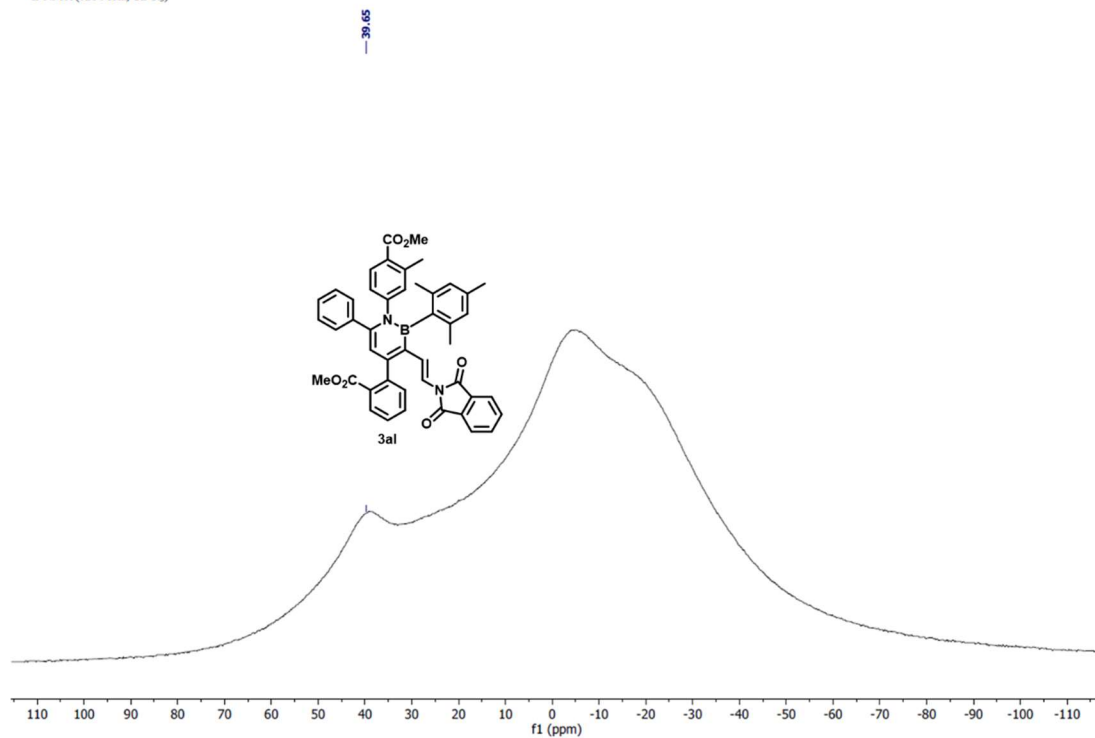
¹³C NMR of 3al

¹³C NMR (126 MHz, CDCl₃)



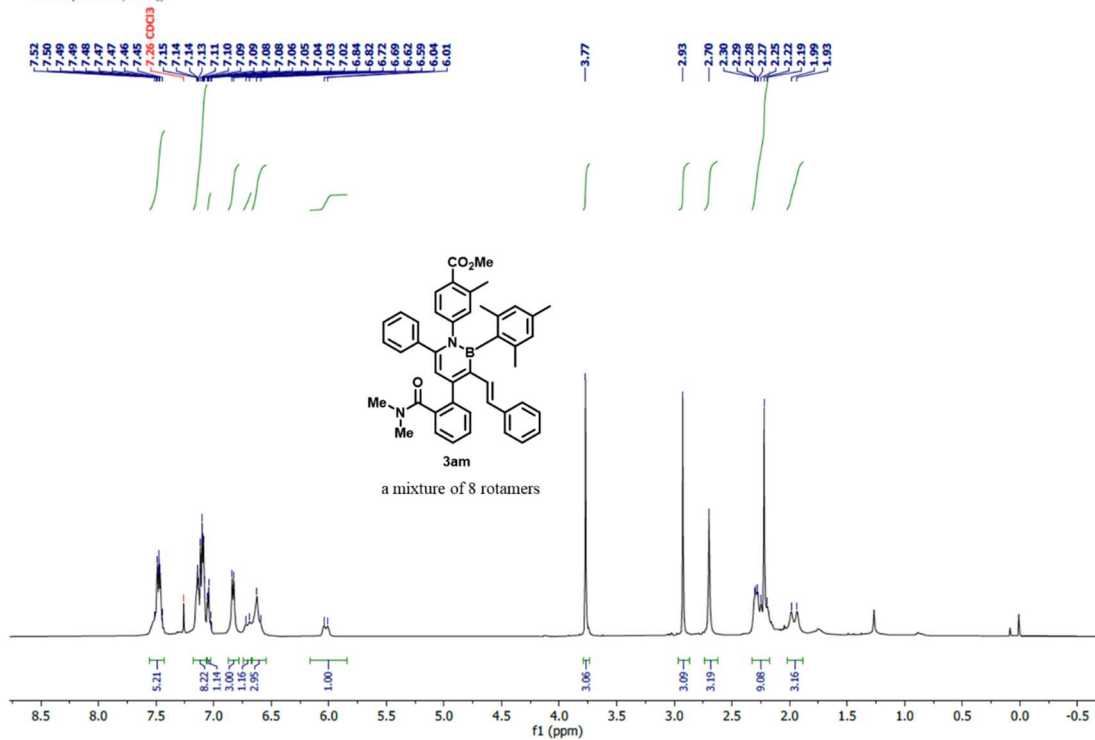
^{11}B NMR of 3al

^{11}B NMR (128 MHz, CDCl_3)



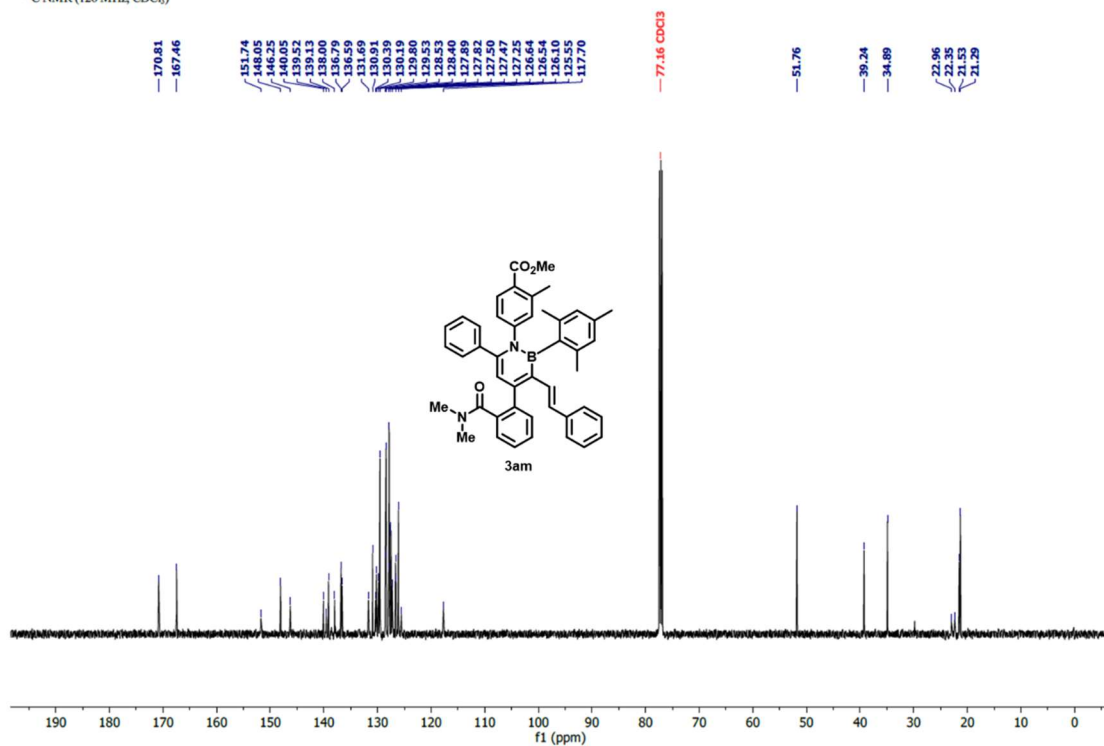
^1H NMR of 3am

^1H NMR (500 MHz, CDCl_3)



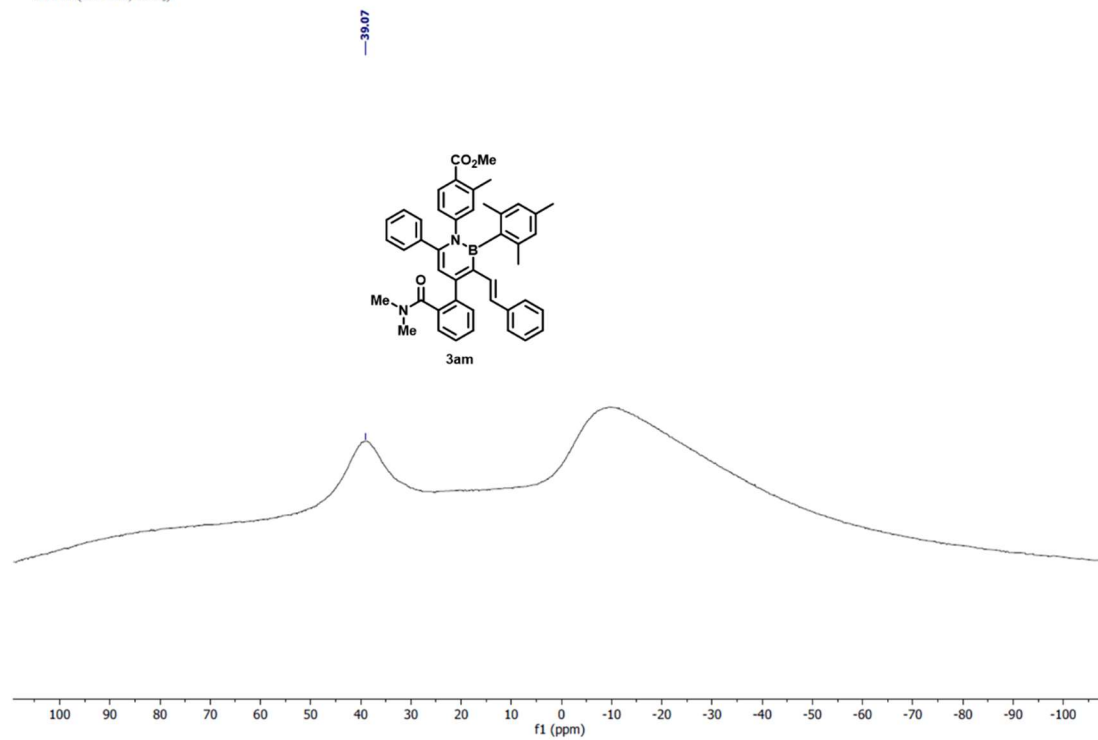
¹³C NMR of 3am

¹³C NMR (126 MHz, CDCl₃)

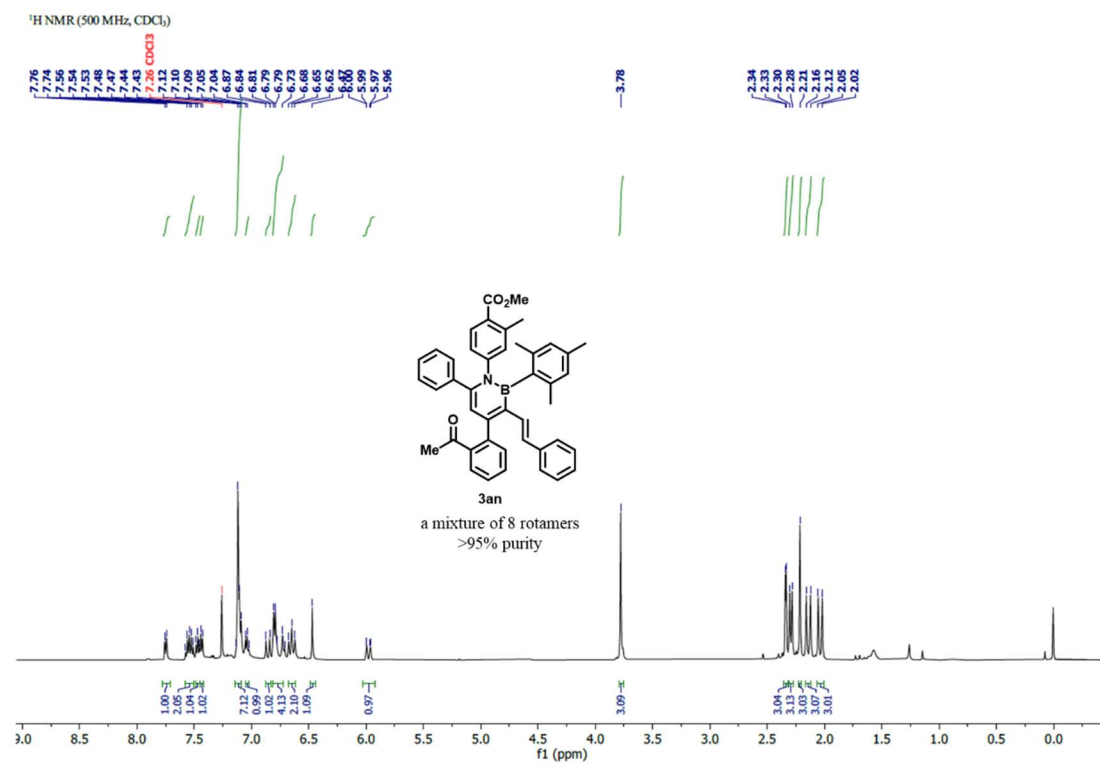


¹¹B NMR of 3am

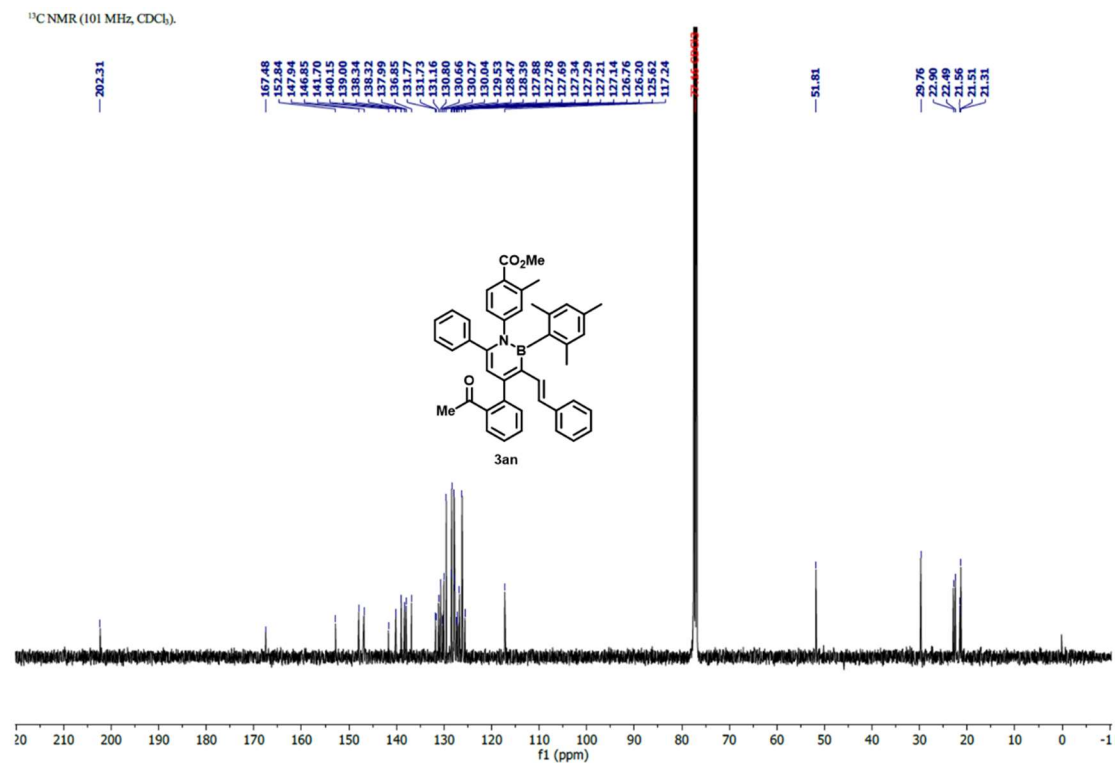
¹¹B NMR (160 MHz, CDCl₃)



¹H NMR of 3an

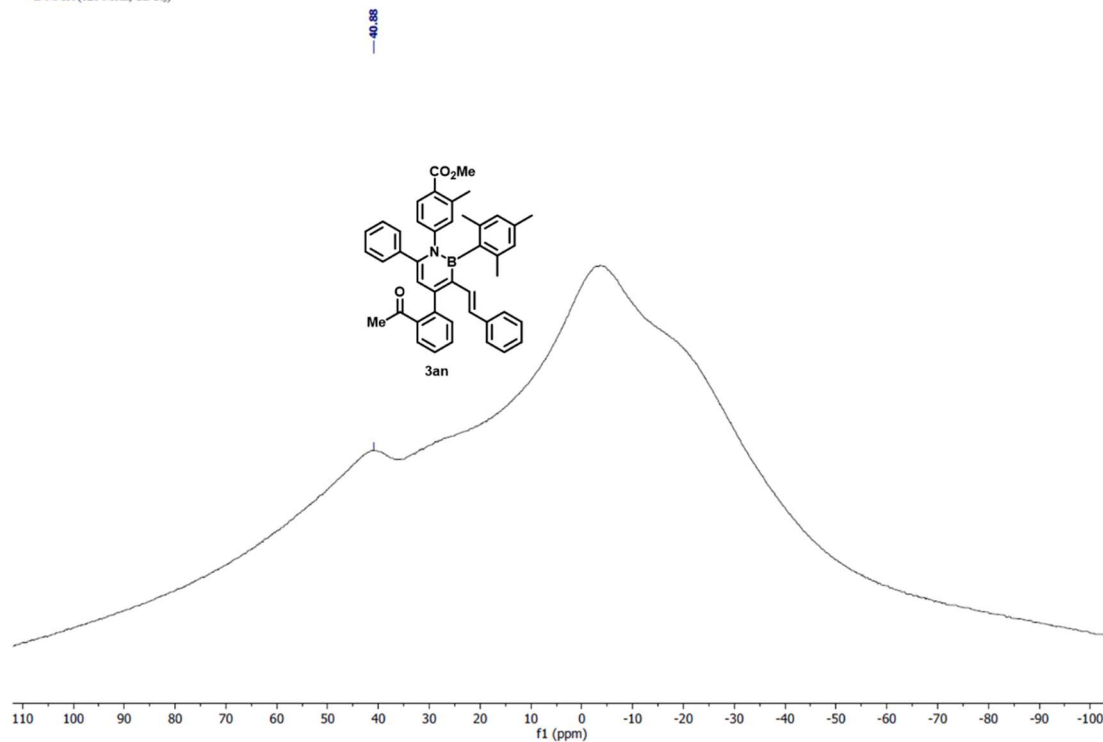


¹³C NMR of 3an



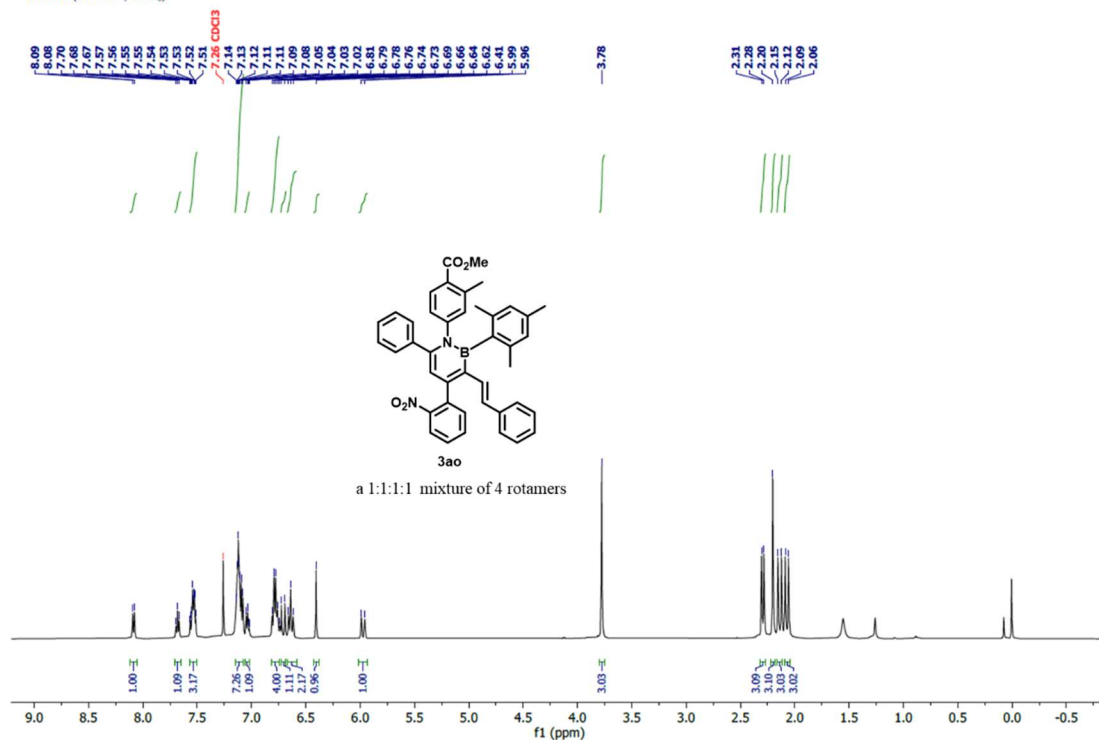
^{11}B NMR of 3an

^{11}B NMR (128 MHz, CDCl_3)



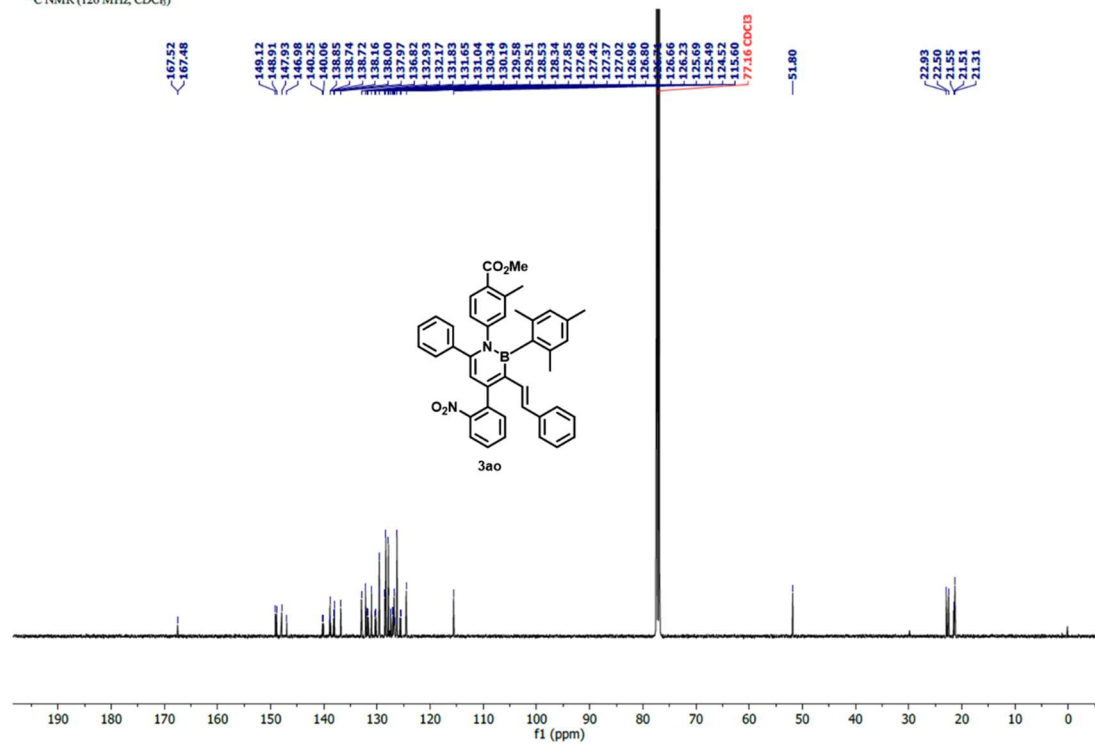
^1H NMR of 3ao

^1H NMR (500 MHz, CDCl_3)



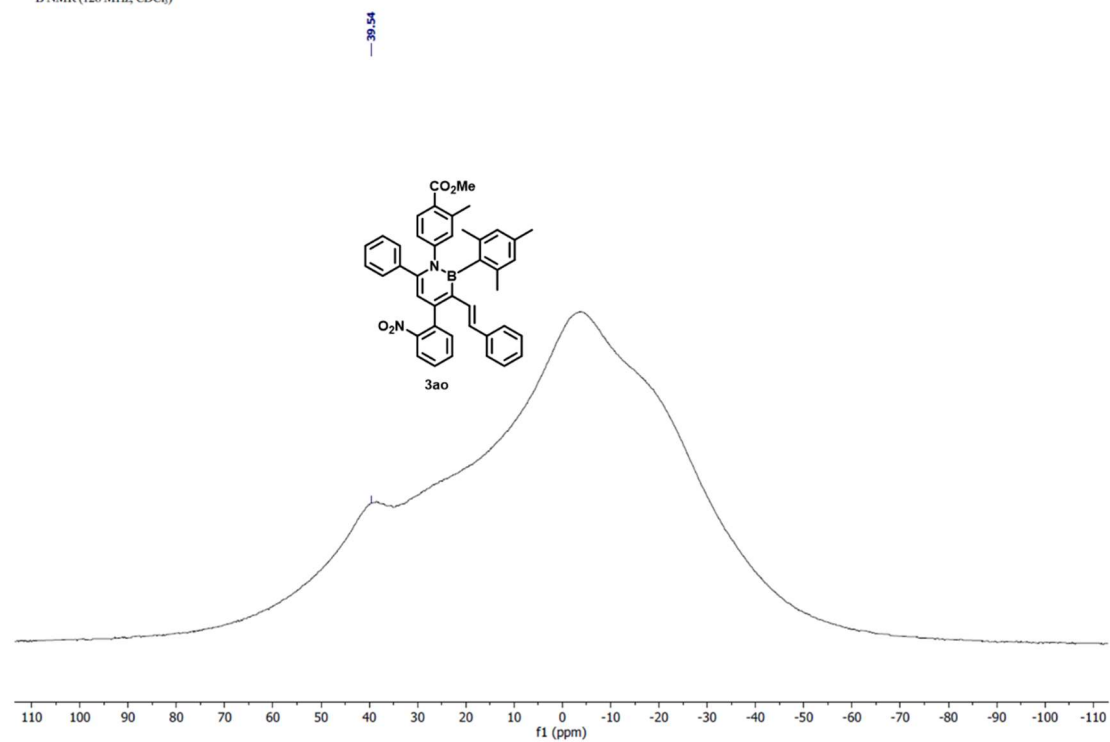
¹³C NMR of 3ao

¹³C NMR (126 MHz, CDCl₃)



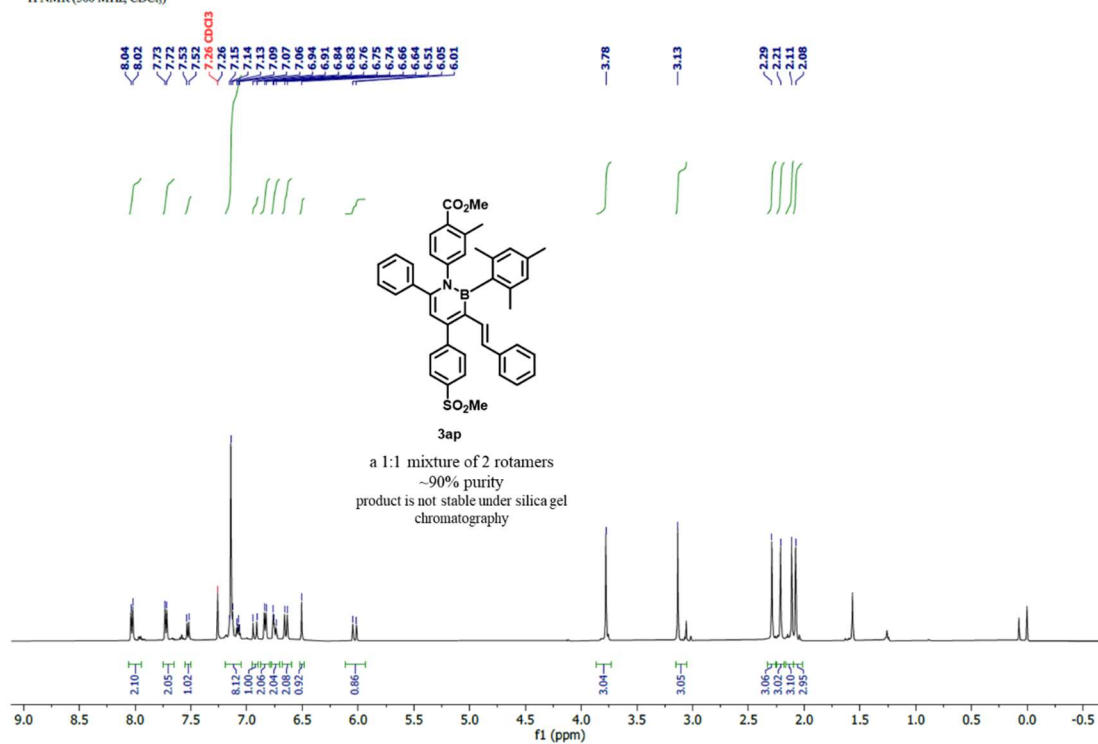
¹¹B NMR of 3ao

¹¹B NMR (128 MHz, CDCl₃)



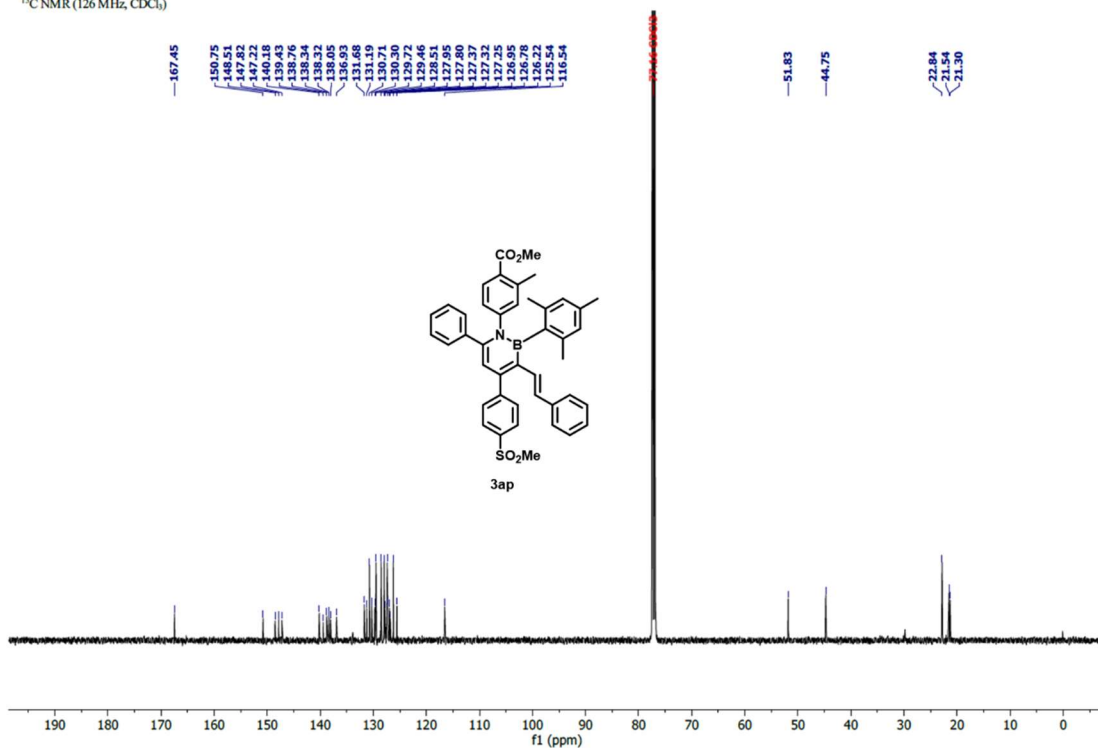
¹H NMR of 3ap

¹H NMR (500 MHz, CDCl₃)



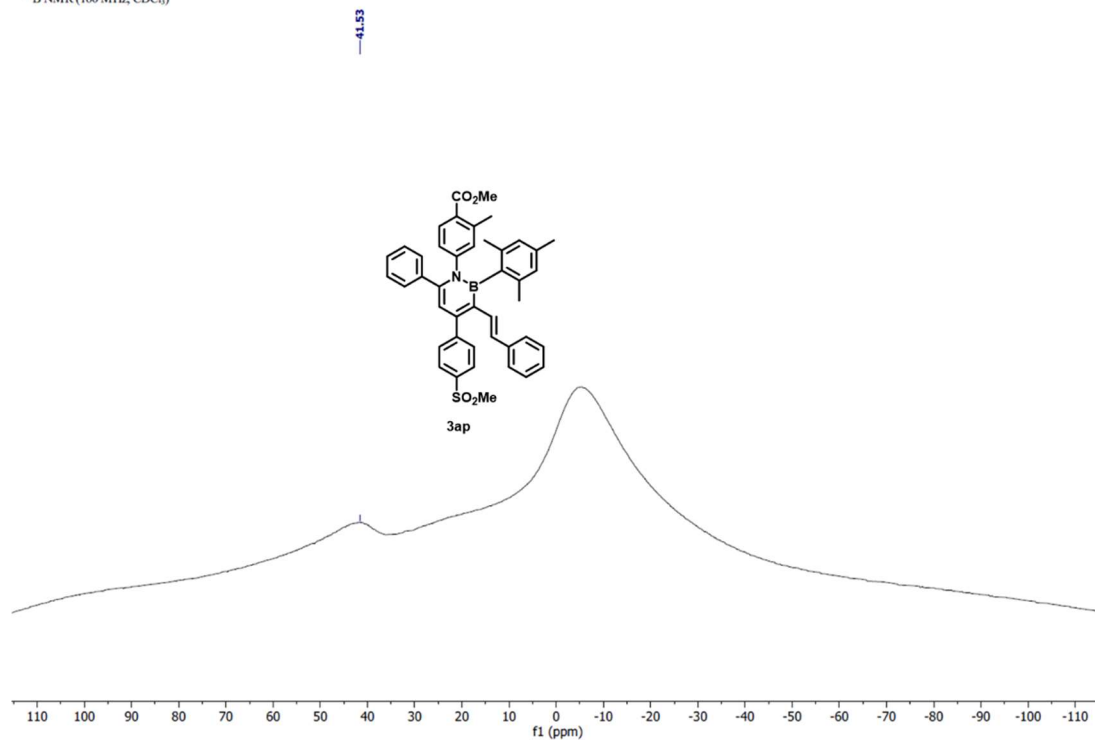
¹³C NMR of 3ap

¹³C NMR (126 MHz, CDCl₃)



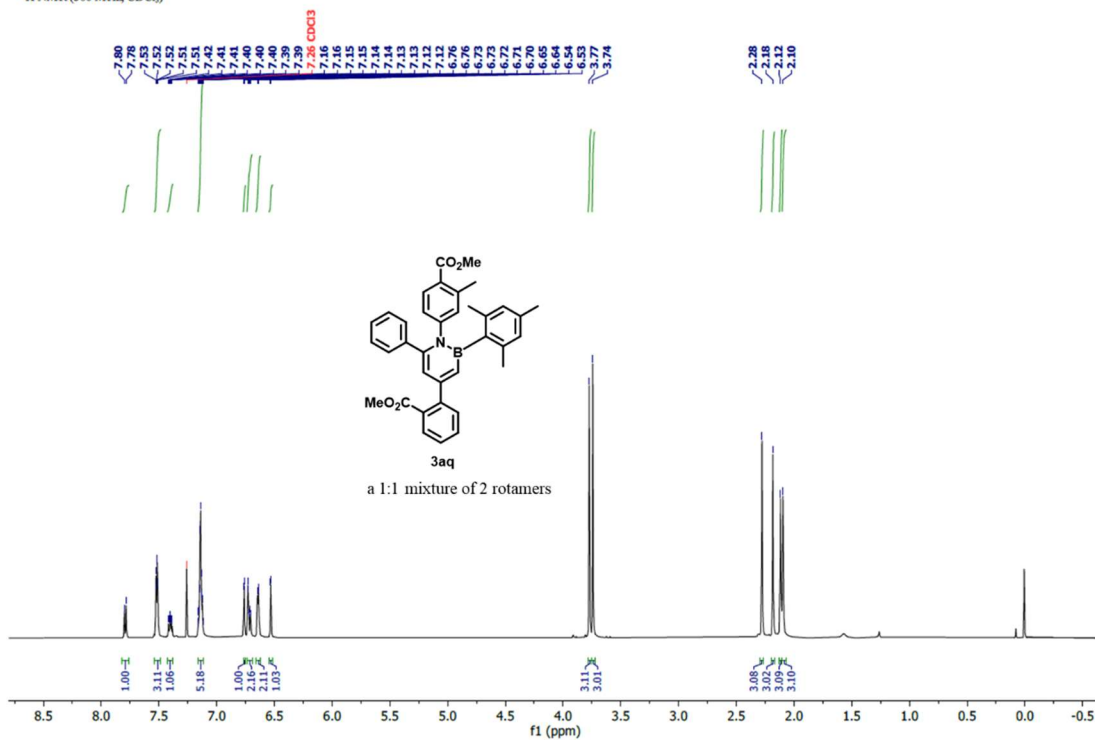
^{11}B NMR of **3ap**

^{11}B NMR (160 MHz, CDCl_3)



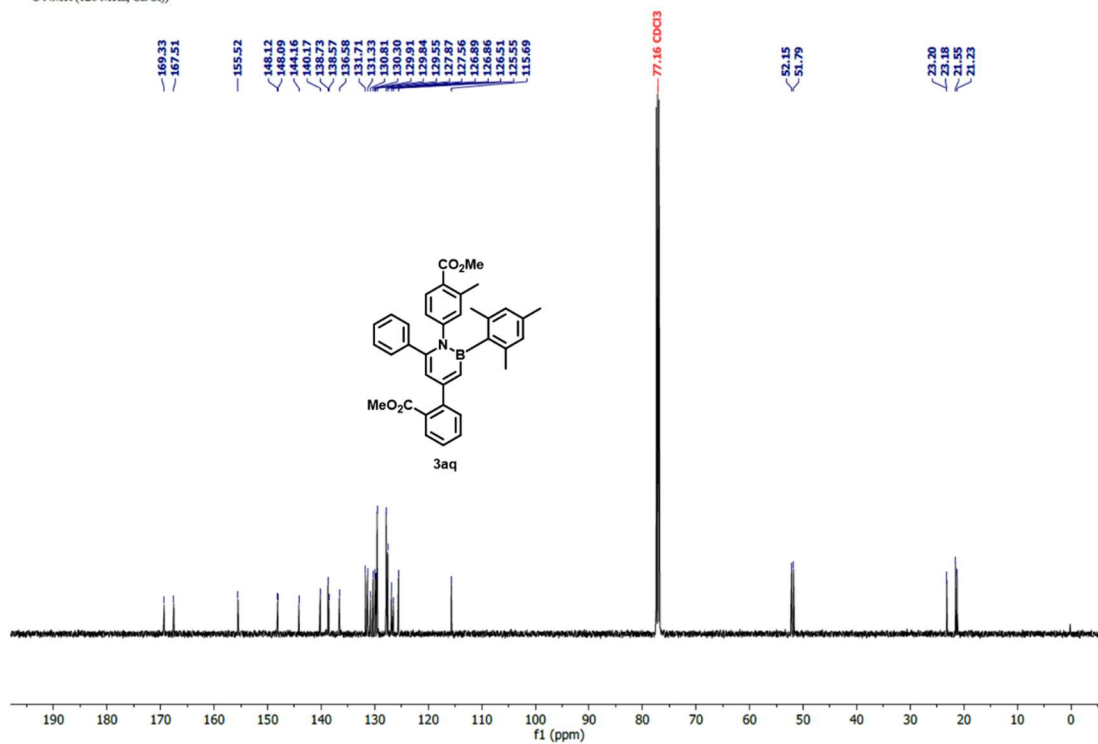
^1H NMR of **3aq**

^1H NMR (500 MHz, CDCl_3)



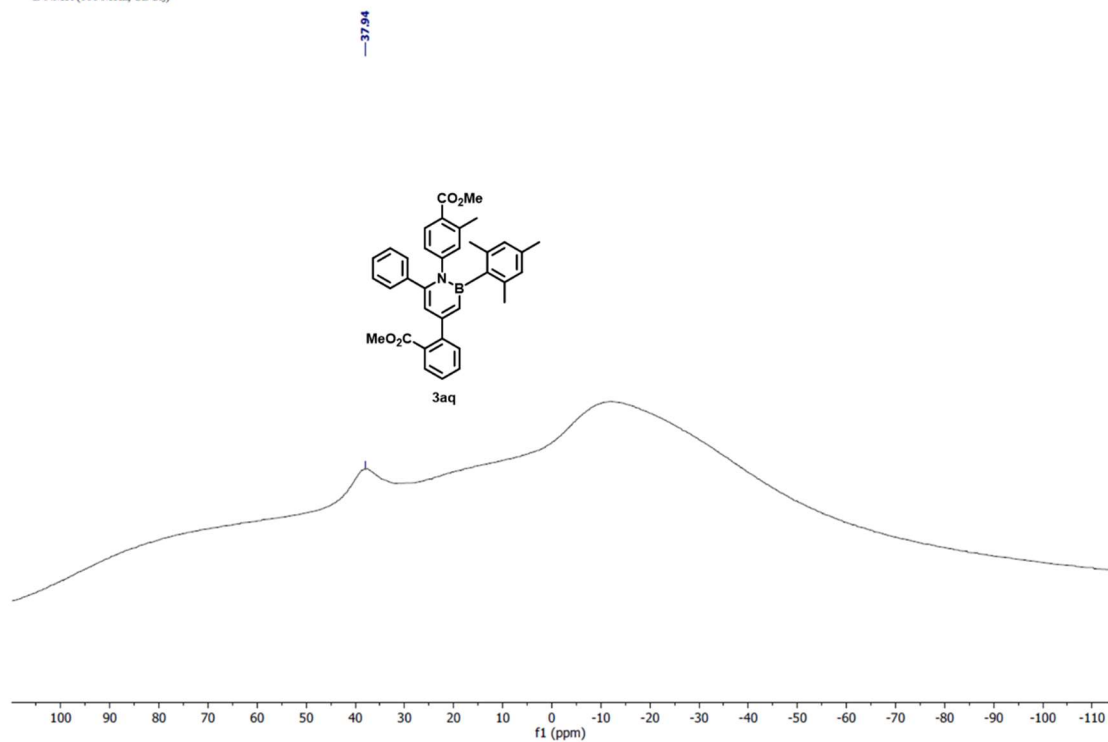
¹³C NMR of 3aq

¹³C NMR (126 MHz, CDCl₃)



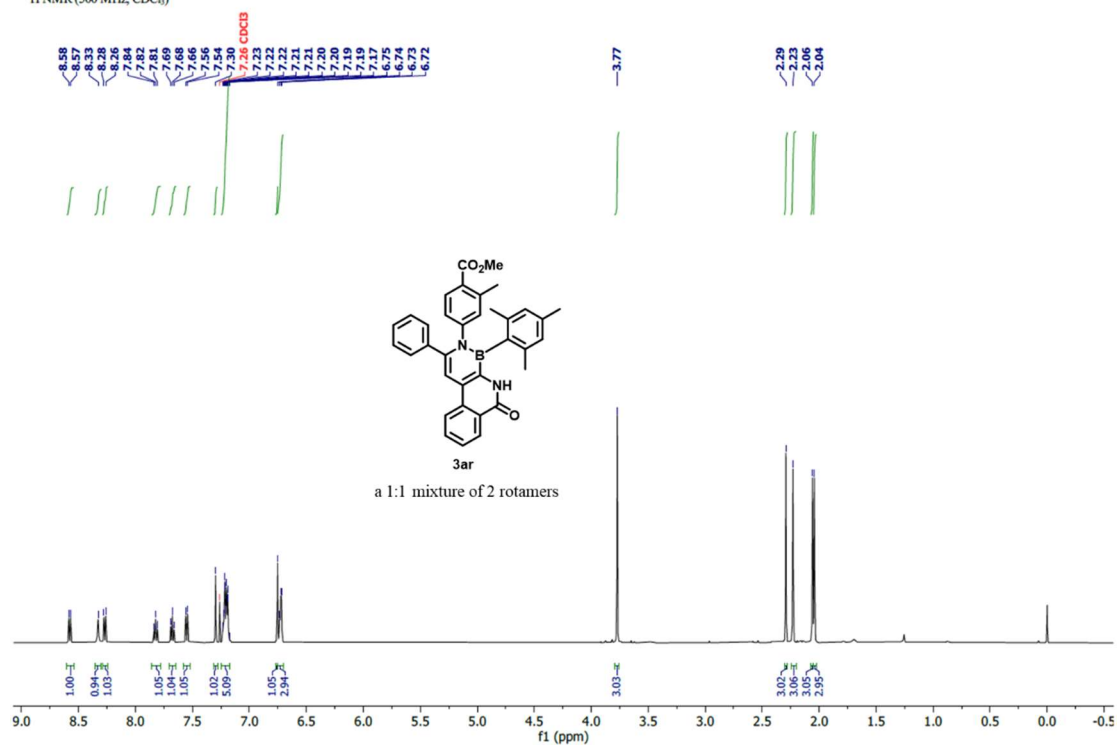
¹¹B NMR of 3aq

¹¹B NMR (160 MHz, CDCl₃)



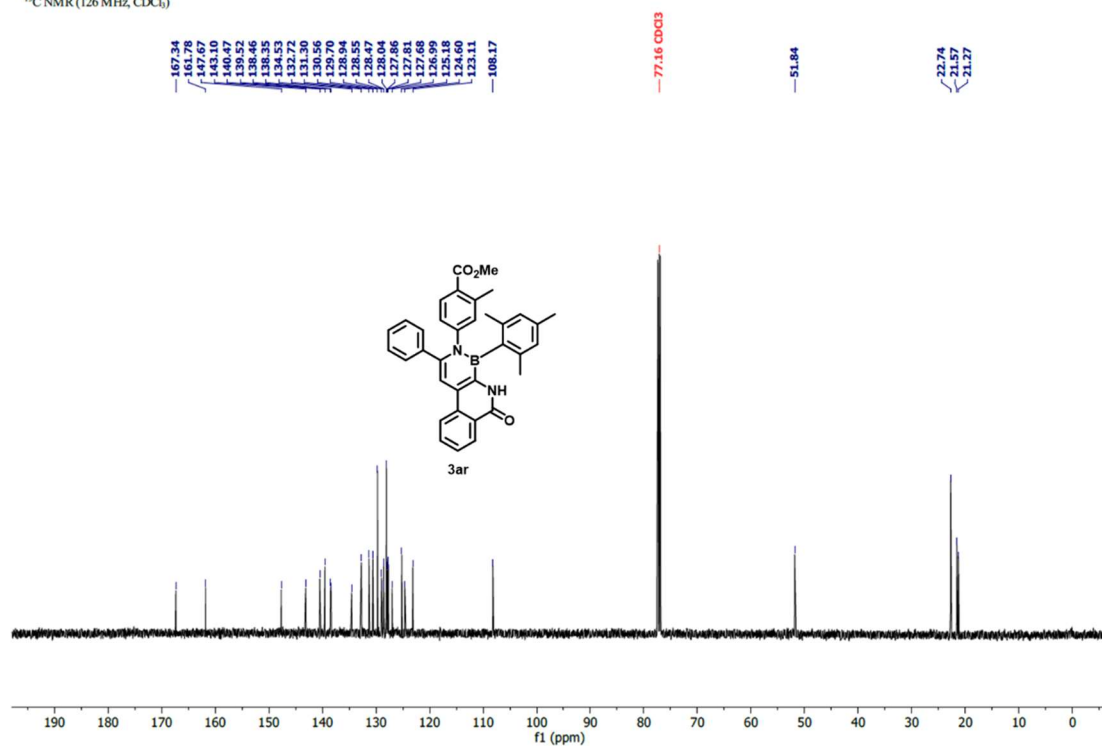
¹H NMR of 3ar

¹H NMR (500 MHz, CDCl₃)



¹³C NMR of 3ar

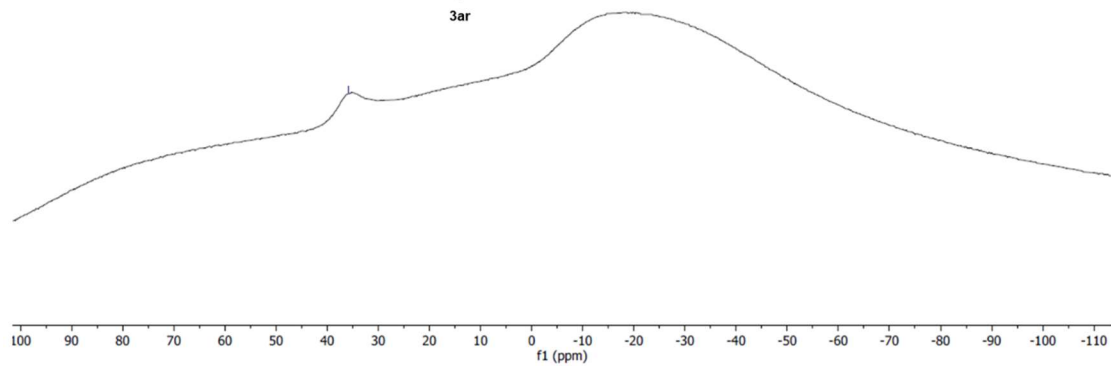
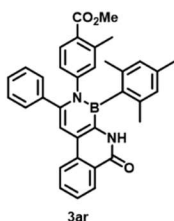
¹³C NMR (126 MHz, CDCl₃)



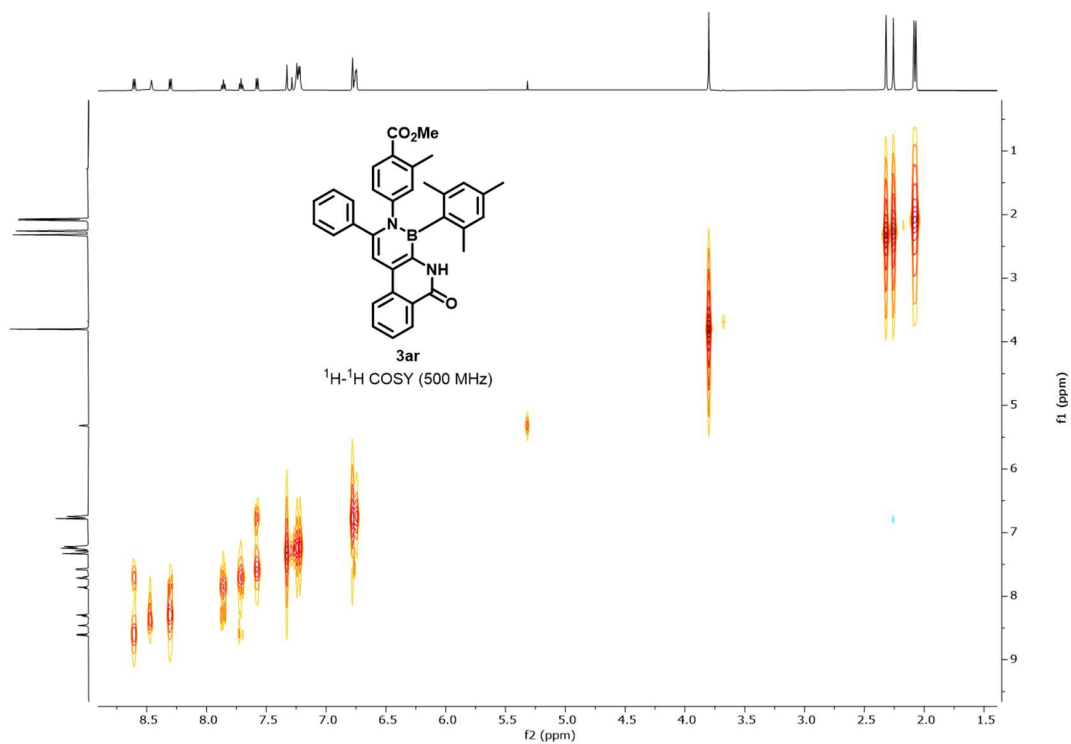
^{11}B NMR of **3ar**

^{11}B NMR (160 MHz, CDCl_3)

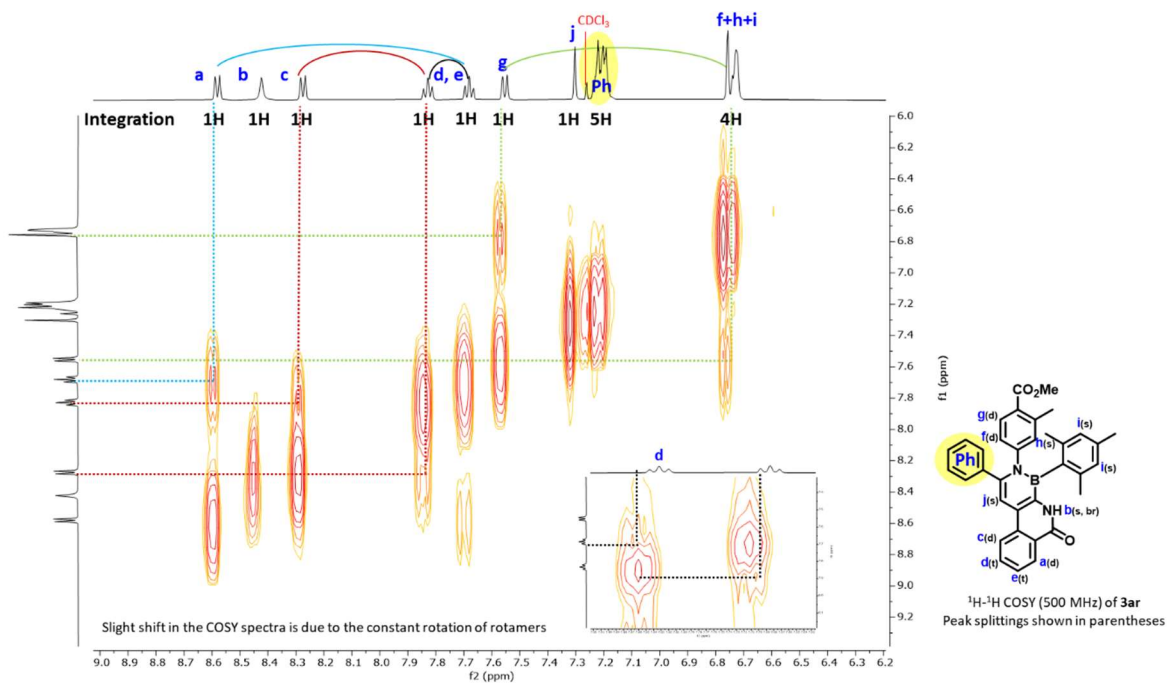
— 35.76



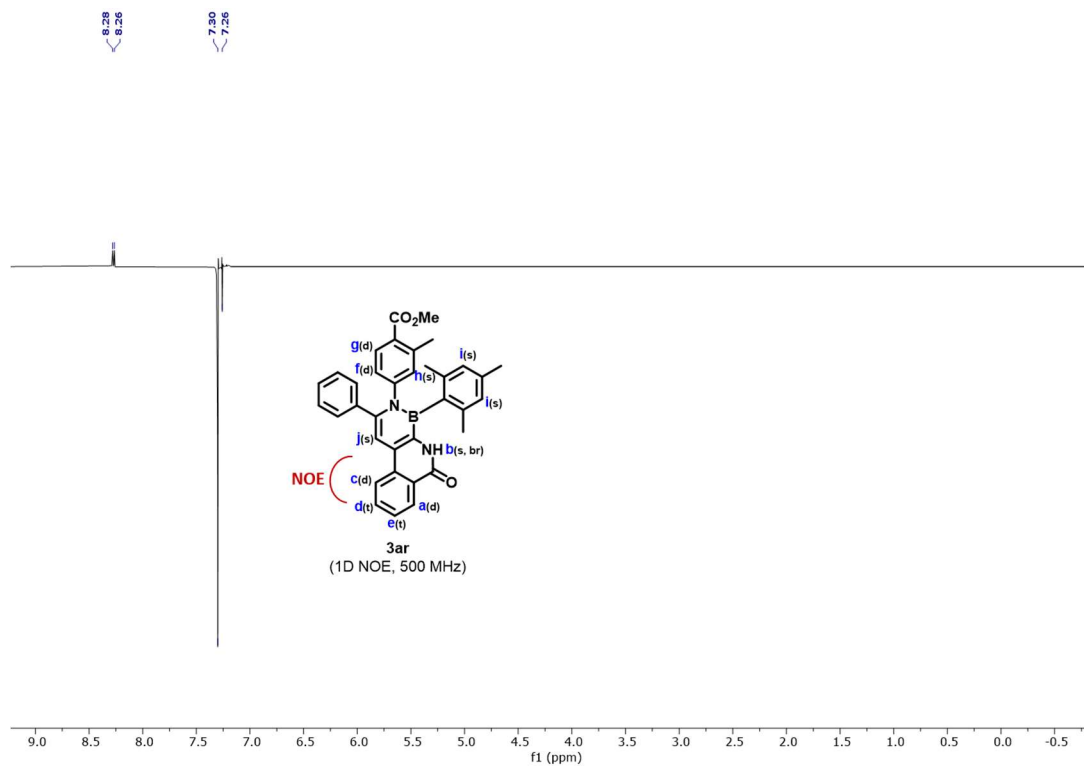
$^1\text{H} - ^1\text{H}$ COSY NMR of **3ar**



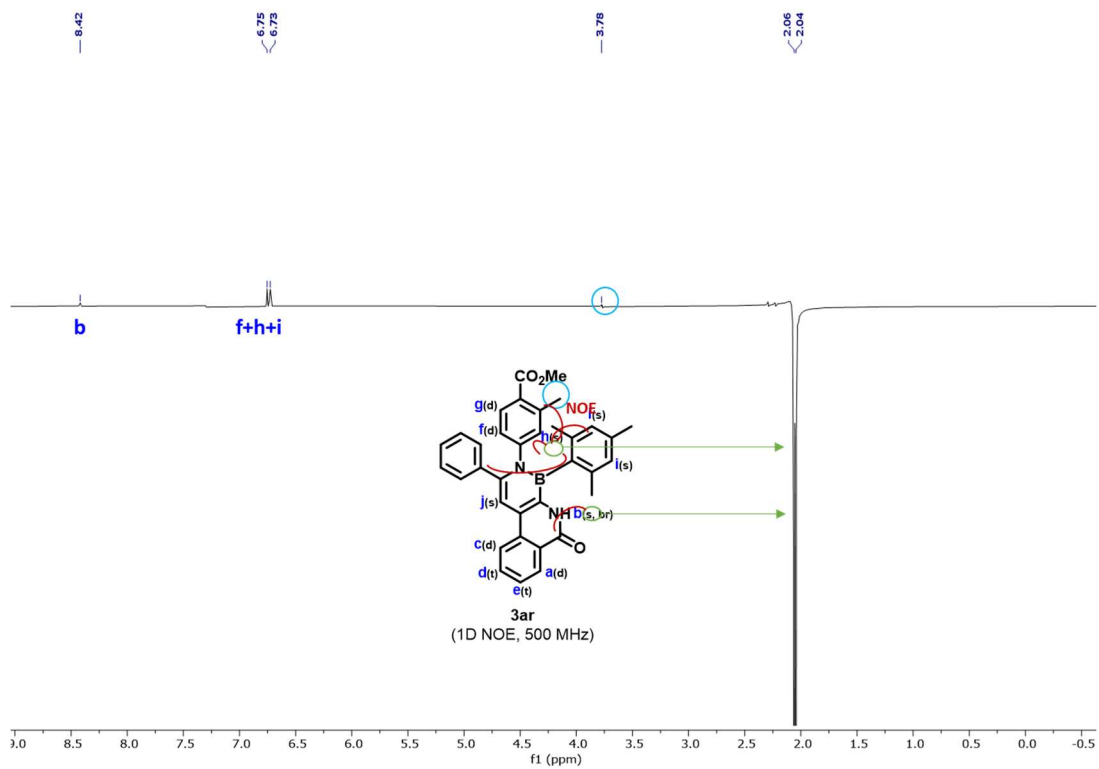
$^1\text{H} - ^1\text{H}$ COSY NMR (enlarged aromatic region) of **3ar**



$^1\text{H} - ^1\text{H}$ NOE NMR of **3ar**

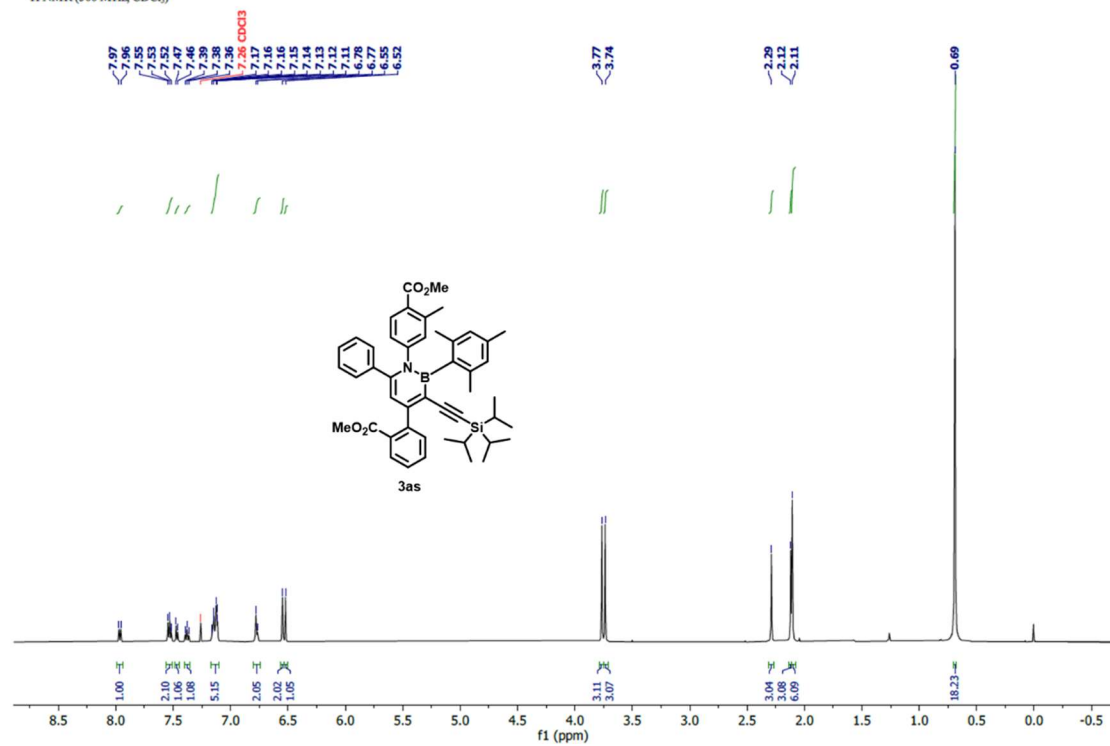


$^1\text{H} - ^1\text{H}$ NOE NMR of **3ar**



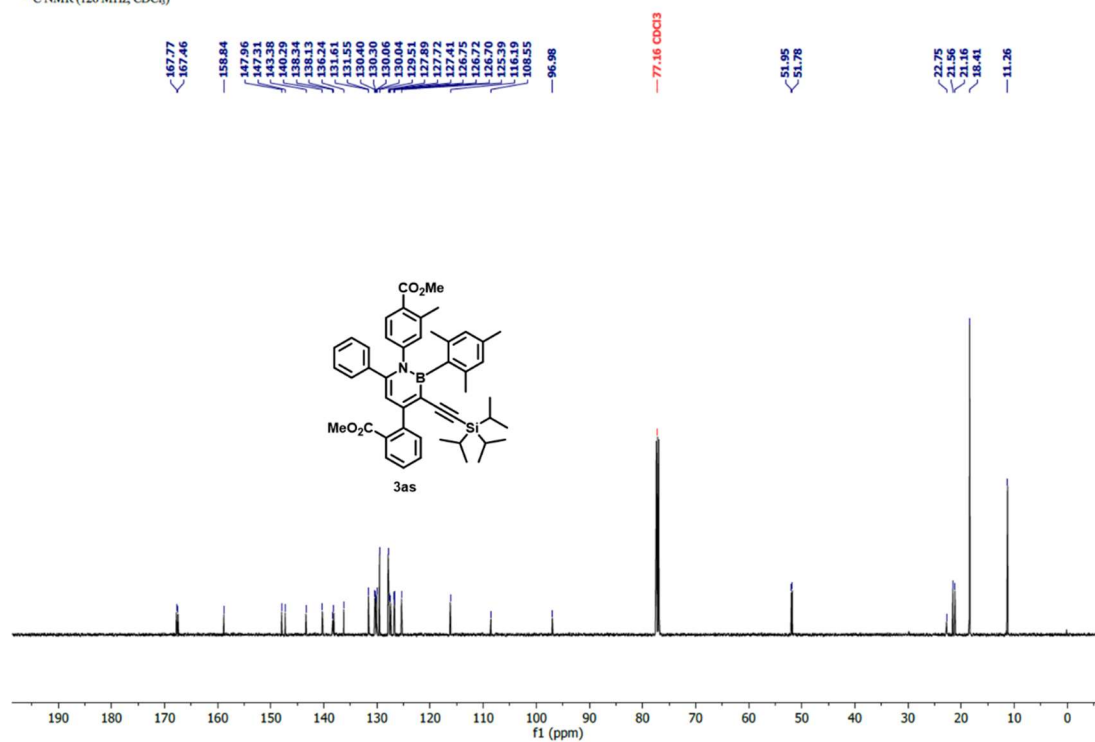
^1H NMR of **3as**

^1H NMR (500 MHz, CDCl_3)



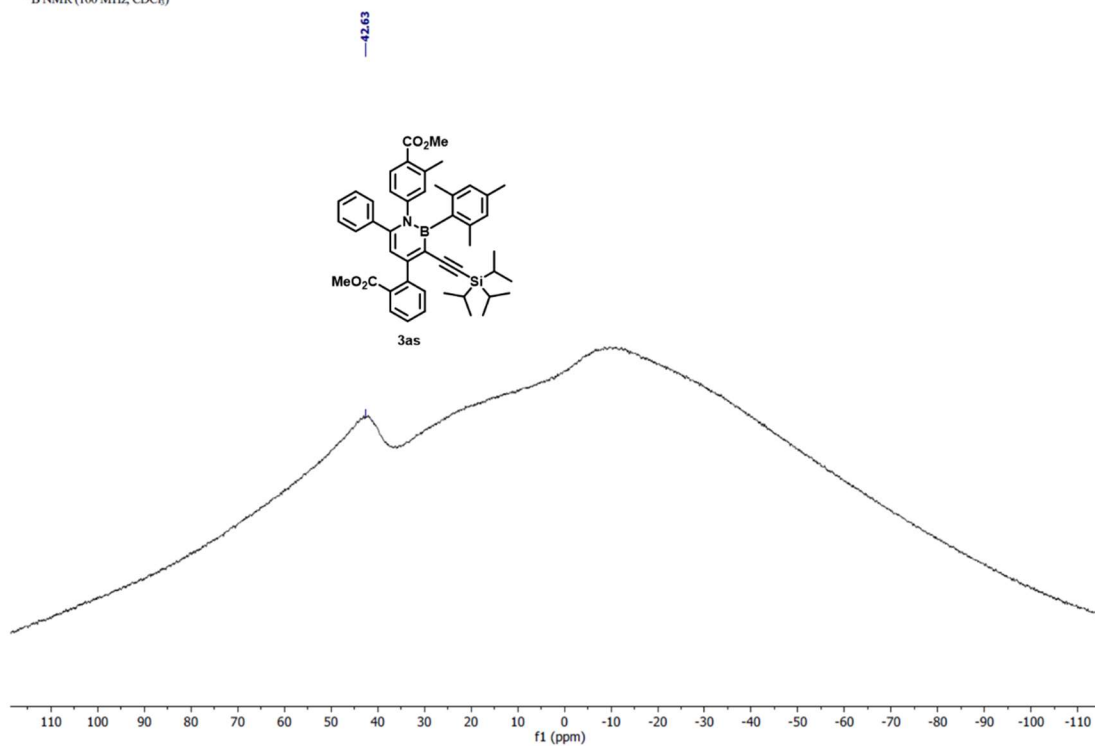
^{13}C NMR of **3as**

^{13}C NMR (126 MHz, CDCl_3)



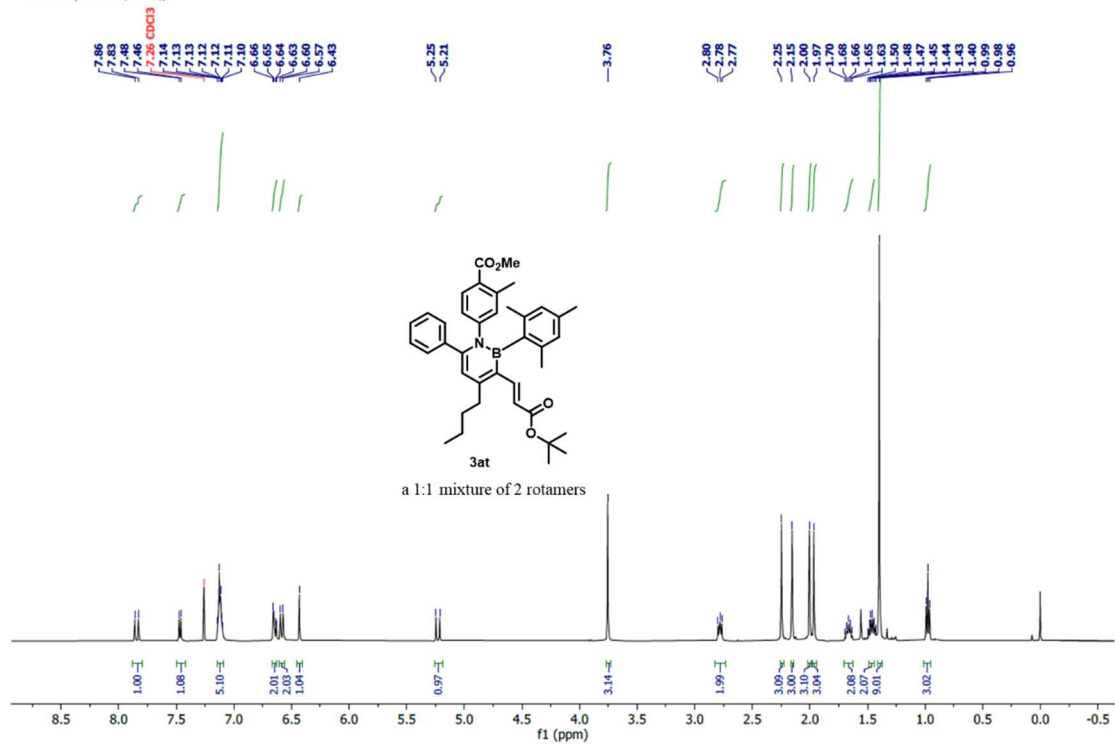
^{11}B NMR of **3as**

^{11}B NMR (160 MHz, CDCl_3)



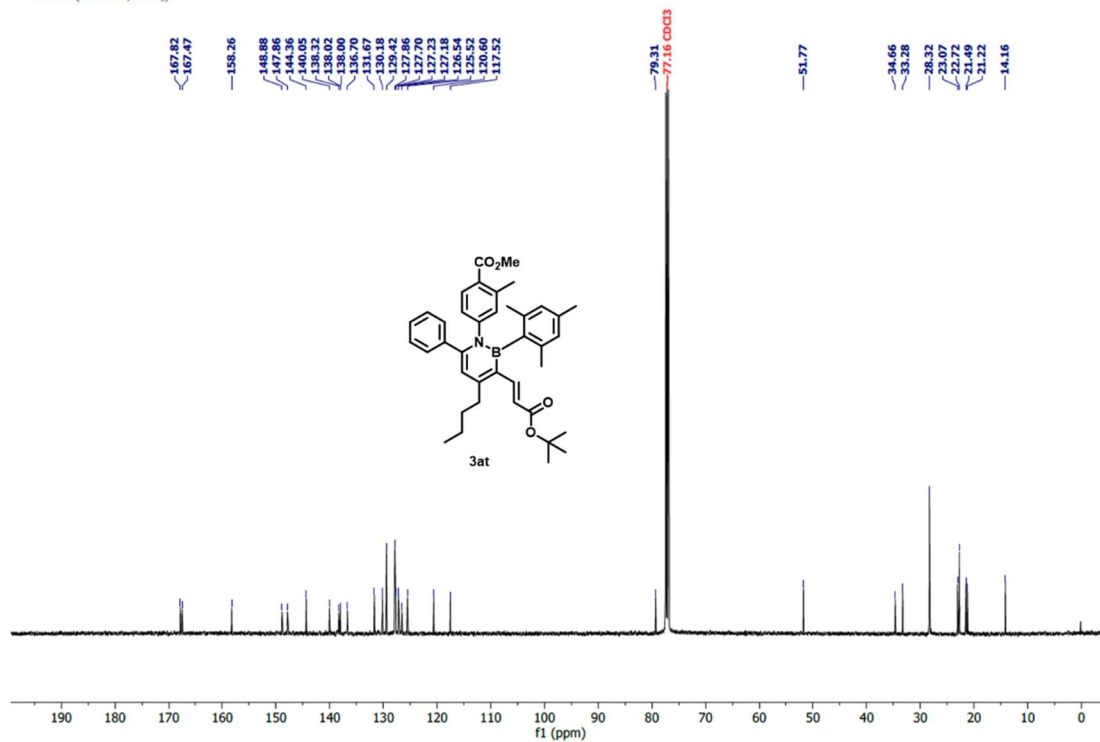
¹H NMR of 3at

¹H NMR (500 MHz, CDCl₃)



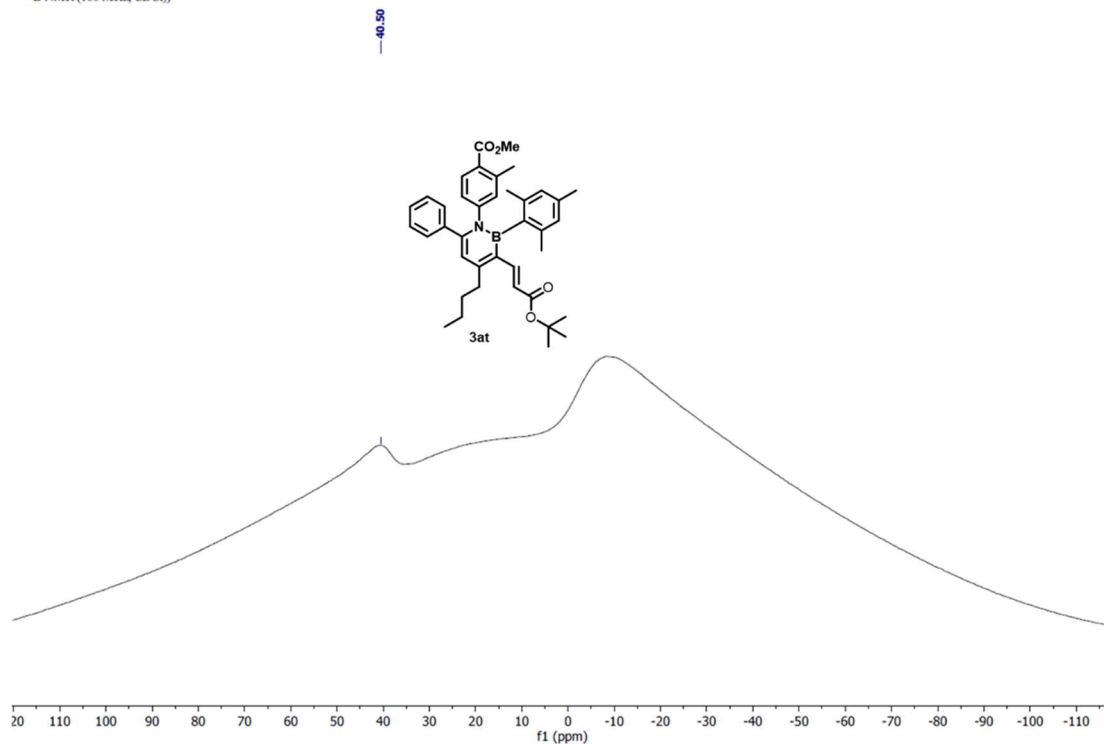
¹³C NMR of 3at

¹³C NMR (126 MHz, CDCl₃)



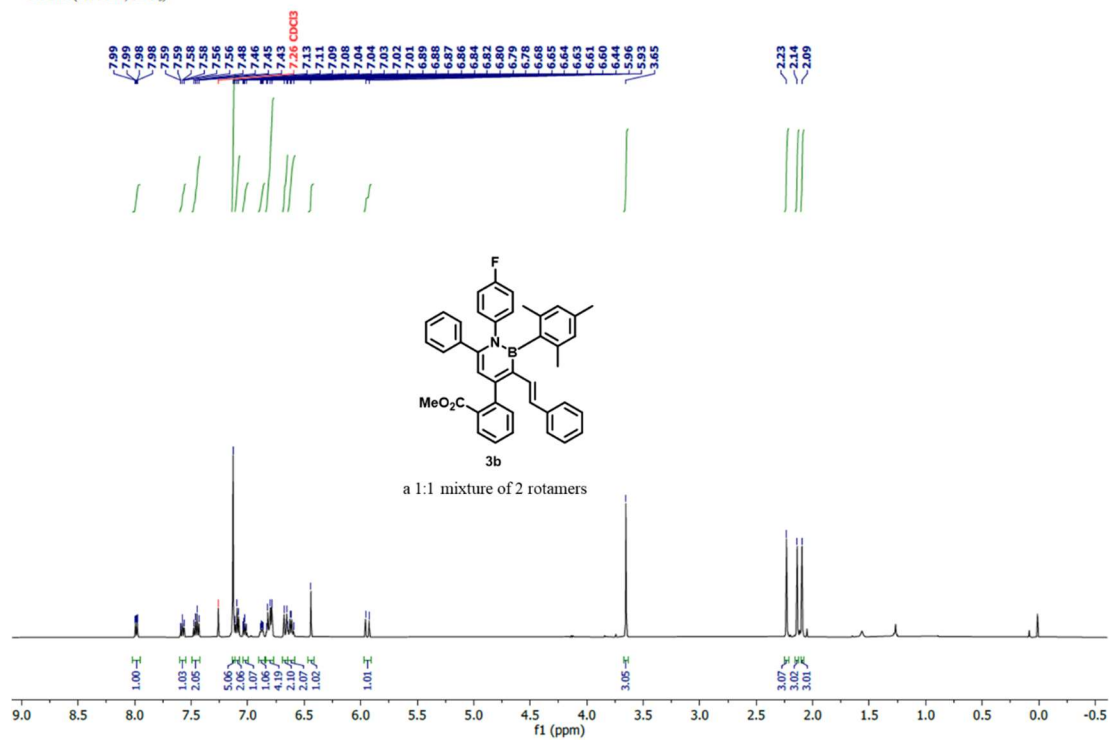
^{11}B NMR of **3at**

^{11}B NMR (160 MHz, CDCl_3)



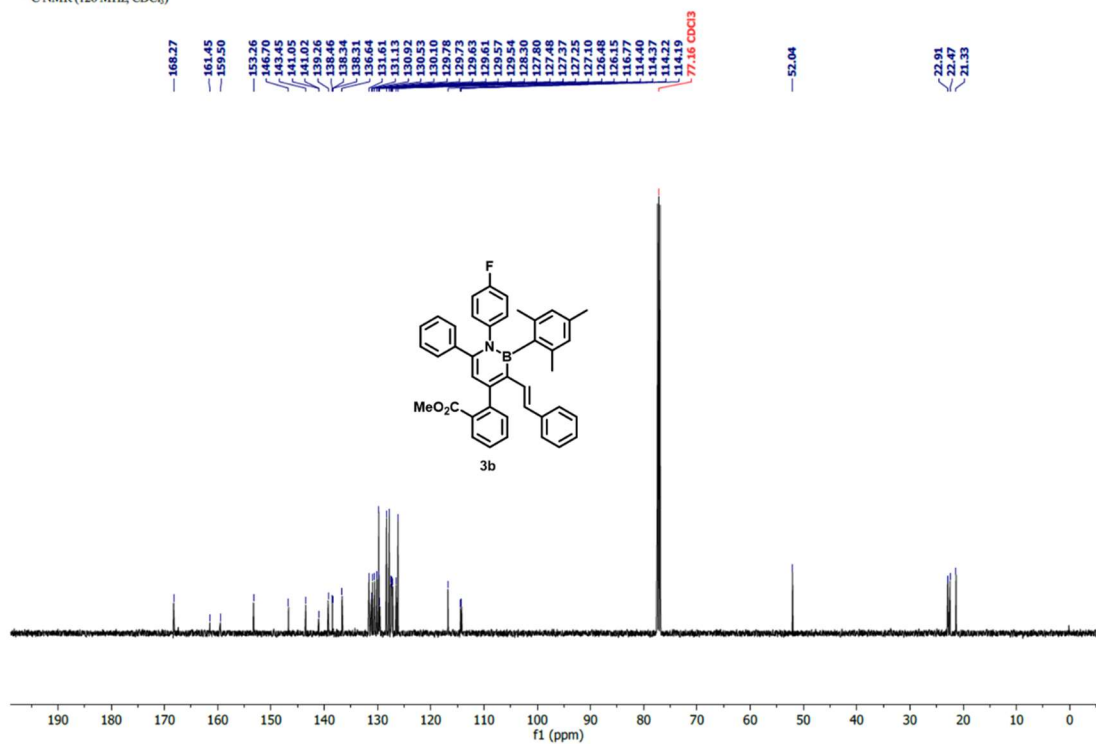
^1H NMR of **3b**

^1H NMR (500 MHz, CDCl_3)



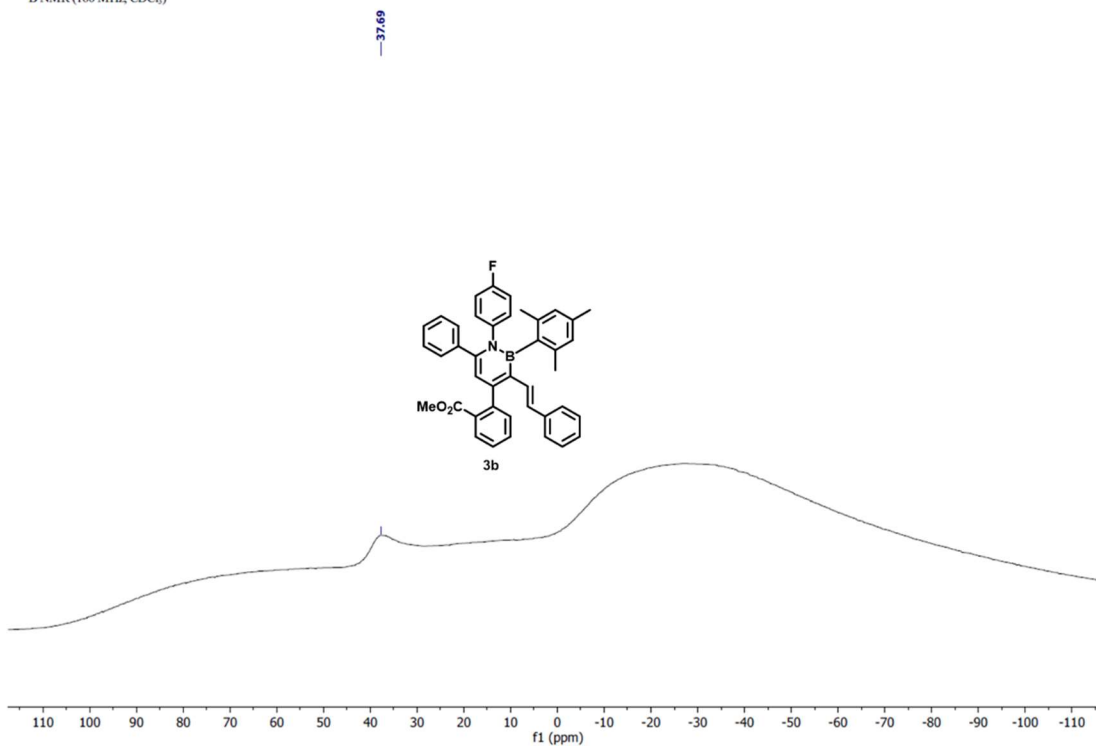
^{13}C NMR of **3b**

^{13}C NMR (126 MHz, CDCl_3)



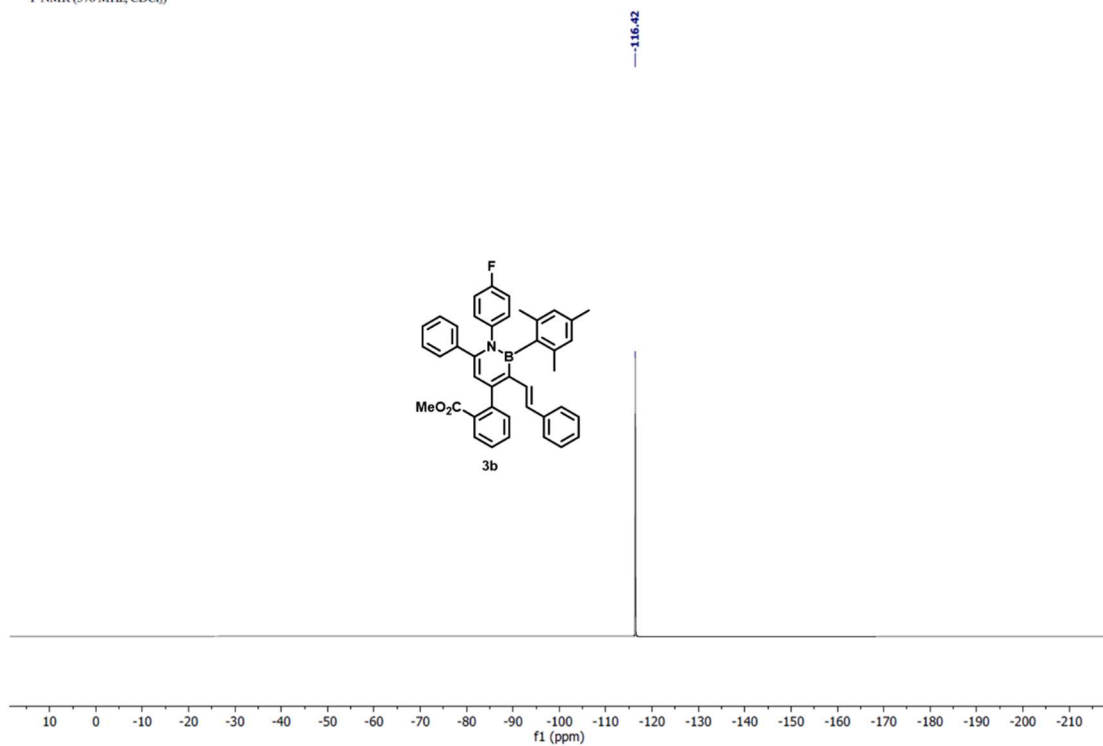
^{11}B NMR of **3b**

^{11}B NMR (160 MHz, CDCl_3)



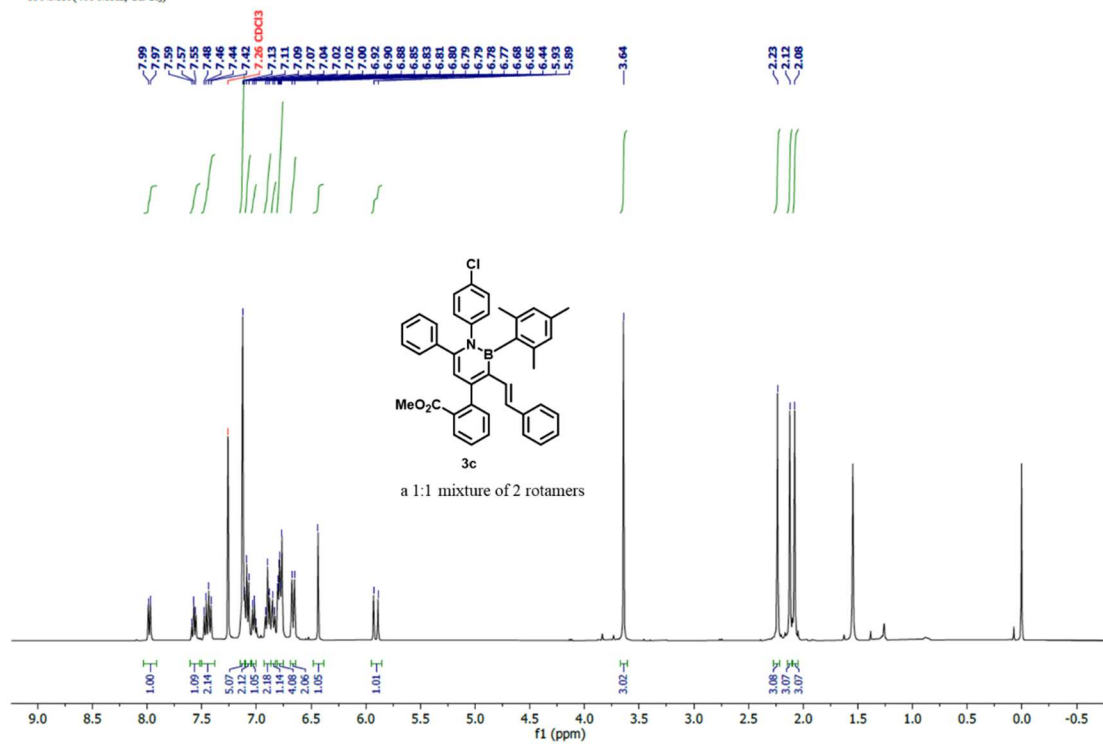
¹⁹F NMR of 3b

¹⁹F NMR (376 MHz, CDCl₃)



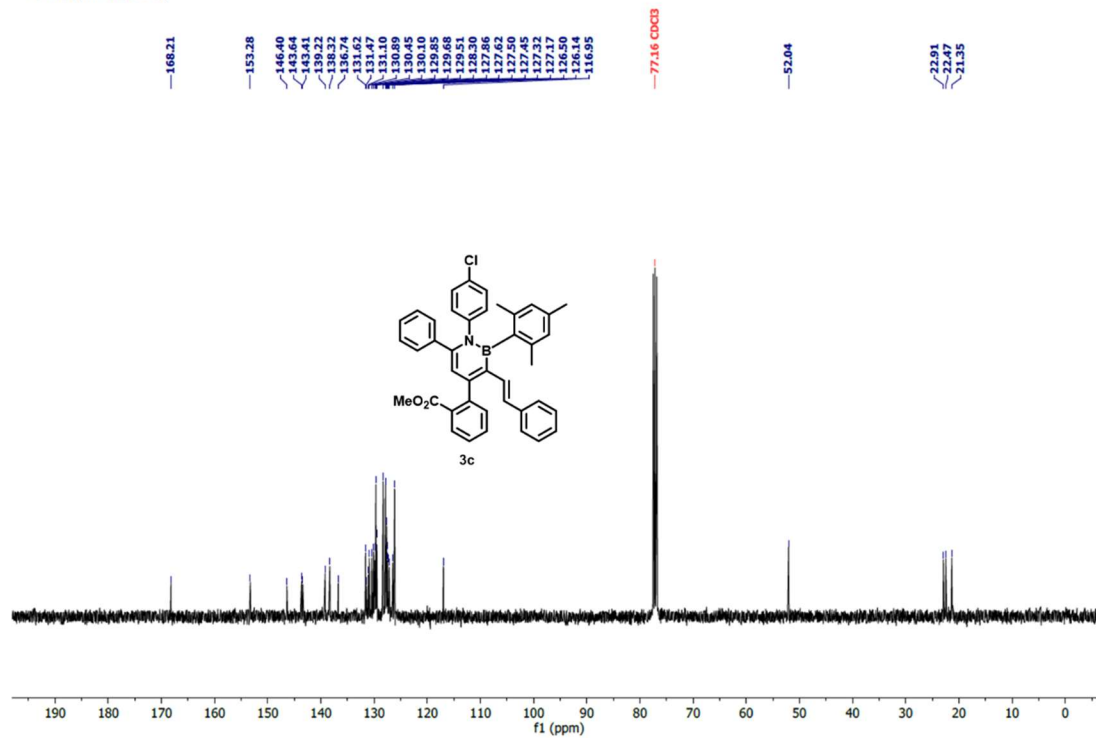
¹H NMR of 3c

¹H NMR (400 MHz, CDCl₃)



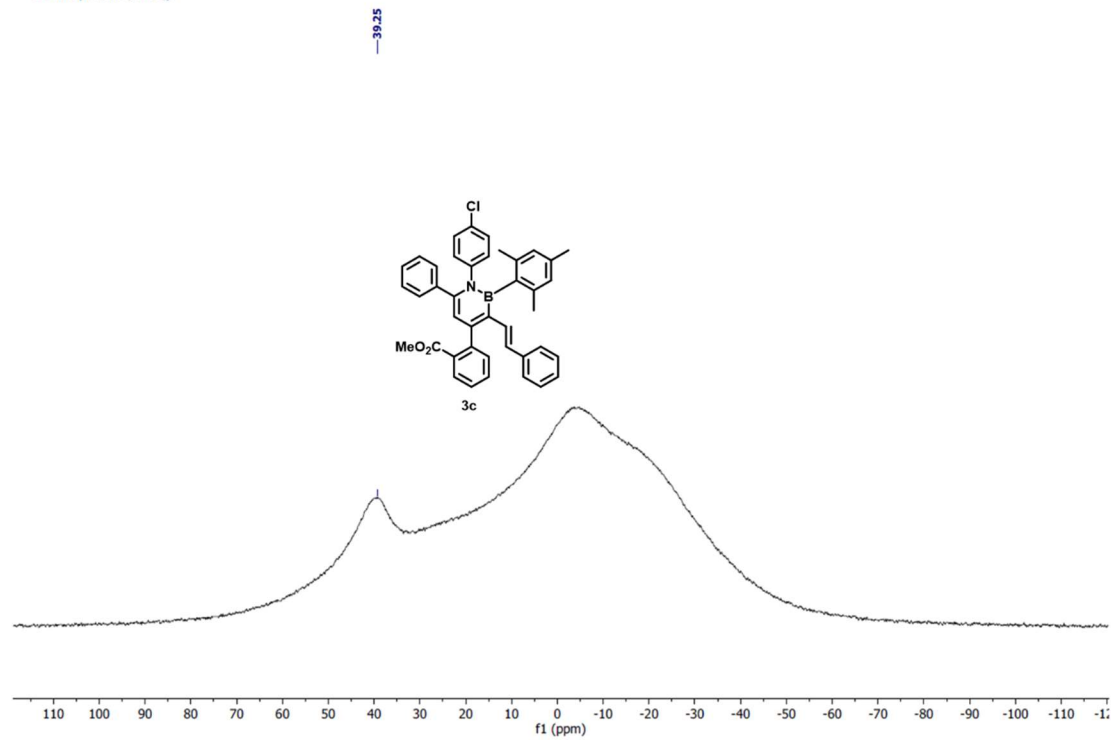
^{13}C NMR of **3c**

^{13}C NMR (101 MHz, CDCl_3)



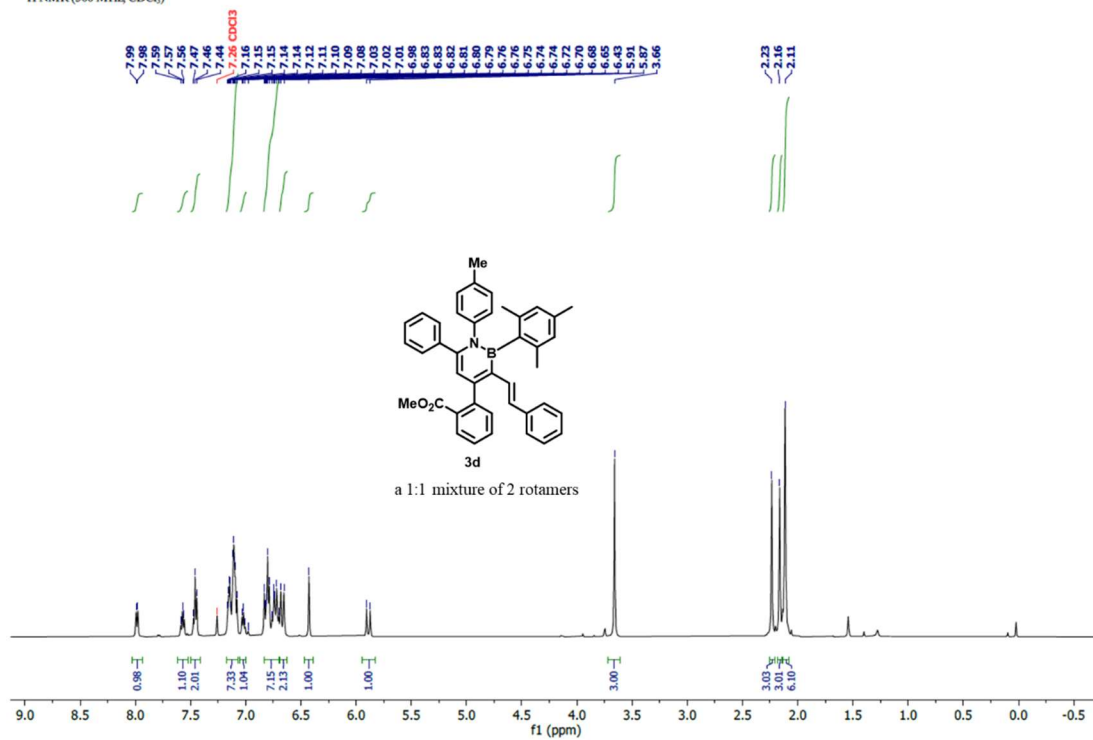
^{11}B NMR of **3c**

^{11}B NMR (128 MHz, CDCl_3)



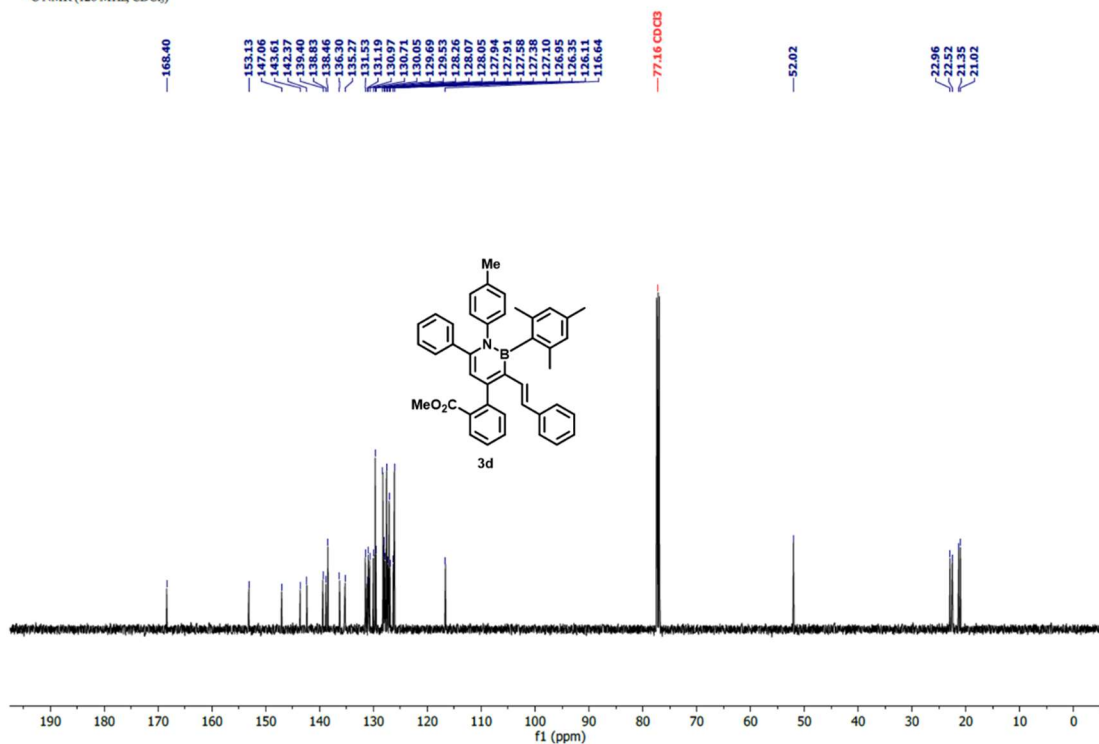
¹H NMR of 3d

¹H NMR (500 MHz, CDCl₃)



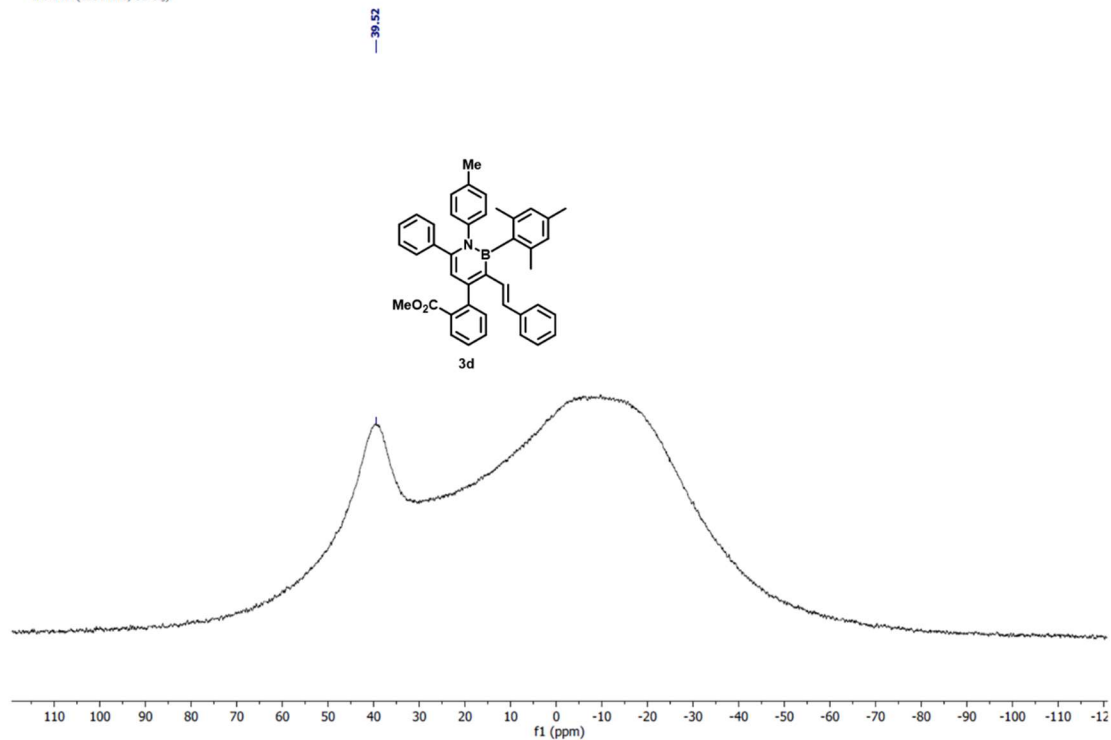
¹³C NMR of 3d

¹³C NMR (126 MHz, CDCl₃)



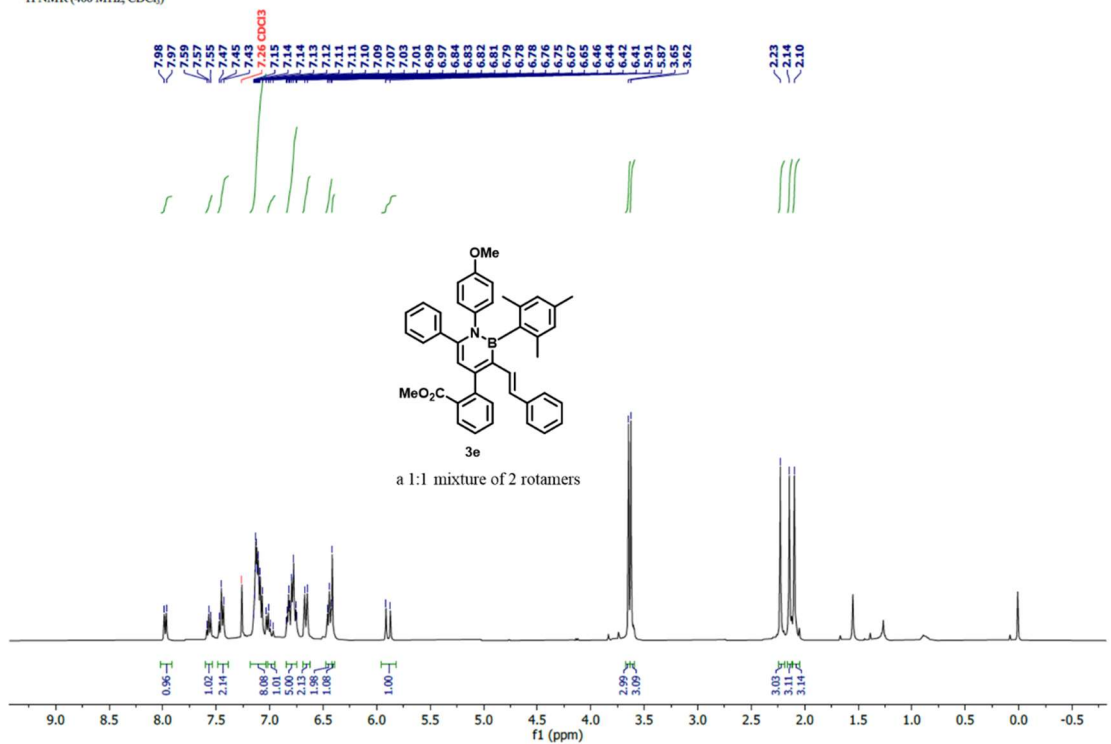
^{11}B NMR of **3d**

^{11}B NMR (128 MHz, CDCl_3).



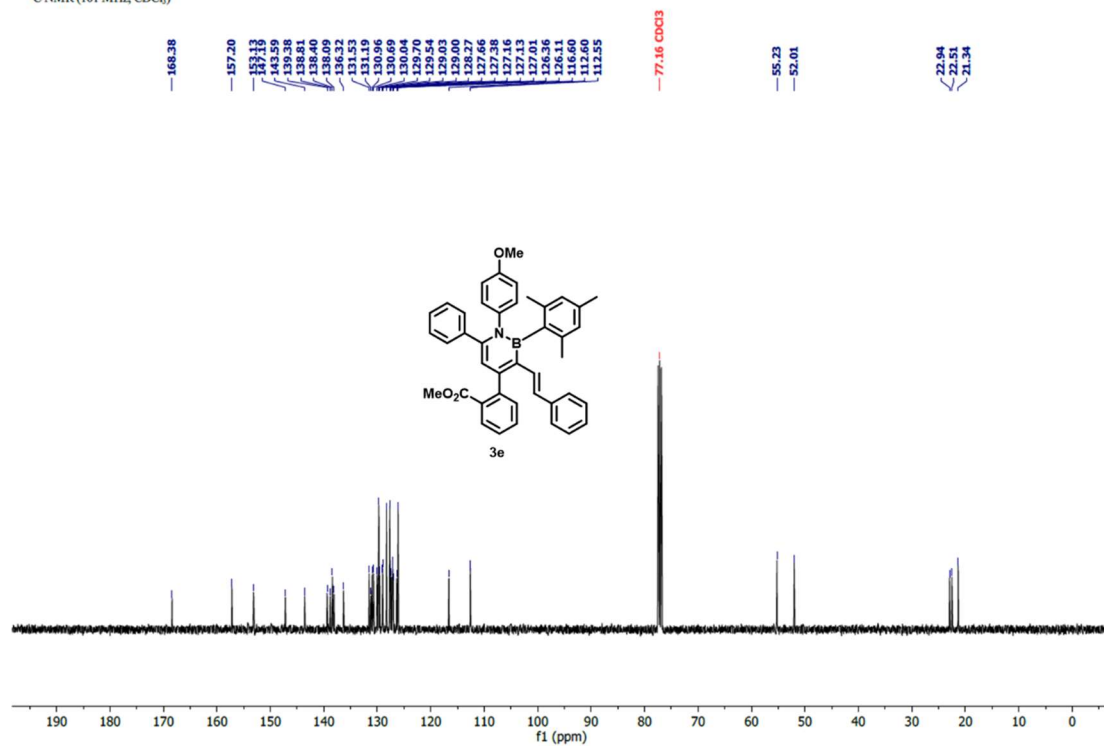
^1H NMR of **3e**

^1H NMR (400 MHz, CDCl_3)



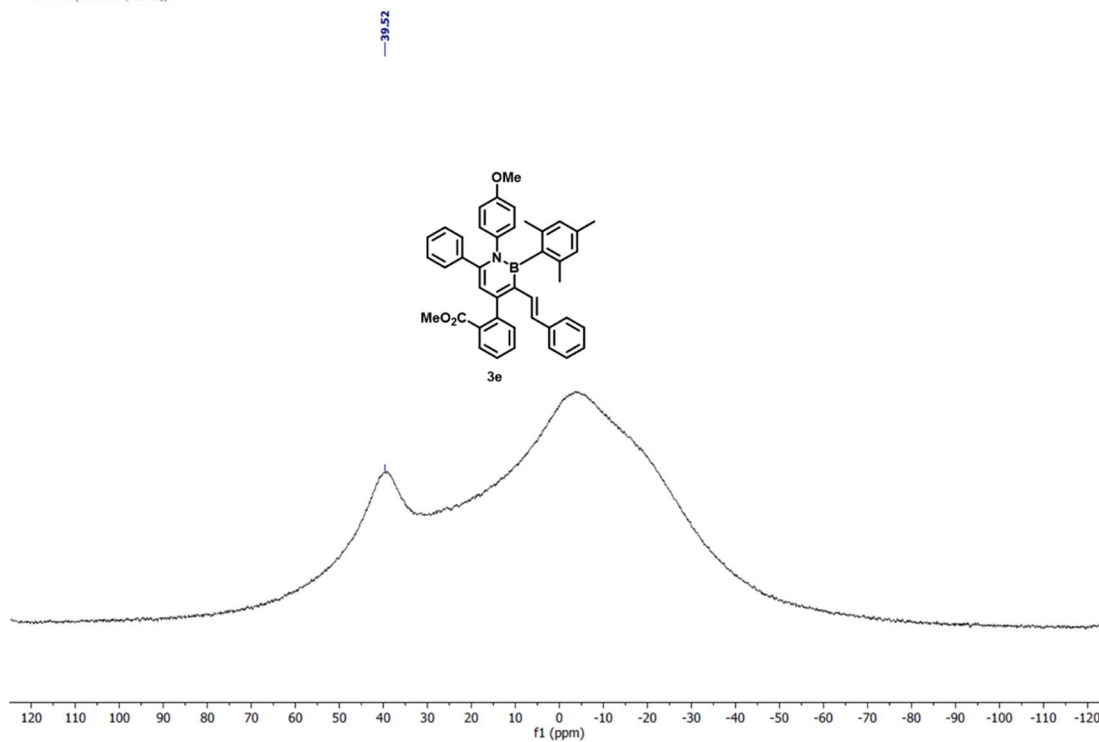
^{13}C NMR of **3e**

^{13}C NMR (101 MHz, CDCl_3)



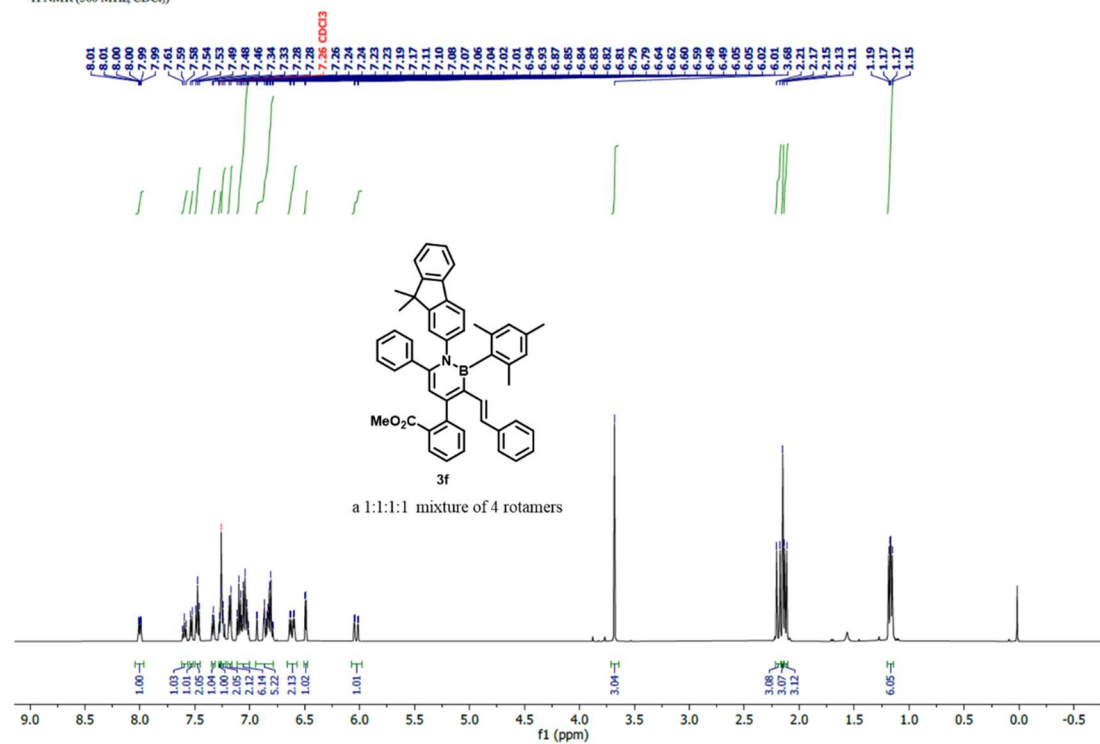
^{11}B NMR of **3e**

^{11}B NMR (128 MHz, CDCl_3)



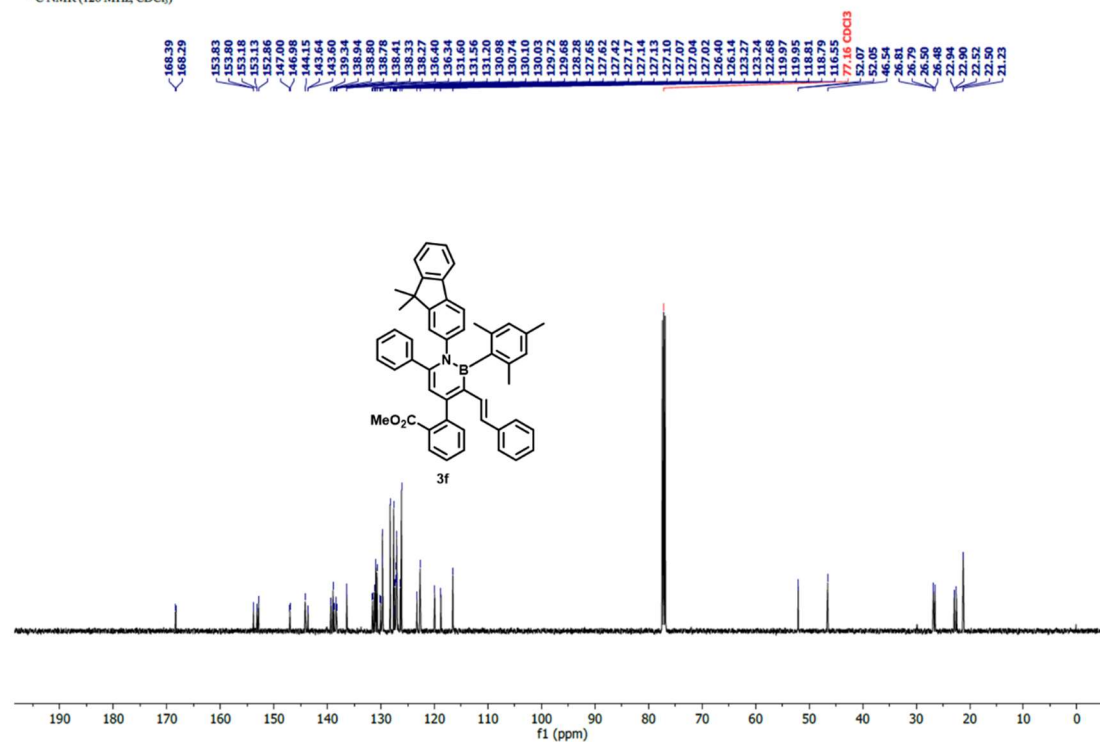
¹H NMR of 3f

¹H NMR (500 MHz, CDCl₃)



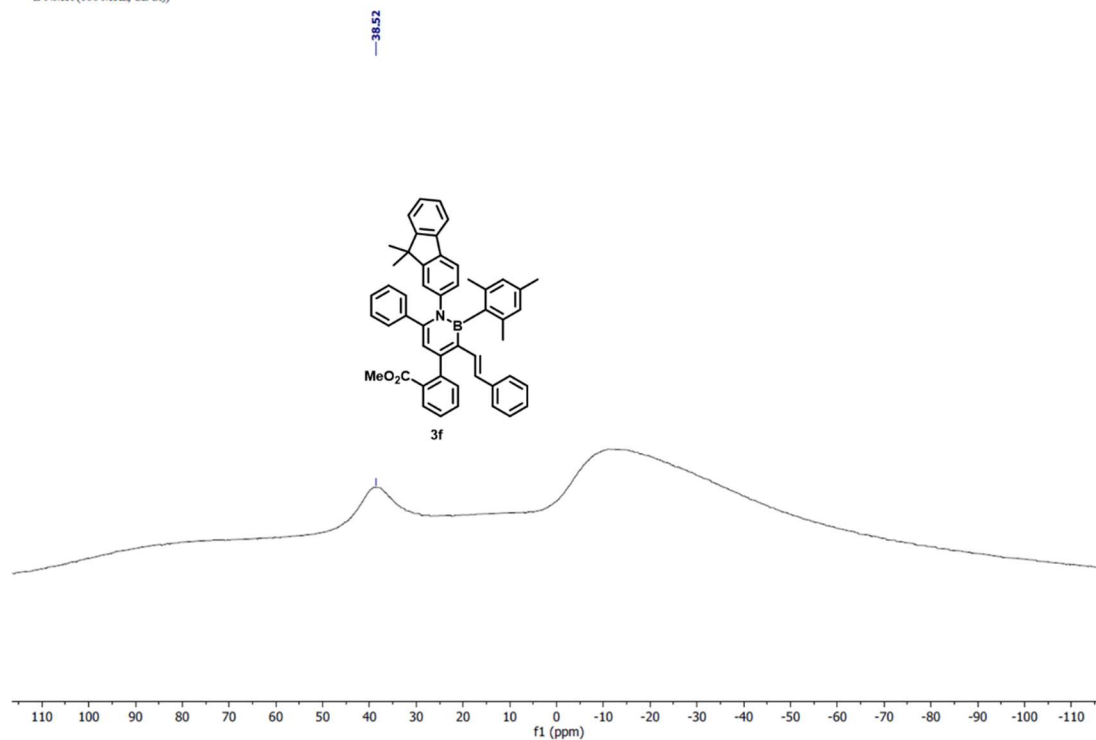
¹³C NMR of 3f

¹³C NMR (126 MHz, CDCl₃)



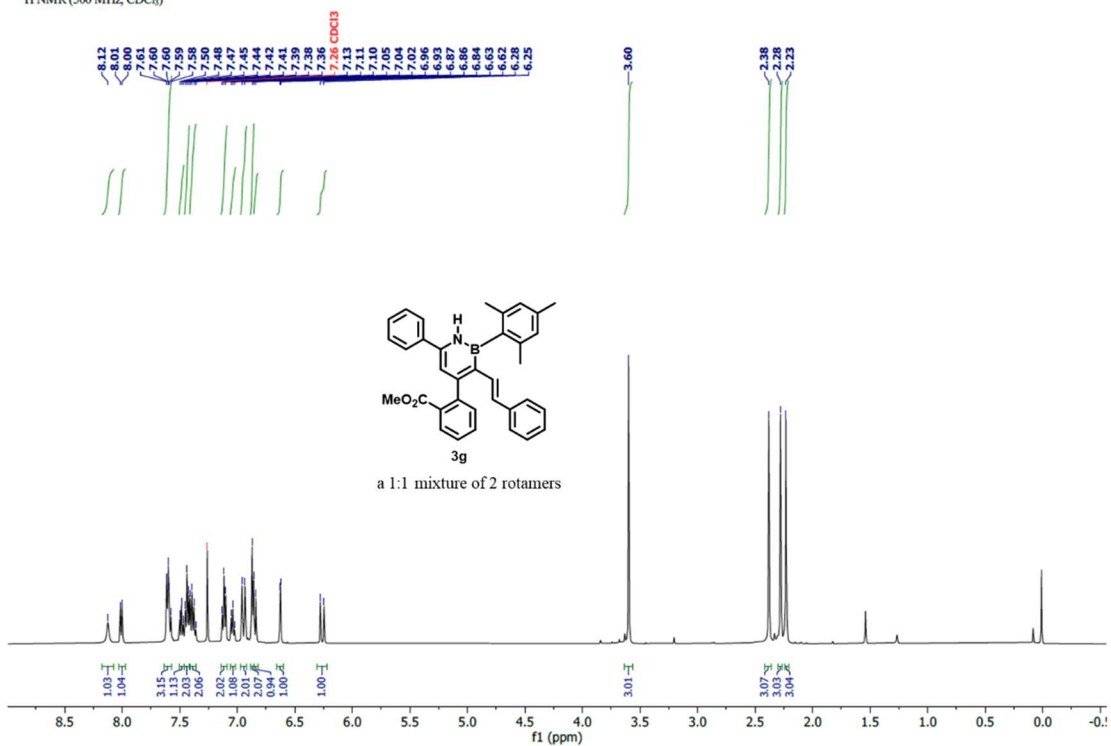
^{11}B NMR of **3f**

^{11}B NMR (160 MHz, CDCl_3)



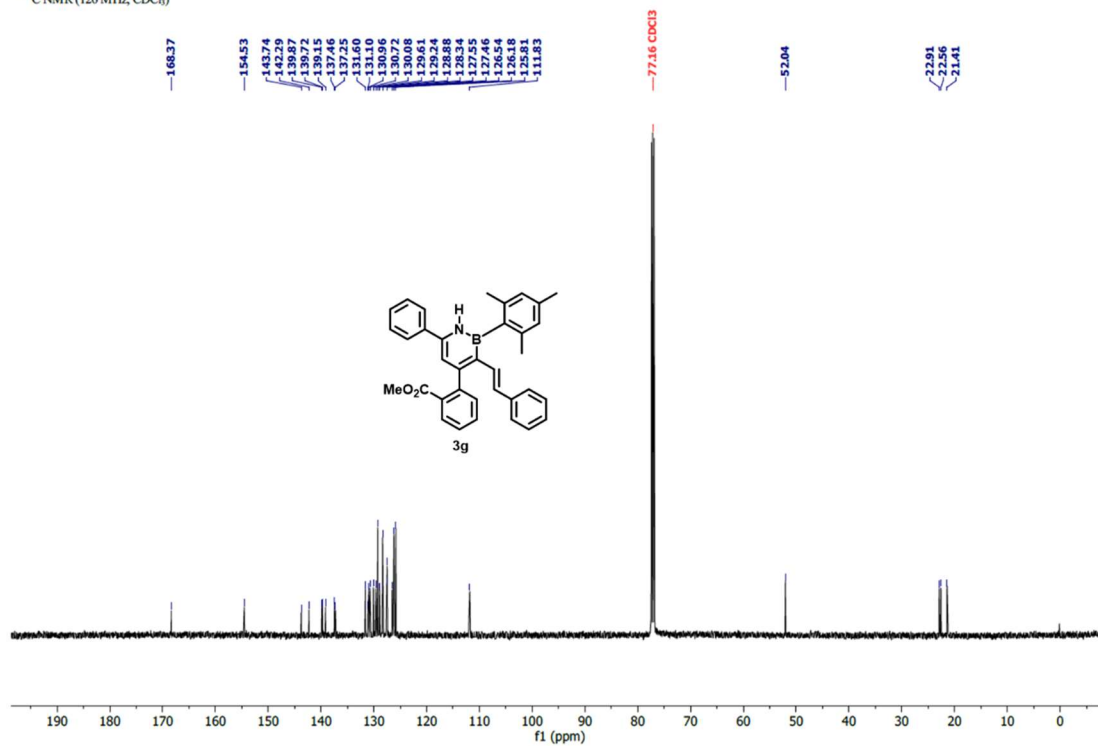
^1H NMR of **3g**

^1H NMR (500 MHz, CDCl_3)



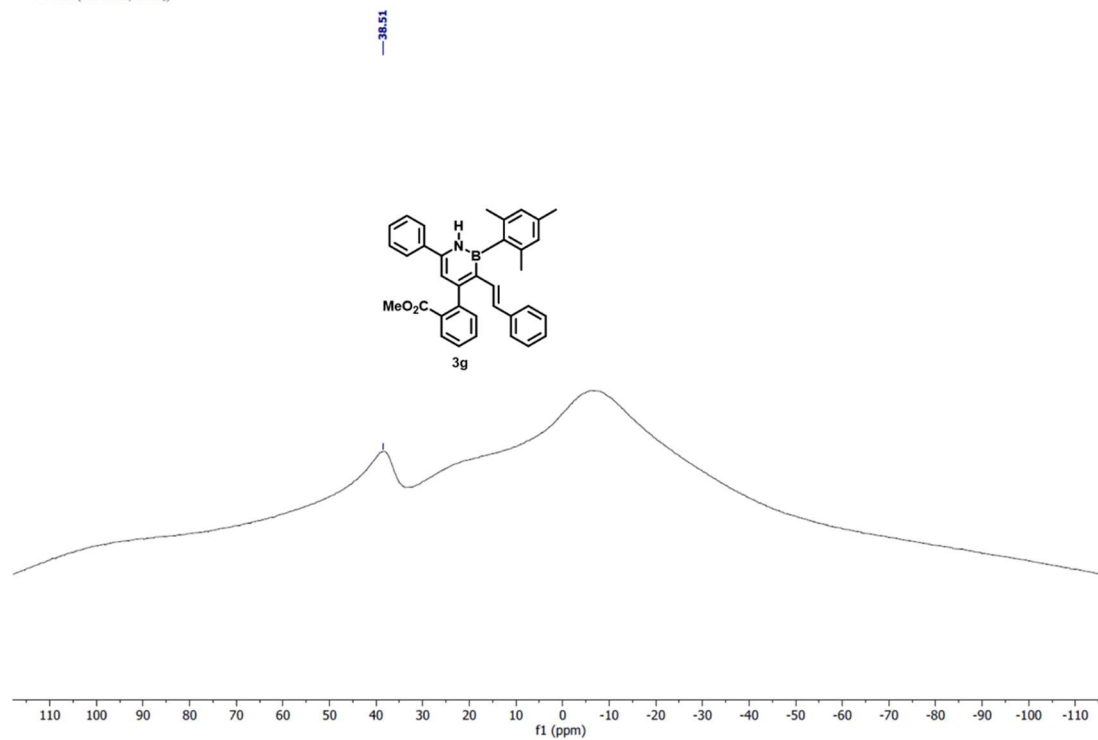
¹³C NMR of 3g

¹³C NMR (126 MHz, CDCl₃)



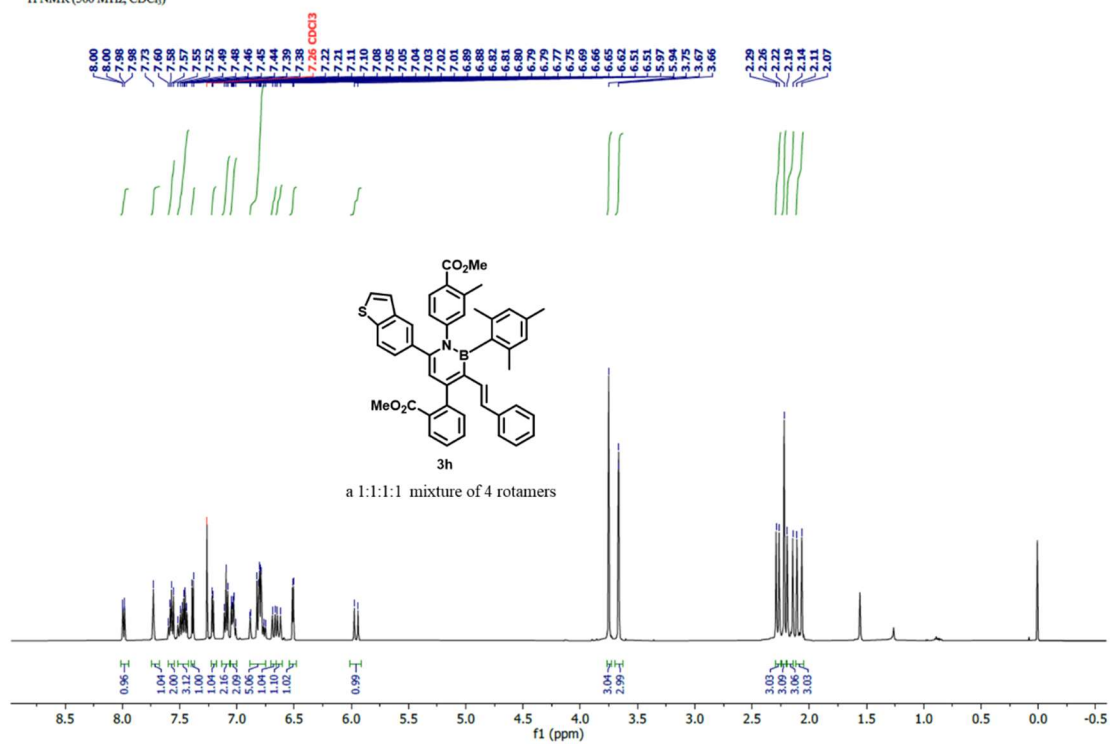
¹¹B NMR of 3g

¹¹B NMR (160 MHz, CDCl₃)



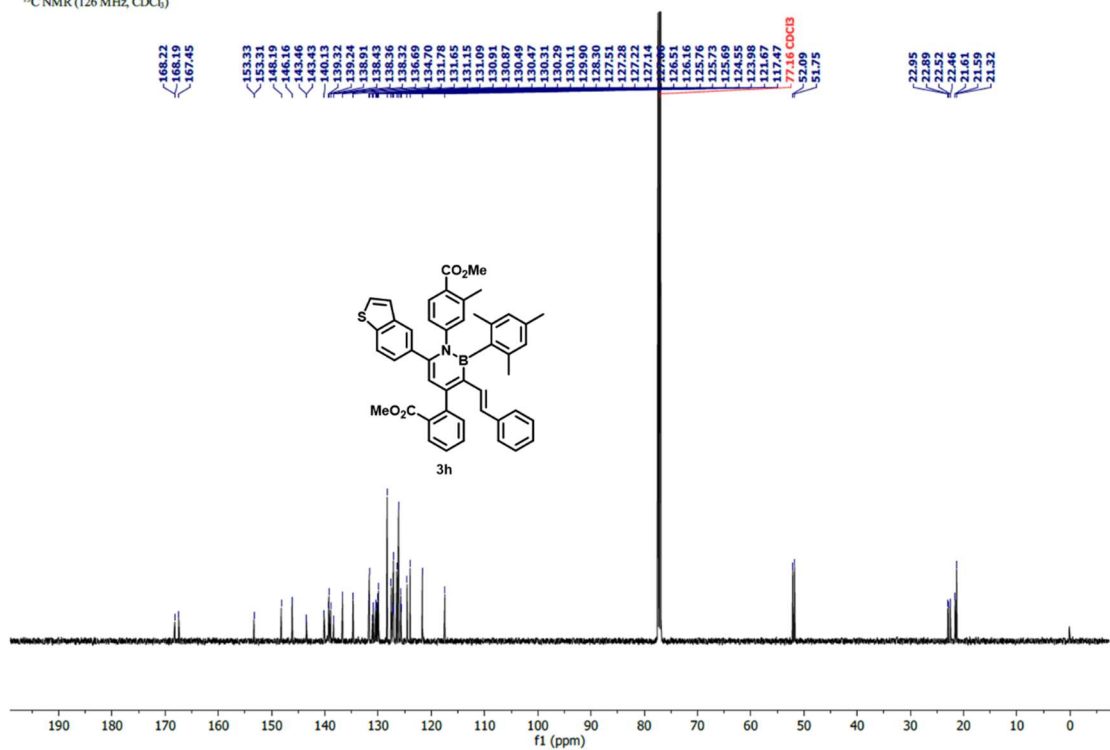
¹H NMR of 3h

¹H NMR (500 MHz, CDCl₃)



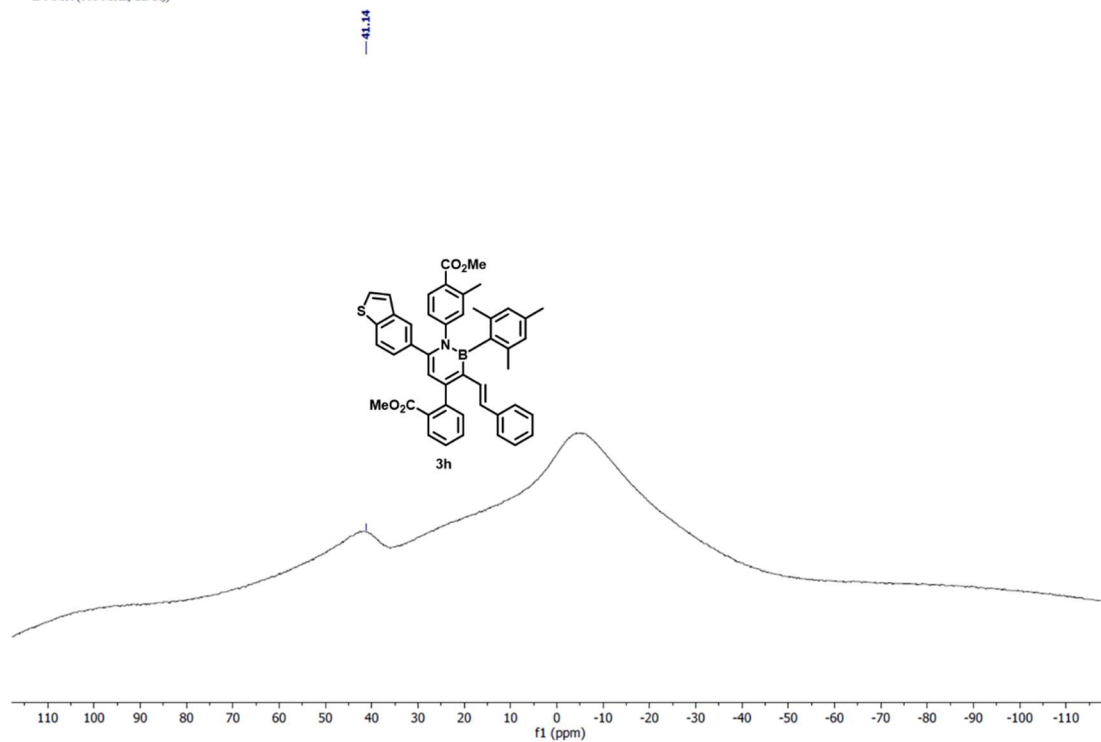
¹³C NMR of 3h

¹³C NMR (126 MHz, CDCl₃)



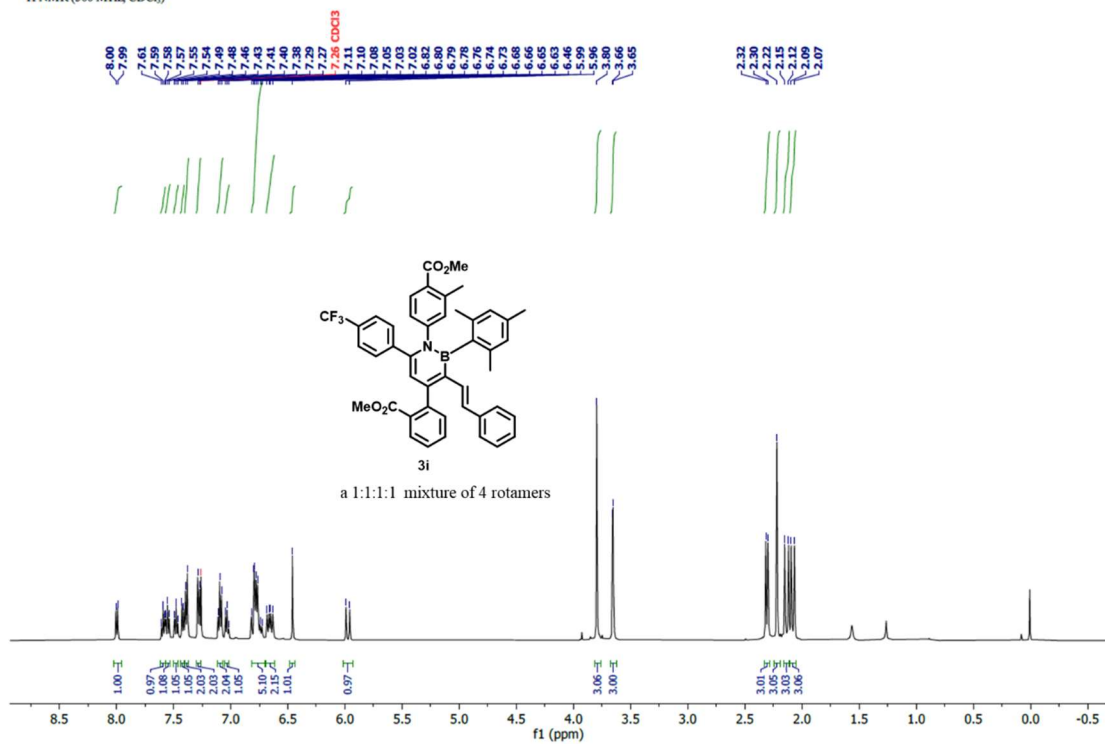
^{11}B NMR of **3h**

^{11}B NMR (160 MHz, CDCl_3)



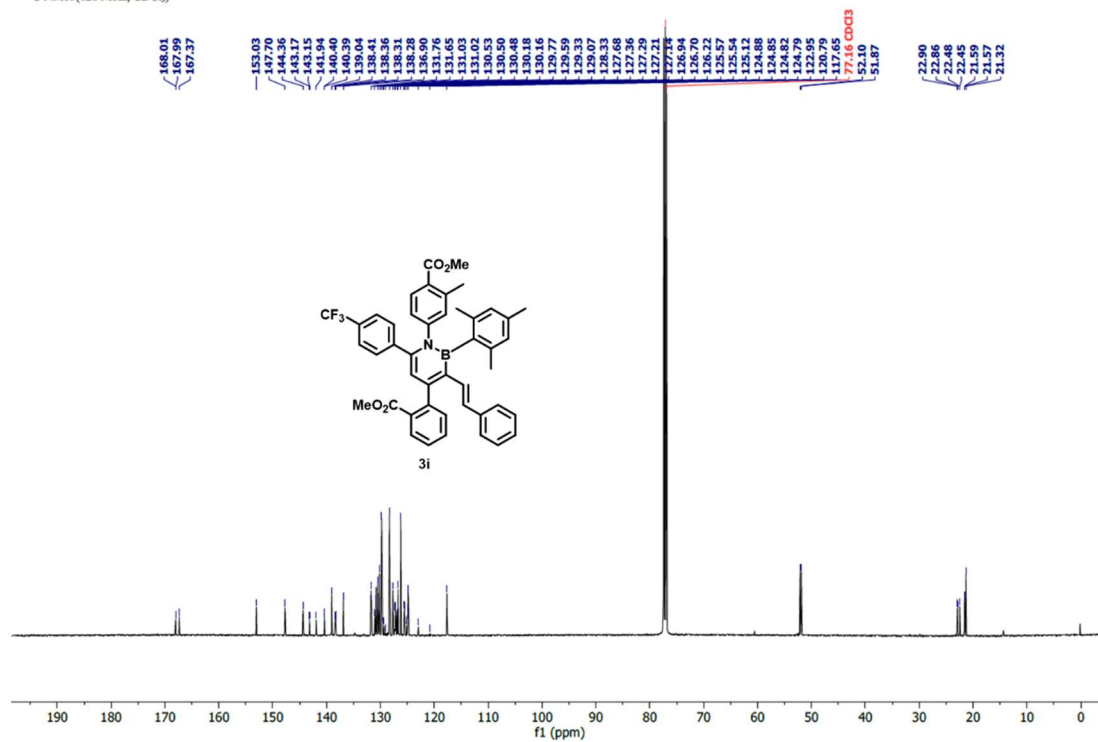
^1H NMR of **3i**

^1H NMR (500 MHz, CDCl_3)



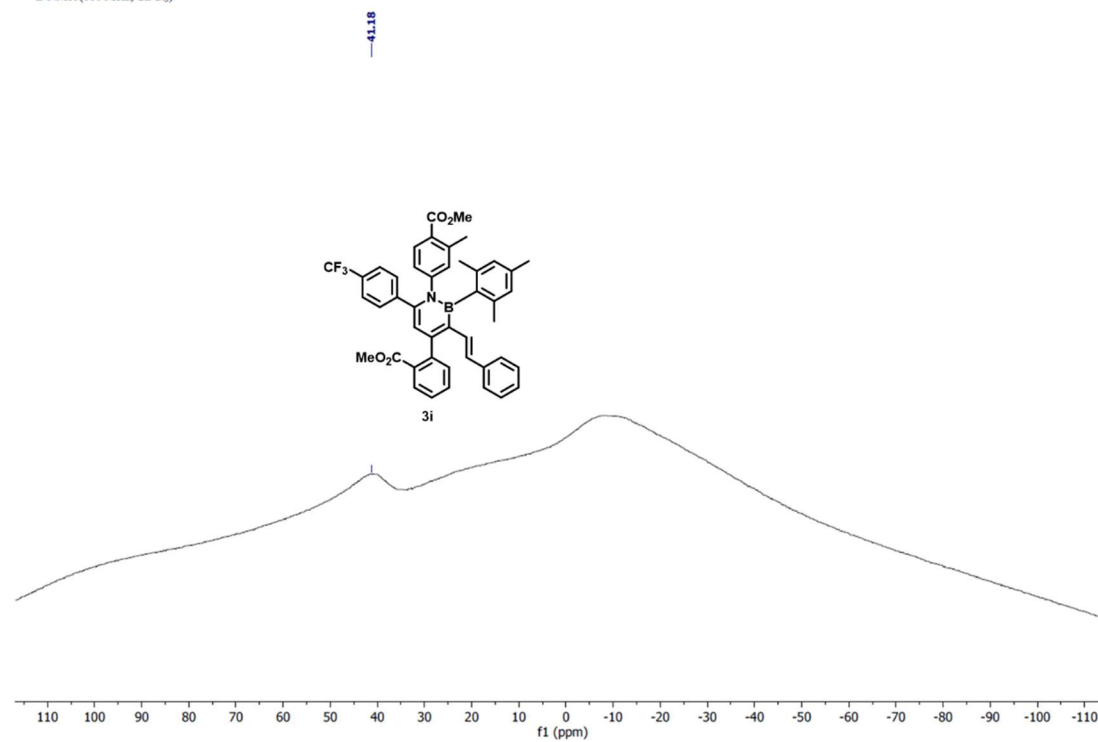
¹³C NMR of **3i**

¹³C NMR (126 MHz, CDCl₃)



¹¹B NMR of **3i**

¹¹B NMR (160 MHz, CDCl₃)



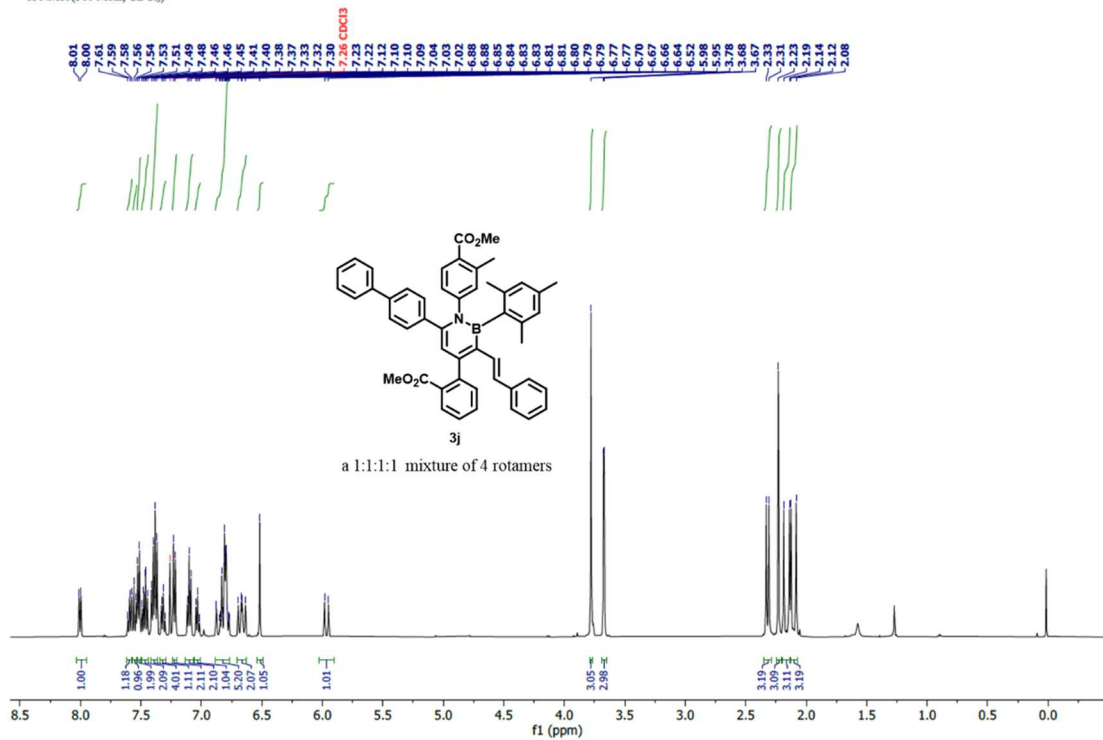
¹⁹F NMR of **3i**

¹⁹F NMR (376 MHz, CDCl₃)



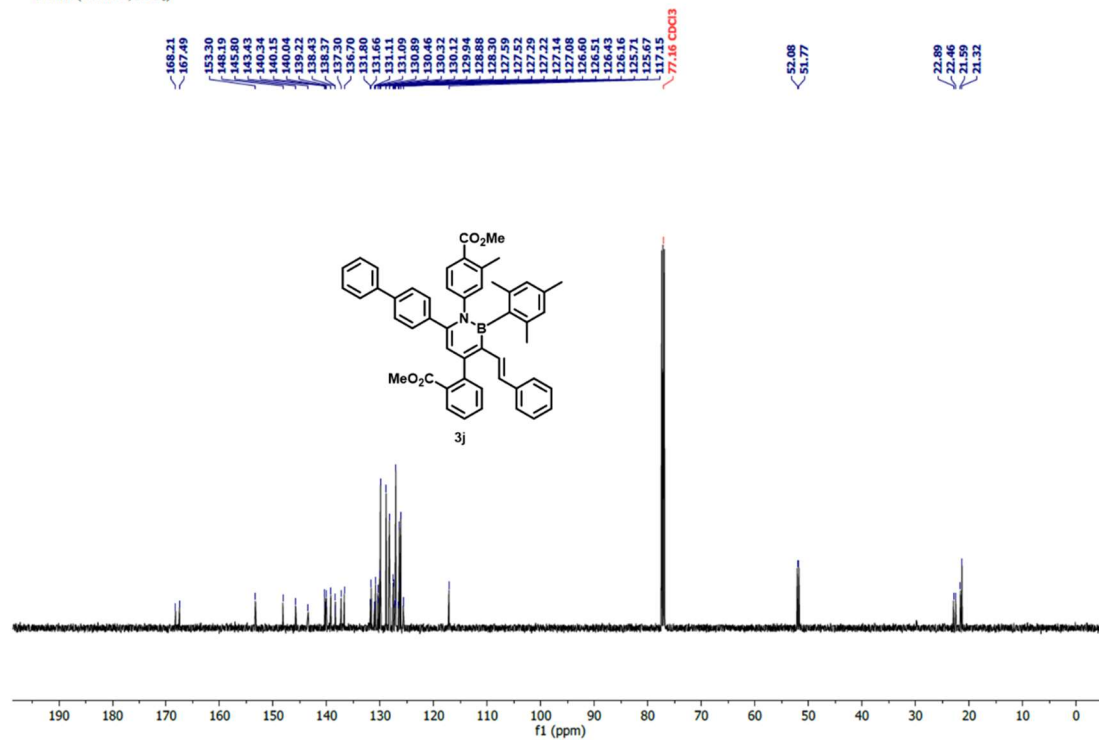
¹H NMR of **3j**

¹H NMR (500 MHz, CDCl₃)



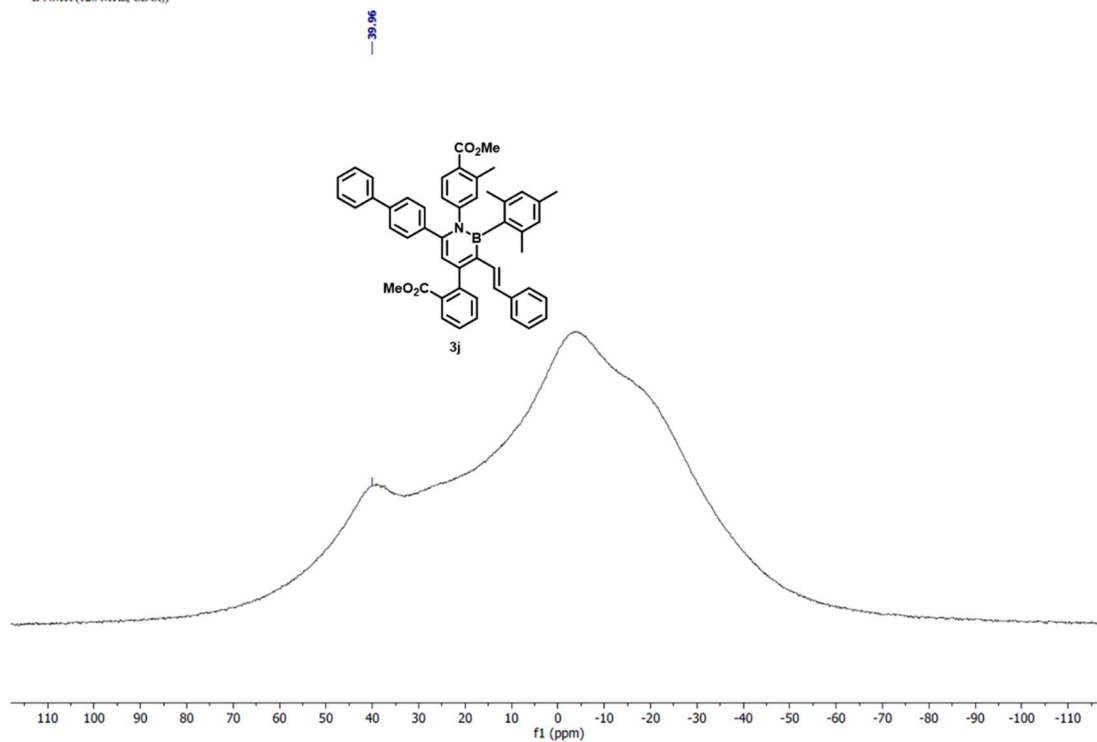
¹³C NMR of **3j**

¹³C NMR (126 MHz, CDCl₃)



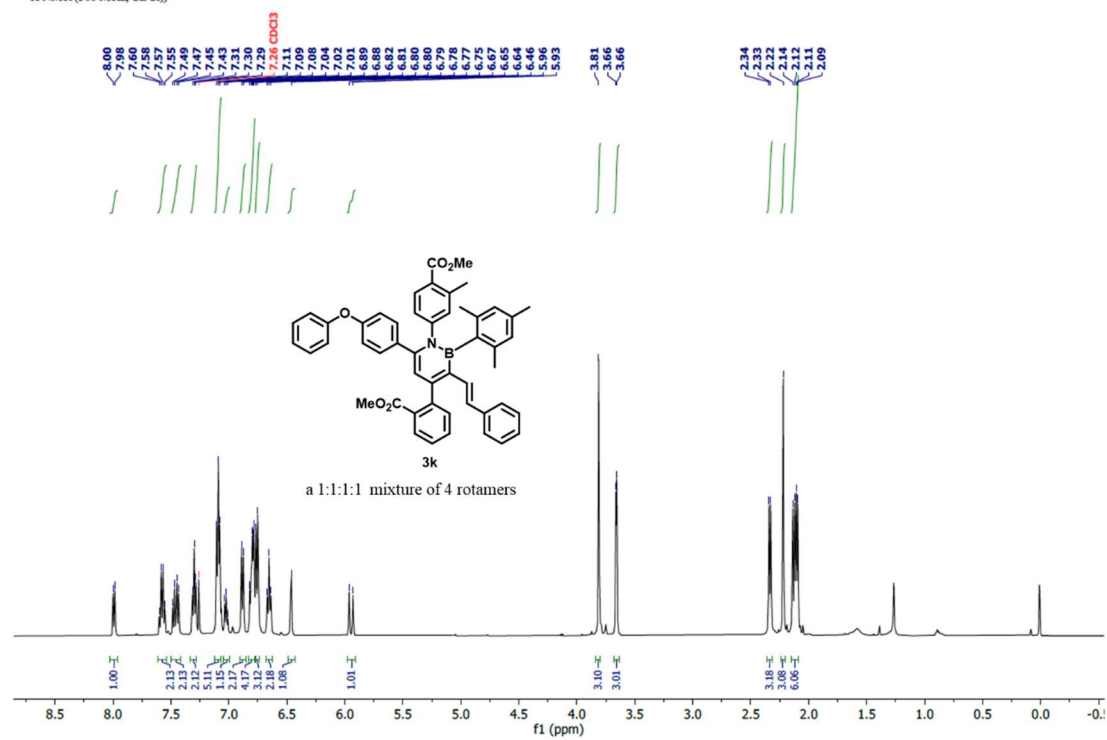
¹¹B NMR of **3j**

¹¹B NMR (128 MHz, CDCl₃)



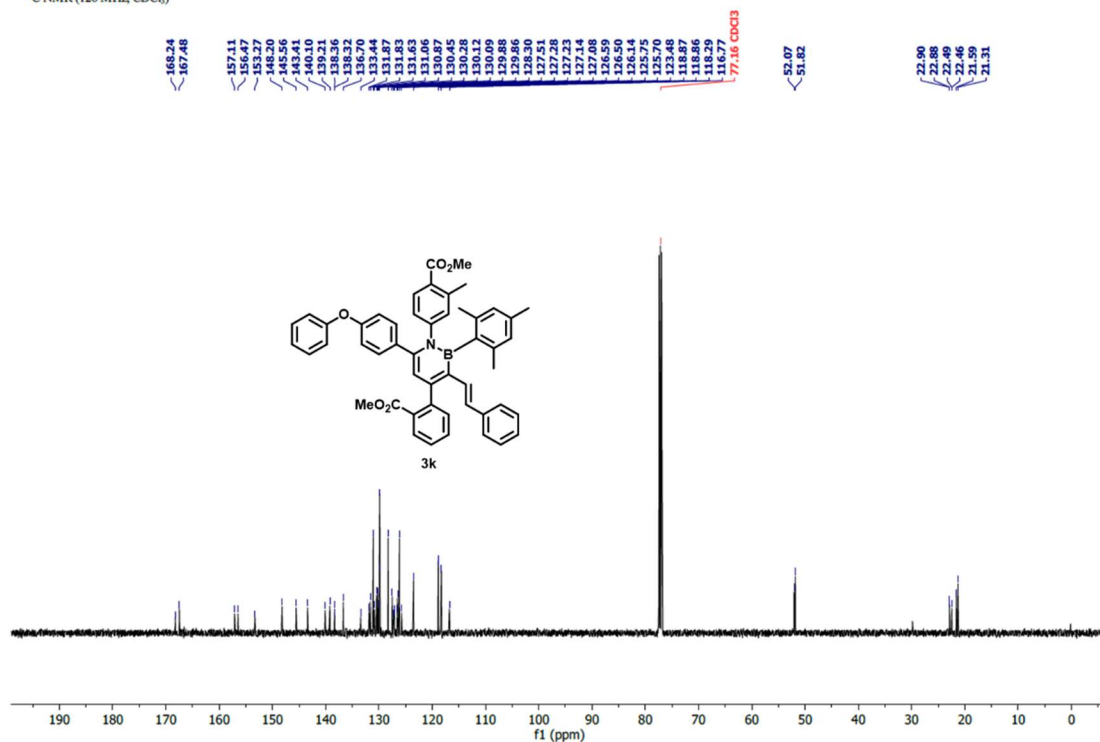
¹H NMR of 3k

¹H NMR (500 MHz, CDCl₃)



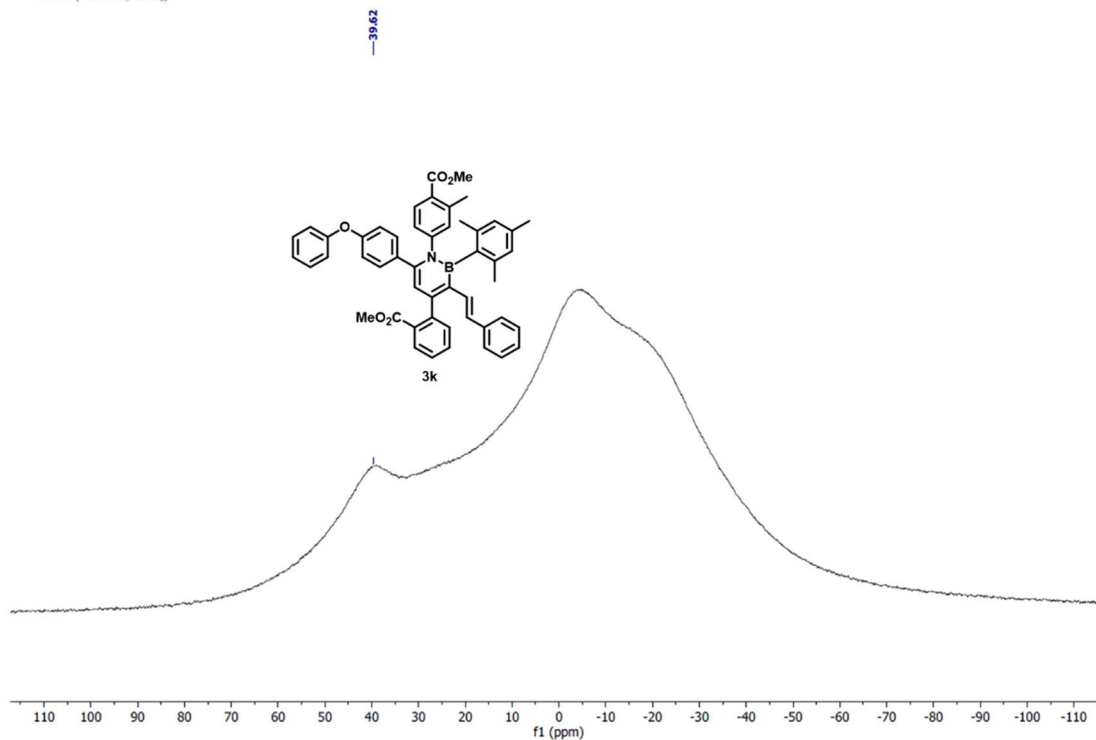
¹³C NMR of 3k

¹³C NMR (126 MHz, CDCl₃)



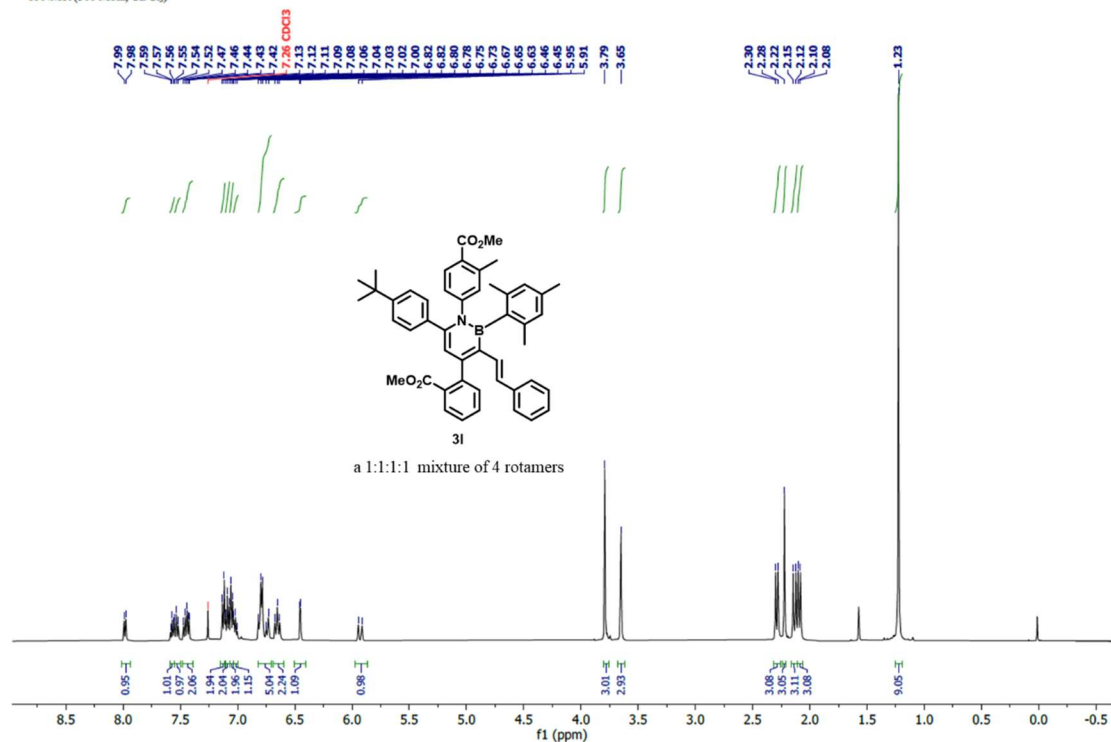
^{11}B NMR of **3k**

^{11}B NMR (128 MHz, CDCl_3)



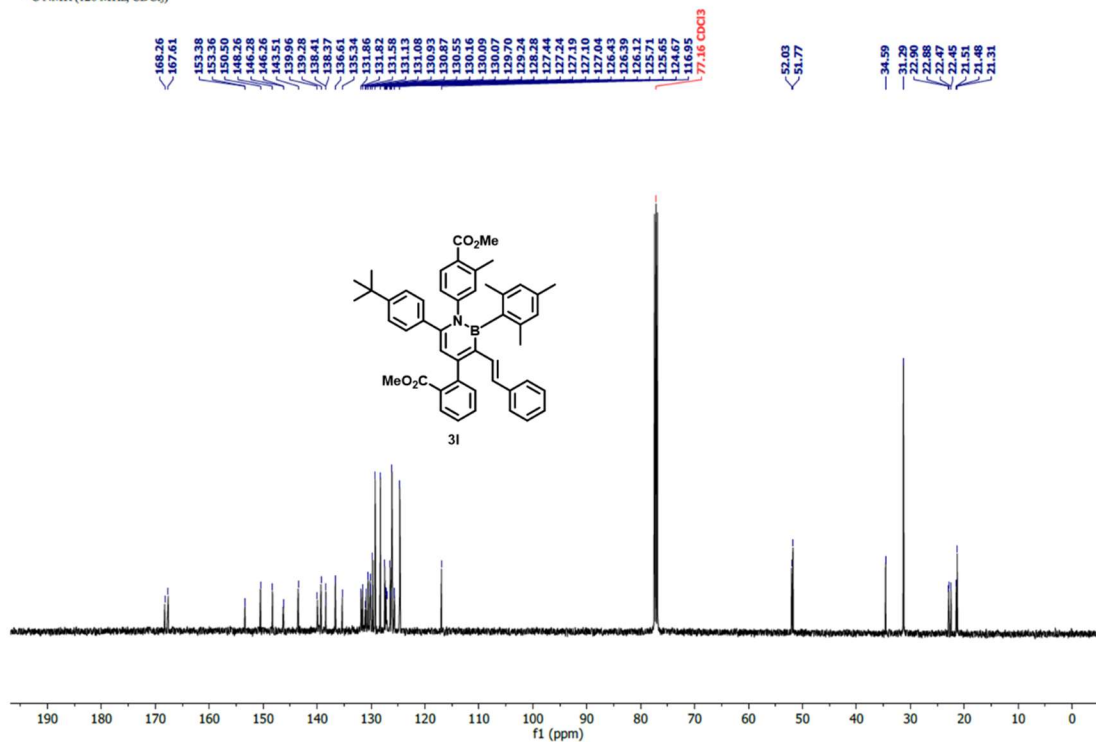
^1H NMR of **3l**

^1H NMR (500 MHz, CDCl_3)



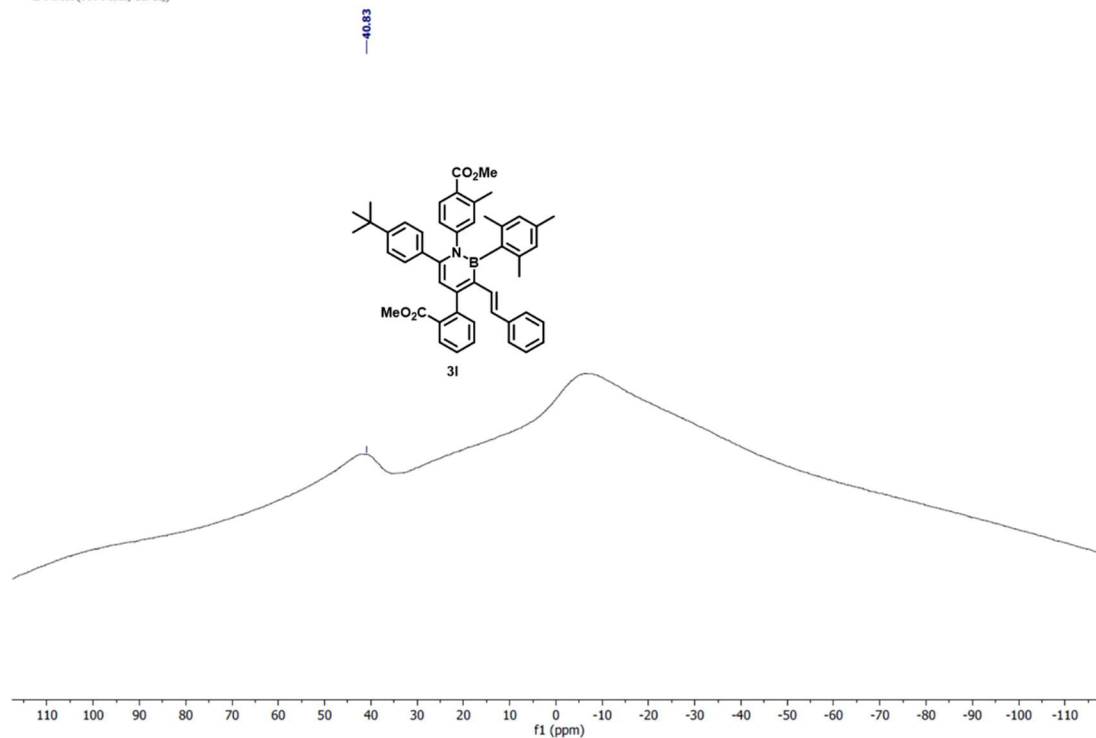
^{13}C NMR of **3I**

^{13}C NMR (126 MHz, CDCl_3)



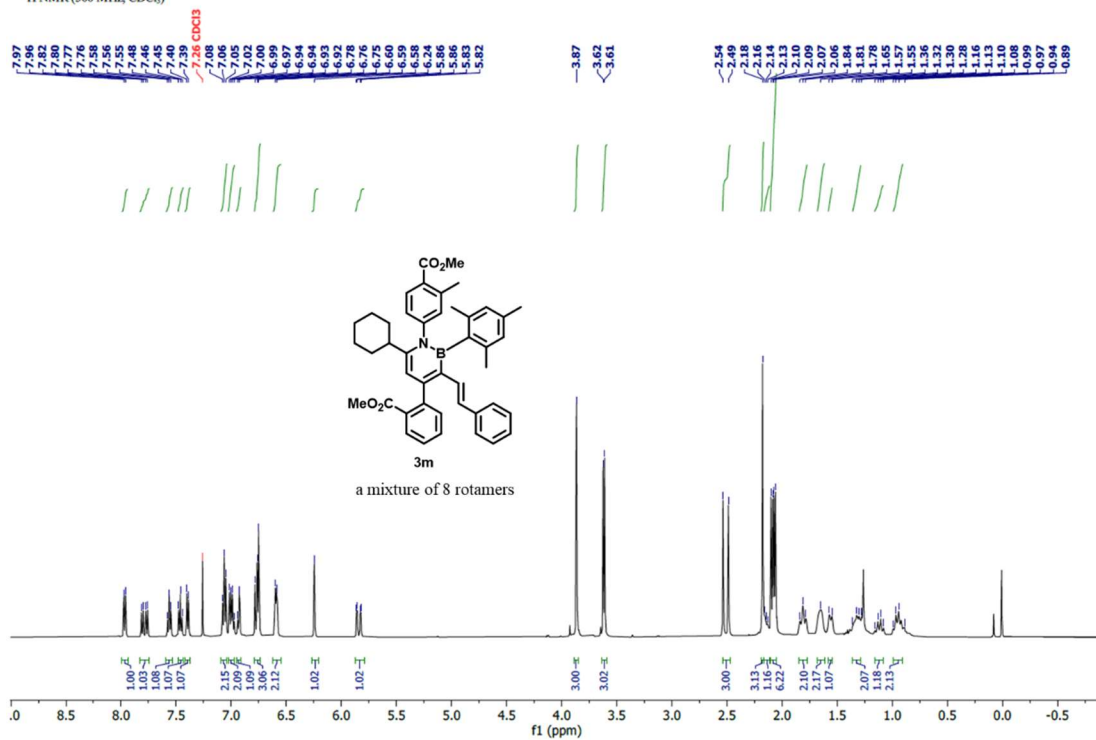
^{11}B NMR of **3I**

^{11}B NMR (160 MHz, CDCl_3)



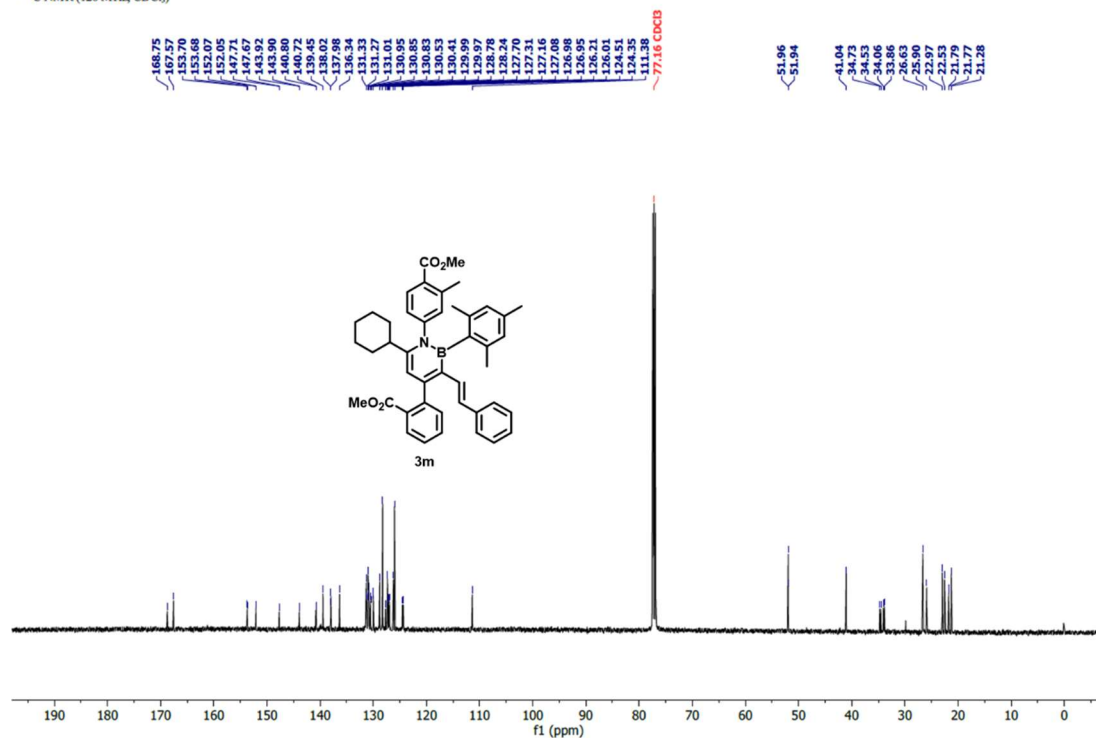
¹H NMR of 3m

¹H NMR (500 MHz, CDCl₃)



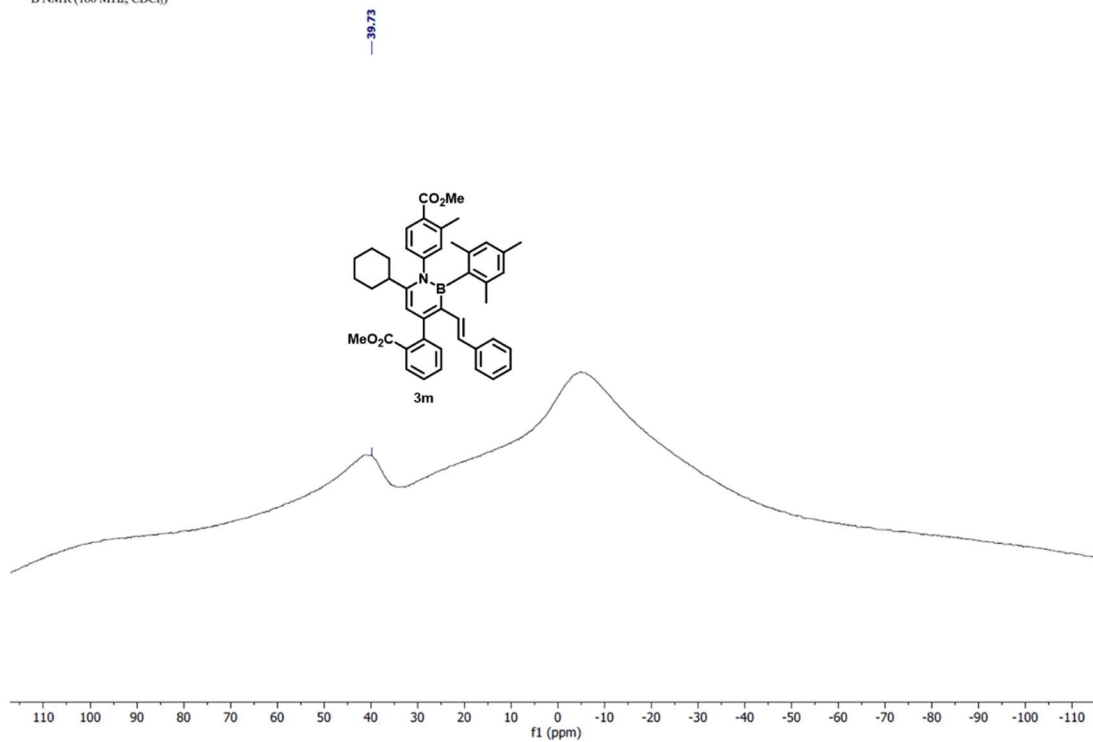
¹³C NMR of 3m

¹³C NMR (126 MHz, CDCl₃)



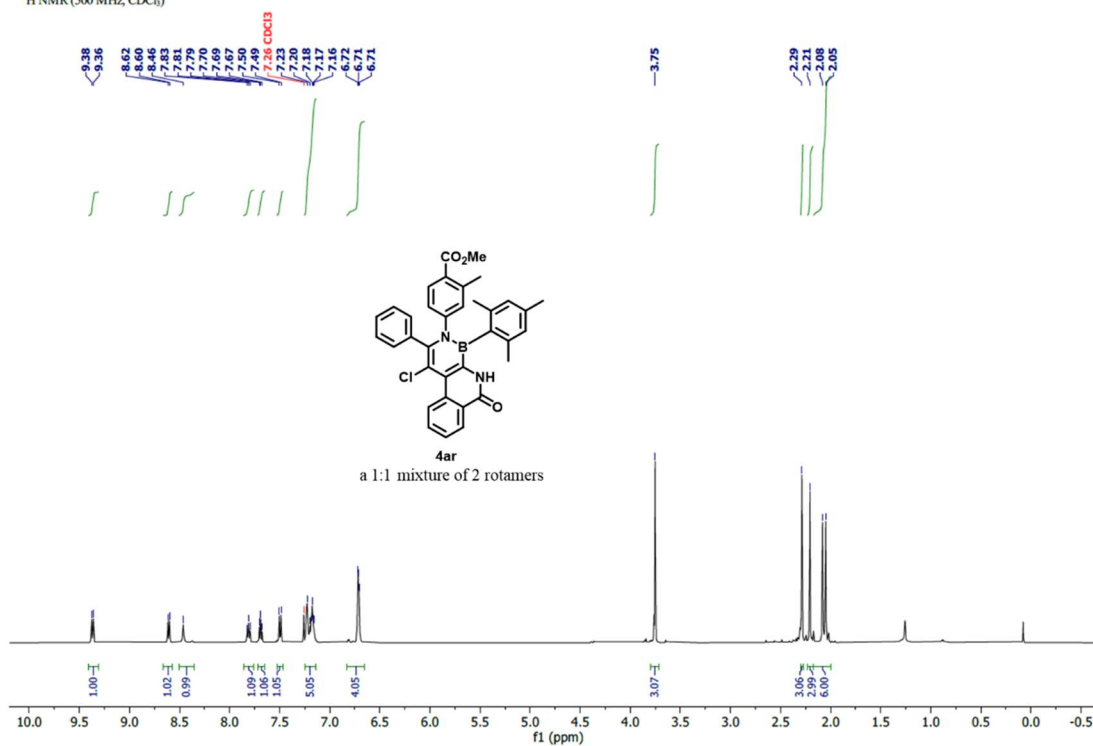
^{11}B NMR of **3m**

^{11}B NMR (160 MHz, CDCl_3)



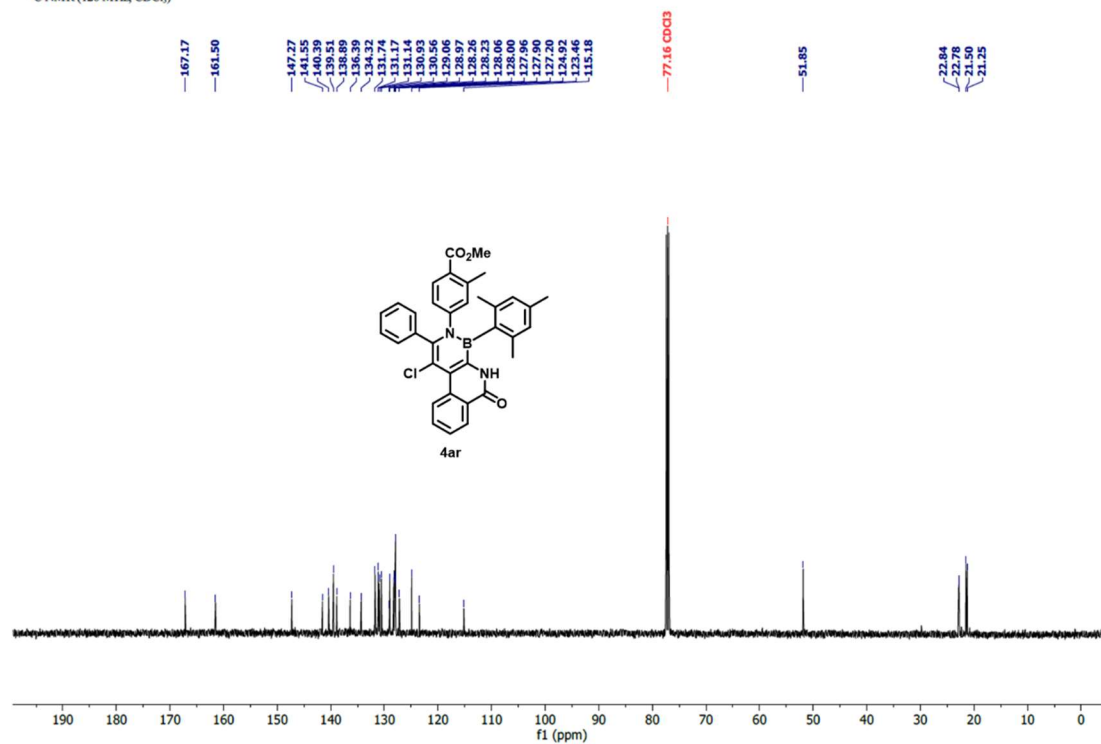
^1H NMR of **4ar**

^1H NMR (500 MHz, CDCl_3)



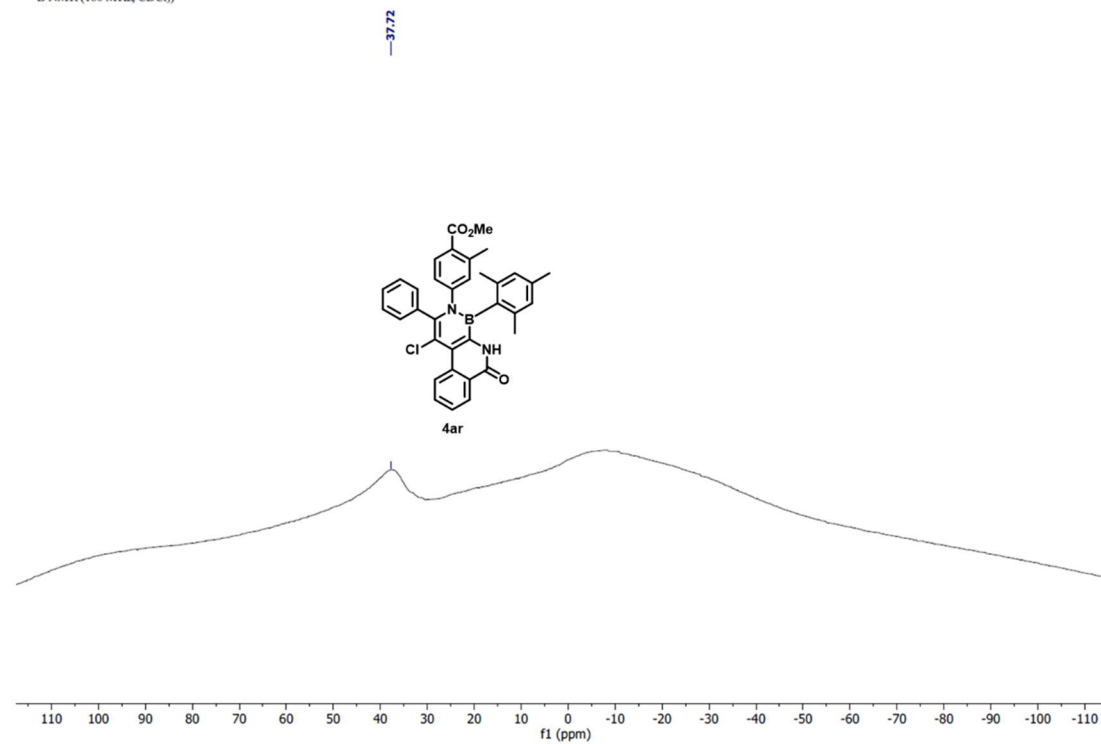
^{13}C NMR of 4ar

^{13}C NMR (126 MHz, CDCl_3)



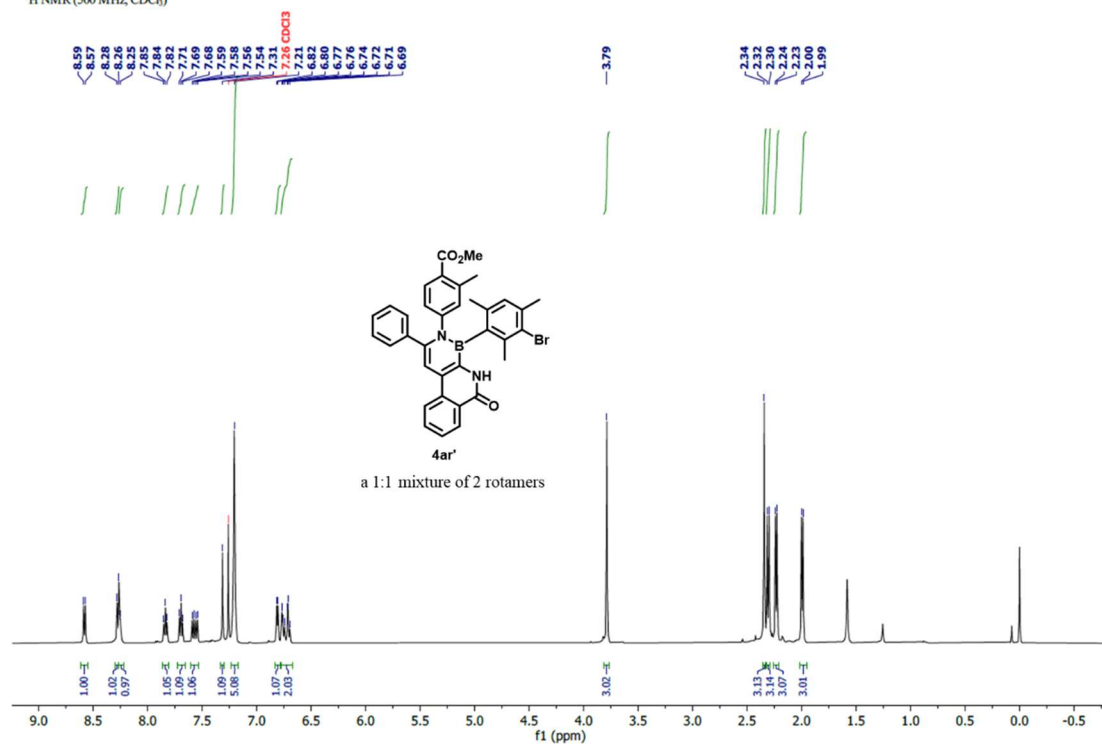
^{11}B NMR of 4ar

^{11}B NMR (160 MHz, CDCl_3)



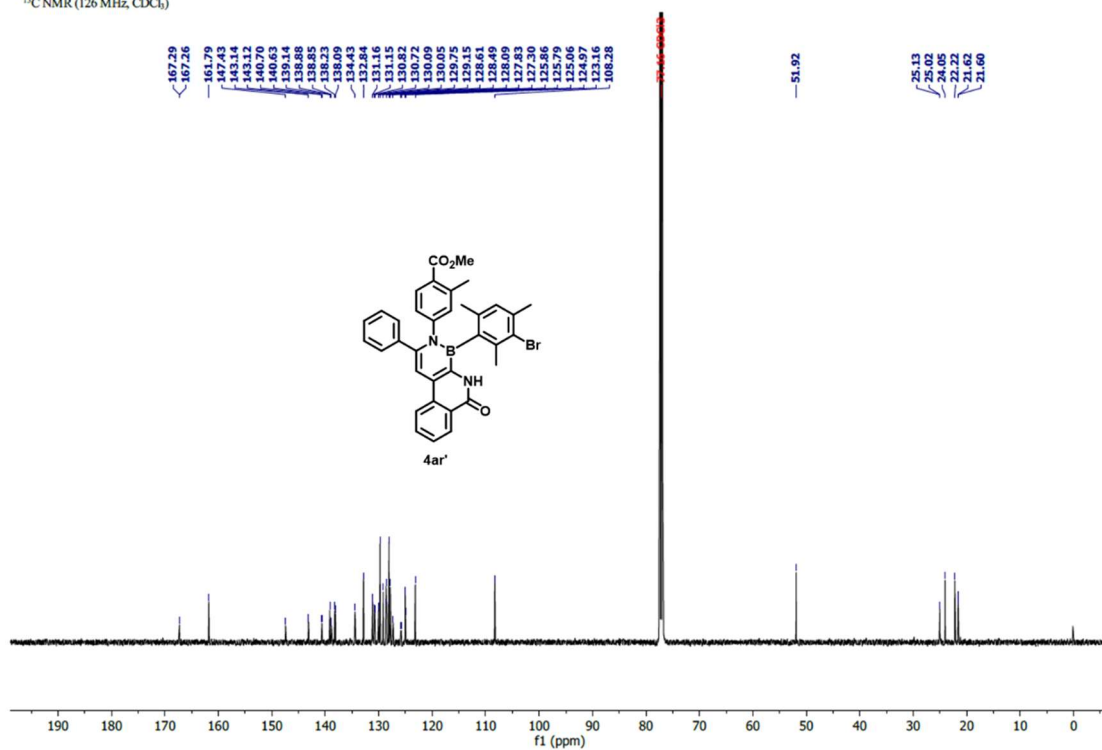
¹H NMR of 4ar'

¹H NMR (500 MHz, CDCl₃)



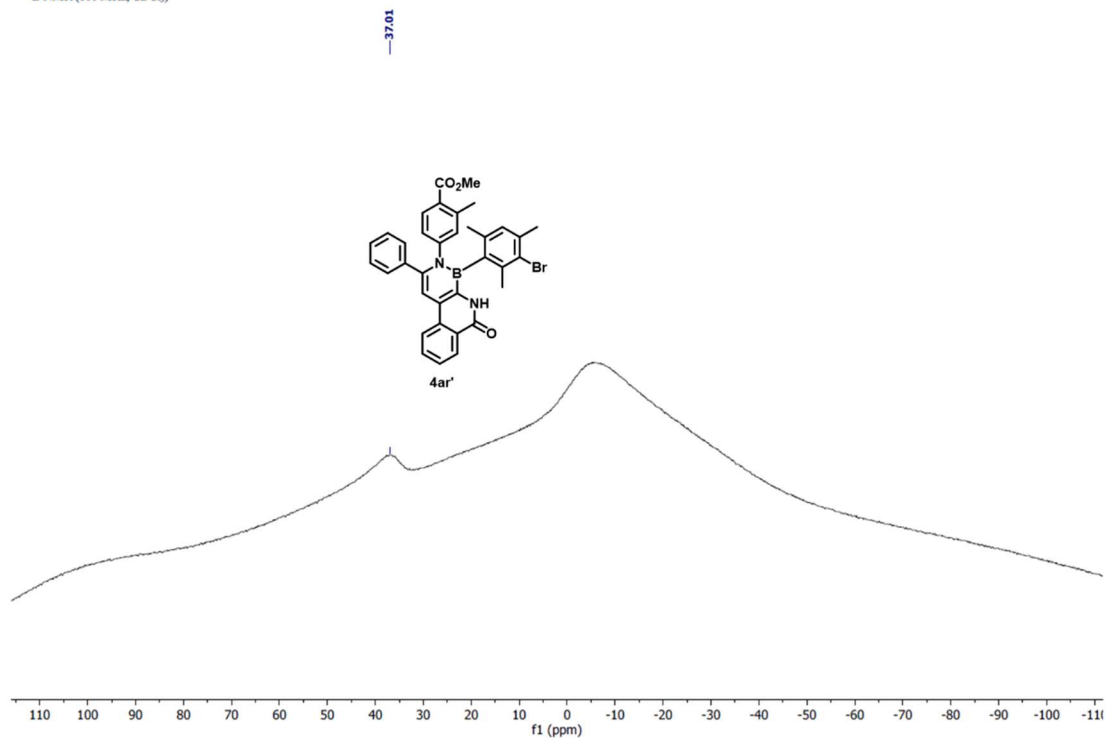
¹³C NMR of 4ar'

¹³C NMR (126 MHz, CDCl₃)



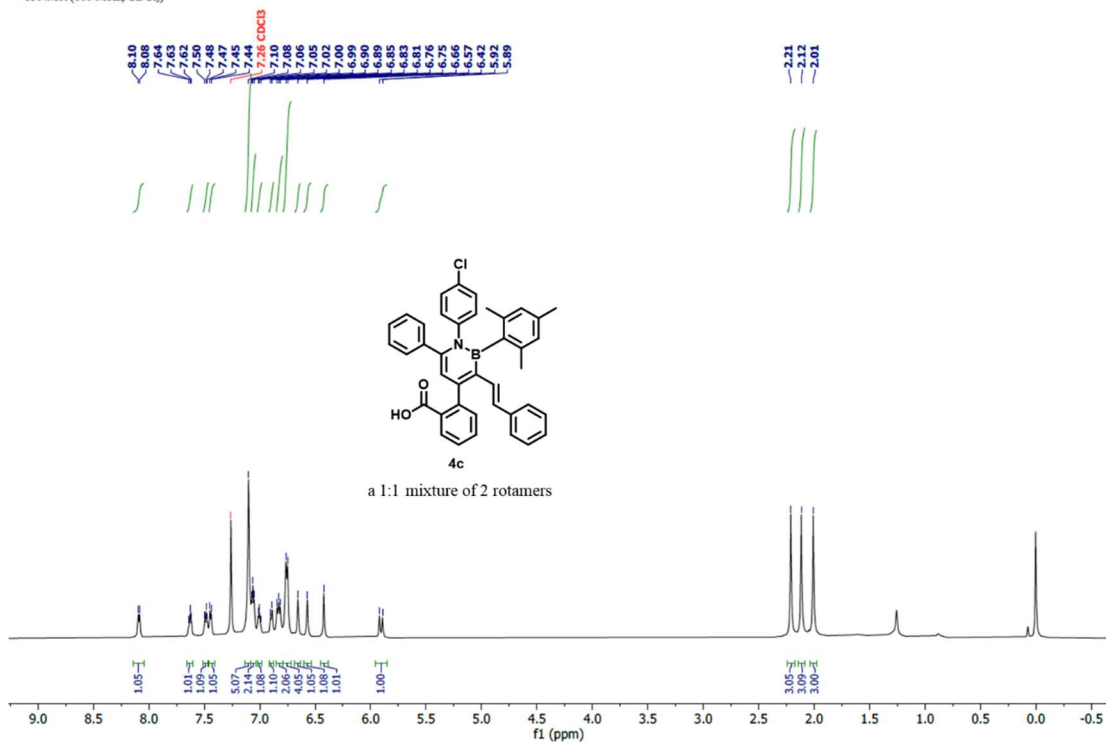
^{11}B NMR of **4ar'**

^{11}B NMR (160 MHz, CDCl_3)



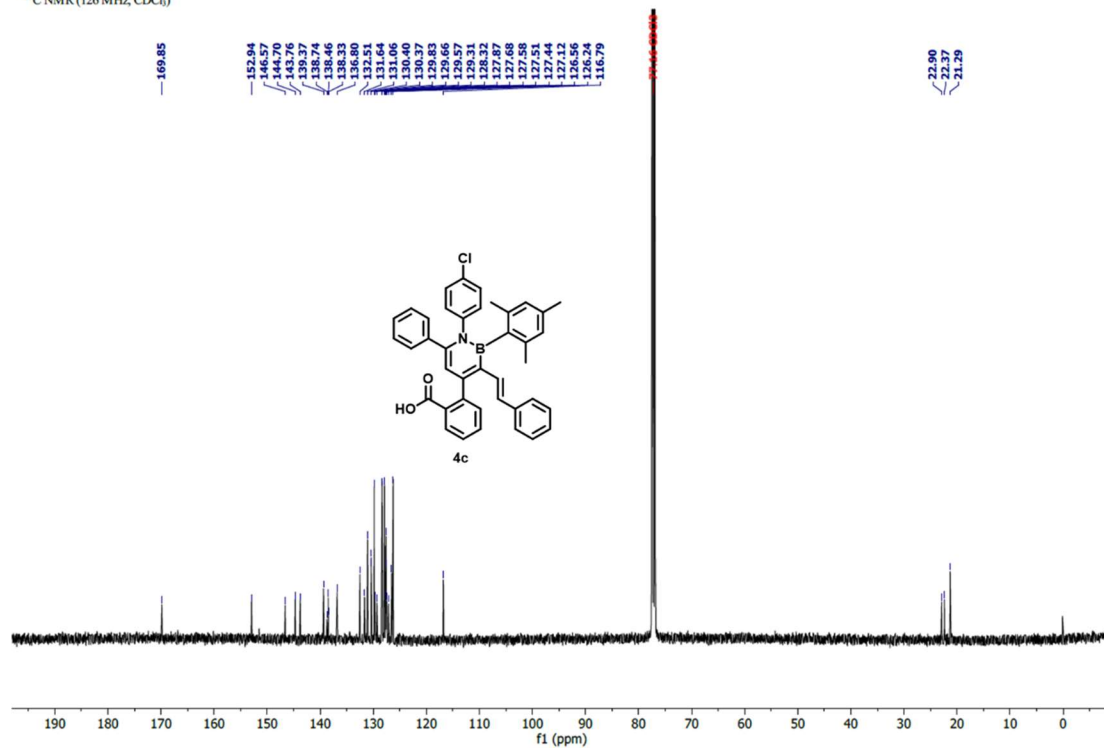
^1H NMR of **4c**

^1H NMR (600 MHz, CDCl_3)



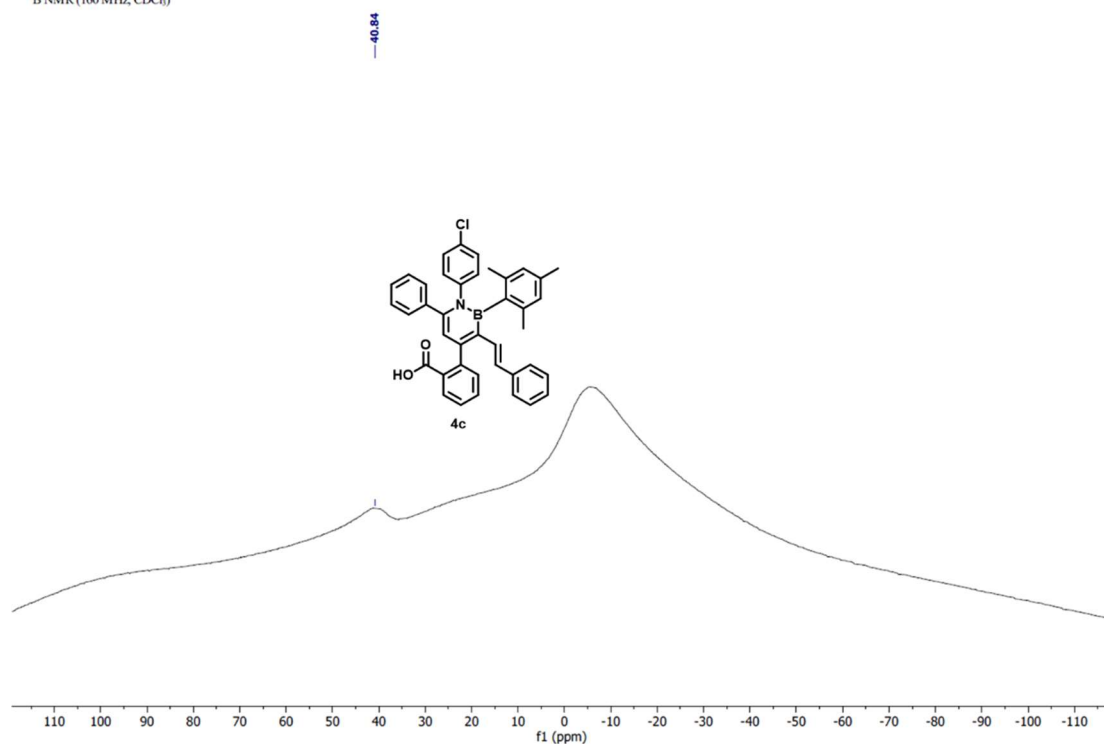
^{13}C NMR of **4c**

^{13}C NMR (126 MHz, CDCl_3)



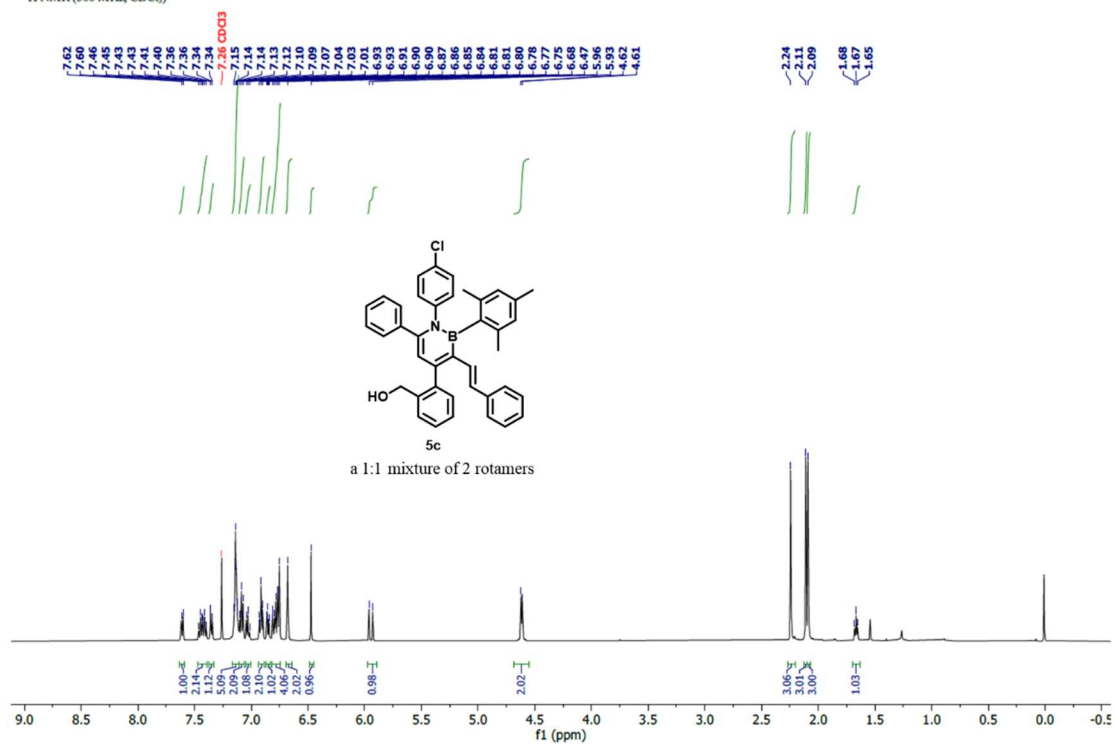
^{11}B NMR of **4c**

^{11}B NMR (160 MHz, CDCl_3)



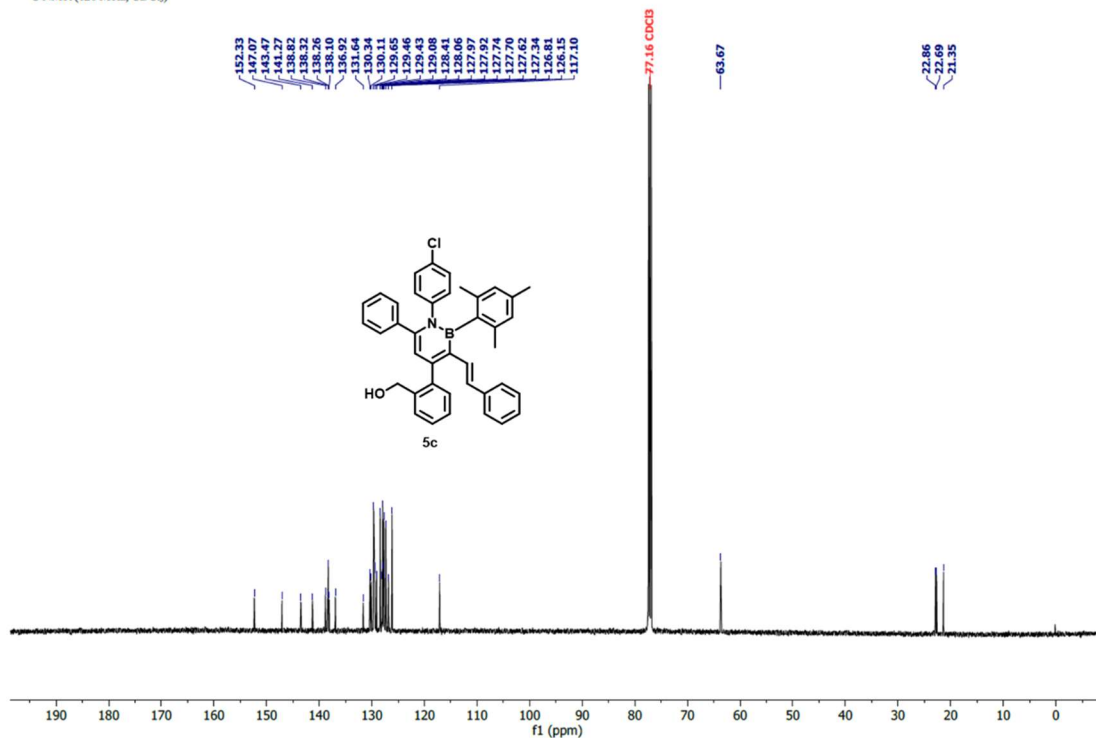
¹H NMR of 5c

¹H NMR (500 MHz, CDCl₃)



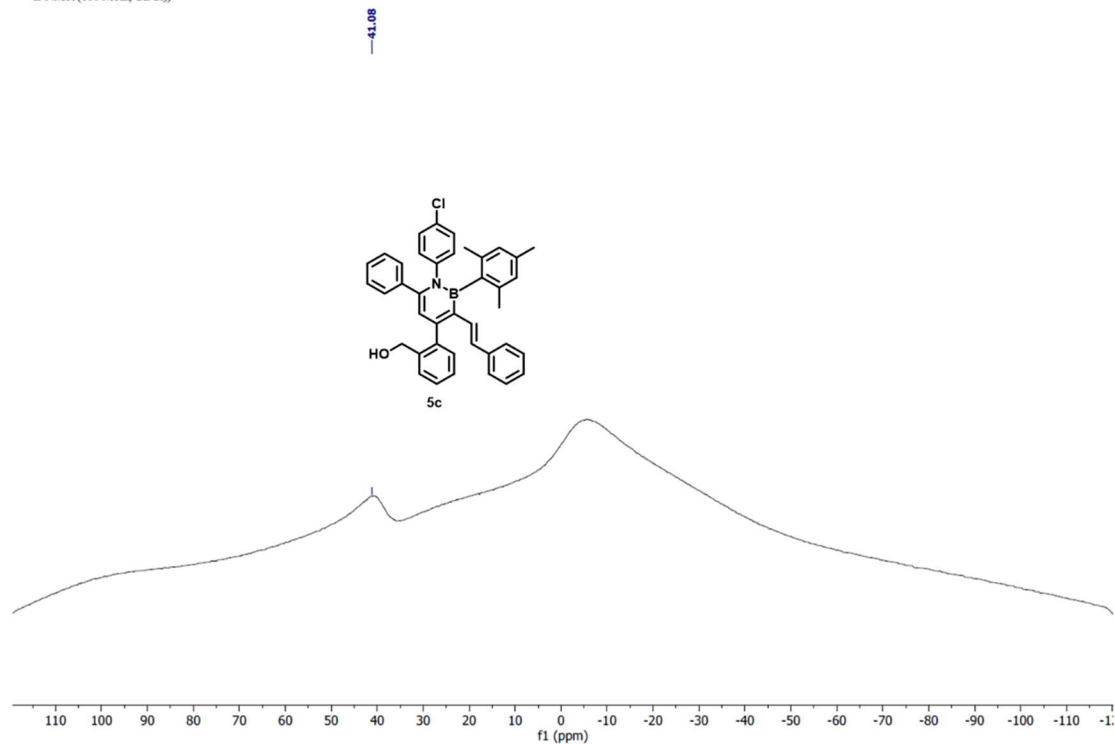
¹³C NMR of 5c

¹³C NMR (126 MHz, CDCl₃)



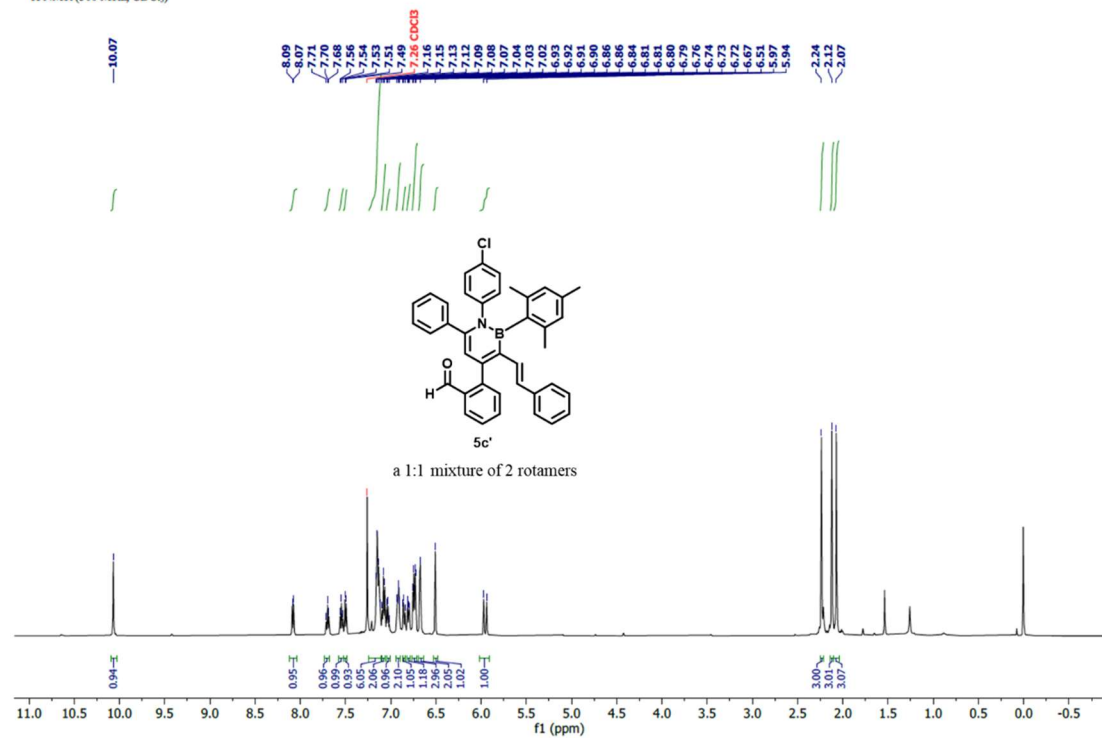
^{11}B NMR of **5c**

^{11}B NMR (160 MHz, CDCl_3)

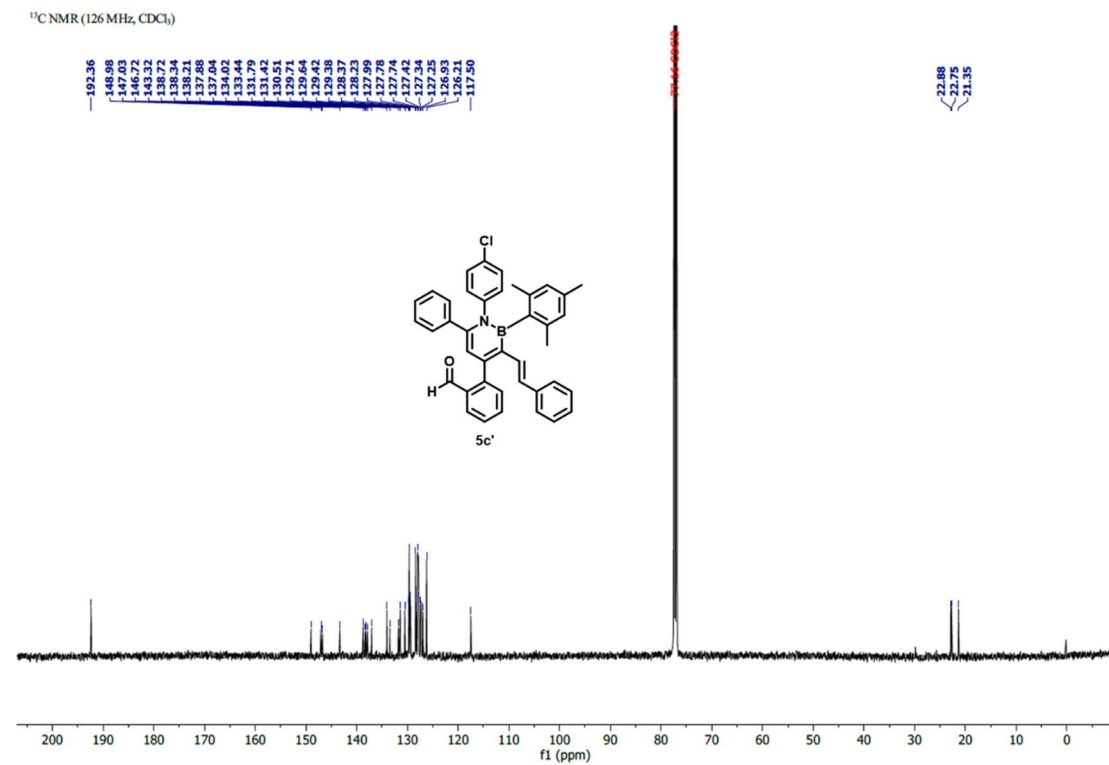


^1H NMR of **5c'**

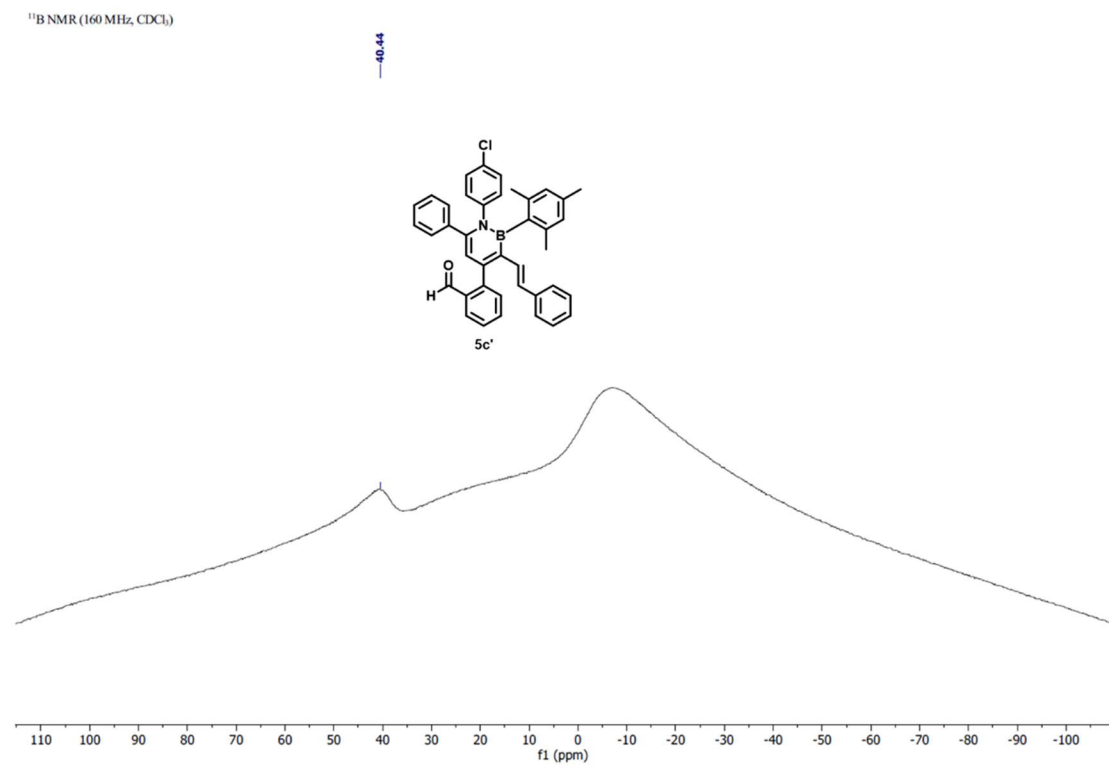
^1H NMR (500 MHz, CDCl_3)



^{13}C NMR of **5c'**

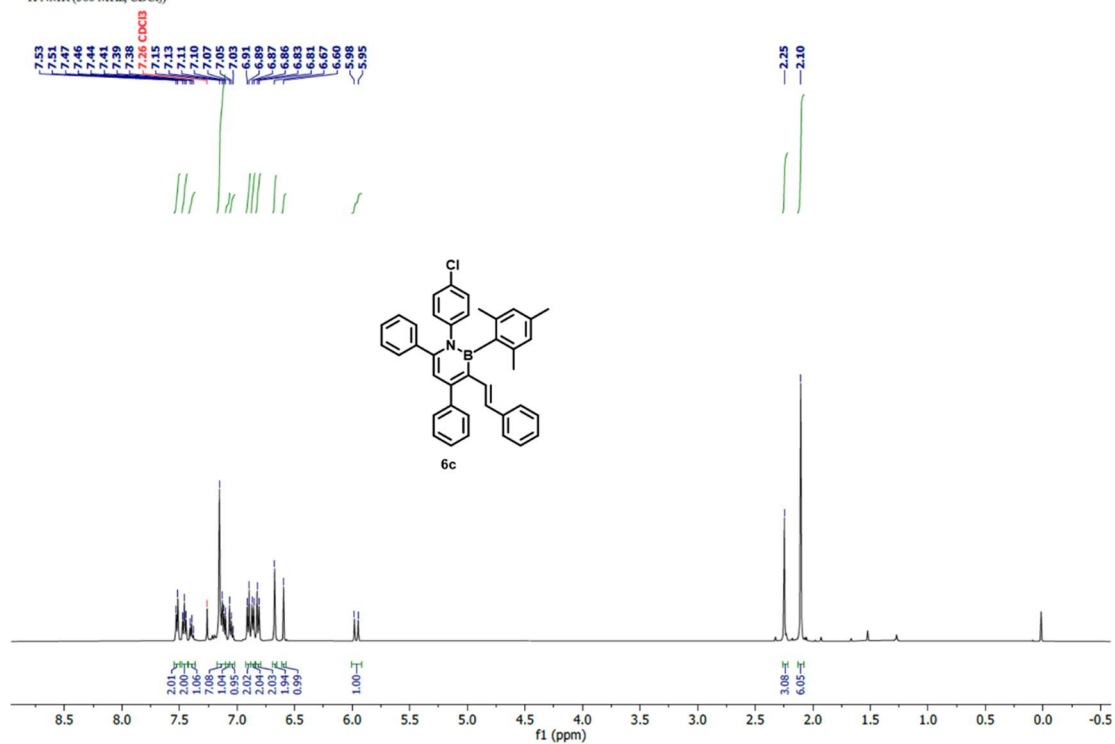


^{11}B NMR of **5c'**



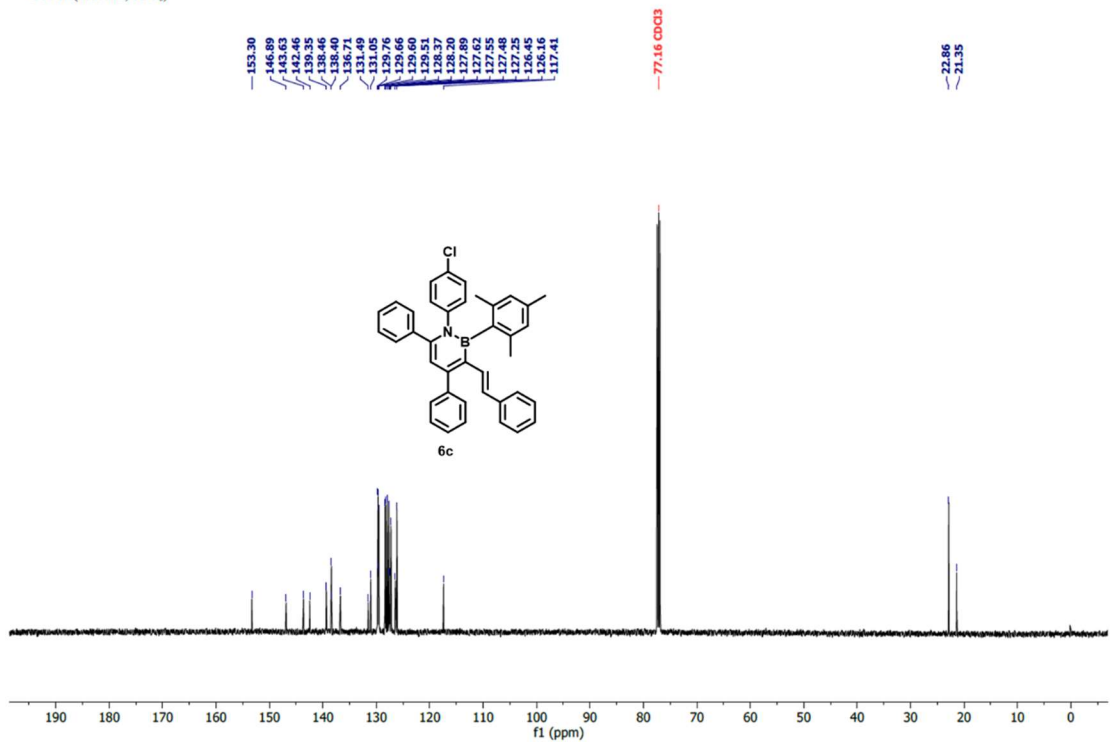
¹H NMR of 6c

¹H NMR (500 MHz, CDCl₃)



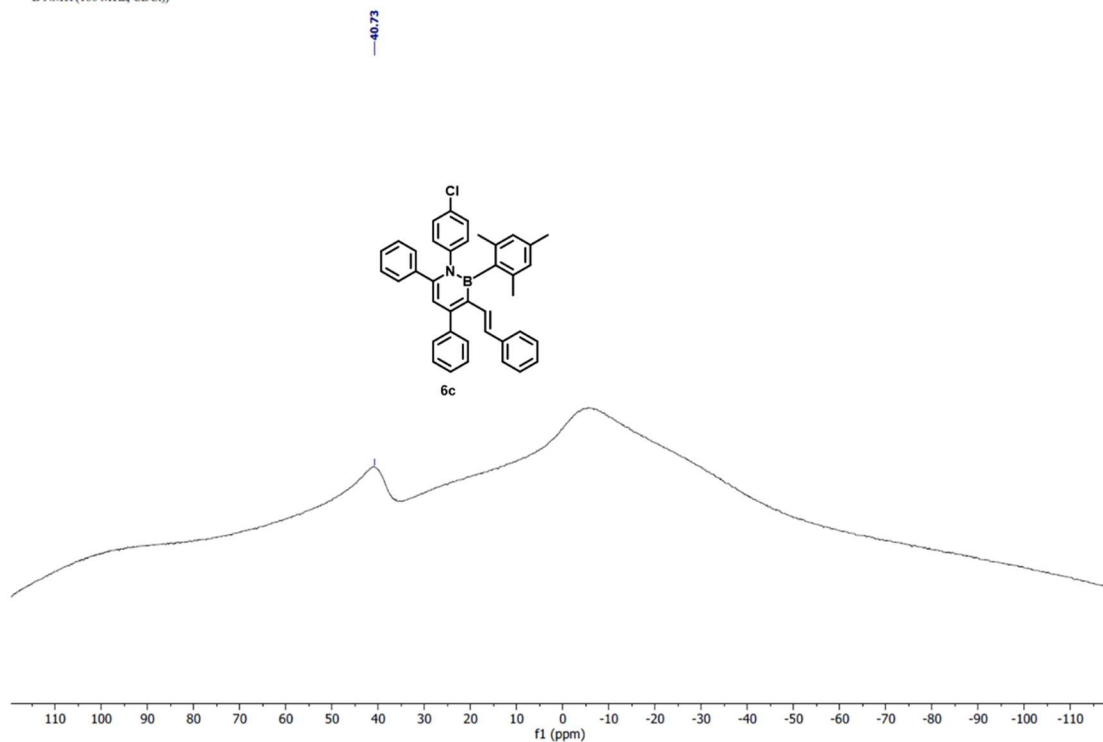
¹³C NMR of 6c

¹³C NMR (126 MHz, CDCl₃)



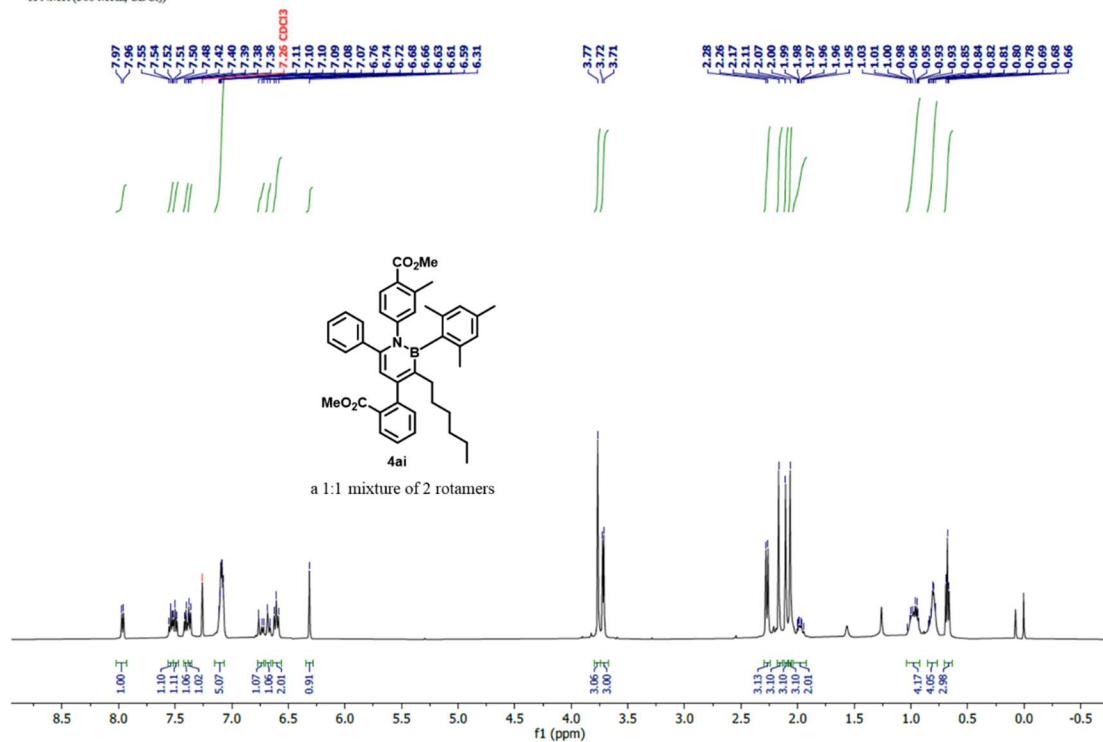
^{11}B NMR of **6c**

^{11}B NMR (160 MHz, CDCl_3)



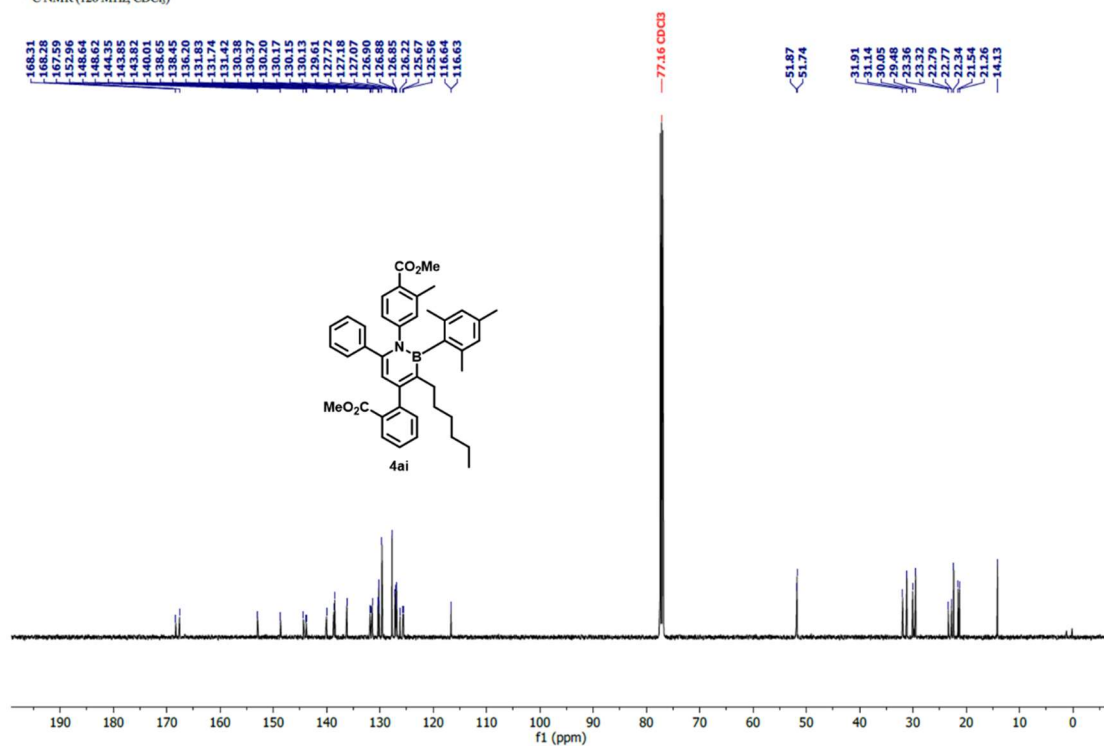
^1H NMR of **4ai**

^1H NMR (500 MHz, CDCl_3)



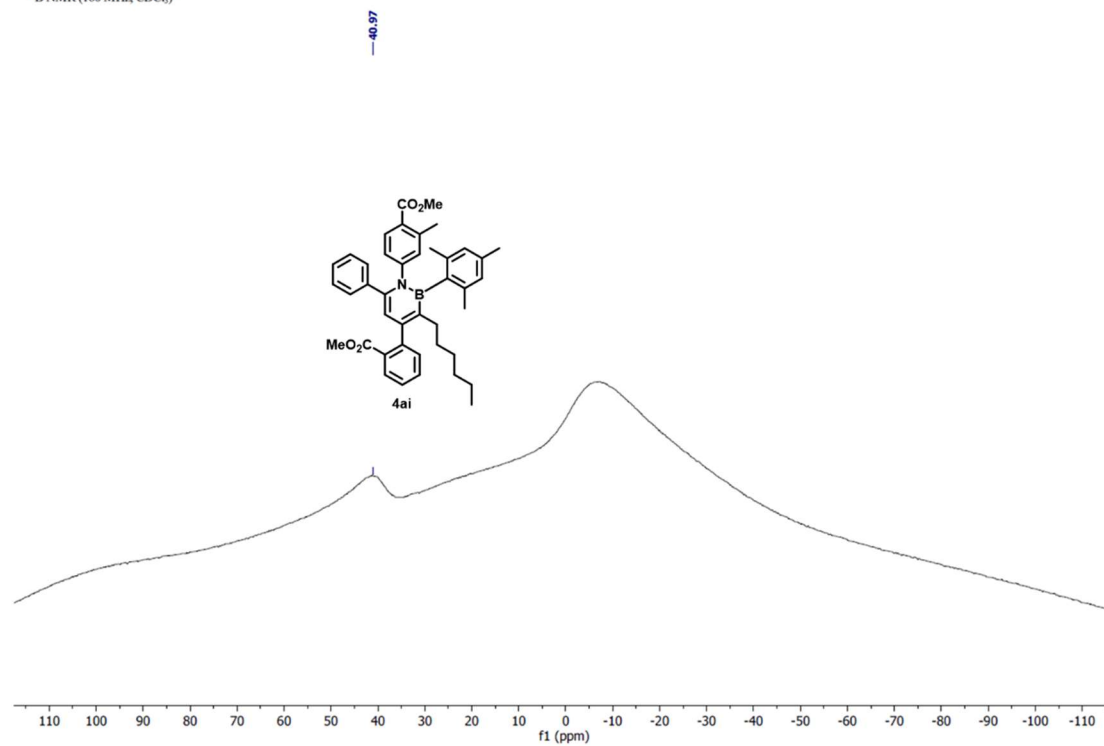
¹³C NMR of 4ai

¹³C NMR (126 MHz, CDCl₃)



¹¹B NMR of 4ai

¹¹B NMR (160 MHz, CDCl₃)



1.7. References

1. Wang, Z.; Zhang, C.; Wu, J.; Li, B.; Chrostowska, A.; Karamanis, P.; Liu, S.-Y. trans-Hydroalkynylation of Internal 1, 3-Enynes Enabled by Cooperative Catalysis. *J. Am. Chem. Soc.* **2023**, *145*, 5624-5630.
2. For examples of applications of 1,2-azaborines in medicinal chemistry, see: (a) Knack, D. H.; Marshall, J. L.; Harlow, G. P.; Dudzik, A.; Szaleniec, M.; Liu, S. Y.; Heider, J. BN/CC Isosteric Compounds as Enzyme Inhibitors: *N*- and *B*-Ethyl-1,2-azaborine Inhibit Ethylbenzene Hydroxylation as Nonconvertible Substrate Analogues. *Angew. Chem. Int. Ed.* **2013**, *52*, 2599-2601. (b) Zhao, P.; Nettleton, D. O.; Karki, R. G.; Zécéri, F. J.; Liu, S. Y. Medicinal Chemistry Profiling of Monocyclic 1,2-Azaborines. *ChemMedChem* **2017**, *12*, 358-361. (c) Boknevitc, K.; Italia, J. S.; Li, B.; Chatterjee, A.; Liu, S.-Y. Synthesis and characterization of an unnatural boron and nitrogen-containing tryptophan analogue and its incorporation into proteins. *Chem. Sci.* **2019**, *10*, 4994-4998. (d) Liu, Y.; Liu, S.-Y. Exploring the strength of a hydrogen bond as a function of steric environment using 1,2-azaborine ligands and engineered T4 lysozyme receptors. *Org. Biomol. Chem.* **2019**, *17*, 7002-7006.
3. Subbaiah, M. A.; Meanwell, N. A. Bioisosteres of the phenyl ring: recent strategic applications in lead optimization and drug design. *J. Med. Chem.* **2021**, *64*, 14046-14128.
4. For selected examples, see: (a) Marwitz, A. J.; Jenkins, J. T.; Zakharov, L. N.; Liu, S.-Y. 1,2-Azaborine Cations. *Angew. Chem. Int. Ed.* **2010**, *49*, 7444-7447. (b) Wan, W.-M.; Baggett, A. W.; Cheng, F.; Lin, H.; Liu, S.-Y.; Jäkle, F. Synthesis by free radical polymerization and properties of BN-polystyrene and BN-poly(vinylbiphenyl). *Chem. Commun.* **2016**, *52*, 13616-13619. (c) Lin, H.; McConnell, C. R.; Jilus, B.; Liu, S.-Y.; Jäkle, F. Changing up BN-polystyrene: effect of substitution pattern on the free-radical polymerization and polymer properties. *Macromolecules*

- 2019**, *52*, 4500-4509. (d) Chen, M.; Unikela, K. S.; Ramalakshmi, R.; Li, B.; Darrigan, C.; Chrostowska, A.; Liu, S. Y. A BN-Doped Cycloparaphenylene Debuts. *Angew. Chem. Int. Ed.* **2021**, *60*, 1556-1560.
5. Hatakeyama, T.; Hashimoto, S.; Oba, T.; Nakamura, M. Azaboradibenzo[6]helicene: carrier inversion induced by helical homochirality. *J. Am. Chem. Soc.* **2012**, *134*, 19600-19603.
6. Braunschweig, H.; Hörl, C.; Mailänder, L.; Radacki, K.; Wahler, J. Antiaromaticity to Aromaticity: From Boroles to 1,2-Azaborinines by Ring Expansion with Azides. *Chem. -Eur. J.* **2014**, *20*, 9858-9861.
7. Schäfer, M.; Schäfer, J.; Dewhurst, R. D.; Ewing, W. C.; Krahfuß, M.; Kuntze-Fechner, M. W.; Wehner, M.; Lambert, C.; Braunschweig, H. Regioselective Catalytic and Stepwise Routes to Bulky, Functional-Group-Appended, and Luminescent 1, 2-Azaborinines. *Chem. -Eur. J.* **2016**, *22*, 8603-8609.
8. Heß, M.; Krummenacher, I.; Dellermann, T.; Braunschweig, H. Rhodium-Mediated Stoichiometric Synthesis of Mono-, Bi-, and Bis-1,2-Azaborinines: 1-Rhoda-3,2-azaboroles as Reactive Precursors. *Chem. -Eur. J.* **2021**, *27*, 9503-9507.
9. For selected reviews on 1,2-azaborine chemistry, see: (a) Campbell, P. G.; Marwitz, A. J.; Liu, S. Y. Recent advances in azaborine chemistry. *Angew. Chem. Int. Ed.* **2012**, *51*, 6074-6092. (b) Bélanger-Chabot, G.; Braunschweig, H.; Roy, D. K. Recent developments in azaborinine chemistry. *Eur. J. Inorg. Chem.* **2017**, *2017*, 4353-4368. (c) Giustra, Z. X.; Liu, S.-Y. The state of the art in azaborine chemistry: new synthetic methods and applications. *J. Am. Chem. Soc.* **2018**, *140*, 1184-1194. (d) McConnell, C. R.; Liu, S.-Y. Late-stage functionalization of BN-heterocycles. *Chem. Soc. Rev.* **2019**, *48*, 3436-3453.

10. Pan, J.; Kampf, J. W.; Ashe, A. J. 1,2-Azaboratabenzene: A heterocyclic π -ligand with an adjustable basicity at nitrogen. *Organometallics* **2004**, *23*, 5626-5629.
11. Pan, J.; Kampf, J. W.; Ashe III, A. J. The Preparation and Crystal Structures of η^1 -Derivatives of 2-Phenyl-1, 2-azaboratabenzene. *Organometallics* **2008**, *27*, 1345-1347.
12. Abbey, E. R.; Lamm, A. N.; Baggett, A. W.; Zakharov, L. N.; Liu, S.-Y. Protecting group-free synthesis of 1,2-azaborines: a simple approach to the construction of BN-benzenoids. *J. Am. Chem. Soc.* **2013**, *135*, 12908-12913.
13. Burford, R. J.; Li, B.; Vasiliu, M.; Dixon, D. A.; Liu, S. Y. Diels–Alder Reactions of 1,2-Azaborines. *Angew. Chem. Int. Ed.* **2015**, *54*, 7823-7827.
14. Baggett, A. W.; Liu, S.-Y. A Boron Protecting Group Strategy for 1,2-Azaborines. *J. Am. Chem. Soc.* **2017**, *139*, 15259-15264.
15. Marwitz, A. J.; Abbey, E. R.; Jenkins, J. T.; Zakharov, L. N.; Liu, S.-Y. Diversity through isosterism: the case of boron-substituted 1,2-dihydro-1,2-azaborines. *Org. Lett.* **2007**, *9*, 4905-4908.
16. Marwitz, A. J.; McClintock, S. P.; Zakharov, L. N.; Liu, S.-Y. BN benzonitrile: an electron-deficient 1,2-dihydro-1,2-azaborine featuring linkage isomerism. *Chem. Commun.* **2010**, *46*, 779-781.
17. Rudebusch, G. E.; Zakharov, L. N.; Liu, S. Y. Rhodium-Catalyzed Boron Arylation of 1,2-Azaborines. *Angew. Chem. Int. Ed.* **2013**, *52*, 9316-9319.
18. Brown, A. N.; Zakharov, L. N.; Mikulas, T.; Dixon, D. A.; Liu, S.-Y. Rhodium-catalyzed B–H activation of 1,2-azaborines: synthesis and characterization of BN isosteres of stilbenes. *Org. Lett.* **2014**, *16*, 3340-3343.

19. Pan, J.; Kampf, J. W.; Ashe, A. J. Electrophilic aromatic substitution reactions of 1,2-dihydro-1,2-azaborines. *Org. Lett.* **2007**, *9*, 679-681.
20. Brown, A. N.; Li, B.; Liu, S.-Y. Negishi cross-coupling is compatible with a reactive B–Cl bond: development of a versatile late-stage functionalization of 1,2-azaborines and its application to the synthesis of new BN isosteres of naphthalene and indenyl. *J. Am. Chem. Soc.* **2015**, *137*, 8932-8935.
21. Brown, A. N.; Li, B.; Liu, S.-Y. Expanding the functional group tolerance of cross-coupling in 1,2-dihydro-1,2-azaborines: Installation of alkyl, alkenyl, aryl, and heteroaryl substituents while maintaining a B–H bond. *Tetrahedron* **2019**, *75*, 580-583.
22. Baggett, A. W.; Vasiliu, M.; Li, B.; Dixon, D. A.; Liu, S.-Y. Late-stage functionalization of 1,2-dihydro-1,2-azaborines via regioselective iridium-catalyzed C–H borylation: the development of a new N,N-bidentate ligand scaffold. *J. Am. Chem. Soc.* **2015**, *137*, 5536-5541.
23. Zhang, Y.; Dan, W.; Fang, X. Metal nitrate mediated regioselective nitration of BN-substituted arenes. *Organometallics* **2017**, *36*, 1677-1680.
24. Zhang, Y.; Sun, F.; Dan, W.; Fang, X. Friedel–Crafts Acylation Reactions of BN-Substituted Arenes. *J. Org. Chem.* **2017**, *82*, 12877-12887.
25. (a) The C-H borylation method gave a mixture of C4 and C5 products, see: McConnell, C. R.; Haeffner, F.; Baggett, A. W.; Liu, S.-Y. 1,2-Azaborine's Distinct Electronic Structure Unlocks Two New Regioisomeric Building Blocks via Resolution Chemistry. *J. Am. Chem. Soc.* **2019**, *141*, 9072-9078. (b) For a single example of C4-selective borylation with a bulky substrate, see: Robichaud, H. M.; Ishibashi, J. S. A.; Ozaki, T.; Lamine, W.; Miqueu, K.; Liu, S.-Y. The aromatic Claisen rearrangement of a 1,2-azaborine. *Org. Biomol. Chem.* **2023**, *21*, 3778-3783.

26. Lyu, H.; Tugwell, T. H.; Chen, Z.; Kukier, G. A.; Turlik, A.; Wu, Y.; Houk, K.; Liu, P.; Dong, G. Modular synthesis of 1,2-azaborines via ring-opening BN-isostere benzannulation. *Nat. Chem.* **2024**, *16*, 269-276.
27. For selected reviews on Pd/norbornene chemistry, see: (a) Catellani, M. Catalytic Multistep Reactions via Palladacycles. *Synlett* **2003**, *3*, 298-313. (b) Martins, A.; Mariampillai, B.; Lautens, M. Synthesis in the Key of Catellani: Norbornene-Mediated *ortho* C-H Functionalization. *Top. Curr. Chem.* **2009**, *292*, 1-33. (c) Ye, J.; Lautens, M. Palladium-Catalysed Norbornene-Mediated C-H Functionalization of Arenes. *Nat. Chem.* **2015**, *7*, 863-870. (d) Della Ca', N.; Fontana, M.; Motti, E.; Catellani, M. Pd/Norbornene: A Winning Combination for Selective Aromatic Functionalization via C-H Bond Activation. *Acc. Chem. Res.* **2016**, *49*, 1389-1400. (e) Liu, Z.-S.; Gao, Q.; Cheng, H.-G.; Zhou, Q. Alkylating Reagents Employed in Catellani-Type Reactions. *Chem. -Eur. J.* **2018**, *24*, 15461-15476. (f) Zhao, K.; Ding, L.; Gu, Z. Development of New Electrophiles in Palladium/Norbornene-Catalyzed *ortho*-Functionalization of Aryl Halides. *Synlett* **2019**, *30*, 129-140. (g) Wang, J.; Dong, G. Palladium/Norbornene Cooperative Catalysis. *Chem. Rev.* **2019**, *119*, 7478-7528. (h) Li, R.; Dong, G. Structurally Modified Norbornenes: A Key Factor to Modulate Reaction Selectivity in the Palladium/Norbornene Cooperative Catalysis. *J. Am. Chem. Soc.* **2020**, *142*, 17859-17875. (i) Chen, Z.; Zhang, F. Recent progress on Catellani reaction. *Tetrahedron* **2023**, *134*, 133307.
28. For the seminal study by Catellani, see: Catellani, M.; Frignani, F.; Rangoni, A. A Complex Catalytic Cycle Leading to a Regioselective Synthesis of *o,o'*-Disubstituted Vinylarenes. *Angew. Chem. Int. Ed. Engl.* **1997**, *36*, 119-122.
29. Catellani, M.; Chiusoli, G. P. Palladium-(II) and-(IV) complexes as intermediates in catalytic C-C bond-forming reactions. *J. Organomet. Chem.* **1988**, *346*, C27-C30.

30. For selected examples of 1,2-difunctionalization of heterocycles by Pd/NBE catalysis, see: (a) Mitsudo, K.; Thansandote, P.; Wilhelm, T.; Mariampillai, B.; Lautens, M. Selectively Substituted Thiophenes and Indoles by a Tandem Palladium-Catalyzed Multicomponent Reaction. *Org. Lett.* **2006**, *8*, 3939-3942. (b) Wilson, J. E. Palladium-catalyzed Catellani-type couplings using methylating reagents for the synthesis of highly substituted *ortho*-methyl-arenes and heteroarenes. *Tetrahedron Lett.* **2016**, *57*, 5053-5056. (c) Li, R.; Zhou, Y.; Xu, X.; Dong, G. Direct Vicinal Difunctionalization of Thiophenes Enabled by the Palladium/Norbornene Cooperative Catalysis. *J. Am. Chem. Soc.* **2019**, *141*, 18958-18963. (d) Padhi, B.; Kang, G.; Kim, E.; Ha, J.; Kim, H. T.; Lim, J.; Joo, J. M. Pd-Catalyzed C-H Annulation of Five-Membered Heteroaryl Halides with Norbornene Derivatives. *ACS Catal.* **2020**, *10*, 1792-1798. (e) Li, R.; Dong, G. Redox-Neutral Vicinal Difunctionalization of Five-Membered Heteroarenes with Dual Electrophiles. *Angew. Chem. Int. Ed.* **2021**, *60*, 26184-26191. (f) Liu, X.; Zhou, Y.; Qi, X.; Li, R.; Liu, P.; Dong, G. Palladium/Norbornene-Catalyzed Direct Vicinal Di-Carbo-Functionalization of Indoles: Reaction Development and Mechanistic Study. *Angew. Chem. Int. Ed.* **2023**, *62*, e202310697.
31. Campbell, P. G.; Abbey, E. R.; Neiner, D.; Grant, D. J.; Dixon, D. A.; Liu, S.-Y. Resonance stabilization energy of 1,2-azaborines: a quantitative experimental study by reaction calorimetry. *J. Am. Chem. Soc.* **2010**, *132*, 18048-18050.
32. Attempts to use non-*B*-Mes-substituted 1,2-azaborines as substrates were unsuccessful at this stage due to rapid decomposition under the Pd/NBE catalysis conditions.
33. Cárdenas, D. J.; Martín-Matute, B.; Echavarren, A. M. Aryl transfer between Pd (II) centers or Pd (IV) intermediates in Pd-catalyzed domino reactions. *J. Am. Chem. Soc.* **2006**, *128*, 5033-5040.

34. (a) Wang, J.; Zhou, Y.; Xu, X.; Liu, P.; Dong, G. Entry to 1,2,3,4-tetrasubstituted arenes through addressing the “*meta* constraint” in the palladium/norbornene catalysis. *J. Am. Chem. Soc.* **2020**, *142*, 3050-3059. (b) Wang, J.; Dong, Z.; Yang, C.; Dong, G. Modular and regioselective synthesis of all-carbon tetrasubstituted olefins enabled by an alkenyl Catellani reaction. *Nat. Chem.* **2019**, *11*, 1106-1112.
35. Wang, P.; Farmer, M. E.; Yu, J. Q. Ligand-Promoted *meta*-C–H Functionalization of Benzylamines. *Angew. Chem. Int. Ed.* **2017**, *56*, 5125-5129.
36. Shen, P.-X.; Wang, X.-C.; Wang, P.; Zhu, R.-Y.; Yu, J.-Q. Ligand-enabled *meta*-C–H alkylation and arylation using a modified norbornene. *J. Am. Chem. Soc.* **2015**, *137*, 11574-11577.
37. Besides arylation and alkylation, amination and acylation have also been initially explored for the ortho coupling, which, however, remain unfruitful at this stage.
38. Nicolaou, K.; Estrada, A. A.; Zak, M.; Lee, S. H.; Safina, B. S. A mild and selective method for the hydrolysis of esters with trimethyltin hydroxide. *Angew. Chem. Int. Ed.* **2005**, *44*, 1378-1382.
39. Efforts to remove the Mes group from boron were unfruitful at this stage, which will be further explored.
40. Wessjohann, L.; Giller, K.; Zuck, B.; Skatteboel, L.; de Meijere, A. Facile synthesis of stable analogs of 2-oxocyclobutanecarboxylates: 2-[(diphenylmethylene)amino]cyclobutenecarboxylates, derivatives and reactions. *J. Org. Chem.* **1993**, *58*, 6442-6450.
41. Devillard, M.; Brousses, R.; Miqueu, K.; Bouhadir, G.; Bourissou, D. A Stable but Highly Reactive Phosphine-Coordinated Borenium: Metal-free Dihydrogen Activation and Alkyne 1, 2-Carboboration. *Angew. Chem. Int. Ed.* **2015**, *54*, 5722-5726.

42. Wang, J.; Dong, Z.; Yang, C.; Dong, G. Modular and regioselective synthesis of all-carbon tetrasubstituted olefins enabled by an alkenyl Catellani reaction. *Nat. Chem.* **2019**, *11*, 1106-1112.
43. Verkruijsse, H.; Brandsma, L. Preparative metallation of norbornene and norbornadiene. *Recl. Trav. Chim. Pays-Bas.* **1986**, *105*, 66-68.
44. Wang, J.; Zhou, Y.; Xu, X.; Liu, P.; Dong, G. Entry to 1,2,3,4-tetrasubstituted arenes through addressing the “*meta* constraint” in the palladium/norbornene catalysis. *J. Am. Chem. Soc.* **2020**, *142*, 3050-3059.

CHAPTER 2

Modular Synthetic Platform for Interior-Functionalized Dendritic Macromolecules Enabled by the Palladium/Norbornene Catalysis

2.1. Introduction

Materials with a demanding synthetic process are often avoided for practicality reasons, despite exhibiting promising properties. In general, it is until the synthetic burden is alleviated by a more efficient and user-friendly method that the value of these materials can be better recognized. One such example is multi-functionalized dendronized macromolecules (*e.g.* dendrimers, dendronized polymers).¹ Building on the unique properties of the bulky monodisperse dendronized three-dimensional architecture, the addition of multiple functional groups (FGs) to each layer can synergistically influence their solubility,^{2a,b} viscosity,^{2c} chain conformation,^{2d} core-shell compartmentation,^{2e} and other properties.² Thus, they offer an excellent platform for enabling high-end applications in drug delivery, sensing, and nanotechnology.³ Unfortunately, this promise is hampered by lengthy synthetic routes to access these materials and inefficiency of introducing FGs.¹⁻²

While it is straightforward to introduce FGs to the core of dendrimers or the periphery of dendrons,⁴ incorporating different FGs into interior layers (*i.e.* generations) of dendrons, which can maximize versatility offered by the layered architecture, has been challenging. To date, two

strategies are known for internal functionalization of dendrons. The first one, namely the pre-functionalization strategy, employs tetrafunctionalized monomers prepared in advance (Figure 2.1A).^{4a,5} The accessibility of such highly functionalized branched monomers could be a concern. In addition, the functionalization reaction needs to be chemically orthogonal to the dendron growth reaction, which is another strict requirement.^{4a} The alternative post-functionalization strategy—FGs are coupled at dendrons' reactive sites after the macromolecular synthesis—was less time-consuming, yet unlikely suitable for generation-specific modification, and prone to defects (Figure 2.1B).^{4a,6} Hence, a more straightforward paradigm, in which the internal FGs are modularly installed onto a simple difunctionalized monomer during the dendron growth (Figure 2.1C), would serve as an almost ideal approach to prepare interior-functionalized dendritic macromolecules. Herein, we describe the first and preliminary development of a modular *in-situ* functionalization strategy for convergent synthesis of dendritic macromolecules containing generation-specific FGs and all-carbon backbones.

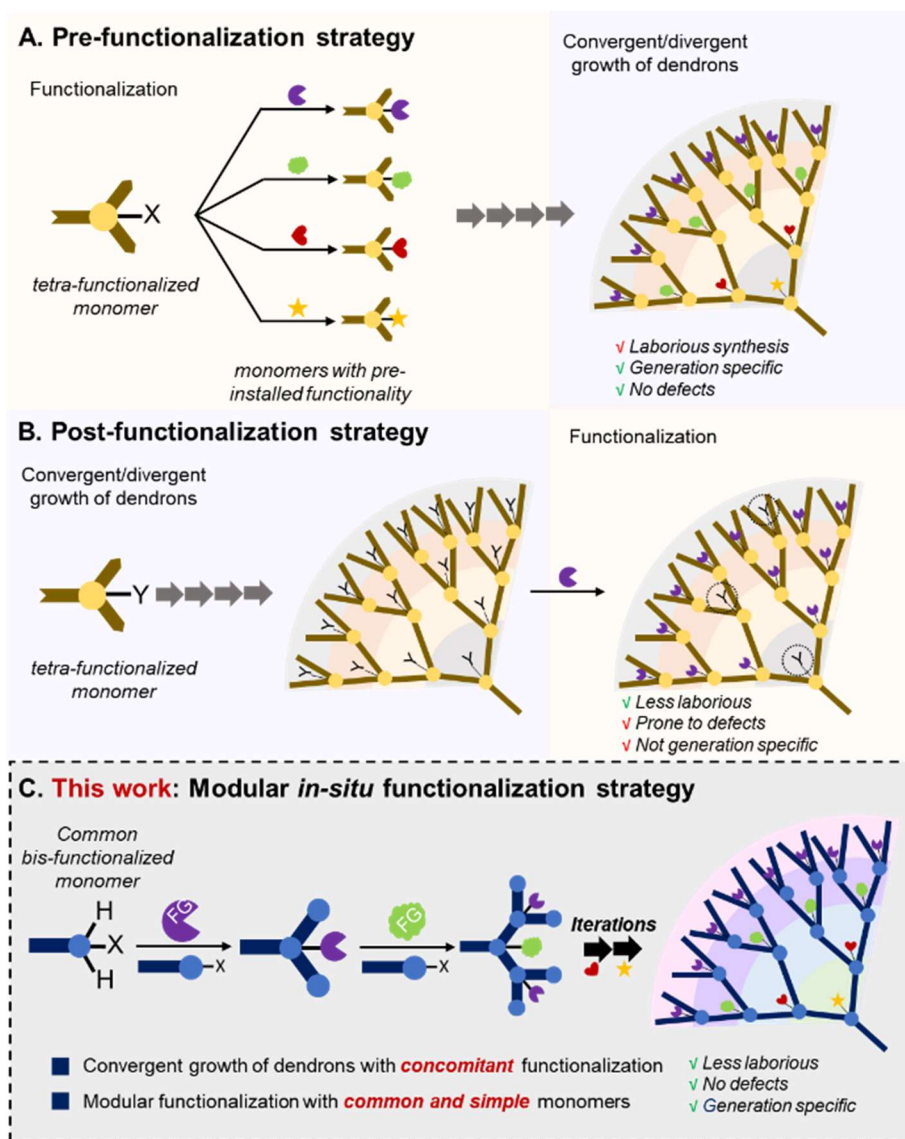


Figure 2.1. Synthetic strategies for the interior-layer functionalization of dendrons.

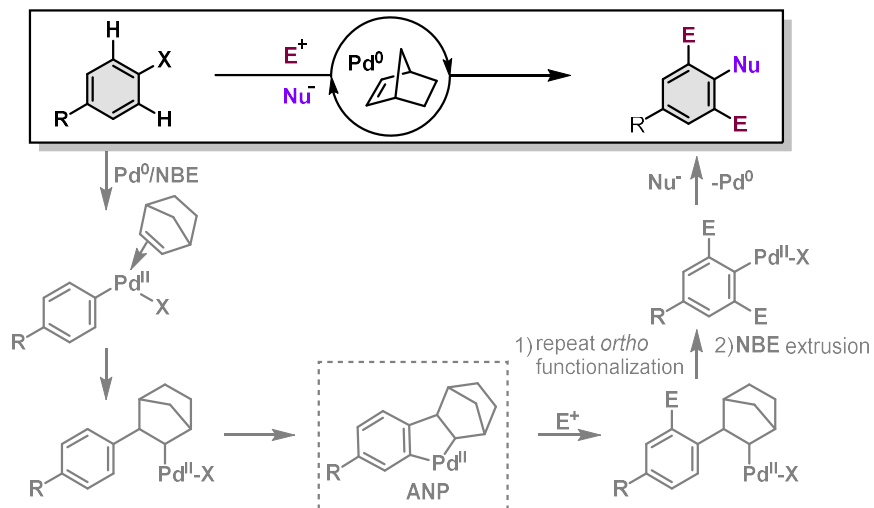
2.2. Results and Discussion

Palladium/norbornene (Pd/NBE)-catalyzed functionalization of *para*-substituted aryl halides provides a unique and efficient method to install three adjacent FGs to the aromatic core (Scheme 2.1A).⁷ Through an aryl-norbornyl palladacycle (ANP) intermediate, various electrophiles and various nucleophiles (including alkenes) can be coupled at the *ortho* and *ipso* positions, respectively.⁸ The branching selective coupling mode renders the Pd/NBE catalysis well suited for

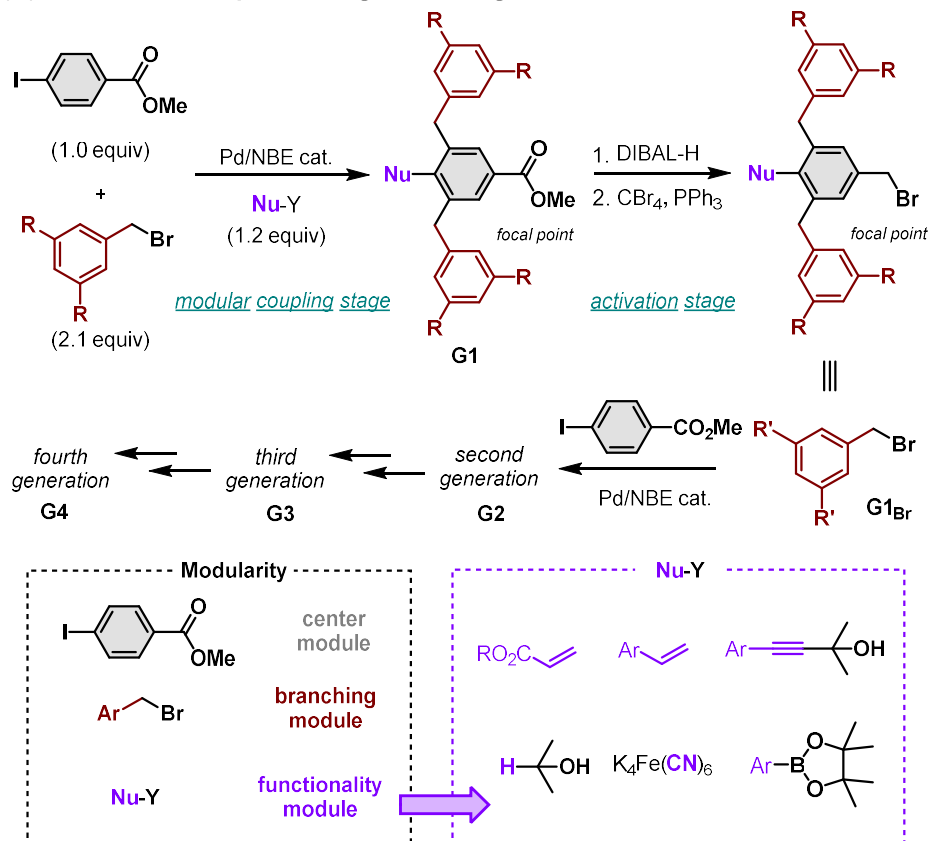
the development of modular *in-situ* functionalization synthesis of interior-functionalized dendritic macromolecules.

Scheme 2.1. Pd/NBE-catalyzed generation growth of interior-functionalized dendrons.

(A) The Pd/NBE catalysis

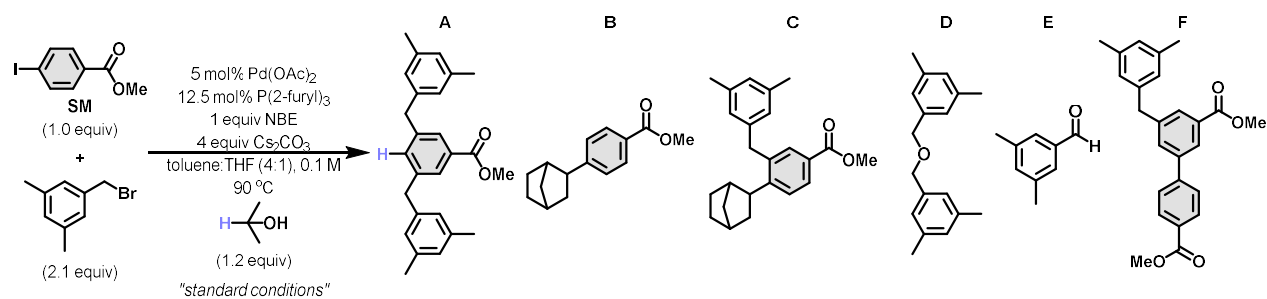


(B) Strategic development for generation growth of dendrons



At this initial stage of exploration, the Pd/NBE-catalyzed double *ortho*-C–H alkylation using benzyl bromides was employed as the dendron growth reaction to access branching networks (Scheme 2.1B). 4-Iodobenzoate serves as an excellent center module because it can be easily converted to a benzyl bromide moiety after a sequence of reduction and bromination, which can participate in the Pd/NBE reaction again as the branching module for the next dendron generation. In each dendron generation synthesis, different FGs can be introduced to the *ipso* position using different nucleophiles. This approach should provide dendrons with all-carbon backbones, which, to the best of our knowledge, have not been accessed previously with the traditional dendron synthesis methods. The benzyl-linked framework is also structurally complementary and chemically adaptable to the benzyl ether-based dendrons pioneered by Hawker and Fréchet, which also utilizes benzyl-type electrophiles.⁹ Additionally, the robust all-carbon dendritic scaffold offers the opportunity for post-modifications under harsher conditions that benzyl ethers may not survive (see page 291).¹⁰

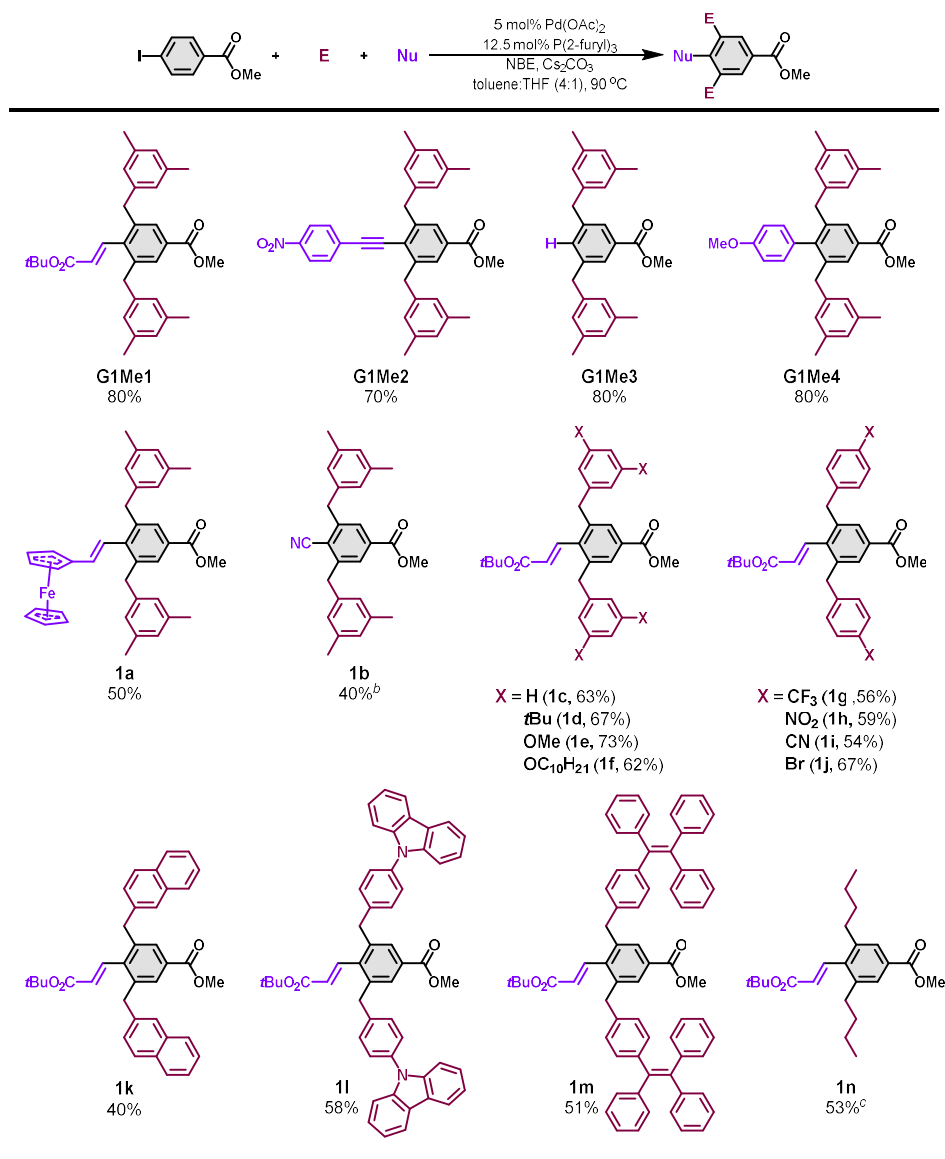
Table 2.1. Selected optimization of the model study.^a



Entry	Changes from the “standard conditions”	A	B	C	D	E	F	SM
1	None	75	0	0	1	2	6	0
2	Toluene instead of toluene:THF (4:1)	62	0	0	1	2	6	0
3	Toluene:THF (1:1) instead of toluene:THF (4:1)	68	0	0	0	7	3	0
4	DME instead of toluene:THF (4:1)	39	0	0	0	21	0	0
5	Toluene:glyme (4:1) instead of toluene:THF (4:1)	56	0	0	1	5	5	0
6	Toluene:dioxane (4:1) instead of toluene:THF (4:1)	20	0	0	6	18	3	33
7	PPh ₃ instead of P(2-furyl) ₃	60	0	0	1	2	7	0
8	P(<i>p</i> MeO-C ₆ H ₄) ₃ instead of P(2-furyl) ₃	17	31	0	4	17	0	29
9	P(<i>p</i> CF ₃ -C ₆ H ₄) ₃ instead of P(2-furyl) ₃	64	4	0	1	1	4	0
10	dppe instead of P(2-furyl) ₃	50	2	0	1	1	4	0
11	Cyclopentanol instead of <i>i</i> PrOH	55	0	0	1	2	9	0
12	No <i>i</i> PrOH	34	2	0	2	46	5	23
13	^b CsOAc instead of Cs ₂ CO ₃	7	0	0	12	0	5	27
14	2.5 mol% Pd(OAc) ₂ , 6.25 mol% P(2-furyl) ₃ instead of 5 mol% Pd(OAc) ₂ , 12.5 mol% P(2-furyl) ₃	21	9	10	25	33	1	18
15	10 mol% Pd(OAc) ₂ , 25 mol% P(2-furyl) ₃ instead of 5 mol% Pd(OAc) ₂ , 12.5 mol% P(2-furyl) ₃	62	0	0	0	9	5	0
16	2.5 equiv 3,5-dimethylbenzyl bromide instead of 2.1 equiv	51	0	0	3	14	6	0
17	3,5-dimethylbenzyl chloride instead of 3,5-dimethylbenzyl bromide	13	0	0	0	0	10	0
18	0.05 M instead of 0.1 M	61	0	0	2	3	7	0

^aNMR yields (%) determined using 1,1,2,2-tetrachloroethane as the internal standard. Reactions were run at 0.1 mmol scale based on the methyl 4-iodobenzoate. ^b3,5-dimethylbenzyl acetate was formed in 89% yield.

Table 2.2. Reaction scope of various electrophiles and nucleophiles.^a



Reaction conditions: ^amethyl 4-iodobenzoate (0.15 mmol), electrophile (0.315 mmol), nucleophile (0.18 mmol), Pd(OAc)₂ (0.0075 mmol), P(2-furyl)₃ (0.0188 mmol), norbornene (0.15 mmol), Cs₂CO₃ (0.60 mmol), toluene/THF (4:1, 1.5 mL), 90 °C, 24 h. ^bK₄Fe(CN)₆·3H₂O (0.30 mmol), Pd(OAc)₂ (0.015 mmol), P(2-furyl)₃ (0.033 mmol), norbornene (0.90 mmol), K₂CO₃ (0.45 mmol), 1,2-dimethoxyethane (1.5 mL), 90 °C, 48 h. ^c1,4-Dioxane was used as the solvent.

To make the Pd/NBE catalysis more suitable for dendron synthesis, our initial effort was to optimize the *ortho*-C–H benzylation of 4-iodobenzoate with 3,5-dimethylbenzyl bromide as the electrophile to achieve higher efficiency (Table 2.1). Palladium acetate and tri(2-furyl)phosphine were found to be a better combination of catalyst and ligand. Only 2.1 equivalents of the benzyl bromide electrophile were needed. A survey of the solvent effect revealed that 20% THF in toluene was optimal. To understand the scope of FGs that can be introduced to the peripheral and interior positions, different nucleophiles and alkyl electrophiles as functionality and branching modules, respectively, were explored (Table 2.2). First, alkenyl (**G1Me1** and **1a**), alkynyl (**G1Me2**), hydrogen (**G1Me3**), aryl (**G1Me4**) and cyano groups (**1b**) can all be smoothly installed at the *ipso* position. Next, a range of benzyl bromides with various substituents at the *meta* positions such as hydrogen (**1c**), methyl (**G1Me1**), *tert*-butyl (**1d**), methoxy (**1e**), and long alkoxy chain (**1f**), proved to be feasible coupling partners. In addition, electron-withdrawing groups at the *para* position, including trifluoromethyl (**1g**), nitro (**1h**), cyano (**1i**), and bromide (**1j**), can be tolerated. Gratifyingly, extended π systems such as naphthalene (**1k**), phenyl carbazole (**1l**), and tetraphenyl ethylene (**1m**) were also compatible to the Pd/NBE catalysis. Besides benzylation, *ortho*-C–H alkylation with *n*-butyl iodide was successfully achieved (**1n**), using 1,4-dioxane as solvent.

To demonstrate the feasibility of this *in-situ* functionalization platform for dendritic molecule synthesis, three prototypes of higher-generation multifunctional dendrons containing different FGs at the periphery/interior/core were prepared (Scheme 2.2). For the peripheral functionalization, we employed benzyl bromides bearing -OMe, -Me, or -CF₃ FGs as branching modules, and three different masked alkynes as functionality modules. To our delight, the first-generation synthesis proceeded smoothly to afford **G1OMe1**, **G1CF₃1**, and **G1Me2** on a multi-gram scale, and all the products can be purified by recrystallization without chromatography. The following ester

reduction and Appel reactions afforded all three **G1_{Br}** compounds in high yields (73 to 98% over two steps). Afterwards, these **G1_{Br}** compounds were subjected to the next generation synthesis of **G2** dendrons, in which hydrogen is introduced to the *ipso* position using isopropanol as the hydride source. The same reduction and bromination sequence was applied to prepare **G2_{Br}** compounds. We note that functional groups other than hydrogen can also be tolerated for further generation growth of dendrons (page 293). Similarly, the third-generation dendrons (**G3**) were synthesized by the same iteration, except using the *ipso*-Suzuki quench in the Pd/NBE catalysis to introduce an aryl FG. Lastly, 1-bromo-4-iodobenzene was used as a center module to connect two G3 dendrons, generating the 4th-generation dendritic macromolecule (**G4_{PhBrOMe}**). Notably, the *ipso*-position was still functionalized even in this more sterically hindered environment after adjusting the co-solvent ratio from toluene:THF (1:4) to toluene:THF (4:1). The remaining aryl bromide moiety in **G4_{PhBrOMe}** can potentially be used for further functionalization. The structure of **G4_{PhBrOMe}** was characterized and supported by NMR spectroscopy, MALDI-MS, and size exclusion chromatography (SEC).

Owing to the high versatility of the Pd/NBE catalysis, this *in-situ* functionalization platform allows convenient exploration of structure–property relationships in some applications, which is difficult to achieve otherwise. For example, considering that benzyl ether-based dendrons are known to form organogels as light harvesting or stimuli-responsive materials,¹¹ six different interior-functionalized 2nd-generation dendritic “gelators” were prepared using this method (Table 2.3). The driving forces for gelation (π - π and C-H/ π interactions)¹² were reported to be affected by structural variations, such as dendron generations, peripheral FGs, or substitution patterns,¹³⁻¹⁴ and yet the effect of interior-functionalization on gelation efficiency remains unexplored. Interestingly, the dendrons with *ipso*-functionalization at the 1st generation exhibited superior gelation ability

compared to the corresponding non-functionalized one. In contrast, the *ipso*-functionalization at the 2nd generation had a negative impact on gelation efficiency. This negative impact was even higher when the *ipso*-position was functionalized with more electron-deficient groups.

Scheme 2.2. Synthetic pathways to access three prototypes of multifunctional dendrons.

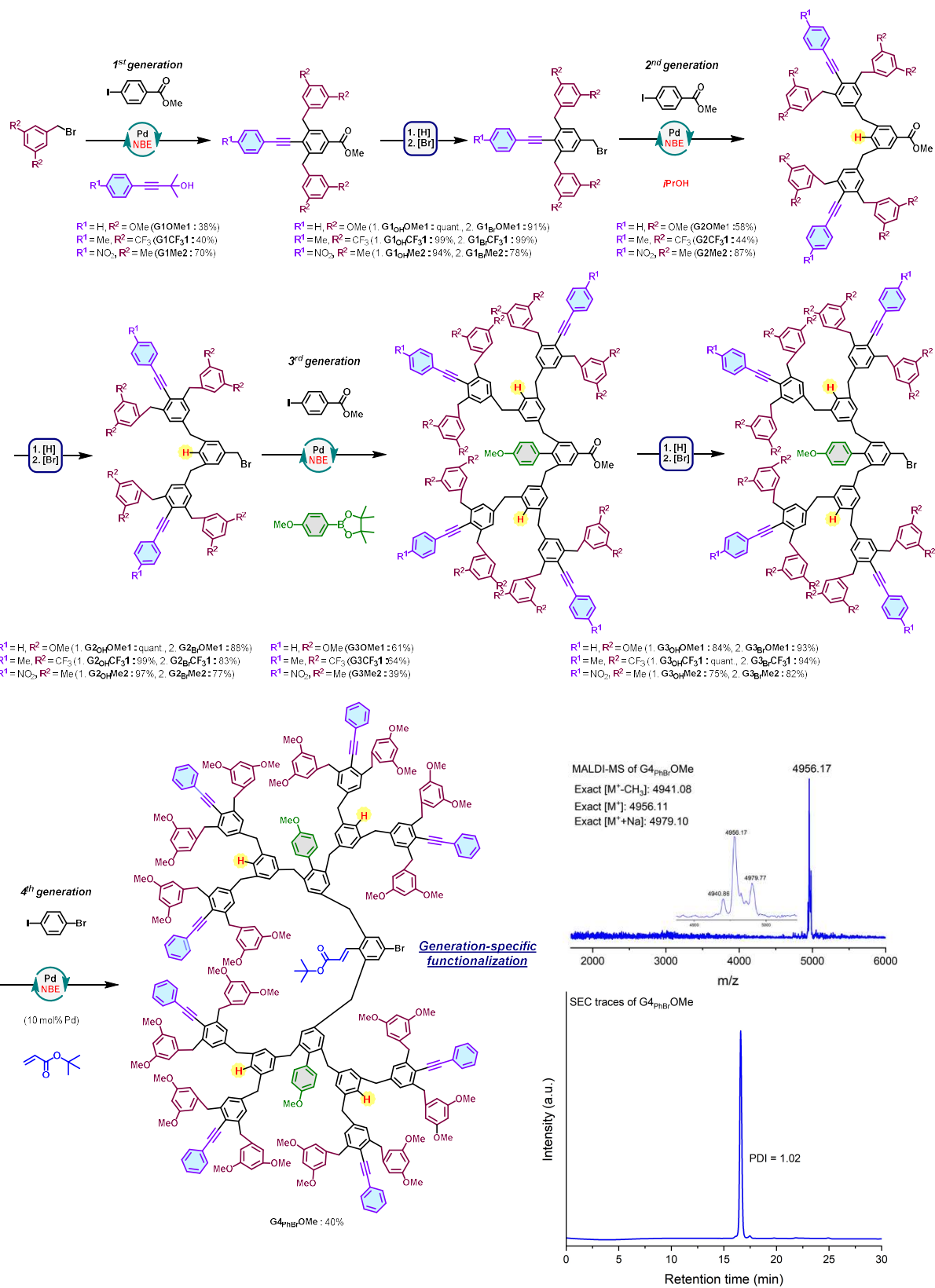
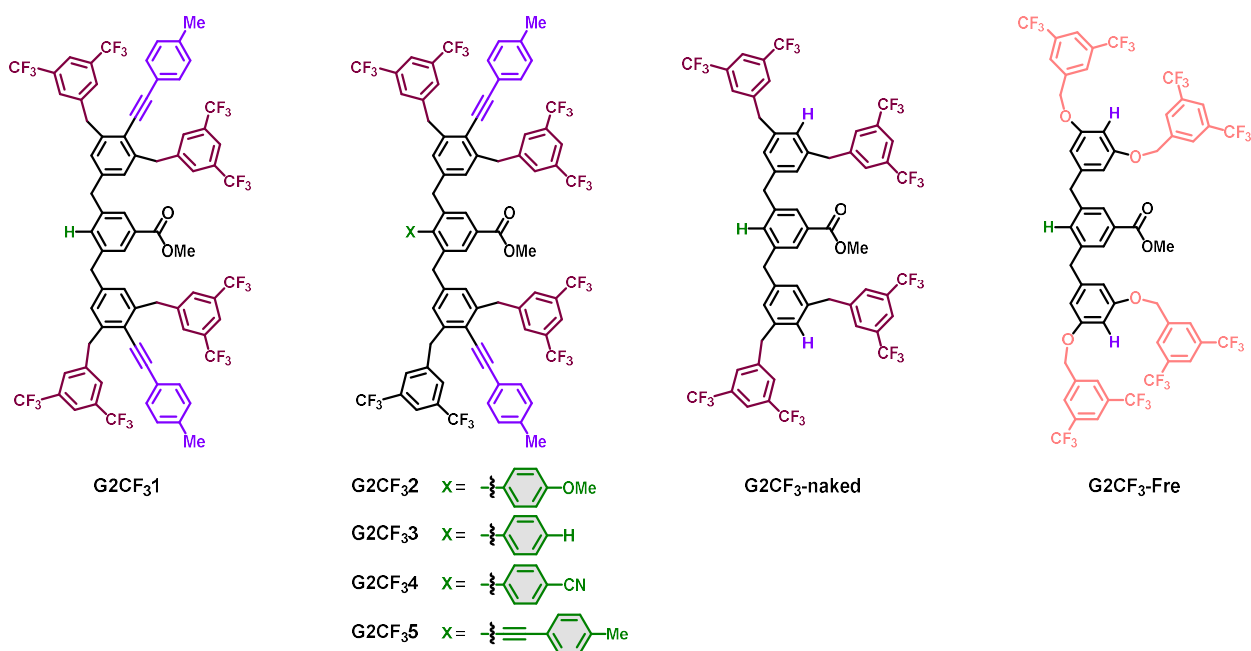


Table 2.3. Gelation behavior in toluene. The lowest critical gelation concentrations (CGC) were measured in toluene by the “stable to inversion” method. To 0.01173 mmol of each dendron, toluene was added in 0.1 mL increments during the test. The vial was heated to 90 °C and then cooled down to r.t. Although gelation typically occurred within 4 hours, we monitored the process for up to 24 hours. In general, dendrons with additional ipso-functionalization (1-ethynyl-4-methylbenzene) in the 1st generation (**G2CF₃1**, **G2CF₃2**, **G2CF₃3**, and **G2CF₃5**) exhibited superior gelation ability compared to the non-functionalized dendrons (**G2CF₃-naked** and **G2CF₃-Fre**). **G2CF₃1** showed a lower CGC compared to **G2CF₃2** and **G2CF₃5**, suggesting that the ipso-functionalization in the 2nd generation had a negative impact on gelation properties. Electronic effect also appeared to be a significant factor: the presence of electron-neutral (**G2CF₃3**) or electron-deficient groups (**G2CF₃4**) instead of an electron-rich group (**G2CF₃2** and **G2CF₃5**) attached to the core hindered the gelation process.



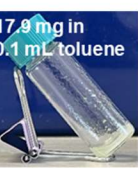
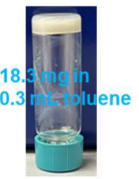
G2CF ₃ 1	G2CF ₃ 2	G2CF ₃ 3	G2CF ₃ 4	G2CF ₃ 5	G2CF ₃ -naked	G2CF ₃ -Fre
G (34.0)	G (91.0)	PG	P	G (61.0)	S	S
						
G: gelation; PG: partial gelation; S: soluble (100.0 mg/mL), I: insoluble upon heating; P: precipitation. The value given in parentheses indicate the CGC in mg/mL.						

Figure 2.2 illustrates another example of using the interior functionalization to enhance the aggregation-induced-emission (AIE) effect by introducing more steric bulk around the rotatable benzyl or phenyl groups.¹⁵ The aryl iodide attached to a well-investigated AIE moiety (Figure 2.2A, **TPE-Ph-I**), tetraphenylethylene,¹⁶ successfully provided three dendron variants: a non-functionalized dendron (**AIE-1**), a dendron with *ipso*-functionalization at the 1st generation (**AIE-2**), and a dendron *ipso*-functionalized in both generations (**AIE-3**) (Figure 2.2B). The AIE behavior of each dendron was examined by measuring the fluorescence in THF/H₂O mixed solvents upon varying the volume fraction of water (f_w) (Figure 2.2C-F). The formation of aggregates upon increasing f_w was confirmed using UV-vis absorption spectroscopy (Figure 2.3). For **AIE-1**, upon increasing f_w from 80% to 95%, emission intensity was approximately 56-fold higher than that of the emission in pure THF. Gratifyingly, interior-functionalized dendrons **AIE-2** and **AIE-3** exhibited a greater enhancement in emission intensity at $f_w = 95\%$, approximately 93-fold and 113-fold, respectively. The absolute quantum yields (ϕ_f) exhibited a similar pattern, giving 2.8%, 13.6%, and 29.7% for **AIE-1**, **AIE-2**, and **AIE-3**, respectively. These two examples clearly showed that changes of the *ipso*-functionalization in such benzyl-type dendrons could make a significant difference of their properties. This highlights the importance of interior functionalization of dendritic materials, as well as the convenience of this new synthetic platform.

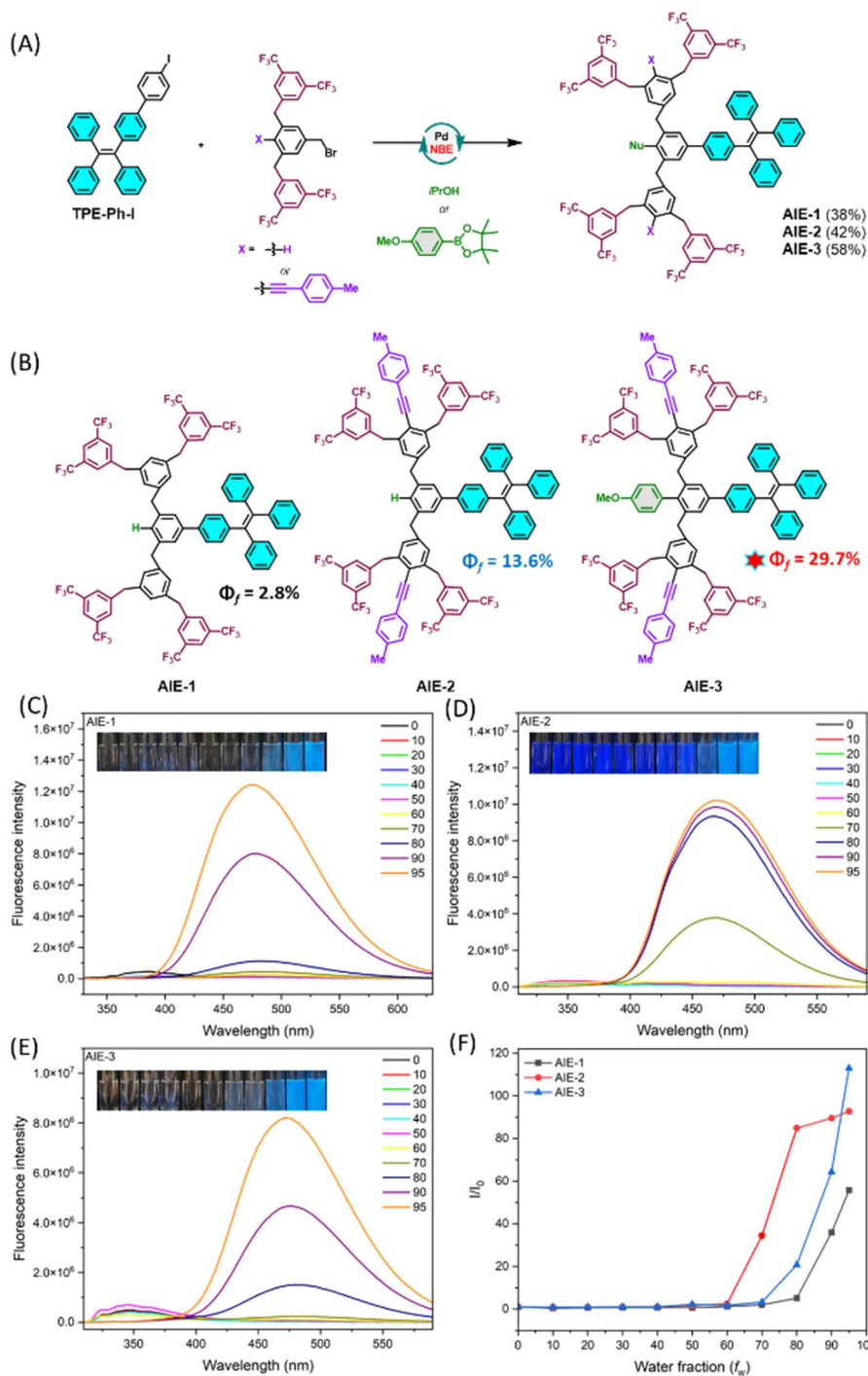


Figure 2.2. Structure-property relationship study of the AIE effect of 2nd-generation dendrons:

(A) Rapid synthesis of the dendritic AIE compounds. (B) The chemical structures of three dendrons along with their respective fluorescence quantum yields. Fluorescence intensity of (C) AIE-1 (excitation: 327 nm, emission = 475 nm), (D) AIE-2 (excitation: 300 nm, emission = 470

nm), and (E) **AIE-3** (excitation: 300 nm, emission = 473 nm) with varying f_w . Inset: fluorescence images of THF-H₂O mixtures (from left to right, $f_w = 0$ to 95 vol%) taken under 365 nm UV illumination. (F) Relative increase in fluorescence intensity compared to that of the material in pure THF solution (I_0).

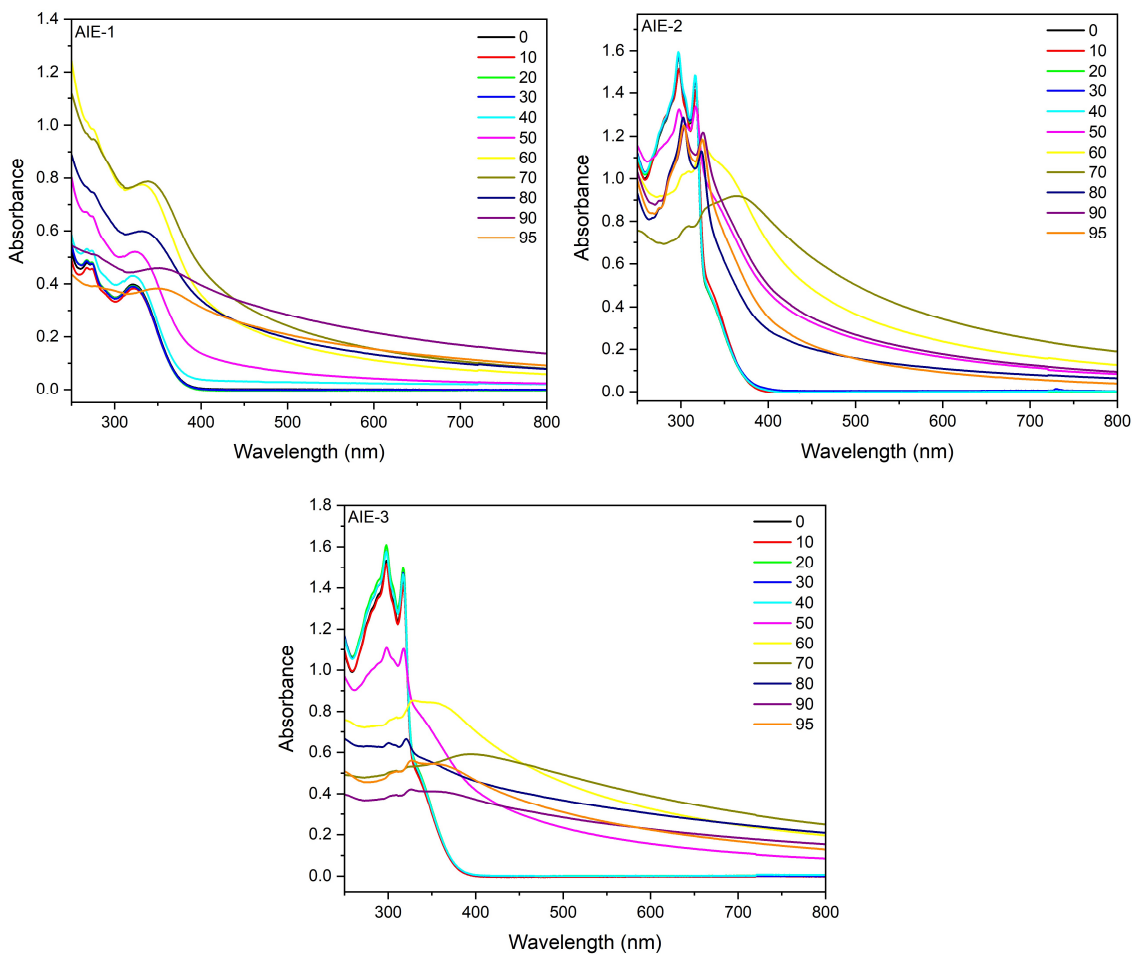


Figure 2.3. UV-Vis spectra of AIE compounds. Absorption maxima in THF: **AIE-1** (321 nm), **AIE-2** (297 nm), and **AIE-3** (298 nm). Upon the addition of water, the Mie scattering effect arising from the formation of aggregates became noticeable. In general, the absorption maxima showed a bathochromic shift in respect to increasing f_w , indicating the formation of J-aggregates, which are advantageous for achieving higher fluorescence.¹⁷

2.3. Conclusion

In summary, we have described the first use of the Pd/NBE catalysis for synthesis of dendritic macromolecules, enabling generation-specific multi-layered interior functionalization in a streamlined and scalable manner. This unique platform simplifies the access to a series of dendrons with similar structures but having different internal and peripheral FGs precisely installed, showing potential to build dendron libraries for systematic structure-property-relationship studies. It is our hope that, by mitigating the synthetic burdens, this convenient platform could catalyze a renaissance in the field of advanced multi-functional dendritic macromolecules.

2.4. General Information

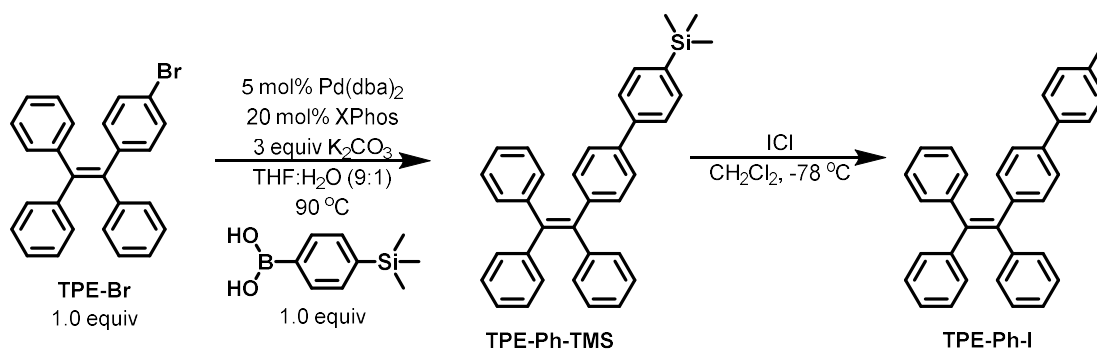
All reagents unless otherwise noted were purchased from Combi-blocks, Sigma-Aldrich, Fisher Scientific, TCI chemicals, Oakwood, or Ambeed, and used as received. Toluene, THF, and 1,4-dioxane used for palladium/norbornene reactions were distilled over sodium and benzophenone. Dry isopropanol (purchased from Sigma-Aldrich) used as the hydride source was degassed and stored in a Schlenk flask. Toluene and DMF used for Appel reactions were processed through a Pure-Solve MD-5 solvent purification system (Inert Corporation). Reaction vials with PTFE lined caps were purchased from Qorpak and flame-dried with a propane torch prior to use. Temperature of the reactions using pie-blocks (Chemglass) were determined using a thermometer placed in a separate vial filled with silicon oil and placed inside the pie-block. Analytical thin-layer chromatography (TLC) was carried out using 0.2 mm silica plates (silica gel 60, F254, EMD chemical), and visualized by irradiation with 254 nm UV light. Column chromatography was performed using silica gel purchased from Macherey-Nagel (Silica 60M, particle size: 0.04-0.063 mm). FT-IR spectra were recorded on a Nicolet iS5 FT-IR spectrometer as a thin film on KBr salt plates. High resolution mass spectra (HRMS) were obtained from Agilent 6223 TOF mass spectrometer (fragmentation voltage set to 70 V or 130 V) by electrospray ionization (ESI) or atmospheric pressure chemical ionization (APCI) and processed with an Agilent MassHunter Operating System. THF size exclusion chromatography (SEC) was carried out with two Agilent PLgel MIXED-B 300 × 7.5 mm columns with 10 μm beads, connected to an Agilent 1260 Series pump, a Wyatt 18- angle DAWN HELEOS light scattering detector, and Optilab rEX differential refractive index detector. Online determination of dn/dc assumed 100% mass elution under the peak of interest. Matrix-assisted laser desorption/ionization time-of-flight (MALDI-TOF) mass spectra were obtained on a Bruker Ultraflex extreme MALDI-TOF instrument in reflection mode or

linear mode, using 2,5-dihydroxybenzoic acid (DHB), 2-[(2*E*)-3-(4-*tert*-butylphenyl)-2-methylprop-2-enylidene]malononitrile (DCTB), or α -Cyano-4-hydroxycinnamic acid (HCCA) as the matrix. The absorption spectra were recorded on a Shimadzu UV3600 Plus UV-Vis-NIR spectrophotometer. Fluorescence studies were conducted using a HORIBA Jobin Yvon Fluorolog-3 spectrofluorometer. The fluorescence quantum yields (ϕ_f) of the compounds were measured using the absolute method with an Edinburgh FLS1000 instrument (N-M01 integrating sphere). Nuclear magnetic resonance (NMR) spectra were recorded with a Bruker Avance 400 (^1H at 400 MHz, ^{13}C at 101 MHz, ^{19}F at 376 MHz), and Bruker Avance 500 (^1H at 400 MHz, ^{13}C at 101 MHz, ^{19}F at 470 MHz). Chemical shifts are reported in parts per million (ppm, δ) in reference to the NMR solvent (CDCl_3 $\delta=7.26$ ppm (^1H) and 77.16 ppm (^{13}C), C_6D_6 $\delta=7.16$ ppm (^1H) and 128.06 ppm (^{13}C)). Coupling constants were reported in Hertz (Hz). Data for ^1H NMR spectra were reported as follows: chemical shift (ppm, referenced to protium, s = singlet, d = doublet, t = triplet, q = quartet, quin = quintet, dd = doublet of doublets, td = triplet of doublets, ddd = doublet of doublets, m = multiplet, coupling constant (Hz), and integration).

2.5. Experimental Procedure and Data

2.5.1. Starting material preparation

2-methyl-4-phenylbut-3-yn-2-ol derivatives¹⁸ and benzyl bromide electrophiles used for the synthesis of **1e**,¹⁹ **1k**,²⁰ and **1l**²¹ were prepared according to reported literature procedures. **TPE-Ph-I** was synthesized in a two-step procedure (see below) from a known compound, **TPE-Br**.²² All other materials were purchased and directly used from the commercial bottles.



A flame-dried 20 mL reaction vial was charged with **TPE-Br** (263.4 mg, 0.73 mmol, 1.0 equiv), (4-(trimethylsilyl)phenyl)boronic acid (124.3 mg, 0.73 mmol, 1.0 equiv), Pd(dba)₂ (18.4 mg, 0.036 mmol, 5 mol%), XPhos (61.1 mg, 0.15 mmol, 20 mol%), and K₂CO₃ (265.5 mg, 2.19 mmol, 3.0 equiv). A THF:H₂O (9:1) solution (6.4 mL) was added to the reaction vial under a nitrogen atmosphere. The solution was stirred and heated at a preheated pie-block set to 90 °C for 24 h. After cooling down to room temperature, the crude mixture was passed through a plug of celite and washed with EtOAc. The organic solvents were removed under reduced pressure. The crude product was directly subjected to the next reaction, as the resulting product is prone to hydrolysis in column chromatography on silica gel. The crude mixture was diluted with 10.0 mL of CH₂Cl₂, and the reaction solution was cooled down to -78 °C. ICl solution (1 M in CH₂Cl₂, 0.6 mL) was added dropwise at -78 °C. Then, the solution was stirred at r.t. overnight. The organic solvents were removed under reduced pressure, and the crude product was purified by flash column chromatography on silica gel (hexanes:CH₂Cl₂ = 2:1).

Yield: 333.1 mg (85% over two steps)

Physical appearance: white solid

R_f: 0.4 (CH₂Cl₂:hexanes = 1:4)

¹H NMR (500 MHz, CDCl₃): δ 7.72 (d, *J* = 8.0 Hz, 2H), 7.30 (d, *J* = 9.1 Hz, 2H), 7.29 (d, *J* = 9.2 Hz, 2H), 7.14 – 7.03 (m, 17H).

¹³C NMR (126 MHz, CDCl₃): δ 143.81, 143.78, 143.75, 143.42, 141.49, 140.48, 140.32, 137.89, 137.80, 132.04, 131.53, 131.46, 128.85, 127.93, 127.86, 127.79, 126.70, 126.67, 126.62, 126.09, 92.96.

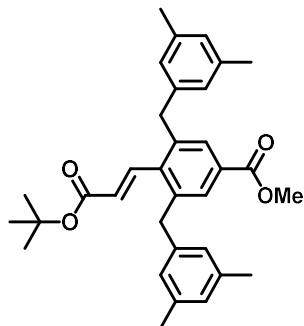
IR (KBr, neat): 3052, 3024, 1597, 1490, 1478, 1442, 1387, 1279, 1155, 1113, 1374, 1028, 1000, 907, 856, 810, 775, 760, 733, 699, 641, 627, 581 cm⁻¹.

HRMS (ESI-TOF): m/z calcd for C₃₂H₂₄I⁺ [M+H⁺]: 535.0917. Found: 535.0916.

2.5.2. General synthetic procedure for the substrate scope

A flame-dried 4 mL reaction vial was charged with methyl 4-iodobenzoate (39.3 mg, 0.15 mmol, 1.0 equiv), electrophile (0.315 mmol, 2.1 equiv), nucleophile (0.18 mmol, 1.2 equiv), Pd(OAc)₂ (1.7 mg, 0.0075 mmol, 5 mol%), and tri(2-furyl)phosphine (4.4 mg, 0.0188 mmol, 12.5 mol%). The vial was brought into the glovebox, and anhydrous Cs₂CO₃ (195.5 mg, 0.60 mmol, 4 equiv), norbornene (14.1 mg, 0.15 mmol, 1 equiv), toluene (1.2 mL), and THF (0.3 mL) were added. The reaction mixture in the sealed vial was stirred at r. t. for 10 mins, was taken out of the glove box, and then was stirred and heated at a preheated pie-block set to 90 °C for 24 h. After cooling down to room temperature, the crude mixture was passed through a plug of celite and washed with EtOAc. The organic solvents were removed under reduced pressure. The crude product was purified by flash column chromatography on silica gel.

G1Me1:



Yield: 80%

Physical appearance: white solid, **m.p.:** 118-120 °C

R_f: 0.5 (EtOAc:hexanes = 1:5)

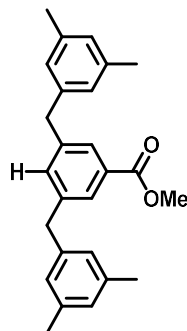
¹H NMR (400 MHz, CDCl₃): δ 7.77 (s, 2H), 7.58 (d, *J* = 16.4 Hz, 1H), 6.81 (s, 2H), 6.68 (s, 4H), 5.75 (d, *J* = 16.4 Hz, 1H), 3.94 (s, 4H), 3.88 (s, 3H), 2.24 (s, 12H), 1.49 (s, 9H).

¹³C NMR (101 MHz, CDCl₃): δ 167.16, 165.23, 141.51, 140.24, 139.97, 139.86, 138.04, 129.68, 129.63, 128.01, 127.57, 126.81, 80.76, 52.26, 39.81, 28.29, 21.43.

IR (KBr, neat): 3010, 2976, 2950, 2919, 2869, 1723, 1643, 1606, 1568, 1456, 1435, 1415, 1392, 1367, 1314, 1297, 1256, 1218, 1151, 1105, 1033, 1004, 902, 845, 770, 693 cm⁻¹.

HRMS (ESI-TOF): *m/z* calcd for C₃₃H₃₈NaO₄⁺ [*M*+Na⁺]: 521.2662. Found: 521.2666.

G1Me3:



Yield: 80%

Physical appearance: colorless oil

R_f: 0.5 (EtOAc:hexanes = 1:5)

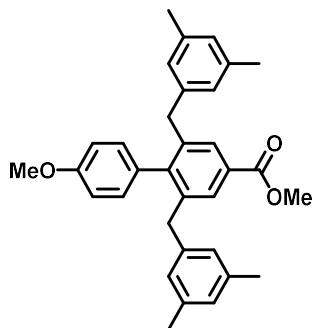
¹H NMR (400 MHz, CDCl₃): δ 7.73 (s, 2H), 7.24 (s, 1H), 6.84 (s, 2H), 6.78 (s, 4H), 3.90 (s, 4H), 3.88 (s, 3H), 2.27 (s, 12H).

¹³C NMR (101 MHz, CDCl₃): δ 167.46, 141.90, 140.62, 138.15, 134.47, 130.61, 128.08, 128.01, 126.79, 52.16, 41.71, 21.41.

IR (KBr, neat): 3013, 2948, 2916, 2860, 1722, 1600, 1433, 1375, 1328, 1299, 1248, 1214, 1113, 1003, 884, 844, 772, 725, 687, 669 cm⁻¹.

HRMS (ESI-TOF): m/z calcd for C₂₆H₂₉O₂⁺ [M+H⁺]: 373.2162. Found: 373.2157.

G1Me4:



Yield: 80%

Physical appearance: colorless oil

R_f: 0.5 (EtOAc:hexanes = 1:9)

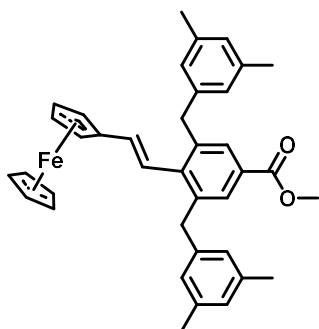
¹H NMR (500 MHz, CDCl₃): δ 7.83 (s, 2H), 6.85 (d, *J* = 8.7 Hz, 2H), 6.81 (d, *J* = 8.7 Hz, 2H), 6.76 (s, 2H), 6.47 (s, 4H), 3.90 (s, 3H), 3.85 (s, 3H), 3.69 (s, 4H), 2.20 (s, 12H).

^{13}C NMR (126 MHz, CDCl_3): δ 167.48, 158.84, 146.63, 140.71, 140.66, 137.59, 131.32, 130.58, 129.13, 127.55, 126.83, 113.58, 55.39, 52.16, 39.87, 21.35.

IR (KBr, neat): 3014, 2949, 2916, 2837, 2731, 1722, 1608, 1567, 1516, 1463, 1435, 1415, 1376, 1327, 1300, 1247, 1210, 1176, 1114, 1038, 1002, 897, 833, 800, 772, 737, 702, 638, 592, 576, 527 cm^{-1} .

HRMS (ESI-TOF): m/z calcd for $\text{C}_{33}\text{H}_{34}\text{NaO}_3^+$ [$\text{M}+\text{Na}^+$]: 501.2400. Found: 501.2397.

1a:



Yield: 50%

Physical appearance: orange oil

R_f : 0.45 (EtOAc:hexanes = 1:9)

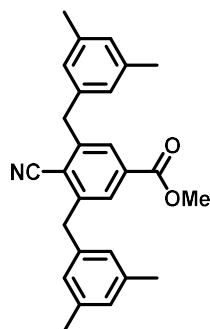
^1H NMR (400 MHz, C_6D_6): δ 8.22 (s, 2H), 6.82 (s, 4H), 6.75 (d, $J = 16.6$ Hz, 1H), 6.70 (s, 2H), 6.30 (d, $J = 16.5$ Hz, 1H), 4.16 (t, $J = 1.9$ Hz, 2H), 4.07 (s, 4H), 4.03 (t, $J = 1.8$ Hz, 2H), 3.95 (s, 5H), 3.44 (s, 3H), 2.10 (s, 12H).

^{13}C NMR (101 MHz, CDCl_3): δ 167.49, 143.36, 140.71, 139.44, 137.97, 133.24, 129.87, 128.21, 127.84, 126.72, 123.03, 83.24, 69.17, 69.09, 66.91, 52.13, 40.06, 21.48.

IR (KBr, neat): 3094, 3015, 2948, 2918 2854, 2730, 1720, 1636, 1604, 1566, 1457, 1434, 1414, 1376, 1327, 1295, 1246, 1216, 1202, 1170, 1106, 1042, 1025, 1003, 967, 932, 901, 839, 818, 771, 737, 692, 587 cm^{-1} .

HRMS (ESI-TOF): m/z calcd for $\text{C}_{38}\text{H}_{38}\text{FeNaO}_2^+$ [$\text{M}+\text{Na}^+$]: 605.2113. Found: 605.2106.

1b:



* $\text{K}_4\text{Fe}(\text{CN})_6 \cdot 3\text{H}_2\text{O}$ (0.30 mmol, 2.0 equiv) was used as the nucleophile. $\text{Pd}(\text{OAc})_2$ (0.015 mmol, 10 mol%), $\text{P}(2\text{-furyl})_3$ (0.033 mmol, 22 mol%), norbornene (0.90 mmol, 6.0 equiv), K_2CO_3 (0.45 mmol, 3.0 equiv), and 1,2-dimethoxyethane (1.5 mL) were used. Reaction was performed at 90 °C for 24 h.

Yield: 40% (>90% purity)

Physical appearance: white solid, **m.p.:** 156-158 °C

R_f: 0.35 (EtOAc:hexanes = 1:4)

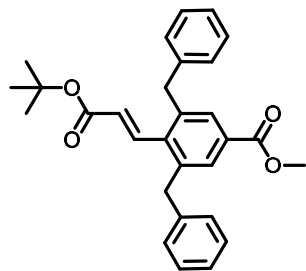
¹H NMR (500 MHz, CDCl₃): δ 7.78 (s, 2H), 6.87 (s, 2H), 6.85 (s, 4H), 4.17 (s, 4H), 3.88 (s, 3H), 2.28 (s, 12H).

¹³C NMR (126 MHz, CDCl₃): δ 166.02, 146.25, 138.46, 138.39, 133.78, 128.69, 128.67, 126.87, 116.97, 116.94, 52.71, 40.51, 21.43.

IR (KBr, neat): 3015, 2952, 2921, 2854, 2732, 2221 (C≡N), 1728, 1606, 1572, 1457, 1435, 1377, 1327, 1264, 1221, 1168, 1096, 1037, 997, 896, 849, 802, 770, 738, 699, 689, 613 cm⁻¹.

HRMS (ESI-TOF): m/z calcd for C₂₇H₂₈NO₂⁺ [M+H⁺]: 398.2115. Found: 398.2112.

1c:



Yield: 63%

Physical appearance: white solid, **m.p.:** 122-124 °C

R_f: 0.3 (EtOAc:hexanes = 1:9)

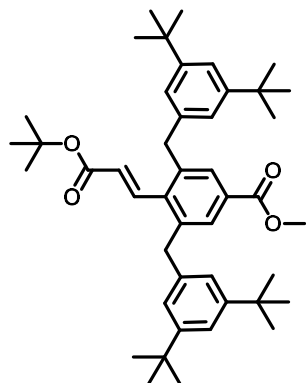
¹H NMR (400 MHz, CD₂Cl₂): δ 7.73 (s, 2H), 7.52 (d, *J* = 16.4 Hz, 1H), 7.25 (t, *J* = 7.4 Hz, 4H), 7.19 – 7.15 (m, 2H), 7.06 (d, *J* = 7.2 Hz, 4H), 5.70 (d, *J* = 16.3 Hz, 1H), 4.02 (s, 4H), 3.82 (s, 3H), 1.46 (s, 9H).

¹³C NMR (126 MHz, CDCl₃): δ 166.94, 165.09, 141.24, 140.26, 140.03, 139.68, 129.68, 128.95, 128.62, 127.67, 126.35, 126.34, 80.85, 52.25, 39.93, 28.24.

IR (KBr, neat): 3085, 3062, 3028, 2977, 2951, 2930, 1716, 1643, 1604, 1569, 1495, 1453, 1435, 1417, 1392, 1315, 1292, 1259, 1220, 1151, 1106, 1076, 1030, 1001, 910, 861, 770, 734, 698 605, 562 cm⁻¹.

HRMS (ESI-TOF): m/z calcd for C₂₉H₃₀NaO₄⁺ [M+Na⁺]: 465.2036. Found: 465.2027.

1d:



Yield: 67%

Physical appearance: white solid, **m.p.:** 135-137 °C

R_f: 0.5 (EtOAc:hexanes = 1:9)

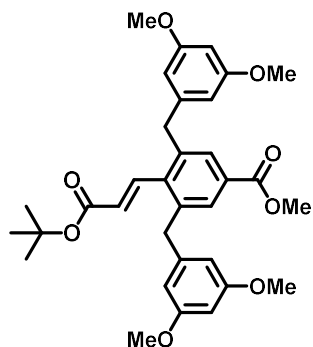
¹H NMR (400 MHz, CD₂Cl₂): δ 7.75 (s, 2H), 7.70 (d, *J* = 16.4 Hz, 1H), 7.23 (t, *J* = 1.5 Hz, 2H), 6.95 (d, *J* = 1.8 Hz, 4H), 5.90 (d, *J* = 16.3 Hz, 1H), 4.00 (s, 4H), 3.81 (s, 3H), 1.46 (s, 9H), 1.24 (s, 36H).

¹³C NMR (101 MHz, CDCl₃): δ 167.12, 165.21, 150.93, 142.05, 140.06, 140.02, 139.11, 129.63, 129.40, 127.66, 123.14, 120.24, 80.83, 52.17, 40.26, 34.89, 31.60, 28.30.

IR (KBr, neat): 2964, 2905, 2868, 1724, 1643, 1599, 1568, 1478, 1458, 1434, 1393, 1364, 1314, 1291, 1249, 1219, 1151, 1105, 1007, 977, 937, 888, 867, 770, 738, 713 cm⁻¹.

HRMS (ESI-TOF): *m/z* calcd for C₄₅H₆₂NaO₄⁺ [M+Na⁺]: 689.4540. Found: 689.4548.

1e:



Yield: 73%

Physical appearance: white solid, **m.p.:** 136-138 °C

R_f: 0.15 (EtOAc:hexanes = 1:4)

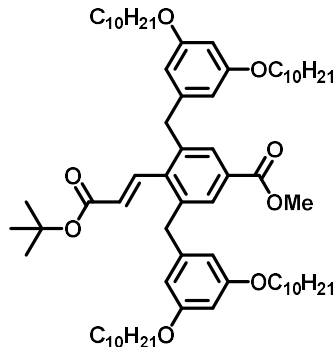
¹H NMR (400 MHz, CDCl₃): δ 7.78 (s, 2H), 7.58 (d, J = 16.4 Hz, 1H), 6.29 (s, 2H), 6.22 (d, J = 2.3 Hz, 4H), 5.76 (d, J = 16.4 Hz, 1H), 3.95 (s, 4H), 3.88 (s, 3H), 3.72 (s, 12H), 1.47 (s, 9H).

¹³C NMR (101 MHz, CDCl₃): δ 166.96, 165.19, 160.99, 142.49, 141.24, 140.27, 139.35, 129.81, 129.79, 127.61, 107.15, 98.25, 80.90, 55.35, 52.28, 40.17, 28.19.

IR (KBr, neat): 2097, 2837, 1726, 1709, 1645, 1605, 1595, 1457, 1432, 1389, 1368, 1348, 1324, 1288, 1220, 1208, 1159, 1066, 1057, 1033, 1004, 941, 841, 765, 736, 692 cm⁻¹.

HRMS (ESI-TOF): m/z calcd for C₃₃H₃₈NaO₈⁺ [M+Na⁺]: 585.2459. Found: 585.2461.

1f:



Yield: 62%

Physical appearance: white solid, **m.p.:** 68-70 °C

R_f: 0.5 (EtOAc:hexanes = 1:9)

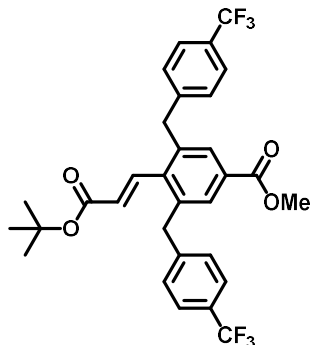
¹H NMR (500 MHz, CDCl₃): δ 7.76 (s, 2H), 7.59 (d, *J* = 16.4 Hz, 1H), 6.28 (s, 2H), 6.20 (d, *J* = 2.2 Hz, 4H), 5.76 (d, *J* = 16.4 Hz, 1H), 3.92 (s, 4H), 3.86 (d, *J* = 6.9 Hz, 8H), 3.84 (s, 3H), 1.72 (p, *J* = 6.8 Hz, 8H), 1.48 (s, 9H), 1.41 (p, *J* = 6.9 Hz, 8H), 1.33 – 1.27 (m, 48H), 0.88 (t, *J* = 6.8 Hz, 12H).

¹³C NMR (101 MHz, CDCl₃): δ 167.01, 165.19, 160.51, 142.25, 141.36, 140.23, 139.38, 129.72, 127.59, 107.63, 99.12, 80.77, 68.06, 52.21, 40.20, 32.04, 29.72, 29.70, 29.57, 29.46, 29.43, 28.23, 26.20, 22.82, 14.24.

IR (KBr, neat): 2925, 2854, 1724, 1595, 1458, 1389, 1367, 1316, 1290, 1218, 1164, 1106, 1060, 828, 770, 721, 688 cm⁻¹.

HRMS (ESI-TOF): *m/z* calcd for C₆₉H₁₁₀NaO₈⁺ [*M*+Na⁺]: 1089.8093. Found: 1089.8095.

1g:



Yield: 56%

Physical appearance: white solid, **m.p.:** 147-149 °C

R_f: 0.25 (EtOAc:hexanes = 1:9)

¹H NMR (400 MHz, CDCl₃): δ 7.80 (s, 2H), 7.51 (d, J = 7.9 Hz, 4H), 7.47 (d, J = 16.5 Hz, 1H), 7.17 (d, J = 8.0 Hz, 4H), 5.62 (d, J = 16.4 Hz, 1H), 4.07 (s, 4H), 3.90 (s, 3H), 1.46 (s, 9H).

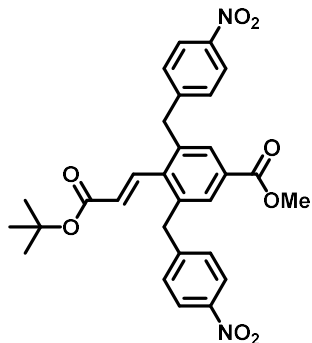
¹³C NMR (101 MHz, CDCl₃): δ 166.64, 164.77, 144.07, 140.59, 140.39, 138.87, 130.16, 130.05, 129.22, 128.73 (q, ²J_{C-CF₃} = 32.5 Hz), 128.25, 125.48 (q, ³J_{C-CF₃} = 3.9 Hz), 121.49 (q, ¹J_{C-CF₃} = 271.9 Hz), 81.23, 52.43, 39.79, 28.16.

¹⁹F NMR (376 MHz, CDCl₃): -62.43.

IR (KBr, neat): 2986, 2953, 1716, 1643, 1618, 1569, 1437, 1416, 1393, 1370, 1326, 1270, 1222, 1161, 1124, 1109, 1068, 1019, 1004, 915, 852, 822, 772, 740, 642, 596 cm⁻¹.

HRMS (ESI-TOF): m/z calcd for C₃₁H₂₈F₆NaO₄⁺ [M+Na⁺]: 601.1784. Found: 601.1777.

1h:



Yield: 59%

Physical appearance: white solid, **m.p.:** 182-184 °C

R_f: 0.3 (EtOAc:hexanes = 1:2)

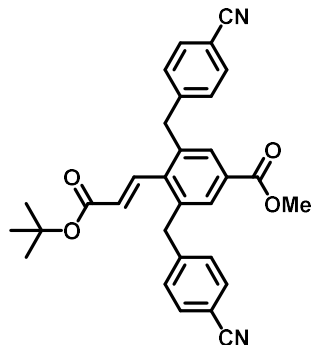
¹H NMR (400 MHz, CDCl₃): δ 8.13 (d, *J* = 8.7 Hz, 4H), 7.81 (s, 2H), 7.46 (d, *J* = 16.4 Hz, 1H), 7.23 (d, *J* = 8.7 Hz, 4H), 5.61 (d, *J* = 16.4 Hz, 1H), 4.13 (s, 4H), 3.90 (s, 3H), 1.47 (s, 9H).

¹³C NMR (101 MHz, CDCl₃): δ 166.39, 164.58, 147.48, 146.80, 140.31, 140.25, 138.41, 130.46, 130.25, 129.74, 128.55, 123.98, 81.56, 52.56, 39.84, 28.23.

IR (KBr, neat): 2977, 2950, 1718, 1643, 1607, 1570, 1487, 1434, 1403, 1392, 1368, 1315, 1288, 1258, 1220, 1152, 1104, 1072, 1011, 911, 846, 795, 768, 733 cm⁻¹.

HRMS (ESI-TOF): *m/z* calcd for C₂₉H₂₈N₂NaO₈⁺ [M+Na⁺]: 555.1738. Found: 555.1732.

1i:



Yield: 54% (>95% purity)

Physical appearance: white solid, **m.p.:** 148-150 °C

R_f: 0.15 (EtOAc:hexanes = 1:4)

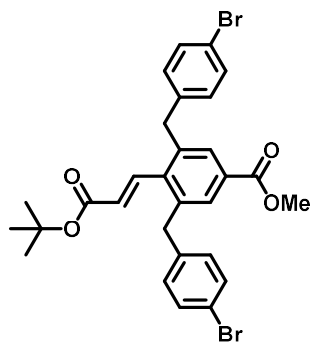
¹H NMR (400 MHz, CDCl₃): δ 7.78 (s, 2H), 7.55 (d, *J* = 8.3 Hz, 4H), 7.44 (d, *J* = 16.4 Hz, 1H), 7.17 (d, *J* = 8.3 Hz, 4H), 5.60 (d, *J* = 16.4 Hz, 1H), 4.07 (s, 4H), 3.90 (s, 3H), 1.48 (s, 9H).

¹³C NMR (126 MHz, CDCl₃): δ 166.43, 164.61, 145.41, 140.31, 138.43, 132.59, 132.50, 130.32, 130.18, 129.67, 128.37, 118.87, 110.55, 81.45, 52.52, 40.03, 28.23.

IR (KBr, neat): 2979, 2951, 2228 (C≡N), 1715, 1646, 1607, 1570, 1506, 1435, 1413, 1393, 1368, 1316, 1296, 1222, 1152, 1105, 1020, 1002, 912, 853, 816, 770, 734, 669, 649, 596, 547 cm⁻¹.

HRMS (ESI-TOF): *m/z* calcd for C₃₁H₂₈N₂NaO₄⁺ [M+Na⁺]: 515.1941. Found: 515.1942.

1j:



Yield: 67%

Physical appearance: white solid, **m.p.:** 68-70 °C

R_f: 0.3 (EtOAc:hexanes = 1:9)

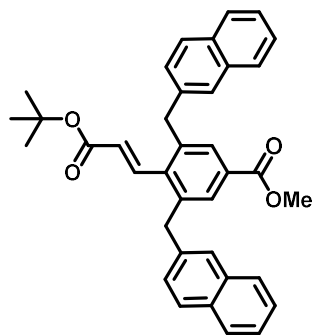
¹H NMR (400 MHz, CDCl₃): δ 7.75 (s, 2H), 7.48 (d, *J* = 16.4 Hz, 1H), 7.37 (d, *J* = 8.4 Hz, 4H), 6.93 (d, *J* = 8.4 Hz, 4H), 5.65 (d, *J* = 16.4 Hz, 1H), 3.96 (s, 4H), 3.89 (s, 3H), 1.49 (s, 9H).

¹³C NMR (101 MHz, CDCl₃): δ 166.70, 164.88, 140.78, 140.18, 139.21, 138.95, 131.71, 130.64, 129.95, 129.76, 127.95, 120.28, 81.11, 52.36, 39.36, 28.23.

IR (KBr, neat): 2977, 2950, 1718, 1643, 1607, 1570, 1487, 1434, 1403, 1392, 1368, 1315, 1288, 1258, 1220, 1152, 1104, 1072, 1011, 911, 846, 795, 768, 733 cm⁻¹.

HRMS (ESI-TOF): *m/z* calcd for C₂₉H₂₈Br₂NaO₄⁺ [M+Na⁺]: 621.0247. Found: 621.0235.

1k:



Yield: 40%

Physical appearance: light yellow solid, **m.p.:** 144-146 °C

R_f: 0.25 (EtOAc:hexanes = 1:9)

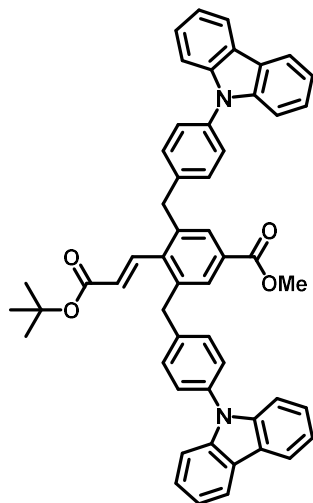
¹H NMR (400 MHz, CDCl₃): δ 7.86 (s, 2H), 7.80 – 7.78 (m, 2H), 7.76 – 7.72 (m, 4H), 7.65 (d, *J* = 16.4 Hz, 1H), 7.51 (s, 2H), 7.46 – 7.41 (m, 4H), 7.24 (dd, *J* = 8.4, 1.8 Hz, 2H), 5.77 (d, *J* = 16.4 Hz, 1H), 4.20 (s, 4H), 3.86 (s, 3H), 1.43 (s, 9H).

^{13}C NMR (101 MHz, CDCl_3): δ 166.97, 165.10, 141.20, 140.39, 139.68, 137.55, 133.66, 132.25, 129.89, 129.82, 128.31, 127.81, 127.74, 127.73, 127.42, 126.13, 125.59, 80.89, 52.28, 40.14, 28.18.

IR (KBr, neat): 3053, 2977, 2950, 1716, 1634, 1601, 1568, 1508, 1435, 1415, 1392, 1367, 1316, 1289, 1220, 1151, 1105, 1004, 910, 855, 816, 770, 740 cm^{-1} .

HRMS (ESI-TOF): m/z calcd for $\text{C}_{37}\text{H}_{34}\text{iNaO}_4^+$ [$\text{M}+\text{Na}^+$]: 565.2349. Found: 565.2343.

11:



Yield: 58%

Physical appearance: white solid, m.p.: 115-117 °C

R_f : 0.4 (EtOAc:hexanes = 1:9)

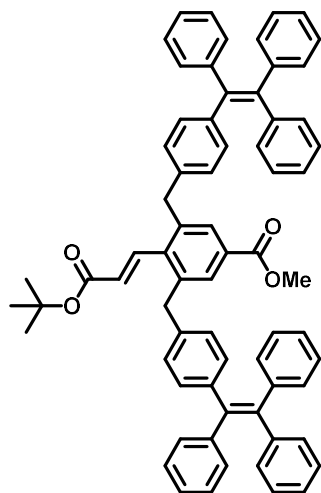
^1H NMR (400 MHz, CDCl_3): δ 8.14 (d, $J = 7.7$ Hz, 4H), 7.96 (s, 2H), 7.73 (d, $J = 16.4$ Hz, 1H), 7.48 (d, $J = 8.1$ Hz, 4H), 7.39 (d, $J = 4.6$ Hz, 8H), 7.34 (d, $J = 8.1$ Hz, 4H), 7.28 (dd, $J = 8.1, 4.1$ Hz, 4H), 5.86 (d, $J = 16.4$ Hz, 1H), 4.21 (s, 4H), 3.95 (s, 3H), 1.50 (s, 9H).

^{13}C NMR (101 MHz, CDCl_3): δ 166.88, 165.09, 141.13, 141.05, 140.46, 139.50, 136.02, 130.35, 130.14, 130.11, 128.04, 127.39, 126.03, 123.43, 120.40, 119.98, 109.89, 81.18, 52.46, 39.74, 28.32.

IR (KBr, neat): 3047, 2977, 2949, 1716, 1645, 1625, 1597, 1570, 1515, 1479, 1452, 1435, 1392, 1365, 1335, 1316, 1290, 1265, 1230, 1150, 1119, 1104, 1018, 1003, 914, 859, 770, 750, 725, 704, 625, 566, 530 cm^{-1} .

HRMS (ESI-TOF): m/z calcd for $\text{C}_{53}\text{H}_{44}\text{N}_2\text{NaO}_4^+$ [$\text{M}+\text{Na}^+$]: 795.3193. Found: 795.3183.

1m:



Yield: 51%

Physical appearance: off-white solid, **m.p.:** 202-204 $^\circ\text{C}$

R_f: 0.25 (EtOAc:hexanes = 1:9)

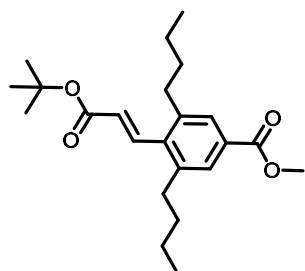
^1H NMR (400 MHz, CDCl_3): δ 7.69 (s, 2H), 7.50 (d, J = 16.4 Hz, 1H), 7.11 – 7.06 (m, 18H), 7.05 – 7.00 (m, 12H), 6.92 (d, J = 8.2 Hz, 4H), 6.78 (d, J = 8.3 Hz, 4H), 5.60 (d, J = 16.3 Hz, 1H), 3.92 (s, 4H), 3.90 (s, 3H), 1.50 (s, 9H).

¹³C NMR (101 MHz, CDCl₃): δ 166.91, 165.08, 143.91, 143.83, 143.78, 141.74, 141.16, 140.92, 140.72, 140.23, 139.58, 138.38, 131.59, 131.45, 129.61, 129.56, 128.27, 127.74, 127.72, 127.54, 126.55, 126.48, 126.46, 80.83, 52.24, 39.62, 28.32.

IR (KBr, neat): 2958, 2923, 2852, 1716, 1645, 1598, 1507, 1491, 1463, 1444, 1378, 1290, 1219, 1150, 1104, 1075, 1002, 888, 763, 746, 699 cm⁻¹.

HRMS (ESI-TOF): m/z calcd for C₆₉H₅₈O₄⁺ [M⁺]: 950.4330. Found: 950.4327.

1n:



*Dioxane was used as the solvent instead of toluene:THF (4:1)

Yield: 53%

Physical appearance: colorless oil

R_f: 0.7 (EtOAc:hexanes = 1:4)

¹H NMR (500 MHz, C₆D₆): δ 8.00 (d, *J* = 15.2 Hz, 1H), 7.98 (s, 2H), 6.09 (d, *J* = 16.3 Hz, 1H), 3.56 (s, 3H), 2.52 – 2.49 (m, 4H), 1.44 – 1.38 (m, 4H), 1.42 (s, 9H), 1.18 (h, *J* = 7.3 Hz, 4H), 0.79 (t, *J* = 7.4 Hz, 6H).

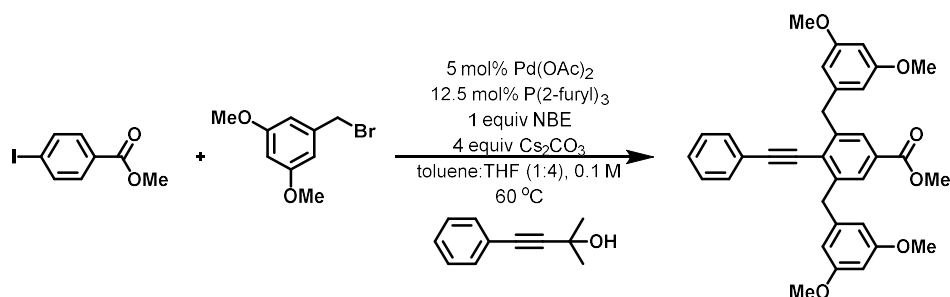
¹³C NMR (126 MHz, CDCl₃): δ 166.85, 165.23, 142.12, 141.74, 139.11, 130.22, 128.48, 127.29, 80.39, 51.63, 33.66, 33.38, 28.16, 22.76, 13.98.

IR (KBr, neat): 2954, 2871, 1723, 1644, 1608, 1569, 1435, 1456, 1392, 1367, 1311, 1279, 1253, 1213, 1150, 1007, 904, 848, 770, 668 cm⁻¹.

HRMS (ESI-TOF): m/z calcd for $C_{23}H_{34}NaO_4^+$ [$M+Na^+$]: 397.2349. Found: 397.2346.

2.5.3. Synthetic procedure for the three prototypes of multifunctional dendrons

Synthesis of compound **G1OMe1**



A flame-dried 350 mL Schlenk flask was charged with methyl 4-iodobenzoate (5.40 g, 20.61 mmol, 1.0 equiv), 3,5-dimethoxybenzyl bromide (10.0 g, 43.27 mmol, 2.1 equiv), 2-methyl-4-phenylbut-3-yn-2-ol (5.30 g, 25.83 mmol, 1.2 equiv), Pd(OAc)₂ (231.3 mg, 1.03 mmol, 5 mol%), and tri(2-furyl)phosphine (598.0 mg, 2.56 mmol, 12.5 mol%). The flask was brought into the glovebox, and anhydrous Cs₂CO₃ (26.86 g, 82.43 mmol, 4 equiv), norbornene (1.94 g, 20.61 mmol, 1 equiv), toluene (40.0 mL), and THF (160.0 mL) were added. The reaction mixture in the sealed flask was stirred at r. t. for 10 mins, was taken out of the glove box, and then was stirred and heated at a 60 °C oil-bath for 48 h. After cooling down to room temperature, the crude mixture was passed through a Büchner funnel packed with celite and washed with EtOAc. The organic solvents were removed under reduced pressure until a small amount of solvent was left. Methanol was added carefully to the crude mixture, and the recrystallized product was filtered to give the desired product.

Yield: 4.17 g (38%)

Physical appearance: white solid, **m.p.:** 143-145 °C

R_f: 0.45 (EtOAc:hexanes = 1:1)

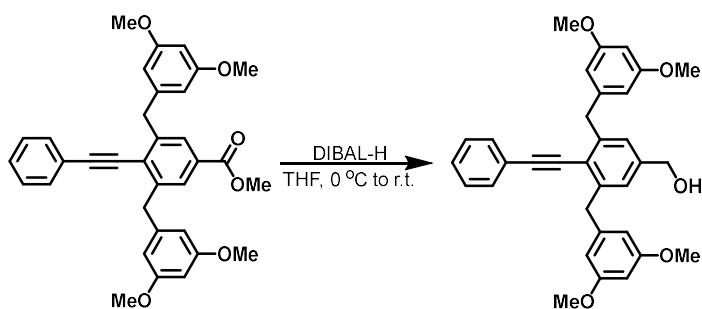
¹H NMR (500 MHz, CDCl₃): δ 7.78 (s, 2H), 7.45 (dd, *J* = 6.5, 2.9 Hz, 2H), 7.34 (dd, *J* = 4.9, 2.0 Hz, 3H), 6.43 (d, *J* = 2.3 Hz, 4H), 6.30 (t, *J* = 2.3 Hz, 2H), 4.22 (s, 4H), 3.87 (s, 3H), 3.70 (s, 12H).

¹³C NMR (101 MHz, CDCl₃): δ 166.85, 160.94, 143.58, 142.59, 131.69, 129.60, 128.91, 128.60, 128.58, 127.60, 123.04, 107.18, 100.69, 98.37, 87.00, 55.34, 52.31, 41.08.

IR (KBr, neat): 2999, 2951, 2837, 2209, 1720, 1606, 1595, 1564, 1492, 1460, 1430, 1319, 1289, 1258, 1206, 1156, 1097, 1066, 1004, 947, 916, 831, 770, 758, 726, 691 cm⁻¹.

HRMS (ESI-TOF): *m/z* calcd for C₃₄H₃₂NaO₆⁺ [*M*+Na⁺]: 559.2091. Found: 559.2094.

Synthesis of compound G1_{OH}OMe1



A flame-dried 250 mL round-bottom flask was charged with **G1OMe1** (4.13 g, 7.70 mmol, 1.0 equiv) and anhydrous THF (77.0 mL) under nitrogen. At 0 °C, DIBAL-H (1 M solution in hexanes, 16.9 mL, 16.93 mmol, 2.2 equiv) was added dropwise. The reaction mixture was then stirred at room temperature for 10 min. The conversion was monitored by TLC. Upon completion of the reaction, the crude mixture was diluted with ether (100 mL) and cooled down to 0 °C. A saturated aqueous solution of Rochelle's salt was added, and the mixture was stirred until phase separation was observed. The organic layer was washed with water (200 mL) and brine (200 mL), dried over

MgSO₄, and concentrated under reduced pressure. The crude product was purified by flash column chromatography on silica gel (EtOAc:hexanes = 1:1).

Yield: 3.91 g (quant.)

Physical appearance: white solid, **m.p.:** 99-101 °C

R_f: 0.1 (EtOAc:hexanes = 1:2)

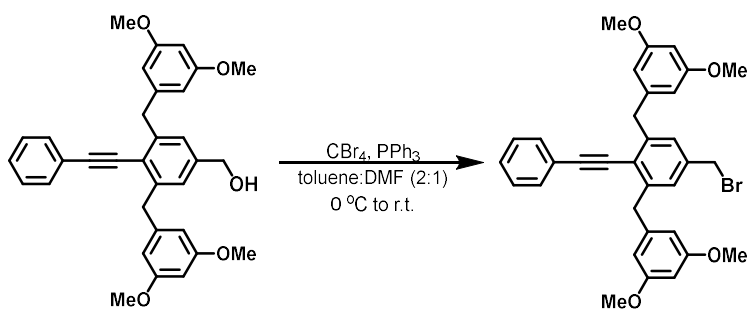
¹H NMR (400 MHz, CDCl₃): δ 7.47–7.44 (m, 2H), 7.32 (dd, *J* = 4.9, 1.9 Hz, 3H), 7.07 (s, 2H), 6.45 (d, *J* = 2.3 Hz, 4H), 6.31 (t, *J* = 2.3 Hz, 2H), 4.60 (s, 2H), 4.20 (s, 4H), 3.71 (s, 12H).

¹³C NMR (101 MHz, CDCl₃): δ 160.81, 143.58, 143.06, 141.26, 131.47, 128.44, 128.36, 125.88, 123.49, 121.90, 107.20, 98.13, 97.89, 87.49, 64.91, 55.21, 41.04.

IR (KBr, neat): 3419 (br), 2998, 2935, 2835, 2209, 1594, 1492, 1459, 1428, 1344, 1291, 1205, 1155, 1065, 831, 757, 690, 668 cm⁻¹.

HRMS (ESI-TOF): *m/z* calcd for C₃₃H₃₂NaO₅⁺ [*M*+Na⁺]: 531.2142. Found: 531.2145.

Synthesis of compound **G1_{Br}OMe1**



A 250 mL round bottom flask was charged with **G1_{OH}OMe1** (3.91 g, 7.70 mmol, 1.0 equiv) and triphenylphosphine (2.42 g, 9.24 mmol, 1.2 equiv). After adding toluene (51.2 mL) and DMF (25.6 mL), CBr₄ (3.06 g, 9.24 mmol, 1.2 equiv) was added at 0 °C. The reaction mixture was stirred at room temperature for 40 min. The conversion was monitored by TLC. Upon completion of the

reaction, the crude mixture was diluted with EtOAc (50 mL) and washed with water (100 mL × 3). The organic layer was dried over MgSO₄ and concentrated under reduced pressure. The crude product was purified by flash column chromatography on silica gel (EtOAc:hexanes = 1:4).

Yield: 3.99 g (91%)

Physical appearance: sticky white solid, **m.p.:** 123-125 °C

R_f: 0.35 (EtOAc:hexanes = 1:4)

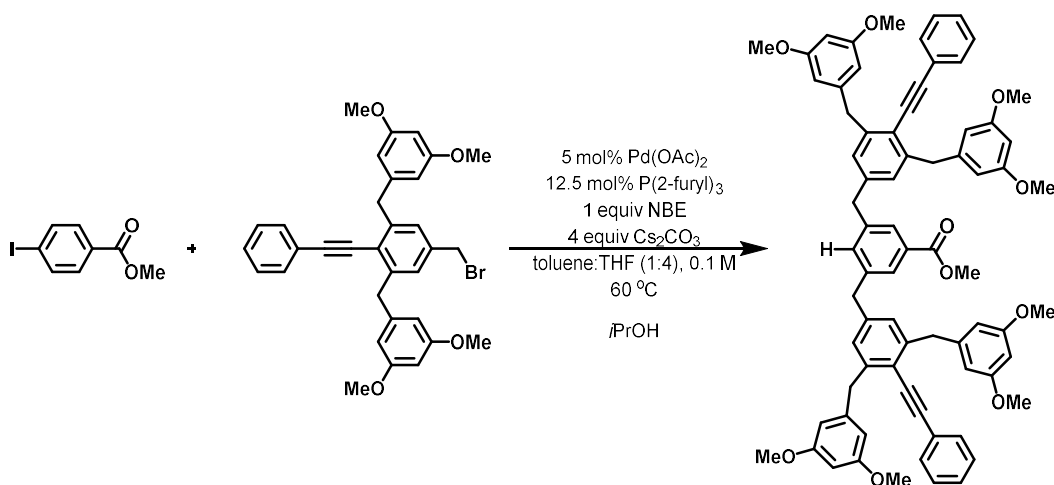
¹H NMR (500 MHz, CDCl₃): δ 7.46 – 7.45 (m, 2H), 7.34 – 7.33 (m, 3H), 7.09 (s, 2H), 6.44 (d, *J* = 2.3 Hz, 4H), 6.32 (t, *J* = 2.4 Hz, 2H), 4.39 (s, 2H), 4.18 (s, 4H), 3.72 (s, 12H).

¹³C NMR (126 MHz, CDCl₃): δ 160.95, 143.88, 142.68, 137.84, 131.61, 128.60, 128.54, 128.14, 123.39, 123.14, 107.26, 98.90, 98.42, 87.05, 55.36, 41.00, 33.50.

IR (KBr, neat): 2999, 2936, 2836, 2208 1595, 1492, 1460, 1428, 1345, 1323, 1291, 1205, 1156, 1066, 991, 945, 914, 831, 777, 757, 691, 663, 632 cm⁻¹.

HRMS (ESI-TOF): *m/z* calcd for C₃₃H₃₂BrO₄⁺ [M+H⁺]: 571.1478. Found: 571.1484.

Synthesis of compound G2OMe1



A flame-dried 40 mL reaction vial was charged with methyl 4-iodobenzoate (752.5 mg, 2.87 mmol, 1.0 equiv), **G1_{Br}OMe1** (3.45 g, 6.03 mmol, 2.1 equiv), isopropanol (0.26 mL, 3.45 mmol, 1.2 equiv), Pd(OAc)₂ (32.2 mg, 0.14 mmol, 5 mol%), and tri(2-furyl)phosphine (83.3 mg, 0.36 mmol, 12.5 mol%). The vial was brought into the glovebox, and anhydrous Cs₂CO₃ (3.74 g, 11.49 mmol, 4 equiv), norbornene (270.4 mg, 2.87 mmol, 1 equiv), toluene (5.7 mL), and THF (22.8 mL) were added. The reaction mixture in the sealed vial was stirred at r. t. for 10 mins, was taken out of the glove box, and then was stirred and heated at a preheated pie-block set to 60 °C for 7 days. After cooling down to room temperature, the crude mixture was passed through a Büchner funnel packed with celite and washed with EtOAc. The organic solvents were removed under reduced pressure. The crude product was purified by flash column chromatography on silica gel (hexanes:CH₂Cl₂:acetone = 3:1:1).

Yield: 1.85 g (58%, 40% yield can be achieved with a reaction time of 2 days)

Physical appearance: off-white solid, **m.p.:** 63-65 °C

R_f: 0.45 (Hexanes:CH₂Cl₂:acetone = 3:1:1)

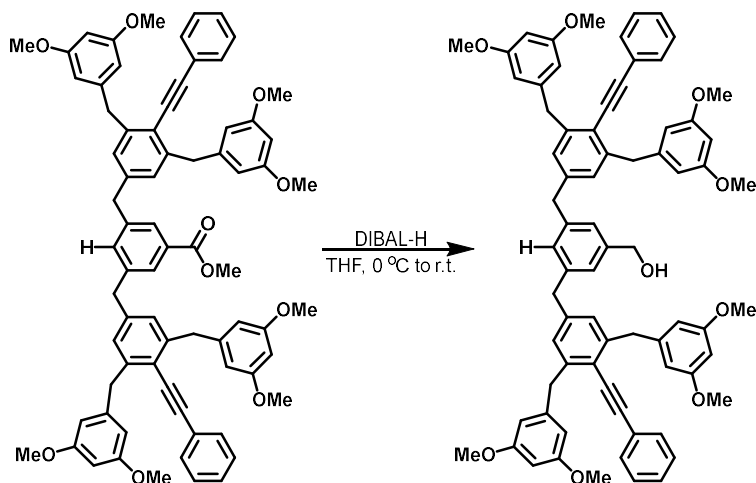
¹H NMR (400 MHz, CDCl₃): δ 7.63 (s, 2H), 7.41 (dd, *J* = 6.6, 3.0 Hz, 4H), 7.32 – 7.29 (m, 6H), 7.06 (s, 1H), 6.86 (s, 4H), 6.39 (d, *J* = 2.3 Hz, 8H), 6.27 (t, *J* = 2.3 Hz, 4H), 4.12 (s, 8H), 3.86 (s, 7H), 3.65 (s, 24H).

¹³C NMR (126 MHz, CDCl₃): δ 167.07, 160.78, 143.55, 143.10, 141.40, 140.82, 134.17, 131.46, 130.61, 128.43, 128.26, 128.22, 127.92, 123.65, 120.90, 107.07, 98.19, 97.70, 87.50, 55.19, 52.09, 41.47, 41.02.

IR (KBr, neat): 2999, 2936, 2836, 2208, 1720, 1595, 1561, 1492, 1459, 1428, 1344, 1292, 1265, 1205, 1155, 1115, 1066, 1005, 914, 831, 757, 736, 691 cm⁻¹.

HRMS (ESI-TOF): *m/z* calcd for C₇₄H₆₉O₁₀⁺ [M+H⁺]: 1117.4885. Found: 1117.4884.

Synthesis of compound **G2OHOMe1**



A flame-dried 50 mL round-bottom flask was charged with **G2OMe1** (1.85 g, 1.66 mmol, 1.0 equiv) and anhydrous THF (16.6 mL) under nitrogen. At 0 °C, DIBAL-H (1 M solution in hexanes, 3.64 mL, 3.64 mmol, 2.2 equiv) was added dropwise. The reaction mixture was then stirred at room temperature for 10 min. The conversion was monitored by TLC. Upon completion of the reaction, the crude mixture was diluted with ether (20 mL) and cooled down to 0 °C. A saturated aqueous solution of Rochelle's salt was added, and the mixture was stirred until phase separation was observed. The organic layer was washed with water (40 mL) and brine (40 mL), dried over MgSO₄, and concentrated under reduced pressure. The crude product was purified by flash column chromatography on silica gel (hexanes:CH₂Cl₂:acetone = 3:1:1).

Yield: 1.80 g (quant.)

Physical appearance: white solid, **m.p.:** 146-148 °C

R_f: 0.3 (Hexanes:CH₂Cl₂:acetone = 3:1:1)

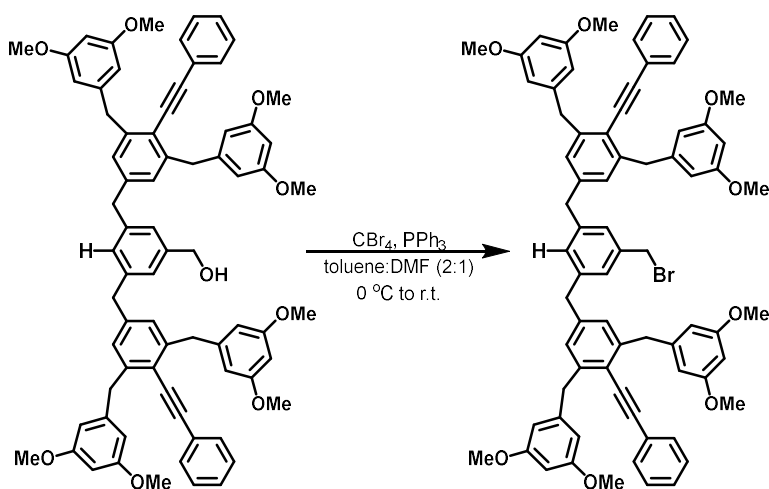
¹H NMR (400 MHz, CDCl₃): δ 7.45 – 7.42 (m, 4H), 7.33 – 7.30 (m, 6H), 6.89 (s, 6H), 6.85 (s, 1H), 6.40 (d, *J* = 2.3 Hz, 8H), 6.28 (t, *J* = 2.3 Hz, 4H), 4.53 (s, 2H), 4.13 (s, 8H), 3.84 (s, 4H), 3.67 (s, 24H).

^{13}C NMR (126 MHz, CDCl_3): δ 160.77, 143.42, 143.24, 141.85, 141.35, 141.30, 131.48, 128.82, 128.46, 128.35, 128.26, 125.18, 123.73, 120.66, 107.25, 98.08, 97.59, 87.57, 65.17, 55.27, 41.65, 41.02.

IR (KBr, neat): 3514 (br), 3053, 2999, 2936, 2836, 2208, 1595, 1560, 1492, 1459, 1428, 1345, 1322, 1291, 1265, 1205, 1155, 1066, 991, 915, 831, 777, 757, 736, 691, 664 cm^{-1} .

HRMS (ESI-TOF): m/z calcd for $\text{C}_{73}\text{H}_{69}\text{O}_9^+$ $[\text{M}+\text{H}^+]$: 1089.4927. Found: 1089.4936.

Synthesis of compound **G2BrOMe1**



A 50 mL round bottom flask was charged with **G2OHOMe1** (1.80 g, 1.65 mmol, 1.0 equiv) and triphenylphosphine (520.1 g, 1.98 mmol, 1.2 equiv). After adding toluene (11.0 mL) and DMF (5.5 mL), CBr_4 (657.6 g, 1.98 mmol, 1.2 equiv) was added at $0\text{ }^\circ\text{C}$. The reaction mixture was stirred at room temperature for 40 min. The conversion was monitored by TLC. Upon completion of the reaction, the crude mixture was diluted with EtOAc (20 mL) and washed with water ($30\text{ mL} \times 3$). The organic layer was dried over MgSO_4 and concentrated under reduced pressure. The crude

product was purified by flash column chromatography on silica gel (hexanes:CH₂Cl₂:acetone = 3:1:1).

Yield: 1.67 g (88%)

Physical appearance: white solid, **m.p.:** 137-139 °C

R_f: 0.5 (Hexanes:CH₂Cl₂:acetone = 3:1:1)

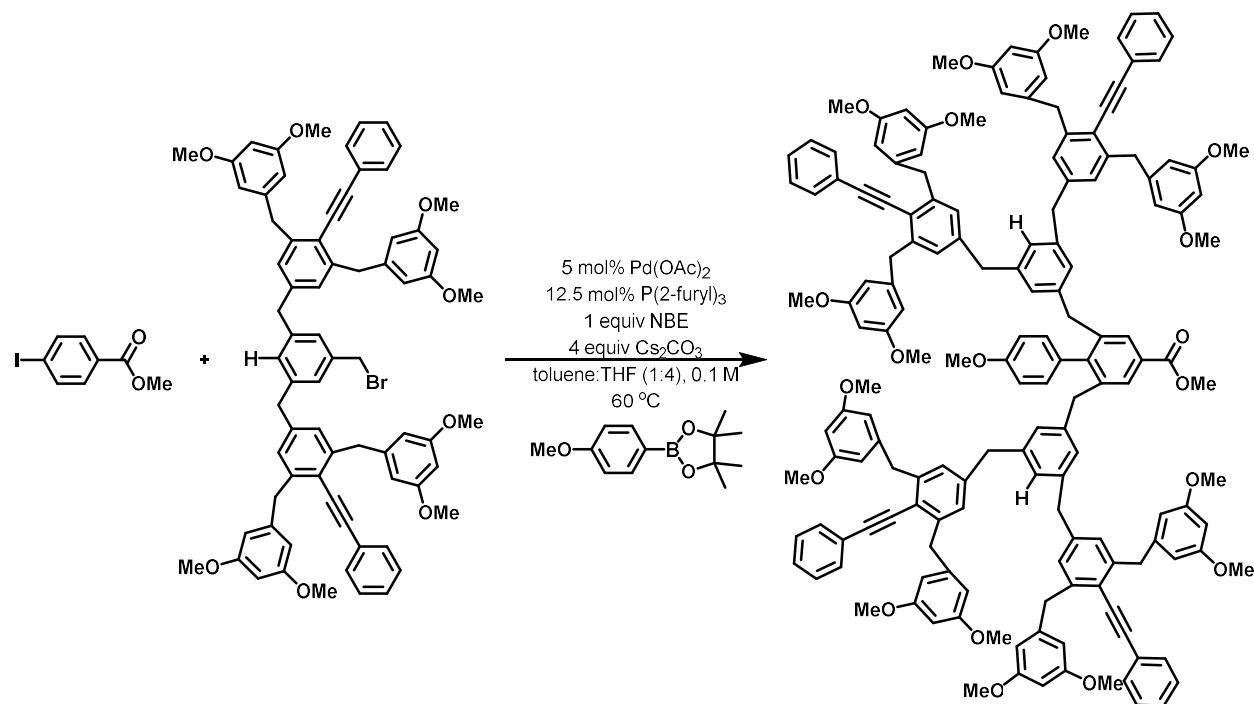
¹H NMR (400 MHz, CDCl₃): δ 7.44 – 7.42 (m, 4H), 7.33 – 7.30 (m, 6H), 6.94 (s, 2H), 6.89 (s, 4H), 6.83 (s, 1H), 6.41 (d, *J* = 2.3 Hz, 8H), 6.29 (t, *J* = 2.3 Hz, 4H), 4.36 (s, 2H), 4.14 (s, 8H), 3.82 (s, 4H), 3.66 (s, 24H).

¹³C NMR (101 MHz, CDCl₃): δ 160.82, 143.52, 143.20, 141.60, 140.88, 138.23, 131.49, 129.68, 128.45, 128.36, 128.27, 127.33, 123.70, 120.83, 107.16, 98.14, 97.65, 87.57, 55.25, 41.48, 41.04, 33.54.

IR (KBr, neat): 2998, 2935, 2835, 2208, 1595, 1560, 1492, 1459, 1428, 1345, 1322, 1291, 1205, 1155, 1066, 992, 914, 831, 757, 691, 664 cm⁻¹.

HRMS (ESI-TOF): *m/z* calcd for C₇₃H₆₈BrO₈⁺ [M+H⁺]: 1151.4092. Found: 1151.4067.

Synthesis of compound **G3OMe1**



A flame-dried 20 mL reaction vial was charged with methyl 4-iodobenzoate (153.8 mg, 0.59 mmol, 1.0 equiv), **G2BrOMe1** (1.42 g, 1.23 mmol, 2.1 equiv), 4-methoxyphenylboronic acid pinacol ester (164.9 mg, 0.70 mmol, 1.2 equiv), Pd(OAc)₂ (6.6 mg, 0.029 mmol, 5 mol%), and tri(2-furyl)phosphine (17.0 mg, 0.073 mmol, 12.5 mol%). The vial was brought into the glovebox, and anhydrous Cs₂CO₃ (764.9 mg, 2.35 mmol, 4 equiv), norbornene (55.3 mg, 0.59 mmol, 1 equiv), toluene (1.2 mL), and THF (4.8 mL) were added. The reaction mixture in the sealed vial was stirred at r. t. for 10 mins, was taken out of the glove box, and then was stirred and heated at a preheated pie-block set to 60 °C for 5 days. After cooling down to room temperature, the crude mixture was passed through a Büchner funnel packed with celite and washed with EtOAc. The organic solvents were removed under reduced pressure. The crude product was purified by flash column chromatography on silica gel (hexanes:CH₂Cl₂:acetone = 3:1:1).

Yield: 856.9 mg (61%)

Physical appearance: white solid, **m.p.:** 80-82 °C

R_f: 0.4 (Hexanes:CH₂Cl₂:acetone = 3:1:1)

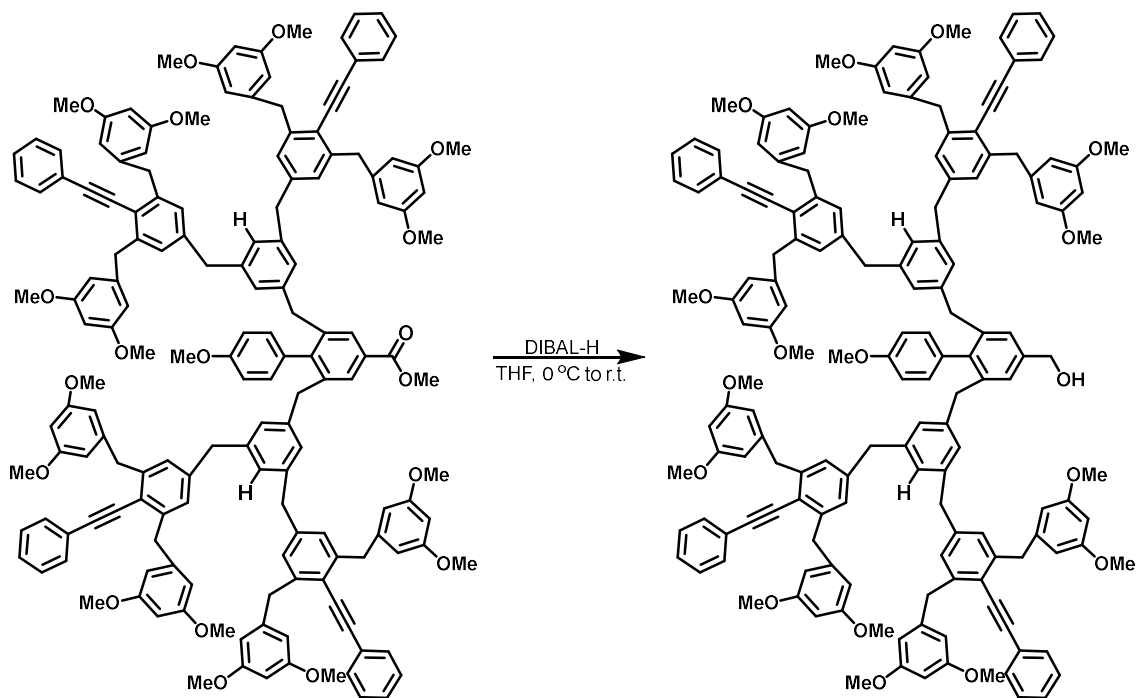
¹H NMR (500 MHz, CDCl₃): δ 7.79 (s, 2H), 7.43 – 7.41 (m, 8H), 7.33 – 7.30 (m, 12H), 6.84 (s, 8H), 6.64 (s, 4H), 6.62 (s, 2H), 6.44 (s, 4H), 6.39 (d, *J* = 2.4 Hz, 16H), 6.27 (t, *J* = 2.3 Hz, 8H), 4.11 (s, 16H), 3.83 (s, 3H), 3.71 (s, 8H), 3.67 (s, 3H), 3.65 (s, 4H), 3.62 (s, 48H).

¹³C NMR (126 MHz, CDCl₃): δ 167.21, 160.79, 158.78, 146.52, 143.35, 143.30, 141.56, 141.00, 140.70, 140.58, 131.49, 131.03, 130.45, 129.20, 129.08, 128.46, 128.40, 128.22, 127.41, 127.16, 123.78, 120.59, 113.66, 107.09, 98.16, 97.48, 87.76, 55.20, 52.15, 41.58, 41.06, 39.78.

IR (KBr, neat): 2998, 2935, 2835, 2208, 1719, 1595, 1561, 1514, 1492, 1459, 1428, 1344, 1321, 1291, 1246, 1265, 1205, 1155, 1066, 1002, 914, 831, 756, 736, 691 cm⁻¹.

MALDI-TOF-MS: m/z calcd for C₁₆₁H₁₄₆NaO₁₉⁺ [M+Na⁺]: 2406.04. Found: 2406.62.

Synthesis of compound **G3OHOMe1**



A flame-dried 10 mL round-bottom flask was charged with **G3OMe1** (826.9 mg, 0.35 mmol, 1.0 equiv) and anhydrous THF (3.5 mL) under nitrogen. At 0 °C, DIBAL-H (1 M solution in hexanes, 0.76 mL, 0.76 mmol, 2.2 equiv) was added dropwise. The reaction mixture was then stirred at room temperature for 10 min. The conversion was monitored by TLC. Upon completion of the reaction, the crude mixture was diluted with ether (5 mL) and cooled down to 0 °C. A saturated aqueous solution of Rochelle's salt was added, and the mixture was stirred until phase separation was observed. The organic layer was washed with water (10 mL) and brine (10 mL), dried over MgSO₄, and concentrated under reduced pressure. The crude product was purified by flash column chromatography on silica gel (hexanes:CH₂Cl₂:acetone = 2:1:1).

Yield: 685.0 mg (84%)

Physical appearance: white solid, **m.p.:** 73-75 °C

R_f: 0.25 (Hexanes:CH₂Cl₂:acetone = 4:2:1)

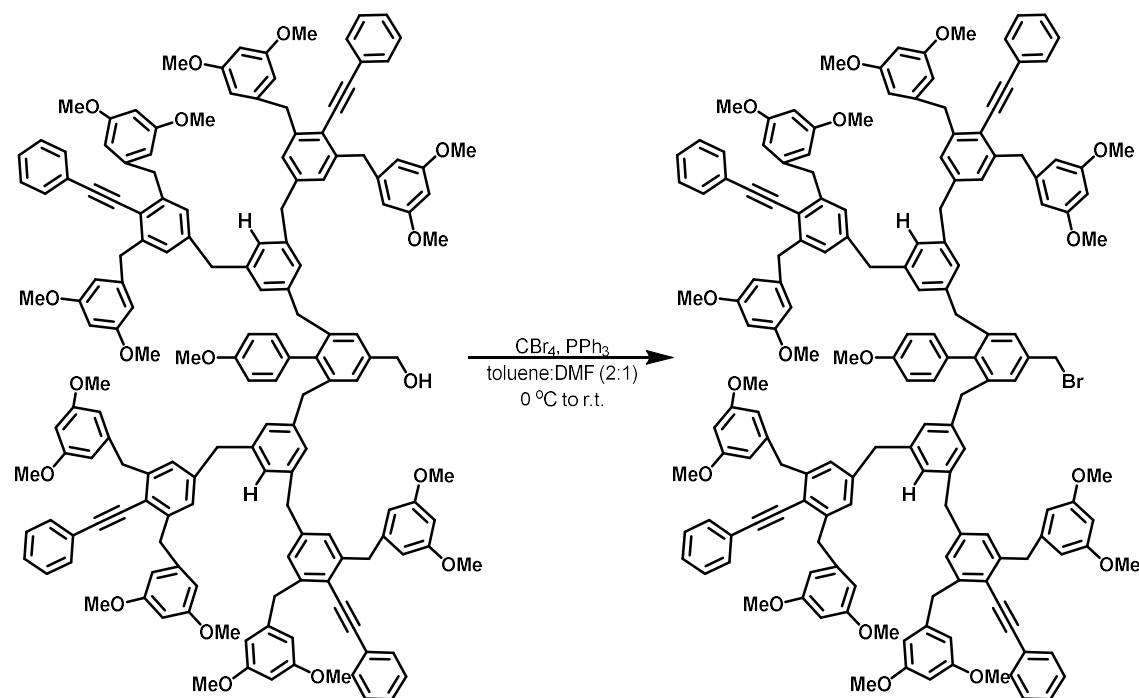
¹H NMR (500 MHz, CDCl₃): δ 7.42 – 7.40 (m, 8H), 7.31 – 7.29 (m, 12H), 7.00 (s, 2H), 6.85 (s, 8H), 6.72 (d, *J* = 8.6 Hz, 2H), 6.68 (d, *J* = 8.6 Hz, 2H), 6.62 (s, 2H), 6.48 (s, 4H), 6.39 (d, *J* = 2.3 Hz, 16H), 6.26 (t, *J* = 2.3 Hz, 8H), 4.53 (d, *J* = 6.0 Hz, 2H), 4.11 (s, 16H), 3.71 (s, 8H), 3.68 (s, 3H), 3.61 (s, 48H), 3.59 (s, 4H), 1.96 (-OH, t, *J* = 6.1 Hz, 1H).

¹³C NMR (126 MHz, CDCl₃): δ 160.79, 158.56, 143.34, 143.30, 141.64, 141.44, 140.83, 140.64, 140.25, 140.11, 131.82, 131.49, 130.97, 128.46, 128.39, 128.23, 127.56, 127.05, 126.33, 123.77, 120.58, 113.63, 107.12, 98.16, 97.50, 87.73, 65.21, 55.23, 41.63, 41.07, 39.87.

IR (KBr, neat): 3519 (br), 2999, 2935, 2836, 2208, 1595, 1514, 1492, 1459, 1428, 1345, 1322, 1291, 1243, 1205, 1155, 1066, 992, 910, 831, 757, 732, 691 cm⁻¹.

MALDI-TOF-MS: *m/z* calcd for C₁₆₀H₁₄₆NaO₁₈⁺ [*M*+Na⁺]: 2378.04. Found: 2378.60.

Synthesis of compound **G3_{Br}OMe1**



A 5 mL round bottom flask was charged with **G3OHOMe1** (635.0 mg, 0.27 mmol, 1.0 equiv) and triphenylphosphine (84.8 mg, 0.32 mmol, 1.2 equiv). After adding toluene (1.8 mL) and DMF (0.9 mL), CBr₄ (107.2 mg, 0.32 mmol, 1.2 equiv) was added at 0 °C. The reaction mixture was stirred at room temperature for 40 min. The conversion was monitored by TLC. Upon completion of the reaction, the crude mixture was diluted with EtOAc (3 mL) and washed with water (6 mL × 3). The organic layer was dried over MgSO₄ and concentrated under reduced pressure. The crude product was purified by flash column chromatography on silica gel (Hexanes:CH₂Cl₂:acetone = 3:1:1).

Yield: 607.1 mg (93%)

Physical appearance: white solid, **m.p.:** 81-83 °C

R_f: 0.55 (Hexanes:CH₂Cl₂:acetone = 3:1:1)

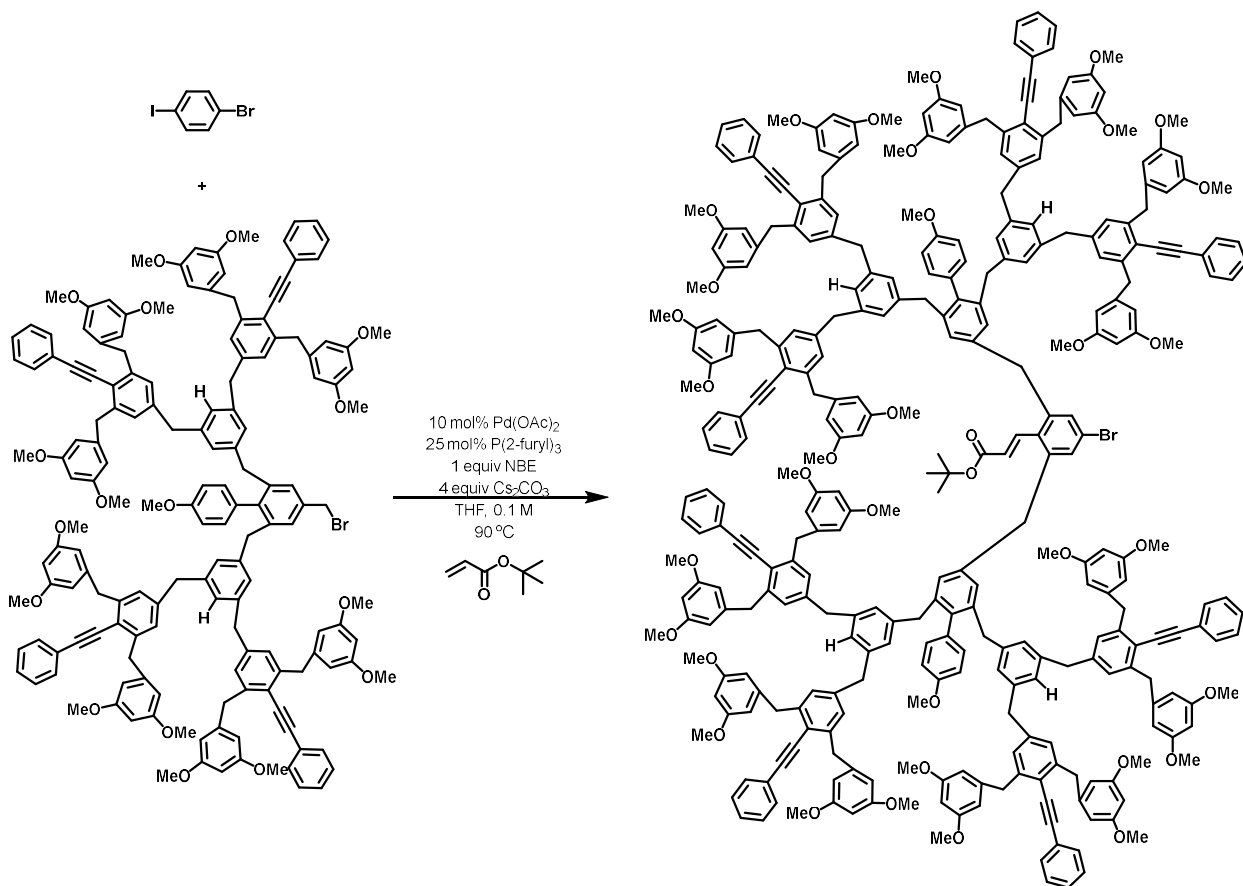
¹H NMR (500 MHz, CDCl₃): δ 7.43 – 7.41 (m, 8H), 7.31 – 7.30 (m, 12H), 7.04 (s, 2H), 6.86 (s, 8H), 6.70 (d, *J* = 8.6 Hz, 2H), 6.67 (d, *J* = 8.7 Hz, 2H), 6.64 (s, 2H), 6.48 (s, 4H), 6.40 (d, *J* = 2.3 Hz, 16H), 6.27 (t, *J* = 2.1 Hz, 8H), 4.35 (s, 2H), 4.12 (s, 16H), 3.72 (s, 8H), 3.68 (s, 3H), 3.62 (s, 48H), 3.58 (s, 4H).

¹³C NMR (126 MHz, CDCl₃): δ 160.80, 158.66, 143.35, 143.30, 141.82, 141.60, 141.10, 140.72, 140.58, 136.76, 131.49, 130.82, 128.45, 128.41, 128.22, 127.51, 127.12, 123.78, 120.62, 113.65, 107.11, 98.15, 97.49, 87.74, 55.22, 41.64, 41.08, 39.76, 33.97.

IR (KBr, neat): 2998, 2934, 2835, 2208, 1595, 1514, 1492, 1459, 1428, 1345, 1291, 1244, 1205, 1155, 1066, 911, 831, 757, 735, 691 cm⁻¹.

MALDI-TOF-MS: m/z calcd for C₁₆₀H₁₄₆BrO₁₇⁺ [M+H⁺]: 2417.97. Found: 2417.35.

Synthesis of compound **G4PhBrOMe**



A flame-dried 4 mL reaction vial was charged with 1-bromo-4-iodobenzene (7.1 mg, 0.025 mmol, 1.0 equiv), **G3BrOMe1** (127.0 mg, 0.0525 mmol, 2.1 equiv), *tert*-butyl acrylate (3.8 mg, 0.03 mmol, 1.2 equiv), Pd(OAc)₂ (0.56 mg, 0.03 mmol, 10 mol%), and tri(2-furyl)phosphine (1.45 mg, 0.00625 mmol, 25 mol%). The vial was brought into the glovebox, and anhydrous Cs₂CO₃ (32.6 mg, 0.1 mmol, 4 equiv), norbornene (2.4 mg, 0.025 mmol, 1 equiv), and THF (1.0 mL) were added. The reaction mixture in the sealed vial was stirred at r. t. for 10 mins, was taken out of the glove box, and then was stirred and heated at a preheated pie-block set to 90 °C for 2 days. After cooling down to room temperature, the crude mixture was passed through a Büchner funnel packed with celite and washed with EtOAc. The organic solvents were removed under reduced pressure. The

crude product was purified by flash column chromatography on silica gel (hexanes:CH₂Cl₂:acetone = 3:1:1).

Yield: 50.2 mg (40%)

Physical appearance: light yellow solid, **m.p.:** 90-92 °C

R_f: 0.2 (CH₂Cl₂:hexanes:acetone = 3:1:1)

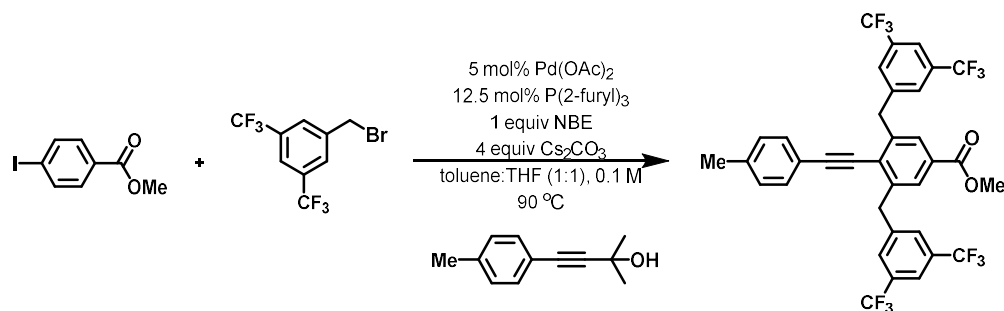
¹H NMR (500 MHz, CDCl₃): δ 7.70 (d, *J* = 16.3 Hz, 1H), 7.38 – 7.36 (m, 16H), 7.27 – 7.26 (m, 24H), 7.09 (s, 2H), 6.89 (s, 4H), 6.82 (s, 16H), 6.61 (d, *J* = 8.7 Hz, 4H), 6.56 (d, *J* = 8.8 Hz, 4H), 6.53 (s, 4H), 6.40 (s, 8H), 6.35 (d, *J* = 2.3 Hz, 32H), 6.22 (t, *J* = 2.3 Hz, 16H), 5.91 (d, *J* = 16.3 Hz, 1H), 4.06 (s, 32H), 3.88 (s, 4H), 3.68 (s, 16H), 3.61 (s, 6H), 3.58 (s, 8H), 3.55 (s, 96H), 1.42 (s, 9H).

¹³C NMR (126 MHz, CDCl₃): δ 165.36, 160.77, 158.45, 143.31, 141.94, 141.71, 141.54, 141.29, 140.53, 140.33, 140.09, 138.38, 133.92, 131.65, 131.48, 131.09, 130.62, 129.14, 128.48, 128.43, 128.18, 127.54, 127.39, 126.85, 123.80, 122.51, 120.57, 113.39, 107.06, 98.13, 97.42, 87.82, 80.86, 55.15, 41.61, 41.07, 39.98, 39.32, 28.27.

IR (KBr, neat): 2997, 2931, 2835, 1701, 1595, 1560, 1541, 1515, 1492, 1458, 1428, 1345, 1318, 1290, 1243, 1205, 1155, 1066, 992, 915, 831, 756, 691, 669 cm⁻¹.

HRMS (ESI-TOF): *m/z* calcd for C₃₃₃H₃₀₃BrNa₂O₃₆²⁺ [M+2Na²⁺]: 2501.0423. Found: 2501.0635.

Synthesis of compound **G1CF31**



A flame-dried 350 mL Schlenk flask was charged with methyl 4-iodobenzoate (5.24 g, 20.00 mmol, 1.0 equiv.), 3,5-bis(trifluoromethyl)benzyl bromide (12.90 g, 42.00 mmol, 2.1 equiv), 2-methyl-4-(*p*-tolyl)but-3-yn-2-ol (4.18 g, 24.0 mmol, 1.2 equiv), Pd(OAc)₂ (224.5 mg, 1.00 mmol, 5 mol%), and tri(2-furyl)phosphine (580.4 mg, 2.50 mmol, 12.5 mol%). The flask was brought into the glovebox, and anhydrous Cs₂CO₃ (26.07 g, 80.00 mmol, 4 equiv), norbornene (1.88 g, 20.00 mmol, 1 equiv), toluene (100.0 mL), and THF (100.0 mL) were added. The reaction mixture in the sealed flask was stirred at r. t. for 10 mins, was taken out of the glove box, and then was stirred and heated at a 90 °C oil-bath for 48 h. After cooling down to room temperature, the crude mixture was passed through a Büchner funnel packed with celite and washed with EtOAc. The organic solvents were removed under reduced pressure. Methanol was added carefully to the crude mixture, and the flask was cooled down to 0 °C. The recrystallized product was filtered to give the desired product.

Yield: 5.56 g (40%)

Physical appearance: white solid, **m.p.:** 187-189 °C

R_f: 0.4 (EtOAc:hexanes = 1:9)

¹H NMR (500 MHz, CDCl₃): δ 7.88 (s, 2H), 7.72 (s, 2H), 7.67 (s, 2H), 7.17 (d, *J* = 8.1 Hz, 2H), 7.14 (d, *J* = 8.1 Hz, 2H), 4.37 (s, 4H), 3.93 (s, 3H), 2.37 (s, 3H).

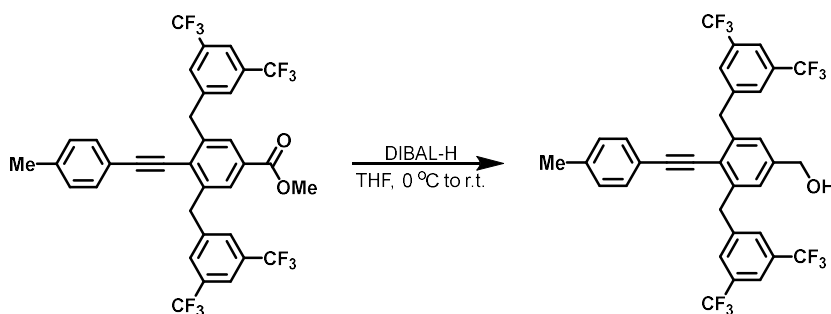
¹³C NMR (101 MHz, CDCl₃): δ 166.30, 142.45, 142.02, 140.00, 131.90 (q, ²J_{C-CF₃} = 33.2 Hz), 130.14, 129.50, 128.96 (q, ³J_{C-CF₃} = 3.8 Hz), 128.22, 123.43 (q, ¹J_{C-CF₃} = 272.8 Hz), 120.69, 118.73, 102.62, 85.08, 52.60, 40.64, 21.70.

¹⁹F NMR (376 MHz, CDCl₃): -62.85.

IR (KBr, neat): 2958, 2924, 2853, 2205, 1728, 1513, 1463, 1438, 1374, 1287, 1220, 1169, 1128, 1003, 907, 891, 879, 844, 814, 768, 727, 706, 684, 649 cm⁻¹.

HRMS (ESI-TOF): m/z calcd for C₃₅H₂₃F₁₂O₂⁺ [M+H⁺]: 703.1501. Found: 703.1489.

Synthesis of compound **G1_{OH}CF₃1**



A flame-dried 250 mL round-bottom flask was charged with **G1CF₃1** (5.28 g, 7.51 mmol, 1.0 equiv) and anhydrous THF (75.0 mL) under nitrogen. At 0 °C, DIBAL-H (1 M solution in hexanes, 16.5 mL, 16.52 mmol, 2.2 equiv) was added dropwise. The reaction mixture was then stirred at room temperature for 10 min. The conversion was monitored by TLC. Upon completion of the reaction, the crude mixture was diluted with ether (100 mL) and cooled down to 0 °C. A saturated aqueous solution of Rochelle's salt was added, and the mixture was stirred until phase separation was observed. The organic layer was washed with water (200 mL) and brine (200 mL), dried over MgSO₄, and concentrated under reduced pressure. The crude product was purified by flash column chromatography on silica gel (EtOAc:hexanes = 1:1).

Yield: 5.0 g (99%)

Physical appearance: white solid, **m.p.:** 195-197 °C

R_f: 0.2 (EtOAc:hexanes = 1:4)

¹H NMR (400 MHz, CDCl₃): δ 7.71 (s, 2H), 7.70 (s, 4H), 7.18 (d, *J* = 7.1 Hz, 2H), 7.18 (s, 2H), 7.13 (d, *J* = 8.1 Hz, 2H), 4.72 (s, 2H), 4.34 (s, 4H), 2.36 (s, 3H).

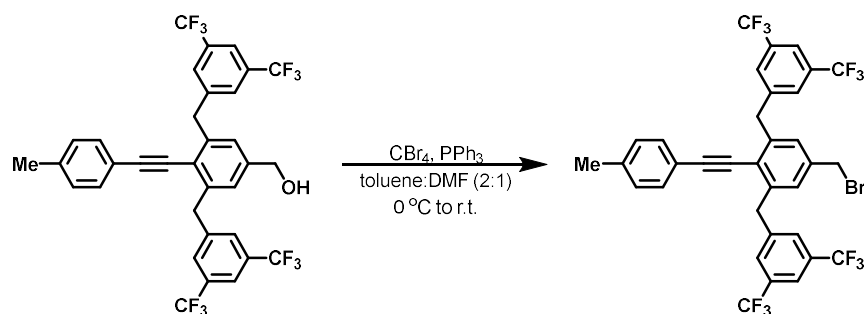
¹³C NMR (126 MHz, CDCl₃): δ 143.09, 142.17, 142.01, 139.42, 131.99 (q, ²*J*_{C-CF₃} = 33.1 Hz), 131.29, 129.44, 129.06, 126.77, 123.56 (q, ¹*J*_{C-CF₃} = 272.7 Hz), 122.85, 120.55, 120.52, 119.44, 99.75, 85.51, 64.78, 40.78, 21.60.

¹⁹F NMR (376 MHz, CDCl₃): -62.82.

IR (KBr, neat): 3329 (br), 3240 (br), 2957, 2924, 2853, 2358, 2341, 2205, 1507, 1465, 1457, 1437, 1375, 1289, 1171, 1128, 1042, 974, 927, 907, 889, 880, 813, 778, 708, 684 cm⁻¹.

HRMS (ESI-TOF): *m/z* calcd for C₃₄H₂₂F₁₂O⁺ [*M*⁺]: 674.1474. Found: 674.1466.

Synthesis of compound **G1_{Br}CF₃1**



A 250 mL round bottom flask was charged with **G1_{OH}CF₃1** (4.18 g, 6.19 mmol, 1.0 equiv) and triphenylphosphine (1.95 g, 7.43 mmol, 1.2 equiv). After adding toluene (41.2 mL) and DMF (20.6 mL), CBr₄ (2.46 g, 7.43 mmol, 1.2 equiv) was added at 0 °C. The reaction mixture was stirred at room temperature for 40 min. The conversion was monitored by TLC. The crude mixture was

diluted with EtOAc (50 mL) and washed with water (100 mL × 3). The organic layer was dried over MgSO₄ and concentrated under reduced pressure. The crude product was purified by recrystallization in CH₂Cl₂/MeOH.

Yield: 4.54 g (99%)

Physical appearance: white solid, **m.p.:** 145-147 °C

R_f: 0.7 (EtOAc:hexanes = 1:4)

¹H NMR (400 MHz, CDCl₃): δ 7.72 (s, 2H), 7.69 (s, 4H), 7.20 (s, 2H), 7.19 (d, *J* = 7.8 Hz, 2H), 7.13 (d, *J* = 8.0 Hz, 2H), 4.46 (s, 2H), 4.33 (s, 4H), 2.37 (s, 3H).

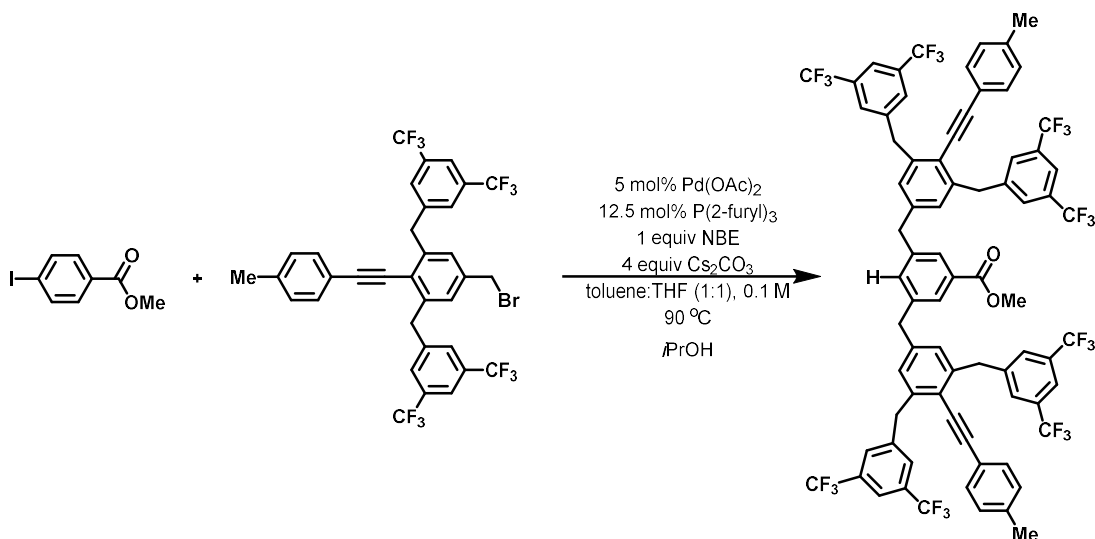
¹³C NMR (126 MHz, CDCl₃): δ 142.60, 142.35, 139.59, 138.62, 131.86 (q, ²*J*_{C-CF₃} = 33.3 Hz), 131.27, 129.44, 129.04, 123.72, 123.44 (q, ¹*J*_{C-CF₃} = 272.7 Hz), 120.63, 119.09, 100.49, 85.08, 40.56, 32.58, 21.68.

¹⁹F NMR (376 MHz, CDCl₃): -62.85.

IR (KBr, neat): 2925, 2853, 2205, 1511, 1465, 1438, 1374, 1287, 1167, 1128, 927, 907, 897, 881, 844, 814, 778, 740, 728, 706, 684 cm⁻¹.

MALDI-TOF-MS: *m/z* calcd for C₃₄H₂₁BrF₁₂Na⁺ [M+Na⁺]: 759.05. Found: 758.97.

Synthesis of compound **G2CF31**



A flame-dried 40 mL reaction vial was charged with methyl 4-iodobenzoate (766.5 mg, 2.93 mmol, 1.0 equiv.), **G1BrCF31** (4.53 g, 6.14 mmol, 2.1 equiv), isopropanol (0.27 mL, 3.51 mmol, 1.2 equiv), Pd(OAc)₂ (32.8 mg, 0.15 mmol, 5 mol%), and tri(2-furyl)phosphine (84.9 mg, 0.37 mmol, 12.5 mol%). The vial was brought into the glovebox, and anhydrous Cs₂CO₃ (3.81 g, 11.70 mmol, 4 equiv), norbornene (275.4 mg, 2.93 mmol, 1 equiv), toluene (14.6 mL), and THF (14.6 mL) were added. The reaction mixture in the vial was stirred at r. t. for 10 mins, was taken out of the glove box, and then was stirred and heated at a preheated pie-block set to 90 °C for 24 h. After cooling down to room temperature, the crude mixture was passed through a Büchner funnel packed with celite and washed with EtOAc. The organic solvents were removed under reduced pressure. The crude product was purified by recrystallization in CH₂Cl₂/MeOH.

Yield: 1.85 g (44%)

Physical appearance: light yellow solid, **m.p.:** 217-219 °C

R_f: 0.6 (CH₂Cl₂:hexanes = 1:2)

¹H NMR (500 MHz, C₆D₆): δ 7.94 (s, 2H), 7.59 (s, 4H), 7.50 (s, 8H), 7.32 (d, *J* = 7.8 Hz, 4H), 6.97 (s, 1H), 6.93 (d, *J* = 7.7 Hz, 4H), 6.70 (s, 4H), 3.81 (s, 8H), 3.62 (s, 4H), 3.60 (s, 3H), 1.99 (s, 6H).

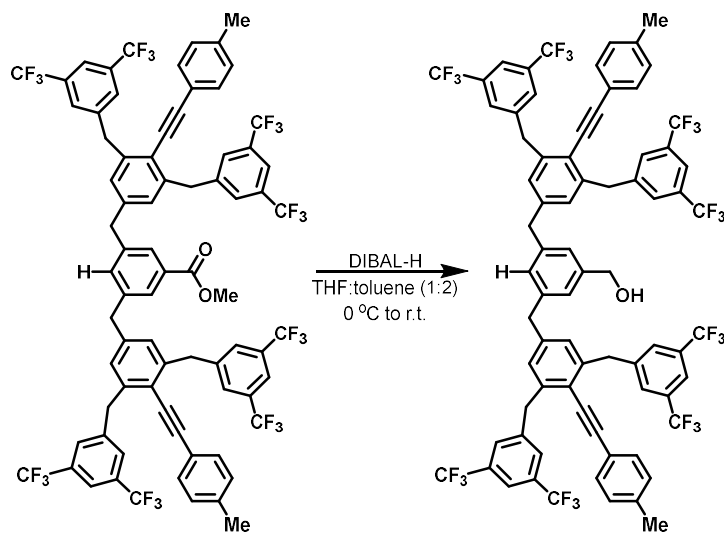
¹³C NMR (126 MHz, C₆D₆): δ 166.36, 143.38, 142.63, 142.06, 141.60, 139.69, 133.69, 132.04 (q, ²*J*_{C-CF₃} = 32.8 Hz), 131.45, 129.74, 129.24, 129.21, 129.04, 128.59, 123.96 (q, ¹*J*_{C-CF₃} = 272.8 Hz), 121.93, 120.49, 120.46, 120.43, 119.82, 100.16, 85.86, 51.77, 41.47, 40.50, 21.29.

¹⁹F NMR (376 MHz, CDCl₃): -62.87.

IR (KBr, neat): 2958, 2924, 2853, 2205, 1724, 1559, 1540, 1508, 1457, 1374, 1286, 1229, 1178, 1129, 1006, 905, 889, 879, 844, 813, 777, 728, 706, 684 cm⁻¹.

HRMS (ESI-TOF): *m/z* calcd for C₇₆H₄₉F₂₄O₂⁺ [M+H⁺]: 1449.3344. Found: 1449.3309.

Synthesis of compound **G2_{OH}CF₃1**



A flame-dried 50 mL round-bottom flask was charged with **G2CF₃1** (1.81 g, 1.25 mmol, 1.0 equiv), anhydrous THF (8.3 mL), and anhydrous toluene (16.6 mL) under nitrogen. At 0 °C, DIBAL-H (1 M solution in hexanes, 2.75 mL, 2.75 mmol, 2.2 equiv) was added dropwise. The

reaction mixture was then stirred at room temperature for 10 min. The conversion was monitored by TLC. Upon completion of the reaction, the crude mixture was diluted with EtOAc (10 mL) and cooled down to 0 °C. A saturated aqueous solution of Rochelle's salt was added, and the mixture was stirred until phase separation was observed. The organic layer was washed with water (20 mL) and brine (20 mL), dried over MgSO₄, and concentrated under reduced pressure. The crude product was purified by recrystallization in CH₂Cl₂/hexanes.

Yield: 1.75 g (99%)

Physical appearance: white solid, **m.p.:** 215-217 °C

R_f: 0.6 (CH₂Cl₂:hexanes = 2:1)

¹H NMR (400 MHz, CDCl₃): δ 7.69 (s, 4H), 7.64 (s, 8H), 7.16 (d, *J* = 8.0 Hz, 4H), 7.12 (d, *J* = 8.0 Hz, 4H), 6.98 (s, 6H), 6.87 (s, 1H), 4.59 (d, *J* = 5.2 Hz, 2H), 4.26 (s, 8H), 3.92 (s, 4H), 2.36 (s, 6H).

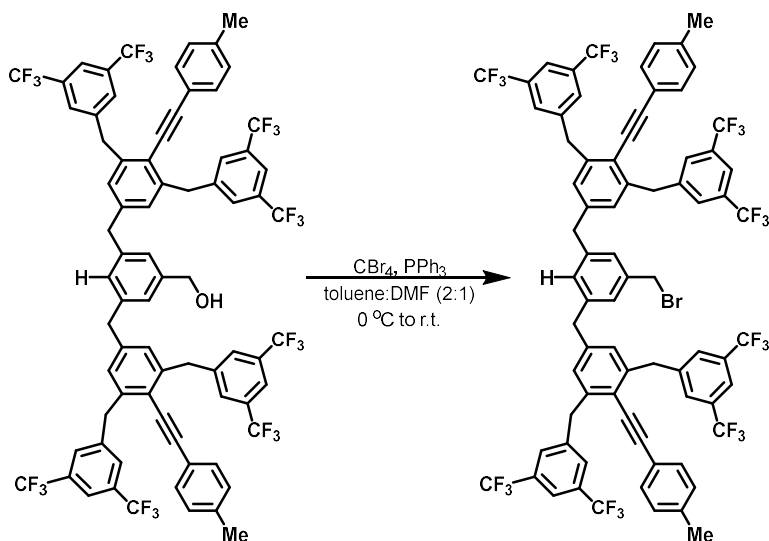
¹³C NMR (126 MHz, C₆D₆): δ 143.49, 143.10, 142.71, 142.50, 141.19, 139.63, 132.01 (q, ²*J*_{C-CF₃} = 32.9 Hz), 131.45, 129.73, 129.23, 125.64, 123.98 (q, ¹*J*_{C-CF₃} = 272.7 Hz), 121.74, 120.44, 119.86, 100.00, 85.95, 64.69, 41.80, 40.53, 21.28.

¹⁹F NMR (376 MHz, CDCl₃): -62.85.

IR (KBr, neat): 3385 (br), 2957, 2924, 2853, 2205, 1508, 1465, 1437, 1374, 1284, 1175, 1129, 906, 885, 813, 706, 684 cm⁻¹.

HRMS (ESI-TOF): *m/z* calcd for C₇₅H₄₉F₂₄O⁺ [M+H⁺]: 1421.3395. Found: 1421.3389.

Synthesis of compound **G2BrCF31**



A 25 mL round bottom flask was charged with **G2OHCf31** (1.36 g, 0.96 mmol, 1.0 equiv) and triphenylphosphine (301.9 mg, 1.15 mmol, 1.2 equiv). After adding toluene (6.4 mL) and DMF (3.2 mL), CBr_4 (381.7 mg, 1.15 mmol, 1.2 equiv) was added at $0\text{ }^\circ\text{C}$. The reaction mixture was stirred at room temperature for 40 min. The conversion was monitored by TLC. The crude mixture was diluted with EtOAc (10 mL) and washed with water ($20\text{ mL} \times 3$). The organic layer was dried over MgSO_4 and concentrated under reduced pressure. The crude product was purified by flash column chromatography on silica gel (hexanes: CH_2Cl_2 :acetone = 3:1:1).

Yield: 1.18 g (83%)

Physical appearance: white solid, **m.p.:** 207-209 $^\circ\text{C}$

R_f: 0.9 (hexanes: CH_2Cl_2 :acetone = 3:1:1)

$^1\text{H NMR}$ (500 MHz, CDCl_3): δ 7.69 (s, 4H), 7.64 (s, 8H), 7.16 (d, $J = 8.2\text{ Hz}$, 4H), 7.12 (d, $J = 8.0\text{ Hz}$, 4H), 7.01 (s, 2H), 6.96 (s, 4H), 6.84 (s, 1H), 4.36 (s, 2H), 4.26 (s, 8H), 3.91 (s, 4H), 2.36 (s, 6H).

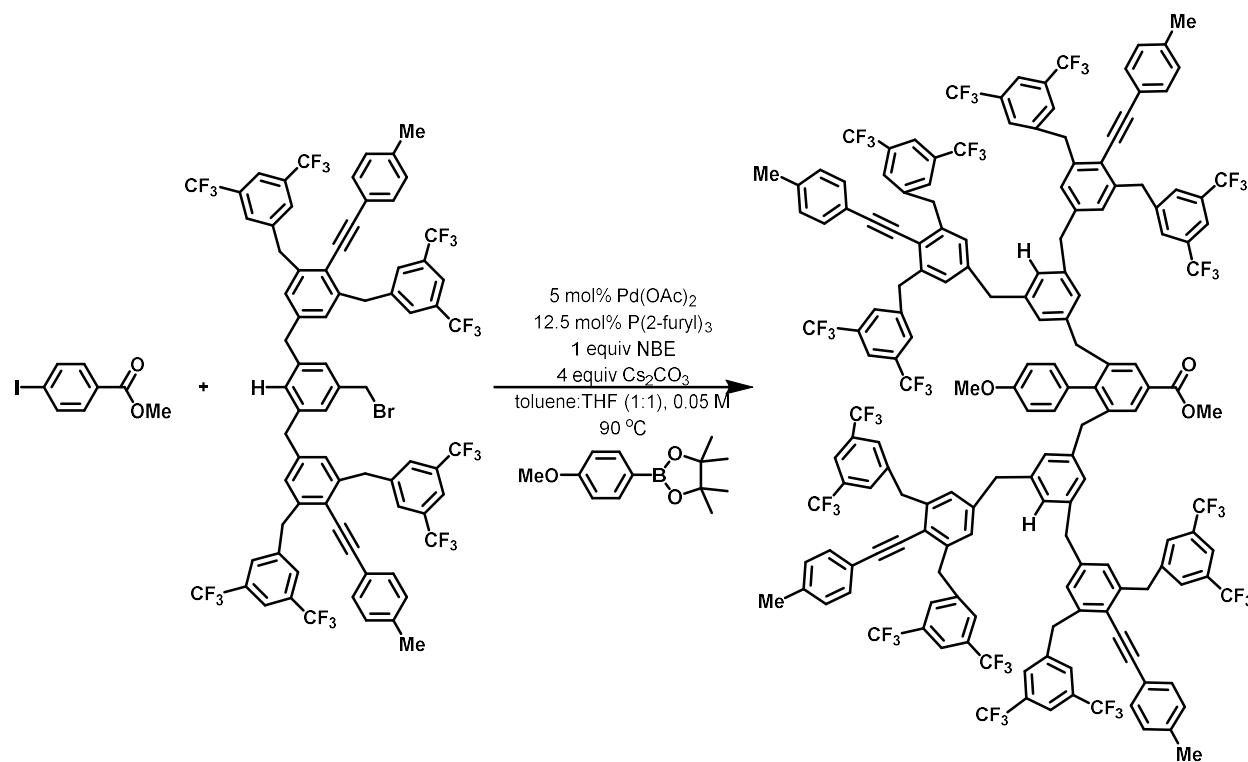
^{13}C NMR (126 MHz, C_6D_6): δ 143.45, 142.58, 142.16, 141.64, 139.69, 139.55, 132.05 (q, $^2J_{\text{C-CF}_3}$ = 32.8 Hz), 131.45, 129.74, 129.51, 129.18, 123.98 (q, $^1J_{\text{C-CF}_3}$ = 272.8 Hz), 121.89, 120.47, 119.80, 100.11, 85.87, 41.47, 40.52, 32.70, 21.28.

^{19}F NMR (376 MHz, CDCl_3): -62.84.

IR (KBr, neat): 2924, 2853, 2205, 1559, 1540, 1511, 1459, 1437, 1373, 1281, 1175, 1130, 1004, 906, 886, 843, 814, 706, 684 cm^{-1} .

MALDI-TOF-MS: m/z calcd for $\text{C}_{75}\text{H}_{48}\text{BrF}_{24}^+$ $[\text{M}+\text{H}^+]$: 1483.26. Found: 1483.78.

Synthesis of compound **G3CF31**



A flame-dried 20 mL reaction vial was charged with methyl 4-iodobenzoate (110.2 mg, 0.42 mmol, 1.0 equiv.), **G2BrCF31** (1.31 g, 0.88 mmol, 2.1 equiv), 4-methoxyphenylboronic acid pinacol ester (118.1 mg, 0.50 mmol, 1.2 equiv), $\text{Pd}(\text{OAc})_2$ (4.7 mg, 0.021 mmol, 5 mol%), and

tri(2-furyl)phosphine (12.2 mg, 0.053 mmol, 12.5 mol%). The vial was brought into the glovebox, and anhydrous Cs₂CO₃ (548.1 mg, 1.68 mmol, 4 equiv), norbornene (39.6 mg, 0.42 mmol, 1 equiv), toluene (4.2 mL), and THF (4.2 mL) were added. The reaction mixture in the vial was stirred at r. t. for 10 mins, was taken out of the glove box, and then was stirred and heated at a preheated pie-block set to 90 °C for 24 h. After cooling down to room temperature, the crude mixture was passed through a Büchner funnel packed with celite and washed with EtOAc. The crude product was purified by flash column chromatography on silica gel (loaded with toluene, then eluted with CH₂Cl₂:hexanes = 1:2).

Yield: 806.3 mg (64%)

Physical appearance: white solid, **m.p.:** 166-168 °C

R_f: 0.7 (CH₂Cl₂:hexanes = 1:1)

¹H NMR (500 MHz, CDCl₃): δ 7.74 (s, 2H), 7.67 (s, 8H), 7.62 (s, 16H), 7.15 (d, *J* = 8.3 Hz, 8H), 7.11 (d, *J* = 8.2 Hz, 8H), 6.91 (s, 8H), 6.76 (d, *J* = 8.7 Hz, 2H), 6.71 (d, *J* = 8.8 Hz, 2H), 6.65 (s, 2H), 6.54 (s, 4H), 4.23 (s, 16H), 3.81 (s, 8H), 3.73 (s, 3H), 3.71 (s, 3H), 3.67 (s, 4H), 2.35 (s, 12H).

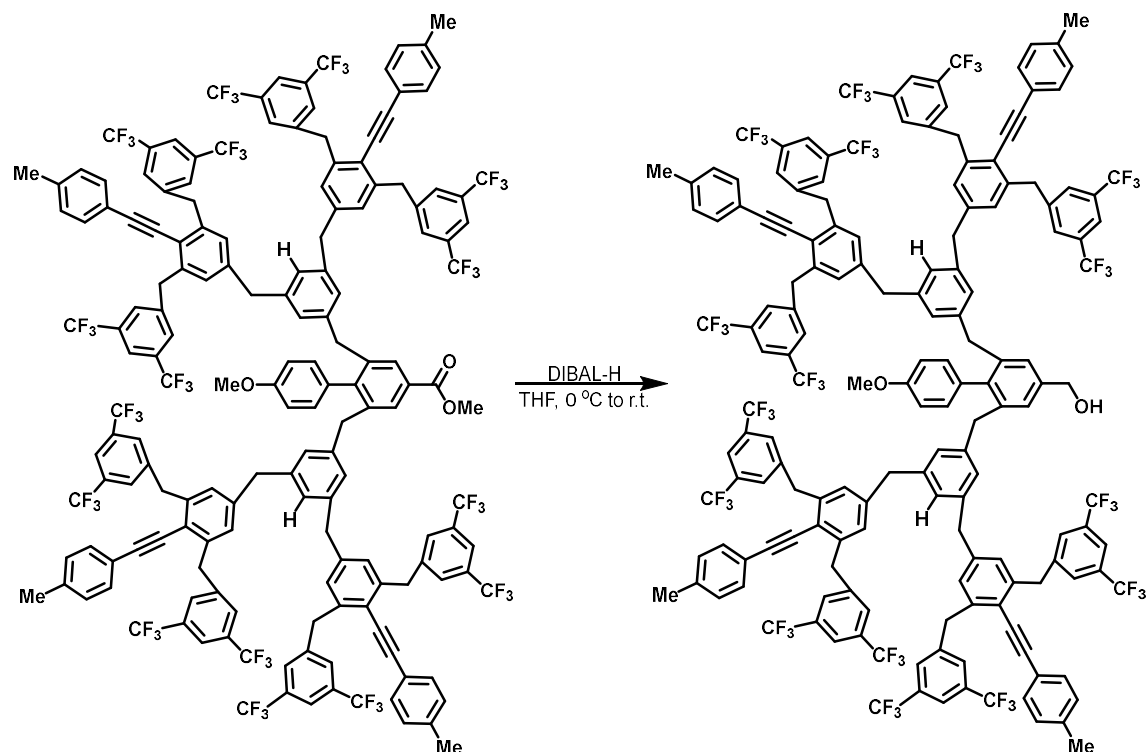
¹³C NMR (126 MHz, CDCl₃): δ 167.19, 158.84, 146.49, 143.10, 142.29, 141.87, 141.37, 140.59, 140.50, 139.25, 131.50 (q, ²*J*_{C-CF₃} = 33.1 Hz), 131.15, 130.43, 129.38, 129.15, 128.91, 127.82, 127.08, 123.32 (q, ¹*J*_{C-CF₃} = 272.7 Hz), 121.27, 120.35, 119.38, 113.68, 99.19, 85.47, 55.18, 52.01, 41.48, 40.57, 39.74, 21.63.

¹⁹F NMR (376 MHz, CDCl₃): -62.87.

IR (KBr, neat): 2925, 2205, 1718, 1654, 1599, 1512, 1541, 1458, 1437, 1374, 1278, 1172, 1131, 1040, 1004, 905, 843, 884, 815, 776, 726, 705, 683, 669 cm⁻¹.

MALDI-TOF-MS: m/z calcd for C₁₆₅H₁₀₆F₄₈O₃⁺ [M⁺]: 3046.74. Found: 3046.83.

Synthesis of compound **G3OHCF31**



A flame-dried 10 mL round-bottom flask was charged with **G3CF₃1** (779.2 mg, 0.26 mmol, 1.0 equiv) and anhydrous THF (2.6 mL) under nitrogen. At 0 °C, DIBAL-H (1 M solution in hexanes, 0.56 mL, 0.56 mmol, 2.2 equiv) was added dropwise. The reaction mixture was then stirred at room temperature for 10 min. The conversion was monitored by TLC. Upon completion of the reaction, the crude mixture was diluted with ether (5 mL) and cooled down to 0 °C. A saturated aqueous solution of Rochelle's salt was added, and the mixture was stirred until phase separation was observed. The organic layer was washed with water (10 mL) and brine (10 mL), dried over MgSO₄, and concentrated under reduced pressure. The crude product was purified by flash column chromatography on silica gel (CH₂Cl₂:hexanes = 1:1).

Yield: 772.0 mg (quant.)

Physical appearance: white solid, **m.p.:** 177-179 °C

R_f: 0.4 (CH₂Cl₂:hexanes = 1:1)

¹H NMR (500 MHz, CDCl₃): δ 7.67 (s, 8H), 7.62 (s, 16H), 7.14 (d, J = 8.3 Hz, 8H), 7.10 (d, J = 8.1 Hz, 8H), 7.03 (s, 2H), 6.91 (s, 8H), 6.79 (d, J = 8.6 Hz, 2H), 6.71 (d, J = 8.7 Hz, 2H), 6.63 (s, 2H), 6.55 (s, 4H), 4.53 (s, 2H), 4.22 (s, 16H), 3.80 (s, 8H), 3.70 (s, 3H), 3.63 (s, 4H), 2.35 (s, 12H).

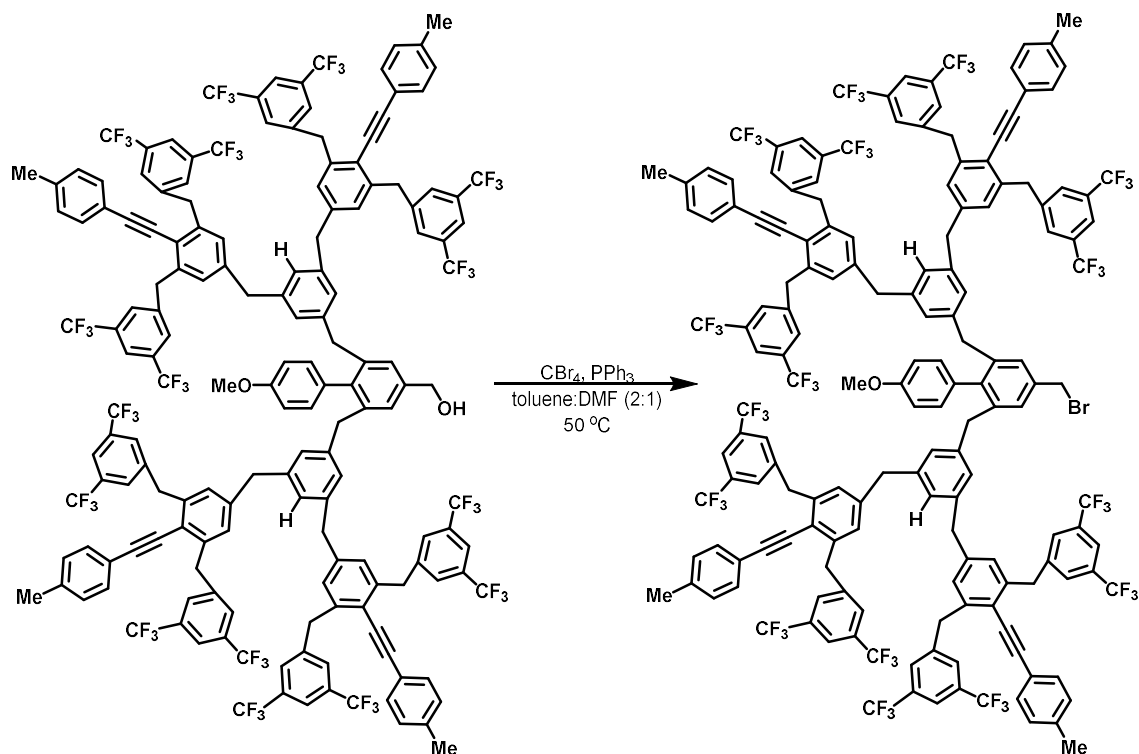
¹³C NMR (126 MHz, CDCl₃): δ 158.58, 142.99, 142.24, 141.73, 140.97, 140.28, 140.24, 139.81, 139.12, 131.62 (q, ²J_{C-CF₃} = 33.0 Hz), 131.02, 130.84, 129.23, 129.02, 128.79, 128.76, 127.76, 126.76, 126.60, 123.35 (q, ¹J_{C-CF₃} = 272.6 Hz), 121.21, 120.22, 119.28, 113.53, 99.18, 85.34, 65.14, 55.03, 41.42, 40.48, 39.76, 21.40.

¹⁹F NMR (376 MHz, CDCl₃): -62.86.

IR (KBr, neat): 3560 (br), 2925, 2206, 1595, 1560, 1513, 1465, 1438, 1373, 1328, 1280, 1174, 1130, 1040, 1020, 1003, 950, 895, 883, 843, 814, 777, 731, 725, 705, 683 cm⁻¹.

MALDI-TOF-MS: m/z calcd for C₁₆₄H₁₀₇F₄₈O₂⁺ [M+H⁺]: 3019.75 Found: 3019.76.

Synthesis of compound **G3BrCF31**



A 10 mL round bottom flask was charged with **G3OHCF31** (750.0 mg, 0.25 mmol, 1.0 equiv) and triphenylphosphine (78.2 mg, 0.30 mmol, 1.2 equiv). After adding toluene (3.2 mL) and DMF (1.6 mL), CBr_4 (98.9 mg, 0.30 mmol, 1.2 equiv) was added at $0\text{ }^\circ\text{C}$. The reaction mixture was then heated to $50\text{ }^\circ\text{C}$ and stirred for 40 min. The conversion was monitored by TLC. The crude mixture was diluted with EtOAc (5 mL) and washed with water ($10\text{ mL} \times 3$). The organic layer was dried over MgSO_4 and concentrated under reduced pressure. The crude product was purified by flash column chromatography on silica gel (CH_2Cl_2 :hexanes = 1:1).

Yield: 720.0 mg (94%)

Physical appearance: white solid, **m.p.:** $170\text{-}172\text{ }^\circ\text{C}$

R_f: 0.8 (CH_2Cl_2 :hexanes = 1:1)

¹H NMR (500 MHz, CDCl₃): δ 7.67 (s, 8H), 7.62 (s, 16H), 7.14 (d, *J* = 8.0 Hz, 8H), 7.10 (d, *J* = 8.0 Hz, 8H), 7.02 (s, 2H), 6.92 (s, 8H), 6.79 (d, *J* = 8.2 Hz, 2H), 6.72 (d, *J* = 8.4 Hz, 2H), 6.65 (s, 2H), 6.55 (s, 4H), 4.31 (s, 2H), 4.23 (s, 16H), 3.81 (s, 8H), 3.71 (s, 3H), 3.61 (s, 4H), 2.35 (s, 12H).

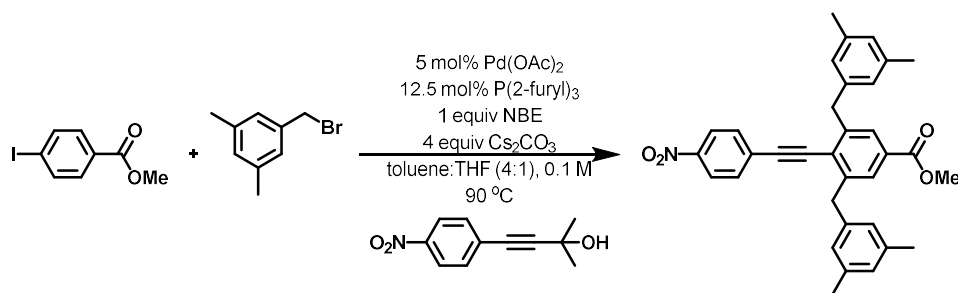
¹³C NMR (126 MHz, CDCl₃): δ 158.72, 143.08, 142.32, 141.87, 141.49, 140.66, 140.55, 139.27, 136.70, 131.67 (q, ²*J*_{C-CF₃} = 33.1 Hz), 131.16, 130.82, 129.38, 129.18, 128.94, 128.31, 127.86, 126.96, 123.48 (q, ¹*J*_{C-CF₃} = 272.7 Hz), 121.32, 120.38, 119.37, 113.67, 99.24, 85.45, 55.18, 41.56, 40.62, 39.76, 33.79, 21.63.

¹⁹F NMR (376 MHz, CDCl₃): -62.86.

IR (KBr, neat): 3033, 2925, 2855, 2207, 1597, 1560, 1513, 1465, 1437, 1374, 1280, 1173, 1130, 1039, 1019, 1103, 905, 883, 843, 814, 777, 726, 705, 683 cm⁻¹.

MALDI-TOF-MS: *m/z* calcd for C₁₆₄H₁₀₆BrF₄₈O⁺ [M+H⁺]: 3081.67. Found: 3081.71.

Synthesis of compound G1Me2



A flame-dried 350 mL Schlenk flask was charged with methyl 4-iodobenzoate (4.22 g, 16.11 mmol, 1.0 equiv), 3,5-dimethylbenzyl bromide (6.74 g, 33.83 mmol, 2.1 equiv), 2-methyl-4-(4-nitrophenyl)but-3-yn-2-ol (3.97 g, 19.33 mmol, 1.2 equiv), Pd(OAc)₂ (180.9 mg, 0.81 mmol, 5 mol%), and tri(2-furyl)phosphine (467.6 mg, 2.01 mmol, 12.5 mol%). The flask was brought into the glovebox, and anhydrous Cs₂CO₃ (21.00 g, 64.45 mmol, 4 equiv), norbornene (1.52 g, 16.11

mmol, 1 equiv), toluene (32.0 mL), and THF (128.0 mL) were added. The reaction mixture in the sealed flask was stirred at r. t. for 10 mins, was taken out of the glove box, and then was stirred and heated at a 90 °C oil-bath for 48 h. After cooling down to room temperature, the crude mixture was passed through a Büchner funnel packed with celite and washed with EtOAc. The organic solvents were removed under reduced pressure until a small amount of solvent was left. Methanol was added carefully to the crude mixture, and the recrystallized product was filtered to give the desired product.

Yield: 5.83 g (70%)

Physical appearance: yellow solid, **m.p.:** 189-191 °C

R_f: 0.7 (EtOAc:hexanes = 1:3)

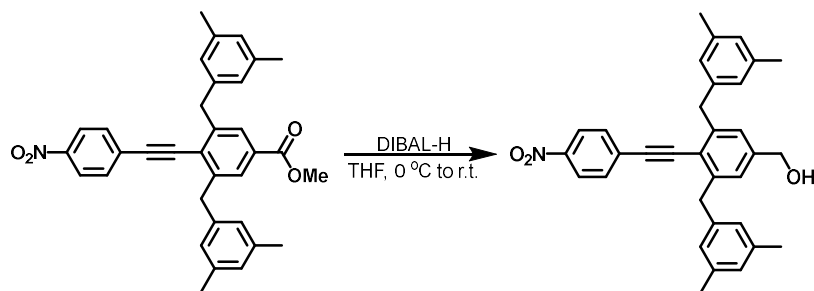
¹H NMR (500 MHz, CDCl₃): δ 8.20 (d, *J* = 8.5 Hz, 2H), 7.81 (s, 2H), 7.50 (d, *J* = 8.4 Hz, 2H), 6.85 (s, 2H), 6.83 (s, 4H), 4.20 (s, 4H), 3.89 (s, 3H), 2.25 (s, 12H).

¹³C NMR (126 MHz, CDCl₃): δ 166.84, 147.35, 144.48, 139.78, 138.12, 132.30, 130.45, 129.99, 128.81, 128.17, 126.83, 126.52, 123.80, 98.13, 92.20, 52.42, 40.78, 21.45.

IR (KBr, neat): 2957, 2924, 2854, 2210, 1722, 1593, 1564, 1519, 1464, 1435, 1377, 1342, 1296, 1260, 1213, 1144, 1095, 1005, 899, 854, 770, 749, 687 cm⁻¹.

HRMS (ESI-TOF): *m/z* calcd for C₃₄H₃₁NO₄⁺ [M⁺]: 517.2248. Found: 517.2245.

Synthesis of compound G1_{OH}Me₂



A flame-dried 250 mL round-bottom flask was charged with **G1Me2** (5.83 g, 11.26 mmol, 1.0 equiv) and anhydrous THF (110.0 mL) under nitrogen. At 0 °C, DIBAL-H (1 M solution in hexanes, 24.8 mL, 24.78 mmol, 2.2 equiv) was added dropwise. The reaction mixture was then stirred at room temperature for 10 min. The conversion was monitored by TLC. Upon completion of the reaction, the crude mixture was diluted with ether (100 mL) and cooled down to 0 °C. A saturated aqueous solution of Rochelle's salt was added, and the mixture was stirred until phase separation was observed. The organic layer was washed with water (200 mL) and brine (200 mL), dried over MgSO₄, and concentrated under reduced pressure. The crude product was purified by recrystallization in CH₂Cl₂ and MeOH.

Yield: 5.18 g (94%)

Physical appearance: yellow solid, **m.p.:** 166-168 °C

R_f: 0.3 (EtOAc:hexanes = 1:2)

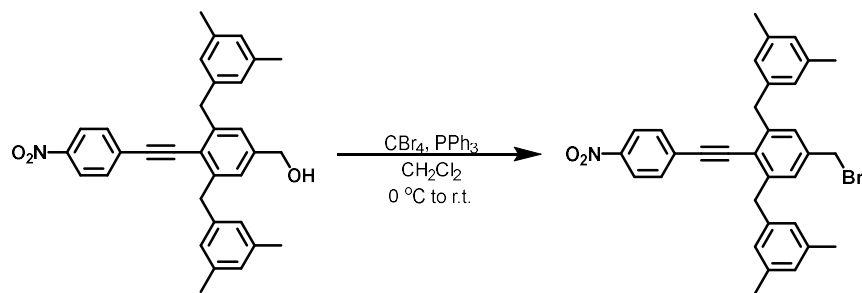
¹H NMR (400 MHz, CDCl₃): δ 8.19 (d, *J* = 8.8 Hz, 2H), 7.50 (d, *J* = 8.8 Hz, 2H), 7.10 (s, 2H), 6.86 (s, 6H), 4.64 (d, *J* = 4.8 Hz, 2H), 4.18 (s, 4H), 2.27 (s, 12H).

¹³C NMR (101 MHz, CDCl₃): δ 147.02, 144.62, 142.16, 140.24, 138.07, 132.11, 130.63, 128.05, 126.92, 126.11, 123.77, 121.08, 95.92, 93.13, 65.11, 40.78, 21.46.

IR (KBr, neat): 3358 (br), 2922, 2852, 2209, 1592, 1516, 1495, 1465, 1375, 1340, 1171, 1105, 1035, 850, 778, 749, 687 cm⁻¹.

HRMS (ESI-TOF): *m/z* calcd for C₃₃H₃₂NO₃⁺ [M+H⁺]: 490.2377. Found: 490.2382.

Synthesis of compound **G1_{Br}Me₂**



A 100 mL round bottom flask was charged with **G1_{OH}Me₂** (5.18 g, 10.58 mmol, 1.0 equiv) and triphenylphosphine (3.33 g, 12.70 mmol, 1.2 equiv). After adding CH_2Cl_2 (52.9 mL), CBr_4 (4.21 g, 12.70 mmol, 1.2 equiv) was added at $0\text{ }^\circ\text{C}$. The reaction mixture was stirred at room temperature for 40 min. The conversion was monitored by TLC. Upon completion of the reaction, the crude mixture was washed with water ($50\text{ mL} \times 3$). The organic layer was dried over MgSO_4 and concentrated under reduced pressure. The crude product was purified by recrystallization in CH_2Cl_2 and MeOH.

Yield: 4.58 g (78%)

Physical appearance: yellow solid, **m.p.:** 185-187 $^\circ\text{C}$

R_f: 0.7 (EtOAc:hexanes = 1:2)

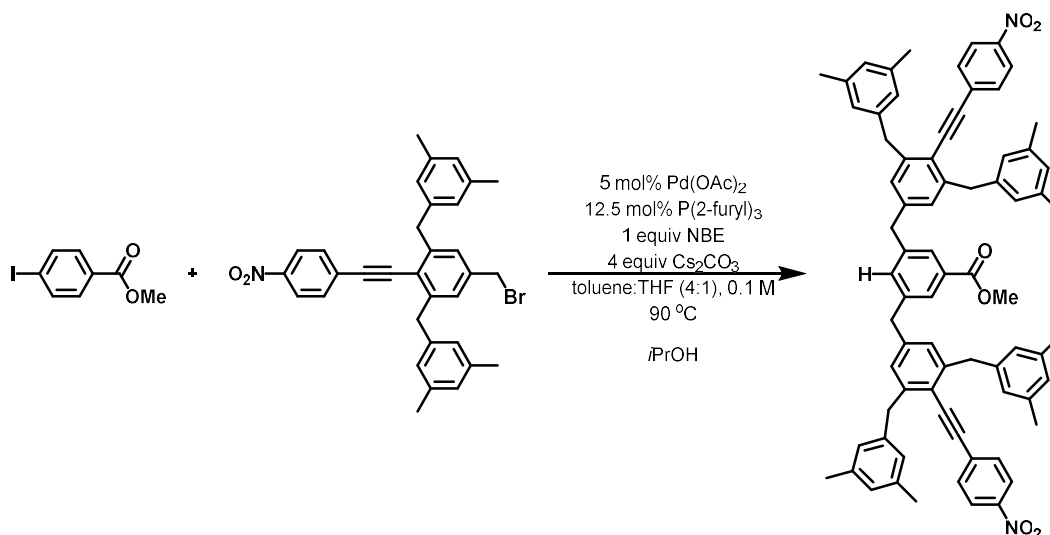
¹H NMR (400 MHz, CDCl_3): δ 8.19 (d, $J = 8.8$ Hz, 1H), 7.50 (d, $J = 8.8$ Hz, 2H), 7.10 (s, 2H), 6.86 (s, 2H), 6.84 (s, 4H), 4.40 (s, 2H), 4.16 (s, 4H), 2.27 (s, 12H).

¹³C NMR (101 MHz, CDCl_3): δ 147.09, 144.77, 139.84, 138.80, 138.09, 132.14, 130.35, 128.34, 128.10, 126.93, 123.74, 122.04, 96.62, 92.57, 40.63, 33.25, 21.43.

IR (KBr, neat): 2916, 2208, 1593, 1517, 1494, 1437, 1375, 1341, 1211, 1172, 1105, 851, 749, 687 cm^{-1} .

HRMS (ESI-TOF): m/z calcd for $\text{C}_{33}\text{H}_{31}\text{BrNO}_2^+$ [$\text{M}+\text{H}^+$]: 552.1533. Found: 552.1523.

Synthesis of compound **G2Me2**



A flame-dried 100 mL Schlenk flask was charged with methyl 4-iodobenzoate (1.02 g, 3.90 mmol, 1.0 equiv), **G1BrMe2** (4.53 g, 8.19 mmol, 2.1 equiv), isopropanol (0.36 mL, 4.68 mmol, 1.2 equiv), Pd(OAc)₂ (43.8 mg, 0.20 mmol, 5 mol%), and tri(2-furyl)phosphine (113.2 mg, 0.49 mmol, 12.5 mol%). The vial was brought into the glovebox, and anhydrous Cs₂CO₃ (5.08 g, 15.60 mmol, 4 equiv), norbornene (367.2 mg, 3.90 mmol, 1 equiv), toluene (31.2 mL), and THF (7.8 mL) were added. The reaction mixture in the sealed vial was stirred at r. t. for 10 mins, was taken out of the glove box, and then was stirred and heated at a 90 °C oil-bath for 48 h. After cooling down to room temperature, the crude mixture was passed through a Büchner funnel packed with celite and washed with EtOAc. The organic solvents were removed under reduced pressure. The crude product was purified by recrystallization in CH₂Cl₂ and hexanes.

Yield: 3.66 g (87%)

Physical appearance: yellow solid, **m.p.:** 186-188 °C

R_f: 0.55 (CH₂Cl₂:hexanes = 1:2)

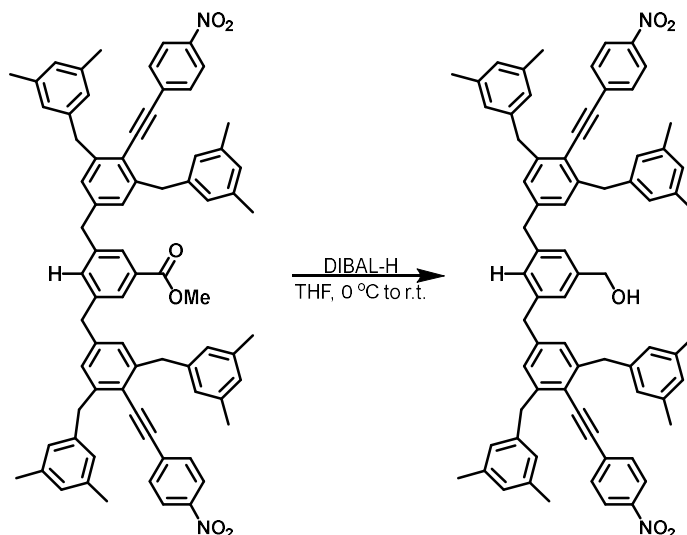
^1H NMR (400 MHz, CDCl_3): δ 8.17 (d, $J = 8.9$ Hz, 4H), 7.67 (s, 2H), 7.46 (d, $J = 8.9$ Hz, 4H), 7.10 (s, 1H), 6.87 (s, 4H), 6.82 (s, 4H), 6.79 (s, 8H), 4.10 (s, 8H), 3.90 (s, 4H), 3.87 (s, 3H), 2.23 (s, 24H).

^{13}C NMR (101 MHz, CDCl_3): δ 167.08, 146.93, 144.46, 141.85, 141.18, 140.23, 137.93, 134.25, 132.01, 130.76, 130.70, 128.43, 128.12, 127.93, 126.84, 123.72, 120.00, 95.76, 93.21, 52.20, 41.63, 40.70, 21.41.

IR (KBr, neat): 2916, 2207, 1722, 1592, 1517, 1495, 1434, 1375, 1215, 1106, 1010, 852, 770, 749, 688 cm^{-1} .

HRMS (ESI-TOF): m/z calcd for $\text{C}_{74}\text{H}_{69}\text{O}_{10}^+$ [$\text{M}+\text{H}^+$]: 1079.4994. Found: 1079.5005.

Synthesis of compound **G2OHMe2**



A flame-dried 50 mL round-bottom flask was charged with **G2Me2** (3.66 g, 3.39 mmol, 1.0 equiv) and anhydrous THF (18.0 mL) under nitrogen. At 0 °C, DIBAL-H (1 M solution in hexanes, 7.46 mL, 7.46 mmol, 2.2 equiv) was added dropwise. The reaction mixture was then stirred at room temperature for 10 min. The conversion was monitored by TLC. Upon completion of the reaction,

the crude mixture was diluted with ether (20 mL) and cooled down to 0 °C. A saturated aqueous solution of Rochelle's salt was added, and the mixture was stirred until phase separation was observed. The organic layer was washed with water (40 mL) and brine (40 mL), dried over MgSO₄, and concentrated under reduced pressure. The crude product was purified by flash column chromatography on silica gel (CH₂Cl₂:hexanes = 3:1).

Yield: 3.45 g (97%)

Physical appearance: yellow solid, **m.p.:** 113-115 °C

R_f: 0.1 (CH₂Cl₂:hexanes = 1:2)

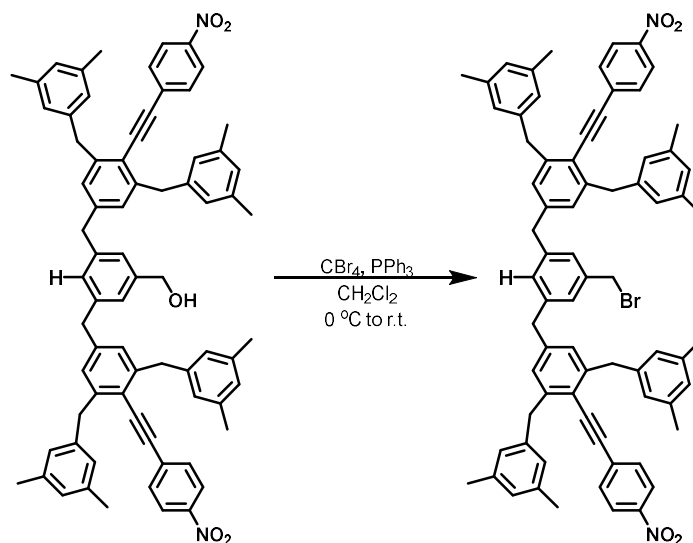
¹H NMR (500 MHz, CDCl₃): δ 8.17 (d, *J* = 8.8 Hz, 4H), 7.46 (d, *J* = 8.8 Hz, 4H), 6.93 (s, 2H), 6.91 (s, 4H), 6.87 (s, 1H), 6.83 (s, 4H), 6.80 (s, 8H), 4.55 (s, 2H), 4.10 (s, 8H), 3.87 (s, 4H), 2.23 (s, 24H).

¹³C NMR (101 MHz, CDCl₃): δ 146.90, 144.35, 142.28, 141.50, 141.15, 140.34, 137.92, 132.00, 130.73, 128.93, 128.54, 127.89, 126.84, 125.41, 123.71, 119.83, 95.67, 93.31, 65.32, 41.79, 40.70, 21.42.

IR (KBr, neat): 3383 (br), 3015, 2917, 2207, 1592, 1560, 1517, 1436, 1375, 1341, 1172, 1105, 909, 851, 777, 749, 732, 688 cm⁻¹.

HRMS (ESI-TOF): *m/z* calcd for C₇₃H₆₆N₂O₅⁺ [M⁺]: 1050.4966. Found: 1050.4962.

Synthesis of compound **G2BrMe2**



A 50 mL round bottom flask was charged with **G2OHMe2** (3.45 g, 3.28 mmol, 1.0 equiv) and triphenylphosphine (1.03 g, 3.94 mmol, 1.2 equiv). After adding CH_2Cl_2 (16.4 mL), CBr_4 (1.31 g, 3.94 mmol, 1.2 equiv) was added at $0\text{ }^\circ\text{C}$. The reaction mixture was stirred at room temperature for 40 min. The conversion was monitored by TLC. Upon completion of the reaction, the crude mixture was washed with water ($20\text{ mL} \times 3$). The organic layer was dried over MgSO_4 and concentrated under reduced pressure. The crude product was purified by recrystallization in CH_2Cl_2 and MeOH.

Yield: 2.80 g (77%)

Physical appearance: yellow solid, **m.p.:** 119-121 $^\circ\text{C}$

R_f: 0.3 (EtOAc:hexanes = 1:9)

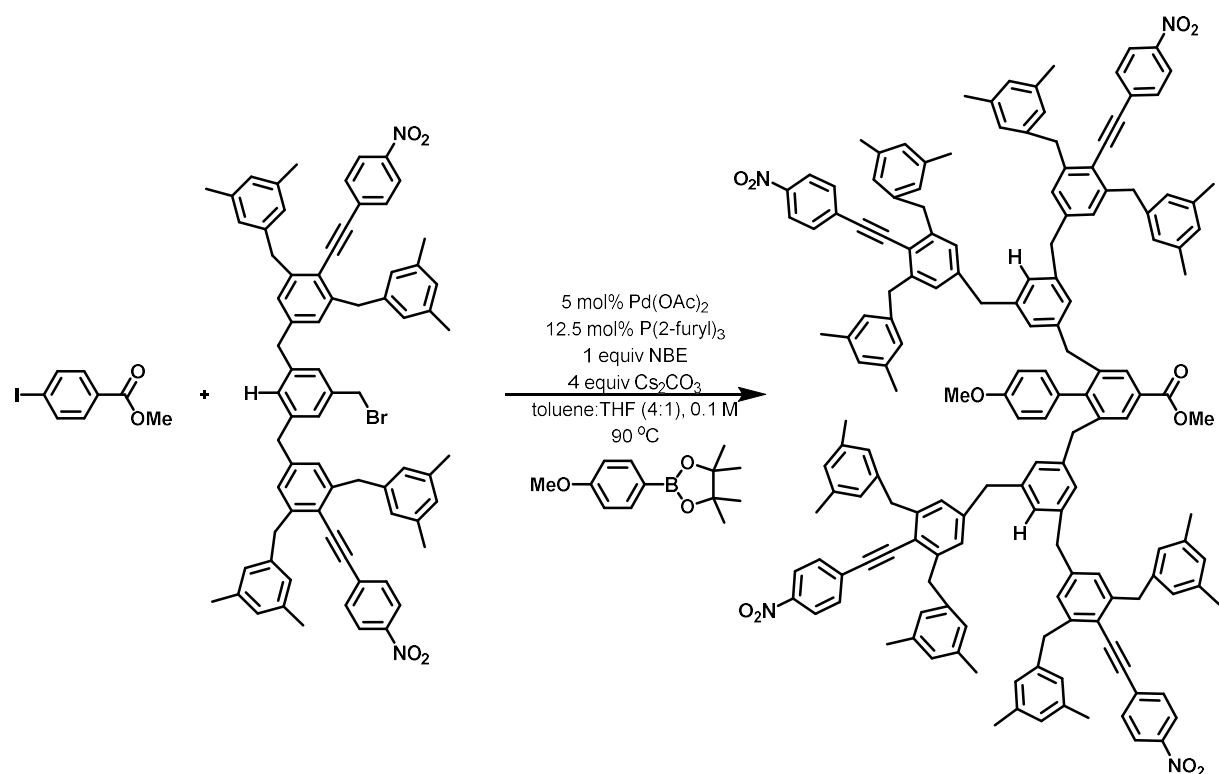
^1H NMR (400 MHz, CDCl_3): δ 8.17 (d, $J = 8.7\text{ Hz}$, 4H), 7.46 (d, $J = 8.8\text{ Hz}$, 4H), 6.96 (s, 2H), 6.90 (s, 4H), 6.85 (s, 1H), 6.83 (s, 4H), 6.81 (s, 8H), 4.35 (s, 2H), 4.11 (s, 8H), 3.85 (s, 4H), 2.23 (s, 24H).

^{13}C NMR (101 MHz, CDCl_3): δ 146.92, 144.43, 141.89, 141.41, 140.30, 138.31, 137.94, 132.02, 130.72, 129.75, 128.55, 127.94, 127.47, 126.85, 123.73, 119.93, 95.72, 93.27, 41.63, 40.72, 33.51, 21.46.

IR (KBr, neat): 3015, 2916, 2207, 1592, 1560, 1517, 1495, 1458, 1437, 1375, 1341, 1284, 1265, 1212, 1172, 1105, 1036, 852, 776, 749, 736, 688 cm^{-1} .

HRMS (ESI-TOF): m/z calcd for $\text{C}_{73}\text{H}_{66}\text{BrN}_2\text{O}_4^+$ [$\text{M}+\text{H}^+$]: 1113.4200. Found: 1113.4198.

Synthesis of compound **G3Me2**



A flame-dried 8 mL reaction vial was charged with methyl 4-iodobenzoate (131.0 mg, 0.50 mmol, 1.0 equiv), **G2BrMe2** (1.17 g, 1.05 mmol, 2.1 equiv), 4-methoxyphenylboronic acid pinacol ester (140.5 mg, 0.60 mmol, 1.2 equiv), $\text{Pd}(\text{OAc})_2$ (5.6 mg, 0.025 mmol, 5 mol%), and tri(2-furyl)phosphine (14.5 mg, 0.0625 mmol, 12.5 mol%). The vial was brought into the glovebox, and

anhydrous Cs₂CO₃ (651.6 mg, 2.00 mmol, 4 equiv), norbornene (47.0 mg, 0.50 mmol, 1 equiv), toluene (4.0 mL), and THF (1.0 mL) were added. The reaction mixture in the sealed vial was stirred at r. t. for 10 mins, was taken out of the glove box, and then was stirred and heated at a preheated pie-block set to 90 °C for 48 h. After cooling down to room temperature, the crude mixture was passed through a Büchner funnel packed with celite and washed with EtOAc. The organic solvents were removed under reduced pressure. The crude product was purified by flash column chromatography on silica gel (hexanes:CH₂Cl₂:acetone = 3:1:1).

Yield: 450.0 mg (39%)

Physical appearance: yellow solid, **m.p.:** 106-108 °C

R_f: 0.7 (CH₂Cl₂:hexanes = 1:4)

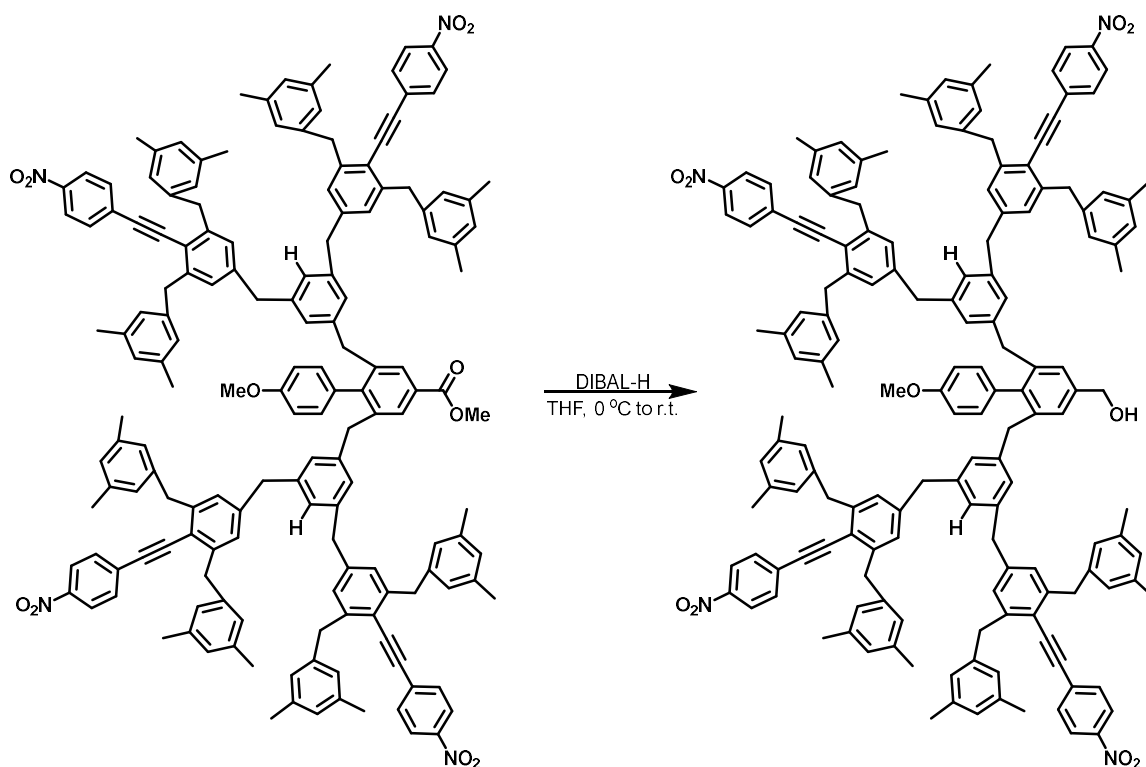
¹H NMR (400 MHz, CDCl₃): δ 8.15 (d, *J* = 8.8 Hz, 8H), 7.76 (s, 2H), 7.42 (d, *J* = 8.9 Hz, 8H), 6.83 (s, 8H), 6.79 (s, 8H), 6.77 (s, 16H), 6.64 (s, 2H), 6.62 (s, 4H), 6.46 (s, 4H), 4.06 (s, 16H), 3.78 (s, 3H), 3.73 (s, 8H), 3.63 (s, 7H), 2.19 (s, 48H).

¹³C NMR (126 MHz, CDCl₃): δ 167.10, 158.76, 146.85, 146.45, 144.21, 142.50, 140.97, 140.47, 140.33, 137.83, 137.62, 131.93, 130.69, 130.36, 129.03, 128.52, 127.86, 127.54, 127.28, 126.99, 126.78, 123.67, 119.66, 113.65, 112.29, 95.60, 93.38, 55.15, 52.10, 41.68, 40.70, 39.90, 21.39.

IR (KBr, neat): 3013, 2951, 2918, 2207, 1719, 1592, 1560, 1541, 1496, 1458, 1436, 1375, 1341, 1307, 1246, 1211, 1174, 1105, 1037, 1012, 853, 770, 749, 687 cm⁻¹.

MALDI-TOF-MS: m/z calcd for C₁₆₁H₁₄₂N₄NaO₁₁⁺ [M+Na⁺]: 2330.06. Found: 2330.64.

Synthesis of compound **G3OHMe2**



A flame-dried 10 mL round-bottom flask was charged with **G3Me2** (450.0 mg, 0.19 mmol, 1.0 equiv) and anhydrous THF (1.95 mL) under nitrogen. At 0 °C, DIBAL-H (1 M solution in hexanes, 0.43 mL, 0.43 mmol, 2.2 equiv) was added dropwise. The reaction mixture was then stirred at room temperature for 10 min. The conversion was monitored by TLC. Upon completion of the reaction, the crude mixture was diluted with ether (5 mL) and cooled down to 0 °C. A saturated aqueous solution of Rochelle's salt was added, and the mixture was stirred until phase separation was observed. The organic layer was washed with water (10 mL) and brine (10 mL), dried over MgSO₄, and concentrated under reduced pressure. The crude product was purified by flash column chromatography on silica gel (EtOAc:hexanes = 1:2).

Yield: 332.2 mg (75%)

Physical appearance: yellow solid, **m.p.:** 121-123 °C

R_f: 0.15 (EtOAc:hexanes = 1:4)

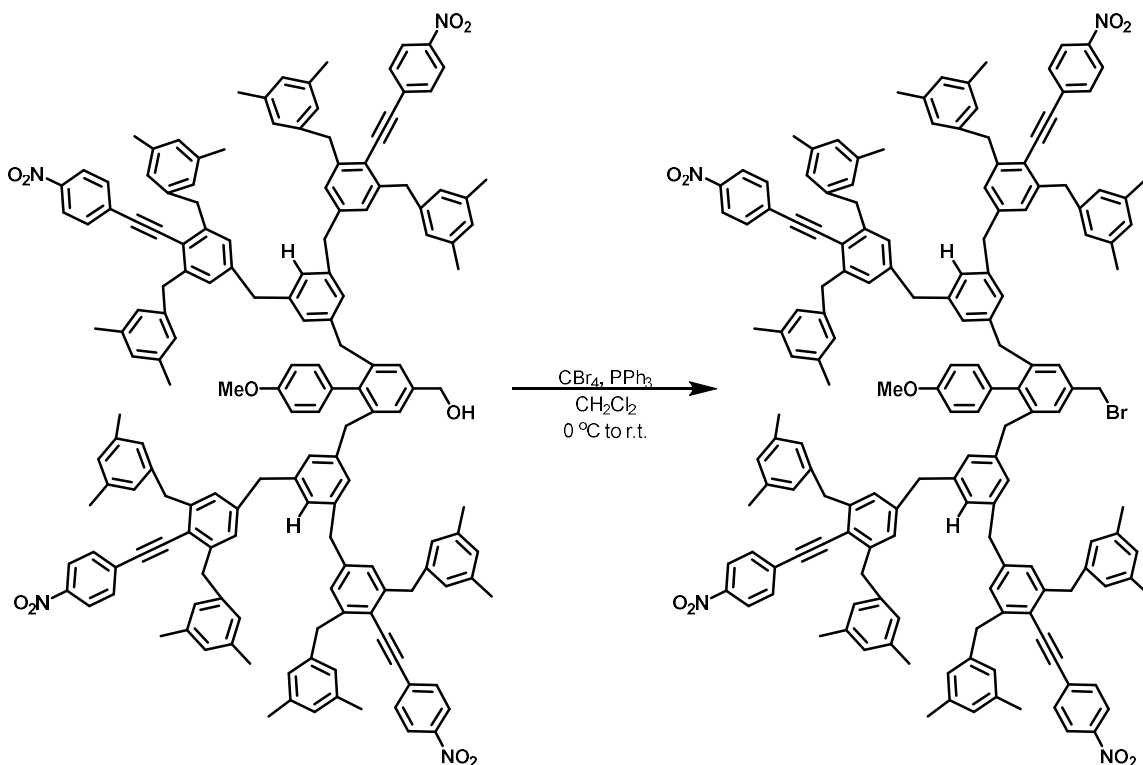
¹H NMR (500 MHz, CDCl₃): δ 8.15 (d, *J* = 8.8 Hz, 8H), 7.42 (d, *J* = 8.8 Hz, 8H), 6.96 (s, 2H), 6.84 (s, 8H), 6.79 (s, 8H), 6.77 (s, 16H), 6.72 (s, 2H), 6.66 (s, 4H), 6.51 (s, 4H), 4.45 (s, 2H), 4.07 (s, 16H), 3.75 (s, 8H), 3.65 (s, 3H), 3.59 (s, 4H), 2.19 (s, 48H).

¹³C NMR (101 MHz, CDCl₃): δ 158.58, 146.88, 144.21, 142.58, 141.38, 140.87, 140.47, 140.35, 140.28, 137.88, 137.67, 131.97, 130.88, 130.71, 128.57, 127.89, 127.73, 127.20, 127.01, 126.79, 126.24, 123.70, 119.70, 113.68, 95.62, 93.36, 65.26, 55.18, 41.74, 40.73, 40.00, 21.42.

IR (KBr, neat): 3568 (br), 3014, 2917, 2207, 1592, 1560, 1517, 1495, 1458, 1437, 1375, 1341, 1284, 1243, 1173, 1105, 1137, 853, 749, 688 cm⁻¹.

MALDI-TOF-MS: *m/z* calcd for C₁₆₀H₁₄₂N₄NaO₁₀⁺ [M+Na⁺]: 2302.06. Found: 2302.65.

Synthesis of compound **G3BrMe2**



A 5 mL round bottom flask was charged with **G3OHMe2** (57.0 mg, 0.025 mmol, 1.0 equiv) and triphenylphosphine (7.9 mg, 0.03 mmol, 1.2 equiv). After adding CH_2Cl_2 (2.5 mL), CBr_4 (9.9 mg, 0.03 mmol, 1.2 equiv) was added at $0\text{ }^\circ\text{C}$. The reaction mixture was stirred at room temperature for 40 min. The conversion was monitored by TLC. Upon completion of the reaction, the crude mixture was washed with water ($3\text{ mL} \times 3$). The organic layer was dried over MgSO_4 and concentrated under reduced pressure. The crude product was purified by flash column chromatography on silica gel (EtOAc:hexanes = 1:4).

Yield: 48.0 mg (82%)

Physical appearance: yellow solid, **m.p.:** 105-107 $^\circ\text{C}$

R_f: 0.6 (EtOAc:hexanes = 1:4)

¹H NMR (400 MHz, CDCl₃): δ 8.15 (d, *J* = 8.9 Hz, 8H), 7.43 (d, *J* = 8.8 Hz, 8H), 6.98 (s, 2H), 6.85 (s, 8H), 6.79 (s, 8H), 6.77 (s, 16H), 6.72 (s, 2H), 6.67 (s, 4H), 6.50 (s, 3H), 4.24 (s, 2H), 4.07 (s, 16H), 3.75 (s, 8H), 3.65 (s, 3H), 3.56 (s, 4H), 2.19 (s, 48H).

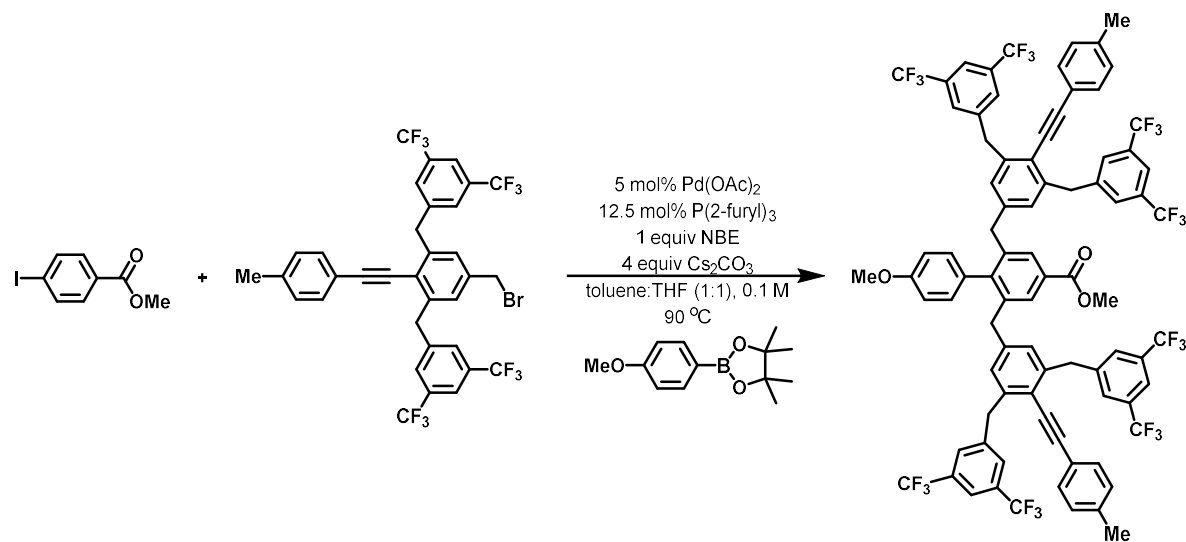
¹³C NMR (126 MHz, CDCl₃): δ 158.69, 146.90, 144.24, 142.54, 141.76, 141.07, 140.56, 140.35, 137.89, 136.76, 132.78, 131.98, 131.37, 130.73, 128.57, 128.27, 127.90, 127.68, 127.25, 127.02, 126.80, 123.72, 119.74, 113.72, 95.63, 93.37, 55.20, 41.77, 40.75, 39.88, 33.75, 21.44.

IR (KBr, neat): 3014, 2917, 2852, 2297, 1592, 1560, 1517, 1495, 1458, 1437, 1375, 1341, 1307, 1284, 1265, 1244, 1173, 1105, 1037, 853, 749, 737, 688 cm⁻¹.

MALDI-TOF-MS: *m/z* calcd for C₁₆₀H₁₄₁BrN₄NaO₉⁺ [*M*+Na⁺]: 2363.98. Found: 2365.27.

2.5.4. Synthetic procedures for G2CF₃2 to G2CF₃4

Synthesis of compound G2CF₃2



A flame-dried 4 mL reaction vial was charged with methyl 4-iodobenzoate (39.3 mg, 0.15 mmol, 1.0 equiv.), G1BrCF₃1 (232.3 mg, 0.315 mmol, 2.1 equiv), 4-methoxyphenylboronic acid pinacol ester (42.1 mg, 0.18 mmol, 1.2 equiv), Pd(OAc)₂ (1.7 mg, 0.0075 mmol, 5 mol%), and tri(2-

furyl)phosphine (4.4 mg, 0.01875 mmol, 12.5 mol%). The vial was brought into the glovebox, and anhydrous Cs₂CO₃ (195.5 mg, 0.6 mmol, 4 equiv), norbornene (14.1 mg, 0.15 mmol, 1 equiv), toluene (0.75 mL), and THF (0.75 mL) were added. The reaction mixture in the vial was stirred at r. t. for 10 mins, was taken out of the glove box, and then was stirred and heated at a preheated pie-block set to 90 °C for 24 h. After cooling down to room temperature, the crude mixture was passed through a Büchner funnel packed with celite and washed with EtOAc. The crude product was purified by recrystallization in CH₂Cl₂/MeOH.

Yield: 163.4 mg (70%)

Physical appearance: white solid, **m.p.:** 241-248 °C

R_f: 0.45 (EtOAc:hexanes = 1:9)

¹H NMR (500 MHz, CDCl₃): δ 7.80 (s, 2H), 7.69 (s, 4H), 7.58 (s, 8H), 7.14 (d, *J* = 8.1 Hz, 4H), 7.11 (d, *J* = 8.3 Hz, 4H), 6.67 (d, *J* = 7.5 Hz, 1H), 6.57 (s, 4H), 6.56 (d, *J* = 7.8 Hz, 2H), 4.18 (s, 8H), 3.90 (s, 4H), 3.74 (s, 3H), 3.73 (s, 3H), 2.35 (s, 6H).

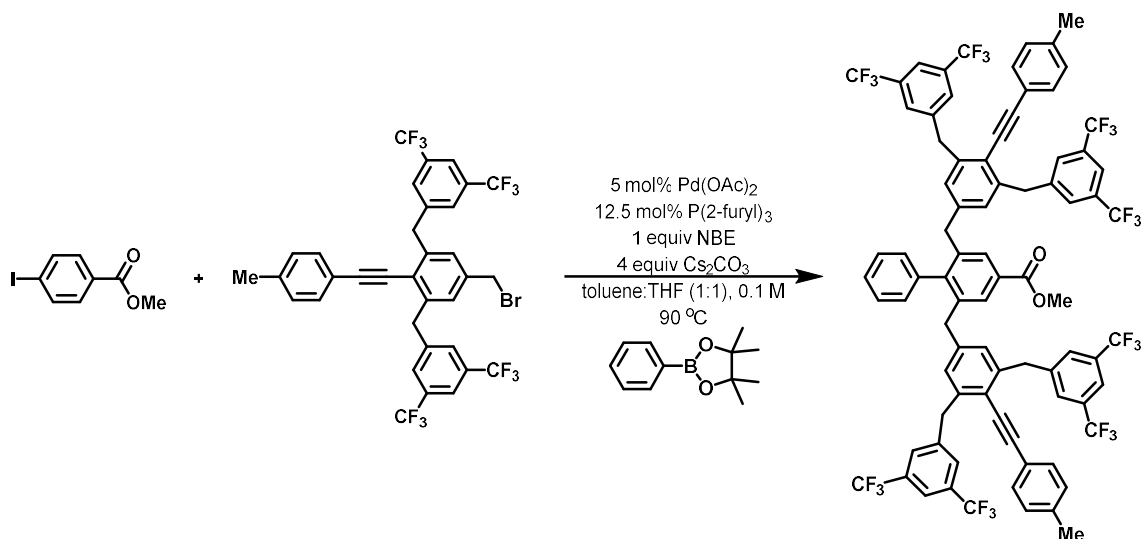
¹³C NMR (126 MHz, CDCl₃): δ 166.93, 159.06, 146.46, 143.08, 141.78, 141.52, 139.89, 139.20, 131.66 (q, ²*J*_{C-CF₃} = 33.2 Hz), 131.15, 130.72, 130.20, 129.59, 129.46, 129.36, 128.95, 128.90, 123.48 (q, ¹*J*_{C-CF₃} = 272.7 Hz), 121.08, 120.34, 119.42, 113.71, 99.08, 85.45, 55.25, 52.27, 40.50, 39.87, 21.65.

¹⁹F NMR (470 MHz, CDCl₃): -62.84.

IR (KBr, neat): 3004, 2999, 2706, 2692, 1717, 1610, 1558, 1511, 1463, 1373, 1275, 1260, 1223, 1168, 1125, 1039, 897, 878, 842, 814, 767, 760, 744, 725, 706, 684 cm⁻¹.

HRMS (ESI-TOF): *m/z* calcd for C₈₃H₅₅F₂₄O₃⁺ [M+H⁺]: 1555.3762. Found: 1555.3766.

Synthesis of compound **G2CF33**



A flame-dried 4 mL reaction vial was charged with methyl 4-iodobenzoate (39.3 mg, 0.15 mmol, 1.0 equiv.), **G1BrCF31** (232.3 mg, 0.315 mmol, 2.1 equiv), phenylboronic acid pinacol ester (36.7 mg, 0.18 mmol, 1.2 equiv), Pd(OAc)₂ (1.7 mg, 0.0075 mmol, 5 mol%), and tri(2-furyl)phosphine (4.4 mg, 0.01875 mmol, 12.5 mol%). The vial was brought into the glovebox, and anhydrous Cs₂CO₃ (195.5 mg, 0.6 mmol, 4 equiv), norbornene (14.1 mg, 0.15 mmol, 1 equiv), toluene (0.75 mL), and THF (0.75 mL) were added. The reaction mixture in the vial was stirred at r. t. for 10 mins, was taken out of the glove box, and then was stirred and heated at a preheated pie-block set to 90 °C for 24 h. After cooling down to room temperature, the crude mixture was passed through a Büchner funnel packed with celite and washed with EtOAc. The crude product was purified by recrystallization in CH₂Cl₂/MeOH.

Yield: 172.8 mg (76%)

Physical appearance: white solid, **m.p.:** 223-225 °C

R_f: 0.15 (EtOAc:hexanes = 1:9)

¹H NMR (500 MHz, CDCl₃): δ 7.85 (s, 2H), 7.70 (s, 4H), 7.58 (s, 8H), 7.15 (d, *J* = 8.0 Hz, 4H), 7.11 (d, *J* = 8.0 Hz, 4H), 7.08 (d, *J* = 7.4 Hz, 1H), 7.02 (t, *J* = 7.4 Hz, 2H), 6.58 (d, *J* = 7.5 Hz, 2H), 6.51 (s, 4H), 4.17 (s, 8H), 3.92 (s, 4H), 3.72 (s, 3H), 2.35 (s, 6H).

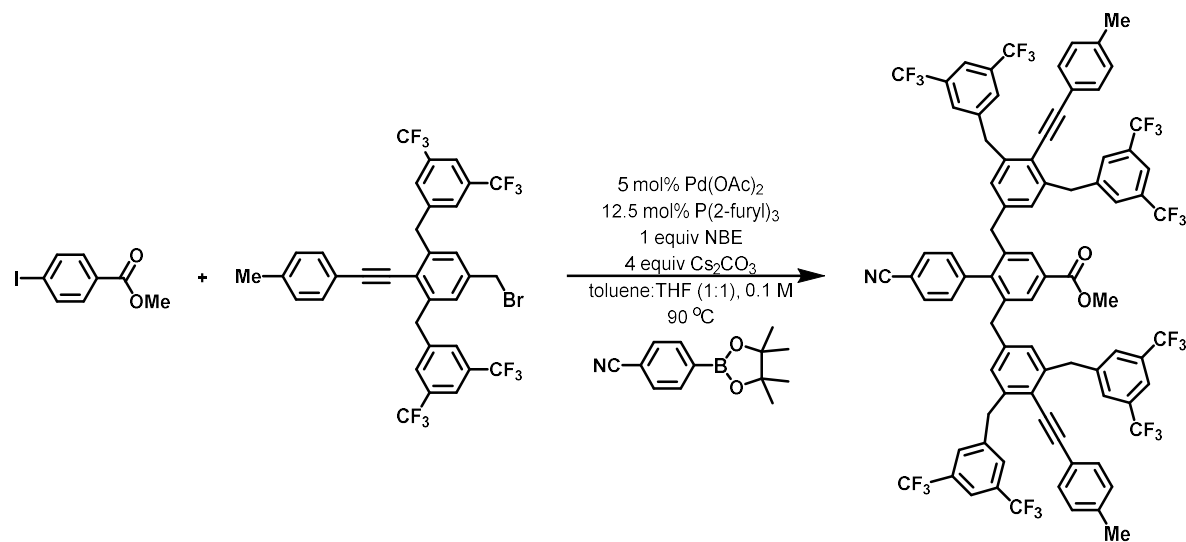
¹³C NMR (126 MHz, CDCl₃): δ 166.91, 146.76, 143.08, 141.63, 141.51, 139.42, 139.21, 138.41, 131.67 (q, ²*J*_{C-CF₃} = 33.1 Hz), 131.16, 129.68, 129.37, 129.02, 128.98, 128.77, 128.10, 127.31, 123.48 (q, ¹*J*_{C-CF₃} = 272.7 Hz), 121.04, 120.35, 119.43, 99.09, 85.48, 52.31, 40.49, 39.91, 21.64.

¹⁹F NMR (470 MHz, CDCl₃): -62.85.

IR (KBr, neat): 3004, 2989, 2706, 1722, 1622, 1605, 1559, 1512, 1464, 1436, 1373, 1275, 1261, 1215, 1168, 1129, 1009, 897, 843, 815, 767, 757, 745, 726, 705, 683 cm⁻¹.

HRMS (ESI-TOF): *m/z* calcd for C₈₂H₅₃F₂₄O₂⁺ [M+H⁺]: 1525.3657. Found: 1525.3654.

Synthesis of compound **G2CF₃4**



A flame-dried 4 mL reaction vial was charged with methyl 4-iodobenzoate (39.3 mg, 0.15 mmol, 1.0 equiv.), **G1BrCF₃1** (232.3 mg, 0.315 mmol, 2.1 equiv), 4-cyanophenylboronic acid pinacol ester (41.2 mg, 0.18 mmol, 1.2 equiv), Pd(OAc)₂ (1.7 mg, 0.0075 mmol, 5 mol%), and tri(2-

furyl)phosphine (4.4 mg, 0.01875 mmol, 12.5 mol%). The vial was brought into the glovebox, and anhydrous Cs₂CO₃ (195.5 mg, 0.6 mmol, 4 equiv), norbornene (14.1 mg, 0.15 mmol, 1 equiv), toluene (0.75 mL), and THF (0.75 mL) were added. The reaction mixture in the vial was stirred at r. t. for 10 mins, was taken out of the glove box, and then was stirred and heated at a preheated pie-block set to 90 °C for 24 h. After cooling down to room temperature, the crude mixture was passed through a Büchner funnel packed with celite and washed with EtOAc. The crude product was purified by flash column chromatography on silica gel (CH₂Cl₂:hexanes = 1:1).

Yield: 75.4 mg (32%)

Physical appearance: white solid, **m.p.:** 200-202 °C

R_f: 0.5 (CH₂Cl₂:hexanes = 1:1)

¹H NMR (500 MHz, CDCl₃): δ 7.84 (s, 2H), 7.70 (s, 4H), 7.58 (s, 8H), 7.42 (d, J = 6.9 Hz, 2H), 7.16 (d, J = 8.5 Hz, 4H), 7.12 (d, J = 8.0 Hz, 4H), 6.73 (d, J = 7.8 Hz, 2H), 6.52 (s, 4H), 4.19 (s, 8H), 3.92 (s, 3H), 3.68 (s, 4H), 2.36 (s, 6H).

¹³C NMR (126 MHz, CDCl₃): δ 166.51, 144.54, 143.71, 142.87, 141.84, 140.86, 139.38, 138.84, 131.98, 131.74 (q, ²J_{C-CF₃} = 33.2 Hz), 131.19, 130.59, 129.95, 129.92, 129.40, 128.92, 128.89, 128.62, 123.44 (q, ¹J_{C-CF₃} = 272.7 Hz), 121.56, 120.45, 119.24, 118.22, 111.72, 99.56, 85.13, 52.44, 40.46, 39.74, 21.66.

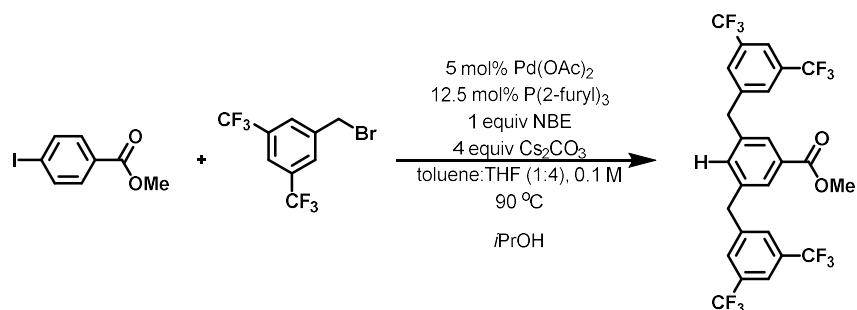
¹⁹F NMR (470 MHz, CDCl₃): -62.84.

IR (KBr, neat): 3004, 2988, 2706, 2230, 1725, 1605, 1558, 1512, 1463, 1436, 1374, 1276, 1260, 1215, 1170, 1131, 1006, 897, 842, 816, 766, 745, 725, 705, 683 cm⁻¹.

HRMS (ESI-TOF): m/z calcd for C₈₃H₅₂F₂₄NO₂⁺ [M+H⁺]: 1550.3609. Found: 1550.3599.

2.5.5. Synthetic procedures for GXCF₃-naked and GXCF₃-Fre

Synthesis of compound G1CF₃-naked



A flame-dried 350 mL Schlenk flask was charged with methyl 4-iodobenzoate (5.24 g, 20.0 mmol, 1.0 equiv), 1-(bromomethyl)-3,5-bis(trifluoromethyl)benzene (12.9 g, 42.0 mmol, 2.1 equiv), isopropanol (1.84 mL, 24.0 mmol, 1.2 equiv), Pd(OAc)₂ (224.5 mg, 1.0 mmol, 5 mol%), and tri(2-furyl)phosphine (580.4 mg, 2.5 mmol, 12.5 mol%). The flask was brought into the glovebox, and anhydrous Cs₂CO₃ (26.07 g, 80.0 mmol, 4 equiv), norbornene (1.88 g, 20.0 mmol, 1 equiv), toluene (40.0 mL), and THF (160.0 mL) were added. The reaction mixture in the sealed flask was stirred at r. t. for 10 mins, was taken out of the glove box, and then was stirred and heated at a 90 °C oil-bath for 48 h. After cooling down to room temperature, the crude mixture was passed through a Büchner funnel packed with celite and washed with EtOAc. The organic solvents were removed under reduced pressure until a small amount of solvent was left. Methanol was added carefully to the crude mixture, and the recrystallized product was filtered to give the desired product.

Yield: 5.58 g (47%)

Physical appearance: white solid, **m.p.:** 83-85 °C

R_f: 0.25 (EtOAc:hexanes = 1:9)

¹H NMR (400 MHz, CDCl₃): δ 7.79 (s, 2H), 7.74 (s, 2H), 7.58 (s, 4H), 7.13 (s, 1H), 4.13 (s, 4H), 3.91 (s, 3H).

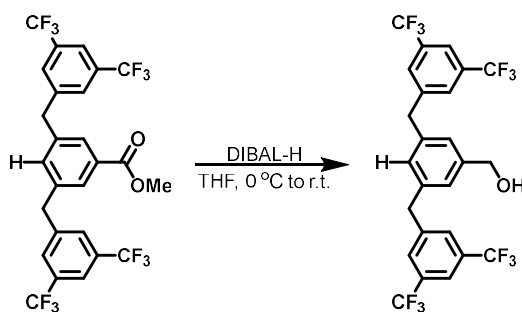
¹³C NMR (126 MHz, CDCl₃): δ 166.65, 142.73, 140.16, 133.90, 132.12 (q, ²J_{C-CF₃} = 33.3 Hz), 131.73, 129.03, 128.91, 123.36 (q, ¹J_{C-CF₃} = 272.8 Hz), 120.83, 52.50, 41.26.

¹⁹F NMR (376 MHz, CDCl₃): -62.94.

IR (KBr, neat): 2956, 1724, 1623, 1603, 1457, 1437, 1376, 1279, 1223, 1173, 1132, 1004, 924, 903, 888, 841, 772, 735, 707, 683 cm⁻¹.

MALDI-TOF-MS: m/z calcd for C₂₆H₁₅F₁₂O₂⁻ [M-H⁻]: 587.09. Found: 586.36.

Synthesis of compound G1_{OH}CF₃-naked



A flame-dried 250 mL round-bottom flask was charged with **G1CF₃-naked** (5.17 g, 8.79 mmol, 1.0 equiv) and anhydrous THF (87.8 mL) under nitrogen. At 0 °C, DIBAL-H (1 M solution in hexanes, 19.3 mL, 19.33 mmol, 2.2 equiv) was added dropwise. The reaction mixture was then stirred at room temperature for 10 min. The conversion was monitored by TLC. Upon completion of the reaction, the crude mixture was diluted with ether (100 mL) and cooled down to 0 °C. A saturated aqueous solution of Rochelle's salt was added, and the mixture was stirred until phase separation was observed. The organic layer was washed with water (200 mL) and brine (200 mL),

dried over MgSO_4 , and concentrated under reduced pressure. The crude product was found pure by NMR.

Yield: 4.92 g (quant.)

Physical appearance: off-white solid, **m.p.:** 123-125 °C

R_f: 0.25 (EtOAc:hexanes = 1:4)

¹H NMR (400 MHz, CDCl₃): δ 7.73 (s, 2H), 7.59 (s, 4H), 7.09 (s, 2H), 6.88 (s, 1H), 4.68 (d, $J = 5.4$ Hz, 2H), 4.08 (s, 4H), 1.72 (t, $J = 5.8$ Hz, 1H).

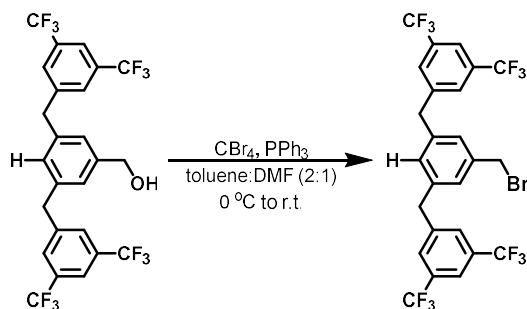
¹³C NMR (101 MHz, CDCl₃): δ 143.25, 142.53, 140.09, 131.97 (q, $^2J_{\text{C-CF}_3} = 33.2$ Hz), 129.06, 128.71, 126.14, 123.43 (q, $^1J_{\text{C-CF}_3} = 272.6$ Hz), 120.63, 64.98, 41.47.

¹⁹F NMR (376 MHz, CDCl₃): -62.91.

IR (KBr, neat): 3315 (br, OH), 3004, 2988, 1622, 1603, 1557, 1463, 1374, 1275, 1260, 1169, 1128, 1107, 963, 897, 841, 767, 760, 745, 725, 705, 683 cm^{-1} .

MALDI-TOF-MS: m/z calcd for $\text{C}_{25}\text{H}_{15}\text{F}_{12}\text{O}^-$ [M-H]: 559.09. Found: 558.41.

Synthesis of compound **G1_{Br}CF₃-naked**



A 250 mL round bottom flask was charged with **G1_{OH}CF₃-naked** (4.97 g, 8.87 mmol, 1.0 equiv) and triphenylphosphine (2.79 g, 10.64 mmol, 1.2 equiv). After adding toluene (59.2 mL) and DMF (29.6 mL), CBr_4 (3.53 g, 10.64 mmol, 1.2 equiv) was added at 0 °C. The reaction mixture was

stirred at room temperature for 40 min. The conversion was monitored by TLC. Upon completion of the reaction, the crude mixture was diluted with EtOAc (50 mL) and washed with water (100 mL \times 3). The organic layer was dried over MgSO₄ and concentrated under reduced pressure. The crude product was purified by recrystallization in CH₂Cl₂/MeOH.

Yield: 4.72 g (85%)

Physical appearance: white solid, **m.p.:** 110-112 °C

R_f: 0.7 (EtOAc:hexanes = 1:4)

¹H NMR (500 MHz, CDCl₃): δ 7.74 (s, 2H), 7.59 (s, 4H), 7.12 (s, 2H), 6.86 (s, 1H), 4.44 (s, 2H), 4.08 (s, 4H).

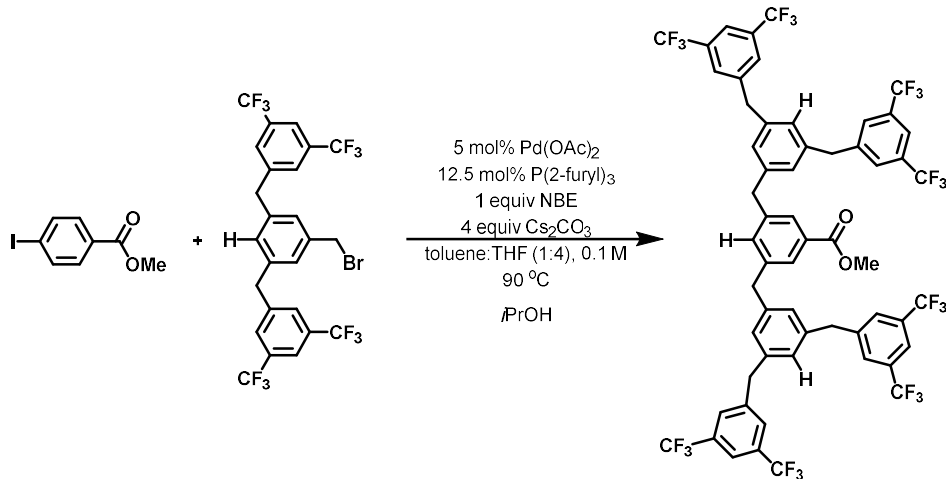
¹³C NMR (126 MHz, CDCl₃): δ 142.86, 140.39, 139.47, 131.89 (q, ²J_{C-CF₃} = 33.2 Hz), 129.51, 129.06, 128.35, 123.25 (q, ¹J_{C-CF₃} = 272.7 Hz), 120.74, 41.27, 32.83.

¹⁹F NMR (376 MHz, CDCl₃): -62.92.

IR (KBr, neat): 3005, 2989, 1621, 1597, 1463, 1435, 1375, 1322, 1276, 1261, 1210, 1163, 1130, 1113, 969, 936, 896, 859, 838, 759, 744, 722, 705, 683 628, 575, 563, 547 cm⁻¹.

MALDI-TOF-MS: m/z calcd for C₂₅H₁₅BrF₁₂Na⁺ [M+Na⁺]: 645.01. Found: 645.04.

Synthesis of compound **G2CF₃-naked**



A flame-dried 4 mL reaction vial was charged with methyl 4-iodobenzoate (39.3 mg, 0.15 mmol, 1.0 equiv.), **G1BrCF₃-naked** (196.3 mg, 0.315 mmol, 2.1 equiv), isopropanol (13.8 μ L, 0.18 mmol, 1.2 equiv), Pd(OAc)₂ (1.7 mg, 0.0075 mmol, 5 mol%), and tri(2-furyl)phosphine (4.4 mg, 0.01875 mmol, 12.5 mol%). The vial was brought into the glovebox, and anhydrous Cs₂CO₃ (195.5 mg, 0.6 mmol, 4 equiv), norbornene (14.1 mg, 0.15 mmol, 1 equiv), toluene (0.3 mL), and THF (1.2 mL) were added. The reaction mixture in the vial was stirred at r. t. for 10 mins, was taken out of the glove box, and then was stirred and heated at a preheated pie-block set to 90 °C for 24 h. After cooling down to room temperature, the crude mixture was passed through a Büchner funnel packed with celite and washed with EtOAc. The crude product was purified by flash column chromatography on silica gel (CH₂Cl₂:hexanes = 1:1).

Yield: 138.7 mg (76%)

Physical appearance: white solid, **m.p.:** 105-107 °C

R_f: 0.6 (CH₂Cl₂:hexanes = 1:1)

¹H NMR (500 MHz, CDCl₃): δ 7.71 (s, 4H), 7.68 (s, 2H), 7.54 (s, 8H), 7.14 (s, 1H), 6.86 (s, 4H), 6.76 (s, 2H), 4.01 (s, 8H), 3.93 (s, 4H), 3.86 (s, 3H).

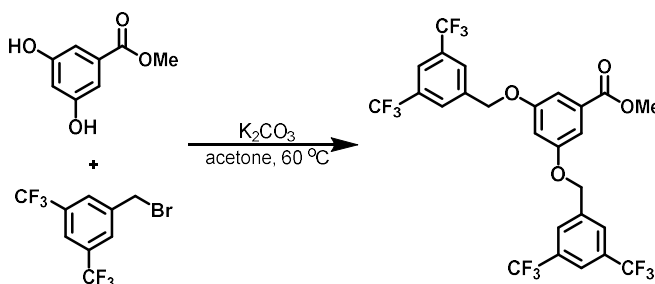
¹³C NMR (126 MHz, CDCl₃): δ 167.09, 143.27, 142.18, 141.35, 140.00, 134.09, 131.90 (q, ²J_{C-CF₃} = 33.1 Hz), 131.02, 129.00, 128.22, 128.20, 127.52, 123.42 (q, ¹J_{C-CF₃} = 272.7 Hz), 120.53, 52.22, 41.47, 41.35.

¹⁹F NMR (470 MHz, CDCl₃): -62.94.

IR (KBr, neat): 3004, 2989, 1721, 1599, 1463, 1375, 1275, 1260, 1219, 1171, 1129, 897, 840, 766, 756, 746, 725, 707, 683 cm⁻¹.

MALDI-TOF-MS: m/z calcd for C₅₈H₃₆F₂₄NaO₂⁺ [M+Na⁺]: 1243.22. Found: 1242.92.

Synthesis of compound **G1CF₃-Fre**



A 250 mL round-bottom flask was charged with methyl 3,5-dihydroxybenzoate (2.0 g, 11.89 mmol, 1.0 equiv), 1-(bromomethyl)-3,5-bis(trifluoromethyl)benzene (8.03 g, 26.17 mmol, 2.2 equiv), K₂CO₃ (4.93 g, 35.68 mmol, 3.0 equiv) and acetone (79.3 mL, 0.15 M). The reaction mixture was then stirred and heated in a 60 °C oil bath overnight. The conversion was monitored by TLC. Upon completion of the reaction, all solids were filtered off. The filtrate was concentrated under reduced pressure. The crude product was purified by recrystallization in CH₂Cl₂/MeOH.

Yield: 6.65 g (90%)

Physical appearance: white solid, **m.p.:** 146-148 °C

R_f: 0.3 (EtOAc:hexanes = 1:9)

¹H NMR (400 MHz, CDCl₃): δ 7.92 (s, 4H), 7.87 (s, 2H), 7.35 (d, *J* = 2.3 Hz, 2H), 6.86 (t, *J* = 2.4 Hz, 1H), 5.21 (s, 4H), 3.94 (s, 3H).

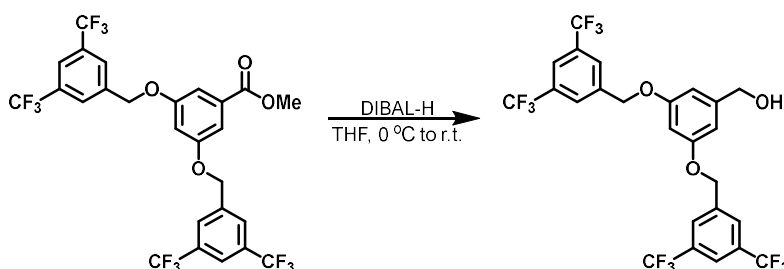
¹³C NMR (101 MHz, CDCl₃): δ 166.44, 159.32, 139.13, 132.78, 132.21 (q, ²*J*_{C-CF₃} = 33.5 Hz), 127.42, 123.35 (q, ¹*J*_{C-CF₃} = 272.5 Hz), 122.25, 108.83, 107.46, 68.87, 52.60.

¹⁹F NMR (376 MHz, CDCl₃): -.

IR (KBr, neat): 3067, 2957, 2913, 1720, 1598, 1458, 1444, 1395, 1362, 1324, 1302, 1279, 1255, 1173, 1131, 1112, 1066, 1003, 972, 925, 886, 843, 781, 768, 734, 705, 683 cm⁻¹.

HRMS (ESI-TOF): *m/z* calcd for C₂₆H₁₇F₁₂O₄⁺ [*M*+*H*⁺]: 621.0930. Found: 621.0914.

Synthesis of compound G1_{OH}CF₃-Fre



A flame-dried 250 mL round-bottom flask was charged with **G1CF₃-Fre** (6.0 g, 9.67 mmol, 1.0 equiv) and anhydrous THF (96.7 mL) under nitrogen. At 0 °C, DIBAL-H (1 M solution in hexanes, 21.3 mL, 21.28 mmol, 2.2 equiv) was added dropwise. The reaction mixture was then stirred at room temperature for 10 min. The conversion was monitored by TLC. Upon completion of the reaction, the crude mixture was diluted with ether (100 mL) and cooled down to 0 °C. A saturated aqueous solution of Rochelle's salt was added, and the mixture was stirred until phase separation was observed. The organic layer was washed with water (200 mL) and brine (200 mL), dried over MgSO₄, and concentrated under reduced pressure. The crude product was found pure by NMR.

Yield: 5.68 g (99%)

Physical appearance: white solid, **m.p.:** 123-125 °C

R_f: 0.15 (EtOAc:hexanes = 1:4)

¹H NMR (400 MHz, CDCl₃): δ 7.91 (s, 4H), 7.86 (s, 2H), 6.69 (d, *J* = 2.3 Hz, 2H), 6.58 (t, *J* = 2.3 Hz, 1H), 5.17 (s, 4H), 4.69 (d, *J* = 5.8 Hz, 2H), 1.78 (t, *J* = 5.9 Hz, 1H).

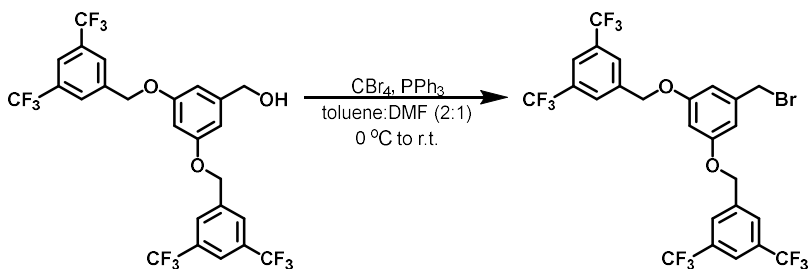
¹³C NMR (101 MHz, CDCl₃): δ 159.67, 144.22, 139.51, 132.14 (q, ²*J*_{C-CF₃} = 33.5 Hz), 127.40, 123.37 (q, ¹*J*_{C-CF₃} = 272.7 Hz), 122.13, 106.20, 101.50, 68.69, 65.14.

¹⁹F NMR (376 MHz, CDCl₃): -62.91.

IR (KBr, neat): 3004, 2988, 1596, 1473, 1452, 1368, 1324, 1276, 1261, 1199, 1161, 1126, 1111, 1077, 1015, 995, 953, 926, 909, 882, 843, 833, 806, 748, 724, 704, 684, 662 cm⁻¹.

HRMS (ESI-TOF): *m/z* calcd for C₂₅H₁₇F₁₂O₃⁺ [M+H⁺]: 593.0981. Found: 593.0984.

Synthesis of compound G1_{Br}CF₃-Fre



A 250 mL round bottom flask was charged with G1OHCF₃-Fre (5.68 g, 9.59 mmol, 1.0 equiv) and triphenylphosphine (3.02 g, 11.51 mmol, 1.2 equiv). After adding toluene (64.0 mL) and DMF (32.0 mL), CBr₄ (3.82 g, 11.51 mmol, 1.2 equiv) was added at 0 °C. The reaction mixture was stirred at room temperature for 40 min. The conversion was monitored by TLC. Upon completion of the reaction, the crude mixture was diluted with EtOAc (50 mL) and washed with water (100 mL × 3). The organic layer was dried over MgSO₄ and concentrated under reduced pressure. The crude product was purified by recrystallization in CH₂Cl₂/MeOH.

Yield: 5.26 g (84%)

Physical appearance: white solid, **m.p.:** 134-136 °C

R_f: 0.7 (EtOAc:hexanes = 1:4)

¹H NMR (500 MHz, CDCl₃): δ 7.91 (s, 4H), 7.87 (s, 2H), 6.70 (s, 2H), 6.59 (s, 1H), 5.16 (s, 4H), 4.44 (s, 2H).

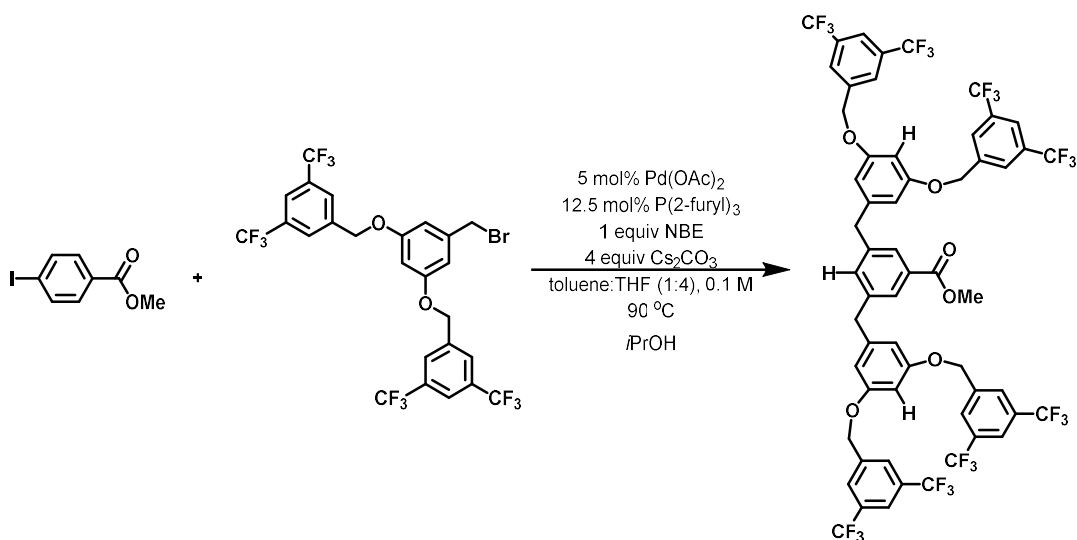
¹³C NMR (126 MHz, CDCl₃): δ 159.58, 140.66, 139.26, 132.18 (q, ²J_{C-CF₃} = 33.5 Hz), 127.41, 123.36 (q, ¹J_{C-CF₃} = 272.9 Hz), 122.21, 108.72, 102.40, 68.75, 33.10, 132.18 (q, J = 33.5 Hz), 123.36 (d, J = 272.9 Hz).

¹⁹F NMR (470 MHz, CDCl₃): -62.92.

IR (KBr, neat): 3004, 2988, 1611, 1598, 1449, 1393, 1362, 1328, 1275, 1261, 1196, 1156, 1110, 995, 968, 922, 911, 885, 861, 842, 764, 704, 683, 662, 645, 611, 582 cm⁻¹.

HRMS (ESI-TOF): m/z calcd for C₂₅H₁₆BrF₁₂O₂⁺ [M+H⁺]: 655.0137. Found: 655.0122.

Synthesis of compound G2CF₃-Fre



A flame-dried 4 mL reaction vial was charged with methyl 4-iodobenzoate (39.3 mg, 0.15 mmol, 1.0 equiv.), **G1_{Br}CF₃-Fre** (206.4 mg, 0.315 mmol, 2.1 equiv), isopropanol (13.8 μ L, 0.18 mmol, 1.2 equiv), Pd(OAc)₂ (1.7 mg, 0.0075 mmol, 5 mol%), and tri(2-furyl)phosphine (4.4 mg, 0.01875 mmol, 12.5 mol%). The vial was brought into the glovebox, and anhydrous Cs₂CO₃ (195.5 mg, 0.6 mmol, 4 equiv), norbornene (14.1 mg, 0.15 mmol, 1 equiv), toluene (0.3 mL), and THF (1.2 mL) were added. The reaction mixture in the vial was stirred at r. t. for 10 mins, was taken out of the glove box, and then was stirred and heated a preheated pie-block set to 90 °C for 24 h. After cooling down to room temperature, the crude mixture was passed through a Büchner funnel packed with celite and washed with EtOAc. The crude product was purified by flash column chromatography on silica gel (CH₂Cl₂:hexanes = 1:2).

Yield: 112.3 mg (58%)

Physical appearance: off-white solid, **m.p.:** 119-121 °C

R_f: 0.2 (EtOAc:hexanes = 1:9)

¹H NMR (500 MHz, CDCl₃): δ 7.85 (s, 8H), 7.84 (s, 4H), 7.77 (s, 2H), 7.25 (s, 1H), 6.49 (s, 2H), 6.47 (s, 4H), 5.06 (s, 8H), 3.96 (s, 4H), 3.90 (s, 3H).

¹³C NMR (126 MHz, CDCl₃): 167.16, 159.60, 143.77, 141.15, 139.38, 134.20, 132.08 (q, ²J_{C-CF₃} = 33.5 Hz), 131.03, 128.40, 127.38, 123.34 (q, ¹J_{C-CF₃} = 272.7 Hz), 122.11, 108.74, 100.13, 68.62, 52.32, 42.00.

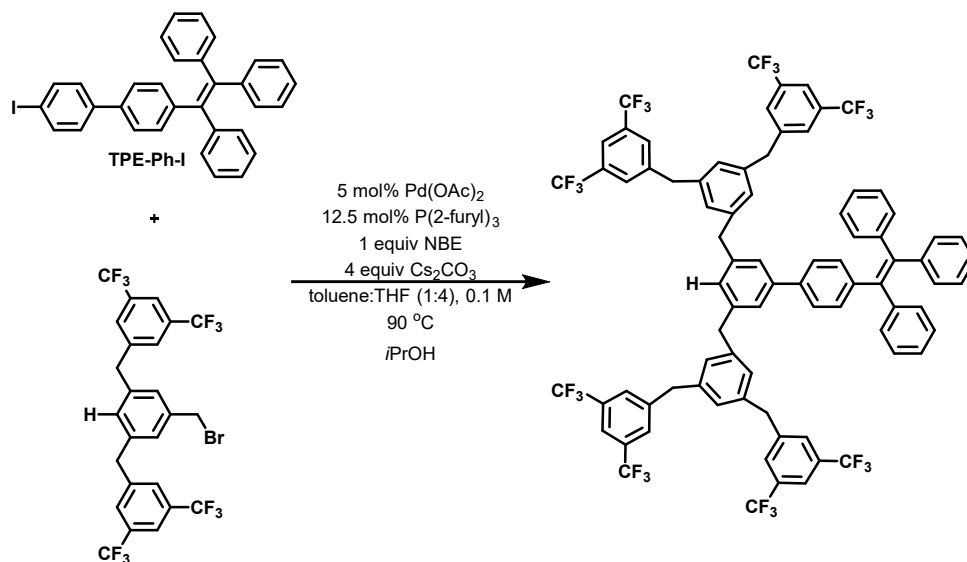
¹⁹F NMR (470 MHz, CDCl₃): -62.93.

IR (KBr, neat): 3005, 2989, 1720, 1596, 1463, 1361, 1276, 1260, 1173, 1230, 1069, 923, 886, 843, 767, 756, 745, 725, 705, 683 cm⁻¹.

HRMS (ESI-TOF): m/z calcd for C₅₈H₃₇F₂₄O₆⁺ [M+H⁺]: 1285.2201. Found: 1285.2212.

2.5.6. Synthetic procedures for AIE compounds

Synthesis of compound AIE-1



A flame-dried 4 mL reaction vial was charged with **TPE-Ph-I** (53.4 mg, 0.1 mmol, 1.0 equiv.), **G1BrCF₃-naked** (130.9 mg, 0.21 mmol, 2.1 equiv), isopropanol (9.2 μ L, 0.12 mmol, 1.2 equiv), Pd(OAc)₂ (1.1 mg, 0.005 mmol, 5 mol%), and tri(2-furyl)phosphine (2.9 mg, 0.0125 mmol, 12.5 mol%). The vial was brought into the glovebox, and anhydrous Cs₂CO₃ (130.3 mg, 0.4 mmol, 4 equiv), norbornene (9.4 mg, 0.1 mmol, 1 equiv), toluene (0.2 mL), and THF (0.8 mL) were added. The reaction mixture in the vial was stirred at r. t. for 10 mins, was taken out of the glove box, and then was stirred and heated at a preheated pie-block set to 90 °C for 24 h. After cooling down to room temperature, the crude mixture was passed through a plug of celite and washed with EtOAc. The crude product was purified by flash column chromatography on silica gel (CH₂Cl₂:hexanes = 1:10).

Yield: 56.5 mg (38%)

Physical appearance: light yellow solid, **m.p.:** 70-72 °C

R_f: 0.35 (EtOAc:hexanes = 1:9)

¹H NMR (500 MHz, CDCl₃): δ 7.71 (s, 4H), 7.55 (s, 8H), 7.23 (d, *J* = 8.3 Hz, 2H), 7.20 (s, 1H), 7.14 – 7.03 (m, 19H), 6.90 (s, 4H), 6.74 (s, 2H), 4.02 (s, 8H), 3.92 (s, 4H).

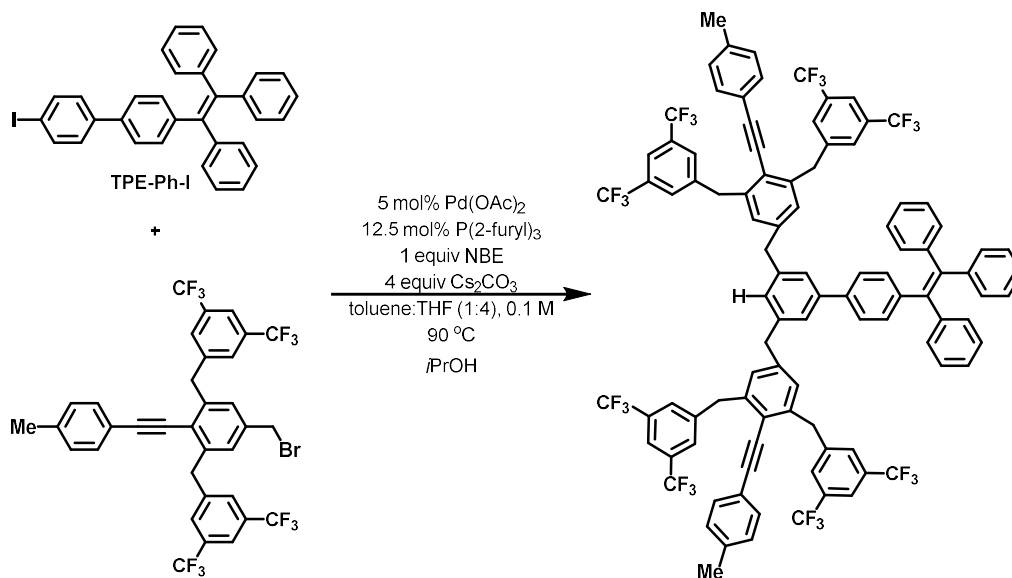
¹³C NMR (126 MHz, CDCl₃): δ 143.90, 143.34, 143.10, 142.73, 141.37, 141.32, 141.28, 140.61, 139.85, 138.56, 132.28, 132.01, 131.88, 131.75, 131.51, 131.48, 129.02, 128.99, 128.54, 128.24, 127.90, 127.84, 127.78, 127.30, 126.63, 126.59, 126.23, 125.70, 123.42 (q, ¹*J*_{C-CF₃} = 272.7 Hz), 120.51, 41.78, 41.38.

¹⁹F NMR (470 MHz, CDCl₃): -62.91.

IR (KBr, neat): 3021, 2924, 2853, 1623, 1598, 1492, 1464, 1444, 1375, 1277, 1172, 1132, 1007, 977, 890, 841, 764, 751, 702, 683 cm⁻¹.

MALDI-TOF-MS: *m/z* calcd for C₈₂H₅₂F₂₄⁺ [*M*⁺]: 1492.37. Found: 1491.85.

Synthesis of compound AIE-2



A flame-dried 4 mL reaction vial was charged with **TPE-Ph-I** (53.4 mg, 0.1 mmol, 1.0 equiv.), **G1BrCF31** (154.9 mg, 0.21 mmol, 2.1 equiv), isopropanol (9.2 μL, 0.12 mmol, 1.2 equiv), Pd(OAc)₂ (1.1 mg, 0.005 mmol, 5 mol%), and tri(2-furyl)phosphine (2.9 mg, 0.0125 mmol, 12.5

mol%). The vial was brought into the glovebox, and anhydrous Cs₂CO₃ (130.3 mg, 0.4 mmol, 4 equiv), norbornene (9.4 mg, 0.1 mmol, 1 equiv), toluene (0.2 mL), and THF (0.8 mL) were added. The reaction mixture in the vial was stirred at r. t. for 10 mins, was taken out of the glove box, and then was stirred and heated at a preheated pie-block set to 90 °C for 24 h. After cooling down to room temperature, the crude mixture was passed through a plug of celite and washed with EtOAc. The crude product was purified by flash column chromatography on silica gel (EtOAc:hexanes = 1:9).

Yield: 71.1 mg (42%)

Physical appearance: light yellow solid, **m.p.:** 134-136 °C

R_f: 0.5 (EtOAc:hexanes = 1:9)

¹H NMR (500 MHz, CDCl₃): δ 7.68 (s, 4H), 7.65 (s, 8H), 7.24 (d, *J* = 8.3 Hz, 2H), 7.22 (s, 2H), 7.17 (d, *J* = 8.2 Hz, 2H), 7.16 (s, 2H), 7.13 – 7.04 (m, 21H), 6.98 (s, 4H), 6.84 (s, 1H), 4.26 (s, 8H), 3.96 (s, 4H), 2.37 (s, 6H).

¹³C NMR (126 MHz, CDCl₃): δ 143.93, 143.90, 143.88, 143.17, 143.04, 142.27, 141.95, 141.59, 141.32, 141.04, 140.63, 139.25, 138.44, 132.08, 131.92, 131.82, 131.56, 131.53, 131.49, 131.29, 131.18, 129.38, 129.07, 128.98, 128.33, 127.91, 127.83, 127.78, 126.72, 126.63, 126.60, 126.25, 125.78, 123.47 (q, ¹*J*_{C-CF₃} = 272.8 Hz), 121.39, 120.41, 119.40, 99.25, 85.46, 41.74, 40.62, 21.65.

¹⁹F NMR (470 MHz, CDCl₃): -62.83.

IR (KBr, neat): 2923, 2852, 1465. 1374, 1278, 1175, 1131, 881, 814, 764, 750, 704, 683 cm⁻¹.

HRMS (ESI-TOF): *m/z* calcd for C₁₀₀H₆₄F₂₄Na⁺ [M+Na⁺]: 1743.4517. Found: 1743.4526.

^1H NMR (500 MHz, CDCl_3): δ 7.68 (s, 4H), 7.60 (s, 8H), 7.34 (s, 2H), 7.29 (d, $J = 8.3$ Hz, 2H), 7.16 – 7.03 (m, 27H), 6.67 (d, $J = 8.6$ Hz, 2H), 6.62 (s, 2H), 6.60 (d, $J = 8.6$ Hz, 2H), 4.19 (s, 8H), 3.75 (s, 7H), 2.36 (s, 6H).

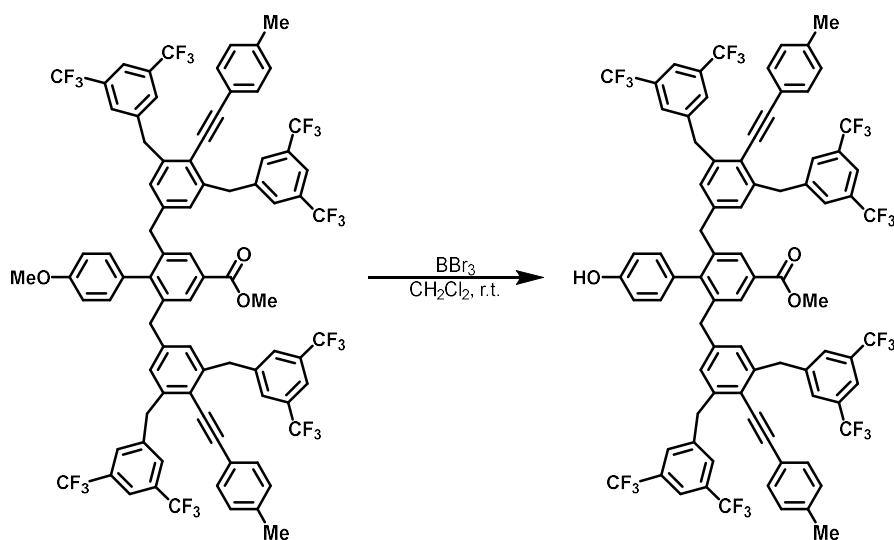
^{13}C NMR (126 MHz, CDCl_3): δ 158.78, 143.93, 143.91, 143.17, 142.41, 141.39, 141.34, 140.80, 140.65, 139.97, 139.68, 139.15, 138.18, 132.04, 131.96, 131.78, 131.52, 131.14, 130.75, 129.35, 128.97, 128.95, 128.91, 127.92, 127.85, 127.78, 126.91, 126.74, 126.64, 126.61, 126.58, 126.11, 125.81, 123.48 (q, $^1J_{\text{C-CF}_3} = 272.7$ Hz), 120.88, 120.33, 119.48, 113.55, 112.96, 98.94, 85.60, 55.22, 40.53, 40.20, 21.64.

^{19}F NMR (470 MHz, CDCl_3): -62.80.

IR (KBr, neat): 2923, 2853, 1604, 1512, 1465, 1443, 1374, 1277, 1246, 1172, 1134, 1107, 1037, 902, 842, 816, 753, 703, 682 cm^{-1} .

HRMS (ESI-TOF): m/z calcd for $\text{C}_{83}\text{H}_{55}\text{F}_{24}\text{O}_3^+$ [$\text{M}+\text{Na}^+$]: 1849.4936. Found: 1849.4903.

2.5.7. Post-modification of **G2CF₃2**



A flame-dried 1.7 mL reaction vial was charged with **G2CF₃2** (20.0 mg, 0.0129 mmol, 1.0 equiv.). In the glovebox, 0.18 mL of CH₂Cl₂ was added to the vial. Then, BBr₃ (0.06 mL, 0.645 M solution in CH₂Cl₂, 3 equiv) was added dropwise at r.t. The vial was taken out of the glovebox and the reaction mixture was stirred at r.t. for 12 h. The crude mixture was then quenched with MeOH and extracted with CH₂Cl₂ (0.5 mL) and H₂O (0.5 mL × 3). The organic layer was dried over MgSO₄, filtered, and concentrated under reduced pressure. The crude product was purified by flash column chromatography on silica gel (EtOAc:hexanes = 1:5) to afford **G2CF₃2-mod**.

Yield: 14.9 mg (75%, purity >95%)

Physical appearance: off-white solid, **m.p.:** 256-258 °C

R_f: 0.15 (EtOAc:hexanes = 1:9)

¹H NMR (500 MHz, CDCl₃): δ 7.82 (s, 2H), 7.69 (s, 4H), 7.59 (s, 8H), 7.14 (d, *J* = 8.0 Hz, 4H), 7.11 (d, *J* = 8.2 Hz, 4H), 6.56 (d, *J* = 8.3 Hz, 2H), 6.53 (s, 4H), 6.46 (d, *J* = 8.1 Hz, 2H), 4.67 (s, 1H, -OH), 4.18 (s, 8H), 3.91 (s, 3H), 3.72 (s, 4H), 2.35 (s, 6H).

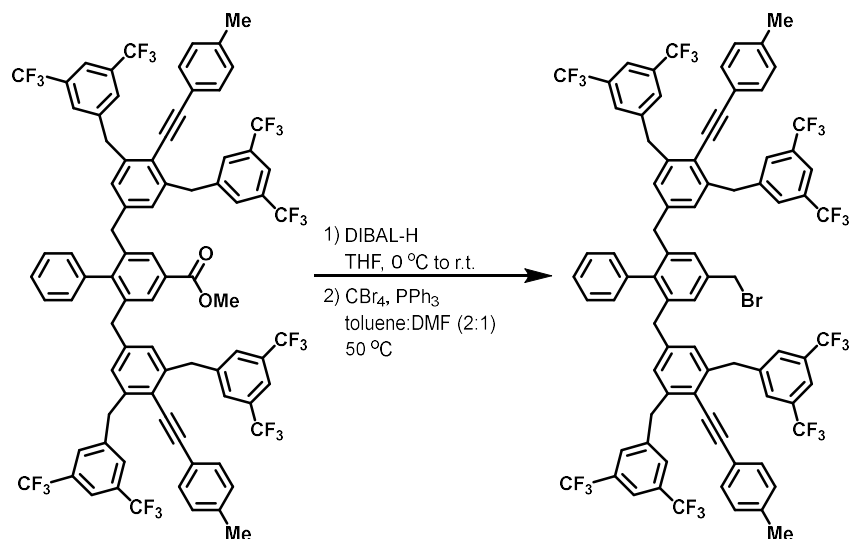
¹³C NMR (126 MHz, CDCl₃): δ 166.94, 154.95, 146.40, 143.08, 141.71, 141.52, 139.87, 139.21, 131.65 (q, ²*J*_{C-CF₃} = 33.0 Hz), 131.21, 131.16, 130.91, 130.40, 129.61, 128.97, 128.78, 123.49 (q, ¹*J*_{C-CF₃} = 272.7 Hz), 121.04, 120.35, 119.42, 115.04, 99.12, 85.44, 52.29, 40.49, 39.93, 21.65.

¹⁹F NMR (470 MHz, CDCl₃): -62.81.

IR (KBr, neat): 3387 (br), 3032, 2953, 2926, 2856, 2209, 1719, 1701, 1711, 1589, 1560, 1541, 1513, 1466, 1491, 1437, 1414, 1374, 1278, 1214, 1171, 1132, 1108, 1404, 1006, 904, 886, 841, 816, 774, 735, 727, 705, 683, 649 cm⁻¹.

HRMS (ESI-TOF): *m/z* calcd for C₈₂H₅₂F₂₄NaO₃⁺ [*M*+Na⁺]: 1563.3425. Found: 1563.3423.

2.5.8. Synthetic procedure for **G3CF33**



A flame-dried 4 mL reaction vial was charged with **G2CF33** (90.0 mg, 0.059 mmol, 1.0 equiv) and anhydrous THF (0.6 mL) under nitrogen. At 0 °C, DIBAL-H (1 M solution in hexanes, 0.13 mL, 0.13 mmol, 2.2 equiv) was added dropwise. The reaction mixture was then stirred at room temperature for 10 min. The conversion was monitored by TLC. Upon completion of the reaction, the crude mixture was diluted with ether (1 mL) and cooled down to 0 °C. A saturated aqueous solution of Rochelle's salt was added, and the mixture was stirred until phase separation was observed. The organic layer was washed with water (1 mL) and brine (1 mL), dried over MgSO₄, and concentrated under reduced pressure. The crude **G2OHCF33** was directly used for the following reaction.

To a 4 mL reaction vial charged with **G2OHCF33** was added triphenylphosphine (18.6 mg, 0.0708 mmol, 1.2 equiv). After adding toluene (0.4 mL) and DMF (0.2 mL), CBr₄ (23.5 mg, 0.0708 mmol, 1.2 equiv) was added at r.t.. The reaction mixture was stirred at 50 °C for 10 min. The conversion was monitored by TLC. Upon completion of the reaction, the crude mixture was diluted with EtOAc (1 mL) and washed with water (1 mL × 3). The organic layer was dried over MgSO₄

and concentrated under reduced pressure. The crude product was purified by recrystallization in $\text{CH}_2\text{Cl}_2/\text{MeOH}$ to afford **G2_{Br}CF₃3**.

Yield: 82.9 mg (90% over two steps)

Physical appearance: white solid, **m.p.:** 192-194 °C

R_f: 0.6 (EtOAc:hexanes = 1:9)

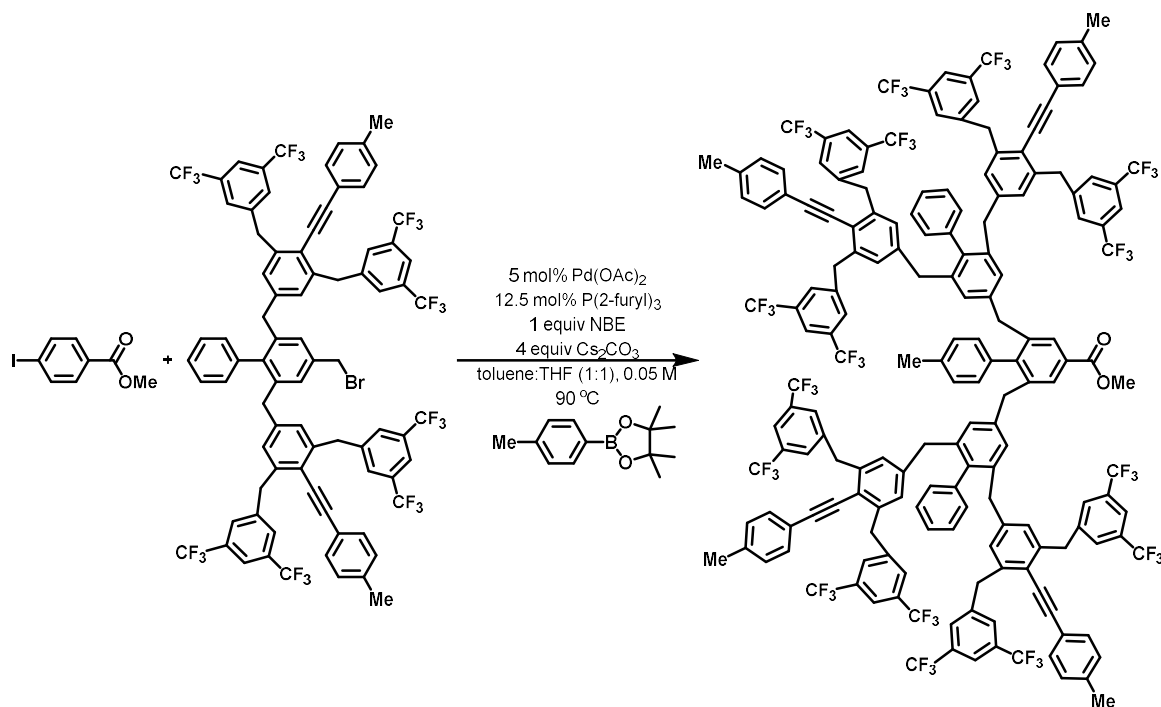
¹H NMR (500 MHz, CDCl₃): δ 7.71 (s, 4H), 7.61 (s, 8H), 7.16 (d, $J = 7.0$ Hz, 4H), 7.15 – 7.13 (m, 3H), 7.12 (d, $J = 8.2$ Hz, 4H), 7.07 (t, $J = 7.4$ Hz, 2H), 6.66 (d, $J = 6.9$ Hz, 2H), 6.58 (s, 4H), 4.45 (s, 2H), 4.20 (s, 8H), 3.67 (s, 4H), 2.36 (s, 6H).

¹³C NMR (126 MHz, CDCl₃): δ 143.13, 142.23, 141.80, 141.54, 139.51, 139.21, 138.75, 137.45, 131.68 (q, $^2J_{\text{C-CF}_3} = 33.1$ Hz), 131.17, 129.45, 129.37, 129.02, 128.96, 128.92, 128.15, 127.17, 123.50 (q, $^1J_{\text{C-CF}_3} = 272.7$ Hz), 121.02, 120.37, 119.45, 99.07, 85.52, 40.53, 39.90, 33.13, 21.64.

¹⁹F NMR (470 MHz, CDCl₃): -62.82.

IR (KBr, neat): 3030, 2927, 2857, 2209, 1623, 1605, 1452, 1534, 1522, 1491, 1466, 1438, 1374, 1278, 1171, 1132, 1108, 904, 886, 843, 816, 778, 765, 726, 705, 683 cm^{-1} .

HRMS (ESI-TOF): m/z calcd for $\text{C}_{81}\text{H}_{52}\text{BrF}_{24}^+$ [$\text{M}+\text{H}^+$]: 1559.2864. Found: 1559.2862.



A flame-dried 1.7 mL reaction vial was charged with methyl 4-iodobenzoate (3.2 mg, 0.0122 mmol, 1.0 equiv.), **G2BrCF₃3** (40.0 mg, 0.0256 mmol, 2.1 equiv), 4-methylphenylboronic acid pinacol ester (3.2 mg, 0.0147 mmol, 1.2 equiv), Pd(OAc)₂ (0.14 mg, 0.000611 mmol, 5 mol%), and tri(2-furyl)phosphine (0.35 mg, 0.000153 mmol, 12.5 mol%). The vial was brought into the glovebox, and anhydrous Cs₂CO₃ (15.9 mg, 0.0488 mmol, 4 equiv), norbornene (1.1 mg, 0.0122 mmol, 1 equiv), toluene (0.12 mL), and THF (0.12 mL) were added. The reaction mixture in the vial was stirred at r. t. for 10 mins, was taken out of the glove box, and then was stirred and heated at a preheated pie-block set to 90 °C for 24 h. After cooling down to room temperature, the crude mixture was passed through a Büchner funnel packed with celite and washed with EtOAc. The crude product was purified by flash column chromatography on silica gel (loaded with toluene, then eluted with EtOAc:hexanes = 1:9) to afford **G3CF₃3**.

Yield: 24.3 mg (62%, purity >95%)

Physical appearance: amorphous colorless solid

R_f: 0.35 (EtOAc:hexanes = 1:1)

¹H NMR (500 MHz, CDCl₃): δ 7.82 (s, 2H), 7.68 (s, 8H), 7.57 (s, 16H), 7.12 (d, *J* = 8.1 Hz, 8H), 7.09 (d, *J* = 8.2 Hz, 8H), 7.02 (dd, *J* = 7.7, 5.5 Hz, 4H), 6.95 (t, *J* = 7.3 Hz, 4H), 6.87 (d, *J* = 7.6 Hz, 2H), 6.72 (s, 4H), 6.52 (d, *J* = 7.1 Hz, 4H), 6.48 (s, 8H), 4.14 (s, 16H), 3.75 (s, 4H), 3.66 (s, 3H), 3.56 (s, 8H), 2.34 (s, 12H), 2.28 (s, 3H).

¹³C NMR (126 MHz, CDCl₃): δ 167.16, 146.79, 143.24, 142.42, 141.31, 140.43, 140.07, 139.92, 139.15, 138.66, 136.99, 136.17, 131.61 (q, ²*J*_{C-CF₃} = 33.1 Hz), 131.11, 130.23, 129.81, 129.64, 129.35, 129.22, 129.07, 128.90, 128.87, 127.85, 127.26, 126.95, 126.74, 123.48 (q, ¹*J*_{C-CF₃} = 272.7 Hz), 120.67, 120.24, 119.47, 98.87, 85.65, 51.94, 40.47, 39.98, 39.41, 21.62, 21.19.

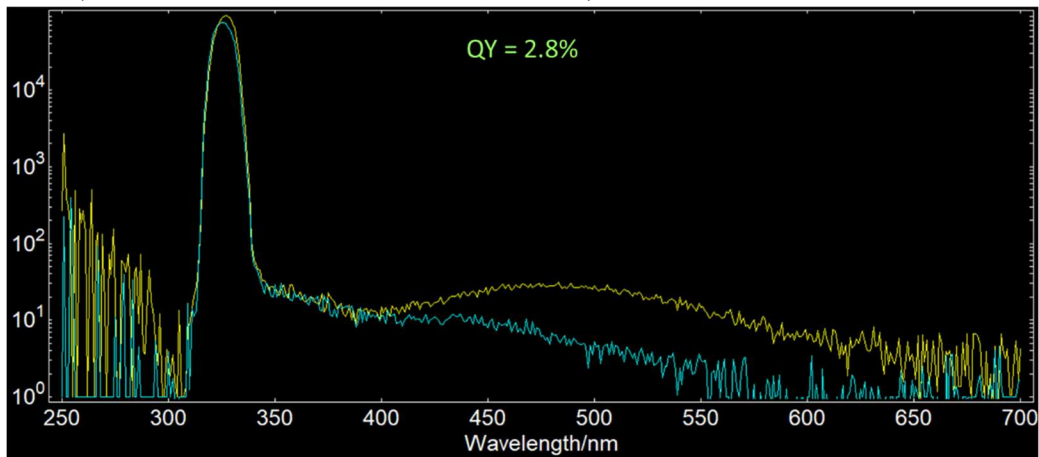
¹⁹F NMR (470 MHz, CDCl₃): -62.84.

IR (KBr, neat): 3029, 2925, 2209, 1797, 1720, 1622, 1606, 1564, 1512, 1466, 1436, 1374, 1277, 1171, 1133, 1108, 1008, 907, 843, 816, 772, 735, 705, 683, 651, 543, 524 cm⁻¹.

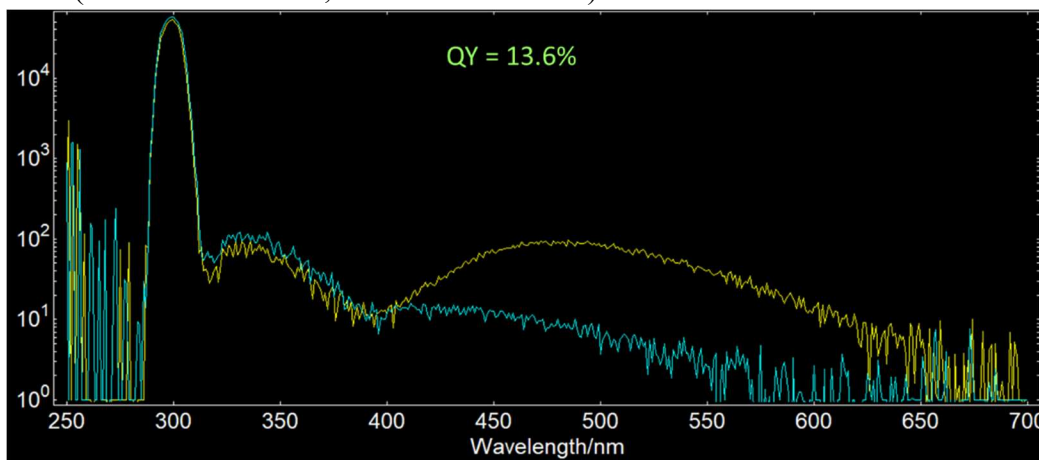
HRMS (ESI-TOF): *m/z* calcd for C₁₇₇H₁₁₅F₄₈O₂⁺ [M+H⁺]: 3183.8025. Found: 3183.7997.

2.6. Absolute Fluorescence Quantum Yield Measurements of AIE Compounds

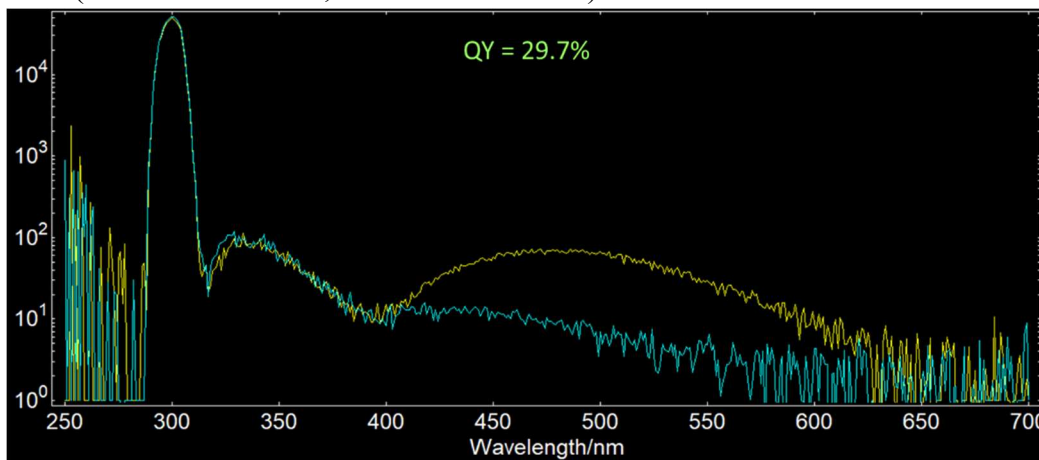
AIE-1 (excitation: 327 nm, bandwidth 10.0 nm)



AIE-2 (excitation: 300 nm, bandwidth 10.0 nm)

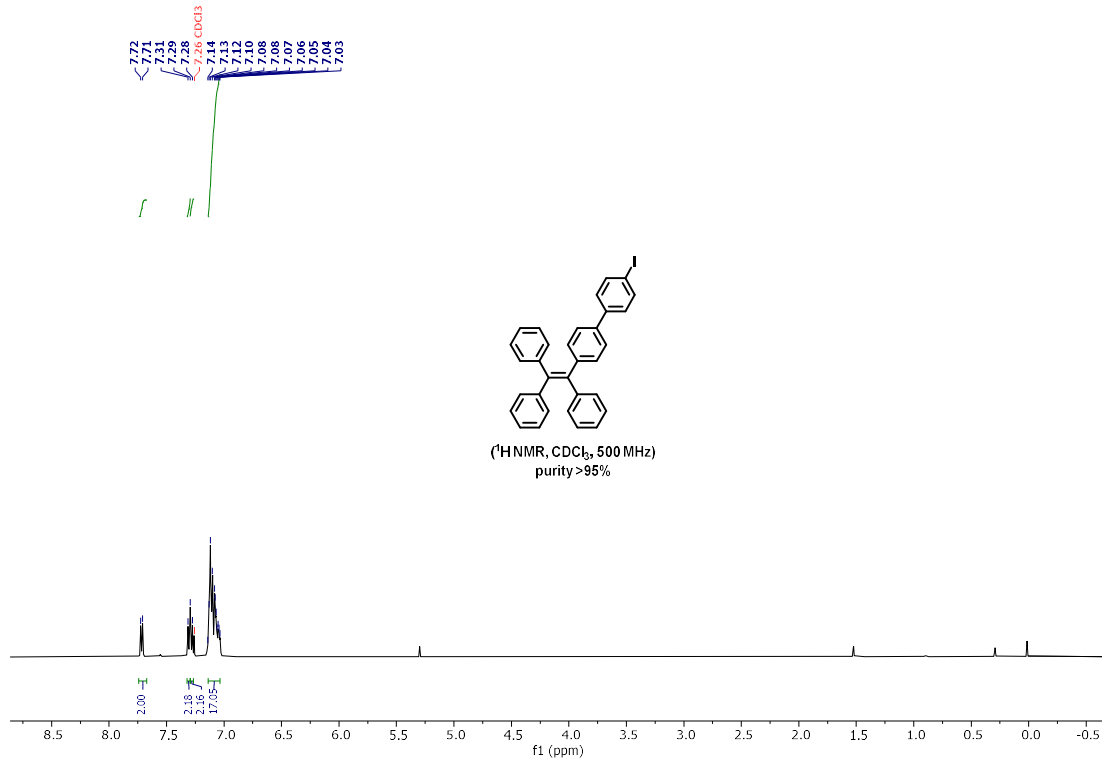


AIE-3 (excitation: 300 nm, bandwidth 10.0 nm)

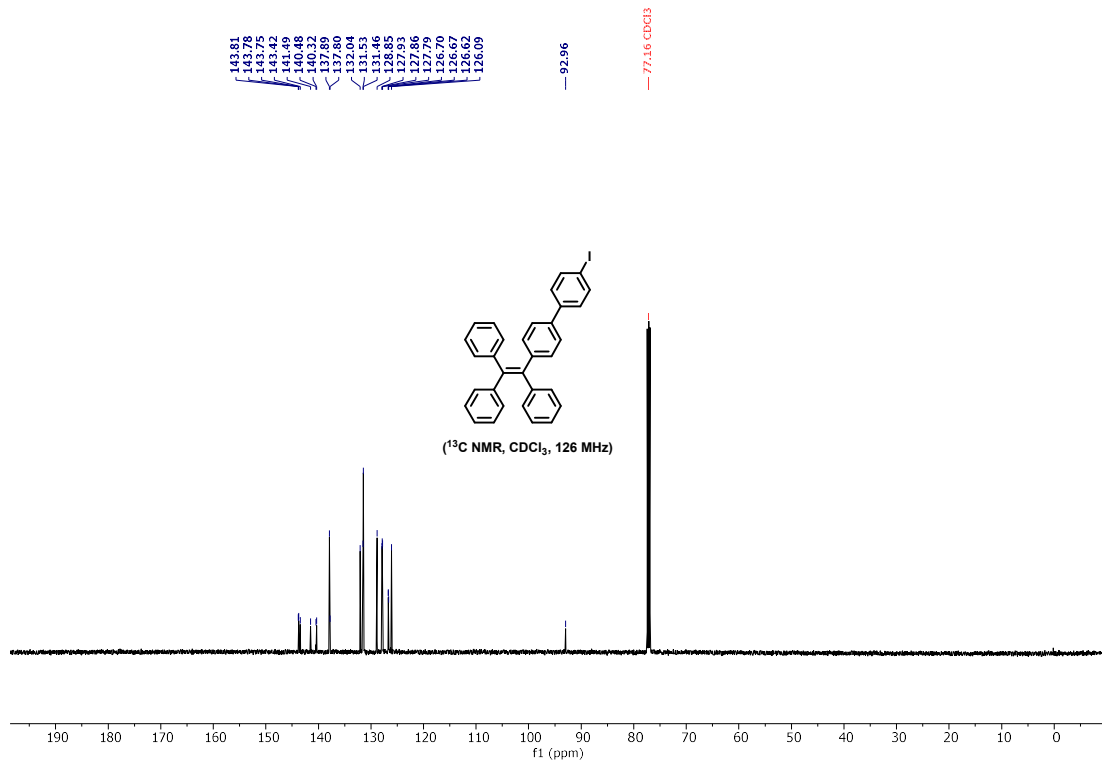


2.7. NMR Spectra

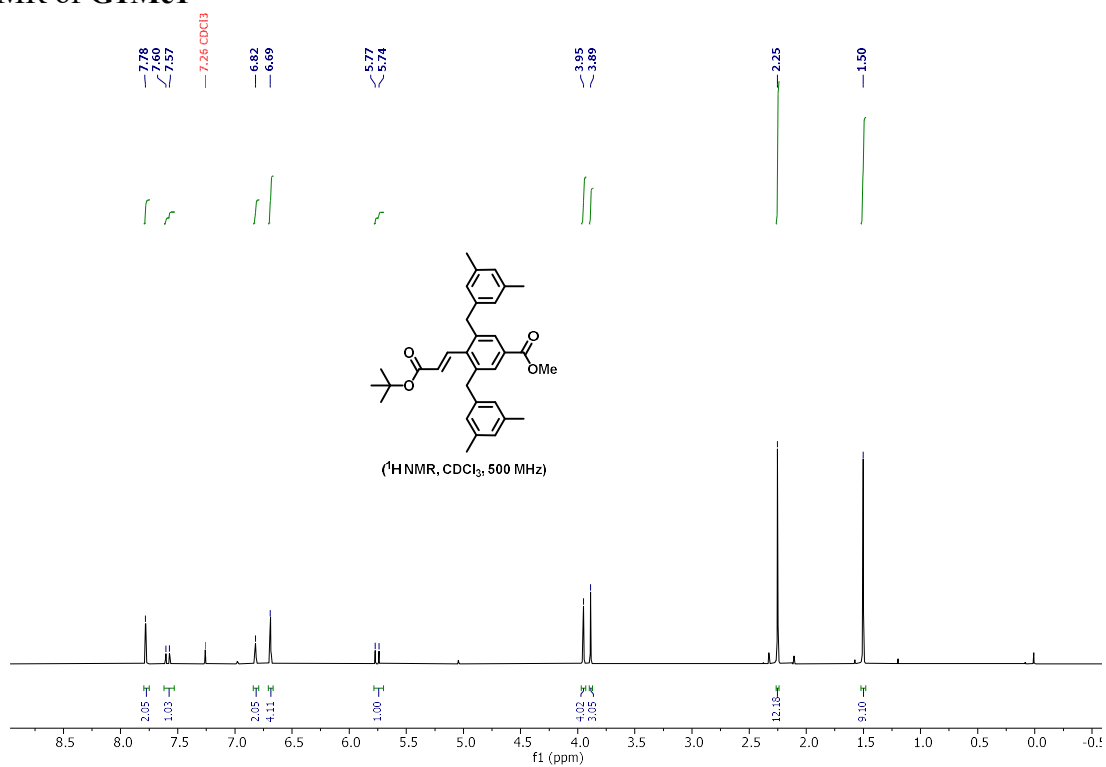
^1H NMR of TPE-Ph-I



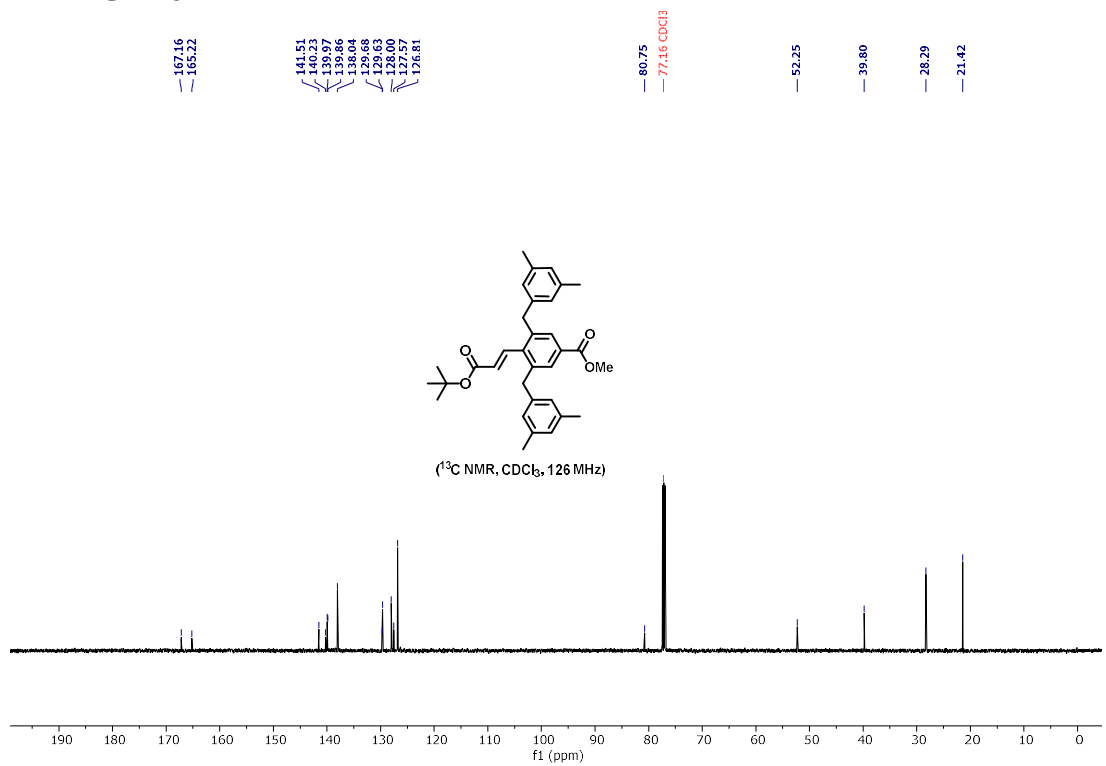
^{13}C NMR of TPE-Ph-I



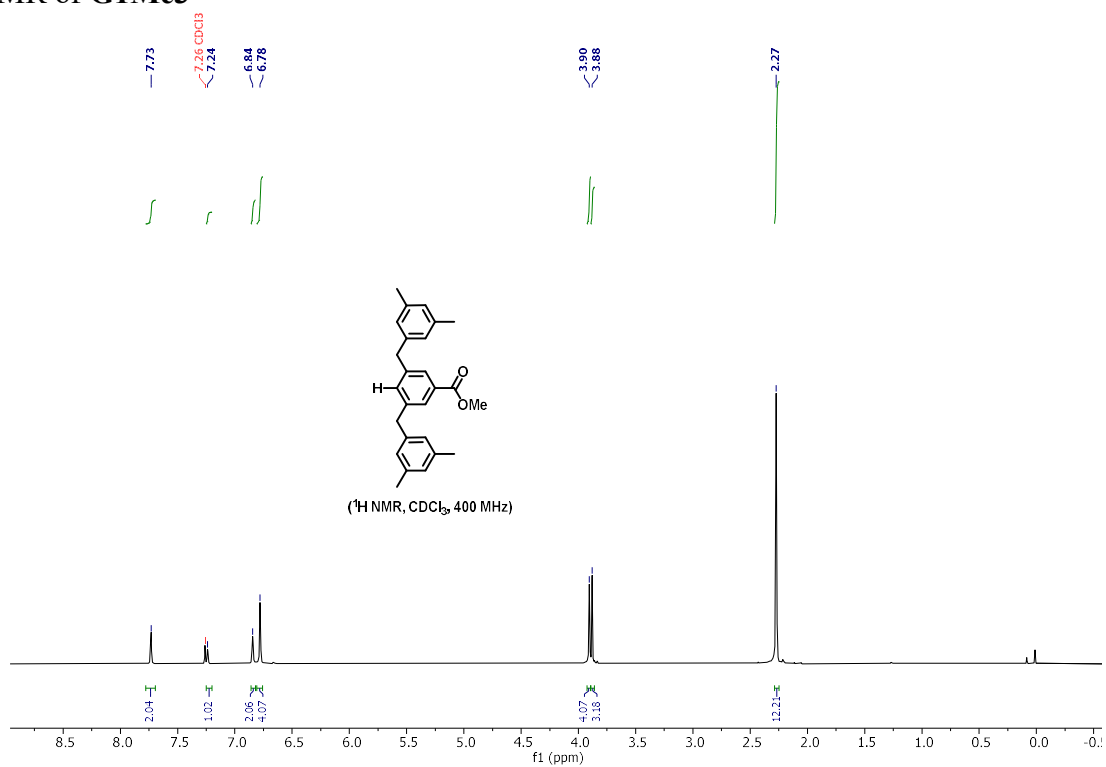
¹H NMR of G1Me1



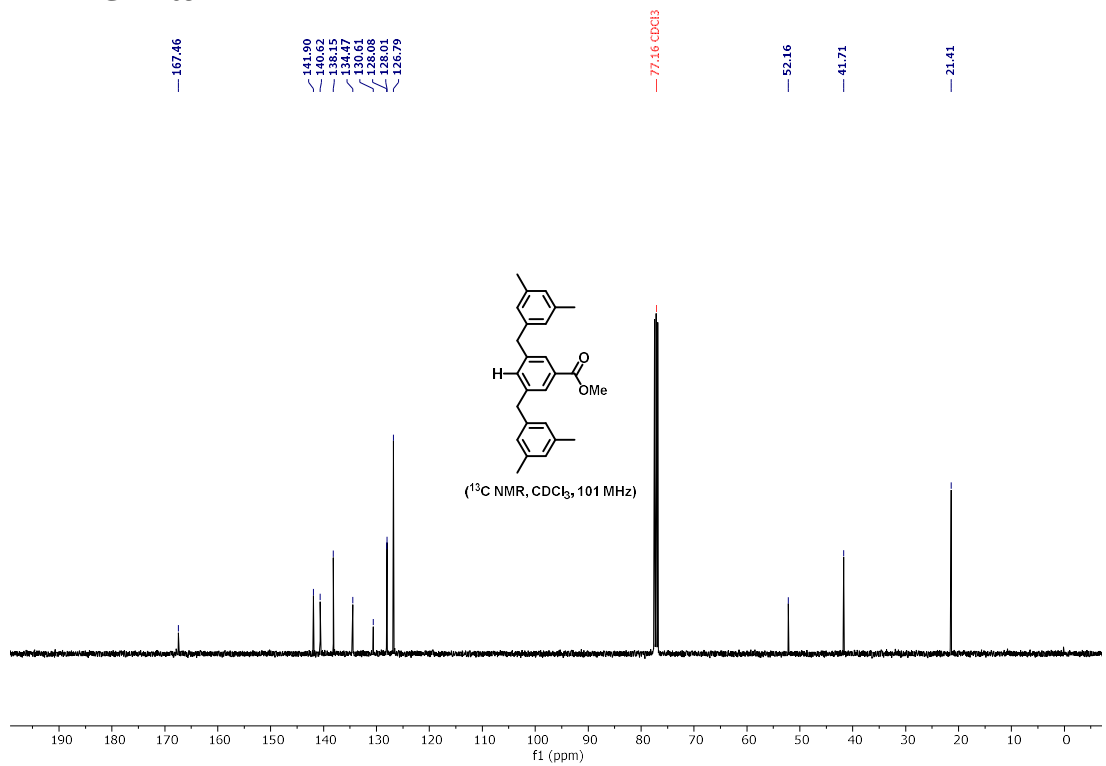
¹³C NMR of G1Me1



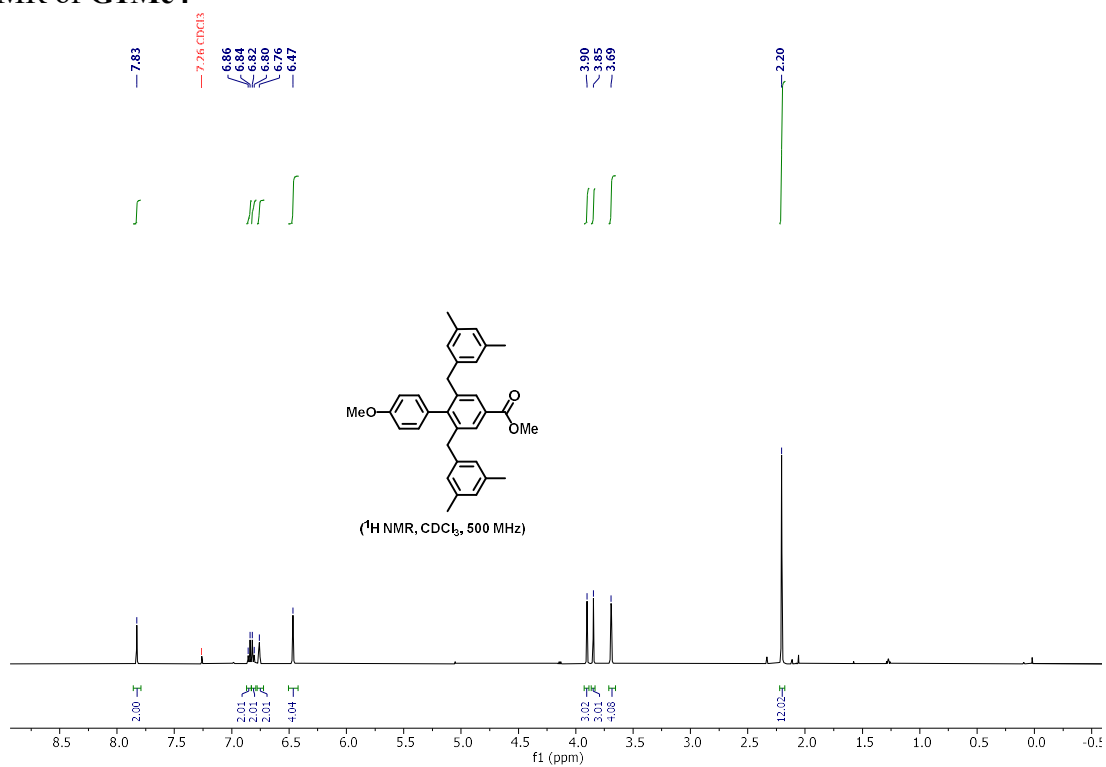
¹H NMR of G1Me3



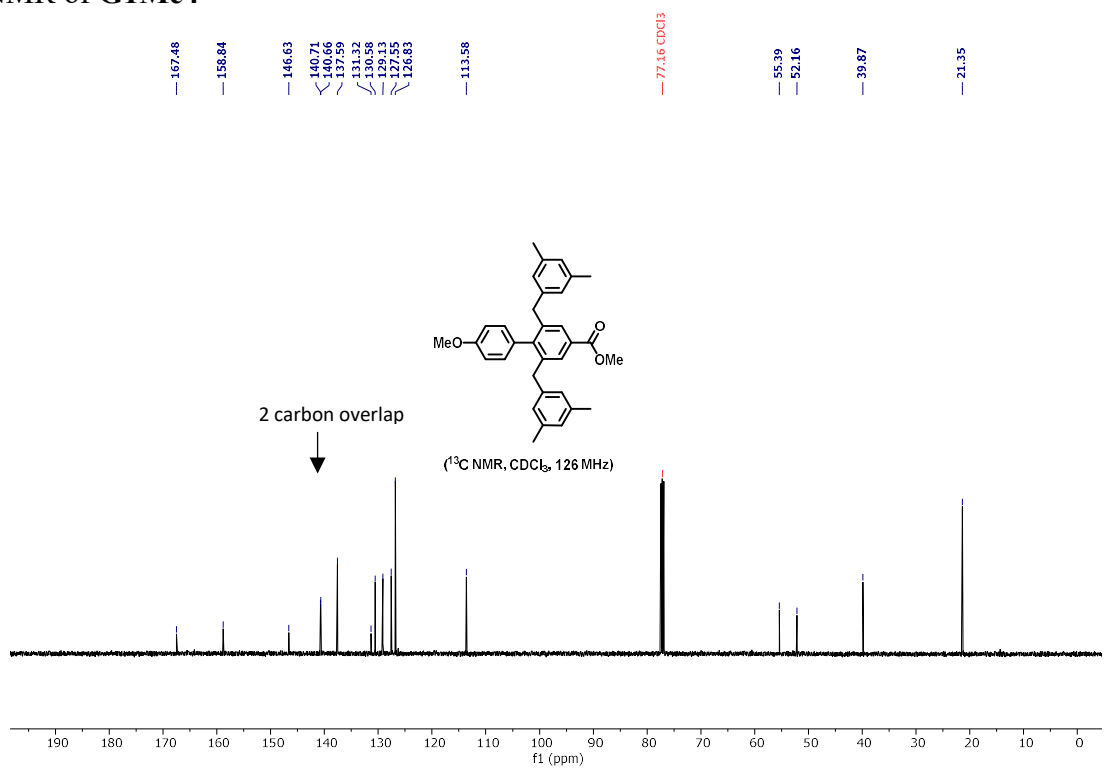
¹³C NMR of G1Me3



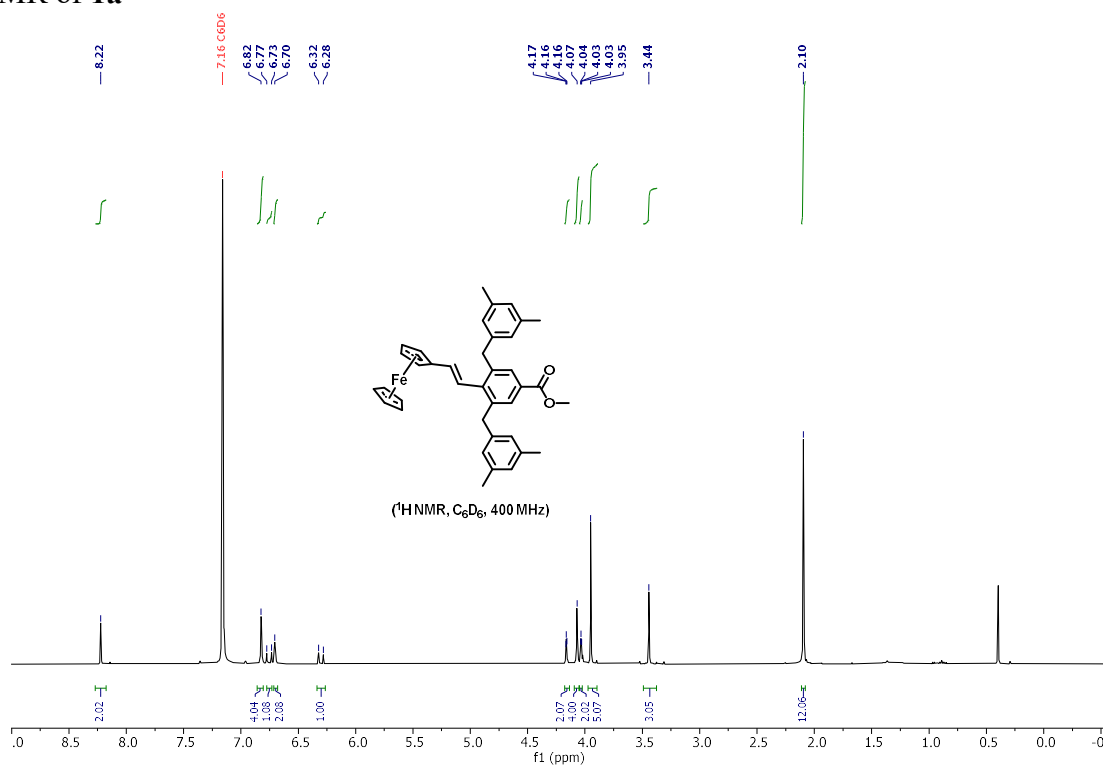
¹H NMR of G1Me4



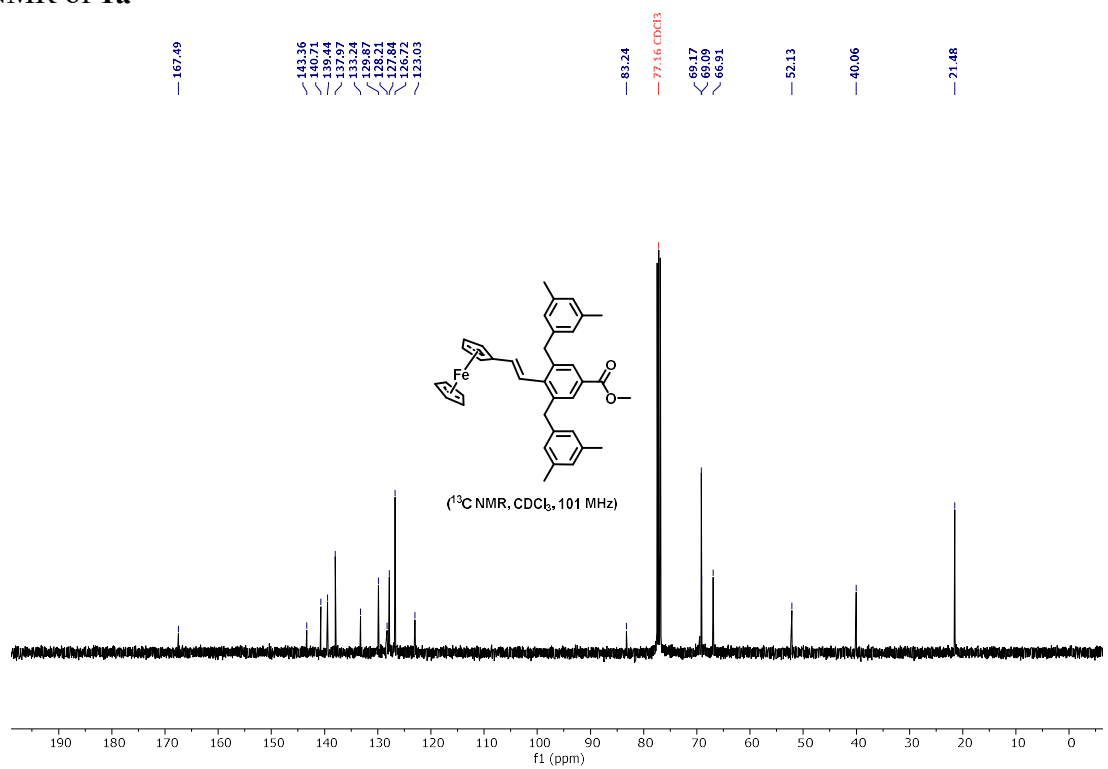
¹³C NMR of G1Me4



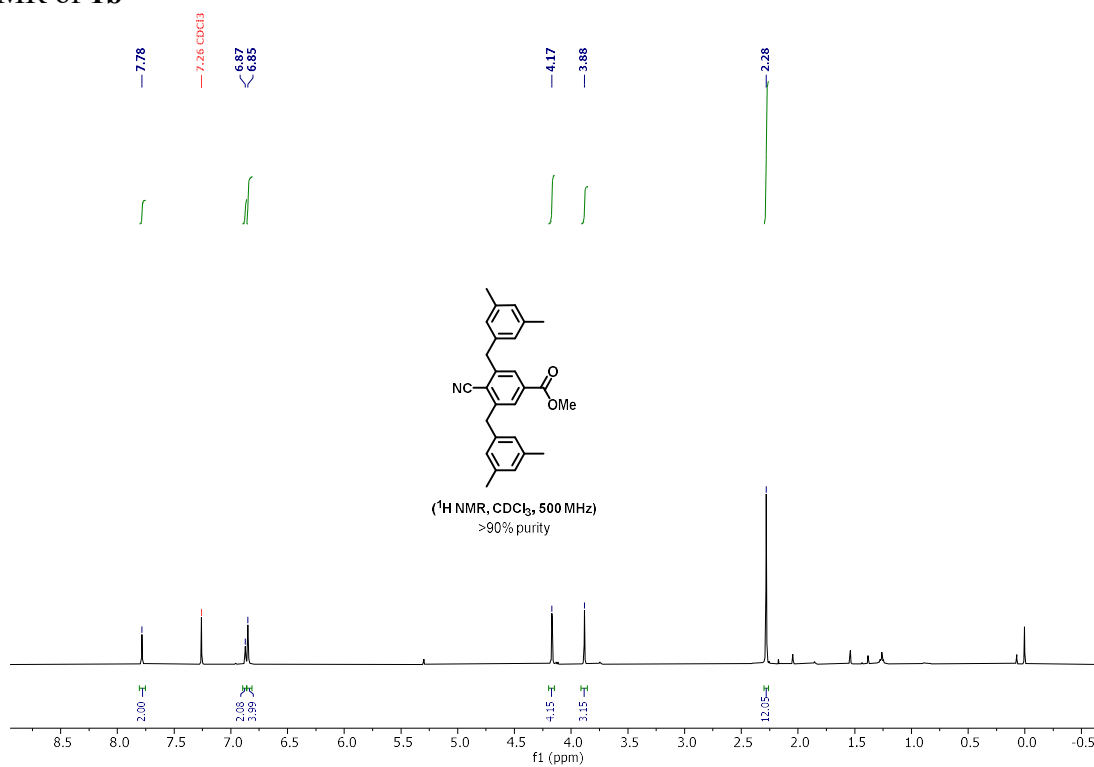
¹H NMR of 1a



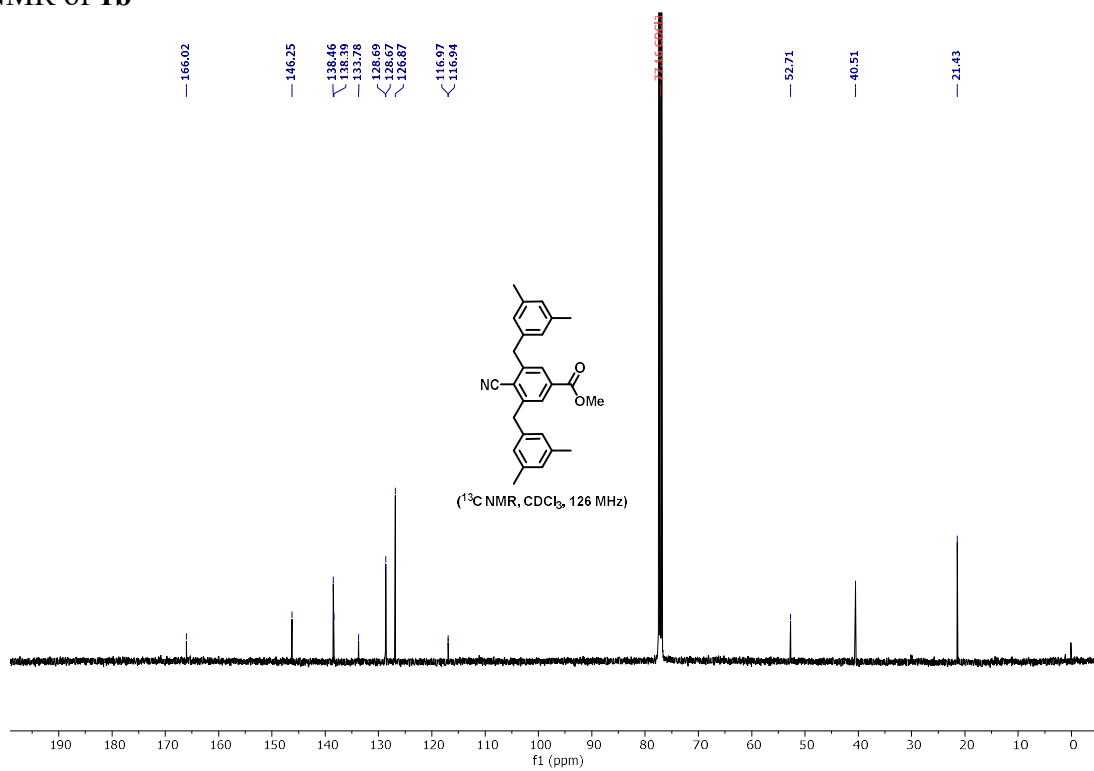
¹³C NMR of 1a



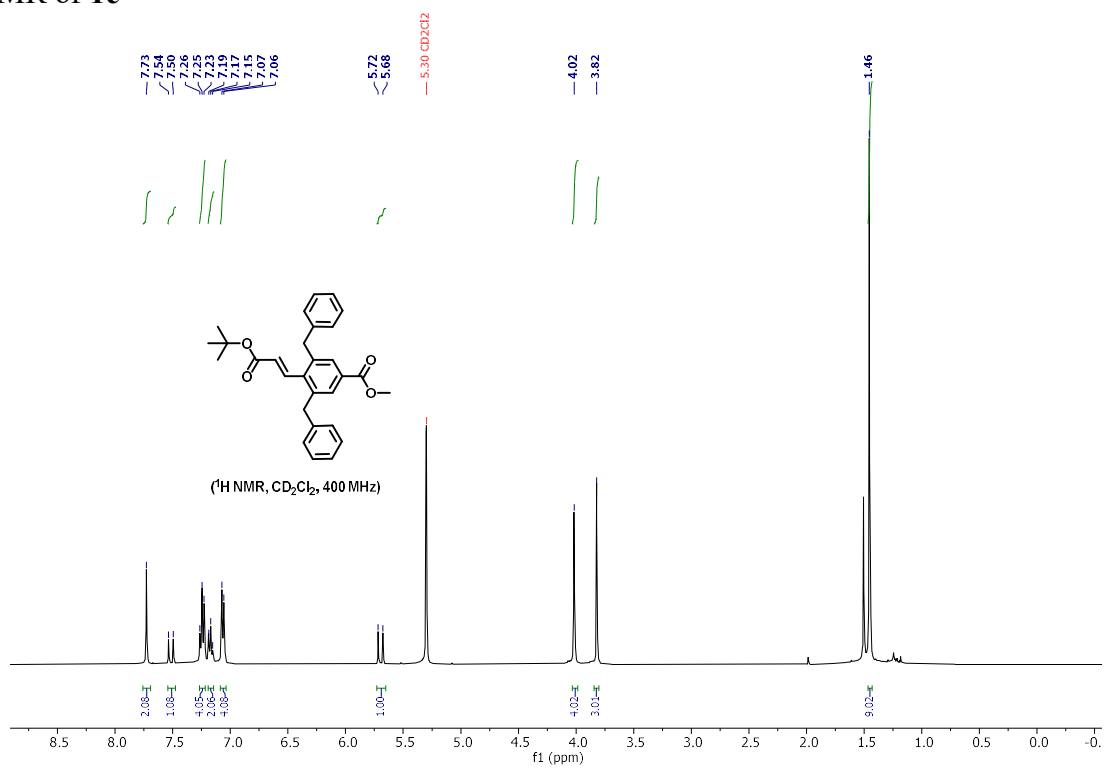
¹H NMR of **1b**



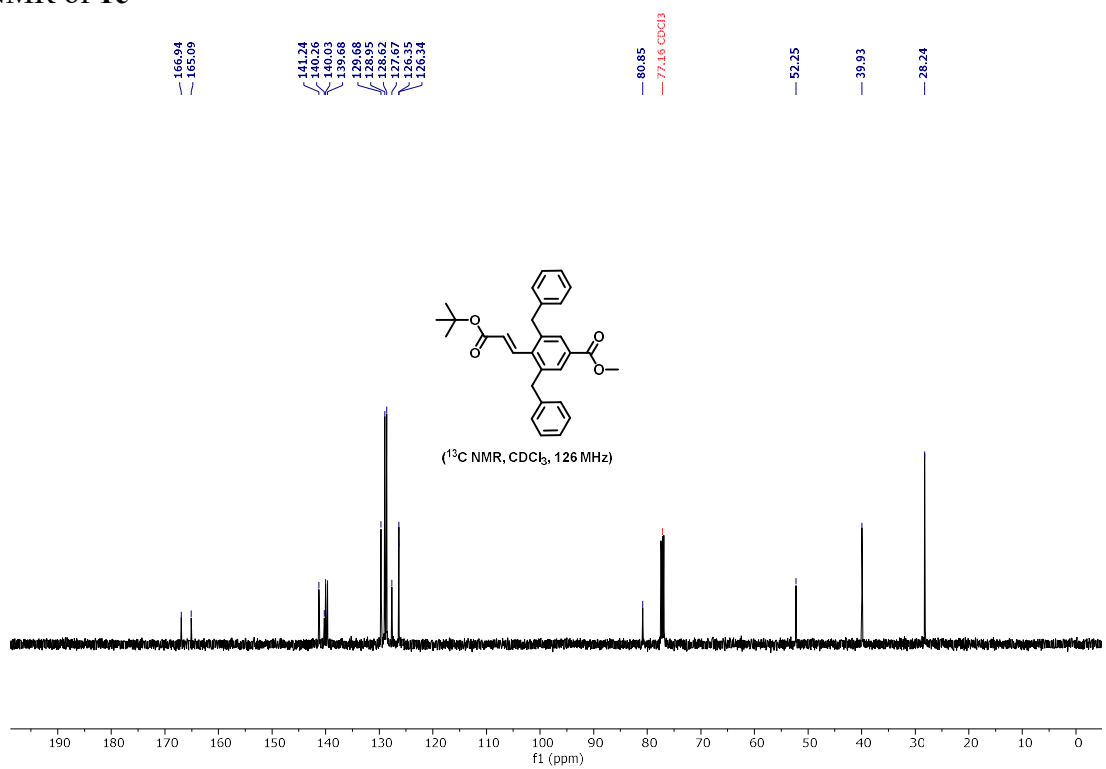
¹³C NMR of **1b**



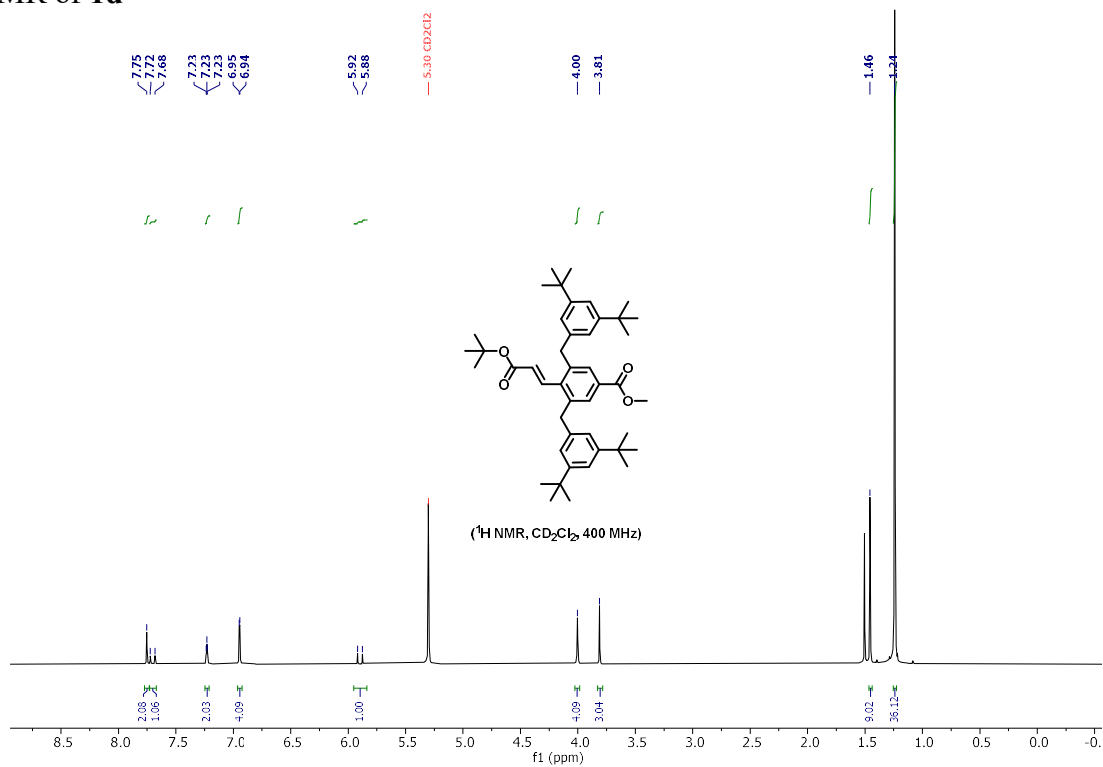
¹H NMR of 1c



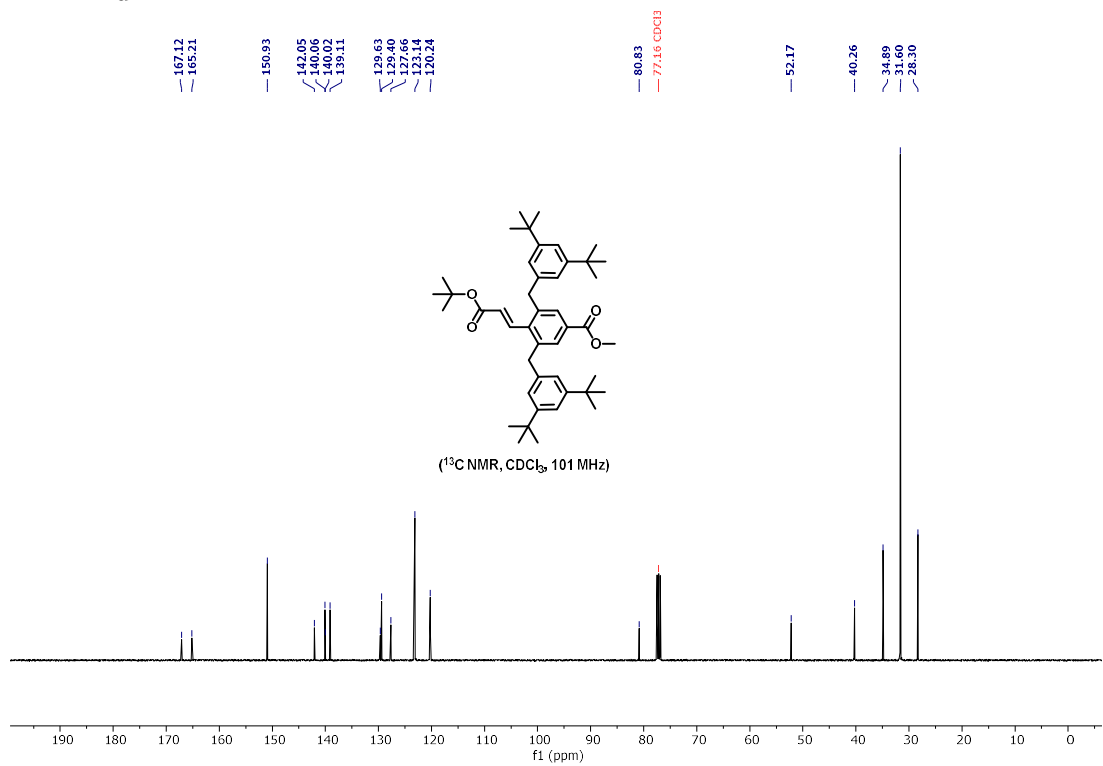
¹³C NMR of 1c



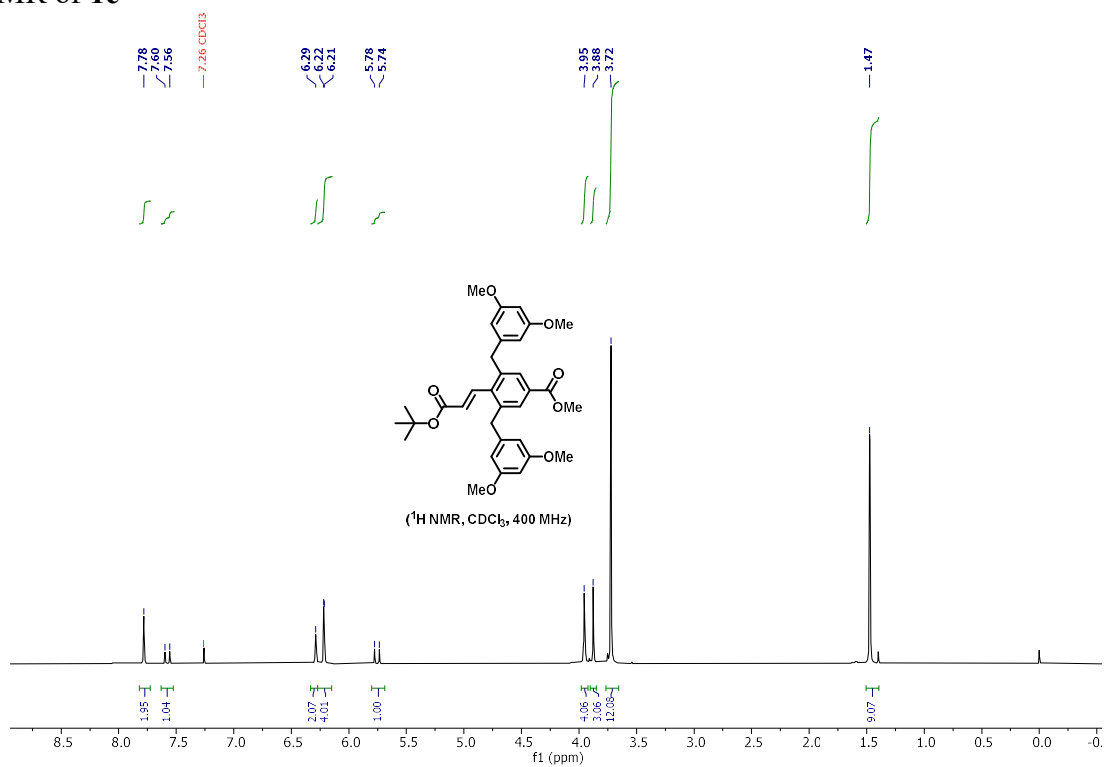
¹H NMR of 1d



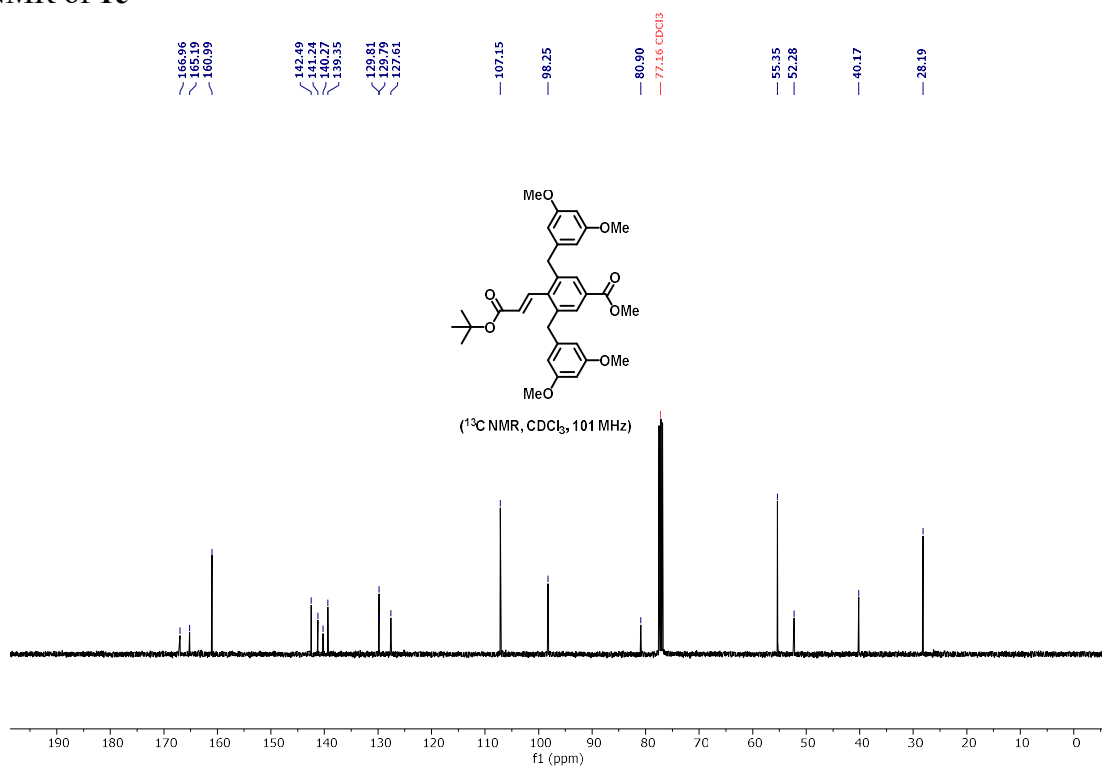
¹³C NMR of 1d



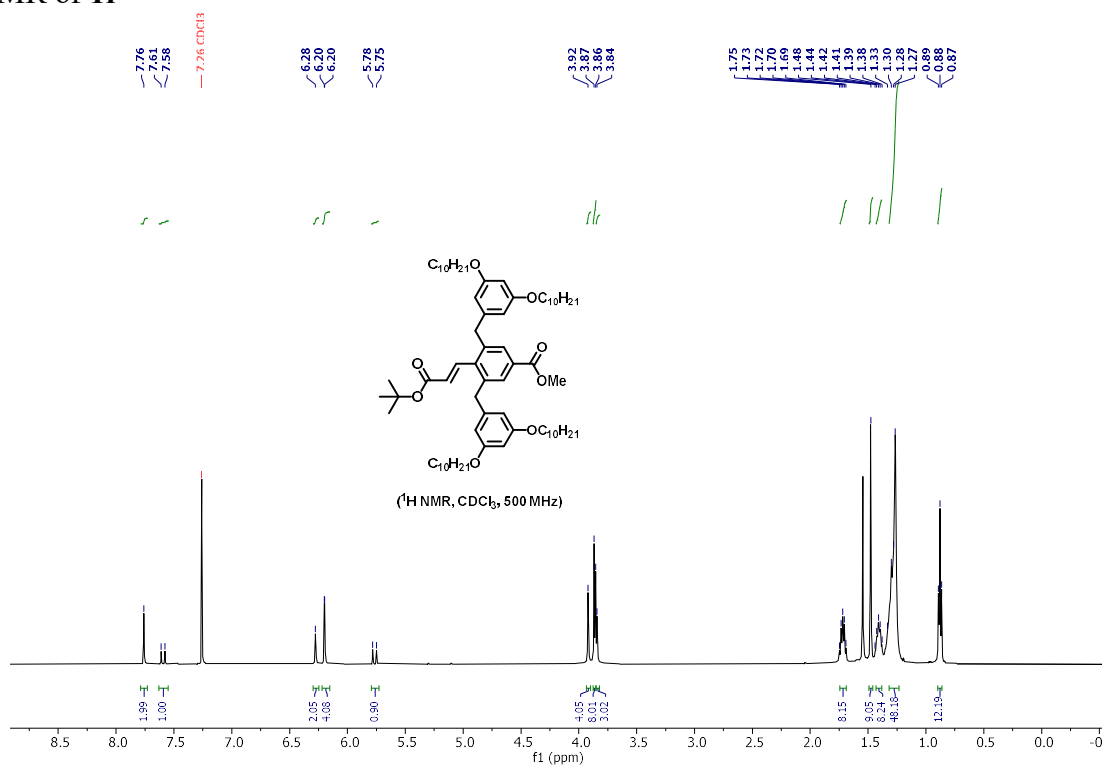
¹H NMR of 1e



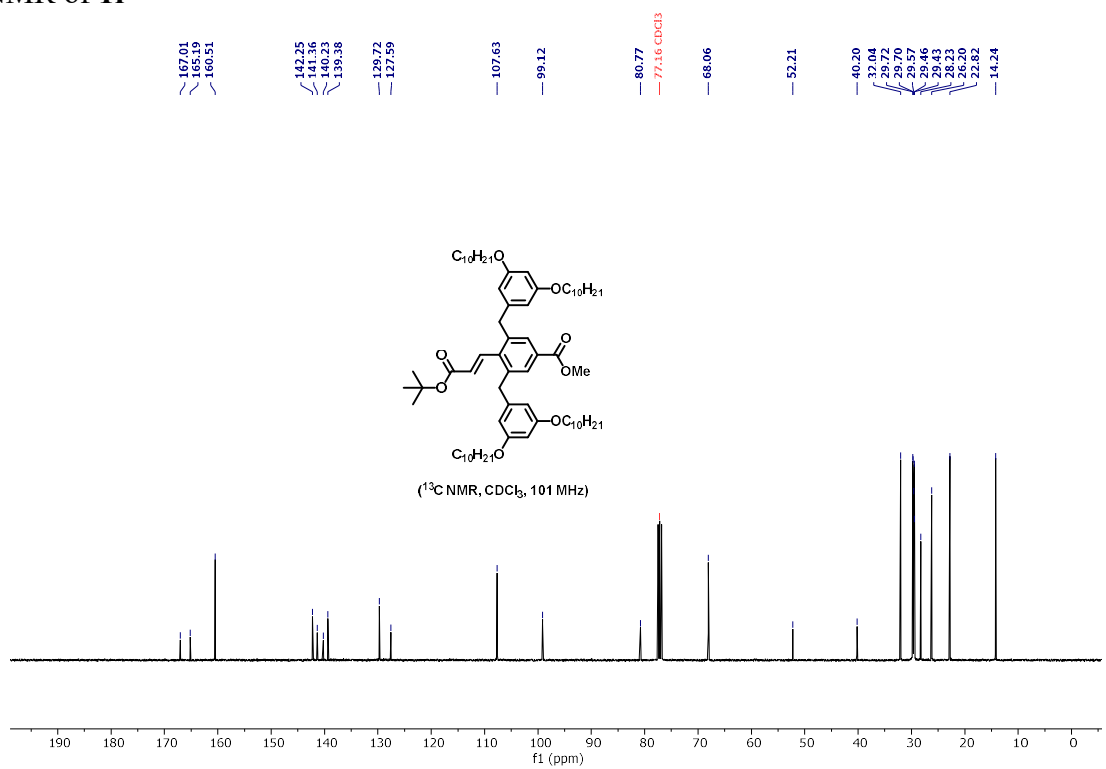
¹³C NMR of 1e



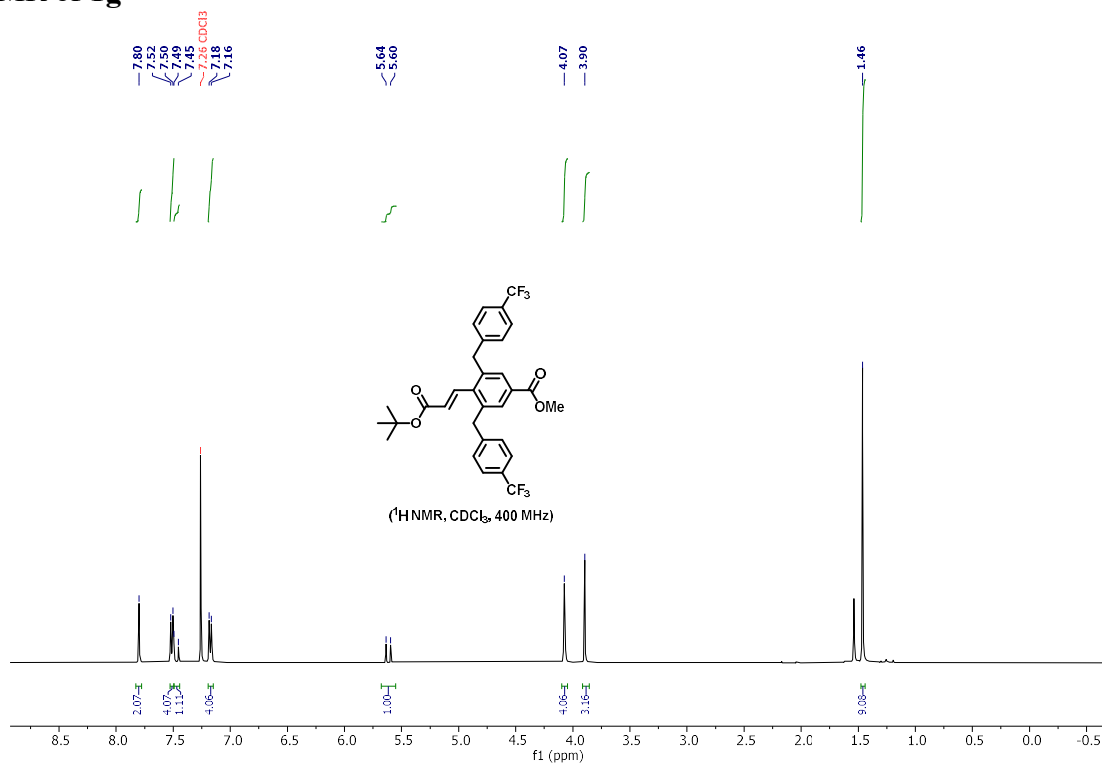
¹H NMR of **1f**



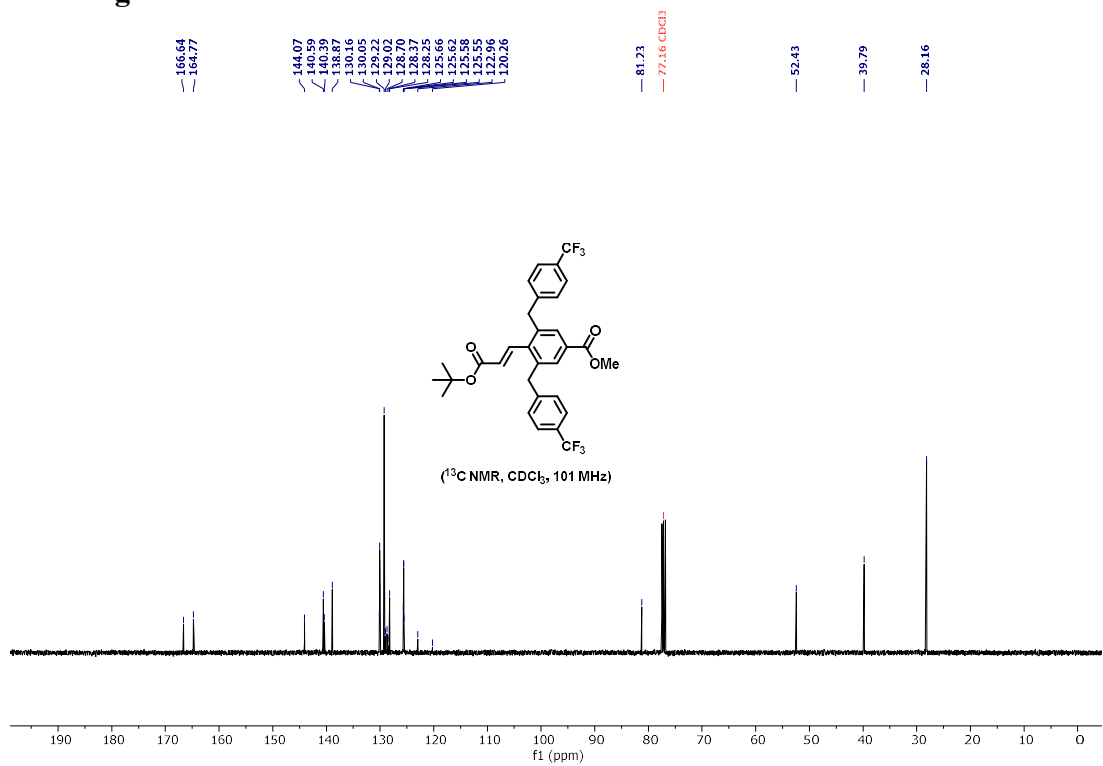
¹³C NMR of **1f**



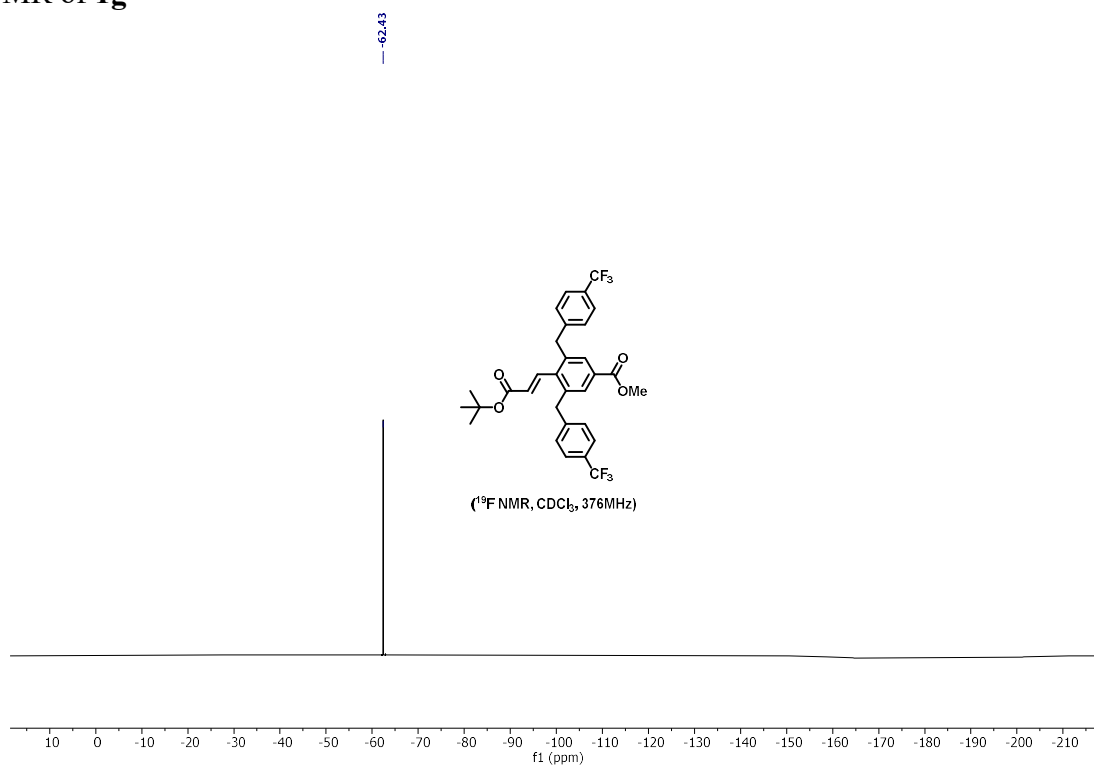
¹H NMR of **1g**



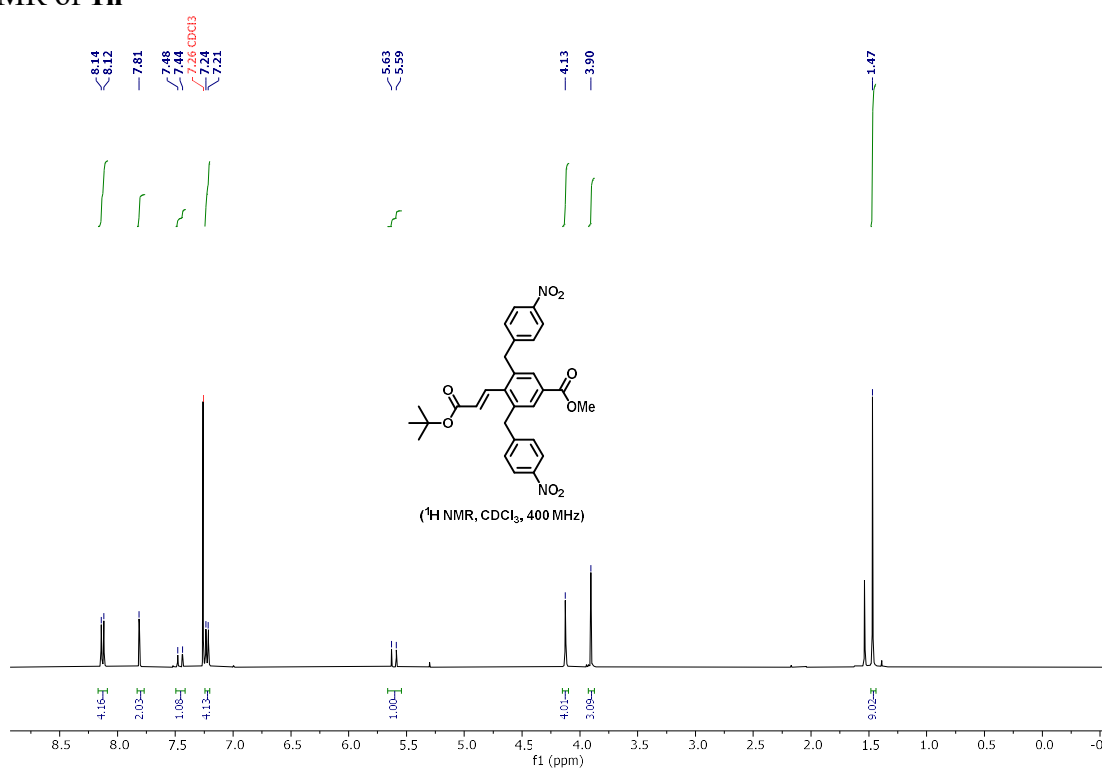
¹³C NMR of **1g**



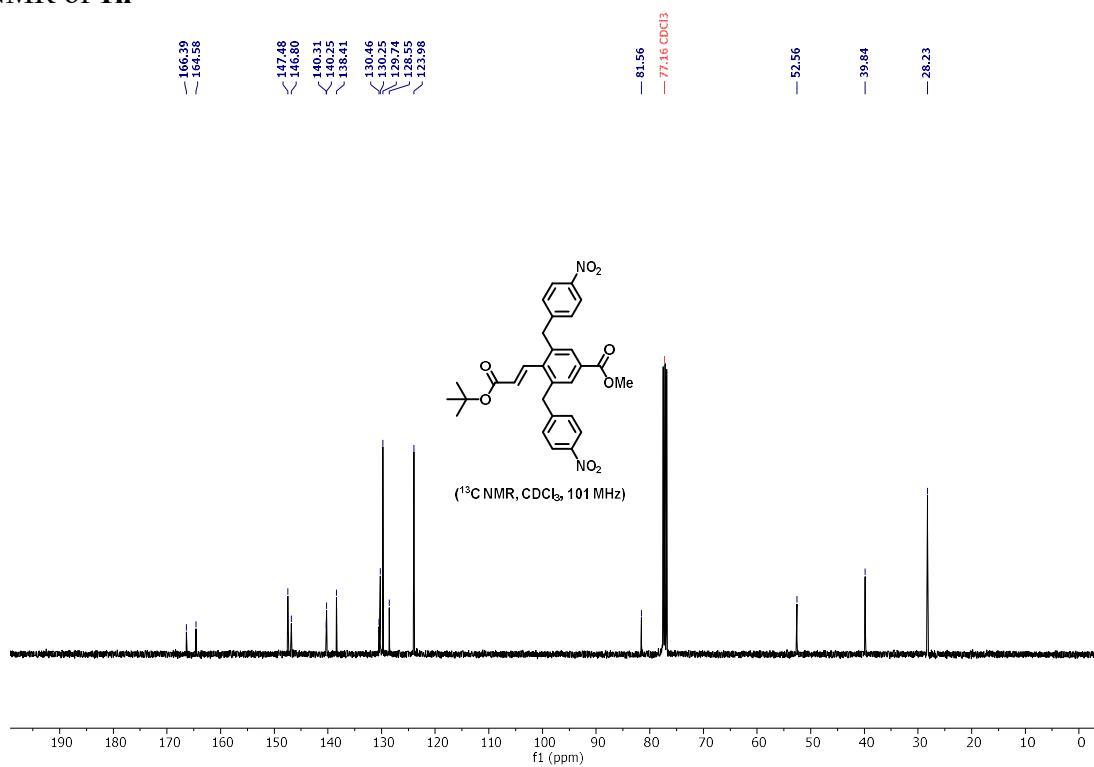
^{19}F NMR of **1g**



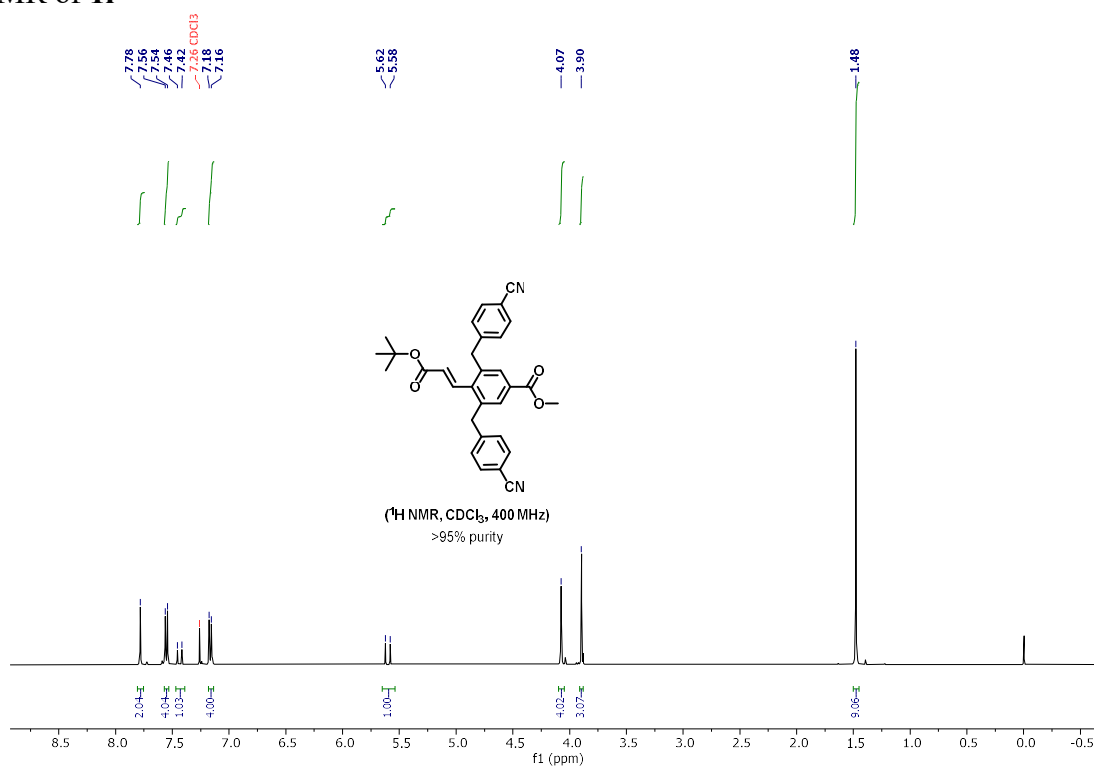
^1H NMR of **1h**



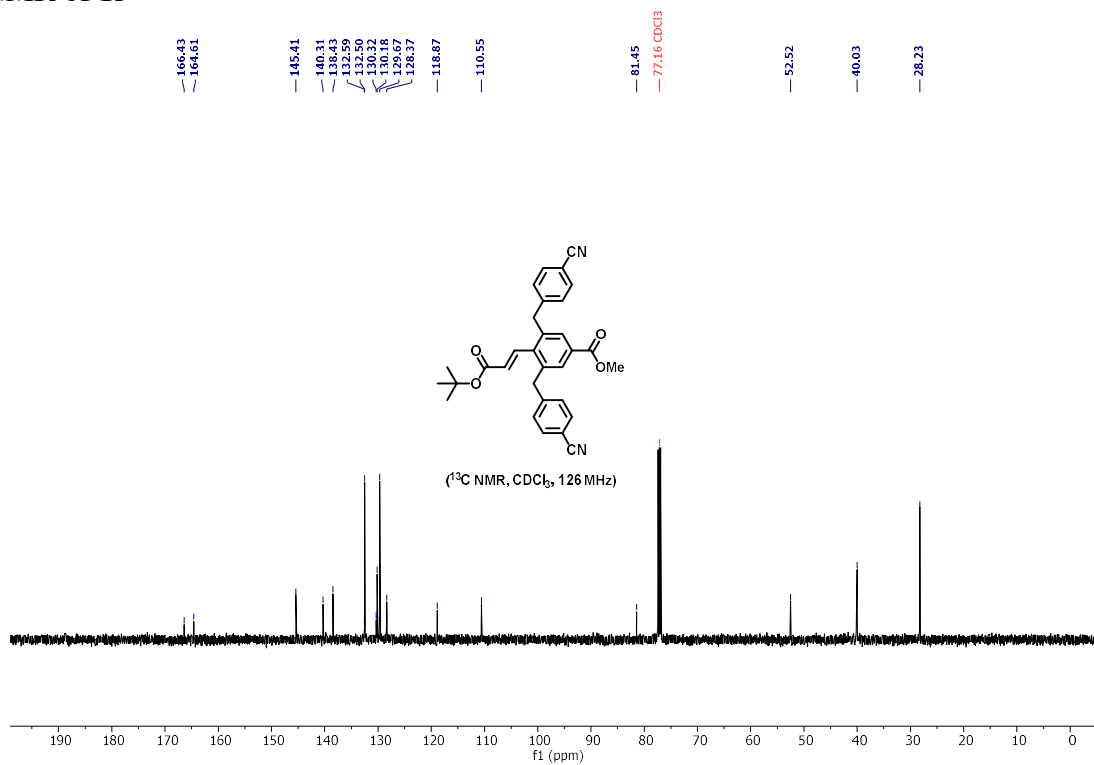
^{13}C NMR of **1h**



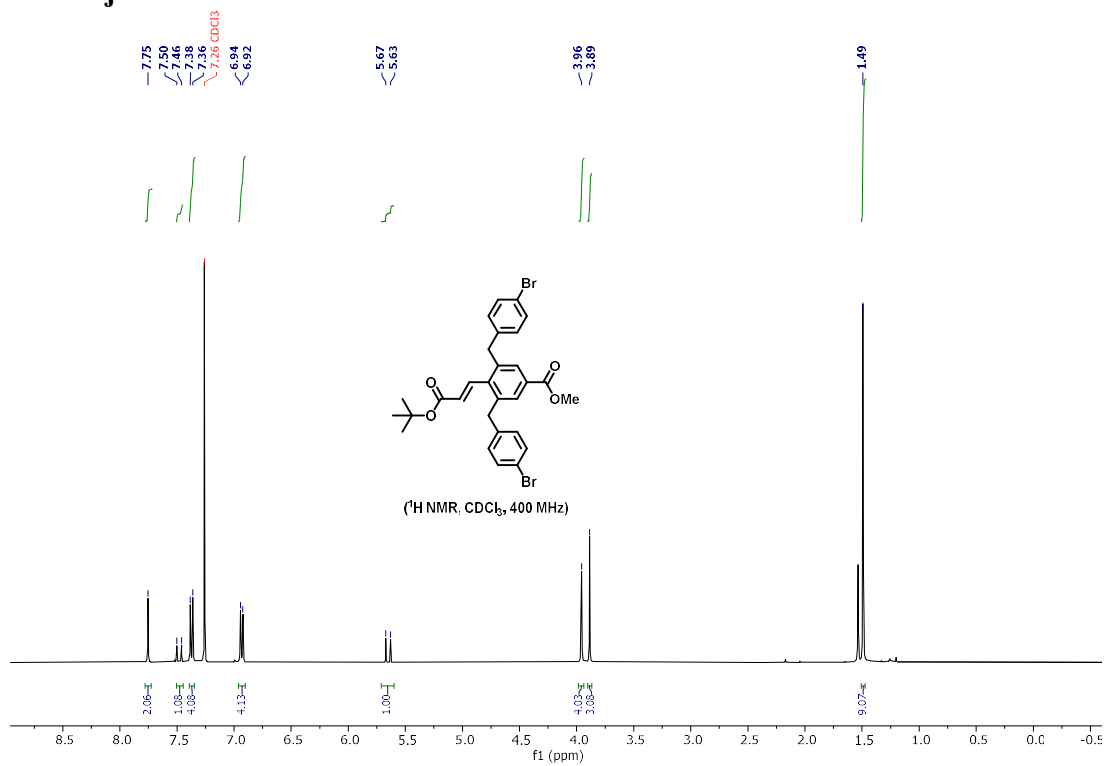
^1H NMR of **1i**



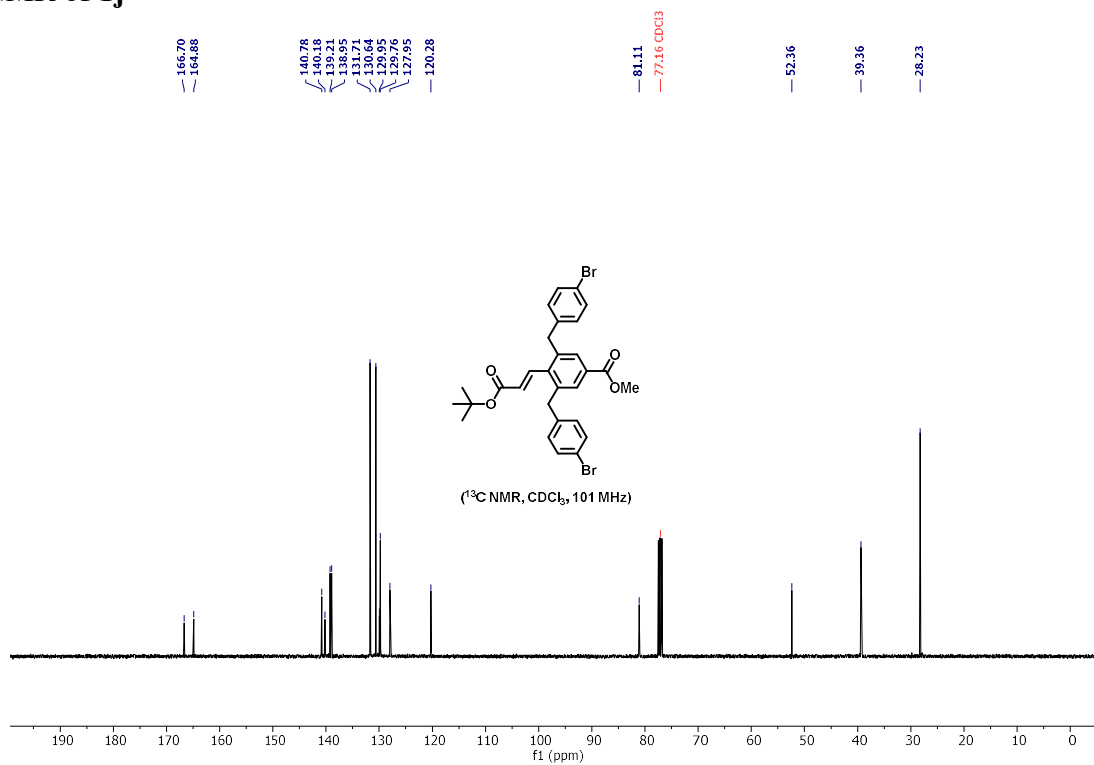
^{13}C NMR of **1i**



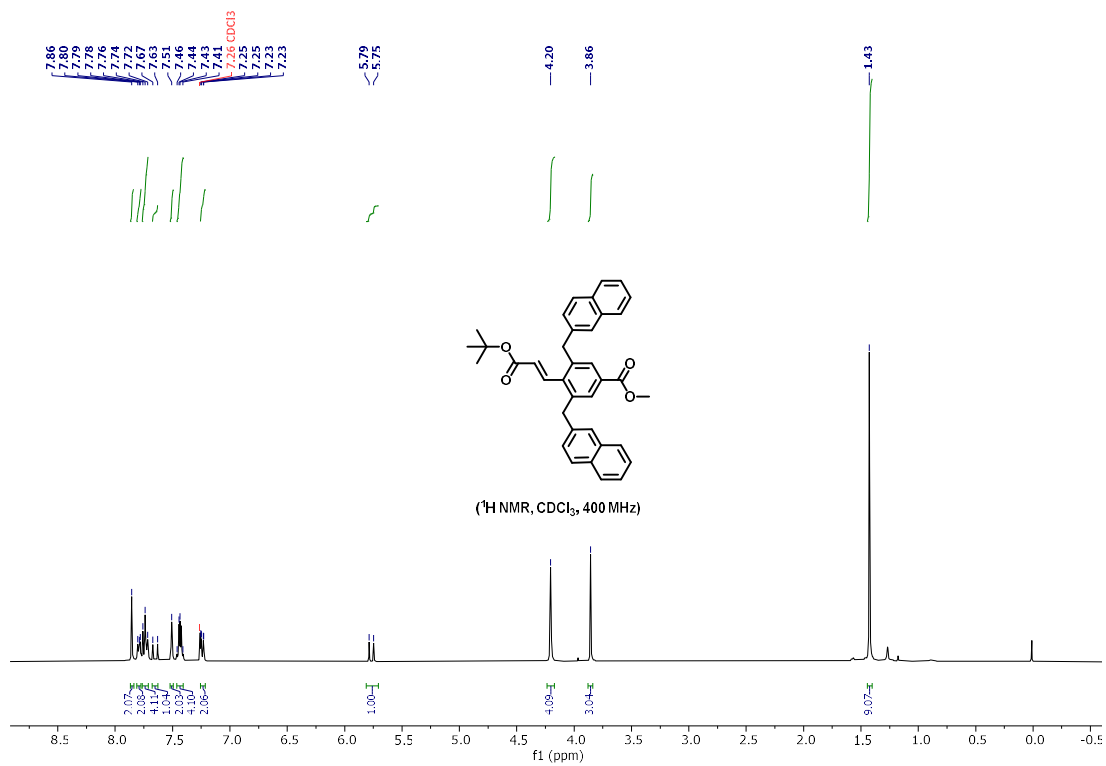
^1H NMR of **1j**



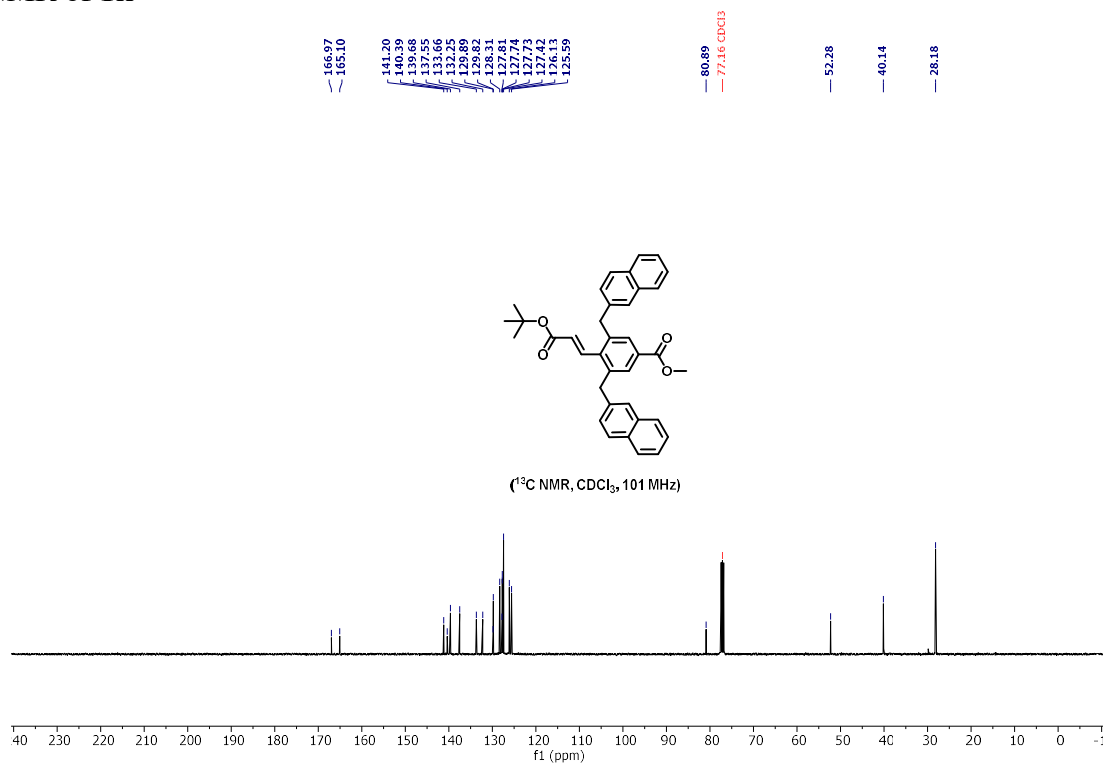
^{13}C NMR of **1j**



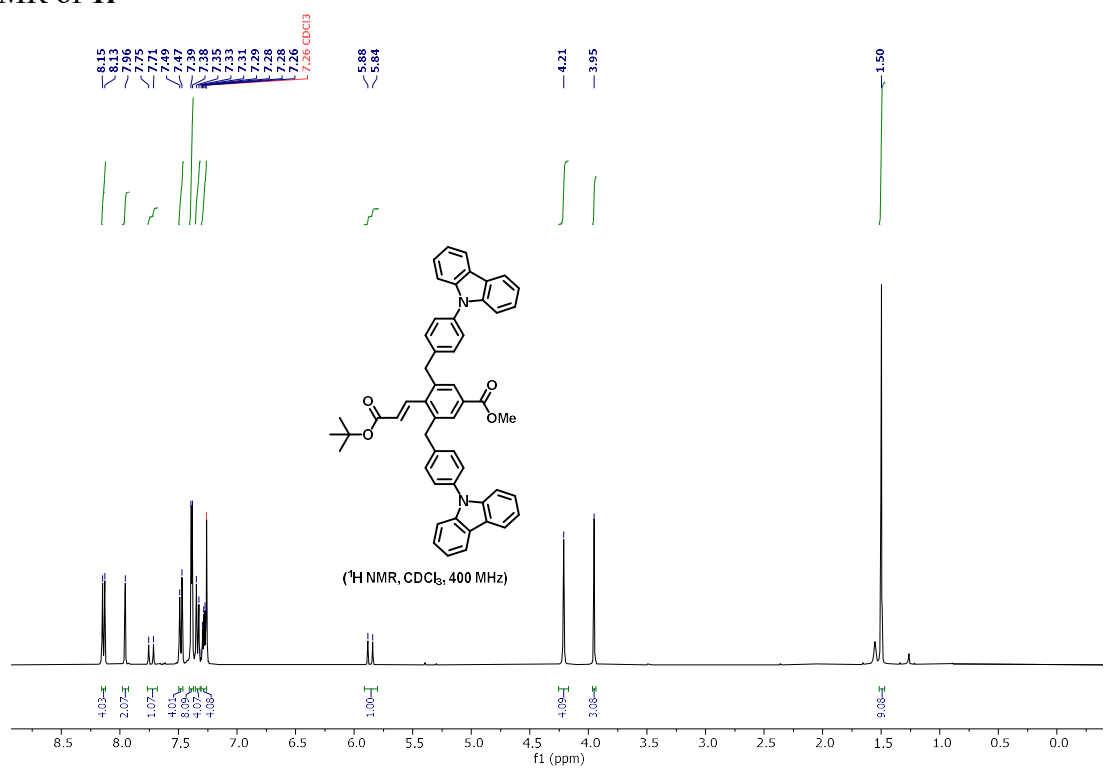
^1H NMR of **1k**



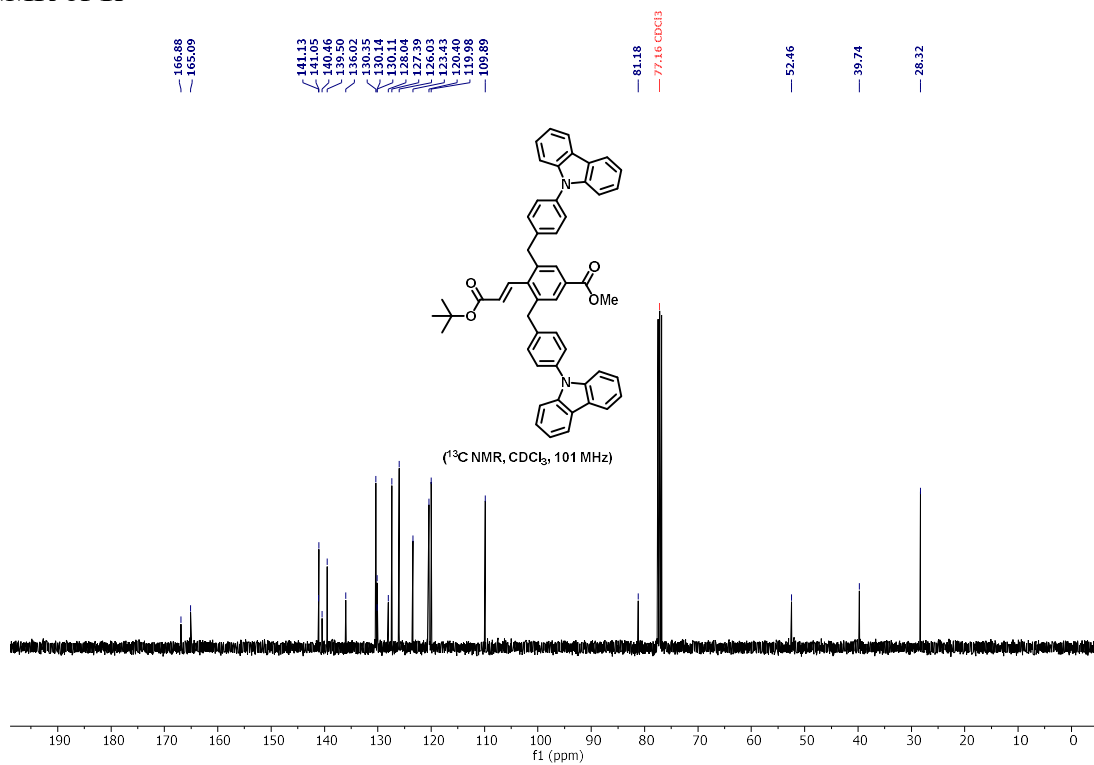
^{13}C NMR of **1k**



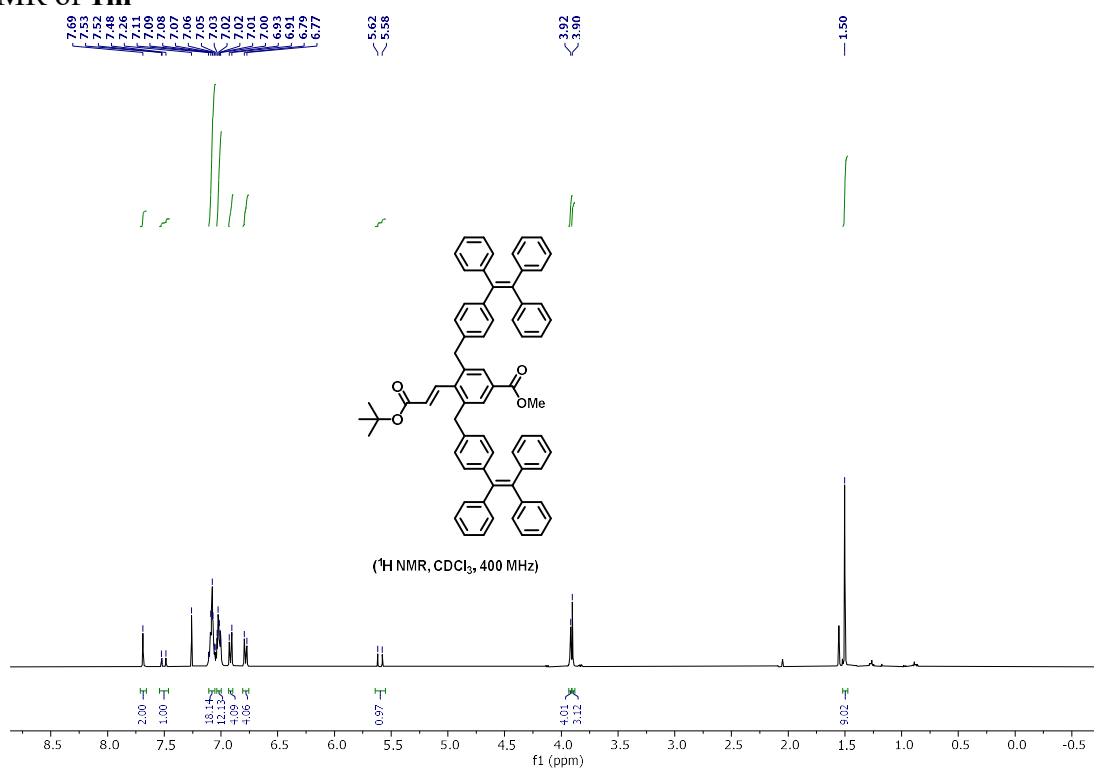
^1H NMR of **1l**



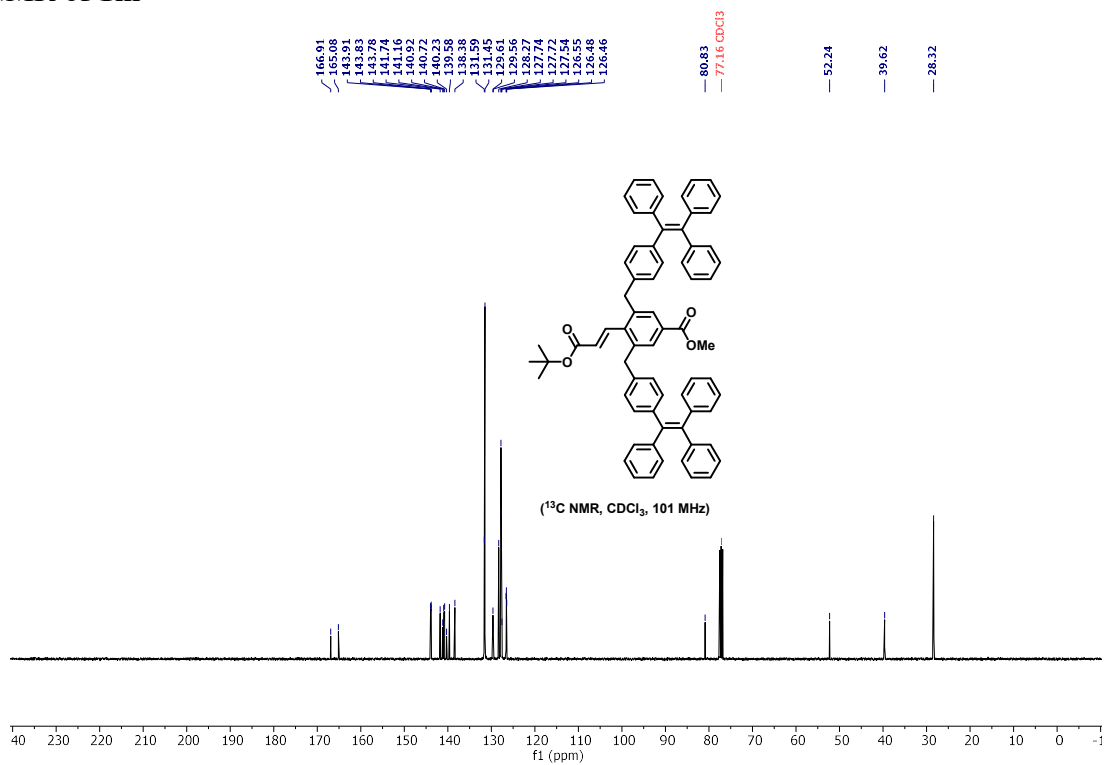
^{13}C NMR of **1l**



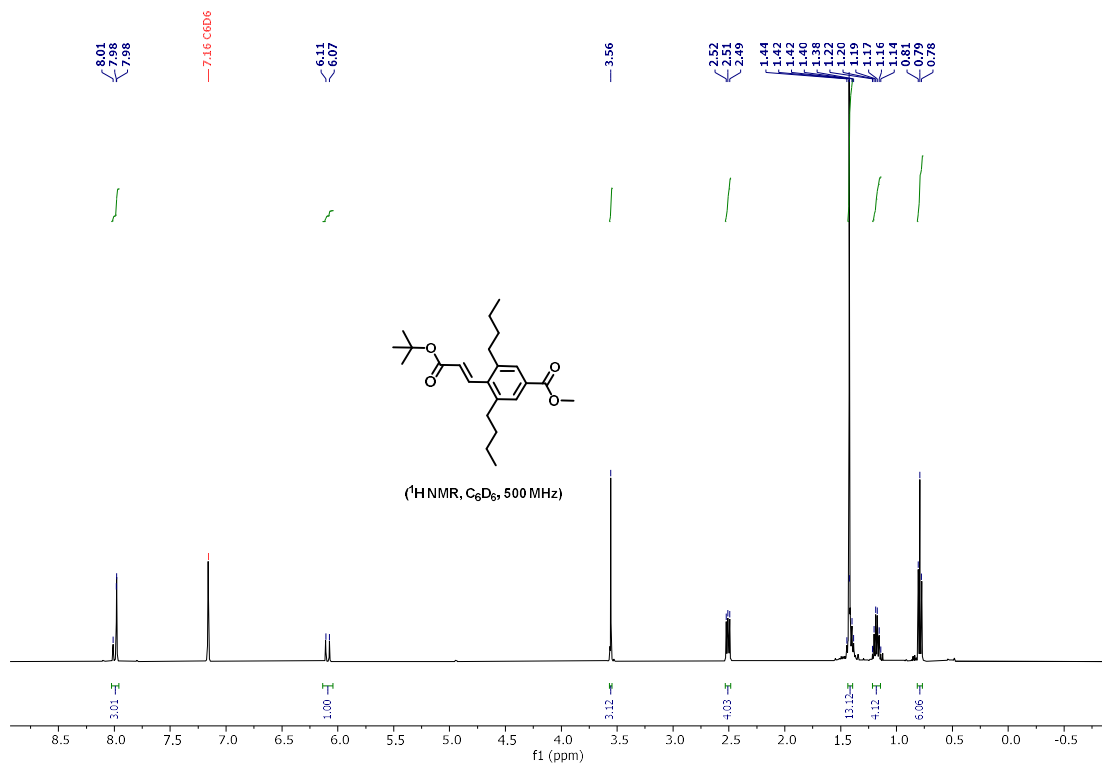
^1H NMR of **1m**



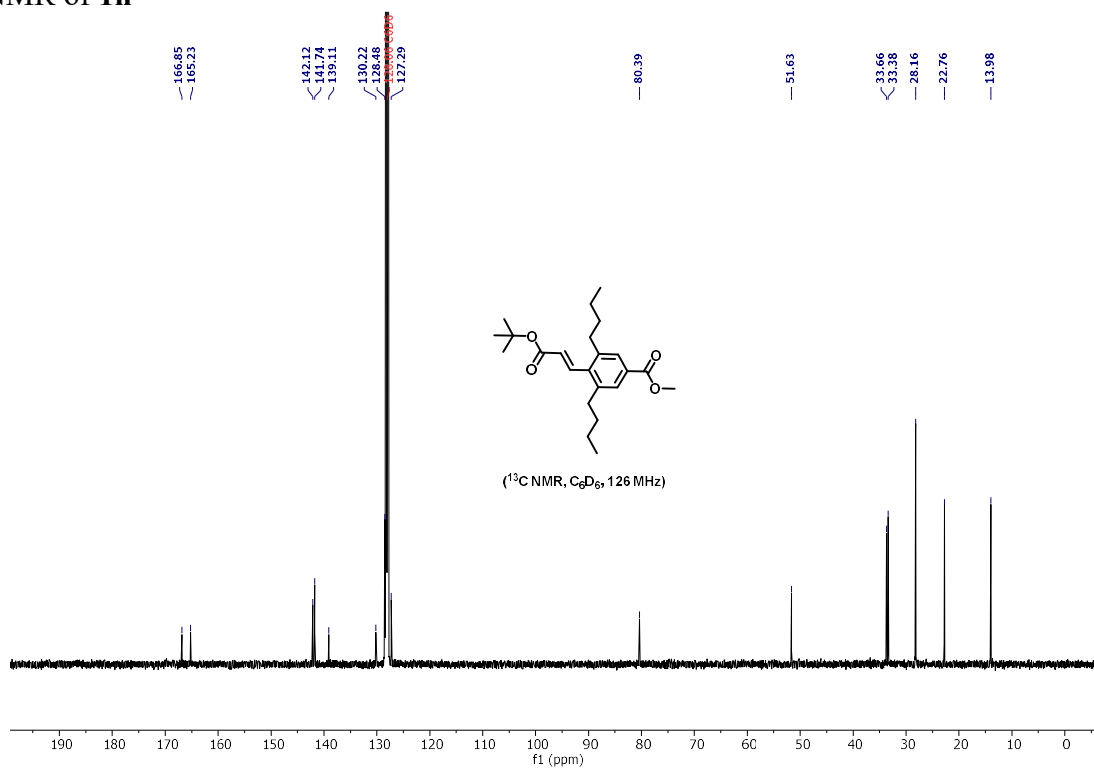
^{13}C NMR of **1m**



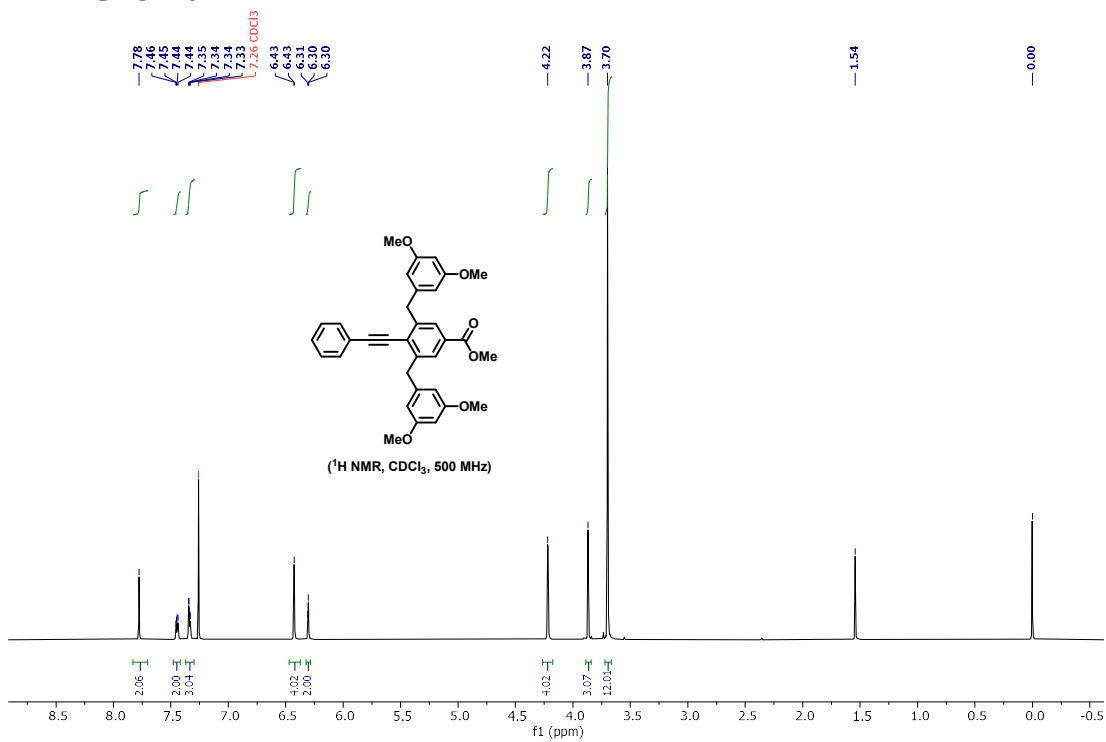
^1H NMR of **1n**



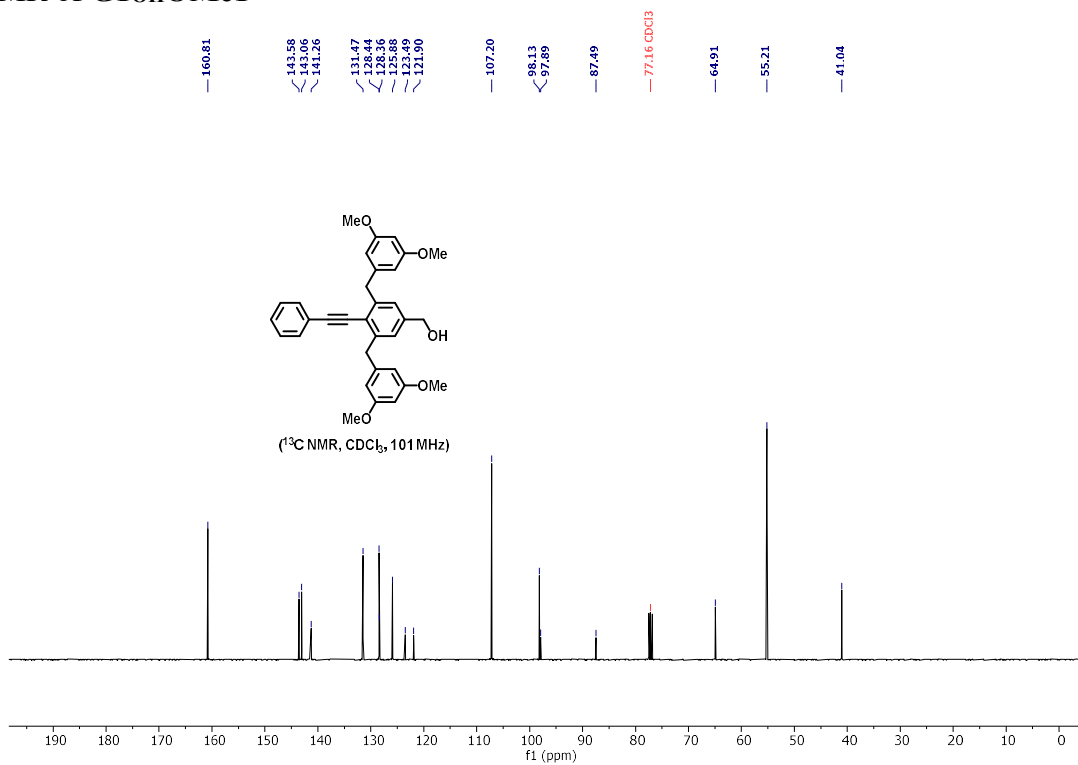
^{13}C NMR of **1n**



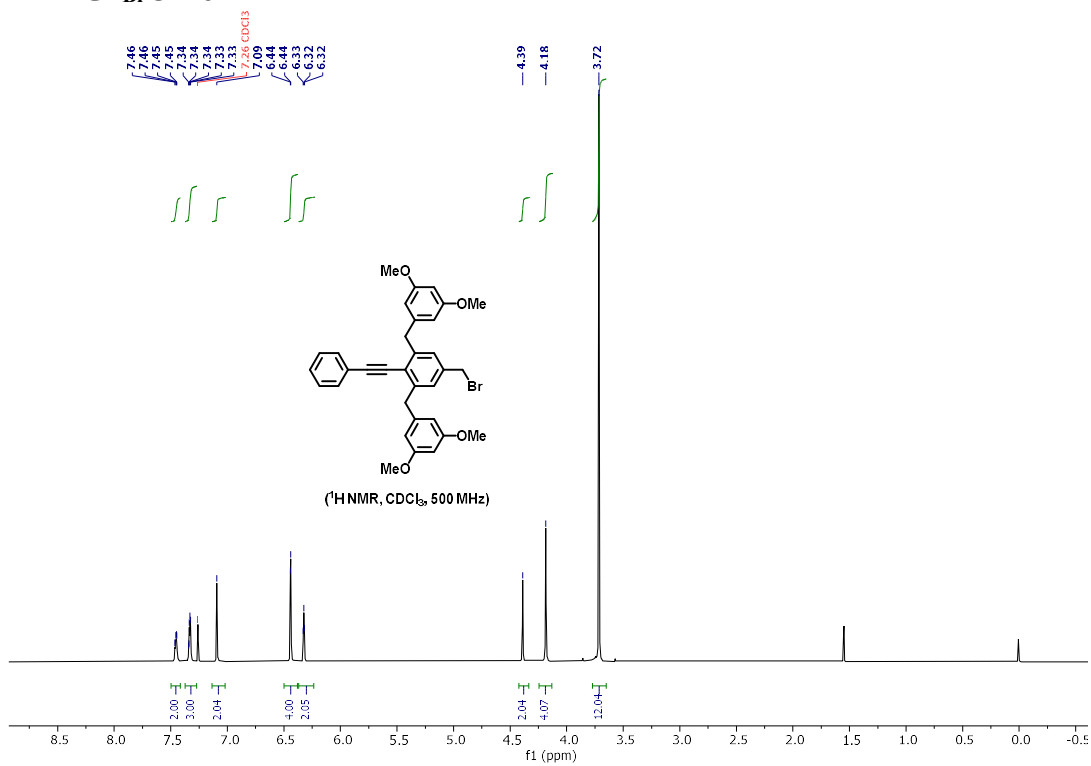
^1H NMR of **G1OMe1**



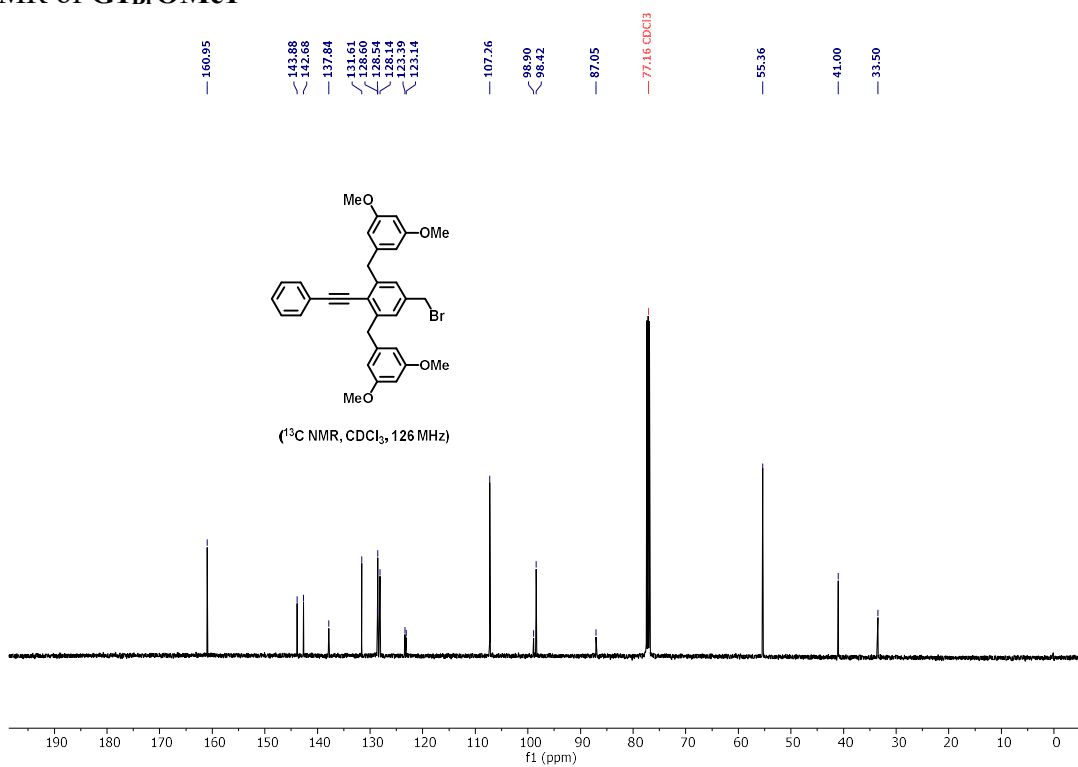
^{13}C NMR of **G1_{OH}OMe1**



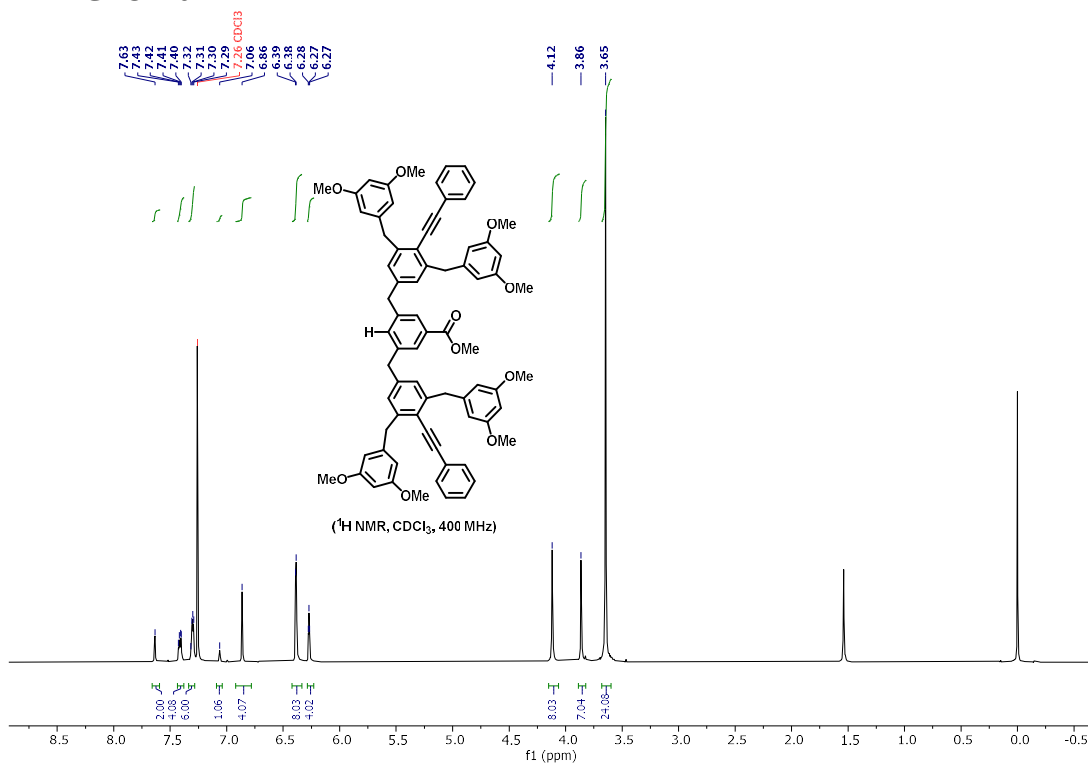
^1H NMR of **G1_{Br}OMe1**



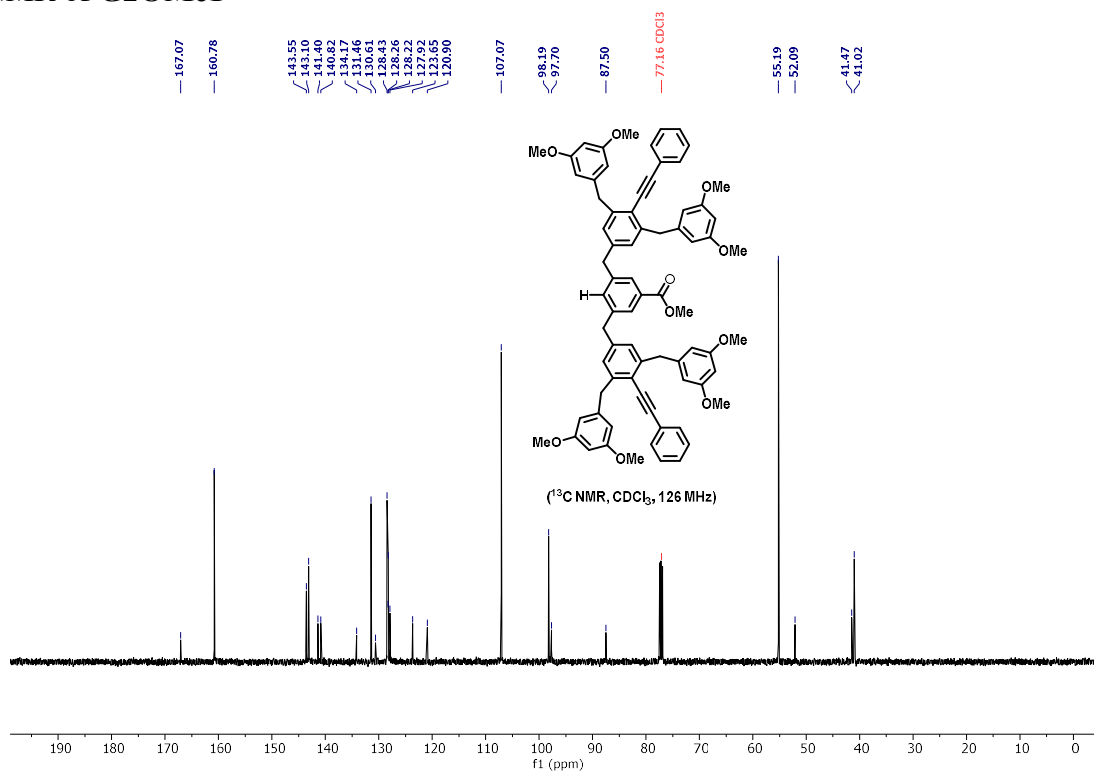
^{13}C NMR of G1BrOMe1



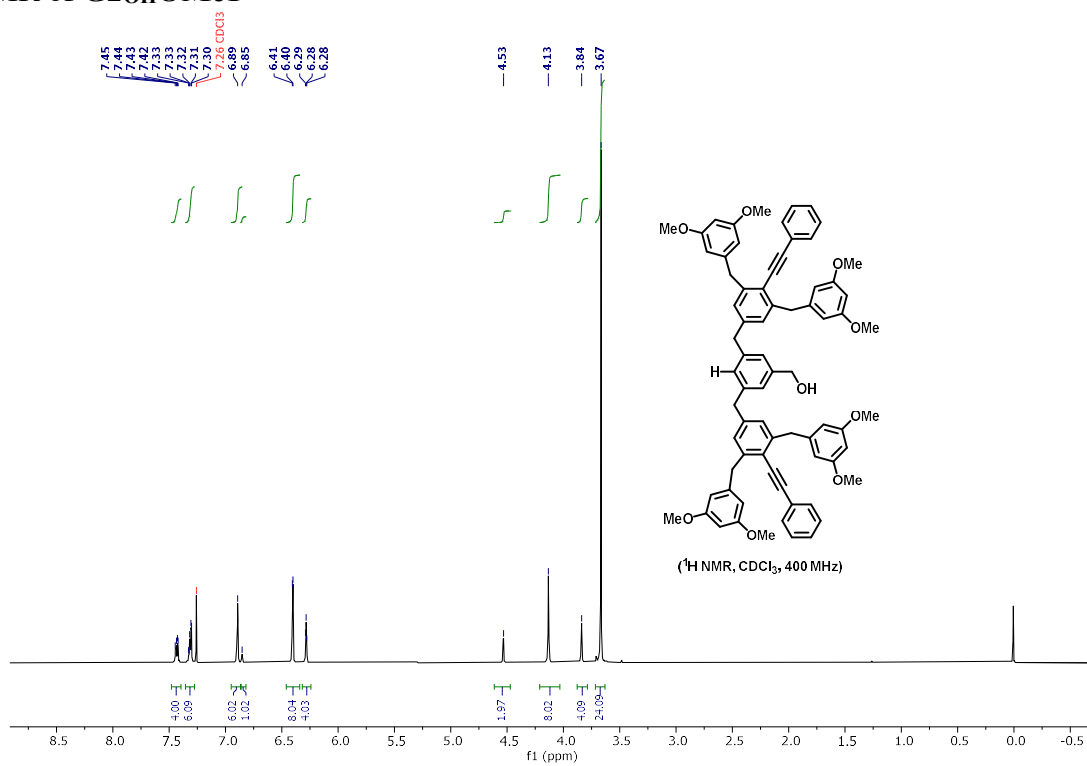
^1H NMR of G2OMe1



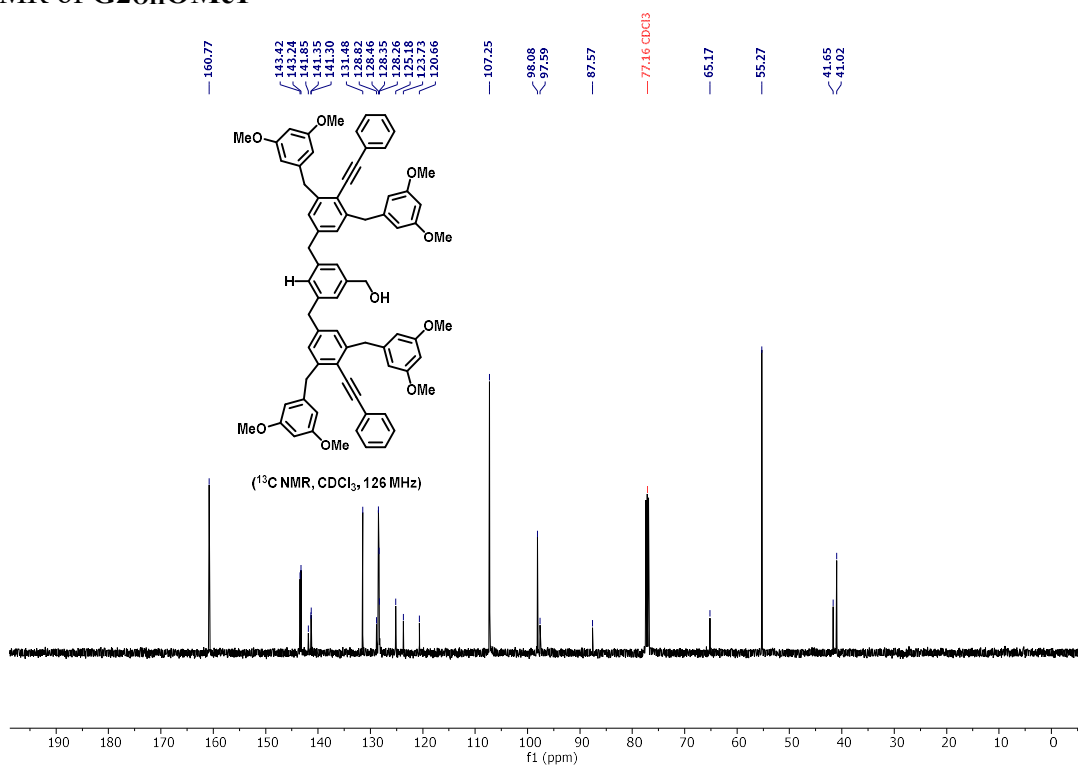
¹³C NMR of G2OMe1



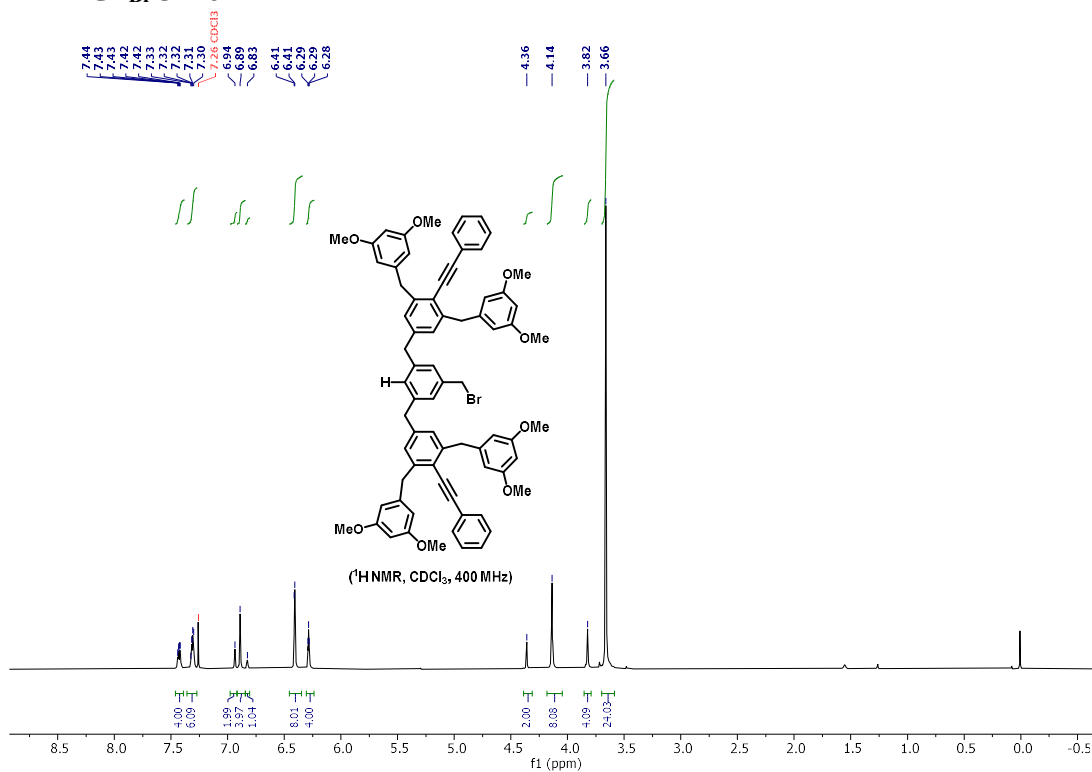
¹H NMR of G2OHMe1



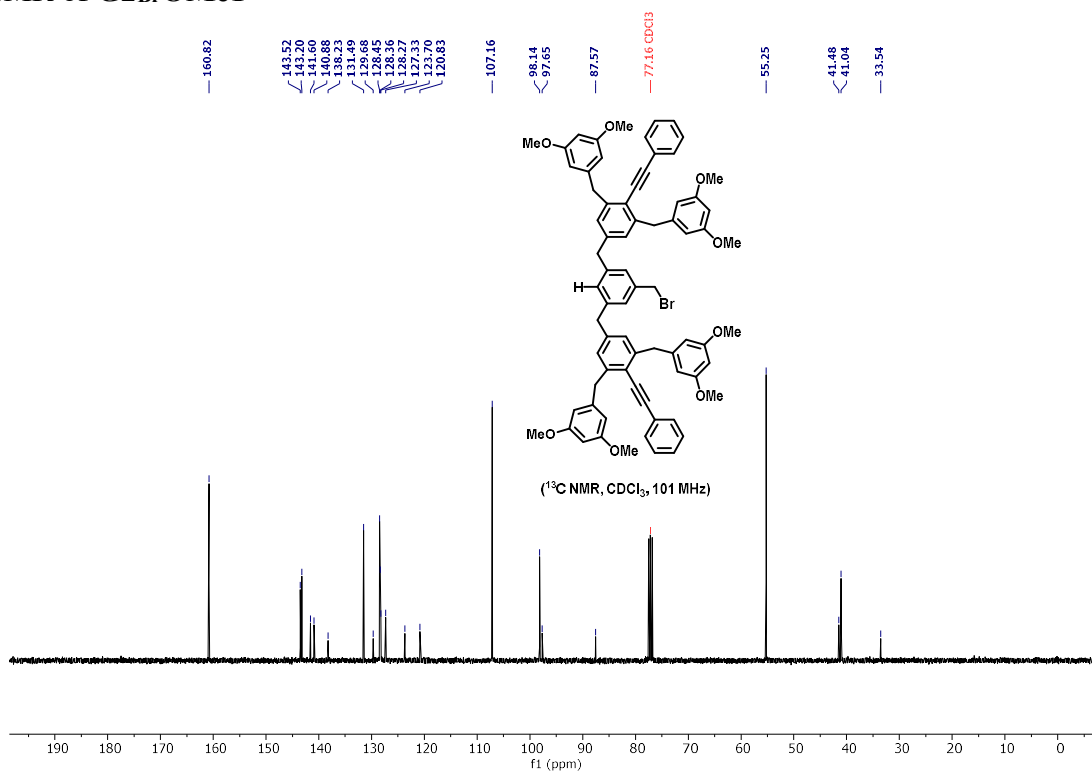
^{13}C NMR of **G2_{OH}OMe1**



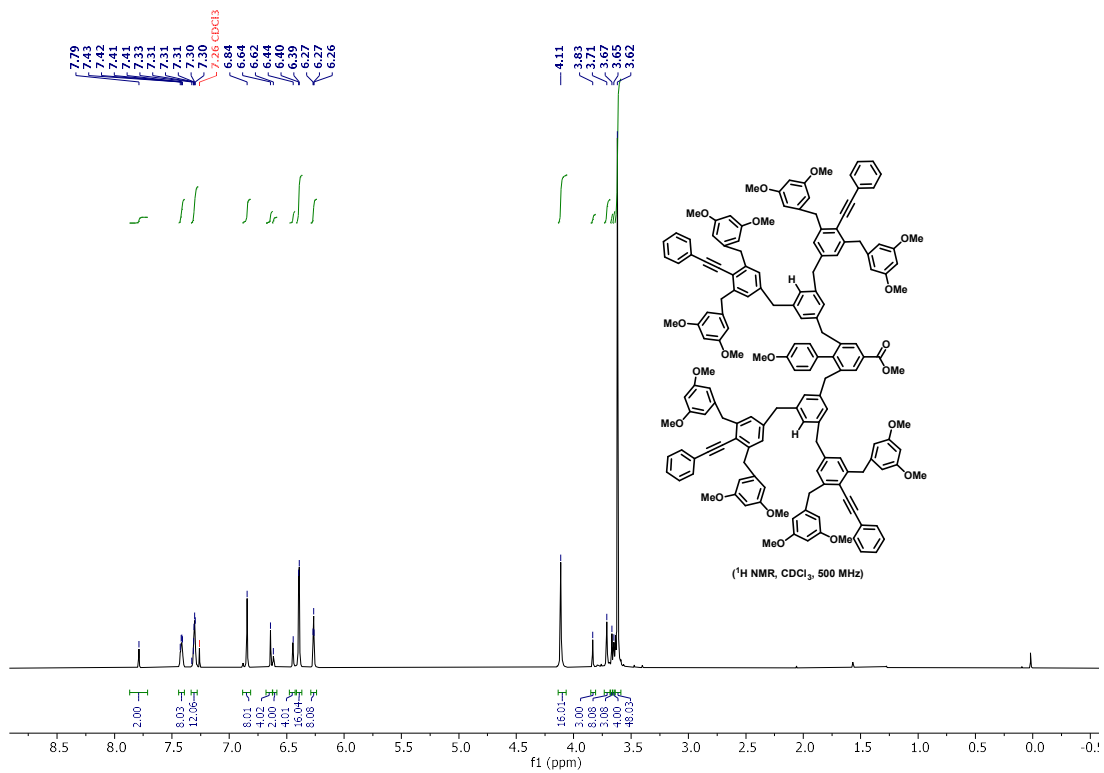
^1H NMR of **G2_{Br}OMe1**



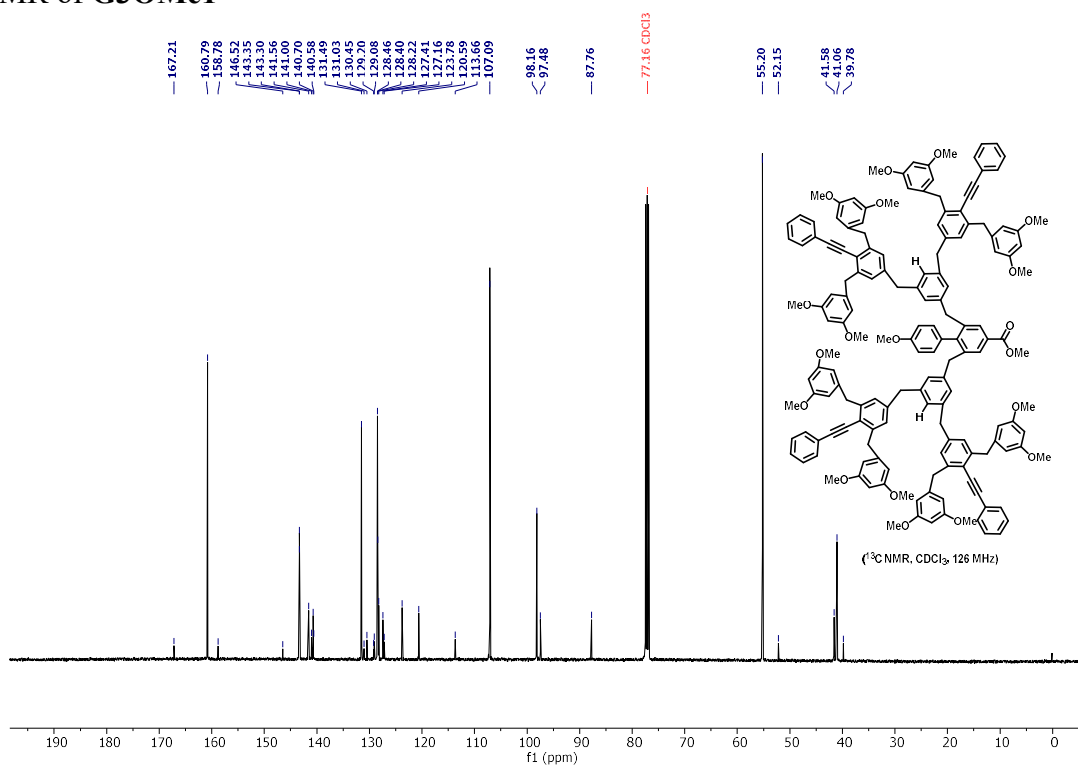
¹³C NMR of G2BrOMe1



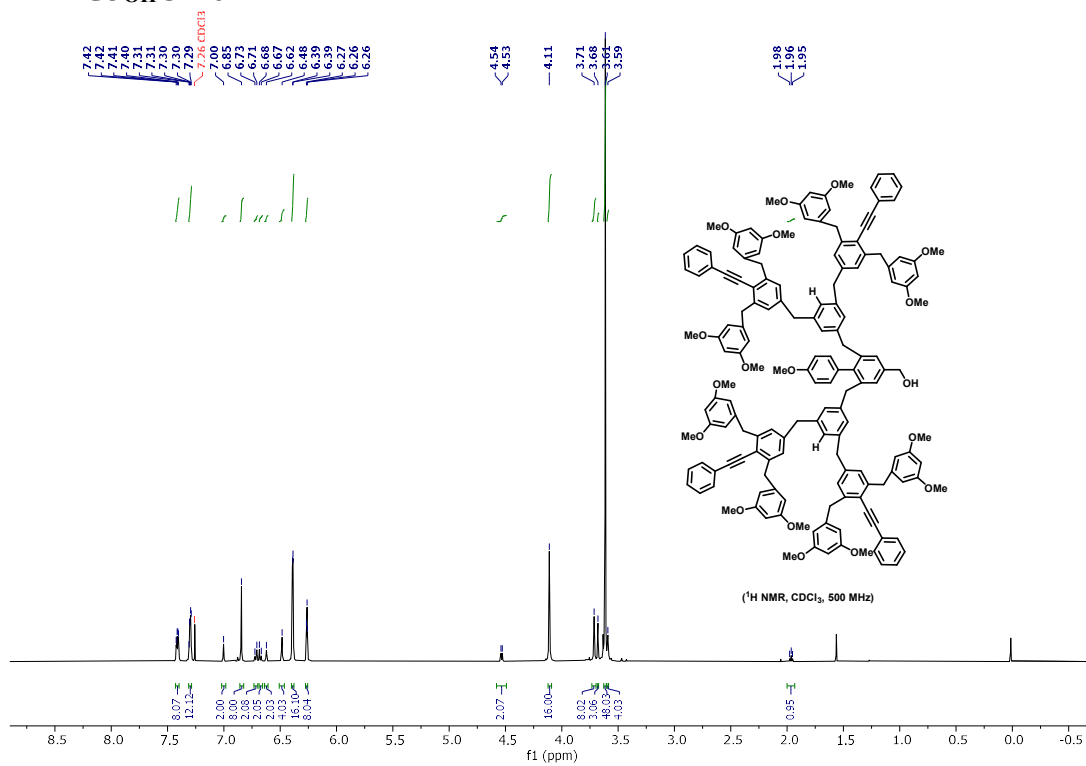
¹H NMR of G3OMe1



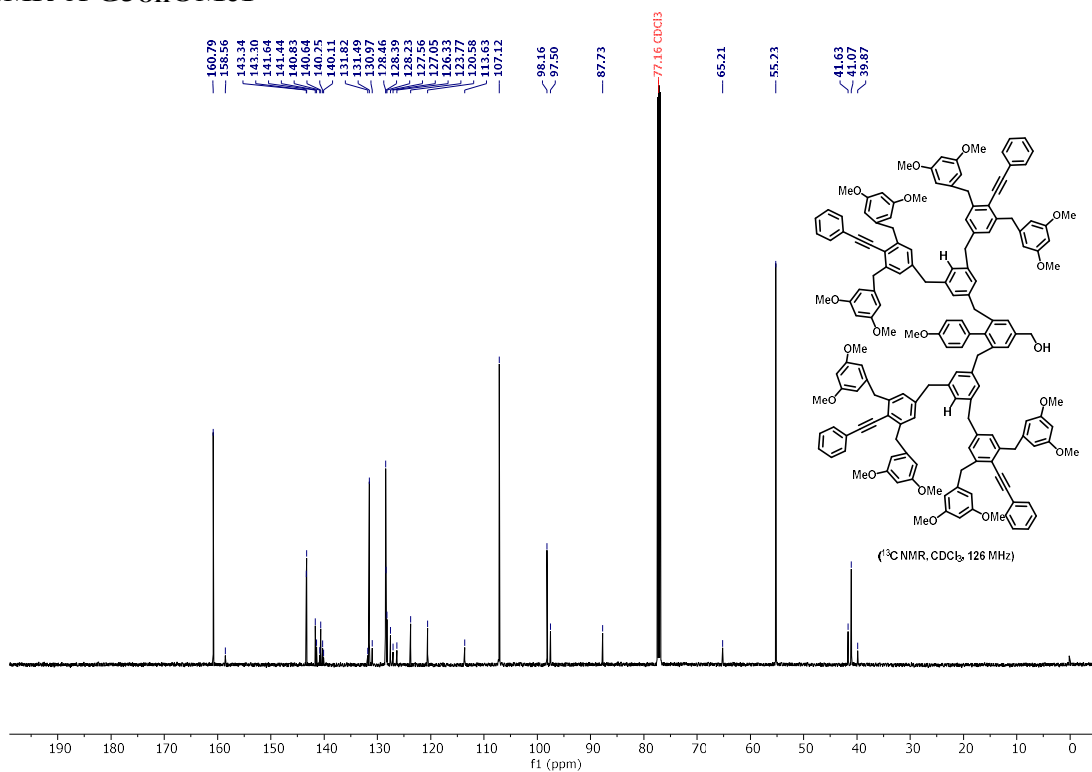
¹³C NMR of G3OMe1



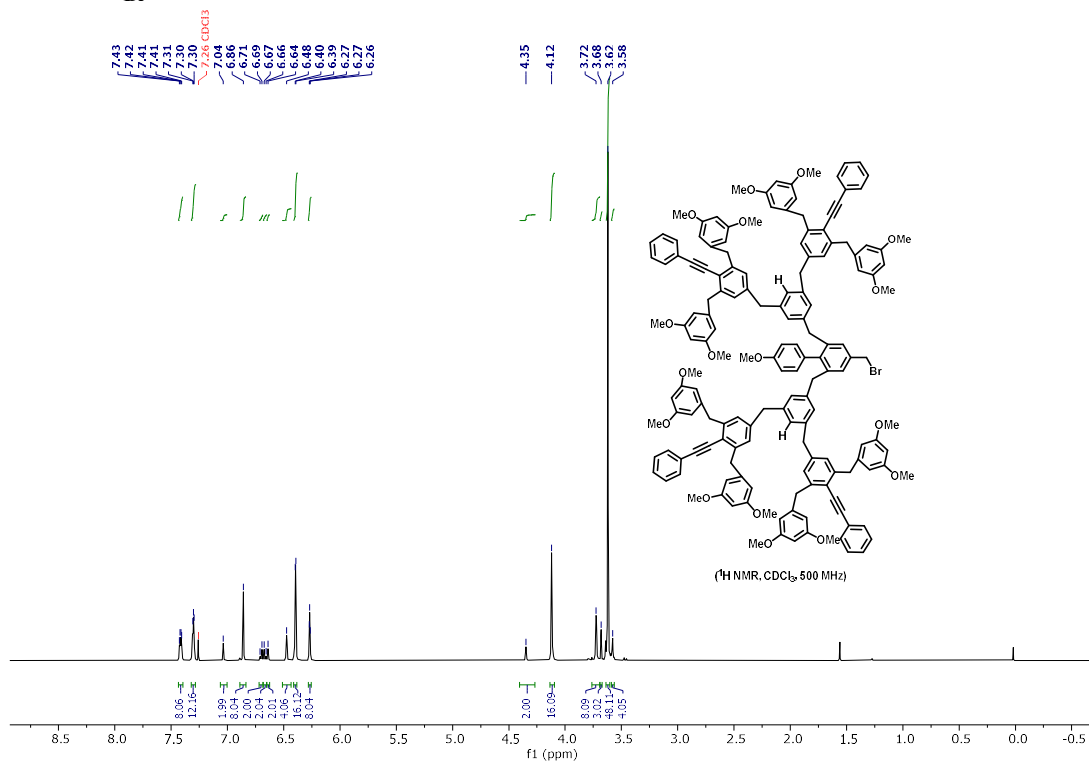
¹H NMR of G3OHOMe1



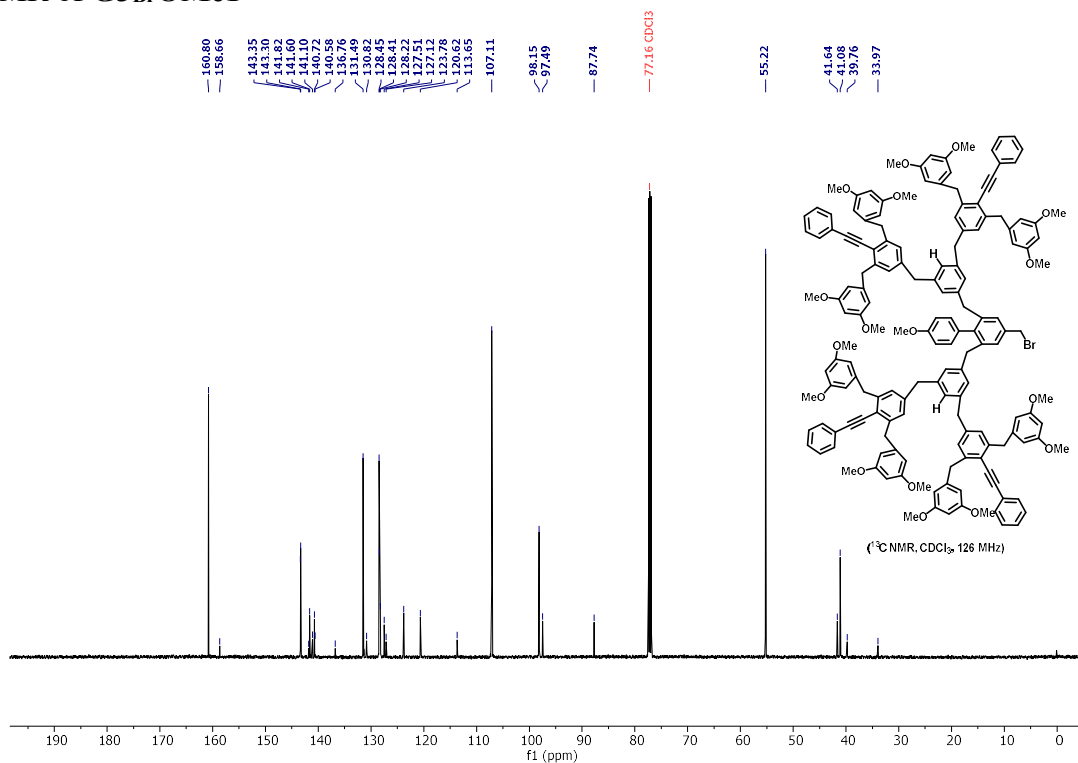
¹³C NMR of G3_{OH}OMe1



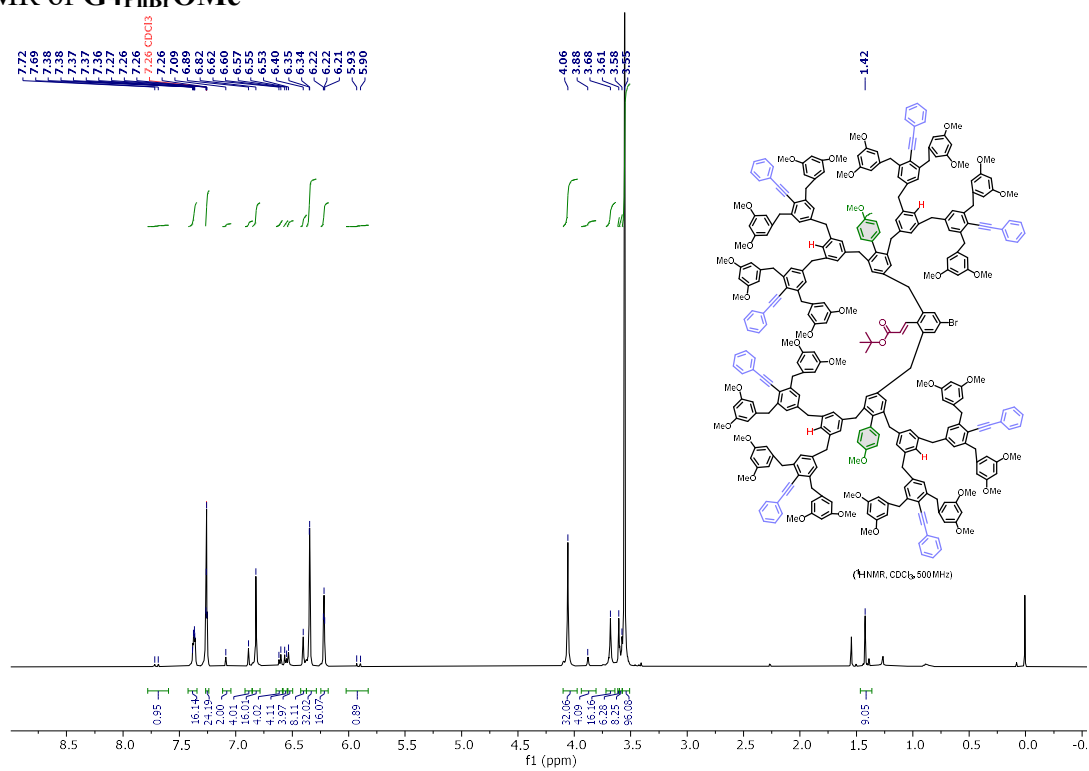
¹H NMR of G3_{Br}OMe1



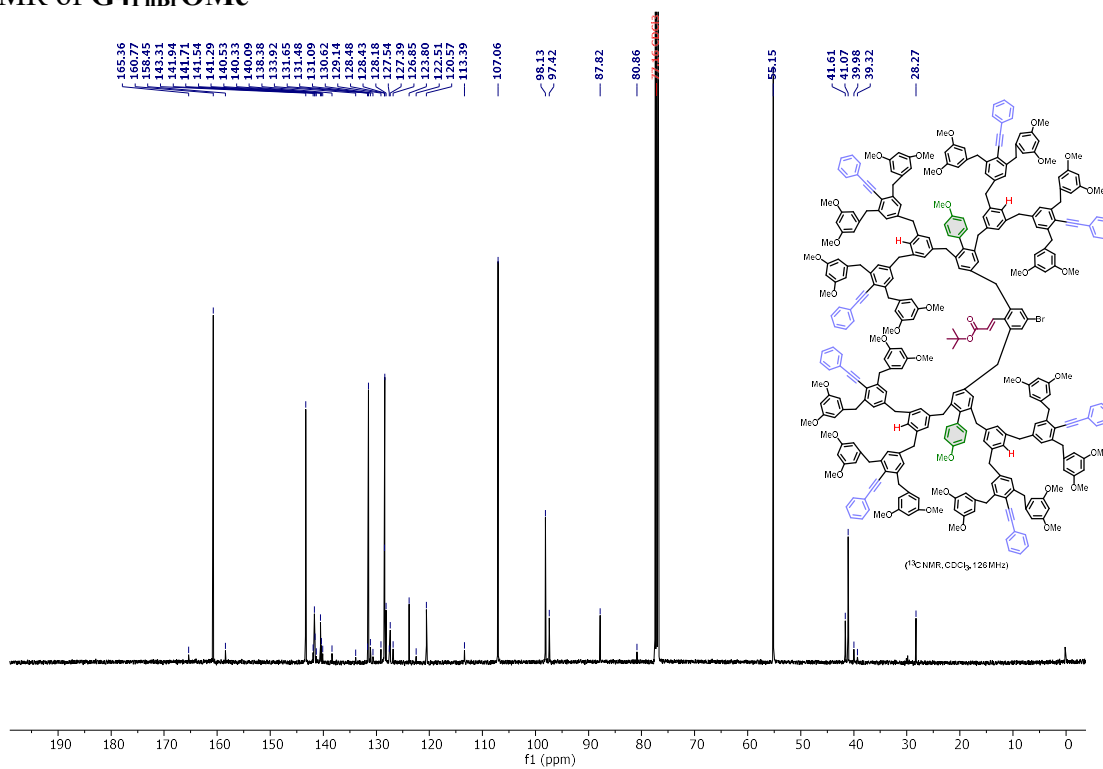
^{13}C NMR of G3BrOMe1



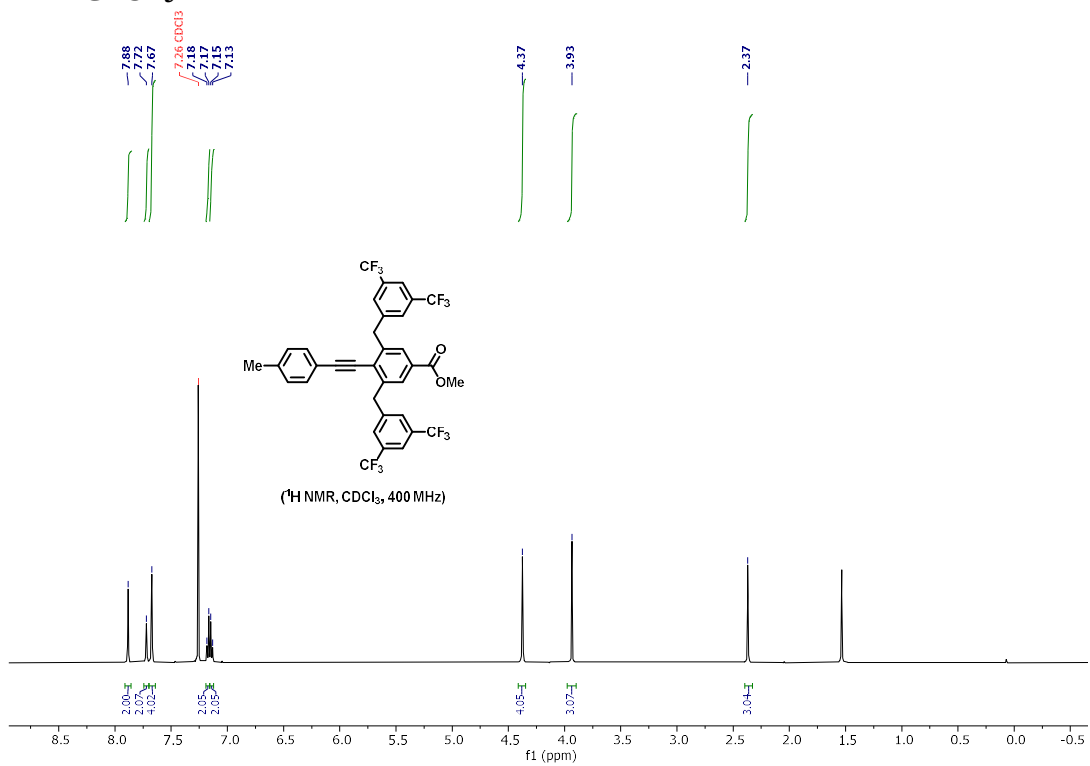
^1H NMR of G4_{Ph}BrOMe



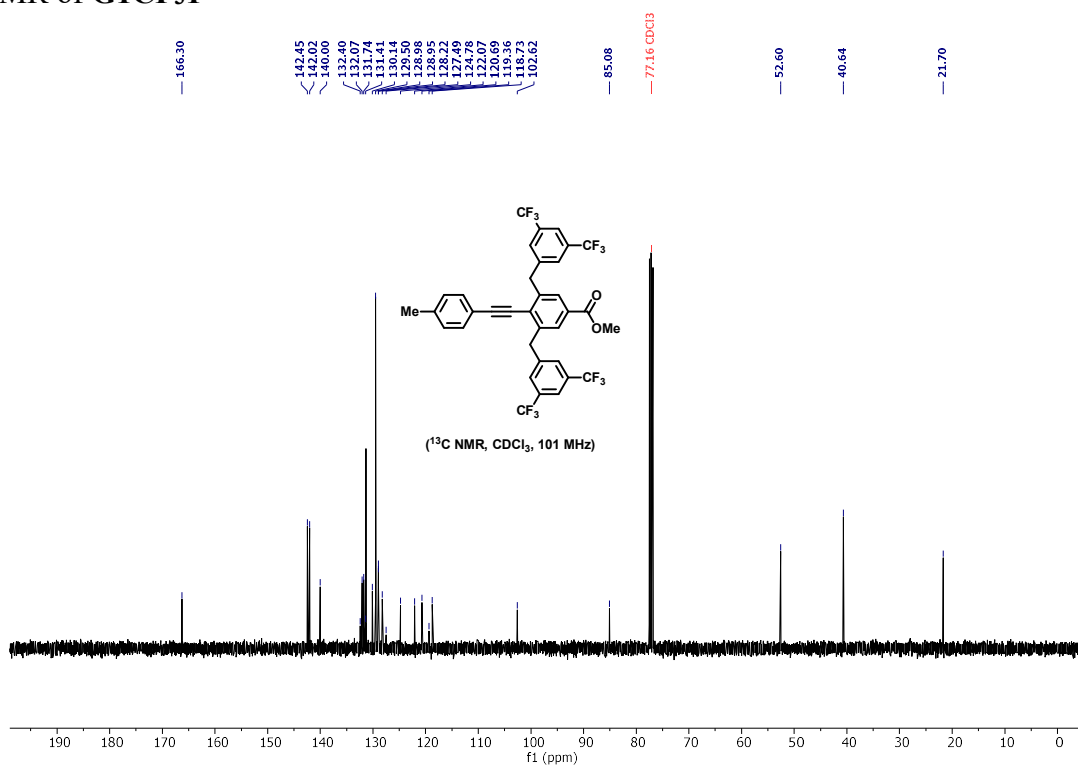
¹³C NMR of G4PhBrOMe



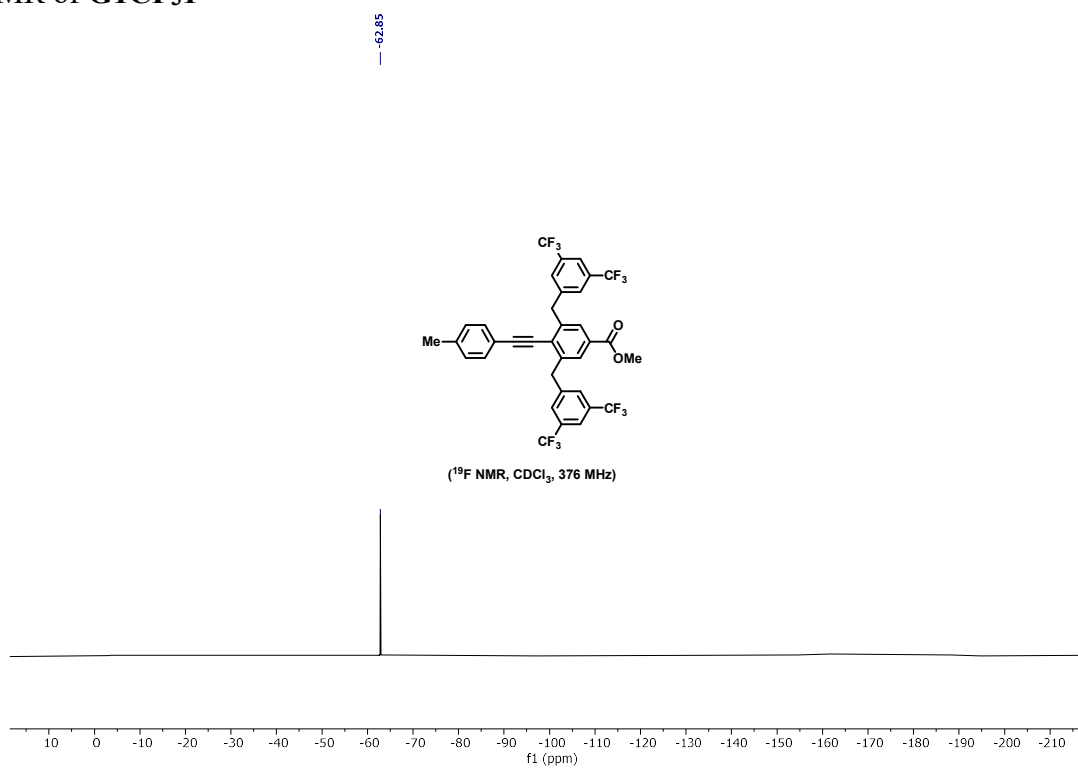
¹H NMR of G1CF₃1



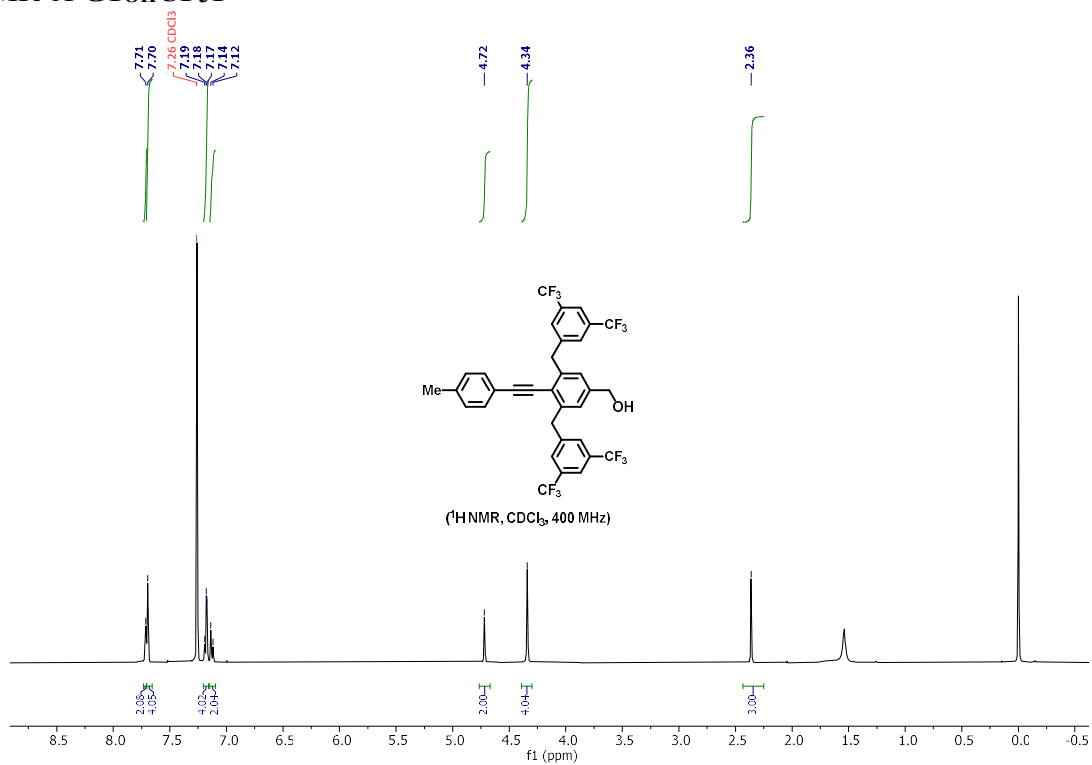
^{13}C NMR of G1CF₃1



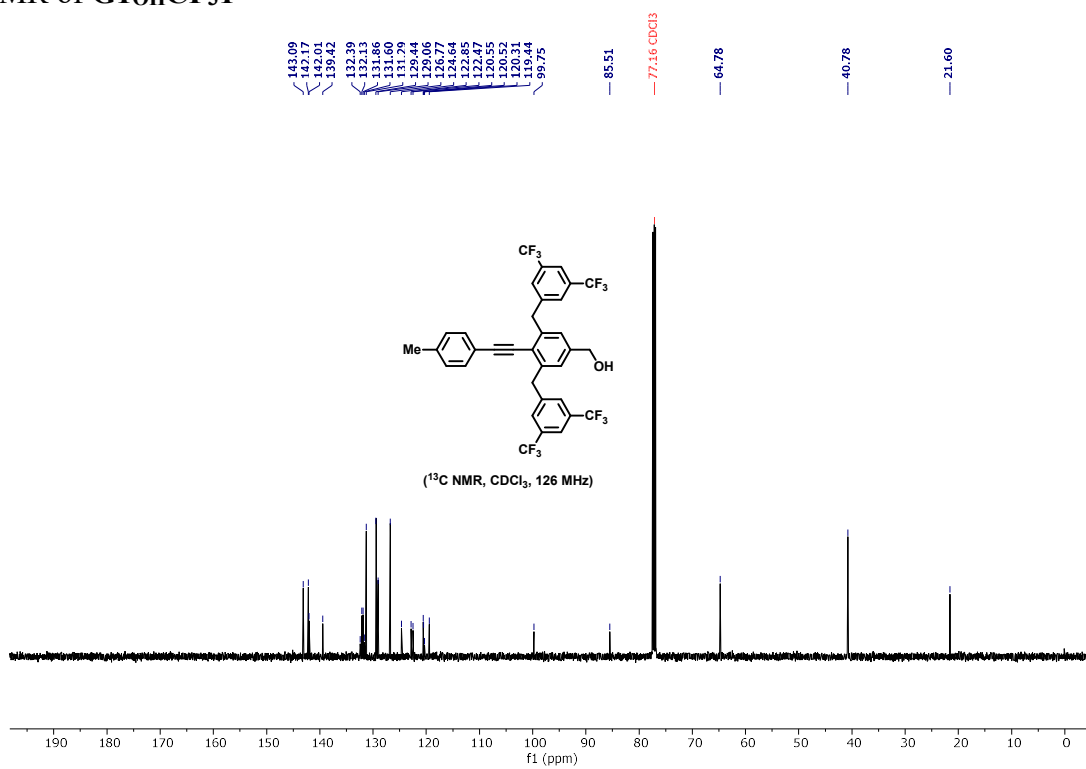
^{19}F NMR of G1CF₃1



¹H NMR of G1_{OH}CF₃1

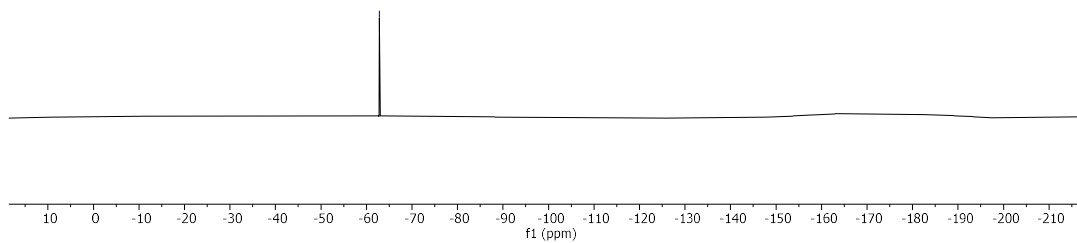
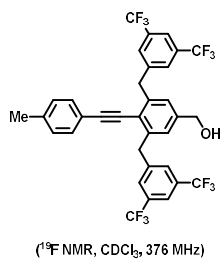


¹³C NMR of G1_{OH}CF₃1

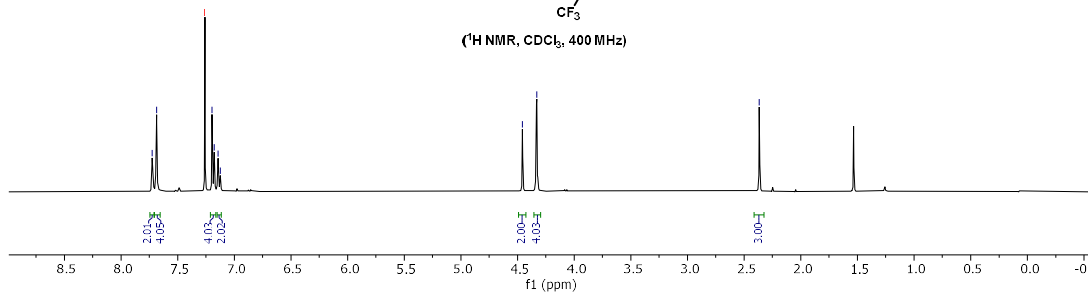
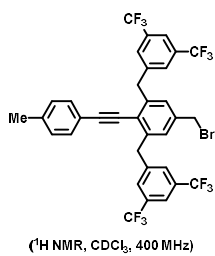
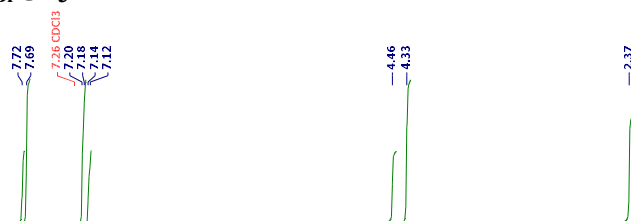


^{19}F NMR of **G1_{OH}CF₃1**

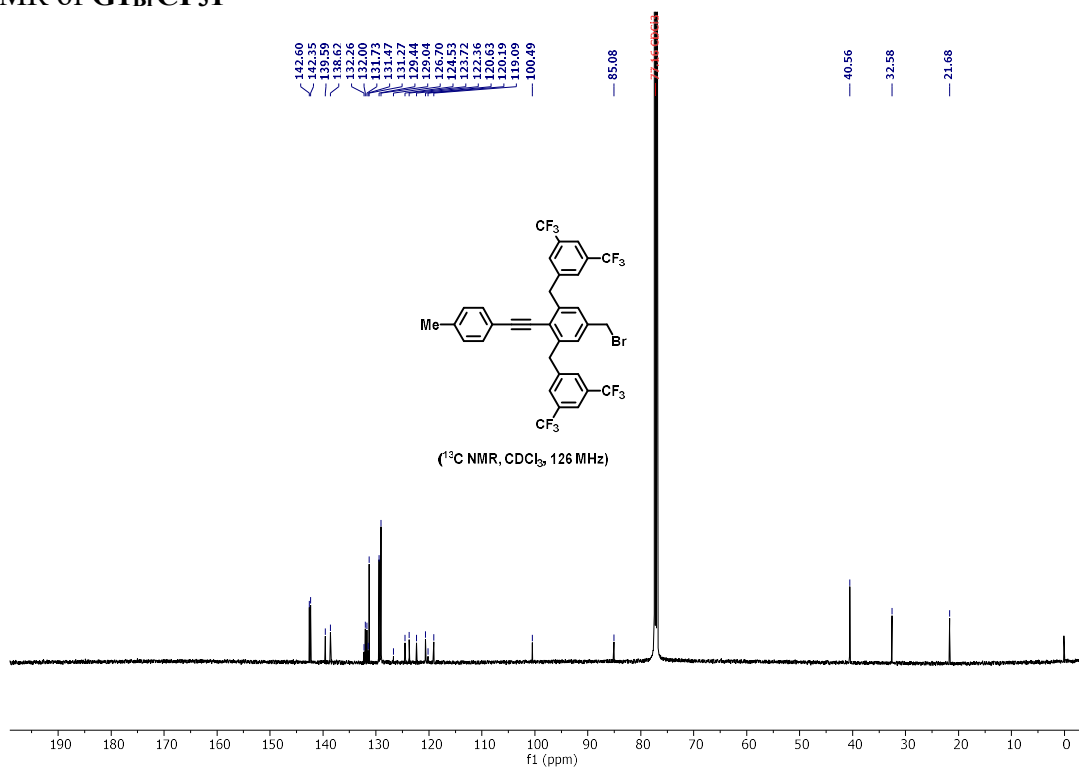
-62.82



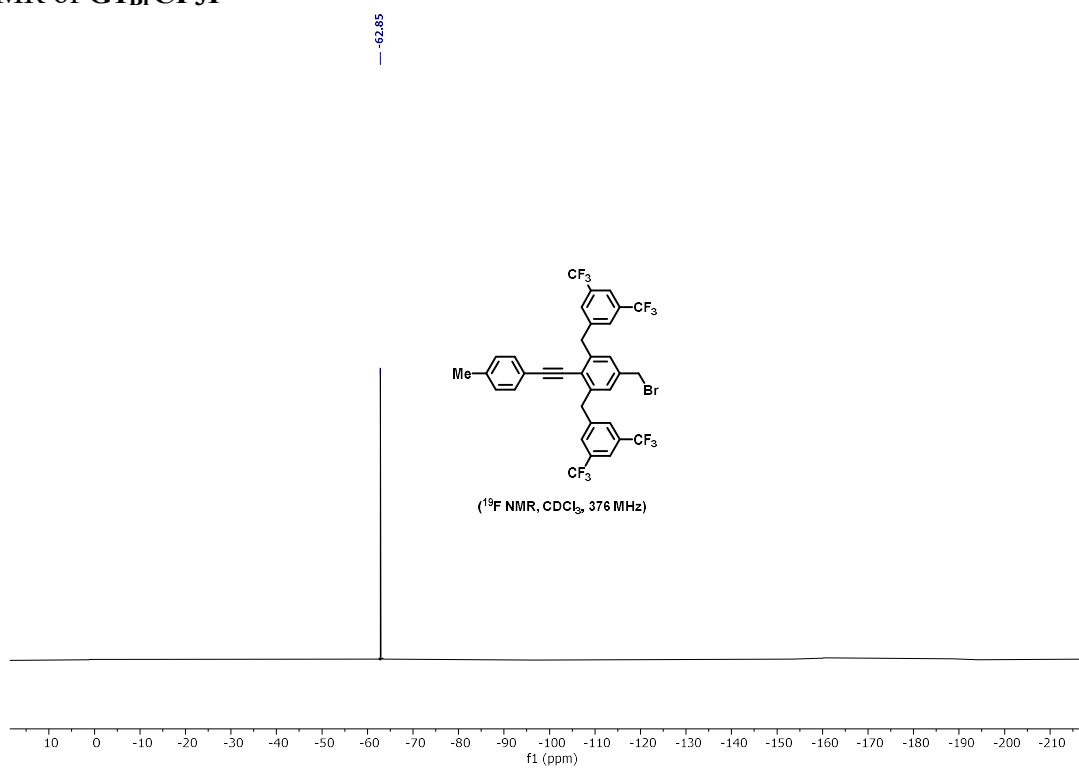
^1H NMR of **G1_{Br}CF₃1**



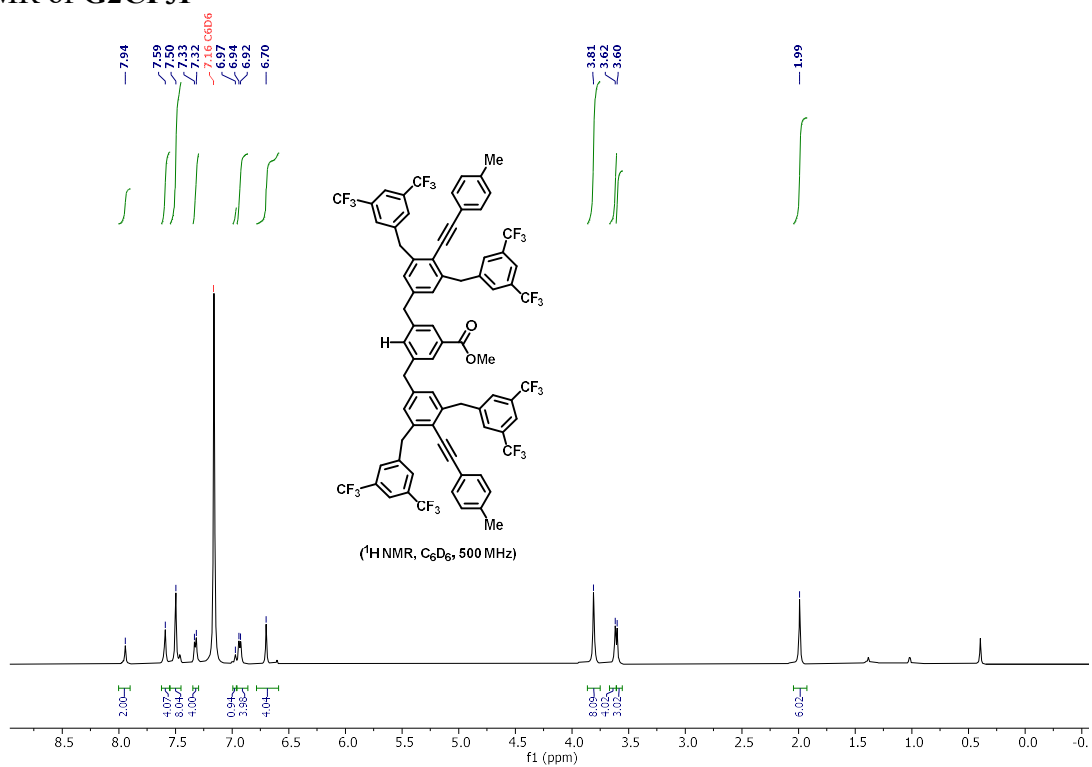
^{13}C NMR of $\text{G1BrCF}_3\mathbf{1}$



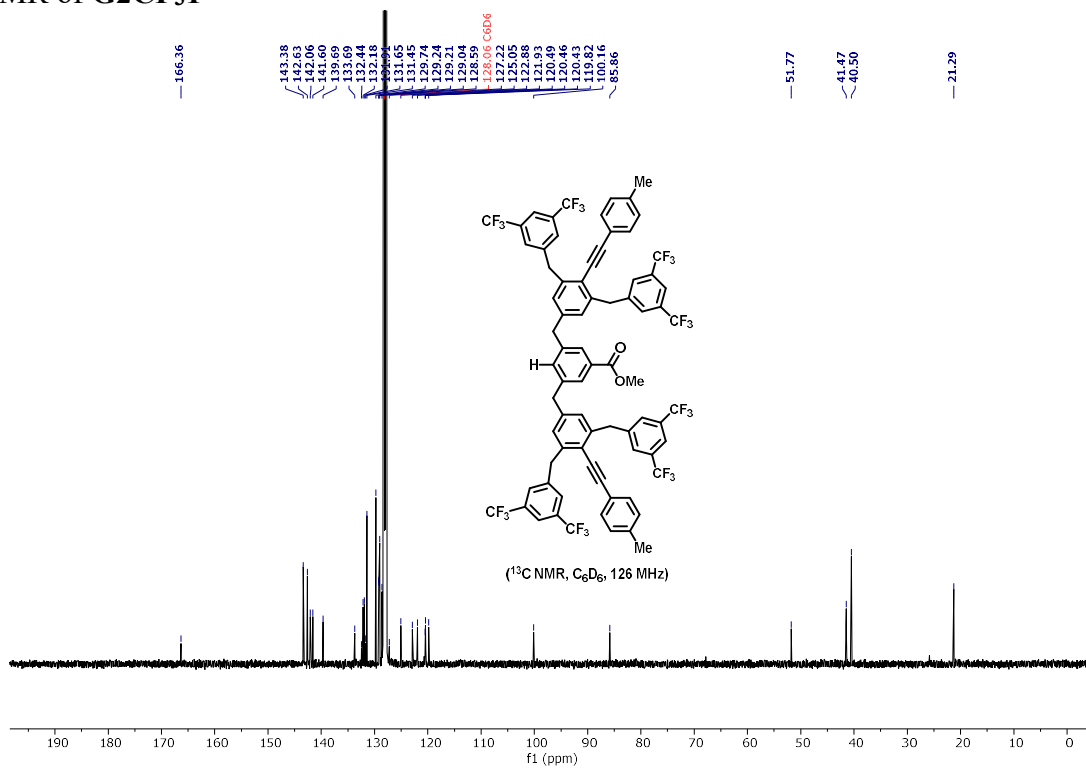
^{19}F NMR of $\text{G1BrCF}_3\mathbf{1}$



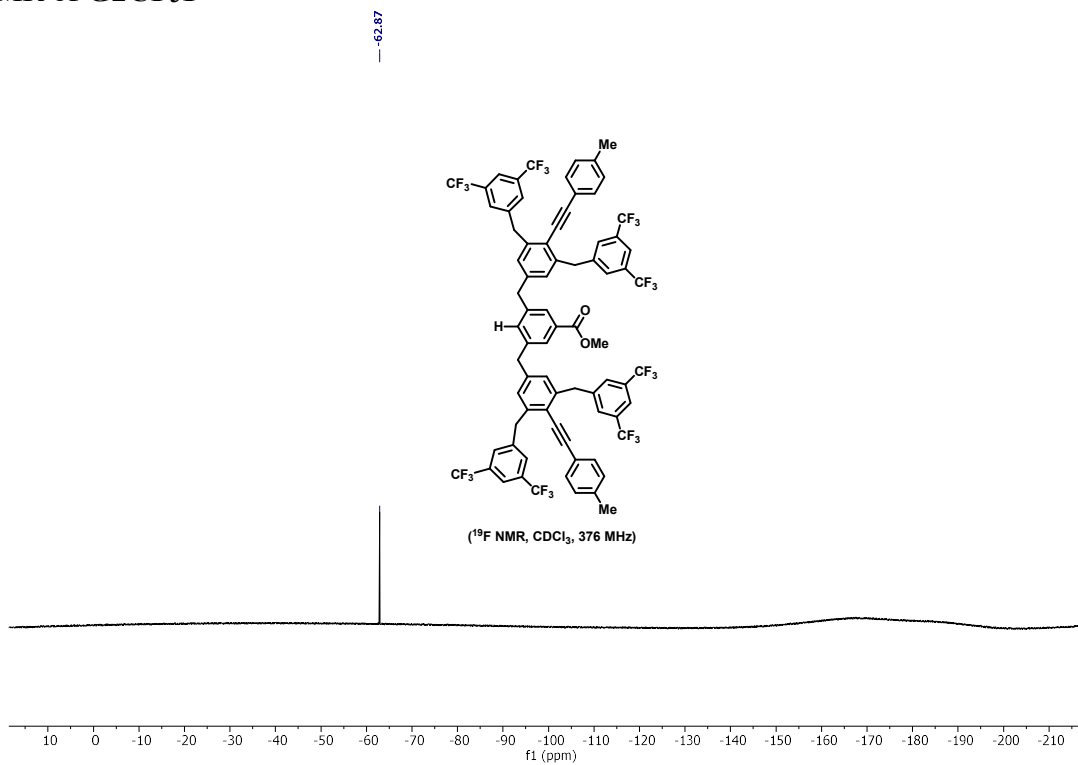
¹H NMR of G2CF₃1



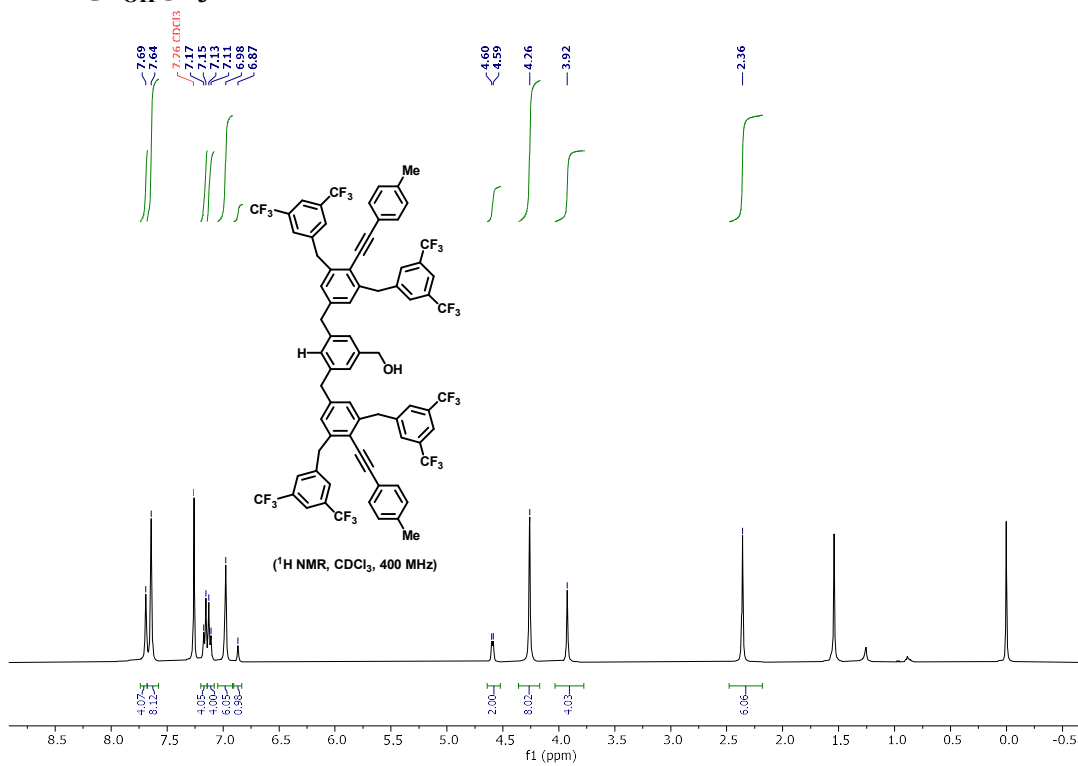
¹³C NMR of G2CF₃1



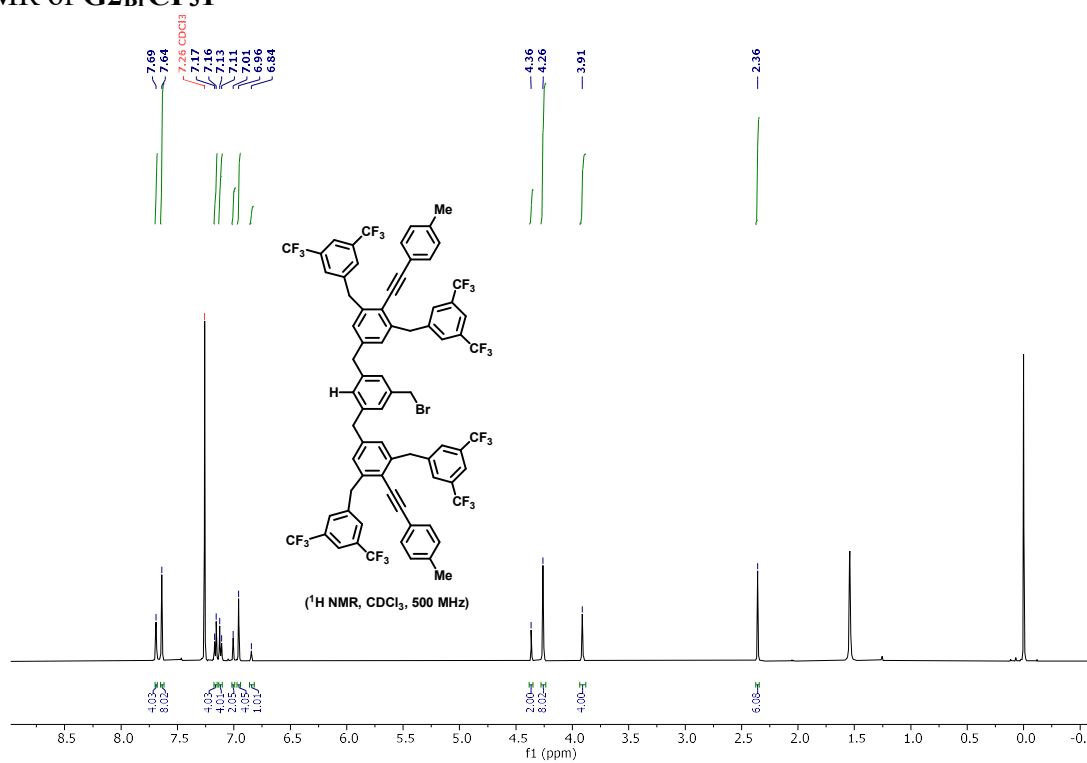
^{19}F NMR of $\text{G2CF}_3\text{1}$



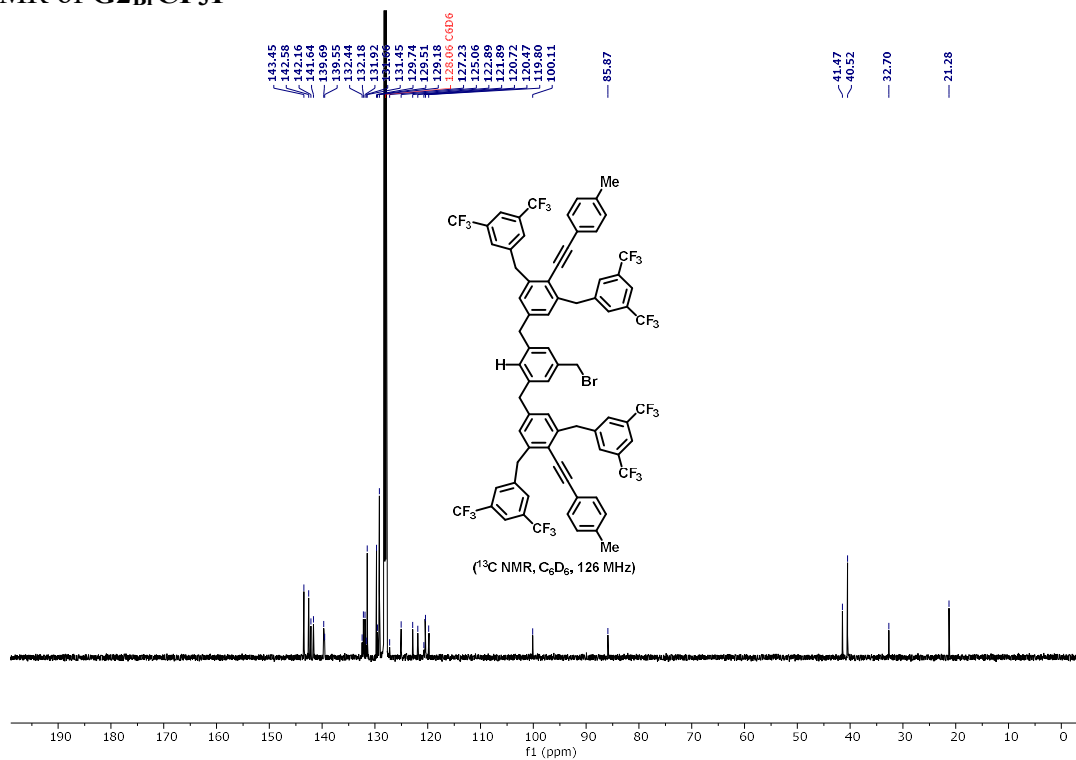
^1H NMR of $\text{G2OHCF}_3\text{1}$



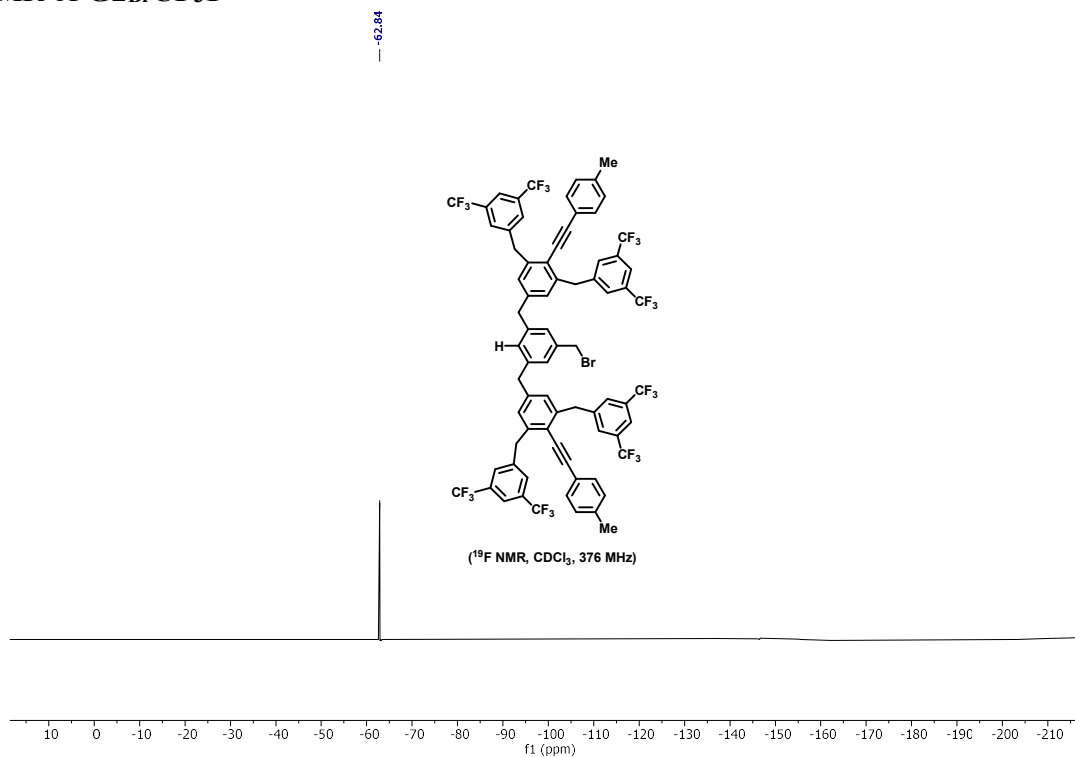
^1H NMR of $\text{G2BrCF}_3\text{1}$



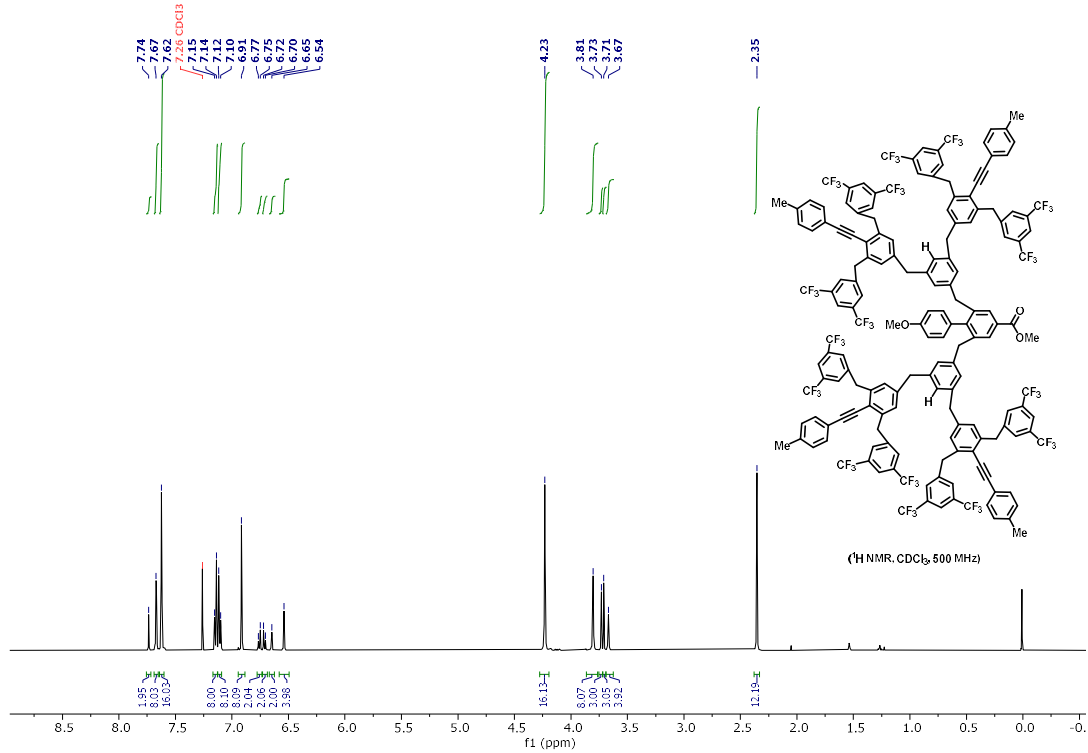
^{13}C NMR of $\text{G2BrCF}_3\text{1}$



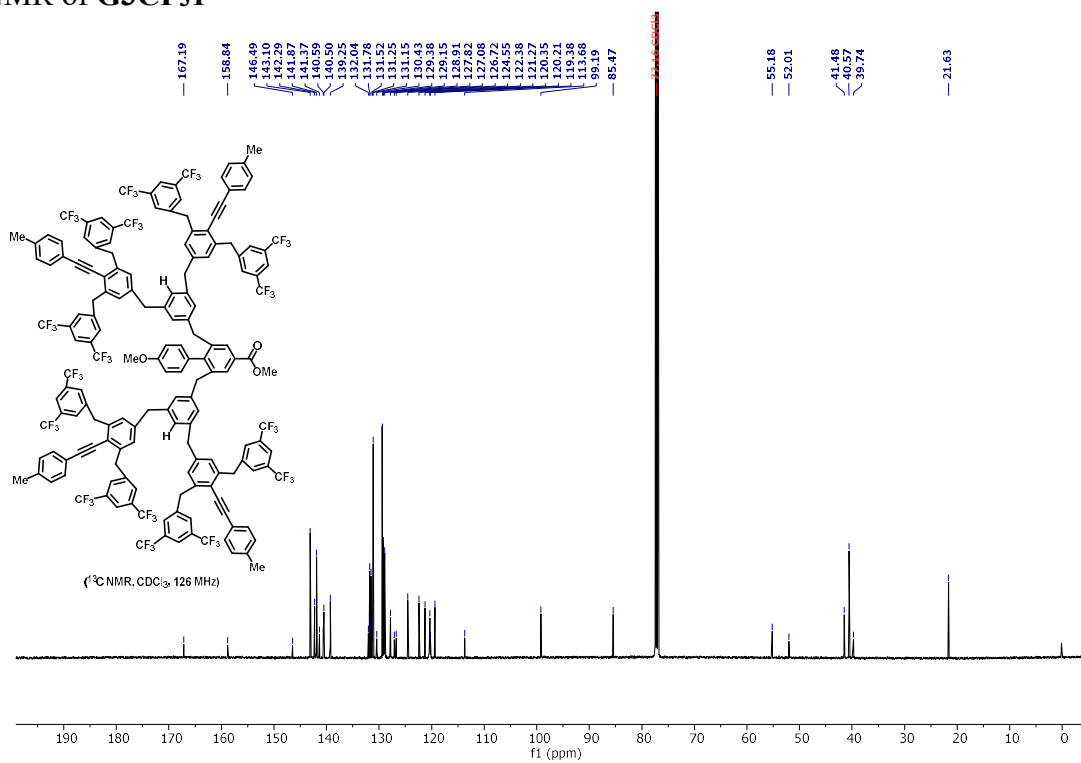
^{19}F NMR of $\text{G2BrCF}_3\mathbf{1}$



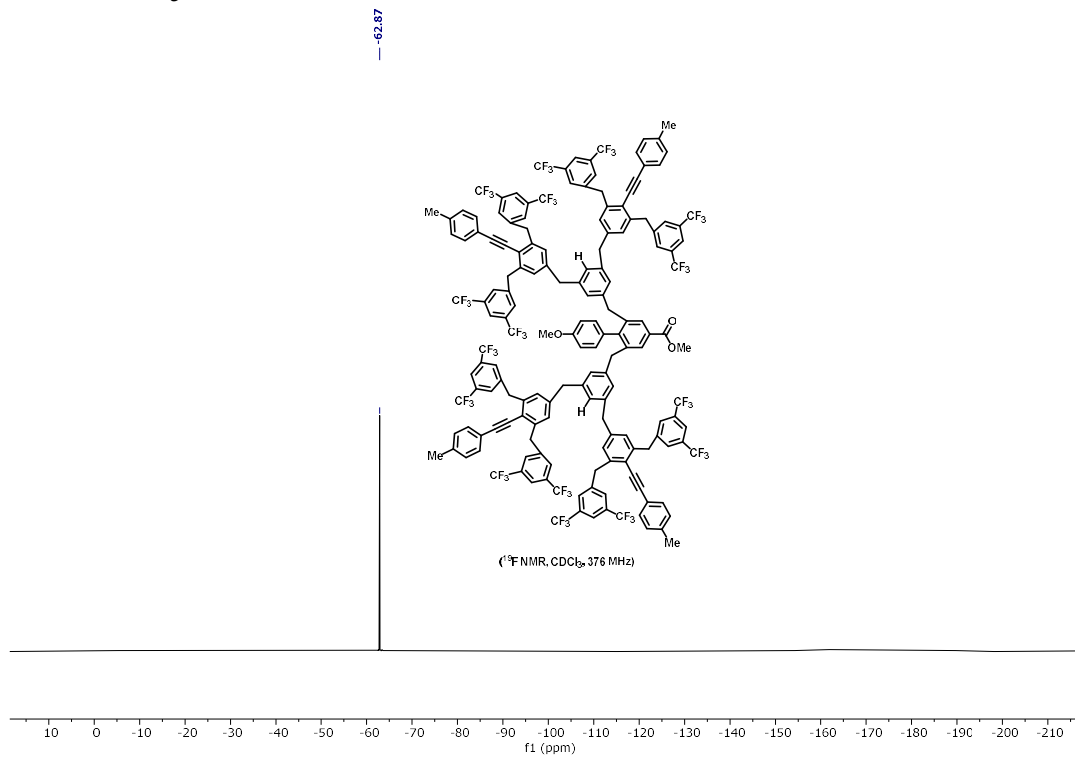
^1H NMR of $\text{G3CF}_3\mathbf{1}$



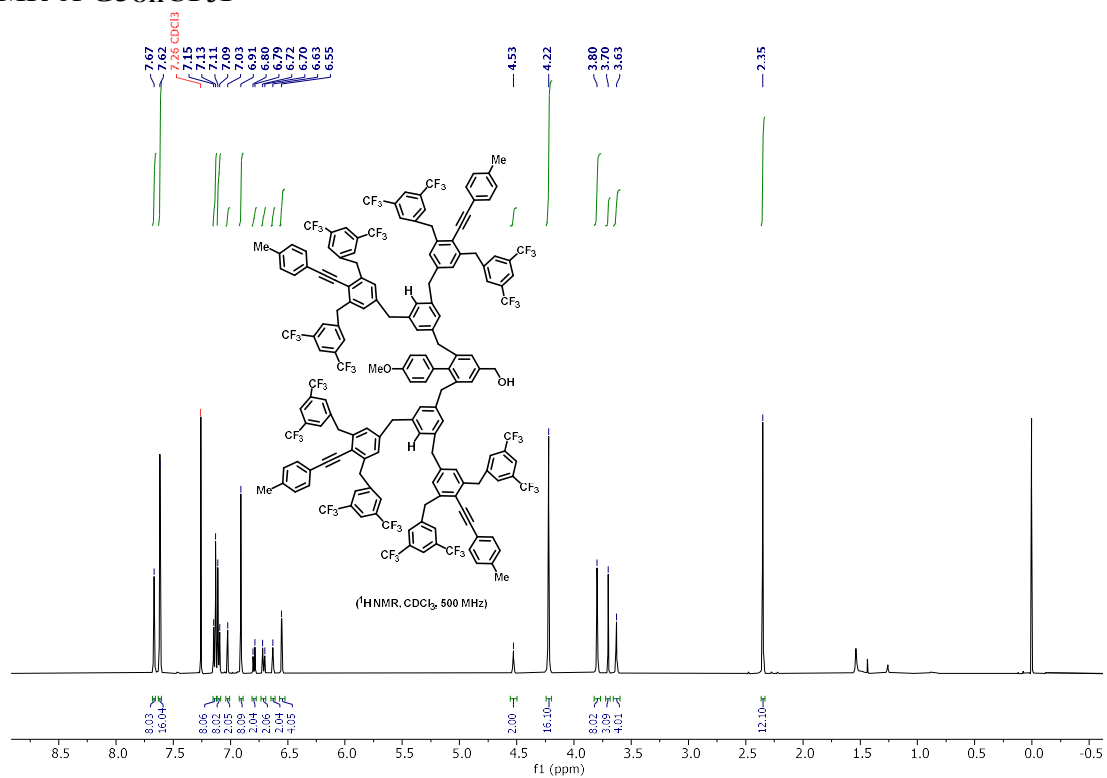
¹³C NMR of G3CF₃1



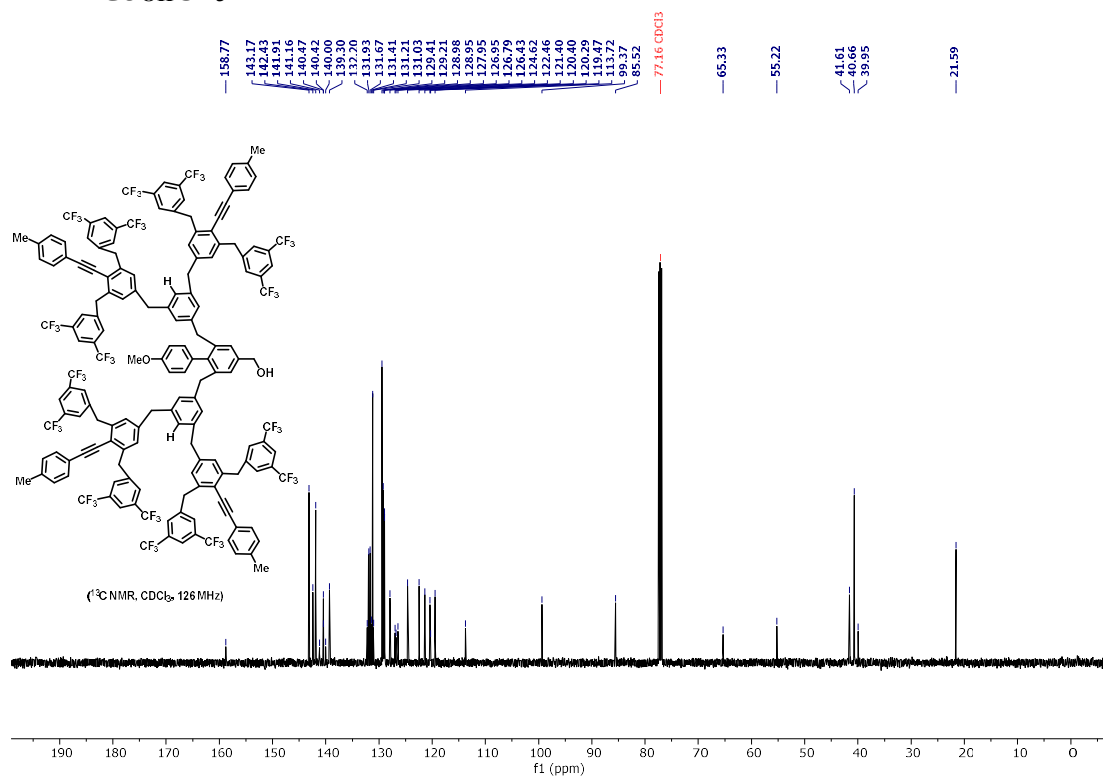
¹⁹F NMR of G3CF₃1



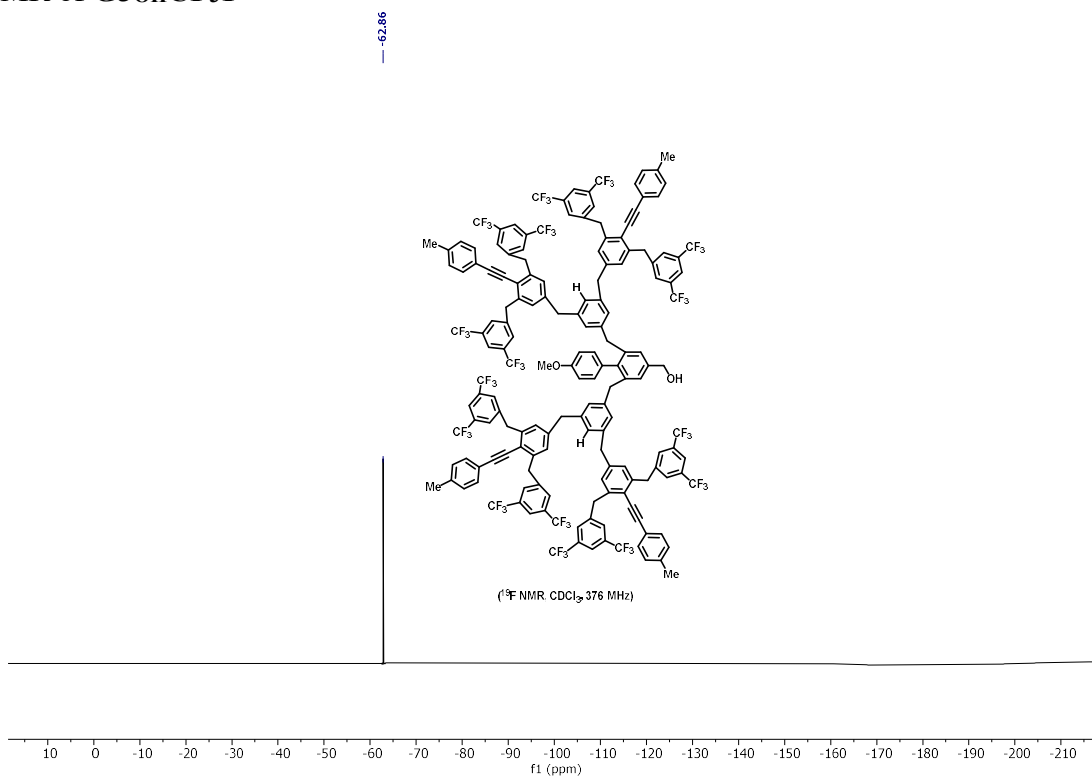
^1H NMR of G3OHCF_3



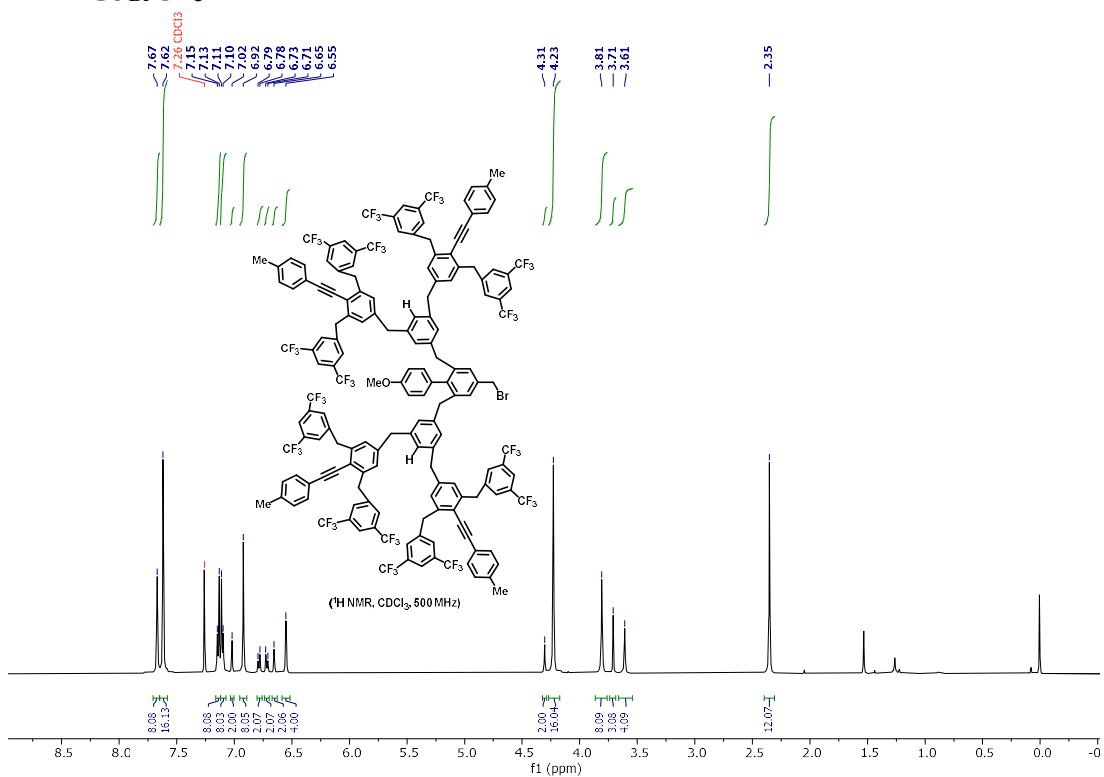
^{13}C NMR of G3OHCF_3



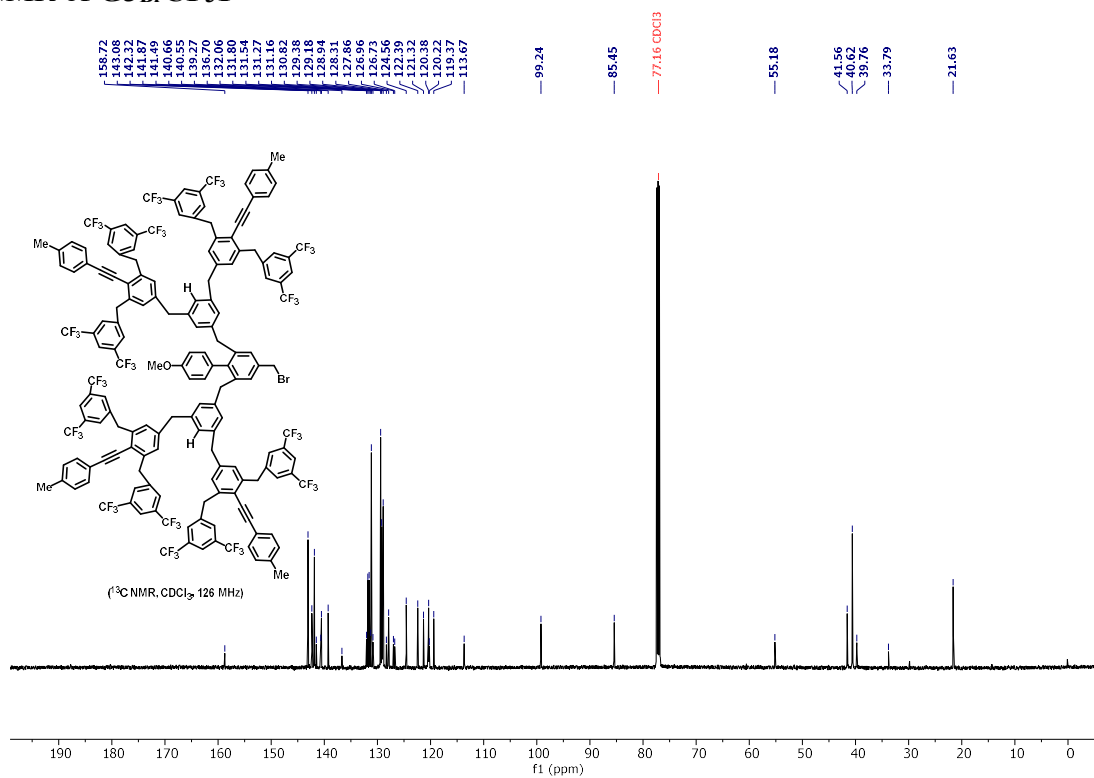
^{19}F NMR of $\text{G3}_{\text{OH}}\text{CF}_3\text{1}$



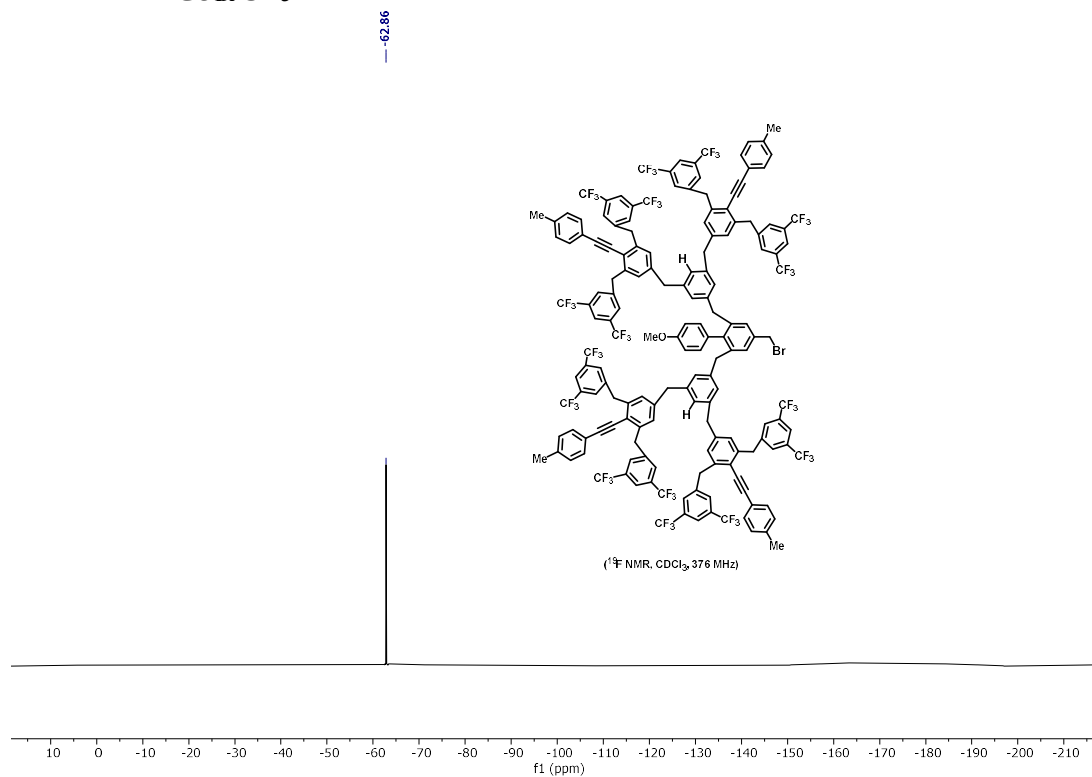
^1H NMR of $\text{G3}_{\text{Br}}\text{CF}_3\text{1}$



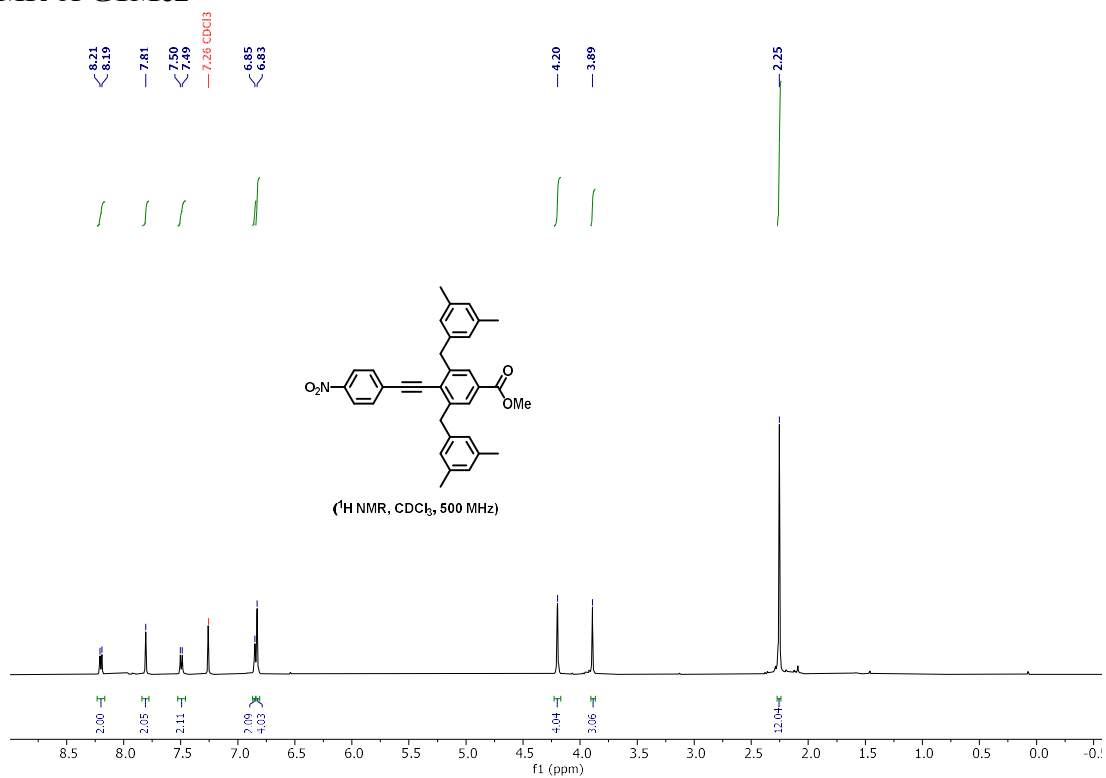
^{13}C NMR of **G3BrCF31**



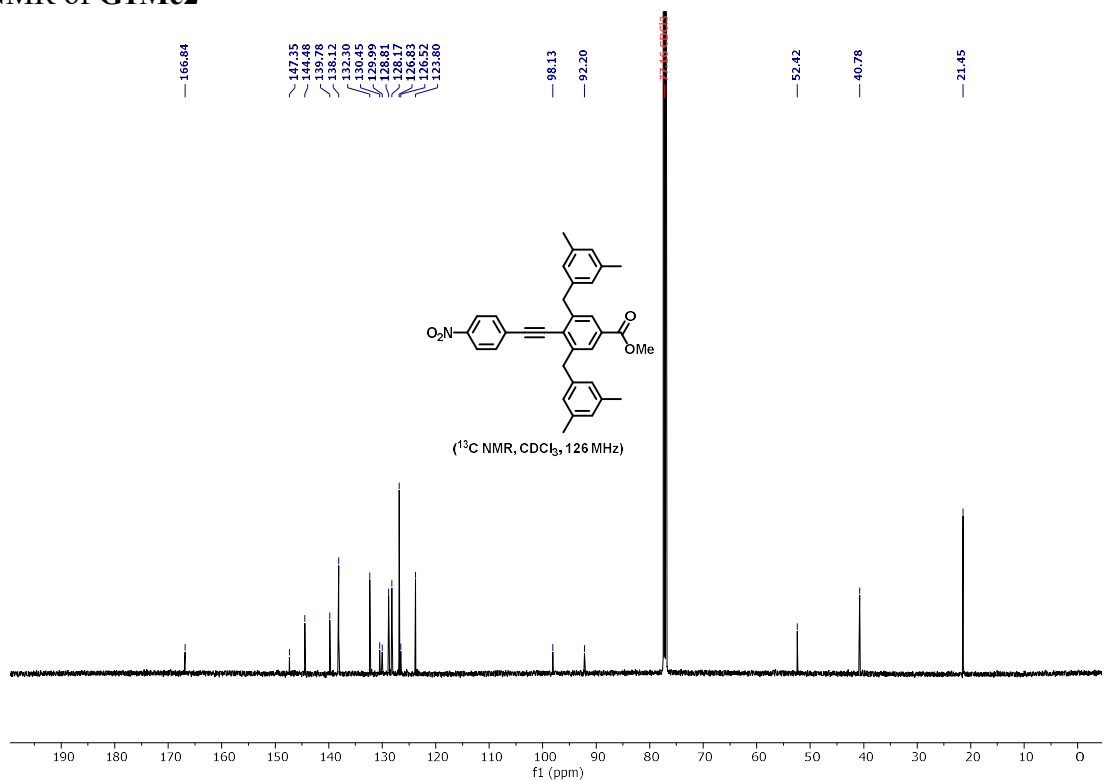
^{19}F NMR of **G3BrCF31**



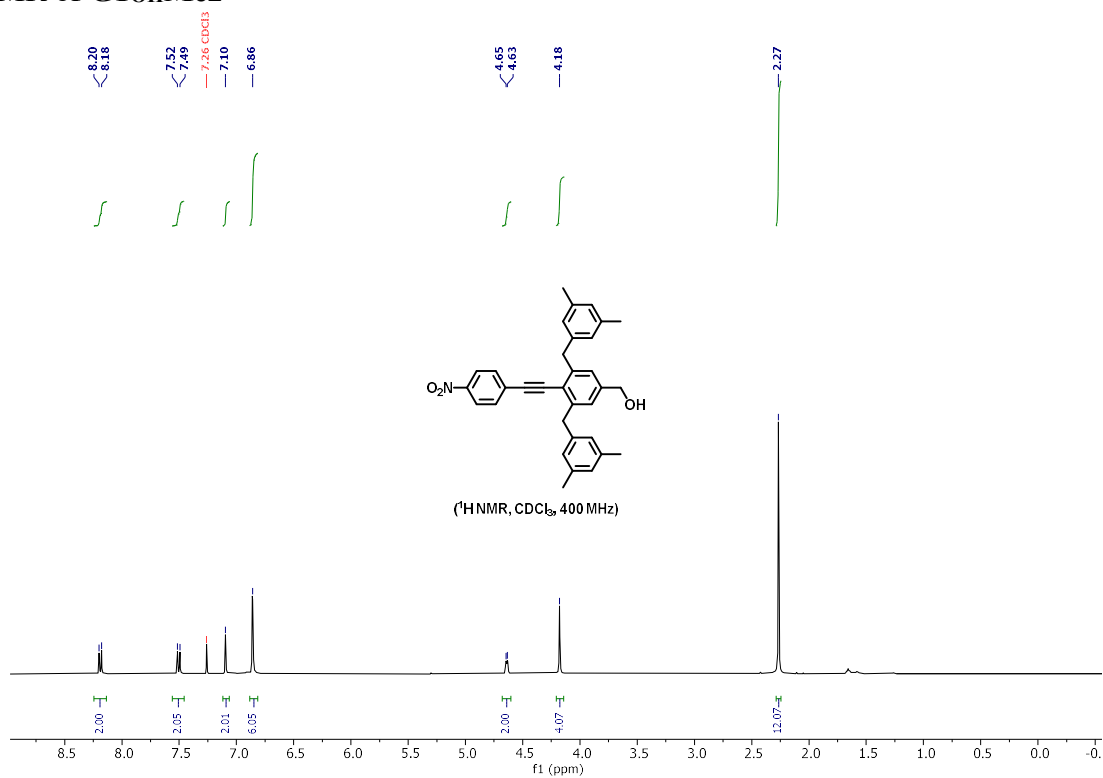
¹H NMR of G1Me2



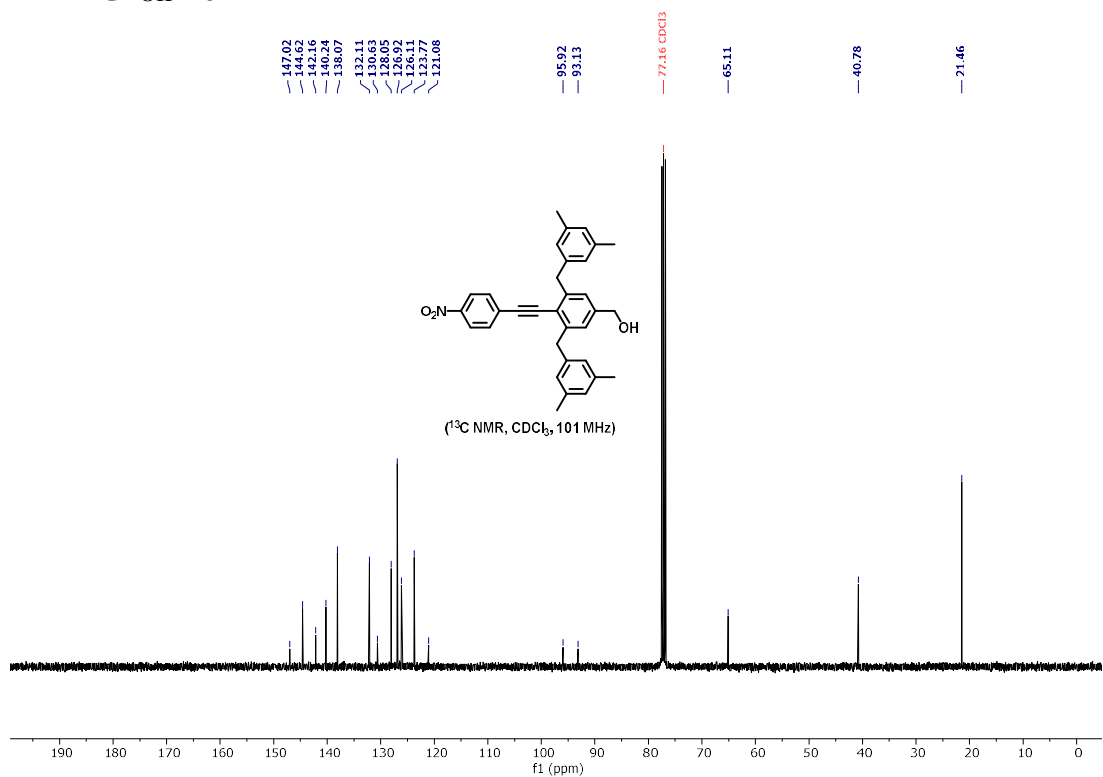
¹³C NMR of G1Me2



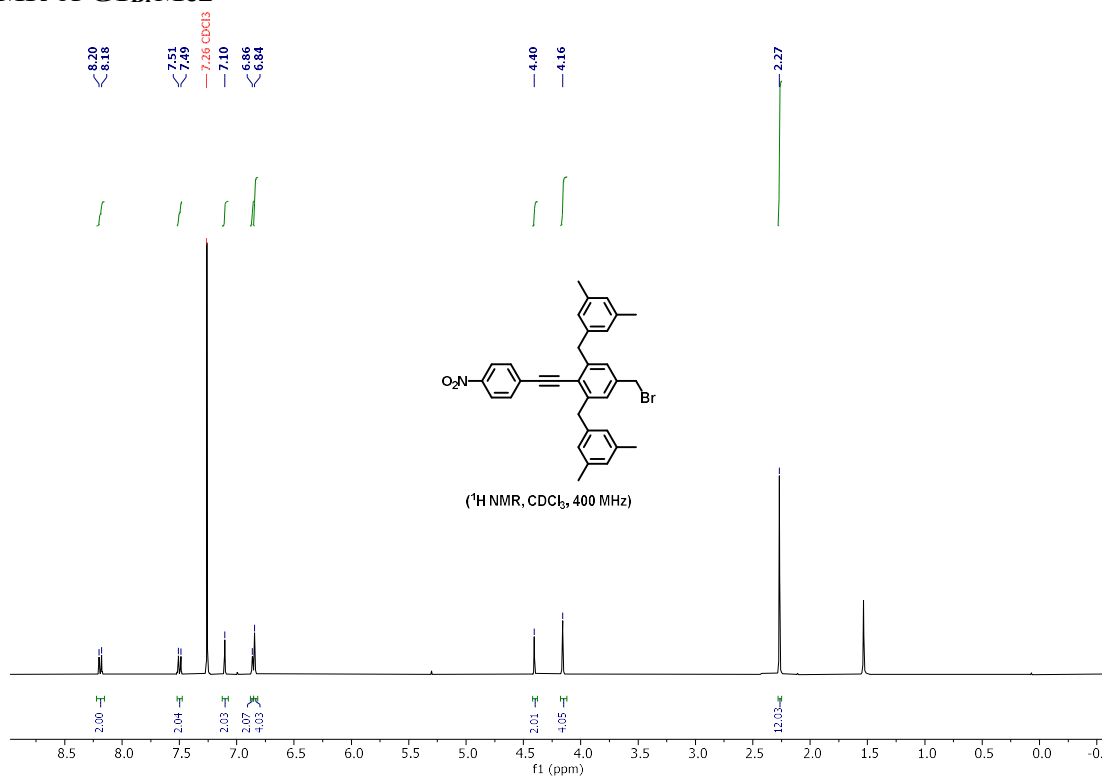
¹H NMR of G1OHMe2



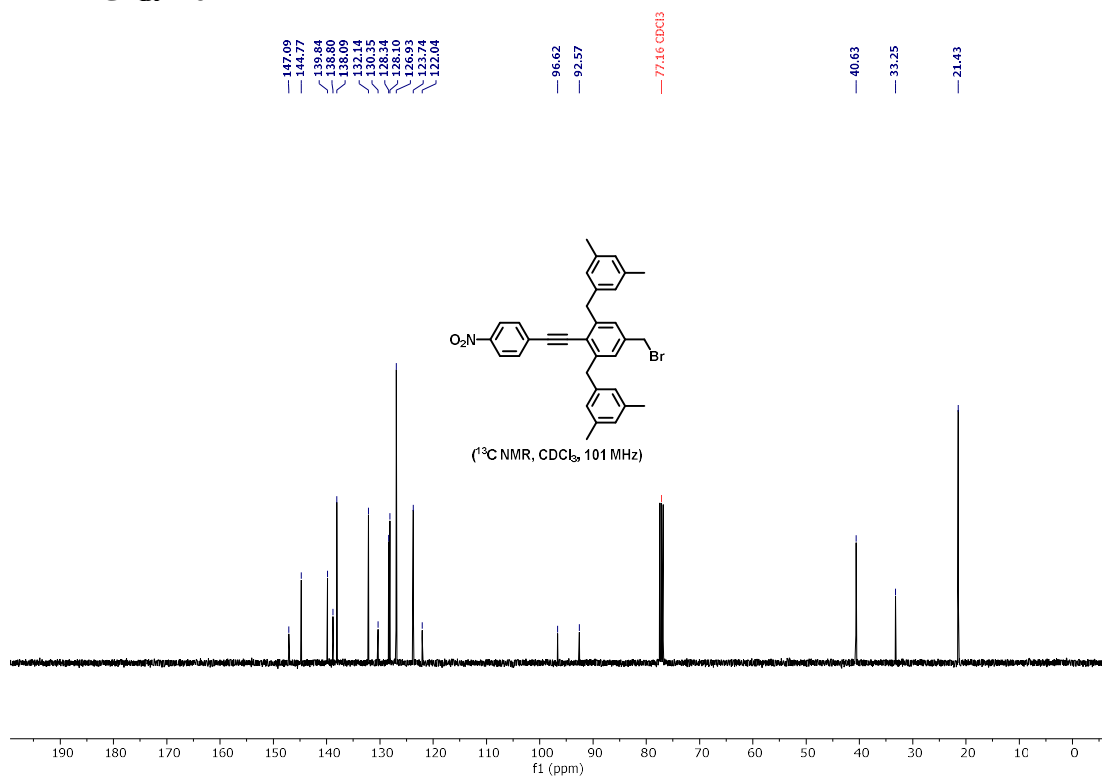
¹³C NMR of G1OHMe2



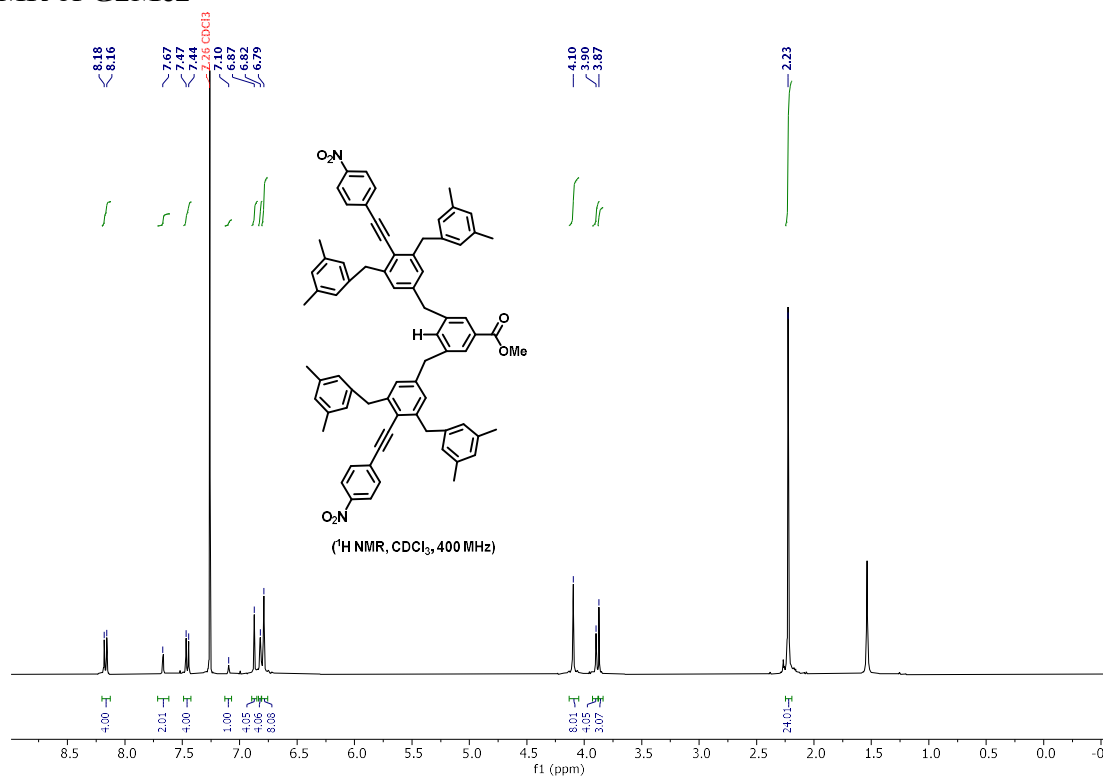
¹H NMR of G1BrMe2



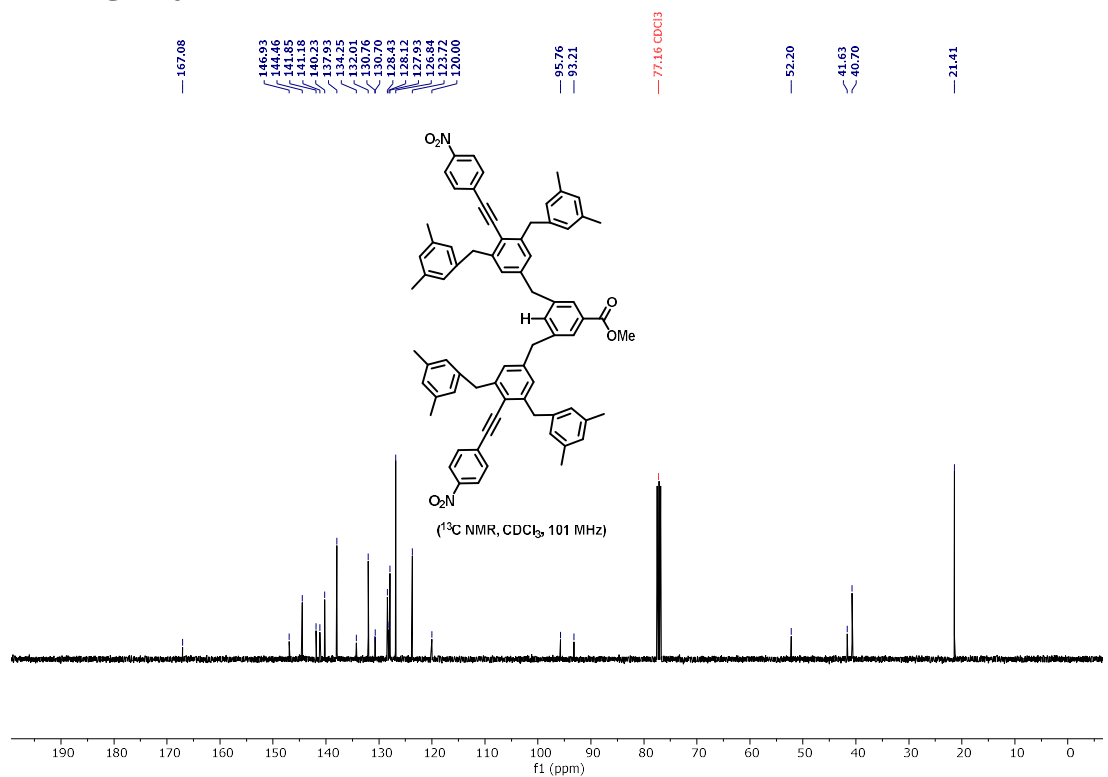
¹³C NMR of G1BrMe2



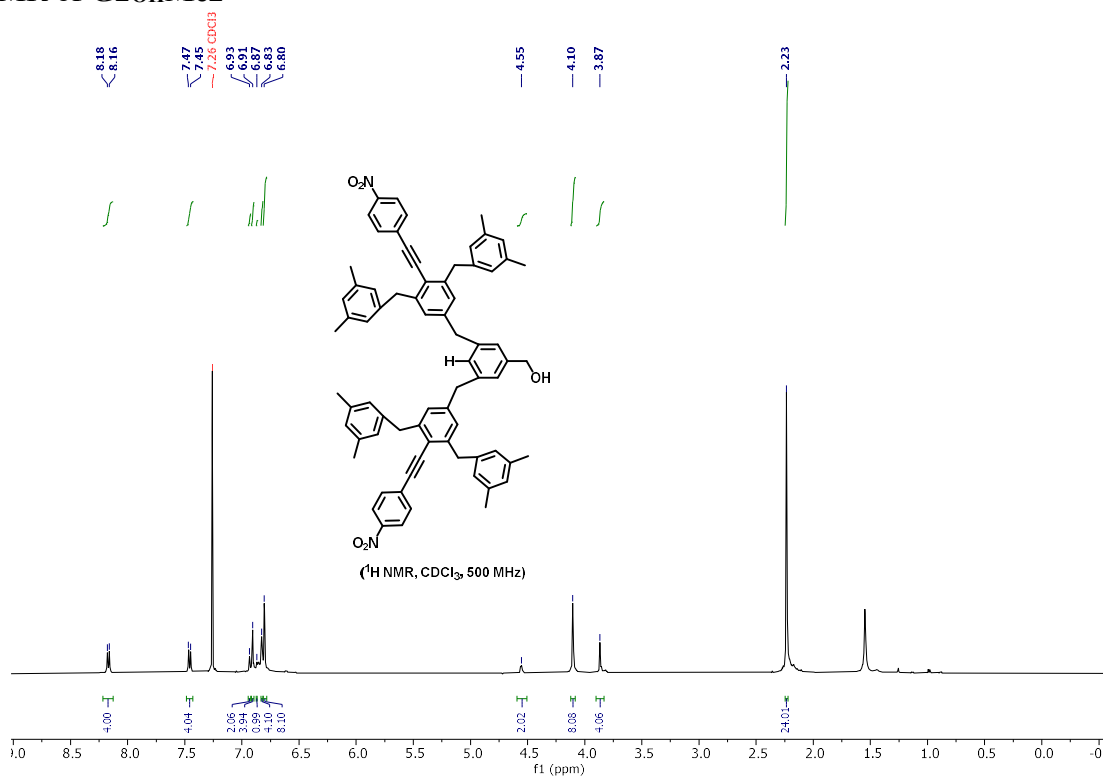
¹H NMR of G2Me2



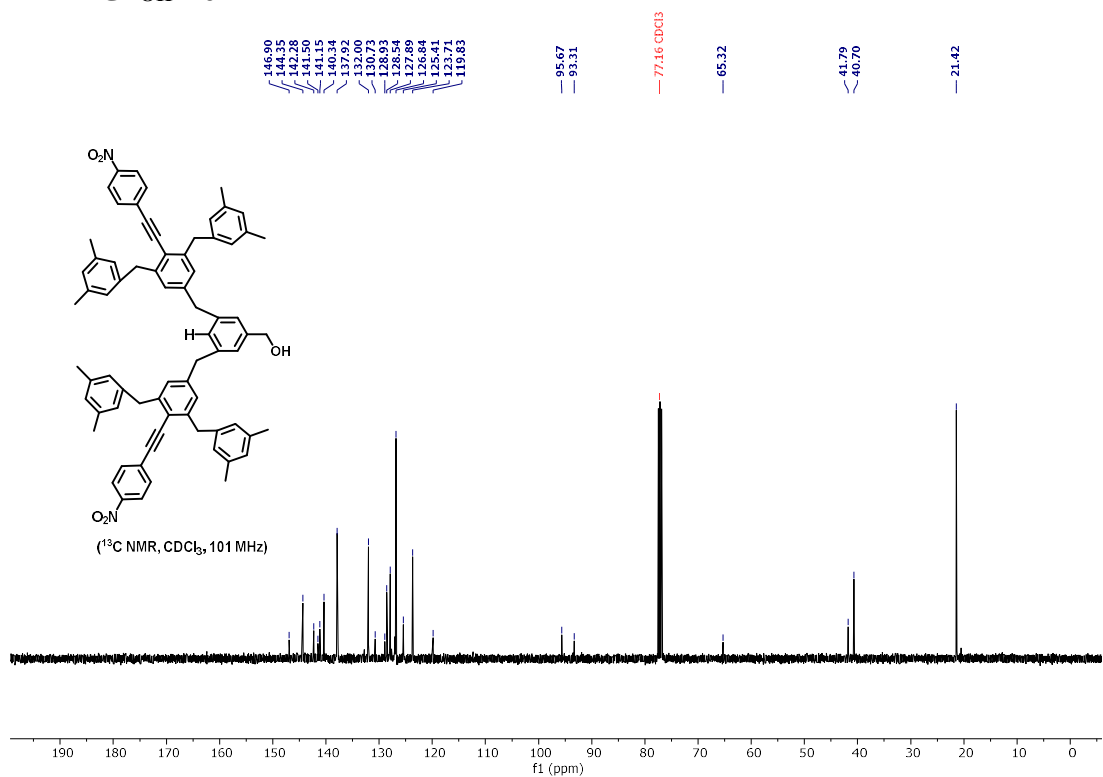
¹³C NMR of G2Me2



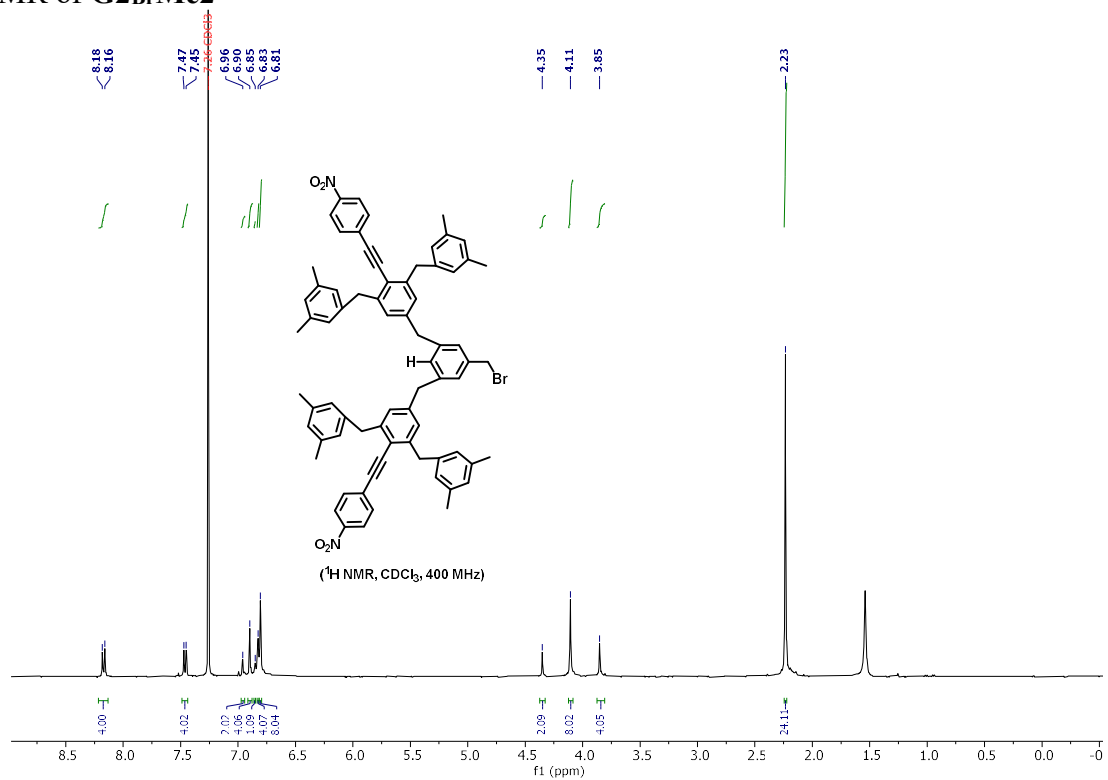
¹H NMR of G2OHMe2



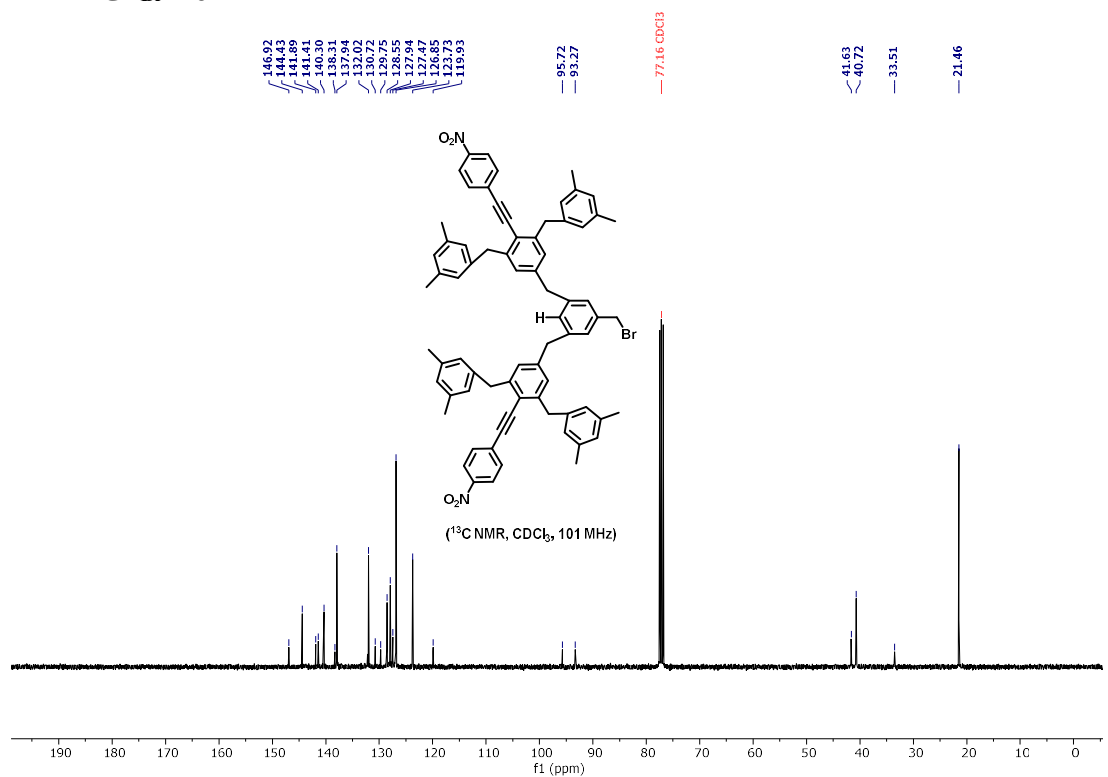
¹³C NMR of G2OHMe2



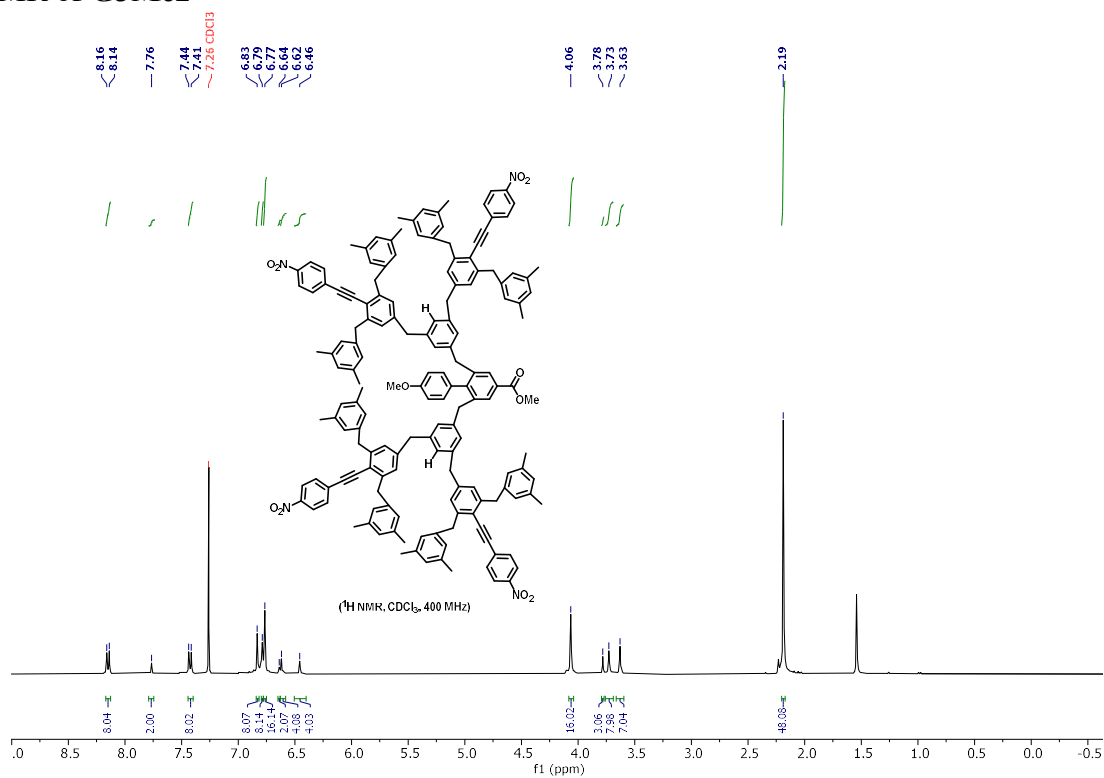
¹H NMR of G2BrMe2



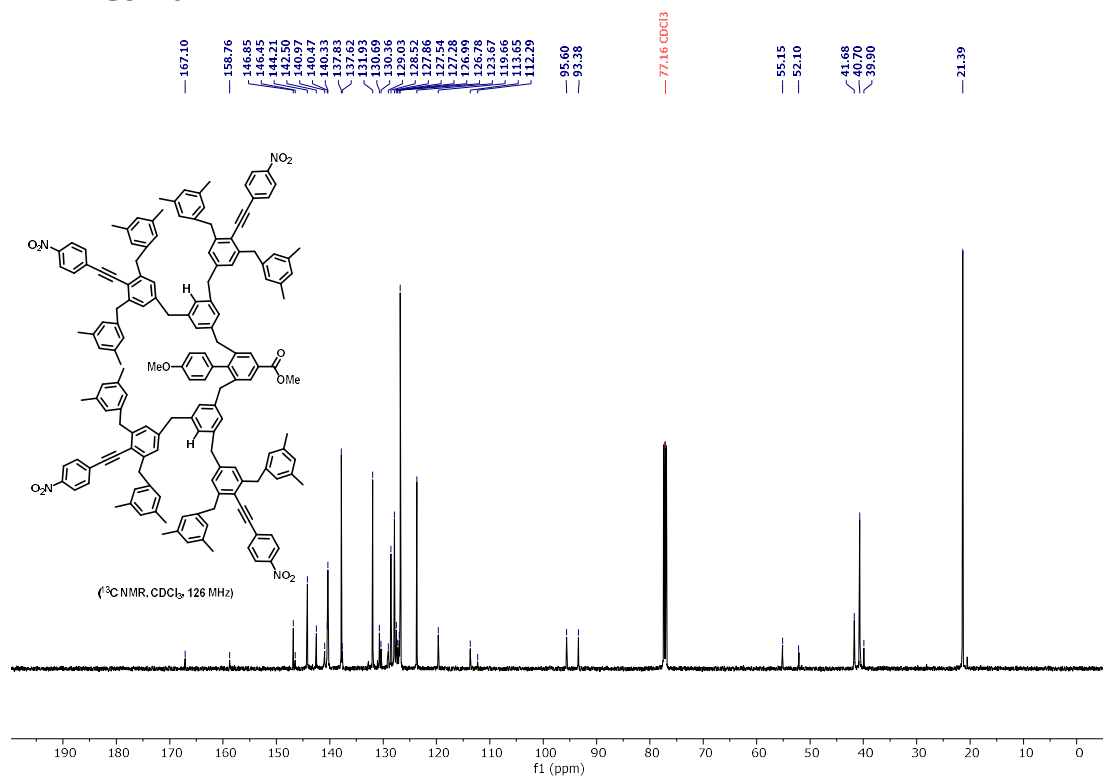
¹³C NMR of G2BrMe2



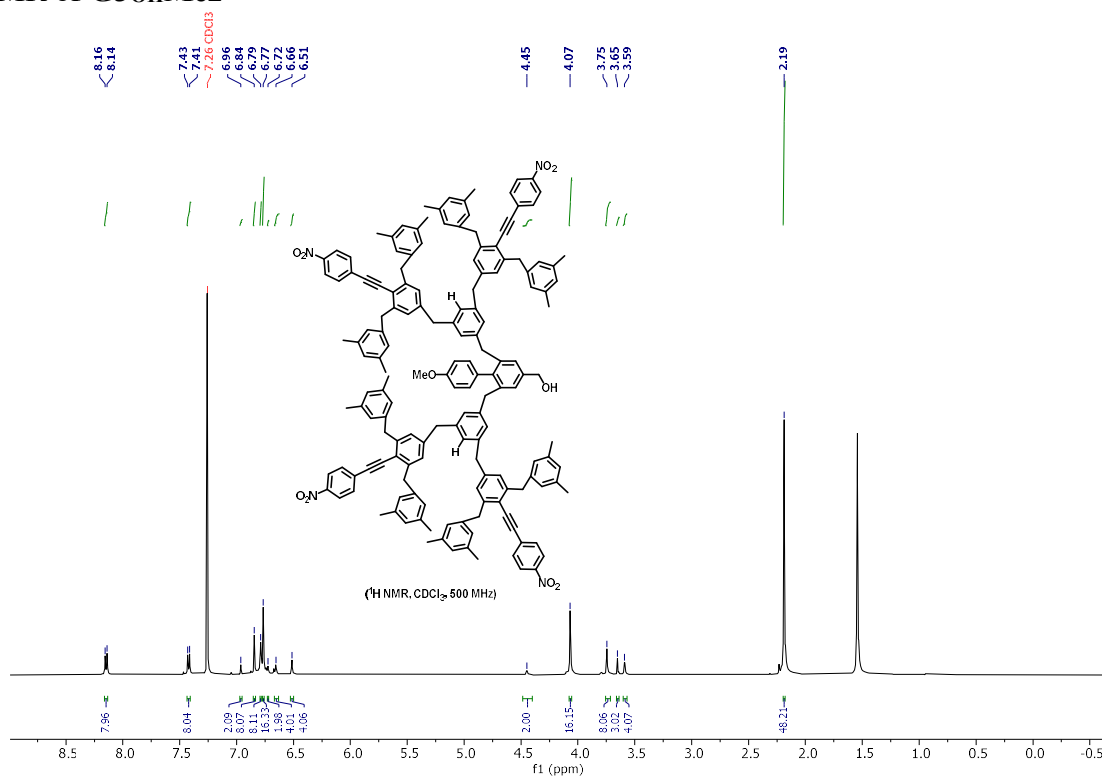
¹H NMR of G3Me2



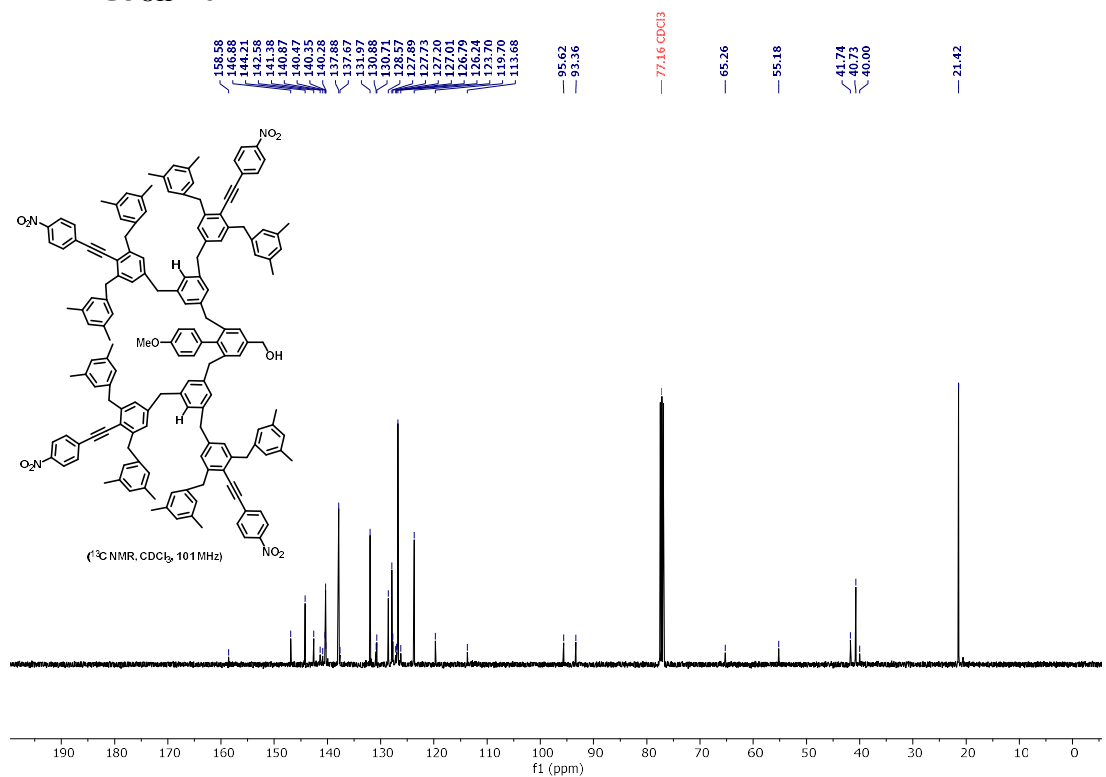
¹³C NMR of G3Me2



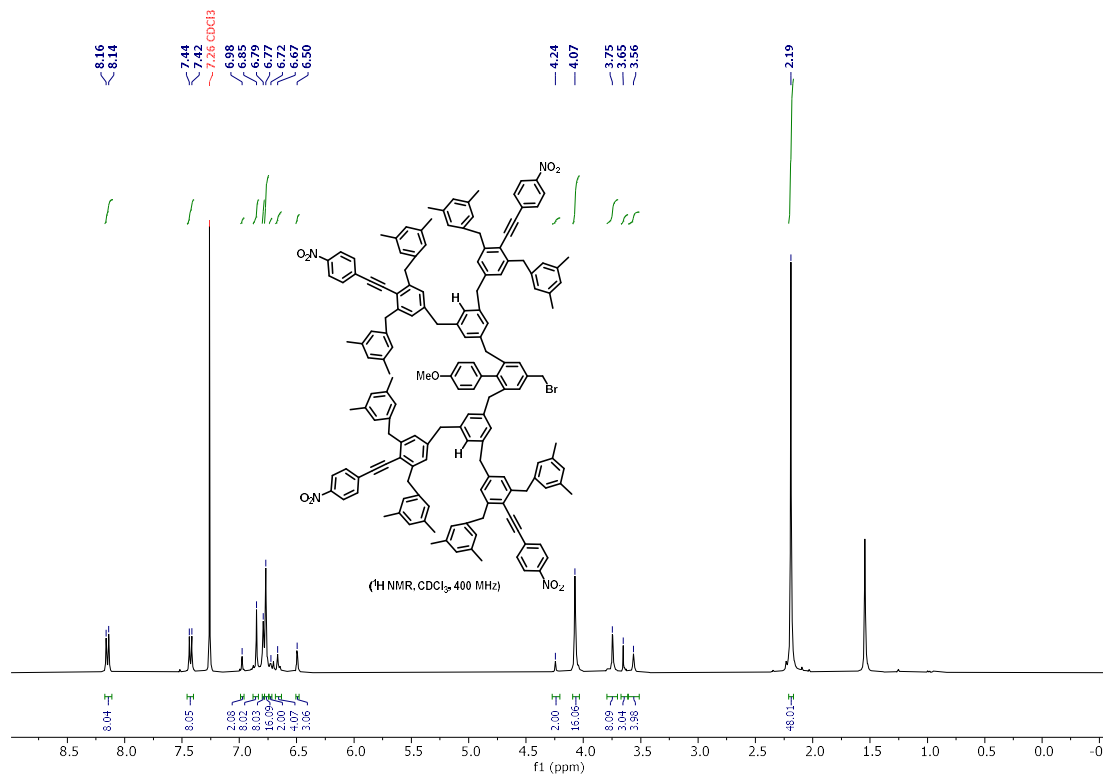
¹H NMR of G3OHMe2



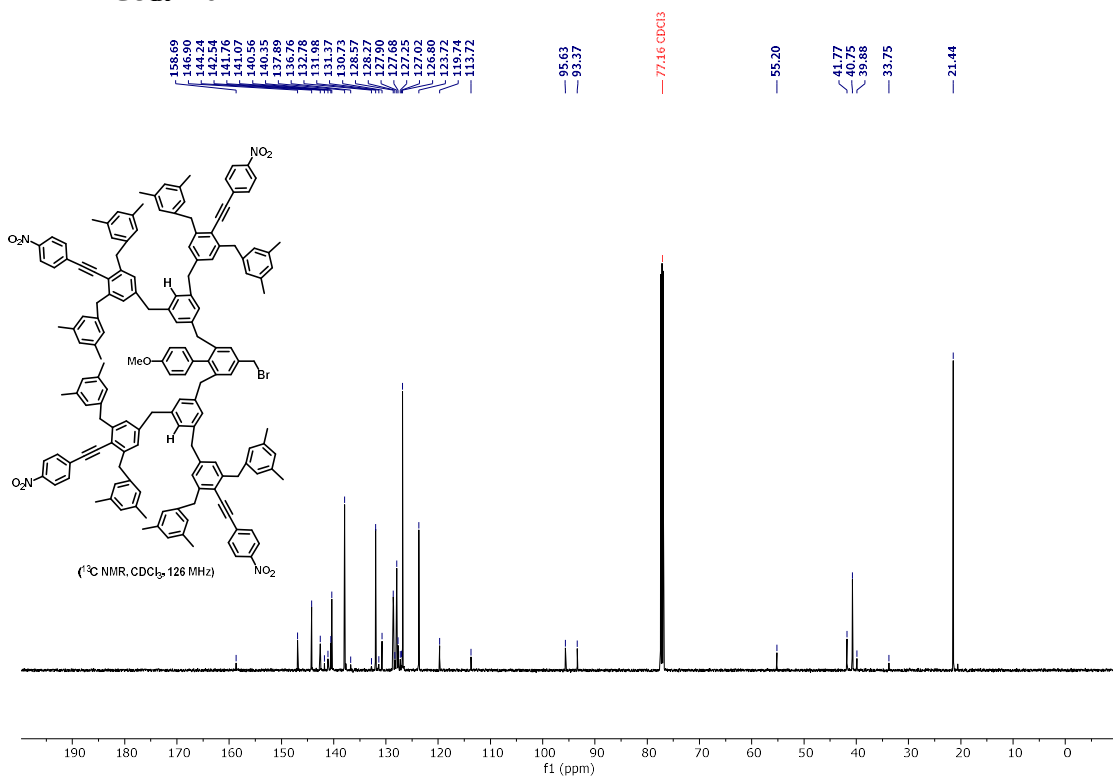
¹³C NMR of G3OHMe2



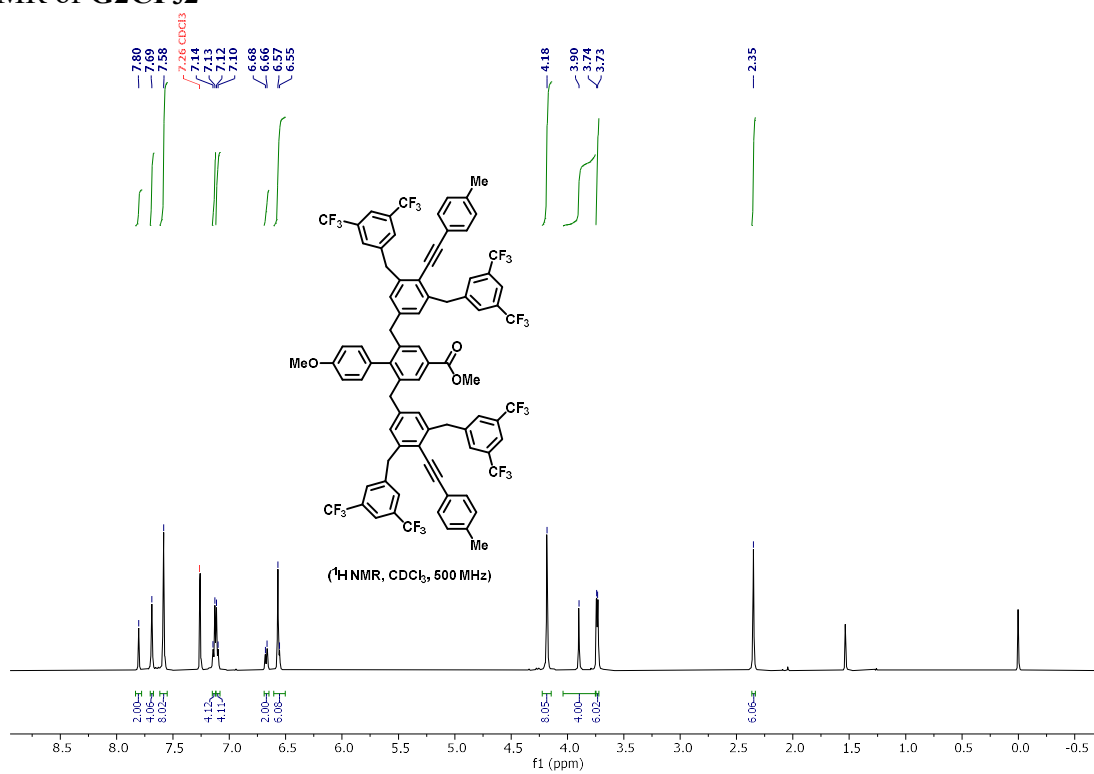
¹H NMR of G3BrMe2



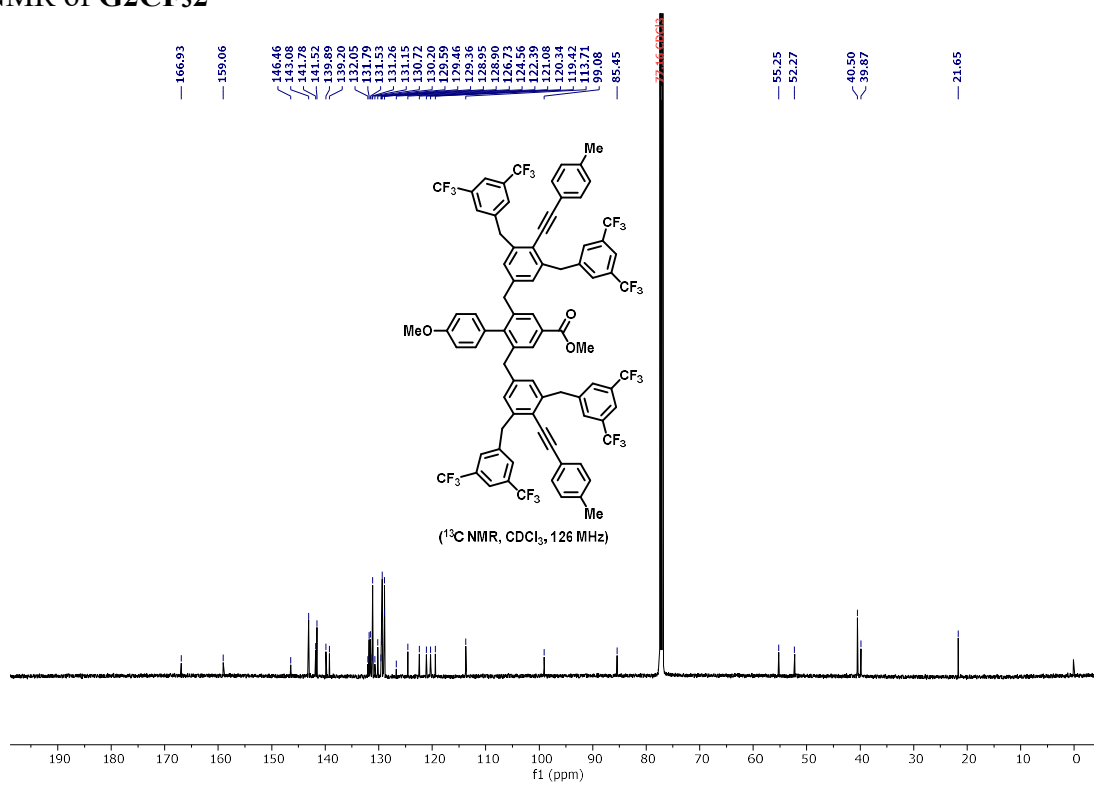
¹³C NMR of G3BrMe2



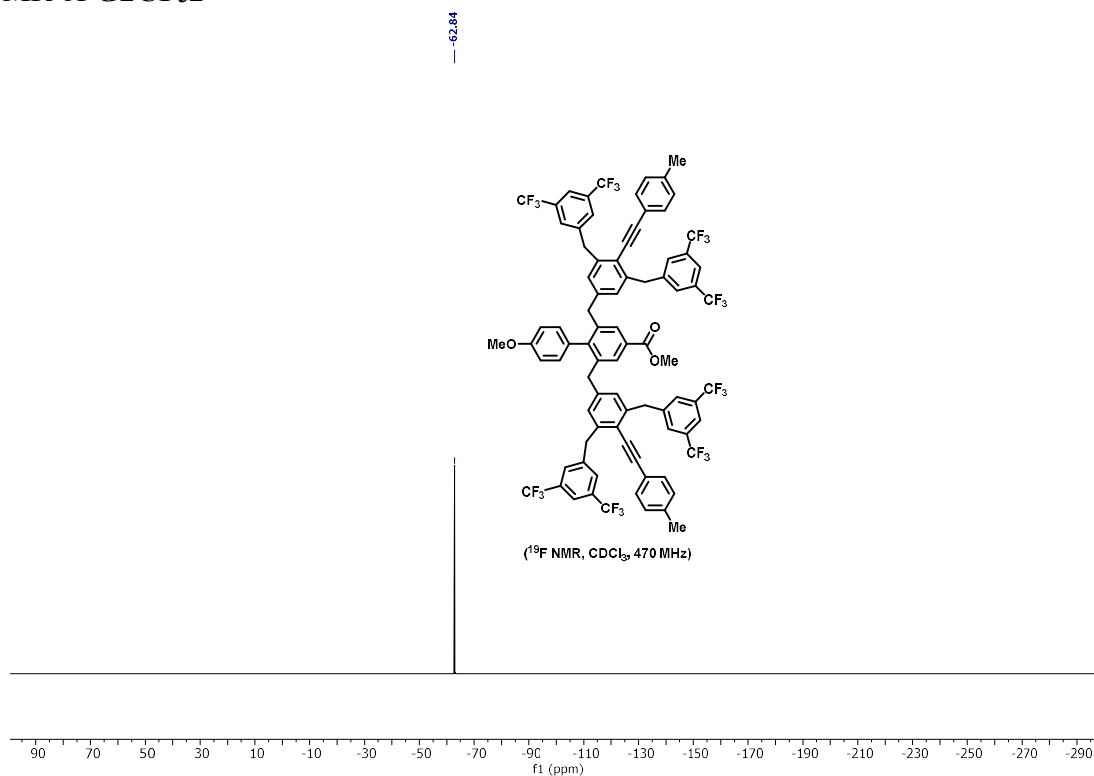
^1H NMR of G2CF₃2



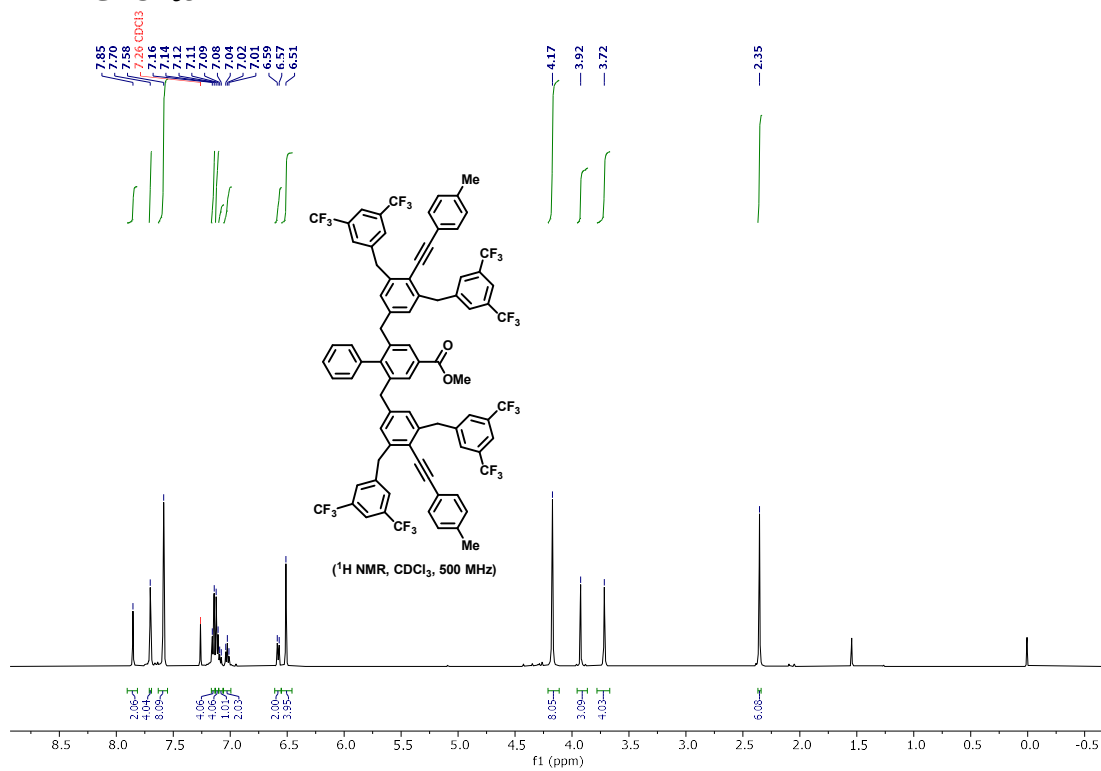
^{13}C NMR of G2CF₃2



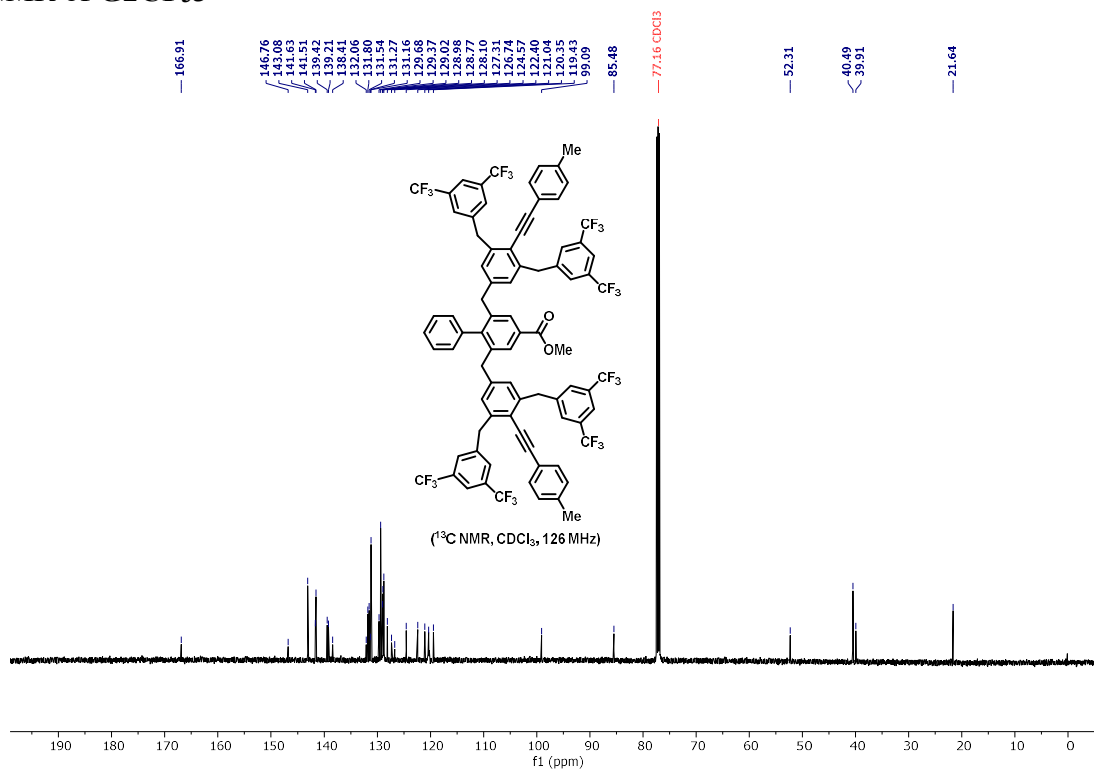
^{19}F NMR of $\text{G2CF}_3\text{2}$



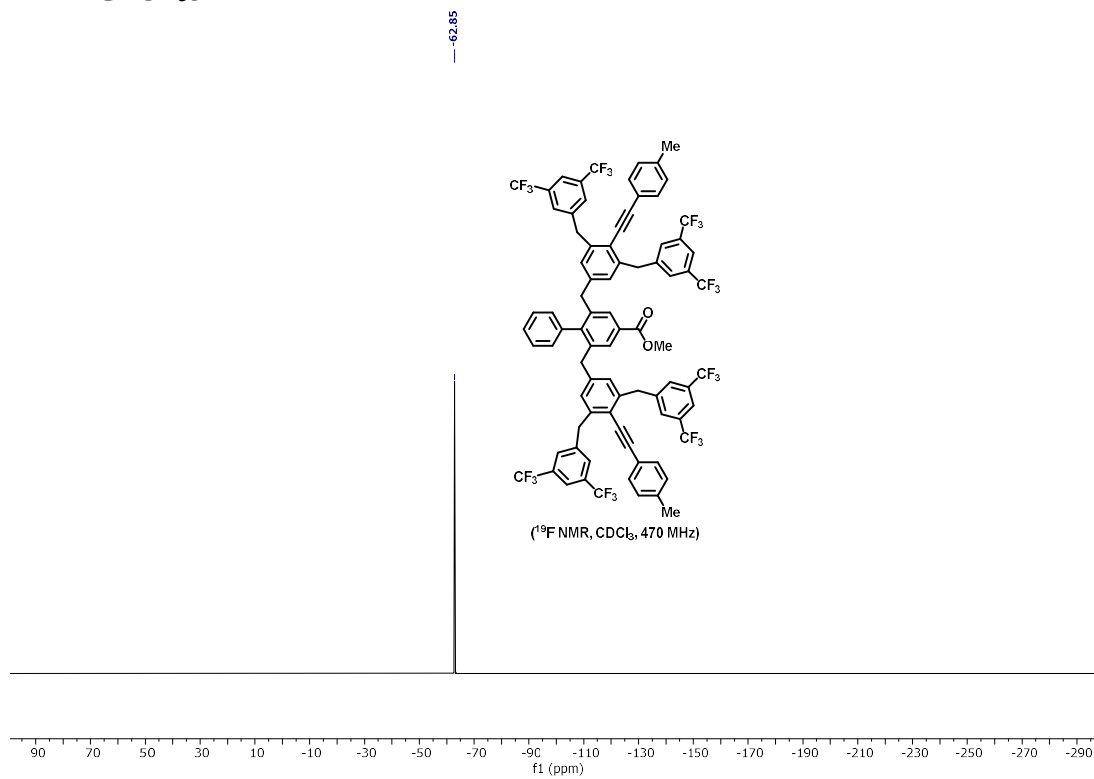
^1H NMR of $\text{G2CF}_3\text{3}$



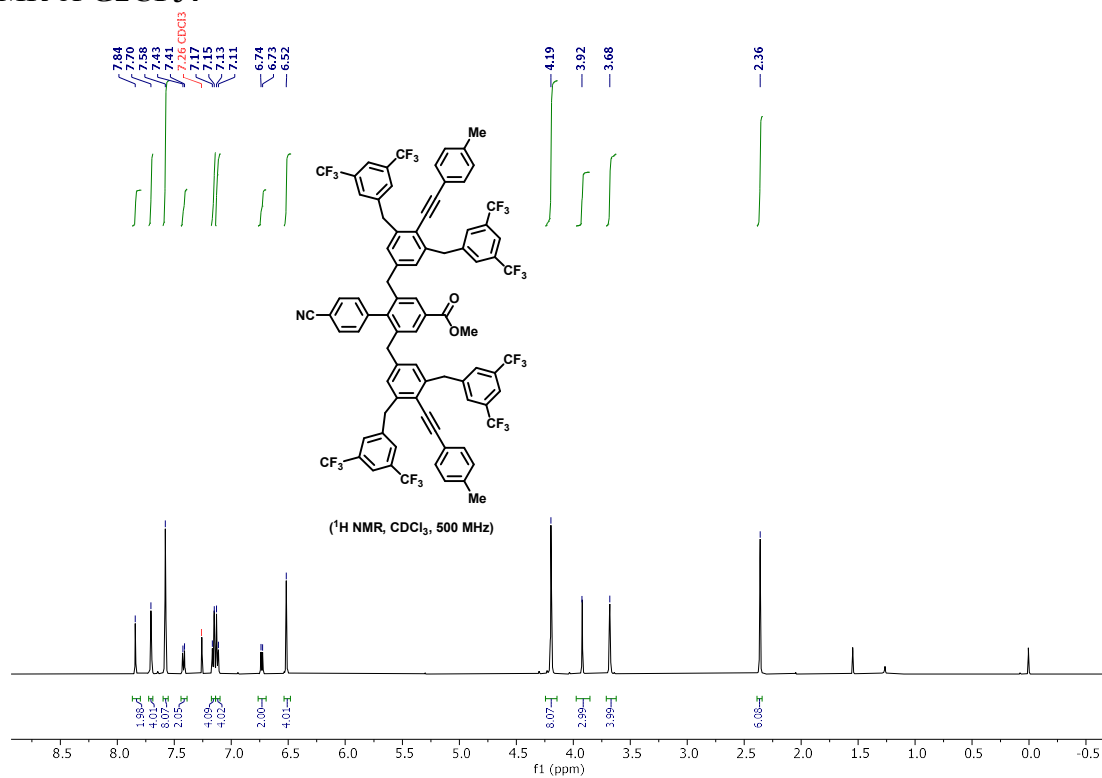
^{13}C NMR of G2CF₃3



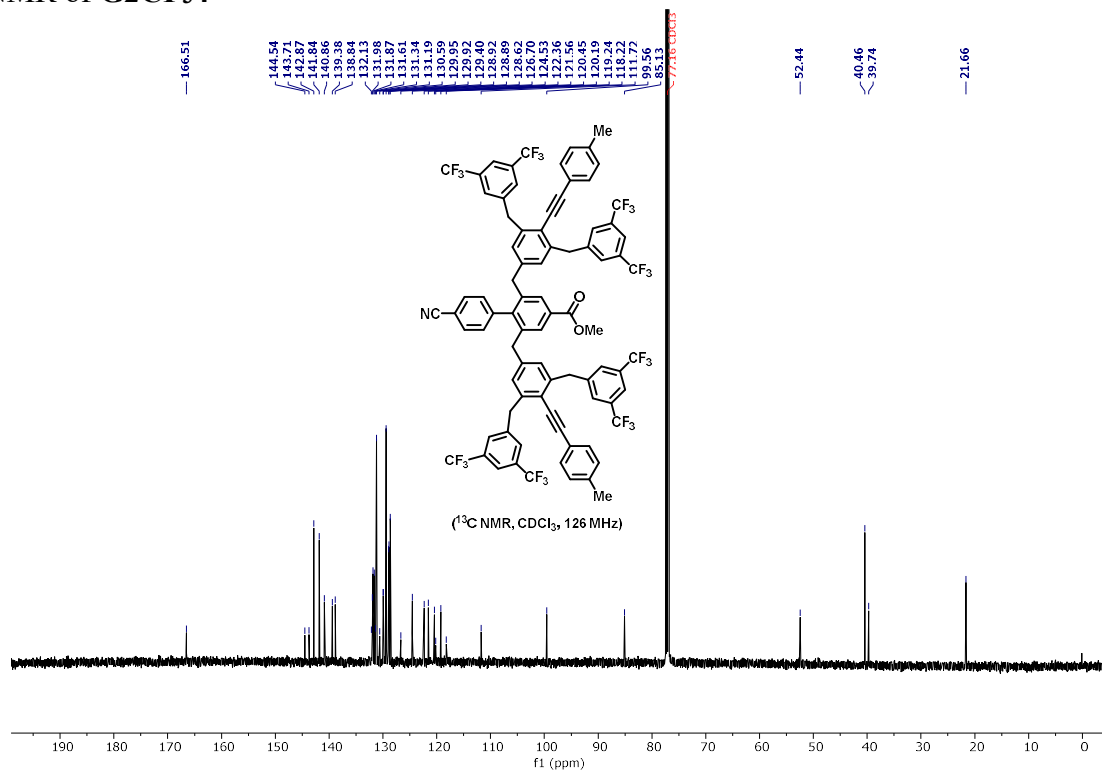
^{19}F NMR of G2CF₃3



¹H NMR of G2CF₃4

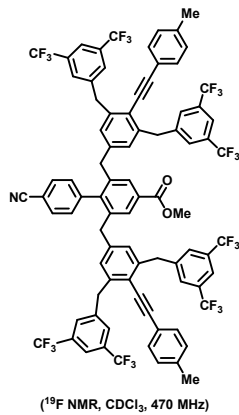


¹³C NMR of G2CF₃4



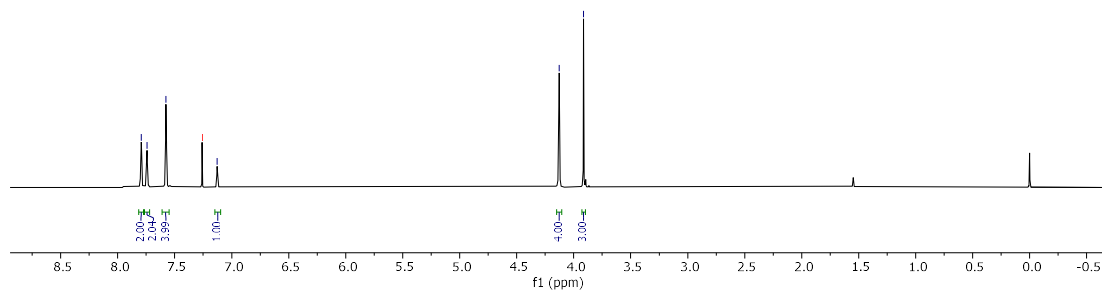
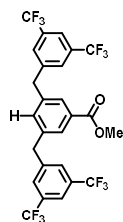
^{19}F NMR of G2CF_3

-62.84

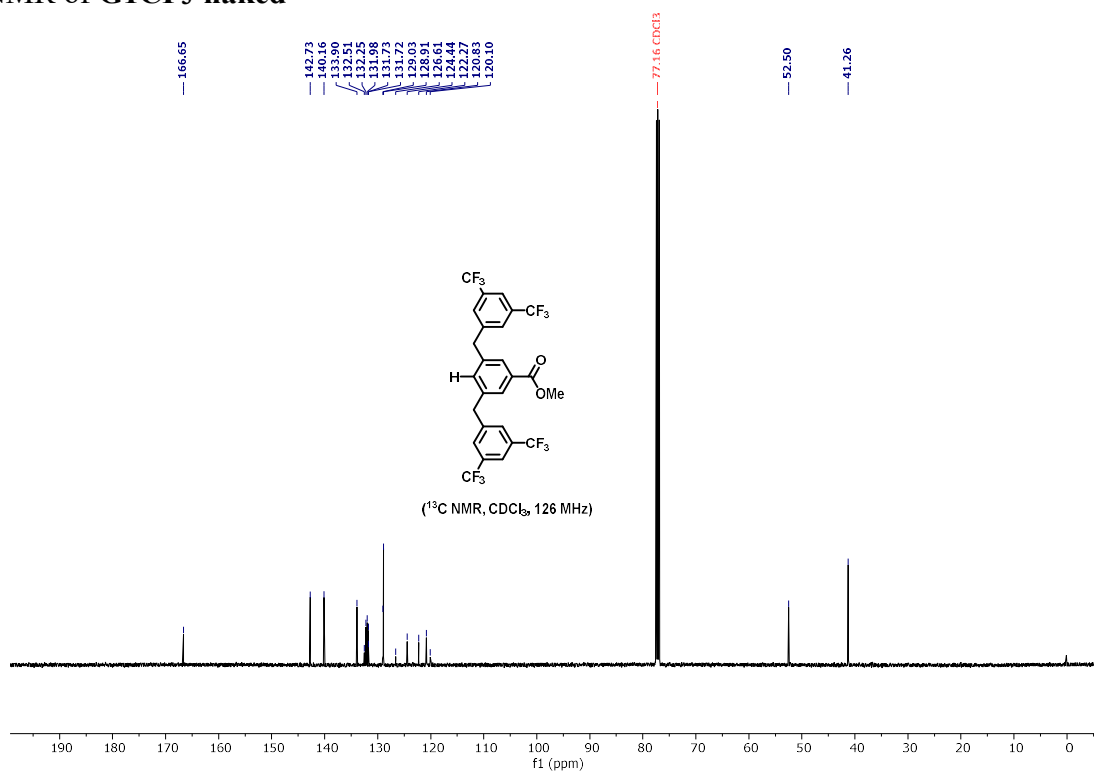


90 70 50 30 10 -10 -30 -50 -70 -90 -110 -130 -150 -170 -190 -210 -230 -250 -270 -290
f1 (ppm)

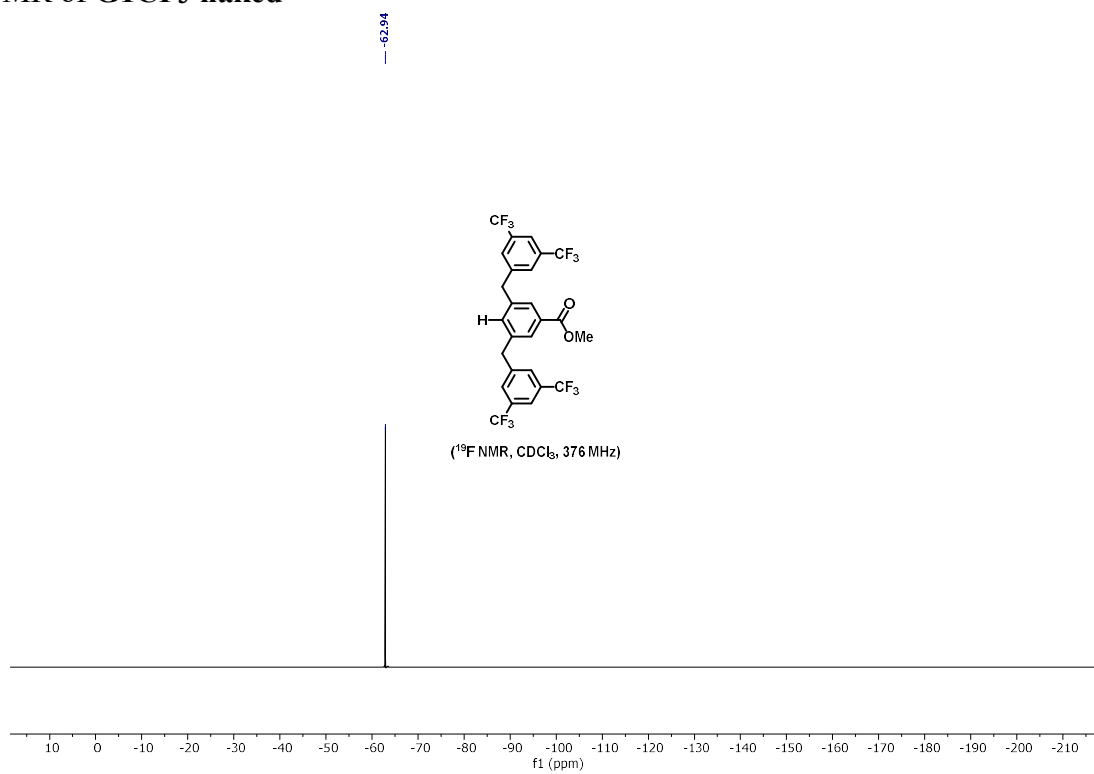
^1H NMR of G1CF_3 -naked



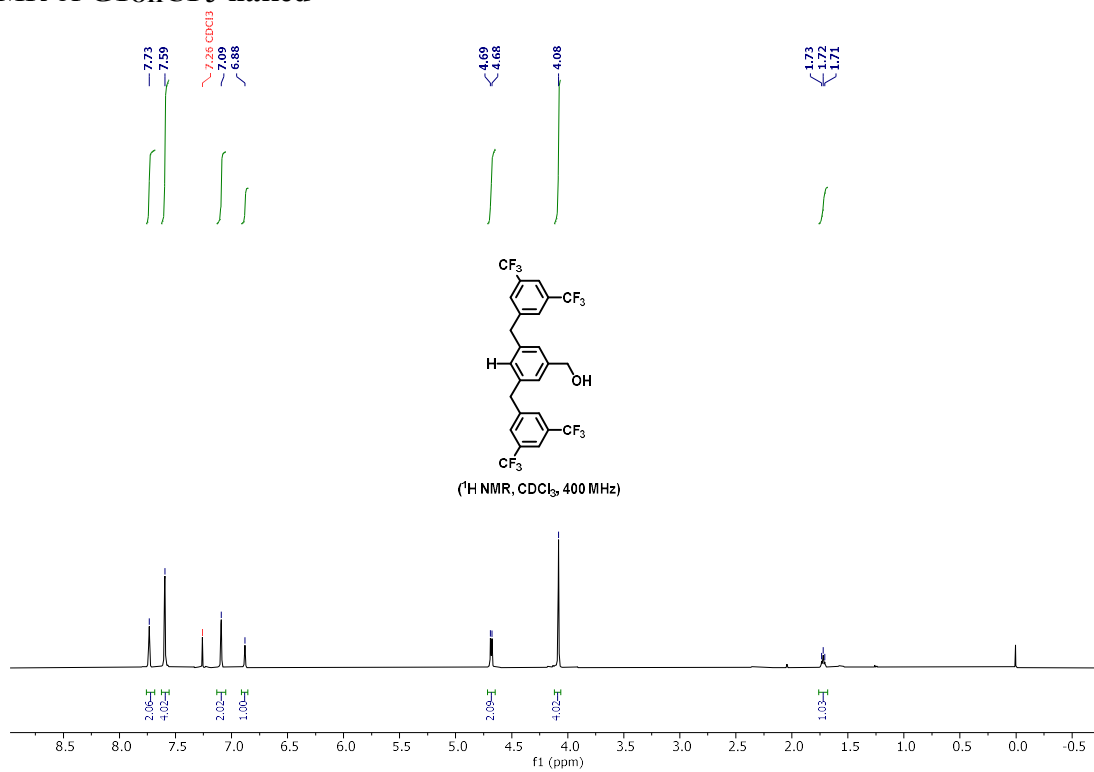
^{13}C NMR of G1CF₃-naked



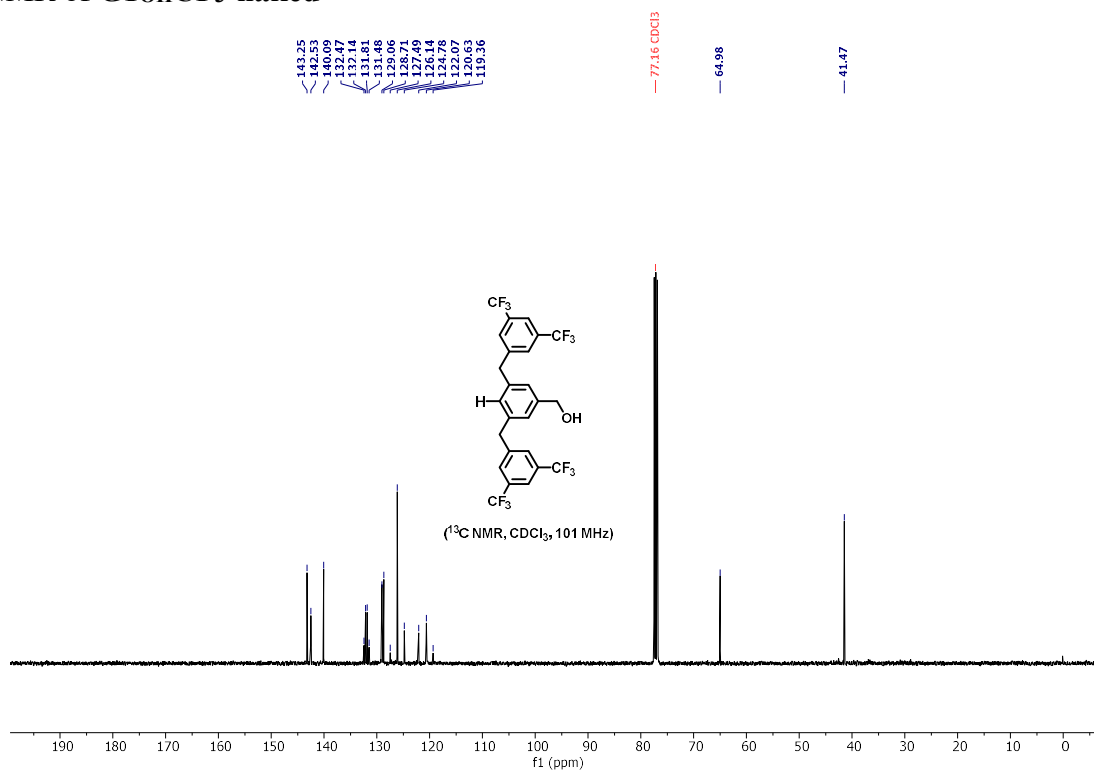
^{19}F NMR of G1CF₃-naked



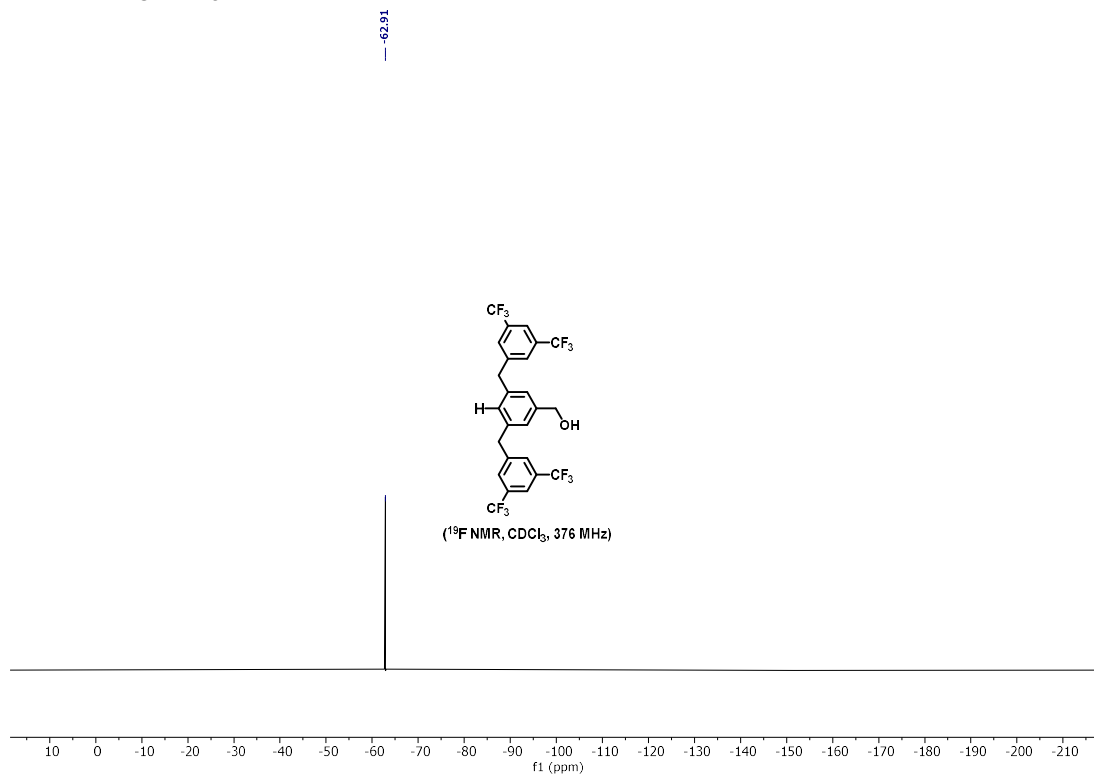
¹H NMR of G1OHCF₃-naked



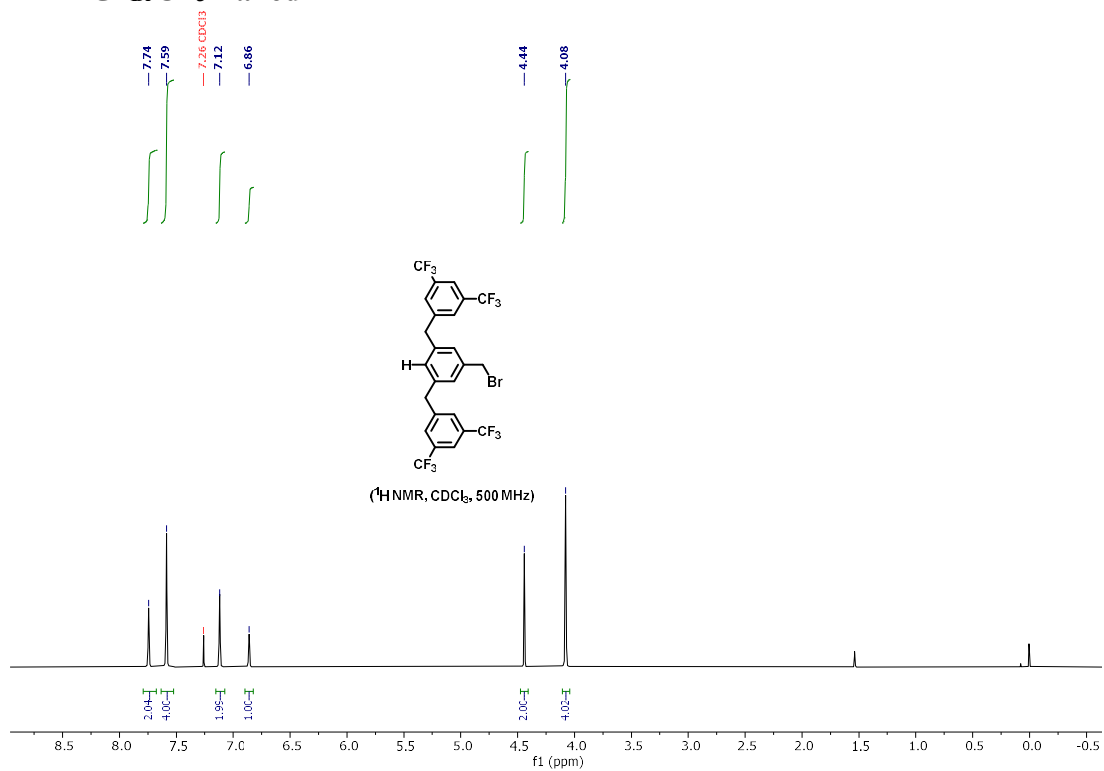
¹³C NMR of G1OHCF₃-naked



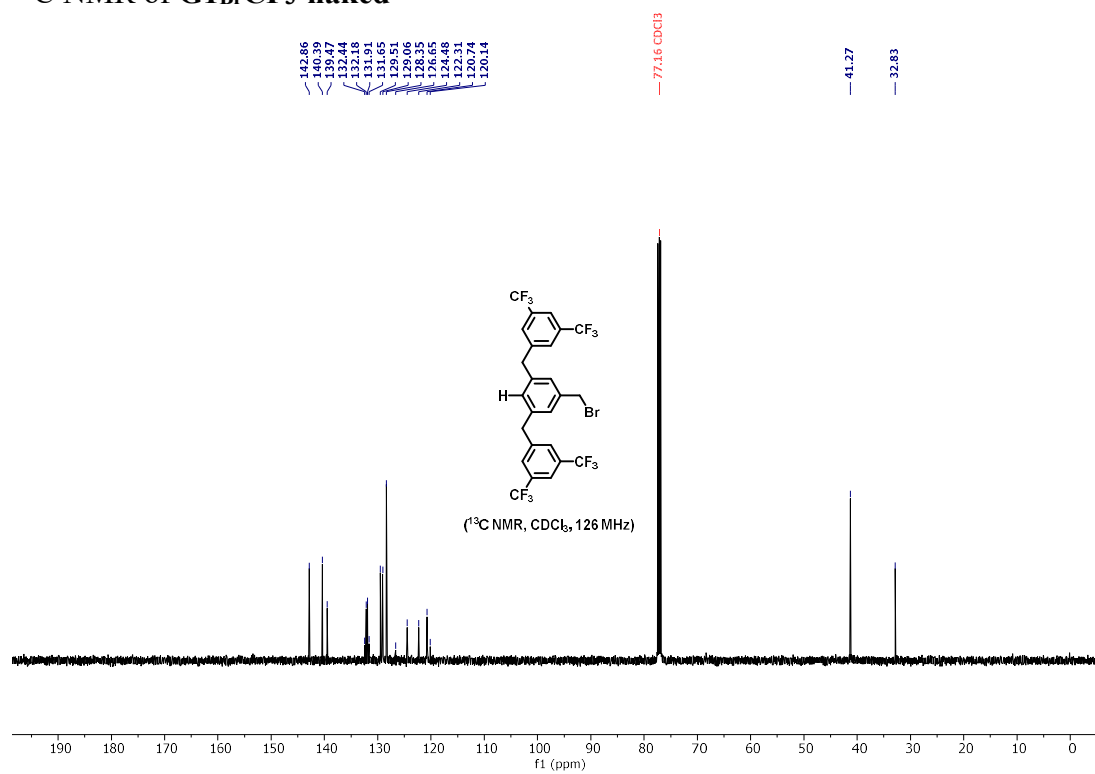
^{19}F NMR of $\text{G1}_{\text{OH}}\text{CF}_3$ -naked



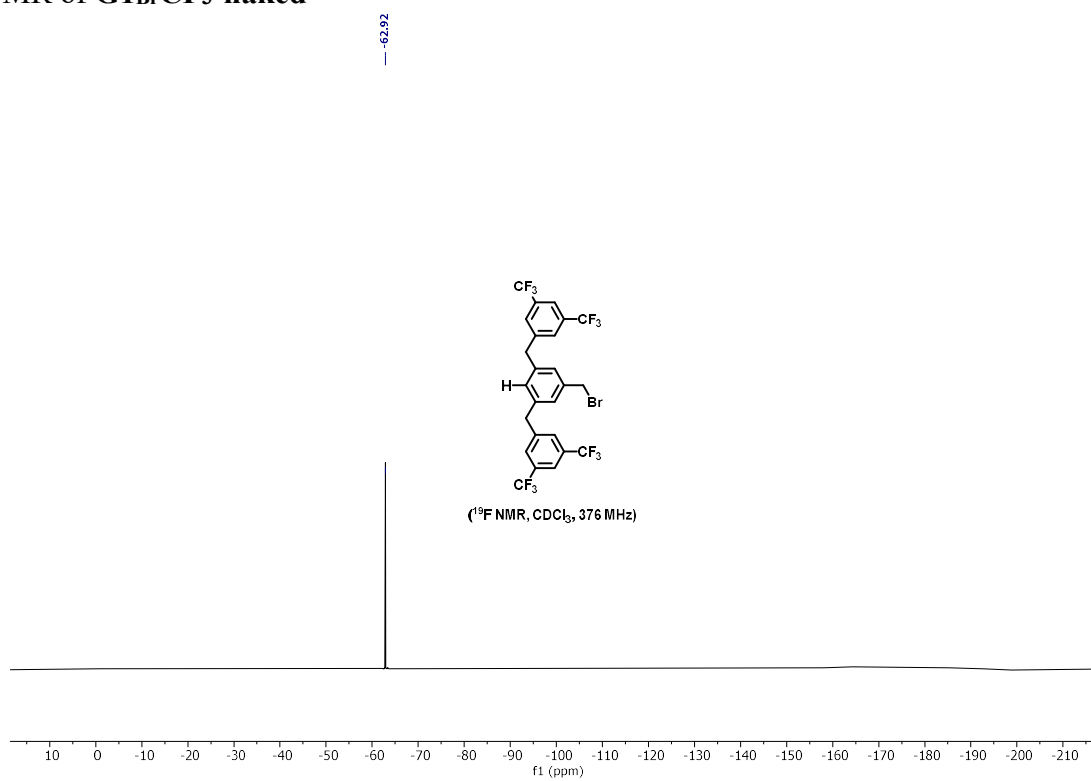
^1H NMR of $\text{G1}_{\text{Br}}\text{CF}_3$ -naked



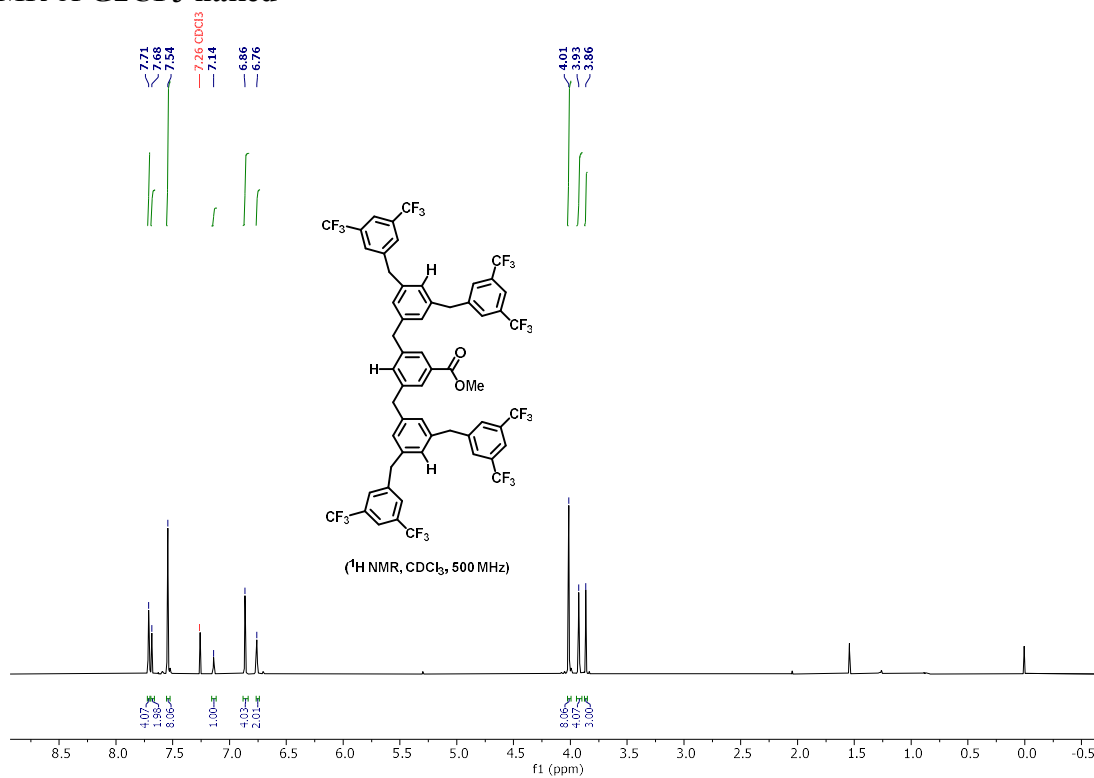
¹³C NMR of G1BrCF₃-naked



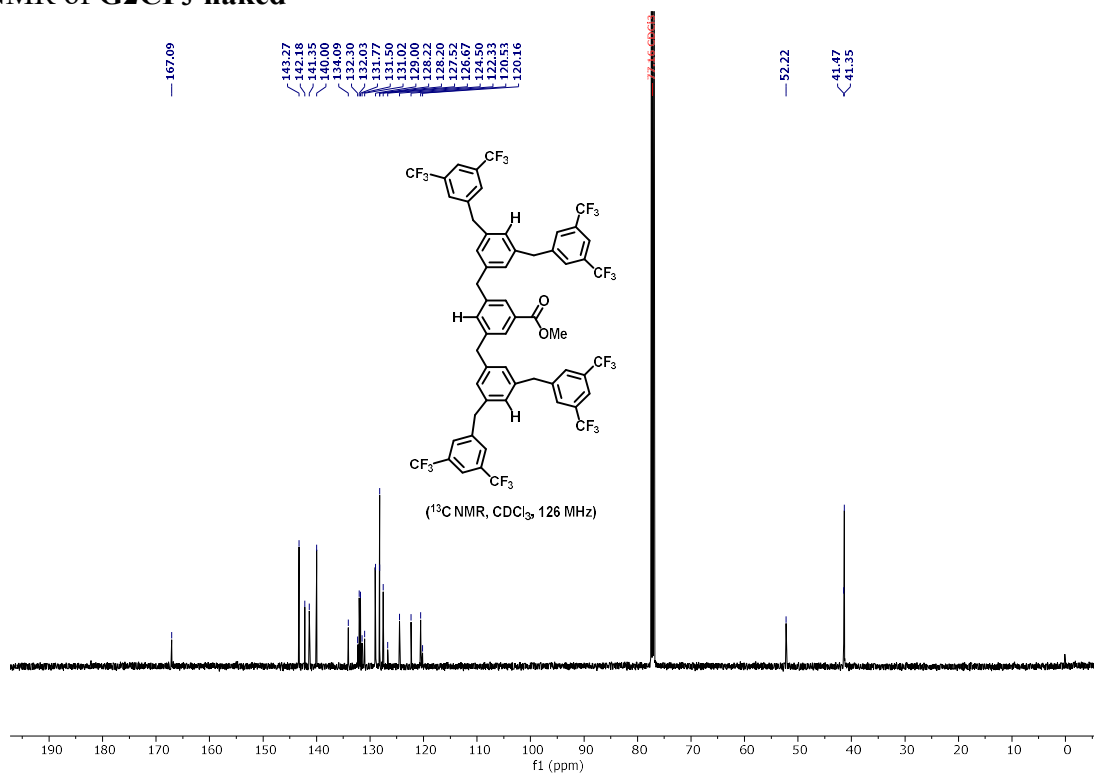
¹⁹F NMR of G1BrCF₃-naked



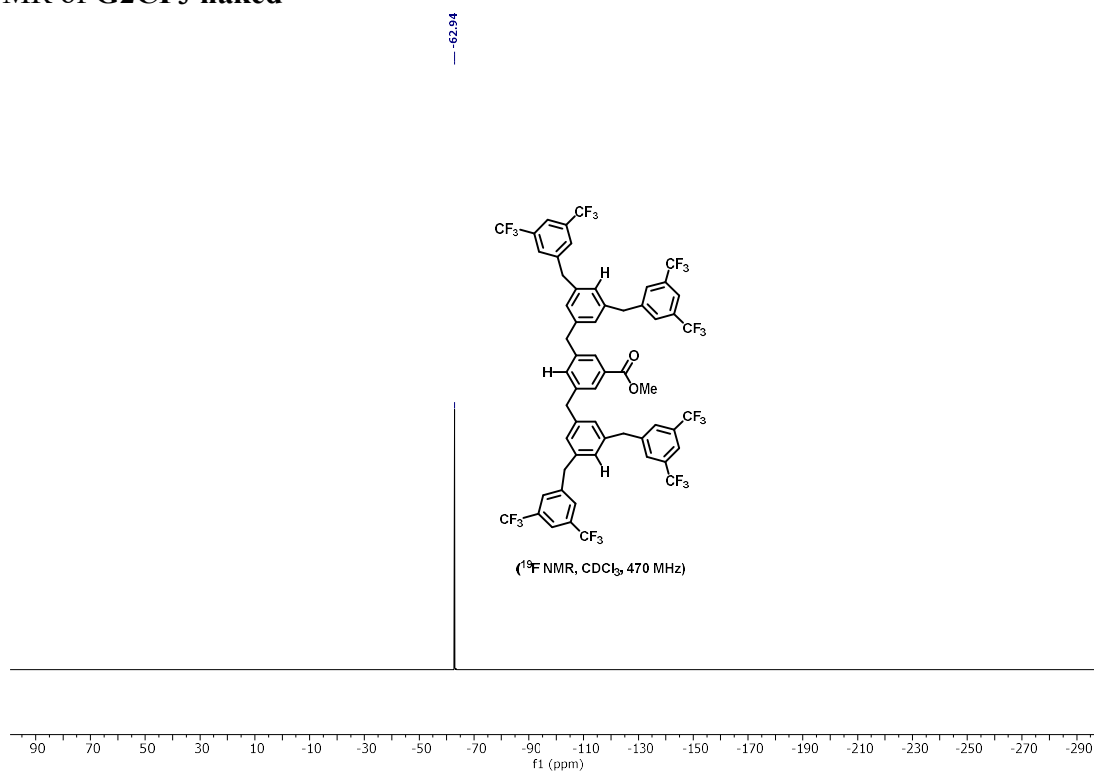
¹H NMR of G2CF₃-naked



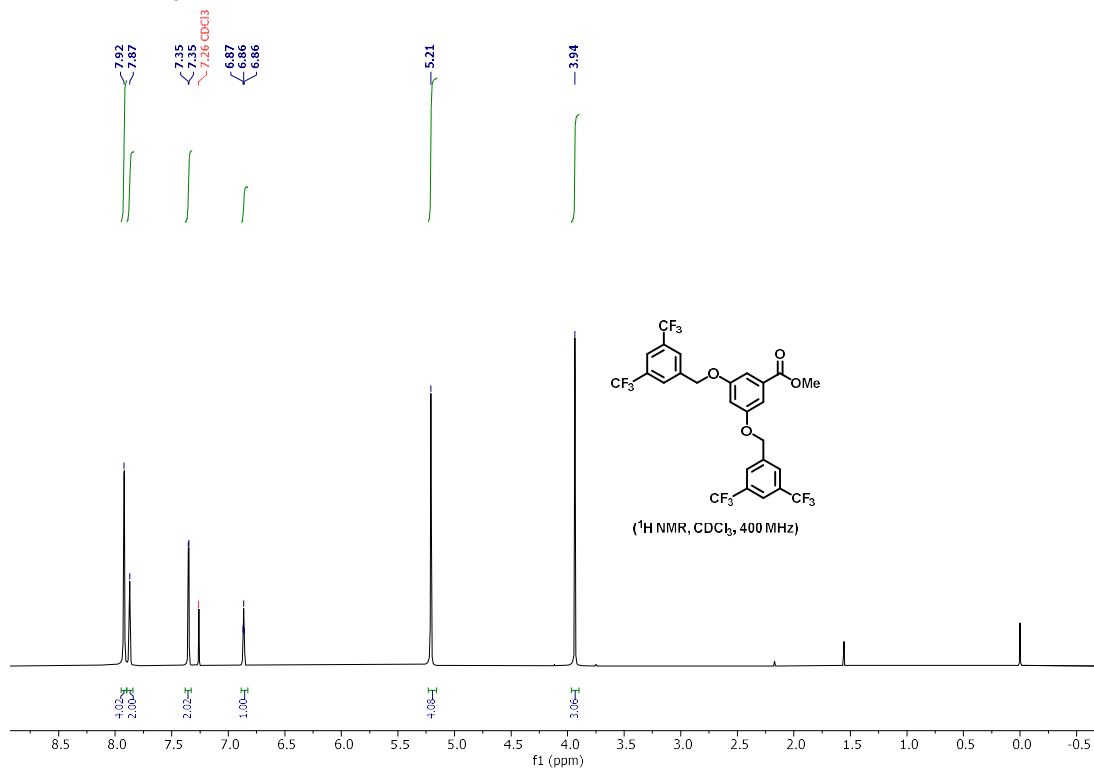
¹³C NMR of G2CF₃-naked



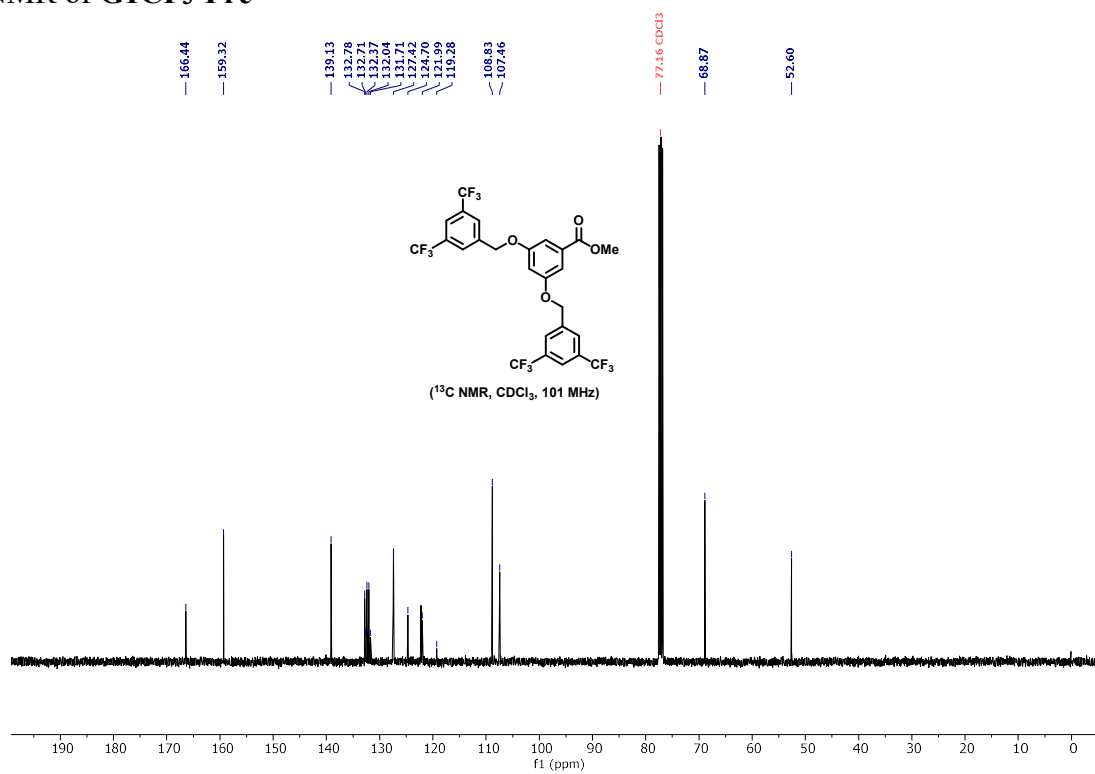
^{19}F NMR of **G2CF₃-naked**



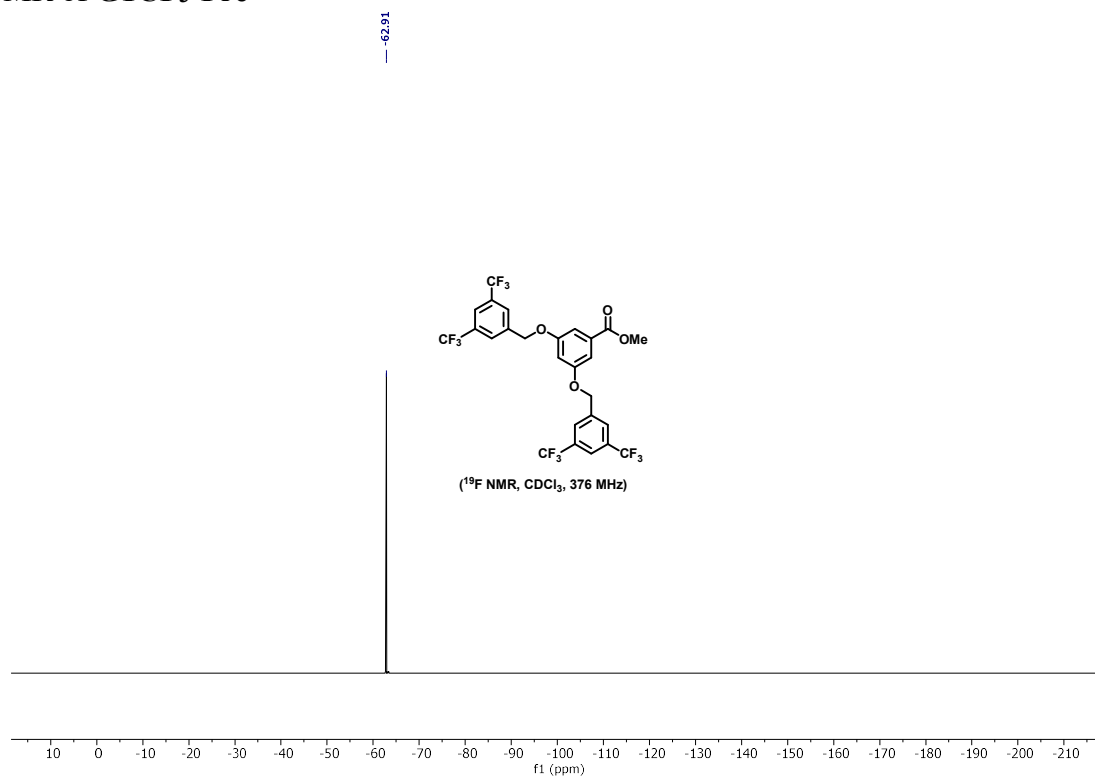
^1H NMR of **G1CF₃-Fre**



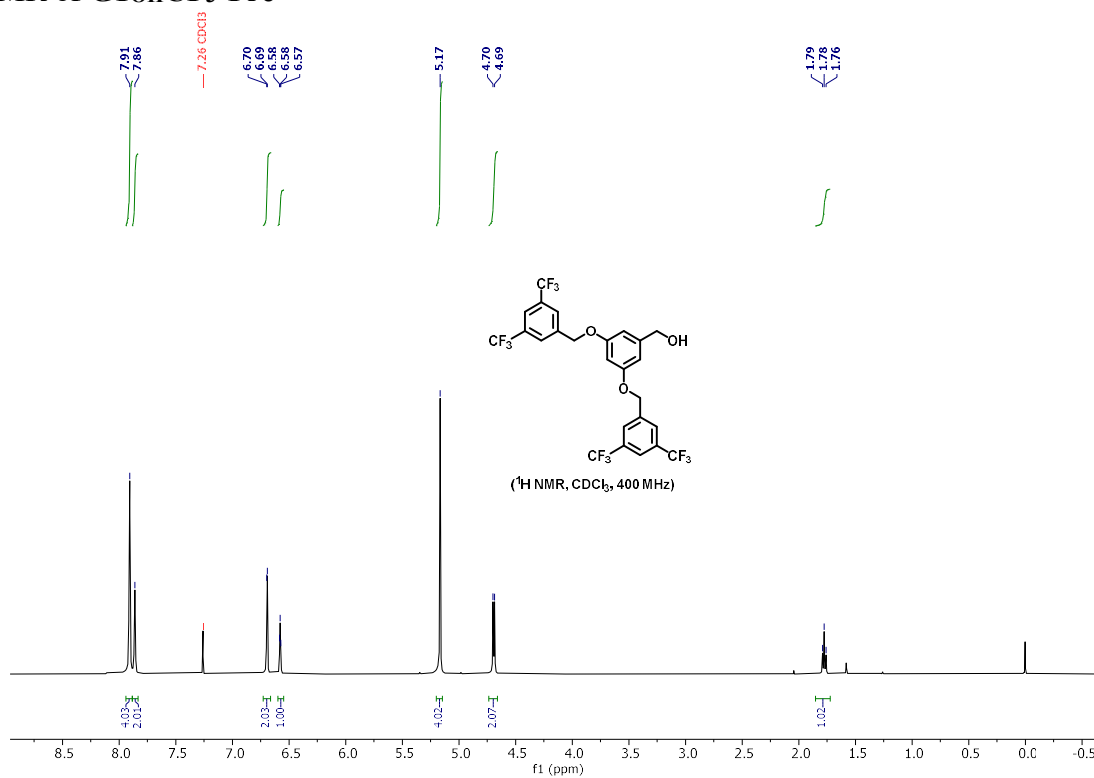
¹³C NMR of G1CF₃-Fre



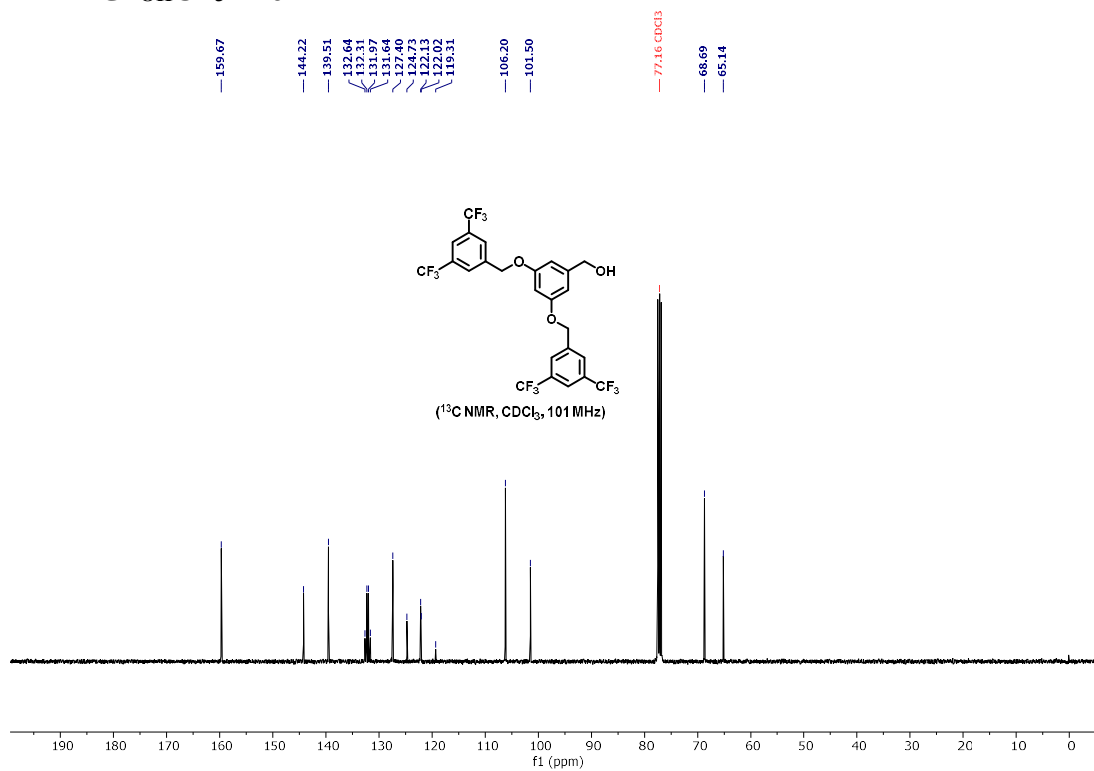
¹⁹F NMR of G1CF₃-Fre



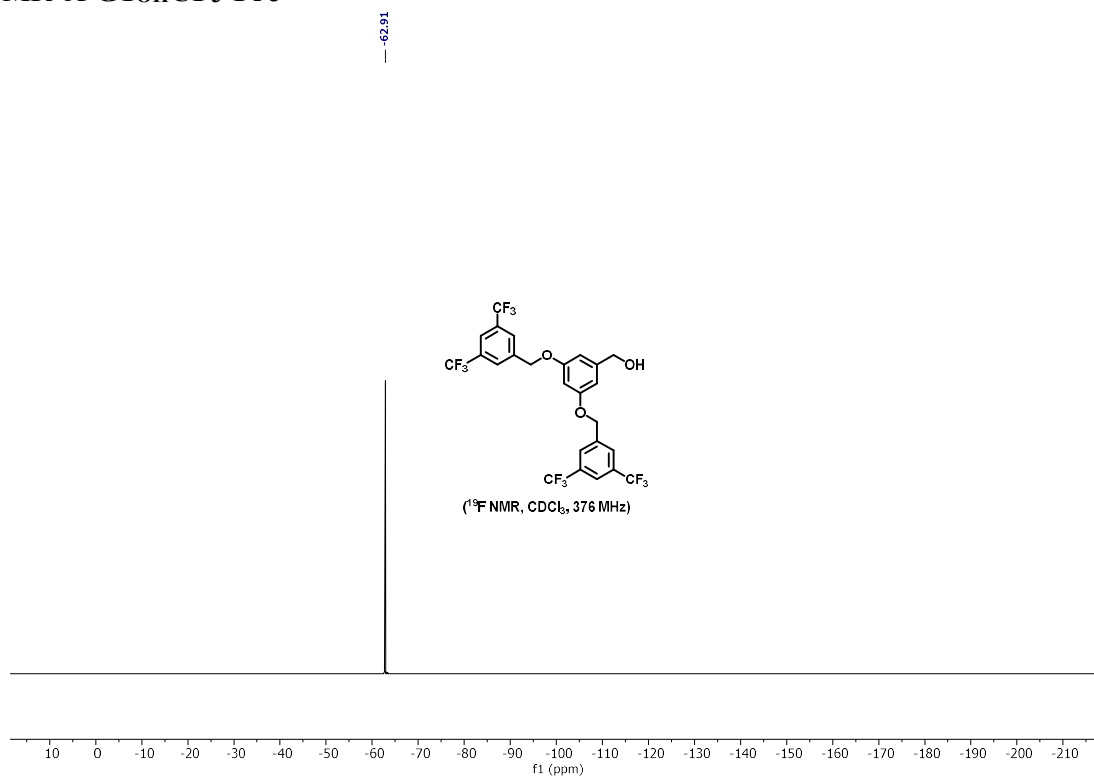
¹H NMR of G1_{OH}CF₃-Fre



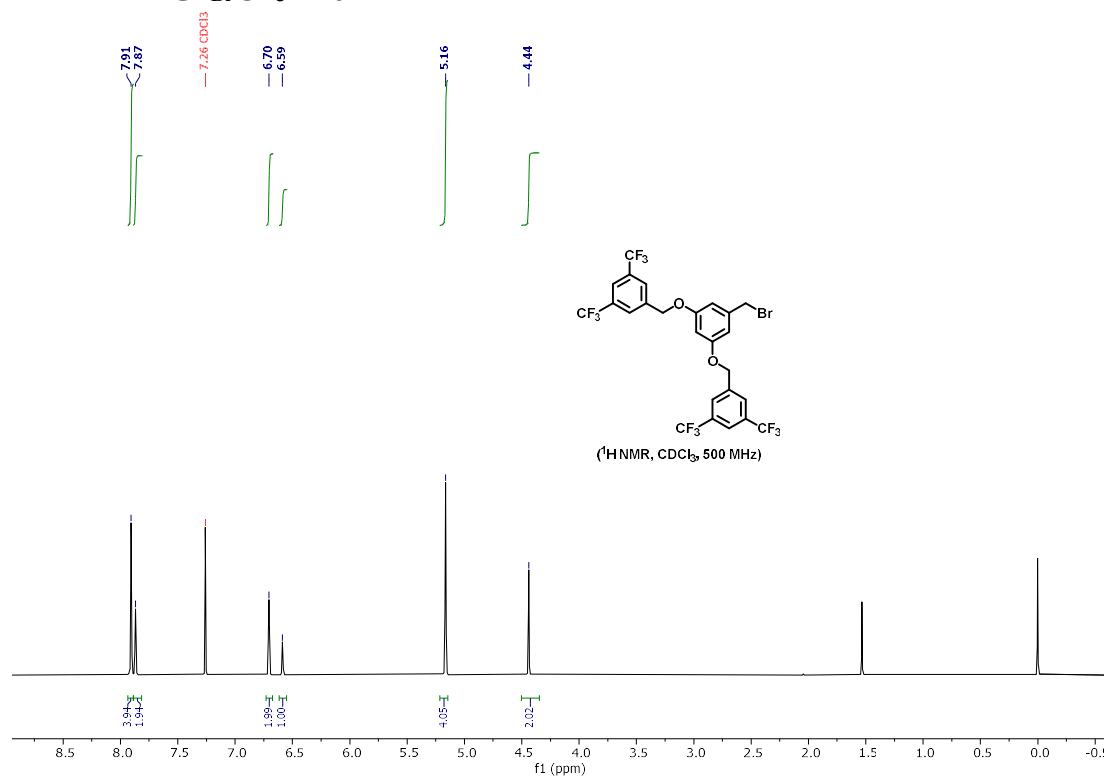
¹³C NMR of G1_{OH}CF₃-Fre



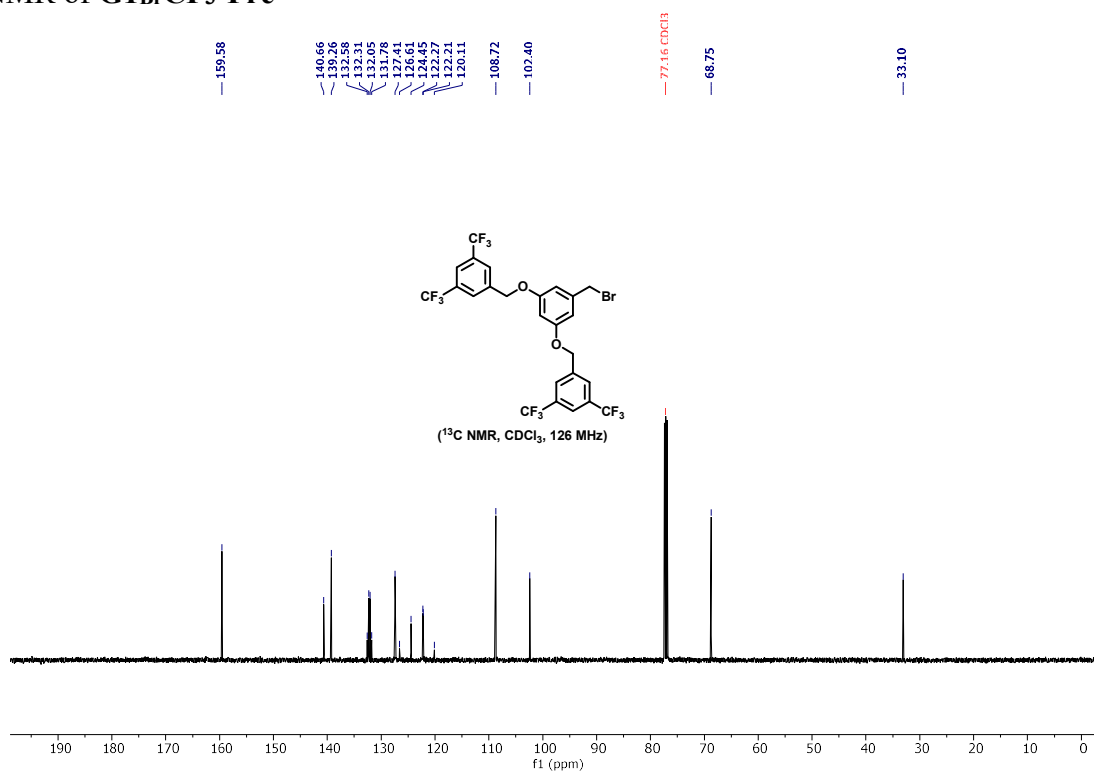
^{19}F NMR of $\text{G1}_{\text{OH}}\text{CF}_3\text{-Fre}$



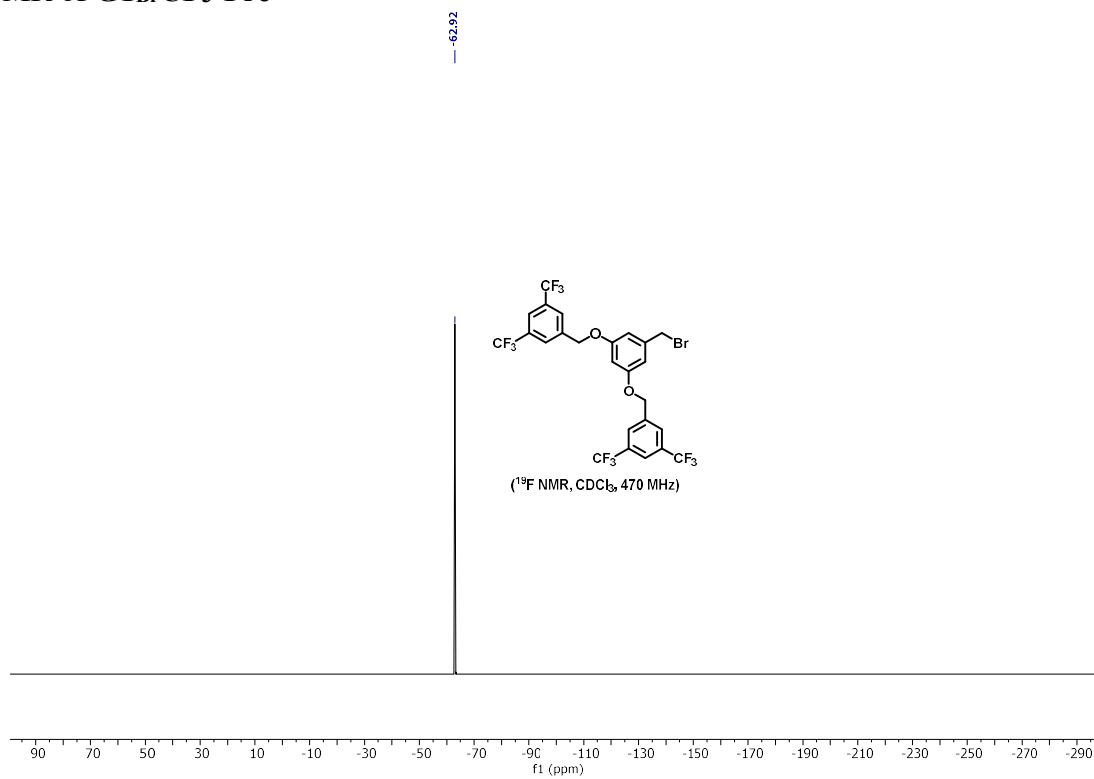
^1H NMR of $\text{G1}_{\text{Br}}\text{CF}_3\text{-Fre}$



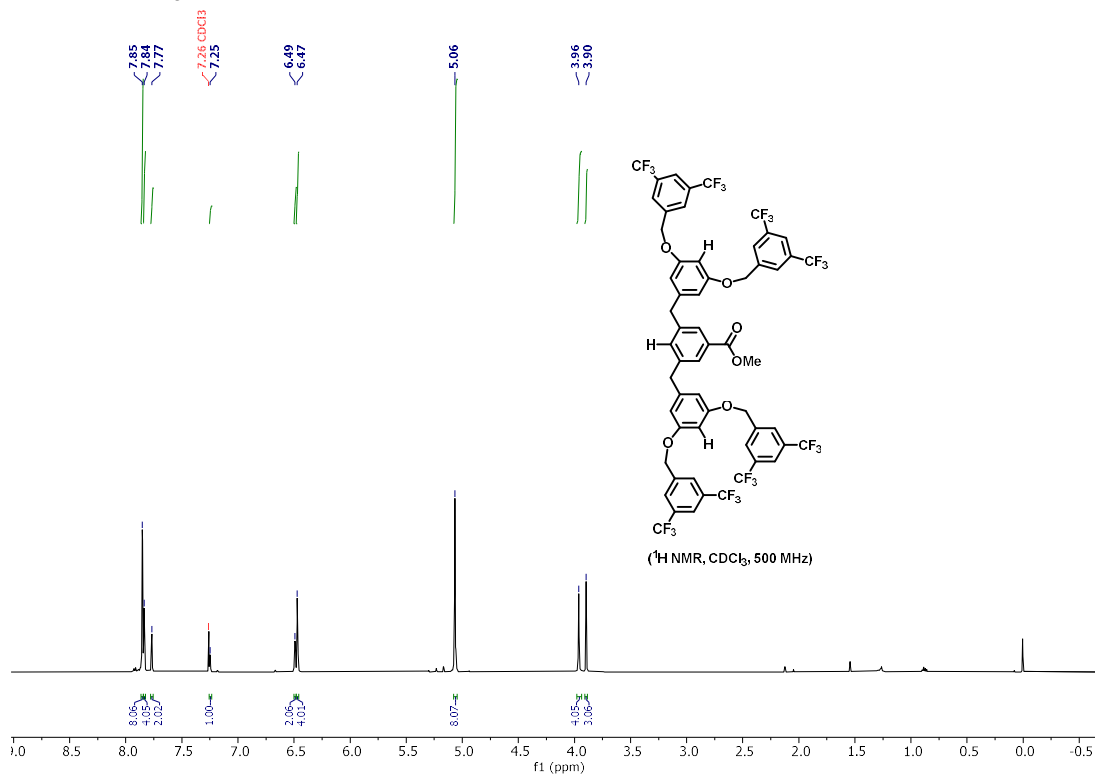
^{13}C NMR of $\text{G1BrCF}_3\text{-Fre}$



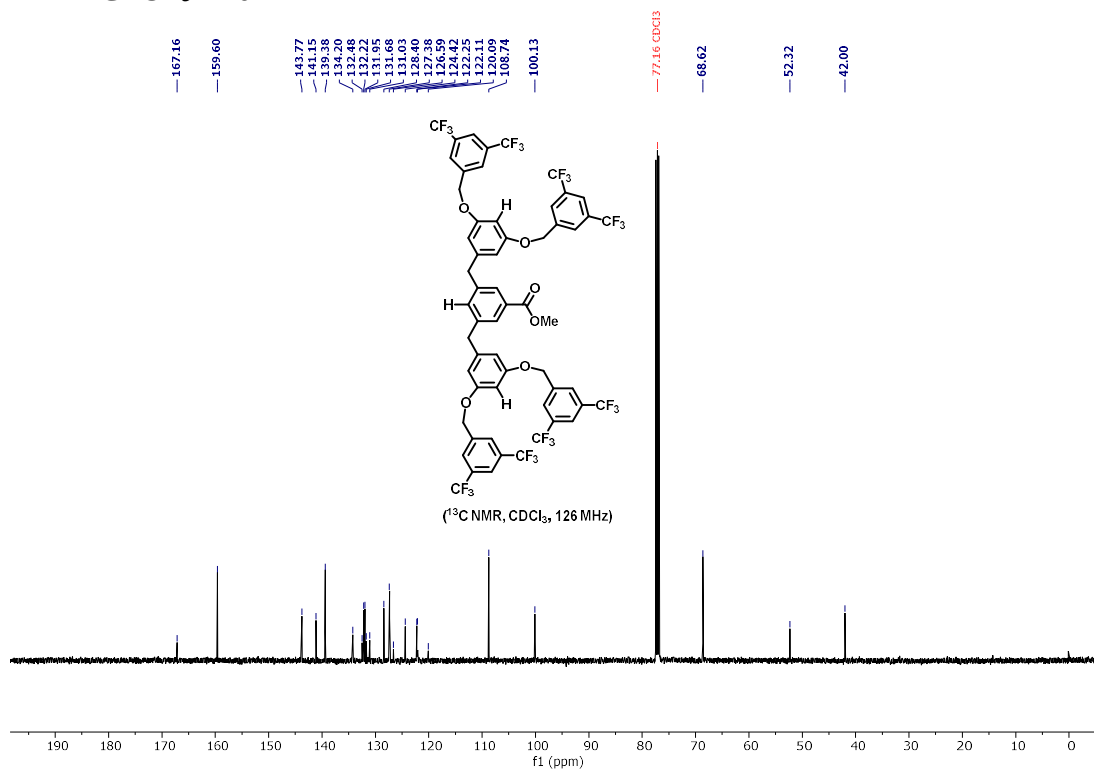
^{19}F NMR of $\text{G1BrCF}_3\text{-Fre}$



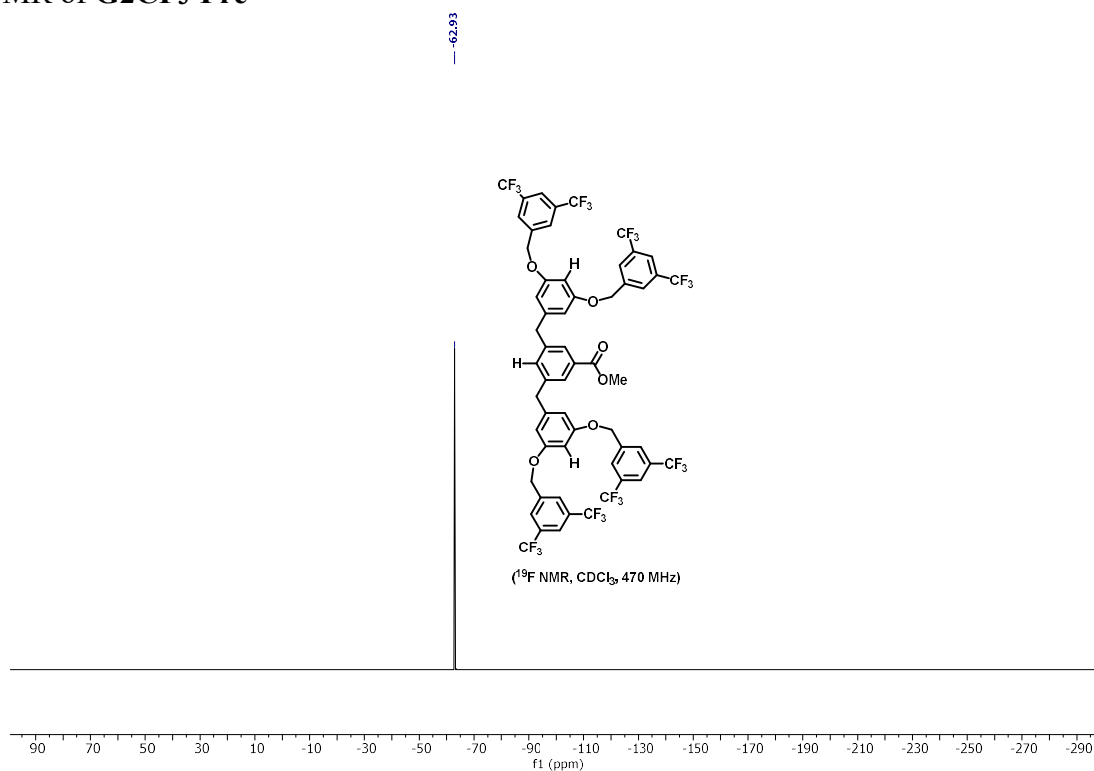
¹H NMR of G2CF₃-Fre



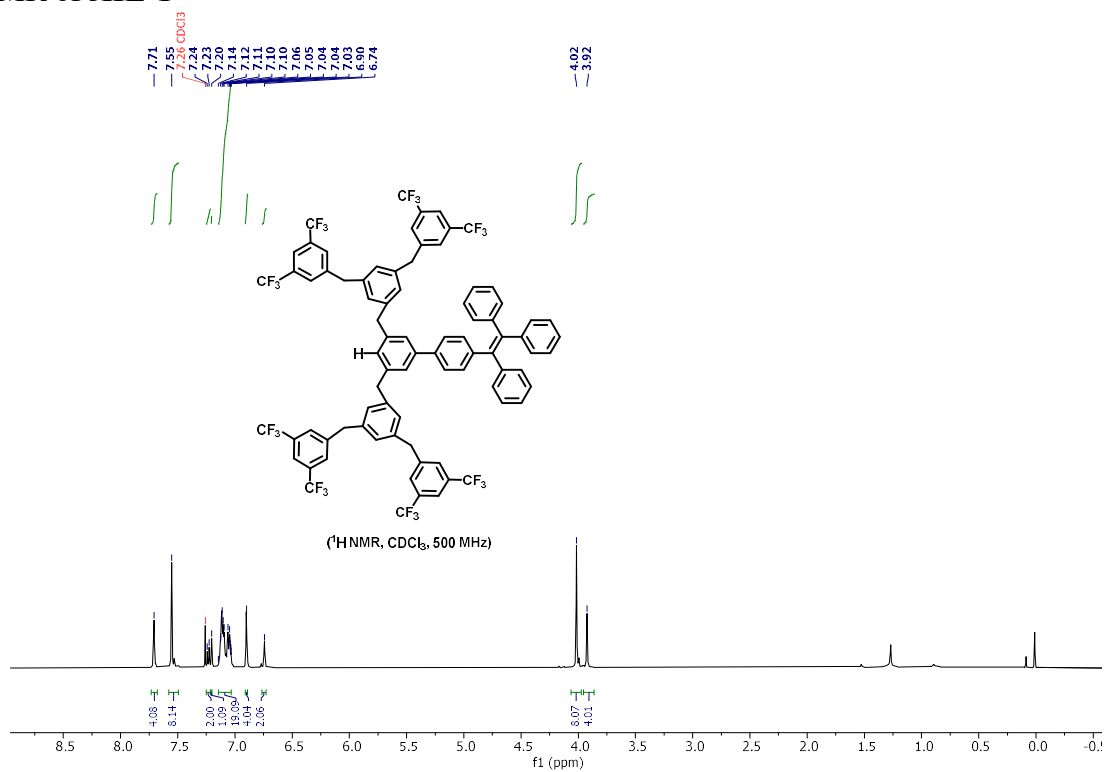
¹³C NMR of G2CF₃-Fre



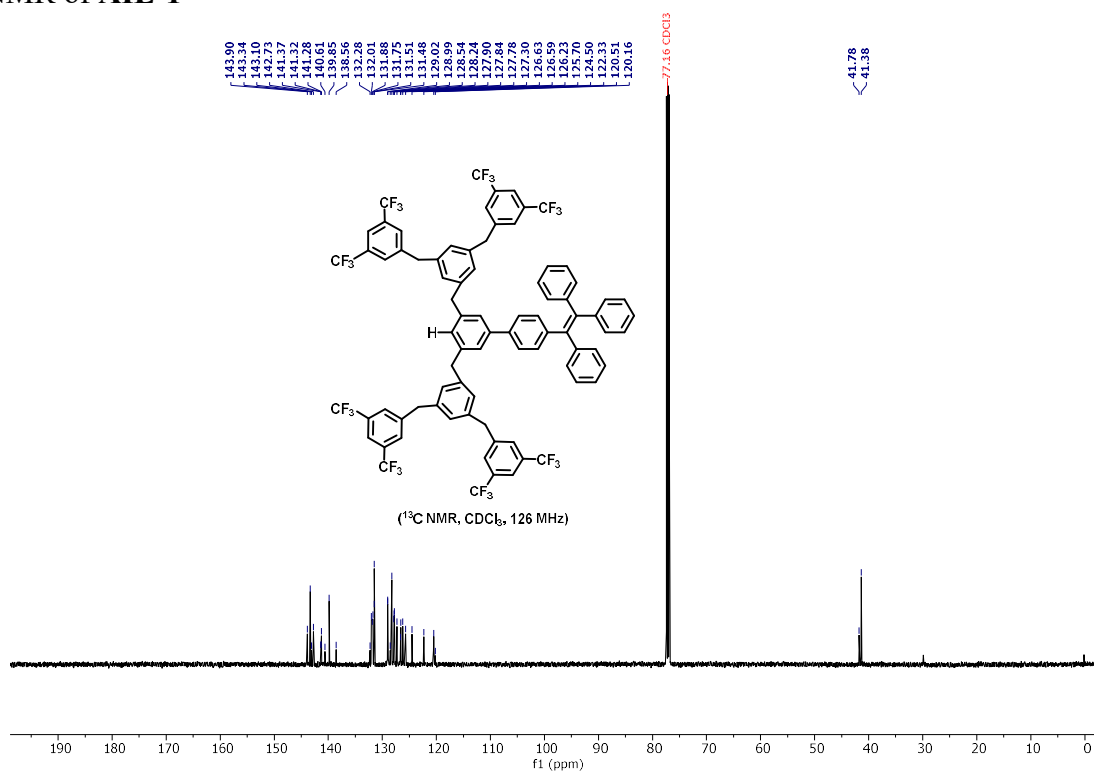
^{19}F NMR of G2CF₃-Fre



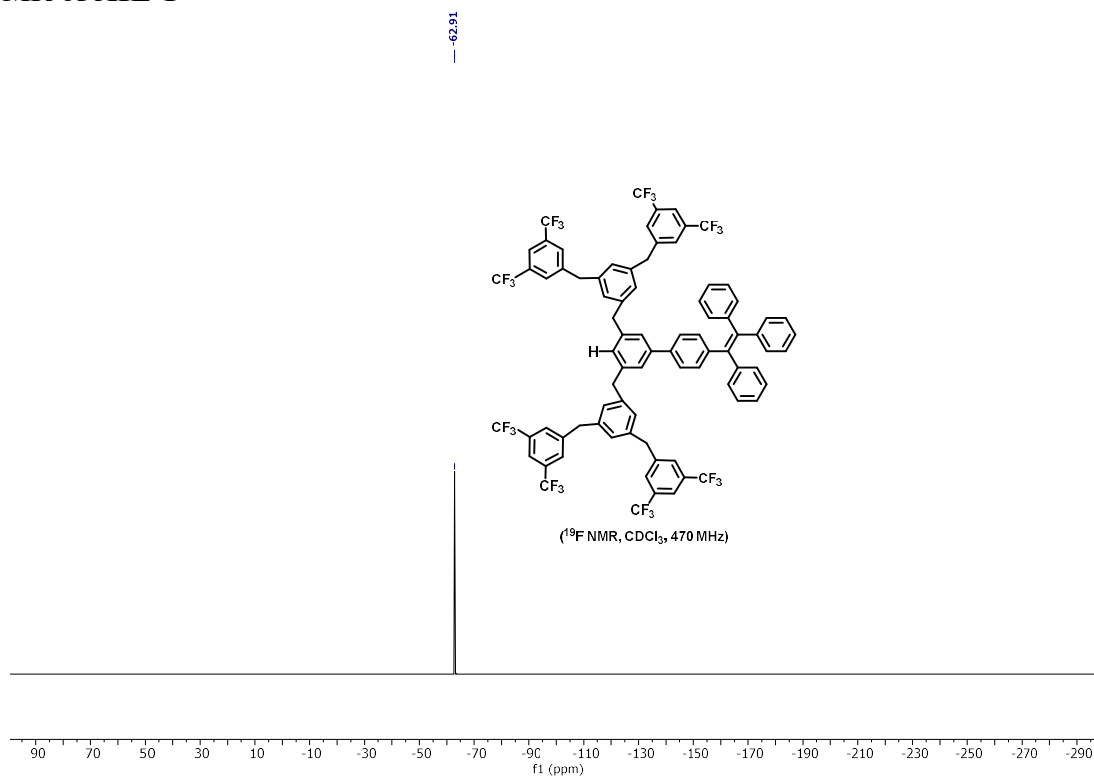
^1H NMR of AIE-1



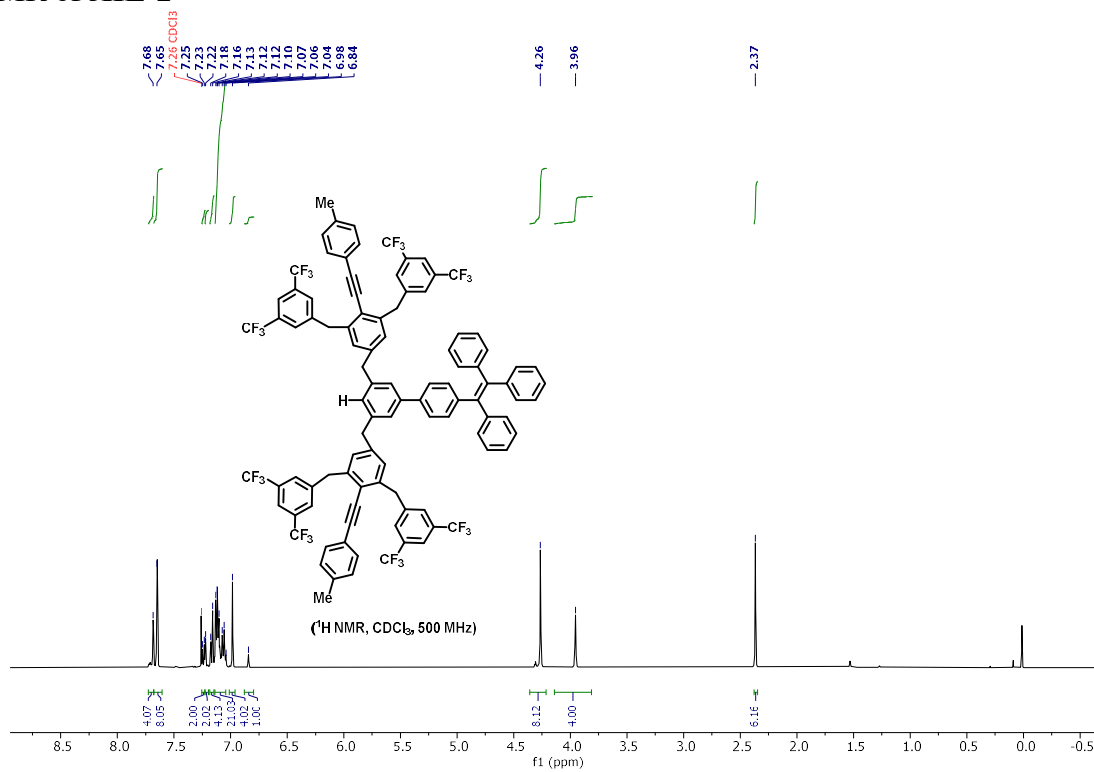
¹³C NMR of AIE-1



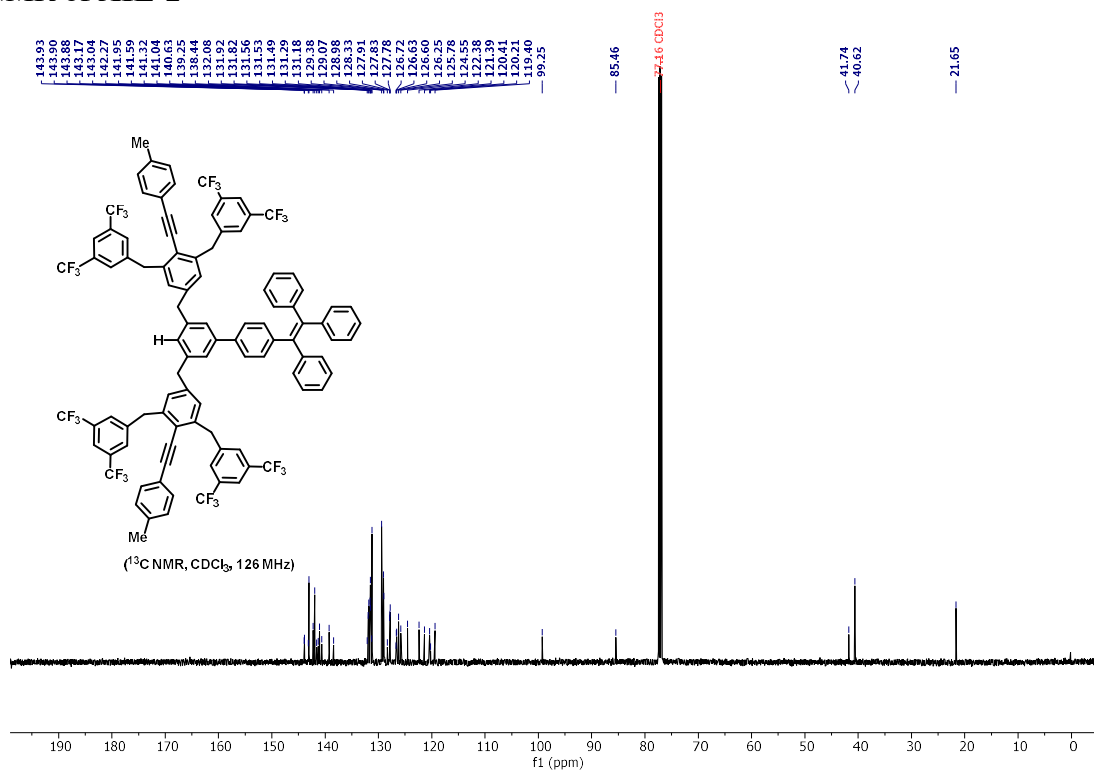
¹⁹F NMR of AIE-1



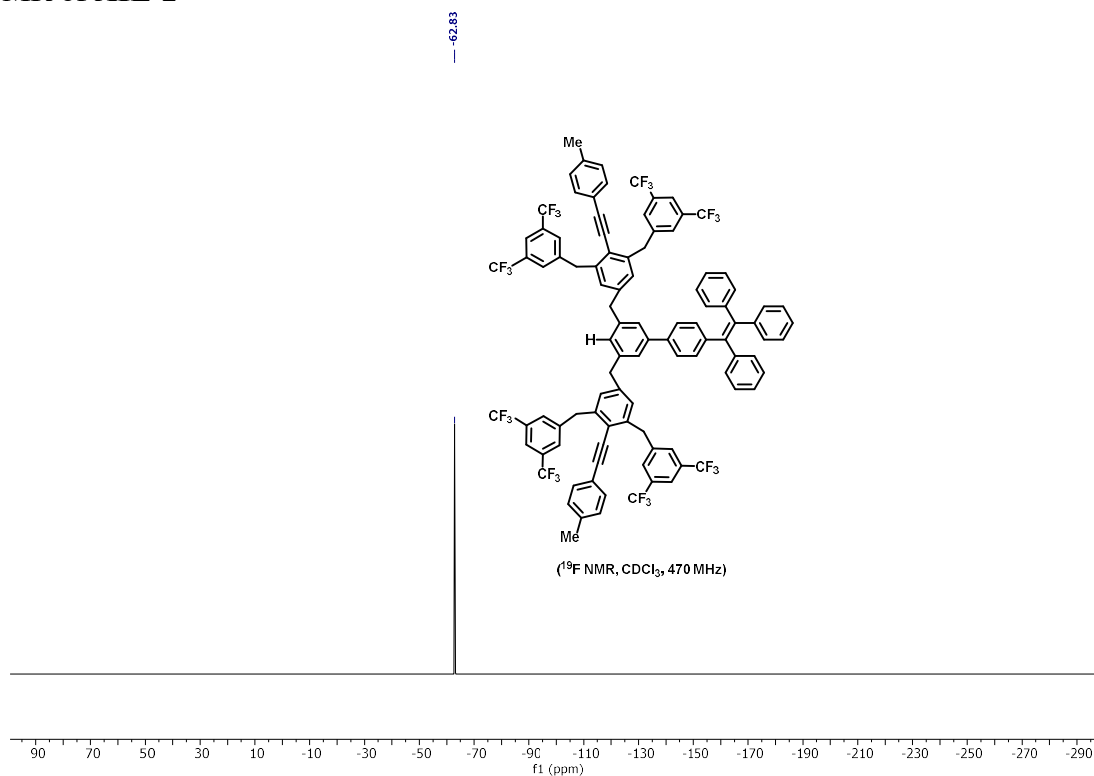
¹H NMR of AIE-2



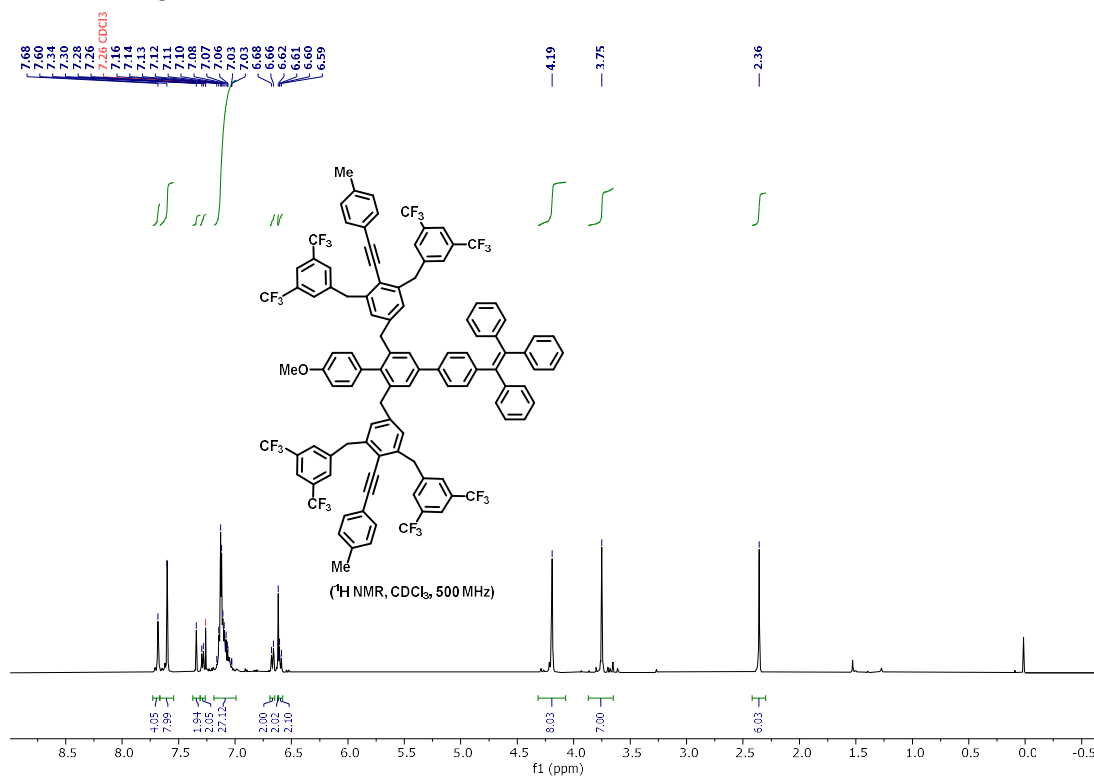
¹³C NMR of AIE-2



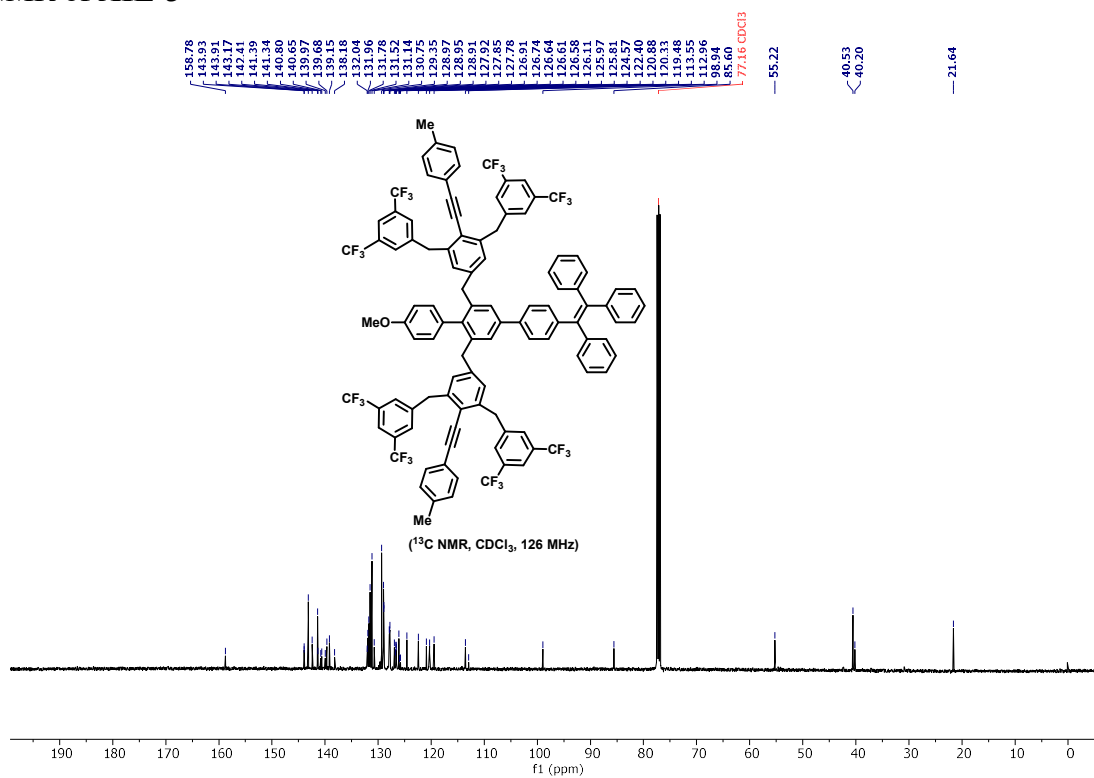
^{19}F NMR of AIE-2



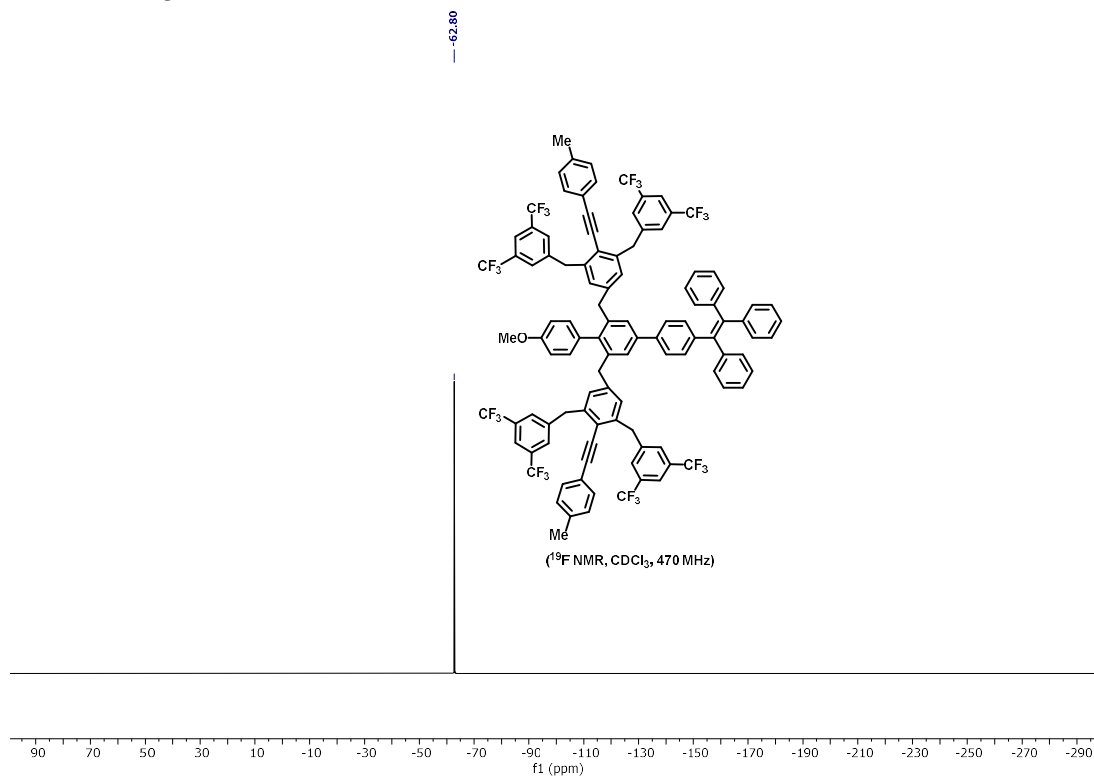
^1H NMR of AIE-3



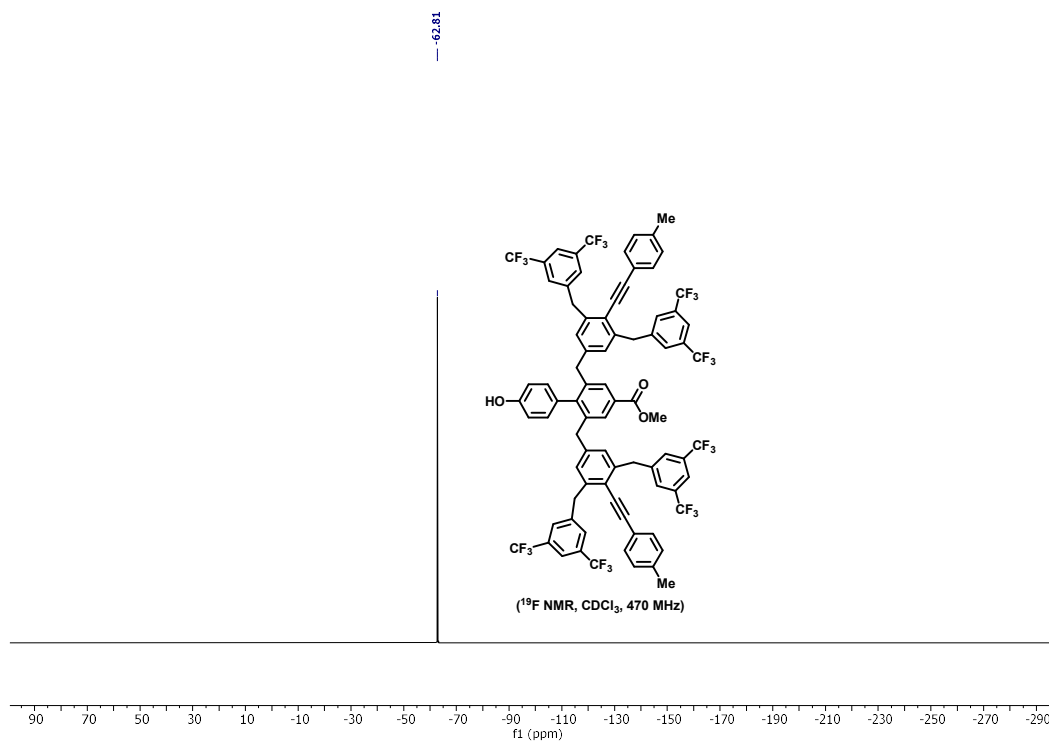
¹³C NMR of AIE-3



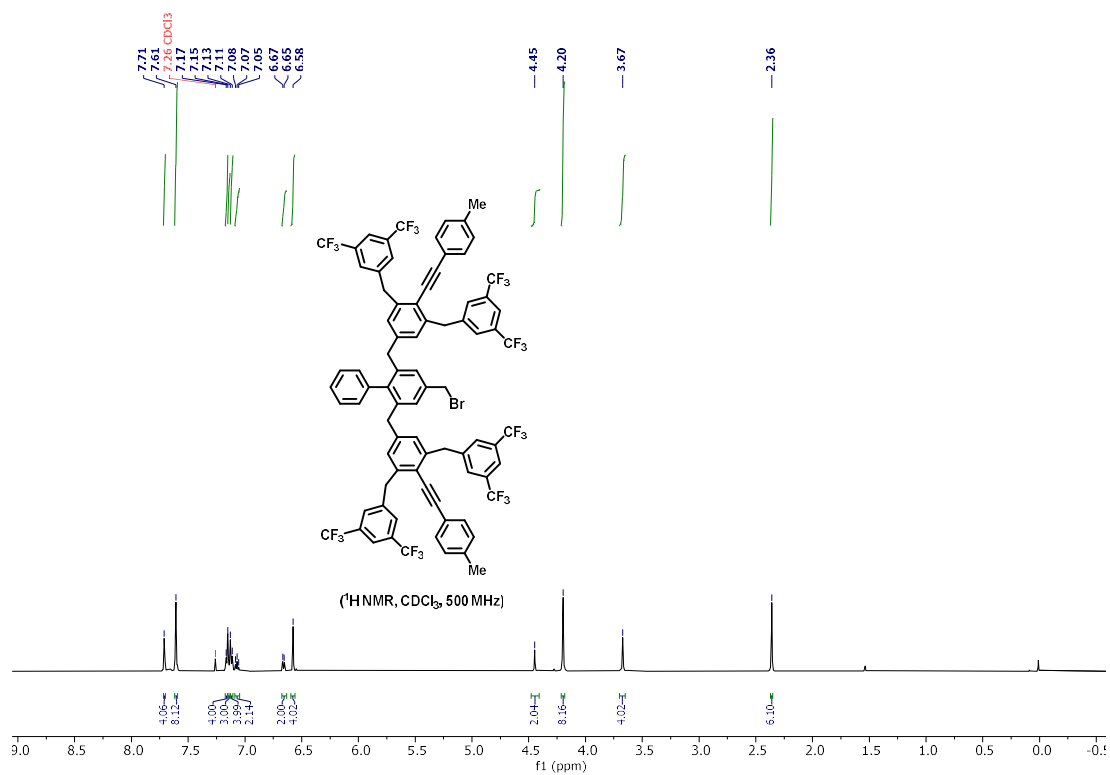
¹⁹F NMR of AIE-3



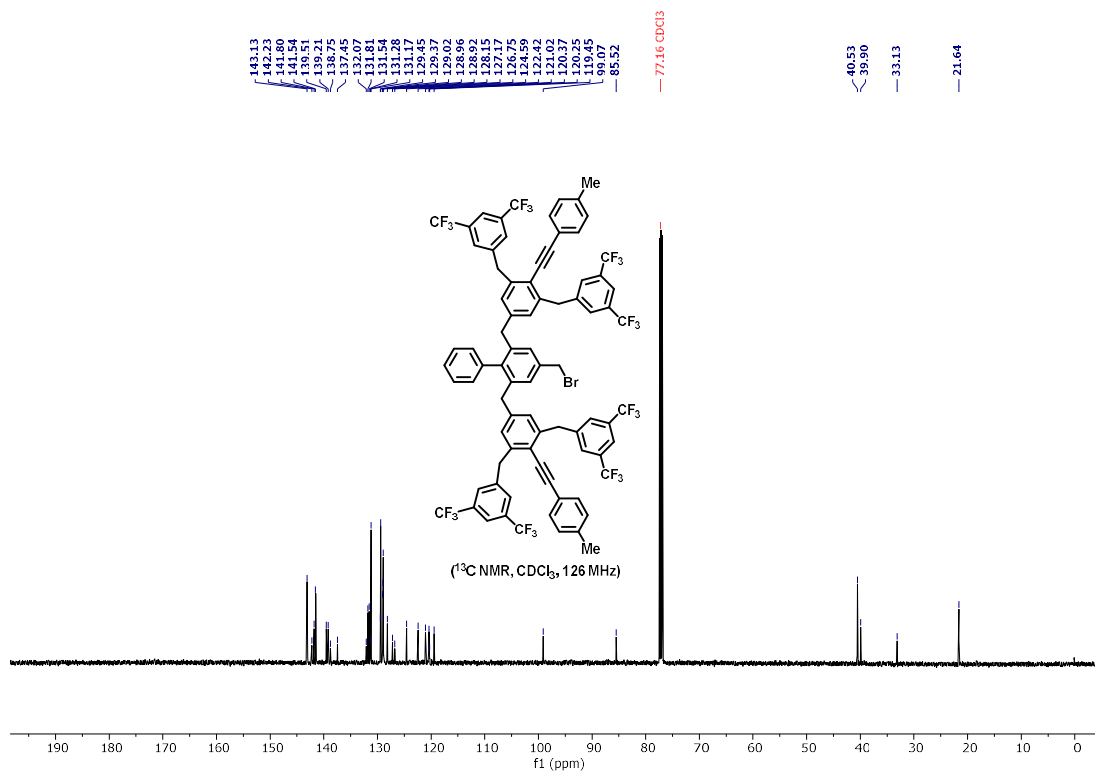
^{19}F NMR of $\text{G2CF}_3\text{2-mod}$



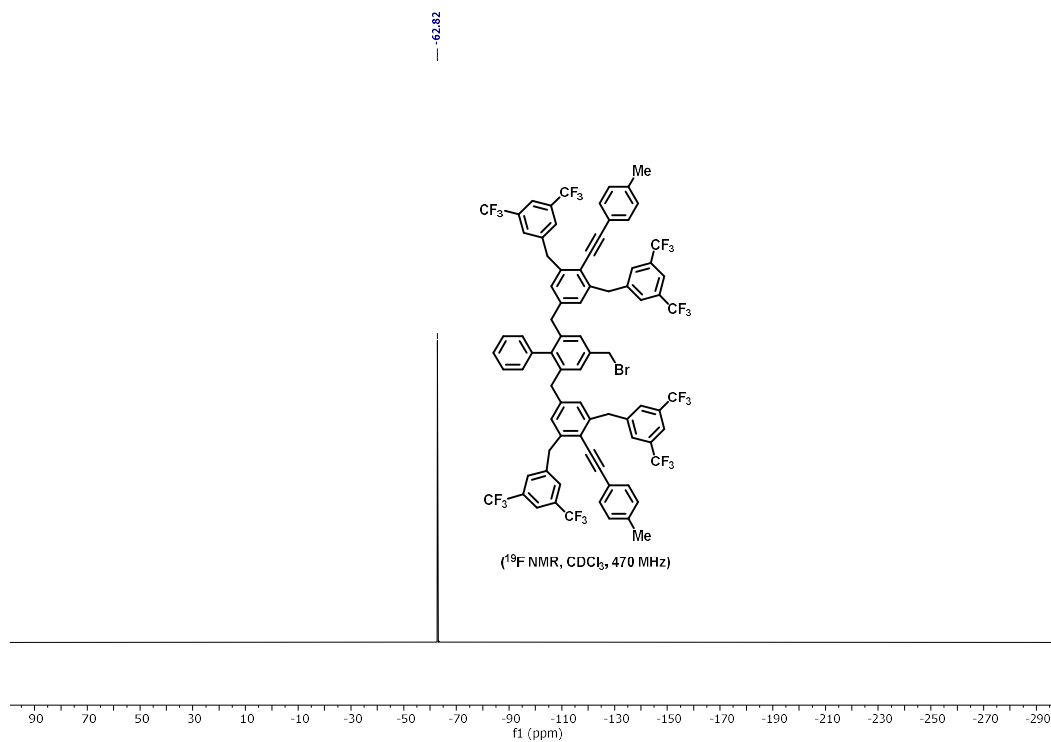
^1H NMR of $\text{G2BrCF}_3\text{3}$



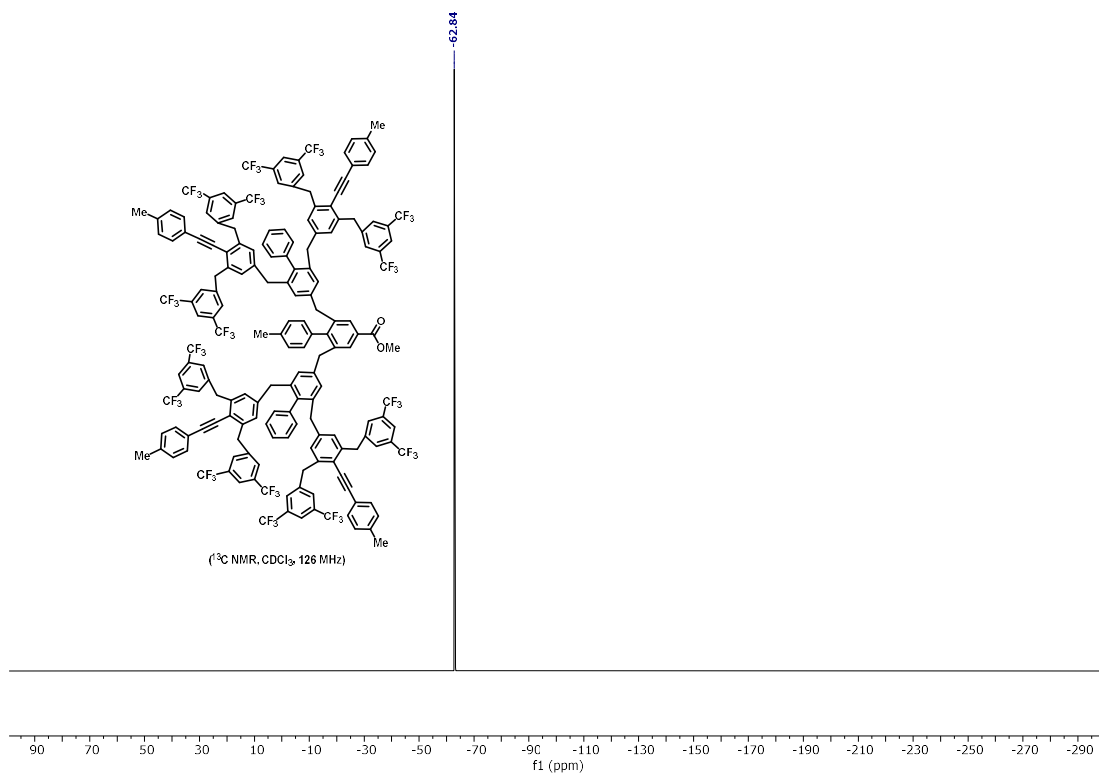
^{13}C NMR of $\text{G2}_{\text{Br}}\text{CF}_3\text{3}$



^{19}F NMR of $\text{G2}_{\text{Br}}\text{CF}_3\text{3}$

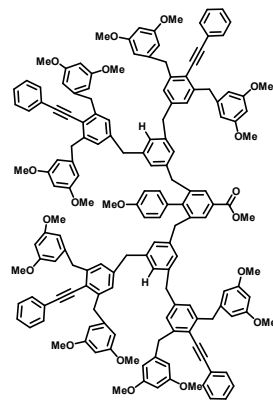
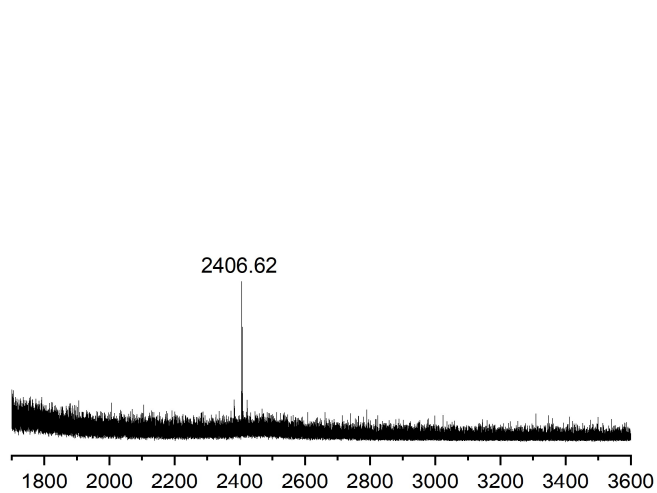


^{19}F NMR of G3CF₃



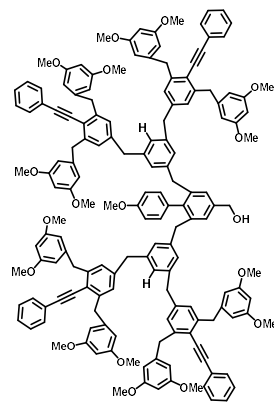
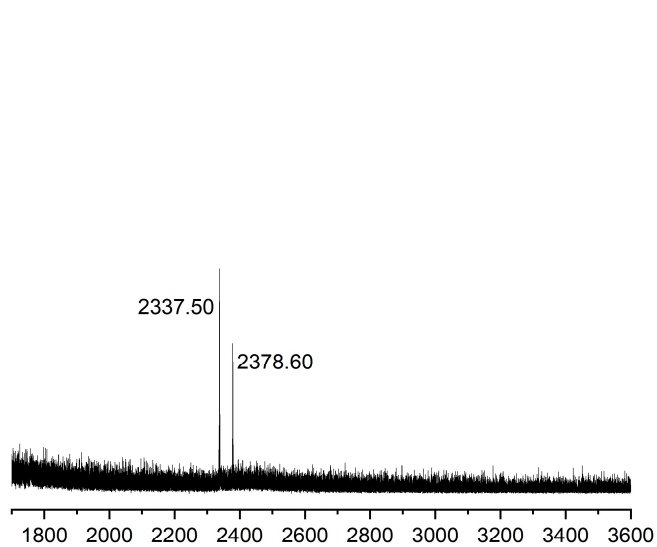
2.8. MALDI-TOF Data

G3OMe1



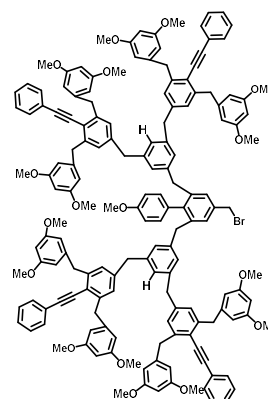
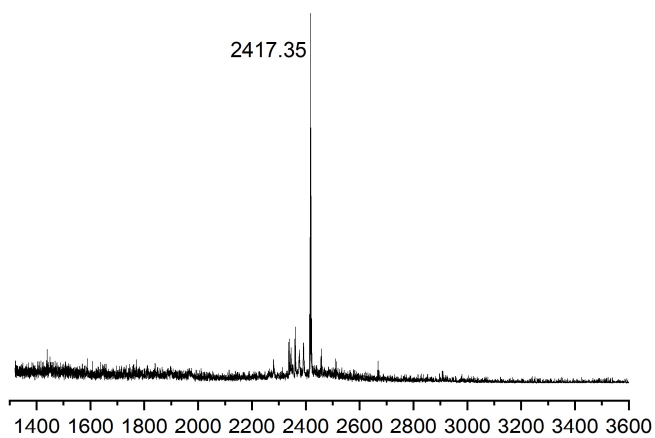
Chemical formula of $[M+Na]^+$: $C_{161}H_{146}NaO_{19}^+$
Exact Mass: 2406.04

G3OHOMe1



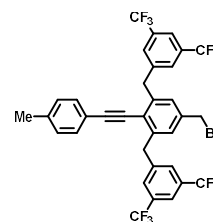
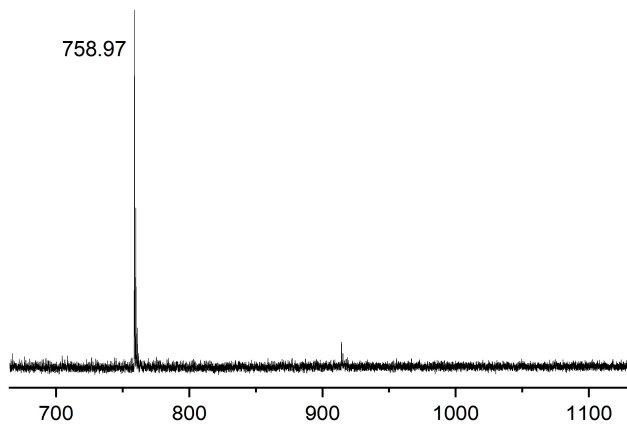
Chemical formula of $[M^+-H_2O]$: $C_{160}H_{144}O_{17}^+$
Exact Mass: 2337.04
Chemical formula of $[M+Na]^+$: $C_{160}H_{142}NaO_{18}^+$
Exact Mass: 2378.04

G3BrOMe1



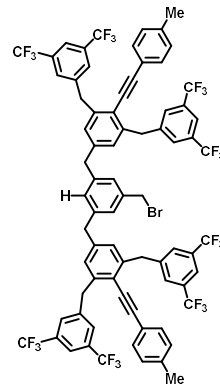
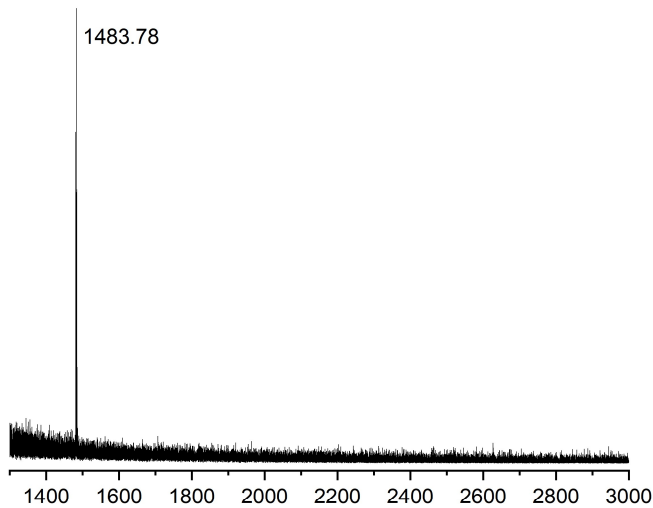
Chemical formula of $[M+H]^+$: $C_{160}H_{146}BrO_{17}^+$
Exact Mass: 2417.97

G1BrCF31



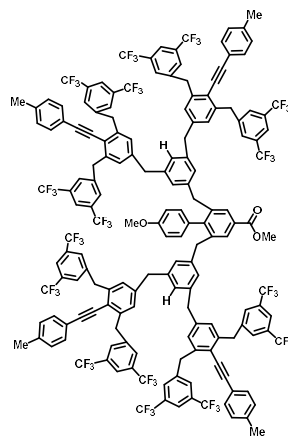
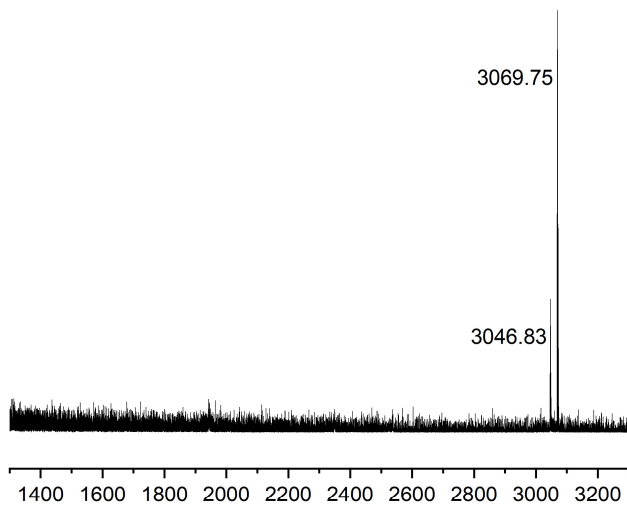
Chemical formula of $[M+Na]^+$: $C_{34}H_{21}BrF_{12}Na^+$
Exact Mass: 759.05

G2BrCF31



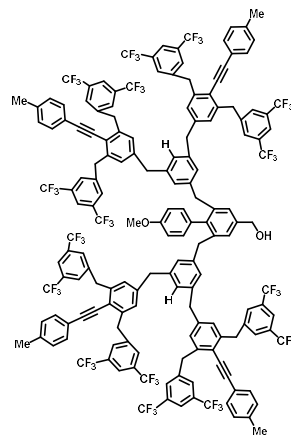
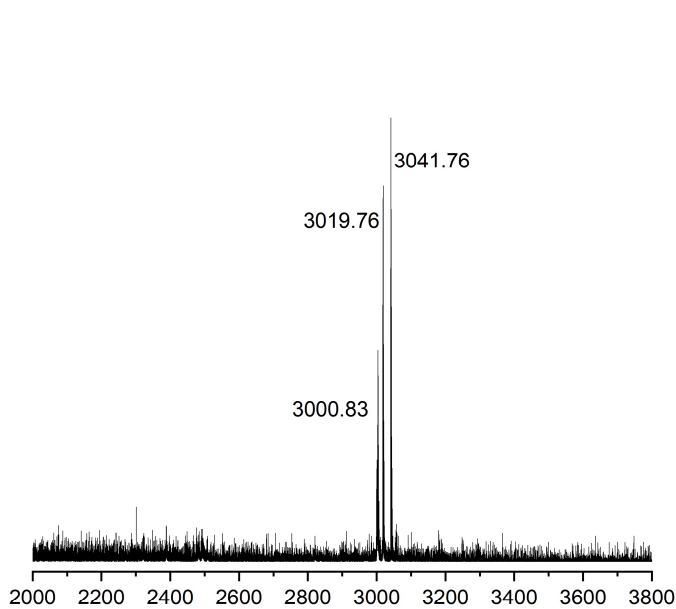
Chemical formula of [M+H]⁺: C₇₅H₄₈BrF₂₄⁺
Exact Mass: 1483.26

G3CF31



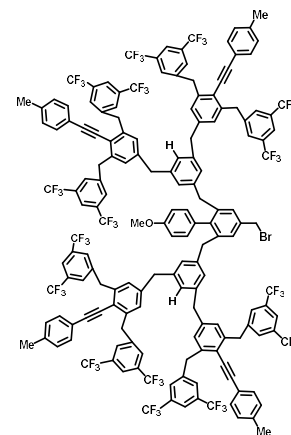
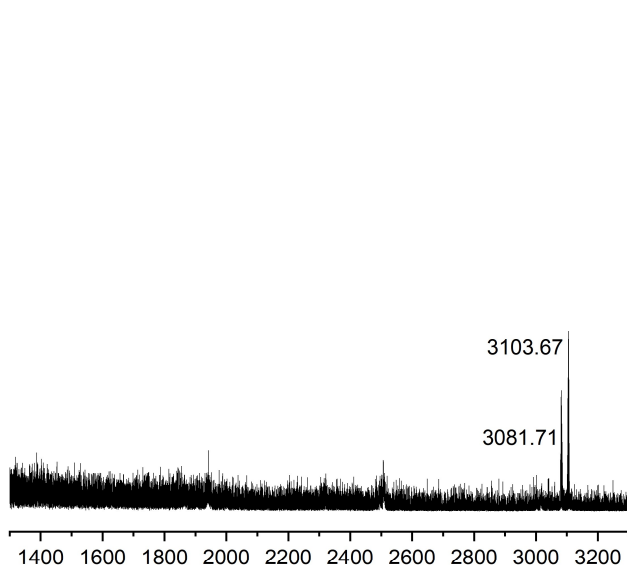
Chemical formula of [M]⁺: C₁₆₅H₁₀₈F₄₈O₃⁺
Exact Mass: 3046.74
Chemical formula of [M+Na]⁺: C₁₆₅H₁₀₈F₄₈NaO₃⁺
Exact Mass: 3069.73

G3_{OH}CF₃1



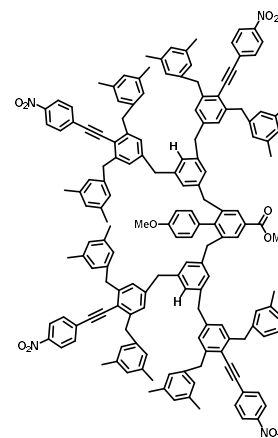
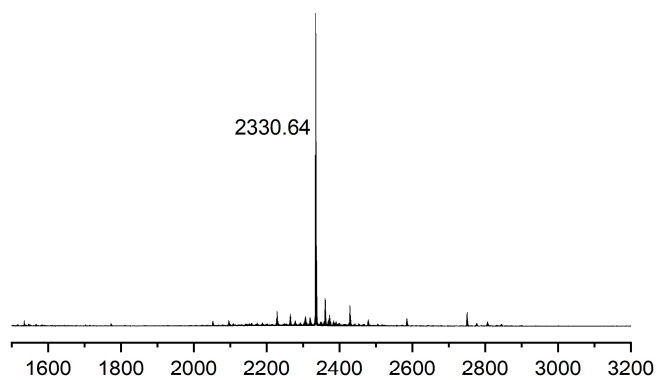
Chemical formula of [M⁺-H₂O]: C₁₆₄H₁₀₄F₄₅O⁺
Exact Mass: 3000.73
Chemical formula of [M+H⁺]: C₁₆₄H₁₀₇F₄₅O₂⁺
Exact Mass: 3019.75
Chemical formula of [M+Na⁺]: C₁₆₄H₁₀₆F₄₅NaO₂⁺
Exact Mass: 3041.73

G3_{Br}CF₃1



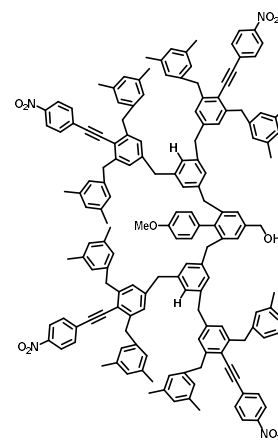
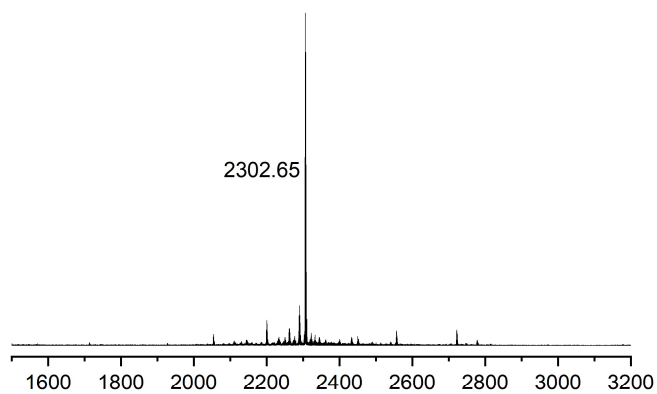
Chemical formula of [M+H⁺]: C₁₆₄H₁₀₅BrF₄₅O⁺
Exact Mass: 3081.67
Chemical formula of [M+Na⁺]: C₁₆₄H₁₀₅BrF₄₅NaO⁺
Exact Mass: 3103.65

G3Me2



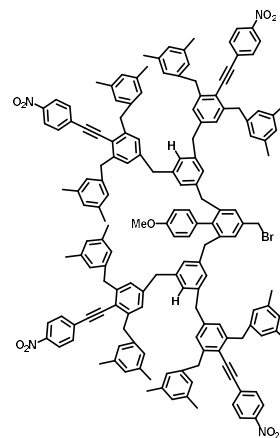
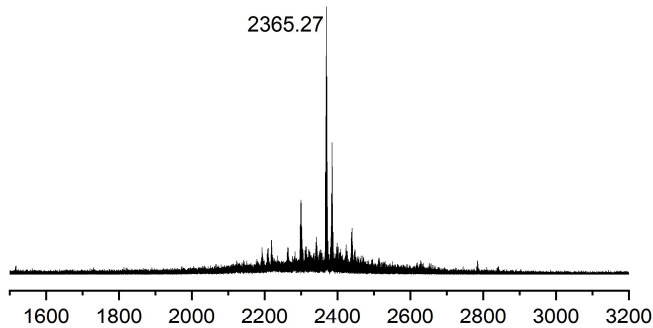
Chemical formula of $[M+Na]^+$: C₁₆₁H₁₄₂N₄NaO₁₁⁺
Exact Mass: 2330.06

G3OHMe2



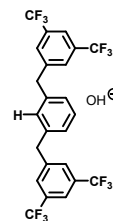
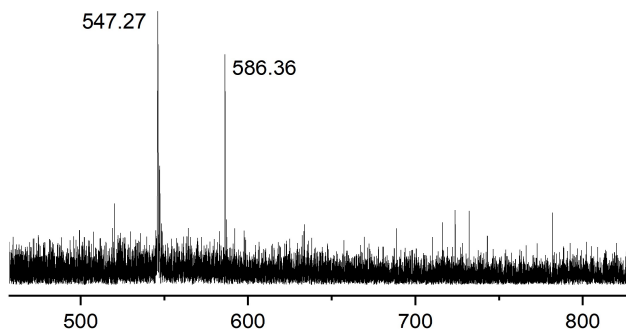
Chemical formula of $[M+Na]^+$: C₁₆₀H₁₄₂N₄NaO₁₀⁺
Exact Mass: 2302.06

G3BrMe2

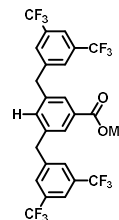


Chemical formula of [M+Na⁺]: C₁₆₀H₁₄₁BrN₄NaO₉⁺
Exact Mass: 2363.98

G1CF₃-naked

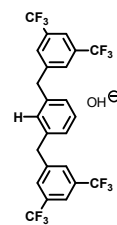
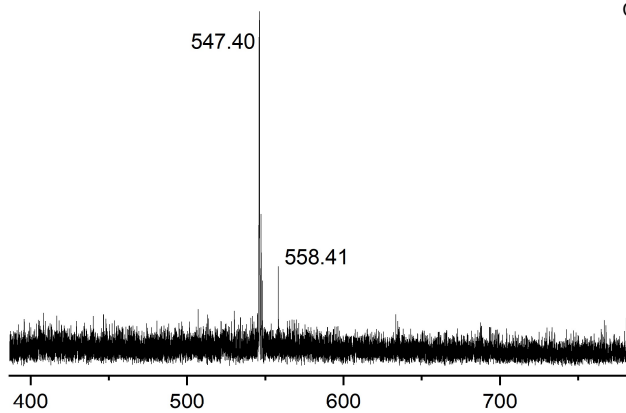


Chemical formula of [M-CH₂+OH⁻]: C₂₄H₁₅F₁₂O⁻
Exact Mass: 547.09

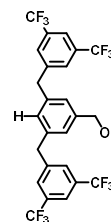


Chemical formula of [M-H⁻]: C₂₆H₁₅F₁₂O₂⁻
Exact Mass: 587.09

G1_{OH}CF₃-naked

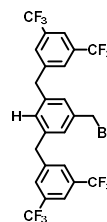
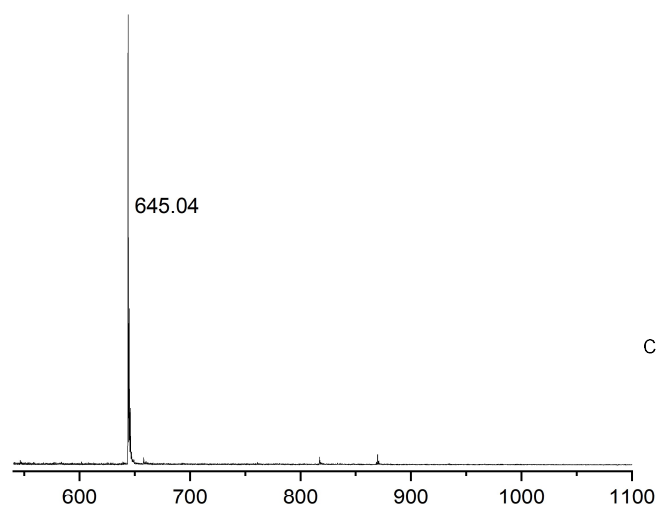


Chemical formula of [M-CH₂+OH]⁻: C₂₄H₁₅F₁₂O⁻
Exact Mass: 547.09



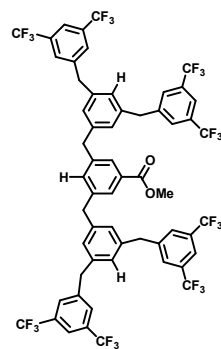
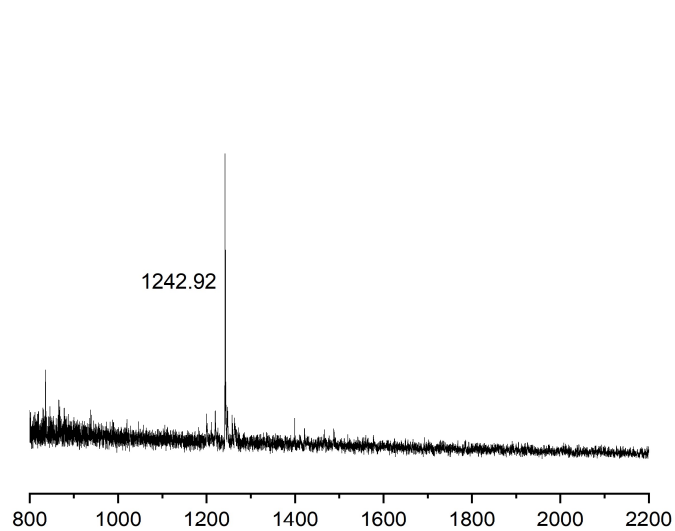
Chemical formula of [M-H]⁻: C₂₅H₁₅F₁₂O⁻
Exact Mass: 559.09

G1_{Br}CF₃-naked



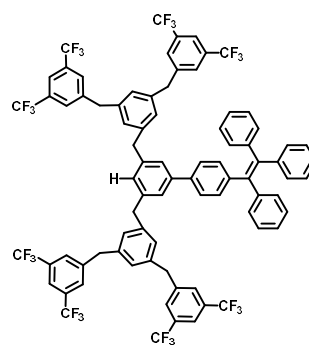
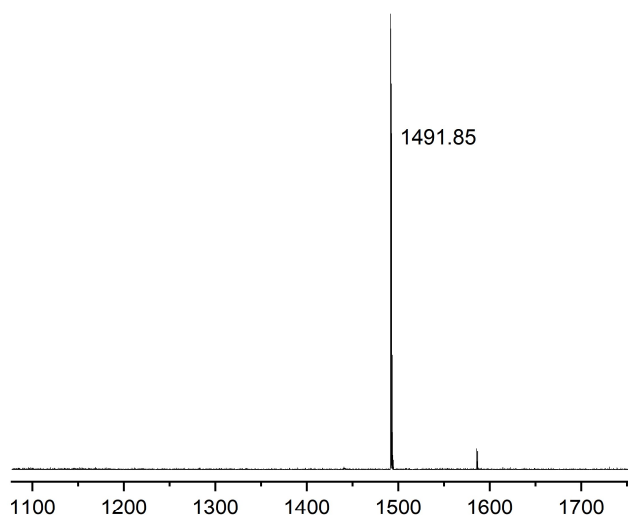
Chemical formula of [M+Na]⁺: C₂₅H₁₅BrF₁₂Na⁺
Exact Mass: 645.01

G2CF₃-naked



Chemical formula of [M+Na⁺]: C₅₈H₃₆F₂₄NaO₂⁺
Exact Mass: 1243.22

AIE-1



Chemical formula of [M⁺]: C₈₂H₅₂F₂₄⁺
Exact Mass: 1492.37

2.9. References

1. Saraswat, V.; Jacobberger, R. M.; Arnold, M. S. Materials science challenges to graphene nanoribbon electronics. *ACS Nano* **2021**, *15*, 3674-3708.
2. Yoon, K.-Y.; Dong, G. Liquid-phase bottom-up synthesis of graphene nanoribbons. *Mater. Chem. Front.* **2020**, *4*, 29-45.
3. For reviews on the applications of dendrimers, see: a) Li, L.; Deng, Y.; Zeng, Y.; Yan, B.; Deng, Y.; Zheng, Z.; Li, S.; Yang, Y.; Hao, J.; Xiao, X.; Wang, X. The application advances of dendrimers in biomedical field. *View* **2023**, *4*, 20230023. b) Yamamoto, K.; Imaoka, T.; Tanabe, M.; Kambe, T. New horizon of nanoparticle and cluster catalysis with dendrimers. *Chem. Rev.* **2019**, *120*, 1397-1437. c) Mignani, S.; Kazzouli, S. E.; Bousmina, M. M.; Majoral, J. -P. Dendrimer space exploration: an assessment of dendrimers/dendritic scaffolding as inhibitors of protein-protein interactions, a potential new area of pharmaceutical development. *Chem. Rev.* **2014**, *114*, 1327-1342. d) Astruc, D.; Boisselier, E.; Ornelas, C. Dendrimers designed for functions: from physical, photophysical, and supramolecular properties to applications in sensing, catalysis, molecular electronics, photonics, and nanomedicine. *Chem. Rev.* **2010**, *110*, 1857-1959.
4. Yoon, K.-Y.; Xue, Y.; Dong, G. Three-Step Synthesis of a Less-Aggregated Water-Soluble Poly (*p*-phenylene ethynylene) with *Meta* Side Chains via Palladium/Norbornene Cooperative Catalysis. *Macromolecules* **2019**, (4), 1663-1670.
5. Grzybowski, M.; Skonieczny, K.; Butenschön, H.; Gryko, D. T. Comparison of oxidative aromatic coupling and the Scholl reaction. *Angew. Chem. Int. Ed.* **2013**, *52*, 9900-9930.
6. Jassas, R. S.; Mughal, E. U.; Sadiq, A.; Alsantali, R. I.; Al-Rooqi, M. M.; Naeem, N.; Moussa, Z.; Ahmed, S. A. Scholl reaction as a powerful tool for the synthesis of nanographenes: a systematic review. *RSC Adv.* **2021**, *11*, 32158-32202.

7. Skraba-Joiner, S. L.; McLaughlin, E. C.; Ajaz, A.; Thamam, R.; Johnson, R. P. Scholl cyclizations of aryl naphthalenes: rearrangement precedes cyclization. *J. Org. Chem.* **2015**, *80*, 9578-9583.
8. Yang, W.; Lucotti, A.; Tommasini, M.; Chalifoux, W. A. Bottom-up synthesis of soluble and narrow graphene nanoribbons using alkyne benzannulations. *J. Am. Chem. Soc.* **2016**, *138*, 9137-9144.
9. Jänsch, D.; Ivanov, I.; Zagranjarski, Y.; Duznovic, I.; Baumgarten, M.; Turchinovich, D.; Li, C.; Bonn, M.; Müllen, K. Ultra-Narrow Low-Bandgap Graphene Nanoribbons from Bromoperylene—Synthesis and Terahertz-Spectroscopy. *Chem. Eur. J.* **2017**, *23*, 4870-4875.
10. For examples of benzyl deprotection, see: a) Okano, K.; Okuyama, K.; Fukuyama, T.; Tokuyama, H. Mild debenzoylation of aryl benzyl ether with BCl_3 in the presence of pentamethylbenzene as a non-Lewis-basic cation scavenger. *Synlett* **2008**, *13*, 1977-1980. b) Angibeaud, P.; Defaye, J.; Gadelle, A.; Utille, J. Mild deprotection of benzyl ether protective groups with ozone. *Synthesis* **1985**, *12*, 1123-1125. c) Mandal, P. K.; McMurray, J. S. Pd-C-induced catalytic transfer hydrogenation with triethylsilane. *J. Org. Chem.* **2007**, *72*, 6559-6601.
11. Feng, Y.; Liu, Z.-X.; Chen, H.; Fan, Q.-H. Functional supramolecular gels based on poly (benzyl ether) dendrons and dendrimers. *Chem. Commun.* **2022**, *58*, 8736-8753.
12. Feng, Y.; Liu, Z.-T.; Liu, J.; He, Y.-M.; Zheng, Q.-Y.; Fan, Q.-H. Peripherally dimethyl isophthalate-functionalized poly (benzyl ether) dendrons: a new kind of unprecedented highly efficient organogelators. *J. Am. Chem. Soc.* **2009**, *131*, 7950-7951.
13. Feng, Y.; Liu, Z. X.; Chen, H.; Yan, Z. C.; He, Y. M.; Liu, C. Y.; Fan, Q. H. A Systematic Study of Peripherally Multiple Aromatic Ester-Functionalized Poly (benzyl ether) Dendrons for

the Fabrication of Organogels: Structure–Property Relationships and Thixotropic Property. *Chem. Eur. J.* **2014**, *20*, 7069-7082.

14. Feng, Y.; Liu, Z.; Wang, L.; Chen, H.; He, Y.; Fan, Q. Poly (benzyl ether) dendrons without conventional gelation motifs as a new kind of effective organogelators. *Chin. Sci. Bull.* **2012**, *57*, 4289-4295.

15. For selected reviews on AIE effect, see: a) Mei, J.; Leung, N. L. C.; Kwok, R. T. K.; Lam, J. W. Y.; Tang, B. J. Aggregation-Induced Emission, Together We Shine, United We Soar! *Chem. Rev.* **2015**, *115*, 11718-11940. b) Suman, G. R.; Pandey, M.; Chakravarthy, A. S. J. Review on new horizons of aggregation induced emission: from design to development. *Mater. Chem. Front.* **2021**, *5*, 1541-1584. c) Zhang, G.; Fu, X.; Zhou, D.; Hu, R.; Zin, A.; Tang, B. Z. Smart aggregation-induced emission polymers: Preparation, properties and bio-applications. *Smart Mol.* **2023**, *1*, e20220008.

16. Dong, Y.; Lam, J. W.; Qin, A.; Liu, J.; Li, Z.; Tang, B. Z.; Sun, J.; Kwok, H. S. Aggregation-induced emissions of tetraphenylethene derivatives and their utilities as chemical vapor sensors and in organic light-emitting diodes. *Appl. Phys. Lett.* **2007**, *91*, 011111.

17. Ma, S.; Du, S.; Pan, G.; Dai, S.; Xu, B.; Tian, W. Organic molecular aggregates: From aggregation structure to emission property. *Aggregate* **2021**, *2*, e96.

18. Li, Y.; Zou, H.; Gong, J.; Xiang, J.; Luo, T.; Quan, J.; Wang, G.; Yang, Z. Efficient synthesis of maleimides and carbazoles via Zn(OTf)₂-catalyzed tandem annulations of isonitriles and allenic esters. *Org. Lett.* **2007**, *9*, 4057-4060.

19. Mahmud, I. M.; Zhou, N.; Wang, L.; Zhao, Y. Triazole-linked dendro [60] fullerenes: modular synthesis via a ‘click’ reaction and acidity-dependent self-assembly on the surface. *Tetrahedron* **2008**, *64*, 11420-11432.

20. Yu, T.; Chai, H.; Zhao, Y.; Zhang, C.; Liu, P.; Fan, D. Synthesis, crystal structure and photoluminescence of phosphorescent copper (I) complexes containing hole-transporting carbazoly moiety. *Spectrochim. Acta A Mol. Biomol. Spectrosc.* **2013**, *109*, 179-185.
21. Liu, Y.; Qin, A.; Chen, X.; Shen, X. Y.; Tong, L.; Hu, R.; Sun, J. Z.; Tang, B. Z. Specific Recognition of β -Cyclodextrin by a Tetraphenylethene Luminogen through a Cooperative Boronic Acid/Diol Interaction. *Chem. Eur. J.* **2011**, *17*, 14736-14740.
22. Biesen, L.; May, L.; Nirmalanathan-Budau, N.; Hoffmann, K.; Resch-Genger, U.; Müller, T. J. Communication of Bichromophore Emission upon Aggregation—Aroyl-*S,N*-ketene Acetals as Multifunctional Sensor Merocyanines. *Chem. Eur. J.* **2021**, *27*, 13426-13434.

CHAPTER 3

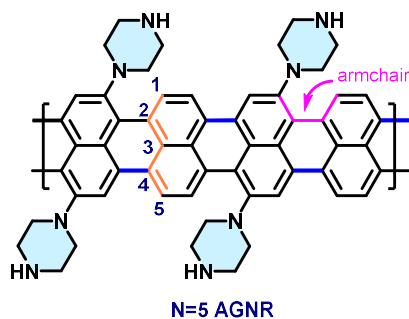
Studies Towards the Bottom-Up Solution-Phase Synthesis of Water/Alcohol Soluble N=5 Armchair Graphene Nanoribbons by the Palladium/Norbornene Catalysis

3.1. Introduction

In recent years, graphene nanoribbons (GNRs) have attracted great interest due to their intriguing electronic properties.¹ Theoretical predictions suggest that GNRs may even have the potential to supplant silicon-based field-effect transistors (FETs) due to their superior thermal conductivity, maximum current density, cut-off frequency, transconductance, electron mobility, and comparable on/off current ratio.² However, the integration of them into state-of-the-art devices is hindered by a range of challenges, including structural control, large-scale production, and device fabrication.² The electronic properties of GNRs are intricately linked to their width, length, edge types, heteroatom doping, and topology, making precise control over their chemical structures crucial for achieving the desired properties.^{1,3-6} In the past decade, great progress has been made in realizing structurally well-defined GNRs through bottom-up approaches such as surface-assisted synthesis and solution-phase synthesis.¹ Currently, the surface-assisted protocol is the most advanced method to obtain atomically precise GNRs from organic monomers on Au(III) or Ag(III) single crystals.⁵ While on-surface methods can yield long GNRs and allow for the direct monitoring of their chemical structure as well as the electronic properties, such a metal-surface based strategy requires high temperatures (>300 °C), limiting the installation of various functional groups on GNRs, and large-scale preparation is not feasible.⁷ Compared to the surface-assisted synthesis, solution-phase synthesis offers several advantages: 1) milder reaction conditions enable the

installation of functional groups, heteroatoms, or side chains that may not survive on-surface, 2) large-scale production, and 3) enhanced solution-processability.^{1b,8}

While several reports have demonstrated GNRs showing improved dispersion in organic solvents through the introduction of bulky groups,⁹⁻¹⁰ long alkyl chains,^{7,11-12} or dendrons,¹³ "truly soluble" GNRs have not yet been realized, which hampers the solution fabrication of devices. The low solubility of GNRs can be attributed to strong π - π interactions between the highly conjugated GNR backbones. In 2019, our group reported the synthesis of a less aggregated, water-soluble poly(*p*-phenylene ethynylene) utilizing the Pd/NBE *ortho*-amination *ipso*-alkynylation reaction.¹⁴ The piperazine side chains could undergo double-protonation in acidic media, thereby attenuating the aggregation of polymer chains in water. This strategy motivated us to design a new monomer for water/alcohol-soluble GNRs, potentially yielding valuable materials for biomedical applications¹⁵⁻¹⁶ that can be solution-processed, particularly in a more environmentally friendly manner. Among various types of GNRs, we selected the N=5 armchair GNR (AGNR, Scheme 3.1), the narrowest AGNR of the N=3k+2 family,^{1b} which is predicted and experimentally proven to exhibit a narrow bandgap (<1.0 eV) suitable for high-performance electronics.^{9,17-20} In addition, the narrower width of the N=5 AGNRs, compared to other wider ribbons, is expected to decrease the inter-ribbon interactions.



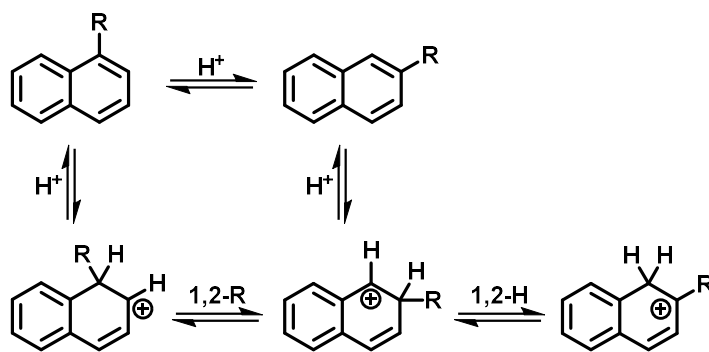
Scheme 3.1. Structure of the proposed N=5 AGNR bearing piperazine side chains.

While a good number of literatures reported the synthesis of N=5 AGNRs on surface,¹⁹⁻²⁴ limited reports exist for the solution-phase synthesis of them.^{9, 17-18} In the following section, challenges associated with the solution-phase synthesis of N=5 AGNRs are summarized.

3.2. Challenges in the Solution-Phase Synthesis of N=5 AGNRs

In the solution-phase synthesis of GNRs, the most common approach to achieve graphitic structures involves the dehydrogenative coupling of their polymer precursors in the presence of various Lewis acids, or oxidants in combination with Brønsted or Lewis acids.²⁵ Although the mechanism is still unclear, some examples suggest that depending on the nature of the reagents involved and the electronic structure of the substrates, two different mechanisms can operate.²⁵⁻²⁶ One involves a radical cation intermediate, while the other proceeds through the formation of a σ -complex. Often, the two mechanisms cannot be distinguished, as Lewis acids can also serve as mild oxidants.

While various nanographenes or GNRs have been successfully achieved by dehydrogenative coupling reactions in solution, certain substrates present greater challenges due to the possibility of rearrangement reactions in the process. In particular, naphthalene, which can be considered as a repeating unit in the N=5 AGNRs, are susceptible to acid-catalyzed 1,2-rearrangement, resulting in the formation of the most stable cationic species, placing the substituent on the β position of the naphthalene (Scheme 3.2).²⁷

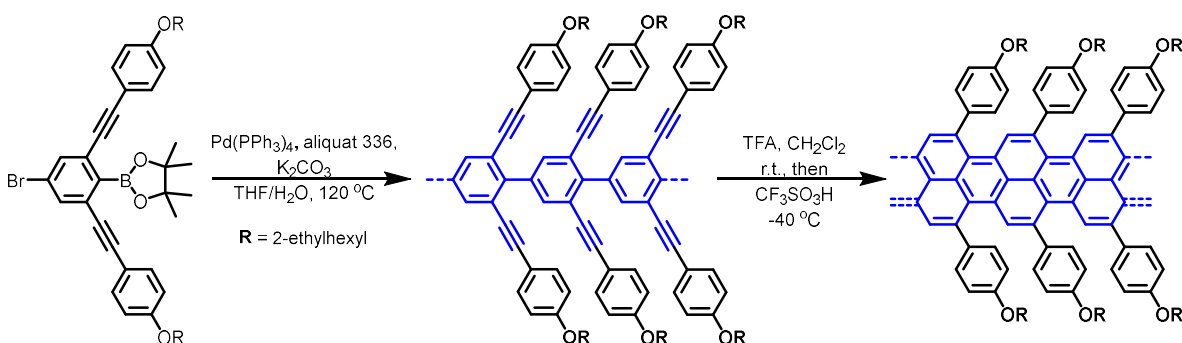


Scheme 3.2. Acid-catalyzed rearrangement of naphthalene derivatives.

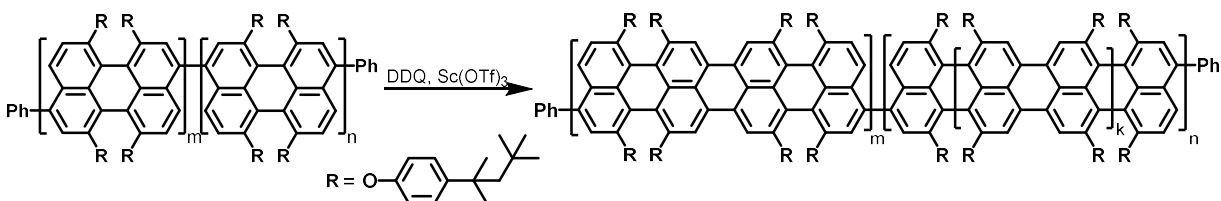
To date, only three examples of solution-phase synthesis of N=5 AGNRs have been reported. The first example by Chalifoux in 2016 involves a complex monomer synthesized over multiple steps, followed by Suzuki coupling and subsequent alkyne benzannulation under acidic condition (Scheme 3.3A).⁹ The presence of branched alkyl chains on the phenyl rings improved the solubility of the ribbon, enabling NMR measurements in CDCl₃. In the following year, Müllen group reported the synthesis of poly(rylene) from functionalized poly(perylene) polymers (Scheme 3.3B).¹⁷ Additionally, they showcased a Ni-catalyzed Yamamoto coupling of a tetrabromoperylene monomer under microwave conditions, resulting in a "defect-free" 5-AGNR. By comparing the UV-vis-NIR absorption spectra, they discovered that by treating poly(perylene) with DDQ/Sc(OTf)₃ in xylene could yield a high cyclodehydrogenation efficiency. Following Müllen's report, Wu group reported the synthesis of cyclopenta-fused poly(rylene)s using the same reaction condition (Scheme 3.3C).¹⁸ All these strategies avoid the direct use of naphthalene-based monomers to access N=5 AGNRs, although the utilization of "precyclized" perylene may be acceptable. Compounds with precyclized structures exhibit lower oxidation potentials, resulting in the emergence of a slippery slope effect as cyclodehydrogenation progresses further.²⁸ However, none of the reports clearly show the radial-breathing-like-mode (RBLM) peaks in their Raman spectra (514.5 nm⁹ or 532 nm¹⁷ laser), which are directly correlated to the respective width of each

GNR.²⁹ A recent report by Fischer raised concerns regarding solution-grown GNRs due to the absence of such signals, casting doubt on the structural integrity of these GNRs.³⁰ However, it's essential to approach this statement with caution, as the observation of RBLM peaks is highly dependent on the laser used during measurement. These peaks are only clearly observable when the GNRs are coherently excited at photon energies near their lowest optical transitions.³¹ Specifically for N=5 AGNRs, RBLM peaks can only be detected using a 785 nm laser.^{21, 23}

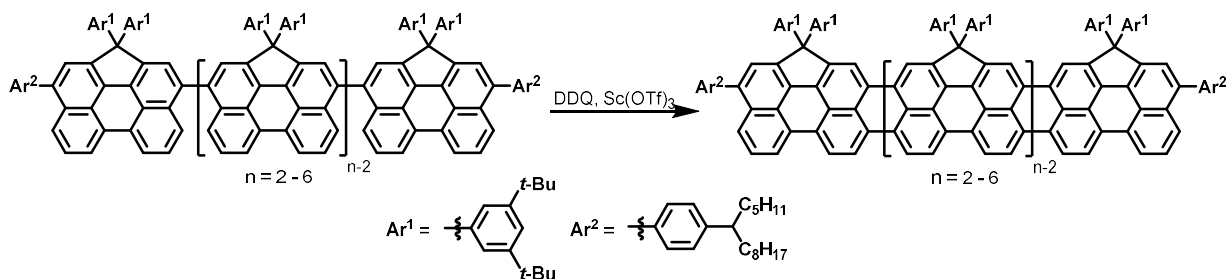
A. Alkyne benzannulation strategy (Chalifoux, 2016)



B. Synthesis of poly(rylene) (Müllen, 2017)



C. Synthesis of cyclopenta-fused poly(rylene) (Wu, 2017)



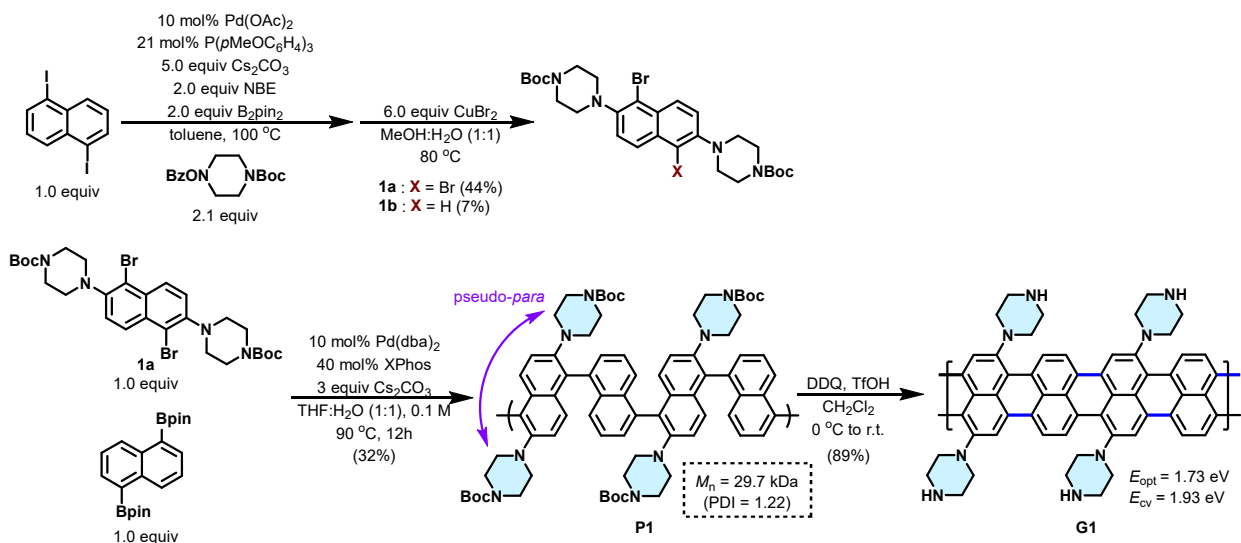
Scheme 3.3. Reported solution-phase syntheses of N=5 AGNRs.

3.3. Results and Discussion

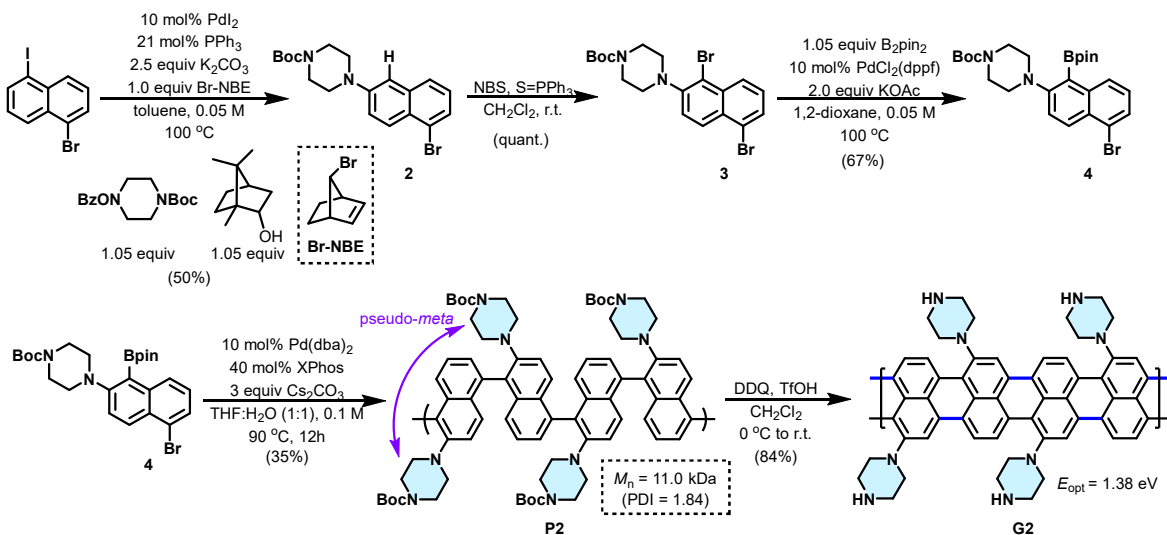
Initially, we designed and synthesized a straightforward naphthalene-based monomer, **1a**, starting from readily available 1,5-diiodonaphthalene (Scheme 3.4A). This was achieved using the palladium/NBE *ortho*-amination *ipso*-borylation reaction followed by the direct conversion of the C-B bond to C-Br bond, as reported by Ritter in 2015.³² Then, Suzuki-Miyaura coupling of **1a** and 1,5-bis(Bpin)naphthalene resulted in the formation of the pseudo-*para* GNR polymer precursor (**P1**) in a yield of 32% after precipitation in MeOH. Under the oxidative cyclodehydrogenation condition (DDQ/TfOH), **G1** was obtained as graphenized black solids. Considering the acidic reaction condition, it was anticipated that the Boc protecting group on the piperazine would be removed during this step. Unfortunately, we discovered that treatment with acids (HCl, TFA, BARF, HBF₄, etc.) in methanol did not lead to successful solubilization of **G1**, even with various counterions, including large anions. Considering the long length of the polymer (degree of polymerization ~48), the observed bandgap appeared larger than expected ($E_{\text{opt}} = 1.73$ eV, $E_{\text{cv}} = 1.93$ eV), in comparison to Mullen's report ($E_{\text{opt}} = 0.88$ eV).¹⁷ At the time, such a discrepancy was believed to stem from the low graphenization efficiency due to the low solubility of **G1** during the oxidation process. Building on our previous study, which demonstrated that the relative positions of piperazine groups can influence the stacking behaviors between polymers, we designed a less symmetric pseudo-*meta* AGNR, **G2** (Scheme 3.4B). From 1-bromo-5-iodonaphthalene, we struggled to obtain compound **3** following the same condition used for 1,5-diiodonaphthalene. Ultimately, we optimized the reaction for *ipso*-hydride termination instead of borylation, which gave compound **2** in 50% yield. Following Gustafson's intriguing report,³³ we found that bromination in the presence of a mild phosphine sulfide Lewis base could selectively give compound **3** in a quantitative yield. Subsequent Miyaura borylation was selective for the bromide

adjacent to the piperazine to give monomer **4**, possibly due to a directing effect. Finally, monomer **4** was subjected to Suzuki-Miyaura polymerization, followed by cyclodehydrogenation, resulting in the formation of **G2**. To our delight, **G2** was found soluble in HCl/MeOH solution after sonication. Additionally, the observed optical bandgap was much lower ($E_{\text{opt}} = 1.38$ eV), suggesting that the graphenization efficiency may have been higher.

A. Synthesis of pseudo-*para* AGNR



B. Synthesis of pseudo-*meta* AGNR



Scheme 3.4. Synthetic routes toward **G1** and **G2**.

To further characterize the precursor polymers and GNRs, measurements and analyses were conducted using techniques such as Raman spectroscopy, FT-IR, and MALDI-TOF. Figure 3.1 shows the Raman spectroscopy data of the two GNRs, displaying two prominent peaks around 1360 and 1590 cm^{-1} , corresponding to the D and G bands of graphitic materials, respectively. The ratios of the D band intensity relative to the G band intensity (I_D/I_G) reflect the presence of “edge defects”. Given that **G1** and **G2** have the same number of piperazines per naphthalene unit, it is reasonable that the I_D/I_G values are almost identical. However, we did not observe any RBLM or overtone/combination modes (such as 2D, D+G, 2G), even with the 785 nm laser.

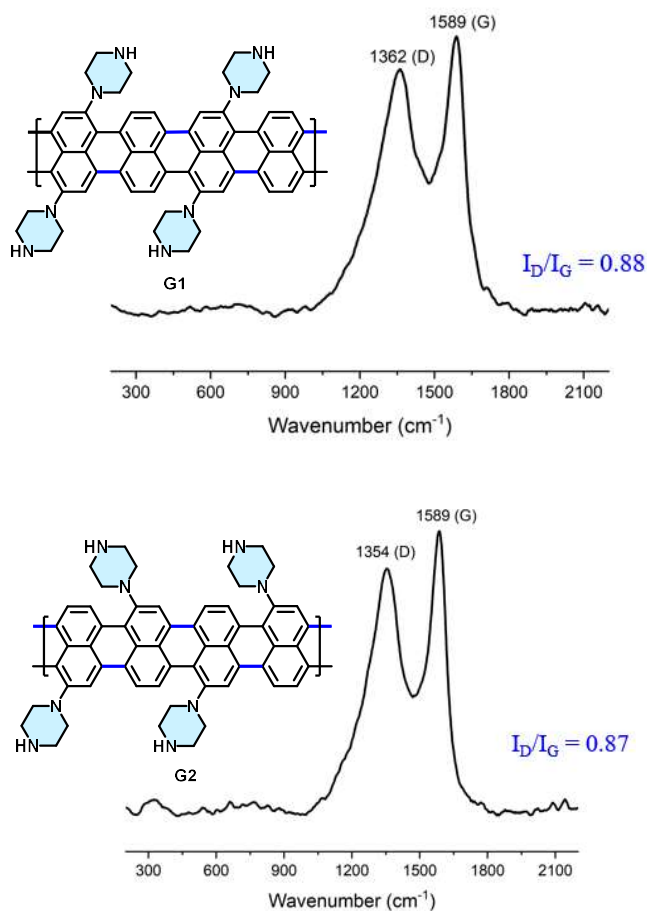


Figure 3.1. Raman spectroscopy data of **G1** and **G2** (laser: 532 nm).

The MALDI-TOF data of the polymer precursors (Figure 3.2) clearly revealed the intervals of unit masses of each polymer, indicating successful polymerization. The mass range observed was lower compared to the results obtained from size exclusion chromatography (SEC), which can be attributed to the inherent challenges in ionizing higher molecular weight polymers. In contrast to the polymer precursors, the MALDI-TOF results of **G1** and **G2** were more complex (Figure 3.3): intervals of the unit masses did not align well with the expected value. FT-IR analysis of **G1** indicated that compared to the polymer precursor **P1**, signal triads (3059-3039 cm^{-1}) from the aryl C-H stretching vibrations were significantly diminished, suggesting cyclodehydrogenation had occurred (Figure 3.4). For **P2** and **G2**, changes in the signal triads were unclear due to the very broad N-H peak (Figure 3.5). Upon treating **G2** with HCl, we observed a significant suppression of the peaks from the secondary N-H wag and the sp^2 C-H bend, and also detected a 40 cm^{-1} shift of the N-H stretching mode, suggestive of the successful formation of the amine salts. However, the FT-IR analysis of the **G2** salt revealed a hidden peak corresponding to C=O, indicating that Boc-deprotection was incomplete. This partial deprotection could, in part, explain the irregular intervals observed in the MALDI-TOF spectra of the GNRs. Based solely on the ensemble of these characterization methods, it was challenging to conclusively determine the formation of the N=5 AGNRs, especially given the absence of desired peaks in the Raman spectra and the ambiguity of the MALDI-TOF results.

To validate our proposed structure, we conducted several additional studies. We performed a control experiment with a model compound to investigate the possibility of a 1,2-rearrangement (Scheme 3.5). After refluxing the material in 1,2-dichloroethane in the presence of excess TfOH (22.9 equiv), no rearrangement was observed. Subsequent Boc protection resulted in the recovery of 74% of the starting material. This observation suggests that 1,2-rearrangement is not the major

side reaction in the graphenization step. However, all oxidative dehydrogenation products obtained from each model study we attempted were complex and insoluble (Scheme 3.6), exhibiting unusual masses upon MALDI-TOF analysis. As a result, we ultimately concluded that undesired intermolecular reactions may have occurred during the oxidative cyclodehydrogenation step.

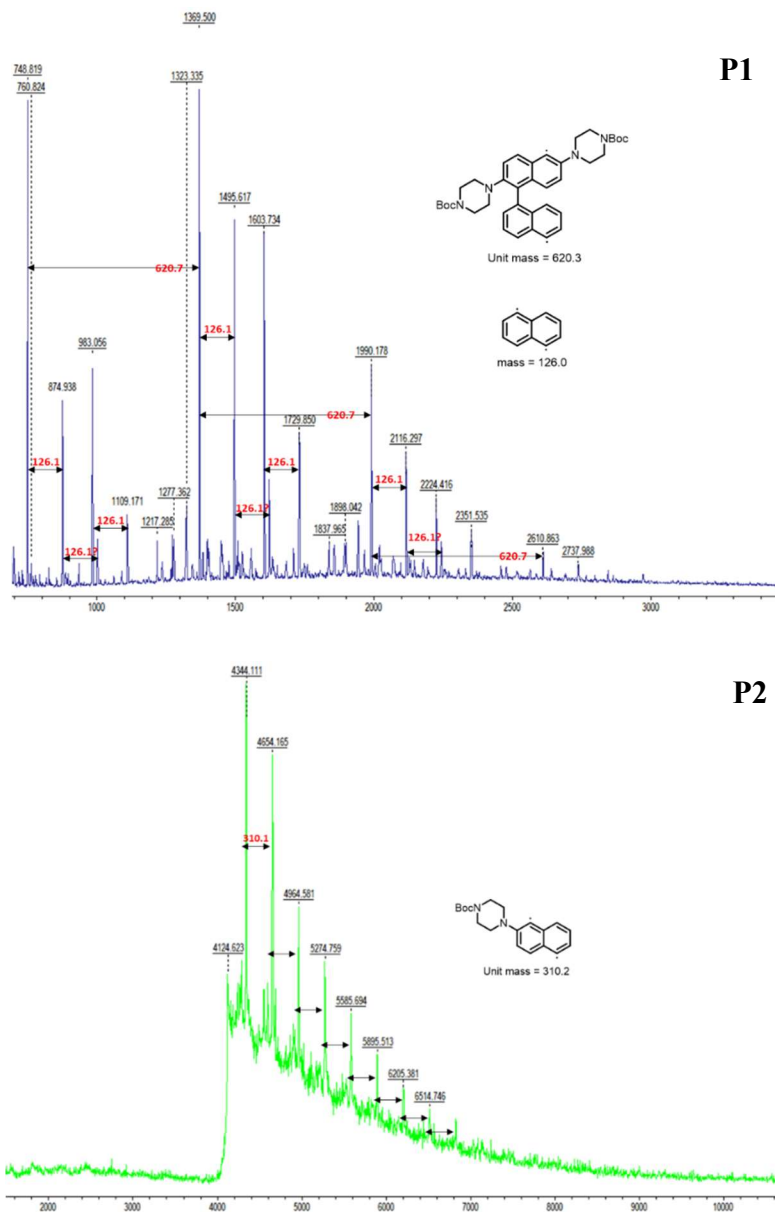


Figure 3.2. MALDI-TOF spectra of **P1** and **P2** (matrix: DCTB).

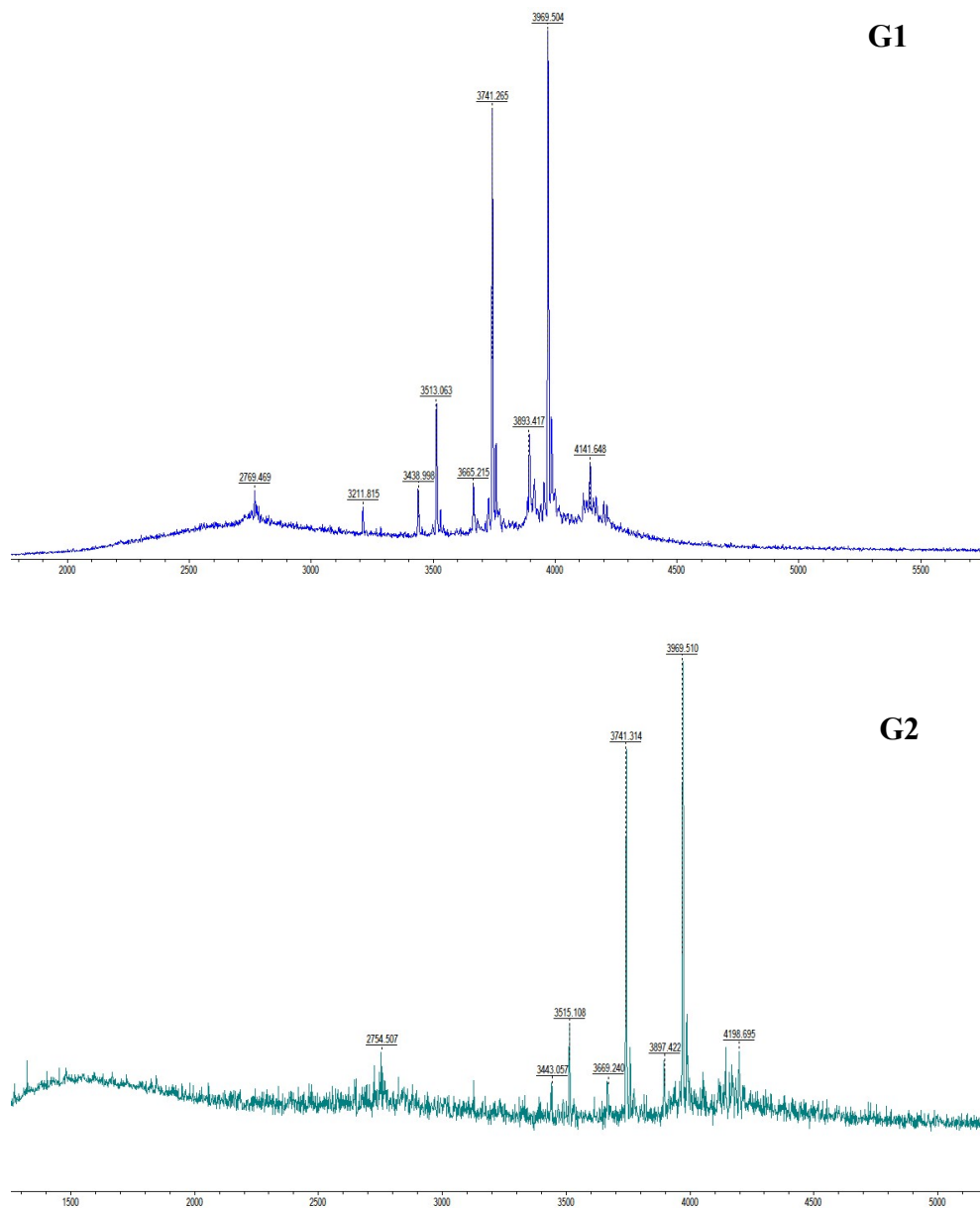


Figure 3.3. MALDI-TOF spectra of **G1** and **G2** (matrix: DCTB).

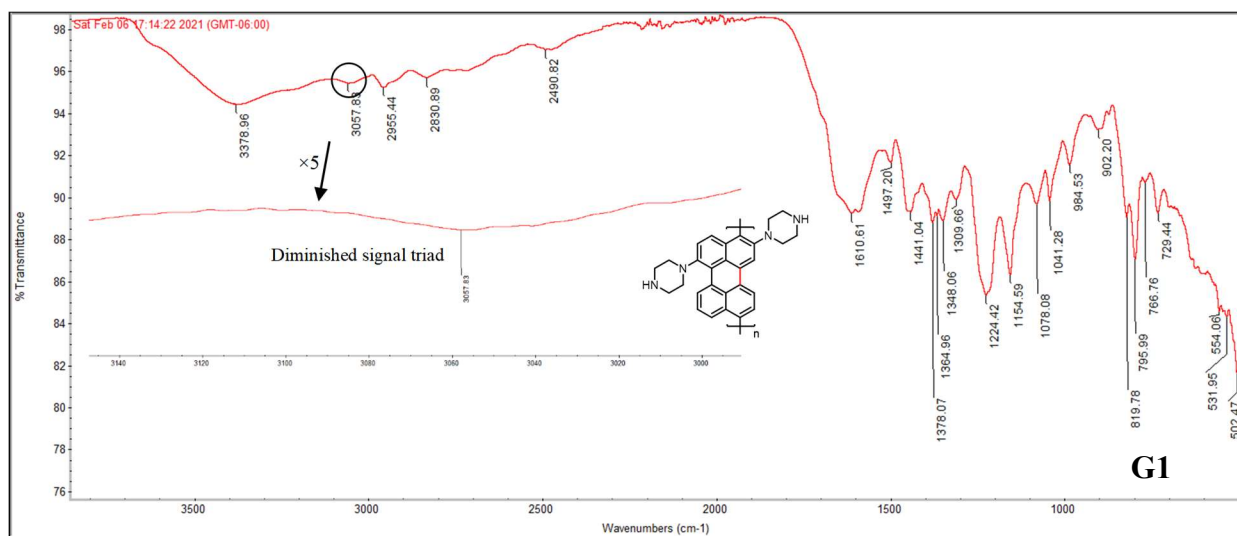
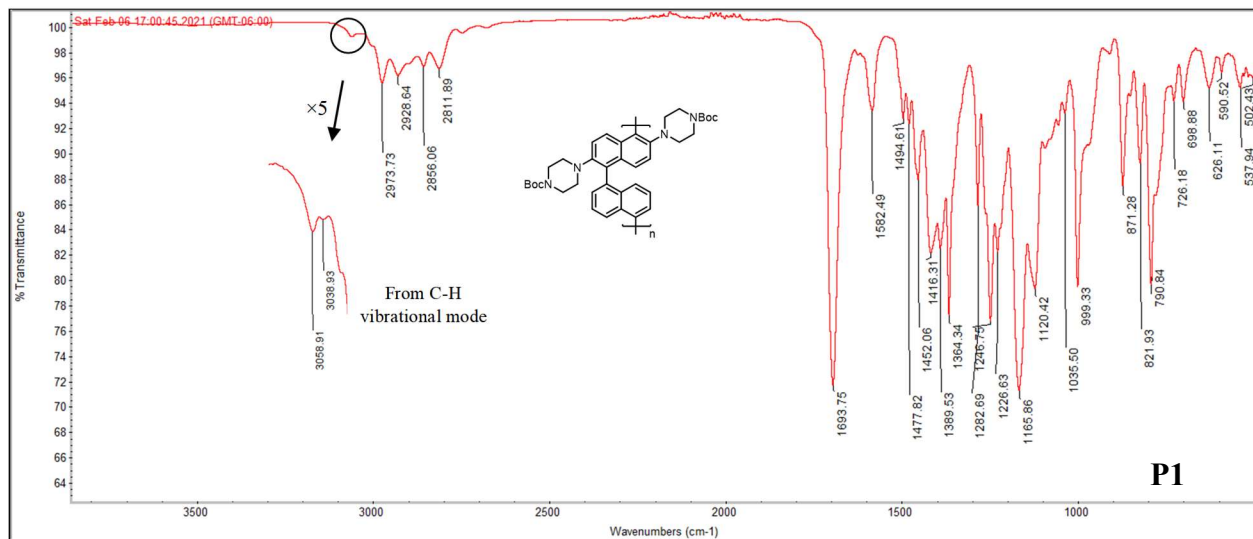


Figure 3.4. IR spectra of P1 and G1.

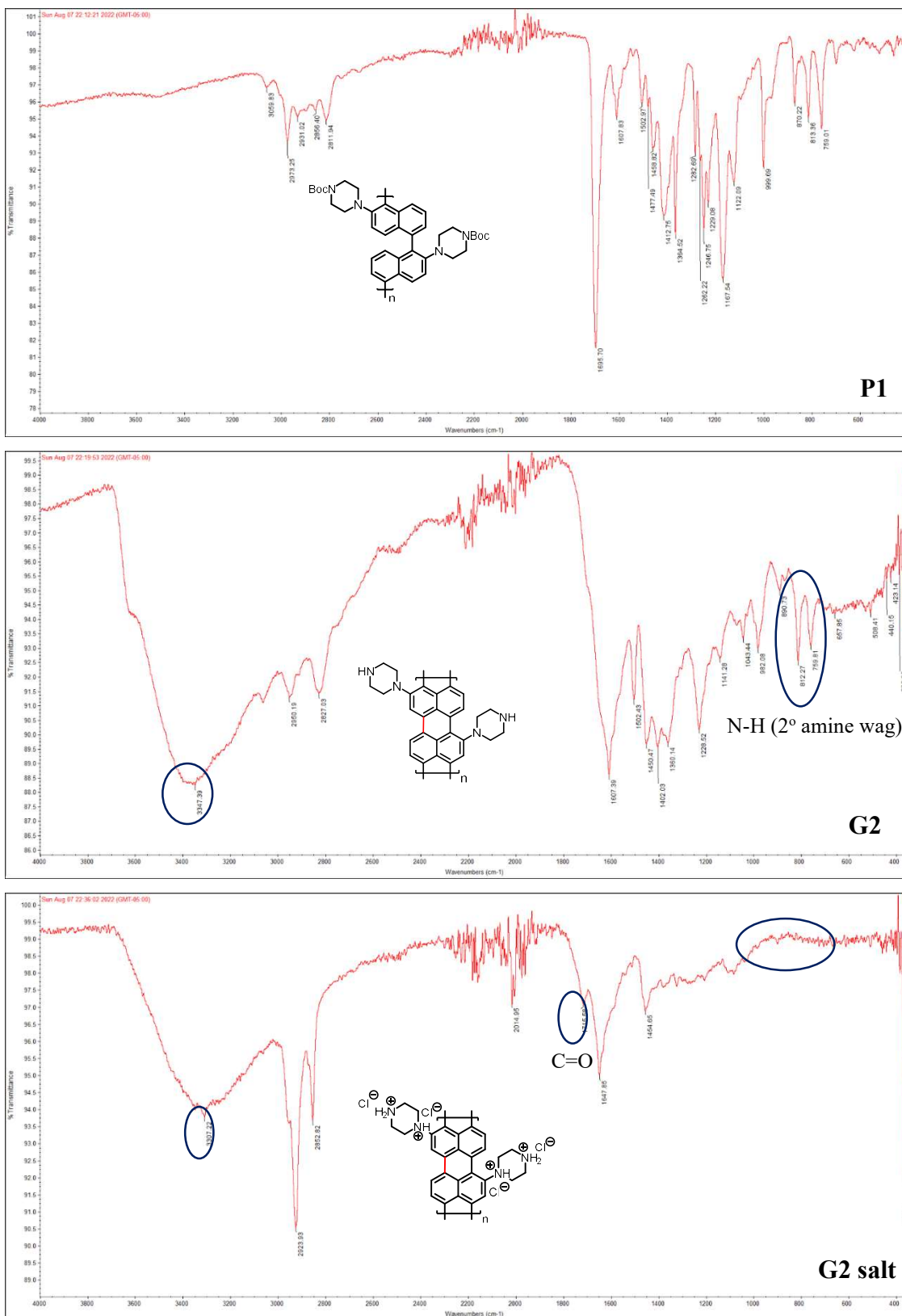
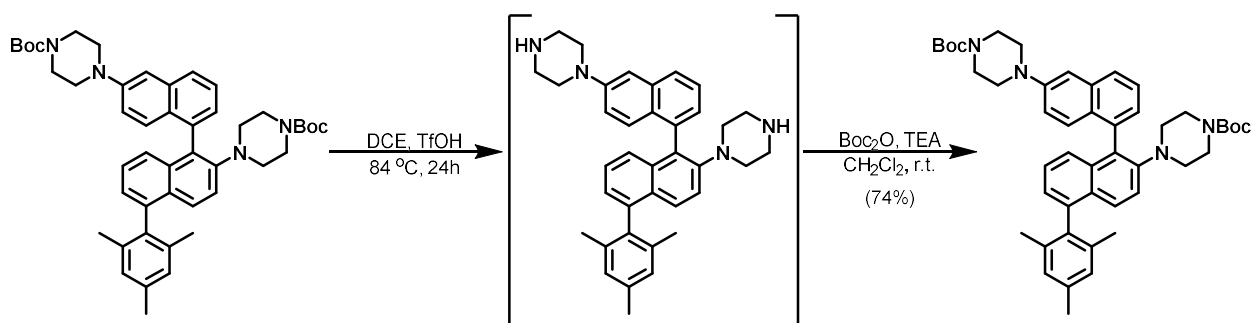
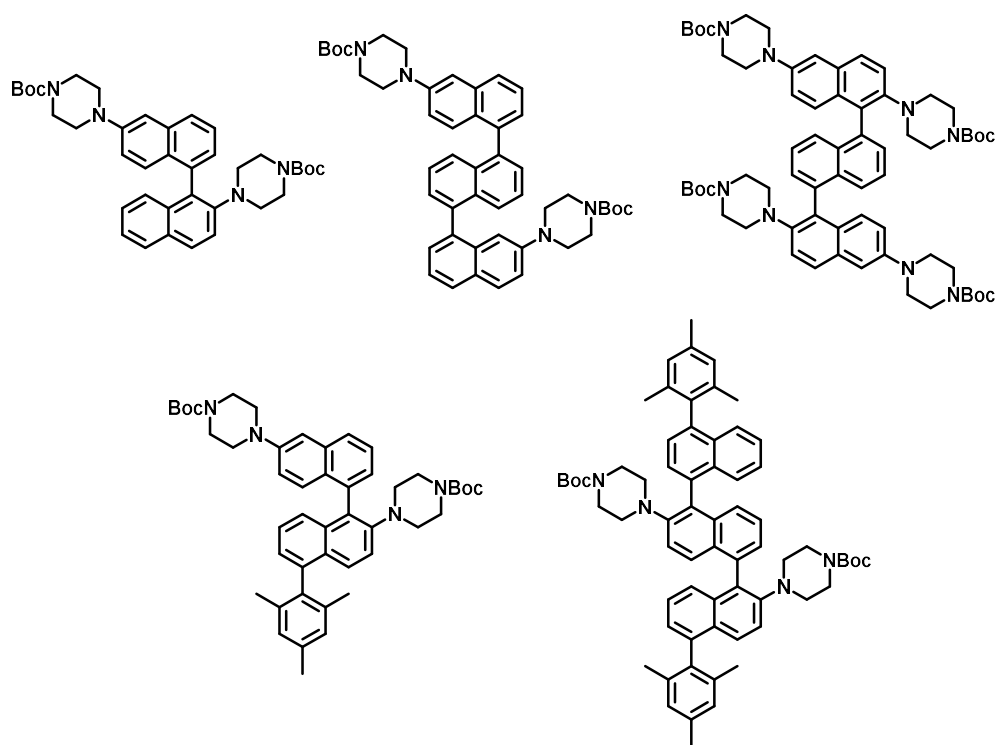


Figure 3.5. IR spectra of P2, G2, and salt form of G2.



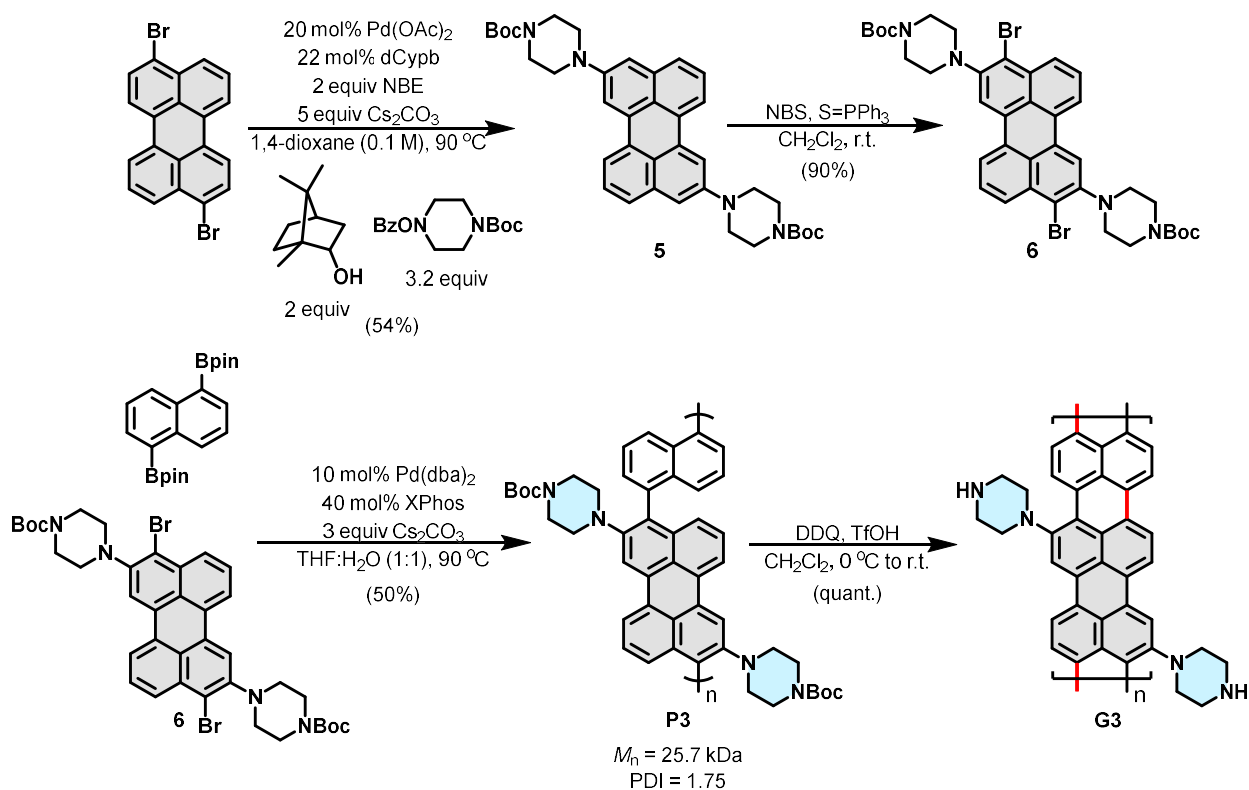
Scheme 3.5. Control experiment excluding 1,2-rearrangement under our reaction condition.



Scheme 3.6. Selected examples of model substrates for the cyclodehydrogenation reaction.

The aforementioned results have prompted doubts about the potential success of naphthalene-based monomers in synthesizing $N=5$ AGNRs in the foreseeable future. This uncertainty has motivated us to search for a "precyclized" monomer that may exhibit greater reactivity in the cyclodehydrogenation step.^{17-18, 28} From a known compound, dibromoperylene, compound **5** was efficiently prepared by palladium/NBE catalysis following our prior report (Scheme 3.7). Next,

bromination smoothly provided monomer **6** in 90% yield. With the new monomer in hand, Suzuki-Miyaura polymerization followed by graphenization yielded **G3** in 50% over two steps.



Scheme 3.7. Synthetic route towards **G3**.

To characterize **G3**, we initially examined the MALDI-TOF spectra. Unlike the messy results observed for **G1** and **G2**, we observed a clear periodicity corresponding to the M^{3+} ion of the unit mass (Figure 3.6). Raman spectra (Figure 3.7) obtained with a 532 nm laser clearly displayed the D and G bands, along with the overtone bands (2D, D+G, and 2G). More importantly, we observed a promising peak that may correspond to the RBLM of **G3** (506 cm^{-1}) using the 785 nm laser excitation. Although this value is slightly shifted from the reported RBLM of pristine $N=5$ aGNRs (530 cm^{-1})^{21, 23}, it is plausible that the presence of the piperazine groups on the edges affected the RBLM.⁹ Further theoretical calculations are necessary to elucidate both the RBLM and the peak at 294 cm^{-1} . The optical bandgap of **G3**, calculated from the onset of absorption in the UV-vis-

NIR spectra (Figure 3.8), was determined to be 1.29 eV, corresponding to 8 to 10 consecutive cyclized naphthalene units.¹⁷ This observation suggests the presence of potential uncyclized defects, indicating that further optimization of the cyclodehydrogenation step may be necessary.

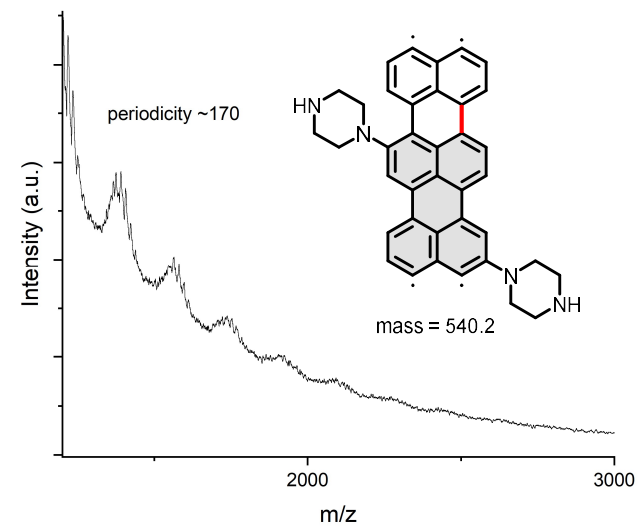


Figure 3.6. MALDI-TOF spectra of **G3**.

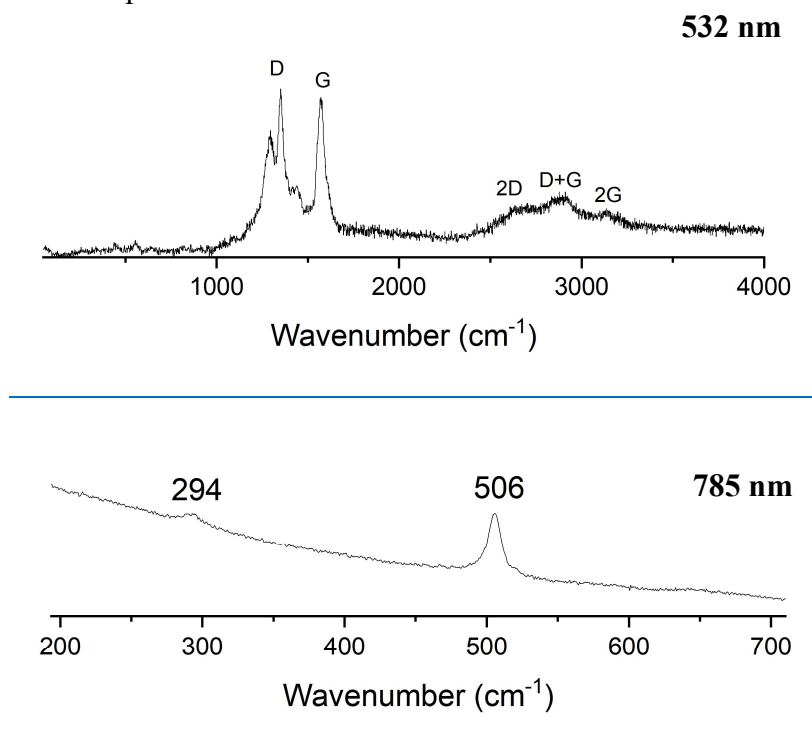


Figure 3.7. Raman spectra of **G3**.

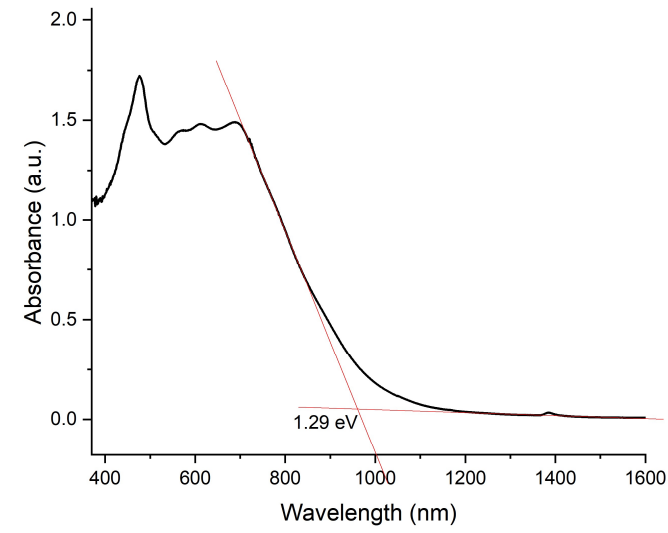


Figure 3.8. UV-vis-NIR spectra of **G3**.

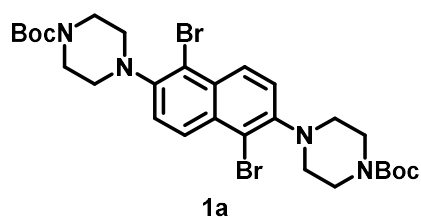
3.4. Conclusion

In summary, this study outlines the journey towards solution-phase synthesis of N=5 AGNRs, supported by detailed analyses using various spectroscopic tools. Unfortunately, **G3** was found insoluble in various acidic conditions, however, this could potentially be solved by continuous exploration of different precyclized monomers. Although this project remains incomplete, it has provided valuable insights into the synthesis of water/alcohol soluble N=5 AGNRs in the near future.

3.5. Characterization Data

Starting material preparation

1,5-diiodonaphthalene,³⁴ 1-bromo-5-iodonaphthalene,³⁵ 1,5-bis(4,4,5,5-tetramethyl-1,3,2-dioxaborolan-2-yl)naphthalene,³⁶ tert-butyl 4-(benzoyloxy)piperazine-1-carboxylate,³⁷ (1R,4S,7r)-7-bromobicyclo[2.2.1]hept-2-ene,³⁸ and 3,9-dibromoperylene²¹ were synthesized according to literature procedures.



Yield: 44%, **m.p.** = 239-241 °C

Physical appearance: white solid

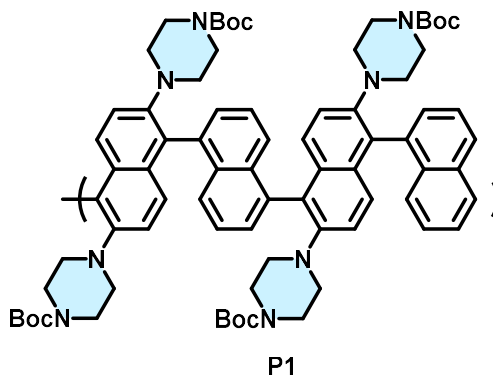
R_f: 0.35 (CH₂Cl₂:hexanes = 1:4)

¹H NMR (400 MHz, CDCl₃): δ 8.30 (d, *J* = 8.0 Hz, 2H), 7.36 (d, *J* = 8.0 Hz, 2H), 3.67 (br, 8H), 3.08 (br, 8H), 1.50 (s, 18H).

¹³C NMR (101 MHz, CDCl₃): δ 155.04, 147.87, 131.32, 128.13, 121.70, 118.57, 80.00, 52.00, 28.62.

IR (KBr, neat): 2973, 2927, 2819, 1689, 1587, 1478, 1452, 1422, 1365, 1319, 1283, 1248, 1206, 1173, 1123, 1084, 1054, 1000, 986, 913, 869, 811, 766, 727, 683, 539 cm⁻¹.

HRMS (ESI-TOF): *m/z* calcd for C₂₈H₃₉Br₂N₄O₄⁺ [M+H⁺]: 653.1338. Found: 653.1337.



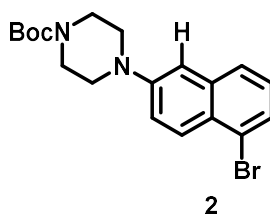
Yield: 32% (fractionized by Soxhlet extraction with boiling methanol for two days)

SEC data: $M_n = 29.7$ kDa, PDI = 1.22

Physical appearance: tan solid

^1H NMR (500 MHz, CDCl_3): δ 7.98-7.32 (br, 10H), 3.65-2.83 (br, 16H), 1.51-1.26 (br, 18H).

^{13}C NMR (126 MHz, CDCl_3): 154.82, 154.50, 147.36, 136.88, 133.93, 133.28, 132.89, 131.35, 128.71, 128.48, 126.66, 126.15, 125.85, 125.53, 120.54, 79.59, 51.99, 51.54, 44.62, 43.59, 29.82, 28.58, 28.48, 28.15.



Yield: 50%, **m.p.** = 127-129 °C

Physical appearance: yellow solid

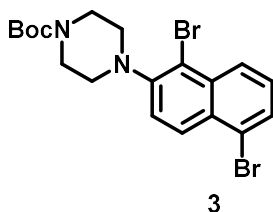
R_f : 0.50 (CH_2Cl_2 :hexanes = 1:4)

^1H NMR (500 MHz, CDCl_3): δ 8.11 (d, $J = 9.2$ Hz, 1H), 7.64 (d, $J = 8.2$ Hz, 1H), 7.57 (d, $J = 7.3$ Hz, 1H), 7.35 (d, $J = 8.7$ Hz, 1H), 7.23 (d, $J = 7.9$ Hz, 1H), 7.10 (s, 1H), 3.64 (t, $J = 5.2$ Hz, 4H), 3.27 (t, $J = 5.2$ Hz, 4H), 1.50 (s, 8H).

¹³C NMR (126 MHz, CDCl₃): δ 154.84, 149.65, 135.98, 128.29, 127.53, 127.19, 126.89, 126.83, 122.66, 120.73, 110.76, 80.16, 49.43, 28.58.

IR (KBr, neat): 2974, 2858, 1695, 1622, 1593, 1559, 1505, 1457, 1422, 1389, 1365, 1286, 1234, 1168, 1140, 1123, 1045, 1001, 963, 868, 815, 775, 748, 666 cm⁻¹.

HRMS (ESI-TOF): m/z calcd for C₁₉H₂₄BrN₂O₂⁺ [M+H⁺]: 391.1016. Found: 391.1016.



Yield: quant.

Physical appearance: sticky white liquid

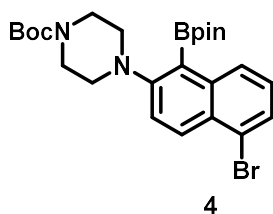
R_f: 0.4 (CH₂Cl₂:hexanes = 1:4)

¹H NMR (500 MHz, CDCl₃): δ 8.32 (d, *J* = 8.6 Hz, 1H), 8.24 (d, *J* = 9.1 Hz, 1H), 7.73 (d, *J* = 7.4 Hz, 1H), 7.50 – 7.32 (m, 2H), 3.67 (t, *J* = 4.9 Hz, 4H), 3.11 (t, *J* = 5.2 Hz, 4H), 1.50 (s, 9H).

¹³C NMR (126 MHz, CDCl₃): δ 155.02, 149.08, 134.57, 129.94, 129.45, 128.18, 127.79, 127.36, 122.81, 121.48, 118.67, 80.01, 51.91, 28.61.

IR (KBr, neat): 2974, 2927, 2858, 2822, 1695, 1611, 1588, 1492, 1457, 1420, 1396, 1365, 1332, 1283, 1249, 1232, 1200, 1170, 1143, 1122, 990, 868, 816, 793, 748, 717, 691 cm⁻¹.

HRMS (ESI-TOF): m/z calcd for C₁₉H₂₃Br₂N₂O₂⁺ [M+H⁺]: 496.0121. Found: 496.0123.



Yield: 67%, **m.p.** = 195-197 °C

Physical appearance: white crystal

R_f: 0.6 (CH₂Cl₂:hexanes = 1:4)

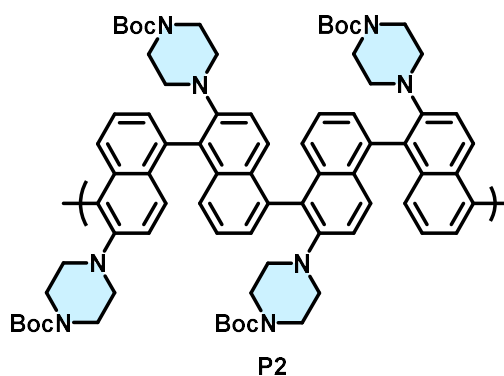
¹H NMR (500 MHz, CDCl₃): δ 8.76 (d, *J* = 9.0 Hz, 1H), 8.46 (d, *J* = 8.6 Hz, 1H), 8.02 (dd, *J* = 6.8, 1.2 Hz, 1H), 7.54 (dd, *J* = 8.6, 6.8 Hz, 1H), 7.36 (d, *J* = 9.1 Hz, 1H), 3.67 (s, 4H), 3.08 (s, 4H), 1.50 (s, 9H), 1.42 (s, 12H).

¹³C NMR (126 MHz, CDCl₃): δ 155.09, 147.94, 135.27, 135.18, 133.22, 130.67, 129.27, 126.78, 120.63, 119.14, 84.04, 79.89, 52.04, 28.61, 25.08.

¹¹B NMR (128 MHz, CDCl₃): δ 31.51.

IR (KBr, neat): 2977, 2928, 2821, 1695, 1610, 1561, 1498, 1453, 1421, 1366, 1354, 1319, 1295, 1282, 1249, 1233, 1206, 1168, 1139, 999, 960, 871, 806, 732, 759, 684 cm⁻¹.

HRMS (ESI-TOF): *m/z* calcd for C₂₅H₃₄BBr₂N₂NaO₄⁺ [M+Na⁺]: 539.1687. Found: 539.1691.



Yield: 35% (fractionized by Soxhlet extraction with boiling methanol for two days)

SEC data: $M_n = 11.0$ kDa, PDI = 1.84

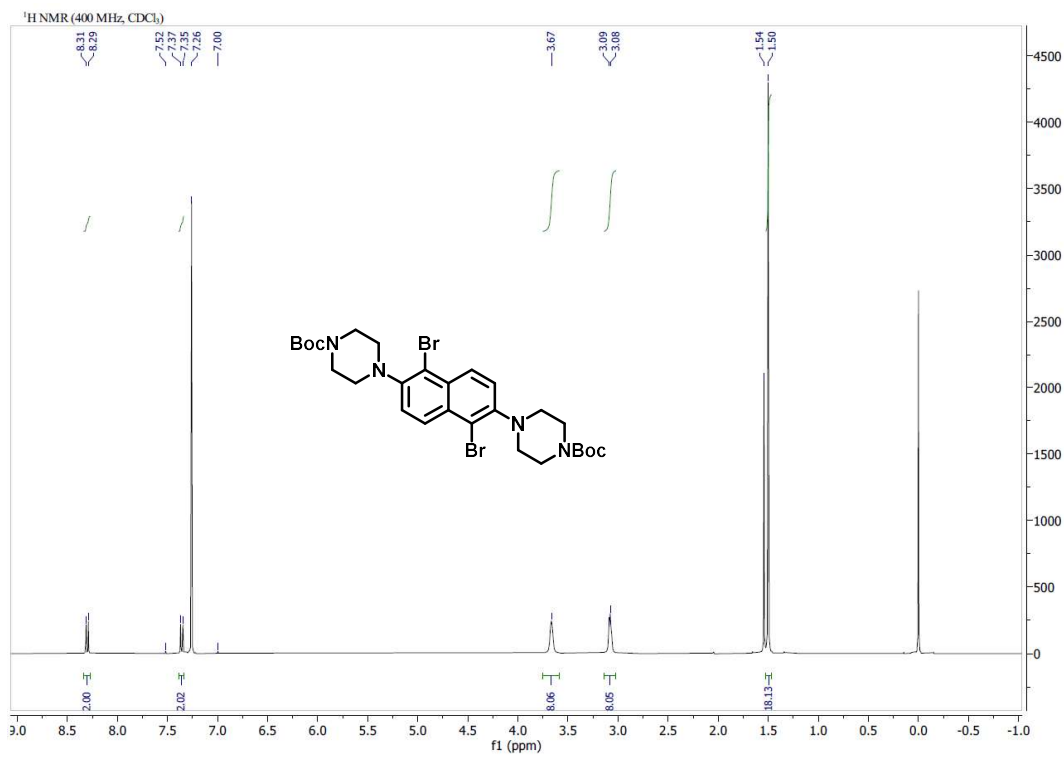
Physical appearance: tan solid

^1H NMR (500 MHz, CDCl_3): δ 8.00-7.26 (br, 5H), 3.65-2.88 (br, 8H), 1.52-1.25 (br, 9H).

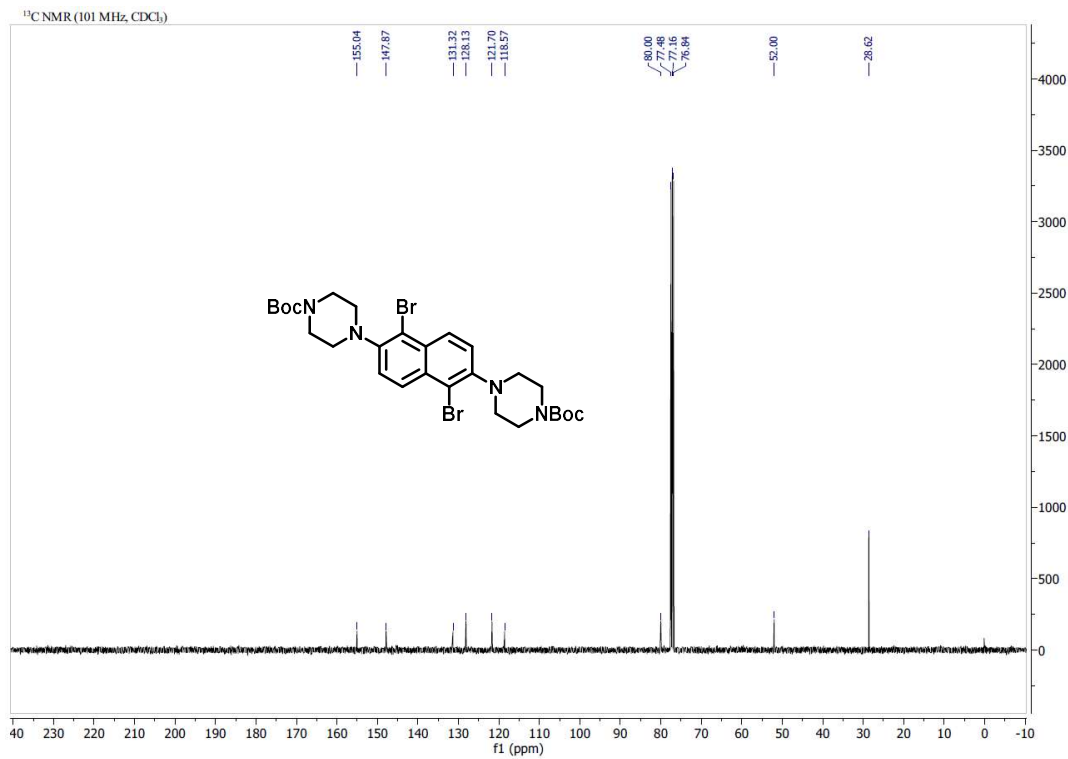
^{13}C NMR (126 MHz, CDCl_3): 154.89, 148.83, 148.24, 136.49, 134.58, 130.60, 129.96, 129.10, 127.95, 125.86, 119.72, 80.09, 79.68, 51.51, 49.67, 43.55, 29.83, 28.60, 28.52.

3.6. NMR Spectra

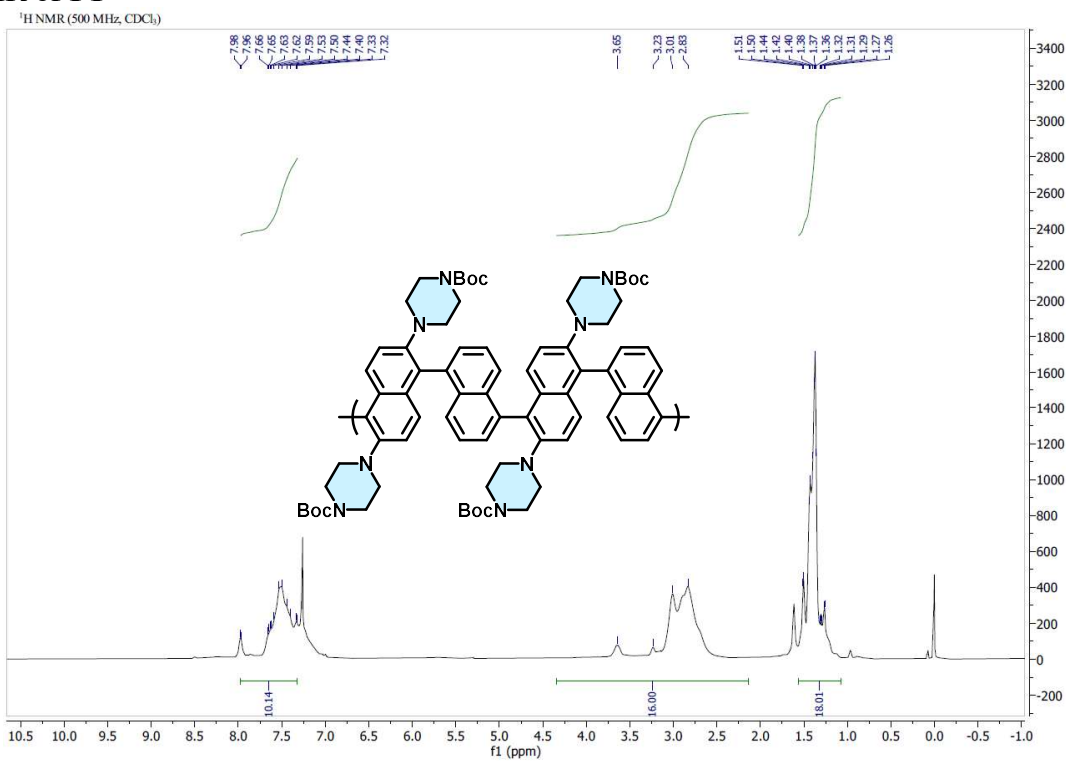
^1H NMR of **1a**



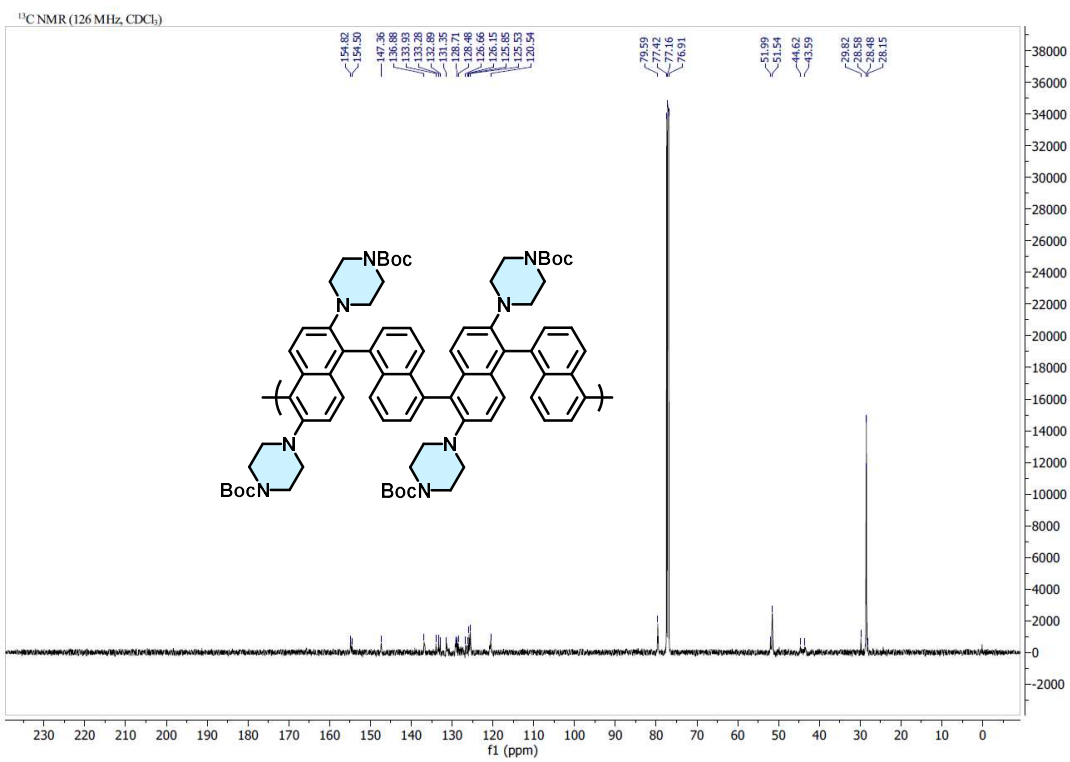
^{13}C NMR of **1a**



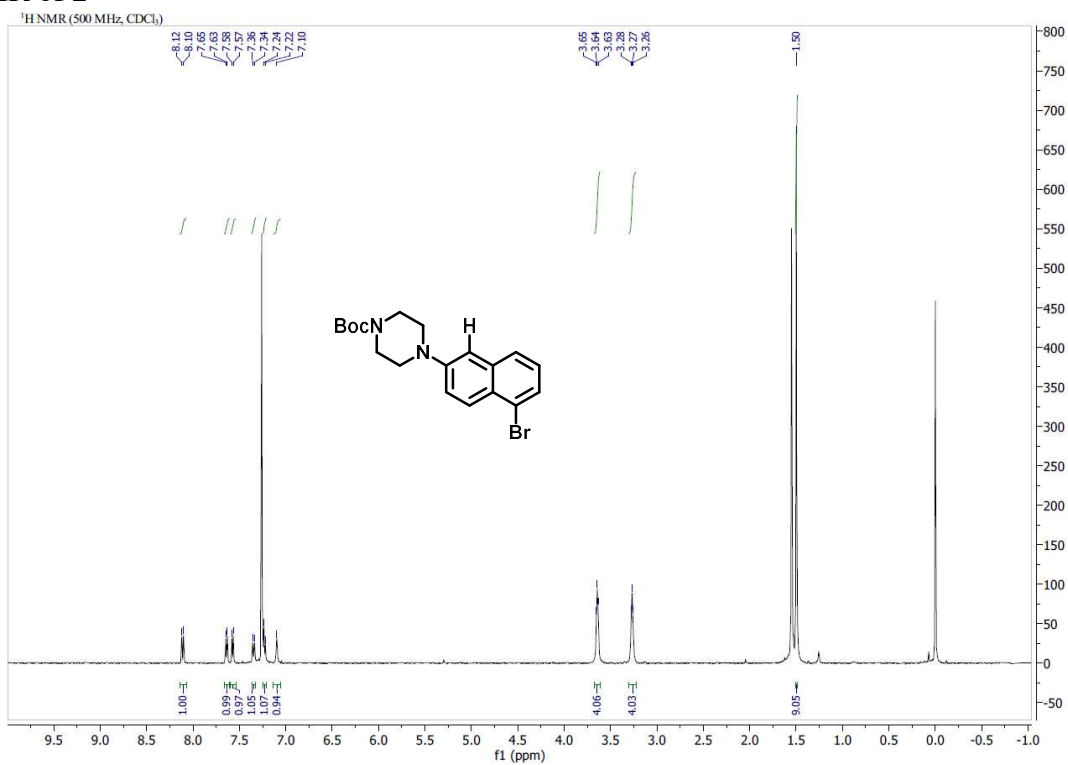
¹H NMR of P1



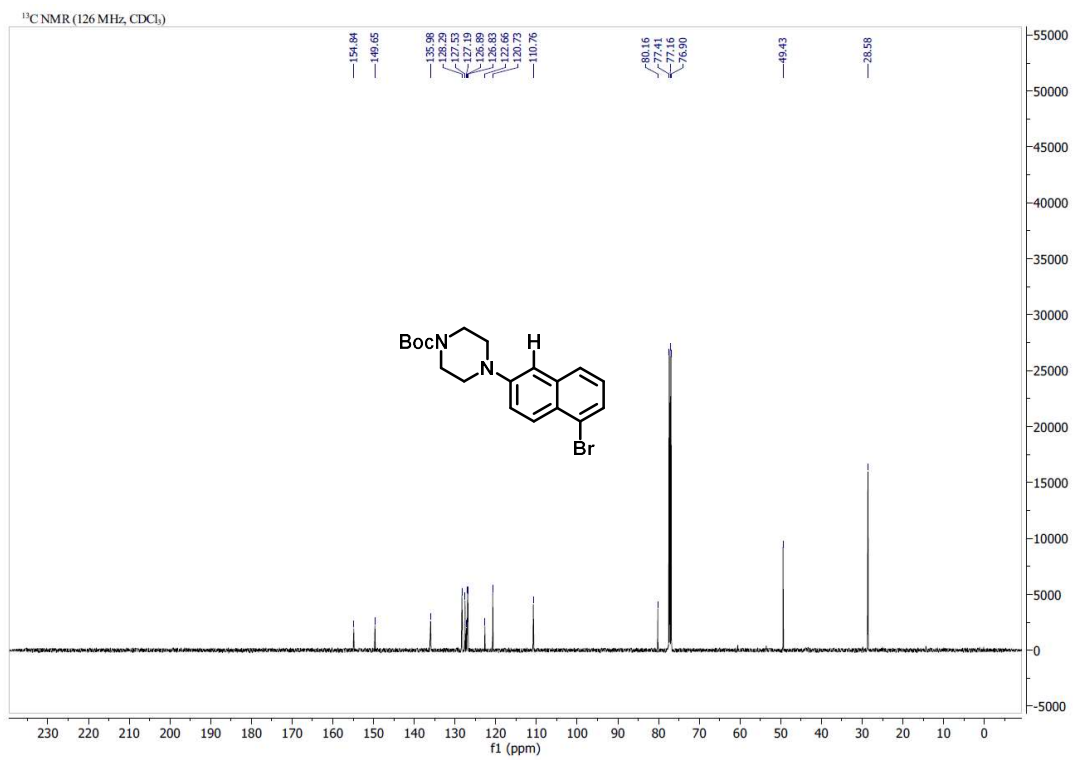
¹³C NMR of P1



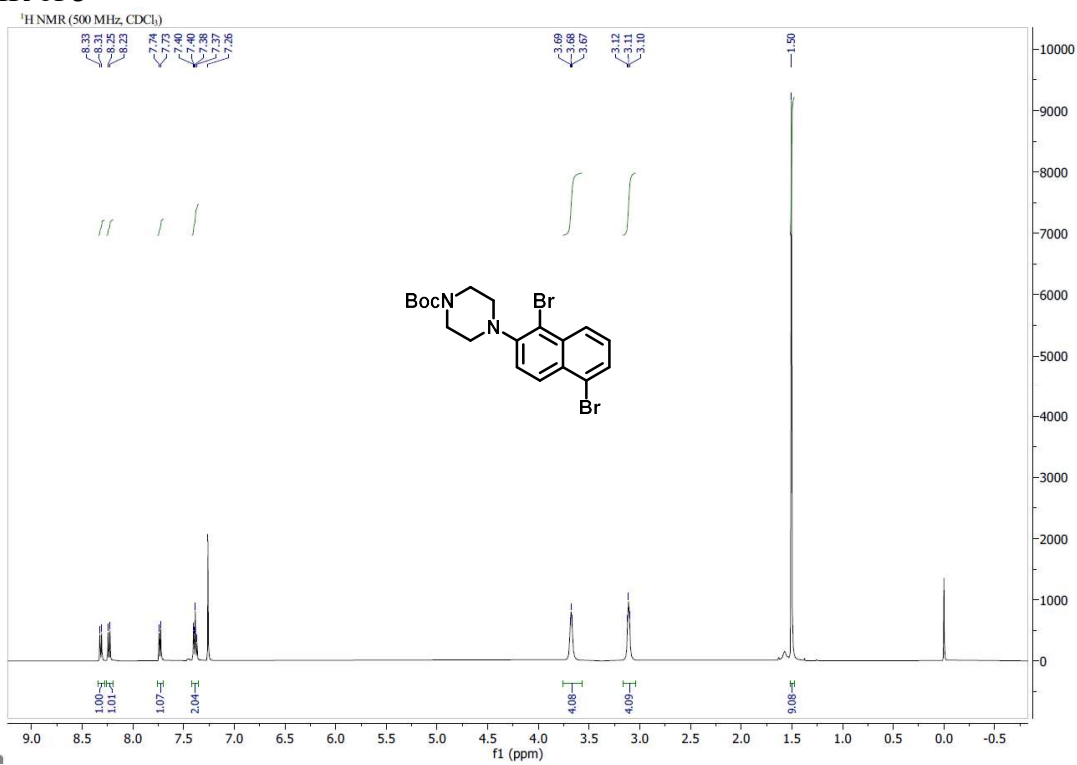
¹H NMR of 2



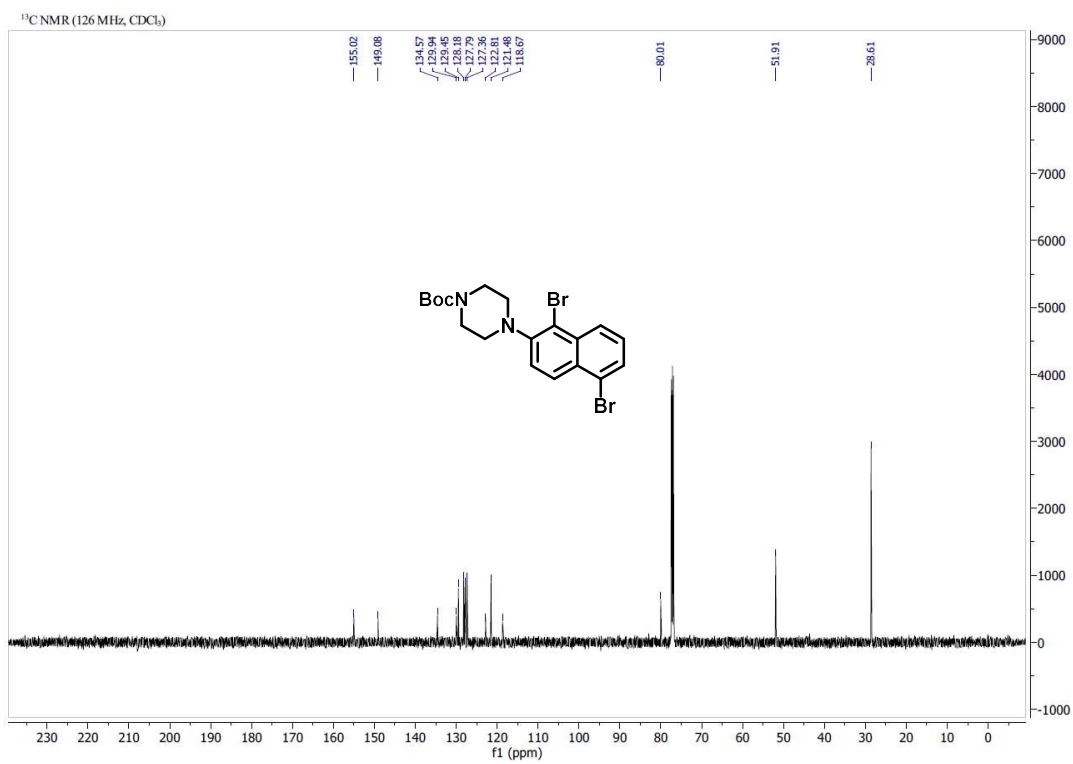
¹³C NMR of 2



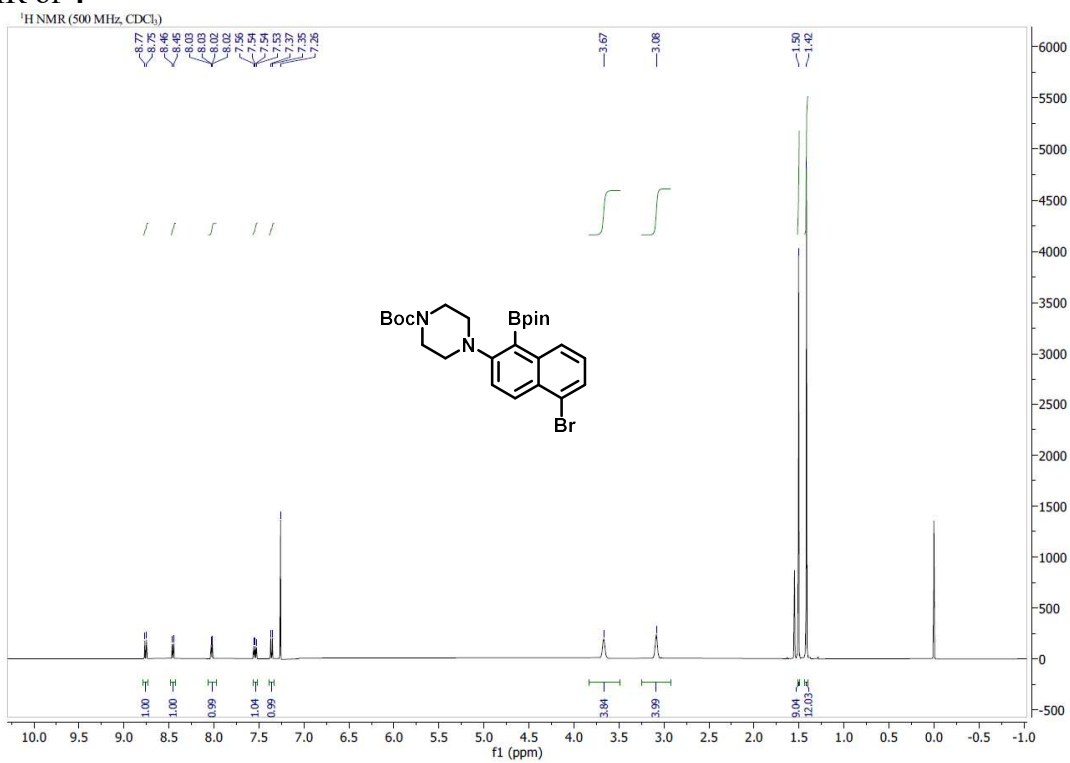
¹H NMR of 3



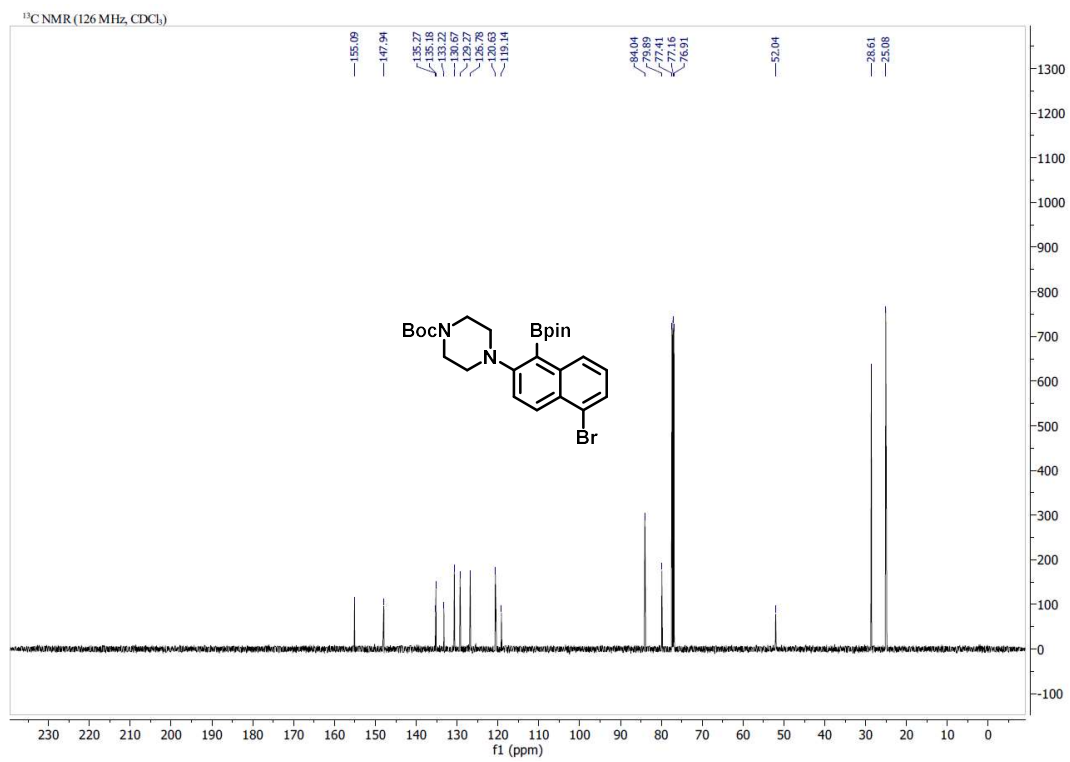
¹³C NMR of 3



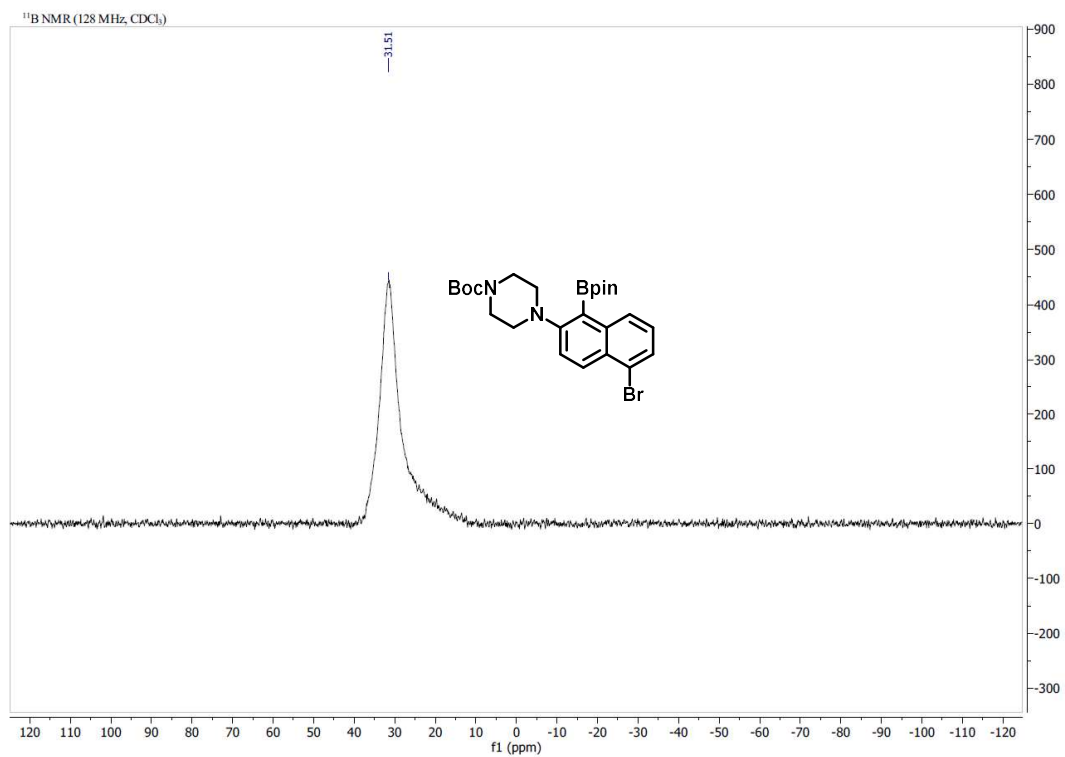
¹H NMR of 4



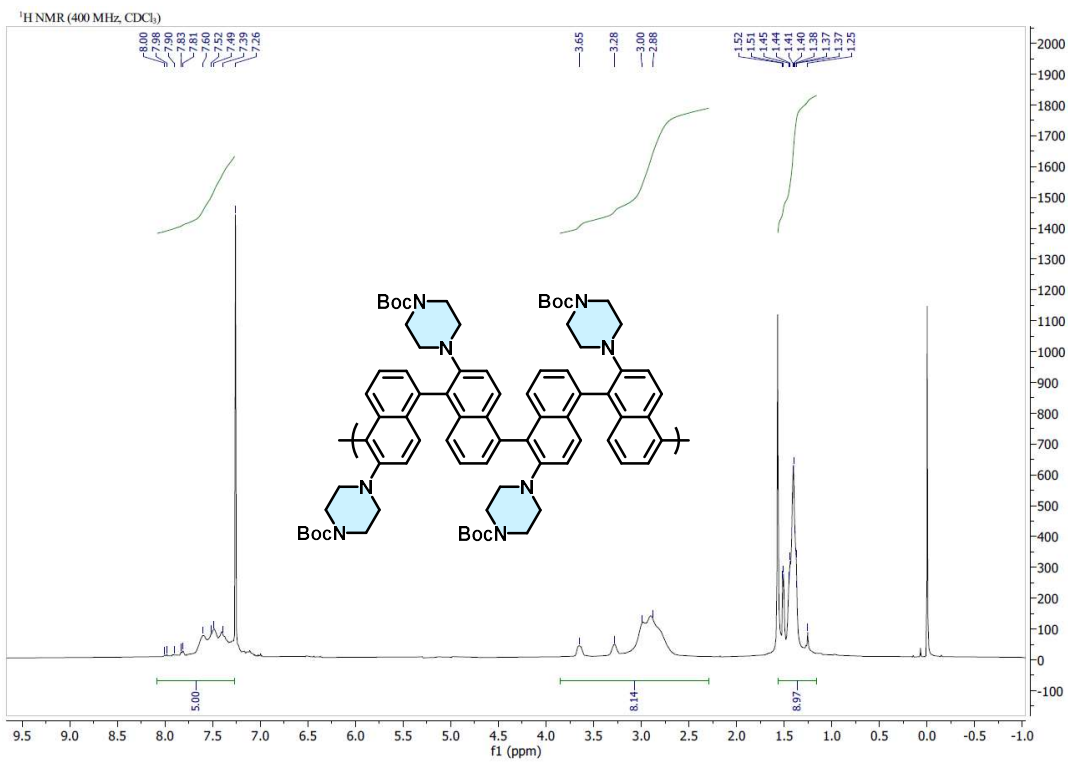
¹³C NMR of 4



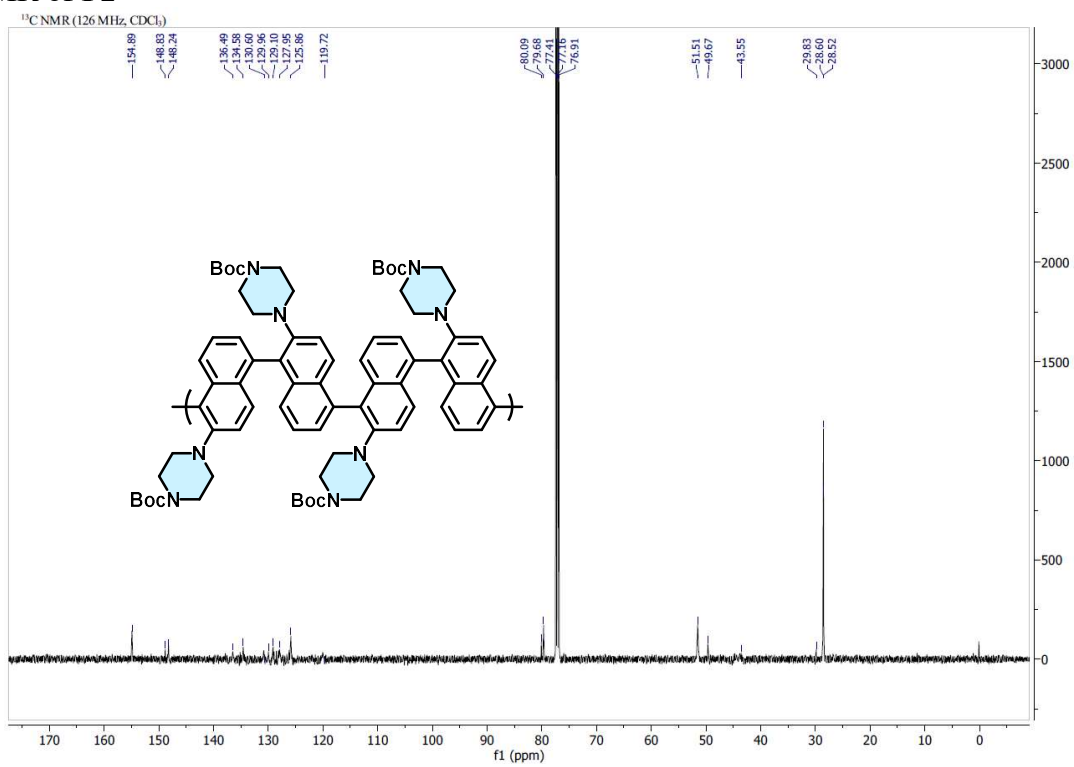
^{11}B NMR of 4



^1H NMR of P2



^{13}C NMR of P2



3.7. References

1. For recent reviews on graphene nanoribbons, see: a) Narita, A.; Wang, X. -Y.; Feng, X.; Müllen, K. New advances in nanographene chemistry. *Chem. Soc. Rev.* **2015**, *44*, 6616-6643. b) Liquid-phase bottom-up synthesis of graphene nanoribbons. *Mater. Chem. Front.* **2020**, *4*, 29-45. c) Yano, Y.; Mitoma, N.; Ito, H.; Itami, K. A Quest for Structurally Uniform Graphene Nanoribbons: Synthesis, Properties, and Applications. *J. Org. Chem.* **2020**, *85*, 4-33. d) Houtsma, R. K.; de la Rie, J.; Stöhr, M. Atomically precise graphene nanoribbons: interplay of structural and electronic properties. *Chem. Soc. Rev.* **2021**, *50*, 6541-6568. e) Liu, Z.; Fu, S.; Liu, X.; Narita, A.; Samori, P.; Bonn, M.; Wang, H. I. Small Size, Big Impact: Recent Progress in Bottom-Up Synthesized Nanographenes for Optoelectronic and Energy Applications. *Adv. Sci.* **2022**, *9*, 2106055.
2. Saraswat, V.; Jacobberger, R. M.; Arnold, M. S. Materials science challenges to graphene nanoribbon electronics. *ACS Nano* **2021**, *15*, 3674-3708.
3. Li, G.; Yoon, K.-Y.; Zhong, X.; Wang, J.; Zhang, R.; Guest, J. R.; Wen, J.; Zhu, X.-Y.; Dong, G. A modular synthetic approach for band-gap engineering of armchair graphene nanoribbons. *Nat. Commun.* **2018**, *9*, 1687.
4. Cai, J.; Ruffieux, P.; Jaafar, R.; Bieri, M.; Braun, T.; Blankenburg, S.; Muoth, M.; Seitsonen, A. P.; Saleh, M.; Feng, X.; Müllen, K.; Fasel, R. Atomically precise bottom-up fabrication of graphene nanoribbons. *Nature* **2010**, *466*, 470-473.
5. Talirz, L.; Ruffieux, P.; Fasel, R. On-surface synthesis of atomically precise graphene nanoribbons. *Adv. Mater.* **2016**, *28*, 6222-6231.
6. Bronner, C.; Stremlau, S.; Gille, M.; Brauße, F.; Haase, A.; Hecht, S.; Tegeder, P. Aligning the band gap of graphene nanoribbons by monomer doping. *Angew. Chem. Int. Ed.* **2013**, *52*, 4422-4425.

7. Narita, A.; Feng, X.; Hernandez, Y.; Jensen, S. A.; Bonn, M.; Yang, H.; Verzhbitskiy, I. A.; Casiraghi, C.; Hansen, M. R.; Koch, A. H. R.; Fytas, G.; Ivasenko, O.; Li, B.; Mali, K. S.; Balandina, T.; Mahesh, S.; De Feyter, S.; Müllen, K. Synthesis of structurally well-defined and liquid-phase-processable graphene nanoribbons. *Nat. Chem.* **2014**, *6*, 126-132.
8. Yoon, K.-Y.; Dong, G. Liquid-phase bottom-up synthesis of graphene nanoribbons. *Mater. Chem. Front.* **2020**, *4*, 29-45.
9. Yang, W.; Lucotti, A.; Tommasini, M.; Chalifoux, W. A. Bottom-up synthesis of soluble and narrow graphene nanoribbons using alkyne benzannulations. *J. Am. Chem. Soc.* **2016**, *138*, 9137-9144.
10. Huang, Y.; Xu, F.; Ganzer, L.; Camargo, F. V.; Nagahara, T.; Teyssandier, J.; Van Gorp, H.; Basse, K.; Straasø, L. A.; Nagyte, V.; Casiraghi, C.; Hansen, M. R.; De Feyter, S.; Yan, D.; Müllen, K.; Feng, X.; Cerullo, G.; Mai, Y. Intrinsic properties of single graphene nanoribbons in solution: synthetic and spectroscopic studies. *J. Am. Chem. Soc.* **2018**, *140*, 10416-10420.
11. El Gemayel, M.; Narita, A.; Dössel, L. F.; Sundaram, R. S.; Kiersnowski, A.; Pisula, W.; Hansen, M. R.; Ferrari, A. C.; Orgiu, E.; Feng, X.; Müllen, K.; Samori, P. Graphene nanoribbon blends with P3HT for organic electronics. *Nanoscale* **2014**, *6*, 6301-6314.
12. Huang, Y.; Mai, Y.; Beser, U.; Teyssandier, J.; Velpula, G.; Van Gorp, H.; Straasø, L. A.; Hansen, M. R.; Rizzo, D.; Casiraghi, C.; Yang, R.; Zhang, G.; Wu, D.; Zhang, F.; Yan, D.; De Feyter, S.; Müllen, K.; Feng, X. Poly(ethylene oxide) functionalized graphene nanoribbons with excellent solution processability. *J. Am. Chem. Soc.* **2016**, *138*, 10136-10139.
13. Xu, F.; Yu, C.; Tries, A.; Zhang, H.; Kläui, M.; Basse, K.; Hansen, M. R.; Bilbao, N.; Bonn, M.; Wang, H. I.; Mai, Y. Tunable superstructures of dendronized graphene nanoribbons in liquid phase. *J. Am. Chem. Soc.* **2019**, *141*, 10972-10977.

14. Yoon, K.-Y.; Xue, Y.; Dong, G. Three-Step Synthesis of a Less-Aggregated Water-Soluble Poly (*p*-phenylene ethynylene) with *Meta* Side Chains via Palladium/Norbornene Cooperative Catalysis. *Macromolecules* **2019**, *52*, 1663-1670.
15. Feng, X.; Liu, L.; Wang, S.; Zhu, D. Water-soluble fluorescent conjugated polymers and their interactions with biomacromolecules for sensitive biosensors. *Chem. Soc. Rev.* **2010**, *39*, 2411-2419.
16. Zhu, C.; Liu, L.; Yang, Q.; Lv, F.; Wang, S. Water-soluble conjugated polymers for imaging, diagnosis, and therapy. *Chem. Rev.* **2012**, *112*, 4687-4735.
17. Jansch, D.; Ivanov, I.; Zagranjarski, Y.; Duznovic, I.; Baumgarten, M.; Turchinovich, D.; Li, C.; Bonn, M.; Müllen, K. Ultra-Narrow Low-Bandgap Graphene Nanoribbons from Bromoperylenes—Synthesis and Terahertz-Spectroscopy. *Chem. Eur. J.* **2017**, *23*, 4870-4875.
18. Zeng, W.; Phan, H.; Heng, T. S.; Gopalakrishna, T. Y.; Aratani, N.; Zeng, Z.; Yamada, H.; Ding, J.; Wu, J. Rylene ribbons with unusual diradical character. *Chem* **2017**, *2*, 81-92.
19. Lawrence, J.; Brandimarte, P.; Berdonces-Layunta, A.; Mohammed, M. S.; Grewal, A.; Leon, C. C.; Sanchez-Portal, D.; de Oteyza, D. G. Probing the magnetism of topological end states in 5-armchair graphene nanoribbons. *ACS Nano* **2020**, *14*, 4499-4508.
20. Kimouche, A.; Ervasti, M. M.; Drost, R.; Halonen, S.; Harju, A.; Joensuu, P. M.; Sainio, J.; Liljeroth, P. Ultra-narrow metallic armchair graphene nanoribbons. *Nat. Commun.* **2015**, *6*, 10177.
21. Chen, Z.; Wang, H. I.; Bilbao, N.; Teyssandier, J.; Pechtl, T.; Cavani, N.; Tries, A.; Biagi, R.; De Renzi, V.; Feng, X.; Kläui, M.; De Feyter, S.; Bonn, M.; Narita, A.; Müllen, K. Lateral fusion of chemical vapor deposited *N* = 5 armchair graphene nanoribbons. *J. Am. Chem. Soc.* **2017**, *139*, 9483-9486.

22. Zhang, H.; Lin, H.; Sun, K.; Chen, L.; Zagranyarski, Y.; Aghdassi, N.; Duhm, S.; Li, Q.; Zhong, D.; Li, Y.; Müllen, K.; Fuchs, H.; Chi, L. On-surface synthesis of rylene-type graphene nanoribbons. *J. Am. Chem. Soc.* **2015**, *137*, 4022-4025.
23. Richter, N.; Chen, Z.; Tries, A.; Prechtel, T.; Narita, A.; Müllen, K.; Asadi, K.; Bonn, M.; Kläui, M. Charge transport mechanism in networks of armchair graphene nanoribbons. *Sci. Rep.* **2020**, *10*, 1988.
24. Berdonces-Layunta, A.; Schulz, F.; Aguilar-Galindo, F.; Lawrence, J.; Mohammed, M. S.; Muntwiler, M.; Lobo-Checa, J.; Liljeroth, P.; De Oteyza, D. G. Order from a mess: the growth of 5-armchair graphene nanoribbons. *ACS Nano* **2021**, *15*, 16552-16561.
25. Jassas, R. S.; Mughal, E. U.; Sadiq, A.; Alsantali, R. I.; Al-Rooqi, M. M.; Naeem, N.; Moussa, Z.; Ahmed, S. A. Scholl reaction as a powerful tool for the synthesis of nanographenes: a systematic review. *RSC Adv.* **2021**, *11*, 32158-32202.
26. Grzybowski, M.; Skonieczny, K.; Butenschön, H.; Gryko, D. T. Comparison of oxidative aromatic coupling and the Scholl reaction. *Angew. Chem. Int. Ed.* **2013**, *52*, 9900-9930.
27. Skraba-Joiner, S. L.; McLaughlin, E. C.; Ajaz, A.; Thamatam, R.; Johnson, R. P. Scholl cyclizations of aryl naphthalenes: rearrangement precedes cyclization. *J. Org. Chem.* **2015**, *80*, 9578-9583.
28. Solórzano, P. C.; Baumgartner, M. T.; Puiatti, M.; Jimenez, L. B. Arenium cation or radical cation? An insight into the cyclodehydrogenation reaction of 2-substituted binaphthyls mediated by Lewis acids. *RSC Adv.* **2020**, *10*, 21974-21985.
29. Gillen, R.; Mohr, M.; Maultzsch, J. Symmetry properties of vibrational modes in graphene nanoribbons. *Phys. Rev. B* **2010**, *81*, 205426.

30. Pun, S. H.; Delgado, A.; Dadich, C.; Cronin, A.; Fischer, F. R. Controlled catalyst-transfer polymerization in graphene nanoribbon synthesis. *Chem* **2024**, *10*, 675-685.
31. Borin Barin, G.; Fairbrother, A.; Rotach, L.; Bayle, M.; Paillet, M.; Liang, L.; Meunier, V.; Hauert, R.; Dumsclaff, T.; Narita, A.; Müllen, K.; Sahabudeen, H.; Berger, R.; Feng, X.; Fasel, R.; Ruffieux, P. Surface-synthesized graphene nanoribbons for room temperature switching devices: substrate transfer and *ex situ* characterization. *ACS Appl. Nano Mater.* **2019**, *2*, 2184-2192.
32. Shi, H.; Babinski, D. J.; Ritter, T. Modular C–H functionalization cascade of aryl iodides. *J. Am. Chem. Soc.* **2015**, *137*, 3775-3778.
33. Maddox, S. M.; Nalbandian, C. J.; Smith, D. E.; Gustafson, J. L. A practical Lewis base catalyzed electrophilic chlorination of arenes and heterocycles. *Org. Lett.* **2015**, *17*, 1042-1045.
34. Rodríguez, J. G.; Tejedor, J. L. Carbon networks based on 1,5-naphthalene units. Synthesis of 1,5-naphthalene nanostructures with extended π -conjugation. *J. Org. Chem.* **2002**, *67*, 7631-7640.
35. Klemm, L.; Sprague, J.; Mak, E. Syntheses and Ultraviolet Spectra of 1-(5-and 8-Methyl-1-naphthyl)-1-cyclopentenes and 1-Cyclohexenes. *J. Org. Chem.* **1957**, *22*, 161-166.
36. Más-Montoya, M.; Ortiz, R. P.; Curiel, D.; Espinosa, A.; Allain, M.; Facchetti, A.; Marks, T. J. Isomeric carbazolocarbazoles: synthesis, characterization and comparative study in Organic Field Effect Transistors. *J. Mater. Chem. C* **2013**, *1*, 1959-1969.
37. Dong, Z.; Dong, G. *Ortho* vs *ipso*: site-selective Pd and norbornene-catalyzed arene C–H amination using aryl halides. *J. Am. Chem. Soc.* **2013**, *135*, 18350-18353.
38. Liu, X.; Wang, J.; Dong, G. Modular entry to functionalized tetrahydrobenzo[*b*]azepines via the palladium/norbornene cooperative catalysis enabled by a C7-modified norbornene. *J. Am. Chem. Soc.* **2021**, *143*, 9991-10004.

CHAPTER 4

A Review on the Graphene-Based Nanomaterials for Biomedical Applications

4.1. Introduction

Graphene, a class of two-dimensional nanomaterials, has garnered widespread attention across diverse fields owing to its exceptional inherent properties ever since its first isolation by Novoselov and Geim in 2004.¹⁻¹⁰ Properties such as high conductivity, large surface area, tunable surface chemistry, high mechanical strength, optical characteristics, and biodegradability have facilitated their integration into various applications, including transparent conductors, wearable electronics, energy storage and conversion, catalysis, and biomedical applications. The physicochemical properties of graphene-based materials (GBMs) highly depend on their structures generated by the manufacturing processes. In conventional top-down approaches, the reduction of higher-dimensional carbon materials are achieved by mechanical/sonochemical/electrochemical exfoliation, unzipping of single or multi-walled carbon nanotubes (SWCNT, MWCNT), lithographic cutting, oxidative exfoliation (e.g. Hummer's method), or reduction of graphene oxides to generate two-dimensional GBMs.^{1, 11-16} Top-down methods have the capability to produce large quantities of GBMs; however, they frequently lead to poorly defined structures. Conversely, the bottom-up approach involves chemical vapor deposition (CVD) on an active metal surface or the use of meticulously designed monomers to construct structurally defined GBMs,

either on-surface or in solution.^{6, 16-19} Both on-surface and solution-phase syntheses enable precise control over the width and edge structures of the resulting GBMs (Figure 4.1a).

Due to their high structural tunability and outstanding intrinsic chemical/physical properties, various graphene derivatives have been actively investigated in the field of biomedicine (Figure 4.1b).^{7-8, 20-29 30-33} The exceptional conductivity of graphenes has spurred the development of highly sensitive sensors for biomarkers or various ions.^{29-30, 34-35} Graphene derivatives exhibiting high near-infrared (NIR) absorbance can function as effective photothermal agents for photothermal therapy against cancers.^{8, 22} The substantial surface area of GBMs facilitates the efficient loading of a diverse range of biomolecules or drugs, making them particularly advantageous for gene/drug delivery applications.^{7, 21-23, 33} Additional properties such as optical features for bioimaging, magnetic attributes for targeted delivery, or enhancement of antimicrobial activities can be further achieved by anchoring various inorganic nanoparticles.^{20, 22, 25, 31, 36}

Given the recent excellent reviews on graphene quantum dot (GQD) and graphene oxide (GO) for biosensing and bioimaging,²⁸⁻²⁹ this article will focus on the summary of therapeutic applications of GBMs, including graphene, nanographenes (NG), GO, reduced GO (rGO), and graphene nanoribbon (GNR) based nano-scaffolds. We begin by elaborating on the antimicrobial activity of GBMs, which, while beneficial in its own, is directly linked to their toxicity. Next, delving into how surface functionalization can impart diverse properties to GBMs while simultaneously reducing system toxicity, we provide a comprehensive overview of their applications in cancer therapeutics and bone regeneration, considering these are the most widely studied therapies mediated by GBMs. Furthermore, future perspectives on the potential benefits and risks of using GBMs will also be discussed.

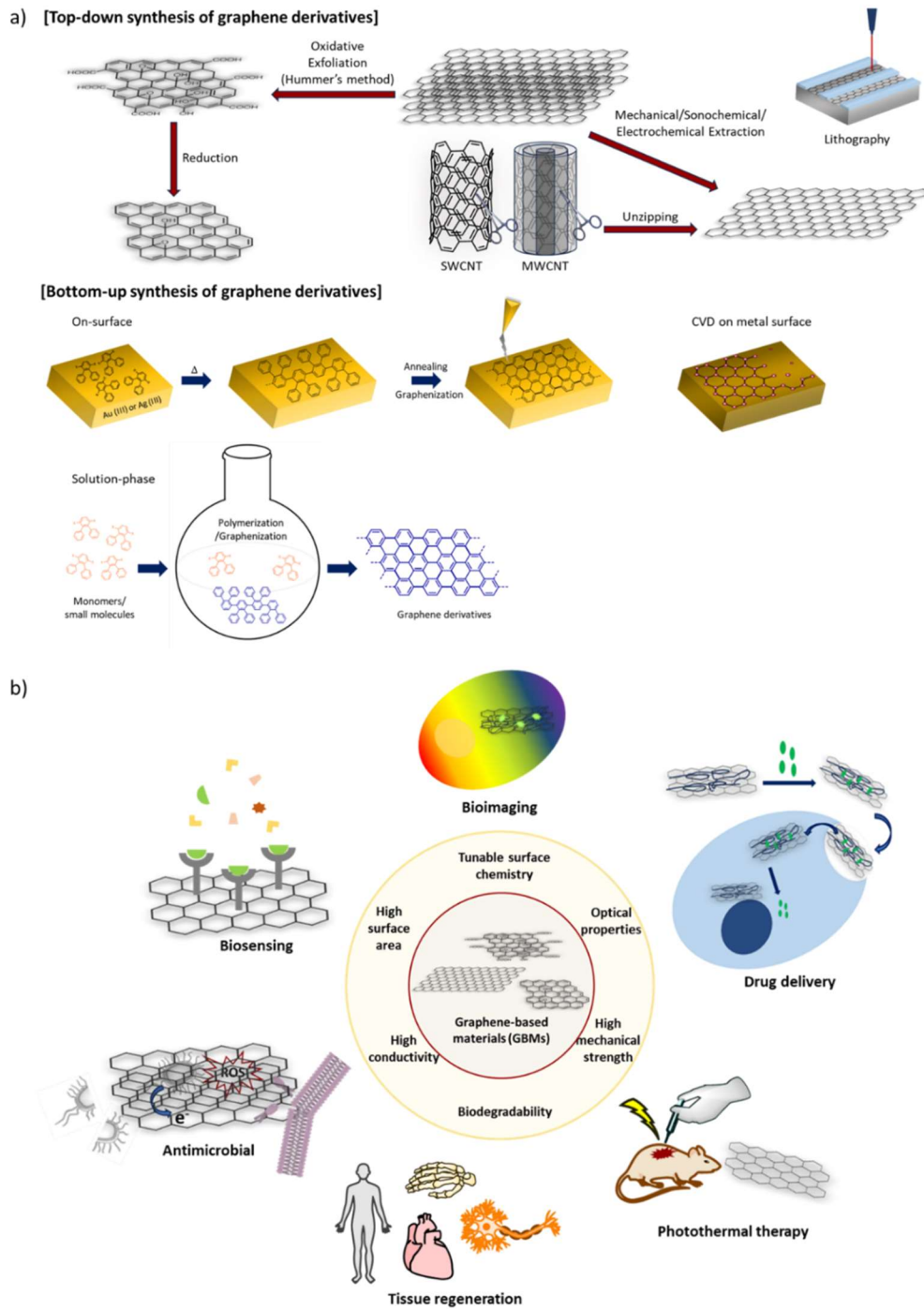


Figure 4.1. Schematic illustration of a) Top-down and bottom-up synthesis of graphene derivatives. b) Biomedical applications of graphene-based materials and their physicochemical properties.

4.2. Antimicrobial Activity

Microorganisms play diverse roles, with some being beneficial and others capable of causing life-threatening diseases and global pandemics. Although various antimicrobial agents, including antibiotics, quaternary ammonium compounds, or metal/metal oxide nanoparticles have been developed, they are plagued by issues such as high cost, environmental pollution, and, most critically, antimicrobial resistance.³⁷⁻⁴¹ Therefore, there is a necessity for the development of a new class of antimicrobial agents. In this context, graphene-based materials stand out as highly promising candidates due to their excellent intrinsic microbial properties.^{25-27, 36} The efficiency of the antimicrobial activities of GBMs depend on several factors, including the size of graphene,⁴²⁻⁴³ number of graphene sheets,⁴⁴⁻⁴⁵ concentration of GBMs,⁴⁶⁻⁴⁹ surface modification,^{47, 50-52} dispersibility of GBMs,^{47, 53} and the type of microbial species.^{49, 54-56} To design novel scaffolds with enhanced properties, comprehending the mechanism behind the antiseptic action exhibited by GBMs is crucial. The subsequent sections are focused and organized based on distinct mechanisms of cell death, involving the most extensively studied bacterial species, followed by examples of applications.

4.2.1. Physical Damage

The most straightforward mechanism involves physical damage caused by the direct contact of cell membranes with the sharp edges of graphene “nano-knives”, as initially reported by Hu et al.⁴⁶ TEM images revealed that membrane walls of *E. coli* were significantly damaged upon simple exposure to 85 µg/mL of GO and rGO, leading to significantly decreased metabolic activities and very low cell viabilities of 1.5% and 15%, respectively (Figure 4.2b). Amongst Gram-positive (*S.*

aureus) and Gram-negative (*E. coli*) bacterial models, the membrane of *S. aureus* was more significantly damaged compared to *E. coli* due to the lack of an outer membrane in Gram-positive bacteria.⁵⁴

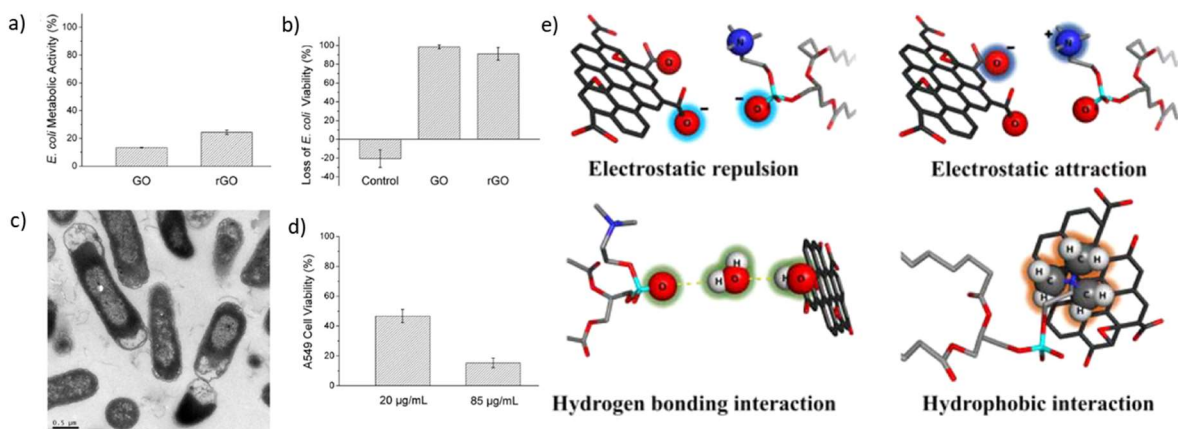


Figure 4.2. Antibacterial activity and cytotoxicity of rGO nanosheets. a) Metabolic activity of *E. coli* treated with 85 µg/mL GO and rGO nanosheets, respectively. b) Antibacterial activity of 85µg/mL GO and rGO nanosheets against *E. coli*. c) TEM image of *E. coli* exposed to 85µg/mL rGO nanosheets at 37 °C for 2 h. d) Viability of A549 cell incubated with 20 and 85µg/mL rGO nanosheets, respectively. e) Schematic illustration of molecular interactions between GO and lipid membrane. a-d) Reproduced with permission.⁴⁶ Copyright 2010, American Chemical Society. e) Reproduced with permission.⁵⁷ Copyright 2015, American Chemical Society.

Tu and colleagues conducted a comprehensive investigation into the molecular mechanism underlying the degradation of bacterial membranes induced by graphene.⁵⁸ Utilizing a combination of molecular dynamics simulations and transmission electron microscopy (TEM) analysis, two distinct pathways leading to death of *E. coli* cells (cultured with a 100 µg/mL GO solution at 37°C for 2.5 hours) were determined. The first pathway involves a well-established insertion and cutting,

while the second pathway entails partial damage to the cell membrane followed by the destructive extraction of phospholipids, ultimately resulting in bacterial death. Simulated trajectories demonstrated that initially, the tail end of the graphene sheets oscillates back and forth across the membrane surface. Subsequently, the sheet becomes trapped by the membrane due to the strong Van der Waals/hydrophobic interactions between the membrane and graphene. In this state, the nanosheet can extract phospholipid molecules from the lipid bilayers onto the graphene surface, gradually causing deformation in the membrane. In another molecular dynamics simulation conducted by Chen et al., a comparison was made between pristine graphene sheets and GO.⁵⁰ Pristine graphene sheets exhibited rapid insertion into the lipid bilayer within a 100 ns timeframe. Conversely, GO showed a preference for remaining at the hydrophilic interface due to the presence of oxygen-containing functional groups on its surface. Only half of the GO was observed to be inserted into the bilayer within a 1000 ns timescale. Further energy analysis unveiled that the cytotoxicity of GO stems from the robust dispersion interactions between graphene and lipid tails, consistent with previous observations by Tu et al.⁵⁸ This observation could further elucidate why the incorporation of biocompatible polymers, such as PEG, enhances the biocompatibility of GBMs as well as reducing its toxicity. Another physical damage pathway by Pham et al. suggested that the cutting of cell membranes by graphene nanosheets could lead to the formation of pores within the membrane, causing osmotic imbalance and eventual cell death through swelling.⁵⁹ The validity of their findings is supported by other molecular dynamics simulations and experimental findings.^{50, 60}

Akhavan reported that bacteria can be entrapped within aggregated graphene nanosheets, isolating them from the surrounding environment and impeding their access to necessary nutrients for survival.⁶¹ Atomic force microscopy (AFM) imaging clearly illustrated *E. coli* encapsulated

between the sheets. They further demonstrated that the captured bacteria could be photothermally inactivated through irradiation with a NIR laser at 808 nm. In a similar context, Mangadlao demonstrated a relationship between antibacterial efficacy and the number of GO layers. An increase in the number of layers resulted in greater bacteria encapsulation, leading to enhanced antibacterial activity.⁴⁴ The nature of the interaction between GO and lipid membrane of *E. coli* was experimentally proven by surface-enhanced infrared absorption spectroscopy, an ultrasensitive technique which allows for an *in situ* investigation of molecular interactions.⁵⁷ These involve electrostatic repulsion/attraction between GO and lipid phosphate group, hydrogen bonding with water molecules in between lipid layers and GO, and hydrophobic interaction between GO and choline group on the phospholipid (Figure 4.2e). In a more recent study, Pulingam and colleagues explored the distinct antibacterial mechanisms of GO towards Gram-positive and Gram-negative bacteria.⁶² The dominant cause of death for Gram-positive bacteria was identified as the wrapping mechanism. In contrast, Gram-negative bacteria were primarily destroyed through physical contact, resulting in membrane damage. This difference was attributed to the presence of an outer membrane layer in Gram-negative bacteria, functioning as a barrier that prevents close interaction with GO sheets.

4.2.2. Chemical Damage

Graphene can induce antimicrobial activities by causing oxidative stress through generation of ROS, such as hydroxyl radicals ($\text{OH}\cdot$), H_2O_2 , singlet oxygen ($^1\text{O}_2$), and superoxide anions ($\text{O}_2^{\cdot-}$).²⁶ ROS can trigger DNA damage, cell membrane depolarization affecting ATP synthesis, lipid peroxidation, protein deactivation, and mitochondrial inefficiency.^{48, 63-65} Gurunathan and colleagues conducted a study on the antibacterial effects of GO and rGO in *Pseudomonas aeruginosa*.⁴⁸ Their observations revealed DNA destruction, evidenced by distinct band formation under agarose gel electrophoresis. Additionally, they assessed ROS generation by monitoring the reduction of nitro blue tetrazolium (NBT), which reacts with superoxide anions, producing a water-soluble species detectable by UV at 470 nm. The findings revealed an increase in ROS, as evidenced by a 3.8-fold and 2.7-fold higher absorption in cells treated with GO and rGO, respectively, compared to the control cells. Apart from NBT, intracellular redox indicators such as GSH, *N*-acetylcystein, α -tocopherol, or dichlorodihydrofluorescein diacetate have been employed to assess ROS generation to date.^{42, 48, 66-73} In another study, Musico and colleagues observed that oxygen groups on GO can contribute to the generation of ROS.⁶⁸ They tested poly(*N*-vinylcarbazole) (PVK) modified derivatives of graphenes, specifically PVK-G and PVK-GO. The PVK-GO membrane showed a more significant decrease in GSH compared to PVK-G. The increased oxidative stress induced by GO may be attributed to its high defect density and excellent dispersibility, as also demonstrated by other studies.^{48, 72, 74} Krishnamoorthy and colleagues conducted a lipid peroxidation assay using ultrasonic irradiation to measure the free radical modulation activity of graphene nanosheets.⁶⁵ The assay included the observation of conjugated dienes, lipid hydroperoxides, and malondialdehydes, which are produced at different stages of lipid peroxidation processes. An intriguing study by Castrillon et al. employed a polydopamine-

assisted AFM probe to investigate the interaction between GO and *E. coli* membranes.⁶⁹ The dominant repulsive force between GO and the bacterial membrane was identified, stemming from the negatively charged carboxylate on GO and the negatively charged membrane of *E. coli*. These findings suggested that physical damage may not be a prerequisite for cell death. Further examination through oxidation studies using GSH indicated an oxidative mechanistic pathway.

Despite numerous reports that support the ROS-mediated pathway, such a mechanism remains controversial and lacks universal acceptance among scientists. Liu et al. observed a very low concentration of $O_2^{\cdot-}$ under NBT testing, suggesting that the source of oxidative stress on bacteria membranes are likely superoxide anion-independent.⁴⁷ Ellman's assay demonstrated that rGO exhibits a stronger oxidation capability towards GSH compared to GO, likely stemming from its higher conductivity, facilitating efficient electron transfer from the bacterial membrane to the graphene sheet. As such, the ROS-independent mechanism involves graphene functioning as an electron pump, extracting electrons from the cellular membrane. Notably, Li et al. investigated the antibacterial activities and the *I-V* characteristics of graphene films on Cu (conducting), Ge (semiconducting), and SiO₂ (insulating) (Figure 4.3). Graphene films on Cu and Ge demonstrated successful inhibition in the growth of *S. aureus* and *E. coli*, which can be attributed to the steady pumping away of electrons (Figure 4.3b-c). Conversely, the graphene-SiO₂ junction exhibited Ohmic contact and proved ineffective in restricting the proliferation of both bacteria (Figure 4.3d).⁷⁵ The electron transfer theory found further support in fullerene derivatives, with membrane destruction observed exclusively in the presence of positively charged fullerenes.⁷⁶⁻⁷⁷

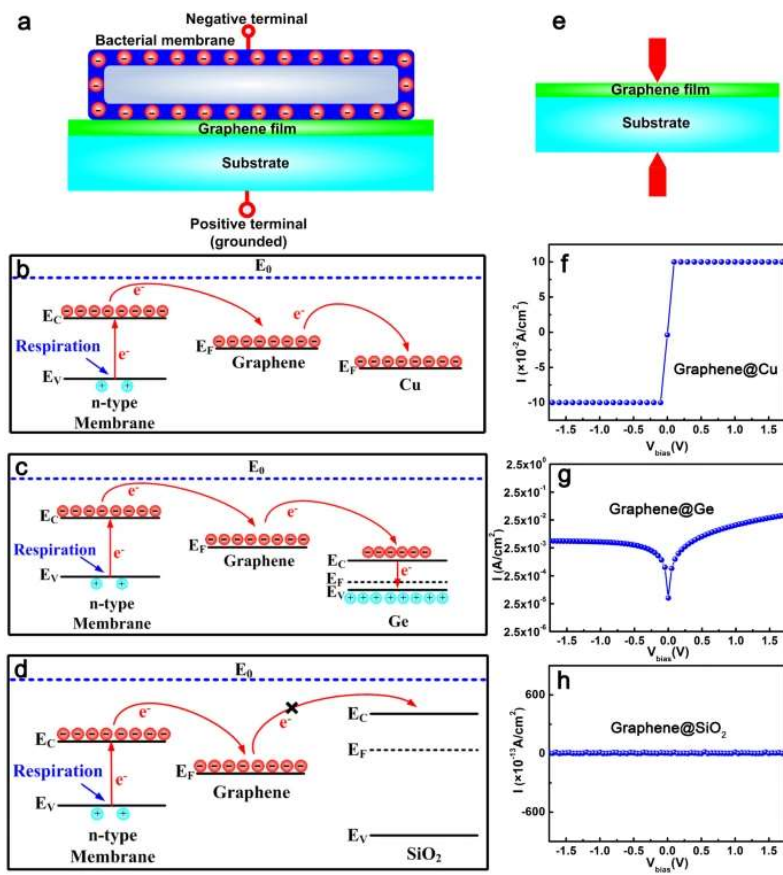


Figure 4.3. a) Schematic circuitry to illustrate the proposed mechanism for the observed phenomena. Energy band diagrams of these graphene-on-substrate junctions are shown: b) on conductor Cu, c) semiconductor Ge, d) and insulator SiO₂. e) Schematic illustration of the circuitry to obtain the current–voltage (I – V) characteristics of f) Graphene@Cu g) Graphene@Ge and h) Graphene@SiO₂ contacts at room temperature, respectively, indicating three different contacts of graphene films with the underlying substrates. Reproduced under a Creative Commons license (Attribution-Noncommercial).⁷⁵ Copyright 2014, Springer Nature.

Hui and colleagues suggested that membrane destruction is attributed to the interaction between the bacteria and the basal plane of GO.⁷⁸ When the basal plane was completely masked with tryptophan or Luria-Bertani broth, the bactericidal activity was completely abolished, leading to

an increase in bacterial count. Similarly, Mangadlao et al. noted that physical damage caused by edges is not a fundamental mechanism for killing bacterial cells.⁴⁴ GO sheets deposited using the Langmuir-Blodgett (LB) method were immobilized, including the edges, which prevents their insertion into or wrapping around the bacteria. GO-LB films exhibited a high antibacterial effect, suggesting that bacterial contact with GO edges is not the primary cause of destruction. Their findings indicated a strong correlation between the availability of basal planes and the bactericidal properties of graphene-based materials.

4.2.3. Applications

Due to the excellent antimicrobial activities of GBMs, various applications have been explored to date. Given the presence of comprehensive reviews on the applications, a concise summary of these applications is provided.^{25, 27, 36} Following the work of Hu et al., various forms of antiseptic “papers” or films have been reported.⁴⁶ Antimicrobial films based on GBMs can be largely categorized into three forms: those leveraging the inherent antimicrobial characteristics of GBMs, deactivation by light (thermal), and those enhanced with antimicrobial additives such as silver nanoparticles (AgNP).^{25, 79} To tailor the properties for specific purposes, GBM films can be incorporated with various polymers, drugs, in addition to inorganic nanoparticles. For example, antiseptic food packaging requires film flexibility, mechanical strength, and water resistance. Graphene-based nanocomposites combined with plastic-like polymers such as PLA, PVA, and poly(ethylene-co-vinyl alcohol) have been explored for food preservation purposes.⁸⁰⁻⁸² In a similar context, diverse applications of surfaces coated with bactericidal GBM-films have been proposed, including their use as membranes for blood purification, water purification, disinfection

of common objects, coating for biomedical implants, and smart disinfecting masks.⁸³⁻⁸⁶ These films have been generated by diverse methods, encompassing CVD, assembly under electric field, spin coating, solvent casting, immersion, roll-to-roll processes, and laser scribing (laser-induced graphenes), demonstrating the ease of large-area fabrication.^{80-81, 86-89}

As an effect of antimicrobial performance, graphene-based nanomicrobial agents could help minimize infections in wounded areas, accelerating the healing process. As such, bandages and dressings functionalized with GBMs have been developed as a proof-of-concept. Several strategies have been explored including: 1) taking advantage of the peroxidase-like activity of GBMs (by hybrids of GBM-H₂O₂), 2) incorporation of GBM-Ag nanoparticles, 3) reinforcement of structural stability of wound dressings, 4) utilizing the photothermal activities of GBMs, and 5) designing of antibacterial polymer-GBM composites.²⁷ Although clinical trials should precede the real-life application, it is clear that GBMs exhibit promising antimicrobial activities that deserve further investigation.

4.3. Cancer Therapeutics

4.3.1. Drug Delivery

Modern drug delivery technology has a relatively brief history, spanning approximately 70 years since the introduction of Spansule® sustained-release capsule technology by Smith, Kline & French Laboratories.⁹⁰⁻⁹¹ Key challenges in drug delivery encompass accurate dosing, efficient delivery to the intended cell/tissue/organ, and precise control over the release of the drug.⁹¹ The evolution of nanotechnology within the biomedical field, particularly in the context of cancer treatment through the development of drug delivery platforms, has gained significant attention.

Utilizing nanocarriers for drug transport stands as one of the most successful strategies in cancer treatment, primarily due to its ability to mitigate side effects and enhance therapeutic efficacy by addressing the difficulties including: 1) drug resistance, 2) cytotoxicity to the body system, and 3) drug clearance from the bloodstream.⁹²

For nanomaterials to serve as effective drug carriers, hydrophilicity is essential to facilitate their prolonged circulation in the bloodstream. GBMs are widely recognized for their ease of surface functionalization through both covalent and non-covalent bonding, enabling the attainment of hydrophilicity.⁹³⁻⁹⁶ In addition, surface functionalization can diminish the direct interaction between GBMs and biological systems, thereby reducing toxicity of the system.⁵⁸ To achieve enhanced stability and biocompatibility in physiological conditions, a diverse array of biocompatible polymers have been employed in conjunction with GBMs including polyethyleneimine, polyethylene glycol, dendrimers, chitosan, polydopamine, and hydrophilic peptides.⁹⁷⁻¹⁰⁹ The regulation of drug delivery/release relies on the specific properties of the incorporated materials or drugs within each tailored nanocarrier. The following sections are organized based on the stimuli-responsive drug delivery behavior of GBMs triggered by various stimuli, including pH, reactive oxygen species (ROS), redox activity, biomolecules, magnetic field, and temperature. Light-responsive systems are frequently integrated with photothermal therapy, and consequently, they are collectively summarized in Section 4.3.2.

4.3.1.1. pH-Responsive Drug Delivery

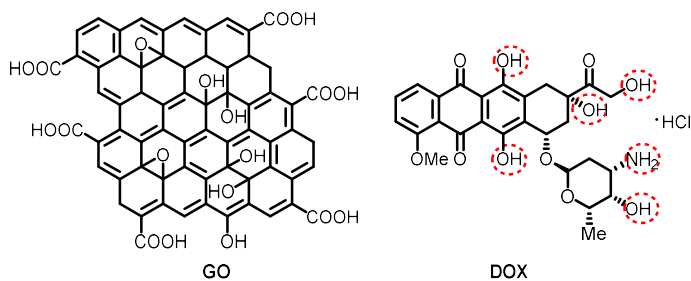


Figure 4.4. Chemical structures of GO and DOX.

Different organs, tissues, and cells exhibit unique pH levels, offering specific stimuli for pH-sensitive drug delivery systems. For instance, typical blood and tissues maintain a pH of 7.4, while tumor tissues exhibit a notable decrease in pH (5.5-6.8) attributed to the accumulation of lactic acid.¹¹⁰ Under such acidic conditions, drug molecules may undergo protonation, reducing their hydrophobic interactions and π - π stacking with the graphene surface. This, in turn, triggers a pH-responsive release of the drug. In a seminal work by Yang and colleagues in 2008, an anticancer drug, doxorubicin (DOX), was loaded onto GO for the first time.¹¹¹ In an aqueous solution, a mixture of GO and DOX was subjected to sonication, followed by centrifugation to achieve a high loading of DOX on GO. The notable loading efficiency was ascribed to the following factors: 1) the π - π stacking between GO sheets and the quinone portion of DOX, 2) hydrophobic interactions, and 3) hydrogen bonding between the amine/hydroxyl groups on DOX and carboxyl/hydroxyl groups on GO (Figure 4.4). DOX release was observed upon exposure to both acidic and basic environments. More recently, Gooneh-Farahani et al. demonstrated that bovine serum albumin (BSA)-stabilized graphene/chitosan (CS) nanocomposites loaded with DOX could sustain a consistent drug release over the course of 28 days.¹¹² In this case, release was activated by exposure

to acidic pH conditions. Additionally, oxidized graphene nanoribbons (OGNRs), derived from longitudinally MWCNTs, have been employed as nanocarriers for drug delivery. An OGNR functionalized with folic acid (FA) and tamoxifen citrate (TC) exhibited a moderate drug loading efficiency of 56%, as reported by Lila and colleagues.¹¹³ Similar to GO, OGNRs displayed pH-dependent release of TC. While this system holds promise as a platform for breast cancer treatment, further research is required to determine the *in vivo* toxicity of this nanocarrier. The same group also published a study in the same year involving a raloxifene (RXF)-loaded FA-OGNR for treating breast cancer.¹¹⁴ Likewise, simple nanocarrier systems, utilizing biocompatible material/GBM hybrids, have been reported for the delivery of various drugs including DOX,¹¹⁵ chlorambucil (CLB),¹¹⁶ cisplatin (CisPt),¹¹⁷ metformin (Met),¹¹⁸ paclitaxel (PTX),¹¹⁹ ulvan,¹²⁰ and erlotinib¹²¹. In the following examples, more intricate systems incorporating diverse functionalities are summarized.

Integration of materials with special properties

Leveraging biocompatible polymers for drug delivery can alleviate the cytotoxicity associated with graphene-based drug nanocarriers, prolong the duration of blood circulation, and impart additional properties aligned with the chosen polymer's characteristics.^{8, 22-23, 92} An example of GO functionalized with a pH-sensitive polymer, poly(2-(diethylamino ethyl methacrylate) (PDEA) by atom transfer radical polymerization was demonstrated by Kavitha et al.¹²² GO-PDEA was used as a nanocarrier to transport a water-insoluble drug, camptothecin (CPT) with a loading capacity of 15 wt%. Drug release profile demonstrated the controlled release under acidic pH conditions, due to the expansion of polymers by the protonation of amine groups. In another system

by Hashemi and Namazi, GO non-covalently functionalized with citric acid G3 dendrimer was presented.¹²³ The GO-G3 system exhibited an impressive DOX encapsulation capacity of 160% given by the high cavity of dendrimers, and the drug release profile showcased a pH-dependent release in acidic media. Intriguingly, the nanocomposite displayed fluorescence properties, providing the potential for straightforward tracing and detection of the nanocarrier in prospective *in vivo* studies. The same group has contributed several dendrimer-based systems for pH-responsive delivery of drugs, including a review article on the topic.¹⁰⁷⁻¹⁰⁹

Ghamkhari and coworkers designed a novel DOX-loaded poly(ethylene glycol) (PEG)/GO nanocomposite functionalized with a biodegradable polymer, (PHEMA-g-PLA)-b-PEG-b-(PHEMA-g-PLA) for possible oral administration to treat breast cancer.¹²⁴ The highlight of this work includes high drug encapsulation efficiency of 85%, sustained release of DOX, pH-responsiveness, and great biocompatibility.

A pH-responsive nanocarrier, comprised of highly fluorinated graphene oxide, linoleic acid, and curcumin (an anticancer drug), was assessed as a promising candidate for a negative magnetic resonance imaging (MRI) contrast agent.¹²⁵ This system harnessed the intrinsic paramagnetism of the ¹⁹F atom, with fluorination accomplished by HF. This material demonstrated tumor suppression *in vivo* without any observable side effects, highlighting its potential as a dual agent for both cancer treatment and simultaneous imaging.

Biomolecules as coating

As mentioned earlier, various biocompatible polymers have been employed to coat the GO surface, as pure GO can trigger immune responses and be rapidly cleared from the body. Another method to achieve stability in physiological conditions is by coating GO with biomolecules such as red blood cell (RBC) membrane (Xie et al).¹²⁶ DOX loaded on GO-RBC maintained good stability with a pH-dependent DOX release profile. MCF-7 cells showed strong concentration dependent cytotoxicity towards the nanomaterial. In another example by Prabakaran et al., ovalbumin (OVA) extracted from quail egg whites was employed to enhance cell permeability in GO-polymethyl methacrylate (PMMA)-OVA-DOX system.¹²⁷ The nanosystem demonstrated pH-responsiveness *in vitro*, and the efficiency of cell death increased by 17% compared to free DOX.

Self-degradation

The Bianco group presented a notable illustration of a multifunctional nanocarrier with inherent self-degradation capabilities.¹²⁸ Their approach involved the modification of GO with *N*-formyl-methionyl-leucyl-phenylalanine (fMLP), a molecule recognized for its affinity to the formyl peptide receptor prevalent on the membranes of various cancer cells. In addition to its targeting effects, fMLP is recognized for its ability to activate neutrophils, e.g., polymorphonuclear neutrophils (PMN).¹²⁹⁻¹³⁰ Neutrophils have been reported to enzymatically degrade carbonaceous materials by inducing the secretion of human myeloperoxidase (MPO). *In vitro* studies of GO and GO/fMLP degradation were conducted using freshly isolated human PMN. Detailed analysis with Raman spectroscopy showed that characteristic features (D and G band) of graphene materials

disappeared within a short time frame for GO/mLMP-PMN, in contrast to GO-PMN (Figure 4.5). In addition, the release of DOX in acidic conditions (pH 5.0) was 3 times higher for GO/mLMP-DOX compared to GO-DOX, due to the peptide-modified surface. Besides exhibiting biodegradability and pH-responsiveness, the nanomaterial was efficiently internalized by cancer cells and effectively induced apoptosis *in vitro*.

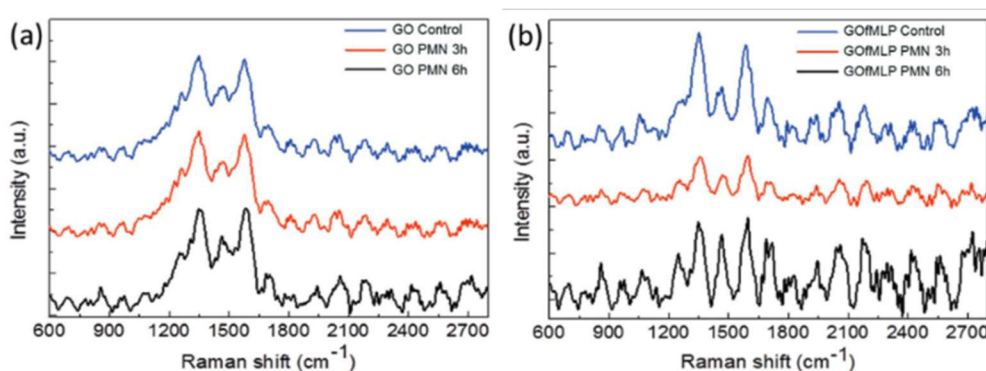


Figure 4.5. a) Neutrophil degradation of GO and b) GO/mLMP monitored by Raman spectroscopy.

Reproduced with permission.¹²⁸ Copyright 2019, John Wiley & Sons, Inc.

Dual drug loading

Many graphene-based drug delivery systems typically carry a single drug, often requiring a high dose for efficient treatment, leading to an increased *in vivo* toxicity. In addition, tumors may develop resistance to drugs over time, diminishing the efficacy of a single-drug system.²² To address this, a promising approach involves a nanocarrier capable of delivering multiple drugs for combined chemotherapy. For instance, chitosan (CS) loaded on rGO exhibited high drug encapsulation efficiency (>90%) for both curcumin (CUR) and 5-fluorouracil (5-FU), successfully

inhibiting the growth of HT-29 colon cancer cells.¹³¹ A similar system employed intrinsically bioactive sodium alginate beads and CS beads embedded on rGO to encapsulate CUR and 5-FU, synergistically combating MCF-7 cancer cells.¹³² Pourjavadi et al. designed a co-delivery system for hydrophobic CUR and hydrophilic DOX.¹³³ The edges of GO were functionalized with poly(epichlorohydrin)-*graft*-hyperbranched polyglycerol (PCH-g-HPG), followed by replacing the chlorines with hydrazine. DOX was covalently connected to hydrazine, and CUR was loaded onto GO through π - π stacking interactions. This nanocarrier exhibited pH-sensitive behavior for both drugs, making it a promising approach for enhanced therapeutic outcomes. Another example of combined chemotherapy by Pei and their team involved a PEGylated NGO-CisPt-DOX nanoparticle system.⁹⁷ The loadings of CisPt and DOX were optimized to a 1:1 weight ratio. At pH 5.3, approximately 65% drug release was observed for both CisPt and DOX after 72 h. In *in vivo* studies, a profound suppression of tumor cell proliferation was observed in the presence of the dual drug-loaded system, surpassing the efficacy of individual pGO or CisPt/DOX administrations. In a similar vein, an array of studies on the synergistic effects of combined chemotherapeutic approaches has been reported, with notable examples including co-delivery of camptothecin/gefitinib, quercetin/gefitinib, CUR/paclitaxel, CUR/DOX, CisPt/DOX, mitoxantrone/DOX, and protocatechuic acid/chlorogenic acid.^{97, 134-140} These investigations underscore the growing interest and potential for enhanced cancer treatment through the combination of multiple therapeutic agents.

Dual stimuli-responsive system

Zhang et al. presented a dual-sensitive GO-based drug delivery system that responded to both pH and redox conditions.¹⁴¹ This system was designed for the co-delivery of DOX and a proapoptotic peptide (KLA). KLA was covalently linked to GO through a disulfide bond, and the system was enveloped with BSA to ensure stability under physiological conditions. *In vitro* experiments indicated that drug release could be induced either by acidic pH conditions or exposure to a reductive agent, dithiothreitol (an alternative to glutathione, which is also a reductant abundant around cancer cells capable of cleaving the disulfide bond). The experimental results suggest that GO-SS-KLA/BSA nanoparticle could be efficiently taken up by MCF-7 cancer cells and exhibit synergistic action of KLA and DOX.

Targeted delivery system

The surfaces of cancer cells are rich in biotin receptors. In a study by Vinothini et al., a DOX-biotin-GO nanocarrier was designed for targeted delivery to cervical cancer cells.¹⁴² GO was coated with κ -Carrageenan, a negatively charged natural polysaccharide, to enhance potential degradability. A substantial drug loading efficiency of 94% was achieved and the nanosystem demonstrated effective pH-sensitive drug release in *in vitro* experiments. Another targeted system by Suryaprakash and coworkers revealed that tumor-trophic mesenchymal stem cells (MSCs) could serve as a highly effective targeted carrier for drugs loaded onto GO.¹⁴³ Both DOX and mitoxantrone (MTX) were loaded onto GO with similar efficiencies of >30%, with drug release occurring when exposed to the acidic tumor microenvironment. To demonstrate the cancer cell

recognition capability of this nanocarrier, three different models were investigated (Figure 4.6a). In both the co-culture and migration models, high LN18 cell deaths of 54% and 53%, respectively, were observed (Figure 4.6c). The migration model exhibited a delay in the killing (Figure 4.6b). In the transwell model, a lower cell death of 27% was observed, proving the specificity of MSCs towards cancer cells (Figure 4.6c).

Tumor-derived exosomes (EXO) are recognized for their inherent “homing ability” to the original cancer cells. Leveraging these properties, a nanosystem composed of GO/MTX/EXO, chito oligosaccharide, and γ -polyglutamic acid, demonstrated significant potential for breast cancer treatment (Chen et al.).¹⁴⁴ Their drug carrier reported an impressive 73% encapsulation efficiency for MTX. Furthermore, they observed a controlled drug release profile, with 57% of the drug released at pH 5.0, while only 7% was released at pH 7.4 over a 120-hour period, demonstrating excellent pH-responsive drug release behavior. To achieve further enhanced targeting specificity, a very small HN-1 peptide (TSPLNIHNGQKL), capable of penetrating through tumor tissue, was loaded onto the DOX@NGO-PEG system. The nanocarrier was capable of targeting CAL-27 and SCC-25 oral squamous cell carcinoma cells, and exhibited pH-responsive release of DOX under acidic environments.¹⁴⁵

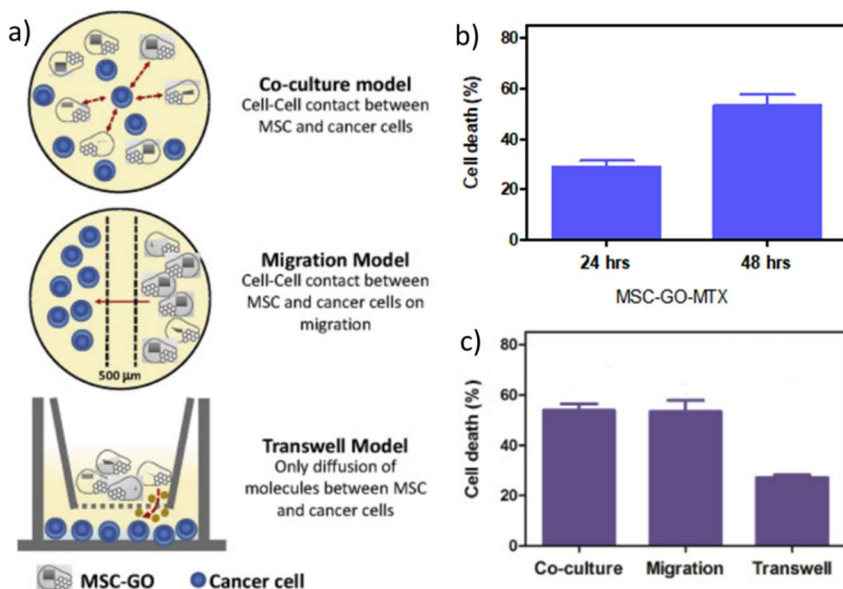


Figure 4.6. a) Three different toxicity models for testing MSC-GO-Drug. b) Delay in cell death in the migration model. c) Toxicity test of LN18 under the three models. Reproduced with permission.¹⁴³ Copyright 2018, Elsevier.

Enhancing the loading efficiency

Samadi and colleagues have demonstrated the use of high-force electric devices for electrospinning to enhance the drug loading capacity of graphene-based nanocarriers.¹⁴⁶ They employed this technique to fabricate nano-scale fibers containing a combination of chitosan, GO, TiO₂, poly(lactic acid) (PLA), and DOX, creating nanopores suitable for drug encapsulation. The SEM images (Figure 4.7a-f) showed that incorporation of TiO₂ nanoparticles result in an increase in diameter of the fiber, due to higher viscosity of the electrospinning solution. When GO was loaded, beads were observed on the fibers. Such porous nanofibers allowed for a remarkable

loading efficiency of over 90% for a 50 mg drug payload. The release profile suggested that the release rate was greatly decreased by increasing fiber thickness (Figure 4.7g). The initial rapid release of the drug is attributed to the release of DOX from the surface of the fiber, while the gradual release results from the slow diffusion from the inside of the nanofiber cavities. A higher sustained release of DOX was achieved with nanofibers thicker than 30 μm . The electrospun nanofiber also exhibited a mildly pH-responsive release characteristic (Figure 4.7h).

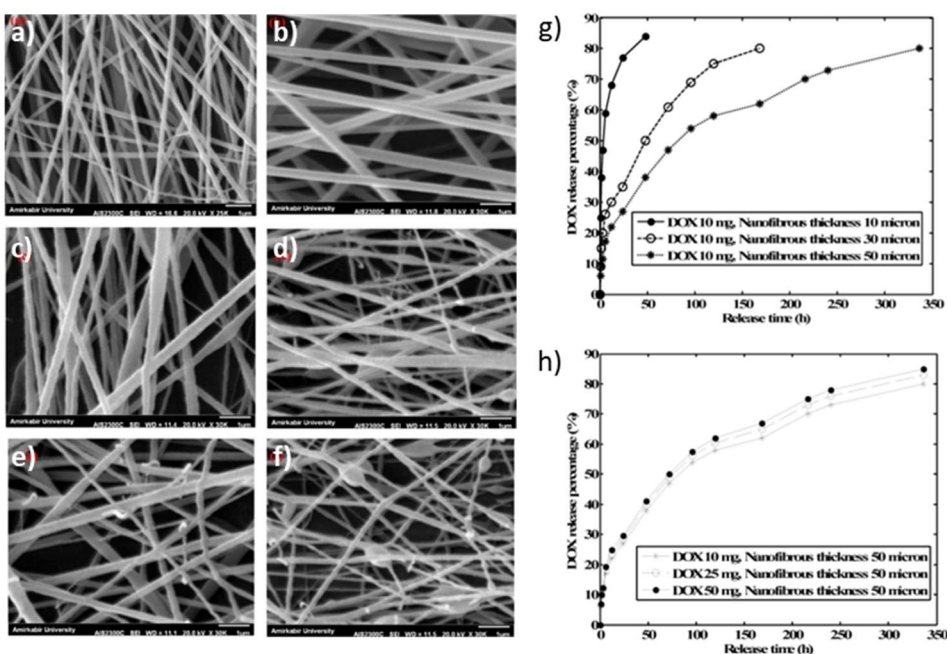


Figure 4.7. SEM images of a) PLA/chitosan, b) PLA/chitosan/TiO₂, c) PLA/chitosan/TiO₂/DOX, d) PLA/chitosan/TiO₂/DOX/GO 500 mg, e) PLA/chitosan/TiO₂/DOX/GO 1000 mg and f) PLA/chitosan/TiO₂/DOX/GO 1500 mg nanofibers. DOX release profiles from g) different thicknesses of nanofibers and h) pH values of 7.4 and 5.3. Reproduced with permission.¹⁴⁶ Copyright 2018, Elsevier.

4.3.1.2. ROS-Responsive Drug Delivery

Reactive oxygen species refer to highly reactive oxygen ions or free radicals such as singlet oxygen ($^1\text{O}_2$), hydrogen peroxide (H_2O_2), hydroxyl radical ($\bullet\text{OH}$), superoxide (O_2^-), and hypochlorite ion (OCl^-). While elevated ROS levels can contribute to conditions like cancer or cellular inflammation, biological systems naturally produce ROS at low levels for purposes such as cell signaling and proliferation.²³ Traditional ROS-responsive drug delivery systems, like nanoparticles or hydrogels, often fall short in delivering effective treatment due to their susceptibility to rapid degradation/clearance and limited bioavailability. Consequently, there are limited reports available on ROS-responsive delivery methods. In 2022, Wu et al. reported a ROS-responsive nanofiber membrane based on rGO as a nanocarrier for the treatment of osteoarthritis.¹⁴⁷ Poly(ethylene glycol) diacrylate (PEGDA)-1,2-ethanediol (EDT) copolymer (PEGDA-EDT) is a ROS-responsive material, where the hydrophobic thioether group is converted into hydrophilic sulfone/sulfoxide groups when exposed to ROS. Poly(lactic acid), which is a biodegradable and biocompatible polyester approved by the Food and Drug Administration (FDA), served as the backbone of the (PEGDA-EDT) nanofiber.¹⁴⁸ Fucoxanthin (Fx) was loaded onto rGO-(PEGDA-EDT)-PLA, and the nanomaterial exhibited low toxicity and a long-term release of Fx over 66 days in response to H_2O_2 *in vitro*.

4.3.1.3. Redox-Responsive Drug Delivery

It is well known that the cellular redox environment is regulated by glutathione (GSH).¹⁴⁹ There are different concentrations of GSH in the exterior (10 mM) and interior (2 mM) of cells. Notably,

some tumor cells possess GSH levels that are at least 4-fold higher than those observed in normal cells.¹⁵⁰ The significant contrast in GSH levels presents a promising stimulus for triggering drug release. The Shi group presented a unique system composed of NGO with a methoxy polyethylene glycol (mPEG) attached via a disulfide linkage (SS). As illustrated in Figure 4.8, NGO-SS-mPEG was first internalized by cancer cells through endocytosis, and the heightened GSH concentration within the cancer cells triggered the cleavage of the disulfide bond, releasing the loaded DOX.¹⁵¹ It is worth noting that this system holds the potential for facilitating the biodegradation of GO. In a related system documented by the Liu group, the redox-responsive surface coating of the GO-SS-PEG system experienced progressive degradation through oxidation induced by horseradish peroxidase (HRP).¹⁵²

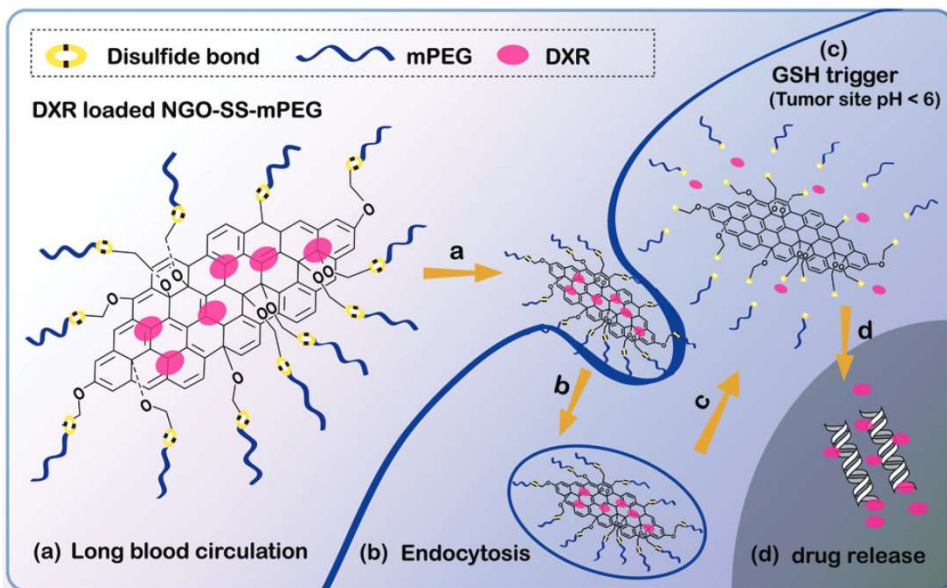


Figure 4.8. Schematic diagram of redox-sensitive NGO-SS-mPEG-DXR showing antitumor activity. a) PEG-shielded NGO with disulfide linkage for prolonged blood circulation. b)

Endocytosis of nanocarrier into tumor cells via the EPR effect. c) GSH triggers PEG detachment. d) Rapid DOX release on the tumor site. Reproduced with permission.¹⁵¹ Copyright 2012, Wiley.

Another work by Chen and coworkers demonstrated a drug carrier based on nanoscale GO (NGO)-polyethylene imine (PEI)-SS-DOX loaded with silver nanoparticles.¹⁵³ The intracellular real-time drug release of NGO-PEI-SS-DOX was monitored by a combination of surface-enhanced Raman scattering (SERS)-fluorescence spectroscopy. The liberation of DOX was significantly contingent on the concentration of GSH, with pH exerting minimal influence on DOX release (Figure 4.9a-c). Analysis through SERS spectroscopy revealed the disappearance of characteristic DOX peaks (461, 790, 1090, 1210 cm^{-1}) within 6 hours, indicative of the complete release of DOX within that time frame (Figure 4.9d). Additional fluorescence imaging provided further confirmation of DOX release within a comparable time frame. This was evidenced by the restoration of DOX fluorescence following S-S cleavage.

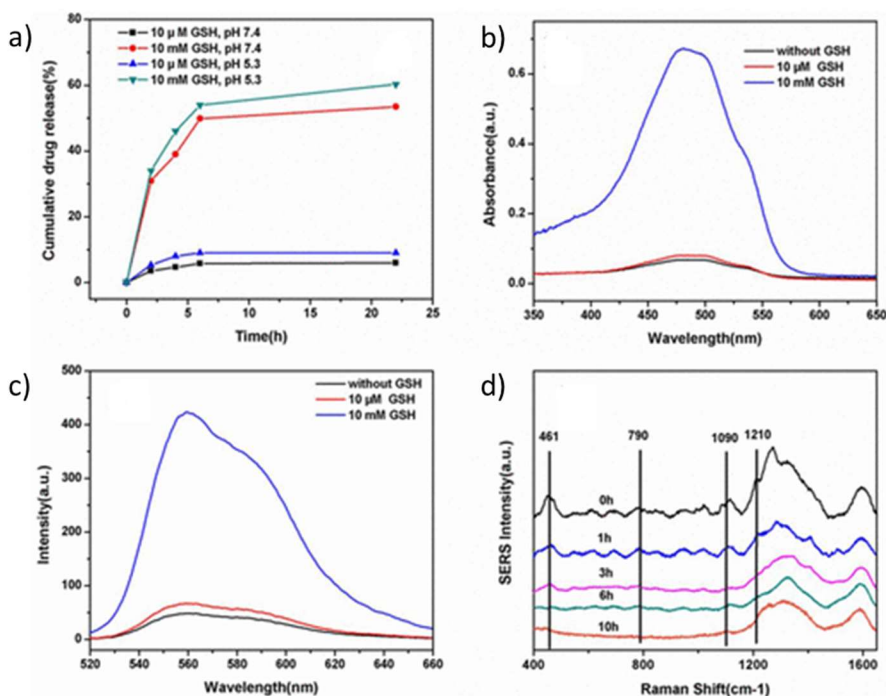


Figure 4.9. a) GSH-responsive drug release profile at pH 7.4 and 5.3. b) Absorbance and c) fluorescence of the released DOX after nanoparticle was dialyzed for 24 h under various GSH concentrations. d) Average SERS spectra ($n = 10$) of the nanoparticle solution after being dialyzed for different time periods. Reproduced with permission.¹⁵³ Copyright 2014, American Chemical Society.

4.3.1.4. Biomolecule-Responsive Drug Delivery

Biomolecules can also serve as stimuli to induce drug release in smart delivery systems based on GBMs. Gu and colleagues employed adenosine-5'-triphosphate (ATP), the principal energy molecule, as a trigger for drug release.¹⁵⁴ A nanoaggregate comprising GO sheets crosslinked by two single-stranded DNA molecules (ssDNA, designated as DNA1 and DNA2) and an ATP aptamer was laden with DOX, as shown in Figure 4.10a. Upon exposure to ATP, the interaction with the ATP aptamer led to the disassembly of the structure, facilitating the release of DOX. *In vitro* studies demonstrated a sustained release of DOX; nevertheless, the free DOX solution exhibited the highest toxicity against HeLa cells, suggesting a somewhat inefficient release of DOX from the GO surface. The same group reported a follow-up work utilizing a furin (cellular protease) cleavable peptide mediated GO (fGO) for co-delivery of DOX and tumor-necrosis-factor-related apoptosis-inducing ligand (TRAIL) for a synergistic combined therapy.¹⁵⁵ As illustrated in Figure 4.10b-c, the nanocarrier accumulates at the tumor site following intravenous administration, facilitated by both passive and active targeting effects. Subsequently, there is a site-specific delivery of TRAIL to the death receptor on the cell membrane. The membrane-bound furin enzyme cleaves the peptide, releasing TRAIL, which, in turn, induces cell apoptosis.

Simultaneously, the liberated GO-PEG-DOX can undergo internalization into the cells, contributing to the chemotherapy process. *In vivo* studies revealed that this synergistic therapeutic approach exerted a potent effect in suppressing tumor growth, with no observed abnormalities in other normal organs.

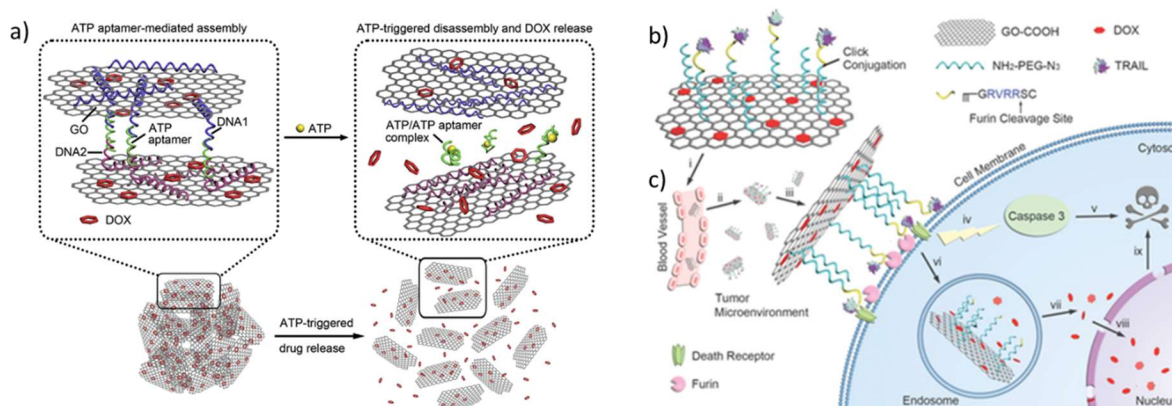


Figure 4.10. a) A schematic illustration of ATP-responsive delivery system. b) Structure of furin-cleavable peptide-conjugated TRAIL/fGO-PEG-DOX nanocarrier. c) Systematic co-delivery of TRAIL and DOX to the tumor site. i: intravenous administration of the nanocarrier; ii: accumulation of GO at the tumor site, iii: binding of TRAIL on the death receptor followed by consumption of peptide linker by furin; iv: activation of caspase-mediated apoptosis; v: cell death; vi: endocytosis of GO by tumor cells; vii: pH-responsive DOX release in endosome; viii: DOX release into the nucleus; ix: DNA damage-mediated apoptosis. a) Reproduced with permission.¹⁵⁴

Copyright 2015, Elsevier., b-c) Reproduced with permission.¹⁵⁵ Copyright 2014, Wiley

4.3.1.5. Magnetic Field-Responsive Drug Delivery

Numerous graphene-based drug delivery systems exhibit excellent control over drug loading and release. However, achieving specificity for targeting desired cancer cells remains a challenge. Conventional targeting systems utilize ligands specific to receptors or antibodies to enhance specificity, but the limited stability of these ligands within the body system constrains their applications. Magnetic nanoparticles such as Fe_3O_4 , Fe_2O_3 , Prussian blue, FeS , and Fe -polyphenols can be magnetically controlled by an external magnetic field for targeted drug delivery.¹⁵⁶⁻¹⁵⁷ In addition iron is biocompatible and has the potential to induce ferroptosis.¹⁵⁸ In this sense, graphene nanocarriers bearing such magnetic materials have been developed for targeted drug delivery. In 2009, Yang et al. synthesized an external field-responsive GO-DOX- Fe_3O_4 nanoparticles (Figure 4.11a).¹⁵⁹ The hybrid material exhibited pH-controlled magnetic behavior (Figure 4.11b): 1) under neutral conditions, the particles were well dispersed in water and did not respond to the magnetic field, 2) in acidic (pH 2-3) conditions, strong hydrogen bonding interaction between the GO sheets triggered aggregation of GO- Fe_3O_4 , and responded to the magnetic field, and 3) in basic conditions (pH 8-9), charge repulsion between negatively charged GO led to redispersion of nanoparticles. Following this work, the same group published a GO- Fe_3O_4 covalently functionalized with folic acid for dual-targeted delivery towards tumor cells.¹⁶⁰

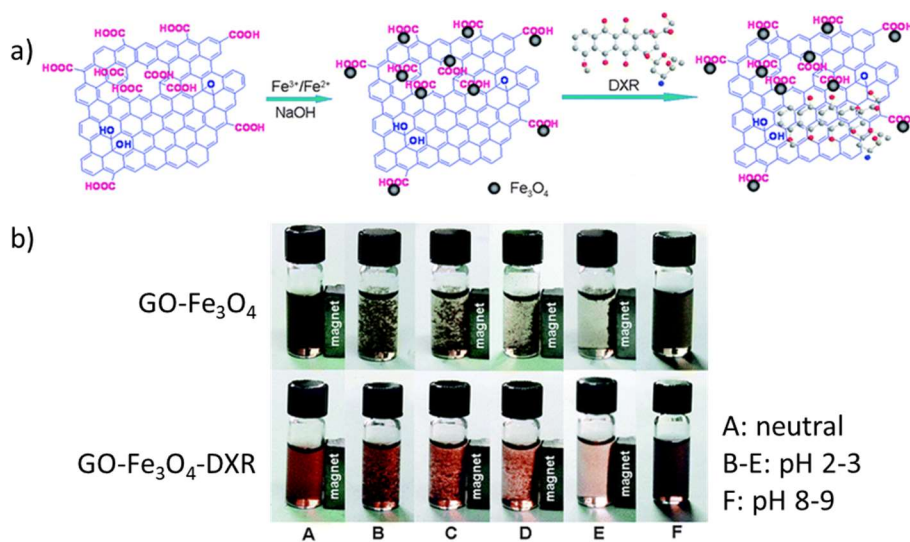


Figure 4.11. a) Schematic representation of GO loaded with Fe_3O_4 nanoparticles and DOX (DXR in the figure). b) Photographic images of the $\text{GO-Fe}_3\text{O}_4$ or $\text{GO-Fe}_3\text{O}_4\text{-DOX}$ in the magnetic field under different pH conditions. Reproduced with permission.¹⁵⁹ Copyright 2009, Royal Society of Chemistry.

Simple systems

Paknia and colleagues developed a $\text{GO-Fe}_3\text{O}_4$ nanocarrier modified with hyperbranched polyglycerol (HPG) polymer through anionic ring-opening multi-branching polymerization (ROMBP).¹⁶¹ The incorporation of HPG significantly enhanced the biocompatibility of GO, and this nanocarrier exhibited an impressive CUR loading capacity of 198%. A comprehensive analysis, which included bioinformatics investigations, suggested that this system has the potential to be an effective approach for cancer treatment. Matiyani and their team successfully developed a polyvinylpyrrolidone (PVP) grafted $\text{GO@Fe}_3\text{O}_4$ nanosystem, which demonstrated intelligent delivery of quercetin, an antioxidant used in cancer treatment.¹⁶² This nanosystem exhibited selectivity towards MDA-MB-231 breast cancer cells while maintaining biocompatibility with

normal HEK 293T cells. This suggests its potential as a targeted and biocompatible platform for cancer treatment. Makharza and their research team successfully achieved selective delivery of CisPt to glioblastoma cancer cells using a designed nanomaterial, $\gamma\text{-Fe}_2\text{O}_3@\text{NGO}$.¹⁶³ This nanomaterial demonstrated a strong binding affinity for CisPt, enabling a sustained release of the drug, with 80% released over a span of 250 hours. Additionally, magnetization measurements indicated the superparamagnetic properties of this magnetic nanoparticle, with a magnetic saturation (MS) of 15 emu/g and a magnetic field (MF) of 7 tesla.

Dual loading of drugs

Dual-drug delivery systems have been explored in magnetic nanoparticle systems as well. Astani et al. grafted polyhydroxyethyl methacrylate (PHEMA) onto reduced graphene oxide (rGO) and subsequently converted the hydroxy groups to succinyloxy groups through polyesterification with succinic anhydride.¹⁴⁰ This unique nanocomposite structure facilitated high encapsulation of DOX (75%) and CisPt (82%) through $\pi\text{-}\pi$ interactions, hydrogen bonding, and ionic interactions. The resulting combinatorial system demonstrated significant cytotoxicity in MCF-7 cells *in vitro*.

More precise dual targeting

To further enhance the precision of dual-targeting magnetic delivery systems, various approaches have been explored. Jiang group constructed a dual targeting GO based on boronic acid grafted magnetic GO (MGO).¹⁶⁴ MGO was additionally functionalized with molecularly

imprinted polymers (MIPs), which are polymers designed with specific recognition sites for particular substances. MGO-MIP-DOX showed a remarkable selectivity for tumor cells over normal cells, indicating the safety of chemotherapy. In addition to high specificity, the nanocarrier exhibited resistance to enzymatic attack and degradation in harsh environments. The inhibition of mitochondrial activity is a widely used strategy in anticancer treatment. In this context, Zhu and coworkers developed a system involving $\text{Fe}_2\text{O}_3@\text{GO}$, functionalized with a mitochondrion targeting peptide (MitP) and loaded with MTX.¹⁶⁵ They successfully demonstrated mitochondrial targeting *in vitro*, and when exposed to an alternating magnetic field, the release of MTX resulted in a decrease in the mitochondria membrane potential. This, in turn, led to a reduction in ATP production, ultimately triggering apoptosis.

Nanocarriers with additional functionalities

A biocompatible $\text{Fe}_3\text{O}_4\text{-GO}$ furnished with copolymer brushes of *N*-isopropylacrylamide (NIPAM) and acrylated β -cyclodextrin (Ac- β -CD) was designed by Pooresmaeil and Namazi. The stimuli-responsive polymers displayed a lower critical solution temperature (see Section 4.2.1.6 for details) of 35 °C. Under conditions of 40°C and pH 5.0, a controlled drug release profile was observed, with 65% DOX release. Further analysis of the system revealed that a magnetic saturation of 10.31 emu/g can respond to the external magnetic field.¹⁶⁶

Ali and their team demonstrated that zinc ferrite (ZnFe_2O_4) nanoparticles can serve as contrast agents for magnetic resonance imaging in a GO based drug delivery system for DOX.¹⁶⁷ Their research also revealed that the system induced the generation of ROS, which in turn led to nucleus

and mitochondrial dysfunction, ultimately triggering apoptosis in HeLa cancer cells. This suggests the potential of the system for cancer therapy and imaging.

Magnetic nanoparticles are recognized for their capability to produce heat when subjected to an alternating magnetic field.¹⁶⁸⁻¹⁷⁰ An iron oxide-GO nanocarrier stabilized with PVP and poly(vinyl alcohol) (PVA) demonstrated a magnetic hyperthermia effect (Swain and coworkers).¹⁷¹ Additionally, this magnetic nanocarrier exhibited high loading efficiencies of 87% for DOX and 91% for PTX. The synergistic impact of thermo- and chemotherapy proved effective in killing cancerous cells. The authors highlighted that the composite had the ability to induce cancer cell death through hyperthermia alone.

4.3.1.6. Thermal-Responsive Drug Delivery

PNIPAM, or poly(*N*-isopropylacrylamide), stands as one of the most extensively studied temperature-sensitive polymers. It undergoes a hydrophilic-hydrophobic transition at a lower critical solution temperature (LCST) around 32 °C.¹⁷² The tuning of this LCST can be achieved by co-polymerization with other monomers or by modifying the hydrophobic end-groups.¹⁷³⁻¹⁷⁵ Therefore, the incorporation of PNIPAM onto GBMs can bestow tunable thermo-responsive characteristics to the drug carrier. A GO-PVP-NIPAM-lysine hybrid system for the delivery of fluorouracil, a chemotherapeutic agent to treat MCF-7 breast cancer cells, was designed by Ashjarian and colleagues.¹⁷⁶ In this system, the impact of pH was observed to be mild, whereas a mere 3-degree increase in temperature substantially augmented drug release at both pH levels (Figure 4.12). Currently, the majority of thermo-responsive drug delivery systems based on GBMs

are constructed using PNIPAM.^{166, 177-181} Few exceptions include systems incorporating poly(*N*-vinylcaprolactam), thermosensitive hydrogels, poloxamers, etc.¹⁸²⁻¹⁸⁵

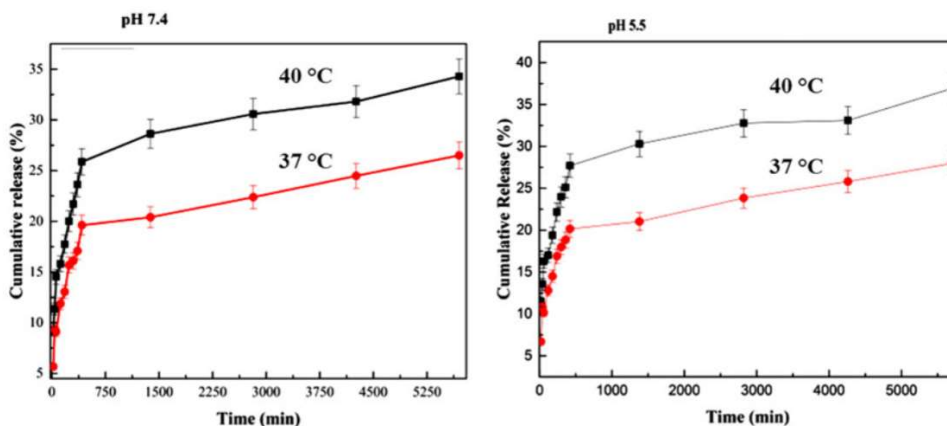


Figure 4.12. A thermal-responsive release of GO-PVP-NIPAM-lysine hybrid system. Reproduced under the terms of the CC-BY license.¹⁷⁶ Copyright 2019, The Authors, published by Taylor & Francis.

Table 4.1. A summary of graphene based nanocarriers for drug delivery applications.

Mono drug delivery		Drug	Target	Highlights	Ref.
GBMs	GO-BSA-chitosan	DOX	SKBR-3	- pH-responsive - Reduced cell viability of SKBR-3	112
	AGO-CS-FA	DOX	L929, HeLa, MCF-7	- High drug loading of 95% - pH-responsive - Amine functionalized GO (AGO) serves as a cationic polyelectrolyte under acidic conditions	115
	rGO-CHA	DOX	KB (<i>in vivo</i>)	- Cholesteryl hyaluronic acid (CHA) to reduce GO - 4-fold increase in DOX loading compared to rGO	186
	GO/(PHEMA-g-PLA)-b-PEG-b-(PHEMA-g-PLA)	DOX	4T1 breast cancer cells (<i>In vivo</i>)	- Stable dispersion in physiological solutions - Oral administration - 85% drug loading - Sustained release of DOX - pH-responsive	124

GO-RBC	DOX	MCF-7	- Biocoating with red blood cell (RBC) membrane - Stable under physiological conditions	126
GO-PMMA-OVA	DOX	CACO-2	- pH-responsive - Biocoating with ovalbumin extracted from quail egg whites - Enhanced permeability	127
GO-fLMP	DOX	HeLa	- pH-responsive - Self-degradation by inducing neutrophil enzymatic degranulation - 3-fold increase of DOX under acidic conditions - Targeted delivery of drug by formyl peptide receptor recognition of fLMP	128
GO-SS-KLA-BSA	DOX	MCF-7	- pH-responsive - Redox-responsive (S-S bond cleavage)	141
GO- κ -Car-biotin	DOX	HeLa	- High stability achieved by coating of BSA - High drug loading (94%) - pH-responsive - Targeted delivery by biotin - Potential degradability by κ -Carrageenan	142
NGO-PEG-HN-1	DOX	CAL-27, SCC-15	- High selectivity towards specific cancer cell targeting by HN-1 peptide - pH-responsive	145
GO-CS-PLA-TiO ₂	DOX	A549	- Nanofibrous scaffold allows for a high drug loading capacity (98%) - pH-responsive	146
GO-Fe ₃ O ₄ -MIP	DOX	HepG2, L02	- High recognition towards carcino-embryonic tumor markers by MIP - pH-responsive	164
GO-Fe ₃ O ₄ -PB	DOX	MCF-7, MCF-10A	- Excellent biocompatibility - Featuring copolymer brushes of NIPAM and Ac- β -CD - Heat and pH-responsive - Successful cell uptake and higher killing effect compared to pristine DOX	166
GO-ZnFe ₂ O ₄	DOX	HeLa	- Serves as contrast agents for MRI - ROS generation	167
NGO-SS-mPEG	DOX	HeLa	- 10 mM GSH triggers reductive cleavage of disulfide linkage (redox-responsive) - High physiological stability and solubility	151
NGO-Ag-PEI-SS	DOX	HeLa	- 10 mM GSH triggers reductive cleavage of disulfide linkage (redox-responsive) - DOX release monitored by SERS, fluorescence spectroscopy - Insignificant cytotoxicity of the nanoparticle (without DOX) up to a high concentration of 1.0 mg/mL	153
GO-DNA-ATP aptamer	DOX	HeLa	- ATP-responsive - Highlights a unique crosslinked structure created by self-assembly	154
fGO-TRAIL-PEG	DOX	A549 (<i>in vivo</i>)	- Furin-responsive - Effective combined therapy of TRAIL and DOX <i>in vivo</i> - No visible damage in other normal organs	155
GO-G3	DOX	T47D, MCF10A	- G3 dendrimer synthesized in three steps - pH-responsive - High loading efficiency (160%) - Exhibits fluorescence in acidic media	123
GO-MSc	DOX or MTX	LN18	- Effective targeting by mesenchymal stem cells - Similar loading efficiencies for both drugs (>30%) - pH-responsive	143
GO-CO- γ -PGA-EXO	MTX	MDA-MB-231	- High selectivity for LN18 over MSC cells - Enhanced targeting by tumor-derived exosomes - High encapsulation efficiency (73%) - Excellent pH-responsive behavior	144
GO-Fe ₂ O ₃ -MitP	MTX	HeLa MCF-7	- Preferential targeting towards mitochondria by MitP	165

GO-PDEA	CPT	N2a cells	- Loading capacity (19%) - Alternating magnetic field assisted MTX release - pH-responsive (no release in acidic or basic conditions)	122
GS-PNIPAM	CPT	A-5RT3	- 15% drug loading - Negligible cytotoxicity - Temperature responsive (33 °C)	179
FA-gelatin-GO (FAGGO)	CLB	Siha cervical cancer cell line	- Loading capacity (18.5 wt%) - Insignificant toxicity of GS-PNIPAM - pH-responsive, prolonged release	116
GO-PVP-NIPAM-lysine	5-FU	MCF-7	- Nontoxic and stable - Very slightly pH-responsive	176
FGO-linoleic acid	CUR	Breast cancer cells	- Temperature responsive - pH-responsive	125
GO-Fe ₃ O ₄ -HPG	CUR	SH-SY5Y, MCF-7	- can serve as an MRI contrast agent - negligible side effects <i>in vivo</i> - Impressive CUR loading (198%)	161
GO-g-MA/FA	PTX	MDA-MB-231 (<i>in vivo</i>)	- pH-responsive - High biocompatibility with no toxicity	119
OGNR-FA	TC	MCF-7, MDA-MB-231 (<i>in vivo</i>)	- Folate receptor targeting - Mildly pH-responsive	113
OGNR-FA	RXF	MCF-7, MDA-MB-231	- pH-responsive - Enhanced targeting by folic acid	114
GO-(PEGDA-EDT)-PLA	Fx	Osteoarthritis	- Drug loading efficiency (56%), slow release - <i>In vivo</i> toxicity not determined	147
GO-Fe ₃ O ₄	TMZ	C6	- Dose, time, pH dependent drug release - <i>In vivo</i> toxicity not determined	187
NGO-Fe ₃ O ₄	CisPt	Glioblastoma U87 cells	- ROS-responsive (PEGDA-EDT) - Long-term release of Fx over 66 days - Negligible toxicity (40–120 µg/mL) <i>in vitro</i>	163
GO-CS	CisPt	HeLa	- pH-responsive - Prolonged release (80% over 250 h)	117
GO-Fe ₃ O ₄ -PVP	QSR	MDA-MB-231	- Magnetic targeting - No toxicity observed for NGO- Fe ₃ O ₄ itself	162
GO-HA	Met	MDA-MB-231, TNBC cells (<i>in vivo</i>)	- pH-responsive - Triggers apoptosis by ROS generation	118
GO-CS-Ma	Ulvan	U87	- Biocompatible with normal HEK 293T cells - pH-responsive	120
GO-PEG	Erlonitib	NPC cell line	- No significant toxicity on normal cells - No side effects on other organs	121
GO-PNIPAM	Ibuprofen	-	- Nanoparticle induced apoptosis and inhibited cell migration of cancerous cells - Mannose (Ma) enables targeting of glioblastoma cancer cells	177
GO-PNP	Adriamycin	MC3T3-E1	- pH-controlled release - Drug loading capacity (88%) - Effective suppression of NPC cell proliferation, migration, and invasion	178
			- Exceptional drug loading capacity (280 wt%) - Temperature-responsive (transition temperature of 22 °C)	
			- Temperature-responsive polymer nanoparticles (PNP) - Biocompatible - Loading efficiency (87%)	

Dual drug delivery				
GBMs	Drug	Target	Highlights	Ref.
GO-PCH-g-HPG	DOX/CUR	MCF-7	- pH-responsive - Covalent loading of DOX and non-covalent loading of CUR	133
NGO-PEG	DOX/CisPt	CAL-27 and MCF-7 (<i>in vivo</i>)	- High cell internalization - Optimized 1:1 drug loading - Efficient cancer cell apoptosis and necrosis	97
rGO-PHEMA-Fe ₃ O ₄	DOX/CisPt	MCF-7	- Attenuated toxicity towards normal organs compared to individual free drugs - High drug encapsulation of DOX (75%) and CisPt (82%)	140

GO	DOX/CUR	AGS (gastric), PC3 (prostate), A2780 (ovarian), HFF cell lines	- Fast cell uptake due to small nanoparticle size (<70 nm) - pH-responsive - pH-responsive - High loading of both drugs - Lower release profile of CUR due to its hydrophobicity	138
rGO-CS	CUR/5-FU	HT-29 colon cancer cells	- High drug encapsulation efficiency (>90%) - Negligible cytotoxicity	131
rGO-SA-CS bead	CUR/5-FU	MCF-7	- Drug encapsulated microbeads - ROS-generation by the bioactive beads	132
GO-PCH-g-HPG	CUR/PTX	MCF-7	- pH-responsive - Sustained release (92 h) at neutral pH - Drugs loaded onto electrospun nanofibers	136
KGO	CPT/GEF	MDA-MB-231	- Potassium containing GO exhibiting intrinsic fluorescence - Low cell viability (18%) - Superb aqueous solubility	134
GO-PVP	QSR/GEF	PA-1 ovarian cancer cells (<i>in vivo</i>)	- Drug cocktail exhibits higher cytotoxicity/drug release profile compared to single drug administration	135
GO-PEG-FA	PCA/CA	HEPG2 (liver cancer), HT-29 (colon cancer)	- Sustained release over 100 h - FA targeting folate receptors	139

4.3.2. Photothermal Therapy

Photothermal therapy (PTT) is a physicochemical therapy that converts optical radiation in the NIR range into heat energy to eliminate cancer cells. The non-invasive characteristics of PTT, coupled with its capacity for selective treatment targeting specific cancer sites, have garnered significant research attention in the past decade.^{22, 188-189} Graphene emerges as a promising material for such applications owing to its exceptional NIR absorbent property, extensive surface area, high thermal conductivity, biocompatibility, low toxicity, and the potential for additional functionalization, such as incorporating drugs or nucleic acid sequences, facilitating targeted delivery.^{22, 188-190}

A seminal report by Yang et al. demonstrated an *in vivo* tumor ablation through the intravenous administration of PEGylated nanographene sheets (NGS).¹⁹¹ In this study, a fluorescent dye was conjugated to the PEG chain, enabling simultaneous bioimaging. Within 24 hours, NGS predominantly accumulated in the tumor cells, attributed to the enhanced permeability and

retention (EPR) effect of cancer cells. Notably, strong fluorescence in the kidneys suggested the potential for renal excretion of NGS. Following the injection, mice treated with NGS-PEG were subjected to an 808 nm NIR irradiation (2 W/cm^2 , 24 h), elevating the surface temperature of tumor cells to $50 \text{ }^\circ\text{C}$ for effective cell ablation. Remarkably, all irradiated tumors detached within a day, and no tumor regrowth was observed over a 40-day period. Further histological examination of mice revealed no apparent side effects. In 2012, the same research group highlighted the critical importance of both the size of the graphene sheet and the surface chemistry in achieving an effective photothermal treatment.¹⁹² rGO-PEG, nano rGO-PEG, and nano GO-PEG (with respective sizes of 65, 23, and 27 nm) were evaluated in terms of their NIR absorption at 808 nm. The findings revealed that both sizes of rGOs exhibited 3-4 times greater absorption compared to GO. This observation is in line with the findings reported by the Dai group, which demonstrated that rGO exhibits a 6-fold higher photothermal conversion efficiency than GO.¹⁹³ Furthermore, the surface coating of nano rGO-PEG enabled extended blood circulation, and its small size facilitated efficient accumulation in tumor cells while reducing retention by the reticuloendothelial system (RES). These pioneering studies have laid the essential groundwork, providing a critical foundation for future advancements in the field of photothermal therapy utilizing graphene. In general, graphene derivatives with less disrupted π conjugation demonstrate higher optical absorbance in the NIR region and exhibit enhanced heat generation capacities. The superior efficacy of reduced forms compared to oxidized forms of graphene for PTT has been elucidated in several reports.¹⁹³⁻¹⁹⁶

Despite the excellent properties of rGO, its utilization has been constrained by its limited stability in biological fluids, primarily attributed to its hydrophobic nature.¹⁹⁷⁻²⁰⁰ To overcome such a limitation, a wide range of synthetic and biological polymers have been employed to coat rGO

sheets, such as PEG,^{191-193, 201} poly(dopamine),²⁰²⁻²⁰³ phospholipid-polyethylene glycol,²⁰⁴ polystyrene-*co*-poly-4-vinylpyridine,²⁰⁴ polystyrene-*co*-polyacrylic acid²⁰⁴, amino-terminated hyperbranched polymer,¹⁹⁶ dextran,²⁰⁵ heparin,²⁰⁶ and hyaluronic acids.¹⁸⁶ Although polymer surfactants play a role in stabilizing rGO in aqueous solutions, targeted delivery to tumor cells cannot be solely accomplished by surface molecules alone. Non-specific delivery of therapeutic agents can result in inadequate dosing or unintended side effects, such as the removal of healthy cells. In the subsequent sections, examples primarily centered around targeted PTT will be provided.

4.3.2.1. Selective/Targeted Photothermal Therapy

The first example of rGO used for PTT was reported by Dai group in 2011.¹⁹³ An increased conjugation by the reduction of GO enhanced the NIR absorption by 6-fold (Figure 4.13a), which is comparable to that of gold or carbon nanotube. To bestow the material with solubility and stability in biological buffer solutions, nanosized (~20 nm) RGO sheets were enveloped in amphiphilic PEG surfactants. The surfactants were further functionalized with a targeting peptide (RGD) specific to U87MG cancer cells (Figure 4.13b), resulting in a three-fold increase in selectivity. Notably, the heightened photothermal capability of RGOs enabled even a low concentration of 20 mg/L to achieve the photoablation temperature within 8 minutes at low laser power (808 nm, 0.6 W/cm²).

In 2021, Dou et al. demonstrated the use of structurally well-defined GNRs as photothermal agents for the first time.²⁰⁷ Carboxylate functionalized GNR was grafted with glycoconjugates such as mannose (Man) or galactose (Gal), which allows for selective binding with carbohydrate

receptors (Figure 4.13c). GNR-Man underwent self-assembly with pyrene-functionalized PRGD ($\alpha_v\beta_3$ integrin receptor targeting ligand) under sonication, endowing the material with dual-receptor targeting functionalities (Figure 4.13d-e). Both *in vitro/in vivo* studies evidenced the potential of dual-receptor targeting, structurally well-defined GNRs for effective cancer therapy.

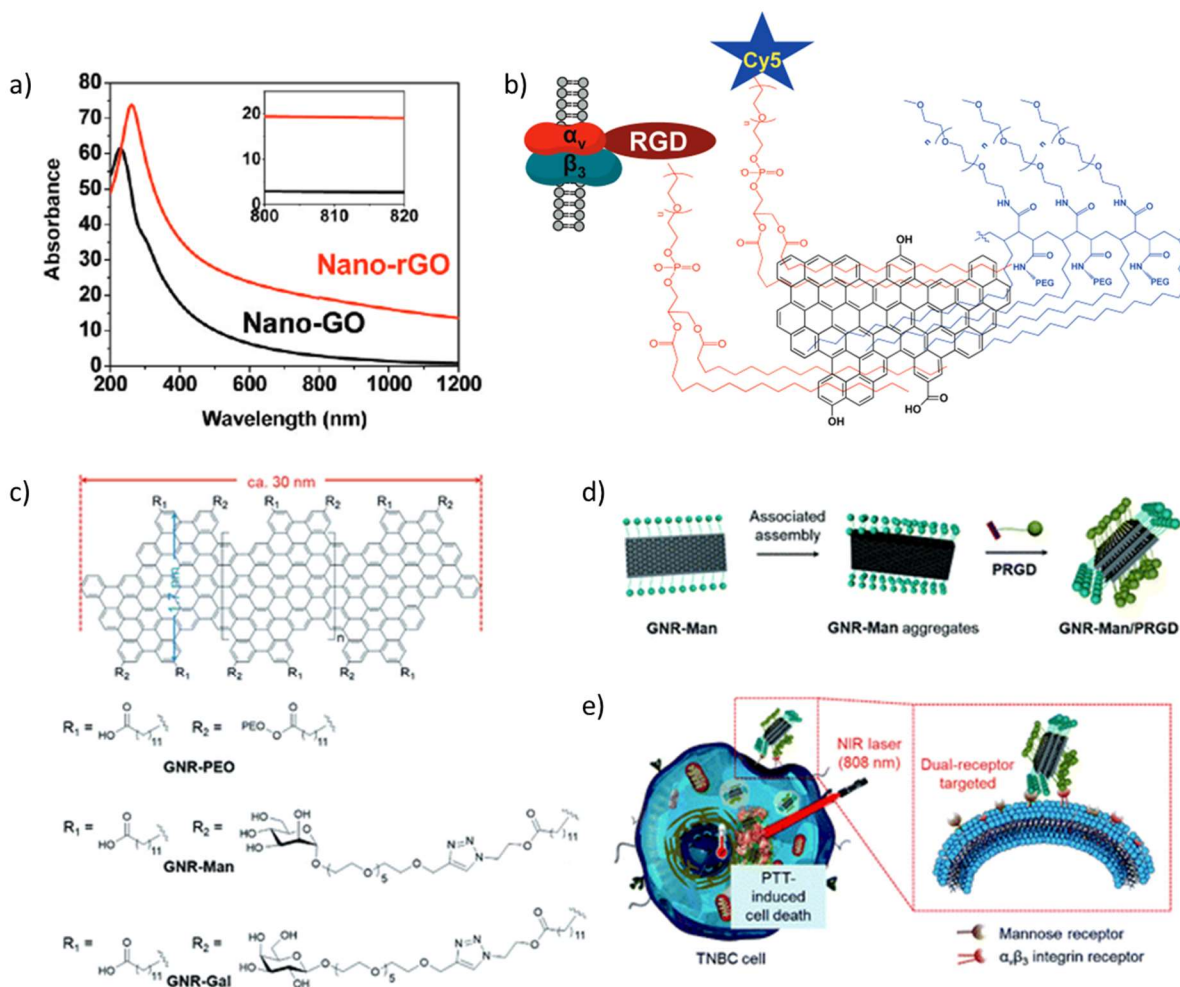


Figure 4.13. a) UV-vis absorption of nano-GO and nano-rGO. b) Schematic representation of nano-RGO-RGD-cy5 interacting with $\alpha_v\beta_3$ integrin receptors located on U87MG cell membrane. Reproduced with permission.¹⁹³ Copyright 2011, American Chemical Society. c) Chemical structures of GNR-PEO, GNR-Gal, and GNR-Man. The GNR exhibits a well-defined structure

with an average length of 30 nm and a uniform width of 1.7 nm. d) Supramolecular self-assembly of GNR-Man with PRGD. e) Illustration of a photothermal treatment of TNBC cells by dual-targeting of GNR-Man/PRGD under NIR exposure. Reproduced under terms of the CC-BY license.²⁰⁷ Copyright 2021, The Authors, published by The Royal Society of Chemistry.

In recent developments, PTT using GO-PEG-FA nanocomposites, delivered through adipose-derived stem cells (ADSC), has shown promise in the treatment of breast cancer.²⁰⁸ In comparison to nanocomposites lacking ADSC, GO-PEG-FA-laden ADSC demonstrated heightened selectivity for tumors *in vivo*, resulting in more effective tumor suppression. The migration of ADSCs toward MCF-7 cells was examined using an *in vivo* fluorescence imaging system (rhodamine B as fluorescence marker), revealing an initial presence in the lungs, followed by localization in the liver. At the 14-day mark, a notable decrease in the fluorescence signal was noted in the liver, while a higher fluorescence level persisted at the tumor sites. After 32 days, fluorescence signals were exclusively observed in the tumors, illustrating the systematic bio-delivery and its capacity to selectively aggregate within the targeted tumor cells. Notably, all radiated tumors in mice treated with PEG-FA-laden-GO-ADSC vanished within 2 days, leaving behind black scars that subsequently fell off after a week.

In addition to biorecognition for targeted PTT, magnetic particles have also been utilized. A notable example by the Liu group in 2012 showed that rGO-iron oxide nanoparticle (IONP)-PEG served as an effective material for a multimodal imaging guided PTT.²⁰ By harnessing the strong NIR absorbance of reduced graphene, the nanoparticle demonstrated dual functionality as a PTT agent and a high-contrast agent for photoacoustic tomography (PAT). Furthermore, IONP served as a magnetic resonance contrast agent for MRI, and the nanocarrier was enhanced with Cy5, a

fluorescence label, facilitating *in vivo* fluorescence imaging. Similarly, Barrera and coworkers synthesized a nanostructure composed of rGO sheets as the photothermal agent and Fe₃O₄ particles to provide magnetic properties.²⁰⁹ *In vitro* studies demonstrated that when HeLa cells were treated with 50 µg/mL and 100 µg/mL of rGO-Fe₃O₄ and exposed to 804 nm laser (1 W/cm², 5 min), their cell viability was reduced to 32.6% and 23.7%, respectively. These studies highlight the potential of carbon-based magnetic nanoparticles for future magnetic resonance imaging and targeted drug delivery. In addition to the use for PTT, the GBM-magnetic particle systems have also been employed in conjunction with other modes of therapy, demonstrating synergistic effects. Such examples are summarized in the following section (4.3.2.2).

4.3.2.2. Combined photothermal therapy

Chemo-photothermal therapy

The utilization of graphene-based nanomaterials in a dual approach involving both chemo- and photothermal therapy could generate synergistic effects. Zhang and coworkers compared the effect of NGO-PEG-DOX nanoparticles to the separate use of DOX or NGO-PEG against EMT6 cells.²¹⁰ Under NIR laser, NGO-PEG-DOX exhibited higher inhibition rate compared to NGO-PEG system at all concentrations examined (Figure 4.14a). At concentrations above 10 µg/mL, NGO-PEG-DOX+NIR demonstrated higher therapeutic efficacy compared to free DOX. They attributed the heightened impact to the accelerated release of DOX from the NGO-PEG system at elevated temperatures, combined with the PTT effect. Subsequent *in vivo* studies demonstrated the remarkable synergistic effect of chemo-PTT (Figure 4.14b), with the NGO-PEG-DOX+NIR group showing complete destruction of the tumor site (no tumor regrowth observed in the following 40 days). Zhu et al. also documented comparable findings using a GO/CS thermosensitive hydrogel

loaded with docetaxel, which demonstrated stability in a physiological solution and exhibited a pH-responsiveness.¹⁸² When this hydrogel was employed in conjunction with NIR laser irradiation at 808 nm (2.5 W), it resulted in a greater inhibition rate in MCF-7 cells compared to using either method alone.

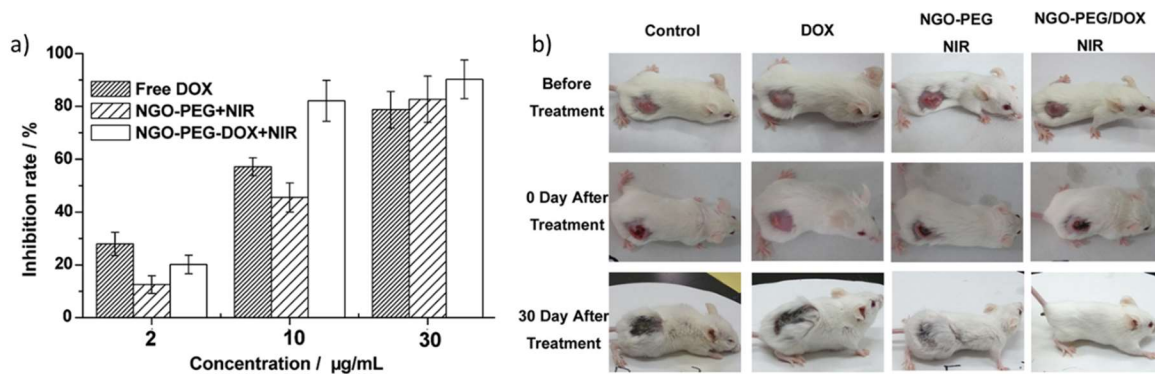


Figure 4.14. a) Relative cell viability of EMT6 cells 24h after treatment with free DOX, NGO-PEG, and NGO-PEG-DOX with NIR laser (808 nm, 2 W/cm²) at various concentrations. B) *In vivo* studies of tumors on mice. Note that irradiated tumor on NGO-PEG/DOX group was completely removed. Reproduced with permission.²¹⁰ Copyright 2011, Elsevier.

Targeted chemo-photothermal therapy

A multifunctional nanocarrier, composed of transferrin-conjugated GO-PEG-DOX, demonstrated synergistic therapeutic effects when exposed to NIR irradiation against glioma cancer cells.²¹¹ Transferrin served as a key targeting molecule, which can transport the nanomaterial across the blood brain barrier. The observed thermal change (4 °C) upon exposure to NIR (2.5 W/cm², 5 min) was not substantial, a phenomenon they attributed to either the limited

amount of drug delivery into the brain or the low thermal response due to the protective barrier of the skull. However, the inherent limited thermal response of GO to NIR should be considered. A recent study involving a novel macrophage-mediated branched polyethyleneimine (BPEI)-PEG-rGO-DOX delivery system showed great potential.²¹² This system maintained stability in the body prior to NIR irradiation, with only a trace amount of DOX released. The majority of DOX was delivered to the tumor site and released on-demand upon NIR irradiation. A 5 min exposure to 808 nm laser (1 W/cm²) at 50 µg/mL resulted in an increase in tumor temperature to 55.8 °C. *In vivo* investigations of the antitumor efficacy in mice bearing tumors revealed that the combination of DOX and PTT significantly reduced tumor volume within 15 days. SreeHarsha et al. presented another system that leveraged the natural site selectivity of chitosan for PC-3 prostate cancer cells.²¹³ The rGO-DOX system stabilized with chitosan hybrid nanoparticle (rGOD-HNP) achieved a high loading efficiency (>60%) for DOX. *In vitro* investigations of drug release revealed that this hybrid material could retain the drug for an extended period, with 60% released over 48 hours. Upon NIR irradiation (808 nm), the system rapidly reached cell ablation temperature within 100 seconds. As anticipated, the combined therapy demonstrated the highest therapeutic efficacy.

Apart from DOX, other anticancer drugs have also been explored in the combined therapy approaches. For instance, resveratrol (RSV), used in the treatment of ovarian cancer, was integrated into an acid/heat-responsive nanomaterial consisting of NGO, IR780 (a mitochondrion-targeting molecule), and ferritin (FRT).²¹⁴ FRT is a natural protein known for its hollow-cage-like nanostructure, which disassembles under neutral or acidic conditions. IR780 was conjugated onto NGO followed by the loading of RSV. Then NGO-IR780-RSV was caged into the FRT. The FRT first releases NGO-IR780-RSV near the acidic environment of cancer cells, followed by RSV

release upon NIR exposure. This hybrid material exhibited exceptional physiological stability and biocompatibility. Its acid/heat-triggered RSV release demonstrated a significant synergistic suppression of tumor growth, as confirmed in *both in vitro* and *in vivo* studies, with minimal toxicity observed in normal organs. Zhan et al. reported a biocompatible NGO-CO-CD47 (targeting B16-F10 melanoma cells) system loaded with anti-melanoma drug dacarbazine (DTIC) which showed efficient targeted/combined therapeutic effect against melanoma.²¹⁵ Du et al. employed a berberine 9-*O*-pyrazole alkyl derivative (**B3**) developed by their own group for chemo/PTT, which demonstrated anti-cancer activity towards HeLa and A549 cell lines (Figure 4.15).²¹⁶ **B3**-GO was further covalently linked to the AS1411 aptamer, serving as a targeting agent. In cellular experiments, the survival rate of A549 cells was 51% without the application of NIR laser, and it reduced to 28% with the NIR irradiation.

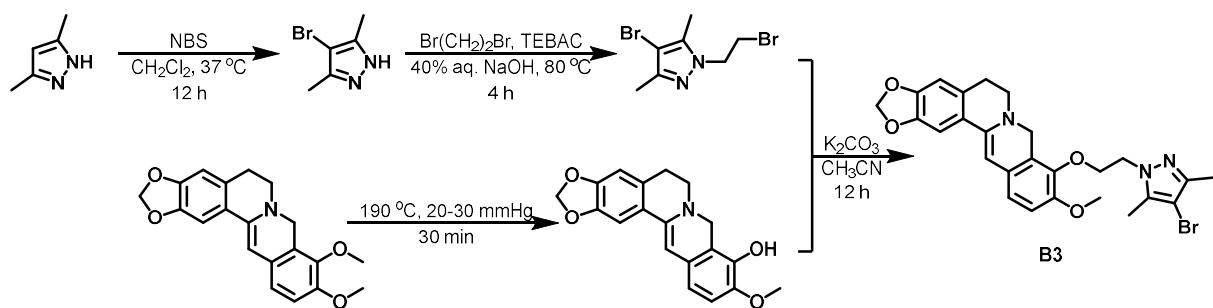


Figure 4.15. Structure and synthesis of berberine derivative (**B3**).

Temperature sensitive chemo-photothermal therapy

The Park group recently introduced a nanogel system composed of GO-PNIPAM framework.²¹⁷ *In vitro* studies demonstrated that the temperature-responsive behavior of PNIPAM remained

consistent even with the inclusion of GO in the hydrogel network. This retained thermoresponsiveness allowed for the efficient release of DOX from the PNIPAM-GO-DOX system at temperatures above the LCST, achieved through the contraction of the hydrophobic polymer.

Inorganic particles as additives in chemo-photothermal therapy

Hybrid combinations of graphene materials²¹⁸ with other functional nanomaterials are recognized for their capacity to enhance the photothermal response such as gold,²¹⁹⁻²²³ graphene quantum dots,²²⁴ and Cu-Se nanoparticles.²²⁵ The Wang group presented a system composed of GO-DOX-MUC1 (targeting aptamer) loaded with gold nanoparticles (AuNP) for targeted PTT and chemotherapy.²²⁰ The loading of DOX was achieved through intercalation within the double-stranded aptamer, as well as adsorption onto the GO surface. *In vitro* studies revealed that among MCF-7, A549, and HepG2 cells, only the MUC1-positive (MCF-7 and A549) cells were targeted. In an irradiation time-dependent assay, the viability of targeted cells remained at 90% after 5 min of irradiation, but with extended irradiation of 15 min, only 20% of the cells survived.

Mesoporous silica-coated nanostructures (MSNs) are commonly employed as drug carriers due to their excellent biocompatibility, high loading capacity, and flexibility to control drug release by versatile surface functionalization.²²⁶⁻²³¹ A notable example by Chen and colleagues demonstrated a novel nanocookie-like structure by coating amorphous carbon on a rGO-mesoporous silica support (Figure 4.16a).²³⁰ While the abundant pores of MSNs enable a large drug loading capacity, there is a potential risk of easy drug leakage from the open shell without any surface modification.

The supplementary carbon layer demonstrated effectiveness in enhancing drug loading, as evidenced by comparing the nanocookie to porous silica sheet (PSS) or rGO (Figure 4.16c). NIR irradiation on the suspension of nanoparticles revealed that the nanocookie behaved similarly to rGO. However, a slower temperature increase was observed for rGO@PSS, presumably due to some blocking effect of silica (Figure 4.16b). This suggests that the added carbon layer helps reduce such a blocking effect. Figure 4.16d shows that without NIR, no drug release is observed from rGO or the nanocookie. Photon heating exhibited a bursting effect on the drug release of the nanocookie, showing an on-off response to NIR stimulation (Figure 4.16e). Further *in vitro* and *in vivo* studies against MDA-MB 231 cancer cells demonstrated successful elimination of tumors by the combined chemo/PTT effect.

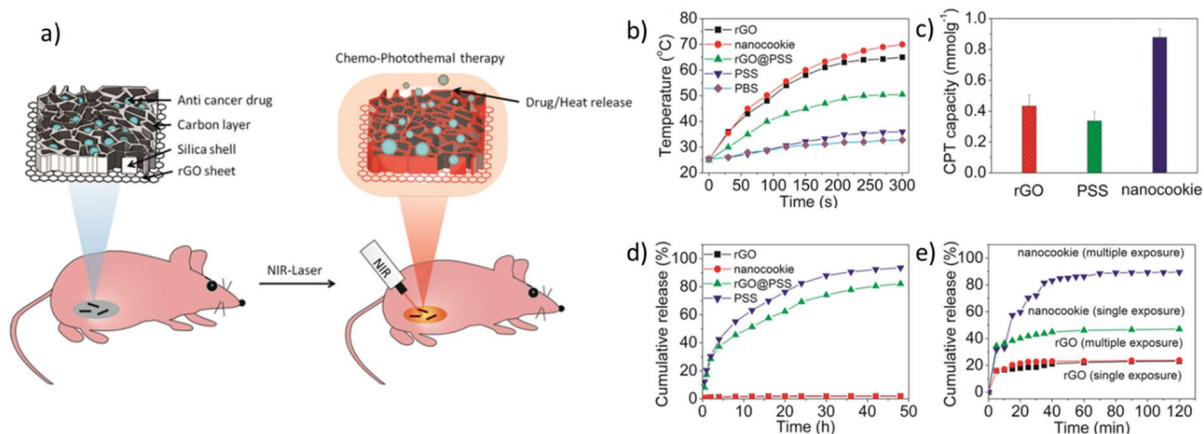


Figure 4.16. a) Schematic illustration depicting chemo-PTT using rGO/carbon/mesoporous silica nanocookie under NIR irradiation. b) Heat-generation kinetics of rGO suspension in phosphate buffer saline (PBS), nanocookie, rGO@PSS, PSS, and PBS (control). 808 nm, 2 W/cm² laser was used. c) CPT loading capacity in rGO, PSS, and nanocookie. d) CPT release profiles of four different nanocarriers. e) Drug release profiles upon NIR irradiation. Single exposure: 5 min NIR

exposure initiated at time 0. Multiple exposures: repeated 5 times after waiting 5 min following previous exposure. Reproduced with permission.²³⁰ Copyright 2014, Wiley.

Magnetic graphene materials have also been utilized in combined therapy for enhanced targeting effect.^{22-23, 232-233} GO-Fe₃O₄ modified with PEG, DOX, and cetuximab (CET, epidermal growth factor receptor antibody that is highly expressed on tumor cell surfaces), was employed for dual targeted delivery.²³³ The *in vivo* investigation demonstrated improved targeting achieved through both ligand recognition and magnetic guidance, leading to a reduction in the rate of tumor growth with dual targeting. In all conditions without NIR exposure, tumor growth was not suppressed. However, when combined with NIR irradiation, the tumor size significantly decreased over a period of 14 days (Figure 4.17a-b). No significant changes or differences in body weight was observed between groups (Figure 4.17c). Only the control group exhibited a slight weight gain, which could be attributed to the common adverse effects of chemotherapy observed in the other groups. Wang et al. functionalized fluorinated GO (FGO) by covalently linking HA with an adipic acid dihydrazide bridge, followed by loading of Fe₃O₄ and DOX to create a dual-targeting combined therapy system.²³⁴ Their *in vitro* studies showed that DOX loading could be tracked through the “switch off” of fluorescence, where the photoluminescence of DOX was quenched upon interaction with the nanocarrier. This efficient quenching was attributed to the formation of an effective fluorescence resonance energy transfer system, established through π - π stacking and hydrogen bonding interactions between DOX and FGO. As a result of the targeting effect of HA towards A549 cancer lines, the nanosystem exhibited notable selectivity towards A549 over the BEAS-2B normal cells. Under dual treatment involving NIR irradiation and DOX, nearly 92% of the cancer cells were eliminated within 48 hours. Similarly, dual-targeting effect of graphitic

hybrid materials were shown by other reports using gastrin-releasing peptide receptor²³⁵ or folic acid²³⁶ in conjunction with magnetic nanoparticles.

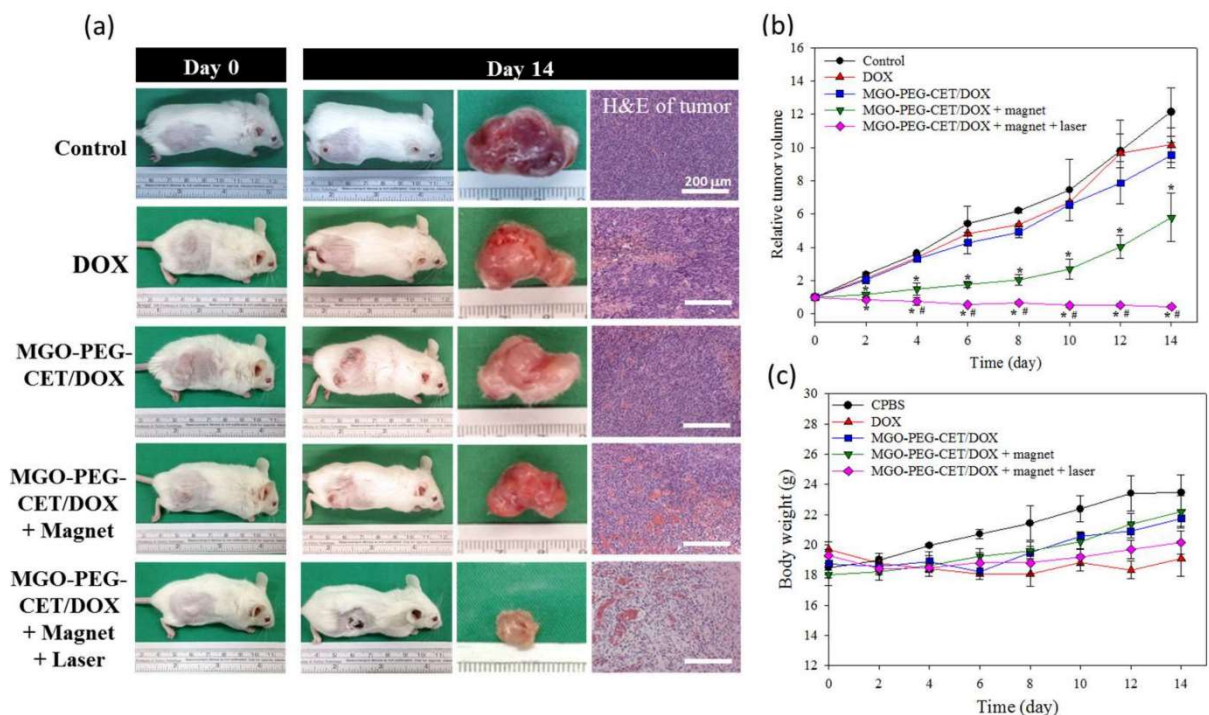


Figure 4.17. a) The observation of tumor-bearing BALB/c mice on days 0 to 14. Incised tumor and H&E staining of the tumor are shown. b) Relative tumor volumes and c) body weight changes from each group were recorded. Reproduced under the terms of the CC-BY license.²³³ Copyright 2018, The Authors, published by MDPI.

Işıkhan and coworkers presented the pioneering use of magnetic GO in conjunction with gelatin.²³⁷ Gelatin, a natural biopolymer derived from the partial hydrolysis of collagen, possesses a cationic nature due to the presence of multiple amine groups. The positively charged polymer enabled easy cellular entry through adsorptive endocytosis into the negatively charged plasma membrane. Furthermore, the cationic nature of gelatin facilitated the release of paclitaxel in response to acidic environments through charge repulsion, resulting in the relaxation of the gelatin

material. A low cell viability of 38% for MCF-7 cells was detected in the presence of NIR laser (0.1 W/cm²) for a very short period of 3 min, due to the synergistic impact of PTT and chemotherapy.

Ardakani and coworkers studied the combinatorial effect of PTT and radiotherapy using Fe₃O₄@Au/rGO nanostructures towards KB oral squamous carcinoma cell line.²³⁸ Gold exhibits high absorption properties towards X-ray, which allows for the lowering of the dose of X-ray, reducing the side effects. No significant cytotoxicity was observed for low concentrations of nanoparticles (5-20 µg/mL), and high cell destruction was observed under radiotherapy (49.8% viability) as well as PTT (27.0% viability). Combined application of radiotherapy and PTT further decreased the cell viability to 11.9%.

Photodynamic-photothermal therapy

Photodynamic therapy (PDT), as another form of phototherapy, has gained considerable interest in recent years. In PDT, cancer cells are destroyed by the ROS generated through the energy transfer from photosensitizers to oxygen species upon light irradiation.²³⁹⁻²⁴⁰ Due to the ease of utilizing light as a common source of stimuli, synergistic combinations of PDT-PTT have been explored with GBMs.^{22, 240-242} Sahu et al. designed a NGO sheet non-covalently functionalized with Pluronic block copolymer (Pluronic F127, FDA-approved polymer for use in human) complexed with methylene blue as a photosensitizer.²⁴¹ Pluronic F127 provided high stability of the nanomaterial in biological environments. *In vivo* cancer therapy against HeLa cells revealed superior efficacy of the combined therapy, as illustrated in Figure 4.18. After 15 days, complete

tumor regression was observed in the PDT+PTT group. In a similar vein, Bianco group reported that a nanocarrier composed of Chlorine C6 (Ce6) photosensitizer covalently grafted onto GO-FA-PEG exhibits excellent dual phototherapy.²⁴² Notably, *in vitro* experiments demonstrated a substantial cellular uptake of GO-FA-Ce6 by MCF-7 cells, attributed to favorable ligand-receptor interactions. The combination of PDT-PTT yielded a remarkable killing efficiency of 94% when tested against RAW 264.7 macrophages. In addition to the provided examples, photosensitizers including methylene blue,²⁴³ indocyanine green,^{231, 244-246} and 4-hydroxycoumarine,²⁴⁷ have been utilized for PDT.

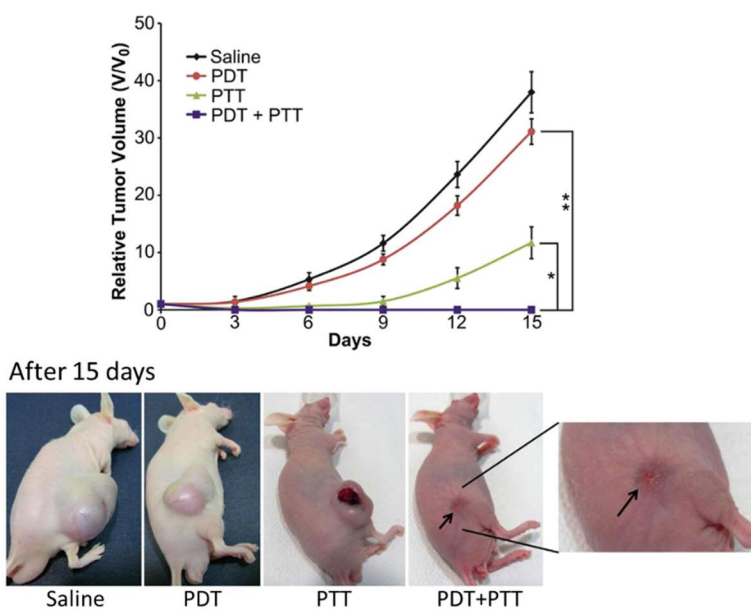


Figure 4.18. *In vivo* treatment against mice bearing HeLa tumor: changes in relative tumor volumes (depicted in a graph) and photographs of the tumors after 15 days of treatment of each therapy methods are shown. Reproduced with permission.²⁴¹ Copyright 2013, Elsevier.

Ion interference-photothermal therapy

In recent years, ion interference therapy (IIT) has surfaced as a promising approach for cancer treatment. Cells harbor a diverse range of ions, which play pivotal roles in regulating critical biological processes. Maintaining the precise ion concentrations is essential for proper cellular function.²⁴⁸⁻²⁴⁹ IIT disrupts normal bioprocesses by overwhelming cells with ions using inorganic nanoparticles such as CaCO₃, NaCl, or zeolitic frameworks (Zn²⁺). However, these materials tend to easily aggregate or crystallize under physiological conditions. The surface of GO has nucleation points that could facilitate the formation of small nanoparticles of inorganic salts. An excellent illustration of GO utilization in a tandem approach of IIT-PTT was provided by Lv et al.²⁵⁰ They incorporated a pH-sensitive Zn²⁺ source, Zeolitic imidazolate framework-8 (ZIF-8), onto GO sheets. Subsequently, GO was reduced to rGO using Vitamin C and subjected to surface modification with BSA. This nanocarrier exhibited minimal systemic toxicity and effectively induced cell apoptosis through a combination of the photothermal effects of rGO and zinc ion-triggered cellular dysfunctions.

Chemodynamic-photothermal therapy

Chemodynamic therapy (CDT) takes advantage of the overproduction of H₂O₂ around tumors. A Fenton-type catalytic reaction, involving highly reactive hydroxyl radicals, induces apoptosis in cancer cells while having minimal impact on healthy cells. A study by the Bianco group demonstrated that a rGO-MnO₂ nanoparticle system combined with PTT could efficiently act against HeLa cells.²⁵¹ GSH molecules, which are abundant in cancerous environments, are

oxidized by MnO₂. Subsequently, Mn²⁺ mediated Fenton reactions generate ROS, and the reaction rate accelerates under NIR irradiation due to the rise in temperature. This strategy leverages the unique features of the tumor microenvironment for targeted treatment, making it a promising approach for cancer therapy.

Triple-synergetic therapy

In addition to dual-therapy, several examples of triple synergetic treatments have been reported. Guo et al. reported a well-designed chemo/PTT/PDT system utilizing GO-PEG-oxidized sodium alginate (OSA) nanocarrier loaded with PTX for the treatment of gastric cancer.²⁵² In gastric cells, the P-glycoprotein (P-gp) actively pumps PTX out, contributing to drug resistance. Consequently, inhibiting this process is essential to overcome drug resistance and enhance the effectiveness of PTX in treating gastric cancer. The generated ROS by PDT depolarized the membrane potential of mitochondria, resulting in reduced ATP generation. As the energy supply for P-gp decreased, gastric cancer cells became re-sensitive to PTX. Combined with enhanced drug sensitivity achieved by chemo/PDT, additional NIR irradiation further suppressed tumor growth, as demonstrated in their *in vivo* studies.

In a study conducted by Zhou and coworkers, a promising strategy for both treating and potentially “vaccinating” against metastatic tumors was demonstrated.²⁵³ They achieved a multipronged approach by combining chemo/PTT, and immune therapy using rGO loaded with MTX, a transforming growth factor beta inhibitor (TGF-β), and immune-stimulating agent (SB-431542). They noted that with NIR irradiation in conjunction with the nanocarrier, it resulted in an impressive 70% long-term survival rate among mice bearing 4T1 tumors. Importantly, tumor-

type-specific immunity was achieved, which allows for an effective combat towards regenerated tumor cells. Such promising approach of tri-combined therapy has shown its effectiveness in multiple reports.^{243, 252, 254-255}

Table 4.2. A summary of graphene based nanocarriers for photothermal therapy applications.

PTT				
GBMs	Additives	Target	Highlights	Ref
NGS-PEG	Cy7	4T1 (<i>in vivo</i>)	- Fluorescence imaging by Cy7 - 808 nm, 2 W/cm ² - Highly effective <i>in vivo</i> treatment	191
rGO-PEG nano rGO-PEG nano rGO-PEG	Cy7	4T1 (<i>in vivo</i>)	- Fluorescence imaging by Cy7 - Smaller size (23-27 nm) sheets exhibit prolonged blood circulation and efficiently accumulate in tumor cells - RGO has higher PTT effect compared to GO	192
nano-GO-PEG nano-rGO-PEG	Cy5, RGD/RAD peptides	U87MG	- Cy5 as a fluorescent tag - RGD/RAD peptide targets $\alpha_v\beta_3$ integrin receptors - 6-fold increase in NIR absorbance for rGO in comparison to GO	193
rGO-Arg GO		MD-MB-231	- Improved physiological stability and cancer cell uptake by arginine - 3.2 times stronger NIR absorbance by rGO-Arg in comparison to GO	194
P-DOPA-rGO		MCF-7	- Dopamine as a reductant to produce rGO - self-polymerization of dopamine in the reduction process - poly-dopamine acts as an additional NIR absorber	203
GNR-Man GNR-Gal	PRGD	MDA-MB-231 (<i>in vivo</i>), Hep-G2, HeLa, MCF-7	- Dual targeting by PRGD peptide recognition by $\alpha_v\beta_3$ integrin receptors and glycoconjugate binding towards carbohydrate receptors - First example of a structurally defined GNR utilized for targeted tumor therapy	207
rGO-AuNP-PEG		SKOV-3 (<i>in vivo</i>)	- NIR-II photoacoustic imaging <i>in vivo</i> - 1061 nm laser, 0.25 W/cm ² - Excellent tumor cell ablation - Clearance of accumulated rGO-AuNP from all the normal organs after 10 days	223
GO-PEG-FA	ADSC, rhodamine B	MCF-7 (<i>in vivo</i>)	- Fluorescence imaging by Rhodamine B - Targeted delivery enabled by cellular therapy (adipose-derived stem cell)	208
rGO-IONP-PEG	Cy5	4T1 (<i>in vivo</i>)	- Multimodal imaging guided PTT (fluorescence, photoacoustic tomography, and MR imaging) - IONP serves as MR imaging contrast agent - Cy5 as a fluorescence label - 0.5 W/cm ² , 808 nm irradiation resulted in highly effective <i>in vivo</i> treatment	20
rGO-Fe ₃ O ₄		HeLa	- rGO-Fe ₃ O ₄ was found to aggregate on the cell membranes - 0.5 W/cm ² , 804 nm irradiation (5 min) - 50 μ g/mL and 100 μ g/mL of nanomaterial led to 32.6% and 23.7% cell viability, respectively.	209
Chemo-PTT				
GBMs	Additives	Target	Highlights	Ref
NGO-PEG	DOX	EMT6	- pH/NIR-responsive release	210

			(<i>in vivo</i>)	- 2 W/cm ² , 808 nm irradiation - Stable in physiological solutions for weeks	195
rGO-BSA	DOX	U87MG		- pH/NIR-responsive release - Negligible cytotoxic effect	
NCGO-FA	DOX	HeLa, MCF-7		- 5.5 W/cm ² , 808 nm irradiation - pH/thermal-responsive release - Good photothermal conversion and photostability	243
GO-PEG-transferrin	DOX	MCF-7 (<i>in vivo</i>)		- pH/NIR-responsive release - Negligible toxicity of GO-PEG-transferrin - Weak thermal change <i>in vivo</i> (2.5 W/cm ² , 808 nm, 4 °C increase in 5 min)	211
rGO-BPEI-PEG-macrophage	DOX	RAW264.7 (<i>in vivo</i>)		- Macrophage mediated targeted delivery - On-demand (NIR) release of DOX - 1 W/cm ² , 808 nm irradiation	212
rGOD-HNP	DOX	PC-3		- Site selectivity achieved by chitosan - Loading efficiency of DOX (>60%) - Sustained release of DOX (60% over 48 h)	213
NrGO	DOX	HeLa		- pH/NIR-responsive release - Amino-terminated hyperbranched polymer used as a reductant to generate rGO	196
GO-GA@Au nanorod	DOX	HeLa, A549		- pH/NIR-responsive release - Gum 476 rabic (GA) extracted from plant enhanced biocompatibility of GO and served as a natural reductant for GO	219
GO-Apt@AuNP	DOX	MCF-7, A549, HepG2		- NIR-responsive release - Excellent targeting towards MUC1-overexpressing cancer cells (MCF-7, A549)	220
rGO-FA-Cu _{2-x} Se	DOX	Hep-2, A549		- pH/NIR-responsive release - Copper chalcogenide as an additional photothermal agent	225
GO-MSN-PDA	DOX	HMCC-97L, HMCC-97H		- 980 nm irradiation - pH-responsive release - 2W/cm ² , 808 nm irradiation	229
GO-Apt-MSN	DOX	MCF-7		- NIR-responsive release - Cy5.5-labeled AS1411 aptamer enabled fluorescence monitoring	227
MGMSPI	DOX	U251 (<i>in vivo</i>)		- pH/photothermal-responsive release - High specificity towards glioma U251 cells over normal cells (1800) - Magnetic graphene allows for MR imaging - Sustained DOX release (<25% after 24 h)	228
MGO-CS-SA	DOX	A549		- loading efficiency (43%) by mesoporous silica - pH-responsive release - Well-dispersed in physiological solutions - Magnetically targeted cellular uptake observed <i>in vitro</i>	232
MGO-PEG-CET	DOX	CT-26 (<i>in vivo</i>)		- pH-responsive release - Dual targeting achieved by magnetic guidance and cetuximab targeting antibody - Efficient intracellular uptakes	233
MrGO-GRPR	DOX	U87 (<i>in vivo</i>)		- pH-responsive release - Dual targeting achieved by magnetic guidance and GRPR peptide - Highest efficacy achieved in chemo/PTT group, minimum systemic toxicity observed	235
MGO-TCA-FA	DOX	HepG2 (<i>in vivo</i>)		- pH/NIR-responsive release - TCA: triformyl cholic acid - High DOX loading (1040 mg/g) - High synergistic therapy tumor inhibition rate (85%)	236
FGO-ADH-HA-Fe ₃ O ₄	DOX	A549		- Fluorescence quenching upon DOX loading - High targeting towards A549 cancer lines over the normal BEAS-2B cells	234
rGO-carbon-MSN	CPT	MDA-MB 231 (<i>in vivo</i>)		- Burst-like drug release upon exposure to NIR - Nanocookie-like structure - Successful eradication of tumors within 2 weeks by combined chemo/PTT (no distal damage)	230

MGO@GEL	PTX	MCF-7	- pH-responsive release by expansion of cationic gelatin under acidic conditions - Low cell viability (38%) achieved with PTX and 3 min exposure to 808 nm, 0.1 W/cm ² laser	237
GO-CS	DTX	MCF-7, Glioma cancer cells (<i>in vivo</i>)	- pH-responsive release - High stability in physiological solutions - No obvious toxic effects found in normal organs	182
NGO-IR780-FRT	RSV	SKOV-3 (<i>in vivo</i>)	- Systematic pH/NIR-responsive release - Ferritin used as a cage to transfer the drug-carrier - No noticeable organ damage	214
NGO-CO-CD47	DTIC	B16-F10 (melanoma)	- pH/NIR-responsive release - High combined therapeutic efficacy <i>in vitro</i> (cell viability 3%) - ROS-mediated apoptosis	215
GO-AS1411	B3	A549, L929	- pH/NIR-responsive release - Berberine 9- <i>O</i> -pyrazole alkyl derivative as anticancer drug	216
PDT-PTT				
GBMs	Photosensitizer	Target	Highlights	Ref
NGO-Pluronic F127	Methylene blue	HeLa (<i>in vivo</i>)	- pH-responsive release of MB photosensitizer - Usage of FDA-approved Pluronic block-copolymer to achieve stability in physiological conditions - High efficacy of combined therapy	241
GO-PEG-FA	Ce6	MCF-7, RAW 264.7 macrophage	- High cellular uptake by MCF-7 - High killing efficiency for RAW 264.7 macrophage (up to 94%)	242
GO-PEG-FA	Indocyanine Green	Ehrlich tumors	- <i>In vivo</i> fluorescence imaging by Rhodamine B fluorescence marker - 808 nm, 1.8 W/cm ² - PDT-PTT resulted in reduction and impediment of tumor growth	244
rGO-FA-mesoporous silica	Indocyanine Green	CT-26 (<i>in vivo</i>)	- Mesoporous silica enhanced indocyanine green encapsulation - Negligible damage to normal cells	231
NCGO-FA	Methylene blue	HeLa, MCF-7	- pH/thermal-responsive release - Good photothermal conversion and photostability	243
Radiotherapy-PTT				
GBMs	Additives	Target	Highlights	Ref
rGO-Fe ₃ O ₄ @Au	DOX	KB cell lines	- X-ray absorption by Au - No significant cytotoxicity (5- 20 µg/mL) - Low cell viability (12%) under synergistic application	238
II-PTT				
GBMs	Additives	Target	Highlights	Ref
rGO-(ZIF-8)-BSA	-	SCC25, HeLa, Cal27 xenografts (<i>in vivo</i>)	- GO was reduced to rGO by Vitamin C - Minimal systemic toxicity - Zinc ion-triggered cellular dysfunctions	250
CDT-PTT				
GBMs	Additives	Target	Highlights	Ref
rGO-MnO ₂	-	HeLa	- Oxidation of intracellular GSH generates Mn ²⁺ - Mn ²⁺ Fenton-type reaction induces cell apoptosis - Combined PTT gives rise in temperature, enhancing the rate of the Fenton reaction	251
Chemo-PDT				
GBMs	Photosensitizer	Target	Highlights	Ref
GO-PEG-FA-TH287-DOX	Indocyanine Green	SaOS-2, MNNG/HOS, U2OS, MG63	- Induces ROS mediated apoptosis via the JNK/p53/p21 pathway - Suppression of MTH1 protein by MTH1 inhibitor (TH287) enhances cellular sensitivity towards ROS	245
GO-PEG-FA-Rg3	Indocyanine Green	Osteosarcoma cells (<i>in vivo</i>)	- Rg3: traditional Chinese natural anticancer drug - Synergistic effect of dual therapy effectively reduced tumor progression	246
MrGO-AA-g-4-HC	4-hydroxycoumarine	MCF-7 (<i>in vivo</i>)	- pH-responsive drug release	247

- 365 nm, 20 mW/cm², 3 min irradiation was found efficacious in tumor growth suppression

Tri-synergetic therapy				
GBMs	Additives	Target	Highlights	Ref
GO-PEG-OSA-PTX	-	HGC-27 (<i>in vivo</i>)	-Chemo/PDT/PTT - pH/thermal-responsive release - ROS generation damages mitochondria, resulting in reduction of ATP - Stops P-gp from pumping out PTX	252
rGO-(TGF-β)-MTX	Immune stimulating agent (SB-431542)	4T1 (<i>in vivo</i>)	-Chemo/PTT/immune - “Vaccination” strategy- generation of tumor type specific immunity	253

4.4. Bone regeneration

As detailed in the preceding sections, GBMs display notable biocompatibility, low toxicity, remarkable mechanical properties, and antimicrobial activity, which are useful for their application in regenerative engineering. To date, GBMs have been utilized in regeneration of bones, skins, neural, and cardiac tissues.²⁵⁶⁻²⁵⁸ Among tissues, bone stands out due to its unique stiffness, making the mechanical strength of graphene materials particularly advantageous in this context. To design nanomaterials for bone regeneration, a fundamental understanding of both bone structure and the intricacies of the bone healing process is imperative. At a macroscopic level, the outer shell consists of dense cortical bone, while the inner region is comprised of a spongy and porous cancellous bone, also known as trabecular bone (Figure 4.19a). Microscopically, long nanoscale fibers composed of collagen and fibers form rod-like structures, which further pack into lamellar structures that arrange into cylinders parallel to the long axis of the cortical bone, and irregular woven arrays in the cancellous bone. Bone tissues are highly dynamic, undergoing constant remodeling orchestrated by osteolysis by osteoclasts and osteogenesis by osteoblasts. The illustration of this remodeling process in an injured bone is depicted in Figure 4.19b. Following the initial acute inflammatory response, a collagen rich, cartilage-like tissues form bridges across the defective gap. Subsequently, this delicate preliminary tissue undergoes mineralization

(calcification) over several weeks, resembling the trabecular bone. Over several months, final remodeling strengthens the bone structure, resulting in a denser and more ordered configuration. As such, bone regeneration is a prolonged process that necessitates a rigid and stable support for efficient healing.

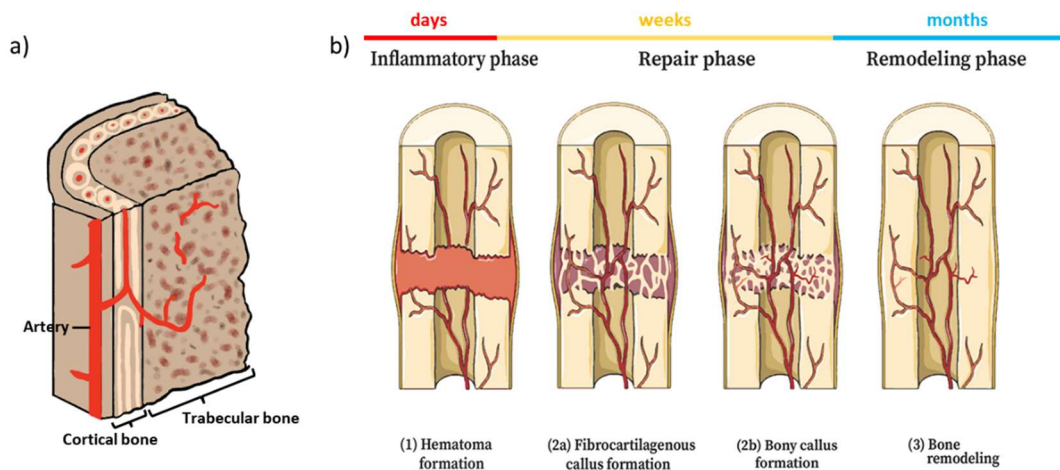


Figure 4.19. a) Illustration of a simplified bone structure. b) Timeline of the bone repair process.

b) was reproduced and adapted under the terms of the CC-BY license.²⁵⁹ Copyright 2020, The Authors, Published by Frontiers.

Traditionally, the gold standard for bone support during regeneration process has been autograft material.²⁶⁰ This approach, involving the use of grafts harvested from the patients' own tissue, typically ensures a complication-free healing process. However, the availability of autograft material can be limited, and its use also introduces an increased risk of additional infections.^{24, 261} Allografts, regarded as the next alternative, are materials harvested from another individual. To mitigate the risks of immune rejection and infection, these materials undergo an extensive sterilization process post-harvest.²⁶¹ However, this sterilization process can significantly diminish

their mechanical strength. Hence, several synthetic scaffolds, including bioceramics, natural polymers, or synthetic polymers, have been extensively explored as natural graft materials due to their accessibility, tunability, stability, and affordability.^{24, 258} Additionally, alternative implants such as titanium alloys, quartz, or bioactive glass have also been reported.²⁶²⁻²⁶⁸ Owing to the brittle nature of these graft materials, they have not been able to achieve a fracture toughness comparable to that of bone. Since the encouraging studies in 2011, demonstrating osteogenic differentiation and proliferation by graphene materials, the incorporation of GBMs into synthetic scaffolds has gained considerable research interest in recent years owing to their capacity to provide mechanical support and enhance biological properties throughout the bone healing process.²⁶⁹⁻²⁷⁰

The mechanism behind enhanced cell differentiation is understood to involve graphene's ability to chemically interact with biomolecules, utilizing hydrophobic, π - π interactions, and hydrogen bonding. This facilitates the sequestering/concentrating/protecting of relevant biomolecules for improved bioactivity.^{257, 269} Another pathway is associated with the excellent electronic properties of graphene, which facilitate enhanced electrical transmission of signals related to osteogenic activities.^{257, 271} Additionally, a recent review article summarized GBM-mediated immunomodulation as a key factor in the tissue engineering process.²⁵⁶

4.4.1. Calcium Based Scaffolds

Calcium phosphate-based materials are regarded as particularly straightforward and biocompatible scaffolds in the realm of bone tissue engineering, owing to their chemical affinity to native bone composition and bioresorbable nature.²⁷² Most frequently employed calcium phosphate compounds are hydroxyapatite (HA) and tricalcium phosphate (TCP). The first *in vivo*

assessment of enhanced osteogenesis by rGO-HA grafts demonstrated the repair of calvarial defects without eliciting inflammatory responses.²⁷³ Additionally, it was reported that the osteogenesis and osteodifferentiation of MC3T3-E1 preosteoblasts were promoted without the use of additional osteoinductive agents *in vitro*, indicating the osteoinductive potential of rGO. A simple nanohydroxyapatite (nHA)-OGNR system by Medeiros et al. showed dose-dependent osteogenesis process owing to the high bioactivity and large surface area of the graphitic material.²⁷⁴ Establishing a safety threshold, a controlled dosage range of 100-200 $\mu\text{g mL}^{-1}$ nHA-OGNR was employed as a parameter for assessing osteogenic potentials across five distinct genes (ALP, OPN, OCN, COL1, and RUNX2). Ghorai et al. employed a salt leaching technique to fabricate a GO sheet customized with nHA, spermine, and polyurethane-urea (PUU), resulting in the formation of a porous scaffold.²⁷⁵ Spermine was selected as a crucial growth factor, and PUU was chosen for its biocompatibility attributed to its chemical resemblance to proteins. Notably, an ultra-low percentage of 0.15% GO significantly enhanced mechanical properties, cell viability, cell proliferation, and surface wettability. *In vivo* studies conducted over an 8-week period demonstrated no signs of toxicity and revealed nearly complete closure of bone wounds, underscoring the scaffold's potential for successful bone regeneration. While further prolonged *in vivo* studies have not been implemented, the authors noted that such low loading of GO will likely have a negligible long-term impact. GO-HA system has been reported in conjunction with other materials such as chitosan,²⁷⁶ poly(butylene-adipate-co-terephthalate),²⁷⁷ polyetheretherketone,²⁷⁸ and carboxymethyl chitosan.²⁷⁹

Li et al. utilized a nHA-rGO hydrogel system for tandem PTT cancer therapy and bone regeneration.²⁸⁰ *In vitro* investigations showcased the successful elimination of osteosarcoma cells upon a 20 min exposure to NIR laser (808 nm, 1 W/cm²). Moreover, the nanoscaffold demonstrated

its capability to promote adhesion, cell proliferation, and mineralization of rat bone marrow stem cells. Ma and coworkers demonstrated a multifunctional GO/nHA/chitosan (CS) network exhibiting excellent PTT efficacy against osteosarcoma cells under NIR irradiation (808 nm, 0.6 W/cm²).²⁸¹ Beyond its anticancer properties, the NIR exposure was identified to stimulate osteogenesis in human bone marrow mesenchymal stem cells (hBMSCs) by generating mild localized heat, consequently activating the BMP2/Smad signaling pathway. The photothermally controlled scaffold showcased its potential utility in tissue regeneration for patients with osteosarcoma.

Ou and coworkers reported a PEI-GO construct laden with a miR-214 inhibitor, which was subsequently incorporated into a porous silk fibroin (SF)/HAP scaffold.²⁸² Given that microRNAs (miRNA) play a role as posttranscriptional repressors in the osteogenic differentiation process, the inhibitor actively suppressed miRNA, leading to an upregulation in the expression of activating transcription factor 4 (ATF4) *in vitro*. Furthermore, the Akt and ERK1/2 signaling pathways were activated. To better assess the potential of this system, further *in vivo* studies should be performed.

A study by Weng et al. introduced a 3D porous AgNP-rGO-nHA composite for bone tissue engineering. Notably, a 4% incorporation of AgNP onto the scaffold showed the highest antibacterial activity and significantly reduced inflammation. Minimization of infection led to efficient bone repair in rabbits upon 12 weeks of treatment.²⁸³ In addition to silver-enhanced scaffolds, other inorganic materials such as zinc-based graphene biomaterials are known to upregulate the expression of bone-specific genes (alkaline phosphatase, osteocalcin, and osteopontin), promote antibacterial activity, and induce osteoconductive and osteoinductive properties.²⁸⁴ Furthermore, the cost-effectiveness of zinc makes it a potentially more economical

option compared to incorporating expensive growth factors, and it offers the additional advantage of an extended shelf life. Among various bioactive elements, strontium is considered essential for maintaining human tissue functions, particularly in bone, by enhancing the osteoinductive properties and cell differentiation.²⁸⁵⁻²⁸⁶ Sr^{2+} exhibits the ability to decrease osteoclast activity and prevent bone degradation, a characteristic not shared by calcium.²⁸⁷⁻²⁸⁸ Other bioactive metal ions including copper, lithium, potassium, sodium, magnesium, cobalt, manganese, and silicon have been explored for their ability to enhance the bone regrowth based on their inherent mechanisms.^{263, 289-294}

A system with GO-copper (Cu) coating uniformly distributed on the calcium phosphate cement (CPC) surface demonstrated by Zhang et al, showed that the slow release of Cu ion could significantly enhance the bone healing process.²⁹⁰ An upregulation of Hif-1 α by GO-Cu-CPC led to enhanced expression of VEGF and BMP-2 proteins, two regulators for angiogenesis and osteogenesis. *In vivo* studies clearly evidenced the superior bone growth promotion capability of GO-Cu-CPC compared to GO-CPC. Notably, the GO-Cu nanocomposite exhibited no apparent cytotoxicity, despite the recognized cellular toxicity associated with excess Cu, known to induce oxidative damage. This observation is attributed to the controlled release of Cu, ensuring the maintenance of Cu ions at a low concentration, thus mitigating potential cytotoxic effects.

Tricalcium phosphate (TCP) bioceramics are recognized as an excellent bone material source. In a study by Wu and colleagues, GO-modified β -TCP disks presented the first finding of the activation of the Wnt signaling pathway induced by GO.²⁹⁵ This activation mechanism was likely facilitated by the interaction of bioactive groups on the GO surface, such as hydroxy or carboxy groups. This interaction partially elucidates the osteogenic stimulation mechanism of GO.

Biphasic calcium phosphates (BCP, combination of HA and TCP) are widely used materials for bone regeneration. Kim and colleagues conducted a study to investigate the impact of GO concentration within the GO-BCP nanocomposite on bone regrowth.²⁹⁶ Three distinct weight ratios of rGO:BCP (2:1000, 4:1000, and 10:1000) were examined. Histological analysis of the *in vivo* results revealed significantly higher bone regeneration with the 4:1000 nanocomposite, suggesting the importance of optimizing the scaffold composition for achieving optimal treatment outcomes.

An Inspiring strategy for fabricating future high-performance biomaterials was demonstrated by Xue et al.²⁹⁷ A bottom-up fabricated microstructure of GO/CS/calcium silicate mirrored the layered structure of nacre, a natural material known for its exceptional strength derived from its “brick and mortar” composition. The resulting macrostructure resembled a multilayered helical cylinder. Notably, the mechanical properties were similar to the natural cortical bone, showing high flexural strength (137.2 Mpa), compressive strength (80.2 Mpa), toughness (1.46 MJ/m³), and specific strength (124.7 Mpa Mg⁻¹ m⁻³). Similarly, nacre-inspired biomimetic materials with strong mechanical properties have been demonstrated for bone engineering in other studies.^{294, 298-}

300

Zhou and colleagues conducted a study demonstrating the fabrication of bone-like structures through biomimetic mineralization utilizing simulated body fluid (SBF) and apatite.³⁰¹ In their investigation, a combination of GO and collagen (Col) was immersed in SBF-apatite for varying durations (1, 7, and 14 days). Notably, no significant differences in apatite composition were observed between 7 and 14 days, prompting the selection of the 7-day treatment for subsequent experiments. Among different loadings of GO, the nanocomposite containing 0.1% GO-Col-

apatite exhibited a composition most closely resembling natural bone tissue. *In vivo* studies further revealed that the porous 0.1-0.2% GO-Col-apatite nanocomposite achieved a two-fold higher bone volume compared to Col-apatite alone. Biomimetic mineralization has consistently proven to be a reliable method for incorporating calcium phosphate derivatives, as evidenced in numerous reports.³⁰²⁻³⁰⁵

Inspired by the seminal report of electrochemical delamination method to transfer 2D-graphene films from metal to other substrates,³⁰⁶ Wang group successfully applied the same bubbling process to 3D-rGO films, and the films facilitated osteogenic differentiation and cell proliferation for pre-osteoblast (MC3T3-E1) cells *in vitro*.³⁰⁷ The same group reported the synthesis of a 3D-rGO-HA membrane with two different sides using their two-step electrochemical method.³⁰⁸ The formed 3D rGO membrane possessed plasticity and maintained the bended shape, a crucial characteristic for guided bone regeneration. One side, adjacent to the bone defect, featured rGO-HA to enhance cell proliferation and osteogenic differentiation, while the other side presented a dense 2D rGO surface to prevent fibroblasts from migrating into the bone defect. Both *in vitro* and *in vivo* investigations demonstrated the significant potential of this nanosystem in promoting the bone healing process.

4.4.2. Natural Polymer Based Scaffolds

Collagen (Col)-based scaffolds are among the most widely used natural polymers due to their biocompatibility, biodegradability, and biological activity. Considering that bone is naturally comprised of collagen, these scaffolds exhibit low immunogenicity; however, they lack

mechanical strength.^{258, 309} Similar to calcium-based bioceramic scaffolds, GBMs have been found to be effective in providing sufficient stiffness required for bone regeneration purposes.

Mechanical enhancement of collagen system can be achieved by cross-linking of biopolymers. Kang and coworkers designed a 3D collagen system by cross-linking GO flakes onto collagen by 1-ethyl-3-(3-dimethylaminopropyl)carbodiimide (EDC) coupling. The elastic modulus of the 3D network increased 2.5-fold (38.7 kPa).³¹⁰ The scaffold exhibited negligible cytotoxicity and was found to enhance the osteogenic differentiation of human MSCs by promoting mechanosensing in MSCs adhered to the stiff GO-Col substrates.

Natural polymers other than collagen have also been combined with GO. Saravanan et al. prepared a 0.25 wt% GO in CS/gelatin (Gn) scaffold by freeze-drying method.³⁰³ Their scaffold effectively promoted osteogenic differentiation of mouse MSCs by upregulating RUNX2 transcription factor. *In vivo* healing of rat tibial bone defects showed successful initiation of the healing process as early as 2 weeks, with higher collagen deposition was observed compared to CS/Gn scaffolds. Similarly, Hermenean and coworkers reported that GO-CS 3D scaffold increased the expression of RUNX2 and bone morphogenic protein (BMP-2).³¹¹ Synergistic promotion of alkaline phosphatase activity was observed in both *in vitro* and *in vivo* analyses. Significantly, substantial bone regeneration was observed in a large calvarial defect in mice over 18 weeks (3 wt% GO).

Hydrogels are a unique class of 3D material with the capability of absorbing large amounts of water without disintegration. Injectable hydrogels have demonstrated great potential for tissue regeneration owing to their similarity to the natural extracellular matrix and porous structure.³¹²⁻
³¹³ Both natural and synthetic polymer based hydrogels have been utilized for tissue engineering.³¹⁴

A natural thermosensitive hydrogel based on GO-chitosan/glycerophosphate (GP) was explored as a bone graft material, capable of gelation at physiological temperature.³¹⁵ The inclusion of GO into the hydrogel network resulted in improved hydration and protein adsorption, while maintaining its thermosensitive and injectable nature. The *in vitro* studies suggested biocompatibility with MSCs with no significant cytotoxicity observed at 0.5% GO.

4.4.3. Synthetic Polymer Based Scaffolds

Exploiting the inherent mechanical strength of graphene-based materials, Lin et al. demonstrated the 3D-printing of a porous scaffold composed of GO-calcium silicate-poly(caprolactone) (PCL).³¹⁶ This scaffold was observed to stimulate the expression of Wharton's Jelly MSCs by enhancing fibroblast growth factor receptors, showing its capability for bone regeneration in both *in vitro* and *in vivo* settings. Similarly, Hou and Wang devised a dual functional PCL/graphene scaffold for both the treatment of bone cancer and bone repair process.³¹⁷ After the bone cancer region is removed, the 3D printed structure can be implanted into the region. The outer layer is constructed with a fibrous structure, while the inner layer is designed to provide structural support. Graphene, gradually released from the surface of the fibrous scaffold, is expected to induce the apoptosis of any remaining cancer cells. Following the degradation of the outer layer, the inner core scaffold is anticipated to slowly dissolve, allowing new bone tissue to replace the region. While further *in vivo* demonstrations are requisite, such bilayer scaffold, created through 3D printing technology, holds significant potential for bone cancer treatment and bone repair. While up to approximately 10% concentrations of GBMs can be incorporated into PCL due to limitations in fluidity, much higher concentrations (>32 wt%) have been successfully fabricated with other

biocompatible elastomers, such as polylactide-*co*-glycolide, for tissue regeneration purposes.³¹⁶

318

Duan et al. explored the osteogenic effects of PLA nanofibrous scaffolds containing graphene or CNTs, fabricated through thermal-induced phase separation.³¹⁹ Both scaffolds promoted osteogenic differentiation of bone MSCs (BMSCs), with graphene demonstrating a stronger effect compared to CNT both *in vitro* and *in vivo*. The 3 wt% graphene/PLA scaffold was found to significantly enhance the production of type I collagen. No visible signs of necrosis or inflammatory response were observed.

Zhou and colleagues investigated the effect of the loading of GO on the morphology of an electrospun nanofibrous scaffold containing GO and poly(3-hydroxybutyrate-*co*-4-hydroxybutyrate) (P34HB).³²⁰ GO was found to reduce the diameter of the fiber, and enhance the porosity, mechanical strength, cellular activities, and osteodifferentiation of the electrospun scaffolds. Large calvarial defects were filled with the scaffolds, and by 8 weeks, almost complete regeneration of bone was achieved without noticeable signs of inflammation.

A thermoresponsive hydrogel scaffold composed of GO-poly(polyethylene glycol citrate-*co*-N-isopropylacrylamide) and gelatin (PPCNg), developed by Chen et al., demonstrated increased ALP activity and gene expression in BMP9-stimulated adipose-derived MSCs.³²¹ *In vivo* results showed the formation of a highly vascularized and mineralized trabecular bone in 4 weeks. They noted that the addition of GO did not affect the thermoresponsive behavior of the hybrid material. Another work by Kim et al. showcased a hydrogel based on PEG-GO molded at a low temperature of -20 °C followed by freeze-drying.³²² Such “cryogel”, named PEGDA-GO, was found to promote osteodifferentiation of human tonsil-derived MSCs, improve cell adhesion, and activate focal

adhesion kinase (FAK) signaling. *In vivo* studies using a mice calvarial defect model demonstrated that a 10 µg/mL GO-incorporated PEGDA displayed a 1.9-fold higher volume of regenerated bone compared to PEGDA cryogels.

Table 4.3. A summary of graphene based bone regeneration systems.

Calcium based bioceramics			
GBMs	Bioceramic	Comments	Ref
rGO	HA (<i>in vivo</i>)	- Enhance the osteogenesis of MC3T3-E1 preosteoblasts - First example to examine the <i>in vivo</i> osteogenic potency of rGO/HA nanocomposites	273
OGNR	nHA (<i>in vivo</i>)	- Dose-dependent osteogenesis - Osteogenic potentials determined across 5 genes (ALP, OPN, OCN, COL1, and RUNX2) - <i>In vivo</i> studies demonstrated higher bone regeneration of nHA/GONR across all groups	274
GO-PUU-spermine	nHA (<i>in vivo</i>)	- Non-toxicity - Porous bone-like scaffold - Ultra-low concentration of 0.15% GO achieved improved mechanical properties, cell viability, cell proliferation, and surface wettability	275
GO-CS	nHA (<i>in vivo</i>)	- High MG-63 osteoblast cell viability (>95%) - One-step in situ generation of GO/CS/nHA scaffold - Uniform dispersion of nHA achieved in nanometer scale in the scaffold - <i>In vitro</i> demonstration of great biological performance in terms of biodegradation, cell proliferation, cell differentiation, hemolysis ratio	276
GO-CMC	nHA (<i>in vivo</i>)	- <i>In vivo</i> bone repair achieved in calvarial defects with scaffolds containing low amount of GO (0.09%) - Carboxymethyl groups on chitosan enhanced the surface chemistry and roughness	279
GNR-PBAT	nHA (<i>in vivo</i>)	- Roughness measured by atomic force microscopy ($R_q = 74.1$ nm) - Higher cell adhesion observed in rougher surfaces, leading to enhanced cell proliferation and osteoinductivity	277
GO-PEEK	HA (<i>in vivo</i>)	- Poly(butylene-adipate-co-terephthalate) (PBAT) utilized for its fast biodegradability and good mechanical properties - Ultrathin fibers of GNR/PBAT/nHA generated by electrospinning - Improved <i>in vivo</i> formation of trabecular bones upon treatment for 2 weeks	278
rGO-AgNP	nHA (<i>in vivo</i>)	- Strong π - π interaction formed between GO and benzene rings on polyetheretherketone (PEEK) - Cell adhesion, proliferation, and differentiation were better for GO-PEEK-HA compared to PEEK-HA - <i>In vivo</i> defect repair in rabbits observed over 60 days	283
rGO	Zinc-doped HA (H _{ap} Z)	- 4% AgNP exhibited high antibacterial activity - AgNP have negligible impact on scaffold topography - Inhibitory effect was observed against MRSA	284
rGO	nHA (<i>in vivo</i>)	- Upregulation of bone-specific genes - Antimicrobial activity against <i>S. aureus</i> - <i>In vivo</i> studies showed enhanced bone regeneration and neovascularization (induction of proangiogenic genes such as VEGF and PDGF) by the nanocomposite	280
rGO	nHA (<i>in vivo</i>)	- Both <i>in vitro</i> and <i>in vivo</i> experiments show effective PTT against MG-63 cells - Simultaneous promotion of bone cell proliferation and differentiation, resulting in large-format tumor-related cranial bone defect repairment	

GO-PEI-SF	HA	<ul style="list-style-type: none"> - Suppression of miRNAs by mir-214 inhibitor led to increased expression of activating transcription factor 4 (ATF4) <i>in vitro</i> - Fluorescence imaging achieved by functionalizing mir-214 with Cy3 - Controlled release of miRNA from the cationic PEI network - Porous structure achieved with silk fibroin/HA - Activation of Akt and ERK1/2 signaling pathway 	282
GO-CS	HA (<i>in vivo</i>)	<ul style="list-style-type: none"> - Nacre-inspired “brick and mortar” layered structure - High flexural strength (161 MPa) compressive strength (95 MPa), and toughness (1.1 MJ/m³) - Angiogenesis and osteogenesis capabilities observed <i>in vivo</i> 	294
GO-CS	HA (<i>in vivo</i>)	<ul style="list-style-type: none"> - Biomimetic mineralization in simulated body fluid (SBF) - Higher osteogenic differentiation achieved for GO-CS-HA-SBF compared to GO-CS-HA - Negligible toxicity against normal epidermal tissue 	302
rGO	HA	<ul style="list-style-type: none"> - Electrochemical delamination by bubbling to transfer rGO films - Enhanced ALP activity and osteogenic genes (ALP, OPN, Runx2) expressions observed in MC3T3-E1 cells 	307
rGO	HA (<i>in vivo</i>)	<ul style="list-style-type: none"> - Two-step electrochemical transfer synthesis of two-sided 3D-rGO-HA membrane (porous side/dense side) - Good biocompatibility with MC3T3-E1 and HUVEC cells 	308
GO-CS	nHA	<ul style="list-style-type: none"> - <i>In vivo</i> demonstration of treatment of calvarial defects - NIR irradiation promoted the osteogenesis by stimulating the BMP2/Smad signaling pathway - Efficient PTT against osteosarcoma cells 	281
GO	TCP (<i>in vivo</i>)	<ul style="list-style-type: none"> - Enhanced alkaline phosphatase activity, osteogenic gene expression (hBMSCs), and cell proliferation - Activation of Wnt/β-catenin signaling pathway induced by bioactive groups (OH⁻ or COO⁻) on GO 	295
rGO	BCP (<i>in vivo</i>)	<ul style="list-style-type: none"> - Effect of rGO concentration within the nanocomposite on bone regeneration was investigated <i>in vivo</i> - low cytotoxicity (cell viability of >80% at concentrations <62.5 μg/mL) 	296
GO-CS	Calcium silicate (<i>in vivo</i>)	<ul style="list-style-type: none"> - Nacre-inspired “brick and mortar” layered structure - Flexibility of material enabling the formation of desired shape - High flexural strength (137.2 MPa), compressive strength (80.2 MPa), toughness (1.46 MJ/m³), and specific strength (124.7 MPa Mg⁻¹ m⁻³) - <i>In vivo</i> osteogenic ability observed on rat femoral defects 	297
GO-Cu	CPC (<i>in vivo</i>)	<ul style="list-style-type: none"> - Upregulation of Hif-1α by activating the Erk1/2 signaling pathway in BMSCs - GO-Cu-CPC promoted angiogenesis and osteogenesis in critical-sized calvarial defects of rats - Negligible cytotoxicity associated with toxic copper, due to long-term controlled release of Cu ions 	290
GO-Col	Apatite (<i>in vivo</i>)	<ul style="list-style-type: none"> - Biomimetic mineralization achieved in simulated body fluid - 0.1% GO imbedded in the scaffold most closely resembled the natural bone tissue - 0.1% GO-Col-Ap exhibited high therapeutic efficacy for the treatment of critical-sized rat cranial defects 	301

Natural polymers			
GBMs	Polymer	Comments	Ref
GO-Sr	Col (<i>in vivo</i>)	<ul style="list-style-type: none"> - Long-term release of Sr²⁺ reinforces collagen scaffold by cross-linking - Osteogenesis and angiogenesis promoted by activation of the MAPK signaling pathway - Highly vascularized bone regeneration, increased expression of RUNX2, OCN, OPN, and CD31-positive vessels in a rat calvarial defect model 	288
GO	Col	<ul style="list-style-type: none"> - Stiff 3D-network formed by cross-coupling of GO and Col mediated by EDC coupling - 2.5-fold increase in elastic modulus - Cell-adhesion promoted proliferation of hMSCs 	310
GO	Col (<i>in vivo</i>)	<ul style="list-style-type: none"> - Collagen sponge coated with thin layer of GO - GO was found to accelerate the degradation process of GO-Col 	323
GO	CS-Gn (<i>in vivo</i>)	<ul style="list-style-type: none"> - Increased collagen deposition compared to CS-Gn scaffold - Cyto-friendly to rat osteoprogenitor cells - Enhanced osteogenic cell differentiation by upregulation of RUNX2 	303
GO	CS (<i>in vivo</i>)	<ul style="list-style-type: none"> - <i>In vivo</i> assessment of critical sized calvarial defect of mice over 18 weeks 	311

GO	CS/GP	<ul style="list-style-type: none"> - Upregulation of RUNX2 and BMP-2 detected - Thermoresponsive hydrogel network with improved physico-chemical properties by incorporation of GO - Osteogenic differentiation of mouse MSCs increased by upregulation of RUNX2, ALP, COL-1, and osteocalcin 	315
Synthetic polymers			
GBMs	Polymer	Comments	Ref
rGO-Sr	PCL (<i>in vivo</i>)	<ul style="list-style-type: none"> - Significantly higher osteoblast proliferation and differentiation for rGO-Sr-PCL scaffolds in comparison to neat PCL and rGO-PCL scaffolds - <i>In vivo</i> studies showed that hydrolytic degradation of PCL was enhanced by Sr nanoparticles 	286
rGO-Cu	PCL	<ul style="list-style-type: none"> - Copper oxide (CuO, Cu₂O) decorated nanocomposite exhibited sustained release of Cu ions - Bactericidal activity against <i>Escherichia coli</i> (22% cell viability) - <i>In vitro</i> studies showed improved mineralization, angiogenesis, and osteogenesis by the scaffold 	291
GO-calcium silicate	PCL (<i>in vivo</i>)	<ul style="list-style-type: none"> - Good mechanical property and controlled structure achieved by 3D-printing - < 10 wt% of graphene incorporation (difficulty in printing at higher concentrations) - Enhanced expression of Wharton's Jelly MSCs - Excellent <i>in vitro/in vivo</i> bone regeneration and angiogenic ability 	316
Graphene	PCL	<ul style="list-style-type: none"> - 3D printing of a dual-functional bilayer scaffold - 5-9 wt% of graphene incorporation - Further <i>in vivo</i> evaluation is prerequisite 	317
Graphene or CNT	PLA (<i>in vivo</i>)	<ul style="list-style-type: none"> - Higher osteogenic effect of graphene compared to CNT both <i>in vitro</i> and <i>in vivo</i> - Increased ALP activity, type I collagen generation and calcium deposition observed for both carbon materials - Negligible inflammatory response, fibrous membrane formation, or necrosis 	319
GO	P34HB	<ul style="list-style-type: none"> - Investigation of the loading of GO on the electrospun fiber morphology - Increased expression of osteogenic genes of rat BMSCs - 8 weeks of <i>in vivo</i> investigation showed almost fully regenerated bone without visible signs of immunological response 	320
GO	PPCNg (<i>in vivo</i>)	<ul style="list-style-type: none"> - Gelatin/citrate-based synthetic polymer network to construct thermoresponsive hydrogel - Induction of ALP and BMP9 expression and enhanced angiogenic factor (VEGF) - Successful <i>in vivo</i> bone defect repairment (high mineralization and vascularization observed) 	321
GO	PEGDA (<i>in vivo</i>)	<ul style="list-style-type: none"> - Cryogel formation at low temperature - Osteogenic differentiation enhanced by higher gene expression (RUNX2, OCN, COL1, ALP) 	322

4.5. Summary and Outlook

GBMs can be readily functionalized through both covalent and non-covalent approaches, leveraging their substantial surface area for the loading of diverse drugs, polymers, biomolecules, or inorganic nanoparticles. This chemical tunability facilitates a spectrum of therapeutic applications, encompassing antimicrobial activities, targeted delivery, combined therapy, bone regeneration, and simultaneous imaging enabled by the multifunctionality of GBMs. However, despite extensive literature supporting their potential, GBMs are currently still at the "proof-of-concept" stage, contrasting with other nanoparticles that have progressed to clinical trials.³²⁴ To advance into clinical evaluation and real-world applications, a thorough investigation of the health and environmental impact of GBMs is essential. Presently, the toxicity evaluation of GBMs presents several controversial aspects. For instance, the mechanism of antimicrobial activities of GO is not fully understood, primarily attributed to the inconsistencies among reported studies. As previously mentioned, a debate persists between the ROS-mediated membrane stress and the electron transfer mechanism. In another case, one study reports that smaller-sized GO exhibits increased antimicrobial activity due to a higher defect density inducing stronger oxidative stress, while another suggests that larger-sized GO can effectively inactivate bacteria by easier wrapping.^{42,325} Such inconsistencies could be attributed to 1) variability in the methods employed for assessing bacterial growth and viability, and 2) differences in the structure of GBMs used in the studies, which may vary significantly based on the synthesis methods employed. For deeper insights into these conflicts, we recommend readers refer to the relevant reviews.³²⁶⁻³²⁷ Despite such contradictory findings, the consensus is that the toxicity of GBMs depends on factors such as lateral size, applied dose, and purity of the material.^{27, 43, 328-329}

The majority of GBMs employed in biomedical applications heavily rely on materials prepared through top-down methods. While well-established methods such as Hummer's method may be reliable for long-term industrialization due to scalability, it may not be the most suitable for therapeutic applications, where safety is of utmost importance. Top-down generation of GBMs result in random structures with batch-to-batch variations in sizes and edges, even when the same protocol is used. Ensuring reproducible evaluations of GBMs for biomedical applications necessitates precise control over both functionalization and the size of the generated graphene materials. The solution-phase synthesis of GBMs could be a promising avenue for the future, enabling the generation of well-controlled, defined graphene-based nanomaterials. Alongside numerous commendable reports on GBM synthesis in solution, some well-controlled approaches, such as programmable synthesis of monodisperse GNRs and iterative binomial synthesis of monodisperse conjugated polymers, have been realized by us.³³⁰⁻³³¹ Both works showcase precise control over both the structure, sequence, and length of target molecules, offering the potential for further extension to automated solid-phase synthesis for industrial applications. Finally, in conjunction with the development of structurally-defined GBMs featuring tailored physicochemical properties and precise surface functionalization, a thorough assessment of potential benefits and long-term risks will be crucial to ensure both safety and maximum therapeutic efficiency.

4.6. References

1. Novoselov, K. S.; Geim, A. K.; Morozov, S. V.; Jiang, D.; Zhang, Y.; Dubonos, S. V.; Grigorieva, I. V.; Firsov, A. A. Electric field effect in atomically thin carbon films. *Science* **2004**, *306*, 666-669.
2. Saraswat, V.; Jacobberger, R. M.; Arnold, M. S. Materials science challenges to graphene nanoribbon electronics. *ACS Nano* **2021**, *15*, 3674-3708.
3. Loh, K. P.; Bao, Q.; Eda, G.; Chhowalla, M. Graphene oxide as a chemically tunable platform for optical applications. *Nat. Chem.* **2010**, *2*, 1015-1024.
4. Wang, H.; Liang, Y.; Mirfakhrai, T.; Chen, Z.; Casalongue, H. S.; Dai, H. Advanced asymmetrical supercapacitors based on graphene hybrid materials. *Nano Res.* **2011**, *4*, 729-736.
5. Wu, J.; Pisula, W.; Müllen, K. Graphenes as potential material for electronics. *Chem. Rev.* **2007**, *107*, 718-747.
6. Chen, Z.; Narita, A.; Müllen, K. Graphene nanoribbons: on-surface synthesis and integration into electronic devices. *Adv. Mater.* **2020**, *32*, 2001893.
7. Feng, L.; Liu, Z. Graphene in biomedicine: opportunities and challenges. *Nanomed.* **2011**, *6*, 317-324.
8. Cheng, L.; Wang, C.; Feng, L.; Yang, K.; Liu, Z. Functional nanomaterials for phototherapies of cancer. *Chem. Rev.* **2014**, *114*, 10869-10939.
9. Huang, C.; Li, C.; Shi, G. Graphene based catalysts. *Energy Environ. Sci.* **2012**, *5*, 8848-8868.
10. Han, J.; Johnson, I.; Chen, M. 3D continuously porous graphene for energy applications. *Adv. Mater.* **2022**, *34*, 2108750.
11. Jiao, L.; Zhang, L.; Wang, X.; Diankov, G.; Dai, H. Narrow graphene nanoribbons from carbon nanotubes. *Nature* **2009**, *458*, 877-880.

12. Kosynkin, D. V.; Higginbotham, A. L.; Sinitskii, A.; Lomeda, J. R.; Dimiev, A.; Price, B. K.; Tour, J. M. Longitudinal unzipping of carbon nanotubes to form graphene nanoribbons. *Nature* **2009**, *458*, 872-876.
13. Behabtu, N.; Lomeda, J. R.; Green, M. J.; Higginbotham, A. L.; Sinitskii, A.; Kosynkin, D. V.; Tsentelovich, D.; Parra-Vasquez, A. N. G.; Schmidt, J.; Kesselman, E.; Cohen, Y.; Talmon, Y.; Tour, J. M.; Pasquali, M. Spontaneous high-concentration dispersions and liquid crystals of graphene. *Nat. Nanotechnol.* **2010**, *5*, 406-411.
14. Zhong, Y. L.; Swager, T. M. Enhanced electrochemical expansion of graphite for in situ electrochemical functionalization. *J. Am. Chem. Soc.* **2012**, *134*, 17896-17899.
15. Ma, L.; Wang, J.; Ding, F. Recent progress and challenges in graphene nanoribbon synthesis. *ChemPhysChem* **2013**, *14*, 47-54.
16. Ambrosi, A.; Chua, C. K.; Bonanni, A.; Pumera, M. Electrochemistry of graphene and related materials. *Chem. Rev.* **2014**, *114*, 7150-7188.
17. Yoon, K.-Y.; Dong, G. Liquid-phase bottom-up synthesis of graphene nanoribbons. *Mater. Chem. Front.* **2020**, *4*, 29-45.
18. Zhou, X.; Yu, G. Modified engineering of graphene nanoribbons prepared via on-surface synthesis. *Adv. Mater.* **2020**, *32*, 1905957.
19. Yano, Y.; Mitoma, N.; Ito, H.; Itami, K. A quest for structurally uniform graphene nanoribbons: synthesis, properties, and applications. *J. Org. Chem.* **2019**, *85*, 4-33.
20. Yang, K.; Hu, L.; Ma, X.; Ye, S.; Cheng, L.; Shi, X.; Li, C.; Li, Y.; Liu, Z. Multimodal imaging guided photothermal therapy using functionalized graphene nanosheets anchored with magnetic nanoparticles. *Adv. Mater.* **2012**, *24*, 1868-1872.
21. Feng, L.; Zhang, S.; Liu, Z. Graphene based gene transfection. *Nanoscale* **2011**, *3*, 1252-1257.

22. Moghadam, N. B.; Avatefi, M.; Karimi, M.; Mahmoudifard, M. Graphene family in cancer therapy: recent progress in cancer gene/drug delivery applications. *J. Mater. Chem. B* **2023**, *11*, 2568-2613.
23. Yang, K.; Feng, L.; Liu, Z. Stimuli responsive drug delivery systems based on nano-graphene for cancer therapy. *Adv. Drug Deliv. Rev.* **2016**, *105*, 228-241.
24. Cheng, J.; Liu, J.; Wu, B.; Liu, Z.; Li, M.; Wang, X.; Tang, P.; Wang, Z. Graphene and its derivatives for bone tissue engineering: In vitro and in vivo evaluation of graphene-based scaffolds, membranes and coatings. *Front. Bioeng. Biotechnol.* **2021**, *9*, 734688.
25. Han, W.; Wu, Z.; Li, Y.; Wang, Y. Graphene family nanomaterials (GFNs)—promising materials for antimicrobial coating and film: A review. *J. Chem. Eng.* **2019**, *358*, 1022-1037.
26. Zou, X.; Zhang, L.; Wang, Z.; Luo, Y. Mechanisms of the antimicrobial activities of graphene materials. *J. Am. Chem. Soc.* **2016**, *138*, 2064-2077.
27. Karahan, H. E.; Wiraja, C.; Xu, C.; Wei, J.; Wang, Y.; Wang, L.; Liu, F.; Chen, Y. Graphene materials in antimicrobial nanomedicine: current status and future perspectives. *Adv. Healthc. Mater.* **2018**, *7*, 1701406.
28. Chung, S.; Revia, R. A.; Zhang, M. Graphene quantum dots and their applications in bioimaging, biosensing, and therapy. *Adv. Mater.* **2021**, *33*, 1904362.
29. Morales-Narváez, E.; Merkoçi, A. Graphene oxide as an optical biosensing platform: A progress report. *Adv. Mater.* **2019**, *31*, 1805043.
30. Zhang, X.; Jing, Q.; Ao, S.; Schneider, G. F.; Kireev, D.; Zhang, Z.; Fu, W. Ultrasensitive field-effect biosensors enabled by the unique electronic properties of graphene. *Small* **2020**, *16*, 1902820.

31. Cheng, L.; Wang, X.; Gong, F.; Liu, T.; Liu, Z. 2D nanomaterials for cancer theranostic applications. *Adv. Mater.* **2020**, *32*, 1902333.
32. Gu, Z.; Zhu, S.; Yan, L.; Zhao, F.; Zhao, Y. Graphene-based smart platforms for combined Cancer therapy. *Adv. Mater.* **2019**, *31*, 1800662.
33. Imani, R.; Mohabatpour, F.; Mostafavi, F. Graphene-based nano-carrier modifications for gene delivery applications. *Carbon* **2018**, *140*, 569-591.
34. Fu, L.; Zheng, Y.; Li, X.; Liu, X.; Lin, C.-T.; Karimi-Maleh, H. Strategies and Applications of Graphene and Its Derivatives-Based Electrochemical Sensors in Cancer Diagnosis. *Molecules* **2023**, *28*, 6719.
35. Mohammadpour-Haratbar, A.; Boraei, S. B. A.; Zare, Y.; Rhee, K. Y.; Park, S.-J. Graphene-based electrochemical biosensors for breast cancer detection. *Biosensors* **2023**, *13*, 80.
36. Fatima, N.; Qazi, U. Y.; Mansha, A.; Bhatti, I. A.; Javaid, R.; Abbas, Q.; Nadeem, N.; Rehan, Z. A.; Noreen, S.; Zahid, M. Recent developments for antimicrobial applications of graphene-based polymeric composites: A review. *J. Ind. Eng. Chem.* **2021**, *100*, 40-58.
37. Hutchings, M. I.; Truman, A. W.; Wilkinson, B. Antibiotics: past, present and future. *Curr. Opin. Microbiol.* **2019**, *51*, 72-80.
38. Dadgostar, P. Antimicrobial resistance: implications and costs. *Infect. Drug Resist.* **2019**, *12*, 3903-3910.
39. Jiao, Y.; Niu, L.; Ma, S.; Li, J.; Tay, F. R.; Chen, J. Quaternary ammonium-based biomedical materials: State-of-the-art, toxicological aspects and antimicrobial resistance. *Prog. Polym. Sci.* **2017**, *71*, 53-90.
40. Dizaj, S. M.; Lotfipour, F.; Barzegar-Jalali, M.; Zarrintan, M. H.; Adibkia, K. Antimicrobial activity of the metals and metal oxide nanoparticles. *Mater. Sci. Eng. C* **2014**, *44*, 278-284.

41. Taubes, G. The bacteria fight back. *Science* **2008**, *321*, 356-361.
42. Perreault, F.; De Faria, A. F.; Nejati, S.; Elimelech, M. Antimicrobial properties of graphene oxide nanosheets: why size matters. *ACS Nano* **2015**, *9*, 7226-7236.
43. Russier, J.; Treossi, E.; Scarsi, A.; Perrozzi, F.; Dumortier, H.; Ottaviano, L.; Meneghetti, M.; Palermo, V.; Bianco, A. Evidencing the mask effect of graphene oxide: a comparative study on primary human and murine phagocytic cells. *Nanoscale* **2013**, *5*, 11234-11247.
44. Mangadlao, J. D.; Santos, C. M.; Felipe, M. J. L.; de Leon, A. C. C.; Rodrigues, D. F.; Advincula, R. C. On the antibacterial mechanism of graphene oxide (GO) Langmuir–Blodgett films. *Chem. Commun.* **2015**, *51*, 2886-2889.
45. Wang, J.; Wei, Y.; Shi, X.; Gao, H. Cellular entry of graphene nanosheets: the role of thickness, oxidation and surface adsorption. *RSC Adv.* **2013**, *3*, 15776-15782.
46. Hu, W.; Peng, C.; Luo, W.; Lv, M.; Li, X.; Li, D.; Huang, Q.; Fan, C. Graphene-based antibacterial paper. *ACS Nano* **2010**, *4*, 4317-4323.
47. Liu, S.; Zeng, T. H.; Hofmann, M.; Burcombe, E.; Wei, J.; Jiang, R.; Kong, J.; Chen, Y. Antibacterial activity of graphite, graphite oxide, graphene oxide, and reduced graphene oxide: membrane and oxidative stress. *ACS Nano* **2011**, *5*, 6971-6980.
48. Gurunathan, S.; Han, J. W.; Dayem, A. A.; Eppakayala, V.; Kim, J.-H. Oxidative stress-mediated antibacterial activity of graphene oxide and reduced graphene oxide in *Pseudomonas aeruginosa*. *Int. J. Nanomed.* **2012**, *7*, 5901-5914.
49. Sawangphruk, M.; Srimuk, P.; Chiochan, P.; Sangsri, T.; Siwayaprahm, P. Synthesis and antifungal activity of reduced graphene oxide nanosheets. *Carbon* **2012**, *50*, 5156-5161.

50. Chen, J.; Zhou, G.; Chen, L.; Wang, Y.; Wang, X.; Zeng, S. Interaction of graphene and its oxide with lipid membrane: a molecular dynamics simulation study. *J. Phys. Chem. C* **2016**, *120*, 6225-6231.
51. Santos, C. M.; Tria, M. C. R.; Vergara, R. A. M. V.; Ahmed, F.; Advincula, R. C.; Rodrigues, D. F. Antimicrobial graphene polymer (PVK-GO) nanocomposite films. *Chem. Commun.* **2011**, *47*, 8892-8894.
52. Karahan, H. E.; Wei, L.; Goh, K.; Wiraja, C.; Liu, Z.; Xu, C.; Jiang, R.; Wei, J.; Chen, Y. Synergism of water shock and a biocompatible block copolymer potentiates the antibacterial activity of graphene oxide. *Small* **2016**, *12*, 951-962.
53. Assali, M.; Almasri, M.; Kittana, N.; Alsouqi, D. Covalent functionalization of graphene sheets with different moieties and their effects on biological activities. *ACS Biomater. Sci. Eng.* **2019**, *6*, 112-121.
54. Akhavan, O.; Ghaderi, E. Toxicity of graphene and graphene oxide nanowalls against bacteria. *ACS Nano* **2010**, *4*, 5731-5736.
55. Sengupta, I.; Bhattacharya, P.; Talukdar, M.; Neogi, S.; Pal, S. K.; Chakraborty, S. Bactericidal effect of graphene oxide and reduced graphene oxide: Influence of shape of bacteria. *Coll. Interface Sci. Commun.* **2019**, *28*, 60-68.
56. Ye, S.; Shao, K.; Li, Z.; Guo, N.; Zuo, Y.; Li, Q.; Lu, Z.; Chen, L.; He, Q.; Han, H. Antiviral activity of graphene oxide: how sharp edged structure and charge matter. *ACS Appl. Mater. Interfaces* **2015**, *7*, 21571-21579.
57. Wu, L.; Zeng, L.; Jiang, X. Revealing the nature of interaction between graphene oxide and lipid membrane by surface-enhanced infrared absorption spectroscopy. *J. Am. Chem. Soc.* **2015**, *137*, 10052-10055.

58. Tu, Y.; Lv, M.; Xiu, P.; Huynh, T.; Zhang, M.; Castelli, M.; Liu, Z.; Huang, Q.; Fan, C.; Fang, H.; Zhou, R. Destructive extraction of phospholipids from *Escherichia coli* membranes by graphene nanosheets. *Nat. Nanotechnol.* **2013**, *8*, 594-601.
59. Pham, V. T.; Truong, V. K.; Quinn, M. D.; Notley, S. M.; Guo, Y.; Baulin, V. A.; Al Kobaisi, M.; Crawford, R. J.; Ivanova, E. P. Graphene induces formation of pores that kill spherical and rod-shaped bacteria. *ACS Nano* **2015**, *9*, 8458-8467.
60. Moghayedi, M.; Goharshadi, E. K.; Ghazvini, K.; Ahmadzadeh, H.; Jorabchi, M. N. Antibacterial activity of Ag nanoparticles/phosphomolybdate/reduced graphene oxide nanocomposite: Kinetics and mechanism insights. *Mater. Sci. Eng. B* **2020**, *262*, 114709.
61. Akhavan, O.; Ghaderi, E.; Esfandiari, A. Wrapping bacteria by graphene nanosheets for isolation from environment, reactivation by sonication, and inactivation by near-infrared irradiation. *J. Phys. Chem. B* **2011**, *115*, 6279-6288.
62. Pulingam, T.; Thong, K. L.; Ali, M. E.; Appaturi, J. N.; Dinshaw, I. J.; Ong, Z. Y.; Leo, B. F. Graphene oxide exhibits differential mechanistic action towards Gram-positive and Gram-negative bacteria. *Colloids Surf. B Biointerfaces* **2019**, *181*, 6-15.
63. West, J. D.; Marnett, L. J. Endogenous reactive intermediates as modulators of cell signaling and cell death. *Chem. Res. Toxicol.* **2006**, *2*, 173-194.
64. Jana, A. K.; Agarwal, S.; Chatterjee, S. The induction of lipid peroxidation in liposomal membrane by ultrasound and the role of hydroxyl radicals. *Radiat. Res.* **1990**, *124*, 7-14.
65. Krishnamoorthy, K.; Veerapandian, M.; Zhang, L.-H.; Yun, K.; Kim, S. J. Antibacterial efficiency of graphene nanosheets against pathogenic bacteria via lipid peroxidation. *J. Phys. Chem. C* **2012**, *116*, 17280-17287.

66. Liu, X.; Sen, S.; Liu, J.; Kulaots, I.; Geohegan, D.; Kane, A.; Poretzky, A. A.; Rouleau, C. M.; More, K. L.; Palmore, G. T. R.; Hurt, R. H. Antioxidant deactivation on graphenic nanocarbon surfaces. *Small* **2011**, *7*, 2775-2785.
67. Perreault, F.; De Faria, A. F.; Elimelech, M. Environmental applications of graphene-based nanomaterials. *Chem. Soc. Rev.* **2015**, *44*, 5861-5896.
68. Musico, Y. L. F.; Santos, C. M.; Dalida, M. L. P.; Rodrigues, D. F. Surface modification of membrane filters using graphene and graphene oxide-based nanomaterials for bacterial inactivation and removal. *ACS Sustain. Chem. Eng* **2014**, *2*, 1559-1565.
69. Castrillón, S. R.; Perreault, F.; de Faria, A. F.; Elimelech, M. Interaction of graphene oxide with bacterial cell membranes: insights from force spectroscopy. *Environ. Sci. Technol. Lett.* **2015**, *2*, 112-117.
70. Zhang, Y.; Ali, S. F.; Dervishi, E.; Xu, Y.; Li, Z.; Casciano, D.; Biris, A. S. Cytotoxicity effects of graphene and single-wall carbon nanotubes in neural pheochromocytoma-derived PC12 cells. *ACS Nano* **2010**, *4*, 3181-3186.
71. Li, Y.; Liu, Y.; Fu, Y.; Wei, T.; Le Guyader, L.; Gao, G.; Liu, R.-S.; Chang, Y.-Z.; Chen, C. The triggering of apoptosis in macrophages by pristine graphene through the MAPK and TGF-beta signaling pathways. *Biomater.* **2012**, *33*, 402-411.
72. Chen, J.; Wang, X.; Han, H. A new function of graphene oxide emerges: inactivating phytopathogenic bacterium *Xanthomonas oryzae* pv. *Oryzae*. *J. Nanopart. Res.* **2013**, *15*, 1658.
73. Nanda, S. S.; An, S. S. A.; Yi, D. K. Oxidative stress and antibacterial properties of a graphene oxide-cystamine nanohybrid. *Int. J. Nanomed.* **2015**, *10*, 549-556.

74. Gurunathan, S.; Han, J. W.; Dayem, A. A.; Eppakayala, V.; Park, M.-R.; Kwon, D.-N.; Kim, J.-H. Antibacterial activity of dithiothreitol reduced graphene oxide. *J. Ind. Eng. Chem.* **2013**, *19*, 1280-1288.
75. Li, J.; Wang, G.; Zhu, H.; Zhang, M.; Zheng, X.; Di, Z.; Liu, X.; Wang, X. Antibacterial activity of large-area monolayer graphene film manipulated by charge transfer. *Sci. Rep.* **2014**, *4*, 4359.
76. Lyon, D. Y.; Brunet, L.; Hinkal, G. W.; Wiesner, M. R.; Alvarez, P. J. J. Antibacterial activity of fullerene water suspensions (nC₆₀) is not due to ROS-mediated damage. *Nano Lett.* **2008**, *8*, 1539-1543.
77. Tang, Y. J.; Ashcroft, J. M.; Chen, D.; Min, G.; Kim, C.-H.; Murkhejee, B.; Larabell, C.; Keasling, J. D.; Chen, F. F. Charge-associated effects of fullerene derivatives on microbial structural integrity and central metabolism. *Nano Lett.* **2007**, *7*, 754-760.
78. Hui, L.; Piao, J.-G.; Auletta, J.; Hu, K.; Zhu, Y.; Meyer, T.; Liu, H.; Yang, L. Availability of the basal planes of graphene oxide determines whether it is antibacterial. *ACS Appl. Mater. Interfaces* **2014**, *6*, 13183-13190.
79. Zhou, Y.; Yang, J.; He, T.; Shi, H.; Cheng, X.; Lu, Y. Highly stable and dispersive silver nanoparticle-graphene composites by a simple and low-energy-consuming approach and their antimicrobial activity. *Small* **2013**, *9*, 3445-3454.
80. Arfat, Y. A.; Ahmed, J.; Ejaz, M.; Mullah, M. Polylactide/graphene oxide nanosheets/clove essential oil composite films for potential food packaging applications. *Int. J. Biol. Macromol.* **2018**, *107*, 194-203.
81. Wang, H.; Chen, M.; Jin, C.; Niu, B.; Jiang, S.; Li, X.; Jiang, S. Antibacterial [2-(methacryloyloxy) ethyl] trimethylammonium chloride functionalized reduced graphene

oxide/poly (ethylene-co-vinyl alcohol) multilayer barrier film for food packaging. *J. Agrig. Food Chem.* **2018**, *66*, 732-739.

82. Rossa, V.; Ferreira, L. E. M.; da Costa Vasconcelos, S.; Shimabukuro, E. T. T.; da Costa Madriaga, V. G.; Carvalho, A. P.; Pergher, S. B. C.; de Carvalho da Silva, F.; Ferreira, V. F.; Junior, C. A. C.; de Melo Lima, T. Nanocomposites based on the graphene family for food packaging: historical perspective, preparation methods, and properties. *RSC Adv.* **2022**, *12*, 14084-14111.

83. He, C.; Shi, Z.-Q.; Cheng, C.; Lu, H.-Q.; Zhou, M.; Sun, S.-D.; Zhao, C.-S. Graphene oxide and sulfonated polyanion co-doped hydrogel films for dual-layered membranes with superior hemocompatibility and antibacterial activity. *Biomater. Sci.* **2016**, *4*, 1431-1440.

84. Yu, L.; Zhang, Y.; Zhang, B.; Liu, J.; Zhang, H.; Song, C. Preparation and characterization of HPEI-GO/PES ultrafiltration membrane with antifouling and antibacterial properties. *J. Membr. Sci.* **2013**, *447*, 452-462.

85. Hui, L.; Auletta, J. T.; Huang, Z.; Chen, X.; Xia, F.; Yang, S.; Liu, H.; Yang, L. Surface disinfection enabled by a layer-by-layer thin film of polyelectrolyte-stabilized reduced graphene oxide upon solar near-infrared irradiation. *ACS Appl. Mater. Interfaces* **2015**, *7*, 10511-10517.

86. Huang, L.; Xu, S.; Wang, Z.; Xue, K.; Su, J.; Song, Y.; Chen, S.; Zhu, C.; Tang, B. Z.; Ye, R. Self-reporting and photothermally enhanced rapid bacterial killing on a laser-induced graphene mask. *ACS Nano* **2020**, *14*, 12045-12053.

87. Zhao, C.; Deng, B.; Chen, G.; Lei, B.; Hua, H.; Peng, H.; Yan, Z. Large-area chemical vapor deposition-grown monolayer graphene-wrapped silver nanowires for broad-spectrum and robust antimicrobial coating. *Nano Res.* **2016**, *9*, 963-973.

88. Li, R.; Mansukhani, N. D.; Guiney, L. M.; Ji, Z.; Zhao, Y.; Chang, C. H.; French, C. T.; Miller, J. F.; Hersam, M. C.; Nel, A. E.; Xia, T. Identification and optimization of carbon radicals on hydrated graphene oxide for ubiquitous antibacterial coatings. *ACS Nano* **2016**, *10*, 10966-10980.
89. Jung, Y.; Min, J.; Choi, J.; Bang, J.; Jeong, S.; Pyun, K. R.; Ahn, J.; Cho, Y.; Hong, S.; Hong, S.; Lee, J.; Ko, S. H. Smart paper electronics by laser-induced graphene for biodegradable real-time food spoilage monitoring. *Appl. Mater. Today* **2022**, *29*, 101589.
90. Ullyot, G. E.; Ullyot, B. H.; Slater, L. B. The metamorphosis of Smith-Kline & French laboratories to Smith Kline Beecham: 1925–1998. *Bull. Hist. Chem.* **2000**, *25*, 16-20.
91. Park, H.; Otte, A.; Park, K. Evolution of drug delivery systems: From 1950 to 2020 and beyond. *J. Control. Release* **2022**, *342*, 53-65.
92. Liu, L.; Ma, Q.; Cao, J.; Gao, Y.; Han, S.; Liang, Y.; Zhang, T.; Song, Y.; Sun, Y. Recent progress of graphene oxide-based multifunctional nanomaterials for cancer treatment. *Cancer Nanotechnol.* **2021**, *12*, 1-31.
93. Shan, C.; Yang, H.; Han, D.; Zhang, Q.; Ivaska, A.; Niu, L. Water-soluble graphene covalently functionalized by biocompatible poly-L-lysine. *Langmuir* **2009**, *25*, 12030-12033.
94. Namvari, M.; Biswas, C. S.; Galluzzi, M.; Wang, Q.; Du, B.; Stadler, F. J. Reduced graphene oxide composites with water soluble copolymers having tailored lower critical solution temperatures and unique tube-like structure. *Sci. Rep.* **2017**, *7*, 44508.
95. Si, Y.; Samulski, E. T. Synthesis of water soluble graphene. *Nano Lett.* **2008**, *8*, 1679-1682.
96. Becerril, H. A.; Mao, J.; Liu, Z.; Stoltenberg, R. M.; Bao, Z.; Chen, Y. Evaluation of solution-processed reduced graphene oxide films as transparent conductors. *ACS Nano* **2008**, *2*, 463-470.

97. Pei, X.; Zhu, Z.; Gan, Z.; Chen, J.; Zhang, X.; Cheng, X.; Wan, Q.; Wang, J. PEGylated nanographene oxide as a nanocarrier for delivering mixed anticancer drugs to improve anticancer activity. *Sci. Rep.* **2020**, *10*, 2717.
98. Liu, Z.; Robinson, J. T.; Sun, X.; Dai, H. PEGylated nanographene oxide for delivery of water-insoluble cancer drugs. *J. Am. Chem. Soc.* **2008**, *130*, 10876-10877.
99. Sun, X.; Liu, Z.; Welsher, K.; Robinson, J. T.; Goodwin, A.; Zaric, S.; Dai, H. Nano-graphene oxide for cellular imaging and drug delivery. *Nano Res.* **2008**, *1*, 203-212.
100. Wang, F.; Zhang, B.; Zhou, L.; Shi, Y.; Li, Z.; Xia, Y.; Tian, J. Imaging dendrimer-grafted graphene oxide mediated anti-miR-21 delivery with an activatable luciferase reporter. *ACS Appl. Mater. Interfaces* **2016**, *8*, 9014-9021.
101. Sayyar, S.; Murray, E.; Thompson, B.; Chung, J.; Officer, D. L.; Gambhir, S.; Spinks, G. M.; Wallace, G. G. Processable conducting graphene/chitosan hydrogels for tissue engineering. *J. Mater. Chem. B* **2015**, *3*, 481-490.
102. Fan, H.; Wang, L.; Zhao, K.; Li, N.; Shi, Z.; Ge, Z.; Jin, Z. Fabrication, mechanical properties, and biocompatibility of graphene-reinforced chitosan composites. *Biomacromolecules* **2010**, *11*, 2345-2351.
103. Wei, L.; Ma, J.; Zhang, W.; Bai, S.-L.; Ren, Y.; Zhang, L.; Wu, Y.; Qin, J. pH triggered hydrogen bonding for preparing mechanically strong, electromagnetic interference shielding and thermally conductive waterborne polymer/graphene@ polydopamine composites. *Carbon* **2021**, *181*, 212-224.
104. Ren, Q.; Shen, X.; Sun, Y.; Fan, R.; Zhang, J. A highly sensitive competitive immunosensor based on branched polyethyleneimine functionalized reduced graphene oxide and gold nanoparticles modified electrode for detection of melamine. *Food Chem.* **2020**, *304*, 125397.

105. Joshi, S.; Siddiqui, R.; Sharma, P.; Kumar, R.; Verma, G.; Saini, A. Green synthesis of peptide functionalized reduced graphene oxide (rGO) nano bioconjugate with enhanced antibacterial activity. *Sci. Rep.* **2020**, *10*, 9441.
106. Joshi, S.; Sharma, P.; Siddiqui, R.; Kaushal, K.; Sharma, S.; Verma, G.; Saini, A. A review on peptide functionalized graphene derivatives as nanotools for biosensing. *Microchim. Acta* **2020**, *187*, 1-15.
107. Karimi, S.; Namazi, H. Fe₃O₄@ PEG-coated dendrimer modified graphene oxide nanocomposite as a pH-sensitive drug carrier for targeted delivery of doxorubicin. *J. Alloys Compd.* **2021**, *879*, 160426.
108. Karimi, S.; Namazi, H. Simple preparation of maltose-functionalized dendrimer/graphene quantum dots as a pH-sensitive biocompatible carrier for targeted delivery of doxorubicin. *Int. J. Biol. Macromol.* **2020**, *156*, 648-659.
109. Pooresmaeil, M.; Namazi, H. Advances in development of the dendrimers having natural saccharides in their structure for efficient and controlled drug delivery applications. *Eur. Polym. J.* **2021**, *148*, 110356.
110. Zhu, Y. J.; Chen, F. pH-responsive drug-delivery systems. *Chem. Asian J.* **2015**, *10*, 284-305.
111. Yang, X.; Zhang, X.; Liu, Z.; Ma, Y.; Huang, Y.; Chen, Y. High-efficiency loading and controlled release of doxorubicin hydrochloride on graphene oxide. *J. Phys. Chem. C* **2008**, *112*, 17554-17558.
112. Gooneh-Farahani, S.; Naghib, S. M.; Naimi-Jamal, M. R.; Seyfoori, A. A pH-sensitive nanocarrier based on BSA-stabilized graphene-chitosan nanocomposite for sustained and prolonged release of anticancer agents. *Sci. Rep.* **2021**, *11*, 17404.

113. Lila, A. S. A.; Soliman, M. S.; Kiran, H.; Gangadharappa, H.; Younes, K. M.; Khafagy, E.-S.; Shehata, T. M.; Ibrahim, M. M.; Abdallah, M. H. Tamoxifen-loaded functionalized graphene nanoribbons for breast cancer therapy. *J. Drug Deliv. Sci. Technol.* **2021**, *63*, 102499.
114. Lila, A. S. A.; Abdallah, M. H.; Wani, S. U. D.; Gangadharappa, H.; Younes, K. M.; Khafagy, E.-S.; Shehata, T. M.; Soliman, M. S. Folic acid-conjugated raloxifene-loaded graphene-based nanocarrier: Fabrication, characterization and antitumor screening. *Colloids Surf. A Physicochem. Eng. Asp.* **2021**, *625*, 126971.
115. Anirudhan, T.; Sekhar, V. C.; Athira, V. Graphene oxide based functionalized chitosan polyelectrolyte nanocomposite for targeted and pH responsive drug delivery. *Int. J. Biol. Macromol.* **2020**, *150*, 468-479.
116. Singh, G.; Nenavathu, B. P.; Imtiyaz, K.; Rizvi, M. M. A. Fabrication of chlorambucil loaded graphene-oxide nanocarrier and its application for improved antitumor activity. *Biomed. Pharmacother.* **2020**, *129*, 110443.
117. Vasanthakumar, A.; Rejeeth, C.; Vivek, R.; Ponraj, T.; Jayaraman, K.; Anandasadagopan, S. K.; Vinayaga Moorthi, P. Design of bio-graphene-based multifunctional nanocomposites exhibits intracellular drug delivery in cervical cancer treatment. *ACS Appl. Bio Mater.* **2022**, *5*, 2956-2964.
118. Basu, A.; Upadhyay, P.; Ghosh, A.; Bose, A.; Gupta, P.; Chattopadhyay, S.; Chattopadhyay, D.; Adhikary, A. Hyaluronic acid engrafted metformin loaded graphene oxide nanoparticle as CD44 targeted anti-cancer therapy for triple negative breast cancer. *Biochim. Biophys. Acta, Gen. Subj.* **2021**, *1865*, 129841.
119. Vinothini, K.; Rajendran, N. K.; Ramu, A.; Elumalai, N.; Rajan, M. Folate receptor targeted delivery of paclitaxel to breast cancer cells via folic acid conjugated graphene oxide grafted methyl acrylate nanocarrier. *Biomed. Pharmacother.* **2019**, *110*, 906-917.

120. Kesavan, S.; Meena, K.; Sharmili, S. A.; Govindarajan, M.; Alharbi, N. S.; Kadaikunnan, S.; Khaled, J. M.; Alobaidi, A. S.; Alanzi, K. F.; Vaseeharan, B. Ulvan loaded graphene oxide nanoparticle fabricated with chitosan and D-mannose for targeted anticancer drug delivery. *J. Drug Deliv. Sci. Technol.* **2021**, *65*, 102760.
121. Lan, M.-Y.; Hsu, Y.-B.; Lan, M.-C.; Chen, J.-P.; Lu, Y.-J. Polyethylene glycol-coated graphene oxide loaded with erlotinib as an effective therapeutic agent for treating nasopharyngeal cancer cells. *Int. J. Nanomed.* **2020**, *15*, 7569-7582.
122. Kavitha, T.; Abdi, S. I. H.; Park, S.-Y. pH-sensitive nanocargo based on smart polymer functionalized graphene oxide for site-specific drug delivery. *Phys. Chem. Chem. Phys.* **2013**, *15*, 5176-5185.
123. Hashemi, H.; Namazi, H. Understanding the pH dependent fluorescence and doxorubicin release from graphene oxide functionalized citric acid dendrimer as a highly efficient drug delivery system. *Mater. Today Commun.* **2021**, *28*, 102593.
124. Ghamkhari, A.; Abbaspour-Ravasjani, S.; Talebi, M.; Hamishehkar, H.; Hamblin, M. R. Development of a graphene oxide-poly lactide nanocomposite as a smart drug delivery system. *Int. J. Biol. Macromol.* **2021**, *169*, 521-531.
125. Razaghi, M.; Ramazani, A.; Khoobi, M.; Mortezaadeh, T.; Aksoy, E. A.; Küçükılınç, T. T. Highly fluorinated graphene oxide nanosheets for anticancer linoleic-curcumin conjugate delivery and T2-Weighted magnetic resonance imaging: *In vitro* and *in vivo* studies. *J. Drug Deliv. Sci. Technol.* **2020**, *60*, 101967.
126. Xie, M.; Deng, T.; Li, J.; Shen, H. The camouflage of graphene oxide by red blood cell membrane with high dispersibility for cancer chemotherapy. *J. Colloid Interface Sci.* **2021**, *591*, 290-299.

127. Prabakaran, S.; Jeyaraj, M.; Nagaraj, A.; Sadasivuni, K. K.; Rajan, M. Polymethyl methacrylate–ovalbumin@ graphene oxide drug carrier system for high anti-proliferative cancer drug delivery. *Appl. Nanosci.* **2019**, *9*, 1487-1500.
128. Martín, C.; Ruiz, A.; Keshavan, S.; Reina, G.; Murera, D.; Nishina, Y.; Fadeel, B.; Bianco, A. A biodegradable multifunctional graphene oxide platform for targeted cancer therapy. *Adv. Funct. Mater.* **2019**, *29*, 1901761.
129. Kagan, V. E.; Konduru, N. V.; Feng, W.; Allen, B. L.; Conroy, J.; Volkov, Y.; Vlasova, I. I.; Belikova, N. A.; Yanamala, N.; Kapralov, A.; Tyurina, Y. Y.; Shi, J.; Kisin, E. R.; Murray, A. R.; Franks, J.; Stolz, D.; Gou, P.; Klein-Seetharaman, J.; Fadeel, B.; Star, A.; Shvedova, A. A. Carbon nanotubes degraded by neutrophil myeloperoxidase induce less pulmonary inflammation. *Nature Nanotechnol.* **2010**, *5*, 354-359.
130. Kurapati, R.; Mukherjee, S. P.; Martín, C.; Bepete, G.; Vázquez, E.; Pénicaud, A.; Fadeel, B.; Bianco, A. Degradation of single-layer and few-layer graphene by neutrophil myeloperoxidase. *Angew. Chem. Int. Ed.* **2018**, *57*, 11722-11727.
131. Dhanavel, S.; Revathy, T.; Sivaranjani, T.; Sivakumar, K.; Palani, P.; Narayanan, V.; Stephen, A. 5-Fluorouracil and curcumin *co*-encapsulated chitosan/reduced graphene oxide nanocomposites against human colon cancer cell lines. *Polym. Bull.* **2020**, *77*, 213-233.
132. Boddu, A.; Reddy, O. S.; Zhang, D.; Rao, K. K.; Lai, W.-F. ROS-generating, pH-responsive and highly tunable reduced graphene oxide-embedded microbeads showing intrinsic anticancer properties and multi-drug co-delivery capacity for combination cancer therapy. *Drug Deliv.* **2022**, *29*, 2481-2490.

133. Pourjavadi, A.; Asgari, S.; Hosseini, S. H. Graphene oxide functionalized with oxygen-rich polymers as a pH-sensitive carrier for co-delivery of hydrophobic and hydrophilic drugs. *J. Drug Deliv. Sci. Technol.* **2020**, *56*, 101542.
134. Tiwari, H.; Karki, N.; Tewari, C.; Pandey, N.; Rana, A.; Rana, S.; Pal, M.; Sahoo, N. G. Dual Drug Loaded Potassium-Contained Graphene Oxide as a Nanocarrier in Cocktailed Drug Delivery for the Treatment of Human Breast Cancer. *Curr. Drug Deliv.* **2023**, *20*, 943-950.
135. Tiwari, H.; Karki, N.; Pal, M.; Basak, S.; Verma, R. K.; Bal, R.; Kandpal, N. D.; Bisht, G.; Sahoo, N. G. Functionalized graphene oxide as a nanocarrier for dual drug delivery applications: The synergistic effect of quercetin and gefitinib against ovarian cancer cells. *Colloids Surf. B: Biointerfaces* **2019**, *178*, 452-459.
136. Asgari, S.; Pourjavadi, A.; Setayeshmehr, M.; Boisen, A.; Ajalloueiian, F. Encapsulation of drug-loaded graphene oxide-based nanocarrier into electrospun pullulan nanofibers for potential local chemotherapy of breast cancer. *Macromol. Chem. Phys.* **2021**, *222*, 2100096.
137. Muthoosamy, K.; Abubakar, I. B.; Bai, R. G.; Loh, H.-S.; Manickam, S. Exceedingly higher co-loading of curcumin and paclitaxel onto polymer-functionalized reduced graphene oxide for highly potent synergistic anticancer treatment. *Sci. Rep.* **2016**, *6*, 32808.
138. Yaghoubi, F.; Motlagh, N. S. H.; Naghib, S. M.; Haghirsadat, F.; Jaliani, H. Z.; Moradi, A. A functionalized graphene oxide with improved cytocompatibility for stimuli-responsive co-delivery of curcumin and doxorubicin in cancer treatment. *Sci. Rep.* **2022**, *12*, 1959.
139. Bullo, S.; Buskaran, K.; Baby, R.; Dorniani, D.; Fakurazi, S.; Hussein, M. Z. Dual drugs anticancer nanoformulation using graphene oxide-PEG as nanocarrier for protocatechuic acid and chlorogenic acid. *Pharm. Res.* **2019**, *36*, 1-11.

140. Astani, S.; Salehi, R.; Massoumi, B.; Massoudi, A. Co-delivery of cisplatin and doxorubicin by carboxylic acid functionalized poly (hydroxyethyl methacrylate)/reduced graphene nanocomposite for combination chemotherapy of breast cancer cells. *J. Biomater. Sci. Polym. Ed.* **2021**, *32*, 657-677.
141. Zhang, J.; Chen, L.; Shen, B.; Chen, L.; Mo, J.; Feng, J. Dual-sensitive graphene oxide loaded with proapoptotic peptides and anticancer drugs for cancer synergetic therapy. *Langmuir* **2019**, *35*, 6120-6128.
142. Vinothini, K.; Rajendran, N. K.; Munusamy, M. A.; Alarfaj, A. A.; Rajan, M. Development of biotin molecule targeted cancer cell drug delivery of doxorubicin loaded κ -carrageenan grafted graphene oxide nanocarrier. *Mater. Sci. Eng. C* **2019**, *100*, 676-687.
143. Suryaprakash, S.; Li, M.; Lao, Y.-H.; Wang, H.-X.; Leong, K. W. Graphene oxide cellular patches for mesenchymal stem cell-based cancer therapy. *Carbon* **2018**, *129*, 863-868.
144. Chen, Q.; Che, C.; Liu, J.; Gong, Z.; Si, M.; Yang, S.; Yang, G. Construction of an exosome-functionalized graphene oxide based composite bionic smart drug delivery system and its anticancer activity. *Nanotechnology* **2022**, *33*, 175101.
145. Li, R.; Wang, Y.; Du, J.; Wang, X.; Duan, A.; Gao, R.; Liu, J.; Li, B. Graphene oxide loaded with tumor-targeted peptide and anti-cancer drugs for cancer target therapy. *Sci. Rep.* **2021**, *11*, 1725.
146. Samadi, S.; Moradkhani, M.; Beheshti, H.; Irani, M.; Aliabadi, M. Fabrication of chitosan/poly (lactic acid)/graphene oxide/TiO₂ composite nanofibrous scaffolds for sustained delivery of doxorubicin and treatment of lung cancer. *Int. J. Biol. Macromol.* **2018**, *110*, 416-424.

147. Wu, J.; Qin, Z.; Jiang, X.; Fang, D.; Lu, Z.; Zheng, L.; Zhao, J. ROS-responsive PPGF nanofiber membrane as a drug delivery system for long-term drug release in attenuation of osteoarthritis. *npj Regen. Med.* **2022**, *7*, 66.
148. Tyler, B.; Gullotti, D.; Mangraviti, A.; Utsuki, T.; Brem, H. Polylactic acid (PLA) controlled delivery carriers for biomedical applications. *Adv. Drug Deliv. Rev.* **2016**, *107*, 163-175.
149. Ballatori, N.; Krance, S. M.; Notenboom, S.; Shi, S.; Tieu, K.; Hammond, C. L. Glutathione dysregulation and the etiology and progression of human diseases. *Biol. Chem.* **2009**, *390*, 191-214.
150. Meng, F.; Hennink, W. E.; Zhong, Z. Reduction-sensitive polymers and bioconjugates for biomedical applications. *Biomater.* **2009**, *30*, 2180-2198.
151. Wen, H.; Dong, C.; Dong, H.; Shen, A.; Xia, W.; Cai, X.; Song, Y.; Li, X.; Li, Y.; Shi, D. Engineered redox-responsive PEG detachment mechanism in PEGylated nano-graphene oxide for intracellular drug delivery. *Small* **2012**, *8*, 760-769.
152. Li, Y.; Feng, L.; Shi, X.; Wang, X.; Yang, Y.; Yang, K.; Liu, T.; Yang, G.; Liu, Z. Surface coating-dependent cytotoxicity and degradation of graphene derivatives: Towards the design of non-toxic, degradable nano-graphene. *Small* **2014**, *10*, 1544-1554.
153. Chen, H.; Wang, Z.; Zong, S.; Wu, L.; Chen, P.; Zhu, D.; Wang, C.; Xu, S.; Cui, Y. SERS-fluorescence monitored drug release of a redox-responsive nanocarrier based on graphene oxide in tumor cells. *ACS Appl. Mater. Interfaces* **2014**, *6*, 17526-17533.
154. Mo, R.; Jiang, T.; Sun, W.; Gu, Z. ATP-responsive DNA-graphene hybrid nanoaggregates for anticancer drug delivery. *Biomater.* **2015**, *50*, 67-74.

155. Jiang, T.; Sun, W.; Zhu, Q.; Burns, N. A.; Khan, S. A.; Mo, R.; Gu, Z. Furin-mediated sequential delivery of anticancer cytokine and small-molecule drug shuttled by graphene. *Adv. Mater.* **2015**, *27*, 1021-1028.
156. Jiang, Z.; Jiang, Z.; Jiang, Y.; Cheng, Y.; Yao, Q.; Chen, R.; Kou, L. Fe-involved nanostructures act as photothermal transduction agents in cancer photothermal therapy. *Colloids Surf. B: Biointerfaces* **2023**, *228*, 113438.
157. Montiel Schneider, M. G.; Martín, M. J.; Otarola, J.; Vakarelska, E.; Simeonov, V.; Lassalle, V.; Nedyalkova, M. Biomedical applications of iron oxide nanoparticles: Current insights progress and perspectives. *Pharmaceutics* **2022**, *14*, 204.
158. Zhang, S.; Xin, W.; Anderson, G. J.; Li, R.; Gao, L.; Chen, S.; Zhao, J.; Liu, S. Double-edge sword roles of iron in driving energy production versus instigating ferroptosis. *Cell Death Dis.* **2022**, *13*, 40.
159. Yang, X.; Zhang, X.; Ma, Y.; Huang, Y.; Wang, Y.; Chen, Y. Superparamagnetic graphene oxide-Fe₃O₄ nanoparticles hybrid for controlled targeted drug carriers. *J. Mater. Chem.* **2009**, *19*, 2710-2714.
160. Yang, X.; Wang, Y.; Huang, X.; Ma, Y.; Huang, Y.; Yang, R.; Duan, H.; Chen, Y. Multi-functionalized graphene oxide based anticancer drug-carrier with dual-targeting function and pH-sensitivity. *J. Mater. Chem.* **2011**, *21*, 3448-3454.
161. Paknia, F.; Mohabatkar, H.; Ahmadi-Zeidabadi, M.; Zarrabi, A. The convergence of in silico approach and nanomedicine for efficient cancer treatment; *in vitro* investigations on curcumin loaded multifunctional graphene oxide nanocomposite structure. *J. Drug Deliv. Sci. Technol.* **2022**, *71*, 103302.

162. Matiyani, M.; Rana, A.; Pal, M.; Rana, S.; Melkani, A. B.; Sahoo, N. G. Polymer grafted magnetic graphene oxide as a potential nanocarrier for pH-responsive delivery of sparingly soluble quercetin against breast cancer cells. *RSC Adv.* **2022**, *12*, 2574-2588.
163. Makharza, S. A.; Cirillo, G.; Vittorio, O.; Valli, E.; Voli, F.; Farfalla, A.; Curcio, M.; Iemma, F.; Nicoletta, F. P.; El-Gendy, A. A.; F. Goya, G.; Hampel, S. Magnetic graphene oxide nanocarrier for targeted delivery of cisplatin: a perspective for glioblastoma treatment. *Pharmaceuticals* **2019**, *12*, 76.
164. Han, S.; Teng, F.; Wang, Y.; Su, L.; Leng, Q.; Jiang, H. Drug-loaded dual targeting graphene oxide-based molecularly imprinted composite and recognition of carcino-embryonic antigen. *RSC Adv.* **2020**, *10*, 10980-10988.
165. Zhu, H.; Zhang, B.; Zhu, N.; Li, M.; Yu, Q. Mitochondrion targeting peptide-modified magnetic graphene oxide delivering mitoxantrone for impairment of tumor mitochondrial functions. *Chin. Chem. Lett.* **2021**, *32*, 1220-1223.
166. Pooresmaeil, M.; Namazi, H. Fabrication of a smart and biocompatible brush copolymer decorated on magnetic graphene oxide hybrid nanostructure for drug delivery application. *Eur. Polym. J.* **2021**, *142*, 110126.
167. Ali, R.; Aziz, M. H.; Gao, S.; Khan, M. I.; Li, F.; Batool, T.; Shaheen, F.; Qiu, B. Graphene oxide/zinc ferrite nanocomposite loaded with doxorubicin as a potential theranostic medium in cancer therapy and magnetic resonance imaging. *Ceram. Int.* **2022**, *48*, 10741-10750.
168. Mehdaoui, B.; Meffre, A.; Carrey, J.; Lachaize, S.; Lacroix, L. M.; Gougeon, M.; Chaudret, B.; Respaud, M. Optimal size of nanoparticles for magnetic hyperthermia: a combined theoretical and experimental study. *Adv. Funct. Mater.* **2011**, *21*, 4573-4581.

169. Chen, X.; Klingeler, R. d.; Kath, M.; El Gendy, A. A.; Cendrowski, K.; Kalenczuk, R. J.; Borowiak-Palen, E. Magnetic silica nanotubes: synthesis, drug release, and feasibility for magnetic hyperthermia. *ACS Appl. Mater. Interfaces* **2012**, *4*, 2303-2309.
170. Chang, M.; Hou, Z.; Wang, M.; Li, C.; Lin, J. Recent advances in hyperthermia therapy-based synergistic immunotherapy. *Adv. Mater.* **2021**, *33*, 2004788.
171. Swain, A. K.; Pradhan, L.; Bahadur, D. Polymer stabilized Fe₃O₄-graphene as an amphiphilic drug carrier for thermo-chemotherapy of cancer. *ACS Appl. Mater. Interfaces* **2015**, *7*, 8013-8022.
172. Heskins, M.; Guillet, J. E. Solution properties of poly (N-isopropylacrylamide). *J. Macromol. Sci.* **1968**, *2*, 1441-1455.
173. Rzaev, Z. M. O.; Dincer, S.; Pişkin, E. Functional copolymers of N-isopropylacrylamide for bioengineering applications. *Prog. Polym. Sci.* **2007**, *32*, 534-595.
174. Halperin, A.; Kröger, M.; Winnik, F. M. Poly (N-isopropylacrylamide) phase diagrams: fifty years of research. *Angew. Chem. Int. Ed.* **2015**, *54*, 15342-15367.
175. Ohnsorg, M. L.; Ting, J. M.; Jones, S. D.; Jung, S.; Bates, F. S.; Reineke, T. M. Tuning PNIPAm self-assembly and thermoresponse: Roles of hydrophobic end-groups and hydrophilic comonomer. *Polym. Chem.* **2019**, *10*, 3469-3479.
176. Ashjaran, M.; Babazadeh, M.; Akbarzadeh, A.; Davaran, S.; Salehi, R. Stimuli-responsive polyvinylpyrrolidone-NIPPAm-lysine graphene oxide nano-hybrid as an anticancer drug delivery on MCF7 cell line. *Artif. Cells Nanomed. Biotechnol.* **2019**, *47*, 443-454.
177. Zhu, S.; Li, J.; Chen, Y.; Chen, Z.; Chen, C.; Li, Y.; Cui, Z.; Zhang, D. Grafting of graphene oxide with stimuli-responsive polymers by using ATRP for drug release. *J. Nanopart. Res.* **2012**, *14*, 1-11.

178. Wang, H.; Sun, D.; Zhao, N.; Yang, X.; Shi, Y.; Li, J.; Su, Z.; Wei, G. Thermo-sensitive graphene oxide–polymer nanoparticle hybrids: synthesis, characterization, biocompatibility and drug delivery. *J. Mater. Chem. B* **2014**, *2*, 1362-1370.
179. Pan, Y.; Bao, H.; Sahoo, N. G.; Wu, T.; Li, L. Water-soluble poly (*N*-isopropylacrylamide)–graphene sheets synthesized via click chemistry for drug delivery. *Adv. Funct. Mater.* **2011**, *21*, 2754-2763.
180. Seo, H. I.; Cheon, Y. A.; Chung, B. G. Graphene and thermo-responsive polymeric nanocomposites for therapeutic applications. *Biomed. Eng. Lett.* **2016**, *6*, 10-15.
181. Khoee, S.; Karimi, M. R. Dual-drug loaded Janus graphene oxide-based thermoresponsive nanoparticles for targeted therapy. *Polymer* **2018**, *142*, 80-98.
182. Zhu, X.; Zhang, Y.; Huang, H.; Zhang, H.; Hou, L.; Zhang, Z. Functionalized graphene oxide-based thermosensitive hydrogel for near-infrared chemo-photothermal therapy on tumor. *J. Biomater. Appl.* **2016**, *30*, 1230-1241.
183. Saeednia, L.; Yao, L.; Berndt, M.; Cluff, K.; Asmatulu, R. Structural and biological properties of thermosensitive chitosan–graphene hybrid hydrogels for sustained drug delivery applications. *J. Biomed. Mater. Res. A* **2017**, *105*, 2381-2390.
184. Kazempour, M.; Edjlali, L.; Akbarzadeh, A.; Davaran, S.; Farid, S. S. Synthesis and characterization of dual pH-and thermo-responsive graphene-based nanocarrier for effective anticancer drug delivery. *J. Drug Deliv. Sci. Technol.* **2019**, *54*, 101158.
185. Lima-Sousa, R.; de Melo-Diogo, D.; Alves, C. G.; Cabral, C. S.; Miguel, S. P.; Mendonça, A. G.; Correia, I. J. Injectable in situ forming thermo-responsive graphene based hydrogels for cancer chemo-photothermal therapy and NIR light-enhanced antibacterial applications. *Mater. Sci. Eng. C* **2020**, *117*, 111294.

186. Miao, W.; Shim, G.; Kang, C. M.; Lee, S.; Choe, Y. S.; Choi, H.-G.; Oh, Y.-K. Cholesteryl hyaluronic acid-coated, reduced graphene oxide nanosheets for anti-cancer drug delivery. *Biomater.* **2013**, *34*, 9638-9647.
187. Wang, L.-H.; Sui, L.; Zhao, P.-H.; Ma, H.-D.; Liu, J.-Y.; Wei, Z.; Zhan, Z.-J.; Wang, Y.-L. A composite of graphene oxide and iron oxide nanoparticles for targeted drug delivery of temozolomide. *Pharmazie* **2020**, *75*, 313-317.
188. Liu, S.; Pan, X.; Liu, H. Two-dimensional nanomaterials for photothermal therapy. *Angew. Chem.* **2020**, *132*, 5943-5953.
189. Zhi, D.; Yang, T.; O'hagan, J.; Zhang, S.; Donnelly, R. F. Photothermal therapy. *J. Control. Release* **2020**, *325*, 52-71.
190. de Melo-Diogo, D.; Lima-Sousa, R.; Alves, C. G.; Correia, I. J. Graphene family nanomaterials for application in cancer combination photothermal therapy. *Biomater. Sci.* **2019**, *7*, 3534-3551.
191. Yang, K.; Zhang, S.; Zhang, G.; Sun, X.; Lee, S. T.; Liu, Z. Graphene in Mice: Ultrahigh In Vivo Tumor Uptake and Efficient Photothermal Therapy. *Nano. Lett.* **2010**, *10*, 3318-3323.
192. Yang, K.; Wan, J.; Zhang, S.; Tian, B.; Zhang, Y.; Liu, Z. The influence of surface chemistry and size of nanoscale graphene oxide on photothermal therapy of cancer using ultra-low laser power. *Biomater.* **2012**, *33*, 2206-2214.
193. Robinson, J. T.; Tabakman, S. M.; Liang, Y.; Wang, H.; Casalongue, H. S.; Vinh, D.; Dai, H. Ultrasmall reduced graphene oxide with high near-infrared absorbance for photothermal therapy. *J. Am. Chem. Soc.* **2011**, *133*, 6825-6831.

194. Hashemi, M.; Omid, M.; Muralidharan, B.; Smyth, H.; Mohagheghi, M. A.; Mohammadi, J.; Milner, T. E. Evaluation of the photothermal properties of a reduced graphene oxide/arginine nanostructure for near-infrared absorption. *ACS Appl. Mater. Interfaces* **2017**, *9*, 32607-32620.
195. Cheon, Y. A.; Bae, J. H.; Chung, B. G. Reduced graphene oxide nanosheet for chemophotothermal therapy. *Langmuir* **2016**, *32*, 2731-2736.
196. Zhang, W.; Dai, J.; Zhang, G.; Zhang, Y.; Li, S.; Nie, D. Photothermal/pH dual-responsive drug delivery system of amino-terminated HBP-modified rGO and the chemo-photothermal therapy on tumor cells. *Nanoscale Res. Lett.* **2018**, *13*, 379.
197. Hu, H.; Wang, X.; Lee, K. I.; Ma, K.; Hu, H.; Xin, J. H. Graphene oxide-enhanced sol-gel transition sensitivity and drug release performance of an amphiphilic copolymer-based nanocomposite. *Sci. Rep.* **2016**, *6*, 31815.
198. Singh, S. K.; Singh, M. K.; Kulkarni, P. P.; Sonkar, V. K.; Grácio, J. J.; Dash, D. Amine-modified graphene: thrombo-protective safer alternative to graphene oxide for biomedical applications. *ACS Nano* **2012**, *6*, 2731-2740.
199. Shim, G.; Kim, J.-Y.; Han, J.; Chung, S. W.; Lee, S.; Byun, Y.; Oh, Y.-K. Reduced graphene oxide nanosheets coated with an anti-angiogenic anticancer low-molecular-weight heparin derivative for delivery of anticancer drugs. *J. Control. Release* **2014**, *189*, 80-89.
200. Stankovich, S.; Dikin, D. A.; Piner, R. D.; Kohlhaas, K. A.; Kleinhammes, A.; Jia, Y.; Wu, Y.; Nguyen, S. T.; Ruoff, R. S. Synthesis of graphene-based nanosheets via chemical reduction of exfoliated graphite oxide. *Carbon* **2007**, *45*, 1558-1565.
201. Zhang, L.; Wang, Z.; Lu, Z.; Shen, H.; Huang, J.; Zhao, Q.; Liu, M.; He, N.; Zhang, Z. PEGylated reduced graphene oxide as a superior ssRNA delivery system. *J. Mater. Chem. B* **2013**, *1*, 749-755.

202. Li, X.; Wang, Y.; Liu, T.; Zhang, Y.; Wang, C.; Xie, B. Ultrasmall graphene oxide for combination of enhanced chemotherapy and photothermal therapy of breast cancer. *Colloids Surf. B Biointerfaces* **2023**, *225*, 113288.
203. Lima-Sousa, R.; Alves, C. G.; Melo, B. L.; Moreira, A. F.; Mendonca, A. G.; Correia, I. J.; de Melo-Diogo, D. Poly (2-ethyl-2-oxazoline) functionalized reduced graphene oxide: Optimization of the reduction process using dopamine and application in cancer photothermal therapy. *Mater. Sci. Eng. C* **2021**, *130*, 112468.
204. Imani, R.; Shao, W.; Emami, S. H.; Faghihi, S.; Prakash, S. Improved dispersibility of nano-graphene oxide by amphiphilic polymer coatings for biomedical applications. *RSC Adv.* **2016**, *6*, 77818-77829.
205. Kim, Y.-K.; Kim, M.-H.; Min, D.-H. Biocompatible reduced graphene oxide prepared by using dextran as a multifunctional reducing agent. *Chem. Commun.* **2011**, *47*, 3195-3197.
206. Wang, Y.; Zhang, P.; Liu, C. F.; Zhan, L.; Li, Y. F.; Huang, C. Z. Green and easy synthesis of biocompatible graphene for use as an anticoagulant. *RSC Adv.* **2012**, *2*, 2322-2328.
207. Dou, W. T.; Xu, F.; Xu, C. X.; Gao, J.; Ru, H. B.; Luan, X.; Zhang, J.; Zhu, L.; Sedgwick, A. C.; Chen, G. R.; Zang, Y.; James, T. D.; Tian, H.; Li, J.; Mai, Y.; He, X. P. Graphene nanoribbon-based supramolecular ensembles with dual-receptor targeting function for targeted photothermal tumor therapy. *Chem. Sci.* **2021**, *12*, 11089-11097.
208. Peng, Z.; Chang, Q.; Xing, M.; Lu, F. Active hydrophilic Graphene oxide Nanocomposites delivery mediated by adipose-derived stem cell for elevated Photothermal therapy of breast Cancer. *Int. J. Nanomed.* **2023**, *18*, 971-986.

209. Barrera, C. C.; Groot, H.; Vargas, W. L.; Narváez, D. M. Efficacy and molecular effects of a reduced graphene Oxide/Fe₃O₄ nanocomposite in photothermal therapy against cancer. *Int. J. Nanomed.* **2020**, *15*, 6421-6432.
210. Zhang, W.; Guo, Z.; Huang, D.; Liu, Z.; Guo, X.; Zhong, H. Synergistic effect of chemophotothermal therapy using PEGylated graphene oxide. *Biomater.* **2011**, *32*, 8555-8561.
211. Dong, H.; Jin, M.; Liu, Z.; Xiong, H.; Qiu, X.; Zhang, W.; Guo, Z. In vitro and in vivo brain-targeting chemo-photothermal therapy using graphene oxide conjugated with transferrin for Gliomas. *Lasers Med. Sci.* **2016**, *31*, 1123-1131.
212. Qiang, L.; Cai, Z.; Jiang, W.; Liu, J.; Tai, Z.; Li, G.; Gong, C.; Gao, S.; Gao, Y. A novel macrophage-mediated biomimetic delivery system with NIR-triggered release for prostate cancer therapy. *J. Nanobiotechnol.* **2019**, *17*, 83.
213. SreeHarsha, N.; Maheshwari, R.; Al-Dhubiab, B. E.; Tekade, M.; Sharma, M. C.; Venugopala, K. N.; Tekade, R. K.; Alzahrani, A. M. Graphene-based hybrid nanoparticle of doxorubicin for cancer chemotherapy. *Int. J. Nanomed.* **2019**, *14*, 7419-7429.
214. Guo, X.; Mei, J.; Zhang, C. Development of drug dual-carriers delivery system with mitochondria-targeted and pH/heat responsive capacity for synergistic photothermal-chemotherapy of ovarian cancer. *Int. J. Nanomed.* **2020**, *15*, 301-313.
215. Zhan, X.; Teng, W.; Sun, K.; He, J.; Yang, J.; Tian, J.; Huang, X.; Zhou, L.; Zhou, C. CD47-mediated DTIC-loaded chitosan oligosaccharide-grafted nGO for synergistic chemo-photothermal therapy against malignant melanoma. *Mater. Sci. Eng. C* **2021**, *123*, 112014.
216. Du, P.; Yan, J.; Long, S.; Xiong, H.; Wen, N.; Cai, S.; Wang, Y.; Peng, D.; Liu, Z.; Liu, Y. Tumor microenvironment and NIR laser dual-responsive release of berberine 9-*O*-pyrazole alkyl

derivative loaded in graphene oxide nanosheets for chemo-photothermal synergetic cancer therapy. *J. Mater. Chem. B* **2020**, *8*, 4046-4055.

217. Baipaywad, P.; Ryu, N.; Im, S.-S.; Lee, U.; Son, H. B.; Kim, W. J.; Park, H. Facile preparation of poly (*N*-isopropylacrylamide)/graphene oxide nanocomposites for chemo-photothermal therapy. *Des. Monomers Polym.* **2022**, *25*, 245-253.

218. Anichini, C.; Samorì, P. Graphene-Based Hybrid Functional Materials. *Small* **2021**, *17*, 2100514.

219. Khan, M. S.; Pandey, S.; Bhaisare, M. L.; Gedda, G.; Talib, A.; Wu, H.-F. Graphene oxide@ gold nanorods for chemo-photothermal treatment and controlled release of doxorubicin in mice Tumor. *Colloids Surf. B: Biointerfaces* **2017**, *160*, 543-552.

220. Wang, X.; Han, Q.; Yu, N.; Li, J.; Yang, L.; Yang, R.; Wang, C. Aptamer-conjugated graphene oxide-gold nanocomposites for targeted chemo-photothermal therapy of cancer cells. *J. Mater. Chem. B* **2015**, *3*, 4036-4042.

221. Jia, X.; Xu, W.; Ye, Z.; Wang, Y.; Dong, Q.; Wang, E.; Li, D.; Wang, J. Functionalized Graphene@ Gold Nanostar/Lipid for Pancreatic Cancer Gene and Photothermal Synergistic Therapy under Photoacoustic/Photothermal Imaging Dual-Modal Guidance. *Small* **2020**, *16*, 2003707.

222. Lim, D.-K.; Barhoumi, A.; Wylie, R. G.; Reznor, G.; Langer, R. S.; Kohane, D. S. Enhanced photothermal effect of plasmonic nanoparticles coated with reduced graphene oxide. *Nano Lett.* **2013**, *13*, 4075-4079.

223. Wang, Z.; Sun, X.; Huang, T.; Song, J.; Wang, Y. A sandwich nanostructure of gold nanoparticle coated reduced graphene oxide for photoacoustic imaging-guided photothermal therapy in the second NIR window. *Front. Bioeng. Biotechnol.* **2020**, *8*, 1-10.

224. Kumawat, M. K.; Thakur, M.; Bahadur, R.; Kaku, T.; Prabhuraj, R.; Suchitta, A.; Srivastava, R. Preparation of graphene oxide-graphene quantum dots hybrid and its application in cancer theranostics. *Mater. Sci. Eng. C* **2019**, *103*, 109774.
225. Zhen, S. J.; Wang, T. T.; Liu, Y. X.; Wu, Z. L.; Zou, H. Y.; Huang, C. Z. Reduced graphene oxide coated Cu_{2-x}Se nanoparticles for targeted chemo-photothermal therapy. *J. Photochem. Photobiol. B Biol.* **2018**, *180*, 9-16.
226. Yao, X.; Niu, X.; Ma, K.; Huang, P.; Grothe, J.; Kaskel, S.; Zhu, Y. Graphene quantum dots-capped magnetic mesoporous silica nanoparticles as a multifunctional platform for controlled drug delivery, magnetic hyperthermia, and photothermal therapy. *Small* **2017**, *13*, 1602225.
227. Tang, Y.; Hu, H.; Zhang, M. G.; Song, J.; Nie, L.; Wang, S.; Niu, G.; Huang, P.; Lu, G.; Chen, X. An aptamer-targeting photoresponsive drug delivery system using “off-on” graphene oxide wrapped mesoporous silica nanoparticles. *Nanoscale* **2015**, *7*, 6304-6310.
228. Wang, Y.; Huang, R.; Liang, G.; Zhang, Z.; Zhang, P.; Yu, S.; Kong, J. MRI-visualized, dual-targeting, combined tumor therapy using magnetic graphene-based mesoporous silica. *Small* **2014**, *10*, 109-116.
229. Liu, R.; Zhang, H.; Zhang, F.; Wang, X.; Liu, X.; Zhang, Y. Polydopamine doped reduced graphene oxide/mesoporous silica nanosheets for chemo-photothermal and enhanced photothermal therapy. *Mater. Sci. Eng. C* **2019**, *96*, 138-145.
230. Chen, Y. W.; Chen, P. J.; Hu, S. H.; Chen, I. W.; Chen, S. Y. NIR-triggered synergic photo-chemothermal therapy delivered by reduced graphene oxide/carbon/mesoporous silica nanocookies. *Adv. Funct. Mater.* **2014**, *24*, 451-459.
231. Choi, H. W.; Lim, J. H.; Kim, C. W.; Lee, E.; Kim, J.-M.; Chang, K.; Chung, B. G. Near-infrared light-triggered generation of reactive oxygen species and induction of local hyperthermia

from indocyanine green encapsulated mesoporous silica-coated graphene oxide for colorectal cancer therapy. *Antioxidants* **2022**, *11*, 174.

232. Xie, M.; Zhang, F.; Peng, H.; Zhang, Y.; Li, Y.; Xu, Y.; Xie, J. Layer-by-layer modification of magnetic graphene oxide by chitosan and sodium alginate with enhanced dispersibility for targeted drug delivery and photothermal therapy. *Colloids Surf. B: Biointerfaces* **2019**, *176*, 462-470.

233. Lu, Y.-J.; Lin, P.-Y.; Huang, P.-H.; Kuo, C.-Y.; Shalumon, K.; Chen, M.-Y.; Chen, J.-P. Magnetic graphene oxide for dual targeted delivery of doxorubicin and photothermal therapy. *Nanomater.* **2018**, *8*, 193.

234. Wang, D.; Zhang, Y.; Zhai, M.; Huang, Y.; Li, H.; Liu, X.; Gong, P.; Liu, Z.; You, J. Fluorescence Turn-off Magnetic Fluorinated Graphene Composite with High NIR Absorption for Targeted Drug Delivery. *ChemNanoMat* **2021**, *7*, 71-77.

235. Dash, B. S.; Lu, Y.-J.; Chen, H.-A.; Chuang, C.-C.; Chen, J.-P. Magnetic and GRPR-targeted reduced graphene oxide/doxorubicin nanocomposite for dual-targeted chemo-photothermal cancer therapy. *Mater. Sci. Eng. C* **2021**, *128*, 112311.

236. Gong, T.; Wang, X.; Ma, Q.; Li, J.; Li, M.; Huang, Y.; Liang, W.; Su, D.; Guo, R. Triformyl cholic acid and folic acid functionalized magnetic graphene oxide nanocomposites: Multiple-targeted dual-modal synergistic chemotherapy/photothermal therapy for liver cancer. *J. Inorg. Biochem.* **2021**, *223*, 111558.

237. Işıklan, N.; Hussien, N. A.; Türk, M. Synthesis and drug delivery performance of gelatin-decorated magnetic graphene oxide nanoplatfrom. *Colloids Surf. A Physicochem. Eng. Asp.* **2021**, *616*, 126256.

238. Ardakani, T. S.; Meidanchi, A.; Shokri, A.; Shakeri-Zadeh, A. Fe₃O₄@ Au/reduced graphene oxide nanostructures: Combinatorial effects of radiotherapy and photothermal therapy on oral squamous carcinoma KB cell line. *Ceram. Int.* **2020**, *46*, 28676-28685.
239. Correia, J. H.; Rodrigues, J. A.; Pimenta, S.; Dong, T.; Yang, Z. Photodynamic therapy review: principles, photosensitizers, applications, and future directions. *Pharmaceutics* **2021**, *13*, 1332.
240. Pham, T. C.; Nguyen, V.-N.; Choi, Y.; Lee, S.; Yoon, J. Recent strategies to develop innovative photosensitizers for enhanced photodynamic therapy. *Chem. Rev.* **2021**, *121*, 13454-13619.
241. Sahu, A.; Choi, W. I.; Lee, J. H.; Tae, G. Graphene oxide mediated delivery of methylene blue for combined photodynamic and photothermal therapy. *Biomater.* **2013**, *34*, 6239-6248.
242. Guo, S.; Song, Z.; Ji, D.-K.; Reina, G.; Fauny, J.-D.; Nishina, Y.; Ménard-Moyon, C.; Bianco, A. Combined photothermal and photodynamic therapy for cancer treatment using a multifunctional graphene oxide. *Pharmaceutics* **2022**, *14*, 1365.
243. Liang, J.; Chen, B.; Hu, J.; Huang, Q.; Zhang, D.; Wan, J.; Hu, Z.; Wang, B. pH and thermal dual-responsive graphene oxide nanocomplexes for targeted drug delivery and photothermal-chemo/photodynamic synergetic therapy. *ACS Appl. Bio Mater.* **2019**, *2*, 5859-5871.
244. Romero, M. P.; Buzza, H. H.; Stringasci, M. D.; Estevão, B. M.; Silva, C. C.; Pereira-da-Silva, M. A.; Inada, N. M.; Bagnato, V. S. Graphene oxide theranostic effect: Conjugation of photothermal and photodynamic therapies based on an in vivo demonstration. *Int. J. Nanomed.* **2021**, *16*, 1601-1616.

245. Huang, X.; Chen, J.; Wu, W.; Yang, W.; Zhong, B.; Qing, X.; Shao, Z. Delivery of MutT homolog 1 inhibitor by functionalized graphene oxide nanoparticles for enhanced chemophotodynamic therapy triggers cell death in osteosarcoma. *Acta Biomater.* **2020**, *109*, 229-243.
246. Lu, S.-L.; Wang, Y.-H.; Liu, G.-F.; Wang, L.; Li, Y.; Guo, Z.-Y.; Cheng, C. Graphene Oxide Nanoparticle-Loaded Ginsenoside Rg3 Improves Photodynamic Therapy in Inhibiting Malignant Progression and Stemness of Osteosarcoma. *Front. Mol. Biosci.* **2021**, *8*, 663089.
247. Vinothini, K.; Rajendran, N. K.; Rajan, M.; Ramu, A.; Marraiki, N.; Elgorban, A. M. A magnetic nanoparticle functionalized reduced graphene oxide-based drug carrier system for a chemo-photodynamic cancer therapy. *New J. Chem.* **2020**, *44*, 5265-5277.
248. Liu, Y.; Zhang, M.; Bu, W. Bioactive nanomaterials for ion-interference therapy. *View* **2020**, *1*, e18.
249. Chi, Y.; Sun, P.; Gao, Y.; Zhang, J.; Wang, L. Ion interference therapy of tumors based on inorganic nanoparticles. *Biosensors* **2022**, *12*, 100.
250. Lv, C.; Kang, W.; Liu, S.; Yang, P.; Nishina, Y.; Ge, S.; Bianco, A.; Ma, B. Growth of ZIF-8 nanoparticles in situ on graphene oxide nanosheets: a multifunctional nanoplatform for combined ion-interference and photothermal therapy. *ACS Nano* **2022**, *16*, 11428-11443.
251. Ma, B.; Nishina, Y.; Bianco, A. A glutathione responsive nanoplatform made of reduced graphene oxide and MnO₂ nanoparticles for photothermal and chemodynamic combined therapy. *Carbon* **2021**, *178*, 783-791.
252. Guo, W.; Chen, Z.; Feng, X.; Shen, G.; Huang, H.; Liang, Y.; Zhao, B.; Li, G.; Hu, Y. Graphene oxide (GO)-based nanosheets with combined chemo/photothermal/photodynamic therapy to overcome gastric cancer (GC) paclitaxel resistance by reducing mitochondria-derived adenosine-triphosphate (ATP). *J. Nanobiotechnol.* **2021**, *19*, 146.

253. Zhou, F.; Wang, M.; Luo, T.; Qu, J.; Chen, W. R. Photo-activated chemo-immunotherapy for metastatic cancer using a synergistic graphene nanosystem. *Biomater.* **2021**, *265*, 120421.
254. Ding, Y.-F.; Kwong, C. H.; Li, S.; Pan, Y.-T.; Wei, J.; Wang, L.-H.; Mok, G. S.; Wang, R. Supramolecular nanomedicine derived from cucurbit[7]uril-conjugated nano-graphene oxide for multi-modality cancer therapy. *Biomater. Sci.* **2021**, *9*, 3804-3813.
255. Liang, J.; Liu, J.; Jin, X.; Yao, S.; Chen, B.; Huang, Q.; Hu, J.; Wan, J.; Hu, Z.; Wang, B. Versatile nanoplatform loaded with doxorubicin and graphene quantum dots/methylene blue for drug delivery and chemophotothermal/photodynamic synergetic cancer therapy. *ACS Appl. Bio Mater.* **2020**, *3*, 7122-7132.
256. Ou, L.; Tan, X.; Qiao, S.; Wu, J.; Su, Y.; Xie, W.; Jin, N.; He, J.; Luo, R.; Lai, X.; Liu, W.; Zhang, Y.; Zhao, F.; Liu, J.; Kang, Y.; Shao, L. Graphene-Based Material-Mediated Immunomodulation in Tissue Engineering and Regeneration: Mechanism and Significance. *ACS Nano* **2023**, *17*, 18669-18687.
257. Luong-Van, E. K.; Madanagopal, T. T.; Rosa, V. Mechanisms of graphene influence on cell differentiation. *Mater. Today Chem.* **2020**, *16*, 100250.
258. Daneshmandi, L.; Barajaa, M.; Tahmasbi Rad, A.; Sydlik, S. A.; Laurencin, C. T. Graphene-based biomaterials for bone regenerative engineering: a comprehensive review of the field and considerations regarding biocompatibility and biodegradation. *Adv. Healthc. Mater.* **2021**, *10*, 2001414.
259. Anastasio, A. T.; Paniagua, A.; Diamond, C.; Ferlauto, H. R.; Fernandez-Moure, J. S. Nanomaterial nitric oxide delivery in traumatic orthopedic regenerative medicine. *Front. Bioeng. Biotechnol.* **2021**, *8*, 592008.

260. Gillman, C. E.; Jayasuriya, A. C. FDA-approved bone grafts and bone graft substitute devices in bone regeneration. *Mater. Sci. Eng. C* **2021**, *130*, 112466.
261. Betz, R. R. Limitations of autograft and allograft: new synthetic solutions. *Orthopedics* **2002**, *25*, S561-S570.
262. Wang, W.; Liu, Y.; Yang, C.; Qi, X.; Li, S.; Liu, C.; Li, X. Mesoporous bioactive glass combined with graphene oxide scaffolds for bone repair. *Int. J. Biol. Sci.* **2019**, *15*, 2156.
263. Zhang, Q.; Li, K.; Yan, J.; Wang, Z.; Wu, Q.; Bi, L.; Yang, M.; Han, Y. Graphene coating on the surface of CoCrMo alloy enhances the adhesion and proliferation of bone marrow mesenchymal stem cells. *Biochem. Biophys. Res. Commun.* **2018**, *497*, 1011-1017.
264. Zhao, C.; Lu, X.; Zanden, C.; Liu, J. The promising application of graphene oxide as coating materials in orthopedic implants: preparation, characterization and cell behavior. *Biomed. Mater.* **2015**, *10*, 015019.
265. Li, K.; Yan, J.; Wang, C.; Bi, L.; Zhang, Q.; Han, Y. Graphene modified titanium alloy promote the adhesion, proliferation and osteogenic differentiation of bone marrow stromal cells. *Biochem. Biophys. Res. Commun.* **2017**, *489*, 187-192.
266. Li, M.; Liu, Q.; Jia, Z.; Xu, X.; Cheng, Y.; Zheng, Y.; Xi, T.; Wei, S. Graphene oxide/hydroxyapatite composite coatings fabricated by electrophoretic nanotechnology for biological applications. *Carbon* **2014**, *67*, 185-197.
267. Wang, Y.; Hu, X.; Dai, J.; Wang, J.; Tan, Y.; Yang, X.; Yang, S.; Yuan, Q.; Zhang, Y. A 3D graphene coated bioglass scaffold for bone defect therapy based on the molecular targeting approach. *J. Mater. Chem. B* **2017**, *5*, 6794-6800.
268. Basal, O.; Ozmen, O.; Deliormanlı, A. M. Bone Healing in Rat Segmental Femur Defects with Graphene-PCL-Coated Borate-Based Bioactive Glass Scaffolds. *Polymers* **2022**, *14*, 3898.

269. Lee, W. C.; Lim, C. H. Y.; Shi, H.; Tang, L. A.; Wang, Y.; Lim, C. T.; Loh, K. P. Origin of enhanced stem cell growth and differentiation on graphene and graphene oxide. *ACS Nano* **2011**, *5*, 7334-7341.
270. Nayak, T. R.; Andersen, H.; Makam, V. S.; Khaw, C.; Bae, S.; Xu, X.; Ee, P.-L. R.; Ahn, J.-H.; Hong, B. H.; Pastorin, G.; Özyilmaz, B. Graphene for controlled and accelerated osteogenic differentiation of human mesenchymal stem cells. *ACS Nano* **2011**, *5*, 4670-4678.
271. Du, Z.; Wang, C.; Zhang, R.; Wang, X.; Li, X. Applications of graphene and its derivatives in bone repair: Advantages for promoting bone formation and providing real-time detection, challenges and future prospects. *Int. J. Nanomed.* **2020**, *15*, 7523-7551.
272. Bose, S.; Tarafder, S. Calcium phosphate ceramic systems in growth factor and drug delivery for bone tissue engineering: a review. *Acta Biomater.* **2012**, *8*, 1401-1421.
273. Lee, J. H.; Shin, Y. C.; Lee, S.-M.; Jin, O. S.; Kang, S. H.; Hong, S. W.; Jeong, C.-M.; Huh, J. B.; Han, D.-W. Enhanced osteogenesis by reduced graphene oxide/hydroxyapatite nanocomposites. *Sci. Rep.* **2015**, *5*, 18833.
274. S. Medeiros, J.; Oliveira, A. M.; de Carvalho, J. O.; Ricci, R.; do C. C. Martins, M.; Rodrigues, B. V. M.; Webster, T. J.; Viana, B. C.; Vasconcellos, L. M. R.; Canevari, R. A.; Marciano, F. R.; Lobo, A. O. Nanohydroxyapatite/graphene nanoribbons nanocomposites induce in vitro osteogenesis and promote in vivo bone neof ormation. *ACS Biomater. Sci. Eng.* **2018**, *4*, 1580-1590.
275. Ghorai, S. K.; Maji, S.; Subramanian, B.; Maiti, T. K.; Chattopadhyay, S. Coining attributes of ultra-low concentration graphene oxide and spermine: An approach for high strength, anti-microbial and osteoconductive nanohybrid scaffold for bone tissue regeneration. *Carbon* **2019**, *141*, 370-389.

276. Zhao, Y.; Chen, J.; Zou, L.; Xu, G.; Geng, Y. Facile one-step bioinspired mineralization by chitosan functionalized with graphene oxide to activate bone endogenous regeneration. *J. Chem. Eng.* **2019**, *378*, 122174.
277. Vasconcellos, L. M. R.; Santana-Melo, G. F.; Silva, E.; Pereira, V. F.; Araújo, J. C. R.; Silva, A. D. R.; Furtado, A. S.; Elias, C. d. M. V.; Viana, B. C.; Marciano, F. R.; Lobo, A. O. Electrospun poly (butylene-adipate-co-terephthalate)/nano-hydroxyapatite/graphene nanoribbon scaffolds improved the in vivo osteogenesis of the neofomed bone. *J. Funct. Biomater.* **2021**, *12*, 11.
278. Peng, S.; Feng, P.; Wu, P.; Huang, W.; Yang, Y.; Guo, W.; Gao, C.; Shuai, C. Graphene oxide as an interface phase between polyetheretherketone and hydroxyapatite for tissue engineering scaffolds. *Sci. Rep.* **2017**, *7*, 46604.
279. Yu, Z.; Xiao, C.; Huang, Y.; Chen, M.; Wei, W.; Yang, X.; Zhou, H.; Bi, X.; Lu, L.; Ruan, J.; Fan, X. Enhanced bioactivity and osteoinductivity of carboxymethyl chitosan/nanohydroxyapatite/graphene oxide nanocomposites. *RSC Adv.* **2018**, *8*, 17860-17877.
280. Li, D.; Nie, W.; Chen, L.; McCoul, D.; Liu, D.; Zhang, X.; Ji, Y.; Yu, B.; He, C. Self-assembled hydroxyapatite-graphene scaffold for photothermal cancer therapy and bone regeneration. *J. Biomed. Nanotech.* **2018**, *14*, 2003-2017.
281. Ma, L.; Feng, X.; Liang, H.; Wang, K.; Song, Y.; Tan, L.; Wang, B.; Luo, R.; Liao, Z.; Li, G.; Liu, X.; Wu, S.; Yang, C. A novel photothermally controlled multifunctional scaffold for clinical treatment of osteosarcoma and tissue regeneration. *Mater. Today* **2020**, *36*, 48-62.
282. Ou, L.; Lan, Y.; Feng, Z.; Feng, L.; Yang, J.; Liu, Y.; Bian, L.; Tan, J.; Lai, R.; Guo, R. Functionalization of SF/HAP scaffold with GO-PEI-miRNA inhibitor complexes to enhance bone regeneration through activating transcription factor 4. *Theranostics* **2019**, *9*, 4525-4541.

283. Weng, W.; Li, X.; Nie, W.; Liu, H.; Liu, S.; Huang, J.; Zhou, Q.; He, J.; Su, J.; Dong, Z.; Wang, D. One-step preparation of an AgNP-nHA@ RGO three-dimensional porous scaffold and its application in infected bone defect treatment. *Int. J. Nanomed.* **2020**, *15*, 5027-5042.
284. Chopra, V.; Thomas, J.; Sharma, A.; Panwar, V.; Kaushik, S.; Sharma, S.; Porwal, K.; Kulkarni, C.; Rajput, S.; Singh, H.; Jagavelu, K.; Chattopadhyay, N.; Ghosh, D. Synthesis and evaluation of a zinc eluting rGO/hydroxyapatite nanocomposite optimized for bone augmentation. *ACS Biomater. Sci. Eng.* **2020**, *6*, 6710-6725.
285. Saidak, Z.; Marie, P. J. Strontium signaling: molecular mechanisms and therapeutic implications in osteoporosis. *Pharmacol. Ther.* **2012**, *136*, 216-226.
286. Kumar, S.; Chatterjee, K. Strontium eluting graphene hybrid nanoparticles augment osteogenesis in a 3D tissue scaffold. *Nanoscale* **2015**, *7*, 2023-2033.
287. Yang, F.; Yang, D.; Tu, J.; Zheng, Q.; Cai, L.; Wang, L. Strontium enhances osteogenic differentiation of mesenchymal stem cells and in vivo bone formation by activating Wnt/catenin signaling. *Stem Cells* **2011**, *29*, 981-991.
288. Chen, Y.; Zheng, Z.; Zhou, R.; Zhang, H.; Chen, C.; Xiong, Z.; Liu, K.; Wang, X. Developing a strontium-releasing graphene oxide-/collagen-based organic-inorganic nanobiocomposite for large bone defect regeneration via MAPK signaling pathway. *ACS Appl. Mater. Interfaces* **2019**, *11*, 15986-15997.
289. Bose, S.; Fielding, G.; Tarafder, S.; Bandyopadhyay, A. Understanding of dopant-induced osteogenesis and angiogenesis in calcium phosphate ceramics. *Trends Biotechnol.* **2013**, *31*, 594-605.

290. Zhang, W.; Chang, Q.; Xu, L.; Li, G.; Yang, G.; Ding, X.; Wang, X.; Cui, D.; Jiang, X. Graphene oxide-copper nanocomposite-coated porous CaP scaffold for vascularized bone regeneration via activation of Hif-1 α . *Adv. Healthc. Mater.* **2016**, *5*, 1299-1309.
291. Jaidev, L.; Kumar, S.; Chatterjee, K. Multi-biofunctional polymer graphene composite for bone tissue regeneration that elutes copper ions to impart angiogenic, osteogenic and bactericidal properties. *Colloids Surf. B Biointerfaces* **2017**, *159*, 293-302.
292. Arnold, A. M.; Holt, B. D.; Daneshmandi, L.; Laurencin, C. T.; Sydlik, S. A. Phosphate graphene as an intrinsically osteoinductive scaffold for stem cell-driven bone regeneration. *Proc. Natl. Acad. Sci.* **2019**, *116*, 4855-4860.
293. Santos, C.; Piedade, C.; Uggowitzer, P. J.; Montemor, M. F.; Carmezim, M. J. Parallel nano-assembling of a multifunctional GO/HapNP coating on ultrahigh-purity magnesium for biodegradable implants. *Appl. Surf. Sci.* **2015**, *345*, 387-393.
294. Feng, C.; Xue, J.; Yu, X.; Zhai, D.; Lin, R.; Zhang, M.; Xia, L.; Wang, X.; Yao, Q.; Chang, J.; Wu, C. Co-inspired hydroxyapatite-based scaffolds for vascularized bone regeneration. *Acta Biomater.* **2021**, *119*, 419-431.
295. Wu, C.; Xia, L.; Han, P.; Xu, M.; Fang, B.; Wang, J.; Chang, J.; Xiao, Y. Graphene-oxide-modified β -tricalcium phosphate bioceramics stimulate in vitro and in vivo osteogenesis. *Carbon* **2015**, *93*, 116-129.
296. Kim, J.-W.; Shin, Y. C.; Lee, J.-J.; Bae, E.-B.; Jeon, Y.-C.; Jeong, C.-M.; Yun, M.-J.; Lee, S.-H.; Han, D.-W.; Huh, J.-B. The effect of reduced graphene oxide-coated biphasic calcium phosphate bone graft material on osteogenesis. *Int. J. Mol. Sci.* **2017**, *18*, 1725.

297. Xue, J.; Feng, C.; Xia, L.; Zhai, D.; Ma, B.; Wang, X.; Fang, B.; Chang, J.; Wu, C. Assembly preparation of multilayered biomaterials with high mechanical strength and bone-forming bioactivity. *Chem. Mater.* **2018**, *30*, 4646-4657.
298. Shi, J.-J.; Ge, Y.-W.; Fan, Z.-H.; Li, Y.; Jia, W.-T.; Guo, Y.-P. Graphene oxide-modified layered double hydroxide/chitosan nacre-mimetic scaffolds treat breast cancer metastasis-induced bone defects. *Carbon* **2022**, *200*, 63-74.
299. Yang, H. M.; Jo, S.; Oh, J. H.; Choi, B.-H.; Woo, J. Y.; Han, C.-S. Strong and Tough Nacre-Inspired Graphene Oxide Composite with Hierarchically Similar Structure. *ACS Nano* **2022**, *16*, 10509-10516.
300. Chen, D.; Liu, P.; Li, M.; Zhang, C.; Gao, Y.; Guo, Y. Nacre-mimetic hydroxyapatite/chitosan/gelatin layered scaffolds modifying substance P for subchondral bone regeneration. *Carbohydr. Polym.* **2022**, *291*, 119575.
301. Zhou, C.; Liu, S.; Li, J.; Guo, K.; Yuan, Q.; Zhong, A.; Yang, J.; Wang, J.; Sun, J.; Wang, Z. Collagen functionalized with graphene oxide enhanced biomimetic mineralization and in situ bone defect repair. *ACS. Appl. Mater. Interfaces* **2018**, *10*, 44080-44091.
302. Liu, S.; Li, Z.; Wang, Q.; Han, J.; Wang, W.; Li, S.; Liu, H.; Guo, S.; Zhang, J.; Ge, K.; Zhou, G. Graphene oxide/chitosan/hydroxyapatite composite membranes enhance osteoblast adhesion and guided bone regeneration. *ACS Appl. Bio Mater.* **2021**, *4*, 8049-8059.
303. Saravanan, S.; Chawla, A.; Vairamani, M.; Sastry, T. P.; Subramanian, K. S.; Selvamurugan, N. Scaffolds containing chitosan, gelatin and graphene oxide for bone tissue regeneration *in vitro* and *in vivo*. *Int. J. Biol. Macromol.* **2017**, *104*, 1975-1985.

304. Depan, D.; Pesacreta, T. C.; Misra, R. D. K. The synergistic effect of a hybrid graphene oxide–chitosan system and biomimetic mineralization on osteoblast functions. *Biomater. Sci.* **2014**, *2*, 264-274.
305. Wang, J.; Ouyang, Z.; Ren, Z.; Li, J.; Zhang, P.; Wei, G.; Su, Z. Self-assembled peptide nanofibers on graphene oxide as a novel nanohybrid for biomimetic mineralization of hydroxyapatite. *Carbon* **2015**, *89*, 20-30.
306. Gao, L.; Ren, W.; Xu, H.; Jin, L.; Wang, Z.; Ma, T.; Ma, L.-P.; Zhang, Z.; Fu, Q.; Peng, L.-M.; Bao, X.; Cheng, H.-M. Repeated growth and bubbling transfer of graphene with millimetre-size single-crystal grains using platinum. *Nat. Comm.* **2012**, *3*, 699.
307. Tian, Z.; Huang, L.; Pei, X.; Chen, J.; Wang, T.; Yang, T.; Qin, H.; Sui, L.; Wang, J. Electrochemical synthesis of three-dimensional porous reduced graphene oxide film: preparation and in vitro osteogenic activity evaluation. *Colloids Surf. B Biointerfaces* **2017**, *155*, 150-158.
308. Liu, W.; Dong, X.; Qin, H.; Sui, L.; Wang, J. Three-dimensional porous reduced graphene oxide/hydroxyapatite membrane for guided bone regeneration. *Colloids Surf. B Biointerfaces* **2021**, *208*, 112102.
309. Sarker, B.; Hum, J.; Nazhat, S. N.; Boccaccini, A. R. Combining collagen and bioactive glasses for bone tissue engineering: a review. *Adv. Healthc. Mater.* **2015**, *4*, 176-194.
310. Kang, S.; Park, J. B.; Lee, T.-J.; Ryu, S.; Bhang, S. H.; La, W.-G.; Noh, M.-K.; Hong, B. H.; Kim, B.-S. Covalent conjugation of mechanically stiff graphene oxide flakes to three-dimensional collagen scaffolds for osteogenic differentiation of human mesenchymal stem cells. *Carbon* **2015**, *83*, 162-172.

311. Hermenean, A.; Codreanu, A.; Herman, H.; Balta, C.; Rosu, M.; Mihali, C. V.; Ivan, A.; Dinescu, S.; Ionita, M.; Costache, M. Chitosan-graphene oxide 3D scaffolds as promising tools for bone regeneration in critical-size mouse calvarial defects. *Sci. Rep.* **2017**, *7*, 16641.
312. Cheng, C.; Li, D. Solvated graphenes: an emerging class of functional soft materials. *Adv. Mater.* **2013**, *25*, 13-30.
313. Lu, J.; He, Y. S.; Cheng, C.; Wang, Y.; Qiu, L.; Li, D.; Zou, D. Self-supporting graphene hydrogel film as an experimental platform to evaluate the potential of graphene for bone regeneration. *Adv. Funct. Mater.* **2013**, *23*, 3494-3502.
314. Liu, M.; Zeng, X.; Ma, C.; Yi, H.; Ali, Z.; Mou, X.; Li, S.; Deng, Y.; He, N. Injectable hydrogels for cartilage and bone tissue engineering. *Bone Res.* **2017**, *5*, 1-20.
315. Saravanan, S.; Vimalraj, S.; Anuradha, D. Chitosan based thermoresponsive hydrogel containing graphene oxide for bone tissue repair. *Biomed. Pharmacother.* **2018**, *107*, 908-917.
316. Lin, Y.-H.; Chuang, T.-Y.; Chiang, W.-H.; Chen, I.-W. P.; Wang, K.; Shie, M.-Y.; Chen, Y.-W. The synergistic effects of graphene-contained 3D-printed calcium silicate/poly- ϵ -caprolactone scaffolds promote FGFR-induced osteogenic/angiogenic differentiation of mesenchymal stem cells. *Mater. Sci. Eng. C* **2019**, *104*, 109887.
317. Hou, Y.; Wang, W.; Bártolo, P. Novel poly (ϵ -caprolactone)/graphene scaffolds for bone cancer treatment and bone regeneration. *3D Print Addit. Manuf.* **2020**, *7*, 222-229.
318. Jakus, A. E.; Secor, E. B.; Rutz, A. L.; Jordan, S. W.; Hersam, M. C.; Shah, R. N. Three-dimensional printing of high-content graphene scaffolds for electronic and biomedical applications. *ACS Nano* **2015**, *9*, 4636-4648.

319. Duan, S.; Yang, X.; Mei, F.; Tang, Y.; Li, X.; Shi, Y.; Mao, J.; Zhang, H.; Cai, Q. Enhanced osteogenic differentiation of mesenchymal stem cells on poly (L-lactide) nanofibrous scaffolds containing carbon nanomaterials. *J. Biomed. Mater. Res. A* **2015**, *103*, 1424-1435.
320. Zhou, T.; Li, G.; Lin, S.; Tian, T.; Ma, Q.; Zhang, Q.; Shi, S.; Xue, C.; Ma, W.; Cai, X.; Lin, Y. Electrospun poly (3-hydroxybutyrate-co-4-hydroxybutyrate)/graphene oxide scaffold: enhanced properties and promoted in vivo bone repair in rats. *ACS Appl. Mater. Interfaces* **2017**, *9*, 42589-42600.
321. Zhao, C.; Zeng, Z.; Qazvini, N. T.; Yu, X.; Zhang, R.; Yan, S.; Shu, Y.; Zhu, Y.; Duan, C.; Bishop, E.; Lei, J.; Zhang, W.; Yang, C.; Wu, K.; Wu, Y.; An, L.; Huang, S.; Ji, X.; Gong, C.; Yuan, C.; Zhang, L.; Liu, W.; Huang, B.; Feng, Y.; Zhang, B.; Dai, Z.; Shen, Y.; Wang, X.; Luo, W.; Oliveria, L.; Athiviraham, A.; Lee, M. J.; Wolf, J. M.; Ameer, G. A.; Reid, R. R.; He, T.-C.; Wei, H. Thermoresponsive citrate-based graphene oxide scaffold enhances bone regeneration from BMP9-stimulated adipose-derived mesenchymal stem cells. *ACS Biomater. Sci. Eng.* **2018**, *4*, 2943-2955.
322. Kim, H. D.; Kim, J.; Koh, R. H.; Shim, J.; Lee, J.-C.; Kim, T.-I.; Hwang, N. S. Enhanced Osteogenic commitment of human Mesenchymal stem cells on polyethylene glycol-based Cryogel with Graphene oxide substrate. *ACS Biomater. Sci. Eng.* **2017**, *3*, 2470-2479.
323. Kawamoto, K.; Miyaji, H.; Nishida, E.; Miyata, S.; Kato, A.; Tateyama, A.; Furihata, T.; Shitomi, K.; Iwanaga, T.; Sugaya, T. Characterization and evaluation of graphene oxide scaffold for periodontal wound healing of class II furcation defects in dog. *Int. J. Nanomed.* **2018**, *13*, 2365-2376.

324. Gao, Z.; Qin, S.; Ménard-Moyon, C.; Bianco, A. Applications of graphene-based nanomaterials in drug design: The good, the bad and the ugly. *Expert Opin. Drug Discov.* **2023**, 1-12.
325. Liu, S.; Hu, M.; Zeng, T. H.; Wu, R.; Jiang, R.; Wei, J.; Wang, L.; Kong, J.; Chen, Y. Lateral dimension-dependent antibacterial activity of graphene oxide sheets. *Langmuir* **2012**, *28*, 12364-12372.
326. Hegab, H. M.; ElMekawy, A.; Zou, L.; Mulcahy, D.; Saint, C. P.; Ginic-Markovic, M. The controversial antibacterial activity of graphene-based materials. *Carbon* **2016**, *105*, 362-376.
327. Palmieri, V.; Lauriola, M. C.; Ciasca, G.; Conti, C.; De Spirito, M.; Papi, M. The graphene oxide contradictory effects against human pathogens. *Nanotechnology* **2017**, *28*, 152001.
328. Bussy, C.; Ali-Boucetta, H.; Kostarelos, K. Safety considerations for graphene: lessons learnt from carbon nanotubes. *Acc. Chem. Res.* **2013**, *46*, 692-701.
329. Seabra, A. B.; Paula, A. J.; de Lima, R.; Alves, O. L.; Durán, N. Nanotoxicity of graphene and graphene oxide. *Chem. Res. Toxicol.* **2014**, *27*, 159-168.
330. Yin, J.; Jacobse, P. H.; Pyle, D.; Wang, Z.; Crommie, M. F.; Dong, G. Programmable fabrication of monodisperse graphene nanoribbons via deterministic iterative synthesis. *J. Am. Chem. Soc.* **2022**, *144*, 16012-16019.
331. Yin, J.; Choi, S.; Pyle, D.; Guest, J. R.; Dong, G. Backbone Engineering of Monodisperse Conjugated Polymers via Integrated Iterative Binomial Synthesis. *J. Am. Chem. Soc.* **2023**, *145*, 19120-19128.